Transactions of the ASME

EDITORIAL STAFF
Director, Technical Publishing
JOS. SANSONE
Managing Editor,
CORNELIA MONAHAN
Production Editor, SUZANNE MAGIDA
Prod. Asst., BETH DARCHI

APPLIED MECHANICS DIVISION

Chairman, R. C. DiPRIMA
Secretary, W. G. GOTTENBERG
Technical Editor, C. S. HSU
Associate Editors, S. T. ARIARATNAM
T. BELYTSCHKO
D. B. BOGY
R. J. CLIFTON
L. B. FREUND
M. HOLT
T. R. KANE
A. S. KOBAYASHI
S. LEIBOVICH
P. A. LIBBY
U. S. LINDHOLM
L. E. MALVERN
J. J. McCOY
R. D. NORDGREN
R. T. SHIELD
C. R. STEELE
C. T. SUN
T. C. T. TING
J. S. WALKER
G. A. WEMPNER

BOARD ON COMMUNICATIONS
Chairman and Vice-President
M. J. RABINS

Members-at-Large
W. BEGELL
J. CALLAHAN
M. HELMICH
D. KOENIG
M. KUTZ
F. LANDIS
J. W. LOCKE
J. E. ORTLOFF
C. PHILLIPS
K. REID

Business Staff
345 E. 47th St.
New York, N.Y. 10017
(212)644-7789

Mng. Dir., Pub., J. J. FREY

OFFICERS OF THE ASME
President, ROBERT B. GAITHER
Executive Director and Sec'y.
BURKE E. NELSON
Treasurer, ROBERT A. BENNETT

Journal of Applied Mechanics (ISSN 0021-8936) is edited and published quarterly at the offices of The American Society of Mechanical Engineers, United Engineering Center, 345 E. 47th St., New York, N.Y. 10017. ASME-TWX No. 710-581-5267, New York. Second Class postage paid at New York, N.Y., and at additional mailing offices.

CHANGES OF ADDRESS must be received at Society headquarters seven weeks before they are to be effective. Please send old label and new address.

PRICES: *To members, $30.00, annually; to* nonmembers, $60.00. Single copies, $20.00 each. Add $5.00 for postage to countries outside the United States and Canada.

STATEMENT from By-Laws. The Society shall not be responsible for statements or opinions advanced in papers or . . . printed in its publications (B7.1, Par. 3).

COPYRIGHT © 1982 by the American Society of Mechanical Engineers. Reprints from this publication may be made on condition that full credit be given the TRANSACTIONS OF THE ASME, *JOURNAL OF APPLIED MECHANICS*, and the author, and date of publication be stated.

INDEXED by the Engineering Index, Inc.

Journal of Applied Mechanics

Published Quarterly by The American Society of Mechanical Engineers

VOLUME 49 • NUMBER 1 • MARCH 1982

TECHNICAL PAPERS

1 Incompressible Flow Between Finite Disks
M. L. Adams and A. Z. Szeri

10 Nonlinear Breaking of Wave Fronts in a Vibrationally Relaxing Gas
R. Shyam, V. D. Sharma, and V. V. Menon

13 Rotating Flow Over a Disk Sector
M. Toren, A. Solan, and M. Ungarish

19 Simultaneous Stress Relaxation in Tension and Creep in Torsion of 2618 Aluminum at Elevated Temperature
J. S. Lai and W. N. Findley

26 A Nonlinear Model for the Dynamics of Penetration into Geological Targets
F. R. Norwood and M. P. Sears

31 Inertia Effects on the Ductile Failure of Thin Rings
A. M. Rajendran and I. M. Fyfe

37 On Nonstationary Cumulative Damage Models
J. L. Bogdanoff and F. Kozin

43 Asymmetric Contact Problem Including Wear for Nonhomogeneous Half Space
T. S. Sankar and V. Fabrikant

47 An Educational Elasticity Problem With Friction Part 2: Unloading for Strong Friction and *Reloading*
M. Comninou and J. Dundurs

52 Antiplane Eigenstrain Problem of an Elliptic Inclusion in an Anisotropic Half Space
R. A. Masumura and Y. T. Chou

55 Line Force in a Two-Phase Orthotropic Medium
R. S. Wu and Y. T. Chou

62 Unconventional Internal Cracks Part 1: Symmetric Variations of a Straight Crack
C. H. Wu

69 The Linear Magnetoelastic Problem of Two Coplanar Griffith Cracks in a Soft Ferromagnetic Elastic Strip
Y. Shindo

75 Use of $\hat{J}$-Integral in Dynamic Analysis of Cracked Linear Viscoelastic Solids by Finite-Element Method
K. Kishimoto, S. Aoki, and M. Sakata

81 A Modified Strain-Energy Density Criterion Applied to Crack Propagation
P. S. Theocaris and N. P. Andrianopoulos

87 Complex Stress Intensity Factors in Bent Plates With Cracks
P. S. Theocaris

97 Application of the Line-Spring Model to a Cylindrical Shell Containing a Circumferential or Axial Part-Through Crack
F. Delale and F. Erdogan

103 Circumferential Through-Cracks in Cylindrical Shells Under Tension
J. L. Sanders, Jr.

108 Elasticity Solution for a Multilayered Transversely Isotropic Circular Cylindrical Shell
K. Chandrashekhara and P. Gopalakrishnan

115 A Simple and Efficient Approximation of Shells via Finite Quadrilateral Elements
G. Wempner, D. Talaslidis, and C.-M. Hwang

121 Large Deflection of a Fluid-Filled Spherical Shell Under a Point Load
L. A. Taber

129 Edge Effects in Laminated Composite Plates
S. B. Dong and D. B. Goetschel

136 A Finite Element Formulation for Unbounded Homogeneous Continua
G. Dasgupta

141 Dynamic Behavior of a Buried Pipe in a Seismic Environment
S. K. Datta, A. H. Shah, and N. El-Akily

149 Transverse Impact on Fluid-Filled Cylindrical Tubes
F. Katsamanis and W. Goldsmith

(Contents continued on Page 262)

Downloaded 04 May 2010 to 128.59.114.15. Redistribution subject to ASME license or copyright; see http://www.asme.org/terms/Terms_Use.cfm

157 *Stress Wave Propagation in a Bar of Arbitrary Cross Section*
K. Nagaya

165 *A Simple and Effective Pipe Elbow Element – Interaction Effects*
K. J. Bathe and C. A. Almeida

172 *Membrane Locking and Reduced Integration for Curved Elements*
H. Stolarski and T. Belytschko

177 *Elastic Stability of Simply Supported Rectangular Plates Under Locally Distributed Edge Forces*
G. Baker and M. N. Pavlović

180 **Finite Element Analysis of Magnetoelastic Buckling of Eight-Coil Superconducting Full Torus**
K. Miya, T. Takagi, M. Uesaka, and K. Someya

187 **Dynamic Instability in Ice-Lifting From a Flat Road Surface Through Penetration With a Sharp Blade**
N. C. Huang

191 **Some Principles of Elastic Shaft Stability Including Variational Principles**
R. C. Shieh

197 **Vibration Modes of Centrifugally Stiffened Beams**
A. D. Wright, C. E. Smith, R. W. Thresher, and J. L. C. Wang

203 **Stability Analysis of an Extrapolated Force Correction Method for Nonlinear Structural Dynamics**
D. M. Trujillo

206 **Free Vibration Analysis of Stiffened Plates by Including the Effect of Inplane Inertia**
G. Aksu

213 **A Linear Algebra Approach to the Analysis of Rigid Body Displacement From Initial and Final Position Data**
A. J. Laub and G. R. Shiflett

217 **A Generalized Hill's Method for the Stability Analysis of Parametrically Excited Dynamic Systems**
S. T. Noah and G. R. Hopkins

BRIEF NOTES

Stress Singularities at the Edge of a Cylindrical Slider 224
R. Solecki and R. J. Conant

Rotation of a Free Elastic Rod 225
C.-Y. Wang

Vibration of Simply Supported Shallow Shells on Elliptical Bases 227
J. R. Coleby and J. Mazumdar

The Local Stress State at a Sharp Corner of an Expanding Inclusion 229
C. Gomez and J. Dundurs

Stick/Slip Conditions for a Thin, Incomplete, Elastic Ring Impinging on a Friction Barrier 231
R. C. Benson

On the Derivation of Two-Dimensional Strain Displacement Relations for Small Finite Deformations of Shear-Deformable Plates 232
E. Reissner

Unsteady Incompressible Boundary-Layer Flow Over a Rotating Sphere 234
M. Kumari and G. Nath

Photoelastic Analysis of the Stress Field Around Cuspidal Points of Rigid Inclusion 236
E. E. Gdoutos

Boundary Condition Effect on Forced Torsional Vibrations of a Cylindrical Rod Connected to an Elastic Half Space 238
H. Wada

240 Dynamic Response of Rigid-Plastic Circular Plates in a Damping Medium
A. Kumar and M. Hedge

241 Index Evaluation for Nonlinear Systems of Order Higher Than Two
R. S. Guttalu and C. S. Hsu

243 Large Deflections of Circular Plates of Variable Thickness
B. Banerjee

245 On Nontrivial Solutions for a Compressed Linear Viscoelastic Rod
M. E. Gurtin, V. J. Mizel, and D. W. Reynolds

247 On the Stability of Linear Systems: A Turbulent Flow Classification Scheme for Dilute Polymer Solutions
N. Phan-Thien and J. D. Atkinson

248 Numerical Generation of Curvilinear Coordinate Systems
B. S. Berger and D. M. Curtis

250 Laminar Flow Along a Porous Vertical Wall
P. D. Verma, K. C. Sarangi, and P. D. Ariel

253 Plastic Wave Propagation in a Circular Cylindrical Rod
J. W. Swegle and T. C. T. Ting

(Contents continued on Inside Back Cover)

Downloaded 04 May 2010 to 171.66.16.34. Redistribution subject to ASME license or copyright; see http://www.asme.org/terms/Terms_Use.cfm

CONTENTS (CONTINUED)

DISCUSSIONS

257-258 Discussions on previously published papers by **S. Krenk, A. Maewal, Y. Takeuti** and **T. Furukawa, N. J. Hoff**

BOOK REVIEWS

259 ***Limit Analysis of Structures at Thermal Cycling*** by **D. A. Gokhfeld** and **O. F. Cherniavsky** . . . Reviewed by **P. G. Hodge, Jr.**

Fracture and Fatigue edited by **J. C. Radon** . . . Reviewed by **J. W. Hutchinson**

Computation Methods in Structural Dynamics by **L. Meirovitch** . . . Reviewed by **P. P. Friedmann**

260 ***Topics in Finite Elasticity*** by **M. E. Gurtin** . . . Reviewed by **J. K. Knowles**

261 ***The Dynamics of Arches*** by **Josef Henrych** . . . Reviewed by **G. J. Simitses**

9, 25, 68	Worldwide Mechanics Meeting List
51, 80, 96, 107, 128	Applied Mechanics Symposium Proceedings
140, 148, 156, 186, 212	Applied Mechanics Symposium Proceedings
120	Announcement – Standard International Units
196	Special Notice – Mandatory Excess Page Charge for Transactions
223	Change of Address Form

Downloaded 04 May 2010 to 171.66.16.34. Redistribution subject to ASME license or copyright; see http://www.asme.org/terms/Terms_Use.cfm

M. L. Adams
Associate Professor,
Department of Mechanical Engineering,
University of Akron,
Akron, Ohio 44325
Mem. ASME

A. Z. Szeri
Professor,
Departments of Mechanical Engineering
and Mathematics,
University of Pittsburgh,
Pittsburgh, Pa. 15261
Mem. ASME

Incompressible Flow Between Finite Disks

Solutions were developed and are shown here for the primary laminar steady flow field that occurs in an incompressible, isoviscous, Newtonian fluid which is contained between two finite parallel disks. One of the disks is made to rotate at constant velocity and the other is held stationary, and either a source or a sink is located concentric to the axis of rotation. The analysis is general, containing all terms of the Navier-Stokes equations for rotationally symmetric flows, and produces a four-parameter family of solutions. The high Reynolds number flow contains multiple cells, arranged along the radius, and the flow appears to be uniquely defined by the boundary condition and the Reynolds number.

Introduction

This work describes an analytical study of the laminar incompressible steady flow field between two finite parallel disks, one stationary and the other rotating at constant speed, with net radial throughflow originating either at the inner radius or at the outer radius of the disks. Solutions of such flows have immediate engineering applications, as in the design of viscosity pumps, face seals, thrust bearings, and rotating heat exchangers. These flows are also of fundamental interest in fluid mechanics, because they are Reynolds number dependent and because they are dependent on more than one spatial coordinate.

A flow that is considerably more amenable to theoretical treatment then the flow under consideration is that due to rotation of a single infinite disk. Karman [1] postulated in that case that the axial velocity is independent of the radial coordinate. This led to a similarity transformation which was later shown by Batchelor [2] to be applicable even when the fluid at infinity has a constant angular velocity about the axis of the disk, or when the fluid is enclosed between two rotating infinite disks. Batchelor suggested that as the Reynolds number increased, the steady flow would develop thin boundary layers on each disk and the main body of fluid would rotate with constant angular velocity. This view was later challenged by Stewartson [3] who reasoned that for large Reynolds numbers the flow outside the boundary layers would be purely axial. However, Lance and Rogers [4] supported Batchelor's hypothesis, using numerical methods to solve the two point boundary-value problem that resulted from the Karman similarity transformation. More recently, Nguyen, Ribault, and Florent [5] found both Batchelor-type and Stewartson-type solutions numerically, with the character of the flow depending on what starting values were assumed for the marching integration. Holodniok, et al. [10], identify as many as five solutions to the governing differential equations at a given (high) Reynolds number, two of which are of boundary-layer type. The low Reynolds number solution is unique and the flow is of Batchelor type, with a substantial portion of the fluid rotating as a rigid body. Additional solutions make their appearance as the Reynolds number is increased. Two of these solutions are of two-cell type, and there is a Stewartson-type solution exhibiting boundary layers on both disks. Wilson and Schryer [11] apply uniform suction to the rotating disk in their numerical treatment of disk flows. They find the equilibrium flow approaching the Batchelor-type flow at large Reynolds numbers, but at the same time, they raise the question as to whether other solutions to the time-dependent equations with zero initial conditions are possible. Wilson, et al., exhibit a rotational startup scheme, which leads to an equilibrium solution in which the interior of the fluid rotates in the direction opposing disk rotation.

The question that suggests itself is whether, and if so under what conditions, will infinite disk flows approximate to laboratory flows between finite disks. The similarity solutions that have been demonstrated by various investigators, e.g., the counter-rotating flow of Wilson and Schryer [11] may be correct analytically, but are they physically acceptable? And again, should multiple solutions be accepted as truly such, for although they are shown to exist under ostensibly identical conditions, i.e., at the same Reynolds number, they lead to distinct flow behavior (boundary condition?) at infinity. Perhaps all that has been demonstrated thus far is that the flow, at a given Reynolds number, is completely determined by the behavior of the fluid at infinity, i.e., the boundary conditions there. Holodniok's results would suggest that there is one, and only one, set of boundary conditions at small R_s which yields an axial velocity component that is independent of radial position, whereas at large values of R_s five such sets are possible.

The foregoing viewpoint is not contradicted by the present numerical experiments on the steady-state problem. The flow seems to be well defined by the boundary conditions, the Reynolds number effect mainifesting itself only in the number of cells that appear. But again the relationship between the Reynolds number and the number of cells is seemingly

Contributed by the Applied Mechanics Division for publication in the JOURNAL OF APPLIED MECHANICS.
Discussion on this paper should be addressed to the Editorial Department, ASME, United Engineering Center, 345 East 47th Street, New York, N. Y. 10017, and will be accepted until two months after final publication of the paper itself in the JOURNAL OF APPLIED MECHANICS. Manuscript received by ASME Applied Mechanics Division, February, 1980; final revision, July, 1981.

Copyright © 1982 by ASME
Downloaded 01 May 2010 to 171.66.16.249. Redistribution subject to ASME license or copyright; see http://www.asme.org/terms/Terms_Use.cfm

unique, although no definite conclusion can be drawn at this time. The highest Reynolds number reached in this study is 14,000. Holodniok, et al. [10], first encountered multiple solutions at $R_E = 20{,}500$ (our notation). We have been unable to reach this limit due to convergence problems encountered in the computation, thus the present work is unable to discuss the problem within the Reynolds number range when infinite-disk research predicts multiplicity of solutions.

Governing Equations

Two parallel disks of outer radius r_2, one stationary and the other rotating at the constant rate ω, are located at $z = 0$ and $z = s$, respectively, of the cylindrical coordinate system (r, θ, z), Fig. 1. Relative to this coordinate system, when assuming rotational symmetry, the equations of motion and continuity are as follows:

$$u\frac{\partial u}{\partial r} - \frac{v^2}{r} + w\frac{\partial u}{\partial z} = \nu\left(\nabla^2 u - \frac{u}{r^2}\right) - \frac{1}{\rho}\frac{\partial p}{\partial r}$$

$$\frac{u}{r}\frac{\partial}{\partial r}(rv) + w\frac{\partial v}{\partial z} = \nu\left(\nabla^2 v - \frac{v}{r^2}\right); \quad 0<r_1<r_2; \quad 0<z<s$$

$$u\frac{\partial w}{\partial r} + w\frac{\partial w}{\partial z} = \nu\nabla^2 w - \frac{1}{\rho}\frac{\partial p}{\partial z}$$

$$\frac{\partial}{\partial r}(ru) + \frac{\partial}{\partial z}(rw) = 0 \tag{1}$$

The equation of continuity is identically satisfied by expressing the radial and axial velocities in terms of the stream function Ψ.

$$u = \frac{1}{r}\frac{\partial \Psi}{\partial z}; \qquad w = -\frac{1}{r}\frac{\partial \Psi}{\partial r} \tag{2}$$

Cross-differentiation eliminates the pressure, so that the system of equations (1) can be replaced by the following two equations:

$$\frac{\partial \Psi}{\partial z}\frac{\partial (D^2\Psi)}{\partial r} - \frac{\partial \Psi}{\partial r}\frac{\partial (D^2\Psi)}{\partial z} - \frac{2v}{r}\frac{\partial v}{\partial r} = \nu\left(r^3 D^2 + 4\frac{\partial}{\partial r}\right)D^2\Psi \tag{3}$$

$$\frac{\partial \Psi}{\partial z}\frac{\partial (rv)}{\partial r} - \frac{\partial \Psi}{\partial r}\frac{\partial (rv)}{\partial z} = \nu r^3 D^2(rv) \tag{4}$$

The operator in (3) and (4) is defined by

$$D^2 = \frac{1}{r^2}\left(\nabla^2 - \frac{2}{r}\frac{\partial}{\partial r}\right).$$

The boundary conditions on Ψ and v at the disks are dictated by no slip and by mass conservation.

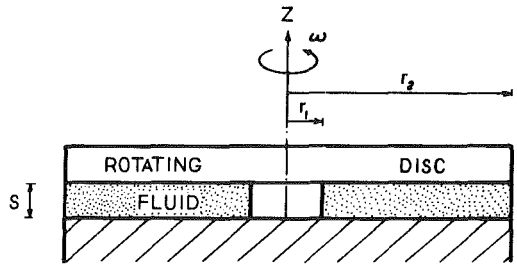


Fig. 1 Configuration of flow domain

$$\frac{\partial \Psi}{\partial r} = \frac{\partial \Psi}{\partial z} = v = 0 \qquad \text{at } z = 0$$

$$\frac{\partial \Psi}{\partial r} = \frac{\partial \Psi}{\partial z} = 0; \quad v = r\omega \quad \text{at } z = s \tag{5}$$

$$\Psi(r,s) - \Psi(r,0) = Q/2\pi$$

The quantity $Q = 2\pi r \int_0^s u(r,z)\,dz$ is the net rate of flow across the arbitrary cylinder r = constant. In addition to (5), boundary conditions must also be specified at some $r = r_1 > 0$ and at $r = r_2 > r_1$.

$$\Psi = \phi(z); \quad v = v_1(z) \qquad \text{at } r = r_1 > 0$$

$$\Psi = \phi(z); \quad v = v_2(z) \qquad \text{at } r = r_2 > r_1 \tag{6}$$

The equations and the boundary conditions are made dimensionless through the following substitutions:

$$z = s\zeta; \qquad r = r_2\rho$$

$$\Psi = s\omega r_2^2\bar{\Psi}; \quad v = r_2\omega\rho\bar{\Omega} \tag{7}$$

The dimensionless form of equations (3) and (4) is

$$\frac{\partial \bar{\Psi}}{\partial \zeta}\frac{\partial (\bar{D}^2\bar{\Psi})}{\partial \rho} - \frac{\partial \bar{\Psi}}{\partial \rho}\frac{\partial (\bar{D}^2\bar{\Psi})}{\partial \zeta} - \sigma^2\frac{\partial (\rho\bar{\Omega}^2)}{\partial \zeta} = \frac{1}{R_E}\left(\rho^3\bar{D}^2 + 4\frac{\partial}{\partial \rho}\right)(\bar{D}^2\bar{\Psi}) \tag{8}$$

and

$$\frac{\partial \bar{\Psi}}{\partial \zeta}\frac{\partial (\rho^2\bar{\Omega})}{\partial \rho} - \frac{\partial \bar{\Psi}}{\partial \rho}\frac{\partial (\rho^2\bar{\Omega})}{\partial \zeta} = \frac{1}{R_E}\rho^3 D^2(\rho^2\bar{\Omega}) \tag{9}$$

where

$$\bar{D}^2 = \frac{1}{\rho^2}\left(\frac{\partial^2}{\partial \rho^2} - \frac{1}{\rho}\frac{\partial}{\partial \rho} + \sigma^2\frac{\partial^2}{\partial \zeta^2}\right)$$

$$\sigma = r_2/s; \quad R_E = \frac{r_2^2\omega}{\nu} \tag{10}$$

Nomenclature

p = pressure
Q = throughflow
R_E = $r_2^2\omega/\nu$, rotational Reynolds number
R_Q = $Q/2\pi s\nu$, throughflow Reynolds number
R_s = gap Reynolds number ($= R_E/\sigma^2$)
$\bar{R}$ = R_Q/R_E
r = radial coordinate
r_1 = inner radial boundary
r_2 = outer radial boundary
s = gap between disks
u = radial velocity
v = circumferential velocity
w = axial velocity
ρ = dimensionless radial coordinate
σ = r_2/s, radius-to-gap ratio
ν = kinematic viscosity
Ψ = stream function
Ω = v/r, angular velocity function
ζ = dimensionless axial coordinate
D^2 = $\frac{1}{r^2}\left(\frac{\partial^2}{\partial r^2} - \frac{1}{r}\frac{\partial}{\partial r} + \frac{\partial^2}{\partial z^2}\right)$

Downloaded 01 May 2010 to 171.66.16.249. Redistribution subject to ASME license or copyright; see http://www.asme.org/terms/Terms_Use.cfm

The dimensionless form of the boundary conditions (5) and (6) is

$$\frac{\partial\bar{\Psi}}{\partial\rho} = \frac{\partial\bar{\Psi}}{\partial\zeta} = \bar{\Omega} = 0 \qquad \text{at } \zeta = 0$$

$$\frac{\partial\bar{\Psi}}{\partial\rho} = \frac{\partial\bar{\Psi}}{\partial\zeta} = 0; \quad \bar{\Omega} = 1 \qquad \text{at } \zeta = 1$$

$$\bar{\Psi} = \bar{\phi}(\zeta); \quad \bar{\Omega} = \bar{\omega}(\zeta) \qquad \text{at } \rho = \rho_1, 1$$

$$\bar{\Psi}(\rho, 1) - \bar{\Psi}(\rho, 0) = \mathrm{R}_Q/\mathrm{R}_E \tag{11}$$

where

$$\mathrm{R}_Q = \frac{Q}{2\pi\nu s} \tag{12}$$

Considerable simplification is achieved in the limit as $\mathrm{R}_Q \to \infty$, termed "thin film" model in [7]. Employing $\hat{r} = r/s\mathrm{R}_Q^{1/2}$ as the dimensionless radial coordinate in this case, the operator D^2 takes the form

$$\hat{D}^2 = \frac{1}{\hat{r}^2}\left[\frac{\partial^2}{\partial\zeta^2} + \frac{1}{\mathrm{R}_Q}\left(\frac{\partial^2}{\partial\hat{r}^2} - \frac{1}{\hat{r}}\frac{\partial}{\partial\hat{r}}\right)\right]$$

and upon passing to the limit

$$\hat{D}^2 = \frac{1}{\hat{r}^2}\frac{\partial^2}{\partial\zeta^2} \tag{13}$$

If in addition we put

$$\Psi = \nu s\mathrm{R}_Q\hat{\Psi}; \quad \Omega = s\omega\mathrm{R}_Q^{1/2}\hat{\Omega}$$

equations (8) and (9) simplify to

$$\frac{\partial\hat{\Psi}}{\partial\zeta}\frac{\partial}{\partial\hat{r}}\left(\frac{1}{\hat{r}^2}\frac{\partial^2\hat{\Psi}}{\partial\zeta^2}\right) - \frac{\partial\hat{\Psi}}{\partial\hat{r}}\frac{\partial}{\partial\zeta}\left(\frac{1}{\hat{r}^2}\frac{\partial^2\hat{\Psi}}{\partial\zeta^2}\right) - \mathrm{R}_s\frac{\partial(\hat{r}\hat{\Omega}^2)}{\partial\zeta} = \frac{1}{\hat{r}}\frac{\partial^4\hat{\Psi}}{\partial\zeta^4}$$

$$\frac{\partial\hat{\Psi}}{\partial\zeta}\frac{\partial(\hat{r}^2\hat{\Omega})}{\partial\hat{r}} - \frac{\partial\hat{\Psi}}{\partial\hat{r}}\frac{\partial(\hat{r}^2\hat{\Omega})}{\partial\zeta} = \hat{r}\frac{\partial^2(\hat{r}^2\hat{\Omega})}{\partial\zeta^2} \tag{14}$$

Implicit in (13) is the assumption of negligible radial variation of shear stress, and is valid when $\mathrm{R}_Q >> 1$.

The resulting thin film equations (14) are of lower order than their thick film counterpart, and the simplified problem is governed by a single parameter, the gap Reynolds number, $s^2\omega/\nu$. The approximation (13) restricts solutions to cases with no reverse radial flow. Nevertheless, present solutions can be compared with the thin film model, when in the appropriate domain of parameter space.

Reduction to Ordinary Differential Equations

The basic flow is shown to be governed by two coupled nonlinear partial differential equations, (8) and (9), of fourth order in each spatial coordinate. Furthermore, the flow requires four dimensionless parameters to characterize it, viz; a rotational Reynolds number R_E, a throughflow Reynolds number R_Q, a radius-to-gap ratio σ, and an inner-radius-to-outer-radius ratio ρ_1.

The partial differential equations (8) and (9) are first reduced to two systems of ordinary differential equations. To this end, two complete sets of functions are considered, $F_n(\zeta)$ and $G_n(\zeta)$, whose elements have continuous derivatives to the required order in $0 < \zeta < 1$ and vanish at both $\zeta = 0$ and at $\zeta = 1$. It is assumed that the Nth approximations $\bar{\Psi}_N$ and $\bar{\Omega}_N$ to $\bar{\Psi}$ and $\bar{\Omega}$, respectively, can be expanded in the series

$$\bar{\Psi}_N = \frac{\mathrm{R}_Q}{\mathrm{R}_E}\bar{\phi}(\zeta) + \sum_{n=1}^{N} F_n(\zeta) f_n(\rho)$$

$$\bar{\Omega}_N = \bar{\omega}(\zeta) + \sum_{n=1}^{N} G_n(\zeta) g_n(\rho) \tag{15}$$

with suitable conditions on $\bar{\phi}(\zeta)$ and $\bar{\omega}(\zeta)$ at $\zeta = 0, 1$ and on $f_n(\rho), f_n'(\rho)$, and $g_n(\rho)$ at $\rho = \rho_1, 1$.

Selecting

$$\bar{\phi}(\zeta) = (1 - \cos(\pi\zeta))/2$$

$$\bar{\omega}(\zeta) = \sin(\pi\zeta/2)$$

$$F_n(\zeta) = \cos((n-1)\pi\zeta) - \cos((n+1)\pi\zeta)$$

$$G_n(\zeta) = \sin(n\pi\zeta) \tag{16}$$

the usual arguments of the Galerkin-Kantorovich method are applied. The approach is similar to that used by Munson and Joseph [9] to solve the somewhat more tractable problem of viscous flow between concentric rotating spheres. Equations (8) and (9) are thus replaced by the following two sets of nonlinear ordinary differential equations.

$$\frac{\pi}{\rho^2}\left(\frac{-2(\bar{\mathrm{R}}\sigma\pi)^2}{\rho}A_k^{(1)} + \bar{\mathrm{R}}\sum_{n=1}^{N}\left(C_{kn}^{(1)}\left(f_n''' - \frac{3}{\rho}f_n'' + \frac{3}{\rho^2}f_n'\right) - \sigma^2\pi^2\left(\frac{2}{\rho}A_{kn}^{(2)}f_n - A_{kn}^{(4)}f_n'\right)\right)\right.$$

$$+ \sum_{n,j=1}^{N} f_n\left(C_{knj}^{(2)}\left(f_j''' - \frac{3}{\rho}f_j'' + \frac{3}{\rho^2}f_j'\right) + \sigma^2\pi^2 A_{knj}^{(3)}\left(f_j' - \frac{2}{\rho}f_j\right)\right)$$

$$\left. - \bar{\mathrm{R}}(\pi\sigma)^2\sum_{n=1}^{N}A_{kn}^{(5)}f_n' - \sum_{n,j=1}^{N}f_j' \times\left(C_{knj}^{(2)}\left(f_n'' - \frac{1}{\rho}f_n'\right) + (\pi\sigma)^2 A_{kjn}^{(6)}f_n\right)\right)$$

$$- 2\pi\sigma^2\rho\left(A_k^{(11)} + \sum_{n=1}^{N}A_{kn}^{(7)}g_n + \sum_{n,j=1}^{N}A_{knj}^{(8)}g_n g_j\right)$$

$$- \frac{1}{\mathrm{R}_E}\sum_{n=1}^{N}\left(\frac{1}{\rho}C_{kn}^{(3)}\left(f_n'''' - \frac{2}{\rho}f_n''' + \frac{3}{\rho^2}f_n'' - \frac{3}{\rho^3}f_n'\right) + \frac{2(\sigma\pi)^2}{\rho}C_{kn}^{(4)}\left(f_n'' - \frac{1}{\rho}f_n'\right) + \frac{(\sigma\pi)^4}{\rho}A_{kn}^{(10)}f_n\right) - \frac{(\pi\sigma)^4\bar{\mathrm{R}}}{\rho\mathrm{R}_E}A_k^{(9)} = 0 \tag{17}$$

$$\mathrm{R}B_k^{(1)} - \frac{\pi\sigma^2}{2\mathrm{R}_E}\rho^2 B_k^{(7)} + \sum_{n=1}^{N}\left(B_{kn}^2 f_n - \frac{1}{2}B_{kn}^{(5)}\rho f_n' + \left(\bar{\mathrm{R}}B_{kn}^{(3)} - \frac{\pi(\sigma\rho)^2}{2\mathrm{R}_E}B_{kn}^{(8)}\right)g_n + \frac{1}{2}\left(\bar{\mathrm{R}}\rho B_{kn}^{(3)} - \frac{3\rho}{\pi\mathrm{R}_E}B_{kn}^{(9)}\right)g_n' - \frac{\rho^2}{2\pi\mathrm{R}_E}B_{kn}^{(9)}g_n''\right)$$

$$+ \sum_{n,j=1}^{N}\left(\frac{1}{2}B_{knj}^{(4)}f_j(2g_n + \rho g_n') - \frac{\rho}{2}B_{knj}^{(6)}g_n f_j'\right) = 0 \tag{18}$$

where $\bar{\mathrm{R}} = \mathrm{R}_Q/\mathrm{R}_E$ and $k = 1, 2, 3, \ldots, N$.

Downloaded 01 May 2010 to 171.66.16.249. Redistribution subject to ASME license or copyright; see http://www.asme.org/terms/Terms_Use.cfm

The coefficients $A_n^{(1)}, \ldots, C_{kn}^{(4)}$ are defined in reference [6].

Approximations $\bar{\Psi}_N$ and $\bar{\Omega}_N$ (15), satisfy all the boundary conditions (11) provided the following conditions are imposed:

$$\begin{aligned} f_n(\rho_1) &= f_n(1) = 0 \\ f_n'(\rho_1) &= f_n'(1) = 0 \\ g_n(\rho_1) &= g_n(1) = 0 \end{aligned} \tag{19}$$

The boundary conditions (19) together with $\bar{\phi}$ and $\bar{\omega}$ (16) specify the velocity components at the inner and outer radii, respectively, as follows:

$$\begin{aligned} \bar{u}_{1,2} &= \left(\frac{1}{\rho}\frac{\partial\bar{\Psi}}{\partial\zeta}\right)_{\rho_1,\rho_2} = \frac{R_Q}{R_E}\frac{\pi}{2\rho_{1,2}}\sin(\pi\zeta) \\ \bar{v}_{1,2} &= (\rho\bar{\Omega})_{\rho_1,\rho_2} = \rho_{1,2}\sin(\pi\zeta/2) \\ \bar{w}_{1,2} &= \left(-\frac{1}{\rho}\frac{\partial\bar{\Psi}}{\partial\rho}\right)_{\rho_1,\rho_2} = 0 \end{aligned} \tag{20}$$

Reduction to Algebraic Equations

Equations (17) - (19) define a two point boundary-value problem for the two sets of functions $[f_n(\rho)]$ and $[g_n(\rho)]$. For the purpose of finding solutions to this boundary-value problem, equations (17) - (19) are replaced by a system of simultaneous algebraic equations via the method of orthononal collocation [8]. To this end we define the transformation,

$$\chi = \frac{\rho - \rho_1}{1 - \rho_1}; \qquad 0 \le \chi \le 1 \tag{21}$$

and assume that $f_n(\chi)$ and $g_n(\chi)$ have the following orthogonal polynomial expansions:

$$f_n(\chi) = \left(\chi(1-\chi)\right)^2 \sum_{m=1}^{M} F_{nm} Q_{m-1}(\chi) \tag{22}$$

$$g_n(\chi) = \chi(1-\chi) \sum_{m=1}^{M} G_{nm} P_{m-1}(\chi) \tag{23}$$

where M is the number of interior collocation points.

Applying the method of orthogonal collocation leads to the following two sets of nonlinear algebraic equations which approximate equations (17) and (18), respectively.

$$\begin{aligned} E_{ik}^{(1)} = D_{ik}^{(1)} &+ \sum_{n=1}^{N}\sum_{t=1}^{M+2} D_{iknt}^{(2)}\alpha_{nt} + \sum_{n=1}^{N}\sum_{t=1}^{M+1} D_{iknt}^{(3)}\beta_{nt} \\ &+ \sum_{n=1}^{N}\sum_{j=1}^{N}\sum_{t=1}^{M+2}\sum_{p=1}^{M+2} D_{iknjtp}^{(4)}\alpha_{nt}\alpha_{jp} \\ &+ \sum_{n=1}^{N}\sum_{j=1}^{N}\sum_{t=1}^{M+1}\sum_{p=1}^{M+1} D_{iknjtp}^{(5)}\beta_{nt}\beta_{jp} + D_{ik}^{(6)} = 0 \end{aligned} \tag{24}$$

and

$$\begin{aligned} E_{ik}^{(2)} = D_{ik}^{(7)} &+ \sum_{n=1}^{N}\sum_{s=1}^{M+2} D_{ikns}^{(8)}\alpha_{ns} + \sum_{n=1}^{N}\sum_{s=1}^{M+1} D_{ikns}^{(9)}\beta_{ns} \\ &+ \sum_{n=1}^{N}\sum_{m=1}^{N}\sum_{s=1}^{M+2}\sum_{r=1}^{M+1} D_{iknmsr}^{(10)}\alpha_{ns}\beta_{mr} = 0 \end{aligned} \tag{25}$$

where

$$i = 1,2,\ldots,M; \quad k = 1,2,\ldots,N.$$

The coefficients $D_{ik}^{(1)}, \ldots, D_{iknmsr}^{(10)}$ are defined in reference [6].

The weighting functions $(\chi(1-\chi))^2$ and $(1-\chi)$ were chosen to satisfy the inner radial boundary conditions (19) at $\rho = \rho_1$. In order to satisfy the outer radial boundary conditions, three additional sets of algebraic equations must be specified.

$$E_k^{(3)} = \sum_{m=1}^{M+2} \alpha_{km} = 0 \tag{26}$$

$$E_k^{(4)} = \sum_{m=1}^{M+2} (m+1)\alpha_{km} = 0 \tag{27}$$

$$E_k^{(5)} = \sum_{m=1}^{M+1} \beta_{km} = 0 \tag{28}$$

The system of equations (24) - (28) constitutes a set of $N(2M+3)$ nonlinear simultaneous algebraic equations which define the $N(M+2)$ elements of $[\alpha_{nm}]$ and the $N(M+1)$ elements of $[\beta_{nm}]$. The unknown functions of f_n and g_n are supplied by the following expressions:

$$f_n(\chi) = \sum_{m=1}^{M+2} \alpha_{nm}\chi^{m+1} \tag{29}$$

$$g_n(\chi) = \sum_{m=1}^{M+1} \beta_{nm}\chi^{m} \tag{30}$$

Solution of the system of equations (24) - (28) were obtained using the Newton-Raphson method.

Having found approximations to the true solutions $\bar{\Psi}$ and $\bar{\Omega}$, we are in the position to calculate the radial variation of the axially averaged dimensionless pressure

$$\bar{P}(\rho) = \frac{P}{\mu\omega R_E} = \int_0^1 \bar{p}(\rho,\zeta)\,d\zeta \tag{31}$$

by integrating the first of the momentum equations (1).

Convergence, Uniqueness, and Verification of Solutions

Test cases were run to investigate the number of terms in the approximating equations (i.e., the values for M and N) required to obtain convergent solutions to flow velocity distributions. The results suggest that for the range of flow parameters under study, $N = 5$ and $M = 6$ is adequate. The corresponding number of nonlinear simultaneous algebraic equations $N(2M+3)$, is 75.

There were no multiple solutions found for the range of flow parameters studied, regardless of the initial conditions used in the Newton-Raphson iteration scheme. This is consistent with the results of Nguyen, et al. [5], who show that for the infinite disk problem only one solution exists below a gap Reynolds number $(s^2\omega/\nu)$ of 300. Though Holodniok, et al. [10], refined this upper limit to 205, this value is still considerably higher than 140, the maximum value of gap Reynolds number used in this study.

The pressure calculated from the thin-film approximation correlates well with measurements by several investigators [7]. In consequence the first verification test choosen for the general analysis was a comparison of present velocity and pressure solutions with thin-film results. In the flow parameter ranges where the thin-film approximation is supported by experimental results, close agreement was exhibited between the two solutions as shown on Table 1 and in Fig. 7.

At another extreme of flow parameter range, comparison

Downloaded 01 May 2010 to 171.66.16.249. Redistribution subject to ASME license or copyright; see http://www.asme.org/terms/Terms_Use.cfm

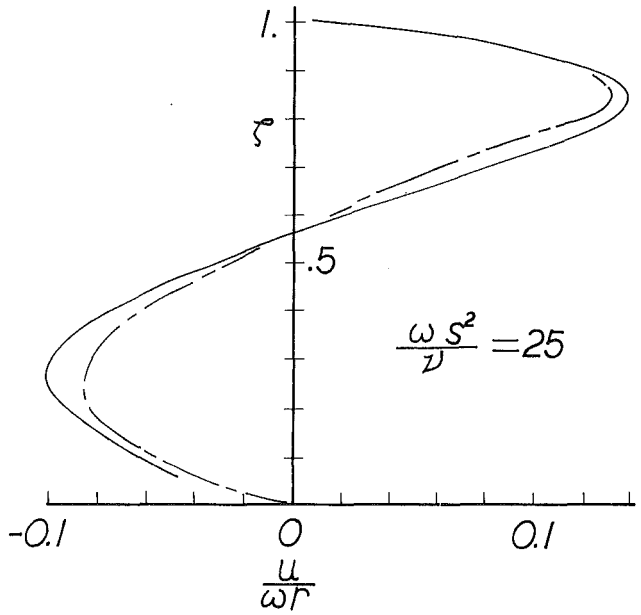


Fig. 2 Comparison of radial velocities; ____ Lance and Rogers [4], infinite disks with no source flow _ _ _ _ Present analysis, finite disks with small soruce flow $R_E = 2500, \sigma = 10, R_Q = 1, \rho_1 = 0.1, \rho = 0.82$

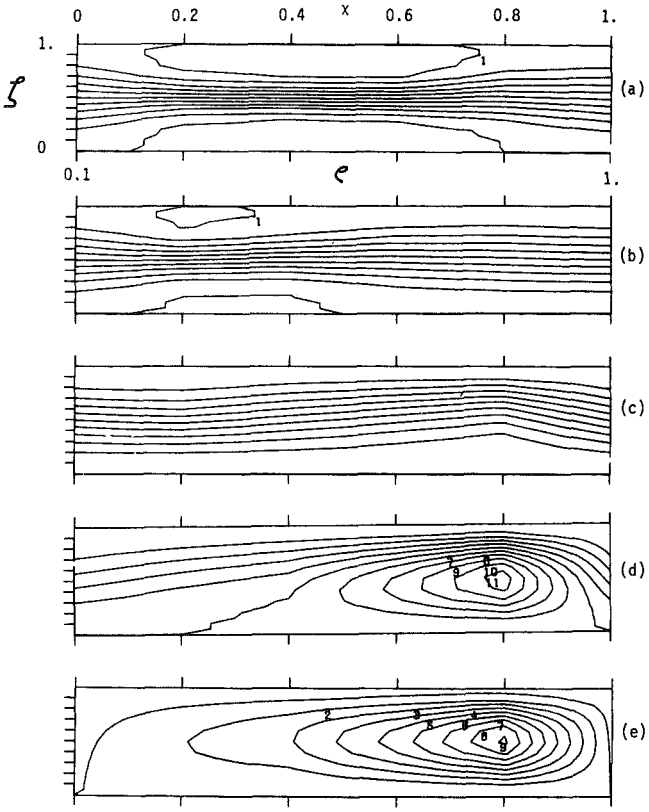


Fig. 3 Equipotential stream function lines (streamlines) for $R_E = 1000, \sigma = 10, \rho_1 = 0.1$; (a) $R_Q = 500$, (b) $R_Q = 250$, (c) $R_Q = 50$, (d) $R_Q = 10$, (e) $R_Q = 1$

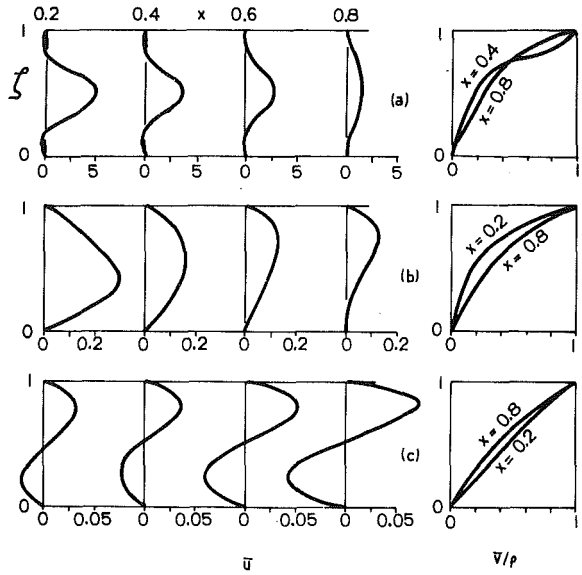


Fig. 4 Radial and tangential velocity profiles, $R_E = 1000, \sigma = 10, \rho_1 = 0.1$; (a) $R_Q = 500$, (b) $R_Q = 50$, (c) $R_Q = 1$

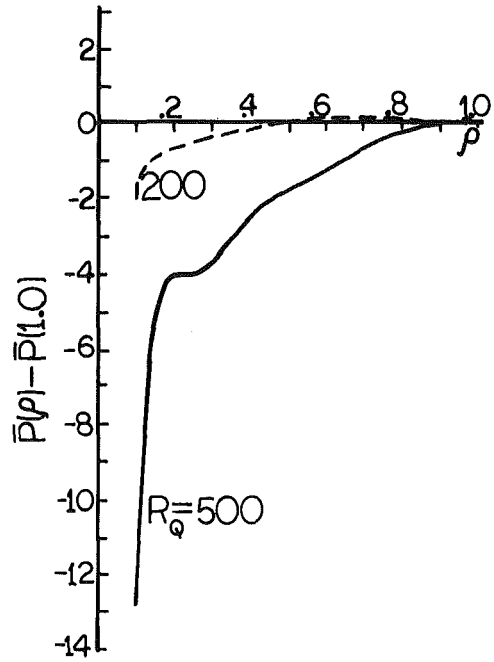


Fig. 5 Radial pressure distribution at $R_E = 1000, \sigma = 10$ and $\rho_1 = 0.1$

was made with infinite-disk solutions [4]. Cases involving low throughflow and high rotation should approach infinite-disk results. A comparison of radial velocity profiles is shown in Fig. 2. One cannot expect exact agreement between the two solutions since radial boundary conditions are specified for the finite disk problem. Nevertheless, the closeness of the agreement lends confidence in the general analyses developed in this study.

Results and Discussion

The problem formulated in the previous sections for thick film disk flows is governed by four parameters: the rotational Reynolds number R_E, the throughflow Reynolds number R_Q and two geometric ratios $\sigma = r_2/s$ and $\rho_1 = r_1/r_2$. Here r_1, $0 < r_1 < r_2$, represents the radial position of the inner boundary. The rotational Reynolds number is related to the gap Reynolds number through $R_s = R_E/\sigma^2$, the latter being employed by researchers working with infinite disk flows.

Our intention here is to explore the effects each of the parameters have on the flow, when ranging over a domain in parameter space that is limited by the accuracy and the convergence properties of the computational scheme employed.

Figure 3 shows contour plots of the normalized stream

Downloaded 01 May 2010 to 171.66.16.249. Redistribution subject to ASME license or copyright; see http://www.asme.org/terms/Terms_Use.cfm

function[1] $\Psi(\rho,\zeta)$ at $R_E = 1000$, $\sigma = 10$ and $\rho_1 = 0.1$ and Fig. 4 shows corresponding velocity profiles. The throughflow Reynolds number R_Q takes the values of 500, 250, 50, 10, and 1. At the highest value of R_Q the convective inertial effects predominate. The pressure increases monotonically with the radius (Fig. 5) and the strong unfavorable pressure gradient induces flow separation on both disks just downstream of the inlet radius. Decreasing R_Q results in a lessening of the relative importance of convective inertia as compared to rotational inertia. At the lowest value of R_Q the flow field is dominated by the centrifugal force field resulting in an outward flow near the rotating disk, and an inflow near the stationary disk. The combination of values $R_E = 1000$ and $\sigma = 10$ is such that the pressure gradient remains unfavorable even at vanishing R_Q, except perhaps at large ρ (Fig. 5). If σ were to be larger and/or R_E smaller, upon decreasing R_Q one would pass into a flow regime where pressure is a monotonically decreasing function of the radius (see the $R_Q = 100$ curve in Fig. 6). This is the normal operating regime of the hydrostatic bearing.

The effect of R_Q on resultant pressure drop form inlet to outlet is shown in Fig. 7. If σ is large, the rotating disk acts as a "pump" when R_Q is small. Upon increasing R_Q, the overall pressure drop increases until reaching a maximum. Thereafter, Δp decreases with increasing R_Q, eventually becoming negative and the rotating disk operates as a "turbine."

When the throughflow is radially inward ($R_Q < 0$), a similar recirculation cell is formed as throughflow magnitude is reduced (Fig. 8). In fact, the same solution is approached as throughflow is reduced, whether approached from positive or negative throughflows. In contrast to the positive throughflow cases (Fig. 3) however, the recirculation cell is initiated on the rotating disk when $R_Q < 0$. This is to be expected since the radially outward flow induced by rotation opposes the inward throughflow. Also, in contrast to the positive throughflow cases, high negative throughflow does not produce separation since radially inward throughflow undergoes a convective acceleration and thus experiences a favorable pressure gradient (Fig. 9). That is, the annulus between disks is a "nozzle" for inward throughflows and a "diffuser" for outward throughflows, an obvious fact consistent with the analytical results.

A 10:1 reduction of rotational Reynolds number ($R_E = 100$) requires approximately 100:1 reduction in throughflow Reynolds number ($R_Q = 0.1$) to establish a recirculation cell (compare Figs. 3(*d*) and 10(*c*)).

When the inner radius is increased by a 5:1 ratio ($\rho_1 = 0.5$), formation of the recirculation cell occurs at approximately the same throughflow Reynolds number (compare Fig. 3(*d*) and 11(*c*)). However, as one might expect, initial formation of the cell occurs over a larger portion of the radial domain when ρ_1 is increased.

The cases discussed thus far show parameter ranges over which significant interaction occurs between throughflow and rotational Reynolds numbers. The analysis was also applied to explore higher rotational Reynolds numbers with very small throughflow. Shown in Figs. 12 and 13 are four cases

[1] In Figs. 3, 8, and 12 particularly, some streamlines appear not to satisfy the $\psi_{1,2} = 0$ boundary conditions. However, this anomaly results from curve-fitting within the contour plotting software package and the number of equipotential lines selected to best display the main structure of the flow pattern.

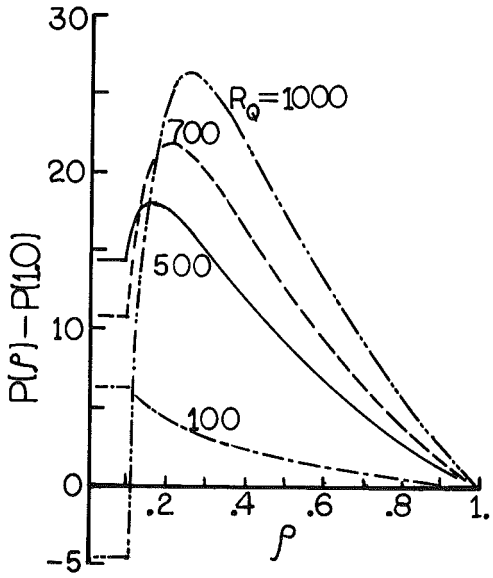


Fig. 6 Radial pressure distribution and $R_E = 1000$, $\sigma = 50$, and $\rho_1 = 0.1$

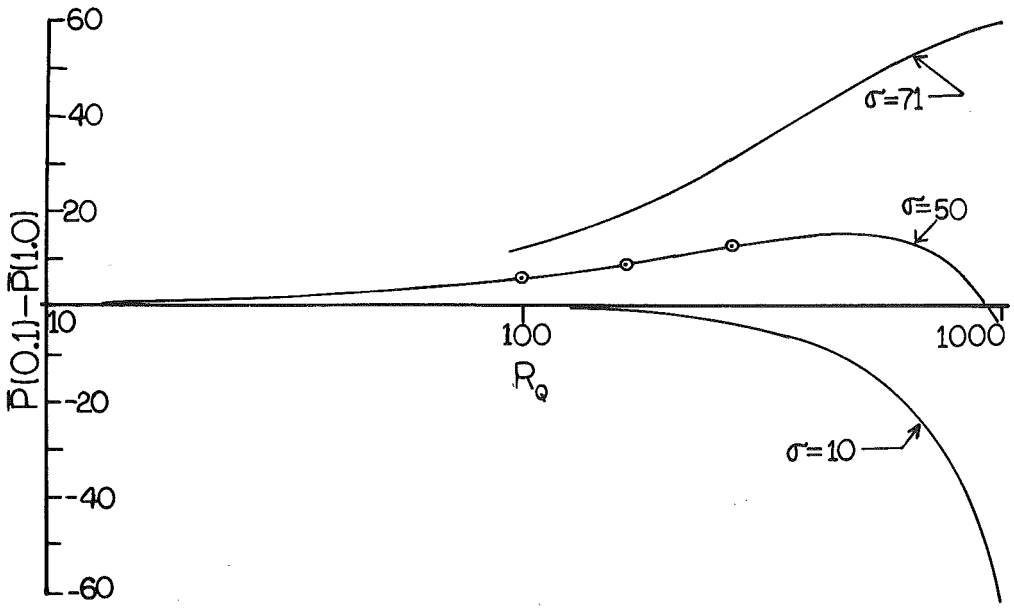


Fig. 7 Variation of pressure drop with R_Q at $R_E = 1000$, and $\rho_1 = 0.1$; (data points shown for thin film solution at $\omega s^2/\nu = 0.4$)

Downloaded 01 May 2010 to 171.66.16.249. Redistribution subject to ASME license or copyright; see http://www.asme.org/terms/Terms_Use.cfm

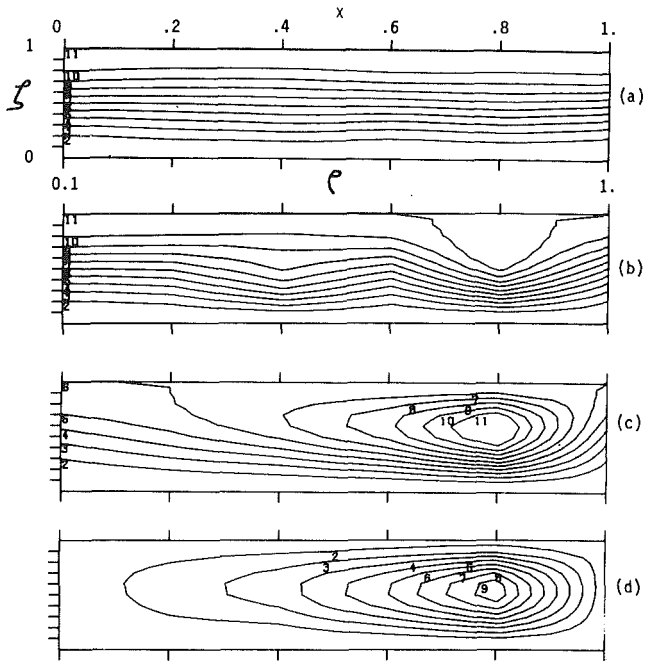


Fig. 8 Equipotential stream function lines (streamlines) for R_E = 1000, σ = 10, ρ_1 = 0.1; (*a*) R_Q = −500, (*b*) R_Q = −50, (*c*) R_Q = −10, (*d*) R_Q = −1

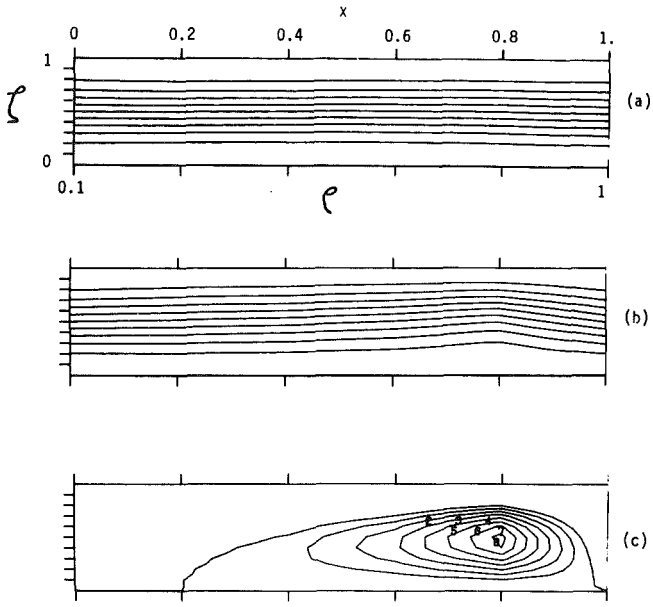


Fig. 10 Equipotential stream function lines (streamlines) for R_E = 100, σ = 10, ρ_1 = 0.1; (*a*) R_Q = 50, (*b*) R_Q = 1, (*c*) R_Q = 0.1

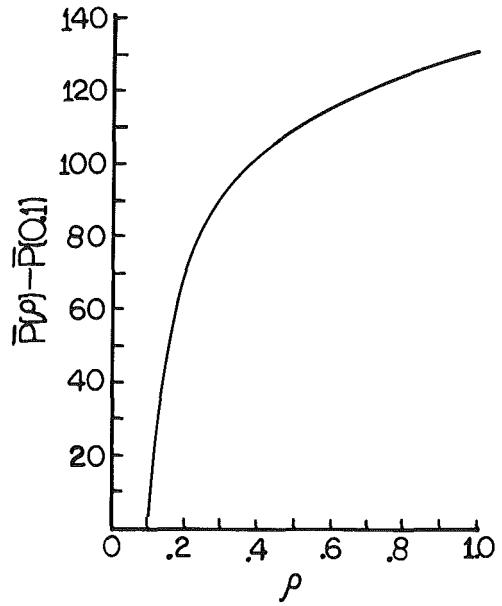


Fig. 9 Radial pressure distribution at R_E = 1000, R_Q = −1000 (radial inflow), and σ = 50

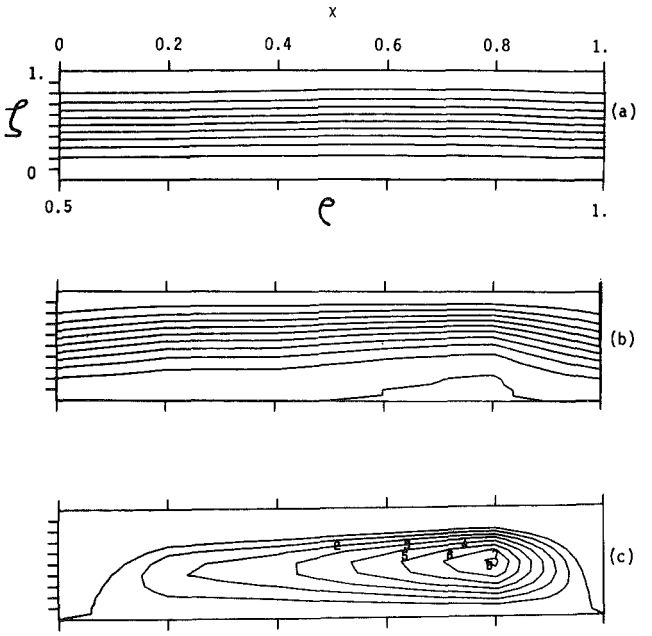


Fig. 11 Equipotential stream function lines (streamlines) for R_E = 1000, σ = 10, ρ_1 = 0.5; (*a*) R_Q = 250, (*b*) R_Q = 50, (*c*) R_Q = 10

with R_Q = 1, σ = 10 and ρ_1 = 0.1 for R_E = 2000 to 14,000 ($20 \leq R_s \leq 140$). The R_E = 14,000 case approaches the upper limit of R_E for which the present algorithm can produce reasonable accuracy with a computationally feasible number of terms in the approximating functions. The stream function contour plots (Fig. 12) show the development of three radially separated recirculation cells. The inner and outer cells have clockwise direction as in the single-cell cases previously discussed. The middle cell (Fig. 12(*d*)) has counterclockwise direction and its radial velocity magnitudes are considerably smaller than the other two cells, apparently because it "opposes" the centrifugal force field. The implication here might be that for even higher rotational Reynolds numbers than shown, more cells would develop, i.e., the cells would "multiply" as R_E is increased. The radial velocity profiles (Fig. 13) are consistent with the flow patterns shown in Fig. 12. It is interesting to note that as R_E is increased from 2000 to 5000, the circumferential velocity profile within the two clockwise cells (x = 0.2, 0.6) is essentially as Batchelor [2] predicted for high Reynolds number flows with infinite disks. However, between these two cells (x = 0.4, R_E = 5000), the circumferential velocity profile is closer to that of considerably lower Reynolds numbers (e.g., Fig. 4). As R_E is increased to 14,000, the circumferential velocity between

Downloaded 01 May 2010 to 171.66.16.249. Redistribution subject to ASME license or copyright; see http://www.asme.org/terms/Terms_Use.cfm

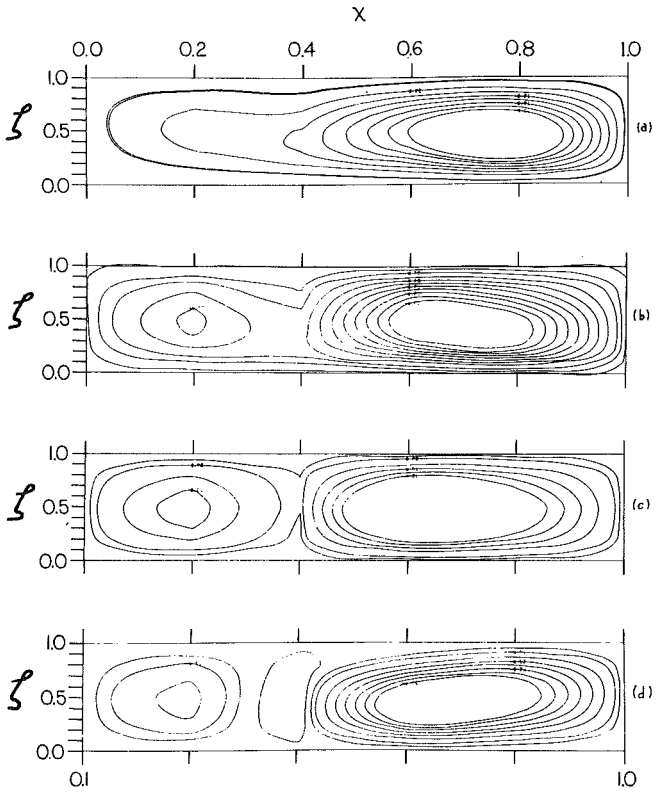


Fig. 12 Stream function contour plots, $R_Q = 1$, $\sigma = 10$, $\rho_1 = 0.1$; (a) $R_E = 2000$, (b) $R_E = 5000$, (c) $R_E = 10{,}000$, (d) $R_E = 14{,}000$

inner and outer cells is counter-rotational. At this time, these results are justifiably subject to question.

Summary

This study of the steady-state problem of rotating disk flows allowed us to follow the formation of recirculation cells with increasing Reynolds number. The contour plots in Fig. 12 are, as far as we know, unique. There is a suggestion here of cell multiplication with increasing Reynolds number. The velocity profiles in Fig. 13 approach Batchelor-type flow within the cells. The present work gives no indication of multiplicity of solutions, but our maximum gap Reynolds number at 140 is still significantly lower than the lower limit of 205, where Holodniok finds multiple solutions between infinite disks. To answer the question of uniqueness of finite disk flows at high Reynolds numbers requires a different numerical approach. A numerical study of the time-dependent problem, coupled with an experimental program, is in progress. (The boundary conditions in this paper were chosen such that they can be easily approximated in the experiments.)

Table 1 Comparison of "thin film" solutions with results of present analysis; ($R_E = 25$, $R_Q = 400$, $\sigma = 50$, $\rho_1 = 0.1$, $N = 5$, $M = 6$)

		Thin Film Solution		Present Solution	
ρ	ζ	$u/r_2\omega$	$v/r_2\omega$	$u/r_2\omega$	$v/r_2\omega$
0.28	0.2	54.08	0.0237	53.92	0.0208
	0.5	87.68	0.0730	88.00	0.0667
	0.8	54.12	0.1752	53.92	0.1710
0.46	0.2	33.36	0.0650	33.40	0.0668
	0.5	52.68	0.1758	52.72	0.1790
	0.8	33.36	0.3304	33.40	0.3328
0.64	0.2	24.05	0.1085	24.00	0.1050
	0.5	37.73	0.2806	37.70	0.2740
	0.8	24.05	0.4844	24.00	0.4800
0.82	0.2	18.79	0.1489	18.90	0.1540
	0.5	29.41	0.3792	29.30	0.3880
	0.8	18.80	0.6340	18.90	0.6390

Acknowledgment

This material is based upon work partially supported by the National Science Foundation under Grant No ENG 78-21853.

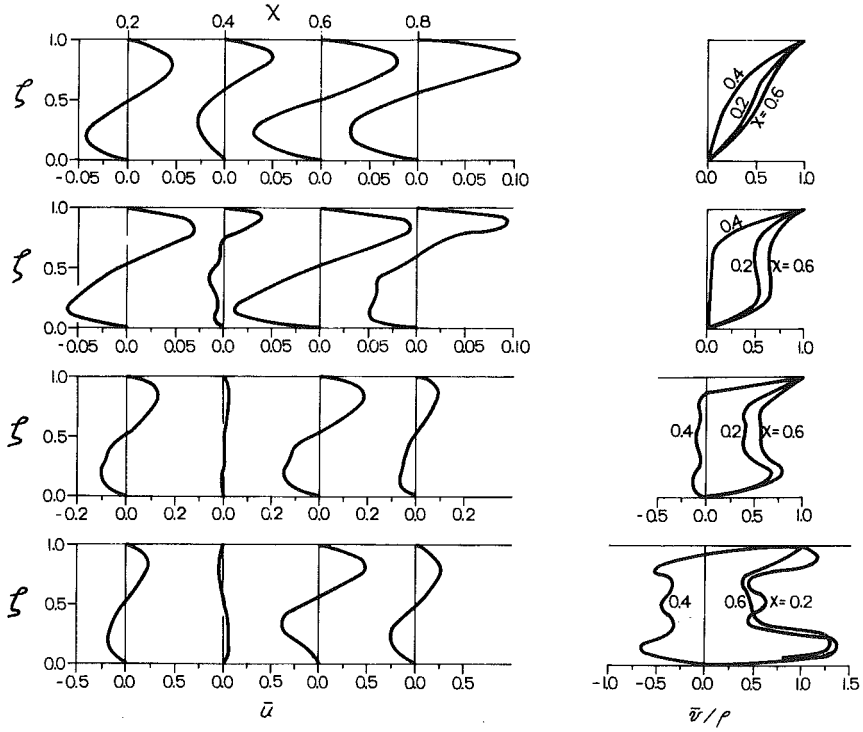


Fig. 13 Radial and tangential velocity profiles, $R_Q = 1$, $\sigma = 10$, $\rho_1 = 0.1$; (a) $R_E = 2000$, (b) $R_E = 5000$, (c) $R_E = 10{,}000$, (d) $R_E = 14{,}000$

Downloaded 01 May 2010 to 171.66.16.249. Redistribution subject to ASME license or copyright; see http://www.asme.org/terms/Terms_Use.cfm

References

1 von Karman, T., "Laminar und Turbulente Reibung," *Zeitschrift für Angewandte Mathematik und Mechanik,* Vol. 1, 1921, pp. 233–240.

2 Batchelor, G. K., "Note on a Class of Solutions of the Navier-Stokes Equations Representing Rotationally Symmetric Flow," *Quarterly Journal of Mechanics and Applied Mathematics,* Vol. 4, Pt. 1, 1951, pp. 29-41.

3 Stewartson, K., "On the Flow Between Two Rotating Coaxial Disks," *Proceedings of the Cambridge Philosophical Society,* Vol. 49, 1953, pp. 333–341.

4 Lance, G. N., and Rogers, M. H., "The Axially Symmetric Flow of a Viscous Fluid Between Two Infinite Rotating Disks," *Proceedings of the Royal Society,* Series A, Vol. 266, 1962, pp. 109–121.

5 Nguyen, N. D., Ribault, J. P., and Florent, P., "Multiple Solutions for Flow Between Coaxial Disks," *Journal of Fluid Mechanics,* 1975, Vol. 68, Pt. 2, pp. 369–388.

6 Adams, M. L., "Incompressible Flow Between Finite Disks," PhD Dissertation, University of Pittsburgh, 1977.

7 Szeri, A. Z., and Adams, M. L., "Laminar Throughflow Between Closely Spaced Rotating Disks," *Journal of Fluid Mechanics,* 1978, Vol. 86, pp. 1–14.

8 Finlayson, B. A., *The Method of Weighted Residuals and Variational Principles,* Academic Press, New York, 1972.

9 Munson, B. R., and Joseph, D. D., "Viscous Incompressible Flow Between Concentric Rotating Spheres. Part 1. Basic Flow," *Journal of Fluid Mechanics,* 1971, Vol. 49, Pt. 2, pp. 289–303.

10 Holodniok, M., Kubicek, M., and Hlavocek, V., "Computation of the Flow Between Two Rotating Coaxial Disks," *Journal of Fluid Mechanics,* 1977, Vol. 81, pp. 689–699.

11 Wilson, L. O., and Schryer, N. L., "Flow Between a Stationary and a Rotation Disk With Suction," *Journal of Fluid Mechanics,* 1978, Vol. 85, pp. 479–496.

Downloaded 01 May 2010 to 171.66.16.249. Redistribution subject to ASME license or copyright; see http://www.asme.org/terms/Terms_Use.cfm

R. Shyam
C.S.I.R. Research Fellow.

V. D. Sharma[1]
Lecturer.

V. V. Menon
Reader.

Applied Mathematics Section,
Institute of Technology,
Banaras Hindu University,
Varanasi 221005, India

Nonlinear Breaking of Wave Fronts in a Vibrationally Relaxing Gas

Using the method of characteristics, some explicit criteria for the nonlinear breaking of wave fronts in a plane, cylindrically or spherically symmetric flows of a vibrationally relaxing gas are obtained. It is shown that except a spherically converging compressive wave, all compressive waves break only when the initial discontinuity at the wave-head exceeds a critical value, and the effects of vibrational relaxation and that of the wave front curvature are to increase the time of their breaking. It is found that the stabilizing influences of vibrational relaxation and that of the wave front curvature are not strong enough to overcome the breaking tendency of a spherically converging compressive wave; in fact, in contrast to a cylindrically converging wave, it always breaks down before the formation of a focus, no matter how small be the initial discontinuity at the wave-head.

Introduction

It is well known that weak discontinuities of the solution of a quasi-linear hyperbolic system of equations propagate along characteristics [1, p. 129] and so the weak discontinuity representing the wave front under discussion will propagate along a characteristic in the (x, t)-plane. The trace of this path (in our discussion) is the leading characteristic bounding the disturbed and undisturbed regions. When the magnitudes of the jumps in the derivatives of the flow variables normal to the leading characteristic become unbounded, the weak discontinuity becomes a strong discontinuity and the propagation then ceases to be along the leading characteristic. The occurrence of such an unbounded jump discontinuity is identified with the physical process of the breaking of a wave (see, for example, Whitham [1, p. 133]).

The problem of breaking of finite amplitude water waves on a sloping beach has been studied previously by Jeffrey [2, 3]. A general method for the study of the development of jump discontinuities in nonlinear hyperbolic equations has been applied by Whitham [1] to the cases where the breaking of finite amplitude shallow water waves, flood waves, and tidal waves takes place; note that all these cases deal with plane waves only. Using the method of characteristics, Chu [4] and Clarke and McChesney [5] have discussed the steepening or the flattening tendencies of plane waves in fluids with internal state variables.

The purpose of the present paper is to discuss the problem of breaking or nonbreaking of wave fronts in plane, cylindrically or spherically symmetric motion of a vibrationally relaxing gas.

General Considerations

The equations, governing an unsteady one-dimensional flow of a vibrationally relaxing gas, are

$$\rho_t + u\rho_x + \rho u_x + j\, x^{-1}\rho u = 0, \tag{1}$$

$$u_t + u\, u_x + \frac{1}{\rho} p_x = 0 \tag{2}$$

$$\rho(h_t + u\, h_x) - p_t - up_x = 0, \tag{3}$$

where ρ is the density, u is the gas velocity, p is the pressure, h is the enthalpy, t is the time, and x is the single spatial coordinate being either axial in flows with planar geometry or radial in cylindrically and spherically symmetric flows. The constant j takes values 0, 1, and 2 according to the dimensions of the respective geometry. The letter subscript denotes partial differentiation unless stated otherwise.

The equations of state, when the gas is capable of being excited in its vibrational made of internal energy, are

$$p = \rho R\, T, \tag{4}$$

$$h = \frac{\nu}{\nu - 1}\frac{p}{\rho} + e_v, \tag{5}$$

where R, T, and ν denote the gas constant, the temperature, and the frozen specific heat ratio, respectively, and e_v is the vibrational energy per unit mass given by

$$e_{v_t} + u\, e_{v_x} = \omega(e^*{}_v(T) - e_v) \equiv \Phi, \tag{6}$$

where $e^*{}_v(T)$ is the equilibrium value of the vibrational energy at the local temperature given by

$$e^*{}_v(T) = R\,\theta_v/\{\exp(\theta_v/T) - 1\}, \tag{7}$$

where θ_v is the characteristic temperature of the molecular vibration. The quantity ω in (6) is the relaxation frequency given by [6, p. 67]

$$\omega = k_1 p \exp(-k_2 T^{-1/3}), \tag{8}$$

where k_1 and k_2 are positive constants depending on the physical properties of the gas only.

[1] Presently, Postdoctoral Fellow, Department of Aerospace Engineering, University of Maryland, College Park, Md. 20742.

Contributed by the Applied Mechanics Division for publication in the JOURNAL OF APPLIED MECHANICS.

Discussion on this paper should be addressed to the Editorial Department, ASME, United Engineering Center, 345 East 47th Street, New York, N.Y. 10017, and will be accepted until final publication of the paper itself in the JOURNAL OF APPLIED MECHANICS. Manuscript received by ASME Applied Mechanics Division, June, 1980; final revision, May, 1981.

Copyright © 1982 by ASME
Downloaded 01 May 2010 to 171.66.16.249. Redistribution subject to ASME license or copyright; see http://www.asme.org/terms/Terms_Use.cfm

Equation (3) with the help of (1), (5), and (6) is conveniently transformed into

$$p_t + up_x + \rho a_f^2 (u_x + j\, x^{-1} u) + \rho(\nu - 1)\Phi = 0, \tag{9}$$

where $a_f = (\nu p/\rho)^{1/2}$ is the frozen speed of sound.

In the matrix notation, equations (1), (2), (6), and (9) can be written as

$$U_t + A\ U_x + B = 0, \tag{10}$$

where U is a column matrix with four components (ρ, u, e_v, p) and the matrices A and B can be read off by inspection of (1), (2), (6), and (9).

Let us now consider a characteristic curve Σ, $x = x(t)$ such that the set of dependent variable U, and the interior derivatives of U may have a jump across Σ. Denoting by $[U]$ the jump of a quantity U across Σ, i.e., the value of U immediately behind Σ minus its value just ahead of Σ, we have along Σ

$$\frac{\delta}{\delta t}[U] = [U_t] + \frac{dx}{dt}[U_x], \tag{11}$$

where the operator $\delta/\delta t$ denotes time derivative as observed from the wave front.

Forming the jumps in the usual way, we obtain from (10) and (11) that

$$\left(A - \frac{dx}{dt} I\right)[U_x] = 0 \tag{12}$$

where use has been made of the condition $[U] = 0$.

Equation (12) shows that if there occurs finite discontinuity in the derivative U_x across the characteristic curve $x = x(t)$, the characteristic speed of propagation, dx/dt, is an eigenvalue of the matrix A. It follows immediately that there are four families of characteristics. Two of these characteristics represent wave propagating in the $\pm$ x-direction with the frozen sound speed a_f, and whose equations are

$$\frac{dx}{dt} = u \pm a_f. \tag{13}$$

The remaining two characteristics form a set of double characteristics

$$\frac{dx}{dt} = u \tag{14}$$

representing the particle path or trajectory.

Since the solutions for the characteristics (13) and (14) are real, the original system of equations (1), (2), (6), and (9) is hyperbolic.

Evolution of the Discontinuity at the Wave Front

In studying wave phenomenon governed by hyperbolic equations, it is usually more natural and convenient to use the characteristics of the governing system as the reference coordinate system, we thus introduce two characteristic variables α and β such that

$$\alpha_t + (u + a_f)\alpha_x = 0, \quad \beta_t + u\,\beta_x = 0.$$

The leading characteristic front can be represented by $\alpha = 0$ and if a material particle crosses this front at time t, its path will be represented by $\beta = t$. Keeping in view the properties of α and β, it is obvious that the functions $x(\alpha, \beta)$ and $t(\alpha, \beta)$ satisfy the following partial differential equations:

$$x_\alpha = u\, t_\alpha, \tag{15}$$

$$x_\beta = (u + a_f) t_\beta. \tag{16}$$

The transformation from the space-time (x, t) plane to the plane of the characteristic parameters (α, β) will be one-to-one if the Jacobian

$$\mathrm{J} = x_\alpha t_\beta - x_\beta t_\alpha = -a_f t_\alpha t_\beta, \tag{17}$$

does not vanish anywhere. The following results are noted for future use

$$f_x = \mathrm{J}^{-1}(f_\alpha t_\beta - f_\beta t_\beta), \tag{18}$$

$$f_t + u\, f_x = -\mathrm{J}^{-1} a_f f_\alpha t_\beta, \tag{19}$$

where f can be either p, ρ, e_v or u.

Since the doubling up or overlapping of fluid particles is prohibited from physical considerations, $t_\beta \neq 0$. Consequently $\mathrm{J} = 0$, if and only if, $t_\alpha = 0$, when two adjoining characteristics merge into a shock wave.

With the help of (17)–(19), equations (1), (2), (6), and (9) may be transformed into the following equivalent system:

$$(a_f \rho_\alpha - \rho u_\alpha) t_\beta + \rho u_\beta t_\alpha + j\, x^{-1} \rho u\, a_f t_\alpha t_\beta = 0, \tag{20}$$

$$(p_\alpha - \rho a_f u_\alpha) t_\beta - p_\beta t_\alpha = 0, \tag{21}$$

$$a_f e_{v_\alpha} t_\beta = 0, \tag{22}$$

$$p_\beta + \rho a_f u_\beta = -\{\rho(\nu - 1)\Phi + j\, x^{-1} \rho u\, a_f^2\} t_\beta, \tag{23}$$

The unperturbed field ahead of the wave Σ is assumed to be uniform and at rest. The boundary conditions are simply

$$p = p_0, \quad \rho = \rho_0, \quad \Phi = \Phi_0, \quad e_v = e_{v_0}, \quad u = 0, \quad t = \beta \tag{24}$$

at $\alpha = 0$, where the subscript "0" indicates a value in the region ahead of Σ. The last condition is, of course, a consequence of the particular method of labeling the particle path. We observe that the boundary conditions (24) at the characteristic wave front $\alpha = 0$ demand that

$$p_\beta = \rho_\beta = e_{v_\beta} = u_\beta = 0, \quad t_\beta = 1 \text{ at } \alpha = 0. \tag{25}$$

Since $\Phi = \Phi_0 = 0$, equation (23) is satisfied identically at $\alpha = 0$. On the other hand, evaluation of (15), (16), and (20)–(22) at the wave front $\alpha = 0$ yields

$$x_\alpha = 0, \quad x_\beta = a_{f_0}, \quad a_{f_0} \rho_\alpha = \rho_0 u_\alpha, \tag{26-28}$$

$$p_\alpha = \rho_0 a_{f_0} u_\alpha, \quad e_{v_\alpha} = 0. \tag{29, 30}$$

To compute $s = [u_x]$ at the wave front $\alpha = 0$, we invoke (17) and (18) which give

$$s = -u_\alpha / a_{f_0} t_\alpha. \tag{31}$$

In order to study the dependence of u_α and t_α on time at the wave front $\alpha = 0$, we differentiate (16) and (23) with respect to α, and (15) and (21) with respect to β, and evaluate at the wave front $\alpha = 0$ to obtain

$$u_{\alpha\beta} = -\left(\Lambda_0 + \frac{j\, a_{f_0}}{2x}\right) u_\alpha, \tag{32}$$

$$t_{\alpha\beta} = -\frac{(\nu + 1)}{2\, a_{f_0}} u_\alpha, \tag{33}$$

where $\Lambda_0 = \nu(\nu - 1)^2\, \omega\, e^{*2}_v \exp(\theta_v / T)/2a^4_{f_0} > 0$. In obtaining (32) and (33) we have made use of (4), (6), (7), and (24)–(30). Integrating (32) with respect to β on the line of constant α (= 0), we obtain

$$u_\alpha = u_{\alpha 0}(x/x_0)^{-j/2} \exp(-\Lambda_0 t). \tag{34}$$

Equation (34) gives the dependence of u_α at the wave front on time, since $t = \beta$ at the wave front. $u_{\alpha 0}$ and x_0 are, of course, the values of u_α and x at $t = 0$, respectively. Moreover,

$$x = x_0 + a_{f_0} t. \tag{35}$$

Making use of (34) in (33) and integrating with respect to β, we get

$$t_\alpha = t_{\alpha 0} - \frac{(\nu + 1)}{2\, a_{f_0}} u_{\alpha 0} \int_0^t (x/x_0)^{-j/2} \exp(-\Lambda_0 \hat{t})\, d\hat{t}, \tag{36}$$

where $t_{\alpha 0}$ is the value of t_α at $t = 0$. In view of equations (34) and (36), (31) yields

$$s = \frac{s_0 (x/x_0)^{-j/2} \exp(-\Lambda_0 t)}{1 + \dfrac{(\nu + 1)}{2} s_0 \displaystyle\int_0^t (x/x_0)^{-j/2} \exp(-\Lambda_0 \hat{t})\, d\hat{t}} \tag{37}$$

where s_0 ($\neq 0$) is the value of s at $t = 0$.

Downloaded 01 May 2010 to 171.66.16.249. Redistribution subject to ASME license or copyright; see http://www.asme.org/terms/Terms_Use.cfm

Discussion (Breaking or Nonbreaking of Waves)

Plane Waves. For a plane wave ($j = 0$), (37) reduces to

$$s = \frac{s_0 \exp(-\Lambda_0 t)}{1 + (s_0/s_c)\{1 - \exp(-\Lambda_0 t)\}}, \tag{38}$$

where $s_c = 2\Lambda_0/(\nu+1)$.

Equation (38) shows that if $s_0 > 0$ (i.e., an expansive wave front) then $s \to 0$ as $t \to \infty$, i.e., the wave attenuates. Also if $s_0 < 0$ (i.e., a compressive wave front) and if it has the magnitude less than s_c then $s \to 0$ as $t \to \infty$, i.e., a compressive wave decays and damps out ultimately. Further if $s_0 = -s_c$ then $s = s_c$ and the wave attains a stable wave form. But if $s_0 < 0$ and has a magnitude greater than s_c then s increases beyond all bounds for a finite time t_c given by

$$t_c = \Lambda_0^{-1} \log\left(1 + \frac{s_c}{s_0}\right)^{-1}. \tag{39}$$

Thus, at the instant t_c, the velocity gradient at the wave front becomes infinite. This predicts the nonlinear breaking of the wave front, and after this time a shock wave with discontinuities in the flow variables p, ρ, and u must be introduced. From (39) it follows that $(\partial t_c/\partial \Lambda_0) > 0$, i.e., an increase in Λ_0 causes an increase in the time t_c of breaking on the wave front. Thus the vibrational relaxation has a stabilizing effect on the breaking of waves.

Cylindrical Waves. For a cylindrical wave ($j = 1$), equation (37) reduces to

$$s = \frac{s_0(1 + k_0 a_{f_0} t)^{-1/2} \exp(-\Lambda_0 t)}{1 + \frac{(\nu+1)}{2} s_0 I(t)} \tag{40}$$

where

$$I(t) = \int_0^t (1 + k_0 a_{f_0} \tau)^{-1/2} \exp(-\Lambda_0 \tau)\, d\tau, \tag{41}$$

and the wave front curvature k_0 ($= 1/x_0$) is either positive or negative, respectively, according as the wave is diverging or converging.

(*i*) *Diverging Waves* ($k_0 > 0$). It is evident that the integral $I(t)$ given by (41) converges to a finite positive limit as $t \to \infty$. Hence, it follows from (40) that if $s_0 > 0$ then $s \to 0$ as $t \to \infty$, i.e., the wave decays and damps out ultimately. But if $s_0 < 0$ then there exists a positive critical value $\hat{s}_c$ given by

$$\hat{s}_c = 2/\{(\nu+1) I(\infty)\}$$

such that for $|s_0| < \hat{s}_c$, $s \to 0$ as $t \to \infty$ (i.e., no breaking is possible at the wave front, rather the wave decays and damps our ultimately), and for $|s_0| > \hat{s}_c$, $|s| \to \infty$ as $t \to \hat{t}_c$, showing that breaking will occur on the wave front in a finite time $\hat{t}_c$, where $\hat{t}_c$ is given by the solution of

$$I(\hat{t}_c) = 2/\{(\nu+1)|s_0|\}. \tag{42}$$

For $|s_0| = \hat{s}_c$, using L'Hospital's rule, it follows from (40) that $|s| \to 2\Lambda_0/(\nu+1)$ as $t \to \infty$ (i.e., no breaking is possible at the wave front, and the wave ultimately takes a stable wave form). Further, it can be seen from (42) that $(\partial \hat{t}_c/\partial \Lambda_0) > 0$ and $(\partial \hat{t}_c/\partial k_0) > 0$ which mean that the effects of vibrational relaxation and that of the wave front curvature are to increase the time of breaking.

(*ii*) *Converging Waves* ($k_0 < 0$). In this case the numerator of (40) becomes unbounded at $t^* = 1/(|k_0| a_{f_0})$, whereas the denominator, for $s_0 > 0$, remains positive and finite since the integral $I(t)$, in this case, converges to a finite positive limit as $t \to t^*$. Hence $s \to \infty$ as $t \to t^*$ when $s_0 > 0$. This corresponds to the formation of a focus but not to the breaking of wave front, since the breaking of a wave front is identified with the intersection of characteristics and hence to the vanishing of t_α. If $s_0 < 0$, then there exists a positive critical value $\tilde{s}_c$ given by

$$\tilde{s}_c = 2/\{(\nu+1) I(t^*)\}$$

such that for $|s_0| < \tilde{s}_c$, $|s| \to \infty$ as $t \to \infty$ (i.e., a focus occurs but no breaking), and for $|s_0| > \tilde{s}_c$, $|s| \to \infty$ as $t \to \tilde{t}_c$, where $\tilde{t}_c < t^*$ is the unique solution of the equation

$$\int_0^{\tilde{t}_c} \{1 - (|k_0| a_{f_0} t)\}^{-1/2} \exp(-\Lambda_0 t)\, dt = 2/\{(\nu+1)|s_0|\}.$$

Since $\tilde{t}_c < t^*$, it follows that the breaking occurs before the formation of the focus. If $|s_0| = \tilde{s}_c$, it follows from (40) that $|s| \to \infty$ as $t \to t^*$, i.e., both breaking and focusing occur simultaneously.

Spherical Waves. In this case ($j = 2$), equation (37) takes the form

$$s = \frac{s_0(1 + k_0 a_{f_0} t)^{-1} \exp(-\Lambda_0 t)}{1 + \frac{(\nu+1)}{2} s_0 \bar{I}(t)}, \tag{43}$$

where

$$\bar{I}(t) = \int_0^t (1 + k_0 a_{f_0} \tau)^{-1} \exp(-\Lambda_0 \tau)\, d\tau. \tag{44}$$

(*i*) *Diverging Waves.* The analysis of the solution of (43) is similar to that for diverging cylindrical waves just discussed, i.e., when $s_0 < 0$, there exists a positive critical value s_c^* such that for $|s_0| < s_c^*$, $|s| \to 0$ as $t \to \infty$; for $|s_0| > s_c^*$, $|s| \to \infty$ as $t \to t_s$ where s_c^* and t_s are, respectively, given by

$$s_c^* = 2/\{(\nu+1)\bar{I}(\infty)\},$$

and

$$\bar{I}(t_s) = 2/\{(\nu+1)|s_0|\}.$$

(*ii*) *Converging Waves.* In this case, both the numerator of (43) and the integral given by (44) become unbounded at a finite time $\hat{t} = 1/(|k_0| a_{f_0})$. Hence, it follows from (43) that for $s_0 > 0$, $|s| \to \infty$ as $t \to \hat{t}$, i.e., a focus is formed. If, however, $s_0 < 0$, the integral $\bar{I}(t)$ is zero at $t = 0$ and increases to ∞ as $t \to \hat{t}$ (since the derivative of $\bar{I}(t)$ is positive), and therefore there must exist a finite time $\bar{t}_s < \hat{t}$ such that the denominator of (43) vanishes at $\bar{t}_s < \hat{t}$ such that the denominator of (43) vanishes at $\bar{t}_s$. In other words, there exists a finite time $\bar{t}_s < \hat{t}$ such that $|s| \to \infty$ as $t \to \bar{t}_s$ where $\bar{t}_s$ is given by

$$\int_0^{\bar{t}_s} \{1 - (|k_0| a_{f_0} t)\}^{-1} \exp(-\Lambda_0 t)\, dt = 2/\{(\nu+1)|s_0|\}.$$

We, thus, find that all spherically converging compressive waves, no matter how small be their initial discontinuity, always break at the wave front before the formation of the focus. This is in contrast to the corresponding case of a cylindrically converging waves.

References

1 Whitham, G. B., *Linear and Nonlinear Waves*, Wiley, New York, 1974.

2 Jeffrey, A., "The Breaking of Waves on a Sloping Beach," *ZAMP*, Vol. 15, 1964, pp. 97–106.

3 Jeffrey, A., "On a Class of Nonbreaking Finite Amplitude Water Waves, *ZAMP*, Vol. 18, 1967, pp. 57–65.

4 Chu, B. T., "Weak Nonlinear Waves in Nonequilibrium Flows," *Nonequilibrium Flows*, Part II, ed., Wegener, P. P., Marcel Dekker, New York, 1970, pp. 33–58.

5 Clarke, J. F., and McChesney, M., *Dynamics of Relaxing Gases*, Butterworths, London, 1976.

6 Bray, K. N. C., "Chemical and Vibrational Nonequilibrium in Nozzle Flows," *Nonequilibrium Flows*, Part II, ed., Wegener, P. P. Marcel Dekker, New York, 1970, pp. 60–157.

Downloaded 01 May 2010 to 171.66.16.249. Redistribution subject to ASME license or copyright; see http://www.asme.org/terms/Terms_Use.cfm

M. Toren
Adjunct Senior Lecturer.

A. Solan[1]
Professor.
Mem. ASME

M. Ungarish[2]

Faculty of Mechanical Engineering,
Technion, Israel Institute of Technology,
Haifa, Israel

Rotating Flow Over a Disk Sector

The rotating boundary layer flow over a plane sector of angle θ_s and infinite radius is solved. For sufficiently large radius the radial coordinate is eliminated by a Von Karman transformation, leaving a nonaxisymmetric flow in (θ,z), which cyclically changes over the full circle, from a Blasius boundary layer, to a Bodewadt flow, and to a rotating wake. Leading terms of the three-dimensional perturbation of the Blasius flow, and of the rotating wake are given, and the matching over the full circle is outlined for limiting values of θ_s.

1 Introduction

Flow over stationary parts in rotating machinery is usually modeled in terms of stationary disks in rotating unbounded flow or disks shrouded by rotating enclosures. Most such analytical models refer to complete full-circle disks (of finite or infinite radius), and thus lead to axisymmetric solutions, independent of the angle (e.g., Bodewadt [1], Rogers and Lance [2, 3]). Here we address ourselves to the problem of rotating flow over a solid surface in the form of a disk sector, of angle $\theta_s < 2\pi$ (Fig. 1). For simplicity, the disk radius is assumed infinite. We assume that the flow far away from the plane of the disk sector is solid body rotation, and the parameters are such that deviations from solid body rotation are confined to a boundary layer near that plane. Clearly, this boundary layer is strongly nonaxisymmetric. To fix ideas, assume the "oncoming" flow at $\theta = 0^-$ to be a nearly undisturbed solid body rotation. This flow meets the "leading edge" of the disk sector at $\theta = 0$ and forms a boundary layer, which starts with a two-dimensional Blasius type asymptotic behavior for $\theta \to 0$, and develops with increasing θ into a three-dimensional flow which tends, for sufficiently large θ, to a Bodewadt layer. As the flow reaches the "trailing edge" of the sector, $\theta = \theta_s$, the boundary layer (either of perturbed Blasius or of Bodewadt type) slides off the solid surface and forms a wake of three-dimensional flow which decays in the circumferential direction and tends to revert to the solid body rotation. If the wake angle $2\pi - \theta_s$ is sufficiently large, the flow at the end of the wake, which is the oncoming flow at the leading edge of the disk sector, is a slightly disturbed solid body rotation. This completes the picture and the geometric cycle repeats itself. To summarize, the flow is a cyclical sequence of nearly Blasius type boundary layer for the circumferential velocity, an approach to a Bodewadt layer, and a rotating wake decaying back to nearly solid body rotation. (The flow over the solid surface near the leading edge is, in a certain sense, related to the flow over a rotating blade in a stationary flow [4, 5].)

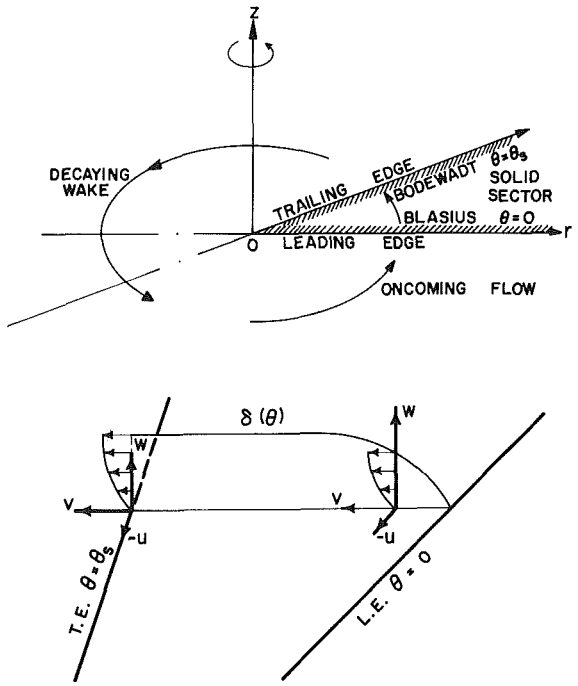


Fig. 1 Regions of rotating flow over a solid plane sector

In the following sections, we shall (1) derive the governing equations for the flow, (2) present the solution for the boundary layer flow over the solid surface, assuming solid body rotation as oncoming flow, (3) present the far downstream solution for the decaying wake, and (4) show how these two flows are modified by their cyclical interaction.

[1] During 1981–1982: Department of Mechanical and Aerospace Engineering, Rutgers University, New Brunswick, N.J. 08903.

[2] During 1981–1982: Department of Mathematics, Massachusetts Institute of Technology, Cambridge, Mass. 02139.

Contributed by the Applied Mechanics Division for publication in the JOURNAL OF APPLIED MECHANICS.

Discussion on this paper should be addressed to the Editorial Department ASME, United Engineering Center, 345 East 47th Street, New York, N.Y. 10017, and will be accepted until two months after final publication of the paper itself in the JOURNAL OF APPLIED MECHANICS. Manuscript received by ASME Applied Mechanics Division, December, 1980; final revision, August 1981.

Copyright © 1982 by ASME
Downloaded 01 May 2010 to 171.66.16.249. Redistribution subject to ASME license or copyright; see http://www.asme.org/terms/Terms_Use.cfm

2 Governing Equations

We consider a steady, incompressible, laminar, rotating flow over a sector of angle θ_s of an infinite plane (Fig. 1) perpendicular to the axis of rotation. Far from the plane the flow is solid body rotation at angular velocity Ω. The cylindrical coordinate system is as shown in Fig. 1. On the solid surface we impose the no-slip condition and at the wake midplane the usual symmetry conditions. Finally, we exclude from our analysis the region near the rotation axis and limit the discussion to r sufficiently large such that $\nu/(\Omega r^2) << 1$, i.e., the flow is limited to a boundary layer.

The problem thus defined admits Von Karman's similarity, viz.,

$$\bar{u}=\Omega r u \quad \bar{v}=\Omega r v \quad \bar{w}=(\Omega\nu)^{1/2} w \quad \bar{z}=(\nu/\Omega)^{1/2} z \tag{1}$$

which eliminates r from the equations. Here $\bar{u}$, $\bar{v}$, $\bar{w}$ are dimensional velocity components and u, v, w are their dimensionless r-independent counterparts. The resulting system of equations, with the two independent variables θ, z, is

$$2u+\frac{\partial v}{\partial\theta}+\frac{\partial w}{\partial z}=0 \tag{2}$$

$$u^2+v\frac{\partial u}{\partial\theta}-v^2+w\frac{\partial u}{\partial z}=-1+\frac{\partial^2 u}{\partial z^2} \tag{3}$$

$$2uv+v\frac{\partial v}{\partial\theta}+w\frac{\partial v}{\partial z}=\frac{\partial^2 v}{\partial z^2} \tag{4}$$

$$z=0\begin{cases}0<\theta<\theta_s: & u=v=w=0 \quad \text{solid surface} \\ \theta_s<\theta<2\pi: & \dfrac{\partial u}{\partial z}=\dfrac{\partial v}{\partial z}=w=0 \quad \text{wake midplane}\end{cases} \tag{5a,b}$$

$$z\to\infty \text{ all } \theta: \quad v\to 1, \quad u\to 0 \tag{6}$$

(Within the boundary layer assumptions the pressure is determined by the external flow, $p = 1/2\,\Omega^2 r^2$.)

To describe the flow field over a full circle we: (*a*) assume an undisturbed flow approaching the leading edge at $\theta = 0^-$ and solve for the boundary layer that grows from $\theta = 0^+$ over the solid surface, (*b*) we solve the wake decaying behind the trailing edge $\theta = \theta_s$, and (*c*) we outline how the flows may be matched.

3 Boundary Layer Over the Solid Surface

Consider equations (2)–(5*a*) and (6), and assume an undisturbed solid body rotation at the leading edge

$$\theta=0^-: \quad v=1, \quad u=w=0 \tag{7}$$

Inspection of these equations shows that for $\theta \to 0$ the system reduces asymptotically to a Blasius problem for $v(\theta,z)$. On the other hand, for θ sufficiently large we expect all terms $\partial/\partial\theta$ to be negligible, thus asymptotically reducing the problem to a Bodewadt flow $v(z)$, $u(z)$. Therefore, we introduce a change of independent variables, from θ, z to

$$\eta=z\theta^{-1/2} \tag{8}$$

and θ, and assume the series expansions

$$u=\theta(u_0+\theta^2 u_2+\theta^4 u_4+\ldots.) \tag{9a}$$

$$v=v_0+\theta^2 v_2+\theta^4 v_4+\ldots. \tag{9b}$$

$$w=\theta^{-1/2}(w_0+\theta^2 w_2+\theta^4 w_4+\ldots.) \tag{9c}$$

where the indexed variables are functions of η only (it can be easily seen that all odd terms vanish). The resulting hierarchy of equations is as follows

0th Order in θ:

$$-\frac{1}{2}\eta v_0'+w_0'=0 \tag{10a}$$

$$v_0''+\frac{1}{2}\eta v_0 v_0'-w_0 v_0'=0 \tag{10b}$$

$$u_0''+\left(\frac{1}{2}\eta v_0-w_0\right)u_0'-v_0 u_0=1-v_0^2 \tag{10c}$$

$$\eta=0: \quad v_0=w_0=u_0=0 \tag{10d}$$

$$\eta\to\infty: \quad v_0\to 1, u_0\to 0 \tag{10e}$$

2nd Order in θ:

$$2v_2-\frac{1}{2}\eta v_2'+w_2'=-2u_0 \tag{11a}$$

$$v_2''+\left(\frac{1}{2}\eta v_0-w_0\right)v_2'-\left(2v_0-\frac{1}{2}\eta v_0'\right)v_2-v_0' w_2=2u_0 v_0 \tag{11b}$$

$$u_2''+\left(\frac{1}{2}\eta v_0-w_0\right)u_2'-3v_0 u_2=u_0^2+\left(u_0-\frac{1}{2}\eta u_0'-2v_0\right)v_2+w_2 u_0' \tag{11c}$$

$$\eta=0: \quad v_2=w_2=u_2=0 \tag{11d}$$

$$\eta\to\infty: \quad v_2\to 0, \quad u_2\to 0 \tag{11e}$$

The equations for orders higher than two can be derived in a quite straightforward manner, and are similar in general structure to (11*a–e*). Note that v_0 and w_0 are determined by the nonlinear system (10*a*,*b*), which can be recognized as the classical Blasius boundary layer. Once this is solved, u_0 can be found from the linear equation (10*c*). This equation is identical to that solved by Mager and Hansen [6] in another problem of boundary layer with crossflow (See also [7] and [8]). From the second-order terms on, all equations are linear, v and w of each order being coupled, and u of the corresponding order to be solved separately. All equations represents two-point boundary value problems and can be solved numerically by standard shooting algorithms. This system of equations is closely related (but not identical) to that considered by Morris [5] in the problem of a rotating blade.

The equations were solved numerically for orders 0, 2, 4, and 6. The results for the unknown boundary values are:

Order	$v_i'(0)$	$u_i'(0)$	$w_i(\infty)$
$i=0$	0.33206	−1.0860	0.86045
2	0.14695	−0.08941	2.31455
4	0.11899	0.05917	−1.37715
6	0.029562	0.01381	−0.76983

The functions $u_i(\eta)$, $v_i(\eta)$ were summed as in equations (9*a*,*b*) for various values of θ. The results are shown in two representations: (1) Figs. 2(*a*),(*b*) show $u(\theta)$ and $v(\theta)$ at $z=1$ as partial sums of one to four terms, i.e., $i = 0, 2, 4$, and 6. Also shown is the corresponding value of the Bodewadt profile (θ- independent); (2) Figs. 3(*a*),(*b*) show the analogous partial sums for $u(z)$ and $v(z)$ at $\theta = 1.2$. (Similar graphs were computed for other values of z or θ, but are not shown.)

As can be expected, for small θ the series converges very fast and the solution is predominantly the Blasius profile. Near $\theta \approx 1.2$ it appears that the three-term and four-term sums are close, indicating convergence, but are significantly different from the zeroth-order Blasius profile. In particular, note how the sixth-order solution in Fig. 3(*b*) differs from the zeroth-order Blasius profile and develops an oscillatory form similar to the Bodewadt profile. Clearly, since the expansion in equations (9*a–c*) is asymptotically valid only for small θ, the series cannot be expected to hold for large θ, as can be seen from the overshoot with respect to the Bodewadt values at the right of Fig. 2(*a*),(*b*). Nevertheless, the present solutions shows how the initial two-dimensional Blasius flow

Downloaded 01 May 2010 to 171.66.16.249. Redistribution subject to ASME license or copyright; see http://www.asme.org/terms/Terms_Use.cfm

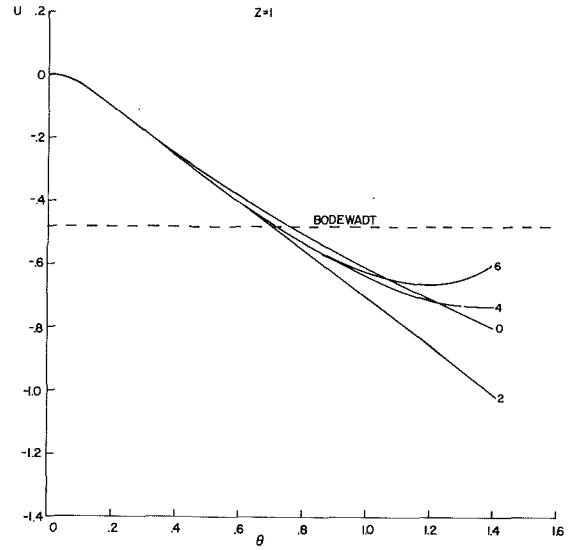


Fig. 2(a) Radial velocity

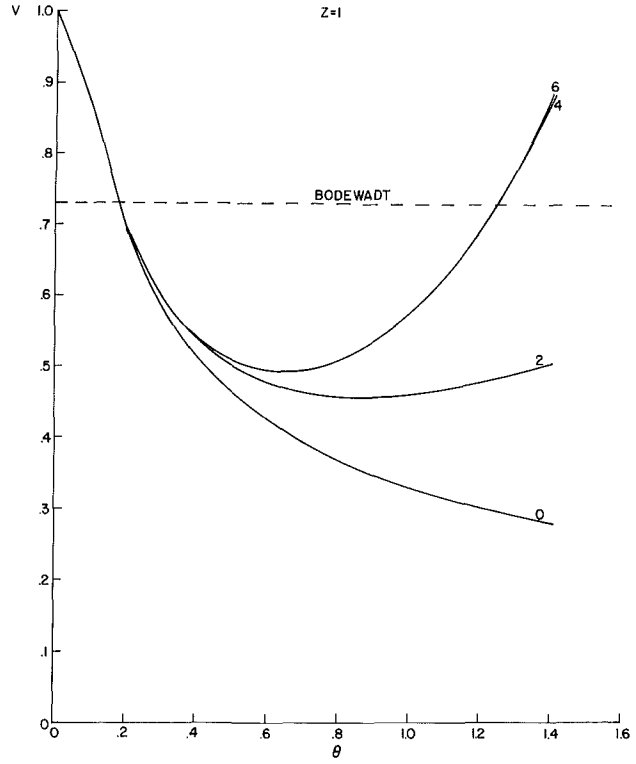


Fig. 2(b) Circumferential velocity

Fig. 2 Boundary layer over solid sector, at $z = 1$; 0, 2, 4, 6 – partial sums of series (9a,b)

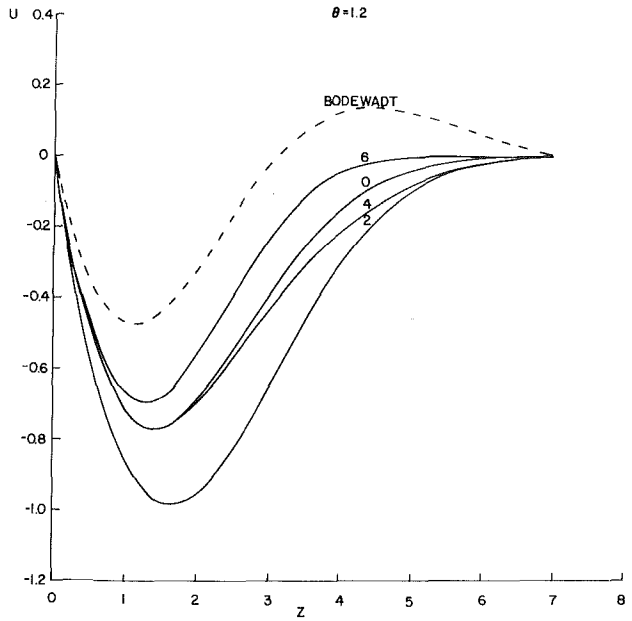


Fig. 3(a) Radial velocity

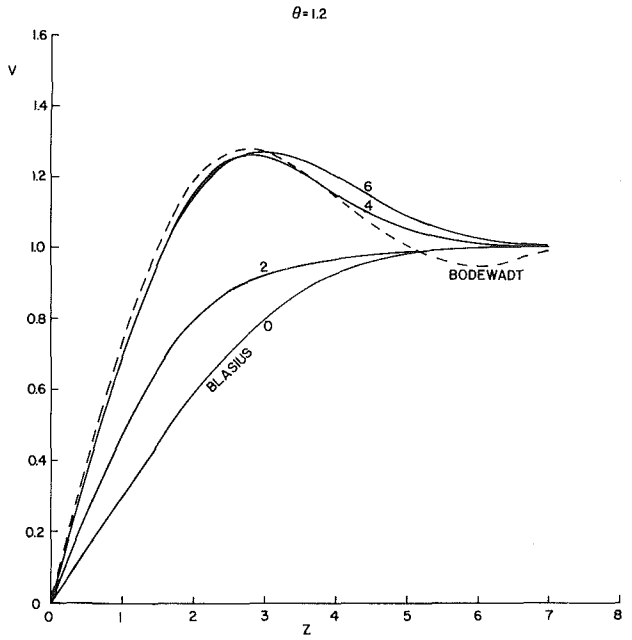


Fig. 3(b) Circumferential velocity

Fig. 3 Boundary layer over solid sector, at $\theta = 1.2$; 0, 2, 4, 6 – partial sums of series (9a,b)

develops, for increasing θ, into the three-dimensional Bodewadt flow, and also provides a rough approximation for the "development angle": inspection of the graphs (including those not shown) indicates that the Bodewadt profile is approached at θ in the range between 0.5 and 1.5, i.e., within the first quadrant. (A more exact answer to this question can be obtained by numerical integration of the governing equations.) It is worthwhile noting that the axial velocity outside the boundary layer is directed away from the solid surface for both the Blasius and Bodewadt flows. (In the inverse problem of a rotating surface in a stationary fluid, the axial velocity is also directed away from the surface at the leading edge, but changes sign at large θ.)

4 Wake

The equations describing the wake are (2)–(4), (5*b*) and (6), with an appropriate initial condition at $\theta = \theta_s$, determined by the flow over the solid surface. Generalizing the classical treatment of wake flow (e.g., [9]) we shall treat separately the near and far wake. Consider the far wake first – here we assume that the flow is a small perturbation on the undisturbed solid body rotation. Thus we introduce

$$v = 1 + \tilde{v} \tag{12}$$

and linearize the equations to obtain

$$2u + \frac{\partial \tilde{v}}{\partial \theta} + \frac{\partial w}{\theta z} = 0 \tag{13a}$$

$$\frac{\partial u}{\partial \theta} - 2\tilde{v} = \frac{\partial^2 u}{\partial z^2} \tag{13b}$$

Downloaded 01 May 2010 to 171.66.16.249. Redistribution subject to ASME license or copyright; see http://www.asme.org/terms/Terms_Use.cfm

$$2u + \frac{\partial \tilde{v}}{\partial \theta} = \frac{\partial^2 \tilde{v}}{\partial z^2} \tag{13c}$$

$$\theta > \theta_s, z = 0: \quad \frac{\partial u}{\partial z} = \frac{\partial \tilde{v}}{\partial z} = w = 0 \tag{13d}$$

$$\theta > \theta_s, z \to \infty: \quad \tilde{v} \to 0, \quad u \to 0 \tag{13e}$$

The initial condition will be obtained by an integral balance, to be discussed later. Note that the two momentum equations (13*b*) and (13*c*) for u, $\tilde{v}$ are coupled. The solution is

$$u = \frac{A}{\sqrt{\pi \theta_w}} \exp\left(-\frac{z^2}{4\theta_w}\right) \sin(2\theta_w + \psi) \tag{14a}$$

$$\tilde{v} = \frac{A}{\sqrt{\pi \theta_w}} \exp\left(-\frac{z^2}{4\theta_w}\right) \cos(2\theta_w + \psi) \tag{14b}$$

$$w = \frac{-Az}{2\sqrt{\pi}\theta_w^{3/2}} \exp\left(-\frac{z^2}{4\theta_w}\right) \cos(2\theta_w + \psi) \tag{14c}$$

where θ_w is the angle in the wake, measured from a virtual origin near the trailing edge

$$\theta_w = \theta - \theta_s + \phi \tag{15}$$

and A, ψ, ϕ are constants, to be determined from the near wake. Note: the angle between the perturbation velocity components u and $\tilde{v}$ changes with θ_w, but at given θ_w it is independent of z (unlike the Ekman layer); the attenuation of u and $\tilde{v}$ in equations (14*a*,*b*) is of the form $1/\sqrt{\theta_w}$, as in two-dimensional flow (e.g., [10, 11]) modified by the trigonometric terms in θ_w, which represent a three-dimensional effect. Thus, since $(\theta_w)_{\max} < 2\pi$, the lower bound for the attenuation of the wake from the trailing edge until it meets the leading edge again is $1/\sqrt{2\pi}$, which is relatively weak.

For the near wake, we integrate equations (2)–(4) with the boundary conditions (5*b*), (6) to obtain the momentum-integral equations

$$3\int_0^\infty dz u^2 + \int_0^\infty dz(1 - v^2) + \frac{d}{d\theta}\int_0^\infty dz uv = 0 \tag{16a}$$

$$4\int_0^\infty dz uv - 2\int_0^\infty dz u + \frac{d}{d\theta}\int_0^\infty dz(v^2 - v) = 0 \tag{16b}$$

with the subsidiary conditions at the midplane

$$\left[u^2 + v\frac{\partial u}{\partial \theta} - v^2 + 1 - \frac{\partial^2 u}{\partial z^2}\right]_{z=0} = 0 \tag{16c}$$

$$\left[2uv + v\frac{\partial v}{\partial \theta} - \frac{\partial^2 v}{\partial z^2}\right]_{z=0} = 0 \tag{16d}$$

These equations were solved by assuming the functional forms

$$u = f(\theta)\Phi(z/\delta) \tag{17a}$$

$$v = 1 + g(\theta)\Phi(z/\delta) \tag{17b}$$

where $\delta = \delta(\theta)$, $\Phi(z=0) = 1$, $\Phi(z \to \infty) \to 0$, and $(\partial\Phi/\partial z)_{z=0} = 0$. Once $\Phi(z/\delta)$ is assumed, the problem is reduced to finding the three unknown functions $\delta(\theta)$, $f(\theta)$, $g(\theta)$, by using three of the four equations (16*a–d*). The initial conditions for the momentum-integral problem, at $\theta = \theta_s^+$, are determined from the flow profiles of the boundary layer over the trailing edge of the solid sector, at $\theta = \theta_s^-$.

For the function $\Phi(z/\delta)$ two alternate forms were assumed: (1) $\Phi(z/\delta) = \exp[-(z/\delta)^2]$, motivated by the far-wake solution, and (2) $\Phi(z/\delta) = 1/2\,[1 + \cos(\pi z/\delta)]$ for $z \le \delta$ and $\Phi(z/\delta) = 0$ for $z > \delta$, used for comparison with (1) as a check of the momentum-integral approach. Since only three of the four equations (16*a–d*) are needed, solutions were attempted with (16 *a*,*b*,*c*) and with (16 *b*,*c*,*d*). It was found that the first combination gave some trouble in regions where

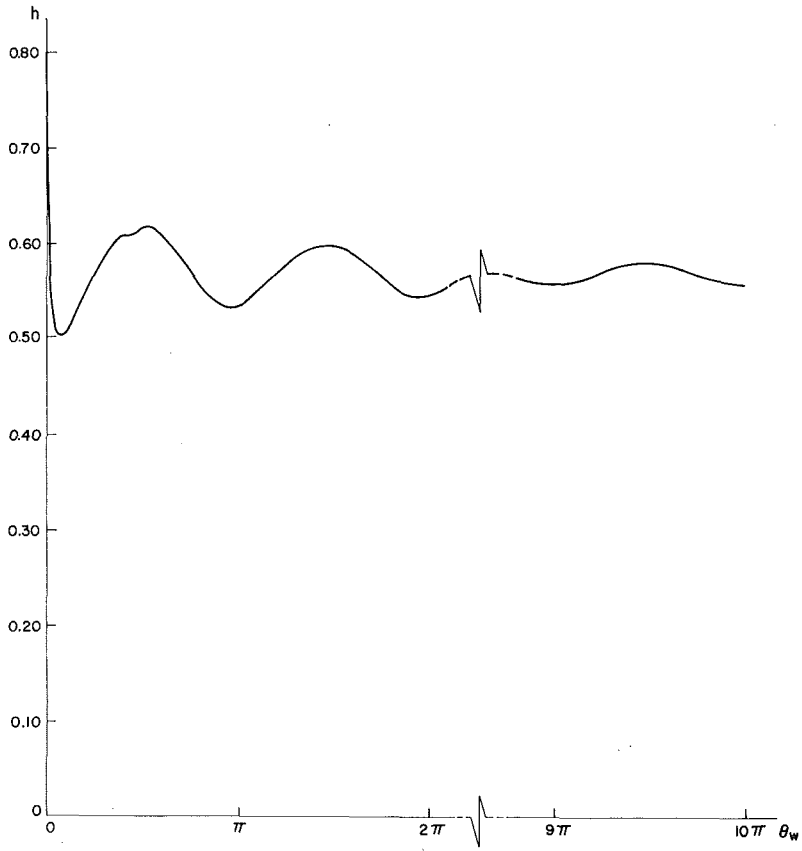


Fig. 4 The function $h(\theta)$ [equation (18)] in the wake of a narrow sector $\theta_s = 0.2$

Downloaded 01 May 2010 to 171.66.16.249. Redistribution subject to ASME license or copyright; see http://www.asme.org/terms/Terms_Use.cfm

$f(\theta)$ approached zero, whereas the second combination gave smooth results in all cases.

Though the initial behavior of the near wake is dependent on the initial conditions, at sufficiently large θ the wake should asymptotically approach the far-wake solution (14 *a–c*). Bearing this in mind, we define a variable

$$h^2(\theta) = \left(\int_0^\infty dzu\right)^2 + \left[\int_0^\infty dz(1-v)\right]^2 \tag{18}$$

In the far wake integration of (14 *a,b*) yields $h(\theta) = A =$ const. Thus, the function $h(\theta)$ obtained from the momentum-integral solution of the near wake should, for large θ, approach a constant value, A. Further comparison with the far wake (14 *a,b*) predicts that for large θ the near wake solution should approach $\delta(\theta) \propto \theta_w^{1/2}$, and $f(\theta)\theta_w^{1/2}$, $g(\theta)\theta_w^{1/2}$ should approach oscillatory functions with period π and constant amplitude. Numerical results, given in the following section, show that this is indeed so.

5 Matching Over the Complete Circle

Having discussed the leading terms of the flows over the solid segment and the wake, we outline the matching of these, to a first approximation, over the complete circle. We consider two extreme cases: (1) a narrow-angle sector ($\theta_s < 0.2$) such that the boundary layer at the trailing edge is nearly Blasius, and (2) a wide-angle sector ($\theta_s > 1$) such that the boundary layer at the trailing edge is Bodewadt.

5.1 Narrow Angle Sector. Assuming undisturbed flow at the leading edge, the velocity components at the trailing edge θ_s are approximately:

$$v_s \simeq v_0(\eta_s) \tag{19a}$$

$$u_s \simeq \theta u_0(\eta_s) \tag{19b}$$

where

$$\eta_s = z\theta_s^{-1/2} \tag{19c}$$

and u_0, v_0 are defined in (10). From these, we obtain the integrals

$$\int_0^\infty dz(v^2 - v) = -0.664\theta_s^{1/2}, \quad \int_0^\infty dzuv = -0.866\theta_s^{3/2},$$

$$\text{and} \quad \int_0^\infty dz(1-v) = 1.72\theta_s^{1/2},$$

which are now used to obtain the initial conditions for $\delta(\theta)$, $f(\theta)$, and $g(\theta)$ at $\theta = \theta_s^+$. The momentum-integral equations were integrated from $\theta - \theta_s = 0$ to 10π for several values of θ_s. (Clearly, $\theta - \theta_s \leq 2\pi$ in physical space, but the integration was continued further to check the asymptotic approach to the far-wake solution.) Typical results for $h(\theta)$ are shown in Fig. 4. It may be seen that, as expected, $h(\theta)$ exhibits a short initial transient and then approaches, in an oscillatory manner, a constant value, which can be identified with A in the far-wake solution. Repeating this computation for different values of θ_s, we obtain $A(\theta_s)$, shown in Fig. 5. To further check the asymptotic behavior, a graph of $\delta\theta_w^{-1/2}$ versus θ_w, assuming $\phi = 0$, was drawn (not shown). Here again, after a short transient, the product $\delta\theta_w^{-1/2}$ tends in an oscillatory manner to a constant (qualitatively similar to Fig. 4). Finally, graphs of $f(\theta)\theta_w^{1/2}$ and $g(\theta)\theta_w^{1/2}$ (Fig. 6) show, after an initial transient, the expected oscillatory behavior with period π and constant amplitude.

The result of these computations is that for $\theta_s \lesssim 0.2$ the far-wake solution is a good approximation for $\theta_w \gtrsim \pi$. Therefore, returning to the complete problem, the far wake can be used to estimate the perturbation of the incoming flow at the leading edge of the solid sector. Now, since for $\theta_s \lesssim 0.2$ $A \lesssim 0.6$ (Fig. 5), and at the leading edge $\theta_w = 2\pi - \theta_s$, we

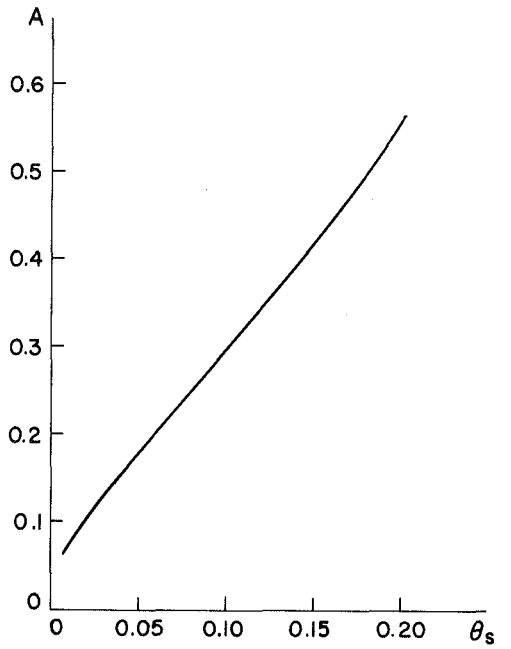


Fig. 5 Amplitude of far wake of narrow sector of angle θ_s

obtain from (14*b*) $|\tilde{v}| \leq 0.6/\sqrt{\pi(2\pi - 0.2)} \simeq 0.1$. Taking this to be the maximum value of the leading edge disturbance which may still be neglected, we obtain the result that for a narrow sector with $\theta_s \lesssim 0.2$ the effect of the wake on the leading edge is not significant. Thus, to the leading order, the flow over the complete circle with a narrow-angle solid sector can be represented by the Blasius series (9 *a*, *b*, *c*) for undisturbed oncoming flow and by the wake (16), (14), with constants obtained from (19).

5.2 Wide Angle Sector. When the solid sector angle is sufficiently large (approximately $\theta_s > 1$) the flow at the trailing edge is Bodewadt, *independent of* θ_s,

$$u_s \simeq F(z) \tag{20a}$$

$$v_s \simeq G(z) \tag{20b}$$

where F, G are the Bodewadt functions [1, 2]. Proceeding as before, we first compute the integrals

$$\int_0^\infty dz(v^2 - v) = -0.376,$$

$$\int_0^\infty dzuv = -0.536,$$

and

$$\int_0^\infty dzu = -0.685$$

and use these as initial conditions to integrate the momentum–integral equations from $\theta - \theta_s = 0$ to 10π. The solution exhibits the same features as in the narrow-angle case described above: for large θ, $h(\theta) \to$ const, $\delta(\theta)\theta_w^{-1/2} \to$ const, and $f(\theta)\theta w^{-1/2}$ and $g(\theta)\theta_w^{-1/2}$ are oscillatory with period π and constant amplitude. The far-wake solution is approached to within less than 10 percent error at $\theta_w^{-1/2} \simeq \pi$. The result for the constant A is $A \simeq 0.96$ (independent of θ_s). Hence, the velocity components at the far end of the wake $\theta_w = 2\pi - \theta_s$, i.e., the oncoming flow at the leading edge, are

$$u = \frac{0.96}{\sqrt{\pi(2\pi - \theta_s)}} \exp\left(-\frac{z^2}{4(2\pi - \theta_s)}\right) \sin[2(2\pi - \theta_s) + \psi] \tag{21a}$$

$$\tilde{v} = \frac{0.96}{\sqrt{\pi(2\pi - \theta_s)}} \exp\left(-\frac{z^2}{4(2\pi - \theta_s)}\right) \cos[2(2\pi - \theta_s) + \psi] \tag{21b}$$

Downloaded 01 May 2010 to 171.66.16.249. Redistribution subject to ASME license or copyright; see http://www.asme.org/terms/Terms_Use.cfm

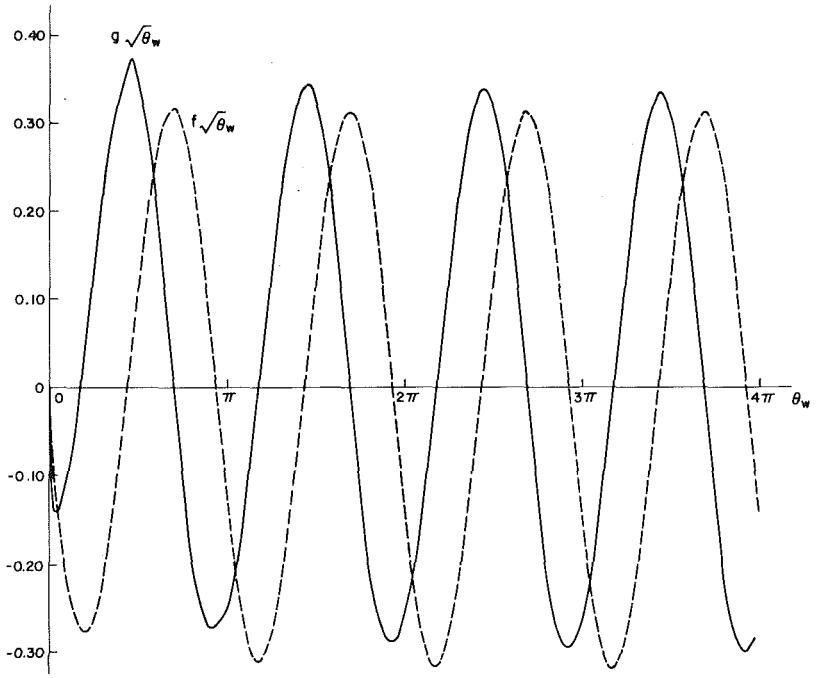


Fig. 6 The functions $f(\theta)\theta_W^{1/2}$, $g(\theta)\theta_W^{1/2}$ in the wake of a narrow sector $\theta_s = 0.2$

In particular, the values at the midplane $z = 0$ are

$$u_{z=0} = \frac{0.96}{\sqrt{\pi(2\pi - \theta_s)}} \sin(-2\theta_s + \psi) \tag{22a}$$

$$v_{z=0} = \frac{0.96}{\sqrt{\pi(2\pi - \theta_s)}} \cos(-2\theta_s + \psi) \tag{22b}$$

To the leading approximation we now have near the leading edge a three-dimensional boundary layer due to a cross flow. Now the leading term of u is $0(1)$ and both u and v are, to the leading order, Blasius scaled by $u_{z=0}$, $v_{z=0}$ from (22*a*) and (22*b*). It may be noted that the deviation from the solution based on "undisturbed oncoming flow" is not negligible. Intuitively, the main effect will be that downstream of the leading edge the Bodewadt flow will be reached sooner, i.e., for values of θ smaller than with the undisturbed flow. The calculation of further terms of the leading edge solution due to the wake-disturbed flow, which has not been attempted here, would be a significant continuation of the present work. It should be noted that the analogous problem in two-dimensional flow, viz., the *near-leading-edge* solution of the flow in a flat-plate boundary layer in the wake of another plate, is an unsolved problem. (The available solutions [12, 13] refer to the *far-downstream* effect of the wake on the boundary layer.)

6 Concluding Remarks

We have shown that the non-axisymmetric rotating flow over a plate sector can be analyzed in terms of a perturbed Blasius boundary layer, a Bodewadt layer, and a rotating wake, cyclically merging into one another over the circumference of the circle. It appears that for plate sector angle $\theta_s \lesssim 0.2$ the boundary layer at the trailing edge is perturbed Blasius and the recursive effect of the far wake on the plate boundary layer is small. Conversely, for plate sector angle $\theta_s \gtrsim 1.0$ the boundary layer at the trailing edge is nearly Bodewadt, and the recursive effect of the far wake on the plate boundary layer cannot be neglected. The results obtained, which are qualitative or exact to the leading order, can be used as starting values for numerical integration of the full problem.

The problem outlined here can be further extended for the case when the plate sector also rotates (either linear or nonlinear problem), or for a plate sector of finite radius.

Acknowledgment

This research was partially supported by the Technion Fund for the Encouragement of Research, Grant 030-278.

References

1 Bodewadt, U. T., "Die Drehstromung uber festem Grunde," *Zeitschrift fur angewandte Mathematik und Mechanik*, Vol. 20, 1940, pp. 241–253.

2 Rogers, M. H., and Lance, G. N., "The Rotationally Symmetric Flow of a Viscous Fluid in the Presence of an Infinite Rotating Disk," *Journal of Fluid Mechanics*, Part 4, Vol. 7, 1960, pp. 617–631.

3 Rogers, M. H., and Lance, G. H., "The Boundary Layer on a Disc of Finite Radius in a Rotating Fluid," *Quarterly Journal of Mechanics and Applied Mathematics,* Part 3, Vol. 17, 1964, pp. 319–330.

4 Miyake, Y., and Fujita, S., "A Laminar Boundary Layer on a Rotating Three-dimensional Blade," *Journal of Fluid Mechanics*, Part 3, Vol. 65, 1974, pp. 481–498.

5 Morris, P. J., "The Three-dimensional Boundary Layer on a Rotating Helical Blade," *Journal of Fluid Mechanics* (to be published).

6 Mager, A., and Hansen, A. G., "Laminar Boundary Layer Over Flat Plate in a Flow Having Circular Streamlines," *NACA TN* No. 2658, 1952.

7 Loos, H. G., "A Simple Laminar Boundary Layer With Secondary Flow," *Journal of the Aeronautical Sciences*, Vol. 22, 1955, pp. 35–40.

8 Rosenhead, L., *Laminar Boundary Layers*, Oxford University Press, 1963, p. 456.

9 Goldstein, S., "Concerning Some Solutions of the Boundary Layer Equations in Hydrodynamics," *Proceedings of the Cambridge Philosophical Society*, Part, 1, Vol. 26, 1930, pp. 1–30.

10 Goldstein, S., "On the Two-dimensional Steady Flow of a Viscous Fluid Behind a Solid Body. Part I," *Proceedings of the Royal Society*, Vol. A142 1933, pp. 545–562.

11 Schlichting, H., *Boundary Layer Theory*, 7th Edition, McGraw-Hill, 1979, p. 175.

12 Stewartson, K., "On Asymptotic Expansions in the Theory of Boundary Layers," *Journal of Mathematics and Physics*, Vol. 36, 1957, pp. 173–191.

13 Libby, P. A., and Fox, H., "Some Perturbation Solutions in Laminar Boundary Layer Theory. Part 1. The Momentum Equation," *Journal of Fluid Mechanics*, Part 3, Vol. 17, 1963, pp. 433–449.

Downloaded 01 May 2010 to 171.66.16.249. Redistribution subject to ASME license or copyright; see http://www.asme.org/terms/Terms_Use.cfm

J. S. Lai
Professor of Civil Engineering,
Georgia Institute of Technology,
Atlanta, Ga. 30332

W. N. Findley
Professor of Engineering,
Box D—Engineering,
Brown University,
Providence, R. I. 02912
Fellow ASME

Simultaneous Stress Relaxation in Tension and Creep in Torsion of 2618 Aluminum at Elevated Temperature

Experiments are reported for stress relaxation and simultaneous stress relaxation and creep with proportional and nonproportional loading and unloading. Results were compared with predictions of a viscous-viscoelastic theory, and modifications, and strain hardening. Predictions were calculated from results of combined constant-stress tension and torsion creep and recovery tests only, which were reported previously. Results showed that a modified viscous-viscoelastic theory predicted all the observed features and predicted the creep and relaxation rates reasonably well.

Introduction

The literature on the time-dependent behavior of metals at elevated temperature mostly deals with creep under uniaxial stress states. Next most numerous are perhaps the works on stress relaxation under simple stress states and least numerous creep under multiaxial stress states. A few have also considered predicting stress relaxation behavior from creep under the same stress state (mostly uniaxial tension). Selected references to the previous investigations of time-dependent behavior of metals under multiaxial stress are given in [1, 2]. No prior work on simultaneous creep and stress relaxation of metals has been found in the literature. The only investigation of simultaneous creep and relaxation was performed by the authors [3, 4] on full density polyurethane.

In previous papers [1, 5, 6] the authors investigated the creep behavior of 2618 aluminum at 200°C (392°F) under combined tension and torsion at moderate stresses. In the first paper the authors developed constitutive equations to describe the creep behavior of the material under multiaxial stress states. The constitutive equations employed five strain components: linear elastic ϵ^e; time-independent plastic ϵ^p; time-dependent positive nonrecoverable ϵ^v_{pos}; and time-dependent negative nonrecoverable ϵ^v_{neg}; time-dependent recoverable ϵ^{ve}. From creep and recovery experiments under combined tension and torsion, the time and stress dependence of these components were evaluated [1] for constant stress. In [5, 6] the constitutive relations developed for a constant stress state were extended for time-dependent stress histories. The extended constitutive equations were used to predict the creep behavior of the material for combined tension and torsion and under varying stress history, including stepup and stepdown stress changes and repeated reversal of shearing stress with and without constant tension. Paper [5] dealt with simple stress states while paper [6] dealt with combined tension and torsion stress states.

In the present paper, experiments involving simultaneous stress relaxation in tension and creep in torsion at moderate stress (strain) levels are reported and discussed. These experiments were performed on the same lot of 2618 aluminum as the experiments in [1, 5, 6]. Methods of predicting simultaneous creep in torsion and stress relaxation in tension from the constitutive equations developed in papers [1, 5, 6] are presented in the present paper. Predictions of stress relaxation and creep under combined tension and torsion stress states using the proposed methods were computed and compared with the experimental results.

Test Material

An aluminum forging alloy 2618-T61 was employed in these experiments. Specimens were taken from the same lot of 63.5 mm (2 1/2 in.) dia forged rod as used in [1, 5, 6] and the same lot as specimen D-H in [7]. Specimens were thin-walled tubes having outside diameter, wall thickness, and gage length of 25.4, 1.52, and 101.6 mm (1.0, 0.060, and 4.00 in.), respectively. A more complete description of material and specimen is given in [1].

Experimental Apparatus and Procedure

The combined tension and torsion creep machine used for the experiments was described in [8] and briefly in [1]. Tension was applied by means of dead weights through a lever. A system of counterbalances permitted torque in either sense to be applied by adding or removing weight from a lever. The tensile and shear strains were monitored by using an extensometer whose sensitivity was 1×10^{-6} and 1.5×10^{-6} for tensile and tensor shear strain, respectively. During a stress relaxation test, the tensile strain was maintained constant by means of a servomechanism whose input was the

Contributed by the Applied Mechanics Division for publication in the JOURNAL OF APPLIED MECHANICS.

Discussion on this paper should be addressed to the Editorial Department, ASME, United Engineering Center, 345 East 47th Street, New York, N. Y. 10017, and will be accepted until two months after final publication of the paper itself in the JOURNAL OF APPLIED MECHANICS. Manuscript received by ASME Applied Mechanics Division, November, 1980; final revision, July, 1981.

Copyright © 1982 by ASME
Downloaded 01 May 2010 to 171.66.16.249. Redistribution subject to ASME license or copyright; see http://www.asme.org/terms/Terms_Use.cfm

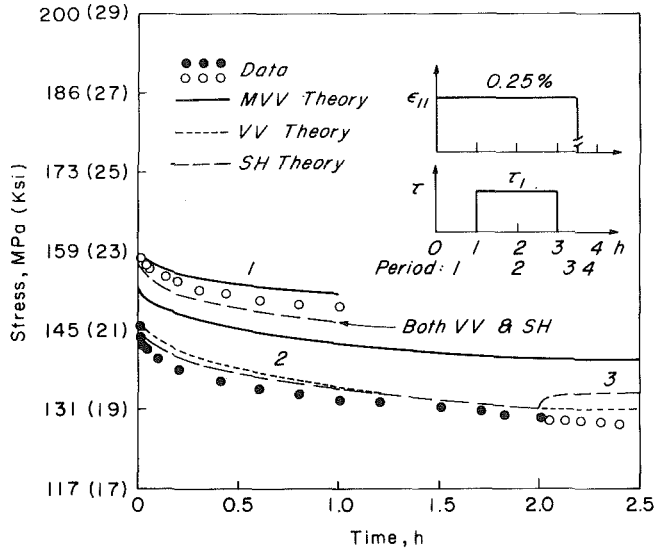


Fig. 1(*a*) Stress relaxation in tension with and without added torsion; τ_1 = 79.63 MPa (11.55 ksi)

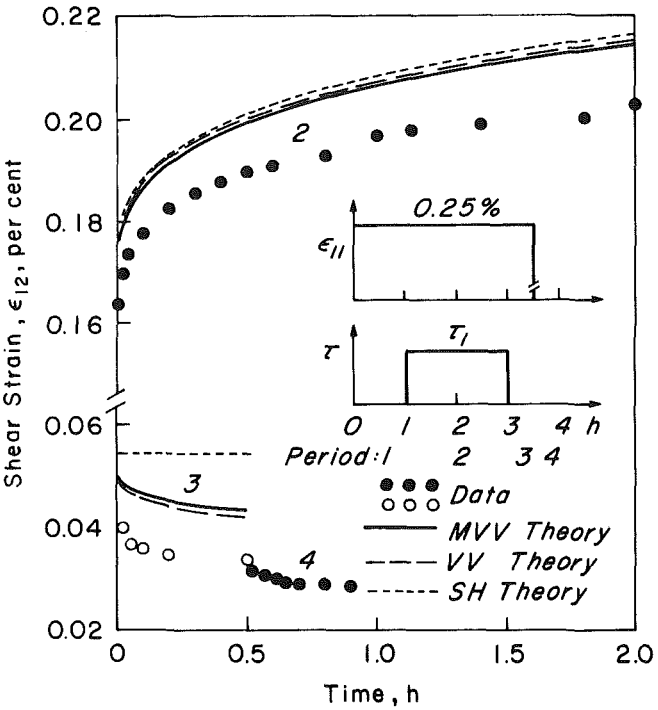


Fig. 1(*b*) Creep in torsion during stress relaxation in tension; τ_1 = 79.63 MPa (11.55 ksi)

difference between the voltage generated from the desired strain level and that from the actual strain response. The output from the servocontroller drove a servovalve which controlled the flow of hydraulic fluid from the pump to a hydraulic cylinder connected in series with a load cell and loading lever. The load applied to the specimen was measured by the load cell to a sensitivity of 9 g (0.02 lb).

The specimen was heated internally by a quartz-tube radiant-heating lamp and externally by two resistance heaters at the ends just outside the gage length. The details of temperature control for the experiment were described in [1, 7]. Measurements made during the experiments indicated a temperature variation of $\pm 0.6°C$ ($\pm 1°F$) both with time and with position along the gage length of the specimen.

After the setup, the specimen was soaked at the test temperature of 200°C for approximately 18 hr prior to testing. The influence of aging on the experimental results discussed in [1, 5] indicated that during the testing time of the experiments reported the creep rate increased about 1/2 percent per hr.[1]

Experimental Results

The results of four combined tension relaxation and torsion creep experiments are shown in Figs. 1–4. The loading and straining programs for each test are shown in inserts on each figure. The "periods" shown are the intervals between load changes, all of which occurred on the hour or half hour, except for periods 4–8, Fig. 2, which were 12 min periods. New time origins are shown for many periods so that data may be properly shown.

In Fig. 1(*a*) a constant tensile strain was maintained in period 1 and a typical stress relaxation curve was observed. In periods 2 and 3, Fig. 1, a constant torque was added and removed while the tensile strain was kept constant. In period 2, Fig. 1(*a*), a new primary-type relaxation occurred. The rate of the stress relaxation continued unchanged into period 3 upon removal of the torque. In Fig. 1(*b*), the usual shape of creep and recovery behavior was observed for the shear strain for periods 2 and 3. In the fourth period, Fig. 1, the tensile stress (not the strain) became zero. The reason that the specimen did not recover at zero strain was that the testing machine was not designed to take the compressive force which would have been required.

The experiment in Fig. 2 involved simultaneously applying constant strain in tension and constant shearing stress in torsion in the first period. Stress relaxation in tension and creep in torsion was observed as shown in Figs. 2(*a*) and 2(*b*), respectively. In the second period, Fig. 2, the shearing stress was increased about 10 percent while the tensile strain remained constant. The results shown indicate that both the stress relaxation and creep behaviors in period 2 continued without significant change in character from the first period. In period 3, the tensile strain was kept constant while the shearing stress was removed. The rate of stress relaxation in period 3, Fig. 2(*a*) continued essentially unchanged from that in period 2. The usual recovery of the shear strain in period 3, Fig. 2(*b*) was observed. In the subsequent periods, a constant shearing stress was repeatedly added and removed three times while the tensile strain was kept constant. In Fig. 2(*a*), periods 4, 6, and 8, (when the shearing stress was on), the stress relaxation behaved as if the shear stress were on continuously from period 4 to 8 (not influenced by the intervals of unloading). Period 5 showed a continued relaxation while period 7 showed a rebound in stress. Other instances of rebound occurred in periods 3 and 5, Fig. 3(*a*). In Fig. 2(*b*), the successive loadings in periods 4, 6, and 8 resulted in decreasing creep rates. In periods 5 and 7, recovery was observed.

In Fig. 3 the first three periods are similar to those of Fig. 1(*a*) except for a higher tensile strain (0.29 percent). The responses of the first three periods in this test were very similar to those shown in Fig. 1. In periods 4 and 5, a constant shearing stress (greater than the shearing stress in period 2) was added and removed. A rapid stress relaxation was observed in period 4, Fig. 3(*a*), while a small increase in stress was observed in periods 3 and 5. The results in period 4 of Fig. 3(*a*) and period 4 of Fig. 2(*a*) indicate that upon reloading in torsion to a higher value while keeping the tensile strain

[1] Two creep tests aged 312 hr, one in tension and one in torsion performed on a different lot of 2618-T61 aluminum since completion of this manuscript showed a decrease in creep rate with age of about 0.01 and 0.03 percent/hr for tension and torsion, respectively. Also a decrease in creep-recovery rate of 0.02 and 0.008 percent/hr was observed from the tension and torsion tests, respectively. This difference between previous results indicating an increase in creep rate and present results showing a small decrease may be due to variable material property between lots. This study of aging is continuing. See reference [9] for a treatment of aging where the effect of aging was pronounced.

Downloaded 01 May 2010 to 171.66.16.249. Redistribution subject to ASME license or copyright; see http://www.asme.org/terms/Terms_Use.cfm

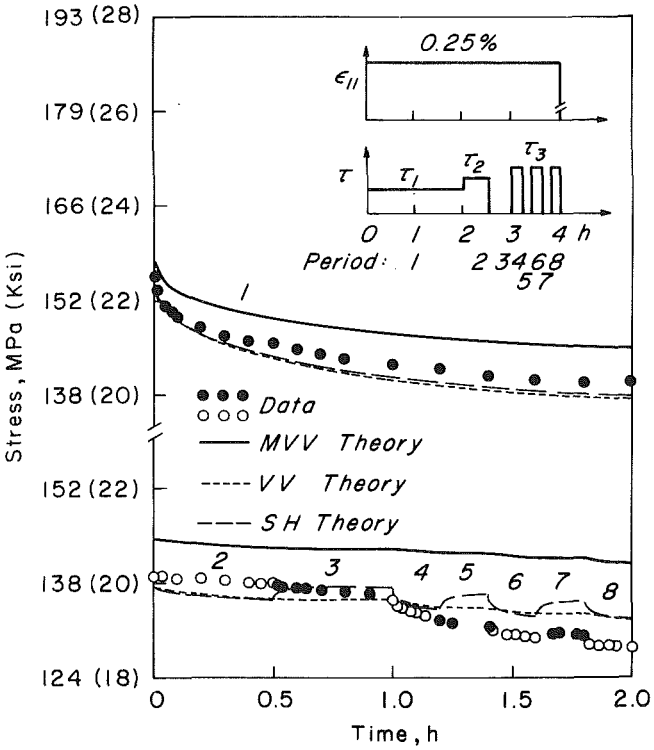


Fig. 2(*a*) Stress relaxation in tension simultaneously with a program of creep in torsion; τ_1 = 55.50 MPa (8.05 ksi); τ_2 = 61.01 MPa (8.85 ksi); τ_3 = 79.63 MPa (11.55 ksi)

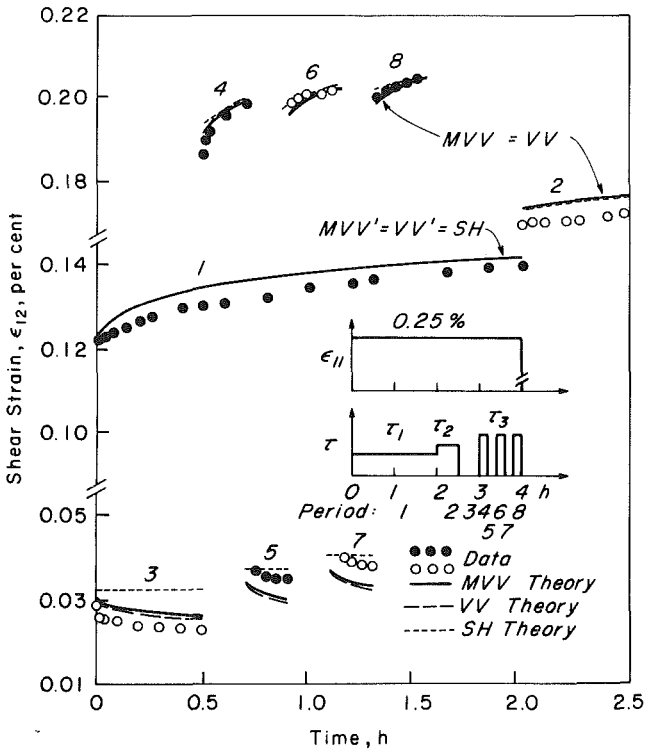


Fig. 2(*b*) Creep in torsion during stress relaxation in tension; τ_1 = 55.50 MPa (8.05 ksi); τ_2 = 61.01 MPa (8.55 ksi); τ_3 = 79.63 MPa (11.55 ksi)

constant, a rapid tensile stress relaxation resulted. On the other hand, if the reloading of torsion was to the same magnitude as in periods 6 and 8 of Fig. 2(*a*), the rate of tensile stress relaxation continued as if the shear stress was uninterrupted. In Fig. 3(*b*), periods 4 and 5 characteristic creep and recovery behavior were observed.

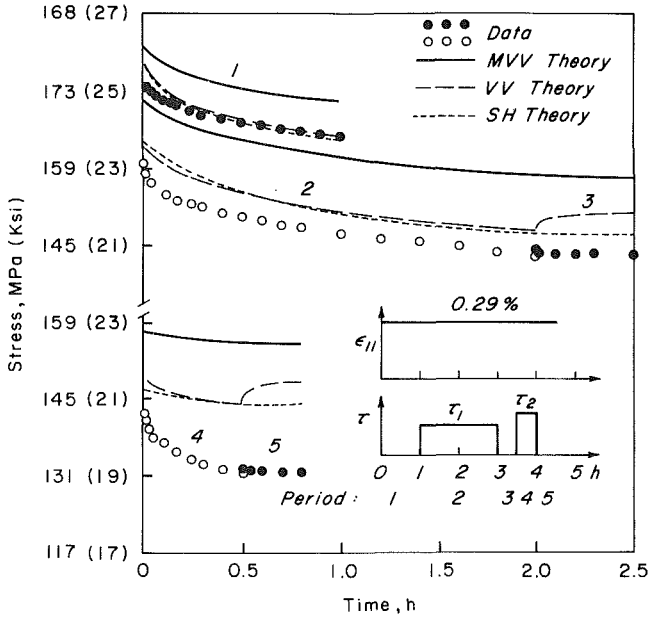


Fig. 3(*a*) Stress relaxation in tension with periods of added torsion; τ_1 = 79.63 MPa (11.55 ksi); τ_2 = 95.55 MPa (13.86 ksi)

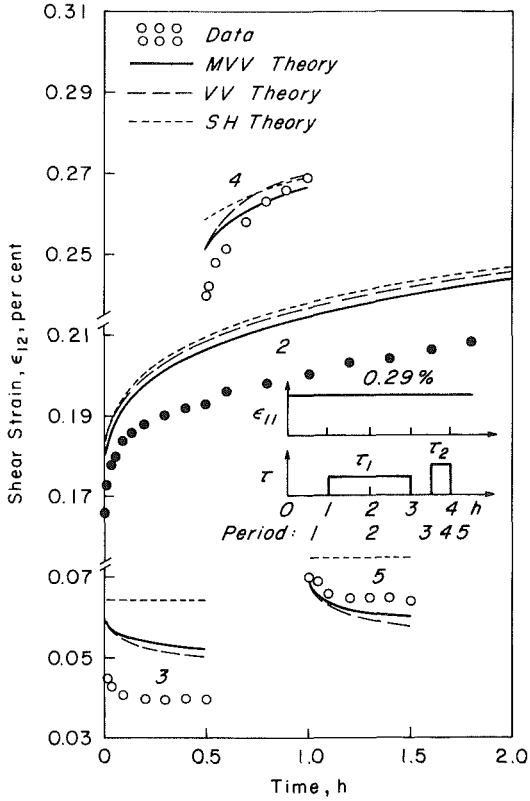


Fig. 3(*b*) Creep in torsion during stress relaxation in tension; τ_1 = 79.63 MPa (11.55 ksi); τ_2 = 95.55 MPa (13.86 ksi)

Figure 4 involved simultaneously applying constant tensile strain and shearing stress in period 1. In period 2 the tensile stress was removed while the shearing stress was kept constant. This was followed by removal of shearing stress in period 3. Characteristic stress relaxation in tension and creep in torsion were observed in period 1. In period 2, Fig. 4(*b*) upon removal of tensile "stress," the creep in torsion was continued as if no removal of tensile "stress" had occurred. In period 3, Fig. 4(*b*), a recovery in shear strain was observed. In periods 2 and 3, Fig. 4(*a*) the stress was reduced to zero rather than the strain being reduced to zero. Thus no further

Downloaded 01 May 2010 to 171.66.16.249. Redistribution subject to ASME license or copyright; see http://www.asme.org/terms/Terms_Use.cfm

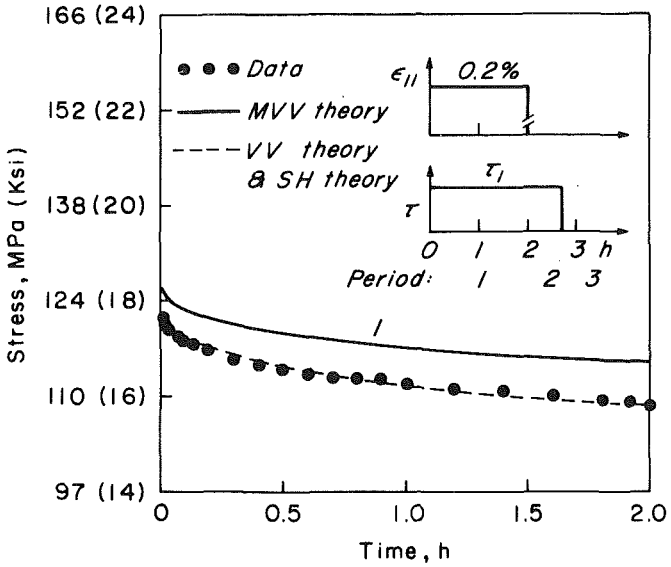


Fig. 4(a) Stress relaxation in tension simultaneously with creep in torsion; τ_1 = 79.63 MPa (11.55 ksi)

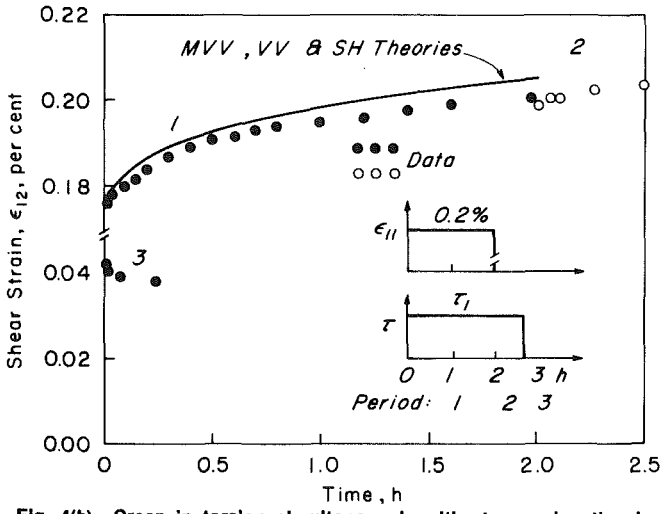


Fig. 4(b) Creep in torsion simultaneously with stress relaxation in tension; τ_1 = 79.63 MPa (11.55 ksi)

stress relaxation occurred. Instead a "creep" recovery occurred at zero stress which is not shown.

In the following sections, the constitutive equations developed in [1, 5, 6] for creep behavior of the same material are presented and used to predict the stress relaxation and creep behaviors shown in the foregoing.

Discussion of Experimental Results; Comparison With Combined Stress Creep

A comparison of the results of the present experiments on histories of variable simultaneous relaxation in tension and creep in torsion shows similar features to those found in variable combined tension and torsion creep [6]. Among these similar features are the following: (*a*) When a shearing stress τ was added to a tensile relaxation at a constant tensile strain ϵ_{11} a new "primary" type stress relaxation resulted as in period 2 Fig. 1(*a*), and periods 2 and 4, Fig. 3(*a*). (*b*) When the shearing stress τ was removed to zero while the tensile strain ϵ_{11} remained constant there was no significant change in the pattern of stress relaxation in tension as shown in period 3, Fig. 1(*a*). Similar but not as well-defined behavior is also shown in period 3, Fig. 2(*a*), and periods 3 and 5, Fig. 3(*a*). (*c*) When the tensile stress σ was changed to zero during tensile relaxation while the shearing stress remained constant the creep ϵ_{12} continued as though there had been no change; see period 2, Fig. 4(*b*) (*d*) When the tensile stress was changed to zero following constant strain relaxation while the shearing strain ϵ_{12} was recovering from prior creep at a shearing stress τ a new recovery type behavior was intitiated in ϵ_{12} as shown in period 4, Fig. 1(*b*).

Constitutive Equations for Creep Under Combined Tension and Torsion

In the previous papers [1, 5, 6] it was shown that creep of specimens of the same lot of 2618 aluminum at 200°C under combined tension and torsion were adequately described by the following relation:

$$\epsilon_{ij}(t) = \epsilon_{ij}^{e} + \epsilon_{ij}^{p} + \epsilon_{ij}^{v}(t) + \epsilon_{ij}^{ve}(t), \tag{1}$$

where ϵ_{ij}^{e}, ϵ_{ij}^{v}, and ϵ_{ij}^{ve} represent the time-independent elastic strain, time-dependent nonrecoverable (viscous) strain and time-dependent recoverable (viscoelastic) strain, respectively, and ϵ_{ij}^{v} was further resolved into positive and negative components [6]. The time-independent plastic strain ϵ_{ij}^{p} was found to be zero in the experiments. The elastic modulus E_0, shear modulus G_0, and Poisson's ratio ν for the elastic strain component ϵ^e for the material at 200°C as reported in [1, 5, 6] is given in Table 1 of reference [6]. The constitutive relations for $\epsilon_{ij}^{v}(t)$ and ϵ_{ij}^{ve} under time-dependent stresses as employed in [1, 5, 6] are reviewed in the following.

Time-Dependent Stress. Under a continuously varying stress σ, the strain response ϵ^{ve} given by the modified superposition principle (derived from the multiple integral representation) was represented for nonliner behavior in [5, 6]. For axial and shear components ϵ^{ve} becomes as follows:

$$\epsilon_{11}^{ve}(t) = \frac{R}{1+R}\int_0^t \frac{\partial}{\partial\sigma(\xi)} F[\bar{\sigma}(\xi), \bar{\tau}(\xi)](t-\xi)^n \dot{\sigma}(\xi)\,d\xi, \tag{2}$$

$$\epsilon_{12}^{ve}(t) = \frac{R}{1+R}\int_0^t \frac{\partial}{\partial\tau(\xi)} G[\bar{\sigma}(\xi), \bar{\tau}(\xi)](t-\xi)^n \dot{\tau}(\xi)\,d\xi. \tag{3}$$

The time-dependent nonrecoverable strain component ϵ^{v} was based on strain hardening [5, 6]. For axial and shear components ϵ^{v} is as follows:

$$\epsilon_{11}^{v}(t) = \frac{1}{1+R}\left[\int_0^t \{F[\bar{\sigma}(\xi), \bar{\tau}(\xi)]\}^{1/n} d\xi\right]^n, \tag{4}$$

$$\epsilon_{12}^{v}(t) = \frac{1}{1+R}\left[\int_0^t \{G[\bar{\sigma}(\xi), \bar{\tau}(\xi)]^{1/n} d\xi\right]^n. \tag{5}$$

A detailed discussion of (2)–(5) was presented in [1, 5, 6]. In (2)–(5), t is time, R is the ratio of the coefficient of the recoverable and nonrecoverable time-dependent strain terms, see reference [1]. The nonlinear functions of F and G in (2)–(5) were derived from a third-order multiple integral representation [4], where

$$F(\bar{\sigma},\bar{\tau}) = F(\sigma-\sigma', \tau-\tau') = F_1(\sigma-\sigma') + F_2(\sigma-\sigma')^2 + F_3(\sigma-\sigma')^3 + F_4(\sigma-\sigma')(\tau-\tau')^2 + F_5(\tau-\tau')^2, \tag{6}$$

$$G(\bar{\sigma},\bar{\tau}) = G(\sigma-\sigma', \tau-\tau') = G_1(\tau-\tau') + G_2(\tau-\tau')^3 + G_3(\sigma-\sigma')(\tau-\tau') + G_4(\sigma-\sigma')^2(\tau-\tau'), \tag{7}$$

and σ', τ' are the components of the creep limit. In the original formulation [1], a Tresca form, as shown in the following, was employed for the creep limits (σ' and τ') under combined tension-torsion stresses.

$$(\sigma')^2 + 4(\tau')^2 = (\sigma^*)^2 = (2\tau^*)^2$$

$$\sigma'/\sigma = \tau'/\tau \tag{8}$$

Downloaded 01 May 2010 to 171.66.16.249. Redistribution subject to ASME license or copyright; see http://www.asme.org/terms/Terms_Use.cfm

Where σ^* and τ^* are the creep limits under pure tension and pure torsion, respectively, and which were found to agree with a Tresca form, i.e., $\sigma^*/\tau^* = 2.00$, see reference [1]. The coefficients of F_i, G_i, and values of σ^*, τ^*, R, and n were derived from constant combined tension-torsion creep and recovery tests reported in [1]. The values of the coefficients corresponding to (6)–(8) were given in [1] and corrected in [5].

It was shown in [6] that using the variable creep limits σ', τ' and (8) did not predict the experimental results quite as accurately as using fixed creep limits σ^* and τ^*. In the present paper, calculations were made using the fixed creep limits, σ^* and τ^*, as well as σ', τ'.

For a series of m step changes in stress as employed in the present work, (3) and (5) become as follows for ϵ_{12} for example:

$$\epsilon_{12}^{ve}(t) = \left(\frac{R}{1+R}\right)\{G(\bar{\sigma}_1, \bar{\tau}_1)[t^n - (t-t_1)^n] + \ldots + G(\bar{\sigma}_{m-1}, \bar{\tau}_{m-1})[(t-t_{m-2})^n - (t-t_{m-1})^n] + G(\bar{\sigma}_m, \bar{\tau}_m)(t-t_{m-1})^n\}, \quad t_{m-1} < t, \tag{9}$$

$$\epsilon_{12}^{v}(t) = \left(\frac{1}{1+R}\right)\{[G(\bar{\sigma}_1, \bar{\tau}_1)]^{1/n}(t_1) + \ldots + G(\bar{\sigma}_{m-1}, \bar{\tau}_{m-1})[(t-t_{m-2})^n - (t-t_{m-1})^n] + [G(\bar{\sigma}_m, \bar{\tau}_m)]^{1/n}(t-t_{m-1})\}^n, \quad t_{m-1} < t. \tag{10}$$

Viscous-Viscoelastic (VV) Theory. The total strain following a time-dependent stress history was found according to (1) by adding to the elastic strain corresponding to the stresses existing at the time of interest the ϵ^{ve} given by (2) or (3) and the ϵ^{v} given by (4) or (5) for axial strain or shear strain.

Modified Viscous-Viscoelastic (MVV) Thoery. In [5, 6] it was found under partial unloading that the observed characteristics of creep behavior of the material were not properly predicted by the *VV* theory. It was found, however, that the *MVV* theory employed in [5] described the creep behavior of the material under partial unloading more closely than the *VV* theory. The basic difference between the *MVV* and the *VV* theories is in the treatment of the creep limits for the recoverable strain ϵ^{ve}; see reference [6] for details.

(*A*) For the *nonrecoverable strain* component ϵ^{v}, the strain hardening rule (4) and (5) was employed unless the current stress σ_C equaled or was less than the creep limit σ^* (or σ'). When $\sigma_C \leq \sigma^*$ (or σ'), the strain rate $\dot{\epsilon}^{v}$ was zero.

Upon reloading from a stress σ_C below to a stress σ_D above the creep limit, the nonrecoverable strain rate $\dot{\epsilon}^{v}$ resumed as though there had been no interval t_x for which $\sigma_C \leq \sigma^*$ (or σ').

(*B*) For the *recoverable strain* component ϵ^{ve}, on *partial unloading* from stress σ_A the recoverable strain rate $\dot{\epsilon}^{ve}$ became and remained zero unless the total change in stress from the highest stress previously encountered to the current stress equaled or exceeded in magnitude the creep limit σ^* (or σ'). When the change in stress was greater than $|\sigma^*|$ or $|\sigma'|$ then recovery would occur followed eventually by creep. Upon increasing the stresss to $\sigma_D \geq \sigma_A$ following a period t_x for which $\dot{\epsilon}^{ve} = 0$, the recoverable strain component ϵ^{ve} continued to creep in accordance with (2) or (3) as though the period t_x never occurred.

(*C*) When one *stress component decreased while the other remained constant,* the material behavior suggested that reducing or removing one stress component, say τ, while the other component, say σ, remained constant affected the *recoverable strain* ϵ^{ve} as follows. The strain corresponding to mixed stress components behaved in accordance with a small stress reduction. That is, the strain, say ϵ_{11}, associated with the mixed stress components, say $\sigma\tau^2$, τ^2, became constant. The strain, say ϵ_{11}, associated with the pure stress terms, say σ, σ^2, σ^3 which were unchanged, continued as though nothing had happened.

Strain-Hardening (SH) Theory. The total strain under this theory was represented by the following,

$$\epsilon_{11}(t) = \frac{\sigma(t)}{E} + \left[\int_0^t \{F[\bar{\sigma}(\xi), \bar{\tau}(\xi)\}^{1/n} d\xi\right]^n, \tag{11}$$

$$\epsilon_{12}(t) = \frac{\tau(t)}{2G} + \left[\int_0^t \{G[\bar{\sigma}(\xi), \bar{\tau}(\xi)^{1/n} d\xi\right]^n, \tag{12}$$

Prediction of Simultaneous Creep in Torsion and Relaxation in Tension From Combined Stress Creep Data. Since creep and stress relaxation behaviors are two aspects of time-dependent behavior of materials, one behavior should be predictable if the other behavior is known. In other words, in a "tensile stress relaxation" test for example, the stress response of a material under a constant axial strain input will be considered as equivalent to a tensile "creep" test with an undetermined time-dependent stress applied to the specimen such that a constant axial strain results throughout the testing period.

Some investigators have considered a relaxation test to be fundamentally different from a creep test; that the material has a constant strain state in relaxation compared to a changing strain state in creep. However, the strain state is not necessarily constant during a relaxation test. In an axial relaxation test only the axial strain component remains constant while the transverse strains are time-dependent [4] unless the relaxation is volume constant, which is not true in general. On the other hand, in a constant-stress creep test all stress components are constant.

The simultaneous stress relaxation in tension and creep in torsion when the specimen is subjected to constant tensile strain and constant shearing stress in torsion can be considered as one of combined tension and torsion creep with variable (time-dependent) tensile stress and constant shearing stress in torsion. The desired time-dependent tensile stress $\sigma(t)$ is unknown, but has to satisfy the condition that the tensile strain produced by the prescribed constant shearing stress and this unknown varying tensile stress $\sigma(t)$ acting together on the specimen must equal the prescribed constant tensile strain. For the *VV* theory this is equivalent to solving a nonlinear equation for $\sigma(t)$ with ϵ_{11} and $\tau(t)$ prescribed. Where the nonlinear equation was: ϵ_{11} equals the elastic strain plus equations (2) and (4). Once $\sigma(t)$ has been determined the corresponding shearing strain is readily obtained by using (3) and (5).

The iterative procedures used to solve for $\sigma(t)$ for the *VV* theory (the other theories were similar) with prescribed tensile strain $\epsilon_{11}(t)$ and shearing stress $\tau(t)$ were as follows. The prescribed $\epsilon_{11}(t)$ and $\tau(t)$ were divided into a number k of intervals of time ($m = 1, \ldots k$). In the first step the $\epsilon_{11}(1)$ and $\tau(1)$ were known. Neglecting the time-dependent responses, the initial tensile stress $S(1) = \epsilon_{11}(1)E$ was determined. With $S(1)$ and $\tau(1)$ for the first step, the $S(t_1)$ and $\tau(t_1)$ at the end of the first interval were computed. Similarly, with $S(t_{m-1})$ at the end of the $m-1$ interval, the $S(t_m)$ and $\tau(t_m)$ were determined using the entire stress history from $t = 0$ to $t = t_m$. The difference between the computed tensile strain and the prescribed tensile strain for the mth interval, $\Delta e(t_m) = e(t_m) = \epsilon_{11}(t_m)$ was computed. $\epsilon_{11}(t_m)$ represented the prescribed tensile strain at $t = t_m$. The $\Delta e(t_m)$ was used to determine the correction for the assumed tensile stress $S(t_m)$. Thus the corrected tensile stress $\sigma(t_m)$ equals $S(t_m) - [\Delta_e(t_m)]E$. The correction was based on the elastic response only. $\sigma(t_m)$ so determined represented the relaxation stress at $t = t_m$. This corrected tensile stress history $\sigma(t)$ and the prescribed

Downloaded 01 May 2010 to 171.66.16.249. Redistribution subject to ASME license or copyright; see http://www.asme.org/terms/Terms_Use.cfm

shearing stress history $\tau(t)$ for $t = 0 \rightarrow t_m$ were used to compute the shearing strain for the *VV* theory.

In the next step ($t = t_{m+1}$), the approximate tensile stress $S(t_{m+1})$ was determined by $S(t_{m+1}) = \sigma(t_m) + [\epsilon_{11}(t_{m+1}) - \epsilon_{11}(t_m)]\ E$. For a constant strain relaxation conditions, $\epsilon_{11}(t_{m+1}) = \epsilon_{11}(t_m)$, thus $S(t_{m+1}) = \sigma(t_m)$. The $S(t_{m+1})$ along with the previous tensile stress history $\sigma(t)$, and the shearing stress history $\tau(t)$ for t from 0 to t_{m+1} were used again to compute the tensile strain response $e(t_{m+1})$. From that the relaxational stress at $t = t_{m+1}$ was determined.

The procedures previously described, were employed to calculate the response of the simultaneous stress relaxation in tension and creep in torsion of 2618 aluminum at 200°C for the histories shown in Figs. 1–4. A sensitivity analysis showed that close to the region where the $\epsilon_{11}(t)$ changed abruptly a time interval greater than 0.001 hr could significantly affect the accuracy of the predictions. Consequently, in all the predictions carried out in this program, the time interval was 0.001 hr.

Comparison of Predictions With Experimental Results

Creep. As shown in Figs. 1(*b*), 2(*b*), 3(*b*), and 4(*b*), the prediction of the shearing creep component (strain ϵ_{12}) for the first application for shear stress compared well with the test data. This was true for all three theories. As noted before these predictions were based on the numerical constants determined entirely from creep and recovery tests under constant combined tension and torsion and reported in reference [1] All of these experiments in Figs. 1–4 included relaxation in tension simultaneously with the shearing creep. In Figs. 2(*b*) and 4(*b*) the creep and relaxation started simultaneoulsy, while in Figs. 1(*b*) and 3(*b*) the relaxation started before the shearing stress was added.

For subsequent periods the shearing strain was reasonably well predicted by either the *VV* or *MVV* theories, but not properly predicted by the *SH* theory when the shearing stress was removed. The *MVV* theory was lower than the *VV* theory when tensile relaxation preceded the torsion creep. No prediction was made for periods 4, Fig. 1(*b*) or periods 2 and 3, Fig. 4(*b*) because the recovery of ϵ_{11} was at constant stress rather than constant strain. The creep in period 4, Fig. 3(*b*) was not well predicted. This is consistent with the observation for combined stress creep under multiple stress changes at high stresses [6], that the predicted creep rate was too low.

Relaxation. Figures 1(*a*), 2(*a*), 3(*a*), and 4(*a*) show that the prediction of the magnitude of the tensile relaxation for the first two periods compared with the test data about as well as the comparison for the creep component of the same tests. The best comparison of magnitudes was found with the *VV* theory (the *SH* theory was usually nearly the same as the *VV* theory).

In Figs. 2(*a*) and 4(*a*) the stress relaxation and creep started simultaneously. In Figs. 1(*a*) and 3(*a*) the creep (shear stress τ) started 1 hr after the start of relaxation. In this case the predicted relaxation rate was somewhat greater than observed and not as close to the test data as in Figs. 2(*a*) and 4(*a*).

When the torque was removed while the tensile strain remained constant, the *VV* theory predicted a reversal of the relaxation which was not observed, see period 3, Fig. 1(*a*), periods 3, 5, and 7, Fig. 2(*a*), and periods 3 and 5, Fig. 3(*a*). This was due to the same feature of the theory that caused a prediction of recovery that was not observed in combined tension-torsion creep [6] when one component went to zero. The reversal of relaxation predicted by the *VV* theory was due to the fact that, upon removal of torque, the last two terms in (6) vanish. This caused a sudden drop in the tensile strain rate. In order to maintain the constant strain imposed by the test program, the tensile stress had to increase accordingly. The *SH* theory predicted no change in stress and the *MVV* theory predicted a small decreasing stress but not as much as observed in period 3, Fig. 1(*a*) for example.

General. The *MVV* theory predicted the character of all of the various features of the test results for both the creep and relaxation components. On the other hand the *VV* theory predicted a trend opposite to that observed during relaxation when the shearing stress was removed while the tensile strain remained constant. The *SH* theory failed to predict the observed recovery when the shearing stress went to zero.

Comparing the magnitudes of creep strains or relaxation stresses predicted with the observed values shows that the *MVV* theory usually predicted higher stresses in relaxation and higher strains in creep than the observed values and generally higher values than predicted by the *VV* and *SH* theories.

However, if comparison is made on the basis of time-dependence alone, that is, on the basis of creep or relaxation rate, it may be shown that in general the prediction of the *MVV* theory is the best. The *MVV* theory was best or the same in this respect as the *VV* theory in the following: Fig. 1; Fig. 2 (except Fig. 2(*a*), period 4); Fig. 3 (except Fig. 3(*a*), period 4, Fig. 3(*b*), period 4) and Fig. 4.

All curves shown in Figs. 1–4 employed variable creep limits σ', τ' (8). The use of fixed values of σ^* and τ^* for creep limits yielded differences which were sometimes improvements and sometimes not. Since fixed values of σ^*, τ^* are not applicable for stress states in which one component is below the creep limit, the results for fixed creep limits are not shown in the figures.

Conclusions

Results of experiments on simultaneous creep in torsion and relaxation in tensions were presented. These included proportional and nonproportional loading, unloading, and reloading. In general the features of the material response were similar to those observed under combined tension and torsion creep.

Three theories were used to predict the material response to the several mixed load-constraint histories tested. These predictions were made using the results of constant load creep and recovery experiments under combined tension and torsion only. Results showed that a modified viscous-viscoelastic (*MVV*) theory predicted all the observed features and in general had the best prediction of creep and relaxation rates.

Acknowledgment

This work was supported by the Army Research Office Research Grant No. DAAG29-79-G-0185. The material was contributed by the Aluminum Company of America. The authors are grateful to C. Kang for performing the experiments and P. C. Capece for typing the manuscript.

References

1 Findley, W. N., and Lai, J. S., "Creep and Recovery of 2618 Aluminum Alloy Under Combined Stress With a Representation by a Viscous-Viscoelastic Model," ASME JOURNAL OF APPLIED MECHANICS, Vol. 45, Sept. 1978, pp. 507–514.

2 Findley, W. N., Cho, U. W., Ding, J. L., "Creep of Metals and Plastic Under Combined Stresses, A Review," ASME *Journal of Engineering Materials and Technology*, Vol. 101, 1979, p. 365.

3 Lai, J. S., and Findley, W. N., "Behavior of Nonlinear Viscoelastic Material Under Simultaneous Stress Relaxation in Tension and Creep in Torsion," ASME JOURNAL OF APPLIED MECHANICS, Vol. 36, 1969, pp. 22–27.

4 Findley, W. N., Lai, J. S., and Onaran, K., *Creep and Relaxation of Nonlinear Viscoelastic Materials*, North-Holland Publishers, 1976.

5 Lai, J. S., and Findley, W. N., "Creep of 2618 Aluminum Under Step Stress Changes Predicted by a Viscous-Viscoelastic Model," ASME JOURNAL OF APPLIED MECHANICS, Vol. 47, Mar. 1980, pp. 21–26.

6 Findley, W. N., and Lai, J. S., "Creep of 2618 Aluminum Under Side Steps of Tension and Torsion and Stress Reversal Predicted by a Viscous-

Downloaded 01 May 2010 to 171.66.16.249. Redistribution subject to ASME license or copyright; see http://www.asme.org/terms/Terms_Use.cfm

Viscoelastic Model," ASME JOURNAL OF APPLIED MECHANICS, Vol. 48, 1981, pp. 47–54.

7 Blass, J. J., and Findley, W. N., "Short-Time Biaxial Creep of an Aluminum Alloy With Abrupt Changes of Temperature and State of Stresses," ASME JOURNAL OF APPLIED MECHANICS, Vol. 38, 1971, pp. 489–501.

8 Findley, W. N., and Gjelsvik, A., "A Biaxial Testing Machine for Plasticity, Creep or Relaxation Under Variable Principal-Stress Ratios," *Proceedings, American Society for Testing and Materials,* Vol. 62, 1962, pp. 1103–1118.

9 Cho, U. W., and Findley, W. N., "Creep and Creep Recovery of 304 Stainless Steel at Low Stresses and Effects of Aging," ASME JOURNAL OF APPLIED MECHANICS, Vol. 48, 1981, pp. 785–790.

Downloaded 01 May 2010 to 171.66.16.249. Redistribution subject to ASME license or copyright; see http://www.asme.org/terms/Terms_Use.cfm

A Nonlinear Model for the Dynamics of Penetration Into Geological Targets[1]

F. R. Norwood
Mem. ASME

M. P. Sears

Computational Physics and Mechanics
Division II-5533,
Sandia National Laboratories,[2]
Albuquerque, N. M. 87185

A general theory is developed for predicting stress and force histories for normal impact and penetration of geological targets by conical-nosed projectiles. To account for general material properties, the target medium is described by arbitrary hydrostat and shear failure-pressure relations. Using the cylindrical cavity approximation, the penetration dynamics reduce to a problem of radially symmetric stress wave propagation involving a nonlinear, ordinary, differential equation in terms of similarity variables. This equation is solved numerically by a shooting technique which is initiated by asymptotic values at the wave front. Numerical results are given for the stresses on the penetrator nose for some specific material models.

1 Introduction

For the study of penetration events by approximate analytical techniques, Norwood [1] introduced the concept of cylindrical cavity expansion (CCE). This concept, which was based on the spherical expansion theory [2], has recently been applied to predict penetration depth, penetrator deceleration history, and stresses on the penetrator nose [3-6]. For the purposes of the present paper, it is important to emphasize that, in addition to the assumption inherent in CCE, these references rely on fairly restrictive constitutive assumptions. Specifically, in references [1, 2, 4, and 6], the target material is assumed to be a locking solid which may be compacted to a critical (locking) density with a minimum of pressure, and further compaction is difficult to effect. Snow, soil, and porous media are examples of materials for which the concept of locking seems to be a reasonable assumption. In reference [3], for the hydrostatic relation, the pressure may be a linear or quadratic function of the volumetric strain, while for the shear failure curve the maximum principal stress difference is assumed to increase with pressure until the von Mises limit is reached and to remain constant thereafter. In reference [5], the target medium is described by a linear hydrostat and a linear shear failure-pressure relation.

The material laws employed in references [1-6] apply only to a limited number of geologic materials and hence it is necessary to develop a theory for arbitrary material laws. This will be done by extending the work [5] for conical-nosed penetrators. As was done in [5], a similarity solution is obtained, but without the need for simplified or restricted material laws. Thus, it is hoped that, by the generality of the constitutive assumptions, the results of the present paper will be applicable to a wide variety of geological targets.

2 Preliminaries

The main purpose of this section is to provide a brief description of the CCE method as it is applied to the problem of penetration [1, 3-6]. In CCE, penetration is assumed to be normal and axisymmetric. It is further assumed that, during penetration, particle motion in the medium is strictly radial and determined by the shape and speed of the projectile. As shown in Fig. 1, the target material is separated into infinitesimal layers. In each layer, a cylindrical cavity is created by the downward motion of the penetrator. The resulting stress on the cavity is used to compute a force on the penetrator at each layer's location. This force is interpreted as the radial component of the total force on the penetrator. More specifically, using a cylindrical coordinate system, with the z-axis along the axis of the penetrator, if the penetrator radius is given by $R(z)$, then the incremental radial ring force on the nose for a thin layer with thickness dz is given by $dF_r = \sigma_{rr}(z)2\pi R(z)dz$, where σ_{rr} is the radial component of stress at the cavity wall. Assuming only a normal force and no surface friction, it follows that the incremental axial force acting on the penetrator is given by

$$dF_z = \frac{dR}{dz}\ dF_r = \sigma_{rr}(z)2\pi R(z)\frac{dR}{dz}dz$$

Thus, to evaluate F_z, it remains to determine the radial component of stress from the present theory.

3 Problem Statement

Using a cylindrical Lagrangian system of coordinates, consider the symmetric expansion of a cylindrical cavity. It will be assumed that the displacements u_z and u_θ vanish everywhere with the displacement u_r independent of z. These assumptions imply a state of plane strain in which the nonzero quantities of interest are

[1] This work was supported by the U.S. Department of Energy under Contract DE-AC04-76-DP00789.

[2] A U.S. Department of Energy facility.

Contributed by the Applied Mechanics Division for publication in the JOURNAL OF APPLIED MECHANICS.

Discussion of this paper should be addressed to the Editorial Department, ASME, United Engineering Center, 345 East 47th Street, New York, N. Y. 10017, and will be accepted until two months after final publication of the paper itself in the JOURNAL OF APPLIED MECHANICS. Manuscript received by ASME Applied Mechanics Division, June, 1981; final revision, October, 1981.

Copyright © 1982 by ASME
Downloaded 01 May 2010 to 171.66.16.249. Redistribution subject to ASME license or copyright; see http://www.asme.org/terms/Terms_Use.cfm

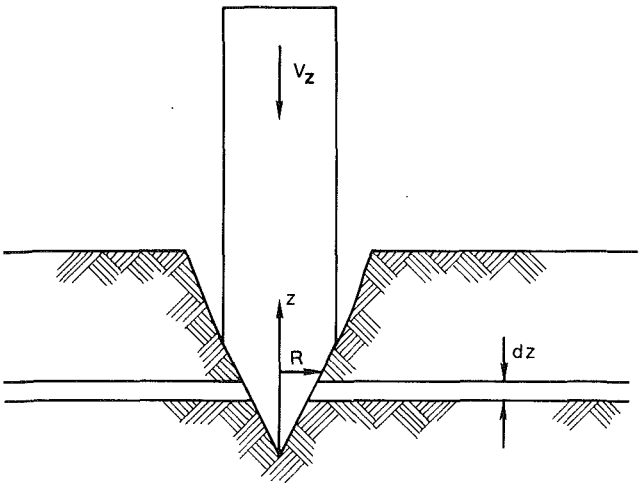


Fig. 1 Geometry of the problem

$$u_r = u(r,t), \quad \sigma_{rr} = \sigma(r,t), \quad \sigma_{\theta\theta} = \sigma_\theta(r,t), \quad \sigma_{zz} = \sigma_z(r,t), \quad (1)$$

where t is time. Using the notation defined by these relations (e.g., $\sigma = \sigma_{rr}$), the governing equations for conservation of mass and momentum are given by

$$\rho_0 r = \rho \frac{\partial}{\partial r}\left[\frac{1}{2}(u+r)^2\right], \quad (2)$$

$$\rho r \frac{\partial^2 u}{\partial t^2} = -(r+u)\frac{\partial \sigma}{\partial r} - (\sigma - \sigma_\theta)\frac{\partial}{\partial r}(r+u), \quad (3)$$

where ρ_0 and ρ are the initial and current densities, respectively, and the stresses are taken positive in compression. The material model selected is given by

$$p = f(\eta), \quad \tau = g(p), \quad (4)$$

where the functions f and g are to be determined from the hydrostat and shear failure-pressure data, and

$$3p = \sigma + \sigma_\theta + \sigma_z, \quad \tau = \sigma - \sigma_\theta, \quad \eta = 1 - \rho_0/\rho, \quad (5)$$

and the elastic strains will be neglected. To complete the material model, it will be assumed that

$$\sigma_z = s\sigma + (1-s)\sigma_\theta, \quad 0 \le s < 1. \quad (6)$$

Equations (4-5) may be combined to give

$$3\sigma = 3f(\eta) + (2-s)\,g(p),$$

$$\sigma_\theta = \sigma - g(p), \quad \sigma_z = \sigma - (1-s)g(p). \quad (7)$$

By restricting the present analysis to conical-nosed penetrators, the boundary conditions for equations (2) and (3) are given by $u(0,t) = Vt$ plus an additional condition yet to be derived for the wave front. In this relation, $V = V_z \tan\phi$, where V_z is the velocity of the penetrator and ϕ is the half cone angle of the penetrator nose (see Fig. 1).

4 Similarity Transformation

In reference [5], the special case of the present theory when $p = f(\eta) = K\eta$ and $\tau = g(p) = \mu p$ was found to possess a similarity solution. In spite of its generality, the present case may also be solved by similarity methods, and, to this effect, we assume the functional forms

$$u = tW(\xi), \quad \rho = \rho(\xi), \quad = r/t, \quad (8)$$

with the boundary condition $W(0) = V$, and W, being related to displacement, is required to be a continuous function of ξ. By (8), equations (2), (3), and (5) may be used to find that

$$\frac{\rho_0}{\rho} = \frac{W+\xi}{\xi}\left(1 + \frac{dW}{d\xi}\right), \quad (9)$$

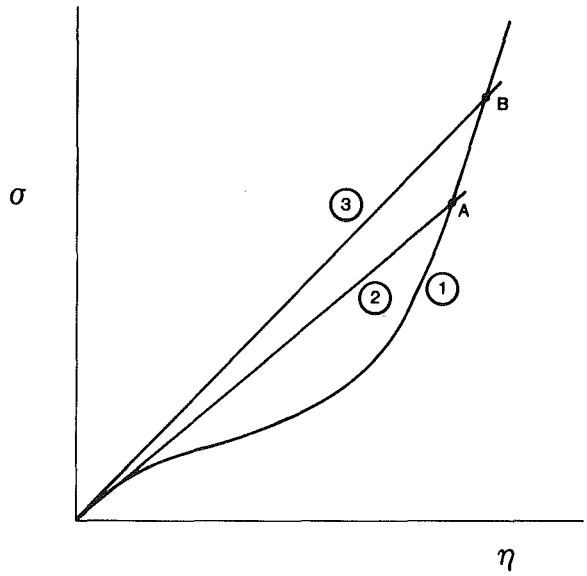


Fig. 2 Schematics for the solution of equation (17)

$$\eta = 1 - \left(1 + \frac{W}{\xi}\right)\left(1 + \frac{dW}{d\xi}\right), \quad (10)$$

$$\rho_0 \xi^3 \frac{d^2W}{d\xi^2} = -(\xi + W)\frac{d\sigma}{d\eta}\frac{d\eta}{d\xi} - (\sigma - \sigma_\theta)\left(1 + \frac{dW}{d\xi}\right), \quad (11)$$

$$\frac{dW}{d\xi} = -\frac{\eta + W/\xi}{1 + W/\xi}. \quad (12)$$

Equations (8)–(12) will be used to treat weak shocks, which have a singularity but no discontinuity at the shock front, and strong shocks, which have a jump discontinuity.

5 Shock Jump Relations

We need to derive Hugonoit jump conditions for the similarity variables. Since we do not require an energy equation, there are only two such jump conditions to be derived as follows. Identify by the subscripts $(+, s, -)$ quantities (ahead, at, behind) the shock front, and by assuming that the shock speed is given by V_s. Conservation of mass across the shock front implies the relation

$$\rho_+(v_+ - V_s) = \rho_-(v_- - V_s), \quad (13)$$

where v is the material velocity defined by

$$v_\pm = \lim_{\xi \to \xi_s \pm}\left[\frac{\partial}{\partial t}(r+u)\right] = \lim_{\xi \to \xi_s \pm}\left[\frac{\partial u}{\partial r}\right] = \left(W - \xi\frac{dW}{d\xi}\right)_\pm. \quad (14)$$

By equations (9), (10), (13), and (14), it is easy to show that $V_s = \xi_s + W_s$, where the requirement that W be continuous across the shock front has been employed.

For the conservation of linear momentum, by integrating equation (11) across the shock, one finds that

$$\rho_0 \xi_s^3\left[\left(\frac{dW}{d\xi}\right)_+ - \left(\frac{dW}{d\xi}\right)_-\right] = -(\sigma_+ - \sigma_-)(\xi_s + W_s). \quad (15)$$

By equation (12) and by the requirement that W be continuous everywhere, equation (15) may be written as

Downloaded 01 May 2010 to 171.66.16.249. Redistribution subject to ASME license or copyright; see http://www.asme.org/terms/Terms_Use.cfm

$$\rho_0 \xi_s^2(\eta_+ - \eta_-) = (\sigma_+ - \sigma_-)(1 + W_s/\xi_s)^2. \tag{16}$$

Of particular interest here is the case when the material ahead of the shock is undisturbed so that $\rho_+ = \rho_0$, and $W_s = \eta_+ = \sigma_+ = 0$. Under these conditions, equation (16) reduces to

$$\sigma_- = \rho_0 \xi_s^2 \eta_-. \tag{17}$$

The solutions to equation (17) with σ defined by equation $(7)_1$ are determined by the similarity variable ξ_s which specifies the position of the shock front. Figure 2 shows a graphical solution of this equation. Curve 1 is a plot of equation (7) for a possible choice of f and g, while curves (straight lines) 2 and 3 are given by $\sigma = \rho_0 c^2 \eta$ and $\sigma = \rho_0 \xi_s^2 \eta$, respectively, where c is the speed of sound in the undisturbed medium [$\rho_0 c^2 = (d\sigma/d\eta)0$; the derivative is evaluated at the origin]. From curves 1 and 3, the origin (trivial case) and point B in Fig. 2 represent solutions to equation (17). From curves 1 and 2, if $\xi_s < c$, then there are two nontrivial solutions. Therefore, for a stable solution, the inequality

$$\xi_s > c \tag{18}$$

must be imposed, resulting in a single shock structure.

6 Weak Shock Conditions

As was shown in [5] for the special case of the theory when $f(\eta) = K\eta$, $g(p) = \mu p$, and $s = 0$, equation (11) admits a weak solution in the neighborhood of $\xi^2 = (1 + 2\mu/3)K/\rho_0$. To derive the corresponding result for the general case, it is necessary to modify equation (11) by the use of equation (10). One finds that

$$\frac{d^2 W}{d\xi^2} = \frac{F(\xi)}{G(\xi)}, \tag{19}$$

where

$$F(\xi) = (\xi + W)\frac{d\sigma}{d\eta}\left[\frac{1}{\xi}\frac{dW}{d\xi}\left(1 + \frac{dW}{d\xi} - \frac{W}{\xi}\right) - \frac{W}{\xi^2}\right] - (\sigma - \sigma_\theta)\left(1 + \frac{dW}{d\xi}\right), \tag{20}$$

$$G(\xi) = \rho_0 \xi^3 - \frac{d\sigma}{d\eta}\frac{(\xi + W)^2}{\xi}. \tag{21}$$

Weak shocks appear as a consequence of zeros in the function G and will be denoted by ξ_0. Assuming again that the material ahead of the shock is undisturbed, one finds that $W_0 = u_0 = \eta_0 = 0$. Hence, the required zeros of G are found by using the asymptotic form of σ, from equation $(7)_1$ in the neighborhood of $\eta = 0$. On the assumption that ξ_0 is a zero of G, then it follows that ξ_0 is a singular point of the differential equation (19). Therefore, in the neighborhood of ξ_0, the expansion required is

$$W(\xi) = a(\xi - \xi_0)^\alpha + 0[(\xi - \xi_0)^{\alpha+1}]. \tag{22}$$

7 Sample Calculation

To illustrate the present theory, two special cases of the constitutive laws will be treated in this section. These cases are selected because, by choosing the coefficients appropriately, functions f and g may be constructed to represent fairly well the corresponding curves for a variety of materials.

Suppose that p is given by either of the relations[3]

$$p = A\eta + B\eta^2, \quad p = A\eta/(1 - B\eta)^2, \tag{23}$$

s is arbitrary, and τ is given by

$$\tau = g(p) = Cp + Dp^2 + Q(1 - e^{\beta p}), \tag{24}$$

[3] The $p - \eta$ relation (23) corresponds to a form used in WONDY [7] and has been found to be useful for representing the hydrostat of many materials.

The weak shock relations may be obtained by using equation (7) and noting that

$$\frac{d\sigma}{d\eta}(\eta = 0) = RA, \quad R = \left[1 + \frac{2 - s}{3}(C + Q\beta)\right]. \tag{25}$$

Since W vanishes at the shock front, the zeros of equation (21) are found from $\rho_0 \xi_0^3 - RA\xi_0 = 0$, with the weak shock solution $\xi_0^2 = RA/\rho_0$. In the neighborhood of ξ_0 the expansions required are

$$W \approx a(\xi - \xi_0)^\alpha,$$
$$G \approx 2RA(\xi - \xi_0),$$
$$F \approx A[R + (C + Q\beta)]a\alpha(\xi - \xi_0)^{\alpha - 1}.$$

The substitution of these expressions into equation (19) results in

$$\alpha = \frac{3R + (C + Q\beta)}{2R}. \tag{26}$$

The values of a and ξ_0 found in [5] may be obtained from the present results by setting Q equal to zero.

For strong shocks, with D and Q set equal to zero for simplicity, equation (17) becomes

$$\sigma = (A\eta_- + B\eta\theta_-^2)[1 + C(2 - s)/3] = \rho_0 \xi_s^2 \eta_-. \tag{27}$$

Hence, using the previous expression for R, one finds that

$$\eta_-[(A + B\eta_-)R - \rho_0 \xi_s^2] = 0, \tag{28}$$

with the trivial solution $\eta_- = 0$, corresponding to the weak shock case, and the strong shock solution

$$\eta_- = (\rho_0 \xi_s^2 - AR)/BR. \tag{29}$$

For this case, no multiple solutions exist. By requiring that $\rho \geq \rho_0$ behind the wave front, and also using the stability condition, equation (18), it follows that

$$\frac{AR}{\rho_0} < \xi_s^2 < \frac{A + B}{\rho_0}R \tag{30}$$

8 Numerical Solution

A shooting technique can be devised for both weak and strong shocks. For the weak shock case, the parameter to be varied is a, the amplitude of the singularity, while for the strong shock case, ξ_s is varied. Thus, the numerical integration of equation (11) proceeds as follows. By comparing a given boundary velocity V with the acoustic speed c it is determined whether to use the strong or weal shock conditions. For the strong shock boundary conditions, a value is selected for ξ_s and equation (17) is then solved for η_-. By equation (10), one now has the boundary conditions for W

$$W(\xi_s) = 0, \quad \frac{dW}{d\xi}(\xi_s) = -\eta_-. \tag{31}$$

These initial estimates are used to solve equation (11) numerically for $W(0)$ and $\sigma(0)$. If, for some small ϵ, $|W(0) - V| > \epsilon V$, then a new trial value of ξ_s is chosen and the process is repeated. Otherwise, we have a point on the curve $\sigma(V)$ and we repeat for a number of values of V.

In the weak shock case, the asymptotic form of the solution is used to provide the boundary conditions

$$W(\xi_0 - \delta) \approx a\delta^\alpha, \quad \frac{dW}{d\xi}(\xi_0 - \delta) \approx a\delta^{\alpha - 1}, \tag{32}$$

Equation (11) is again solved numerically for $W(0)$ and $\sigma(0)$. The same convergence criterion is used, but in this case the parameter a is varied. Note that α and ξ_0 depend on the choice of the functions f and g.

9 Numerical Results

For the special case when $f(\eta) = K\eta$ and $g(p) = \mu p$, we duplicated the results of [5] by the scheme outlined in the

Downloaded 01 May 2010 to 171.66.16.249. Redistribution subject to ASME license or copyright; see http://www.asme.org/terms/Terms_Use.cfm

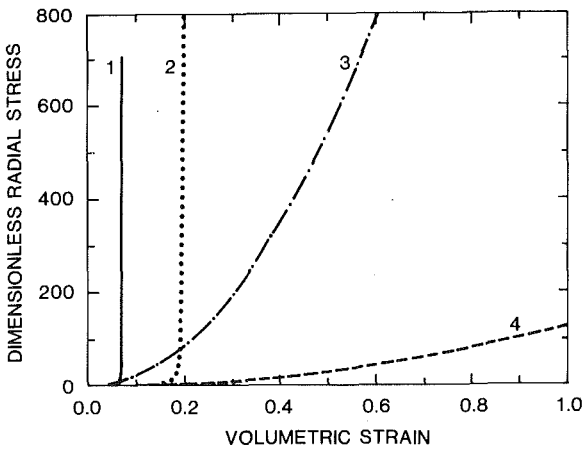


Fig. 3 Hydrostats for nonlinear materials

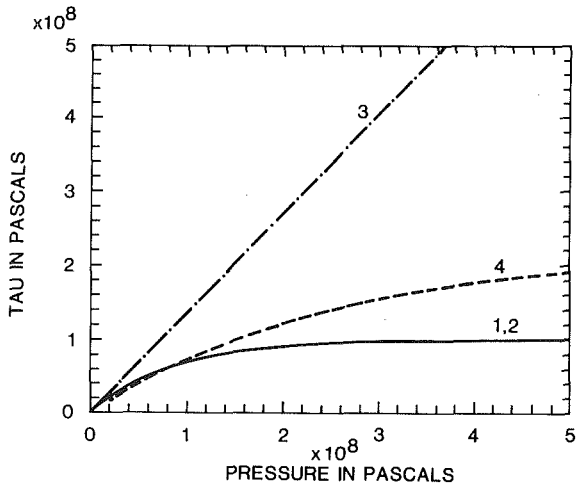


Fig. 4 Failure curves for nonlinear materials

preceding section. For more general cases, consider the relations

$$p = f(\eta) = \frac{A\eta + B_1\eta^2}{(1 - B_2\eta)^2}, \tag{33}$$

$$\tau = g(p) = C_p + D_p{}^2 + Q(1 - e^{-\beta p}) \tag{34}$$

together with equations (7). By a proper choice of $A, B_1, B_2, C, D, Q, \beta$ and s, it is possible to simulate continuous material data more closely than the locking model used in [1-4, 6] or the linear model used in [5]. This is illustrated in Figs. 3 and 4 for the values of the parameters shown on Table 1.[4] The values for curves 1, 3 and 4 in each figure were obtained, respectively, by approximating experimental data for yeso sandstone, Dakota sandstone, and yeso gypsum [10]. The values for curves 2 were obtained from those of curves 1 by changing B_2 from 14 to 5. From these curves it should be apparent that a wide variety of experimental curves may be approximated by the models in equations (33) and (34). The first two curves of Fig. 3 resemble quite closely a locking solid. By the use of equations (7), (33), (34), and the values from Table 1, $\sigma(\eta)$ was calculated and plotted in Fig. 5 for each set of values.[5] The ordinate in this curve is τ/A. The corresponding stresses on conical-nosed penetrators as a function of the radial expansion velocity are shown in Fig. 6. For this figure, the abcissa is V/c_0, where $V = V_z \tan\phi$, and $c_0^2 = A/\rho_0$; the ordinate is the dimensionless ratio σ/A, where σ is the value at the cavity wall. The use of these scaled coordinates enables us to compare different models on a single plot.

The most significant feature of Fig. 6 is the appearance of jumps in the stress-velocity relationship. These jumps are associated with the onset of the strong shock solution. At low speeds the weak shock prevails. Eventually, as the velocity is increased, a point is reached where the strong shock solution must be used instead. The reason for the jump discontinuity is that, for velocities slightly higher than the jump point, both solutions are valid; however, the solution with lower energy and stress is chosen as the physical one. This important behavior is reminiscent of that experienced by an aircraft approaching the sound barrier. As it does so, the stress increases dramatically until the aircraft has passed the sound barrier, when a strong shock forms in the surrounding medium. The stress level is then decreased somewhat.

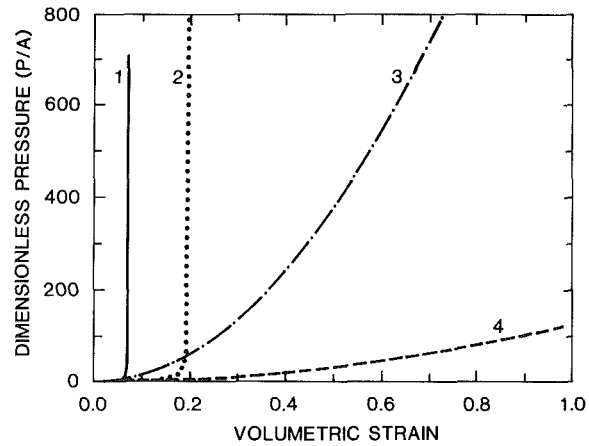


Fig. 5 Radial stress as a function of volumetric strain

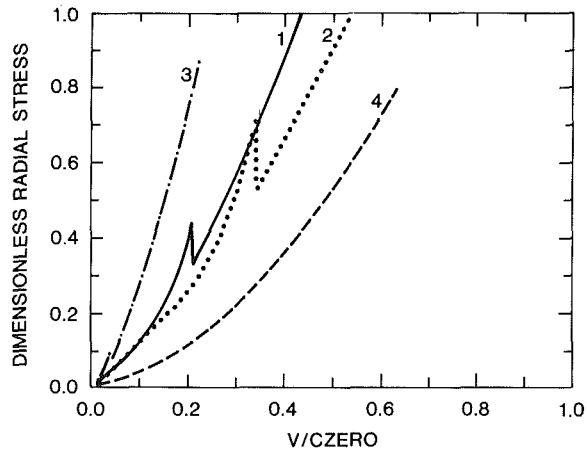


Fig. 6 Radial stress component on the conical nose

10 Conclusions

We have shown how to implement a similarity solution to the cavity expansion approximation using a general material model. Our program can handle both weak and strong shock regimes and we have carried out the solution for parameters that approximate several geological materials of interest. An interesting feature of the results is the appearance of a jump in stress versus velocity due to the transition from the weak to the strong shock regime. Another interesting feature of our model is its ability to handle a general nonlinear material model.

[4] The ordinate in Fig. 3 is the ratio p/A.

[5] In equation $(7)_1$ $f(\eta)$ dominates and therefore Fig. 5 looks very similar to Fig. 3.

Downloaded 01 May 2010 to 171.66.16.249. Redistribution subject to ASME license or copyright; see http://www.asme.org/terms/Terms_Use.cfm

Table 1 Parameter values for generating Fig. 3

Parameter \ Curve	1	2	3	4
A(pascals)	10^8	10^8	4×10^9	4×10^{10}
B_1(pascals)	0	0	6×10^{12}	5×10^{12}
B_2	14	5	0	0
C	0	0	1.35	0
D(pascals^{-1})	0	0	0	0
Q(pascals)	10^8	10^8	0	2.2×10^8
β(pascals^{-1})	1.2×10^{-8}	1.2×10^{-8}	0	4×10^{-9}
s	1	1	1	1
ρ_0(kg/m^3)	2300	2300	2440	2230

1-yeso sandstone
2-yeso sandstone
3-Dakota sandstone
4-yeso gypsum

References

1 Norwood, F. R., "Cylindrical Cavity Expansion in a Locking Solid," SLA-74-0201, Sandia Laboratories, Albuquerque, N. Mex., 1974.

2 Ross, B., and Hanagud, S., "Penetration Studies of Ice with Application to Artic and Subartic Warfare," Final Report, Project NWCR 7000-452-4, Stanford Research Institute, Menlo Park Calif., 1969.

3 Yarrington, P., "A One-Dimensional Approximate Technique for Earth Penetration Calculations," SAND77-1126, Sandia Laboratories, Albuquerque, N. Mex., 1977.

4 Yankelevsky, D. Z., and Adin, M. A., "A Simplified Analytical Method for Soil Penetration Analysis," *International Journal of Numerical and Analytical Methods in Geomechancis*, Vol. 4, 1980, pp. 233–254.

5 Forrestal, M. J., Longcope, D. B., and Norwood, F. R., "A Model to Estimate Forces on Conical Penetrators into Dry Porous Rock," ASME JOURNAL OF APPLIED MECHANICS, Vol. 48, 1981, pp. 25–29.

6 Forrestal, M. J., Norwood, F. R., and Longcope, D. B., "Penetration into Targets Described by Locked Hydrostats and Shear Strength," to appear in the *International Journal of Solids and Structures*.

7 Lawrence, R. J., and Mason, D. S., "WONDY IV-A Computer Program for One-Dimensional Wave Propagation with Rezoning," SC-RR-71 0284, Sandia Laboratories, Reprinted Nov., 1975.

8 Young, C. W., "Depth Prediction for Earth Penetrating Projectiles," *Journal of Soil Mechanics and Foundations*, Division of ASCE, May 1969, 803–817.

9 Young, C. W., "Empirical Equations for Predicting Penetration Performances in Layered Earth Materials for Complex Penetrator Configurations," SC-DR-0523, Sandia Laboratories, Albuquerque, N. Mex., 1972.

10 Hightower, M. M., Sandia National Laboratories, private communication.

Downloaded 01 May 2010 to 171.66.16.249. Redistribution subject to ASME license or copyright; see http://www.asme.org/terms/Terms_Use.cfm

A. M. Rajendran
Research Engineer,
Aerospace Mechanical Division,
University of Dayton Research Institute,
Dayton, Ohio 45469

I. M. Fyfe
Professor,
Department of Aero and Astro,
University of Washington,
Seattle, Wash. 98195
Mem. ASME

Inertia Effects on the Ductile Failure of Thin Rings[1]

The introduction of inertia terms into a theoretical model of thin ring expansion shows that classical plastic instability concepts, defined in terms of the local strain in the necking region, no longer apply. By introducing the role of void growth in triggering local necking, through a recently proposed constitutive equation for porous plastic materials, it is possible to overcome this difficulty. A criterion based on a critical void volume fraction provides the alternative means to predict failure. This theory was applied to a thin ring configuration, and the results were found to compare favorably with experimental values obtained from statically and dynamically loaded rings. The experimental techniques developed to handle the thin ring configuration are also described.

Introduction

Ductile failure as a phenomenon associated with plastic instability dates back to the time of Considére [1] who identified the point of instability as the onset of localized necking brought about when the increment of strain hardening became equal to the geometric softening, at the point of maximum load in a simple tension test. Marciniak and Kuczynski [2] considered this phenomenon in metal sheets under biaxial tension, and developed a mathematical model (*M-K* model) to construct forming limit diagrams. This model is based on an initial geometric imperfection, which is a localized thickness reduction in the sheet lying perpendicular to the major principal strain direction. By this method they predicted that the strain in the uniform region reaches a limiting value at which point the local strain in the defective region becomes unstable. In recent studies by Hutchinson and Neale [3] and Ghosh [4] the analysis was extended to include the effect of strain rate and different viscoplastic constitutive laws on localized necking. The results of this analysis, in its application to the case of uniaxial tension under quasi-static loading, predicted that the strain at necking increases with an increase in the strain-rate sensitivity and the strain-hardening parameter. These results were verified experimentally for different materials by Ghosh [4]. This analysis also predicted, depending on the constitutive equation, either no effect on or minor reduction of uniform strain at necking due to an increase in strain rate. These theoretical results were in agreement with the experiments of Sagat and Taplin [5] for superplastic materials under quasi-static loading conditions.

In the high strain-rate loading regime, where the quasi-static loading assumption no longer applies, considerable evidence exists, Wilson [6], that an increase in strain rate can in fact result in an increase in the ductility of most metals. In a series of experiments at high strain rate, the present authors (Fyfe and Rajendran, [7]) confirmed the increased ductility that occurs in this regime. They also supported this evidence by applying the *M-K* model to thin ring failure when inertia effects were included. Interestingly, the numerical solution of this model predicted the expected slowdown in the imperfection growth rate, but, even though local strain grows faster than the uniform strain, no plastic instability conditions occur before the material has actually failed. In this case, additional information or some other method has to be considered to predict failure. One way is to postulate that failure will occur when some macro/micro parameter reaches a finite critical value. For this purpose, it is essential to consider the failure mechanism at the local site where the failure would eventually occur.

A failure mechanism with growing acceptability is one that considers the process as being initiated by the nucleation of voids around inclusions and their subsequent growth and coalescence. During the last decade, different approaches were initiated by several investigators to apply this mechanism as a means of predicting ductile failure. Among them, Hancock and MacKenzie [8] examined failure in notched tensile specimens using the Rice and Tracey [9] void growth model; and, in the area of high strain-rate failure Seaman, Curran, and Shockey [10] developed models that considered the nucleation and growth of voids in the plate impact configuration.

Encouraged by metallurgical evidence, several other investigators [11, 12] working on the continuum aspect of failure, considered plastic dilatation effects on the yield criterion. This gave a new dimension to the problem of ductile fracture. Following this line of attack, recently Gurson [13] presented a continuum theory of ductile rupture by void nucleation and growth and used a constitutive equation for void-containing materials, which explicitly considered the void volume fracture and matrix stresses. The main advantage of such a theory is its simplicity and its ability to provide direct calculations of these microparameters, which are essential to predict failure.

[1]The results communicated in this paper were obtained in the course of an investigation supported by the U. S. Army Research Office under Grant DA-G29-77-0211.

Contributed by the Applied Mechanics Division for publication in the JOURNAL OF APPLIED MECHANICS.

Discussion on this paper should be addressed to the Editorial Department, ASME, United Engineering Center, 345 East 47th Street, New York, N.Y. 10017, and will be accepted until two months after final publication of the paper itself in the JOURNAL OF APPLIED MECHANICS. Manuscript received by ASME Applied Mechanics Division, March 1981; final revision, September 1981.

Copyright © 1982 by ASME
Downloaded 01 May 2010 to 171.66.16.249. Redistribution subject to ASME license or copyright; see http://www.asme.org/terms/Terms_Use.cfm

This continuum model was employed by Needleman and Triantafyllidis [14] in their examination of necking in biaxially stretched sheets. The initial metallurgical imperfection was described by stipulating a slightly larger value for the void volume fraction in the local site compared to that in the uniform region, with the local site also containing a geometric imperfection. Their results predicted forming limit diagrams in essential agreement with the available experiments.

In the present study the concept of a local imperfection is coupled with the void growth model in the analysis of thin ring specimens. The objective was to determine if this model could be used to predict the onset of plastic instabilities, at the strains associated with high strain-rate failure. The results from a series of experiments designed to determine the failure strain of statically and dynamically loaded thin rings were examined to provide some verification of the proposed failure criterion.

Localized Necking in a Thin Ring

The bulk of the studies investigating plastic instability, in addition to being quasi-static in nature, were quite often applied to the simple tension in a bar. The inclusion of inertia, using the analysis technique described in [3], can best be adapted to the dynamic case by considering the radially symmetric expansion of a thin ring or cylinder. A configuration in which the hoop strain ϵ_θ and the radial strain ϵ_r can be described in terms of the radial displacement u is by

$$\epsilon_\theta = ln(1 + u/R), \qquad \epsilon_r = ln(h(t)/h(0)) \tag{1}$$

where R is the initial radius of the midsurface, $r(t)$ is the instantaneous radius, with $h(0)$ the initial thickness, and $h(t)$ the instantaneous thickness.

Consider two segments of the expanding strip or ring, one with a small geometric defect in the thickness, and other with uniform thickness, as shown in Fig. 1. The variables associated with these two segments can be distinguished by the superscripts "B" and "A" for the local or defected segment and the uniform segment, respectively. A nonuniformity parameter η can then be defined by the relation

$$\eta = (h^A(0) - h^B(0))/h^A(0) \tag{2}$$

The equation of motion for an expanding ring with a given internal pressure $P(t)$ is, for the uniform segment

$$P(t) = \frac{\sigma_\theta{}^A h^A}{r^A} + \rho h^A \ddot{u}^A \tag{3}$$

and if the long, wavelength assumption of [3] is envoked, for the local segment

$$P(t) = \frac{\sigma_\theta{}^B h^B}{r^B} + \rho h^B \ddot{u}^B \tag{4}$$

where σ_θ is the hoop stress, ρ is the mass density, and $\ddot{u}$ is the radial acceleration of the ring. Since the pressure experienced by both segments is the same, we can equate (3) and (4) to obtain

$$\frac{\sigma_\theta{}^A h^A}{r^A} + \rho h^A \ddot{u}^A = \frac{\sigma_\theta{}^B h^B}{r^B} + \rho h^B \ddot{u}^B \tag{5}$$

Expressing u, h, and r in terms of the strains ϵ_θ, ϵ_r and the imperfection η through the use of (1) and (2), the preceding equation can be transformed to the form

$$\ddot{\epsilon}_\theta{}^B + (\dot{\epsilon}_\theta{}^B)^2 = \frac{e^{-(\epsilon_\theta{}^B + \epsilon_\theta{}^A)} \cdot e^{(\epsilon_r{}^A - \epsilon_r{}^B)}}{(1-\eta)\rho R^2} [\sigma_\theta{}^A + \rho R^2 e^{2\epsilon_\theta{}^A} (\ddot{\epsilon}_\theta{}^A + (\dot{\epsilon}_\theta{}^A)^2)] - \frac{e^{-2\epsilon_\theta{}^B}}{\rho R^2} \sigma_\theta{}^B \tag{6}$$

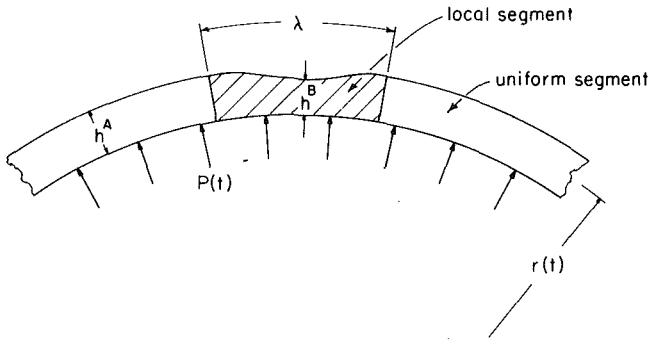


Fig. 1 Thin ring configuration with geometric imperfection

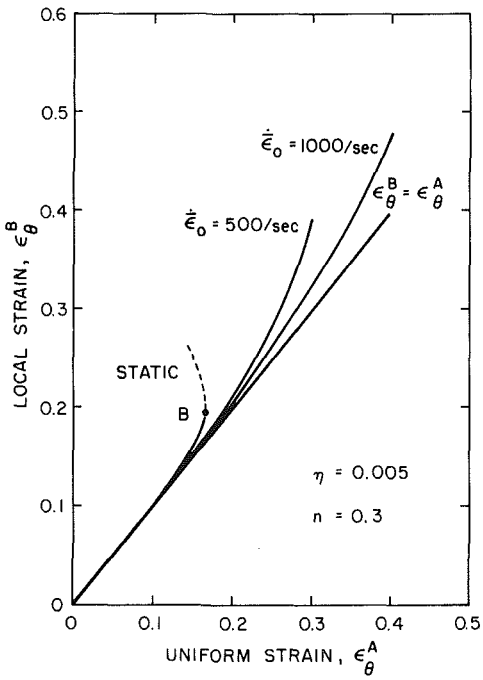


Fig. 2 The influence of inertia on the imperfection growth for a rate-independent material ($\sigma = K\epsilon^n$). B point of static load maximum (Considere's criterion).

The quasi-static case can be considered by neglecting the inertia terms as represented by the strain-rate terms in (6). If the material is assumed to be incompressible ($\epsilon_r = \epsilon_\theta/2$) and obeys the rate-independent power law, $\sigma = K\epsilon^n$ (6) is further reduced to the form

$$(\epsilon_\theta{}^B)^n = \frac{e^{3/2(\epsilon_\theta{}^B - \epsilon_\theta{}^A)}}{(1-\eta)} \cdot (\epsilon_\theta{}^A)^n \tag{7}$$

Using the failure criterion, $d\epsilon^B/d\epsilon^A \to \infty$, as proposed in [3], it can be readily determined that the onset of local necking occurs when $\epsilon_\theta{}^B = 2/3\ n$, which is compatible with the tensile bar results of $\epsilon^B = n$.

The material response of the ring when it expands under dynamic loading conditions can be obtained from the numerical solution of (6). For simplicity, it will be assumed in the following considerations that the ring is expanding at a constant velocity, which implies that $\ddot{u}^A = 0$, and $\ddot{u}^B \neq 0$. Equation (6) is simplified in that $(\ddot{\epsilon}_\theta{}^A + (\dot{\epsilon}_\theta{}^A)^2)$ is zero. The constant velocity of the expanding ring is defined through the initial uniform strain rate $\dot{\bar{\epsilon}}_\theta$. In Fig. 2, curves of the local strain $\epsilon_\theta{}^B$ are plotted against the uniform strain $\epsilon_\theta{}^A$ for different initial strain-rate values. These plots clearly show that the growth of the local strain is inhibited by increasing strain rate, which is in accord with experimental observations. These results also show that the quasi-static failure criterion

Downloaded 01 May 2010 to 171.66.16.249. Redistribution subject to ASME license or copyright; see http://www.asme.org/terms/Terms_Use.cfm

$d\epsilon^B/d\epsilon^A \rightarrow \infty$ is no longer applicable, and some other failure criterion must be introduced. The results presented in Fig. 2 are based on the assumption that the material is strain-rate independent. However, the delay in necking due to inertia occurs regardless of whether the material is represented by a rate-independent or rate-dependent model.

Compressible Materials

Although the stability model for a plastically incompressible material provides the theoretical confirmation that plastic instability is inhibited due to inertia effects, it does not contain an inherent criterion for localized necking or failure. The presence of voids just prior to failure suggests that this difficulty can be overcome by introducing the role played by void growth in triggering local necking directly into the analysis. Following the approach taken by Needleman and Triantafyllidis [14], it will be assumed that the material is a ductile porous one idealized as an aggregate consisting of voids and a ductile matrix. The presence of voids makes the aggregate plastically compressible. The details of this type of constitutive model are described in [13] and [14], so it is only necessary to show how the equations are adapted to the geometry and strain-rate conditions appropriate to dynamically loaded, thin ring specimens.

For a randomly voided material the yield surface has the form

$$\phi = \frac{\sigma_e^{\,2}}{Y_m^{\,2}} + 2f \cdot \cosh\left(\frac{\sigma_{1+\sigma_2+\sigma_3}}{2Y_m}\right) - f^2 - 1 = 0 \quad (8)$$

where Y_m is the flow stress of the matrix material, f is the current volume fraction of voids, σ_i are the principle values of the Cauchy stress acting on an element of the void matrix aggregate, and σ_e is the effective stress.

The increment in Y_m has the form [14],

$$\dot{Y}_m = \frac{E_t E}{(E - E_t)\, Y_m} \cdot \frac{\sigma_i \dot{\epsilon}_i^{\,p}}{(1-f)} \quad (9)$$

where E and E_t are the Young's modulus and tangent modulus, respectively, of the incompressible matrix. It is through E_t that the constitutive model of the incompressible matrix is introduced, and the matrix can either be rate-independent or rate-dependent. In the latter case the aggregate will also be a rate-dependent material, although in an indirect fashion. The increase in the void volume fraction f, due to void growth, is related to the plastic dilation by

$$\dot{f} = (1-f)\,(\dot{\epsilon}_1^{\,p} + \dot{\epsilon}_2^{\,p} + \dot{\epsilon}_3^{\,p}) \quad (10)$$

while the plastic strain rate $\dot{\epsilon}_i^{\,p}$ of the aggregate is given by

$$\dot{\epsilon}_i^{\,p} = \frac{1}{g} \frac{\partial \phi}{\partial \sigma_k} \dot{\sigma}_k \frac{\partial \phi}{\partial \sigma_i} \quad (11)$$

with

$$g = -\left[\frac{\partial \phi}{\partial Y_m} \cdot \frac{E_t E}{E - E_t} \cdot \frac{\sigma_i}{(1-f)\, Y_m} \cdot \frac{\partial \phi}{\partial \sigma_i} + \frac{3f(1-f)}{Y_m} \frac{\partial \phi}{\partial f} \sinh\left(\frac{\sigma_1 + \sigma_2 + \sigma_3}{2Y_m}\right)\right] \quad (12)$$

The constitutive equation of the principal stress components of the aggregate can be written in the following fashion

$$\dot{\sigma}_i = C_{ij} \dot{\epsilon}_j \quad (13)$$

where it has been assumed that the total strain rate is the sum of its elastic and plastic increments. Thus (11) can be combined with the elastic stress-strain relations so that the coefficients C_{ij} are given by,

$$C_{ij} = E_{ij} - \frac{1}{q} E_{ik} \frac{\partial \phi}{\partial \sigma_k} E_{ej} \frac{\partial \phi}{\partial \sigma_i} \quad (14)$$

where

$$q = g + \frac{\partial \phi}{\partial \sigma_i} E_{ij} \frac{\partial \phi}{\partial \sigma_j} \quad (15)$$

and the elastic constants of the matrix are given in terms of Young's modulus E, and Poisson's ration ν, by

$$E_{ij} = \frac{E(1-\nu)}{(1+\nu)(1-2\nu)} \quad i = j$$
$$E_{ij} = \frac{\nu E}{(1+\nu)(1-2\nu)} \quad i \neq j \quad (16)$$

The preceding equations thus describe the compressible material in the necking region. For a plane stress problem these equations can be greatly reduced in complexity, so that the plane stress increments are given by

$$\dot{\sigma}_\alpha = L_{\alpha\beta} \dot{\epsilon}_\beta \quad (17)$$

where the plane stress moduli $L_{\alpha\beta}$ are related to the C_{ij} coefficients by the expressions

$$L_{\alpha\beta} = C_{\alpha\beta} - \frac{C_{\alpha z} C_{z\beta}}{C_{zz}} \quad (18)$$

in which the Greek indices range from 1-2 in contrast to the Latin indices that range from 1-3. Equation (18) can further be reduced for the uniaxial stress case where (17) will then have the form

$$\dot{\sigma} = \left(L_{11} - \frac{L_{12} L_{21}}{L_{22}}\right) \dot{\epsilon} \quad (19)$$

For the thin ring configuration considered in this analysis, the local and uniform segments are assumed to be under plane stress and uniaxial conditions, respectively, so that for both segments $\dot{\sigma}_r = 0$, and from (17) we obtain

$$\dot{\epsilon}_r = \gamma_\theta \dot{\epsilon}_\theta + \gamma_z \dot{\epsilon}_z \quad (20)$$

where

$$\gamma_\theta = -\frac{C_{r\theta}}{C_{rr}}, \gamma_z = -\frac{C_{rz}}{C_{rr}} \quad (21)$$

In addition, the uniaxial section requires that $\dot{\sigma}_z^{\,u} = 0$ leading to

$$\dot{\epsilon}_z^{\,A} = -\frac{L_{z\theta}^A}{L_{zz}} \dot{\epsilon}_\theta^{\,A} \quad (22)$$

Also employing the strain compatibility across the imperfection band, requires that

$$\dot{\epsilon}_z = \dot{\epsilon}_z \quad (23)$$

As mentioned earlier, the matrix material is introduced through E_t, and using the rate-dependent constitutive model proposed in [15], the uniaxial stress form of this model is given by

$$\sigma = K\epsilon^n \left[1 + m \cdot ln\left(1 + \frac{\dot{\epsilon}}{\dot{\epsilon}_{\text{ref}}}\right)\right] \quad (24)$$

so that

$$E_t = n\sigma / \left[\sigma / K\left(1 + m \cdot ln\left(1 + \frac{\dot{\epsilon}}{\dot{\epsilon}_{\text{ref}}}\right)\right)\right]^{1/n} \quad (25)$$

where $\dot{\epsilon}_{\text{ref}}$ is the reference strain rate below which the material is considered to be strain-rate insensitive, and m is a strain-rate sensitivity parameter. It is implied in this analysis that ϕ is strain-rate independent at the strain-rate levels considered. The initial metallurgical imperfection (Δf) is defined as the difference between the initial void volume fractions of local and uniform segments at the point where the uniform section first becomes plastic. This can be incorporated into the solution by initially setting $f^A = 0$, so that $f^B = \Delta f$.

Downloaded 01 May 2010 to 171.66.16.249. Redistribution subject to ASME license or copyright; see http://www.asme.org/terms/Terms_Use.cfm

Equation (6) together with equations (8)–(25) can be solved numerically to determine either the growth of the void volume fraction or the local strain for increasing uniform strain, for any chosen value of the initial strain rate.

Static Case. In determining a void growth failure criterion the behavior of the material under quasi-static stability model can also be obtained for a compressible material by neglecting the inertia terms in (6) to obtain

$$\sigma_\theta{}^B \cdot e^{(\epsilon_r{}^B + \epsilon_\theta{}^A)} = \frac{1}{1-\eta}\,\sigma_\theta{}^A e^{(\epsilon_r{}^A + \epsilon_\theta{}^B)} \tag{26}$$

Differentiating this equation with respect to time, and using (20), (22), and (23) the following expression can be obtained

$$\frac{d\epsilon_\theta{}^B}{d\epsilon_\theta{}^A} = \{\Gamma(L^A_{\theta\theta} + \sigma_\theta{}^A\gamma_\theta{}^A - (L^A_{\theta z} + \sigma_\theta{}^A\gamma_z{}^A)L^A_{z\theta}/L^A_{zz}) - \sigma_\theta{}^B(1-\gamma^B_z L^A_{z\theta}) + L^B_{\theta z}L^A_{z\theta}/L^A_{zz}\}1/\beta \tag{27}$$

where

$$\beta = (L^B_{\theta\theta} + \sigma_\theta{}^B\gamma_\theta{}^B - \Gamma\sigma_\theta{}^A)$$

and

$$\Gamma = \frac{1}{(1-\eta)}\,e^{(\epsilon_r{}^A - \epsilon_r{}^B)e^{(\epsilon_\theta{}^B - \epsilon_\theta{}^A)}}$$

The quasi-static instability condition for the compressible material is then defined in the same way as it was for the incompressible material, i.e., $d\epsilon_\theta{}^B/d\epsilon_\theta{}^A \to \infty$.

The numerical solution of (27) together with equations (8)–(25) can then be carried out with increasing uniform strains until the instability point is reached. Results of these calculations are given in Fig. 3 for various values of the parameter η for a fixed value of Δf. In addition to showing the sensitivity of the instability point to variation in η, these results also show that even if the geometric imperfection is zero, failure can occur because of the metallurgical imperfection. In Fig. 4 the increase of the void volume fraction with increasing uniform strain is given for both the static and dynamic cases, and again it can be seen that the inclusion of inertia inhibits the growth of both these variables.

Void Growth Failure

With the absence of any well-defined point of instability under high strain-rate loading conditions, some alternative failure criterion is required for this case. Two approaches are possible, either to consider a new failure criterion, or find means of extending the quasi-static criterion, $d\epsilon^A/d\epsilon^B \to \infty$, to cover the dynamic case. The latter approach was taken in this study.

Earlier studies by other investigators (e.g. [8]) have led to the proposal that failure will occur when the void volume fraction reaches a critical level. A point of view that appears to be feasible is the dynamic case when metallurgical observations are made on specimens that have failed under high strain-rate conditions. Following this concept, the quasi-static analysis is carried out to the point where instability occurs and the corresponding value of f at this point is designated as the critical void volume fraction, f_{cr}. The dynamic analysis is then carried out for the strain-rate level of interest, until f reaches the value of f_{cr}. The corresponding uniform strain at this point, ϵ^d_{cr}, is considered to be the uniform strain at failure, on the assumption that f_{cr} is independent of the strain rate of the process. This assumption was found to be quite compatible with the experimental observations described in the following section. This procedure is illustrated in Fig. 4, where the void volume fraction is plotted against the uniform strain. The point A in the zero strain-rate case is the point of plastic instability, $d\epsilon^A/d\epsilon^B \to \infty$. From the numerical solution it was also observed that ϵ^d_{cr} approached a limiting condition, and

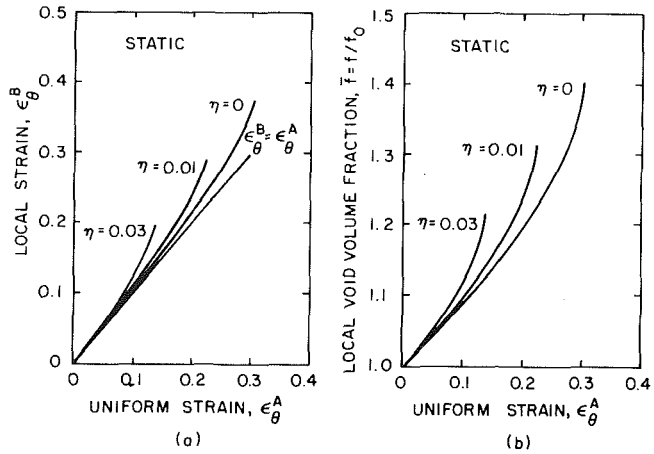


Fig. 3 Imperfections growth as a function of uniform strain for different geometric imperfection levels: (*a*) local strain, (*b*) void growth

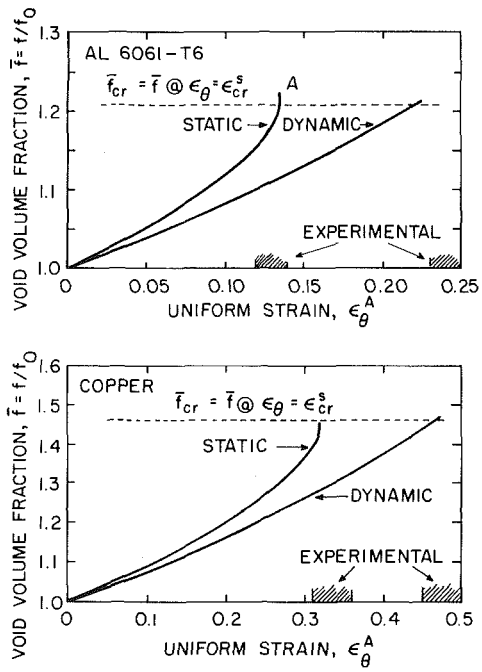


Fig. 4 Critical void volume criterion applied to thin rings of aluminum and copper ($\eta = 0.03$, $\Delta f = 0.01$, $\dot{\epsilon} = 8 \times 10^3$ sec)

did not increase significantly for strain rates greater than $\dot{\epsilon}_0 = 5000$ 1/s.

Experiments on Thin Rings

To check the validity of the criterion proposed in the preceding section, a series of dynamic and static experiments were carried out, with the objective of determining the uniform strain at failure for both types of loading conditions.

The static test apparatus was designed to expand the ring uniformly up to the point of failure. The load was applied indirectly through a polyethylene cylinder, in which the cylinder was internally loaded by oil pressure. The test configuration is shown in Fig. 5(*a*). The radial expansion of the ring was measured using a linear voltage, differential transformer (LVDT) system, whose actuator rod was displaced by the direct expansion of the ring.

Calibration for this system was obtained by moving the LVDT rod against a micrometer which was adjusted to give a voltage-rod displacement curve. The results of these tests were usually recorded on an x-y plotter in which internal pressure as a function of ring displacement was recorded. However, in this case, the pressure had no significance and no attempt was

Downloaded 01 May 2010 to 171.66.16.249. Redistribution subject to ASME license or copyright; see http://www.asme.org/terms/Terms_Use.cfm

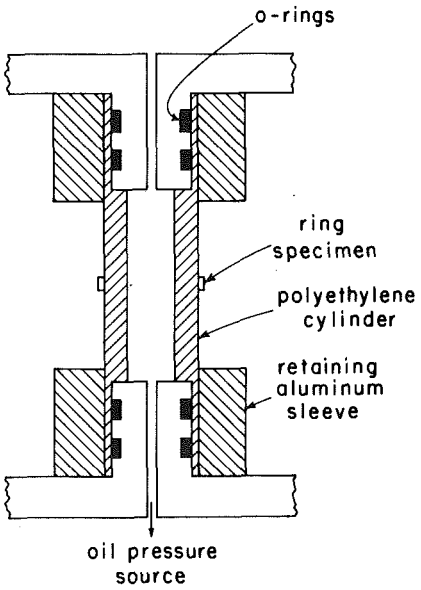


Fig. 5(a) Static

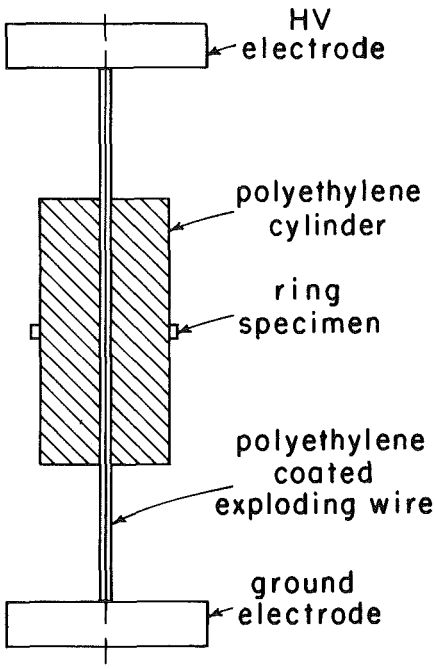


Fig. 5(b) Dynamic

Fig. 5 Specimen configuration

made to find the stress level in the ring. The hoop strain was obtained directly from (1). Although the theory only determines the onset of necking, the difference between the uniform strain values when necking first occurs and failure occurs is quite insignificant. In this configuration it should be pointed out that it is the uniform strain at failure and not the local strain, that is shown in Fig. 4. These tests were carried out for aluminum and annealed copper.

In the dynamic experiments, an exploding wire system was used to generate a symmetric and axially uniform pressure pulse which propagated radially through the medium surrounding the wire to uniformly impinge on the inner surface of the specimen. This system has the advantage over explosive techniques in that the axial variation caused by the finite detonation velocity is eliminated, and the rings expand without variation in the pressure across their width. The basic test configuration is shown in Fig. 5(*b*), in which the wire to be exploded is imbedded in a polyethylene cylinder. The outer diameter of this cylinder was such that the ring specimen could be lightly held in the position shown. The length of the cylinder was not particularly critical, and a length was chosen that produced high strain-rate levels with a uniform displacement of the ring across its width. The general specimen configuration was a ring whose internal diameter was 25.4 mm, width 3 mm, and of different thicknesses varying in value from 0.5–1.0 mm. The polyethylene cylinder was approximately 5 cm in length, with the 10 cm long wire loosely imbedded in the center.

The foregoing assembly was then attached between the high voltage and ground terminals of the capacitor bank system. The capacitor bank system consisted of two or more 15 microfarad capacitors each charged to 20 kV to provide the energy storage of 3000 J per capacitor. These capacitors were mechanically switched to discharge through the 10 cm long copper wire. To reduce ringing in the system, the diameter of the wire was fixed at 0.84 mm, and the resultant pressure pulse was approximately 5 μs in duration.

To obtain the input conditions appropriate to the theoretical analysis described earlier, it was necessary to obtain the strain rate of the uniform section of the ring. The hoop strain rate ($\dot{\epsilon}_\theta{}^A$) was determined by optical techniques to eliminate the magnetic interference associated with exploding wire systems. The system found to be most successful is one that measures the light variation of a small collimated beam passing between the ring, and a fixed knife edge positioned perpendicular to the specimen. The light intensity variation is detected by a photomultiplier tube, located beyond the test section area where the output is amplified and displayed on an oscilloscope. A more detailed description of this apparatus is given in [16].

Results

In the static tests, the uniform hoop strain at failure could be obtained quite readily, but in the dynamic tests the failure strain could not be determined directly, due to the fact that the time of failure could not be determined (a necessary requirement) if the measured value of the radial displacement as a function of time was to be used. To overcome this difficulty the uniform strain at failure was obtained from a post-test examination of the fractured ring using the following procedures.

With the dynamic tests conducted at various voltage levels of the capaciter bank, and thus different strain rate levels, the number of pieces into which the ring broke varied. As was to be expected, the lower the strain rate of loading, the fewer failure points occurred in the specimen. At the highest strain-rate levels, as many as 10 failure points were observed. With the hoop strain values being obtained from a uniform section of the broken ring, it was found that a section, free from necking, could be expected when the strain-rate level produced about five failure points. If the uniform section remained essentially plastically incompressible then ϵ_θ would be twice the value of ϵ_z, which is a measure of the change in the width of the ring. To check this point, a series of experiments were carried out in which the ring was expanded to a diameter just short of failure. Comparing the ϵ_θ obtained from the change in diameter and from the change in the width, it was found that these results were quite compatible with the incompressibility assumption and the scatter was within 3 percent strain.

The possibility that the uniform section could expand sufficiently after failure so that post-test measurements would be significantly larger than the true value was also considered. However, as the section would be in an unloaded state after the unloading wave from the fractured surface reached all parts of the fragment, it was calculated that this additional strain could only introduce an error of about 5 percent.

Downloaded 01 May 2010 to 171.66.16.249. Redistribution subject to ASME license or copyright; see http://www.asme.org/terms/Terms_Use.cfm

The results of these measurements made with an initial strain rate of approximately 1×10^4 1/s for both copper and aluminum samples are shown in Fig. 4, where it can be seen that inertia increased the uniform strain at failure to values very close to those predicted by the theory. This increase in strain, due to inertia, is fairly typical of the results obtained from similar tests carried out on thin cylinders of the same materials. In tests where 9 or 10 failure points did occur, but in which at least one portion of the fractured ring was large enough to allow the calculation of the hoop strain, it was observed that the strain at failure had not increased significantly over those values obtained with about five failure points. This result is compatible with the theoretical prediction that the strain at failure approaches the limiting curve $\epsilon_\theta{}^A = \epsilon_\theta{}^B$ of Fig. 2, and suggests that failure could occur at a critical, void volume fraction that is essentially strain-rate independent.

The uniform strain at failure is very sensitive to the two parameters that define the geometric and metallurgical imperfections, η and Δf. Although η can be found by a careful measurement of the ring specimen, the problem of determining an accurate value of η is directly related to the thickness of the ring, which for thin rings results in a value of η that with care, is a reasonable approximation. On the other hand, the value of Δf is only an educated guess, and the value chosen for this study was one used by Needleman and Triantafyllidis [14], and also by Yamamoto [17], which, although probably unrealistically high, is felt to be compatible with the simplified constitutive model used in the study. So, it may be possible to pick different combinations of η and Δf which would allow the theory to predict a value of ϵ_{cr}^s in agreement with the quasi-static test results in Fig. 4. However, that these same values also accurately predict the dynamic test values for the two materials is encouraging. Since the dimensions of the ring specimens for both the A1. 6061-T6 and the annealed copper are identical, the value of η was naturally the same in both cases, and the same value of Δf was considered to be appropriate lacking any evidence to the contrary.

Conclusions

The use of a constitutive model, which allows for plastic compressibility in the region of either a metallurgical or geometric flaw, although somewhat complex, provides results that appear to be compatible with the more traditional treatment of necking instability. The concept of a critical, void volume level as a means to predict failure is a natural growth of the use of this model, and encouraging results were obtained in its application to thin rings undergoing both static and dynamic expansion.

With the analysis designed to predict the strain at the onset of ductile fracture, no consideration has been given to void nucleation or the particular mode of failure that might ensue beyond this strain level. It is to be expected that this latter aspect of the failure process can only be determined from a more detailed study of the stress field in the necking region. Applying the void growth stability to thin rings does not preclude the possibility that the main failure process will be of the cleavage type. A close examination of the fracture surfaces showed that the dimpled surface, characteristic of void growth failure, was always present although often only in a small area close to the edge. However, it has yet to be shown that the dimpled area was the first section to become unstable.

For a material that is essentially perfectly plastic, the incompressible model predicts the strain at failure to occur at the onset of plastic flow. The compressible model, however, in addition to providing a failure criterion applicable for conditions where inertia is important, also gives a more realistic failure strain for materials of this kind. In the present model, the strain-hardening effect is introduced, rather artificially, through the tangent modulus E_t. However in comparing the results of this analysis in its application to the aluminum and copper rings, it is interesting to note that the theory predicts not only the large ductility expected of the copper, but also the reduced effect of inertia in this material in contrast to the aluminum; a result that is clearly seen in Fig. 4.

The problem of determining meaningful values for the nonuniformity parameter η is essentially more a function of the specimen geometry, and so reasonable values can usually be obtained. Unfortunately, this is not the case for Δf. In principle, this value should be obtainable from metallurgical experiments, but even if values were available, it would still be necessary to incorporate the void nucleation mechanism. As a generally applicable, void nucleation model has as yet to be defined, it appears that for dynamic failure prediction, it must be assumed that the initial value of Δf includes nucleation. As assumption that should have negligible affect on the results obtained if nucleation is complete before the critical static strain is reached.

The extension of the approach outlined in this study to different geometric configurations, in which the role of the nonuniformity parameter η can be neglected is a necessary step to further the efforts to incorporate microstructural features in the analysis of ductile fracture.

References

1 Considère, A., "L'Emploi du Fer et de L'Acier dans les Constructions," *Ann. Ponts Chaussee*, Vol. 9, 1885, p. 574.

2 Marciniak, A., and Kuczynski, K., "Limit Strains in the Process of Stretch Forming Sheet-Metal," *International Journal of the Mechanical Sciences*, Vol. 9, 1967, p. 609.

3 Hutchinson, J. W., and Neale, K. W., "Influence of Strain-Rate Sensitivity on Necking Under Uniaxial Tension," *Acta Metallurgica*, Vol. 25, 1977, p. 839.

4 Ghosh, A. K., "Tensile Instability and Necking in Materials with Strain Hardening and Strain-Rate Hardening," *Acta Metallurgica*, Vol. 25, 1977*a*, p. 1413.

5 Sagat, S., and Taplin, D. M. R., "The Stability of Plastic Flow in Strain-Rate Sensitivity Materials," *Metal Science*, Vol. 10, 1976, p. 94.

6 Wilson, F. W., "High Velocity Forming of Metals," *The American Society of Tool and Manufacturer Engineers*, New York, 1964.

7 Fyfe, I. M., and Rajendran, A. M., "Dynamic Pre-Strain and Inertia Effects on the Fracture of Metals," *Journal of the Mechanics and Physics of Solids*, Vol. 28, 1980, p. 17.

8 Hancock, J. W., and Mackenzie, A. C., "On the Mechanisms of Ductile Rupture in High-Strength Steels Subjected to Multi-Axial Stress-states," *Journal of the Mechanics and Physics of Solids*, Vol. 24, 1976, p. 147.

9 Rice, J. R., and Tracey, D. M., "On the Ductile Englargements of Voids in Triaxial Stress Fields," *Journal of the Mechanics and Physics of Solids*, Vol. 17, 1969, p. 201.

10 Seaman, L., Curran, D. R., and Shockey, D. A., "Computational Models for Ductile and Brittle Fracture," *Journal of Applied Physics*, Vol. 47, No. 11, 1976, p. 4814.

11 Berg, C. A., "Plastic Dilation and Void Interaction," *Proceedings of the Batelle Memorial Institute Symposium on Inelastic Processes in Solids*, 1969, p. 171.

12 Nagpal, V., McClintock, F. A., Berg, C. A., and Subudhi, M., "Traction-Displacement Boundary Conditions for Plastic Fracture by Hole Growth," *International Symposium on Foundations of Plasticity*, Vol. 1, Sawczuk, A., ed, 1972, p. 365.

13 Gurson, A. L., "Porous Rigid-Plastic Materials Containing Rigid Inclusions-Yield Function, Plastic Potential, and Void Nucleation," *Advances in Research on the Strength and Fracture of Materials*, Vol. 2*a*, Tablin, D. M. R., ed., Pergamon Press, New York, 1977, p. 357.

14 Needleman, A., and Triantafyllidis, N., "Void Growth and Local Necking in Biaxially Stretched Sheets," ASME *Journal of Engineering Materials and Technology*, Vol. 100, Apr. 1978, p. 164.

15 Campbell, J. D., Eleiche, A. M., and Tsao, M. C. C., *Fundamental Aspects of Structural Alloy Design*, Jafee, R. J., ed., Plenum Press, New York, 1977, p. 545.

16 Swift, R. P., and Fyfe, I. M., "Elastic/Viscoplastic Theory Examined Using Radial Cylindrical Stress Waves," ASME JOURNAL OF APPLIED MECHANICS, Vol. 37, Series E, 1970, p. 1134.

17 Yamamoto, H., "Conditions for Shear Localization in the Ductile Fracture of Void-Containing Materials," *International Journal of Fracture*, Vol. 14, No. 4, 1978, p. 347.

Downloaded 01 May 2010 to 171.66.16.249. Redistribution subject to ASME license or copyright; see http://www.asme.org/terms/Terms_Use.cfm

J. L. Bogdanoff
Professor of Aero. Engineering,
School of Aero. and Astro.,
Purdue University,
W. Lafayette, Ind. 47907
Fellow ASME

F. Kozin
Professor of Electrical Engineering,
Polytechnical Institute of New York,
333 Jay Street,
Brooklyn, N. Y. 11201

On Nonstationary Cumulative Damage Models

In this paper, we continue our study of embedded Markoff Chain Models of Cumulative Damage. We introduce and discuss a time transformation that leads to a condensation method. This method appears to be unusally comprehensive and a practical way to study nonstationary models of cummulative damage. Further, it allows us to estimate the desired nonstationary transition matrices providing a means of gaining further insights into the cumulative damage process. Examples are presented and further directions of research are indicated.

1 Introduction

The ease with which stationary finite state-discrete time embedded Markoff processes [1-6] can handle constant severity duty cycles (*DC*) stems from the fact that simple formulas can be obtained for the moments of time to reach a given damage level. These moment formulas are used to estimate the parameters of a model from life data by means of the method of moments with refinement in the parameter values by least squares or maximum likelihood if necessary. Excellent descriptions and analysis of life data have been obtained using this model.

Markoff process models are not new as applications of stochastic methods. However, the general structure that we have proposed is new to the description and organization of cumulative damage (*CD*) data. Therefore, we have chosen to call these finite state-discrete time embedded Markoff processes *B*-models to emphasize the importance of the general structure they possess. We believe we are the first group to engage in a systematic study of the consequences of these models and in a systematic application of them to data.

Nonstationary *CD* processes do occur. Typical sources of nonstationary behavior are time-dependent load severity and/or environment, and/or material properties. It is well known that problems concerning nonstationary (time-dependent) models are difficult to handle except for special cases. There seems to be no standard technique for analyzing the finite time properties of nonstationary finite state Markoff Chains (*MC*) possessing one absorbing state with the remaining states transient.

We have used trail and error methods in our previous studies [2] to arrive at acceptable parameter estimates in nonstationary *B*-models that describe and analyze specific life data. Clearly, it is desirable to formulate practical analytical procedures for constructing nonstationary *B*-models that describe *CD* processes coming from nonstationary data.

Several approaches might be considered. For example, we might assume a specific parametric time-varying form for the probabilities in the transition matrices that define the Markoff Chain [2]. This method may be referred to as the direct method. It is easy to use in computation and it is easy to explore, computationally, the consequences for a *CD* process of various assumed changes with time. However, in general, it is very difficult to estimate the unknown parameters of the assumed form of the time-varying probabilities from life data. Another approach embeds or subordinates a stationary Markoff Chain (*MC*) to an independent counting process [7]. Again, the parameter estimation problems, given life data from a nonstationary *CD* process, proves to be quite difficult except in physically uninteresting cases. A third approach to consider is a direct time transformation applied to a stationary *B*-model. It is this third approach that had led us to what appears to be an unusually comprehensive and practical way to study nonstationary *MC*'s of the type used to model *CD* processes. It leads to what we shall refer to as the condensation method of time transformations and allows, not only the estimation of the desired nonstationary transition matrices comprising the *B*-model, but also provides a means of gaining further insight into the *CD* process that generated the given life data.

Thus the purpose of this paper is to describe the time transformation and the condensation method for generating nonstationary *B*-models from stationary *B*-models. A simple graphical procedure is used to determine the nature of the time transformation as well as the proper condensation. We apply the technique to construct a *B*-model that describes and analyzes a specific set of life data. Finally, we show how the method can be used to gain insight into what might be occurring in a *CD* process that generates given data.

It appears that this approach is new. An outline of the method can be found in [6].

To conserve space we only shall repeat in Section 2 material from [1-6] that is absolutely necessary. The interested reader is referred to these references for details.

2 Brief Decription of *B*-Models

B-models are *MC* descriptions of *CD* processes. Let the finite (discrete) damage states be denoted by (1, 2, .., *b*) where

Contributed by the Applied Mechanics Division for publication in the JOURNAL OF APPLIED MECHANICS.

Discussion on this paper should be addressed to the Editorial Department, ASME, United Engineering Center, 345 East 47th Street, New York, N. Y., 10017, and will be accepted until two months after final publication of the paper itself in the JOURNAL OF APPLIED MECHANICS. Manuscript received by ASME Applied Mechanics Division, March, 1981; final revision, July, 1981.

Copyright © 1982 by ASME
Downloaded 01 May 2010 to 171.66.16.249. Redistribution subject to ASME license or copyright; see http://www.asme.org/terms/Terms_Use.cfm

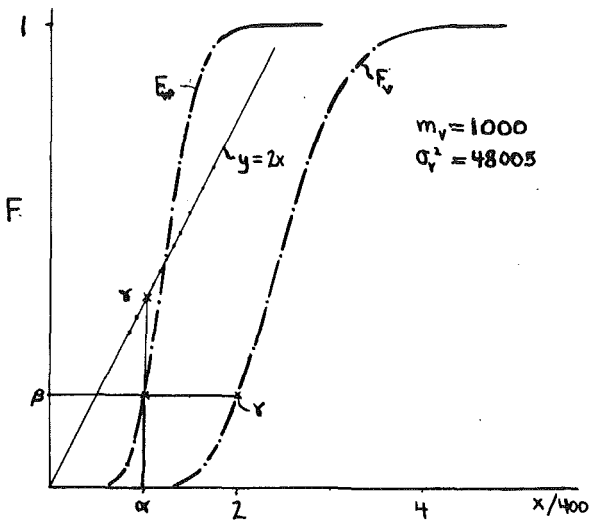


Fig. 1 Graphical procedure for constructing F_V from F_W when $y = 2_x$

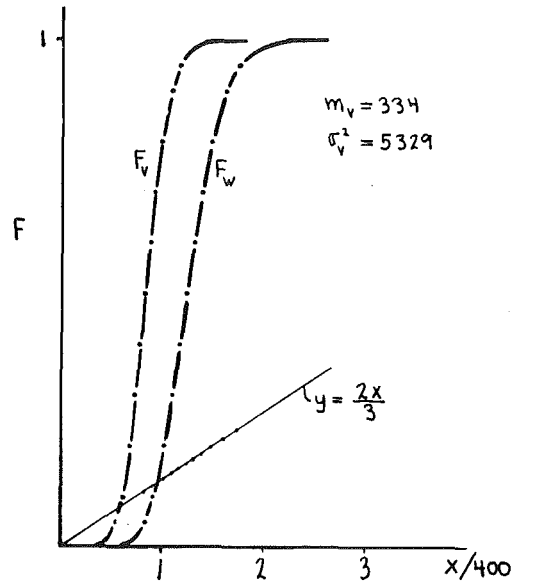


Fig. 2 Influence of transformation $y = 2/3\,x$ on the shape of F_v

b denotes failure. Let the discrete time be $x = 0, 1, 2, \ldots$. The rv D_x denotes the damage state occupied at time x, with Pr $[D_x = j] = p_x(j)$. The $(1 \times b)$ row vector $\mathbf{p}_x = \{p_x(1),\ldots, p_x(b)\}$ denotes the probability distribution of D_x. We denote the initial probability distribution of damage by

$$\mathbf{p}_0 = \{\pi_1,\ldots, \pi_{b-1}, 0\}, \quad \sum_1^{b-1} \pi_j = 1 \tag{1}$$

We set $\pi_b = 0$ since we assume no failed item is put into service at $x = 0$. Let P denote the constant severity DC $(b \times b)$ probability transition matrix defined as

$$P = \begin{Bmatrix} p_1 & q_1 & 0 & \ldots & 0 & 0 \\ 0 & p_2 & q_2 & \ldots & 0 & 0 \\ 0 & 0 & 0 & \ldots & p_{b-1} & q_{b-1} \\ 0 & 0 & 0 & \ldots & - & 1 \end{Bmatrix} \tag{2}$$

where p_j, $q_j > 0$, and $p_j + q_j = 1$. Equation (2) assumes a unit-jump damage accumulation mechanism. We know [1] that

$$\mathbf{P}_x = \mathbf{p}_0 P^x = \mathbf{p}_{x-1} P \tag{3}$$

It is convenient for analytical puposes to assume $\pi_1 = 1$. Let $W_{1,b}$ denote the time to reach state b (or time to failure) given in state 1 at $x = 0$. Let $F_w(x;1,b)$ denote the cumulative distribution function (cdf) of $W_{1,b}$. It follows from (2) and (3) that

$$F_w(x;1,b) = p_x(b) \tag{4}$$

We find, on setting $r_j = p_j/q_j$

$$E\{W_{1,b}\} = \sum_1^{b-1}(1+r_j) \equiv m_w$$

$$\text{Var } W_{1,b} = \sum_1^{b-1} r_j(1+r_j) \equiv \sigma_w^2$$

$$\mu_3\{W_{1,b}\} = \sum_1^{b-1} r_j(1+r_j)(1+2r_j)$$

$$\mu_4\{W_{1,b}\} = 3\sigma_w^4 + \sum_1^{b-1} r_j(1+r_j)(1+2r_j)(1+3r_j)$$

$$+ \sum_1^{b-1} r_j^2(1+r_j) \tag{5}$$

If $\pi_1 \neq 1$, formulas analogous to (5) can be derived, but they become much more complex. When $\pi_1 \neq 1$, we replace $W_{1,b}$ with W_b.

Formulas for the reliability function $\bar{F}_w(x; 1,b)$, the failure rate (hazard) function $h_w(x; 1,b)$, and explicit formulas for $F_w(x; 1,b)$ can be found in [1].

Equation (3) is used for computation and provides the probability distribution of D_x and $F_w(x; 1,b)$. Moments of D_x and $W_{1,b}$ are also easy to evalute at the same time.

$W_{1,b}$ is a discrete rv. Thus F_w, $\bar{F}_w$, and h_w have the usual staircase form. Computer plots of these functions as ordinate against x as absicssa appear as poorly drawn smooth curves for the range x and the values of the p_j encountered with data. We shall therefore always plot model generated F_w, $\bar{F}_w$, and h_w as smoooth curves for reasons of appearance, as previously mentioned in [1].

3 The Method

Consider two discrete times x and y. We are interested in transforming one B-model in x-time to another B-model in y-time. Let the time transformation be

$$y = g(x), \quad g(0) = 0, \quad g'(x) > 0 \tag{6}$$

where g is of class C_1 at least. There are some interesting aspects associated with this transformation. Let us consider a simple case.

Assume

$$y = ax, \quad a > 1 \tag{7}$$

First, consider a graphical procedure.

Figure 1 shows the cdf F_w of the time $W_{1,b}$ to failure for a stationary B-model in x-time, and the line (7); these are the given information. Let $V_{1,b}$ denote the time to failure in y-time, and let it's cdf be F_v. We find F_v as follows: At $x = \alpha$, draw a line parallel to the ordinate; let the intercepts with F_w and g, be β and γ, respectively. The point (γ, β) then lies on F_v as ordinate with γ as absicssa. On taking a succession of α's, we obtain enough points to complete F_v versus y. The crosses marked on g indicate the values of γ used in the construction.

Downloaded 01 May 2010 to 171.66.16.249. Redistribution subject to ASME license or copyright; see http://www.asme.org/terms/Terms_Use.cfm

We have used $a = 2$ in (7) in this figure. Obviously, the graphical procedure is easy to carry out.

Figure 2 shows the construction of F_v, when $a = 2/3$ in (7). Now let us consider how to construct a B-model for y-time in terms of the B-model in x-time.

We assume

$$\mathbf{p}_y = \mathbf{p}_0(P')^y, \quad y = 0, 1, 2, \ldots \tag{8}$$

This equation assumes DC severity in y-time is defined by the probability transition matrix P', and the B-model in y-time is stationary. From the transformation (7), we have

$$(P')^y = (P')^{ax} = P^x; \tag{9}$$

therefore, it follows for $a = 2$ that

$$P' = P^{1/2} \tag{10}$$

Assume, for example,

$$P = \begin{Bmatrix} 0.90 & 0.10 & 0 \\ 0 & 0.80 & 0.20 \\ 0 & 0 & 1 \end{Bmatrix} \tag{11}$$

We find from (10) that

$$P' = \begin{Bmatrix} 0.94868 & 0.05426 & -0.00294 \\ 0 & 0.89443 & 0.10557 \\ 0 & 0 & 1 \end{Bmatrix} \tag{12}$$

which is *not a probability transition matrix* since it has a negative entry, although row sums are still one. This difficulty persists for all $g' > 1$.

We need a method which uses $\mathbf{p}_0$, P, and $y = g(x)$ to produce $\mathbf{p}_y$ and avoids the difficulty illustrated by (12).

Consider the following: let $x_1, x_2, \ldots$ be determined by $j = g(x_j)$, where $j = 1, 2, \ldots$ Now form the intervals $(0, x_1]$, $(x_1, x_2] \ldots$. Define

$$\begin{aligned} Q_j &= I \text{ if } (x_{j-1}, x_j] \text{ contains no integer} \\ &= P \text{ if } (x_{j-1}, x_j] \text{ contains one integer} \\ &= P^2 \text{ if } (x_{j-1}, x_j] \text{ contains two integers, etc.} \end{aligned} \tag{13}$$

Consider the model defined by

$$\mathbf{p}_y = \mathbf{p}_0 \prod_1^y Q_j \tag{14}$$

We observe first that each Q_j defined in this manner is a probability transition matrix. Thus the difficulty illustrated by (12) is avoided. For example, with $a = 2$, we find from (13) that

$$Q_1 = I, \quad Q_2 = P, \quad Q_3 = I, \quad Q_4 = P \ldots \tag{15}$$

which shows that we replace successively the pairs $(P^{1/2}, P^{1/2})$ coming from the exact time transformation with the pairs (I, P). We shall refer to this technique as the *condensation method.*

We shall refer to the chain defined by the transition matrices

$$I, P, I, P, I, P, \ldots .$$

as quasi-stationary as there is a periodicity to the sequence of transition matrices.

Next, note that for any positive integer y

$$\prod^y Q_j$$

is that power of P which is the largest integer equal to or less than $g^{-1}(y)$. This means that (14) does not produce the exact power of P required by the time transformation $y = g(x)$. We find, using (3) and (4), the error in $\mathbf{p}_y$ to be no more than

$$\{q_1 p_y(1), |-q_2 p_y(2) + q_1 p_y(1)|, |-q_3 p_y(3) + q_2 p_y(2)|, \ldots, q_{b-1} p_y(b-1)$$

Since the q_j are typically small and $p(j) \to 0$ as $y \to \infty$, $j = 1, \ldots, b-1$, this error is small and becomes asymptotically zero. We therefore use (14) to define the CD process in y-time with F_v given by $p_y(b)$.

Equation (13) says in particular that we are condensing integer number of jumps of F_w into the units jumps in F_v, which is why we call this a condensation method. We are using an unconventional method for obtaining F_v and F_w using $y = g(x)$. The method has the major advantages of eliminating the difficulty associated with the fractional powers (<1) of P, of providing a simple and unified computational scheme, and of keeping y-time on the nonnegative integers. We will continue to use $y = g(x)$ graphically, however, to get F_v from F_w as illustrated in Figs. 1 and 2. As a matter of fact, the F_v in each of Figs. 1 and 2 were computer drawn using the condensation method (14). These curves lie on top of the curves obtained using the graphical procedure, which further illustrates the negligibly small error introduced by the condensation method.

We should point out that it is possible under certain conditions to determine whether the exact time transformation (14) will yield probability transition matrices. The analysis involved will be discussed in another paper. The beauty of our proposed condensation method, although approximate, is that it always works, and is sufficiently accurate for practical work.

Let us look at the moment problem. Consider

$$V = g(W), \tag{16}$$

which, strictly speaking, is not the exact transformation according to (13). However, (16) can be employed for obtaining useful approximate values for the moments of V in terms of the parameters of the time transformation and the parameters of the stationary B-model, especially when g is restricted to be a polynomial. Examination of the error indicates that EV from (14) will differ from $E\{g(W)\}$ by approximately 1; $E\{V^2\}$ will differ from $E\{g^2(W)\}$ by approximately $E\{V\}$. Typical value of EV and EV^2 encountered in data are 10^3 and 10^6, respectively. Thus these errors are of no significance when compared with the nominal values. We find, for example, that for the linear transformation (7), (16) gives $EV = a\,EW$ and Var $V = a^2$ Var W; and hence, the signal to noise ratio for V is approximately the same as for W. Moment formulas (5) for W of a stationary B-model are readily obtained, especially if the p_j in P are independent of j. If g is a polynomial, it is then easy to find approximate and useful moment formulas for V.

Figures 3 and 4 use the quadratic time transformations.

$$\begin{aligned} y &= x + \frac{x^2}{524}, \quad x \geq 0 \\ y &= x - \frac{x^2}{4000}, \quad 0 \leq x < 2000 \end{aligned} \tag{17}$$

respectively. The computed values of mean and variance of are shown in the figures. The approximate values are (1000, 104,104) and (435, 6550), respectively.

It should be pointed out that the same F_w is used in Figs. 1–4, the stationary B-model employed uses $\pi_1 = 1$, $b-1 = 20$, and $r_j = p_j/q_j = 24$, $j = 1, \ldots, 20$. This gives $m_w = 500$, $\sigma_w^2 = 12{,}000$.

We can now make a number of observations. DC severity in y-time is less (more) severe than in x-time depending upon

Downloaded 01 May 2010 to 171.66.16.249. Redistribution subject to ASME license or copyright; see http://www.asme.org/terms/Terms_Use.cfm

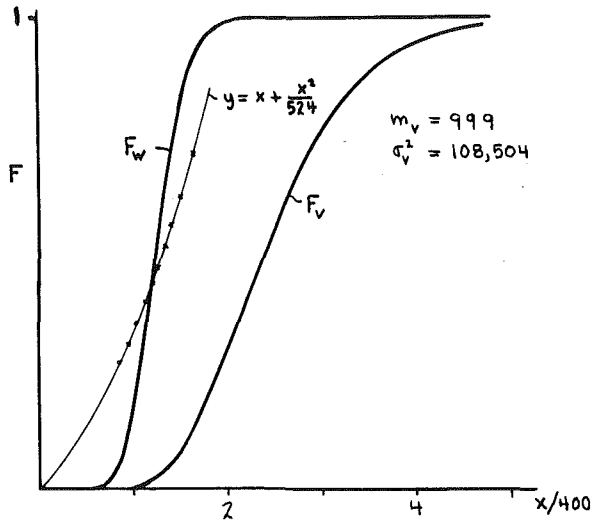


Fig. 3 Influence of transformation $y = x + x^2/524$ on shape of F_v

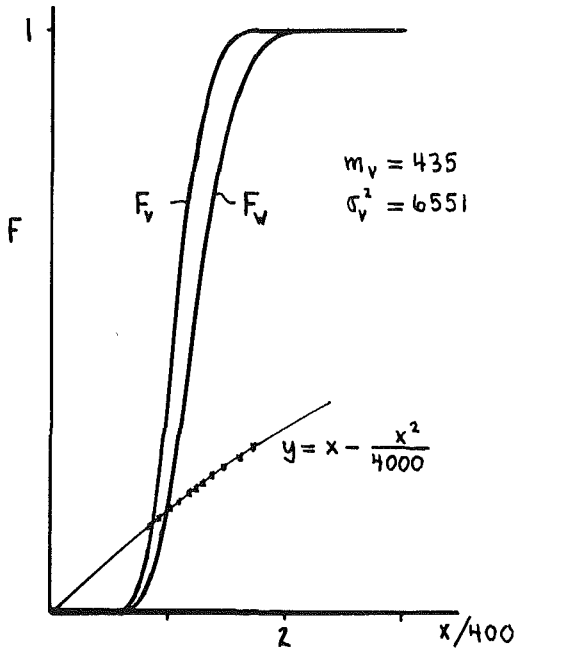


Fig. 4 Influence of transformation $y = x - x^3/4000$ on shape of F_v

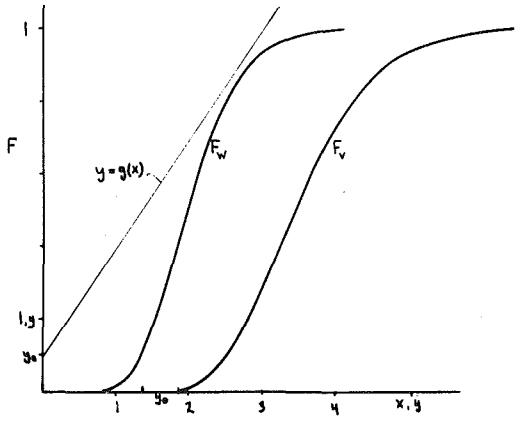


Fig. 5 Influence of vertical discontinuity at origin on shape of F_v

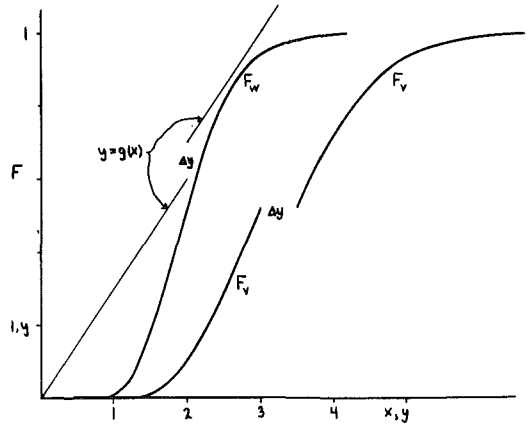


Fig. 6 Influence of vertical discontinuity at $x = 2$ on shape of F_v

whether g' is greater (less) than one. If there is a finite value $g(x)$ for which $g' = 0$ (see Fig. 4), this value of x must be much larger than the abicssa value at which F_w is essentially one. The roll-off of F_v to the asymptote 1 becomes very gradual if $g' > 1$ increases rapidly with x; conversely, the roll-off of F_v to the asymptote 1 becomes very rapid if g' ($0 < g' < 1$) decreases rapidly with x. A little refection reveals that vertical discontinuities (including a jump at the origin) in g causes horizontal discontinuities in F_v such as might occur during periods of no use (see Figs. 5 and 6); and horizontal discontinuities in g cause vertical discontinuities in F_v that might be thought of a period during which testing is conducted out of service. A continuous g made up of segments of straight lines may be thought of as representing time periods during which *DC* severity in y-time is constant but different in the different periods. Obviously, g can be used in a number of different ways.

Given any two of F_w, g, and F_v, we can construct the third. So far, we have used F_w and g to find F_v. Suppose we are given F_w and F_v; we can construct the time transformation g graphically in the same fashion as previously described. The form of g yields important insights into the nature of the B-model that will generate F_v. Indeed, it leads us to one of the most important results of this study.

Suppose the real data are given through the smoothed emperical distribution function (*edf*) F_v. Can this F_v be generated by a stationary B-model, or must it of necessity be modeled by a nonstationary B-model? Let us assume that the corresponding g is linear, yielding the time transformation $y = ax$: it follows that F_v can be obtained from a stationary B-model! To see this, let us consider the graphical procedure.

Given F_v, we choose an F_w with $m_w/\sigma_w = m_v/\sigma_v$. Suppose F_w and F_v generate time transformation $Y = ax$. Note that from this transformation $m_v = am_w$; therefore the slope of the line, a, is given by m_v/m_w. Now choose a stationary B-model with $m_w = m_v$ and the same m_v/σ_v. It follows that the slope of the new line that defines the time transformation connecting this B-model with F_v is unity!! Therefore, x-time and y-time are identical and the F_w generated by this B-model is identical to F_v. The importance of this result for B-models cannot be overestimated.

As an example, consider the F_n shown in Fig. 7, which is a smoothed version of an *edf* obtained in life testing in fatigue [8]. Regard F_n as F_v. The F_w is the *cdf* from a stationary B-model ($\pi_1 = 1$) having the same m_w/σ_w as does F_n. Construct g (shown by crosses). This g is nearly a straight line through the origin. Hence, we conclude that F_n can be described by the *cdf* of a stationary B-model with $\pi_1 = 1$.

Downloaded 01 May 2010 to 171.66.16.249. Redistribution subject to ASME license or copyright; see http://www.asme.org/terms/Terms_Use.cfm

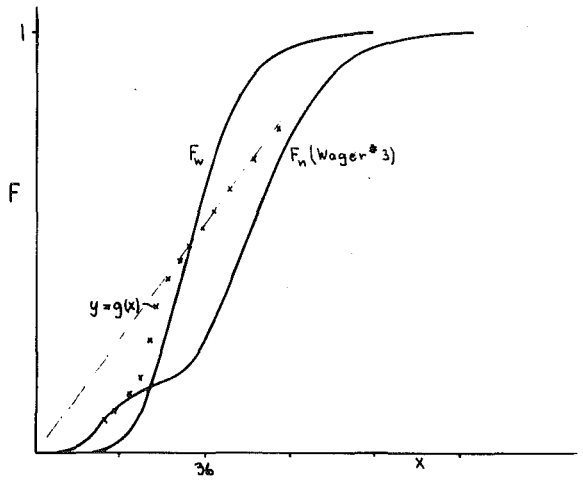


Fig. 7 Time transformation connecting a stationary *B*-model *cdf* F_w and a smoothed *edf* F_n (Sweet-Kozin)

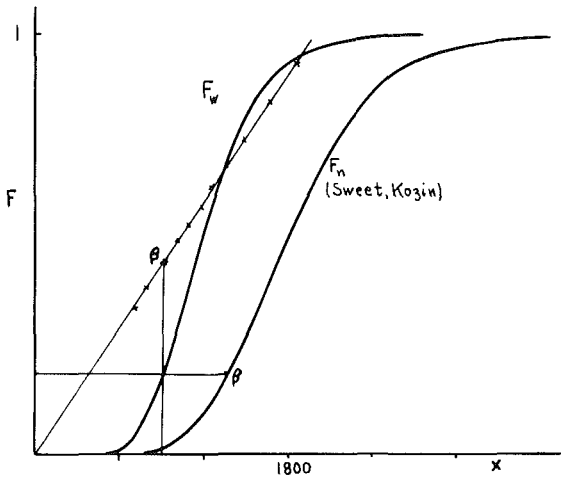


Fig. 8 Time transformation connecting a stationary *B*-model *cdf* F_w with $\pi_1 = 1$ and a smoothed edf F_n (Wager No. 3)

Now consider the F_n as shown in Fig. 8. This is a smoothed version of an *edf* obtained in wear testing [2]. F_w is an arbitrarily selected *cdf* from a stationary *B*-model with $\pi_1 = 1$. Construct g; this g tells us that *DC* severity in y-time first decreases, then increases, and ultimately becomes constant. Any other stationary F_w (with $\pi_1 = 1$) gives the same qualitative results. Naturally, it would be important to appeal directly to the experiment to determine if such behavior is plausible; in this case, it is not. That is, we have obtained a nonstationary model that does not agree with the physical facts. What do we do now? We can proceed in the following way. Consider an F_w obtained from a stationary *B*-model with $\pi_1 \neq 1$; again construct the g. Some numerical experimentations with the π_j ($\pi_1 \neq 1$) or using the computational scheme given in [9] provides a model whose *cdf*, F_w, is shown in Fig. 9, and here we find that g is linear, indicating there exists a stationary *B*-model with $\pi_1 \neq 1$ which fits the data. This model provides a physically plausible explanation of what is observed based upon what is known about the experiment.

We thus see that the g-function will determine for us whether or not to choose a nonstationary *B*-model, and how the *B*-model is to be constructed, whether stationary or not.

4 Describing Nonstationary Life Data

We shall now use the method described in Section 3 to construct a model to describe one set of life data that could have originated from a nonstationary *CD* mechanism.

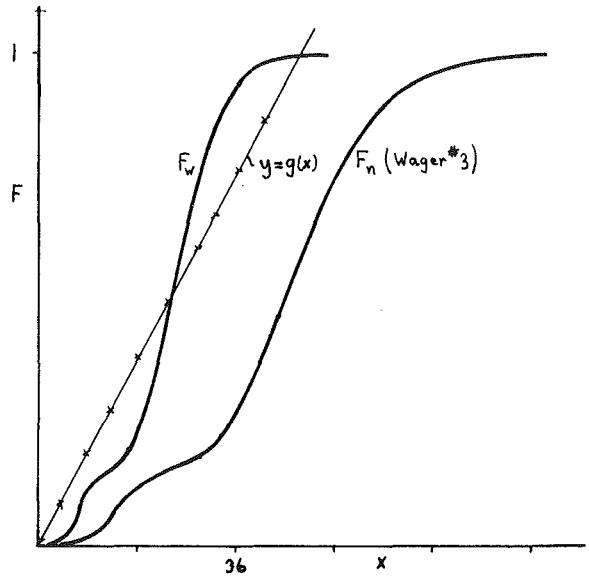


Fig. 9 Time transformation connecting a stationary *B*-model *cdf* F_w with $\pi_1 \neq 1$ and a smoothed *edf* F_n (Wager No. 3)

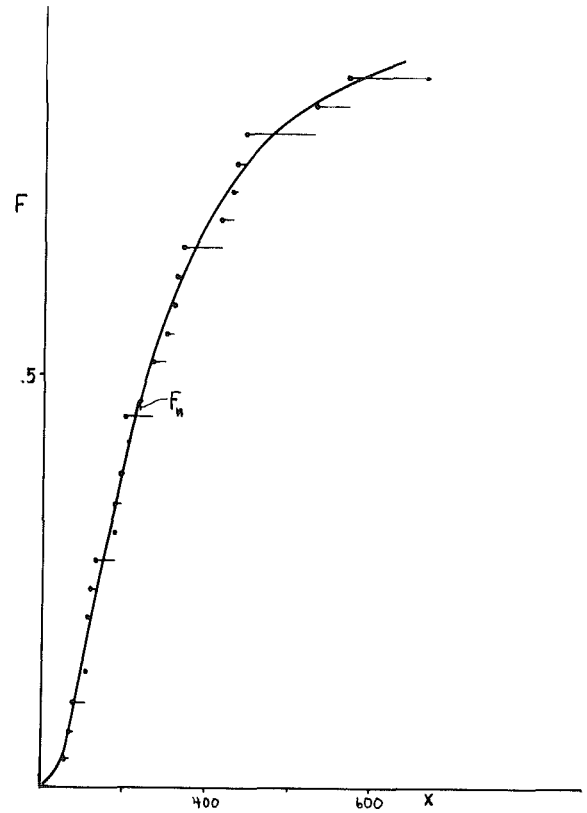


Fig. 10 *Edf* of life data of rolling elements in ball bearings and smoothed F_n

The emperical distribution function (*edf*) of the life data is shown in Fig. 10 (also see the figure in [2]). We have put in a smooth curve F_n to fit this *edf*.

We shall use F_n in y-time. The sharp rise in the toe of F_n and the very slow roll-off to the asymptote strongly suggests that the *CD* process in y-time has a *DC* severity steadily decreasing in time, implying a polynomial time transformation of reasonably high degree. We thus assume

Downloaded 01 May 2010 to 171.66.16.249. Redistribution subject to ASME license or copyright; see http://www.asme.org/terms/Terms_Use.cfm

$$y = x + a_1 x^2 + a_2 x^4, \quad a_1, \quad a_2 > 0 \tag{18}$$

We assume that in x-time P has unit jump, $\pi_1 = 1$, with $r_j =$ constant. It is convenient to use as scale for the abscissa 200 oscillations = 1 *DC*; we can convert back if that is desirable once α_1 and α_2 in (18) are evaluated. A short graphical exploration reveals that with $m_w = 0.35$, $m_w/\sigma_w = 3.00$, the values $a_1 = 1.120$, $a_2 = 67.19$ provide a transformation yielding a F_v which coincides with F_n. It should be mentioned that the values of a_1 and a_2 were found by matching F_v to F_n at the ordinates 0.20 and 0.40. We now have sufficient information to construct the stationary B-model in x-time and the $\{P_j\}$ in y-time. If deemed necessary, we can refine these parameters by maximum likelihood techniques, for example.

Figure 11 shows the *edf* of the life data and the F_v we have obtained. The fit is excellent.

Equation (18) says model *DC* severity in y-time steadily decreases in time. Since physical *DC* severity remains constant, the model indicates the material is work hardening.

Originally [2] we found $\{P_j\}$ by laborious trial-and-error procedure using a digital computer. The present method took under 1 hr of effort using a hand computer and a few graphs.

It is important to observe that in the aforementioned process we did not use the moments estimated from the *edf* and moment formulas for F_v to estimate the parameters as has proved so successful when dealing with stationary life data and stationary B-models. While we could have used the method of moments, it is much more complex than the scheme employed.

We also observe that the $\{Q_j\}$ we have found are not unique. Other choices of P in x-time could have been used, leading to a different time transformation. This nonuniqueness of the $\{Q_j\}$ is due to the fact that a single *edf* of life data does not specify the damage accumulation mechanism, as noted earlier [3, 4].

5 Discussion and Conclusion

This apparently simple and straightforward study of the time transformation of stationary B-models leads us to remarkable results.

In particular, we have shown how one can obtain a nonstationary B-model from real life data in a straightforward manner. The nonstationary model is constructed from a stationary model using a time transformation and a condensation method. The choice of the stationary B-model obviously raises some subtle problems, which are related to the choice of the "best" model and physical reality.

Furthermore, we can determine whether life data represented by an *edf* F_n came from a stationary or a nonstationary *CD* process. We simply find the time transformation connecting F_n with the *cdf* F_w of a suitable B-model. If the transformation is nonlinear, it is natural to represent the *CD* process with a nonstationary model. If the transformation is linear a stationary B-model is the natural model, the appropriate stationary model then gives the transformation $y = x$.

Finally, it is easy to see how to extend the method to account for environmental changes, significant occasional random overloads, etc.

We shall show in a subsequent paper that the techniques discussed opens up the whole field of spectrum (and random) loading and accelerated testing under spectrum loading to a detailed analysis.

Once again we note that B-model provide a powerful and straightforward tool for the examination of a wide variety of aspects of *CD* processes.

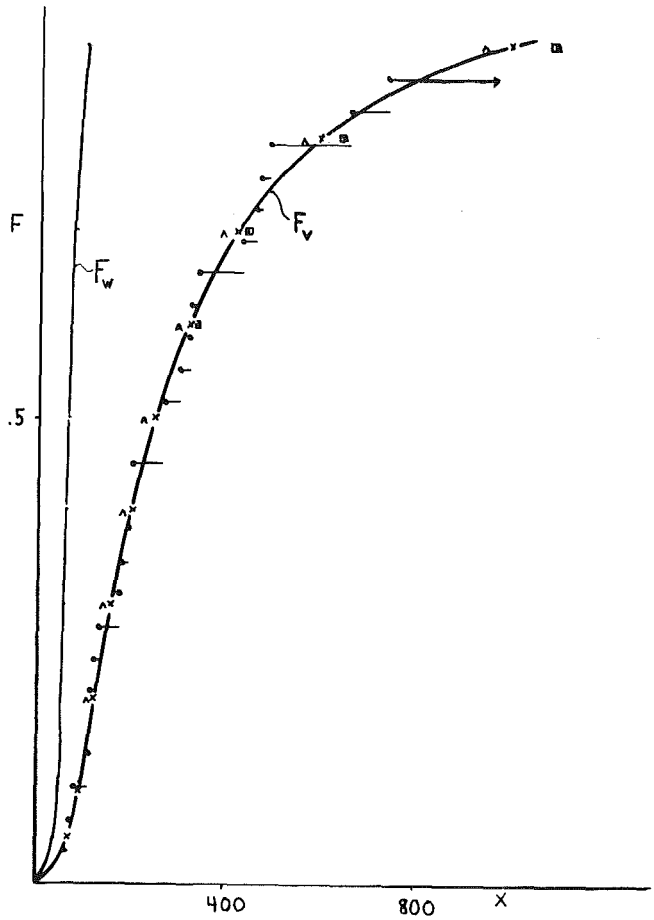


Fig. 11 F_w **and** F_v **from nonlinear transformation for description of** F_n **from Fig. 10**

Acknowledgment

Support from A.F.O.S.R., Dr. I. N. Shimi, Project Manager, under Contract No. F-49670-78-C-0108, is gratefully acknowledged.

References

1 Bogdanoff, J. L., "A New Cumulative Damage Model, Part 1," ASME JOURNAL OF APPLIED MECHANICS, Vol. 45, June 1978, pp. 246–250.

2 Bogdanoff, J. L., and Krieger, W., "A New Cumulative Damage Model, Part 2," ASME JOURNAL OF APPLIED MECHANICS, Vol. 45, June 1978, pp. 251–257.

3 Bogdanoff, J. L., "A New Cumulative Damage Model, Part 3," ASME JOURNAL OF APPLIED MECHANICS, Vol. 45, Dec. 1978, pp. 733–739.

4 Bogdanoff, J. L., and Kozin, F., "A New Cumulative Damage Model, Part 4," ASME JOURNAL OF APPLIED MECHANICS, Vol. 47, Mar. 1980, pp. 40–44.

5 Kozin, F., and Bogdanoff, J. L., "A Critical Analysis of some Probabilistic Models of Fatigue Crack Growth," *Eng. Fract. Mech.* Vol. 14, 1981, pp. 49–89.

6 Bogdanoff, J. L., and Kozin, F., "On a New Cumulative Damage Model for Fatigue," *1981 Proceedings, Annual Reliability and Maintainability Symposium,* pp. 9–17.

7 Cinlar, E., *Introduction to Stochastic Processes,* Prentice-Hall, Inc., Englewood Cliffs, N. J., 1975, pp. 236–237.

8 Sweet, A. L., and Kozin, F., "Experimental Studies of Cumulative Damage," Contract No. NAS8-20105, George C. Marshall Space Flight Center, Huntsville, Ala., Mar. 1967.

9 Alhassid, Y., Agmon, N., and Levine, R. D., "An Upper Bound for the Entropy and Its Application to the Maximal Entropy Problem," *Chem. Phy. Letters,* Vol. 53, No. 1, January 1, 1978, pp. 22–26.

Downloaded 01 May 2010 to 171.66.16.249. Redistribution subject to ASME license or copyright; see http://www.asme.org/terms/Terms_Use.cfm

T. S. Sankar
Professor.
Mem. ASME

V. Fabrikant
Research Associate.

Department of Mechanical Engineering,
Concordia University,
Montreal, Quebec, Canada

Asymmetric Contact Problem Including Wear For Nonhomogeneous Half Space

Contact problem with wear for asymmetric rigid die acting on a half space whose elastic modulus is a power function of depth is considered for the case when the die is rotating according to an arbitrary law. Zone of contact is taken to be a circle, and the wear is proportional to the work done by the tangential stresses obeying Coloumb's law. Integral equation of the problem is derived and an exact solution of the equation is obtained in closed form. The case of inclined flat die is discussed as an illustrative example of the general method of solution that is proposed.

Introduction

Plane and axisymmetric contact problems with wear have been extensively investigated in recent years. The plane contact problem was initially formulated by Galin [1]. He reduced it to an eigenvalue and eigenfunction problem of an integral equation of Fredholm type with singular kernel and showed that solutions can be obtained. Using this technique, Aleksandrov, et al. [2], obtained some numerical results for the case of constant rate of penetration of the die into the half plane and also for the case of constant applied forces.

Axisymmetric contact problem with wear was later formulated by Galin and Goriacheva [3] and was reduced to an eigenfunction problem of a Fredholm integral equation with a symmetrical kernel. They also proved the positive nature of all the generated eigenvalues. These results were then extended by Aleksandrov, et al. [4]. Here, using the Legendre polynomials expansion of the kernel and the eigenfunctions, numerical results were obtained for the same cases, as proposed in [2], considering the embedding of a rotating annular die into an elastic layer.

The important problem of asymmetric contact with wear, for which solutions have not been previously obtained, is considered in this paper and the exact solution of such a problem is obtained in a closed form. Employing the properties of hypergeometric functions, Abel operators and newly introduced L-operators, explicit expression for the inverse operator is given. The details of the calculation procedure are explained in the Appendix.

As an illustrative example, the case of embedding of an inclined rotating cylindrical die is considered. The governing formulas for calculating the axial forces and tilting and rotating moments are obtained for limiting cases of $t=0$ and $t\to\infty$.

Contributed by the Applied Mechanics Division for publication in the JOURNAL OF APPLIED MECHANICS.

Discussion on this paper should be addressed to the Editorial Department, ASME, United Engineering Center, 345 East 47th Street, New York, N.Y. 10017, and will be accepted until two months after final publication of the paper itself in the JOURNAL OF APPLIED MECHANICS. Manuscript received by ASME Applied Mechanics Division, November, 1980; final revision, June, 1981.

Formulation of the Problem

Consider a nonhomogeneous elastic half space $z\geq 0$, elastic modulus of which is a power function of z, namely

$$E=E_0 z^k 0\leq k<1$$

A stamp with the end surface defined by the equation

$$z=f(\rho,\phi)$$

in polar coordinates is situated on this half space, and is acted upon by a force P acting along the z-axis, and M_r is the rotating moment on the stamp about this axis according to a law $\psi=\psi(t)$. Here, the angle of rotation ψ is an increasing positive function of time t with $\psi(0)=0$. It is assumed that the contact area is a circle of radius a and the only frictional forces $\tau_{z\theta}$ are proportional to the normal pressure σ_z with a constant coefficient of friction μ described as

$$\tau_{z\theta}=\mu\sigma_z \tag{1}$$

In this paper, the thermal effect, dynamic effect of rotation, and influence of $\tau_{z\theta}$ on the normal displacement are neglected since the influence of these are not significant. The integral equation of the problem in polar coordinates may be written, as given in [5],

$$H\int_0^a\int_0^{2\pi}\frac{\sigma(\rho_0,\phi_0,t)\rho_0 d\rho_0 d\phi_0}{(\rho^2+\rho_0^2-2\rho\rho_0\cos(\phi-\phi_0))^{\frac{1+k}{2}}}=w(\rho,\phi,t) \tag{2}$$

Here H is an elastic constant [6], and σ denotes the normal pressure σ_z.

When the wear is abrasive, the amount of material removed can be assumed proportional to the work done by the frictional forces, and may be written as

$$w(\rho,\phi,t)=\delta(t)-f(\rho,\phi+\psi(t))-\mu m\rho\int_0^t\sigma(\rho,\phi,\tau)\frac{d\psi(\tau)}{d\tau}d\tau \tag{3}$$

Here $\delta(t)$ is the rigid displacement of the die and m is the coefficient of abrasive wear.

Substitution of equation (3) in (2) results in the type of

Copyright © 1982 by ASME
Downloaded 01 May 2010 to 171.66.16.249. Redistribution subject to ASME license or copyright; see http://www.asme.org/terms/Terms_Use.cfm

integral equation of the problem to be solved for the stresses and moments and is

$$H\int_0^a \int_0^{2\pi} \frac{\sigma(\rho_0,\phi_0,t)\rho_0 d\rho_0 d\phi_0}{(\rho^2+\rho_0^2-2\rho\rho_0\cos(\phi-\phi_0))^{\frac{1+k}{2}}} = \delta(t) - f[\rho,\phi+\psi(t)]$$

$$-\mu m\rho\int_0^t \sigma(\rho,\phi,\tau)\frac{d\psi(\tau)}{d\tau}d\tau \tag{4}$$

It is now possible to consider certain variations of the stated problem, e.g., $\delta(t)$ is a known function and $P(t)$ is to be determined. In practice, this case arises when it is necessary to provide certain rate of embedding of the stamp into the half space. Inverse case is also of interest when the acting force $P(t)$ is known and the rate of penetration is to be determined.

Proposed Solution

For simplicity, equation (4) is rewritten in the form

$$HM\sigma(\rho_0,\phi_0,t) = w_1(\rho,\phi,t) - \mu m\rho\int_0^t \sigma(\rho,\phi,\tau)\frac{d\psi(\tau)}{d\tau}d\tau \tag{5}$$

Here M denotes the left-hand integral operator in equation (4), and

$$w_1(\rho,\phi,t) = \delta(t) - f[\rho,\phi+\psi(t)]$$

Equation (5) with respect to t is equivalent to an ordinary linear differential equation of the first order with varying coefficients. Its solution is known and is written in the standard form

$$\sigma(\rho,\phi,t) = \frac{M^{-1}}{H}\left\{w_1(\rho_0,\phi_0,t) - \beta e^{-\psi(t)\beta}\int_0^t e^{\psi(\tau)\beta}w_1(\rho_0,\phi_0,\tau)\frac{d\psi(\tau)}{d\tau}\right\} \tag{6}$$

Here β denotes the product $H^{-1}\mu m M^{-1}\rho_0$, and M^{-1} is an integral operator indicating inverse of M. Explicit expression for M^{-1} is obtained in the Appendix at the end of the paper and has the form

$$M^{-1}f(\rho_0,\phi_0) = \frac{\cos\frac{\pi k}{2}}{2\pi^3}\int_0^{2\pi}\left\{\frac{f(0,\phi_0)+\Phi(a,\rho,\phi_0,\phi)}{(a^2-\rho^2)^{\frac{1-k}{2}}} - \int_\rho^a \frac{dr}{(r^2-\rho^2)^{\frac{1-k}{2}}}\frac{d}{dr}\Phi(r,\rho,\phi_0,\phi)\right\}d\phi_0$$

$$\Phi(r,\rho,\phi_0,\phi) = r^{1-k}\int_0^r \frac{d\rho_0}{(r^2-\rho_0^2)^{\frac{1-k}{2}}}\frac{d}{d\rho_0}\left[L\left(\frac{\rho\rho_0}{r^2},\phi_0-\phi\right)f(\rho_0,\phi_0)\right] \tag{7}$$

Now, if $\delta(t)$ is a known function, then

$$P(t) = \int_0^a\int_0^{2\pi}\sigma(\rho,\phi,t)\rho d\rho d\phi$$

Analogously, if $\psi(t)$ is a known function, then the rotating moment M_r

$$M_r(t) = J\frac{d^2\psi}{dt^2} + \mu\int_0^a\int_0^{2\pi}\sigma(\rho,\phi,t)\rho^2 d\rho d\phi$$

where J is the moment of inertia of the die.

Hereafter M^{-1} will be denoted as an integral transform of a function of ρ_0,ϕ_0, into a new function of ρ and ϕ. The time parameters t and τ are not affected by this transformation, and the arbitrary function of time $\psi(t)$ remains unchanged after application of the operator M^{-1}. For example, the product of $\beta w_1(\rho_0,\phi_0,\tau)$ is denoted by

$$\beta w_1(\rho_0,\phi_0,\tau) \equiv H^{-1}\mu m M^{-1}[\rho_0 w_1(\rho_0,\phi_0,\tau)]$$

Further β^2 is understood as two consecutive applications of the operator β, and $e^{\psi(t)\beta}$ is interpreted as an expansion of the exponent in the power series.

All of these formulas are valid not only for the case of inhomogeneous half space, but also give the solution for an isotropic body. The latter case is obtained setting $k=0$.

Illustrative Example

As an example, one may consider the case of an inclined cylindrical flat-ended die under the action of an axial force $P(t)$, rotating moment $M_r(t)$, and a tilting moment $M_t(t)$. Let α be the angle between the axis $0z$ and that of the die ($\alpha=$ const). The displacements of the die are then prescribed as follows

$$w_1(\rho,\phi,t) = \delta_0 + \delta_1 t + \alpha\rho\cos\phi$$

where δ_0, δ_1 are constants, and $\psi(t)=\omega t$ with $\omega=$ constant.

In this case, direct use of equation (6) yields the following results

$$\sigma(\rho,\phi,t) = \frac{M^{-1}}{H}e^{-\beta\omega t}(\delta_0+\alpha\rho_0\cos\phi_0) + \frac{\delta_1}{\mu m\omega}(1-e^{-\beta\omega t})\frac{1}{\rho_0}$$

Now, it is possible to obtain the following solutions for the limiting cases $t=0$ and $t\to\infty$ and are

$$\sigma(\rho,\phi,0) = \frac{\cos\frac{\pi k}{2}}{\pi^2 H}\frac{\delta_0+\frac{2\alpha}{1+k}\cos\phi}{(a^2-\rho^2)^{\frac{1-k}{2}}}$$

$$\sigma(\rho,\phi,\infty) = \frac{\delta_1}{\mu m\omega}\frac{1}{\rho}$$

Consequently, the following expressions are valid for the axial force P, the tilting moment M_t, and the rotating moment M_r

$$P(0) = \frac{2\cos\frac{\pi k}{2}}{\pi H}\frac{\delta_0 a^{1+k}}{1+k}, P(\infty) = \frac{2\pi a\delta}{\mu m\omega}$$

$$M_t(0) = \frac{4\alpha a^{3+k}\cos\frac{\pi k}{2}}{\pi H(1+k)^2(3+k)}, M_t(\infty) = 0$$

$$M_r(0) = \mu\frac{\cos\frac{\pi k}{2}}{\pi H}\frac{\Gamma\left(\frac{1+k}{2}\right)\Gamma\left(\frac{3}{2}\right)}{\Gamma(2+k)}\delta_0 a^{2+k}, M_r(\infty) = \frac{\pi a^2\delta_1}{m\omega}$$

Discussion of Results

From the solutions, it may be observed that in the example considered, the stresses under the die change radically with the

Downloaded 01 May 2010 to 171.66.16.249. Redistribution subject to ASME license or copyright; see http://www.asme.org/terms/Terms_Use.cfm

passage of time. At $t=0$, singularity exists on the edge, and at $t\to\infty$ the singularity occurs at the center. This is due to the fact that there is no wear under the die center, and hence there will only be plastic deformation at this point.

Initial axial forces and rotating moments are proportional to the initial displacement of the die, while at $t\to\infty$ they are proportional to the rate of penetration of the die.

Initial tilting moment is proportional to the angle α and disappear with the passage of time. It is of some interest to note that at $t\to\infty$, axial forces, as well as moments, do not depend on the elastic properites of material of the half space.

In this paper, the rotating velocity is assumed to be small to justify the fact that the thermal effects may be neglected. Inclusion of thermodynamic consideration will present an interesting challenge to the present problem.

Acknowledgments

The investigation reported in this paper was partially supported by grant A7104 from the Natural Sciences and Engineering Research Council of Canada.

References

1 Galin, L. A., "Contact Problems of the Theory of Elasticity in the Presence of Wear," *Journal of Applied Mathematics and Mechanics*, Vol. 40, 1976, pp. 981–986.

2 Aleksandrov, V. M., Galin, L. A., and Piriev, N. P., "Plane Contact Problem with Wear for a Thick Elastic Layer," *Mechanics of Solids*, Vol. 13, No. 4, 1978, pp. 60–67.

3 Galin, L. A., and Goriacheva, I. G., "Axisymmetric Contact Problem of the Theory of Elasticity in the Presence of Wear," *Journal of Applied Mathematics and Mechanics*, Vol. 41, No. 5, 1977, pp. 807–812.

4 Aleksandrov, V. M., and Kovalenko, E. V., "Axisymmetric Contact Problem for Linearly Deformable Foundation of General Type with Wear," *Mechanics of Solids*, Vol. 13, No. 5, 1978, pp. 58–66.

5 Rostovtsev, N. A., "An Integral Equation Encountered in the Problem of a Rigid Foundation Bearing on Nohomogeneous Soil," *Journal of Applied Mathematics and Mechanics*, Vol. 25, 1961, pp. 238–246.

6 Rostovtsev, N. A., and Khranevskaia, I. E., "The Solution of the Boussinesq Problem for a Half-Space Whose Modulus of Elasticity is a Power Function of Depth," *Journal of Applied Mathematics and Mechanics*, Vol. 35, 1971, pp. 1053–1061.

7 Bateman, G., and Erdelyi, A., *Higher Transcendental Functions*, Vol. 1, McGraw-Hill, New York, 1954.

APPENDIX

Here explicit expression for the operator M^{-1} inverse to the operator M is derived. Consider the integral equation

$$\int_0^a\int_0^{2\pi}\frac{F(\rho_0,\phi_0)\rho_0 d\rho_0 d\phi_0}{\left[\rho^2+\rho_0^2-2\rho\rho_0\cos(\phi-\phi_0)\right]^{\frac{1+\nu}{2}}}=f(\rho,\phi)\ (0\le\rho\le a, 0\le\phi\le 2\pi)$$

Here, f is the known function and $0\le\nu<1$.

Using the known properties of hypergeometric functions [5], it is possible to transform the kernel as follows

$$\frac{1}{\left(\rho^2+\rho_0^2-2\rho\rho_0\cos(\phi-\phi_0)\right)^{\frac{1+\nu}{2}}}=\sum_{n=-\infty}^{\infty}\frac{e^{in(\phi-\phi_0)}}{2\pi}\int_0^{2\pi}\frac{e^{-in\psi}d\psi}{\left[\rho^2+\rho_0^2-2\rho\rho_0\cos\psi\right]^{\frac{1+\nu}{2}}}$$

$$=\sum_{n=-\infty}^{\infty}\frac{e^{in(\phi-\phi_0)}}{2\pi\rho_0^{1+\nu}}\frac{2\pi\Gamma[n+(1+\nu)/2]}{\Gamma\left(\frac{1+\nu}{2}\right)\Gamma(n+1)}\left(\frac{\rho}{\rho_0}\right)^n {}_2F_1\left(\frac{1+\nu}{2},n+\frac{1+\nu}{2},n+1;\frac{\rho^2}{\rho_0^2}\right)$$

$$=\sum_{n=-\infty}^{\infty}\frac{e^{in(\phi-\phi_0)}}{\rho_0^{1+\nu}}\frac{\Gamma[n+(1+\nu)/2]}{\Gamma\left(\frac{1+\nu}{2}\right)\Gamma(n+1)}\left(\frac{\rho}{\rho_0}\right)^n\frac{2\Gamma(n+1)}{\Gamma[n+(1+\nu)/2]\Gamma\left[1-(1+\nu)/2\right]}$$

$$\times\int_0^1\frac{t^{2n+\nu}(1-t^2)^{-\frac{1+\nu}{2}}}{(1-t^2\rho^2/\rho_0^2)^{\frac{1+\nu}{2}}}dt$$

$$=\sum_{n=-\infty}^{\infty}\frac{2}{\pi}\cos\frac{\pi\nu}{2}\frac{e^{in(\phi-\phi_0)}}{(\rho\rho_0)^n}\int_0^{\rho}\frac{x^{2n+\nu}dx}{\left[(\rho^2-x^2)(\rho_0^2-x^2)\right]^{\frac{1+\nu}{2}}}$$

$$=\frac{2}{\pi}\cos\frac{\rho\pi}{2}\int_0^{\rho}\frac{x^{\nu}dx}{\left[(\rho^2-x^2)(\rho_0^2-x^2)\right]^{\frac{1+\nu}{2}}}\left[\frac{1}{1-\frac{x^2}{\rho\rho_0}e^{i(\phi-\phi_0)}}+\frac{1}{1-\frac{x^2}{\rho\rho_0}e^{-i(\phi-\phi_0)}}-1\right] \tag{9}$$

The last expression is valid if $\rho<\rho_0$. In the case $\rho>\rho_0$, the upper limit of integration will be ρ_0.

Now, substitution of equation (9) into equation (8) yields

$$\frac{2}{\pi}\cos\frac{\pi\nu}{2}\int_0^{\rho}\frac{x^{\nu}dx}{(\rho^2-x^2)^{\frac{1+\nu}{2}}}\int_x^a\frac{\rho_0 d\rho_0}{(\rho_0^2-x^2)^{\frac{1+\nu}{2}}}\times\int_0^{2\pi}\left[\frac{1}{1-\frac{x^2}{\rho\rho_0}e^{i(\phi-\phi_0)}}+\frac{1}{1-\frac{x^2}{\rho\rho_0}e^{-i(\phi-\phi_0)}}-1\right]$$

$$F(\rho_0,\phi_0)d\rho_0=f(\rho,\phi) \tag{10}$$

Here, a change of the order of integration is used accordingly to the scheme

$$\int_0^{\rho}d\rho_0\int_0^{\rho_0}dx+\int_{\rho}^a d\rho_0\int_0^{\rho}dx=\int_0^{\rho}dx\int_x^{\rho}d\rho_0+\int_0^{\rho}dx\int_{\rho}^a d\rho_0=\int_0^{\rho}dx\int_x^a d\rho_0$$

Consider an operator

$$L(k,\phi-\phi_0)f(\phi_0)=\int_0^{2\pi}\left[\left(1-ke^{i(\phi-\phi_0)}\right)^{-1}+\left(1-ke^{-i(\phi-\phi_0)}\right)^{-1}-1\right]f(\phi_0)d\phi_0$$

Downloaded 01 May 2010 to 171.66.16.249. Redistribution subject to ASME license or copyright; see http://www.asme.org/terms/Terms_Use.cfm

It is easy to prove the following properties of L-operators

$$L(k_1,\phi_1-\phi)L(k,\phi-\phi_0)=2\pi L(kk_1,\phi_1-\phi_0)$$
$$L(1,\phi-\phi_0)f(\phi_0)=2\pi f(\phi) \tag{11}$$

Application of the operators

$$\frac{d}{dr}\int_0^r \frac{\rho d\rho}{(r^2-\rho^2)^{\frac{1-\nu}{2}}} L\left(\frac{\rho}{z},\phi_1-\phi\right)$$

to both sides of equation (10) yields

$$2\pi r^\nu \int_r^a \frac{\rho_0 d\rho_0}{(\rho_0^2-r^2)^{\frac{1+\nu}{2}}} \int_0^{2\pi} \left[\left(1-\frac{r^2}{z\rho_0}e^{i(\phi_1-\phi_0)}\right)^{-1}\right.$$

$$+\left(1-\frac{r^2}{z\rho_0}e^{-i(\phi_1-\phi_0)}\right)^{-1}$$

$$\left.-1\right]F(\rho_0\phi_0)d\phi_0=\frac{d}{dr}\int_0^r \frac{\rho d\rho}{(r^2-\rho^2)^{\frac{1-\nu}{2}}}$$

$$L\left(\frac{\rho}{z},\phi_1-\phi\right)f(\rho,\phi)$$

Here the known properties of L and Abel operators [7] are used.

Now after dividing both parts of the last expression by r^ν and applying operators

$$\frac{d}{dy}\int_y^a \frac{rdr}{(r^2-y^2)^{\frac{1-\nu}{2}}} L\left(\frac{z^2}{r^2},\phi_2-\phi_1\right)$$

one obtains

$$-\frac{2\pi^3}{\cos\frac{\pi\nu}{2}} yL(z/y,\phi_2-\phi_0)F(y,\phi_0)$$

$$=\frac{d}{dy}\int_y^a \frac{r^{1-\nu}dr}{(r^2-y^2)^{\frac{1-\nu}{2}}} L\left(\frac{z^2}{r^2},\phi_2-\phi_1\right)$$

$$\frac{d}{dr}\int_0^r \frac{\rho d\rho}{(r^2-\rho^2)^{\frac{1-\nu}{2}}} L\left(\frac{\rho}{z},\phi_1-\phi\right)f(\rho,\phi)$$

0peration$L(y/z,\psi-\phi_2)$ leads to the solution of the problem

$$F(y,\psi)=-\frac{\cos\frac{\pi\nu}{2}}{8\pi^5 y} L\left(\frac{y}{z},\psi-\phi_2\right)\frac{d}{dy}\int_y^a \frac{r^{1-\nu}dr}{(r^2-y^2)^{\frac{1-\nu}{2}}}$$

$$\times L\left(\frac{z^2}{r^2},\phi_2-\phi_1\right)\frac{d}{dr}\int_0^r \frac{\rho d\rho}{(r^2-\rho^2)^{\frac{1-\nu}{2}}} L\left(\frac{\rho}{z},\phi_1-\phi\right)f(\rho,\phi)$$

It is possible to simplify the last formula using the L-operator properties, equation (11), and the rules of differentiation under integral sign and integration by parts. The result is

$$F(y,\psi)=\frac{\cos\frac{\pi\nu}{2}}{2\pi^3}\int_0^{2\pi}\left\{\frac{f(0,\phi)+\Phi(a,y,\phi,\psi)}{(a^2-y^2)^{\frac{1-\nu}{2}}}\right.$$

$$\left.\int_y^a \frac{dr}{(r^2-y^2)^{\frac{1-\nu}{2}}}\frac{d}{dr}\Phi(r,y,\phi,\psi,)\right\}d\phi$$

$$\Phi(r,y,\phi,\psi,)=r^{1-\nu}\int_0^r \frac{d\rho}{(r^2-\rho^2)^{\frac{1-\nu}{2}}}\frac{d}{d\rho}$$

$$\left[L\left(\frac{y\rho}{r^2},\phi-\psi\right)f(\rho,\phi)\right]$$

Downloaded 01 May 2010 to 171.66.16.249. Redistribution subject to ASME license or copyright; see http://www.asme.org/terms/Terms_Use.cfm

Maria Comninou
Associate Professor,
Department of Civil Engineering,
University of Michigan,
Ann Arbor, Mich. 48109
Mem. ASME

John Dundurs
Professor,
Department of Civil Engineering,
Northwestern University,
Evanston, Ill. 60201
Fellow ASME

An Educational Elasticity Problem With Friction Part 2: Unloading for Strong Friction and Reloading

This paper examines the case of unloading with strong friction, and also treats reloading of the unbounded solid with a semi-infinite cut. The solid is compressed uniformly normal to the cut, and a concentrated force acts on the tip of the cut causing localized separation and frictional slip.

Introduction

This paper is a continuation of [1], in which the problem of localized separation and slip at a semi-infinite cut in an unbounded solid were considered. The applied loads were uniform compression normal to the cut and a concentrated force P at the origin. We allowed P to vary as a function of time and first studied the case of *loading* or $\dot{P}(t)>0$. Next we proceeded to examine the case of *unloading* or $\dot{P}(t)<0$ after $P(t)$ had reached a maximum value P_1. To follow unloading we had to decide whether $f_k<\tan\alpha$ or $f_k>\tan\alpha$ in the notation of [1]. The case $f_k<\tan\alpha$, or unloading for weak friction was completed in [1]. Here we consider the case $f_k>\tan\alpha$, or unloading for strong friction. Moreover, we extended our study to *reloading* for both weak and strong friction.

Unloading for Strong Friction

For reference, some of the key results that are required to treat unloading are repeated.

The extent of the separation zone is given by

$$a=\frac{\kappa-1}{\pi(\kappa+1)}\frac{P\cos\alpha}{p\infty} \tag{1}$$

and the normal tractions are

$$N(x)=-p\infty\left(\frac{x-a}{x}\right)^{1/2}H(x-a),\qquad 0<x<\infty \tag{2}$$

The residual or locked-in shear tractions are

$$S_1(x)=f_k p\infty\left\{-\left(\frac{x-a_1}{x}\right)^{1/2}H(x-a_1)+\left(\frac{x-b_1}{x}\right)^{1/2}H(x-b_1)\right\},\qquad 0<x<\infty \tag{3}$$

where a_1 and b_1 determine the extents of separation and slip zones reached at the maximum load P_1. Specifically, a_1 is obtained from (1) upon replacing P with P_1 and

$$b_1=a_1\left(1+\frac{\tan\alpha}{f_k}\right) \tag{4}$$

The correction required to account for the changed conditions of slip due to unloading is sought in the form of a glide dislocation distribution $B_x{}^c(x)$ over the region $0<x<a_1$. It is recalled from [1] that for the case of strong friction, the possible slip zone cannot expand to the right and $b<a_1$. Then, if the corrective quantities are identified by the index c we have for the corrective shear tractions, tangential shift and slip velocity

$$S_c(x) = -\frac{2\mu}{\pi(\kappa+1)}\int_0^{a_1}\frac{B_x^c(\xi)d\xi}{\xi-x},\qquad 0<x<\infty \tag{5}$$

$$h_c(x) = \frac{\kappa-1}{4\mu}(P_1-P)\sin\alpha-\int_0^x B_x^c(\xi)d\xi,\qquad 0<x<\infty \tag{6}$$

$$V(x) = \dot{h}_c(x)=-\frac{\kappa-1}{4\mu}\dot{P}\sin\alpha-\int_0^x \dot{B}_x{}^c(\xi)d\xi,\quad 0<x<\infty \tag{7}$$

Note that the first terms in (6) and (7) represent the contributions from the Airy stress function reflecting the decrease of the concentrated force from P_1 to P. The total shear tractions are then

$$S(x)=S_1(x)+S_c(x) \tag{8}$$

Some clarification is required regarding the interval of definition of $B_x^c(x)$. For the case of weak friction [1], the slip zone *advanced* into a stick zone ($a_1<b$) anihilating the locked-in dislocations on $a_1<x<b$, and the corrective distribution was defined on $0<x<b$. In the present case of strong friction, the slip zone *recedes* from a stick zone (onset of recession at $x=a_1$) leaving behind new locked-in dislocations on $a<x<a_1$, and $B_x^c(x)$ must be defined on $0<x<a_1$.

Although it will be shown that a slip zone is not possible for the case of strong friction, it is instructive to exhibit the contradictions arising from the assumption of slip.

Contributed by the Applied Mechanics Division for publication in the JOURNAL OF APPLIED MECHANICS.

Discussion on this paper should be addressed to the Editorial Department, ASME, United Engineering Center, 345 East 47th Street, New York, N.Y. 10017, and will be accepted until two months after final publication of the paper itself in the JOURNAL OF APPLIED MECHANICS. Manuscript received by ASME Applied Mechanics Division, March 1981.

Copyright © 1982 by ASME
Downloaded 01 May 2010 to 171.66.16.249. Redistribution subject to ASME license or copyright; see http://www.asme.org/terms/Terms_Use.cfm

Slip Zone. If there is slip in the region $a<x<b$, it is anticipated that $V(x)>0$ and hence $S(x)>0$. Therefore we can take

$$S(x) = -f_k N(x), \qquad 0<x<b \tag{9}$$

Since $S_1(x)$ vanishes in $0<x<b$, using (2) and (5), (9) becomes,

$$\int_0^{a_1} \frac{B_x^c(\xi)d\xi}{\xi - x} = -\frac{\pi(\kappa+1)}{2\mu} f_k p_\infty \left(\frac{x-a}{x}\right)^{1/2} H(x-a),$$

$$0<x<b \tag{10}$$

Note that (10) is a Cauchy singular integral equation, valid in an interval smaller than the range of integration. Thus additional information about the unknown function $B_x^c(x)$ is required. Indeed we observe that $B_x^c(x)$ in $b<x<a_1$ must be independent of time (and therefore of a), since conditions of stick prevail on $b<x<a_1$ and the dislocation distribution is locked in. To utilize this information we differentiate (10) with respect to time:

$$\int_0^{a_1} \frac{\dot{B}_x^c(\xi)d\xi}{\xi - x} = \frac{\pi(\kappa+1)}{4\mu} f_k p_\infty \frac{\dot{a}}{x^{1/2}(x-a)^{1/2}} H(x-a),$$

$$0<x<b \tag{11}$$

and since

$$\dot{B}_x^c(x) = 0, \qquad b<x<a_1 \tag{12}$$

equation (11) becomes

$$\int_0^{b} \frac{\dot{B}_x^c(\xi)d\xi}{\xi - x} = \frac{\pi(\kappa+1)}{4\mu} f_k p_\infty \frac{\dot{a}}{x^{1/2}(x-a)^{1/2}} H(x-a),$$

$$0<x<b \tag{13}$$

There are two options for the solution of (13): (*1*) $\dot{B}_x^c(x)$ bounded at b or (*2*) $\dot{B}_x^c(x)$ unbounded at b. In either case $\dot{B}_x^c$ is unbounded at $x=0$. Since similar calculations have been shown in [1], we omit the details and record the results:

Case 1

$$\dot{B}_x^c(x) = -\frac{\kappa+1}{4\mu} f_k p_\infty \frac{\dot{a}}{x^{1/2}(a-x)^{1/2}} H(a-x), 0<x<b \tag{14}$$

$$V(x) = \frac{\pi(\kappa+1)}{4\mu} p_\infty (f_k - \tan\alpha)\dot{a}, \qquad a<x<b \tag{15}$$

Case 2

$$\dot{B}_x^c(x) = \frac{\kappa+1}{4\mu}(f_k - \tan\alpha) p_\infty \frac{\dot{a}}{x^{1/2}(b-x)^{1/2}}$$

$$-\frac{\kappa+1}{4\mu} f_k p_\infty \frac{\dot{a}}{x^{1/2}(a-x)^{1/2}} H(a-x), \qquad 0<x<b \tag{16}$$

$$V(x) = \frac{\kappa+1}{4\mu}(f_k - \tan\alpha) p_\infty \dot{a}\left[\pi - \cos^{-1}\left(1 - \frac{2x}{b}\right)\right],$$

$$a<x<b \tag{17}$$

In both cases, $V(x)$ is only given over the slip zone where it must be checked for consistency with $S(x)$. In the second case it is possible to enforce the condition

$$V(b) = 0 \tag{18}$$

but not so for the first case. However, both cases predict $V(x)<0$ since $\dot{a}<0$ and $f_k - \tan\alpha > 0$, and thus contradict the assumption about the direction of slip. The opposite assumption about the direction of slip leads similarly to contradictions. We then have to conclude that slip is not possible in the case of strong friction and that stick follows immediately the contracting separation zone.

No Slip Zone. In this case (10) becomes

$$\int_0^{a_1} \frac{B_x^c(\xi)d\xi}{\xi - x} = 0, \qquad 0<x<a \tag{19}$$

and differentiation with respect to time yields

$$\int_0^{a} \frac{\dot{B}^c(\xi)d\xi}{\xi - x} = 0, \qquad 0<x<a \tag{20}$$

The solution of (20) singular at $x=a$ is

$$\dot{B}_x^c(x) = \frac{C}{x^{1/2}(a-x)^{1/2}}, \qquad 0<x<a \tag{21}$$

where C is a constant, which is determined from the condition that the slip velocity must vanish at the transition from separation to stick, or using (1) and (7)

$$V(a) = -\frac{\pi(\kappa+1)}{4\mu} p_\infty \dot{a}\tan\alpha - \int_0^a \dot{B}_x^c(\xi)d\xi = 0 \tag{22}$$

Substituting (21) into (22) we obtain

$$C = -\frac{\kappa+1}{4\mu} p_\infty \dot{a}\tan\alpha \tag{23}$$

Then using (23), (21) is written conveniently as

$$dB_x^c = -\frac{\kappa+1}{4\mu} p_\infty \tan\alpha \frac{da}{x^{1/2}(a-x)^{1/2}}, \qquad 0<x<a \tag{24}$$

and upon integration

$$B_x^c(x;a) = B_x^c(x;a_1) + \int_{a_1}^a dB_x^c(x;a), \qquad 0<x<a \tag{25}$$

Observing that

$$B_x^c(x;a_1) = 0 \tag{26}$$

because $a=a_1$ corresponds to $P=P_1$, which was reached upon loading, and integrating we obtain

$$B_x^c(x;a) = \frac{\kappa+1}{2\mu} p_\infty \tan\alpha \left\{-\left(\frac{a-x}{x}\right)^{1/2} + \left(\frac{a_1-x}{x}\right)^{1/2}\right\},$$

$$0<x<a \tag{27}$$

Note that in (25-27), the dependence on time is through a and is denoted in the argument of B_x^c. As the separation zone recedes, the dislocation distribution in the interval $a<x<a_1$ is locked in at its value at the transition from separation to stick, or

$$B_x^c(x)|_{a<x<a_1} = B_x^c(x;x)|_{0<x<a} \tag{28}$$

Thus

$$B_x^c(x) = \frac{\kappa+1}{2\mu} p_\infty \tan\alpha \left(\frac{a_1 - x}{x}\right)^{1/2}, \qquad a<x<a_1 \tag{29}$$

Combining (27) and (29) we obtain

$$B_x^c(x) = \frac{\kappa+1}{2\mu} p_\infty \tan\alpha$$

$$\left\{-\left(\frac{a-x}{x}\right)^{1/2} H(a-x) + \left(\frac{a_1-x}{x}\right)^{1/2}\right\},$$

$$0<x<a_1 \tag{30}$$

where the dependence on a is again suppressed in the argument of B_x^c.

The remaining quantities are then computed as

Downloaded 01 May 2010 to 171.66.16.249. Redistribution subject to ASME license or copyright; see http://www.asme.org/terms/Terms_Use.cfm

$$h_c(x) = -\frac{\kappa+1}{4\mu} p\infty a \tan\alpha\left\{\pi/2 + \sin^{-1}\left(1-\frac{2x}{a}\right) - 2\left[\frac{x}{a}\left(1-\frac{x}{a}\right)\right]^{1/2}\right\} H(a-x) + \frac{\kappa+1}{4\mu} p\infty a_1 \tan\alpha\left\{\pi/2 + \sin^{-1}\left(1-\frac{2x}{a_1}\right) - 2\left[\frac{x}{a_1}\left(1-\frac{x}{a_1}\right)\right]^{1/2}\right\}, \quad 0<x<a_1 \tag{31}$$

$$V(x) = -\frac{\kappa+1}{4\mu} p\infty a \tan\alpha\left[\pi/2 + \sin^{-1}\left(1-\frac{2x}{a}\right)\right], \quad 0<x<a \tag{32}$$

$$S(x) = p\infty\left\{\tan\alpha\left(\frac{x-a}{x}\right)^{1/2} H(x-a) - (f_k+\tan\alpha)\left(\frac{x-a_1}{x}\right)^{1/2} H(x-a_1) + f_k\left(\frac{x-b_1}{x}\right)^{1/2} H(x-b_1)\right\}, \quad 0<x<\infty \tag{33}$$

It is easily verified from these expressions that the inequality

$$|S(x)| < f_k |N(x)| \tag{34}$$

is satisfied in the stick zone. Upon complete removal of the load ($a=0$), we obtain the following expression for the residual shear tractions

$$S(x) = p\infty f_k\left\{\frac{\tan\alpha}{f_k} - \left(1+\frac{\tan\alpha}{f_k}\right)\left(\frac{x-a_1}{x}\right)^{1/2} H(x-a_1) + \left(\frac{x-b_1}{x}\right)^{1/2} H(x-b_1)\right\}, \quad 0<x<\infty \tag{35}$$

It is remarkable that, although there was no slip, part of the residual shear stress is constant but less than $f_k p\infty$. The distributions of the shear tractions for unloading and complete removal of load under strong friction are shown schematically in Fig. 1.

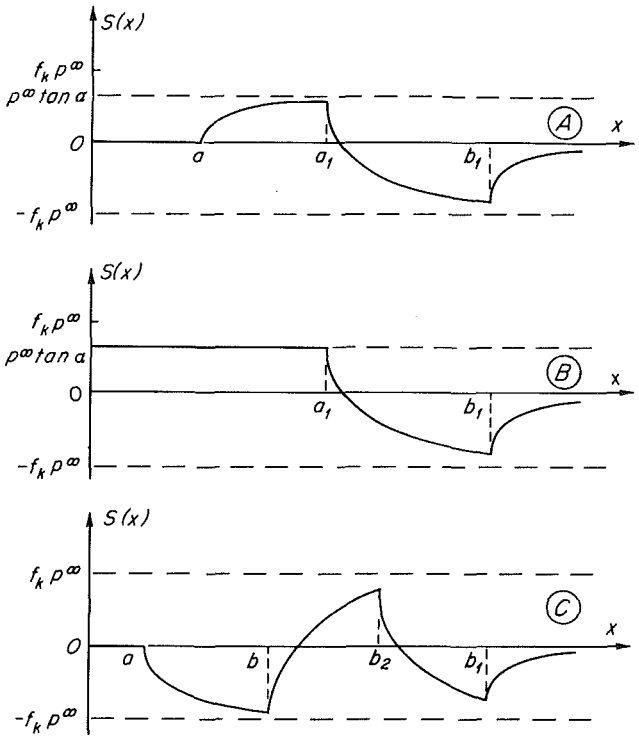


Fig. 1 Schematic distribution of the shear tractions on the cut. (a) Unloading under strong friction; (b) complete removal of load under strong friction; and (c) reloading under weak friction.

Reloading for Strong Friction

Suppose that during unloading $P(t)$ reaches a minimum value P_2, as shown in Fig. 2, and then starts increasing again. We refer to this phase as reloading and consider first the case of strong friction.

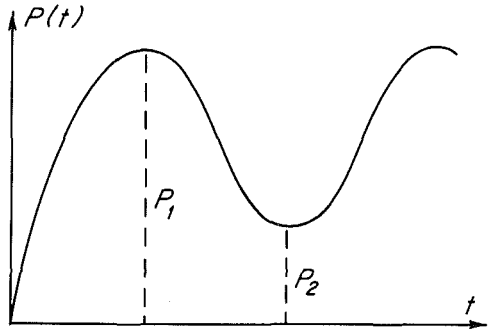


Fig. 2 Applied force *P* versus time

The extent of the current separation zone a still given by (1), while a_1 and a_2 denote the extent of the separation zones attained for loads P_1 and P_2, respectively. Thus

$$a_1 = \frac{\kappa-1}{\pi(\kappa+1)} \frac{P_1\cos\alpha}{p\infty} \tag{36}$$

$$a_2 = \frac{\kappa-1}{\pi(\kappa+1)} \frac{P_2\cos\alpha}{p\infty} \tag{37}$$

The normal tractions are given by (2) and the total shear tractions are

$$S(x) = S_2(x) + S_c(x) \tag{38}$$

where from (33)

$$S_2(x) = p\infty\left\{\tan\alpha\left(\frac{x-a_2}{x}\right)^{1/2} H(x-a_2) - (f_k+\tan\alpha)\left(\frac{x-a_1}{x}\right)^{1/2} H(x-a_1) + f_k\left(\frac{x-b_1}{x}\right)^{1/2} H(x-b_1)\right\}, \quad 0<x<\infty \tag{39}$$

and

$$S_c(x) = -\frac{2\mu}{\pi(\kappa+1)} \int_0^b \frac{B_x^c(\xi)d\xi}{\xi-x}, \quad 0<x<\infty \tag{40}$$

The tangential shift is given by

$$h_c(x) = -\frac{\kappa-1}{4\mu}(P-P_2)\sin\alpha - \int_0^x B_x^c(\xi)d\xi = -\frac{\pi(\kappa+1)}{4\mu} p\infty(a-a_2)\tan\alpha - \int_0^x B_x^c(\xi)d\xi, \quad 0<x<\infty \tag{41}$$

In (40), b denotes the endpoint of the slip zone. However, as long as $a<a_1$, no slip is anticipated since there was no slip upon unloading and $b=a$. If we denote by $B_x^{(2)}(x)$, the locked-in dislocation distribution corresponding to a_2, then the purpose of $B_x^c(x)$ is to anihilate the "excess" in $B_x^{(2)}(x)$.

Downloaded 01 May 2010 to 171.66.16.249. Redistribution subject to ASME license or copyright; see http://www.asme.org/terms/Terms_Use.cfm

Since

$$B_x^{(2)}(x)=\frac{\kappa+1}{2\mu}p\infty\tan\alpha\left\{-\left(\frac{a_2-x}{x}\right)^{1/2}H(a_2-x)+\left(\frac{a_1-x}{x}\right)^{1/2}\right\},\qquad 0<x<a_1 \tag{42}$$

we have

$$B_x^c(x)=\frac{\kappa+1}{2\mu}p\infty\tan\alpha\left\{\left(\frac{a_2-x}{x}\right)^{1/2}H(a_2-x)-\left(\frac{a-x}{x}\right)^{1/2}\right\},\qquad 0<x<a \tag{43}$$

The corrective shear tractions are then computed from (43) with $b=a$, and

$$S_c(x)=p\infty\tan\alpha\left\{-\left(\frac{x-a_2}{x}\right)^{1/2}H(x-a_2)+\left(\frac{x-a}{x}\right)^{1/2}H(x-a)\right\},\qquad 0<x<\infty \tag{44}$$

and the total shear tractions are

$$S(x)=p\infty\left\{\tan\alpha\left(\frac{x-a}{x}\right)^{1/2}H(x-a)-(f_k+\tan\alpha)\left(\frac{x-a_1}{x}\right)^{1/2}H(x-a_1)+f_k\left(\frac{x-b_1}{x}\right)^{1/2}H(x-b_1)\right\},\qquad 0<x<\infty \tag{45}$$

It is seen from (45) that

$$S(x)=0,\qquad 0<x<a \tag{46}$$

$$|S(x)|<f_k|N(x)|,\qquad a<x<\infty \tag{47}$$

Moreover, (41) with (43) gives

$$h_c(a)=0$$

The distribution of the shear tractions under strong friction are the same for reloading as for unloading, which are sketched in Fig. 1.

When a reaches a_1 the shear tractions become

$$S(x)=f_kp\infty\left\{-\left(\frac{x-a_1}{x}\right)^{1/2}H(x-a_1)+\left(\frac{x-b_1}{x}\right)^{1/2}H(x-b_1)\right\},\qquad 0<x<\infty \tag{48}$$

However, equation (48) gives the same shear stress as reached by *loading* directly up to P_1 [compare (48) with (3)]. This means that all traces of unloading have been erased, and if reloading continues beyond P_1 to P, we obtain the same results as if P had been reached by direct loading.

The implication of this for loads that fluctuate periodically about a certain level without reversing direction is that after one cycle the process repeats itself, and that energy is dissipated by friction only on the initial loading path.

Reloading for Weak Friction

For the case of weak friction, we expect slip to occur in the interval $a<x<b$. The arrangement of a and b in relation to a_1, b_1, a_2, and b_2 is shown in Fig. 3. It is recalled from [1] that

$$b_2=\frac{1}{2}(a_1+a_2)+\frac{1}{2}(a_1-a_2)\frac{\tan\alpha}{f_k} \tag{49}$$

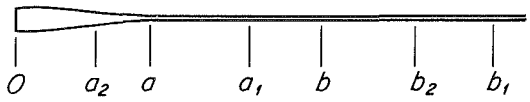


Fig. 3 Arrangement of the separation and slip zones for reloading under weak friction

while a, a_1 a_2, and b_1 are given by (1), (36), (37), and (4), respectively. The total shear tractions are given by (38) with

$$S_2(x)=f_kp\infty\left\{\left(\frac{x-a_2}{x}\right)^{1/2}H(x-a_2)-2\left(\frac{x-b_2}{x}\right)^{1/2}H(x-b_2)+\left(\frac{x-b_1}{x}\right)^{1/2}H(x-b_1)\right\},\qquad 0<x<\infty \tag{50}$$

and $S_c(x)$ given by (40).

We anticipate $V(x)<0$ and hence $S(x)<0$. In the slip zone then

$$S(x)=f_kN(x),\qquad a<x<b \tag{51}$$

while in the separation zone

$$S(x)=0,\qquad 0<x<a \tag{52}$$

From (51), (52), and (1), the governing equation for B_x^c becomes

$$\int_0^b\frac{B_x^c(\xi)\,d\xi}{\xi-x}=\frac{\pi(\kappa+1)}{2\mu}f_kp\infty\left\{\left(\frac{x-a_2}{x}\right)^{1/2}H(x-a_2)+\left(\frac{x-a}{x}\right)^{1/2}H(x-a)-2\left(\frac{x-b_2}{x}\right)^{1/2}H(x-b_2)+\left(\frac{x-b_1}{x}\right)^{1/2}H(x-b_1)\right\},\qquad 0<x<b \tag{53}$$

Before proceeding we must decide whether $a<b<b_2$ (phase 1) or $b_2<b<b_1$ (phase 2). For phase 1 we obtain

$$B_x^c(x)=\frac{\kappa+1}{2\mu}f_kp\infty\left\{\left(\frac{a_2-x}{x}\right)^{1/2}H(a_2-x)+\left(\frac{a-x}{x}\right)^{1/2}H(a-x)-2\left(\frac{b-x}{x}\right)^{1/2}\right\},\qquad 0<x<b \tag{54}$$

Requiring $h_c(b)=0$ yields

$$b=\frac{1}{2}\left[a\left(1+\frac{\tan\alpha}{f_k}\right)-a_2\left(\frac{\tan\alpha}{f_k}-1\right)\right] \tag{55}$$

From (55) it is seen that at the end of phase 1, or for $b=b_2$, $a=a_1$. Moreover, at the end of phase 1, $P=P_1$, $N(x)=N_1(x)$, and $S(x)=S_1(x)$. Hence, loading beyond P_1 (phase 2) gives the same results as direct loading. However, it is interesting to note that a sudden jump in the extent of the slip zone from b_2 to b_1 is involved.

The shear tractions for phase 1 are given by

$$S(x)=f_kp\infty\left\{-\left(\frac{x-a}{x}\right)^{1/2}H(x-a)+2\left(\frac{x-b}{x}\right)^{1/2}H(x-b)-2\left(\frac{x-b_2}{x}\right)^{1/2}H(x-b_2)+\left(\frac{x-b_1}{x}\right)^{1/2}H(x-b_1)\right\},\qquad 0<x<\infty \tag{56}$$

and their distribution is shown in Fig. 1. For completeness we also record $h_c(x)$ and $V(x)$ in the slip zone

$$h_c(x)=-\frac{\kappa+1}{2\mu}f_kp\infty b\left\{\frac{\pi}{2}+\sin^{-1}\left(1-\frac{2x}{b}\right)\right.$$

Downloaded 01 May 2010 to 171.66.16.249. Redistribution subject to ASME license or copyright; see http://www.asme.org/terms/Terms_Use.cfm

$$-2\left[\frac{x}{b}\left(1-\frac{x}{b}\right)\right]^{1/2}\Bigg\}, \qquad a<x<b \tag{57}$$

$$V(x)=-\frac{\kappa+1}{2\mu}f_k p_\infty \dot{b}\left\{\frac{\pi}{2}+\sin^{-1}\left(1-\frac{2x}{b}\right)\right\}, \qquad a<x<b \tag{58}$$

and it is verified that $V(x)<0$ as assumed.

Conclusion

The most interesting implication of the foregoing analysis is in regard to periodically fluctuating loads. In both cases (strong or weak friction) it is found that after one cycle the process is repeated.

Another important aspect that has emerged is the distinction in the analysis for unloading between the case of a slip zone *advancing* into a stick zone (weak friction) or a slip zone *receding* from a stick zone (strong friction). It is perhaps enlightening that a similar observation has been made in the context of convergence of numerical computations involving the finite element technique [2]. In the latter, as well as in theoretical work involving proofs of existence [3], the question of how small f must be for the case of weak friction arises. Clearly, as the present problem indicates, the answer depends on the geometric and loading characteristics of the problem. A better definition for weak friction then is the one just given: for *weak* friction, the slip zone upon unloading *advances* into a stick zone.

In conclusion, we hope that the present analysis serves its purpose to instruct, particularly since the authors themselves missed some points at the beginning and had to retrace their steps.

References

1 Dundurs, J., and Comninou, M., "An Educational Elasticity Problem with Friction. Part 1: Loading, and Unloading for Weak Friction," ASME JOURNAL OF APPLIED MECHANICS, Vol. 48, 1981, pp. 841–845.

2 Kikuchi, N., and Oden, J. T., *Contact Problems in Elasticity*, Chapter 12, SIAM, Philadelphia (1981), in press.

3 Nečas, J., Jarušek, J., and Haslinger, J., "On the Solution of the Variational Inequality to the Signorini Problem With Small Friction," preprint.

Downloaded 01 May 2010 to 171.66.16.249. Redistribution subject to ASME license or copyright; see http://www.asme.org/terms/Terms_Use.cfm

R. A. Masumura
Naval Research Laboratory,
Material Science and
Technology Division,
Washington, D.C. 20375

Y. T. Chou
Department of Metallurgy
and Materials Engineering,
Lehigh University,
Bethlehem, Pa. 18015

Antiplane Eigenstrain Problem of an Elliptic Inclusion in an Anisotropic Half Space

The antiplane eigenstrain problem of an elliptic inclusion in an anisotropic semi-infinite medium is investigated. Expressions for the stresses and elastic energy have been developed using the line force concept and superposition of the image field. It is shown that in the presence of a free surface the stresses inside the inclusion are not constant. In addition, the elastic energy of the system is reduced as the inclusion approaches the free surface.

Introduction

The comprehensive treatment by Eshelby [1] of the ellipsoidal inclusion problem in an infinite medium has generated an extensive investigation in this area. In contrast, the problem of the inclusion in a semi-infinite medium has not been fully investigated due to the added complication of free-surface boundary conditions. Efforts to obviate this difficulty utilized several different types of approaches [2–4].

For a restricted class of generalized plane problems, the ellipsodial inclusion in an anisotropic half space can be examined using the line force concept where the elastic functions depend only on two coordinate variables. This dependency leads to a method employing mapping techniques and producing a closed-form solution for the stresses. Implicit in the solution is the type and kind of transformation strain assumed in the inclusion.

This work deals with a transformation problem in which an elliptic inclusion embedded in a semi-infinite matrix tends to undergo a prescribed uniform deformation. Because of the elastic constraint imposed by its surroundings, the transformed region will reach an equilibrium configuration. We are concerned with the elastic state in the inclusion and matrix.

Formulation-Stress Components

The analysis of this problem is based on the line force concept utilized by Yang and Chou [5] for their analysis of plane problems of inclusions. The anisotropic elastic medium is defined by the half space $x_1 \geq 0$, and the cylindrical axis of the inclusion is parallel with the x_3 axis. The elliptically shaped inclusion is given by $(x_1 - h)^2/a^2 + x_2^2/b^2 = 1$, where h is the distance from the center of the inclusion to the free surface, and a and b are the semi-axes aligned with the x_1 and x_2 axes, respectively, as shown in Fig. 1. For this analysis, only uniform antiplane transformation strains (eigenstrains), e_{13}^0 and e_{23}^0 will be considered, and it is further assumed that the matrix and inclusion have identical elastic properties. The anisotropic medium possesses a two-fold rotation axis of symmetry about x_3, and by the antiplane assumption, only three elastic constants, C_{44}, C_{55}, and C_{45}, are involved in the analysis.

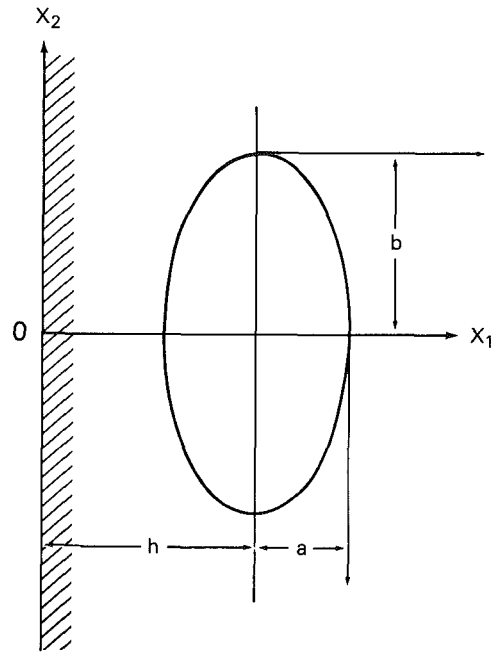


Fig. 1 Cylindrical elliptical inclusion in a semi-infinite medium

Explicit expressions for the elastic field of an antiplane line force in a semi-infinite anisotropic medium have been developed by Chou [6] and form the basis for this analysis. For an antiplane line force per unit length, F_3, acting normal to the $x_1 - x_2$ plane at some point (y_1, y_2), the stresses ρ_{23} and ρ_{13} at (x_1, x_2) are given as the sum of two quantities. The first quality, ρ_{3j}^{+}, results from the line force as if it were acting in an infinite medium, and the second, ρ_{3j}^{-}, results from an

Contributed by the Applied Mechanics Division for publication in the JOURNAL OF APPLIED MECHANICS.

Discussion on this paper should be addressed to the Editorial Department, ASME, United Engineering Center, 345 East 47th Street, New York, N.Y. 10017, and will be accepted until two months after final publication of the paper itself in the JOURNAL OF APPLIED MECHANICS. Manuscript received by ASME Applied Mechanics Division, March, 1981; final revision, August, 1981.

Copyright © 1982 by ASME
Downloaded 01 May 2010 to 171.66.16.249. Redistribution subject to ASME license or copyright; see http://www.asme.org/terms/Terms_Use.cfm

image line force at $(-y_1, y_2)$ required for the free-surface boundary condition, $\mathfrak{p}_{13}^{+} + \mathfrak{p}_{13}^{-} = 0$ at $x_1 = 0$. These forms are,

$$\mathfrak{p}_{3j} = \mathfrak{p}_{3j}^{+} + \mathfrak{p}_{3j}^{+}; \qquad j = 1,2 \tag{1}$$

and

$$\mathfrak{p}_{3j}^{+} = \mathrm{Re}\left\{ -\frac{F_3}{\pi L D^{\pm}} \left[C_{3j31} + \mu C_{3j32} \right] \right\} \tag{2}$$

where

$$D^{\pm} = (x+\bar{x}) - i\mu(x-\bar{x}) \mp (y+\bar{y}) + i\mu(y-\bar{y}), \qquad i = \sqrt{-1} \tag{3}$$

C_{pqrs} are the elastic moduli in the four index notation, $L = (C_{44}C_{55} - C_{45}^2)^{1/2}$, $\mu = (-C_{45} + iL)/C_{44}$, $x = x_1 + ix_2$, $y = y_1 + iy_2$, and the bar denotes complex conjugation.

The antiplane line force is integrated around the contour of the elliptical region to correspond with Eshelby's inclusion problem and hence, the integrated stresses are

$$P_{3j} \oint \mathfrak{p}_{3j}\, ds = \oint \mathfrak{p}_{3j}^{+}\, ds + \oint \mathfrak{p}_{3j}^{-}\, ds \tag{4}$$

where ds is the arc differential (in a counterclockwise direction).

However, the first integral on the right-hand side of (4) is due to the integrated line force as if the force were in an infinite medium, and has been evaluated by Yang and Chou [5] for a coordinate system located at the center of the elliptical region. Thus their solution can be utilized in our case by a simple coordinate translation. Hence, attention will only be focused on the image contribution which can be written as

$$P_{3j}^{-} = \mathrm{Re}\left\{ \lambda_j \oint \frac{F_3}{D^{-}}\, ds \right\} \tag{5}$$

where $\lambda_j = -(C_{3j31} + \mu C_{3j32})/\pi L$. From the stresses, P_{3j}^0, resulting from the eigenstrains, e_{3j}^0, in the inclusion we have by equilibrium of forces,

$$F_3\, ds = -(Q\, dy + \bar{Q}\, d\bar{y})/2 \tag{6}$$

where $Q = P_{23}^0 + iP_{13}^0$ and $P_{3j}^0 = 2(C_{3j31}\, e_{13}^0 + C_{3j32}\, e_{23}^0)$. This leads to

$$P_{3j}^{-} = \mathrm{Re}\{ -\lambda_j (QI^{-} + \bar{Q}J^{-})/2 \} \tag{7}$$

where

$$I^{-} = \oint \frac{dy}{D^{-}} \qquad \text{and } J^{-} = \oint \frac{d\bar{y}}{D^{-}} \tag{8}$$

and evaluation of these integrals will lead to P_{3j}^{-} as required.

The contour integrals given by equation (8) are mapped from a system of confocal ellipses in the x_i frame to a system of concentric circles in the ξ_i frame by

$$x = \zeta(a+b)/2 + \bar{\zeta}(a-b)/2 + h; \qquad \zeta = \xi_1 + i\xi_2 \tag{9}$$

$$y = \sigma(a+b)/2 + \bar{\sigma}(a-b)/2 + h; \qquad \bar{\sigma} = 1/\sigma \tag{10}$$

where σ defines a unit circle in the mapped plane. Thus the integrations required for equation (8) are performed around the unit circle. In the mapped plane,

$$I^{-} = \oint \frac{m_1 d\sigma}{\mathfrak{D}^{-}} \qquad \text{and} \qquad J^{-} = \oint \frac{m_2 d\sigma}{\mathfrak{D}^{-}} \tag{11}$$

where

$$m_1 = \{\sigma(a+b) - (a-b)/\sigma\}/2,$$

$$m_2 = \{\sigma(a-b) - (a+b)/\sigma\}/2 \tag{12}$$

and in the ζ-plane D^{-} becomes,

$$\mathfrak{D}^{-} = g(\sigma) = A\sigma^2 + B\sigma + C \tag{13}$$

with $A = a + i\mu b + a\mu\epsilon$, $B = \zeta(a - i\mu b) + \bar{\zeta}(a + i\mu b) + 2h(2 + \mu\epsilon)$, $C = a - i\mu b + a\mu\epsilon$ and $\epsilon = 2(C_{45}/C_{55})$. The integration follows once the roots of $g(\sigma)$ have been determined.

Root location can be identified by a theorem of Marden [7] and is based on the properties of A, B, and C. Application of this theorem shows that only one root lies within the unit circle and hence the integration proceeds by residue calculus. The resulting calculation yields

$$I^{-} = \gamma^{-}(\alpha - i\mu) S^{-}(x) \quad \text{and} \quad J^{-} = \gamma^{-}(\alpha + i\mu)\, S^{-}(x) \tag{14}$$

where

$$\gamma^{-} = i\pi ab/(\alpha^2 a^2 + \mu^2 b^2), \qquad \alpha = 1 + \mu\epsilon \tag{15}$$

and

$$S^{-}(x) = -(x + \alpha h)/[(x+\alpha h)^2 - (\alpha^2 a^2 + \mu^2 b^2)]^{1/2} + 1 \tag{16}$$

Now the image contributions to the stresses, P_{3j}, are

$$P_{3j}^{-} = \mathrm{Re}\left\{ -\frac{\lambda_j}{2} \Omega^{-} \right\}; \qquad \Omega^{-} = P_{23}^0 (I^{-} + J^{-}) + iP_{13}^0 (I^{-} - J^{-}) \tag{17}$$

These image terms are valid anywhere in the half space $x_1 \geq 0$.

The nonimage components, P_{3j}^{+}, are obtained from Yang and Chou [5] after a shift in coordinate axis from the center of the ellipse to the free surface to conform with the image contribution coordinate system. As expected, their calculations show that inside the inclusion, the stresses are constant. Inside the inclusion one finds,

$$I^{+} = -i\pi(a+b)/(a - i\mu b)$$

and

$$J^{+} = -i\pi(a-b)/(a - i\mu b) \tag{18}$$

with

$$\Gamma = (a + i\mu b)/(a - i\mu b) \qquad \text{and } |\Gamma| < 1. \tag{19}$$

Outside the inclusion, in the matrix, the relevant forms are,

$$I^{+} = \gamma^{+}(i\mu + 1) S^{+}(x) \qquad \text{and} \qquad J^{+} = \gamma^{+}(i\mu - 1) S^{+}(x) \tag{20}$$

where

$$\gamma^{+} = i\pi ab/(a^2 + \mu^2 b^2) \tag{21}$$

and

$$S^{+}(x) = (x-h)/[(x-h)^2 - (a^2 + \mu^2 b^2)]^{1/2} - 1 \tag{22}$$

The nonimage terms can be combined with those in equation (17) to yield,

$$P_{3j} = P_{3j}^{+} + P_{3j}^{-} = \mathrm{Re}\left\{ -\frac{\lambda_j}{2} \Omega \right\} \tag{23}$$

where

$$\Omega = \Omega^{+} + \Omega^{-} \qquad \text{and} \qquad \Omega^{\pm} = P_{23}^0 (I^{\pm} + J^{\pm}) + i\, P_{13}^0 (I^{\pm} + J^{\pm}) \tag{24}$$

As expected, the stresses inside the inclusion are not constant due to the image contributions.

After much algebra, it can be shown the $P_{13}(x_1 = 0) = 0$, indicating that the expressions just developed to satisfy the boundary conditions. A limiting case was examined for $h \to \infty$ and led to the recovery of the Yang and Chou [5] solution as expected.

For a circular inclusion of radius a in a cubic or isotropic ($C_{44} = C_{55}$ and $C_{45} = 0$) semi-infinite medium, the stresses in the matrix are

$$\begin{pmatrix} P_{13} \\ P_{23} \end{pmatrix} = \frac{a^2}{2} \begin{bmatrix} A^{+} - A^{-} & -(B^{+} + B^{-}) \\ B^{+} - B^{-} & A^{+} - A^{-} \end{bmatrix} \begin{pmatrix} P_{13}^0 \\ P_{23}^0 \end{pmatrix} \tag{25}$$

where

$$A^{\pm} = [(x_1 \pm h)^2 - x_2^2]/r_{\pm}^4, \qquad B^{\pm} = (x_1 \pm h) x_2 / r_{\pm}^4$$

Downloaded 01 May 2010 to 171.66.16.249. Redistribution subject to ASME license or copyright; see http://www.asme.org/terms/Terms_Use.cfm

and

$$r_{\pm}^2 = [(x_1 \pm h)^2 + x_2^2] \tag{26}$$

Elastic Energy

Following Eshelby [1], the elastic energy per unit length of the inclusion in a half space, E^h, is given as $E^h = E^\infty + E^*$ where E^∞ is the elastic energy of the inclusion as if it were in an infinite medium and E^* is the image contribution,

$$E^* = -\frac{1}{2}\int P_{ij}^- e_{ij}^0 dV \tag{27}$$

The energy term, E^∞, is simply calculated following Eshelby's formulation.

As an example, consider again the case of the circular inclusion. In this situation,

$$E^\infty = \pi a^2[(e_{23}^0)^2 + (e_{13}^0)^2]C_{44}/2 \tag{28}$$

Substituting P_{ij}^- from equation (17) into equation (27), the image contribution is given as

$$E^* = -E^\infty/(4t^2), \qquad t \geq 1 \tag{29}$$

where $t = h/a$, the normalized distance from the center of the circle to the edge of the half space. Thus the elastic energy of the inclusion is $E^h = E^\infty\,[1 - 1/(4t^2)]$ and shows that as $t \to \infty$, $E^h \to E^\infty$ (infinite medium case). At $t = 1$, when the circular inclusion is at the free boundary, E^h $(t = 1) = 0.75E^\infty$ and the energy is lowered. Eshelby [1] has shown that the elastic energy of a spherical void in an isotropic half space has a similar type of inverse power dependence on t.

For the case of an elliptic inclusion, $a \neq b$, the image contribution, E^*, is calculated from equation (27). Specifically when the medium possesses cubic symmetry, E^* becomes

$$E^* = (K\pi a^2 e^2)[1 - \mathrm{Re}\{\mathfrak{F}\}]/(1 - e^2) \tag{30}$$

where

$$\mathfrak{F} = \mathfrak{F}^+ - \mathfrak{F}^-,$$

$$K = C_{44}[(e_{13}^0)^2 + (e_{23}^0)^2], \qquad e = b/a,$$

and

$$\mathfrak{F}^{\pm} = \frac{1}{\pi}\int_{-1}^{+1} \{[2t \pm (1-\xi^2)^{1/2} + ie\xi]^2 - (1-e^2)\}^{1/2} d\xi \tag{31}$$

Equation (30) is numerically evaluated as $E^{**} = E^*/K\pi a^2$, the normalized image contribution for several values of t and e. This normalization has the interpretation of a fixed a while varying b so that $e << 1$ and $e >> 1$ represent limiting cases of a "slit" and "slab," respectively. Utilizing this normalization, it can be shown that $E^{**} \to 0$ as $e \to 0$ and $E^\infty \to 0$ and $E^\infty \to 1$ as $e \to 1$. Figure 2 shows the results of equation (30) for various b/a ratios, and as seen before, $E^{**} \to 0$ as $t \to \infty$.

Conclusions

The line force concept has been utilized to examine an inclusion in a half-space for a case of uniform antiplane strains. Expressions for the stresses and elastic energy have been developed. It is shown that in the presence of a free surface the stresses inside the inclusion are not constant (in contrast with the result for the ease of an infinite medium). In addition, the elastic energy of the system is reduced as the inclusion approaches the free surface.

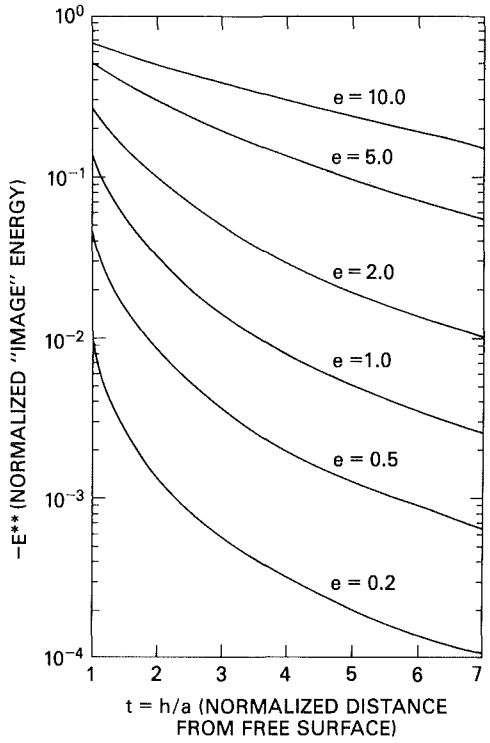


Fig. 2 Normalized "image" energy variation from the free surface for various $e = b/a$ values

References

1 Eshelby, J. D., "Elastic Inclusions and Inhomogenetics," *Progress in Solid Mechanics,* Vol. 2, Sneddon, I. N., and Hill, R., eds., North Holland, 1961, pp. 89–139.

2 Seo, K., and Mura, T., "The Elastic Field in a Half Space Due to Ellipsoidal Inclusions With Uniform Eigenstrains," ASME JOURNAL OF APPLIED MECHANICS, Vol. 46, 1979, pp. 1–5.

3 Chui, Y. P., "On the Stress Field and Surface Deformation in a Half Space with a Cuboidal Zone in Which Initial Strains are Uniform," ASME JOURNAL OF APPLIED MECHANICS, Vol. 45, 1978, pp. 302–306.

4 Aderogba, K., "On Eigenstresses in a Semi-Infinite Solid," *Mathematical Proceedings of the Cambridge Philosophical Society,* Vol. 80, 1976, pp. 555–562.

5 Yang, H. C., and Chou, Y. T., "Antiplane Problems of an Elliptic Inclusion in an Anisotropic Medium," ASME JOURNAL OF APPLIED MECHANICS, Vol. 44, 1977, pp. 437–441.

6 Chou, Y. T., "On Antiplane Line Force in a Two-Phase Anisotropic Medium," *Physica Status Solidi (a),* Vol. 34, 1976, pp. 645–650.

7 Marden, M., *Geometry of Polynomials,* 2nd Ed., American Mathematical Society, 1966, pp. 194–197.

Downloaded 01 May 2010 to 171.66.16.249. Redistribution subject to ASME license or copyright; see http://www.asme.org/terms/Terms_Use.cfm

R. S. Wu
Y. T. Chou

Department of Metallurgy
and Materials Engineering,
Lehigh University,
Bethlehem, Pa. 18015

Line Force in a Two-Phase Orthotropic Medium

Based on the generalized method of images, the elastic field of an in-plane line force acting in a two-phase orthotropic medium is analyzed. Several special cases of technological interest are deduced from the general solution, including the case of a line force applied on the free surface of a half space. Application of the results to the determination of the elastic field of an edge dislocation in a semi-infinite orthotropic medium is illustrated.

1 Introduction

Composite materials, for example, the fiber-reinforced metals and ceramics, are widely used in modern technology. The understanding and improvement of their mechanical behavior are in ever-increasing demand. One of the critical regions where failure of composite materials often takes place is near or at the interphase boundary. On a microscopic scale, this region may be visualized as a two-phase medium of infinite extent, and such a model has been used in numerous analyses in both fundamental and applied research.

In this study, we shall be concerned with the elastic field of a line force in a two-phase anisotropic medium. A line force is the two-dimensional product of a continuous, uniform distribution of point forces acting along a line [1]. The analysis of an in-plane force in a two-phase isotropic medium was reported some years ago by Frasier and Rongved [2]. An extension of their work to take account of the effect of elastic anisotropy is motivated by recent applications of line force to crack and inclusion problems in which the elastic anisotropy plays a dominant role [3-10].

Analyses of the elastic fields of line defects in an anisotropic single-phase medium are in general complex [11]. The complexity is enhanced in the case of a two-phase anisotropic medium, and to effect an explicit solution it is necessary to assume that the anisotropic medium contains certain elements of symmetry [12-18]. In this work we shall assume that both phases of the medium have two planes of symmetry orthogonal to each other (orthotropy).

The basic approach used in the present analysis will follow the work of Eshelby, Read and Shockley [11] and of Pande and Chou [17], as shown in Sections 2 and 3. In Section 4, we shall examine several special cases of technological importance, in particular the case of a line force near a free surface. A direct application of the present solutions could be made to the analysis of elastic inclusions in a two-phase anisotropic medium. However, such an analysis would be much too involved, and we shall present instead a simple example in which the local elastic field of an edge dislocation is determined from the known solutions of a line force, as given in Section 5.

2 Analysis

2.1 Formulation of the Problem. We consider an anisotropic elastic medium comprising two welded half spaces with Phase I in $x>0$ and Phase II in $x<0$ in reference to a Cartesian coordinate system $Oxyz$. A uniform line force parallel to the z-axis is applied at a distance a on the xy plane in Phase I. Since nothing varies with the z-coordinate, the system can be treated as a two-dimensional plane-strain problem with the line force F acting at $(a,0)$. In general, the elastic constants C_{ij} and other parameters pertaining to Phases I and II will be denoted by superscripts (1) and (2), respectively. However, for a statement valid in both phases the superscripts may be omitted for simplicity.

To effect an analytical solution to the problem, we further assume that both phases are orthotropic with the elastic constants given by

$$\begin{bmatrix} C_{11} & C_{12} & C_{13} & 0 & 0 & 0 \\ & C_{22} & C_{23} & 0 & 0 & 0 \\ & & C_{33} & 0 & 0 & 0 \\ & & & C_{44} & 0 & 0 \\ & & & & C_{55} & 0 \\ & & & & & C_{66} \end{bmatrix} \tag{1}$$

A line force in a homogeneous (single-phase) medium with condition (1) has been treated by Hirth [19]. For a two-phase medium the solution is likely to consist of the "homogeneous" term plus an "image" term or terms. A simple approach based on the generalized image method was undertaken by Pande and Chou [17] in the study of edge dislocations in a two-phase anisotropic medium. Their method will be used in the present analysis.

Following the work of Pande and Chou [17], the displacements u and v of the present system can be given as

$$u = \mathrm{Re}\,\{D_1\Psi_+ + D_2\Psi_-\} \tag{2a}$$

Contributed by the Applied Mechanics Division for publication in the JOURNAL OF APPLIED MECHANICS.

Discussion on this paper should be addressed to the Editorial Department, ASME, United Engineering Center, 345 East 47th Street, New York, N. Y. 10017, and will be accepted until two months after final publication of the paper itself in the JOURNAL OF APPLIED MECHANICS. Manuscript received by ASME Applied Mechanics Division, April, 1981; final revision, July, 1981.

Copyright © 1982 by ASME
Downloaded 01 May 2010 to 171.66.16.249. Redistribution subject to ASME license or copyright; see http://www.asme.org/terms/Terms_Use.cfm

$$v = \mathrm{Re}\{-A(D_1\Psi_+ - D_2\Psi_-)\} \tag{2b}$$

where Re denotes the real part of the complex functions and D_1 and D_2 are complex constants. The constant A and the functions Ψ_+ and Ψ_- are defined as

$$A = \frac{\lambda(C_{66}e^{i\alpha} + \bar{C}_{12}e^{-i\alpha})}{C_{12} + C_{66}} \tag{3}$$

$$\Psi_\pm = f(\xi_\pm) = f(x + k_j \pm \lambda e^{i\alpha} y) \tag{4}$$

where k_j are unknown constants to be determined. In equations (3) and (4)

$$\lambda = \left(\frac{C_{11}}{C_{22}}\right)^{1/4} = \left(\frac{\bar{C}_{12}}{C_{22}}\right)^{1/2} \tag{5}$$

$$\bar{C}_{12} = (C_{11}\, C_{22})^{1/2} \tag{6}$$

$$\alpha = \cos^{-1}\left(\frac{1}{2}\sqrt{-C}\right) \quad \text{for } C \le 0$$

$$= \cos^{-1}\left(\frac{i}{2}\sqrt{C}\right) \quad \text{for } C > 0 \tag{7}$$

and

$$C = \frac{(\bar{C}_{12} + C_{12})(\bar{C}_{12} - C_{12} - 2C_{66})}{\bar{C}_{12}\, C_{66}} \tag{8}$$

which has a lower limit of -4 and vanishes in the case of isotropy [20].

Under the condition of orthotropic symmetry the stress components are given by

$$\sigma_{xx} = \mathrm{Re}\{E(D_1\Psi'_+ + D_2\Psi'_-)\} \tag{9a}$$

$$\sigma_{yy} = \mathrm{Re}\{F(D_1\Psi'_+ + D_2\Psi'_-)\} \tag{9b}$$

$$\sigma_{xy} = \mathrm{Re}\{G(D_1\Psi'_+ - D_2\Psi'_-)\} \tag{9c}$$

and

$$\sigma_{zz} = \frac{C_{22}C_{13} - C_{12}C_{23}}{\bar{C}_{12}^2 - C_{12}^2}\sigma_{xx} + \frac{C_{11}C_{23} - C_{12}C_{13}}{\bar{C}_{12}^2 - C_{12}^2}\sigma_{yy} \tag{9d}$$

where

$$E = C_{11} - C_{12}\lambda e^{i\alpha} A \tag{10a}$$

$$F = C_{12} - C_{22}\lambda e^{i\alpha} A \tag{10b}$$

$$G = C_{66}(\lambda e^{i\alpha} - A) \tag{10c}$$

and

$$\Psi'_\pm = \frac{d\Psi_\pm}{d\xi_\pm} \tag{10d}$$

For a welded boundary, the displacements u and v and the stresses σ_{xx} and σ_{xy} are continuous at the interface $x = 0$, i.e.,

$$u^{(1)} = u^{(2)} \tag{11a}$$

$$v^{(1)} = v^{(2)} \tag{11b}$$

$$\sigma_{xx}{}^{(1)} = \sigma_{xx}{}^{(2)} \tag{11c}$$

$$\sigma_{xy}{}^{(1)} = \sigma_{xy}{}^{(2)} \tag{11d}$$

However, for convenience we shall use an alternate version for the displacement continuity,

$$\frac{\partial u^{(1)}}{\partial y} = \frac{\partial u^{(2)}}{\partial y} \tag{11a}'$$

$$\frac{\partial v^{(1)}}{\partial y} = \frac{\partial v^{(2)}}{\partial y} \tag{11b}'$$

The use of equations (11a)′ and (11b)′ may result in a difference in displacements by a constant at the boundary, but the constant can be eliminated by a suitable adjustment of the displacement functions.

Conditions (11a)′, (11b)′, (11c), and (11d) can be rewritten as

$$\mathrm{Re}(\gamma^{(1)}\phi_-{}^{(1)}) = \mathrm{Re}(\gamma^{(2)}\phi_-{}^{(2)}) \tag{12a}$$

$$\mathrm{Re}(A^{(1)}\gamma^{(1)}\phi_+{}^{(1)}) = \mathrm{Re}(A^{(2)}\gamma^{(2)}\phi_+{}^{(2)}) \tag{12b}$$

$$\mathrm{Re}(E^{(1)}\phi_+{}^{(1)}) = \mathrm{Re}(E^{(2)}\phi_+{}^{(2)}) \tag{12c}$$

$$\mathrm{Re}(G^{(1)}\phi_-{}^{(1)}) = \mathrm{Re}(G^{(2)}\phi_-{}^{(2)}) \tag{12d}$$

where

$$\phi_\pm = D_1\Psi'_+ \pm D_2\Psi'_- \tag{13}$$

and

$$\gamma = \lambda e^{i\alpha} \tag{14}$$

To determine the four complex coefficients, $D_1{}^{(1)}$, $D_2{}^{(1)}$, $D_1{}^{(2)}$, $D_2{}^{(2)}$ (eight unknowns) in equations (2a) and (2b), we need four more conditions in addition to equations (12). Two conditions are provided by the conditions of equilibrium,

$$\frac{\partial\sigma_{xx}}{\partial x} + \frac{\partial\sigma_{xy}}{\partial y} = 0 \tag{15a}$$

$$\frac{\partial\sigma_{xy}}{\partial x} + \frac{\partial\sigma_{yy}}{\partial y} = 0 \tag{15b}$$

The other two conditions are obtained from the definition of the line force

$$\oint_c (\sigma_{xx}dy - \sigma_{xy}dx) = F_x \tag{16a}$$

$$\oint_c (\sigma_{xy}dy - \sigma_{yy}dx) = F_y \tag{16b}$$

with the integration contour c enclosing the singularity.

It was found that in the homogeneous case (single-phase), $D_1 = D_2 = D$ for $F = F_x$ and $D_1 = -D_2 = D$ for $F = F_y$. Thus, for a two-phase medium, the unknown coefficients, D's, can be reduced to four and uniquely determined by the boundary conditions, equations (12).

2.2 Method of Solution. The solution of the problem is based on the generalized image method used previously by Head [21] and Pande and Chou [17]. The solution consists of the "homogeneous" term plus the "image" term or terms. The position and strength of the image are determined by the boundary conditions at $x = 0$.

Let us first construct the following trial functions for $\Psi_\pm$,

$$D^{(1)}\Psi'_\pm{}^{(1)} = \frac{K_1}{x - a \pm \lambda^{(1)}e^{i\alpha^{(1)}}y} + \frac{K_2}{x + a \pm \lambda^{(1)}e^{i\alpha^{(1)}}y} + \frac{K_3\, e^{2i\alpha^{(1)}}}{x - ae^{2i\alpha^{(1)}} \pm \lambda^{(1)}e^{i\alpha^{(1)}}y} + \frac{K_4\, e^{2i\alpha^{(1)}}}{x + ae^{2i\alpha^{(1)}} \pm \lambda^{(1)}e^{i\alpha^{(1)}}y} \tag{17}$$

and

$$D^{(2)}\Psi'_\pm{}^{(2)} = \frac{P_1}{\epsilon x - a \pm \lambda^{(1)}e^{i\alpha^{(1)}}y} + \frac{P_2}{\epsilon x + a \pm \lambda^{(1)}e^{i\alpha^{(1)}}y} + \frac{P_3\, e^{2i\alpha^{(1)}}}{\epsilon x - ae^{2i\alpha^{(1)}} \pm \lambda^{(1)}e^{i\alpha^{(1)}}y} + \frac{P_4\, e^{2i\alpha^{(1)}}}{\epsilon x + ae^{2i\alpha^{(1)}} \pm \lambda^{(1)}e^{i\alpha^{(1)}}y} \tag{18}$$

where

$$\epsilon = \gamma^{(1)}/\gamma^{(2)} \tag{19}$$

and K_i and P_i ($i = 1,2,3,4$) are unknown complex coefficients to be determined by the boundary conditions (12). In terms of K_i and P_i, equations (12) become

$$\gamma^{(1)}(K_1 \mp K_2) - \gamma^{(2)}(P_1 \mp P_2) + \overline{\gamma^{(1)}}\,\overline{(K_3 \mp K_4)} - \overline{\gamma^{(2)}}\,\overline{(P_3 \mp P_4)} = 0 \tag{20a}$$

Downloaded 01 May 2010 to 171.66.16.249. Redistribution subject to ASME license or copyright; see http://www.asme.org/terms/Terms_Use.cfm

$$A^{(1)}\gamma^{(1)}(K_1 \pm K_2) - A^{(2)}\gamma^{(2)}(P_1 \pm P_2) + \overline{A^{(1)}\gamma^{(1)}}\,\overline{(K_3 \pm K_4)} - \overline{A^{(2)}\gamma^{(2)}}\,\overline{(P_3 \pm P_4)} = 0 \tag{20b}$$

$$E^{(1)}(K_1 \pm K_2) - E^{(2)}(P_1 \pm P_2) + \overline{E^{(1)}}\,\overline{(K_3 \pm K_4)} - \overline{E^{(2)}}\,\overline{(P_3 \pm P_4)} = 0 \tag{20c}$$

$$G^{(1)}(K_1 \mp K_2) - G^{(2)}(P_1 \mp P_2) + \overline{G^{(1)}}\,\overline{(K_3 \mp K_4)} - \overline{G^{(2)}}\,\overline{(P_3 \mp P_4)} = 0 \tag{20d}$$

where a bar above a complex function denotes the complex conjugate of that function. In equations (20), the upper signs (in $\pm$ or $\mp$) are used for the case of $F = F_x$, whereas the lower signs refer to the case of $F = F_y$.

In the present study, K_4, P_2, and P_3 are set to be zero in order that the stresses may not have a singularity apart from that at the line force site[1] (i.e., at $x=a$) [17]. Furthermore, K_1 is determined from the homogeneous case [11] and is given by

$$K_1 = \frac{-F_x(\bar{C}_{12}{}^{(1)}e^{i\alpha^{(1)}} + C_{66}{}^{(1)}e^{-i\alpha^{(1)}})}{4\pi\lambda^{(1)}\bar{C}_{12}{}^{(1)}C_{66}{}^{(1)}\sin 2\alpha^{(1)}} \quad \text{for } F=F_x \tag{21a}$$

and

$$K_1 = \frac{F_y(C_{12}{}^{(1)} + C_{66}{}^{(1)})}{4\pi\bar{C}_{12}{}^{(1)}C_{66}{}^{(1)}\sin 2\alpha^{(1)}} \quad \text{for } F=F_y \tag{21b}$$

Once K_2, K_3, P_1 and P_4 are determined by equations (20), the Ψ functions and subsequently the displacement and stress fields can be obtained by straightforward substitutions.

3 Results

The results of the problem will be presented in two parts: the line force perpendicular to the interface ($F=F_x$) and that parallel to it ($F=F_y$). The elastic field of a line force in an arbitrary direction can be obtained by superposition of these two solutions, together with the solution for antiplane line force ($F=F_z$) reported previously [18].

For simplicity, only the elastic field in Phase I will be given as follows. We shall omit the superscripts for the elastic constants and parameters except where confusion may arise. The elastic field in Phase II can be obtained by the same approach (though algebraically more complex) and will not be reported in explicit form. Furthermore, a number of elastic parameters which will appear in the solutions are conveniently defined as follows:

$$Q_0 = H_0^{-1}[2(C_{12}{}^{(1)} + \bar{C}_{12}{}^{(1)})(C_{12}{}^{(2)} - \bar{C}_{12}{}^{(2)}) + (C_{12}{}^{(2)2} - \bar{C}_{12}{}^{(2)2})(C_{66}{}^{(1)} + C_{12}{}^{(1)})/C_{66}{}^{(1)} - (C_{12}{}^{(1)2} - \bar{C}_{12}{}^{(1)2})(C_{66}{}^{(2)} + \bar{C}_{12}{}^{(2)})/C_{66}{}^{(2)}] \tag{22}$$

$$Q_1 = (\lambda^{(1)}\lambda^{(2)}H_0)^{-1}[4\sin\alpha^{(1)}\sin\alpha^{(2)}\bar{C}_{12}{}^{(1)} \cdot \bar{C}_{12}{}^{(2)}(\lambda^{(1)2} - \lambda^{(2)2})] \tag{23}$$

$$Q_2 = (\bar{C}_{12}{}^{(2)2} - C_{12}{}^{(2)2})\bar{C}_{12}{}^{(1)}/H_0(\bar{C}_{12}{}^{(1)} + C_{12}{}^{(1)}) \tag{24}$$

$$N = \bar{C}_{12}{}^{(1)}(C_{12}{}^{(2)} - \bar{C}_{12}{}^{(2)})/H_0 \tag{25}$$

and

$$H_0 = \frac{4(\lambda^{(1)2} + \lambda^{(2)2})}{\lambda^{(1)}\lambda^{(2)}}\sin\alpha^{(1)}\sin\alpha^{(2)}\bar{C}_{12}{}^{(1)}\bar{C}_{12}{}^{(2)} + 2(C_{12}{}^{(1)} - \bar{C}_{12}{}^{(1)})(C_{12}{}^{(2)} - \bar{C}_{12}{}^{(2)}) + (\bar{C}_{12}{}^{(2)2} - C_{12}{}^{(2)2})(1 + \bar{C}_{12}{}^{(1)}/C_{66}{}^{(1)}) + (\bar{C}_{12}{}^{(1)2} - C_{12}{}^{(1)2})(1 + \bar{C}_{12}{}^{(2)}/C_{66}{}^{(2)}) \tag{26}$$

[1] Strictly speaking, the vanishing of three constants depends on the range of the C values. For example, $K_3 \neq 0$ and $K_4 = 0$ for $-4 < C < -2$, and $K_3 = 0$ and $K_4 \neq 0$ for $-2 < C < 0$. However, the difference in details does not alter the final solutions.

3.1 Displacement Field ($x \geq 0$).

(*A*) $F=F_x$ (line force perpendicular to the interface)

$$u = \frac{-F_x}{8\pi\lambda}\left\{\left[\frac{\bar{C}_{12}+C_{66}}{2\bar{C}_{12}C_{66}\sin\alpha}\ln\chi_1 + \frac{\bar{C}_{12}-C_{66}}{\bar{C}_{12}C_{66}\cos\alpha}\cdot\tan^{-1}\frac{2\lambda^2y^2\sin 2\alpha}{2(x-a)^2+(C+2)\lambda^2y^2}\right] - (Q_0+Q_1-CQ_2)\left[\frac{\bar{C}_{12}+C_{66}}{2\bar{C}_{12}C_{66}\sin\alpha}\ln\chi_2 + \frac{\bar{C}_{12}-C_{66}}{\bar{C}_{12}C_{66}\cos\alpha}\tan^{-1}\frac{2\lambda^2y^2\sin 2\alpha}{2(x+a)^2+(C+2)\lambda^2y^2}\right] + (Q_0-CQ_2)\left[\frac{(C+2)\bar{C}_{12}-2C_{66}}{C\bar{C}_{12}C_{66}\sin\alpha}\ln\chi_2 + \frac{2}{C_{66}\cos\alpha}\cdot\tan^{-1}\frac{2\lambda^2y^2\sin 2\alpha}{2(x+a)^2+(C+2)\lambda^2y^2}\right] - \frac{2(\bar{C}_{12}-C_{66})}{C\bar{C}_{12}C_{66}}\tan^{-1}\frac{2(x+a)\lambda y\sin\alpha}{(x+a)^2-\lambda^2y^2+Cax}\right]\right\} \tag{27a}$$

$$v = \frac{F_x}{4\pi}\left\{\frac{C_{12}+C_{66}}{\bar{C}_{12}C_{66}\sin 2\alpha}\left[\tanh^{-1}\frac{2(x-a)\lambda y\cos\alpha}{(x-a)^2+\lambda^2y^2} - (Q_0+Q_1-CQ_2)\tanh^{-1}\frac{2(x+a)\lambda y\cos\alpha}{(x+a)^2+\lambda^2y^2}\right] + \frac{C_{12}+C_{66}}{\bar{C}_{12}C_{66}\sin 2\alpha}(Q_0-CQ_2)\left[\tanh^{-1}\frac{2(x+a)\lambda y\cos\alpha}{(x+a)^2+\lambda^2y^2} - \frac{\sin\alpha}{\cos\alpha}\tan^{-1}\frac{2(x+a)\lambda y\sin\alpha}{(x+a)^2-\lambda^2y^2}\right] + (Q_0+CN)\left[\frac{\bar{C}_{12}+C_{66}}{\bar{C}_{12}C_{66}\sin 2\alpha}\tanh^{-1}\frac{2(x-a)\lambda y\cos\alpha}{(x+a)^2+\lambda^2y^2+Cax} - \frac{2(\bar{C}_{12}-C_{66})}{C\bar{C}_{12}C_{66}}\tan^{-1}\frac{2(x+a)\lambda y\sin\alpha}{(x+a)^2-\lambda^2y^2+Cax}\right]\right\} \tag{27b}$$

where

$$\chi_1 = [(x-a)^2+\lambda^2y^2]^2 + C(x-a)^2\lambda^2y^2 \tag{28}$$

$$\chi_2 = [(x+a)^2+\lambda^2y^2]^2 + C(x+a)^2\lambda^2y^2 \tag{29}$$

$$\chi_3 = [(x+a)^2+\lambda^2y^2+Cax]^2 + C(x-a)^2\lambda^2y^2 \tag{30}$$

(*B*) $F=F_y$ (line force parallel to the interface)

$$u = \frac{F_y}{4\pi}\left\{\frac{C_{12}+C_{66}}{\bar{C}_{12}C_{66}\sin 2\alpha}\left[\tanh^{-1}\frac{2(x-a)\lambda y\cos\alpha}{(x-a)^2+\lambda^2y^2} - (Q_0+Q_1-CQ_2)\tanh^{-1}\frac{2(x+a)\lambda y\cos\alpha}{(x+a)^2+\lambda^2y^2}\right] + \frac{C_{12}+C_{66}}{\bar{C}_{12}C_{66}\sin 2\alpha}(Q_0-CQ_2)\left[\tanh^{-1}\frac{2(x+a)\lambda y\cos\alpha}{(x+a)^2+\lambda^2y^2} + \frac{\sin\alpha}{\cos\alpha}\tan^{-1}\frac{2(x+a)\lambda y\sin\alpha}{(x+a)^2-\lambda^2y^2}\right]\right.$$

Downloaded 01 May 2010 to 171.66.16.249. Redistribution subject to ASME license or copyright; see http://www.asme.org/terms/Terms_Use.cfm

$$+(Q_0+CN)\left[\frac{\bar{C}_{12}+C_{66}}{\bar{C}_{12}C_{66}\sin 2\alpha}\right.$$

$$\cdot\tanh^{-1}\frac{2(x-a)\lambda y\cos\alpha}{(x+a)^2+\lambda^2y^2+Cax}$$

$$\left.+\frac{2(\bar{C}_{12}-C_{66})}{\bar{C}_{12}C_{66}C}\tan^{-1}\frac{2(x+a)\lambda y\sin\alpha}{(x+a)^2-\lambda^2y^2+Cax}\right]\Bigg\} \tag{31a}$$

$$v=\frac{-F_y}{8\pi\lambda}\left\{\left[\frac{\bar{C}_{12}+C_{66}}{2\bar{C}_{12}C_{66}\sin\alpha}\ln\chi_1-\frac{\bar{C}_{12}-C_{66}}{\bar{C}_{12}C_{66}\cos\alpha}\right.\right.$$

$$\cdot\tan^{-1}\frac{2\lambda^2y^2\sin 2\alpha}{2(x-a)^2+(C+2)\lambda^2y^2}\Bigg]$$

$$-(Q_0+Q_1-CQ_2)\left[\frac{\bar{C}_{12}+C_{66}}{2\bar{C}_{12}C_{66}\sin\alpha}\ln\chi_2\right.$$

$$\left.-\frac{\bar{C}_{12}-C_{66}}{\bar{C}_{12}C_{66}\cos\alpha}\tan^{-1}\frac{2\lambda^2y^2\sin 2\alpha}{2(x+a)^2+(C+2)\lambda^2y^2}\right]$$

$$+(Q_0-CQ_2)\left[\frac{(C+2)\bar{C}_{12}-2C_{66}}{\bar{C}_{12}C_{66}C\sin\alpha}\ln\chi_2-\frac{2}{C_{66}\cos\alpha}\right.$$

$$\cdot\tan^{-1}\frac{2\lambda^2y^2\sin 2\alpha}{2(x+a)^2+(C+2)\lambda^2y^2}\Bigg]$$

$$\left.-(Q_0+CN)\left[\frac{2(C_{12}+C_{66})}{\bar{C}_{12}C_{66}C\sin\alpha}\ln\chi_3\right]\right\} \tag{31b}$$

3.2 Stress Field ($x \geq 0$). (A) $F=F_x$ (line force perpendicular to the interface)

$$\sigma_{xx}=\frac{-F_x\lambda}{4\pi\sin\alpha}\left\{\frac{(x-a)}{\chi_1}[(C+3+\rho)(x-a)^2+(1-\rho)\lambda^2y^2]\right.$$

$$\left.-\frac{(Q_0+Q_1-CQ_2)(x+a)}{\chi_2}[(C+3+\rho)(x+a)^2+(1-\rho)\lambda^2y^2]\right\}$$

$$-\frac{F_x\lambda}{2\pi C\sin\alpha}\left\{\frac{(Q_0-CQ_2)(x+a)}{\chi_2}[C+2+2\rho)\right.$$

$$\cdot((x+a)^2+\lambda^2y^2)+C(C+3+\rho)(x+a)^2]-\frac{(Q_0+CN)}{\chi_3}$$

$$\cdot[(C+2+2\rho)(x+a)((x+a)^2+\lambda^2y^2)-C\langle C(1-\rho)ax^2$$

$$\left.+x(x+a)((1-\rho)x-(C+1+3\rho)a)+(1-\rho)a\lambda^2y^2\rangle]\right\} \tag{32a}$$

$$\sigma_{yy}=\frac{F_x}{4\pi\lambda\sin\alpha}\left\{\frac{(x-a)}{\chi_1}[(1-\rho)(x-a)^2-(1+(c+3)\rho)\lambda^2y^2]\right.$$

$$-\frac{Q_0+Q_1-CQ_2}{\chi_2}(x+a)[(1-\rho)(x+a)^2$$

$$\left.-(1+(c+3)\rho)\lambda^2y^2]\right\}+\frac{F_x}{2\pi C\lambda\sin\alpha}\left\{\frac{(Q_0-CQ_2)(x+a)}{\chi_2}\right.$$

$$\cdot[(C+2+2\rho)((x+a)^2+\lambda^2y^2)-(1-\rho)C\lambda^2y^2]$$

$$-\frac{(Q_0+CN)}{\chi_3}[(C+2+2\rho)(x+a)((x+a)^2+\lambda^2y^2)$$

$$+C\langle C(C+3+\rho)a^2x+a(a+x)((2C+5+3\rho)x$$

$$\left.+(C+3+\rho)a)+(C+3+\rho)x\lambda^2y^2\rangle]\right\} \tag{32b}$$

$$\sigma_{xy}=\frac{-F_x\lambda}{4\pi\sin\alpha}\left\{\frac{y}{\chi_1}[(C+3+\rho)(x-a)^2+(1-\rho)\lambda^2y^2]\right.$$

$$-\frac{(Q_0+Q_1-CQ_2)y}{\chi_2}\left.[(C+3+\rho)(x+a)^2+(1-\rho)\lambda^2y^2]\right\}$$

$$-\frac{F_x\lambda}{2\pi C\sin\alpha}\left\{\frac{(Q_0-CQ_2)y}{\chi_2}[(C+2+2\rho)((x+a)^2+\lambda^2y^2)\right.$$

$$+C(C+3+\rho)(x+a)^2]-\frac{(Q_0+CN)y}{\chi_3}[(C+2+2\rho)$$

$$\left.\cdot((x+a)^2+\lambda^2y^2)-C\langle(1-\rho)x^2-(C+3+\rho)a^2\rangle]\right\} \tag{32c}$$

where $\rho = C_{12}/\bar{C}_{12}$.

(B) $F = F_y$ (line force parallel to the interface)

$$\sigma_{xx}=\frac{-F_y\lambda^3}{4\pi\sin\alpha}\left\{\frac{y}{\chi_1}[(1+(C+3)\rho)(x-a)^2-(1-\rho)\lambda^2y^2]\right.$$

$$-\frac{(Q_0+Q_1-CQ_2)y}{\chi_2}[(1+(C+3)\rho)(x+a)^2$$

$$\left.-(1-\rho)\lambda^2y^2]\right\}+\frac{F_y\lambda^3}{2\pi C\sin\alpha}\left\{\frac{(Q_0-CQ_2)y}{\chi_2}\right.$$

$$\cdot[(C+2+2\rho)((x+a)^2+\lambda^2y^2)-C(1-\rho)(x+a)^2]$$

$$-\frac{(Q_0+CN)y}{\chi_3}[(C+2+2\rho)((x+a)^2+\lambda^2y^2)$$

$$\left.+C\langle(C+3+\rho)x^2-(1-\rho)a^2\rangle]\right\} \tag{33a}$$

$$\sigma_{yy}=\frac{-F_y\lambda}{4\pi\sin\alpha}\left\{\frac{y}{\chi_1}[(1-\rho)(x-a)^2+(C+3+\rho)\lambda^2y^2]\right.$$

$$-\frac{(Q_0+Q_1-CQ_2)y}{\chi_2}\left.[(1-\rho)(x+a)^2+(C+3+\rho)\lambda^2y^2]\right\}$$

$$-\frac{F_y\lambda}{2\pi C\sin\alpha}\left\{\frac{(Q_0-CQ_2)y}{\chi_2}[(C+2+2\rho)((x+a)^2+\lambda^2y^2)\right.$$

$$+C(C+3+\rho)\lambda^2y^2]-\frac{(Q_0+CN)y}{\chi_3}[(C+2+2\rho)$$

$$\cdot((x+a)^2+\lambda^2)y^2+C\langle(C+4)\rho a^2-2(1-\rho)ax$$

$$\left.-(1-\rho)\lambda^2y^2\rangle]\right\} \tag{33b}$$

$$\sigma_{xy}=\frac{-F_y\lambda}{4\pi\sin\alpha}\left\{\frac{(x-a)}{\chi_1}[(1-\rho)(x-a)^2+(C+3+\rho)\lambda^2y^2]\right.$$

$$-\frac{(Q_0+Q_1-CQ_2)(x+a)}{\chi_2}\left.[(1-\rho)(x+a)^2+(C+3+\rho)\lambda^2y^2]\right\}$$

$$-\frac{F_y\lambda}{2\pi C\sin\alpha}\left\{\frac{(Q_0-CQ_2)(x+a)}{\chi_2}[(C+2+2\rho)\right.$$

$$\cdot((x+a)^2+\lambda^2y^2)+C(C+3+\rho)\lambda^2y^2]-\frac{(Q_0+CN)}{\chi_3}$$

$$\cdot[(C+2+2\rho)(x+a)((x+a)^2+\lambda^2y^2)-C\langle C(1-\rho)$$

Downloaded 01 May 2010 to 171.66.16.249. Redistribution subject to ASME license or copyright; see http://www.asme.org/terms/Terms_Use.cfm

$$\cdot a^2x-a(x+a)\left((C+1+3\rho)x-(1-\rho)a\right.$$

$$\left.+(1-\rho)x\lambda^2y^2\rangle]\right\} \tag{33c}$$

The foregoing results satisfy the equilibrium and the boundary conditions. (The latter were verified by numerical calculation.) For reference, the stress field in Phase II ($x \le 0$) is given in complex functions as follows:

$$\sigma_{xx}=\mathrm{Re}\left\{E^{(2)}\left[P_1\frac{2(\epsilon x-a)[(\epsilon x-a)^2-\lambda^{(1)^2}y^2e^{-2i\alpha^{(1)}}]}{\chi_4}\right.\right.$$

$$\left.\left.-e^{2i\alpha^{(1)}}P_4\frac{2(\epsilon x+ae^{2i\alpha^{(1)}})[(\epsilon x+ae^{-2i\alpha^{(1)}})^2-\lambda^{(1)^2}y^2e^{-2i\alpha^{(1)}}]}{\chi_5}\right]\right\} \tag{34a}$$

$$\sigma_{yy}=\mathrm{Re}\left\{F^{(2)}\left[P_1\frac{2(\epsilon x-a)[(\epsilon x-a)^2-\lambda^{(1)^2}y^2e^{-2i\alpha^{(1)}}]}{\chi_4}\right.\right.$$

$$\left.\left.-e^{2i\alpha^{(1)}}P_4\frac{2(\epsilon x+ae^{2i\alpha^{(1)}})[(\epsilon x+ae^{-2i\alpha^{(1)}})^2-\lambda^{(1)^2}y^2e^{-2i\alpha^{(1)}}]}{\chi_5}\right]\right\} \tag{34b}$$

$$\sigma_{xy}=\mathrm{Re}\left\{G^{(2)}\left[P_1\frac{-2\lambda^{(1)}e^{i\alpha^{(1)}}y[(\epsilon x-a)^2-\lambda^{(1)^2}y^2e^{-2i\alpha^{(1)}}]}{\chi_4}\right.\right.$$

$$\left.\left.-e^{2i\alpha^{(1)}}P_4\frac{-2\lambda^{(1)}e^{i\alpha^{(1)}}y[(\epsilon x+ae^{-2i\alpha^{(1)}})^2-\lambda^{(1)^2}y^2e^{-2i\alpha^{(1)}}]}{\chi_5}\right]\right\} \tag{34c}$$

where

$$\chi_4=[(\epsilon x-a)^2+\lambda^{(1)^2}y^2]+C^{(1)}\lambda^{(1)^2}y^2(\epsilon x-a)^2 \tag{35}$$

$$\chi_5=\{[(\epsilon x-a)^2+\lambda^{(1)^2}y^2]-C^{(1)}a\epsilon x\}^2$$
$$+C^{(1)}\lambda^{(1)^2}y^2(\epsilon x+a)^2 \tag{36}$$

4 Special Cases

There are several simple examples which can be obtained from the general problem analyzed in the preceding section. First of all, if we let $C_{ij}^{(1)}=C_{ij}^{(2)}$, then $Q_1=0$, $Q_0-CQ_2=0$, and $Q_0+CN=0$. The general results then reduce to those for a homogeneous, orthotropic medium treated by Hirth and Hirth and Lothe [19, 22]. Explicit expressions can also be deduced for other special cases as shown in the following.

4.1 The Elastic Field of a Line Force in a Two-Phase Isotropic Medium. In the case of isotropy, $C_{11}=C_{22}=C_{33}=2\mu(1-\nu)/(1-2\nu)$, $C_{12}=C_{13}=2\mu\nu/(1-2\nu)$, $C_{44}=C_{55}=C_{66}=\mu$, and $C=0$ where μ is the shear modulus and ν is the Poisson's ratio. The general solutions given in Section 3 will be simplified considerably.

(*A*) $F=F_x$(line force perpendicular to the interface, $x \ge 0$)

$$u=\frac{-F_x}{16\pi\mu(1-\nu)}\left\{(3-4\nu)\ln[(x-a)^2+y^2]+\frac{2y^2}{(x-a)^2+y^2}\right.$$

$$\left.+(Q_0+M/4)\ln[(x+a)^2+y^2]+2Q_0(3-4\nu)\frac{y^2}{(x+a)^2+y^2}\right\} \tag{37a}$$

$$v=\frac{F_x}{16\pi\mu(1-\nu)}\left\{\frac{2(x-a)y}{(x-a)^2+y^2}+2Q_0(3-4\nu)\frac{(x-a)y}{(x+a)^2+y^2}\right.$$

$$\left.+Q_0\frac{8ax(x+a)y}{[(x+a)^2+y^2]^2}-M\tan^{-1}\frac{2(x+a)y}{(x+a)^2-y^2}\right\} \tag{37b}$$

$$\sigma_{xx}=\frac{-F_x}{4\pi(1-\nu)}\left\{\frac{(x-a)[3(x-a)^2+y^2]}{[(x-a)^2+y^2]^2}\right.$$

$$+Q_0\frac{(x+a)[3(x+a)^2+y^2]}{[(x+a)^2+y^2]^2}$$

$$+2Q_0\frac{x[(x+3a)(x+a)^3-6a(x+a)y^2-y^4]}{[(x+a)^2+y^2]^3}+M\frac{x+a}{(x+a)^2+y^2}$$

$$\left.-2\nu\left[\frac{x-a}{(x-a)^2+y^2}+Q_0\frac{x+a}{(x+a)^2+y^2}\right.\right.$$

$$\left.\left.+2Q_0\frac{x[(x+a)^2-y^2]}{[(x+a)^2+y^2]^2}\right]\right\} \tag{38a}$$

$$\sigma_{yy}=\frac{F_x}{4\pi(1-\nu)}\left\{\frac{(x-a)[3(x-a)^2+y^2]}{[(x-a)^2+y^2]^2}\right.$$

$$-Q_0\frac{(x+a)[3(x+a)^2+y^2]}{[(x+a)^2+y^2]^2}$$

$$-2Q_0\frac{a(x+3a)(x+a)^3+2(x+a)(2x^2+7ax+2a^2)y^2+(4x+a)y^4}{[(x+a)^2+y^2]^3}$$

$$+M\frac{x+a}{(x+a)^2+y^2}-2\nu\left[\frac{x-a}{(x-a)^2+y^2}-Q_0\frac{x+a}{(x+a)^2+y^2}\right.$$

$$\left.\left.-2Q_0\frac{a(x+a)^2+(2x+a)y^2}{[(x+a)^2+y^2]^2}\right]\right\} \tag{38b}$$

$$\sigma_{xy}=\frac{-F_x}{4\pi(1-\nu)}\left\{\frac{y[3(x-a)^2+y^2]}{[(x-a)^2+y^2]^2}-Q_0\frac{y[3(x+a)^2+y^2]}{[(x+a)^2+y^2]^2}\right.$$

$$+4Q_0\frac{xy[(2x+5a)(x+a)^2+(2x+a)y^2]}{[(x+a)^2+y^2]^3}+M\frac{y}{(x+a)^2+y^2}$$

$$-2\nu\left[\frac{y}{(x-a)^2+y^2}-Q_0\frac{y}{(x+a)^2+y^2}\right.$$

$$\left.\left.+4Q_0\frac{(x+a)xy}{[(x+a)^2+y^2]^2}\right]\right\} \tag{38c}$$

where

$$M=\frac{4\mu^{(2)}(1-\nu^{(1)})[\mu^{(1)}(1-2\nu^{(2)})-\mu^{(2)}(1-2\nu^{(1)})]}{[\mu^{(1)}+\mu^{(2)}(3-4\nu^{(1)})][\mu^{(2)}+\mu^{(1)}(3-4\nu^{(2)})]} \tag{39}$$

$$Q_0=\frac{\mu^{(1)}-\mu^{(2)}}{\mu^{(1)}+\mu^{(2)}(3-4\nu^{(1)})} \tag{40}$$

(*B*) $F=F_y$ (line force parallel to the interface, $x \ge 0$)

$$u=\frac{F_y}{16\pi\mu(1-\nu)}\left\{\frac{2(x-a)y}{(x-a)^2+y^2}+2Q_0(3-4\nu)\frac{(x-a)y}{(x+a)^2+y^2}\right.$$

$$\left.-Q_0\frac{8ax(x+a)y}{[(x+a)^2+y^2]^2}+M\tan^{-1}\frac{2(x+a)y}{(x+a)^2-y^2}\right\} \tag{41a}$$

$$v=\frac{-F_y}{16\pi\mu(1-\nu)}\left\{(3-4\nu)\ln[(x-a)^2+y^2]\right.$$

$$-\frac{2y^2}{(x-a)^2+y^2}+(Q_0+M/4)\ln[(x+a)^2+y^2]$$

$$\left.-2Q_0(3-4\nu)\frac{y^2}{(x+a)^2+y^2}\right\} \tag{41b}$$

Downloaded 01 May 2010 to 171.66.16.249. Redistribution subject to ASME license or copyright; see http://www.asme.org/terms/Terms_Use.cfm

$$\sigma_{xx}=\frac{-F_y}{4\pi(1-\nu)}\left\{\frac{y[(x-a)^2-y^2]}{[(x-a)^2+y^2]^2}-Q_0\frac{y[(x+a)^2-y^2]}{[(x+a)^2+y^2]^2}\right.$$
$$+4Q_0\frac{xy[(2x-a)(x+a)^2+(2x+3a)y^2]}{[(x+a)^2+y^2]^3}-M\frac{y}{(x+a)^2+y^2}$$
$$+2\nu\left[\frac{y}{(x-a)^2+y^2}-Q_0\frac{y}{(x+a)^2+y^2}\right.$$
$$\left.\left.-4Q_0\frac{(x+a)xy}{[(x+a)^2+y^2]^2}\right]\right\} \quad (42a)$$

$$\sigma_{yy}=\frac{-F_y}{4\pi(1-\nu)}\left\{\frac{y[(x-a)^2+3y^2]}{[(x-a)^2+y^2]^2}-Q_0\frac{y[(x+a)^2+3y^2]}{[(x+a)^2+y^2]^2}\right.$$
$$+4Q_0\frac{y[(3ax+2y^2)(x+a)^2+(2y^2-ax)y^2]}{[(x+a)^2+y^2]^3}$$
$$+M\frac{y}{(x+a)^2+y^2}-2\nu\left[\frac{y}{(x-a)^2+y^2}-Q_0\frac{y}{(x+a)^2+y^2}\right.$$
$$\left.\left.+4Q_0\frac{y(a^2+ax+y^2)}{[(x+a)^2+y^2]^2}\right]\right\} \quad (42b)$$

$$\sigma_{xy}=\frac{-F_y}{4\pi(1-\nu)}\left\{\frac{(x-a)[(x-a)^2+3y^2]}{[(x-a)^2+y^2]^2}\right.$$
$$-Q_0\frac{(x+a)[(x+a)^2+3y^2]}{[(x+a)^2+y^2]^2}$$
$$+2Q_0\frac{a(3x+a)(x+a)^3+2(x+a)(2x^2+ax+2a^2)y^2+(4x+3a)y^4}{[(x+a)^2+y^2]^3}$$
$$+M\frac{(x+a)}{(x+a)^2+y^2}-2\nu\left[\frac{(x-a)}{(x-a)^2+y^2}-Q_0\frac{(x+a)}{(x+a)^2+y^2}\right.$$
$$\left.\left.+2Q_0\frac{(2x+a)y^2+a(x+a)^2}{[(x+a)^2+y^2]^2}\right]\right\} \quad (42c)$$

Frasier and Rongved [2] reported the stress field under the plane stress condition in bipolar coordinates. The foregoing stress equations have been checked numerically with their results, after the latter had been converted to the plane strain condition.[2]

4.2 The Elastic Field of a Line Force in a Semi-Infinite Medium. Another special case of interest occurs when the second phase is absent. The system thus consists of a line force acting at distance a from the free surface $x = 0$ in a semi-infinite medium. The displacement and stress equations can be obtained from equations (27)–(33) simply by setting $Q_0 = 1$ and $Q_1 = Q_2 = N = 0$.

In particular, if $a = 0$, the line force is acting on the free surface [23]. This case has many practical applications. The stress equations for $F = F_x$ are given in the following:

$$\sigma_{xx}=\frac{-2F_x\lambda\sin\alpha}{\pi}\frac{x^3}{(x^2+\lambda^2y^2)^2+Cx^2\lambda^2y^2} \quad (43a)$$

$$\sigma_{yy}=\frac{-2F_x\sin\alpha}{\pi}\frac{x\lambda^2y^2}{(x^2+\lambda^2y^2)^2+Cx^2\lambda^2y^2} \quad (43b)$$

$$\sigma_{xy}=\frac{-2F_x\sin\alpha}{\pi}\frac{x^2\lambda y}{(x^2+\lambda^2y^2)^2+Cx^2\lambda^2y^2} \quad (43c)$$

which agree with the results of Lekhnitskii [24].

[2] In order to reach the agreement, the term $(1+\nu)K_2(z+c)$ in equation (4) of reference [2] should read $K_2(z+c)$.

5 Application

The basic information expressed in the preceding sections is useful in various applications. For the sake of simplicity, we shall apply the results to the determination of the elastic field of an edge dislocation in a semi-infinite orthotropic medium [25]. The derivation is based on the principle of virtual work through a virtual work cycle. The cycle may begin by introducing a line force F_x at the position (x,y), as shown in Fig. 1. As a result, the system gains an amount of work W_f.

A cut is then made from $x = 0$ to a along the plane $y = 0$. In order to maintain the equilibrium, it is necessary to apply surface tractions on the cut planes with a magnitude equal to the stresses produced by the line force at (x,y). The two cut planes are next displaced relative to each other by an amount b_x in the x-direction and then rejoined together. In this way an edge dislocation is formed at $(a,0)$ with a strain energy W_d. However, during the process of forming the dislocation, two interaction work terms are also involved. The first is the work done by the surface tractions on the cut planes due to the stress field of the line force, $W_{\rm I}=\int_0^a\sigma_{xy}b_x\,dx$. The second term is the work done by the line force at (x,y) in the displacement field of the edge dislocation, $W_{\rm II} = F_x\cdot u_e$. The total strain energy in the system up to this stage is $W_f + W_d + W_{\rm I} + W_{\rm II}$.

Let us now remove the line force and then the edge dislocation from the system. An amount of strain energy $W_f + W_d$ is released accordingly. The system is back to its original state, and by the law of conservation of energy, we have

$$W_f+W_d+W_{\rm I}+W_{\rm II}-W_f-W_d=0 \quad (44)$$

or

$$W_{\rm I}=-W_{\rm II} \quad (45)$$

Consequently

$$u_e=\frac{-b_x}{F_x}\int_0^a\sigma_{xy}(\bar{x},x,\bar{y},y)\,d\bar{x} \quad (46)$$

evaluated at $\bar{y} = 0$, where σ_{xy} can be obtained from equation (32c). Using a similar cycle yields

$$v_e=\frac{-b_x}{F_y}\int_0^a\sigma_{xy}(\bar{x},x,\bar{y},y)\,d\bar{x} \quad (47)$$

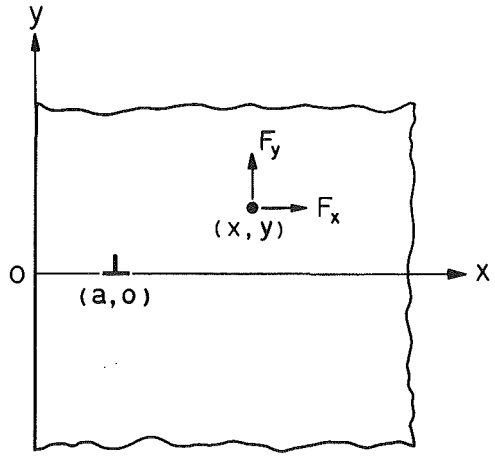


Fig. 1 Interaction of a line force at (x,y) and an edge dislocation at (a, o) in an orthotropic half space

Downloaded 01 May 2010 to 171.66.16.249. Redistribution subject to ASME license or copyright; see http://www.asme.org/terms/Terms_Use.cfm

evaluated at $\bar{y} = 0$, with σ_{xy} derived from equation (33c). The final results are

$$u_e = \frac{b_x}{4\pi}\left\{\frac{C_{12}-\bar{C}_{12}\cos 2\alpha}{2\bar{C}_{12}\sin 2\alpha}\right.$$
$$\cdot\ln\frac{(x-a)^2+\lambda^2y^2+2(x-a)\lambda y\cos\alpha}{(x-a)^2+\lambda^2y^2-2(x-a)\lambda y\cos\alpha}$$
$$+\tan^{-1}\frac{2(x-a)\lambda y\sin\alpha}{(x-a)^2-\lambda^2y^2}-\frac{\sin\alpha}{2\cos\alpha}$$
$$\cdot\ln\frac{(x+a)^2+\lambda^2y^2+2(x+a)\lambda y\cos\alpha}{(x+a)^2+\lambda^2y^2-2(x+a)\lambda y\cos\alpha}$$
$$+\frac{C_{12}-\bar{C}_{12}\cos 2\alpha}{2\bar{C}_{12}\cos^2\alpha}\tan^{-1}\frac{2(x+a)\lambda\sin\alpha}{(x+a)^2-\lambda^2y^2}$$
$$-\frac{C_{12}-\bar{C}_{12}}{2\bar{C}_{12}\sin 2\alpha}$$
$$\cdot\ln\frac{(x+a)^2+\lambda^2y^2+Cax+2(x-a)\lambda y\cos\alpha}{(x+a)^2+\lambda^2y^2+Cax-2(x-a)\lambda y\cos\alpha}$$
$$\left.-\frac{C_{12}+\bar{C}_{12}}{2\bar{C}_{12}\cos^2\alpha}\tan^{-1}\frac{2(x+a)\lambda y\sin\alpha}{(x+a)^2+Cax-\lambda^2y^2}\right\} \tag{48a}$$

$$v_e = \frac{b_x\lambda}{4\pi}\left\{\frac{C_{12}-\bar{C}_{12}}{4\bar{C}_{12}\sin\alpha}\ln[\langle(x-a)^2+\lambda^2y^2\rangle^2\right.$$
$$+C(x-a)^2\lambda^2y^2]+\frac{C_{12}+\bar{C}_{12}}{2\bar{C}_{12}\cos\alpha}$$
$$\cdot\tan^{-1}\frac{\lambda^2y^2\sin 2\alpha}{(x-a)^2-\lambda^2y^2\cos 2\alpha}+\frac{(C_{12}+\bar{C}_{12})\sin\alpha}{4\bar{C}_{12}\cos^2\alpha}$$
$$\cdot\ln[\langle(x+a)^2+\lambda^2y^2\rangle^2+C(x+a)^2\lambda^2y^2]$$
$$-\frac{C_{12}-\bar{C}_{12}}{2\bar{C}_{12}\cos\alpha}\tan^{-1}\frac{\lambda^2y^2\sin 2\alpha}{(x+a)^2-\lambda^2y^2\cos 2\alpha}$$
$$-\frac{C_{12}-\bar{C}_{12}\cos 2\alpha}{2\bar{C}_{12}\sin 2\alpha\cos\alpha}\ln[\langle(x+a)^2+\lambda^2y^2$$
$$+Cax\rangle^2+C(x-a)^2\lambda^2y^2]-\frac{1}{\cos\alpha}$$
$$\left.\cdot\tan^{-1}\frac{2ax\sin 2\alpha-a^2\sin 4\alpha+\lambda^2y^2\sin 2\alpha}{x^2-2ax\cos 2\alpha+a^2\cos 4\alpha-\lambda^2y^2\cos 2\alpha}\right\} \tag{48b}$$

The stress equations derived from equations (48) are in agreement with the previous results of Pande and Chou [25].[3]

6 Conclusions

1 Explict expressions were obtained for the elastic field of an in-plane line force acting in a two-phase orthotropic medium. The stress fields, on approaching isotropy, agree with Frasier and Rongved's results.

2 The general solutions were simplified to special cases including the solution for a line force in a half space of orthotropic symmetry.

3 A simple application of the results was made to determine the elastic field of an edge dislocation in an orthotropic half space.

[3] We take the opportunity to correct some typographical errors in reference 25. The signs of the second terms in the stress equations (29), (30), (31), (35) and (37) should be changed.

Acknowledgment

This work was supported by the National Science Foundation under Grant DMR 76-14998.

References

1 Dundurs, J., and Hetenyi, M., "Transmission of Force Between Two Semi-Infinite Solids," ASME JOURNAL OF APPLIED MECHANICS, Vol. 32, 1965, pp. 671-674.

2 Frasier, J. T., and Rongved, L., "Force in the Plane of Two Joined Semi-Infinite Plates," ASME JOURNAL OF APPLIED MECHANICS, Vol. 24, 1957, pp. 582-584.

3 Eshelby, J. D., "The Determination of the Elastic Field of an Ellipsoidal Inclusion and Related Prolems," *Proceedings of the Royal Society,* London, Series, A., Vol. 241, 1957, pp. 376-396.

4 Gehlen, P. C., Hahn, G. T., and Kanninen, M. F., "Crack Extension by Bond Rupture in a Model of BCC Iron," *Scripta Metallurgica,* Vol. 6, 1972, pp. 1087-1090.

5 Gehlen, P. C., et al., "Nonlinear Effects in the Displacement Field of a Dislocation," *Scripta Metallurgica,* Vol. 6, 1972, pp. 445-446.

6 Gehlen, P. C., et al., "A New Representation of the Strain Field Associated With the Cube-Edge Dislocation in a Model of a α-Iron," *Journal of Applied Physics*, Vol. 43, 1972, pp. 3921-3933.

7 Gehlen, P. C., "Crack Extension in a Model of α-Iron," *Scripta Metallurgica,* Vol. 7, 1973, pp. 1115-1116.

8 Hirth, J. P., Hoagland, R. G., and Gehlen, P. C., "The Interaction Between Line Force Arrays and Planar Cracks," *International Journal of Solids and Structures,* Vol. 10, 1974, pp. 977-984

9 Yang, H. C., and Chou, Y. T., "Generalized Plane Problems of Elastic Inclusions in Anisotropic Solids," ASME JOURNAL OF APPLIED MECHANICS, Vol. 43, 1976, pp. 424-430.

10 Yang, H. C., and Chou, Y. T., "Antiplane Strain Problems of an Elliptic Inclusion in an Anisotropic Medium," ASME JOURNAL OF APPLIED MECHANICS, Vol. 44, 1977, pp. 437-441.

11 Eshelby, J. D., Read, W. T., and Shockley, W., "Anisotropic Elasticity With Applications to Dislocation Theory," *Acta Metallurgica,* Vol. 1, 1953, pp. 251-259.

12 Gemperlová, J., and Saxl, I., "Dislocations in an Inhomogeneous Anisotropic Medium," *Czechoslovak Journal of Physics,* Vol. B18, 1968, pp. 1085-1093.

13 Tucker, M. O., "Plane Boundaries and Straight Dislocations in Elastically Anisotropic Materials," *Philosophical Magazine,* Vol. 19, 1969, pp. 1141-1159.

14 Barnett, D. M., and Lothe, J., "An Image Force Theorem for Dislocations in Anisotropic Bicrystals," *Journal of Physics F: Metal Physics,* Vol. 4, 1974, pp. 1618-1653.

15 Chou, Y. T., "On Dislocation-Boundary Interaction in an Anisotropic Aggregate," *physica status solidi,* Vol. 15, 1966, pp. 123-127.

16 Chou, T. Y., and Barnett, D. M., "Stacked Screw Dislocation Arrays in an Anisotropic Two-Phase Medium," *physica status solidi,* Vol. 21, 1967, pp. 239-246.

17 Pande, C. S., and Chou, Y. T., "Edge Dislocations in Anisotropic Inhomogeneous Media," *Journal of Applied Physics,* Vol. 43, 1972, pp. 840-844.

18 Chou, Y. T., "On Antiplane Line Force in a Two-Phase Anisotropic Medium," *physica status solidi,* Vol. 34, 1976, pp. 645-650.

19 Hirth, J. P., "Anisotropic Elastic Solutions for Line Force Arrays," *Scripta Metallurgica,* Vol. 6, 1972, pp. 535-540.

20 Chou, Y. T., and Sha, G. T., "On the Elastic Field of a Dislocation in an Anisotropic Crystral," *Scripta Metallurgica,* Vol. 5, 1971, pp. 551-558.

21 Head, A. K., "Edge Dislocations in Inhomogeneous Media," *The Proceedings of the Physical Society,* Vol. B66, 1953, pp. 793-801.

22 Hirth, J. P., and Lothe, J., "Anisotropic Elastic Solutions for Line Defects in High-Symmetry Cases," *Journal of Applied Physics,* Vol. 44, 1973, pp. 1029-1032.

23 Barnett, D. M., and Lothe, J., "Line Force Loadings on Anisotropic Half-Spaces and Wedges," *Physica Norvegica,* Vol. 8, 1975, pp. 13-22.

24 Lekhnitskii, S. G., *Theory of Elasticity of an Anistropic Elastic Body,* California, Holden-Day, Inc., 1963.

25 Pande, C. S., and Chou, Y. T., "Edge Dislocations in Semi-Infinite Anisotropic Media," *physica status solidi,* Series (a), Vol. 6, 1971, pp. 499-504.

Downloaded 01 May 2010 to 171.66.16.249. Redistribution subject to ASME license or copyright; see http://www.asme.org/terms/Terms_Use.cfm

Unconventional Internal Cracks Part 1: Symmetric Variations of a Straight Crack

C. H. Wu
Professor,
Department of Materials Engineering,
University of Illinois at Chicago Circle,
P.O. Box 4348,
Chicago, Ill. 60680

The composite mapping function of successive mappings by rational functions is rational but may have poles at more than one location. This method may be exploited to generate many, many new but unconventional cracks for which the associated elasticity problems may be solved exactly. Two families of cracks are examined in detail in this paper. A few more cases will be reported in a follow-up paper.

1 Introduction

One of the tasks involved in carrying out a fracture analysis is the determination of the stress-intensity factors at the tip (or tips) of a crack. In the discussions to follow, we shall extend the conventionally implied meaning of the word crack to include holes with cusps. Thus a crack boundary is in general a simple contour with cusps and the area enclosed by the contour is not necessarily zero. In the context of the linear elastic fracture mechanics, the determination of the stress-intensity factors requires the solution of an elasticity problem. There have been many analytical and numerical methods developed for this purpose. One of the well-established analytical methods is the so-called conformal mapping technique. The advantage of this method is that it gives the exact solution provided the given crack boundary can be mapped onto the unit circle by a sufficiently simple mapping function. However, it is in general impossible to find the needed simple and explicit mapping function for a crack that is commonly considered to be of physical relevance. This realization led Bowie to devise his method of polynomial approximation. A summary of his method as well as many related work can be found in [1].

But what crack configurations are physically relevant and what are not? Natural cracks are very irregular, and any attempt in describing them by the use of a straight crack or a circular-arc crack is an approximation in itself. Information on internal cracks detected by one of the so-called nondestructive methods can never be very precise and complete, and it is therefore desirable to have a large number of exact crack solutions available so that a meaningful parametric study can be carried out for the limited data to determine their worst physical implications. In the various statistical approaches to fracture [2–4], a defect is usually characterized by a single parameter. Increasing the number of parameters in these theories requires the knowledge of families of multiparameter crack solutions. The use of a straight crack, which has a zero enclosure, to study fracture under compression is not very satisfactory because the opposite faces of the crack will come into contact [5, 6]. A crack configuration possessing one or two cusps and a nonzero gap between the opposite faces would be a better model for this investigation. Finally, a straight crack is insensitive to a crack-parallel load. The effect of the crack-parallel load, however, becomes increasingly important as the gap between the opposite faces of a crack increases. In the investigations of the so-called branching phenomenon (see [6] and the many references listed therein), a uniaxial crack-parallel load is interpreted as a pure shear. This interpretation is not applicable even if the crack has only a very small gap. The experimental data available for this study were mostly obtained from a crack with a nonzero enclosure, and the scattering of the data has been the subject of discussion in more than a few papers (see the references of [6]). The foregoing discussion clearly indicates the desirability of generating more exact solutions for multiparameter crack configurations.

Our results are presented in two parts. Part 1 includes a general formulation and solutions for certain symmetric variations of a straight crack. A few more cases will be presented in Part 2.

2 Plane and Antiplane Problems

Let (x_1,x_2,x_3) be rectangular Cartesian coordinates. We consider the plane and antiplane problems in the x_1 and x_2 coordinates, and shall use a complex formulation in terms of the complex variable $z = x_1 + ix_2$. The displacements $u_i(x_1, x_2)$ and stresses $\tau_{ij}(x_1, x_2)$ may be written in terms of three complex functions $Z(z)$, $W(z)$, $w(z)$, viz.,

Antiplane Problems

$$2\mu u_3 = Z(z) + \overline{Z(z)}, \tag{1}$$

$$\tau_{31} - i\tau_{32} = Z'(z); \tag{2}$$

Plane Problem

$$2\mu(u_1 + iu_2) = \kappa W(z) - z\overline{W'(z)} - \overline{w(z)}, \tag{3}$$

$$\tau_{11} + \tau_{22} = 2[W'(z) + \overline{W'(z)}], \tag{4}$$

Contributed by the Applied Mechanics Division for publication in the JOURNAL OF APPLIED MECHANICS.

Discussion on this paper should be addressed to the Editorial Department, ASME, United Engineering Center, 345 East 47th Street, New York, N. Y. 10017, and will be accepted until two months after final publication of the paper itself in the JOURNAL OF APPLIED MECHANICS. Manuscript received by ASME Applied Mechanics Division, March, 1981; final revision, July. 1981.

Copyright © 1982 by ASME
Downloaded 01 May 2010 to 171.66.16.249. Redistribution subject to ASME license or copyright; see http://www.asme.org/terms/Terms_Use.cfm

$$\tau_{22} - i\tau_{12} = W'(z) + \overline{W'(z)} + z\overline{W''(z)} + \overline{w'(z)}. \quad (5)$$

In the previous equations and throughout this paper, prime denotes complex differentiation; Z', W', and w' are holomorphic functions; μ is the shear modulus and

$$\kappa = \begin{cases} 3-4\nu & \text{plane strain} \\ (3-\nu)/(1+\nu) & \text{plane stress} \end{cases} \quad (6)$$

where ν is Poisson's ratio. For an infinite body R_z loaded at infinity by

$$\tau_{\alpha i} = \sigma_{\alpha i} \text{ (constant)} \quad \text{as } |z| \to \infty, \quad (7)^1$$

the three complex functions have the representations

$$Z(z) = Z_1 z + Z_{-1} z^{-1} + \ldots, \quad (8)$$

$$W(z) = W_1 z + W_{-1} z^{-1} + \ldots, \quad (9)$$

$$w(z) = w_1 z + w_{-1} z^{-1} + \ldots, \quad (10)$$

as $|z| \to \infty$, and

$$Z_1 = \sigma_{31} - i\sigma_{32}, \quad (11)$$

$$W_1 = \frac{1}{4}(\sigma_{11} + \sigma_{22}), \quad w_1 = \frac{1}{2}(\sigma_{22} - \sigma_{11}) + i\sigma_{12}. \quad (12)$$

If the infinite body contains a single traction-free hole defined by a simple contour C, then

$$Z(z) - \overline{Z(z)} = 0, \quad (13)^2$$

$$W(z) + z\overline{W'(z)} + \overline{w(z)} = 0, \quad (14)^2$$

for z on C. The problems to be considered in this paper require the determination of the three complex functions satisfying (11)–(14).

If the contour C has a cusp of zero cusp angle at $z = z_c$ (Fig. 1), then it is convenient to introduce a set of local polar coordinates (r_c, θ_c) so that

$$z = z_c + r_c e^{i\theta_c}, \quad -\pi \le \theta_c \le \pi, \quad (15)$$

defines a small r_c – neighborhood of z_c. The stresses in the neighborhood are completely determined in terms of three stress-intensity factors K_i. In particular,

$$\tau_{11} + \tau_{22} = \frac{2}{\sqrt{2\pi r_c}}\left(K_1 \cos\frac{\theta_c}{2} - K_2 \sin\frac{\theta_c}{2}\right), \quad (16)^2$$

$$\tau_{31} - i\tau_{32} = -ie^{-i\alpha_c} e^{-i(\theta_c/2)} \frac{K_3}{\sqrt{2\pi r_c}}, \quad (17)^3$$

where α_c is the orientation of the cusp (Fig. 1). It follows from (16), (17), (2), and (4) that

$$K_1 - iK_2 = \lim_{z \to z_c} 2\sqrt{2\pi}(z - z_c)^{1/2} W'(z) e^{-i\alpha_c/2} \quad (18)$$

$$K_3 = \lim_{z \to z_c} \sqrt{2\pi}(z - z_c)^{1/2} Z'(z) i e^{i\alpha_c/2} \quad (19)$$

In the context of the linear elastic fracture mechanics, the strain energy induced by the presence of the hole is the so-called flaw energy U which may be conveniently determined by the Sih-Liebowitz formula [7]. It is

$$U = -\frac{\pi}{2}(\kappa + 1)\,\mathrm{Re}\,[W_1 w_{-1} + w_1 W_{-1}] + \pi\,\mathrm{Re}\,(Z_1 Z_{-1}) \quad (20)$$

where the constants are defined in (8) - (10).

We now introduce a new complex $\zeta (= \xi + i\eta)$-plane and assume that the region R_ζ^+ $\{|\zeta| > 1\}$ is mapped onto R_z by the function

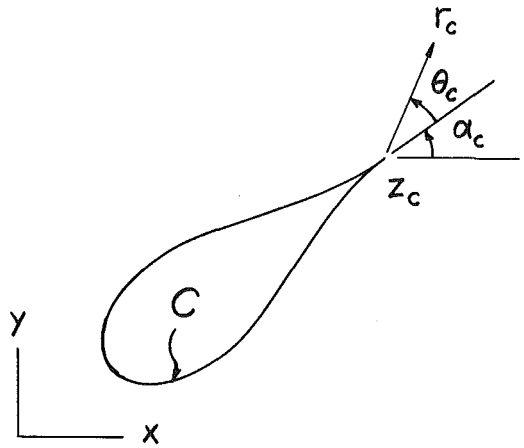


Fig. 1 A crack with a cusp of zero cusp angle

$$z = M(\zeta) = M_1 \zeta + \sum_{i=0}^{I} \sum_{j=1}^{J_i} \frac{M_{ij}}{(\zeta - \zeta_i)^j} \quad (21)^4$$

where M_1, M_{ij} are constants and I, J_i integers. The complex numbers ζ_i satisfy the conditions

$$\zeta_o = 0 \quad \text{and} \quad 0 < |\zeta_i| < 1 \quad \text{for} \quad i > 0. \quad (22)$$

For $|\zeta| > 1$, $M(\zeta)$ has the expansion

$$M(\zeta) = M_1 \zeta + M_{-1} \frac{1}{\zeta} + \ldots \quad (23)^5$$

where

$$M_{-1} = \sum_{i=0}^{I} M_{i1}. \quad (24)$$

Also, since C is assumed to have a cusp at $z_c = M(\zeta_c)$,

$$M(\zeta) = z_c + \frac{1}{2} M''(\zeta_c)(\zeta - \zeta_c)^2 + \ldots \quad (25)$$

as $\zeta \to \zeta_c$.

In the ζ-plane, we define

$$\Psi(\zeta) \equiv Z(M(\zeta)), \quad \Omega(\zeta) \equiv W(M(\zeta)), \quad \omega(\zeta) \equiv w(M(\zeta)). \quad (26)$$

It follows from (8)–(14) and (23) that

$$\Psi(\zeta) = M_1 Z_1 \zeta + \Psi_{-1} \frac{1}{\zeta} + \ldots, \quad (27)$$

$$\Omega(\zeta) = M_1 W_1 \zeta + \Omega_{-1} \frac{1}{\zeta} + \ldots, \quad (28)$$

$$\omega(\zeta) = M_1 w_1 \zeta + \omega_{-1} \frac{1}{\zeta} + \ldots, \quad (29)$$

as $|\zeta| \to \infty$, and

$$\Psi(\zeta) - \overline{\Psi(\zeta)} = 0, \quad (30)$$

$$\Omega(\zeta) + \frac{M(\zeta)}{\overline{M'(\zeta)}} \overline{\Omega'(\zeta)} + \overline{\omega(\zeta)} = 0, \quad (31)$$

for $|\zeta| = 1$. We must now determine holomorphic functions Ψ', Ω', and ω' such that the aforementioned conditions are satisfied. The solution for (27) and (30) is trivial. It is

$$\Psi(\zeta) = M_1 Z_1 \zeta + \overline{M_1 Z_1} \zeta^{-1} \quad (32)$$

where Z_1 and M_1 are given by (11) and (23).

Consider now the functions defined by (28), (29), and (31). We begin by introducing a new function defined by

[1] Greek and latin subscripts range over the integers (1, 2) and (1, 2, 3), respectively.

[2] These are the integrated forms of the traction-free conditions.

[3] These may be considered as the definitions of K_i.

[4] The composite mapping of successive transformations by rational functions is of this form.

[5] By shifting the origin, the constant term can always be made to vanish.

Downloaded 01 May 2010 to 171.66.16.249. Redistribution subject to ASME license or copyright; see http://www.asme.org/terms/Terms_Use.cfm

$$\Omega_H(\zeta) = \begin{cases} \Omega(\zeta) & \zeta \in R_\zeta^+ \\ -\dfrac{M(\zeta)}{\overline{M'\left(\dfrac{1}{\bar\zeta}\right)}}\,\overline{\Omega'\left(\dfrac{1}{\bar\zeta}\right)} - \overline{\omega\left(\dfrac{1}{\bar\zeta}\right)} & \zeta \in R_\zeta^- \end{cases} \tag{33}$$

where R_ζ^+ and R_ζ^- are, respectively, the regions $|\zeta| > 1$ and $|\zeta| < 1$. This is the so-called stress continuation [8], and it is clear that Ω_H' is holomorphic in both R_ζ^+ and R_ζ^-. For ζ in R_ζ^-, however, the function Ω_H must have poles at $\zeta = 0$ and $\zeta = \zeta_i$ which are dictated by the behavior of ω at infinity and the poles of $M(\zeta)$. The solution is therefore given by

$$\Omega_H(\zeta) = \mathrm{M}_1 W_1 \zeta - \overline{M_1 w_1}\,\zeta^{-1} + \sum_{i=0}^{I}\sum_{j=1}^{J_i} \Omega_{ij}(\zeta - \zeta_i)^{-j} \tag{34}$$

where Ω_{ij} are constants to be determined. The second of (33) implies that

$$\omega(\zeta) = -\overline{\Omega_H\left(\frac{1}{\bar\zeta}\right)} - \frac{\overline{M\left(\dfrac{1}{\bar\zeta}\right)}}{M'(\zeta)}\,\Omega_H'(\zeta) \quad (|\zeta| > 1). \tag{35}$$

The constants Ω_{ij} may then be determined by requiring that $\omega'(\zeta)$ is holomorphic in R_ζ^+. This may be accomplished by noticing that both $\overline{\Omega_H(1/\bar\zeta)}$ and $\overline{M(1/\bar\zeta)}$ have poles at $\zeta = 1/\bar\zeta_i$, and hence must be removed. The result is a system of complex algebraic equations governing the unknown constants Ω_{ij}.

The stress-intensity factors (18) and (19) may now be expressed in terms of the properties of (32) and (34). They are

$$K_1 - iK_2 = 2[\pi/M''(\zeta_c)]^{1/2}\,\Omega'(\zeta_c)\,e^{-i\alpha_c/2} \tag{36}$$

$$K_3 = ie^{i\alpha_c/2}[\pi/M''(\zeta_c)]^{1/2}(M_1 Z_1 - \overline{M_1 Z_1}\,\zeta_c^{-2}), \tag{37}$$

where

$$\Omega'(\zeta_c) = M_1 W_1 + \overline{M_1 w_1}\,\zeta_c^{-2} - \sum_{i=0}^{I}\sum_{j=1}^{J_i} j\Omega_{ij}(\zeta_c - \zeta_i)^{-(j+1)}. \tag{38}$$

Similarly, the flaw energy U defined by (20) now becomes

$$U = -\frac{\pi}{2}(\kappa+1)\,\mathrm{Re}\,M_1(\Omega_{-1} w_1 + \omega_{-1} W_1 - 2M_{-1} w_1 W_1) + \pi\,\mathrm{Re}\,(M_1 \bar M_1 Z_1 \bar Z_1 - M_1 M_{-1} Z_1^2). \tag{39}$$

3 Symmetric Variations of a Straight Crack

We begin by introducing another complex ζ^* $(= \xi^* + i\eta^*)$-plane. Let R^* be the region $|\zeta^* - \delta| > 1 - \delta$ $(0 \le \delta < 1)$, then the function

$$z = m^*(\zeta^*) = \frac{(1-\delta^2)a}{2}\left(\frac{\zeta^* - \delta}{1-\delta} + \frac{1-\delta}{\zeta^* - \delta} + \frac{\delta}{1-\delta}\right) \quad (\zeta^* \epsilon R^*) \tag{40}$$

maps R^* onto R_z^*, the infinite region exterior to the straight crack $m^*(-1+2\delta) < x_1 < m^*(+1)$ in the z-plane (Fig. 2). In (40), "a" is to be identified with a typical linear dimension of an actual crack configuration to be considered in the sequel. To construct the actual crack, we draw in the ζ^*-plane an ellipse defined by

$$\xi^{*2} + (\eta^*/\lambda)^2 = 1 \tag{41}$$

which is tangent to the circle $|\zeta^* - \delta| = 1 - \delta$ *at* $\zeta^* = 1$. The

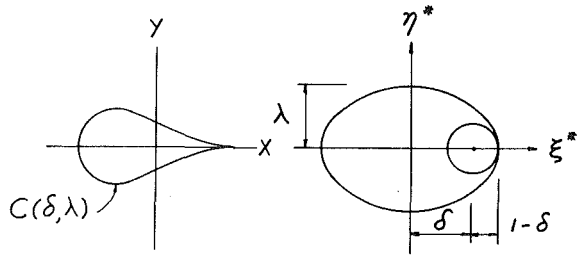


Fig. 2 Construction of the class of cracks $C(\delta,\lambda)$

infinite region exterior to the ellipse in the ζ^*-plane is denoted by R. The function $m^*(\zeta^*)$ maps R onto R_z, the infinite region exterior to a contour C which is just the image of the ellipse in the z-plane. Since C depends on δ and λ, we shall henceforth use $C(\delta,\lambda)$ to denote the class of two-parameter contours. Also, the range of λ will be specified in the development to follow. We note in passing that C has a cusp of zero cusp angle at $z = m^*(1)$ for $\delta > 0$, and two cusps at $z = m^*(\pm 1)$ for $\delta = 0$.

The region R is then remapped onto the region $R_\zeta\{|\zeta| > 1\}$ by the function

$$\zeta^* = m(\zeta) = \frac{1+\lambda}{2}\left(\zeta + \frac{1-\lambda}{1+\lambda}\,\frac{1}{\zeta}\right) \quad (\zeta \epsilon R_\zeta). \tag{42}$$

The function that maps R_ζ onto R_z is just

$$z = M(\zeta) \equiv m^*(m(\zeta)). \tag{43}$$

It has the explicit representations

$$M(\zeta) = \frac{(1-\delta^2)a}{2}\left\{\frac{1}{1-\delta}\left[\frac{1+\lambda}{2}\zeta + \frac{1-\lambda}{2}\,\frac{1}{\zeta}\right] + \frac{2(1-\delta)}{(1+\lambda)(\zeta_1 - \zeta_2)}\left[\frac{\zeta_1}{\zeta - \zeta_1} - \frac{\zeta_2}{\zeta - \zeta_2}\right]\right\} \tag{44}$$

where

$$\left.\begin{matrix}\zeta_1 \\ \zeta_2\end{matrix}\right\} = \frac{1}{1+\lambda}\left[\delta \pm (\lambda^2 + \delta^2 - 1)^{\frac{1}{2}}\right] \quad (\lambda^2 + \delta^2 - 1 \neq 0); \tag{45}$$

and

$$M(\zeta) = \frac{(1-\delta^2)a}{2}\left\{\frac{1}{1-\delta}\left[\frac{1+\lambda}{2}\zeta + \frac{1-\lambda}{2}\,\frac{1}{\zeta}\right] + \frac{2(1-\delta)}{1+\lambda}\left[\frac{1}{\zeta - \zeta_1} + \frac{\zeta_1}{(\zeta - \zeta_1)^2}\right]\right\} \tag{46}$$

where

$$\zeta_1 = \frac{\delta}{1+\lambda} \quad \text{and} \quad \lambda^2 + \delta^2 - 1 = 0. \tag{47}$$

The expressions (45) and (47) are, respectively, the distinct roots and double root of the same equation

$$m(\zeta) - \delta = \frac{1+\lambda}{2\zeta}\left[\zeta^2 - \frac{2\delta}{1+\lambda}\zeta + \frac{1-\lambda}{1+\lambda}\right] = 0. \tag{48}$$

To insure that contours defined by $C(\delta,\lambda)$ are simple, the radius of curvature of the ellipse (41) at $\zeta^* = 1$ must be greater than $1 - \delta$. It follows that

$$\lambda^2 \ge 1 - \delta \tag{49}$$

which indicates that both (44) and (46) are needed to describe the class of admissible contours.

The meaning of "a" may be conceived from

$$M(+1) - M(-1) = m^*(+1) - m^*(-1) = 2a. \tag{50}$$

It follows that $2a$ is just the "crack length" although it no longer carries the meaning in the ordinary sense. It is also convenient to introduce an aspect ratio r defined by

Downloaded 01 May 2010 to 171.66.16.249. Redistribution subject to ASME license or copyright; see http://www.asme.org/terms/Terms_Use.cfm

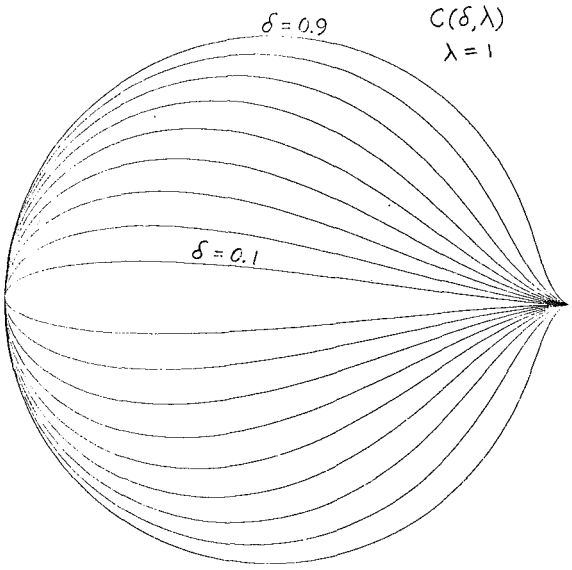


Fig. 3 Symmetric airfoil cracks C(δ,1)

$$r(\delta,\lambda) = \frac{1}{a} \operatorname*{Max}_{|\zeta|=1} \operatorname{Im} M(\zeta) \tag{51}$$

which does not have a simple explicit expression, but can be computed straightforwardly.

For $\lambda = 1$, the ellipse defined by (41) is a circle, and $M(\zeta)$ reduces to the well-known (symmetric) airfoil transformation

$$M(\zeta) = \frac{a}{2}(1-\delta^2)\left[\frac{\zeta-\delta}{1-\delta} + \frac{1-\delta}{\zeta-\delta} + \frac{\delta}{1-\delta}\right] \quad (\text{for } \lambda = 1). \tag{52}$$

A family of the airfoil-shaped configurations $C(\delta, 1)$ is given in Fig. 3.

A few remarks regarding the class of two-parameter contours are in order. The cusp angle is always zero and hence the elasticity solution is square-root singular at the cusp tip. For $\lambda = \lambda_0$ fixed, the variation of the class of contours $C(\delta,\lambda_0)$ as a function of δ is qualitatively the same as $C(\delta, 1)$, with $C(1, \lambda_0)$ being the ellipse of axes a and $\lambda_0 a$. The class of contours $C(\delta, \sqrt{0.9})$ is given in Fig. 4. For $\delta = 0$ and $\lambda > 1$, $C(0, \lambda)$ becomes doubly symmetric and has two tips. This class is shown in Fig. 5.

We proceed to determine the coefficients needed in the solution (34). We shall, however, only consider the case defined by (44) and (45). The function $M(\zeta)$ has simple poles at $\zeta = \zeta_0 = 0$, $\zeta = \zeta_1$, and $\zeta = \zeta_2$. It follows from (34) that

$$\Omega_H(\zeta) = M_1 W_1 \zeta + (\Omega_{01} - \overline{M_1 w_1})\frac{1}{\zeta} + \frac{\Omega_{11}}{\zeta-\zeta_1} + \frac{\Omega_{21}}{\zeta-\zeta_2}. \tag{53}$$

The function $\omega(\zeta)$ may now be obtained by substituting (44) and (53) into (35). The behavior (29) immediately leads to the conclusion that

$$\Omega_{01} = \frac{\lambda-1}{\lambda+1}\overline{M_1 W_1}. \tag{54}$$

The additional conditions needed to remove the apparent poles at $1/\bar{\zeta}_1$ and $1/\bar{\zeta}_2$ are

$$\frac{\bar{\zeta}_1 - \bar{\zeta}_2}{\bar{\zeta}_1^3} F\left(\frac{1}{\bar{\zeta}_1}\right)\bar{\Omega}_{11} - \frac{\Omega_{11}}{(1-\zeta_1\bar{\zeta}_1)^2} - \frac{\Omega_{21}}{(1-\zeta_2\bar{\zeta}_1)^2} = \Omega_{01} - \overline{M_1 w_1} - \frac{M_1 W_1}{\bar{\zeta}_1^2}, \tag{55}$$

$$\frac{\bar{\zeta}_2 - \bar{\zeta}_1}{\bar{\zeta}_2^3} F\left(\frac{1}{\bar{\zeta}_2}\right)\bar{\Omega}_{21} - \frac{\Omega_{11}}{(1-\zeta_1\bar{\zeta}_2)^2} - \frac{\Omega_{21}}{(1-\zeta_2\bar{\zeta}_2)^2} = \Omega_{01} - \overline{M_1 w_1} - \frac{M_1 W_1}{\bar{\zeta}_2^2}, \tag{56}$$

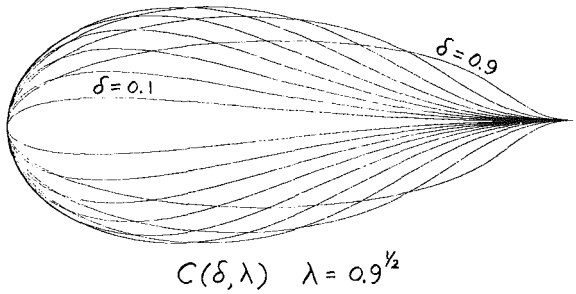


Fig. 4 Symmetric one-tip cracks $C(\delta,\sqrt{0.9})$

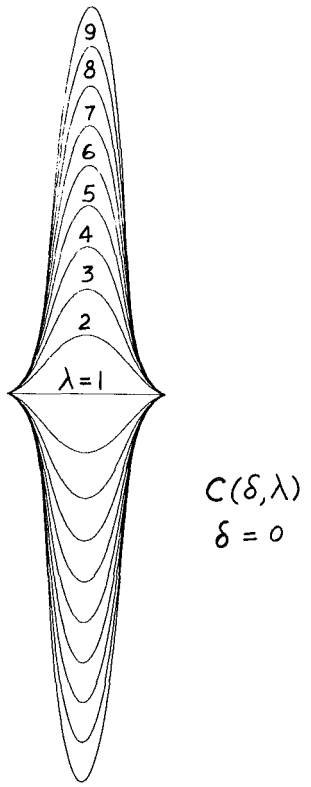


Fig. 5 Doubly symmetric two-tip cracks $C(0,\lambda)$

where

$$F(\zeta) = \frac{1+\lambda}{2(1-\delta)}\frac{2}{(1-\delta^2)a}\frac{dM}{d\zeta} = \left[\frac{1+\lambda}{2(1-\delta)}\right]^2\left(1 - \frac{1-\lambda}{1-\lambda}\frac{1}{\zeta^2}\right)\left\{1 - \left[\frac{1-\delta}{m(\zeta)-\delta}\right]^2\right\}. \tag{57}$$

To facilitate the solution of (55) and (56), it is easier to consider the symmetric and antisymmetric solutions separately.

To this end, we consider Ω_{11} and Ω_{21} as functions of $(\sigma_{11}, \sigma_{22}, \sigma_{12})$ (see (12)). Symmetry considerations, together with the observations that M_1 is real, lead to

$$\left.\begin{array}{l}\Omega_{11}(\sigma_{11},\sigma_{22},0),\quad \Omega_{21}(\sigma_{11},\sigma_{22},0) \text{ real} \\ \Omega_{11}(0,0,\sigma_{12}),\quad \Omega_{21}(0,0,\sigma_{12}) \text{ imaginary}\end{array}\right\} \text{for } \zeta^2+\delta^2-1>0, \tag{58}$$

$$\left.\begin{array}{l}\Omega_{11}(\sigma_{11},\sigma_{22},0) = \bar{\Omega}_{21}(\sigma_{11},\sigma_{22},0) \\ \Omega_{11}(0,0,\sigma_{12}) = -\bar{\Omega}_{21}(0,0,\sigma_{12})\end{array}\right\} \text{for } \zeta^2+\delta^2-1<0. \tag{59}$$

Conditions (58) and (59) are associated with real and distinct, and complex conjugate roots of (55), respectively. The four coupled equations implied by (55) and (56) can now be solved two at a time. We have

Downloaded 01 May 2010 to 171.66.16.249. Redistribution subject to ASME license or copyright; see http://www.asme.org/terms/Terms_Use.cfm

$$\frac{\Omega_{11}}{M_1}=\left[\frac{1+3\lambda}{4(1+\lambda)}\sigma_{11}-\frac{3+\lambda}{4(1+\lambda)}\sigma_{22}\right]\frac{a_{22}-a_{12}}{|a_{\alpha\beta}|}$$

$$-\frac{1}{4}(\sigma_{11}+\sigma_{22})\frac{a_{22}\zeta_2^2-a_{12}\zeta_1^2}{\zeta_1^2\zeta_2^2\,|a_{\alpha\beta}|}-i\sigma_{12}\frac{b_{22}-b_{12}}{|b_{\alpha\beta}|}, \tag{60}$$

$$\frac{\Omega_{21}}{M_1}=\left[\frac{1+3\lambda}{4(1+\lambda)}\sigma_{11}-\frac{3+\lambda}{4(1+\lambda)}\sigma_{22}\right]\frac{a_{11}-a_{21}}{|a_{\alpha\beta}|}$$

$$-\frac{1}{4}(\sigma_{11}+\sigma_{22})\frac{a_{11}\zeta_1^2-a_{21}\zeta_2^2}{\zeta_1^2\zeta_2^2\,|a_{\alpha\beta}|}-i\sigma_{12}\frac{b_{11}-b_{21}}{|b_{\alpha\beta}|}, \tag{61}$$

where

$$\left.\begin{matrix}a_{11}\\ b_{11}\end{matrix}\right\}=\frac{\zeta_1-\zeta_2}{\zeta_1^3}F\left(\frac{1}{\zeta_1}\right)\mp\frac{1}{(1-\zeta_1^2)^2}, \tag{62}$$

$$\left.\begin{matrix}a_{22}\\ b_{22}\end{matrix}\right\}=\frac{\zeta_2-\zeta_1}{\zeta_2^3}F\left(\frac{1}{\zeta_2}\right)\mp\frac{1}{(1-\zeta_2^2)^2}, \tag{63}$$

$$-a_{12}=-a_{21}=b_{12}=b_{21}=\frac{1}{(1-\zeta_1\zeta_2)^2}. \tag{64}$$

These results are written in such a way that they are valid for both (58) and (59). The solution for the very special case defined by (46) and (47) can also be obtained in a straightforward manner, but will not be given here.

4 Results

4(*a*) Symmetric Airfoil Cracks. This class of crack configurations is defined by $C(\delta, 1)$, Fig. 3, and the solution may be deduced from the results of Section 3. Setting $\lambda=1$ in (45), we find that $\zeta_1=\delta$ and $\zeta_2=0$. The solution $\Omega_H(\zeta)$ defined by (53) is just

$$\Omega_H(\zeta)=M_1W_1\zeta-\overline{M_1w_1}\frac{1}{\zeta}+\frac{\Omega_{11}}{\zeta-\delta} \tag{65}$$

where

$$\frac{\Omega_{11}}{M_1}=\frac{(1-\delta^2)^2}{1+2\delta-\delta^2}\left\{\frac{\delta^2}{2}(\sigma_{11}-\sigma_{22})\right.$$

$$\left.-\frac{1}{4}(\sigma_{11}+\sigma_{22})\right\}-i\delta^2(1-\delta)^2\sigma_{12}. \tag{66}$$

Equations (36)–(40), together with

$$\omega_{-1}=\frac{1-2\delta-\delta^2}{\delta^2}M_1W_1+\frac{\bar{\Omega}_{11}}{\delta^2} \tag{67}$$

obtained from (35), yield

$$\left.\begin{matrix}K_1\\ K_2\\ K_3\end{matrix}\right\}=[\pi a(1-\delta^2)]^{1/2}$$

$$\begin{cases}\left[\dfrac{2+4\delta+2\delta^3+\delta^4}{2(1+2\delta-\delta^2)}\sigma_{22}-\dfrac{\delta^3(2+\delta)}{2(1+2\delta-\delta^2)}\sigma_{11}\right]\\ (1-\delta^2)\sigma_{12}\\ \sigma_{32}\end{cases} \tag{68}$$

$$U=\frac{\pi a^2}{2}(\kappa+1)\frac{(1+\delta)^2}{4}\left\{\frac{\delta^2(1-\delta^2)^2+\delta(2+5\delta-4\delta^2)}{4(1+2\delta-\delta^2)}\sigma_{11}^2\right.$$

$$+\frac{\delta^2(1-\delta^2)^2+(4+2\delta-7\delta^2+4\delta^3)}{4(1+2\delta-\delta^2)}\sigma_{22}^2$$

$$\left.-\frac{\delta(2-\delta)+\delta^2(1-\delta^2)^2}{2(1+2\delta-\delta^2)}\sigma_{11}\sigma_{22}+[1-\delta^2(1-\delta)^2]\sigma_{12}^2\right\}$$

$$\left.+\frac{\pi a^2}{4}(1+\delta)^2[(2-2\delta+\delta^2)\sigma_{32}^2+\delta(2-\delta)\sigma_{31}^2]\right]. \tag{69}$$

It can be easily checked that these expressions reduce to those for a crack of length $2a$ when δ is set to zero. For $\delta=1$, the contour $C(1, 1)$ becomes a circle of radius a, and the stress-intensity factors given by (68) are zero, while U deduces to the flaw energy for a circular hole.

For $1-\delta << 1$, the contour $C(\delta, 1)$ may be interpreted as a circular hole with a short radial crack. This may be seen from the fact that the exact mapping function

$$M(\zeta)=\frac{(1-\delta^2)a}{2}\left[\frac{1-\delta}{\zeta-\delta}+\frac{\zeta}{1-\delta}\right] \tag{70}$$

may be approximated by

$$M_0(\zeta)=\frac{(1-\delta)a}{2}\zeta, \tag{71}$$

the image of which in the z-plane is just the circle

$$|z|=R\equiv\frac{(1+\delta)a}{2}. \tag{72}$$

It is clear that $M(-1)-M_0(-1)$ is of the order of $(1-\delta)^2$, and the difference

$$A\equiv M(1)-M_0(1)=(1-\delta)a$$

may be interpreted as the length of the radial crack. As $A/R \to 0$, i.e., $\delta \to 1$, the stress-intensity factors become

$$K_1=(\pi A)^{1/2}\frac{3}{4}\sqrt{2}(3\sigma_{22}-\sigma_{11})$$

$$=(\pi A)^{1/2}\begin{cases}2.121\,\sigma & \sigma_{22}=\sigma_{11}=\sigma\\ 1.061\,(-\sigma) & \text{for}\quad \sigma_{22}=0,\ \sigma_{11}=\sigma\\ 3.182\,\sigma & \sigma_{22}=\sigma,\ \sigma_{11}=0\end{cases} \tag{73}$$

$$K_2=(\pi A)^{1/2}2\sqrt{2}(1-\delta)\sigma_{12}, \tag{74}$$

$$K_3=(\pi A)^{1/2}\sqrt{2}\,\sigma_{32}. \tag{75}$$

The factors appearing in (73) are roughly 5 percent lower than those associated with a very short radial crack originating from the boundary of a true circular hole [9]. For K_3, however, the counterpart of the factor $\sqrt{2}$ is 2 [10], and we have no explanation for such a substantial difference.

Finally, for δ small the contour $C(\delta, 1)$ may be represented by

$$\left(\frac{x_2}{a}\right)=\delta\left(1-\frac{x_1}{a}\right)^{3/2}\left(1+\frac{x_1}{a}\right)^{1/2}\qquad\left|\frac{x_1}{a}\right|\le 1, \tag{76}$$

and

$$\left.\begin{matrix}K_1\\ K_2\\ K_3\end{matrix}\right\}=\sqrt{\pi a}\begin{cases}\left(1+\dfrac{1}{2}\delta^2-\delta^3\right)\sigma_{22}-\delta^3\sigma_{11}\\ \left(1-\dfrac{3}{2}\delta^2\right)\sigma_{12}\\ \left(1-\dfrac{1}{2}\delta^2\right)\sigma_{32}\end{cases} \tag{77}$$

4(*b*) Doubly Symmetric Cracks. This class of cracks is defined by $C(0, \lambda)$, Fig. 5. Setting $\delta=0$ in (45), we find

$$\zeta_1=-\zeta_2=k=\left(\frac{\lambda-1}{\lambda+1}\right)^{1/2}\qquad(\lambda\ge 1). \tag{78}$$

The solution $\Omega_H(\zeta)$ defined by (53) is just

$$\Omega_H(\zeta)=M_1W_1\zeta+(k^2M_1W_1$$

$$-M_1\bar{w}_1)\frac{1}{\zeta}+\frac{\Omega_{11}}{\zeta-k}+\frac{\Omega_{21}}{\zeta+k}, \tag{79}$$

Downloaded 01 May 2010 to 171.66.16.249. Redistribution subject to ASME license or copyright; see http://www.asme.org/terms/Terms_Use.cfm

where

$$\frac{\Omega_{11}}{M_1} = \frac{\Omega_{21}}{M_1} = \frac{(1-k^4)^2(k^4+2k^2-1)}{8(1+k^4)^2}\sigma_{11} + \frac{(1-k^4)^2(k^4-2k^2-1)}{8(1+k^4)^2}\sigma_{22} - i\frac{k^2(1-k^2)^2}{2(1+k^4)}\sigma_{12} \tag{80}$$

Substituting the foregoing relations into (35), we get

$$-\frac{\omega_{-1}}{M_1} = W_1 - \frac{2\bar{\Omega}_{11}}{k^2 M_1} + \left\{1 - \frac{(1-k^2)^2}{k^2} + k^2[k^2-(1-k^2)^2]\right\} W_1 + k^2\left(k^2 W_1 - \bar{w}_1 + \frac{2\Omega_{11}}{M_1}\right). \tag{81}$$

Equations (36)–(40) now yield

$$K_1 = \frac{\sqrt{\pi a}}{1+k^2}\left\{\left[4 + \frac{2k^2(1+k^2)(2+k^2-k^6)}{(1+k^4)^2}\right]\frac{\sigma_{22}}{4} - \left[\frac{2k^4(1+k^2)(3+2k^2+k^4)}{(1+k^4)^2}\right]\frac{\sigma_{11}}{4}\right\}, \tag{82}$$

$$K_2 = \frac{\sqrt{\pi a}}{1+k^2}\frac{1-k^2}{(1+k^2)(1+k^4)}\sigma_{12}, \tag{83}$$

$$K_3 = \frac{\sqrt{\pi a}}{1+k^2}\sigma_{32}, \tag{84}$$

$$U = \frac{\pi a^2}{2}(\kappa+1)\frac{1}{4(1-k^2)^2}\left\{\frac{k^2(1+k^2)(1+2k^2+k^8)}{2(1+k^4)^2}\sigma_{11}^2 + \frac{1}{2}(1-k^2)^2\left[1+\frac{1+2k-k^2}{(1+k^4)^2}\right]\sigma_{22}^2 - \frac{k^2[(2-k^2)+(1-k^4)^2-k^6(2-2k^2+k^4)]}{2(1+k^4)^2}\sigma_{11}\sigma_{22} + \left[1-\frac{k^2(1-k^2)^2}{1+k^4}\right]\sigma_{12}^2\right\} + \frac{\pi a^2}{4(1-k^2)^2}\left\{(2-3k^2+k^4)\sigma_{32}^2 + k^2(3-k^2)\sigma_{31}^2\right\}. \tag{85}$$

These relations reduce to the corresponding expressions for a crack of length $2a$ when k is set to zero, i.e., $\lambda = 1$.

For $\lambda >> 1$ and for points far away from the cusps, $|\zeta^*| >> 1$ and hence the second term in the mapping function

$$z = \frac{a}{2}\left(\zeta^* + \frac{1}{\zeta^*}\right) + \frac{a}{2}\left(m(\zeta) + \frac{1}{m(\zeta)}\right) \tag{86}$$

may be dropped. The image of the unit circle $|\zeta| = 1$ obtained by such an approximation is the ellipse

$$\left(\frac{x_1}{\frac{a}{2}}\right)^2 + \left(\frac{x_2}{\lambda a}\right)^2 = 1 \tag{87}$$

in the z-plane. Thus, as $\lambda \to \infty$, the cusp may be interpreted as an edge crack of crack length $A = 1/2\ a$. The stress-intensity factors may be deduced from (82)–(84) by setting $k = 1$. The results are

$$K_1 = (\pi A)^{1/2}\frac{3}{4}\sqrt{2}\sigma_{22} = (\pi A)^{1/2}1.06(\sigma_{22}-\sigma_{11}), \tag{88}$$

$$K_3 = (\pi A)^{1/2}\frac{1}{\sqrt{2}}\sigma_{32}. \tag{89}$$

The constant factors appearing in (88) and (89) are to be compared with 1.122 [11] and 1 for a true edge crack. Once again we see the rather large difference appearing in K_3. It is noted, however, that the factors appearing in (73) and (75) may be deduced from those appearing in (88) and (89) by using the appropriate stress-concentration factors pertinent to a circular hole (2, 3 and 2 for $\sigma_{11} = \sigma_{22} = \sigma$, $\sigma_{22} = \sigma$, and $\sigma_{11} = 0$ and σ_{32}, respectively).

For $\lambda - 1 << 1$, the crack configuration may be approximated by

$$\frac{x_2}{a} = (\lambda-1)\left[1-\left(\frac{x_1}{a}\right)^2\right]^{3/2}, \tag{90}$$

and the stress-intensity factors become

$$K_1 = (\pi a)^{1/2}\left\{\left[1+\frac{3}{8}(\lambda-1)^2\right]\sigma_{22} - \frac{3}{8}(\lambda-1)^2\sigma_{11}\right\}$$

$$K_2 = (\pi a)^{1/2}\left[1-\frac{3}{2}(\lambda-1)+\frac{7}{4}(\lambda-1)^2\right]\sigma_{12}, \tag{92}$$

$$K_3 = (\pi a)^{1/2}\left[1-\frac{1}{2}(\lambda-1)+\frac{1}{2}(\lambda-1)^2\right]\sigma_{32}. \tag{93}$$

5 Remarks

Two classes of cracks depicted by the configurations shown in Figs. 3–5 are solved. The effect of a crack-parallel load is explicitly reflected in all the formulas. This effect will play an important role in studying the branching of a crack under uniaxial load, especially when the load is almost parallel to the crack. Also, the explicit "thin crack" representations, (76) and (90), provide us with two perfect models for studying the strength of a crack under compression. These problems are now under our investigation.

6 Additional Remarks

The physical interpretations of the limiting cases pertaining to (73)–(75) and (88)–(89) are a short radial crack at the boundary of a circular hole and an edge crack, respectively. These interpretations are substantiated by the numerical coefficients associated with K_1 and K_2, but not K_3 which is out by a factor of $\sqrt{2}$. This latter discrepancy led one of the reviewers to suggest that perhaps a different definition for K_3 was used in the cited references. This was in fact our suspicion at the beginning. However, we have been unable to detect any inconsistency in this regard and the discrepancy remains a puzzling point.

We are indebted to another reviewer for bringing to our attention some closely related results reported in [12]–[15]. These authors are in complete agreement with us in stressing the relevance of the roles of cusps in fracture mechanics. However, they seem to place more attention to the construction of complicated cuspidal contours [13, 15]. This is in contrast to our stated objective of generating more *exact* solutions which, by necessity, can only be obtained for relatively simple cuspidal contours. The underlying elasticity theory and complex method approach are of course the same.

References

1 Bowie, O. L., "Solutions of Plane Crack Problems by Mapping Technique," *Mechanics of Fracture 1* (Methods of Analysis and Solutions of Crack Problems), ed., Sih, G. C., Noordhoff International, 1973.

2 Batdorf, S. B., and Heinisch, H. L., Jr., "Weakest Link Theory Reformulated for Arbutrary Fracture Criterion," *Journal of the American Ceramic Society,* Vol. 61, No. 7, 1978, pp. 335–358.

3 Adams, M., and Sines, G., "A Statistical, Micromechanical Theory of the Compressive Strength of Brittle Materials," *Journal of the American Ceramic Society,* Vol. 61, No. 3-4, 1978, pp. 126–131.

4 Hunt, R. A., and McCartney, L. N., "A New Approach to Weibull's Statistical Theory of Brittle Fracture," *International Journal of Fracture,* Vol. 15, No. 4, 1979, pp. 365–375.

5 McClintock, F., and Walsh, J. B., "Friction on Griffith Cracks in Rocks Under Pressure," *Proceedings, 4th U.S. Congress of Applied Mechanics,* Berkeley, 1962, pp. 1015–1021.

Downloaded 01 May 2010 to 171.66.16.249. Redistribution subject to ASME license or copyright; see http://www.asme.org/terms/Terms_Use.cfm

6 Wu, C. H., "Maximum-Energy-Release-Rate Criterion Applied to a Tension-Compression Specimen With Crack," *Journal of Elasticity,* Vol. 8, No. 3, 1978, pp. 235–257.

7 Sih, G. C., and Liebowiz, H., "On the Griffith Energy Criterion for Brittle Fracture," *International Journal of Solids and Structures,* Vol. 3, 1967, pp. 1–22.

8 England, A. H., *Complex Variable Methods in Elasticity,* Wiley, Interscience, 1971.

9 Bowie, O. L., "Analysis of an Infinite Plate Containing Radial Cracks Originating at the Boundary of an Internal Circular Hole," *Journal of Mathematics and Physics,* Vol. 35, 1956, pp. 66–71.

10 Sih, G. C., "Stress Distribution Near Internal Crack Tips for Longitudinal Shear Problems," ASME JOURNAL OF APPLIED MECHANICS, Vol. 87, 1965, pp. 51–58.

11 Koiter, W. T., "Rectangular Tensile Sheet With Symmetric Edge Cracks," ASME JOURNAL OF APPLIED MECHANICS, Vol. 32, 1965, p. 237.

12 Panasyuk, V. V., and Berezhnitskii, L. T., "Limit Equilibrium of Plates With Sharp Stress Raisers," *Soviet Material Science,* Vol. 1, No. 4, 1965, pp. 293–301.

13 Berezhnitskii, L. T., and Sadivskii, V. M., "Stress Distribution Near Elastic Inclusions With Cuspidal Points on the Outline," *Soviet Material Science,* Vol. 12, No. 3, 1976, pp. 261–265.

14 Berezhnitskii, L. T., and Sadivskii, V. M., "Theory of Sharp-Pointed Stress Concentrations in Anisotropic Plates," *Soviet Material Science,* Vol. 13, No. 3, 1977, pp. 303–311.

15 Berezhnitskii, L. T., "Theory of Cuspidal Defects With Different Types of Angular Cuspidal Points," *Soviet Material Science,* Vol. 13, 4, 1977, pp. 414–420.

Downloaded 01 May 2010 to 171.66.16.249. Redistribution subject to ASME license or copyright; see http://www.asme.org/terms/Terms_Use.cfm

The Linear Magnetoelastic Problem of Two Coplanar Griffith Cracks in a Soft Ferromagnetic Elastic Strip

Y. Shindo
Associate Professor,
Department of Mechanical Engineering II,
Faculty of Engineering,
Tohoku University,
Sendai 980, Japan

Following a linear theory for soft ferromagnetic elastic solids, we consider the problem of determining the stress-intensity factors in an infinite strip of a soft ferromagnetic elastic material containing two coplanar Griffith cracks. We assume that the solid is a homogeneous and isotropic one and it is permeated by a uniform magnetostatic field normal to the cracks surfaces and that the cracks are opened by a constant internal pressure. By the use of Fourier transforms we reduce the problem to that of solving two simultaneous triple integral equations. These equations are reduced to a singular integral equation of the first kind. By expanding the solution into the form of the product of the series of Chebyshev polynomials of the first kind and their weight function, the singular integral equation is further reduced to the infinite system of algebraic equations for the determination of the unknown coefficients. Numerical calculations are carried out and the influence of the magnetic fields on the stress-intensity factors is graphically shown in detail.

Introduction

In recent years, interest in the theory of cracks has grown considerably due to innumerable applications in the field of fracture mechanics. The theory of cracks in a two-dimensional elastic medium was first developed by Griffith [1]. Many papers on the subject are reviewed by the recent book of Sih [2]. The problem of a Griffith crack in an infinitely long elastic strip has been considered by Lowengrub [3]. When the strip contains two coplanar Griffith cracks, the problem is reduced to that of solving a set of triple integral equations. Cook [4] has considered such equations and has reduced to a set of three Fredholm integral equations. Lowengrub and Srivastava [5] have reduced the triple integral equations to a single Fredholm integral equation, which can be solved by a well-known iterative procedure, by using finite Hilbert transform techniques. However, an iterative solution is a valid one when half the width of the strip is much greater than the distance of the far end of the cracks from the origin, so the solution for any thickness of the strip was not verified.

Many technical devices such as motors, generators, MHD devices, and fussion reactors employ elastic structures in magnetic fields. The theory of magnetoelasticity concerns the interacting effects of externally applied magnetic field on the elastic deformation of a solid body. The basic equations of such magnetoelastic deformation theory have been derived by Dunkin and Eringen [6], Pao and Yeh [7], and Hutter and Pao [8]. Pao and Yeh [7] have developed a linear theory for soft ferromagnetic elastic solids and have applied the theory to the magnetoelastic buckling problem of an infinitely extended plate in a transversely applied uniform magnetic field. The author [9–11] used Pao-Yeh's theory [7] to solve the problems of a finite crack, a penny-shaped crack, and two coplanar cracks in an infinite medium.

This paper applies Pao-Yeh's theory [7] to the problem of determining the distribution of stress in an infinitely long strip of a soft ferromagnetic elastic material containing two coplanar Griffith cracks. The problem is considered for a uniform magnetostatic field normal to the edges of the strip. Using Fourier transform techniques, the problem is reduced to that of solving two simultaneous triple integral equations. By the suitable definition of the integral transforms, the triple integral equations are further reduced to a singular integral equation of the first kind. The solution of the singular integral equation is given in the form of the product of the series of Chebyshev polynomials of the first kind and their weight functions and is obtained by solving a system of linear algebraic equations for the determination of unknown coefficients. Making the distance of the near ends of the cracks tend to zero, we solve the linear magnetoelastic problem for a Griffith crack in a strip. Numerical calculations are carried out and the variations of stress-intensity factors with the ratio of half the distance of the near ends of the cracks to the far one for half the strip width and the normalized magnetic induction are shown graphically. The method of solution is such that the numerical results can be obtained at any desired half the strip width.

Contributed by the Applied Mechanics Division for publication in the JOURNAL OF APPLIED MECHANICS.

Discussion on this paper should be addressed to the Editorial Department, ASME, United Engineering Center, 345 East 47th Street, New York, N.Y. 10017, and will be accepted until two months after final publication of the paper itself in the JOURNAL OF APPLIED MECHANICS. Manuscript received by ASME Applied Mechanics Division, December, 1980; final revision, August, 1981.

Copyright © 1982 by ASME
Downloaded 01 May 2010 to 171.66.16.249. Redistribution subject to ASME license or copyright; see http://www.asme.org/terms/Terms_Use.cfm

Basic Equations of the Theory of Magnetoelasticity

Consider a soft ferromagnetic isotropic linear elastic solid. If we consider plane strain perpendicular to the z-axis in a rectangular cartesian coordinate system (x, y, z) and assume that the applied magnetic induction $\mathbf{B}_0$ is of the form $\mathbf{B}_0 = (0, B_0, 0)$ where B_0 is constant, we get the linearized field equations in the perturbation state as

$$\nabla^2 u_x + \frac{1}{1-2\nu}(u_{x,x}+u_{y,y})_{,x} + \frac{2\chi B_0}{\mu\mu_r} h_{x,y} = 0$$

$$\nabla^2 u_y + \frac{1}{1-2\nu}(u_{x,x}+u_{y,y})_{,y} + \frac{2\chi B_0}{\mu\mu_r} h_{y,y} = 0$$

$$\nabla^2 = \partial^2/\partial x^2 + \partial^2/\partial y^2 \tag{1}$$

$$\begin{aligned} h_x &= \phi_{,x} \\ h_y &= \phi_{,y} \\ \nabla^2\phi &= 0 \end{aligned} \tag{2}$$

where $[u_x(x,y), u_y(x,y), 0]$ are the displacement components, $[h_x(x,y), h_y(x,y), 0]$ are the magnetic intensity components, ϕ is the magnetic potential, the Lame constants λ and μ are replaced by ν and μ with $\lambda = 2\mu\nu/(1-2\nu)$, ν is the Poisson's ratio, μ_r is the specific magnetic permeability, χ is the magnetic susceptibility, and a comma denotes partial differentiation with respect to the coordinates. The last terms on the left-hand side of equation (1) are due to the effect of magnetic field which is represented by using a dipole model for magnetization.

The nontrivial components of the stresses and the magnetic quantities are

$$\begin{aligned} t_{xx} &= 2\mu\left[\frac{\nu}{1-2\nu}(u_{x,x}+u_{y,y}) + u_{x,x}\right] \\ t_{xy} &= t_{yx} = \mu(u_{x,y}+u_{y,x}) + (\chi B_0/\mu_r) h_x \\ t_{yy} &= 2\mu\left[\frac{\nu}{1-2\nu}(u_{x,x}+u_{y,y}) + u_{y,y}\right] \\ &\quad + 2\chi B_0/\mu_r) h_y + \chi B_0^2/\mu_0\mu_r^2 \end{aligned} \tag{3}$$

$$\begin{aligned} t_{xx}^M &= -(B_0/\mu_r) h_y - \frac{B_0^2}{\mu_0\mu_r^2} \\ t_{xy}^M &= t_{yx}^M = \mu_0 B_0 h_x \\ t_{yy}^M &= \frac{1+2\chi}{\mu_r} B_0 h_y + \frac{(1+2\chi)B_0^2}{2\mu_0\mu_r^2} \end{aligned} \tag{4}$$

$$\begin{aligned} b_x &= \mu_0\mu_r h_x \\ b_y &= \mu_0\mu_r h_y \end{aligned} \tag{5}$$

where $\mu_0 = 4\pi\times 10^{-7}$ Newton/A^2 (H/m) is the magnetic permeability of the vacuum, t_{xx}, $t_{xy} = t_{yx}$ and t_{yy} are the magnetoelastic stresses, t_{xx}^M, $t_{xy}^M = t_{yx}^M$, t_{yy}^M are the Maxwell stresses and $[b_x, b_y, 0]$ are the magnetic induction components in the perturbation state.

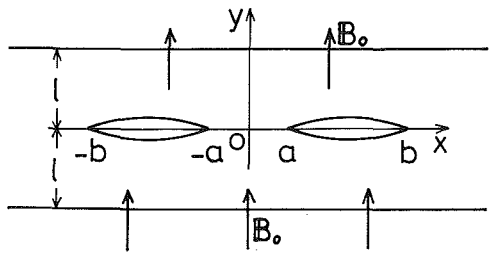


Fig. 1 Two coplanar Griffith cracks in a soft ferromagnetic elastic strip

Statement and Solution of the Magnetoelastic Problem

We consider an infinite strip $-\infty < x < \infty$, $-l \le y \le l$ with two coplanar cracks located on the line $y=0$, $a \le |x| \le b$ as shown in Fig. 1. A uniform magnetic field $\mathbf{B}_0$ is applied perpendicular to the edges of the strip. We assume that the cracks are opened by an internal pressure $p(x)$, which is an even function of x and the edges of the strip are free from mechanical load.

For convenience, all magnetic quantities outside the solid will be denoted by the superscript (e). The magnetic induction $\mathbf{B}_0{}^{(e)}$ outside the solid becomes $\mathbf{B}_0{}^{(e)} = (0, B_0, 0)$. Symmetry arguments are used to allow consideration of only the first quadrant with appropriate boundary conditions along the coordinate axes. The corresponding boundary conditions may be taken as

$$h_x^{(e)}(x,l) - h_x(x,l) = -(\chi B_0/\mu_0\mu_r) u_{y,x}(x,l);\ |x| < \infty$$

$$h_y^{(e)}(x,l) - \mu_r h_y(x,l) = 0;\ |x| < \infty \tag{6}$$

$$t_{yx}(x,l) = 0;\ |x| < \infty$$

$$t_{yy}(x,l) = (\chi^2/\mu_r)\{B_0 h_y(x,l) + B_0^2/2\mu_0\mu_r\};\ |x| < \infty \tag{7}$$

$$h_x^{(e)}(x,0) - h_x(x,0) = -(\chi B_0/\mu_0\mu_r) u_{y,x}(x,0);\ a \le |x| \le b$$

$$\phi(x,0) = 0;\ |x| < a,\ b < |x| \tag{8}$$

$$b_y^{(e)}(x,0) - b_y(x,0) = 0;\ a \le |x| \le b$$

$$\phi^{(e)}(x,0) = 0;\ a \le |x| \le b \tag{9}$$

$$t_{yx}(x,0) = 0;\ |x| < \infty \tag{10}$$

$$t_{yy}(x,0) = (\chi^2/\mu_r)\{B_0 h_y(x,0) + B_0^2/2\mu_0\mu_r\} - p(x);\ a \le |x| \le b$$

$$u_y(x,0) = 0;\ |x| < a,\ b < |x| \tag{11}$$

It is convenient to express the solutions for equations (1) and (2) as follows;

$$\begin{aligned} u_x &= -\nu\frac{\chi(\chi-2)B_0^2}{4\mu_0\mu\mu_r^2} x \\ &\quad - \frac{2}{\pi}\int_0^\infty \left[\left\{B(\alpha) + (3-4\nu)\frac{1}{\alpha}C(\alpha) + yD(\alpha)\right\}\sinh(\alpha y)\right. \\ &\quad + \left\{A(\alpha) + C(\alpha)y + (3-4\nu)\frac{1}{\alpha}D(\alpha)\right\}\cosh(\alpha y) \\ &\quad + 2(1-2\nu)(\chi B_0/\mu\mu_r)\{a(\alpha)\cosh(\alpha y) \\ &\quad \left. + b(\alpha)\sinh(\alpha y)\}\right]\sin(\alpha x)\,d\alpha \end{aligned}$$

$$\begin{aligned} u_y &= (1-\nu)\frac{\chi(\chi-2)B_0^2}{4\mu_0\mu\mu_r^2} y \\ &\quad + \frac{2}{\pi}\int_0^\infty [\{A(\alpha) + C(\alpha)y\}\sinh(\alpha y) \\ &\quad + \{B(\alpha) + D(\alpha)y\}\cosh(\alpha y)]\cos(\alpha x)\,d\alpha \end{aligned} \tag{12}$$

$$\phi = \frac{2}{\pi}\int_0^\infty \{a(\alpha)\sinh(\alpha y) + b(\alpha)\cosh(\alpha y)\}\cos(\alpha x)\,d\alpha \tag{13}$$

Downloaded 01 May 2010 to 171.66.16.249. Redistribution subject to ASME license or copyright; see http://www.asme.org/terms/Terms_Use.cfm

$$\phi^{(e)} = \frac{2}{\pi}\int_0^\infty a_e(\alpha)\sinh(\alpha y)\cos(\alpha x)\,d\alpha;$$

$$y=0,\ a<|x|<b \tag{14}$$

$$\phi^{(e)} = \frac{2}{\pi}\int_0^\infty b_e(\alpha)e^{-\alpha y}\cos(\alpha x)\,d\alpha;\ l\le|y| \tag{15}$$

where $A(\alpha)$, $B(\alpha)$, $C(\alpha)$, $D(\alpha)$, $a(\alpha)$, $b(\alpha)$, $a_e(\alpha)$ and $b_e(\alpha)$ are unknown functions. The boundary conditions (6), (7), and (10) are satisfied if we take

$$\begin{aligned}
A(\alpha) &= \frac{1}{4(1-\nu)\Delta(\alpha)}[\{\beta_4(\alpha)\gamma_1(\alpha)-\beta_2(\alpha)\gamma_3(\alpha)\}B(\alpha)\\
&\quad+\{\beta_4(\alpha)\gamma_2(\alpha)-\beta_2(\alpha)\gamma_4(\alpha)\}(\chi B_0/\mu\mu_r)b(\alpha)]\\
D(\alpha) &= -\frac{1}{4(1-\nu)\Delta(\alpha)}[\{\beta_1(\alpha)\gamma_3(\alpha)\\
&\quad-\beta_3(\alpha)\gamma_1(\alpha)\}\alpha B(\alpha)+\{\gamma_4(\alpha)\beta_1(\alpha)\\
&\quad-\gamma_2(\alpha)\beta_3(\alpha)\}(\chi B_0/\mu\mu_r)\alpha b(\alpha)]\\
C(\alpha) &= \frac{1}{4(1-\nu)}\{2\alpha B(\alpha)+(3-4\nu)(\chi B_0/\mu\mu_r)\alpha b(\alpha)\}\\
a(\alpha) &= \frac{1}{e_1(\alpha l)}[(\chi B_0/\mu\mu_r)\{A(\alpha)\sinh(\alpha l)\\
&\quad+B(\alpha)\cosh(\alpha l)+lC(\alpha)\sinh(\alpha l)\\
&\quad+lD(\alpha)\cosh(\alpha l)\}-b(\alpha)\{\cosh(\alpha l)+\mu_r\sinh(\alpha l)\}]\\
b_e(\alpha) &= \mu_r e^{\alpha l}\{2\alpha B(\alpha)+4(1-\nu)C(\alpha)\}
\end{aligned} \tag{16}$$

where

$$\begin{aligned}
\beta_1(\alpha l) &= \{2+(3-4\nu)(\chi b_c/\mu_r)^2\}\sinh^2(\alpha l)\\
&\quad+2\mu_r\sinh(\alpha l)\cosh(\alpha l)\\
\beta_2(\alpha l) &= 4(1-\nu)\sinh^2(\alpha l)+2\mu_r\alpha l\cosh^2(\alpha l)\\
&\quad+[2\{\alpha l+2(1-\nu)\mu_r\}\\
&\quad+(3-4\nu)(\chi b_c/\mu_r)^2\alpha l]\sinh(\alpha l)\cosh(\alpha l)\\
\beta_3(\alpha l) &= [2\{\sinh(\alpha l)+\mu_r\cosh(\alpha l)\}\\
&\quad+(2-\chi-4\nu)(\chi b_c/\mu_r)^2\sinh(\alpha l)]\sinh(\alpha l)\\
\beta_4(\alpha l) &= 2\{(1-2\nu)\cosh(\alpha l)+\alpha l\sinh(\alpha l)\}e_1(\alpha l)\\
&\quad+(2-\chi-4\nu)(\chi b_c/\mu_r)^2\alpha l\cosh^2(\alpha l)\\
\gamma_1(\alpha l) &= 2[\{2+(3-4\nu)(\chi b_c/\mu_r)^2\}\alpha l\sinh^2(\alpha l)\\
&\quad+2\{\mu_r\alpha l-(1-\nu)(3-4\nu)(\chi b_c/\mu_r)^2\}\\
&\quad\times\sinh(\alpha l)\cosh(\alpha l)]\\
\gamma_2(\alpha l) &= (3-4\nu)[\{2\alpha l+4(1-\nu)\mu_r\\
&\quad+(3-4\nu)(\chi b_c/\mu_r)^2\alpha l\}\sinh^2(\alpha l)\\
&\quad+2\{\mu_r\alpha l+2(1-\nu)\}\\
&\quad\times\sinh(\alpha l)\cosh(\alpha l)]\\
\gamma_3(\alpha l) &= -2[2e_1(\alpha l)\{\sinh(\alpha l)-\alpha l\cosh(\alpha l)\}\\
&\quad+(2-\chi-4\nu)(\chi b_c/\mu_r)^2\{2(1-\nu)\cosh(\alpha l)\\
&\quad-\alpha l\sinh(\alpha l)\}\cosh(\alpha l)]\\
\gamma_4(\alpha l) &= -2e_1(\alpha l)[\{1-2\nu-2(1-\nu)\chi\}\sinh(\alpha l)\\
&\quad-2(1-\nu)\{2(1-2\nu)-\chi\}\cosh(\alpha l)\\
&\quad-(3-4\nu)\alpha l\cosh(\alpha l)]\\
&\quad+(2-\chi-4\nu)(3-4\nu)(\chi b_c/\mu_r)^2\alpha l\\
&\quad\times\sinh(\alpha l)\cosh(\alpha l)\\
\Delta(\alpha l) &= \beta_1(\alpha l)\beta_4(\alpha l)-\beta_2(\alpha l)\beta_3(\alpha l)\\
e_1(\alpha l) &= \sinh(\alpha l)+\mu_r\cosh(\alpha l),\ b_c^2=B_0^2/\mu_0\mu
\end{aligned} \tag{17}$$

The remaining boundary conditions (8) and (11) will be satisfied provided $B(\alpha)$ and $b(\alpha)$ satisfy the simultaneous triple integral equations:

$$\int_0^\infty \alpha b(\alpha)\sin(\alpha x)\,d\alpha$$

$$=(XB_0/\mu_0\mu_r)\int_0^\infty \alpha B(\alpha)\sin(\alpha x)\,d\alpha;\ a\le|x|\le b$$

$$\int_0^\infty b(\alpha)\cos(\alpha x)\,d\alpha=0;\ |x|<a,\ b<|x| \tag{18}$$

$$\int_0^\infty[\alpha B(\alpha)\{1+H_e(\alpha l)\}-\alpha b(\alpha)\{2(1-\nu)\chi-1+2\nu$$

$$+H_m(\alpha l)\}(\chi B_0/2\mu\mu_r)]\cos(\alpha x)\,d\alpha$$

$$=\frac{\pi(1-\nu)}{2\mu}p(x);\ a\le|x|\le b$$

$$\int_0^\infty B(\alpha)\cos(\alpha x)\,d\alpha=0;\ |x|<a,\ b<|x| \tag{19}$$

where

$$\begin{aligned}
H_e(\alpha l) &= -\frac{1}{4e_1(\alpha l)}[\{2e_1(\alpha l)\\
&\quad-(\chi-2+4\nu)(\chi b_c/\mu_r)^2\sinh(\alpha l)\}\\
&\quad\times\{\beta_4(\alpha l)\gamma_1(\alpha l)-\beta_2(\alpha l)\gamma_3(\alpha l)\}/\Delta(\alpha l)\\
&\quad+\{2(1-2\nu)e_1(\alpha l)-(X-2\\
&\quad+4\nu)(\chi b_c/\mu_r)^2\alpha l\cosh(\alpha l)\}\\
&\quad\times\{\beta_1(\alpha l)\gamma_3(\alpha l)-\beta_3(\alpha l)\gamma_1(\alpha l)\}/\Delta(\alpha l)\\
&\quad-2(\chi-2+4\nu)(\chi b_c/\mu_r)^2\{2(1-\nu)\cosh(\alpha l)\\
&\quad-\alpha l\sinh(\alpha l)\}]-1\\
H_m(\alpha l) &= \frac{1}{2e_1(\alpha l)}[[\{2e_1(\alpha l)\\
&\quad-(\chi-2+4\nu)(\chi b_c/\mu_r)^2\sinh(\alpha l)\}\{\beta_4(\alpha l)\gamma_2(\alpha l)\\
&\quad-\beta_2(\alpha l)\gamma_4(\alpha l)\}/\Delta(\alpha l)+\{2(1-2\nu)e_1(\alpha l)\\
&\quad-(\chi-2+4\nu)(\chi b_c/\mu_r)^2\alpha l\cosh(\alpha l)\}\\
&\quad\{\gamma_4(\alpha l)\beta_1(\alpha l)-\gamma_2(\alpha l)\beta_3(\alpha l)\}/\Delta(\alpha l)\\
&\quad+(\chi-2+4\nu)[4(1-\nu)\{\cosh(\alpha l)+\mu_r\sinh(\alpha l)\}\\
&\quad+(3-4\nu)(\chi b_c/\mu_r)^2\alpha l\sinh(\alpha l)]]\\
&\quad-2(1-\nu)X-1+2\nu
\end{aligned} \tag{20}$$

Downloaded 01 May 2010 to 171.66.16.249. Redistribution subject to ASME license or copyright; see http://www.asme.org/terms/Terms_Use.cfm

If we make the integral representations for $b(\alpha)$ and $B(\alpha)$

$$b(\alpha) = \frac{1}{\alpha}\int_a^b h(\xi)\sin(\alpha\xi)\,d\xi$$

$$B(\alpha) = \frac{1}{\alpha}\int_a^b \varphi(\xi)\sin(\alpha\xi)\,d\xi \tag{21}$$

and substitute the equations (21) into the first equation of (18), after some manipulations, we have

$$h(\xi) - (\chi B_0/\mu_0\mu_r)\varphi(\xi) = 0 \tag{22}$$

When we use equation (22), from the first equation of (19) we also have the following singular integral equation of the first kind,

$$\int_a^b \varphi(\xi)\left[\frac{1}{\xi-x}+\frac{1}{\xi+x}+\frac{2}{y_0}S(x,\xi)\right]\alpha\xi = \frac{\pi(1-\nu)}{\mu y_0}p(x) \tag{23}$$

in which the Fredholm kernel $S(x, \xi)$ is bounded in closed interval $a \le x, \xi \le b$ and is given by

$$S(x,\xi) = \int_0^\infty \left[H_e(\alpha l) - \frac{1}{2}(\chi b_c/\mu_r)^2 H_m(\alpha l)\right]\sin(\alpha\xi)\cos(\alpha x)\,d\alpha \tag{24}$$

and

$$y_0 = 1 + \frac{1}{2}(\chi b_c/\mu_r)^2\{1-2\nu-2(1-\nu)\chi\} \tag{25}$$

From the second equations of (18) and (19) and the definitions (21) it is clear that the integral equation (23) must be solved under the following single-valuedness conditions:

$$\int_a^b h(\xi)\,d\xi = 0$$

$$\int_a^b \varphi(\xi)\,d\xi = 0 \tag{26}$$

The singular integral equation of the first kind for $\varphi(\xi)$ will be solved numerically for the case of uniform pressure, i.e., $p(x) = p_0$. For the sake of the convenience, we perform the following nondimensionalization:

$$a_0 = a/b$$

$$R = x/b = \frac{1}{2}(1-a_0)s + \frac{1}{2}(1+a_0)$$

$$T = \xi/b = \frac{1}{2}(1-a_0)\tau + \frac{1}{2}(1+a_0)$$

$$M(s,\tau) = \frac{b-a}{y_0}S(x,\xi) \tag{27}$$

The solution of the set of integral equations (23) and (26) as given in Erdogan [12], is

$$\varphi(\xi) = \frac{(1-\nu)p_0}{\mu y_0(1-\tau^2)^{1/2}}\sum_{n=1}^\infty A_n T_n(\tau) \tag{28}$$

where $T_n(\tau)$ are Chebyshev polynomials of the first kind and A_n are unknown constants obtained from the following infinite system of linear algebraic equations:

$$\sum_{n=1}^\infty (\delta_{kn} + C_{kn})A_n = \delta_{1k} \tag{29}$$

where δ_{kn} is the Kronecker delta and

$$C_{kn} = \frac{2}{\pi^2}\int_{-1}^1 U_{k-1}(s)(1-s^2)^{1/2}\,ds \int_{-1}^1 \times\left[\frac{1}{\tau+s+2(1+a_0)/(1-a_0)} + M(s,\tau)\right]T_n(\tau)\frac{1}{(1-\tau^2)^{1/2}}\,d\tau \tag{30}$$

In equation (30), $U_{k-1}(s)$ are Chebyshev polynomials of the second kind.

The singular part of the complete stress $t_{cyy}(x,0)$ is determined as

$$t_{cyy}(x,0) = t_{yy}(x,0) + t_{yy}^M(x,0) \sim \frac{K_{h1a}}{\{2(a-x)\}^{1/2}} + \frac{K_{h1b}}{\{2(x-b)\}^{1/2}} \tag{31}$$

where K_{h1a} and K_{h1b} are the stress-intensity factors at the inner and the outer tips of the crack, respectively, and are defined by the following equations

$$K_{h1a} = \lim_{x\to a^-}\{2(a-x)\}^{1/2} t_{cyy}(x,0) = -\frac{p_0 b^{1/2}\{(1-a_0)/2\}^{1/2}}{2\chi\mu_r^2 y_0}[2\chi\mu_r^2 + \{2(1-\nu)+(5-6\nu)\chi\}(\chi X b_c)^2]\sum_{n=1}^\infty (-1)^n A_n$$

$$K_{h1b} = \lim_{x\to b^+}\{2(x-b)\}^{1/2} t_{cyy}(x,0) = \frac{p_0 b^{1/2}\{(1-a_0)/2\}^{1/2}}{2\chi\mu_r^2 y_0}[2\chi\mu_r^2 + \{2(1-\nu)+(5-6\nu)\chi\}(\chi b_c)^2]\sum_{n=1}^\infty A_n \tag{32}$$

We might also note that we cannot set $a_0 = 0$ in this analysis. But by extending the definition of the function $\varphi(\xi)$ and the kernels of (23) and (26) from $0 < \xi, x < b$ into $-b < \xi, x < b$ in an appropriate way, we can achieve it. That is,

$$\int_{-b}^b \varphi(\xi)\left[\frac{1}{\xi-x}+\frac{1}{y_0}S(x,\xi)\right]\alpha\xi = \frac{\pi(1-\nu)}{\mu y_0}p(x)$$

$$\int_{-b}^b \varphi(\xi)\,d\xi = 0 \tag{33}$$

where $-\varphi(-\xi)$ is denoted as $\varphi(\xi)$. Performing the following nondimensionalization

$$x = bs$$

$$\xi = b\tau$$

$$M_0(s,\tau) = \frac{b}{y_0}S(bs,b\tau) \tag{34}$$

the solution $\varphi(\xi)$ is also obtained as

$$\varphi(\xi) = \frac{(1-\nu)p_0}{\mu y_0}\sum_{n=1}^\infty B_n T_{2n-1}(\tau) \tag{35}$$

where B_n are determined by

$$\sum_{n=1}^\infty (\delta_{kn} + D_{kn})B_n = \delta_{1k} \tag{36}$$

In equation (36), D_{kn} is

Downloaded 01 May 2010 to 171.66.16.249. Redistribution subject to ASME license or copyright; see http://www.asme.org/terms/Terms_Use.cfm

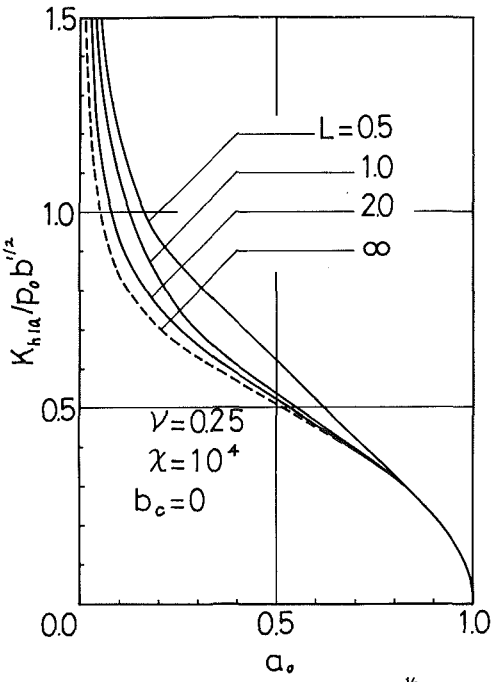


Fig. 2 Normalized stress-intensity factor $K_{h1a}/p_0b^{1/2}$ against a_0 for the case of the absence of the magnetic field

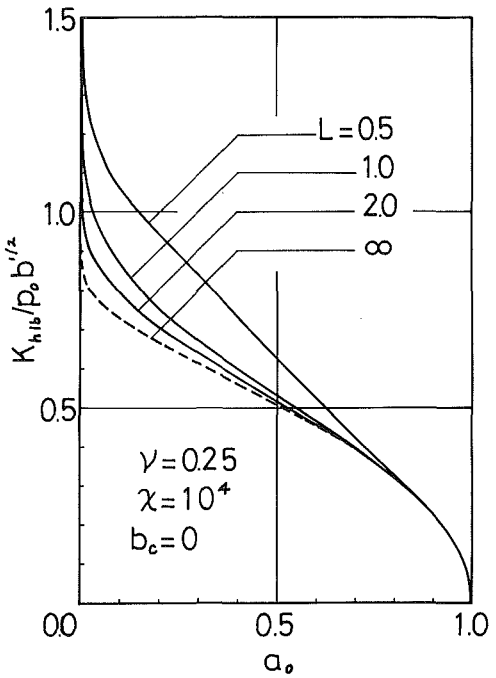


Fig. 3 Normalized stress-intensity factor $K_{h1b}/p_0b^{1/2}$ against a_0 for the case of the absence of the magnetic field

$$D_{kn} = \frac{2}{\pi^2}\int_{-1}^{1} U_{2k-2}(s)(1-s^2)^{1/2}\,ds$$

$$\times \int_{-1}^{1} M_0(s,\tau)\,T_{2n-1}(\tau)\frac{1}{(1-\tau^2)^{1/2}}\,d\tau \tag{37}$$

The stress-intensity factor in this case is also determined as

$$K_{h1b} = \frac{p_0 b^{1/2}}{2X\mu_r^2}[2\chi\mu_r^2 + \{2(1-\nu)$$

$$+(5-6\nu)\chi\}(\chi b_c)^2]\sum_{n=1}^{\infty} B_n \tag{38}$$

Numerical Results and Discussions

To examine the effects of magnetic fields and geometrical configurations on the stress-intensity factors, two infinite systems of simultaneous equations (29) for $a_0 \neq 0$ and (36) for $a_0 = 0$ are solved numerically for Poisson's ratio $\nu = 0.25$ and magnetic susceptibility $\chi = 10^4$. First, the variations of the normalized stress-intensity factor $K_{h1a}/p_0b^{1/2}$ at the inner tip of the crack with a_0 for $b_c = 0$ and $L = 0.5$, 1.0, 2.0, ∞ are shown in Fig. 2. The same kind of results for $K_{h1b}/p_0b^{1/2}$ at the outer tip of the crack is also shown in Fig. 3. While the problem in a purely elastic case was solved by Lowengrub and Srivastava [5], their solution was an iterative one that was valid at $L >> 1$ and did not have a numerical one for any prescribed values of L owing to difficulties of the numerical analysis. The dashed curves for the case $L = \infty$ coincide with the closed-form solutions for the infinite solid with two coplanar Griffith cracks by Lowengrub and Srivastava [13]. $K_{h1a}/p_0b^{1/2}$ becomes very large as $a_0 \to 0$ and decreases monotonously with an increasing a_0 and tends to zero as $a_0 \to 1.0$. $K_{h1b}/p_0b^{1/2}$ tends to the result for the strip with a Griffith crack by Lowengrub [3] as $a_0 \to 0$ and tends to zero as $a_0 \to 1.0$. When a_0 tends to 1.0, both $K_{h1a}/p_0b^{1/2}$ and $K_{h1b}/p_0b^{1/2}$ approach to the normalized stress-intensity factor $(1-a_0/2)^{1/2}$ for a Griffith crack of length $b-a$ in the plane strain state. And $K_{h1a}/p_0b^{1/2}$ and $K_{h1b}/p_0b^{1/2}$ decrease with increasing L and the tendency is more pronounced with decreasing a_0.

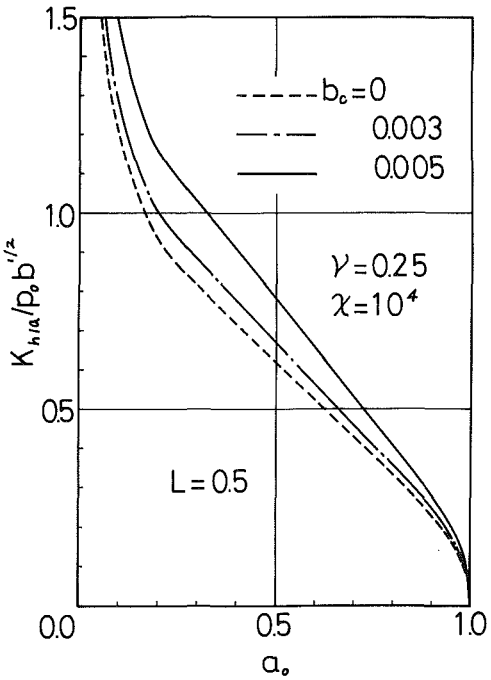


Fig. 4 Effect of magnetic field on normalized stress-intensity factor $K_{h1a}/p_0b^{1/2}$ against a_0 for $L = 0.5$

Next, we examine the effects of magnetic fields on the stress-intensity factors. Figures 4 and 5 show the effects of magnetic fields on the variations of $K_{h1a}/p_0b^{1/2}$ at the inner tip of the crack against a_0 for $L = 0.5$ and 1.0, respectively. The dashed curves show the results for the case of the absence of the magnetic fields, $b_c = 0$, which are the same results as Fig. 2. The same kind of results at $x = b$ is also shown in Figs. 6 and 7. $K_{h1b}/p_0b^{1/2}$ tends to the result for the ferromagnetic strip with a Griffith crack as $a_0 \to 0$ and further tends to that for the infinite solid with a Griffith crack by the author [9] as

Downloaded 01 May 2010 to 171.66.16.249. Redistribution subject to ASME license or copyright; see http://www.asme.org/terms/Terms_Use.cfm

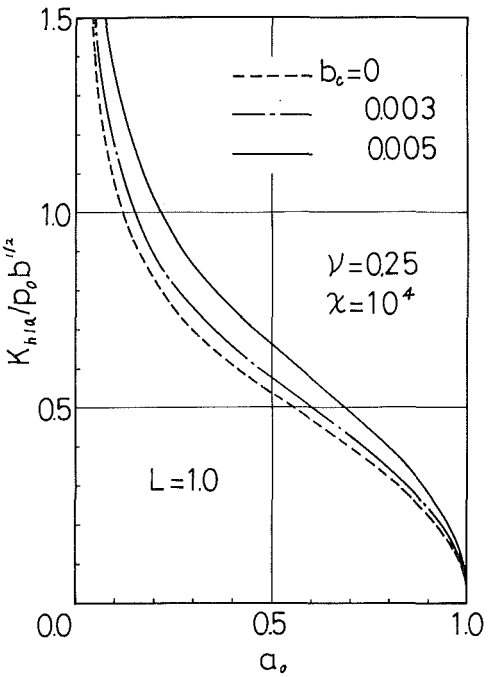


Fig. 5 Effect of magnetic field on normalized stress-intensity factor $K_{h1a}/p_0 b^{1/2}$ against a_0 for $L = 1.0$

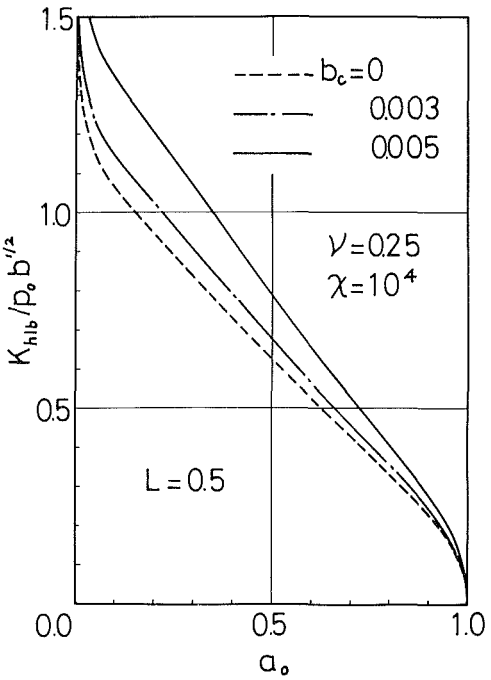


Fig. 6 Effect of magnetic field on normalized stress-intensity factor $K_{h1b}/p_0 b^{1/2}$ against a_0 for $L = 0.5$

$L \to \infty$. And when $L \to \infty$, we solve the problem for the infinite solid with two coplanar Griffith cracks by the author [11]. When we compare the present solution at $L = \infty$ with the closed form solution [11], the computations carried out reveal to be fairly good. As b_c increases, the stress-intensity factors increase depending on the values of ν, χ, a_0 and L. The effects of the magnetic fields on the stress-intensity factors are more pronounced with decreasing a_0 and L.

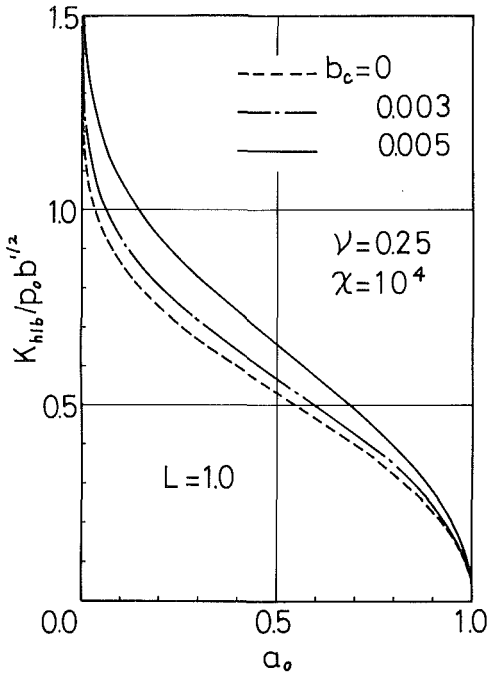


Fig. 7 Effect of magnetic field on normalized stress-intensity factor $K_{h1b}/p_0 b^{1/2}$ against a_0 for $L = 1.0$

Acknowledgment

The author is especially grateful to Prof. Dr. A. Atsumi, Tohoku University, for his invaluable direction, and acknowledges with thanks the support of this study by the Scientific Research Fund of the Ministry of Education for the fiscal year 1979.

References

1 Griffith, A. A., "The Phenomena of Rupture and Flow in Solids," *Philosophical Transactions of the Royal Society of London,* Series A, Vol. 221, 1920, pp. 163–198.

2 Sih, G. C., ed., *Methods of Analysis and Solutions of Crack Problems,* Noordhoff, Leyden, 1973.

3 Lowengrub, M., "A Two Dimensional Crack Problem," *International Journal of Engineering Science,* Vol. 4, 1966, pp. 289–299.

4 Cooke, J. C., "The Solution of Triple Integral Equations in Operational Form," *Quarterly Journal of Mechanics and Applied Mathematics,* Vol. 17, 1965, pp. 57–72.

5 Lowengrub, M., and Srivastava, K. N., "Two Coplanar Griffith Cracks in an Infinitely Long Elastic Strip," *International Journal of Engineering Science,* Vol. 6, 1968, pp. 425–434.

6 Dunkin, J. W., and Eringen, A. C., "On the Propagation of Waves in an Electromagnetic Elastic Solid," *International Journal of Engineering Science,* Vol. 1, 1963, pp. 461–495.

7 Pao, Y.-H., and Yeh, C.-S., "A Linear Theory for Soft Ferromagnetic Elastic Solids," *International Journal of Engineering Science,* Vol. 11, 1973, pp. 415–436.

8 Hutter, K., and Pao, Y.-H., "A Dynamic Theory for Magnetizable Elastic Solids with Thermal and Electrical Conduction," *Journal of Elasticity,* Vol. 4, 1974, pp. 89–114.

9 Shindo, Y., "The Linear Magnetoelastic Problem for a Soft Ferromagnetic Elastic Solid with a Finite Crack," ASME JOURNAL OF APPLIED MECHANICS, Vol. 44, 1977, pp. 47–51.

10 Shindo, Y., "Magnetoelastic Interaction of a Soft Ferromagnetic Elastic Solid with a Penny-Shaped Crack in a Constant Axial Magnetic Field," ASME JOURNAL OF APPLIED MECHANICS, Vol. 45, 1978, pp. 291–296.

11 Shindo, Y., "Singular Stresses in a Soft Ferromagnetic Elastic Solid with Two Coplanar Griffith Cracks," *International Journal of Solids and Structures,* Vol. 16, 1980, pp. 537–543.

12 Erdogan, F., "Approximate Solutions of Systems of Singular Integral Equations," *SIAM Journal on Applied Mathematics,* Vol. 17, 1969, pp. 1041–1059.

13 Lowengrub, M., and Srivastava, K. N., "Research Note on Two Coplanar Griffith Cracks in an Infinite Medium," *International Journal of Engineering Science,* Vol. 6, 1968, pp. 359–362.

Downloaded 01 May 2010 to 171.66.16.249. Redistribution subject to ASME license or copyright; see http://www.asme.org/terms/Terms_Use.cfm

Use of $\hat{J}$-Integral in Dynamic Analysis of Cracked Linear Viscoelastic Solids by Finite-Element Method

K. Kishimoto
Research Associate.

S. Aoki
Associate Professor.

M. Sakata
Professor.

Department of Physical Engineering,
Tokyo Institute of Technology,
Ookayama, Meguro-ku,
Tokyo 152, Japan

A computational method using the path (area)-independent $\hat{J}$-integral is developed to analyze viscoelastic problems. Since the displacement field near the crack tip of a viscoelastic solid is dependent upon the complete past history of the dynamic stress-intensity factors, the $\hat{J}$-integral is represented by a hereditary integral of the dynamic stress-intensity factors. We assume that the stress and strain rates vary in proportion to time during each increment of time and derive a formula to obtain the current value of the dynamic stress-intensity factor from the time increment of the $\hat{J}$-value. Both pure and mixed mode problems of a suddenly loaded crack are analyzed by making use of the formula together with the conventional finite-element method. In order to demonstrate the capability and reliability of the present method, problems of a center crack and an oblique crack in viscoelastic rectangular plates are solved.

Introduction

It is reported that inertia effect is important for estimating the stress-intensity factors due to impact loading. However, only a few idealized cases are amenable to analytic treatment because of mathematical complexities. Thus it is important to develop a numerical method to determine the dynamic stress-intensity factors for a wide range of structures of complex geometries and loading conditions.

In previous papers [1-3], the authors have reported the analysis of the dynamic stress-intensity factor for a cracked linear elastic or viscoelastic isotropic plate by the finite-element method using a singular element in which the displacement shape function has been taken from the analytical crack-tip expansions. Although the method has eliminated the need for a fine grid near the crack tip and is capable of determining accurate values of the dynamic stress-intensity factors, it is inconvenient to use an element of this special type since the singular element deviates in character from the other elements. In order to overcome this, we have attempted to develop an alternative method to solve the elastodynamic problems [4] by combining the conventional finite-element method with the path independent $\hat{J}$-integral [5] which is an extension of the J-integral proposed by Rice which includes the effect of the inertia of materials, etc.

In the present paper, a computational method using the $\hat{J}$-integral is developed to analyze viscoelastic problems.

Contributed by the Applied Mechanics Division for publication in the JOURNAL OF APPLIED MECHANICS.

Discussion on this paper should be addressed to the Editorial Department, ASME, United Engineering Center, 345 East 47th Street, New York, N. Y. 10017, and will be accepted until two months after final publication of the paper itself in the JOURNAL OF APPLIED MECHANICS. Manuscript received by ASME Applied Mechanics Division, March, 1981; final revision, July, 1981.

Formula for Determining Dynamic Stress-Intensity Factors From $\hat{J}$-Integral

Consider a plate of homogeneous, isotropic, and linear viscoelastic material. The plate contains a stationary traction-free crack along the X_1-axis as shown in Fig. 1. For the transient problems as well as static ones, component of the stress σ_{ij} and displacement u_i in the neighborhood of a stationary crack are given as, in a polar coordinate system $0-r, \theta$ with the origin being loated at the crack tip [3],

$$\sigma_{ij} = \frac{K_{\mathrm{I}}(t)}{\sqrt{2\pi r}} f_{ij}^{\mathrm{I}}(\theta) + \frac{K_{\mathrm{II}}(t)}{\sqrt{2\pi r}} f_{ij}^{\mathrm{II}}(\theta) + \frac{K_{\mathrm{III}}(t)}{\sqrt{2\pi r}} f_{ij}^{\mathrm{III}}(\theta) \quad (1a)$$

$$u_i = T_{\mathrm{I}}(t)\sqrt{\frac{r}{2\pi}} g_i^{\mathrm{I}}(\theta,\nu) + T_{\mathrm{II}}(t)\sqrt{\frac{r}{2\pi}} g_i^{\mathrm{II}}(\theta,\nu) + T_{\mathrm{III}}(t)\sqrt{\frac{r}{2\pi}} g_i^{\mathrm{III}}(\theta) \quad (1b)$$

where $K_M(t)$ (M = I, II, III,) denote the stress-intensity factors, and the strain-intensity factors $T_M(t)$ satisfy the relations

$$K_M(t) = 2\int_0^t \mu(t-\tau)\frac{\partial T_M(\tau)}{\partial \tau} d\tau \qquad (M=\mathrm{I,II,III},) \quad (2)$$

with the relaxation moduli for pure shear, $\mu(t)$. The dimensionless function $f_{ij}^{\mathrm{I}}(\theta)$, $g_i^{\mathrm{I}}(\theta,\nu)$, etc., are identical with those associated with the elastic singularity. In deriving equation (1), we have assumed Poisson's ratio ν is constant.

The energy-release rate due to crack extension is given by taking account of the inertia effects as

$$\hat{J} = -\int_\Gamma T_i u_{i,1} d\Gamma + \iint_A (\sigma_{ij}\epsilon_{ij,1} + \rho\ddot{u}_i u_{i,1}) dA \quad (3)$$

where T_i is surface traction, ρ the density, Γ an arbitrary

Copyright © 1982 by ASME
Downloaded 01 May 2010 to 171.66.16.249. Redistribution subject to ASME license or copyright; see http://www.asme.org/terms/Terms_Use.cfm

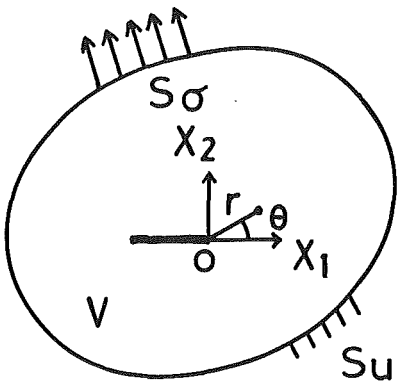


Fig. 1 Cracked linear viscoelastic plate

curve surrounding the crack tip, A the area surrounded by Γ and the crack surfaces. A superposed dot denotes the time derivative. It has been proved theoretically in the previous paper [5] that the $\hat{J}$-integral given by equation (1) is path (area)-independent irrespective of the stress-strain relation. By virtue of path-independence, we can evaluate the $\hat{J}$-integral by taking Γ to be a small path around the crack tip and using equation (1). Thus we obtain

$$\hat{J}=\frac{\kappa+1}{4}[K_{\mathrm{I}}(t)T_{\mathrm{I}}(t)+K_{\mathrm{II}}(t)T_{\mathrm{II}}(t)]+K_{\mathrm{III}}(t)T_{\mathrm{III}}(t) \tag{4}$$

where

$$\kappa=\begin{cases}3-4\nu & \text{plane strain}\\ (3-\nu)/(1+\nu) & \text{plane stress}\end{cases}$$

Since in the case of an elastic solid, the following relation holds:

$$K_M(t)=2\mu T_M(t) \qquad (M=\mathrm{I,II,III},) \tag{5}$$

where μ is the shear modulus, equation (4) becomes

$$\hat{J}=\frac{\kappa+1}{8\mu}[K_{\mathrm{I}}^2(t)+K_{\mathrm{II}}^2(t)]+\frac{1}{2\mu}K_{\mathrm{III}}^2(t)=g \tag{6}$$

This equation indicates that the $\hat{J}$-integral is identical with the elastic energy release rate g provided that the material is elastic.

It is found from equations (2) and (4) that the dynamic stress-intensity factor can be determined by evaluating the $\hat{J}$-integral for pure mode problems. For mixed mode problems, however, equation (4) is not available for determining $K_M(t)$.

In order to obtain a useful formula for determining $K_M(t)$ for a mixed mode problem, we decompose $\hat{J}$ into $\hat{J}^{\mathrm{I}}$, $\hat{J}^{\mathrm{II}}$, and $\hat{J}^{\mathrm{III}}$ as

$$\hat{J}=\hat{J}^{\mathrm{I}}+\hat{J}^{\mathrm{II}}+\hat{J}^{\mathrm{III}} \tag{7}$$

where the superscript I, II, or III denotes each of the deformation modes. Since the components of stress and displacement for Mode III are independent of those for Modes I and II, $\hat{J}^{\mathrm{III}}$ is given by

$$\hat{J}^{\mathrm{III}}=-\int_\Gamma \sigma_{3i}n_i u_{3,1}\,d\Gamma + \iint_A (2\sigma_{3i}\epsilon_{3i,1}+\rho\ddot{u}_3 u_{3,1})dA \,(i=1,2) \tag{8}$$

For the inplane mode, we employ the decomposition procedure which has been used by Ishikawa, et al. [6], for static problems and by the authors [4] for elastodynamic problems. We define σ_{ij}^M, etc., $(M = \mathrm{I, II})$ as

$$\begin{Bmatrix}\sigma_{11}^{\mathrm{I}}\\ \sigma_{22}^{\mathrm{I}}\\ \sigma_{12}^{\mathrm{I}}\end{Bmatrix}=\frac{1}{2}\begin{Bmatrix}\sigma_{11}+\sigma_{11}'\\ \sigma_{22}+\sigma_{22}'\\ \sigma_{12}-\sigma_{12}'\end{Bmatrix},\quad \begin{Bmatrix}u_1^{\mathrm{I}}\\ u_1^{\mathrm{I}}\end{Bmatrix}=\frac{1}{2}\begin{Bmatrix}u_1+u_1'\\ u_2-u_2'\end{Bmatrix},$$

$$\begin{Bmatrix}\epsilon_{11}^{\mathrm{I}}\\ \epsilon_{22}\\ \epsilon_{12}\end{Bmatrix}=\frac{1}{2}\begin{Bmatrix}\epsilon_{11}+\epsilon_{11}'\\ \epsilon_{22}+\epsilon_{22}'\\ \epsilon_{12}-\epsilon_{12}'\end{Bmatrix}$$

$$\begin{Bmatrix}\sigma_{11}^{\mathrm{II}}\\ \sigma_{22}^{\mathrm{II}}\\ \sigma_{12}^{\mathrm{II}}\end{Bmatrix}=\frac{1}{2}\begin{Bmatrix}\sigma_{11}-\sigma_{11}'\\ \sigma_{22}-\sigma_{22}'\\ \sigma_{12}+\sigma_{12}'\end{Bmatrix},\quad \begin{Bmatrix}u_1^{\mathrm{II}}\\ u_2^{\mathrm{II}}\end{Bmatrix}=\frac{1}{2}\begin{Bmatrix}u_1-u_1'\\ u_2+u_2'\end{Bmatrix},$$

$$\begin{Bmatrix}\epsilon_{11}^{\mathrm{II}}\\ \epsilon_{22}^{\mathrm{II}}\\ \epsilon_{12}^{\mathrm{II}}\end{Bmatrix}=\frac{1}{2}\begin{Bmatrix}\epsilon_{11}-\epsilon_{11}'\\ \epsilon_{22}-\epsilon_{11}'\\ \epsilon_{12}+\epsilon_{12}'\end{Bmatrix} \tag{9}$$

where the prime denotes the values at the symmetrical point with respect to the X_1-axis, i.e., $\sigma_{ij}'(X_1, X_2) = \sigma_{ij}(X_1, -X_2)$, etc. From equations (3) and (9) we obtain

$$\hat{J}^M=-\int_\Gamma T_i^M u_i^{M,1}\,d\Gamma + \iint_A (\sigma_{ij}^M\epsilon_{ij,1}^M+\rho\ddot{u}_i^M u_{i,1}^M)dA \quad (i=1,2,\ M=\mathrm{I,II}) \tag{10}$$

where the summation convention is not employed in index M. It is easily proved that $\hat{J}^M$ are path-independent and are related to $K_M(t)$ and $T_M(t)$ as

$$\hat{J}^{\mathrm{I}}=\frac{\kappa+1}{4}K_{\mathrm{I}}(t)T_{\mathrm{I}}(t) \tag{11a}$$

$$\hat{J}^{\mathrm{II}}=\frac{\kappa+1}{4}K_{\mathrm{II}}(t)T_{\mathrm{II}}(t) \tag{11b}$$

$$\hat{J}^{\mathrm{III}}=K_{\mathrm{III}}(t)T_{\mathrm{III}}(t) \tag{11c}$$

From equations (2) and (11), we can determine the dynamic stress-intensity factors $K_M(t)$ for the mixed mode problem by computing the $\hat{J}$-integral. It is noted that since the relationship between $K_M(t)$ and the $\hat{J}$-integral contains the hereditary integral of the dynamic stress-intensity factor for viscoelastic problems, the computational procedure is a little complicated as compared with the elastic problems.

Computational Procedure for Determining Dynamic Stress-Intensity Factor

We consider a standard viscoelastic solid obeying the constitutive equations

$$\dot{s}_{ij}+\beta s_{ij}=2\mu'(\dot{e}_{ij}+\alpha e_{ij}) \tag{12a}$$

$$\dot{\sigma}_{kk}+\beta\sigma_{kk}=\frac{2(1+\nu)}{(1-2\nu)}\mu'(\dot{\epsilon}_{kk}+\alpha\epsilon_{kk}) \tag{12b}$$

where s_{ij} and e_{ij} are the stress and strain deviators, respectively, and μ', α, and β are material constants. In this case, equation (2) becomes

$$\dot{K}_M(t)+\beta K_M(t)=2\mu'(\dot{T}_M(t)+\alpha T_M(t)) \quad (M=\mathrm{I,II,III}) \tag{13}$$

In the particular case, $\alpha = 0$ and $\alpha = \beta = 0$, equations (12) and (13) correspond to the Maxwell model and the elastic solid, respectively.

Assuming the stress and strain rates vary linearly with time in each time interval form $t = t_0$ to $t_0 + \Delta t$ [3], we obtain from equation (13) as

Downloaded 01 May 2010 to 171.66.16.249. Redistribution subject to ASME license or copyright; see http://www.asme.org/terms/Terms_Use.cfm

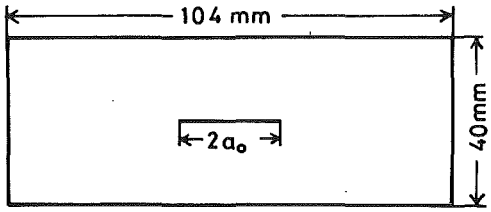


Fig. 2 Cracked viscoelastic rectangular plate; ρ = 2.45Mg/m^3, ν = 0.25, μ' = 29.4 GN/m^2, $2a_0$ = 24 mm; $\alpha = \beta = 0$ (elastic solid), $\alpha = 0.2 \times 10^5$ s^{-1}, $\beta = 0.4 \times 10^5$ s^{-1} (Standard solid), $\alpha = 0$, $\beta = 0.4 \times 10^5$ s^{-1} (Maxwell model)

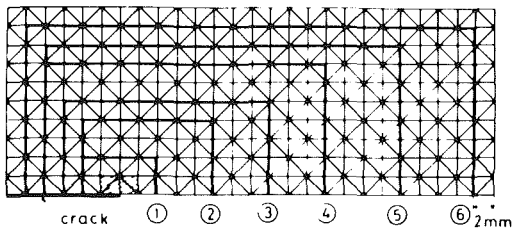


Fig. 3 Finite-element grid pattern (297 nodes, 520 elements) and paths for $\hat{J}$-integral (hatched part represents the singular element used for comparison)

$$\left(\frac{2}{\Delta t}+\beta\right)\Delta K_M = 2\mu'\left\{\left(\frac{2}{\Delta t}+\alpha\right)\Delta T_M + 2\alpha T_1(t_0)\right\} - 2\beta K_M(t_0) \tag{14}$$

where Δ designates the increments from t_0 to $t_0 + \Delta t$. From equation (4), in the case of Mode I, the increment of the $\hat{J}$-integral is given by

$$\Delta\hat{J} = \frac{\kappa+1}{4}\left(T_1(t_0)\Delta K_1 + K_1(t_0)\Delta T_1 + \Delta K_1 \Delta T_1\right) \tag{15}$$

Finally, the combination of equations (14) and (15) yields

$$\Delta K = \frac{-A+\sqrt{A^2-4B}}{2} \tag{16}$$

where

$$A = \frac{2\mu'\left(\frac{2}{\Delta t}-\alpha\right)T_1(t_0) + \left(\frac{2}{\Delta t}+3\beta\right)K_1(t_0)}{\frac{2}{\Delta t}+\beta}$$

$$B = \frac{2\beta K_1^2(t_0) - 4\alpha\mu' K_1(t_0)T_1(t_0) - 2\mu'\left(\frac{2}{\Delta t}+\alpha\right)\frac{4}{\kappa+1}\Delta J}{\frac{2}{\Delta t}+\beta} \tag{17}$$

We have chosen the root so that ΔK_1 and $\Delta\hat{J}$ have the same sign. A similar equation to equation (16) can be obtained for the Mode II, Mode III, or the mixed mode problem. Thus we can evaluate the dynamic stress-intensity factor by computing the $\hat{J}$-integral.

Numerical Examples

To demonstrate capability and reliability of the present method, some of the numerical results will be given in this section. The present analyses are concerned with a center crack (pure mode problem) and an oblique crack (mixed mode problem) in viscoelastic rectangular plates subjected to dynamic loading. The constant strain triangular elements are used in the computation, since they are the simplest. To evaluate the $\hat{J}$-integral from equation (3) or (10), the term $\epsilon_{ij,1}$ or $\epsilon^M_{ij,1}$ is evaluated as follows. First, the strain at each node are determined as the element area weighted average of the strain in all the elements meeting at the common node. Then, $\epsilon_{ij,1}$ or $\epsilon^M_{ij,1}$ are obtained by using the nodal values and the linear interpolating function.

The Newmark-β method [7] with $\beta = 1/6$ (not to be confused with the viscoelastic parameter β) and $\Delta t = 0.2\mu$s has been employed as the time integration scheme in the finite-element computation.

(1) Pure Mode Problem. Computation have been carried out for a cracked retangular plate as shown in Fig. 2 where a tensile stress σ or an inplane shear stress τ are applied to the upper and lower boundaries of the plate at time $t = 0$ with the Heaviside function time-dependence. By virtue of symmetry, only the first quadrant needs to be considered. Figure 3 shows the grid pattern employed and the various paths over which the values of the $\hat{J}$-integral are computed. The computation using a singular element [3] has also been performed for comparison. The hatched part in the figure illustrates the shape of the singular element. It is noted that in the computation using the $\hat{J}$-integral, triangular elements have been employed in this region.

Figure 4 shows the normalized dynamic stress-intensity factor $K_1(t)/\sigma\sqrt{\pi a_0}$ and $K_{II}(t)/\tau\sqrt{\pi a_0}$ that are estimated from the values of the $\hat{J}$-integral computed over the paths illustrated. It is observed that, as can be expected theoretically, both values are almost independent of the paths selected in the computation. Figures 5 and 6 show, respectively, the time variation of $K_1(t)/\sigma\sqrt{\pi a_0}$ and $K_{II}(t)/\tau$

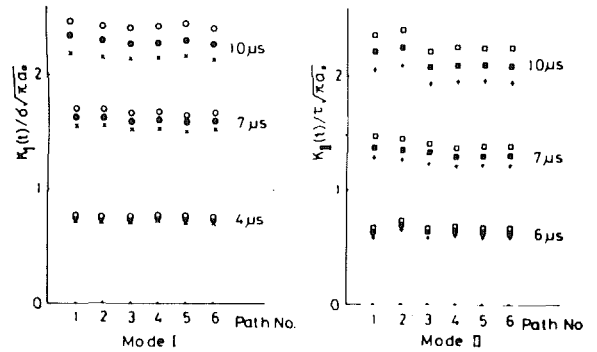


Fig. 4 Path-independence of $\hat{J}$ (pure mode); elastic solid (○, □), standard solid (●, ■), Maxwell model (x, +)

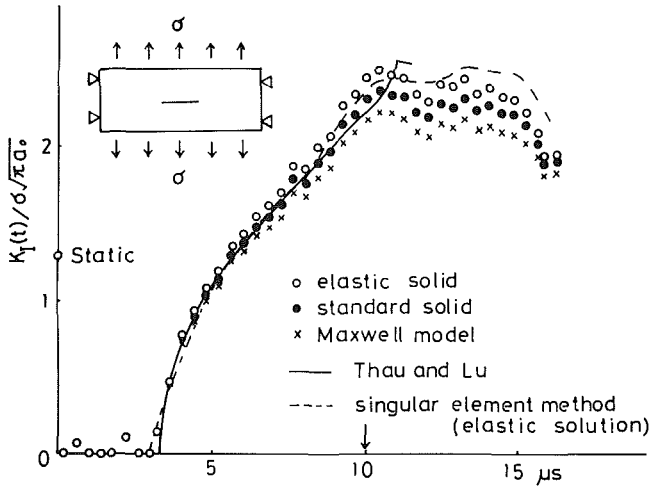


Fig. 5 Time variation of normalized Mode I dynamic stress-intensity factor (Path No. 5)

Downloaded 01 May 2010 to 171.66.16.249. Redistribution subject to ASME license or copyright; see http://www.asme.org/terms/Terms_Use.cfm

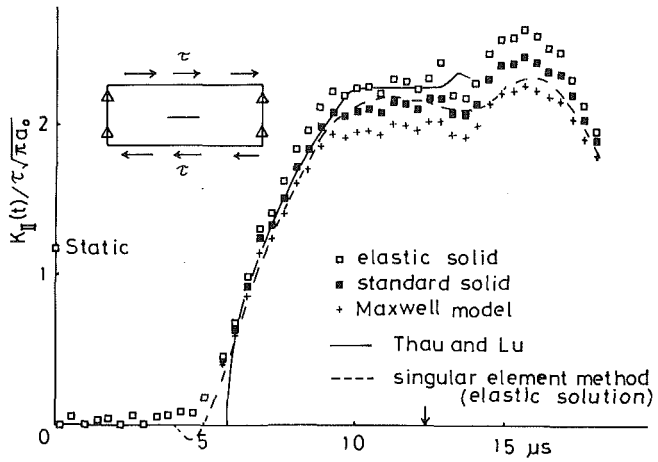


Fig. 6 Time variation of normalized Mode II dynamic stress-intensity factor (Path No. 5)

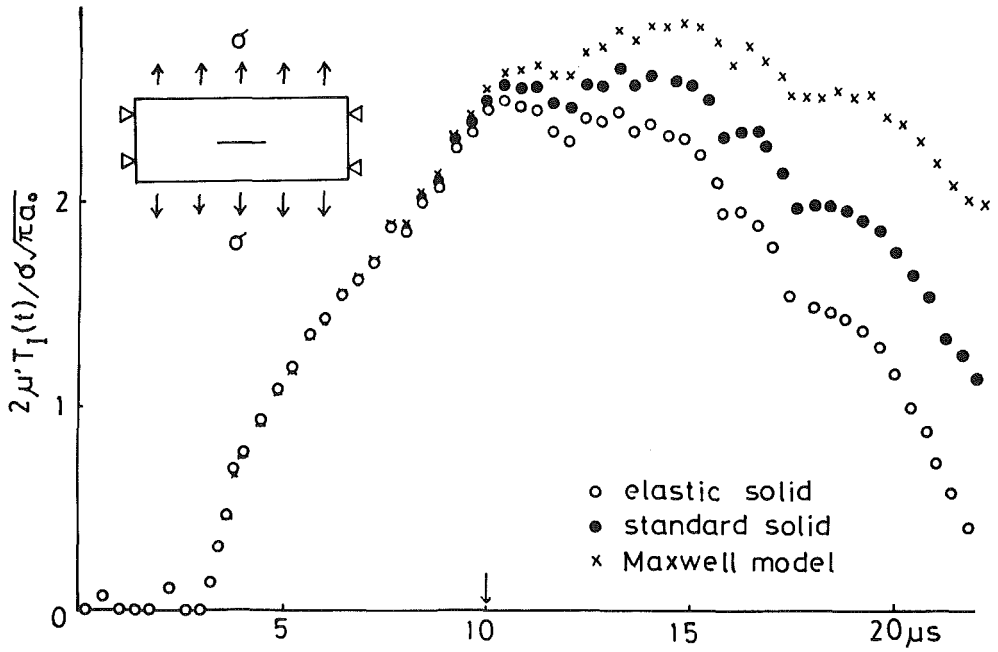


Fig. 7 Time variation of normalized Mode I strain-intensity factor (Path No. 5)

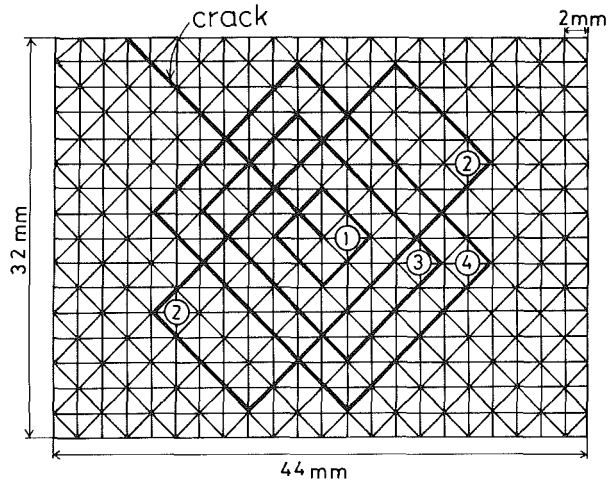


Fig. 8 Finite-element grid pattern (399 nodes, 704 elements) and paths for $\hat{J}$-integral, $\rho = 2.45 Mg/m^3$, $\nu = 0.25$, $\mu' = 29.4\ GN/m^2$, $a_0 = 22.63mm$; $\alpha = \beta = 0$ (elastic solid), $\alpha = 0.2 \times 10^5\ s^{-1}$, $\beta = 0.4 \times 10^5\ s^{-1}$ (standard solid), $\alpha = 0$, $\beta = 0.4 \times 10^5\ s^{-1}$ (Maxwell model)

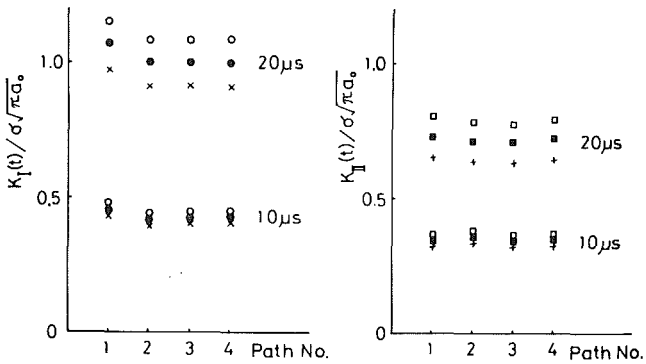


Fig. 9 Path-independence of $\hat{J}^I$ and $\hat{J}^{II}$ (mixed mode); elastic solid (○, □), standard solid (●, ■), Maxwell model (x, +)

Downloaded 01 May 2010 to 171.66.16.249. Redistribution subject to ASME license or copyright; see http://www.asme.org/terms/Terms_Use.cfm

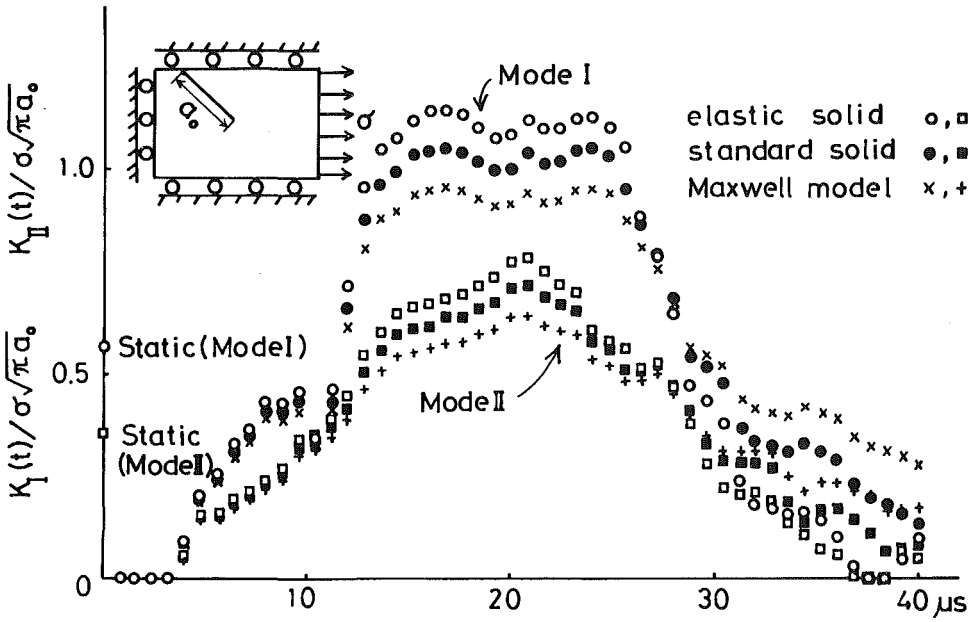


Fig. 10 Time variation of normalized dynamic stress-intensity factors for mixed mode (Path No. 3)

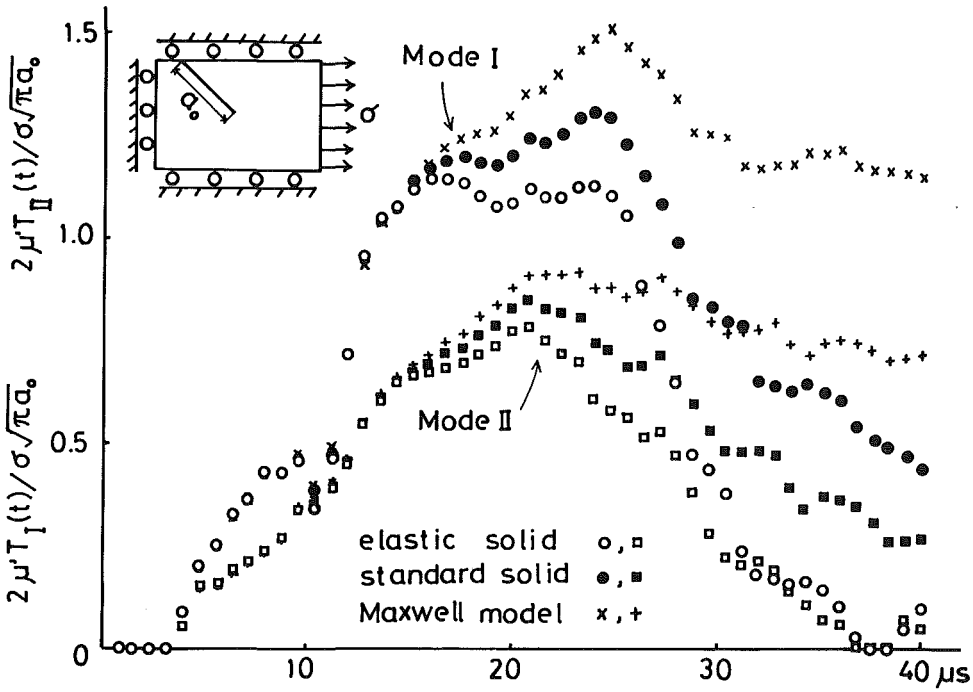


Fig. 11 Time variation of strain-intensity factors for mixed mode (Path No. 3)

$\sqrt{\pi a_0}$ which are calculated from the $\hat{J}$-value over the path No. 5. The analytical results for a finite crack in an elastic plate by Thau and Lu [8] and results by the singular element method are also shown. The symbol (↓) on the time axis denotes the time-of-arrival at the crack tip of the dilational stress waves reflected by the upper and lower boundaries. The results by Thau and Lu are applicable only to this time. It is observed that the present method provides the same accuracy as the method with the singular element. The static solution which is independent of α and β in this case, is also shown. Figure 7 shows the normalized strain-intensity factor $2\mu' T_1(t)/\sigma\sqrt{\pi a_0}$ ($K_1(t) = 2\mu' T_1(t)$ for the elastic problem). It is observed that because of viscosity, the maximum values of the stress-intensity factors for the viscoelastic solids are smaller than those for the elastic solid while the strain intensity factors display the reverse tendencies.

It is generally accepted that the energy-release rate is an important physical quantity to investigate the crack growth and especially in the linear elastic fracture mechanics the fracture criterion using the stress-intensity factor is equivalent to the energy-release rate concept. However, equation (4) indicates that this equivalence does not hold generally for viscoelastic solids. Further studies would be necessary before any definite conclusion can be drawn concerning the crack initiation problem of a viscoelastic material.

(2) Mixed Mode Problem. The problem contains a crack slanted at 45° to the boundary of a rectangular plate loaded by uniform end tension σ at time $t = 0$ with the Heaviside function time-dependence. The element grid pattern and paths over which $\hat{J}^M$ ($M = 1, 2$) are evaluated are shown in Fig. 8. Figure 9 shows the dynamic stress-intensity factors calculated

Downloaded 01 May 2010 to 171.66.16.249. Redistribution subject to ASME license or copyright; see http://www.asme.org/terms/Terms_Use.cfm

from $\hat{J}^M$ for various paths. Those values are path-independent of the path selected to compute $\hat{J}^M$ as anticipated theoretically. Figures 10 and 11, respectively, show the time variation of the dynamic stress-intensity factors and the strain-intensity factors obtained from $\hat{J}^M$-value over the path No. 3. A similar tendency to pure mode problems is observed in these figures.

Summary

A method for estimating the dynamic stress-intensity factor of a viscoelastic solid has been developed by using the finite-element method and the path (area)-independent $\hat{J}$-integral and some examples of its use have been demonstrated.

References

1 Aoki, S., et al., "Elastodynamic Analysis of Crack by Finite-Element Method Using Singular Element," *International Journal of Fracture*, Vol. 14, 1978, pp. 59-68.

2 Kishimoto, K., Aoki, S., and Sakata, M., "Computer Simulation of Fast Crack Propagation in Brittle Material," *International Journal of Fracture*, Vol. 16, 1980, pp. 3-13.

3 Aoki, S., et al., "Dynamic Analysis of Cracked Linear Viscoelastic Solids by Finite-Element Method Using Singular Element," *International Journal of Fracture*, Vol. 16, 1980, pp. 97-109.

4 Kishimoto, K., Aoki, S., and Sakata, M., "Dynamic Stress-Intensity Factors Using J-Integral and Finite-Element Method," *Engineering Fracture Mechanics*, Vol. 13, 1980, pp. 387-394.

5 Kishimoto, K., Aoki, S., and Sakata, M., "On the Path-Independent Integral-$\hat{J}$," *Engineering Fracture Mechanics*, Vol. 13, 1980, pp. 841-850.

6 Ishikawa, H., Kitagawa, H., and Okamura, H., "J-Integral of a Mixed Mode Crack and Its Application," *Proceedings of the Third International Conference on Mechanical Behavior of Materials*, eds., Miller, K. J., and Smith, R. F., Pergamon, Vol. 3, 1980, pp. 447-455.

7 Newmark, N. M., "A Method of Computation for Structural Dynamics," *Transactions of the American Society of Civil Engineers*, Vol. 127, 1962, pp. 1406-1435.

8 Thau, S. A., and Lu, T. H., "Transient Stress-Intensity Factors for a Finite Crack in an Elastic Solid Caused by a Dilatational Wave," *International Journal of Solids and Structures*, Vol. 7, 1971, pp. 731-750.

Downloaded 01 May 2010 to 171.66.16.249. Redistribution subject to ASME license or copyright; see http://www.asme.org/terms/Terms_Use.cfm

A Modified Strain-Energy Density Criterion Applied to Crack Propagation

P. S. Theocaris
Mem. ASME

N. P. Andrianopoulos

Department of Theoretical and Applied Mechanics, The National Technical University of Athens, Zographou, Athens 624, Greece

An exact solution is presented to the problem of the crack-initiation direction by applying the minimum strain-energy density criterion in the case of a slant crack loaded uniaxially. The exact expressions of stresses, obtained from Muskhelishvili's complex functions, are used in evaluating strain energy. Although the position of direction of the minimum density (ϑ_m) was accepted as the probable direction of the next kink of a propagating crack, the mean value of the strain-energy density is also introduced, instead of its minimum value, in the role of the critical quantity for crack initiation. Interesting results were derived for the behavior of this quantity concerning the phenomenon of bifurcation. The ratio of the mean-energy densities above and below the expected path of propagation is introduced as a second factor influencing the exact value of angle ϑ_m of propagation.

Introduction

Several theories have been proposed to describe the manner in which a crack will propagate. Such theories attempt to link the principles of fracture mechanics to the practical problem of fracture. Griffith [1] was the first to discuss the conditions of crack-propagation initiation. Several decades later, Erdogan and Sih [2] investigated the problem of propagation of a slant crack. They made the assumption that the crack will propagate in a direction perpendicular to the maximum value of the tensile stress σ_ϑ. They stated that this direction coincides with the plane of zero-shear stress, $\tau_{r\vartheta} = 0$, i.e., with the plane along which σ_ϑ becomes the principal stress σ_1. They also stated that the crack will propagate to the assigned angle when the value of σ_ϑ (or σ_1) reaches a critical value, which is a material constant. But in the case of uniaxial tensile load, the condition $\sigma_\vartheta \geq \sigma_{\text{crit}}$ is equivalent to $\sigma_1 \geq \sigma_{\text{crit}}$ or $(\sigma_1 - \sigma_2) \geq \sigma'_{\text{crit}}$. The last condition corresponds to the classical Tresca failure criterion.

After this criterion was developed, some energy concepts were also introduced. Again Sih [3] had introduced the idea that the crack will propagate when the minimum strain-energy density around its tip reaches a critical value and that the direction of this minimum density coincides with the expected angle of propagation. He called this criterion the *S*-criterion. The *S*-criterion conceptually is an expansion of the classical *Mises* failure criterion. The only difference between them is that the *S*-criterion considers both parts (*distortional* and *dilatational*) of the strain energy, whereas the Mises criterion only considers its distortional part.

However, it is worthwhile saying that both failure criteria (Tresca and Mises) are valid for ductile materials, whereas the respective fracture criteria are referred to brittle fratures and, so far, there is no other fracture criterion corresponding to the Mohr-type failure criterion which would be more suitable for brittle frature. Nevertheless, both fracture criteria give, more or less, accurate results, lying between the limits of experimental scattering.

It can be said that there is no physical reason supporting the restriction, holding for both criteria, that the core radius r is constant. There must be a low limit of the r-value, but this limit may depend on ϑ if, for example, we consider a small yield zone around the crack tip. Nevertheless, this problem is thoroughly discussed elsewhere [4]. On the other hand, even in the case when $r = \text{const}$, the exact value of r strongly affects the values of stresses around the crack tip and thus the corresponding critical values of σ_ϑ or S_m. Obviously, these critical values can be measured experimentally by recording the fracture load of specimens for different values of angle β. values of angle β.

It can be said, holding for the *S*-criterion, that although the condition $S(\vartheta_m) = S_{\text{cr}}$ is correct from a mathematical point of view, its physical reasoning is somehow peculiar. Namely, this condition must be written as $S(\vartheta_m) \geqq S_{\text{cr}}$. But as the load increases, this condition is first fulfilled at the vicinity of the maximum values of the *S*-distribution, and, last, at the desired angle ϑ_m. So we have to suppose that either the crack possesses a *thinking ability*, since it waits to establish a certain condition only in a certain direction, ignoring any other direction, or to replace this condition by another more physical one. For obvious reasons, we prefer the second alternative and therefore must somehow adapt this condition to a physically sound assumption. This subject will be discussed later in the paper.

Although both criteria roughly give acceptable results, especially for large values of angle β, they diverge

Contributed by the Applied Mechanics Division for publication in the JOURNAL OF APPLIED MECHANICS.

Discussion on this paper should be addressed to the Editorial Department, ASME, United Engineering Center, 345 East 47th Street, New York, N.Y. 10017, and will be accepted until two months after final publication of the paper itself in the JOURNAL OF APPLIED MECHANICS. Manuscript received by ASME Applied Mechanics Division, April, 1981; final revision, July 1981.

Copyright © 1982 by ASME
Downloaded 01 May 2010 to 171.66.16.249. Redistribution subject to ASME license or copyright; see http://www.asme.org/terms/Terms_Use.cfm

significantly from the experimental data for small β. Many attempts [5-8] were made to improve the accuracy of the theoretical predictions. The common characteristic of these attempts is that more terms should be included in the expressions of stresses to either increase the accuracy of these expressions, or to introduce new parameters (namely, to increase the ability to modify), like the value of r or the value of the coefficient of the second term in the asymptotic expansions of the components of stresses. As a result, these attempts had to modify the obtained theoretical predictions to the correct direction.

The final step of this method should be the introduction of all the terms in the series expansions of stresses into the equations of the criteria. The main puprose of this paper is the presentation of an *exact solution*, restricted, for simplicity, in the case of the S-criterion.

Theoretical Considerations

Referring to the geometry of Fig. 1, the stress field can be described by Muskhelishvili's [9] complex functions:

$$\left.\begin{aligned}\Phi(z)&=\frac{1}{2}(2\Gamma+\bar{\Gamma}')\frac{z}{(z^2-\alpha^2)^{1/2}}-\frac{1}{2}\bar{\Gamma}'\\ \Omega(z)&=\frac{1}{2}(2\Gamma+\bar{\Gamma}')\frac{z}{(z^2-\alpha^2)^{1/2}}+\frac{1}{2}\bar{\Gamma}'\end{aligned}\right\}\quad(1)$$

where

$$\frac{1}{2}\bar{\Gamma}'=-\frac{\sigma_{Y,0}}{4}(1-k)e^{2i\beta}$$

$$\frac{1}{2}(2\Gamma+\bar{\Gamma}')=\frac{\sigma_{Y,0}}{4}[(1-e^{2i\beta})+k(1+e^{2i\beta})]$$

and k is the biaxiality ratio $\sigma_{X,0}/\sigma_{Y,0}$ at infinity.

The corresponding stresses are given by:

$$\left.\begin{aligned}&\sigma_X+\sigma_Y=4\mathrm{Re}[\Phi(z)]\\ &\sigma_Y-\sigma_X+2i\tau_{XY}=2[(\bar{z}-z)\Phi'(z)-\Phi(z)+\bar{\Omega}(z)]\end{aligned}\right\}\quad(2)$$

The strain-energy density is expressed by:

$$T=\frac{\partial W}{\partial V}=\frac{1}{8G}\left[\eta(\sigma_1+\sigma_2)^2+(\sigma_1-\sigma_2)^2\right]$$

$$=\frac{1}{2G}\left[4\mathrm{Re}^2[\Phi(z)]+|(\bar{z}-z)\Phi'(z)-\Phi(z)+\bar{\Omega}(z)|^2\right]\quad(3)$$

where η is a constant depending on Poisson's ratio ($\eta=1-\nu/1+\nu$) for plane-stress, and $\eta=(1-2\nu)$ for plane-strain conditions). The dilatational component $(\partial W/\partial V)v$ of the total strain energy density is given by:

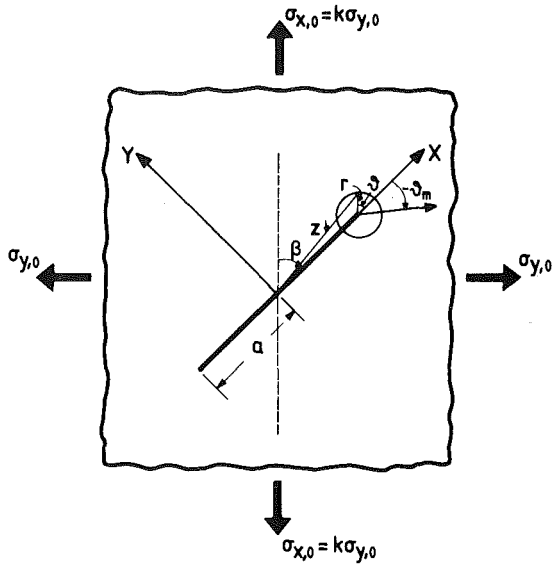


Fig. 1 A slant crack under biaxial load

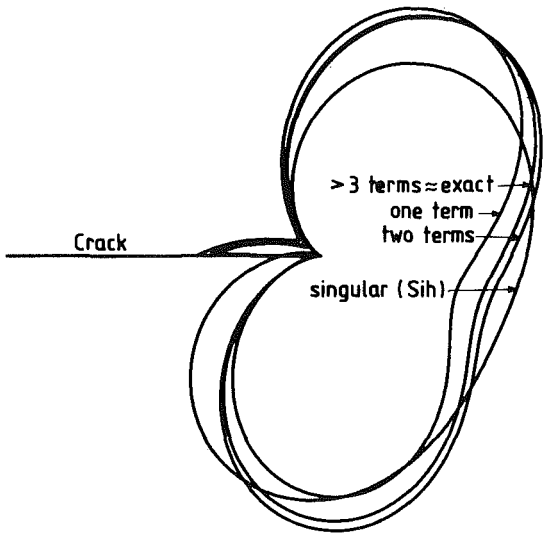


Fig 2 Strain-energy density lobes for β = 75 deg, ν = 0.34, $r/2\alpha$ = 0.05, and various combinations of terms. Constant term Γ' is included.

Nomenclature

E = modulus of elasticity
G = shear modulus
K_I, K_{II} = stress intensity factors
k = biaxiality ratio ($=\sigma_{X,0}/\sigma_{Y,0}$)
(r, ϑ) = polar coordinates around crack-tip
S = strain-energy density reduced to r
$\bar{S}$ = mean value of S
S_{cr} = critical value of S
S_m = minimum value of S
$\bar{S}_1, \bar{S}_2$ = values of $\bar{S}$ at two semilobes
T, T_V, T_D = strain-energy density and its dilatational and distortional components, respectively ($T = S/r$)
r = core region radius
z = complex coordinate
α = half crack-length
β = angle of crack inclination
ϵ = area enveloped by the S-curve
ζ = complex coordinate around crack-tip
ϑ_m = expected angle of propagation
η = Muskhelishvili's constant
ν = Poisson' ratio
$\sigma_\vartheta, \sigma_r, \tau_{r\vartheta}$ = polar stresses around crack-tip
$\sigma_{X,0}, \sigma_{Y,0}$ = stresses at infinity
σ_1, σ_2 = principal stresses around crack-tip
$\Phi(z), \Omega(z)$ = Muskhelishvili's complex stress functions

Downloaded 01 May 2010 to 171.66.16.249. Redistribution subject to ASME license or copyright; see http://www.asme.org/terms/Terms_Use.cfm

$$T_V = \left(\frac{\partial W}{\partial V}\right)_V = \frac{4(1-2\nu)}{3G(1+\nu)} \{\mathrm{Re}[\Phi(z)]\}^2 \tag{4}$$

and the distortional one $(\partial W/\partial V)_D$ by:

$$T_D = \left(\frac{\partial W}{\partial V}\right)_D = \frac{1}{G}\left[\frac{2(1+7\nu)}{3(1+\nu)}\mathrm{Re}^2[\Phi(z)] + |(\bar{z}-z)\Phi'(z) - \Phi(z) + \bar{\Omega}(z)|^2\right] \tag{5}$$

Considering that the quantities expressed by the equations (3)–(5) are evaluated at circles of constant radius r around each crack tip and that $\bar{\Gamma}' = 0$, then these quantities may be reduced to the corresponding S-values.

A typical method to evaluate equations (3)–(5) is to expand the complex functions involved into a Taylor series around the singular point $z = \pm\alpha$ by introducing the variable:

$$\zeta = z - \alpha = re^{i\vartheta} \tag{6}$$

Applying this method we obtain:

$$\left.\begin{aligned}
\Phi(\zeta) &= \frac{1}{2}(2\Gamma+\bar{\Gamma}')\left\{\frac{1}{2}\left(\frac{\zeta}{2\alpha}\right)^{-1/2} + \left(\frac{\zeta}{2\alpha}\right)^{1/2} + \sum_{n=1}^{\infty}(-1)^n\left[\prod_{l=1}^{n}\frac{2l-1}{2(l+2)-4}\right]\left(\frac{\zeta}{2\alpha}\right)^n\right\} - \frac{1}{2}\bar{\Gamma}' \\
\Omega(\zeta) &= \frac{1}{2}(2\Gamma+\bar{\Gamma}')\left\{\frac{1}{2}\left(\frac{\zeta}{2\alpha}\right)^{-1/2} + \left(\frac{\zeta}{2\alpha}\right)^{1/2} + \sum_{n=1}^{\infty}(-1)^n\left[\prod_{l=1}^{n}\frac{2l-1}{2(l+2)-4}\right]\left(\frac{\zeta}{2\alpha}\right)^n\right\} + \frac{1}{2}\bar{\Gamma}' \\
\Phi'(\zeta) &= \frac{1}{2}(2\Gamma+\bar{\Gamma}')\left\{-\frac{1}{8\alpha}\left(\frac{\zeta}{2\alpha}\right)^{-3/2} + \frac{3}{16\alpha}\left(\frac{\zeta}{2\alpha}\right)^{-1/2} - \frac{3}{8\alpha}\left(\frac{\zeta}{2\alpha}\right)^{1/2} + \right. \\
&\left. + \sum_{n=2}^{\infty}(-1)^n\left[\prod_{l=1}^{n}\frac{2l-1}{2(l+2)-4}\right]\left[\frac{n+1/2}{2\alpha}\left(\frac{\zeta}{2\alpha}\right)^{n-1/2} + \frac{n-1/2}{4\alpha}\left(\frac{\zeta}{2\alpha}\right)^{n-3/2}\right]\right\}
\end{aligned}\right\} \tag{7}$$

The simplest and most common way to evaluate the stresses needed is to consider only the terms having negative exponents and to ignore the constant term $1/2\ \bar{\Gamma}'$. The solution obtained is the so-called *singular solution*. It must be emphasized that the singular solution consists of only a part of the first term of the Taylor series.

To expose the role of introducing more terms of stresses into the energy expressions, which affect both values of ϑ_m and S_m, the values of S for $\beta = 75$ deg have been plotted in Fig. 2. In this plot, the difference between the exact and the singular value of ϑ_m is of the order of 40 percent and the corresponding difference in S_{ϑ_m} value is of the order of 30 percent. The same result can be concluded from Fig. 3, where the values of ϑ_m, obtained from the singular solution, are plotted versus β together with those obtained from the exact solution. For comparison purposes, in Fig. 4, the three curves ϑ_m versus β, obtained from the exact expressions for three indicative values of $r/2\alpha$, are plotted along with the singular curve. A common characteristic of all three exact curves is that for $\beta < 45$ deg they give absolutely larger predictions for ϑ_m, and for $\beta > 45$ deg absolutely smaller predictions than the singular (Sih's) curve. This behavior is in better agreement with the experimental results.

In order to overcome the physical peculiarity of the condition $S(\vartheta_m) \geqq S_{cr}$ previously indicated, we introduce a new parameter, the *mean strain-energy density* $(\bar{S})$, around the crack tip.

It seems natural that the whole energy-balance around the crack tip is of more importance than a specific value in a specific direction. Really, one can imagine that there must be a scalar lower threshold of energy density beneath which the crack cannot propagate. When this threshold is reached, the crack propagates along the easier path, i.e., the direction of ϑ_m.

This mean strain-energy density $\bar{S}$ is expressed by:

$$\bar{S} = \frac{1}{2\pi}\int_0^{2\pi} S(\vartheta)\,d\vartheta \tag{8}$$

From a physical point of view, $\bar{S}$ is the radius of the circle around the crack-tip, which is equivalent to the strain-energy density lobe. This quantity possesses the desired property of undirectionality, represents accurately the energy concentration around the crack-tip, and can serve as a threshold for crack initiation.

Now the *modified strain-energy density criterion* can be expressed by the following two hypotheses:

Hypothesis A. A crack propagates when the mean-strain energy density around its tip is larger than a critical value, that is:

$$\bar{S} \geqq \bar{S}_{cr}$$

Hypothesis B. The direction of crack propagation coincides with the direction ϑ_m of the minimum strain energy density around the crack tip, that is:

$$\frac{\partial S}{\partial \vartheta} = 0 \qquad \vartheta = \vartheta_m$$

Nevertheless, it also seems natural that the direction of the minimum strain-energy density is of primary importance in defining the expected angle ϑ_m of propagation, but not the only one. The distribution of energy density in the vicinity of ϑ_m is always insensitive to small variations of ϑ around ϑ_m (Fig. 5). If for some reason the crack fails to expand along the ϑ_m-direction, one may expect that the crack will divert to the side of relatively lower strain-energy density area. Following this reasoning, the whole strain-energy density lobe around the crack-tip was divided into two areas, as indicated in Fig. 5, and the mean value of the strain-energy density for either of the sectors was computed. The corresponding mean densities were denoted by $\bar{S}_1$ and $\bar{S}_2$ for the upper and lower semilobes, respectively, and they are given by:

$$\bar{S}_1 = \frac{1}{\pi - \vartheta_m}\int_{\vartheta_m}^{\pi} S(\vartheta)\,d\vartheta \qquad \bar{S}_2 = \frac{1}{\pi + \vartheta_m}\int_{-\pi}^{\vartheta_m} S(\vartheta)\,d\vartheta \tag{9}$$

In a previous paper [10], a similar attempt was made by evaluating the expression:

$$\epsilon = \int_{\pi-\vartheta_m}^{\pi+\vartheta_m} S^2(\vartheta)\,d\vartheta$$

which corresponds to the area enveloped by the curve $S = S(\vartheta)$. Instead of ϵ, we preferred to introduce $\bar{S}$ measured in energy density units, because it is the same physical quantity as S and can fulfill in a more natural way the requirements of the modified S-criterion introduced here.

Results and Discussion

The modified strain-energy density criterion was applied to the case described in Fig. 1 in order to derive the expected

Downloaded 01 May 2010 to 171.66.16.249. Redistribution subject to ASME license or copyright; see http://www.asme.org/terms/Terms_Use.cfm

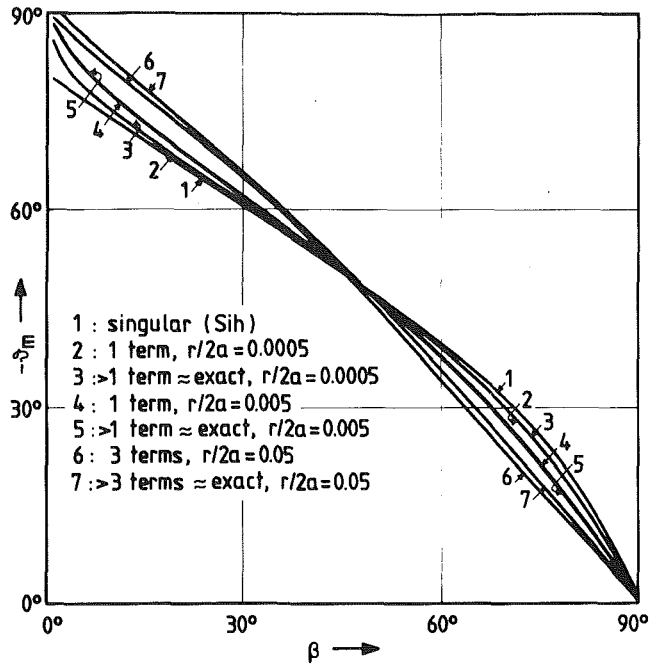


Fig. 3 Expected angle ϑ_m of propagation versus β for three different values of $r/2\alpha$ ($= 0.0005, 0.005, 0.05$) and various combinations of terms compared to singular (Sih) solution. Constant term Γ' is included.

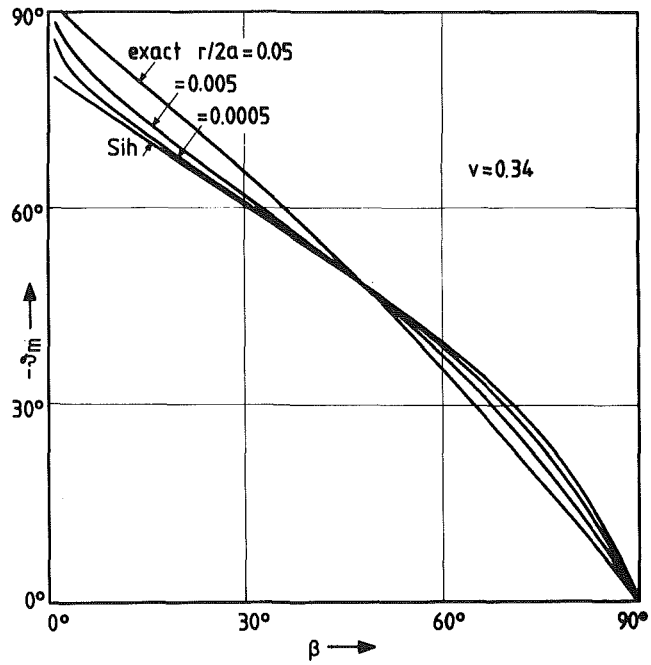


Fig. 4 Expected angle ϑ_m of propagation versus β for three different values of $r/2\alpha$ ($= 0.005, 0.005, 0.05$) when the exact expressions of stresses are used, as compared to the singular (Sih) solution

angles of propagation and the corresponding values of $\bar{S}_{cr}$. To achieve this, we put:

$$z = \alpha\left(1 + \frac{r}{\alpha} e^{i\vartheta}\right) \tag{10}$$

where α is the half-crack length and (r,ϑ) the polar coordinates around the crack-tip. The ratio $r/2\alpha$ was equal to $r/2\alpha = 0.05$.

Although the exact value of this ratio is unknown, we have two reasons to select this rather large value. The first is that, if some yielding exists, its radius would be of the same order. The second, as was pointed out in [11] and [12], is that a good approximation of the ratio $r/2\alpha$ is the radius of the initial

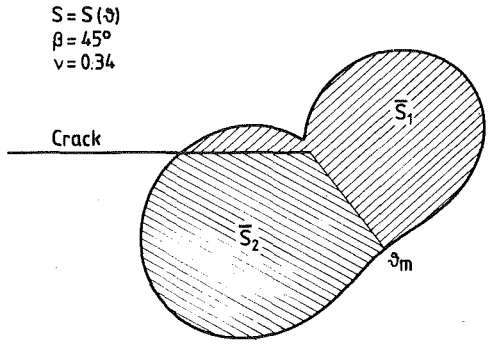


Fig. 5 The two semilobes into which the whole lobe of strain-energy density S is divided in order to compute the relative mean values $\bar{S}_1$ and $\bar{S}_2$

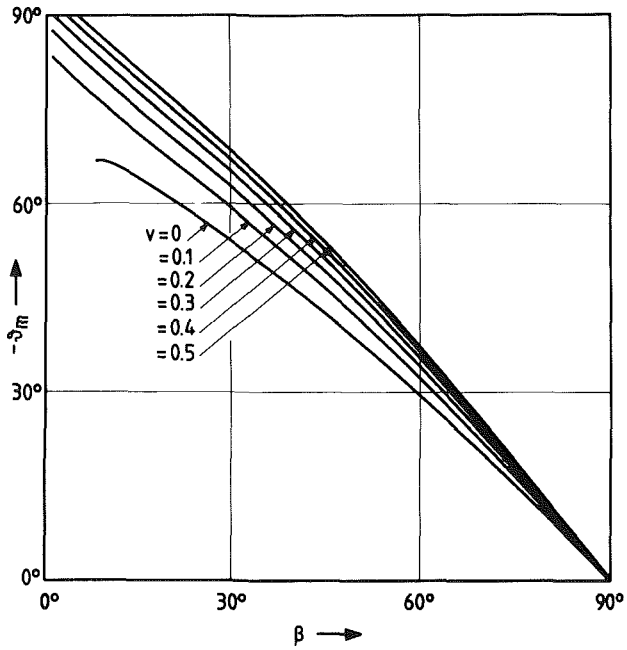


Fig. 6 Expected angle ϑ_m of propagation versus β for $r/2\alpha = 0.05$ and Poisson's ratios $\nu = 0$, 0.1, 0.2, 0.3, 0.4, and 0.5, when the exact formulas are used

curve of the caustics, which is roughly of the same order. Really, the radius of the initial curve of the caustics serves as an envelope for the highly disturbed area very close to the crack-tip. Thus, the radius of this curve is long enough to avoid the rather unknown disturbed area of plastic deformations, but short enough to be dominated by the stress state at the crack-tip.

The expected angles ϑ_m of crack expansion are plotted in Fig. 6 versus angle β for values of Poisson's ratios equal to $\nu = 0$, 0.1, 0.2, 0.3, 0.4, and 0.5. As can be seen from this plot for $\nu \geqq 0.3$ and for small values of angle β, $|\vartheta_m| > 90$ deg. At first, this result seems strange, since no experimental evidence confirms it. But one must remember that the actual angle ϑ_m is also affected by the secondary factor, i.e., the relative value of energy density in the two sectors of Fig. 5. In the case when this factor does not resolve this phenomenon, one is obliged to either accept the necessary results of a theory and perform more accurate experiments or to reject the theory. However, because the S-criterion is well established on a physical basis, for the time being, it seems unrealistic to reject it.

The ratio $\bar{S}_1/\bar{S}_2$ is plotted versus the angle β in Fig. 7 for the same six values of Poisson's ratio. This ratio, starting from $\bar{S}_1/\bar{S}_2 = 1$ at $\beta = 0$ deg, decreases rapidly and, passing

Downloaded 01 May 2010 to 171.66.16.249. Redistribution subject to ASME license or copyright; see http://www.asme.org/terms/Terms_Use.cfm

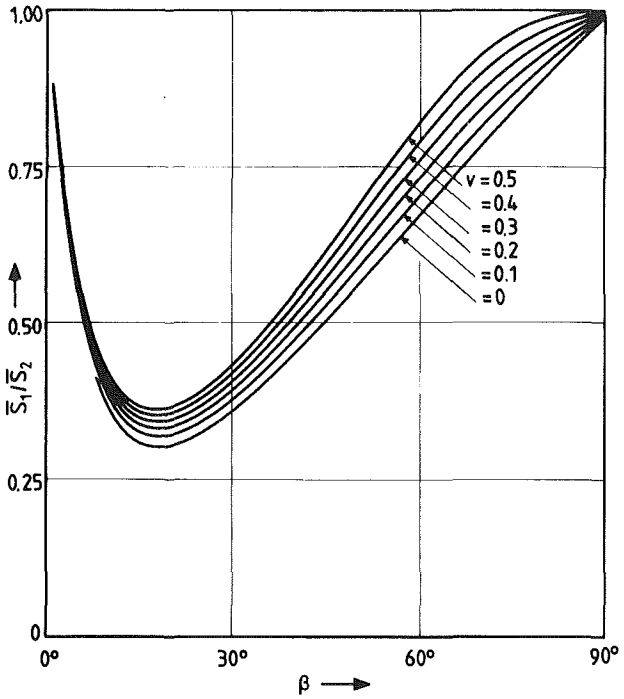


Fig. 7 The ratio of the mean values of strain-energy density of the two semilobes above and below the direction of propagation versus angle β for Poisson's ratio ν = 0, 0.1, 0.2, 0.3, 0.4, and 0.5

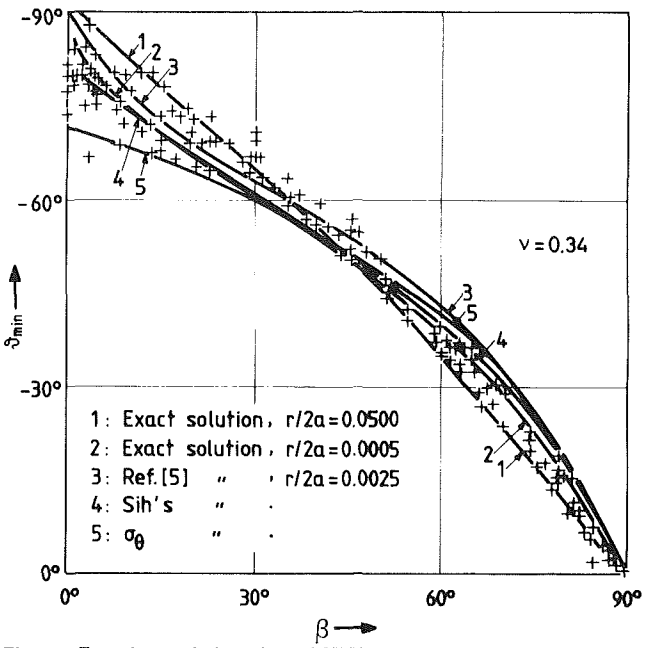


Fig. 8 Experimental data from PMMA (ν = 0.34), as compared to curves $\beta = \vartheta_m$ obtained from the singular, the exact (with $r/2\alpha$ = 0.05 and 0.0005) and Williams and Ewing (with $r/2\beta$ = 0.0025) solutions

through a minimum at about β = 18 deg, increases rather smoothly, reaching its initial value at β = 90 deg. One can conclude from these curves that the second factor $(\bar{S}_1/\bar{S}_2)$ always tends to decrease ϑ_m absolutely and this effect is stronger when $\beta \leqq 18$ deg. It means that values of $|\vartheta_m| > 90$ deg obtained by considering the first factor (S_m) may only be absolutely smaller, a fact that appears frequently in the experiments.

A second remark on these curves is that, since for small angles β the ratio $\bar{S}_1/\bar{S}_2$ is very sensitive, for these angles one may expect strong experimental scattering due to inaccurate definition of angle β. This scattering was observed in the praxis as is shown in Fig. 8.

For the reasonable question, how the second factor affects quantitively the value of ϑ_m, the answer is yet unknown. A probable way to answer this question is to establish an approximate function $\Delta\vartheta_m = \Sigma\alpha_i(\bar{S}_1/\bar{S}_2)^i$ and define the unknown coefficients α_i experimentally.

In Fig. 8, the exact curves for $r/2\alpha$ = 0.05 and 0.0005 of the expected values for ϑ_m are plotted versus β for reference and comparison purposes, together with the original Sih's curve (both for ν = 0.34), and the approximate curve of Williams and Ewing [5]. The experimental points shown were obtained from references [2] and [7].

The values of $\bar{S}/(\bar{S}_\infty \times r/2\alpha)$ are plotted against angle β in Fig. 9. The quantity $\bar{S}_\infty$ is the mean strain-energy density far from the crack and for the case of uniaxial tension expressed by:

$$\bar{S}_\infty = \frac{\sigma_{Y,0}^2}{2E} \tag{11}$$

An important observation in these plots is that at about β = 72 deg, a maximum appears contrary to the monotonous increase of the already well-established corresponding curves of S_m [3]. This weak maximum implies that it is easier for a crack to expand when β = 72 deg, than when β = 90 deg, or at least it is equally difficult. This phenomenon should be expected, since a monotonously increasing curve of S_m or S implies that the contribution of K_{II} in the fracture process is

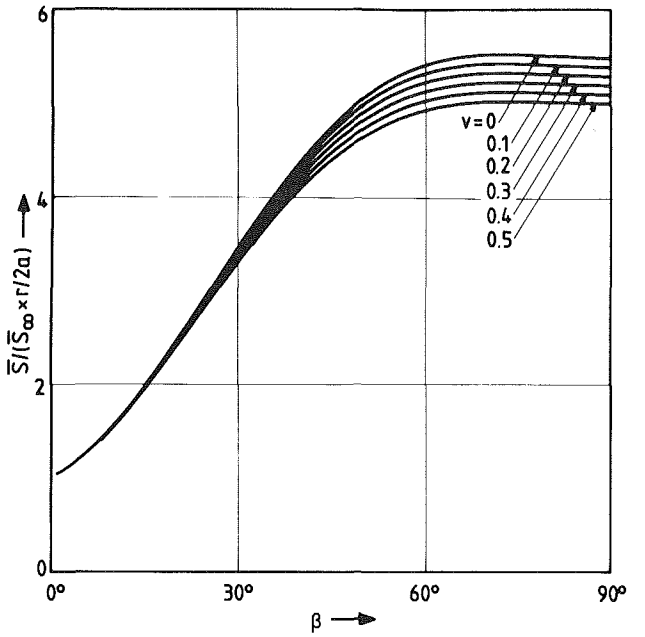


Fig. 9 The reduced value $\bar{S}/(\bar{S}_\infty \times r/2\alpha)$ of the mean value of the strain-energy density versus β, for values of Poisson's ratio ν = 0, 0.1, 0.2, 0.3, 0.4, and 0.5

limited only in modifying the value of ϑ_m. But the existence of K_{II} also implies an offer of energy from a second channel, except the channel represented by K_I. The two energy channels (K_I and K_{II}) are mutually competitive and the calculations resulted in the curves of Fig. 9 show that the maximum of the whole energy offered to the material occurs when β = 72 deg. A similar peak phenomenon at β = 70 deg was indicated by Sih and Kipp [13], where it was pointed out that, while the experimental evidence with plane stress-tensile specimens, as well as the two-term approximation solution by Williams and Ewing [5], indicate this peak of the normalized applied loads, Sih's solution [3], based on the S-criterion, does not present such peak.

The position of $\bar{S}$-maximum also dictates that if the ex-

Downloaded 01 May 2010 to 171.66.16.249. Redistribution subject to ASME license or copyright; see http://www.asme.org/terms/Terms_Use.cfm

ternal offer of energy is much more than what is needed for crack propagation, resulting in a crack bifurcation phenomenon, the easier propagation direction for the two new branches may be somewhere between 0 and 18 deg from the direction of the mother crack. On the other hand, theoretical predictions for already bifurcated cracks [14] have shown that the two branches tend to expel each other when the angle between them is small. Thus, the most probable angle of bifuraction must lie close to 18 deg. This result is in good agreement with previous experimental results [15, 16].

Conclusions

In the present paper, the exact expressions for stresses were used to evaluate the strain-energy density around the crack-tip in the case of an infinite cracked plate under uniaxial tensile load. Generalized plane-stress conditions were assumed. It was pointed out that the values of the expected angle ϑ_m of crack propagation differ significantly from its corresponding values when the singular expressions of stresses are used. The introduction of the exact expressions of stresses, as given by Muskhelishvili's complex functions, is preferable instead of using the a priori "erroneous" one singular or more term approximations commonly used. Also, the computer time needed for exact calculations is comparable to that of the singular one and much less than calculations with more than one term.

On the other hand the ϑ_m predictions obtained from the exact solution do not depend linearly, contrary to the singular solution, on the distance r from the crack-tip, where the evaluation of the strain-energy density is performed. This solution has the advantage that ϑ_m varies depending on the exact value of r, which must be different for each material. In this paper, we propose a value of r comparable to the radius of the yielding zone around the crack-tip or equivalent to the radius of the *initial curve* of the experimentally obtained caustics.

A modified version of the S-criterion was proposed in the sense that the minimum value of strain-energy density S was replaced by its mean value $\bar{S}$ in the role of the critical quantity. This modification removes a logical paradox in the original S-criterion and permits an insight to the complex phenomenon of bifurcation. Indeed, contrary to the minimum strain-energy density S, its mean value $\bar{S}$ possesses a weak maximum at about $\beta = 72$ deg, which corresponds to a bifurcation angle of about 18 deg. This bifurcation angle is in satisfactory agreement to experimental evidence.

Finally, a second factor affecting the value of ϑ_m was introduced. This is the ratio of the mean values of strain-energy densities of the two semilobes above and below the direction of ϑ_m in the strain-energy density distribution. It seems logical that if, for some reason, the crack fails to propagate along the ϑ_m-direction, it will prefer to diverge to the side of the relatively smaller strain-energy density concentrations. Although, for the time being, there is not quantitative description of the influence of this ratio on the value of ϑ_m, experimental evidence, especially for small values of the angle β, shows that this influence must exist.

References

1 Griffith, A. A., "The Phenomena of Rupture and Flow in Solids," *Phi. Trans. Royal Soc. London, A,* Vol. 221, 1921, pp. 163–198.

2 Erogan, F., and Sih, G. C., "On the Crack Extension in Plates Under Plane Loading and Transverse Shear," ASME *Journal of Basic Engineering,* Vol. 85, 1963, pp. 519–527.

3 Sih, G. C., "Some Basic Problems in Fracture Mechanics and New Concepts," *Eng. Fract. Mech.,* Vol. 5, 1973, pp. 365–377.

4 Theocaris, P. S., and Andrianopoulos, N. P., "The Mises Elastic-Plastic Boundary as the Core Region in Fracture Criteria," in press. *Eng. Fract. Mech.,* June 1981.

5 Williams, J. G.. and Ewing, P. D., "Fracture Under Complex Stress—The Angled Crack Problem," *Int. J. Fract. Mech.,* Vol. 8, 1972, pp. 441–446.

6 Cotterell B., "On Brittle Fracture Paths," *Int. J. Fract. Mech.,* Vol. 1, 1965, pp. 96–103.

7 Eftis, J., and Subramonian, N., "The Inclined Crack Under Biaxial Load," *Eng. Fract. Mech.,* Vol. 10, 1978, pp. 43–67.

8 Ewing, P. D., Swedlow, J. L., and Williams, J. G., "Further Results on the Angled Crack Problem," *Int. J. Fract.,* Vol. 12, 1976, pp. 85–93.

9 Muskhelishvili, N. I., *Some Basic Problems of the Mathematical Theory of Elasticity,* Noordhoff, Groningen, 1953.

10 Theocaris, P. S., and Papadopoulos, G., "The Distribution of the Elastic Strain Energy Density at the Crack-Tip for Fracture Modes K_I and K_{II}." Accepted for publication in the *Int. J. Fract.,* Dec. 1980.

11 Theocaris, P. S., "The Caustics as a Means to Define the Core Region in Brittle Fracture." *Eng. Fract. Mech.,* Vol. 14, 1981, pp. 353–362.

12 Theocaris, P. S., "Experimental Determination of the Core Region in Mixed-Mode Fracture." *Proc. U.S.-Greece Symposium on Mixed-Mode Crack Propagation,* eds., G. C. Sih and P. S. Theocaris, Sijthoff and Noordhoff, 1980.

13 Sih, G. C., and Kipp, M. E., Discussion on reference [5], *Int. J. Fract.,* Vol. 10, 1974, pp. 261–265.

14 Theocaris, P. S., and Andrianopoulos, N. P., "Propagation Predictions in Branched Cracks by the Strain-Energy Density Criterion," submitted for publication to the *J. Mech. Phys. Solids,* Oct. 1980.

15 Theocaris, P. S., "Complex Stress-Intensity Factors at Bifuracated Cracks," *J. Mech. Phys. Solids,* Vol. 20, 1972, pp. 265–279.

16 Kalthoff, J. F., "On the Propagation Direction in Bifuracted Cracks," *Dynamic Crack Propagation,* ed., G. C. Sih, Noordhoff, 1973, pp. 449–458.

Downloaded 01 May 2010 to 171.66.16.249. Redistribution subject to ASME license or copyright; see http://www.asme.org/terms/Terms_Use.cfm

Complex Stress Intensity Factors in Bent Plates With Cracks

P. S. Theocaris

Department of Theoretical and Applied Mechanics, The National Technical University of Athens, 5, K. Zographou Street, Zographou, Athens 624, Greece
Mem. ASME

The experimental method of caustics was applied to the study of asymmetric bending of isotropic cracked plates and to the determination of the complex stress intensity factors (S.I.F's) at the crack tips. It was shown that the method of reflected caustics is convenient for detecting and evaluating both K_I and K_{II} stress intensity factors. Based on the singular approximation of the elastic solution around the crack tip, the theory of formation of the caustics was developed and related to the evaluation of both components of stress intensity factors. It was also shown that the generalized method of caustics, known as the method of pseudocaustics, is a potential and simple method for determining S.I.F's in cracked plates submitted to bending. Experimental evidence with specimens made either of optically inert materials, such as plexiglass, or of any opaque material like steel, and elastically loaded, has corroborated the theoretical results.

Introduction

The experimental determination of the complex stress intensity factor in bending of thin elastic plates, containing a line crack of arbitrary orientation in its interior, is of great interest in fracture mechanics. Williams, in a series of papers [1-3], obtained the stress and deflections in bent cracked plates by using classical fourth-order thin plate theory. Sih, Paris, and Erdogan [4] have modified Williams' equations by introducing a bending stress intensity factor. Based on the Reissner theory of bent plates, Knowles and Wang [5] obtained a more rafinated solution to bending problems by making the assumption that the stress intensity factor is constant through the thickness of the plate. The solution was extended later on to account for the variation of the stress intensity factors due to bending through the thickness of the plate by Sih and Hartranft [6]. An experimental investigation of the crack-tip stress intensity factors in plates under cylindrical bending was given in reference [7] using an indirect method of measuring the bending moment and afterward applying a theoretical formula for determining the critical value of S.I.F., which causes the crack growth.

While classical experimental methods like photoelasticity, moire, holography, and interferometry, are incapable of detecting the influence of bending moments in flexed plates because of either the anihilation of the photoelastic effect by bending stresses, or by the lack of thickness variation by bending moments, exclusively, the method of reflected caustics [8, 9] is capable of evaluating the components of K_I and K_{II} stress intensity factors because, in this method, the caustic is created by the reflected rays at the vicinity of the deflected lips of the crack at its tip. Applying this method, the problem of symmetric bending of a plate containing an internal crack was successfully solved in reference [10] using the method of reflected caustics.

The Method of Caustics

The method of caustics, which was extensively used for the study of the singular behavior of stress fields presenting any type of singularity due either to the geometry of the specimen, or the type of loading, is based on a principle of transformation of the stress singularity to an optical singularity that happens at some distance from the singular stress field. At distance z_0, a reference screen is placed that receives all light rays emitted from a point- or parallel-light source, which are either reflected or refracted from the vicinity of the stress singularity.

This transformation is sensitive to the variation of the elastic stress- and strain-gradient near the singularity, which creates abrupt variations of the slope of the lateral faces of the specimen and significant variations of the refractive index for transparent materials.

By applying the simple laws of reflection or refraction from geometric optics and using the condition of zeroing of the respective Jacobian determinant for the expression of reflections on the deformed surface of the specimen, a relation that defines the existance of singularity in the stress field, we can readily obtain that the system of equations expressing the initial curve on the specimen and its caustic at a reference plane are given by [8]:

i Parametric equations for the caustic:

$$X_1 = \lambda x + 2z_0 \frac{\partial w}{\partial x}$$

$$Y_1 = \lambda y + 2z_0 \frac{\partial w}{\partial y} \qquad (1)$$

Contributed by the Applied Mechanics Division for publication in the JOURNAL OF APPLIED MECHANICS.

Discussion on this paper should be addressed to the Editorial Department, ASME, United Engineering Center, 345 East 47th Street, New York, N.Y. 10017, and will be accepted until two months after final publication of the paper itself in the JOURNAL OF APPLIED MECHANICS. Manuscript received by ASME Applied Mechanics Division, June, 1981; final revision; September 1981.

Copyright © 1982 by ASME
Downloaded 01 May 2010 to 171.66.16.249. Redistribution subject to ASME license or copyright; see http://www.asme.org/terms/Terms_Use.cfm

ii Equation for the initial curve:

$$\begin{vmatrix} \frac{\partial X_1}{\partial x} & \frac{\partial X_1}{\partial y} \\ \frac{\partial Y_1}{\partial x} & \frac{\partial Y_1}{\partial y} \end{vmatrix} = 0 \tag{2}$$

where:

$$\lambda = \frac{z_0 + z_i}{z_i} \tag{3}$$

is the magnification factor of the optical set up (equal to 1 for a parallel light beam) [8].

In these relations, X_1 and Y_1 are the coordinates of the caustic in the deflection field $w(x,y)$ of the plate and z_i is the distance between the focus of the light beam and the specimen. On the other hand, the pseudocaustics are similar curves to caustics, which have, as initial curves on the specimen, its boundaries or any other line in the stress field. Thus, while relations (1) express again the caustic relations, (2) yielding the initial curve, should be replaced by the parametric equation of the boundary of any interior line of the stress field. Thus, the pseudocaustics can provide the same amount of informations as the caustics do, and have the further advantage that the coordinates of the points $P(x, y)$ on the plate are chosen by the experimenter himself. This can be achieved by making thin tracings along the lines desired on the plate. The obtained images of these points on the screen are the pseudocaustics.

Introducing a system of polar coordinates indicated in Fig. 1, equations (1) and (2) become [11]:

$$X_1 = \lambda r\cos\vartheta + 2z_0\left(\frac{\partial w}{\partial r}\cos\vartheta - \frac{1}{r}\frac{\partial w}{\partial \vartheta}\sin\vartheta\right) \tag{4}$$

$$Y_1 = \lambda r\sin\vartheta + 2z_0\left(\frac{\partial w}{\partial r}\sin\vartheta + \frac{1}{r}\frac{\partial w}{\partial \vartheta}\cos\vartheta\right) \tag{5}$$

Moreover, equation (2) for the initial curve becomes:

$$1 + \left(\frac{2z_0}{\lambda}\right)^2 (PQ - R^2) + \frac{2z_0}{\lambda}(P+Q) = 0 \tag{6}$$

where the coefficients P, Q, R are given by:

$$P = \frac{\partial^2 w}{\partial r^2} \tag{7}$$

$$Q = \frac{1}{r^2}\frac{\partial^2 w}{\partial \vartheta^2} + \frac{1}{r}\frac{\partial w}{\partial r} \tag{8}$$

$$R = \frac{1}{r}\frac{\partial^2 w}{\partial r \partial \vartheta} - \frac{1}{r^2}\frac{\partial w}{\partial \vartheta} \tag{9}$$

The form and the dimensions of the curve determined by equations (4) and (5) together with equation (6) depend on the stress field near the crack tip (or any other singularity) and they will be used for experimental determination of the complex stress intensity factors.

Caustics Formed by a Mixed-Mode Deformation in Bent Cracked Plates

We now investigate the caustics obtained from reflected rays at the tip of a crack contained in an elastic plate submitted to bending. Consider an infinite orthogonal plate with parallel reflective lateral faces, submitted to two independent bending moments M_x and M_y and containing a through-the-thickness crack of length a in its middle (Fig. 1). The stresses at the crack tips possess singularities of the same order either according to the Kirchoff classical fourth-order theory, or according to the Reissner sixth-order theory [5]. However, the limiting values of stresses near the vertex of the crack differ between the two theories and they are expressed by:

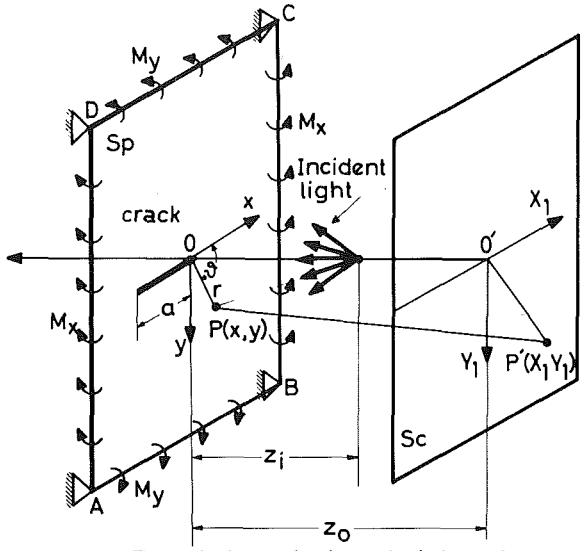


Fig. 1 The optical setup for the method of caustics

i For the Kirchoff-Williams fourth-order theory of bending:

$$\sigma_{x_{b_0}} \simeq -\frac{1-\nu}{3+\nu}\sigma(2r)^{-1/2}\left(\frac{3}{4}\cos\frac{\vartheta}{2} + \frac{1}{4}\cos\frac{5\vartheta}{2}\right)$$

$$\sigma_{y_{b_0}} \simeq \frac{1}{3+\nu}\sigma(2r)^{-1/2}\left(\frac{11+5\nu}{4}\cos\frac{\vartheta}{2} + \frac{1-\nu}{4}\cos\frac{5\vartheta}{2}\right)$$

ii For the Reissner sixth-order theory:

$$\sigma_{x_b} \simeq \frac{1+\nu}{3+\nu}\sigma(2r)^{-1/2}\left(\frac{3}{4}\cos\frac{\vartheta}{2} + \frac{1}{4}\cos\frac{5\vartheta}{2}\right)$$

$$\sigma_{y_b} \simeq \frac{1+\nu}{3+\nu}\sigma(2r)^{-1/2}\left(\frac{5}{4}\cos\frac{\vartheta}{2} - \frac{1}{4}\cos\frac{5\vartheta}{2}\right)$$

The deformation of the plate at the immediate vicinity of the crack tip is governed by the stress invariant $(\sigma_x + \sigma_y)$, which, at this region close to the crack tip takes the same value for both theories, that is:

$$\sigma_{x_b} + \sigma_{y_b} \equiv \sigma_{x_{b_0}} + \sigma_{y_{b_0}} = 2\frac{1+\nu}{3+\nu}\sigma(2r)^{-1/2}\cos\frac{\vartheta}{2}$$

Since the caustic created around the crack tip depends on the stress invariant $(\sigma_x + \sigma_y)$ [8], the identical values of this invariant at the crack tip for both theories indicate that the caustic is independent of the theory used for the analysis of the bent plates.

The procedure employed in this paper was to formulate the elastic deflection field $w(r, \vartheta)$ in terms of the Williams-Kirchoff equations [2] by using the notation proposed by Sih, Paris, and Erdogan [4], which is expressed by:

$$w(r,\vartheta) = r^{3/2}\left\{-\left[\cos\frac{3\vartheta}{2} - \frac{3(1-\nu)}{7+\nu}\cos\frac{\vartheta}{2}\right]b_1 + \left[\sin\frac{3\vartheta}{2} - \frac{3(1-\nu)}{5+3\nu}\sin\frac{\vartheta}{2}\right]b_2\right\} \tag{10}$$

where:

$$b_1 = -K_I\frac{7+\nu}{3\sqrt{2}Gh(3+\nu)}$$

$$b_2 = -K_{II}\frac{5+3\nu}{3\sqrt{2}Gh(3+\nu)} \tag{11}$$

Downloaded 01 May 2010 to 171.66.16.249. Redistribution subject to ASME license or copyright; see http://www.asme.org/terms/Terms_Use.cfm

and K_{II}, K_{II} are the crack-tip stress intensity factors for symmetrical and skew-symmetrical stress distributions, respectively, developed in transverse bending of the plate.

Differentiating equation (10) and introducing relations (7)–(9) we can readily find, from equation (6) the equation of the initial curve expressed by:

$$1+\left(\frac{2z_0}{\lambda}\right)^2 \frac{3}{4} r^{-1}\left(-b_1\cos\frac{3\vartheta}{2}+A\cos\frac{\vartheta}{2}+b_2\sin\frac{3\vartheta}{2}\right.$$
$$\left.-B\sin\frac{\vartheta}{2}\right)\left(-\frac{3}{4}b_1\cos\frac{3\vartheta}{2}+\frac{5}{4}A\cos\frac{\vartheta}{2}\right.$$
$$\left.-\frac{3}{4}b_2\sin\frac{3\vartheta}{2}-\frac{5}{2}B\sin\frac{\vartheta}{2}\right)-r^{-1}\left(\frac{2z_0}{\lambda}\right)^2\left(\frac{3}{4}b_1\sin\frac{3\vartheta}{2}\right.$$
$$\left.-\frac{A}{4}\sin\frac{\vartheta}{2}+\frac{3}{4}b_2\cos\frac{3\vartheta}{2}\right.$$
$$\left.-\frac{B}{4}\cos\frac{\vartheta}{2}\right)^2+\frac{2z_0}{\lambda}r^{-1/2}\left(2A\cos\frac{\vartheta}{2}-2B\sin\frac{\vartheta}{2}\right)=0 \quad (12)$$

In this relation, A and B are expressed by:

$$A=\frac{3(1-\nu)}{7+\nu}b_1$$
$$B=\frac{3(1-\nu)}{5+3\nu}b_2 \quad (13)$$

Relation (12) may be written in the form:

$$r^{1/2}=\frac{2F}{-M\pm(M^2-4F)^{1/2}} \quad (14)$$

where the quantities F and M are given by:

$$F=\left(\frac{2z_0}{\lambda}\right)^2 b_2^2 f\left(\vartheta,\frac{K_I}{K_{II}},\nu\right)$$
$$M=\frac{2z_0}{\lambda}b_2 m\left(\vartheta,\frac{K_I}{K_{II}},\nu\right) \quad (15)$$

where:

$$f\left(\vartheta,\frac{K_I}{K_{II}},\nu\right)=\frac{3}{4}\left(-\frac{K_I}{K_{II}}\frac{7+\nu}{5+3\nu}\cos\frac{3\vartheta}{2}\right.$$
$$\left.+\frac{K_I}{K_{II}}\frac{3(1-\nu)}{5+3\nu}\cos\frac{\vartheta}{2}+\sin\frac{3\vartheta}{2}\right.$$
$$\left.-\frac{3(1-\nu)}{5+3\nu}\sin\frac{\vartheta}{2}\right)\left(\frac{3}{4}\frac{K_I}{K_{II}}\frac{7+\nu}{5+3\nu}\cos\frac{3\vartheta}{2}\right.$$
$$\left.+\frac{5}{4}\frac{K_I}{K_{II}}\frac{3(1-\nu)}{5+3\nu}\cos\frac{\vartheta}{2}\right.$$
$$\left.-\frac{3}{4}\sin\frac{3\vartheta}{2}-\frac{5}{4}\frac{3(1-\nu)}{5+3\nu}\sin\frac{\vartheta}{2}\right)$$
$$-\left(\frac{3}{4}\frac{K_I}{K_{II}}\frac{7+\nu}{5+3\nu}\sin\frac{3\vartheta}{2}-\frac{1}{4}\frac{K_I}{K_{II}}\frac{3(1-\nu)}{5+3\nu}\sin\frac{\vartheta}{2}\right.$$
$$\left.+\frac{3}{4}\cos\frac{3\vartheta}{2}-\frac{1}{4}\frac{3(1-\nu)}{5+3\nu}\cos\frac{\vartheta}{2}\right)^2 \quad (16)$$

$$m\left(\vartheta,\frac{K_I}{K_{II}},\nu\right)=\frac{6(1-\nu)}{5+3\nu}\left(\frac{K_I}{K_{II}}\cos\frac{\vartheta}{2}-\sin\frac{\vartheta}{2}\right)$$

Angle ϑ varies between $-\pi$ and π. Therefore, the sign in front of $r^{1/2}$ in relation (14) should be selected in such a way in combination with the sign of M, to yield a positive value for $r^{1/2}$. The sign of M may be positive or negative, depending on the sign of the stress intensity factors (relations (11) and (13)), the sign of the magnification factor λ, and the value of angle ϑ. The factor λ is positive or negative, if the specimen is illuminated by a divergent or convergent light beam.

By taking into account equation (14) together with equations (15) and (16) the expression for the initial curve is given by:

$$r^{1/2}=\left(\frac{2z_0}{\lambda}\right)b_2 f_1\left(\vartheta,\frac{K_I}{K_{II}},\nu\right) \quad (17)$$

where:

$$f_1\left(\vartheta,\frac{K_I}{K_{II}},\nu\right)=\frac{2f}{-m\pm(m^2-4f)^{1/2}}$$

These equations indicate that the shape of the initial curve depends only on the value of Poisson's ratio ν and the ratio K_I/K_{II} of two stress intensity factors. It does not depend on the distance z_0, or on the magnification factor λ and on the quantity b_1.

We can now derive the equations for the caustic in parametric form. Thus, from equations (4) and (5), and by taking into account equation (10), we have:

$$X_1=\lambda r\cos\vartheta+3z_0 r^{1/2}\left[\left(-\cos\frac{\vartheta}{2}\right.\right.$$
$$\left.+\frac{1-\nu}{7+\nu}\cos\frac{3\vartheta}{2}+2\frac{1-\nu}{7+\nu}\cos\frac{\vartheta}{2}\right)b_1$$
$$\left.+\left(\sin\frac{\vartheta}{2}-\frac{1-\nu}{5+3\nu}\sin\frac{3\vartheta}{2}+2\frac{1-\nu}{5+3\nu}\sin\frac{\vartheta}{2}\right)b_2\right] \quad (18)$$

$$Y_1=\lambda r\sin\vartheta+3z_0 r^{1/2}\left[\left(\sin\frac{\vartheta}{2}\right.\right.$$
$$\left.+\frac{1-\nu}{7+\nu}\sin\frac{3\vartheta}{2}+2\frac{1-\nu}{7+\nu}\sin\frac{\vartheta}{2}\right)b_1$$
$$\left.+\left(\cos\frac{\vartheta}{2}+\frac{1-\nu}{5+3\nu}\cos\frac{3\vartheta}{2}-2\frac{1-\nu}{5+3\nu}\cos\frac{\vartheta}{2}\right)b_2\right]$$

Furthermore, by taking into account equation (17) of the initial curve, we can derive the relations for the coordinates X_1 and Y_1 of the caustic:

$$X_1=\frac{(2z_0b_2)^2}{\lambda}f_2\left(\vartheta,\frac{K_I}{K_{II}},\nu\right)$$
$$Y_1=\frac{(2z_0b_2)^2}{\lambda}f_3\left(\vartheta,\frac{K_I}{K_{II}},\nu\right) \quad (19)$$

where:

$$f_2\left(\vartheta,\frac{K_I}{K_{II}},\nu\right)=f_1^2\cos\vartheta+\frac{3}{2}f_1$$
$$\times\left[\left(-\cos\frac{\vartheta}{2}+\frac{1-\nu}{7+\nu}\cos\frac{3\vartheta}{2}+2\frac{1-\nu}{7+\nu}\cos\frac{\vartheta}{2}\right)\right.$$
$$\left.\times\left(\frac{K_I}{K_{II}}\frac{7+\nu}{5+3\nu}\right)+\left(\sin\frac{\vartheta}{2}-\frac{1-\nu}{5+3\nu}\sin\frac{3\vartheta}{2}+\frac{2(1-\nu)}{5+3\nu}\sin\frac{\vartheta}{2}\right)\right] \quad (20)$$

$$f_3\left(\vartheta,\frac{K_I}{K_I},\nu\right)=f_1^2\sin\vartheta+\frac{3}{2}f_1\left[\left(-\sin\frac{\vartheta}{2}+\frac{1-\nu}{7+\nu}\sin\frac{3\vartheta}{2}\right.\right.$$
$$\left.+2\frac{1-\nu}{7+\nu}\sin\frac{\vartheta}{2}\right)$$
$$\left.\times\left(\frac{K_I}{K_{II}}\frac{7+\nu}{5+3\nu}\right)+\left(\cos\frac{\vartheta}{2}-\frac{1-\nu}{5+3\nu}\cos\frac{3\vartheta}{2}+2\frac{1-\nu}{5+3\nu}\cos\frac{\vartheta}{2}\right)\right]$$

It is clear from relations (19) and (20) that the shape of the caustic depends on the same quantities as the shape of the

Downloaded 01 May 2010 to 171.66.16.249. Redistribution subject to ASME license or copyright; see http://www.asme.org/terms/Terms_Use.cfm

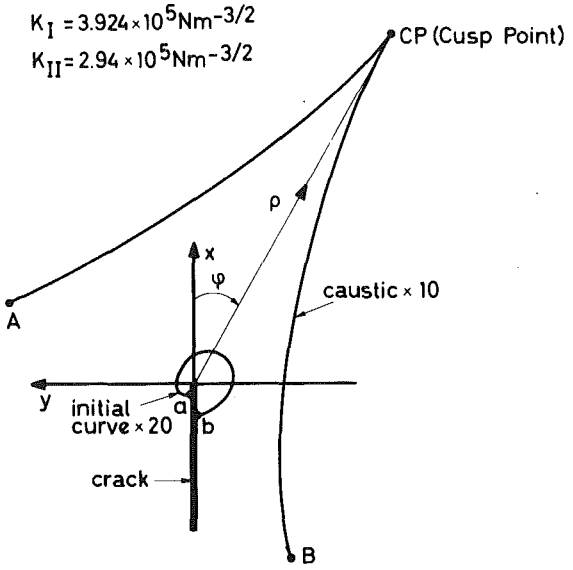


Fig. 2 Theoretical forms of the caustic and the respective initial curve

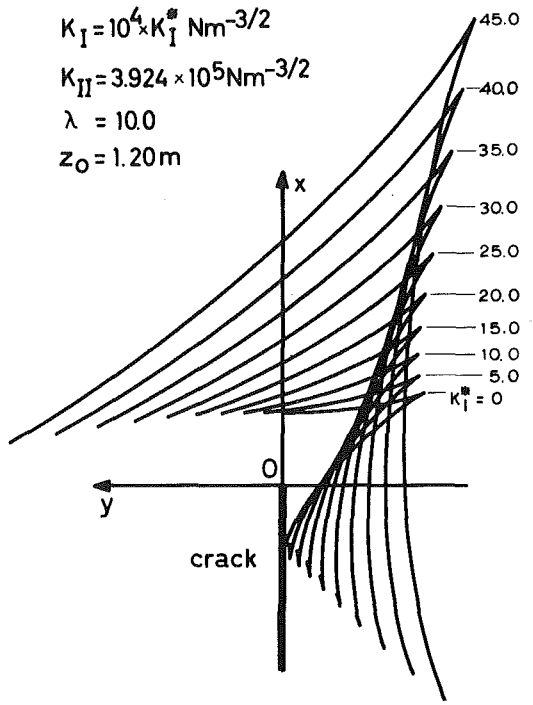


Fig. 3 Theoretical forms of caustics for different values of K_I for the case when K_{II} was kept constant

initial curve. Therefore, the shape of the caustics depends only on Poisson's ratio ν and the ratio K_I/K_{II}, whereas its size depends on the values of stress intensity factors, the geometry of the plate, and the characteristics of the optical set up.

Figure 2 shows the theoretically obtained caustic and its initial curve for a cracked plate of plexiglass with $E = 3.2 \times 10^6 KN/m^2$, $\nu = 0.34$, thickness $h = 0.002m$, $K_I = 3 \times 10^5 N/m^{3/2}$ and $K_{II} = 4 \times 10^5 N/m^{3/2}$, when the screen is placed at a distance $z_0 = 1.200m$ and the magnification factor of the optical system is $\lambda = 10.0$.

The variation of the shape of the caustics with K_I for a constant value of K_{II}, in the case of the same plate as the foregoing, is plotted in Fig. 3. As we can see from this figure, there are three typical points of the caustics that characterize its dependence on the K_I and K_{II} stress intensity factors. These points are the two extremities A and B and its cusp point CP (Fig. 2).

The coordinates X_1 and Y_1 of the extremity points A and B of the caustic are given by relations (18) combined with relation (14) of the initial curve. Extreme points of the caustics are defined as the images on the screen of the points of the specimen where the initial curve crosses the crack lips (points a and b of Fig. 2). Therefore, by introducing the values $\vartheta = +\pi$ and $\vartheta = -\pi$ in equation (14), we can obtain the rays r_a and r_b of the initial curve corresponding to the points a and b, respectively:

$$r_a^{1/2} = \frac{\frac{z_0}{8\lambda}[6(b_2B+b_1A)+9(b_1^2-b_2^2)+15B^2+A^2]}{B \pm \{B^2 - \frac{1}{16}[6(b_2B+b_1A)+9(b_1^2-b_2^2)+15B^2+A^2]\}^{1/2}} \tag{21a}$$

$$r_b^{1/2} = \frac{\frac{z_0}{8\lambda}[6(b_2B-b_1A)-9(b_1^2+b_2^2)+15B^2-A^2]}{-B \pm \{B^2 - \frac{1}{16}[6(b_2B-b_1A)-9(b_1^2+b_2^2)+15B^2-A^2]\}^{1/2}} \tag{21b}$$

The value of $X_{1(\pm\pi)}$ and $Y_{1(\pm\pi)}$ of the extreme points A and B of the caustic can be obtained, from relations (18):

$$\left.\begin{aligned} &i \text{ for } \vartheta = \pi: \\ &X_{1(\pi)} = -\lambda r_a + \frac{24 z_0}{5+3\nu} r_a^{1/2} 2b_2 \\ &Y_{1(\pi)} = +\frac{24 z_0}{7+\nu} r_a^{1/2} b_1 \\ &ii \text{ for } \vartheta = -\pi: \\ &X_{1(-\pi)} = -\lambda r_b - \frac{24 z_0}{5+3\nu} r_b^{1/2} b_2 \\ &Y_{1(-\pi)} = -\frac{24 z_0}{7+\nu} r_b^{1/2} b_1 \end{aligned}\right\} \tag{22}$$

where r_a and r_b are given from equations (21a, b), respectively.

We now define the cusp point CP by evaluating its polar coordinates ρ and φ (Fig. 2). These quantities are given by:

$$\rho = (X_1^2 + Y_1^2)^{1/2} = \rho(\vartheta, r, b_1, b_2) \tag{23a}$$

$$\varphi = \arctan\frac{Y_1}{X_1} = \varphi(\vartheta, r, b_1, b_2) \tag{23b}$$

where X_1, Y_1, or r and ϑ must be determined.

The location of the point CP is determined by defining the angle $\varphi = \varphi_{CP}$ corresponding to a local maximum for the polar radius ρ. The conditions for local maximum ρ are:

$$\frac{d\rho}{d\vartheta} = 0, \quad \frac{d^2\rho}{d\vartheta^2} < 0 \tag{24}$$

They may be evaluated from relations (23a) and (14) and they take the form:

Downloaded 01 May 2010 to 171.66.16.249. Redistribution subject to ASME license or copyright; see http://www.asme.org/terms/Terms_Use.cfm

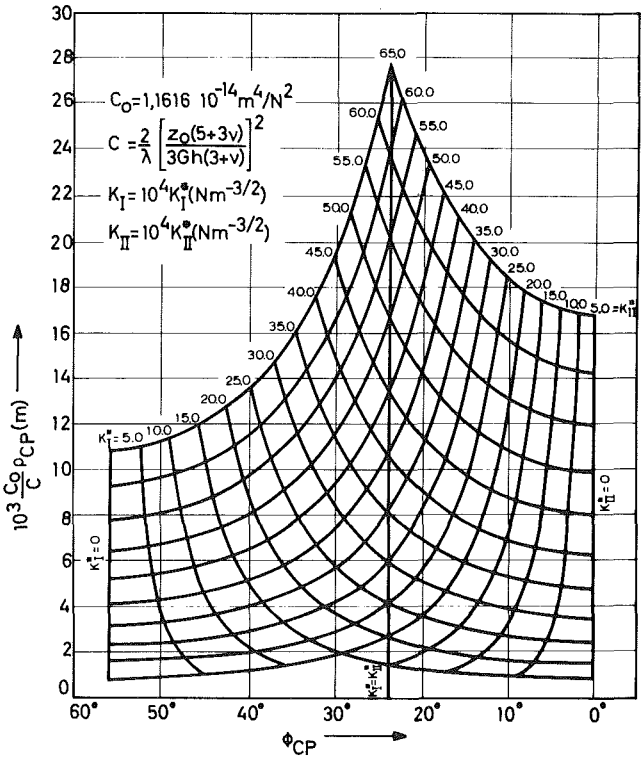


Fig. 4 A nomogram in $\rho_{CP} - \varphi_{CP}$ coordinates of cusp point of caustic for obtaining the value of K_I and K_{II} S.I.F.

$$C=\frac{2}{\lambda}\left[\frac{z_0(5+3\nu)}{3Gh(3+\nu)}\right]^2 \tag{28}$$

The values for $\rho_{\max} = \rho_{CP}$ and φ_{CP}, defined from relations (24) for the cusp point, are presented in Fig. 4, which shows the variations of the ρ_{CP} in terms of the angle φ_{CP} for different values of K_I and K_{II}.

It may be derived from Fig. 4 that for the extreme cases of $K_I \neq 0$ and $K_{II} = 0$ or $K_I = 0$ and $K_{II} \neq 0$ the loci of the cusp points of the caustics are two straight lines with a constant angle for φ equal to $\varphi_{K_{II}=0} = 0$ deg and $\varphi_{K_{I}=0} = 57$ deg, with the direction of the crack, respectively.

This means that, for the case of a plate in bending with bending moments M_x and M_y, for which $K_{II} = 0$ the cusp points for all caustics formed for different values of K_I lie along the crack axis, and, therefore, all these caustics are symmetric to the crack. On the other hand, it may be derived from the nomogram of Fig. 4 that when the plate is submitted to such bending moments creating a state of deformation with $K_I = K_{II}$, the cusp point of all caustics for any pair of K_I and K_{II} subtends a constant angle with the crack axis, which is equal to $\varphi_{KI=KII} = 24$ deg. Finally, for any combination of the values for K_I and K_{II}, angle φ varies between $\varphi_{K_{II}=0} = 0$ deg and $\varphi_{K_I=0} = 57$ deg.

Application of Pseudocaustics to Cracked Plates in Bending

The equations of the caustic, as expressed by relations (18), are convenient for expressing the image on the screen of every point for which the position on the plate is known. To explicitly define the polar coordinates r and ϑ in equation (18), a series of isolate points on the plate, belonging to a grid, is marked on the specimen in the vicinity of the crack tip. The deformation of the plate in the vicinity of the crack tip, which depends on the values of K_I and K_{II}, may be depicted by the change in the form of the pseudocaustic corresponding to the selected in advance points around the crack tip. The method will be illustrated by some examples, where a set of isolated points and lines marked on the specimen are used as reference points or lines for defining the corresponding pseudocaustics formed on the screen.

$$\left.\begin{aligned}
\frac{d\rho}{d\vartheta} &= \frac{\frac{dX_1}{d\vartheta}X_1+\frac{dY_1}{d\vartheta}Y_1}{\rho}=0 \\
\frac{d^2\rho}{d\vartheta^2} &= \frac{\frac{d^2X_1}{d\vartheta^2}X_1+\left(\frac{dX_1}{d\vartheta}\right)^2+\left(\frac{dY_1}{d\vartheta}\right)^2+\frac{d^2Y_1}{d\vartheta^2}Y_1-\left(\frac{\partial\rho}{\partial\vartheta}\right)^2}{(X_1^2+Y_1^2)^{1/2}}<0
\end{aligned}\right\} \tag{25}$$

However, for practical applications, the expressions for ρ and φ should be given in a more convenient form. This can be done by using for X_1, Y_1, and r, the expressions (19) and (17), respectively. In this case we obtain:

$$\left.\begin{aligned}
\rho &= CK_{II}^2 f_4\left(\vartheta,\frac{K_I}{K_{II}},\nu\right) \\
\varphi &= \arctan f_5\left(\vartheta,\frac{K_I}{K_{II}},\nu\right)
\end{aligned}\right\} \tag{26}$$

where:

$$\left.\begin{aligned}
f_4\left(\vartheta,\frac{K_I}{K_{II}},\nu\right) &= \left[f_2^2\left(\vartheta,\frac{K_I}{K_{II}},\nu\right)+f_3^2\left(\vartheta,\frac{K_I}{K_{II}},\nu\right)\right]^{1/2} \\
f_5\left(\vartheta,\frac{K_I}{K_{II}},\nu\right) &= \frac{f_3\left(\vartheta,\frac{K_I}{K_{II}},\nu\right)}{f_2\left(\vartheta,\frac{K_I}{K_{II}},\nu\right)}
\end{aligned}\right\} \tag{27}$$

and:

Figure 5 shows a set of a concurrent lines ss and tt passing through the tip 0 of a crack with equations $y = \pm x$, marked on the plate before deformation and their pseudocaustics s_1s_1 and t_1t_1 after deformation of the plate, together with the respective caustic around the crack tip for $K_1 = 5.88 \times 10^5 \text{Nm}^{-3/2}$, $K_{II} = 3.43 \times 10^5 \text{Nm}^{-3/2}$, $z_0 = 1.20$ m, and $\lambda = 10.0$. On the other hand, Fig. 6 shows a circumference $abcda'$ traced around the crack tip before loading and its pseudocaustic $ABCDA'$ for the same plate under loading conditions as previously. Points b, c, and d at the intersection of the $0x$- and $0y$-axes with the circle $abcda'$ of radius δ, which have before deformation the coordinates:

Downloaded 01 May 2010 to 171.66.16.249. Redistribution subject to ASME license or copyright; see http://www.asme.org/terms/Terms_Use.cfm

$$\text{Point } b: \quad x_b = 0 \quad y_b = \delta$$
$$\text{Point } c: \quad x_c = \delta \quad y_c = 0 \tag{29}$$
$$\text{Point } d: \quad x_d = 0 \quad y_d = -\delta$$

Their images after deformation have the following coordinates, respectively:

Points B and D

$$X_{B,D} = -\frac{z_0 |\delta|^{1/2}}{Gh}(-K_I \pm K_{II})$$
$$Y_{B,D} = \pm\lambda\delta \mp \frac{z_0 |\delta|^{1/2}}{(3+\nu)Gh}[(5-\nu)K_I \pm (3\nu+1)K_{II}] \tag{30}$$

whereas for the point C we have:

$$X_C = \lambda\delta + \frac{4z_0(1+\nu)|\delta|^{1/2}}{(3+\nu)\sqrt{2}Gh}K_I$$
$$Y_C = -\frac{4z_0(1+\nu)|\delta|^{1/2}}{(3+\nu)\sqrt{2}Gh}K_{II} \tag{31}$$

It can be derived from relations (30) and (31) that the coordinates of the pseudocaustic formed from a concentric circle around the crack tip are linearly related to the respective values K_I and K_{II} of the stress intensity factors.

From relation (31) it can be readily seen that either of the components of the stress intensity factor is solely dependent on either of the coordinates X_c and Y_c. Then, it seems reasonable to use this point in front of the crack tip and on the crack axis for defining directly and separately K_I and K_{II}. For this point any variation of either of coordinates X_c and Y_c along the $0x$- and $0y$-axes means a variation of either of the stress intensity factors without influencing the other one.

Finally, it is clear from both relations (31) that the same factor:

$$C_p = \frac{4z_0(1+\nu)|\delta|^{1/2}}{\sqrt{2}(3+\nu)Gh}$$

multiplies both K_I and K_{II} in the two relations. This means that the sensitivity of the method of pseudocaustics in evaluating these two stress intensity factors is identical for both factors. Moreover, since C_p depends on the properties and size of the specimen and, on the other hand, on the geometric characteristics of the optical set up and the radius of the pseudocaustic, it can be readily derived that there could be an optimization process of obtaining the pseudocaustic, yielding the best results for each particular case of cracked plate and loading mode.

Determination of Complex Stress Intensity Factors

Based on the previous theory of caustics and pseudocaustics, a method can be established for determining the K_I and K_{II} stress intensity factors in cracked plates under bending.

i First consider the evaluation of K_I and K_{II} by the method of caustics. The significant geometric dimensions of the caustic are either the coordinates of its extreme points defined by relations (22), or the polar coordinates of their cusp point (relations (23)).

Assuming therefore, that the coordinates of the extreme points of the caustic on the screen have been found, the unknowns K_I and K_{II} factors can be determined by eliminating the additional unknown quantities r_a and r_b from the system of four equations (22). This elimination yields the following simple relations:

$$K_I = \frac{(3+\nu)3\sqrt{2}Gh}{24z_0}\left\{\frac{\lambda[Y_{1(\pi)} - Y_{1(-\pi)}]}{\frac{X_{1(\pi)}}{Y_{1(\pi)}} - \frac{X_{1(-\pi)}}{Y_{1(-\pi)}}}\right\}^{1/2} \tag{32a}$$

$z = 1.20\ \text{m}$
$\lambda = 10$
$K_I = 5.88\times10^5\ \text{Nm}^{-3/2}$
$K_{II} = 3.43\times10^5\ \text{Nm}^{-3/2}$

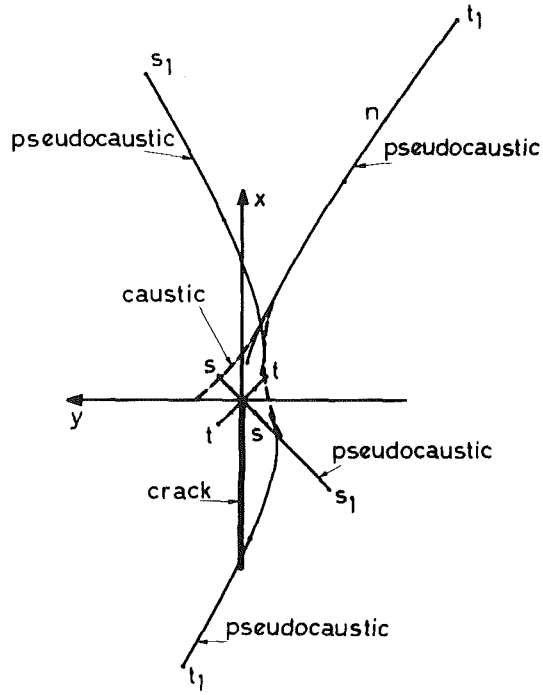


Fig. 5 The theoretical forms of pseudocaustics s_1s_1, t_1t_1 derived from a set of concurrent lines ss, tt passing through the crack tip, together with the caustic corresponding to the same loading and experimental arrangement

$E = 3.129\times10^9\ \text{Nm}^{-2}$
$\nu = 0.33$
$z_o = 1.20\ \text{m}$
$K_I = 5.88\times10^5\ \text{Nm}^{-3/2}$
$K_{II} = 2.94\times10^5\ \text{Nm}^{-3/2}$

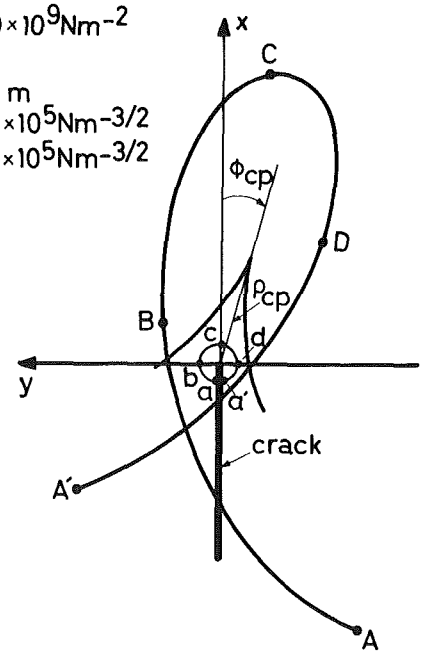


Fig. 6 The theoretical form of the pseudocaustic *ABCDA'* of a concentric with the crack tip circumference *abcda'*

$$\frac{K_{II}}{K_I} = \frac{\left[\frac{X_{1(\pi)}}{Y^2_{1(\pi)}} - \frac{X_{1(-\pi)}}{Y^2_{1(-\pi)}}\right]}{\left[\frac{1}{Y_{1(\pi)}} - \frac{1}{Y_{1(-\pi)}}\right]} \tag{32b}$$

Downloaded 01 May 2010 to 171.66.16.249. Redistribution subject to ASME license or copyright; see http://www.asme.org/terms/Terms_Use.cfm

Relation (32*b*) presents the influence of K_{II} on the shape of the caustic. In the case of a symmetrical loading [11], $X_{1(\pi)} = X_{1(-\pi)}$ and $Y_{1(\pi)} = -Y_{1(-\pi)}$ and, from relation (32*b*), it may be derived that $K_{II}/K_I = 0$. This means that $K_{II} = 0$, a fact that characterizes a symmetrical loading in bending of plates.

An unsymmetric loading ($K_{II} \neq 0$) of a plate under bending can be immediately detected from the shape of the caustic, because in this case the following inequalities are valid:

$$X_{1(\pi)} \neq X_{1(-\pi)} \text{ and } |Y_{1(\pi)}| \neq |Y_{1(-\pi)}|$$

These inequalities are due to the rotation of the caustic about the crack tip created by the existence of the K_{II}-component.

ii Next we consider the coordinates of the cusp point of the caustic. The system of equations (24)–(26) related to the cusp point is much more complicated, than the system (32) corresponding to the extreme points of the caustic. However, the coordinates of the cusp point of the caustic are very accurately defined and yield better accuracy in evaluating K_I and K_{II}. Moreover, in this case only two coordinates are needed for the experimental determination of K_I and K_{II}. These coordinates are the polar radius ρ_{CP} and the polar angle φ_{CP} of the cusp point. To avoid the solution of the system (24)–(26) each time, the nomogram of Fig. 4 was plotted by solving this system numerically for $\nu = 0.34$ (the value of Poisson's ratio for plexiglass). It is easy now, by measuring the polar radius ρ_{CP} and the polar angle φ_{CP} of the cusp point of the experimentally obtained caustic, to normalize it to the appropriate quantities and define from the nomogram both values for K_I and K_{II}. However, since these quantities depend on ν, it is necessary to plot each time for different ν's, the respective nomograms.

The dependence of ρ_{CP} and φ_{CP} on K_I and K_{II} is also exhibited in Fig. 4. It is shown in this figure, as K_I and K_{II} increase, the sensitivity of the method also increases. This is indicated in Fig. 4 by the increasing spaces between two isoparametric lines of either family K_I or K_{II} when the values of these factors increase.

iii Finally, the method of pseudocaustics may be used for determining K_I and K_{II}. By a particular choice of the points *b*, *c*, and *d* of Fig. 6, the value entering in equations (30) and (31) is determined. Moreover, the coordinates X and Y of the pseudocaustics, corresponding to the points *B*, *C*, and *D*, are evaluated on the screen with the plate deformed. From the system of equations (30) and (31) a series of values result for K_I and K_{II}, and the mean value of these series gives a better approximation for K_I and K_{II} as follows:

From equation (30),

$$\left.\begin{aligned} K_I &= -\frac{Gh}{2z_0|\delta|^{1/2}}\left(-\frac{3\nu+1}{3+\nu}X_B + Y_B - \lambda|\delta|\right), \quad K_{II} = \frac{Gh}{2z_0|\delta|^{1/2}}\left(\frac{5-\nu}{3+\nu}X_B + Y_B - \lambda|\delta|\right) \\ K_I &= \frac{Gh}{2z_0|\delta|^{1/2}}\left(\frac{3\nu+1}{3+\nu}X_D + Y_D + \lambda|\delta|\right), \quad K_{II} = -\frac{Gh}{2z_0|\delta|^{1/2}}\left(-\frac{5-\nu}{3+\nu}X_D + Y_D + \lambda|\delta|\right) \end{aligned}\right\} \quad (33)$$

From equation (32),

$$\left.\begin{aligned} K_I &= \frac{\sqrt{2}(3+\nu)}{4(1+\nu)} \qquad \frac{Gh}{z_0|\delta|^{1/2}}(X_c - \lambda|\delta|) \\ K_{II} &= -\frac{\sqrt{2}(3+\nu)}{4(1+\nu)} \qquad \frac{Gh}{z_0|\delta|^{1/2}}Y_c \end{aligned}\right\} \quad (34)$$

Experimental Evidence

To check the validity of the theoretical results, a series of experiments was undertaken. Both plexiglass and stainless steel or aluminum plates were selected as materials of the plates. *Cylindrical bending* was chosen as the type of loading. A series of bending tests were run with specimens of dimensions: 0.50m × 0.20m and nominal thickness h = 0.002m. The cracks of nominal length a = 0.03m were all centrally located in the plate and making an angles of 0, 10, 20, 30, 40, 50, and 60 deg with the direction of the axis of plate bending. The optical constants for the particular plexiglass and steel plates used in the experiments were:

For plexiglass:

$$C_f = \frac{\nu}{E} = 1{,}0512 \times 10^{-10}\text{m}^2/\text{N}$$

For stainless steel:

$$C_f = \frac{\nu}{E} = 1{,}6000 \times 10^{-12}\text{m}^2/\text{N}$$

Figures 7–9 show the caustics obtained for a plexiglass plate, and Fig. 10 shows the caustic for a stainless steel plate with a central crack making an angle of 40, 30, 20, and 30 deg, respectively. The distance z_0 between the screen and the specimen and the magnification factor λ were z_0 = 1.05m and λ = +6.0 for the caustic of Fig. 7, and z_0 = 1.27m, λ = +10.0, for Fig. 9. From Figs. 7 and 9 the polar coordinates of the cusp point were determined as follows:

For Fig. 7: $\rho_{CP} = 0.0515\text{m}$ $\varphi_{CP} = 24$ deg

For Fig. 9: $\rho_{CP} = 0.042\text{m}$ $\varphi_{CP} = 20$ deg

Next, the quantities $C = 2z_0^2(5 + 3\nu)^2/[9\lambda(3 + \nu)^2 G^2h^2]$ and $C_0\rho/C$ were evaluated for every case, where C_0 = 1,1616 × $10^{-14}\text{m}^4/\text{N}^2$. Thus, the values $C_0\rho/C$ = 0, 0252m, φ = 24 deg for Fig. 7, and $C_0\rho/C$ = 0,023436m, φ = 20 deg for Fig. 9 were derived. From the nomogram of Fig. 4 and for the preceding values of $C_0\rho/C$ and φ, the following values for K_I and K_{II} were derived, respectively:

$$K_I = 5.79 \times 10^4\text{Nm}^{-3/2}$$
$$K_{II} = 5.78 \times 10^4\text{Nm}^{-3/2}$$

and

$$K_I = 6376 \times 10^4\text{Nm}^{-3/2}$$
$$K_{II} = 4806 \times 10^4\text{Nm} - 3/2$$

If these values of K_I and K_{II}, for example, K_I = 6376 × $10^4\text{Nm}^{-3/2}$ and K_{II} = 4806 × $10^4\text{Nm}^{-3/2}$ are introduced in the computer program together with the corresponding parameters of the optical setup, then a theoretical caustic of Fig. 9(*a*) is obtained. A superposition of the theoretical caustic of Fig. 9(*a*) and the experimental one of Fig. 9(*b*) shows a very good coincidence between the theory and experiment.

For a complete illustration of the method, it remains to compare the experimental results of the S.I.F.'s K_I and K_{II} determined by the technique of pseudocaustics and the corresponding theoretical values. The method of pseudocaustics requires some identifying points marked on the plate at $y = \pm a$, $x = b$. This is achieved by an identation hardness test using a calibrated machine that forces a hard cone into the surface of the material. After the removal of the load, a permanent conical impression of a small diameter and

Downloaded 01 May 2010 to 171.66.16.249. Redistribution subject to ASME license or copyright; see http://www.asme.org/terms/Terms_Use.cfm

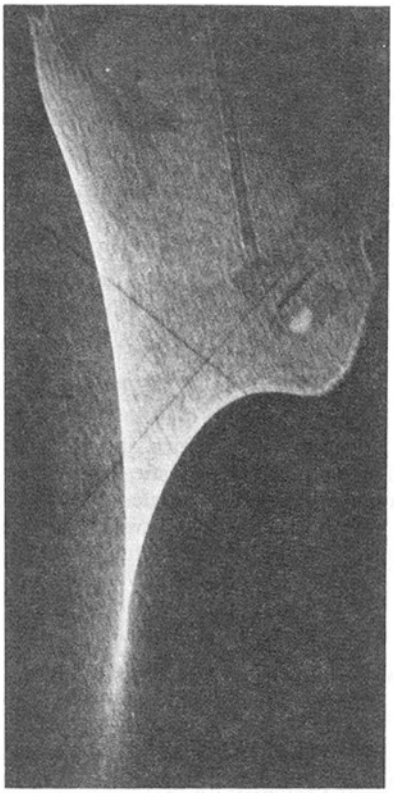


Fig. 7 Experimentally obtained caustic for a plexiglass plate in cylindrical bending containing a central crack subtending an angle of 40 deg with the bending axis

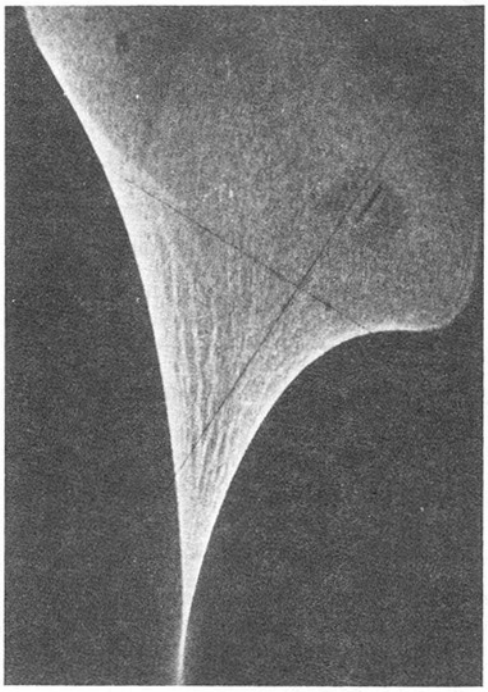


Fig. 8 Experimentally obtained caustic for a plexiglass plate in cylindrical bending which contains a central crack subtending an angle of 30 deg with the bending axis

depth remains on the plate surface. For the specimen of plexiglass plate, a Rockwell hardness machine with a cone was used, which gave an identation with a diameter less than 0.001m and a depth less than 0.0001m. These indentations are so small that there is no influence on the distribution around the crack tip. The position and the dimensions of the iden-

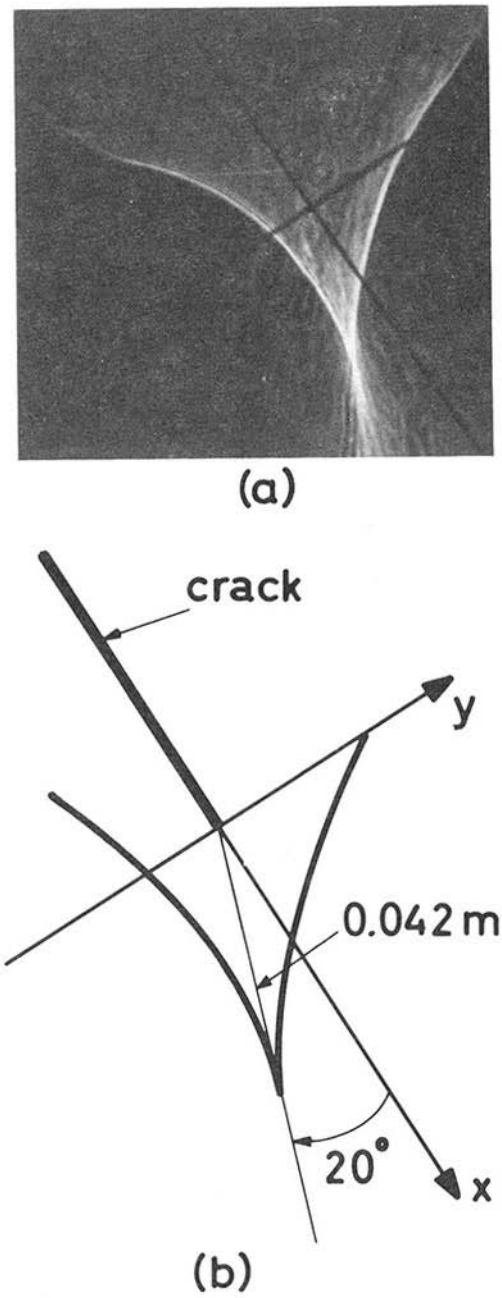


Fig. 9(*a*) Experimentally obtained caustic for a plexiglass plate in cylindrical bending which contains a central crack subtending an angle of 20 deg with the bending axis, and (*b*) the corresponding theoretical caustic for the same loading and optical setup

:ations are showed in Fig. 11(*b*). Figure 11(*a*) shows the image on the screen of the pseudocaustics. This images have a rhomboidal form, which accurately give their centers at the intersection of two diagonals. The coordinates of these centers have found:

Point B	$X=0.0112$m	$Y=0.0150$m
Point C	$X=0.0725$m	$Y=-0.012m$
Point D	$X=0.0320$m	$Y=-0.0268m$

From the system of equations (33) and (34), and for $z_0 = 1.20$m and $\lambda = 10.0$, a series of values were found for K_I and K_{II}, as follows:

From equation (33):

$$K_I = 5.80 \times 10^4 \text{Nm}^{-3/2}$$

Downloaded 01 May 2010 to 171.66.16.249. Redistribution subject to ASME license or copyright; see http://www.asme.org/terms/Terms_Use.cfm

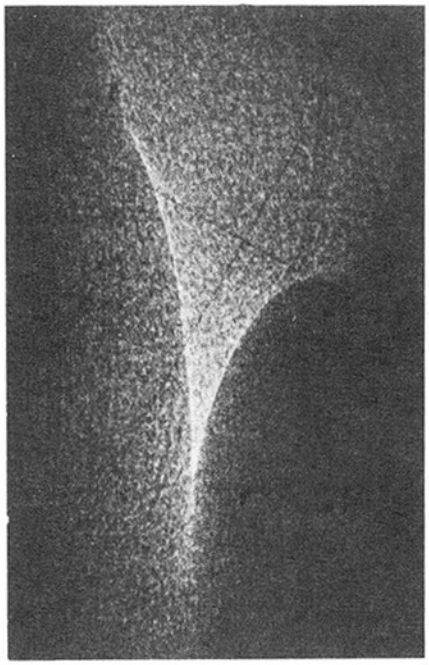


Fig. 10 Experimentally obtained caustic for a stainless steel plate in cylindrical bending that contains a central crack subtending an angle of 30 deg with the bending axis

$$K_{II} = 2.69 \times 10^4 \text{Nm}^{-3/2}$$
$$K_I = 6.00 \times 10^4 \text{Nm}^{-3/2}$$
$$K_{II} = 2.89 \times 10^4 \text{Nm}^{-3/2}$$

From equation (34):

$$K_I = 5.52 \times 10^4 \text{Nm}^{-3/2}$$
$$K_{II} = 2.93 \times 10^4 \text{Nm}^{-3/2}$$

The average values of these factors are:

$$K_I = 5.77 \times 10^4 \text{Nm}^{-3/2}$$
$$K_{II} = 2.84 \times 10^4 \text{Nm}^{-3/2}$$

The theroetical formulas for K_I and K_{II} are respectively, [6]:

$$K_I = \Phi(1) M\sqrt{a}\sin^2\beta$$
$$K_{II} = Y(1) M\sqrt{a}\sin\beta\cos\beta$$

where $\Phi(1)$ and $Y(1)$ are functions given in reference [6] versus $h/a\sqrt{10}$, where h is the plate thickness and a is the crack length. The value of the external distributed moment, acting on the plate boundary, was:

$$M = 8.485 \times 10^4 \text{Nm/m}$$

These quantities yield for the theoretical values of K_I and K_{II} that

$$K_I = 5.95 \times 10^4 \text{Nm}^{-3/2}, \quad K_{II} = 2.99 \times 10^4 \text{Nm}^{-3/2}$$

and these values are in good agreement with the respective experimental values.

Conclusions

An experimental technique, based on the method of caustics, was used to determine the two components K_I and K_{II} of the complex stress intensity factor in cracked plates under bending.

It was derived that there is a significant influence of the S.I.F.'s K_I and K_{II} on the shape and dimensions of the caustic at a crack vertex in asymmetric bending. The effect of K_{II} on the caustic is a deviation of the caustic from the axis of the crack. This deviaiton is evaluated either by measuring the cartesian coordinates of the extreme points of the caustic or by measuring the polar coordinates of its cusp point. A supplemental technique, based on the pseudocaustics method, was also applied for determining K_I and K_{II}. The application of this method is very simple and this implies that it can be used to check the results obtained by the method of caustics. A mean value of the stress intensity factors derived by the two methods may yield more accurate results.

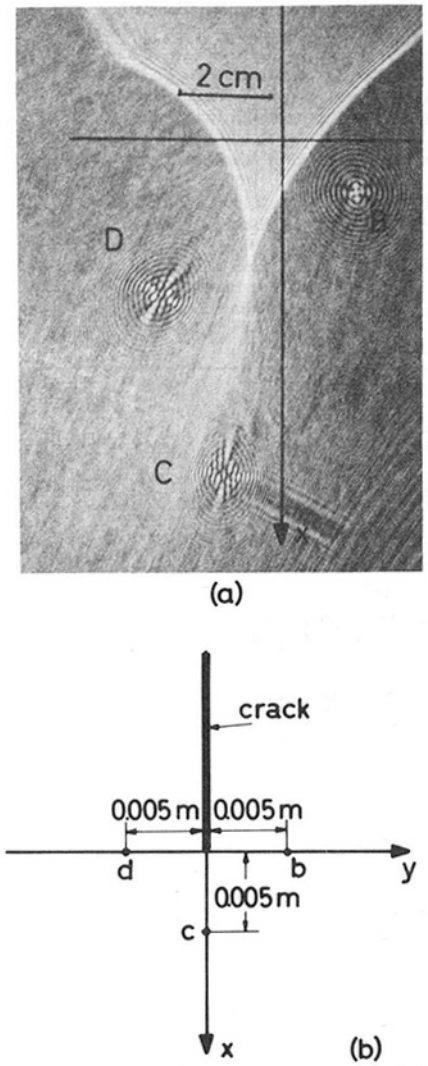


Fig. 11 (a) The caustic and the pseudocaustics (points B, C, D) as obtained experimentally for a set points (b,c,d) marked on a plexiglass plate (b) in cylindrical bending that contains a central crack subtending an angle of 20 deg with the bending axis

Acknowledgments

The author is indebted to his senior research assistant Dr. Constantin Razem for helping him to execute calculations and experiments contained in this paper. He is also grateful for a grant allocated to Dr. Razem by the Hellenic Aluminum Co., which allowed him to participate in this research program.

References

1 Williams, M. L., "Surface Stress Singularities Resulting From Various Boundary Conditions in Angular Corners of Plates Under Bending," *Proceedings, Ist U.S. National Congress of Applied Mechanics,* June 1951, pp. 325-329.

2 Williams, M. L., "The Bending Stress Distribution at the Base of a Stationary Crack," ASME JOURNAL OF APPLIED MECHANICS, Vol. 28, Series E, Mar. 1961, pp. 78-82.

3 Williams, M. L., Invited Discussion of "An Experimental Investigation

Downloaded 01 May 2010 to 171.66.16.249. Redistribution subject to ASME license or copyright; see http://www.asme.org/terms/Terms_Use.cfm

of the Crack Tip Stress-Intensity Factors in Plates Under Cylindrical Bending," by Erdogan, F., Tuncel, O., and Paris, P. C., GALCIT SM62-19, California Institute of Technology, Mar., 1962.

4 Sih, G. C., Paris, P., and Erdogan, F., "Crack Tip Stress-Intensity Factors for Plane Extension and Plate Bending Problems," ASME JOURNAL OF APPLIED MECHANICS, Vol. 29, Series E, June, 1962, pp. 306–312.

5 Knowles, J. K., and Wang, N. M., "On the Bending of an Elastic Plastic Containing a Crack," *Journal of Mathematics and Physics,* Dec., 1961, pp. 223–236.

6 Hartranft, R. J., and Sih, G. C., "Effect of Plate Thickness on the Bending Stress Distribution Around Through Cracks," *Journal of Mathematics and Physics,* Vol. 47, No. 3, Sept., 1968, pp. 276–291.

7 Erdogan, E., Tuncel, O., and Paris, P. C., "An Experimental Investigation of the Crack Tip Stress-Intensity Factors in Plates Under Cylindrical Bending," ASME *Journal of Basic Engineering,* Series D, Vol. 84, 1962, pp. 542–546.

8 Theocaris, P. S., "The Method of Caustics Applied to Elasticity Problems," *Optical Methods Applied to Composite Materials,* Developments in Composite Materials, G. S. Holister ed., Applied Science Publishers, Vol. II, Chapter II, 1981, pp. 27–63.

9 Theocaris, P. S., and Gdoutos, E. E., "Experimental Solution of Flexed Plates by the Method of Caustics, ASME JOURNAL OF APPLIED MECHANICS, Vol. 44, 1977, pp. 107–111.

10 Theocaris, P. S., "Caustic Created from Simply Supported Plates Under Uniform Loading," *Int. J. Solids and Structures,* Vol. 13, No. 4, 1977, pp. 1281–1291.

11 Theocaris, P. S., "Symmetric Bending of Cracked Plates Studied by Caustics," *International Journal of Mechanical Sciences,* Vol. 21, No. 11, 1979, pp. 659–670.

12 Theocaris, P. S., and Razem, C. I., "Deformed Boundaries Determined by the Method of Caustics," *J. of Strain Analysis,* Vol. 12, No. 3, 1977, pp. 223–232.

Downloaded 01 May 2010 to 171.66.16.249. Redistribution subject to ASME license or copyright; see http://www.asme.org/terms/Terms_Use.cfm

Application of the Line-Spring Model to a Cylindrical Shell Containing a Circumferential or Axial Part-Through Crack[1]

F. Delale
Department of Mechanical Engineering and Mechanics,
Drexel University,
Philadelphia, Pa.

F. Erdogan
Department of Mechanical Engineering and Mechanics,
Lehigh University,
Bethlehem, Pa. 18015
Mem. ASME

In this paper the line-spring model developed by Rice and Levy is used to obtain an approximate solution for a cylindrical shell containing a part-through surface crack. It is assumed that the shell contains a circumferential or axial semi-elliptic internal or external surface crack and is subjected to a uniform membrane loading or a uniform bending moment away from the crack region. To formulate the shell problem, a Reissner type theory is used to account for the effects of the transverse shear deformations. The stress intensity factor at the deepest penetration point of the crack is tabulated for bending and membrane loading by varying three-dimensionless length parameters of the problem formed from the shell radius, the shell thickness, the crack length, and the crack depth. The upper bounds of the stress intensity factors are provided by the results of the elasticity solution obtained from the axisymmetric crack problem for the circumferential crack, and that were found from the plane strain problem for a circular ring having a radial crack for the axial crack. Qualitatively the line-spring model gives the expected results in comparison with the elasticity solutions. The results also compare well with the existing finite element solution of the pressurized cylinder containing an internal semi-elliptic surface crack.

1 Introduction

In recent years there has been some renewed interest in the line-spring model which was developed in [1] for obtaining an approximate solution of a plate containing a part-through surface crack. There are a number of reasons for this. First, the accuracy of the results obtained form the model turned out to be better than that shown by the early comparisons with the solutions found from the finite element and the alternating methods [2–6] (see, for example, [7]). Secondly, the technique appears to have the potential for important applications to a great variety of shell structures of rather complex geometries with a relatively small computational effort. Finally, it can be quite useful to study certain aspects of the part-through crack problem in the presence of large-scale plastic deformations (see, for example, the interesting recent work by Parks [7, 9], and [8] and [10]).

In this paper the elastic problem for a relatively thin-walled cylinder containing a semi-elliptic, part-through crack is considered. It is assumed that the crack lies in a plane perpendicular to or containing the axis of the cylinder and may be an external or an internal surface crack. In formulating the problem, the cylinder is approximated by a shallow shell and the effect of transverse shear deformations are taken into

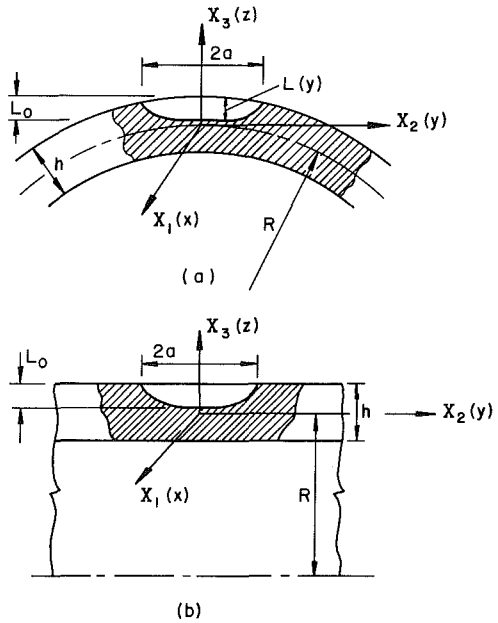


Fig. 1 The geometry of a circumferential or an axial part-through surface crack in a cylindrical shell

[1] This work was supported by the Department of Transportation under the contract DOT-RC-82007, by NSF under the Grant CME-78-08737, and by NASA-Langley under the Grant NGR 39-007-011.

Contributed by the Applied Mechanics Division for publication in the JOURNAL OF APPLIED MECHANICS.

Discussion on this paper should be addressed to the Editorial Department, ASME, United Engineering Center, 345 East 47th Street, New York, N.Y. 10017, and will be accepted until two months after final publication of the paper itself in the JOURNAL OF APPLIED MECHANICS. Manuscript received by ASME Applied Mechanics Division; May 1981; final revision, July 1981.

Copyright © 1982 by ASME
Downloaded 01 May 2010 to 171.66.16.249. Redistribution subject to ASME license or copyright; see http://www.asme.org/terms/Terms_Use.cfm

account [11, 12]. The edge-cracked strip results used in the line-spring model are obtained from an intergral equation solution given in [13].

The stress intensity factor for a part-through axial crack located inside the cylinder is given in [14–16] where in [14] and [15] the finite element, and in [16] the boundary integral equation method is used to solve the problem. The results found in this paper are compared with those given in [14] as well as the related plane strain and axisymmetric elasticity solutions. The stress intensity factors obtained from the elasticity solutions for a ring with a radial crack under plane-strain conditions and for a cylinder containing an axisymmetric circumferential surface crack provide upper bounds for the results corresponding to an axial and a circumferential surface crack of finite length in the cylindrical shell.

2 General Formulation

The part-through crack geometry for the cylindrical shell under consideration is shown in Fig. 1. It is assumed that the external loads are symmetric with respect to the plane of the crack. Thus the only nonzero net ligament stress and moment resultants, which have a constraining effect on the crack surface displacements, would be the membrane resultant N_{11} and the moment resultant M_{11}. The basic idea underlying the line-spring model consists of: (*a*) representing the net ligament stresses by a membrane load N and a bending moment M, and the crack surface displacements by a crack opening δ, and a relative rotation θ, all referred to the midplane of the shell and continuously distributed along the length of the crack; (*b*) approximating the relationship between (N, M) and (δ, θ) by the corresponding plane-strain results obtained from the solution of an edge-cracked strip or a ring; (*c*) reducing the problem to a pair of integral equations for the unknown functions N and M or δ and θ by using the boundary and the continuity conditions for the shell in the plane of the crack.

In the formulation of the crack problem for the shell, the derivatives of the crack surface displacement and rotation are used as the unknown functions, which are defined by

$$\frac{\partial}{\partial y}u(+0,y)=G_1(y),\quad \frac{\partial}{\partial y}\beta_x(+0,y)=G_2(y). \qquad (1a,b)$$

The notation and the dimensionless quantities used in the formulation are given in Fig. 1 and in Appendix A of [17]. It is shown in [17] that the general problem for a symmetrically loaded shell containing a through crack may be reduced to the following system of integral equations:

$$\int_{-1}^{1}\frac{G_1(t)}{t-y}\,dt+\int_{-1}^{1}\sum_{1}^{2}k_{1j}(y,t)G_j(t)\,dt = 2\pi F_1(y),\quad -1<y<1, \qquad (2a)$$

$$\frac{1-\nu^2}{\lambda^4}\int_{-1}^{1}\frac{G_2(t)}{t-y}\,dt+\int_{-1}^{1}\sum_{1}^{2}k_{2j}(y,t)G_j(t)\,dt = 2\pi\frac{h}{a}F_2(y),\quad -1<y<1, \qquad (2b)$$

subject to

$$\int_{-1}^{1}G_1(y)\,dy=0,\quad \int_{-1}^{1}G_2(y)\,dy=0, \qquad (3a,b)$$

where kernels $k_{ij}(y, t)$, $(i, j = 1, 2)$ are known functions. The problem is formulated as a perturbation problem in which the stress and moment resultants applied to the crack surfaces are the only external loads. Thus F_1 and F_2 appearing in (2) are

$$F_1(y)=N_{xx}(+0,y),\quad F_2(y)=M_{xx}(+0,y),\quad -1<y<1. \qquad (4a,b)$$

Table 1 Normalized stress intensity factor k/k_0 at the deepest penetration point $L = L_0$, $y = 0$ of the outer semi-elliptic circumferential crack in a cylinder under uniform membrane loading N_∞; $\lambda_2 = [12(1-\nu^2)]^{1/4}\, a/\sqrt{rh}$, $\nu = 0.3$

	$L_0 = 0.2h$				$L_0 = 0.4h$			
λ_2	a=h	a=2h	a=4h	a=8h	a=h	a=2h	a=4h	a=8h
0	0.817	0.883	0.930	0.961	0.507	0.627	0.741	0.837
0.5	0.817	0.883	0.930	0.961	0.509	0.628	0.742	0.837
0.75	0.816	0.882	0.930	0.961	0.509	0.628	0.742	0.837
1.0		0.880	0.929	0.960		0.626	0.741	0.836
1.5		0.876	0.926	0.959		0.620	0.736	0.833
2.0			0.922	0.956			0.727	0.827
4.0			0.893	0.939			0.670	0.784
6.0				0.916				0.728
8.0				0.893				0.676
	$L_0 = 0.6h$				$L_0 = 0.8h$			
0	0.245	0.336	0.451	0.582	0.073	0.104	0.149	0.216
0.5	0.248	0.339	0.454	0.583	0.074	0.106	0.151	0.219
0.75	0.250	0.341	0.455	0.585	0.076	0.107	0.152	0.220
1.0		0.341	0.455	0.585		0.109	0.154	0.221
1.5		0.341	0.453	0.583		0.112	0.157	0.223
2.0			0.448	0.577			0.158	0.224
4.0			0.408	0.532			0.158	0.214
6.0				0.476				0.197
8.0				0.428				0.182

Table 2 Normalized stress intensity factor k/k_0 at the deepest penetration point $L = L_0$, $y = 0$ of an outer semi-elliptic circumferential crack in a cylindrical shell under uniform bending moment M_∞

	$L_0 = 0.2h$				$L_0 = 0.4h$			
λ_2	a=h	a=2h	a=4h	a=8h	a=h	a=2h	a=4h	a=8h
0	0.804	0.875	0.926	0.959	0.441	0.579	0.710	0.819
0.5	0.804	0.875	0.926	0.959	0.443	0.581	0.712	0.819
0.75	0.803	0.874	0.925	0.958	0.443	0.580	0.711	0.819
1.0		0.872	0.924	0.958		0.578	0.709	0.818
1.5		0.867	0.921	0.956		0.570	0.703	0.814
2.0			0.916	0.953			0.692	0.806
4.0			0.884	0.934			0.621	0.753
6.0				0.909				0.686
8.0				0.883				0.624
	$L_0 = 0.6h$				$L_0 = 0.8h$			
0	0.132	0.238	0.373	0.526	-0.012	0.017	0.065	0.140
0.5	0.135	0.241	0.376	0.529	-0.010	0.019	0.068	0.143
0.75	0.137	0.243	0.377	0.529	-0.008	0.021	0.069	0.145
1.0		0.243	0.377	0.529		0.023	0.071	0.146
1.5		0.242	0.374	0.526		0.027	0.074	0.148
2.0			0.367	0.519			0.075	0.148
4.0			0.313	0.459			0.072	0.132
6.0				0.386				0.108
8.0				0.326				0.088

Table 3 Normalized stress intensity factor k/k_0 at the deepest penetration point $y = 0$, $L = L_0$ of an inner semi-elliptic circumferential surface crack in a cylindrical shell under uniform membrane loading N_∞

	$L_0 = 0.2h$				$L_0 = 0.4h$			
λ_2	a=h	a=2h	a=4h	a=8h	a=h	a=2h	a=4h	a=8h
0	0.817	0.883	0.930	0.961	0.507	0.627	0.741	0.837
0.5	0.810	0.879	0.928	0.960	0.497	0.618	0.735	0.833
0.75	0.804	0.875	0.926	0.959	0.487	0.610	0.729	0.829
1.0		0.870	0.923	0.957		0.600	0.722	0.824
1.5		0.858	0.916	0.953		0.579	0.704	0.812
2.0			0.907	0.948			0.685	0.798
4.0			0.870	0.926			0.613	0.739
6.0				0.902				0.687
8.0				0.881				0.646
	$L_0 = 0.6h$				$L_0 = 0.8h$			
0	0.245	0.336	0.451	0.582	0.073	0.104	0.149	0.216
0.5	0.240	0.330	0.444	0.576	0.073	0.103	0.147	0.213
0.75	0.236	0.324	0.438	0.570	0.073	0.102	0.145	0.210
1.0		0.318	0.431	0.563		0.101	0.143	0.207
1.5		0.305	0.414	0.546		0.101	0.140	0.200
2.0			0.398	0.529			0.137	0.194
4.0			0.350	0.467			0.133	0.177
6.0				0.422				0.168
8.0				0.392				0.163

Downloaded 01 May 2010 to 171.66.16.249. Redistribution subject to ASME license or copyright; see http://www.asme.org/terms/Terms_Use.cfm

The formulation just given refers to a shallow shell containing a crack along the principal plane of curvature coinciding with X_2X_3 plane (Fig. 1). The principal radii of curvature R_1 and R_2 are defined by

$$\frac{1}{R_1} = -\frac{\partial^2 Z}{\partial X_1^2}, \quad \frac{1}{R_2} = -\frac{\partial^2 Z}{\partial X_2^2}, \tag{5a,b}$$

where $Z(X_1, X_2)$ is the distance of the point on the middle surface to the tangent plane X_1X_2. Thus, for the circumferential crack shown in Fig. 1(*a*), $R_2 = R$ and $R_1 = \infty$ (giving $\lambda_1 = 0$), and for the axial crack shown in Fig. 1(*b*), $R_1 = R$ and $R_2 = \infty$ (giving $\lambda_2 = 0$).

Now let

$$N_{11} = N_\infty, \quad M_{11} = M_\infty \tag{6a,b}$$

be the uniform membrane load and the bending moment applied to the shell away from the crack region and $N(X_2)$ and $M(X_2)$ the stress and moment resultants which are equivalent to the net ligament stresses in $-a < X_2 < a$ or $-1 < y < 1$. The input functions, which appear in the integral equations (2), may then be expressed as

$$F_1(y) = \frac{1}{E}(-\sigma_\infty + \sigma), \quad F_2(y) = \frac{1}{6E}(-m_\infty + m), \tag{7a,b}$$

for the crack located on the outside, and

$$F_1(y) = \frac{1}{E}(-\sigma_\infty + \sigma), \quad F_2(y) = \frac{1}{6E}(m_\infty - m), \tag{8a,b}$$

for the crack located inside the cylinder[2] where

$$\sigma_\infty = \frac{N_\infty}{h}, \quad m_\infty = \frac{6M_\infty}{h^2}, \tag{9a,b}$$

and

$$\sigma(y) = \frac{N(X_2)}{h} = \frac{N(ay)}{h}, \quad m(y) = \frac{6M(X_2)}{h^2} = \frac{6M(ay)}{h^2}. \tag{10a,b}$$

The stresses σ and m are linearly related to the crack surface displacement $u(+0, y) = \delta/2$ and rotation $\beta_x(+0, y) = \theta/2$. This relationship may be obtained from the related plane-strain problem by expressing the rate of change of the potential energy in terms of the crack closure energy and the change in gross compliance as follows [1, 18]

$$\frac{1-\nu^2}{E}K^2 = \frac{1}{2}\left[\sigma h\frac{\partial \delta}{\partial L} + \frac{mh^2}{6}\frac{\partial \theta}{\partial L}\right] \tag{11}$$

where K is the total mode I stress intensity factor at the crack tip and L is the length of the edge crack. If we now let

$$K = \sqrt{h}(\sigma g_t + m g_b), \tag{12}$$

from (11) we obtain

$$\sigma(y) = E[\gamma_{tt}(y)u(+0, y) \pm \gamma_{tb}(y)\beta_x(+0, y)],$$
$$m(y) = 6E[\gamma_{bt}(y)u(+0, y) \pm \gamma_{bb}(y)\beta_x(+0, y)], \tag{13a,b}$$

where + and − signs are to be used for the outer and the inner cracks, respectively, and

$$\gamma_{tt} = \frac{a}{h(1-\nu^2)}\frac{\alpha_{bb}}{\Delta}, \quad \gamma_{bb} = \frac{1}{36(1-\nu^2)}\frac{\alpha_{tt}}{\Delta},$$

$$\gamma_{tb} = -\frac{1}{6(1-\nu^2)}\frac{\alpha_{tb}}{\Delta}, \quad \gamma_{bt} = -\frac{a}{6h(1-\nu^2)}\frac{\alpha_{bt}}{\Delta},$$

$$\Delta = \alpha_{tt}\alpha_{bb} - \alpha_{tb}^2, \tag{14a-e}$$

$$\alpha_{ij} = \frac{1}{h}\int_0^L g_i g_j \, dL, \quad (i, j = t, b). \tag{15}$$

The crack depth L is assumed to be a known function of y (Fig. 1).

Referring to the definitions (1), u and β_x may be expressed as

$$u(+0, y) = \int_{-1}^{y} G_1(t)\, dt, \quad \beta_x(+0, y) = \int_{-1}^{y} G_2(t)\, dt. \tag{16a,b}$$

Substituting from (16) and (13) into (2) the final form of the integral equations is found to be

$$-\gamma_{tt}(y)\int_{-1}^{y} G_1(t)\, dt \mp \gamma_{tb}(y)\int_{-1}^{y} G_2(t)\, dt + \frac{1}{2\pi}\int_{-1}^{1}\frac{G_1(t)}{t-y}\, dt$$
$$+ \frac{1}{2\pi}\int_{-1}^{1}[k_{11}(y, t)G_1(t) + k_{12}(y, t)G_2(t)]\, dt$$

Table 4 Normalized stress intensity factor k/k_0 at the deepest penetration point $y = 0$, $L = L_0$ of an inner semi-elliptic circumferential surface crack in a cylindrical shell under uniform bending moment M_∞

	$L_0 = 0.2h$				$L_0 = 0.4h$			
λ_2	a=h	a=2h	a=4h	a=8h	a=h	a=2h	a=4h	a=8h
0	0.804	0.875	0.926	0.959	0.441	0.579	0.710	0.819
0.5	0.797	0.870	0.923	0.957	0.429	0.569	0.703	0.814
0.75	0.789	0.866	0.921	0.956	0.418	0.559	0.696	0.809
1.0		0.860	0.917	0.954		0.547	0.687	0.803
1.5		0.847	0.909	0.950		0.522	0.666	0.789
2.0			0.900	0.945			0.643	0.772
4.0			0.859	0.920			0.557	0.702
6.0				0.894				0.640
8.0				0.871				0.592
	$L_0 = 0.6h$				$L_0 = 0.8h$			
0	0.132	0.238	0.373	0.526	-0.012	0.017	0.065	0.140
0.5	0.125	0.230	0.364	0.518	-0.013	0.015	0.062	0.136
0.75	0.119	0.222	0.356	0.511	-0.013	0.014	0.060	0.133
1.0		0.214	0.347	0.502		0.013	0.057	0.129
1.5		0.197	0.326	0.481		0.012	0.053	0.120
2.0			0.306	0.460			0.049	0.112
4.0			0.244	0.382			0.042	0.089
6.0				0.327				0.078
8.0				0.289				0.070

Table 5 Normalized stress intensity factor k/k_0 at the deepest penetration point $y = 0$, $L = L_0$ of an outer semi-elliptic axial surface crack in a cylindrical shell under uniform membrane loading N_∞

	$L_0 = 0.2h$				$L_0 = 0.4h$			
λ_1	a=h	a=2h	a=4h	a=8h	a=h	a=2h	a=4h	a=8h
0	0.817	0.883	0.930	0.961	0.507	0.627	0.741	0.837
0.5	0.822	0.886	0.932	0.962	0.518	0.635	0.748	0.841
0.75	0.826	0.888	0.933	0.963	0.527	0.642	0.752	0.844
1.0		0.890	0.934	0.963		0.649	0.757	0.847
1.5		0.894	0.936	0.964		0.663	0.766	0.853
2.0			0.938	0.965			0.773	0.857
4.0			0.935	0.964			0.775	0.860
6.0				0.959				0.848
8.0				0.954				0.834
	$L_0 = 0.6h$				$L_0 = 0.8h$			
0	0.245	0.336	0.451	0.582	0.073	0.104	0.149	0.216
0.5	0.255	0.346	0.461	0.590	0.076	0.108	0.154	0.223
0.75	0.264	0.355	0.468	0.597	0.080	0.112	0.159	0.229
1.0		0.364	0.477	0.604		0.118	0.165	0.235
1.5		0.384	0.494	0.619		0.130	0.178	0.250
2.0			0.509	0.631			0.192	0.264
4.0			0.532	0.651			0.225	0.299
6.0				0.641				0.303
8.0				0.622				0.294

[2] In both cases the applied moment M is such that the crack tends to open under bending of the shell, and the net ligament moment is assumed to constrain the crack surface rotation, hence the change in sign of F_2 in (7) and (8).

Downloaded 01 May 2010 to 171.66.16.249. Redistribution subject to ASME license or copyright; see http://www.asme.org/terms/Terms_Use.cfm

$$= -\frac{\sigma_\infty}{E}, \quad -1<y<1,$$

$$\mp\gamma_{bt}(y)\int_{-1}^{y} G_1(t)\,dt - \gamma_{bb}(y)\int_{-1}^{y} G_2(t)\,dt + \frac{a(1-\nu^2)}{2\pi h\lambda^4}\int_{-1}^{1}\frac{G_2(t)}{t-y}\,dt + \frac{a}{2\pi h}\int_{-1}^{1}[k_{21}(y,t)G_1(t)+k_{22}(y,t)G_2(t)]dt$$

$$= \mp\frac{m_\infty}{6E}, \quad -1<y<1 \qquad (17a,b)$$

where the upper (i.e., $-$) and the lower (i.e., $+$) signs are to be used for the outer and the inner crack, respectively.

3 Compliance Coefficients

The functions g_t and g_b, which appear in (12), and which give the membrane and bending components of the stress intensity factor, are obtained from the corresponding plane-strain crack geometry.

For the circumferential crack, the appropriate geometry is that of an infinite strip with an edge crack. On the other hand, for the axial crack, the proper plane-strain problem would be that of a ring having a radial edge crack. In a recent study, the ring problem was formulated in terms of a singular integral equation [19]. The results given in [19] show that for cylinders with values of h/R, which may be considered a "shallow shell," the ring results are reasonably close to the strip results. Also for small values of h/R, the convergence of the numerical solution of the ring problem is not very good. Hence, the complete parametrization of the problem for the purpose of obtaining g_t and g_b (which would be functions of h/R as well as L/h) becomes rather complicated. In this paper, therefore, the edge-cracked strip results will be used for both the axial and the circumferential crack problem.

For the strip, the functions g_t and g_b are obtained from the results given in [13] which are valid for $0 < L/h < 0.8$ and may be expressed as

$$g_t(\xi) = \sqrt{\pi\xi}(1.1216 + 6.5200\xi^2 - 12.3877\xi^4 + 89.0554\xi^4 - 188.6080\xi^8 + 207.3870\xi^{10} - 32.0524\xi^{12}),$$

$$g_b(\xi) = \sqrt{\pi\xi}(1.1202 - 1.8872\xi + 18.0143\xi^2 - 87.3851\xi^3 + 241.9124\xi^4 - 319.9402\xi^5 + 168.0105\xi^6) \qquad (18a,b)$$

where $\xi = L(X_2)/h = L(ay)/h$. From (18) and (15) the functions α_{ij}, $(i,j = t,b)$ may be determined as follows:

$$\alpha_{tt} = \xi^2\sum_{n=0}^{12} C_{tt}^{(n)}\xi^{2n}, \quad \alpha_{bb} = \xi^2\sum_{n=0}^{12} C_{bb}^{(n)}\xi^{n},$$

$$\alpha_{tb} = \alpha_{bt} = \xi^2\sum_{n=0}^{18} C_{tb}^{(n)}\xi^{n}. \qquad (19a\text{-}c)$$

The calculated values of $C_{ij}^{(n)}$ may be found in [18].

4 Solution for the Cylindrical Shell

The solution of the problem is obtained for a uniform membrane loading N_∞ and for a bending moment M_∞ applied to the shell away from the crack region and for the Poisson's ratio $\nu = 0.3$. Even though $L(X_2) = L(ay)$ describing the crack shape can be any single-valued function, the problem is solved only for a semi-elliptic surface crack given by

Table 6 Normalized stress intensity factor k/k_0 at the deepest penetration point $y = 0$, $L = L_0$ of an outer semi-elliptic axial surface crack in a cylindrical shell under uniform bending moment M_∞

	$L_0 = 0.2h$				$L_0 = 0.4h$			
λ_1	a=h	a=2h	a=4h	a=8h	a=h	a=2h	a=4h	a=8h
0	0.804	0.875	0.926	0.959	0.441	0.579	0.710	0.819
0.5	0.810	0.878	0.927	0.960	0.445	0.590	0.718	0.823
0.75	0.814	0.880	0.929	0.960	0.465	0.598	0.723	0.827
1.0		0.883	0.930	0.961		0.606	0.729	0.831
1.5		0.887	0.932	0.962		0.621	0.740	0.837
2.0			0.934	0.963			0.747	0.842
4.0			0.930	0.961			0.747	0.843
6.0				0.956				0.828
8.0				0.951				0.812
	$L_0 = 0.6h$				$L_0 = 0.8h$			
0	0.132	0.238	0.373	0.526	-0.012	0.017	0.065	0.140
0.5	0.143	0.250	0.385	0.536	-0.008	0.022	0.072	0.148
0.75	0.154	0.260	0.394	0.544	-0.003	0.027	0.078	0.155
1.0		0.272	0.405	0.553		0.034	0.085	0.163
1.5		0.295	0.425	0.570		0.047	0.100	0.180
2.0			0.442	0.585			0.115	0.197
4.0			0.464	0.605			0.148	0.232
6.0				0.588				0.231
8.0				0.563				0.217

Table 7 Normalized stress intensity factor k/k_0 at the deepest penetration point $L = L_0$, $y = 0$ of an inner semi-elliptic axial surface crack in a cylindrical shell under uniform membrane loading N_∞

	$L_0 = 0.2h$				$L_0 = 0.4h$			
λ_1	a=h	a=2h	a=4h	a=8h	a=h	a=2h	a=4h	a=8h
0	0.817	0.883	0.930	0.961	0.507	0.627	0.741	0.837
0.5	0.813	0.880	0.929	0.960	0.501	0.621	0.737	0.834
0.75	0.810	0.878	0.927	0.960	0.498	0.618	0.734	0.832
1.0		0.876	0.926	0.959		0.615	0.732	0.830
1.5		0.873	0.924	0.958		0.611	0.728	0.827
2.0			0.922	0.957			0.725	0.825
4.0			0.916	0.953			0.718	0.819
6.0				0.950				0.811
8.0				0.946				0.802
	$L_0 = 0.6h$				$L_0 = 0.8h$			
0	0.245	0.336	0.451	0.582	0.073	0.104	0.149	0.216
0.5	0.243	0.333	0.447	0.578	0.074	0.104	0.148	0.215
0.75	0.243	0.331	0.445	0.576	0.075	0.105	0.149	0.215
1.0		0.331	0.443	0.574		0.107	0.150	0.215
1.5		0.333	0.444	0.572		0.112	0.153	0.217
2.0			0.444	0.571			0.158	0.221
4.0			0.451	0.570			0.177	0.237
6.0				0.569				0.242
8.0				0.561				0.241

Table 8 Normalized stress intensity factor k/k_0 at the deepest penetration point $L = L_0$, $y = 0$ of an inner semi-elliptic axial surface crack in a cylindrical shell under uniform bending moment M_∞

	$L_0 = 0.2h$				$L_0 = 0.4h$			
λ_1	a=h	a=2h	a=4h	a=8h	a=h	a=2h	a=4h	a=8h
0	0.804	0.875	0.926	0.959	0.441	0.579	0.710	0.819
0.5	0.799	0.872	0.924	0.958	0.434	0.573	0.706	0.815
0.75	0.796	0.869	0.923	0.957	0.430	0.568	0.702	0.813
1.0		0.867	0.921	0.956		0.565	0.699	0.811
1.5		0.864	0.919	0.955		0.560	0.694	0.807
2.0			0.917	0.954			0.691	0.805
4.0			0.911	0.950			0.682	0.797
6.0				0.946				0.788
8.0				0.942				0.777
	$L_0 = 0.6h$				$L_0 = 0.8h$			
0	0.132	0.238	0.373	0.526	-0.012	0.017	0.065	0.140
0.5	0.128	0.233	0.368	0.521	-0.012	0.017	0.064	0.139
0.75	0.128	0.231	0.365	0.518	-0.010	0.018	0.064	0.138
1.0		0.230	0.363	0.516		0.019	0.065	0.138
1.5		0.233	0.363	0.513		0.024	0.069	0.141
2.0			0.363	0.513			0.074	0.145
4.0			0.369	0.515			0.091	0.161
6.0				0.507				0.164
8.0				0.495				0.161

Downloaded 01 May 2010 to 171.66.16.249. Redistribution subject to ASME license or copyright; see http://www.asme.org/terms/Terms_Use.cfm

Table 9 Distribution of the normalized stress intensity factor k/k_0 along the crack front in a cylindrical shell containing an inner or outer semi-elliptic circumferential surface crack (see insert in Fig. 4), $\lambda_2 = 2$, $a = 4h$, $L_0 = 0.4h$, $\nu = 0.3$

	Outer Crack		Inner Crack	
$\frac{2\phi}{\pi}$	Membrane Loading	Bending	Membrane Loading	Bending
1.0	0.727	0.692	0.685	0.643
0.894	0.719	0.689	0.678	0.641
0.789	0.694	0.680	0.658	0.637
0.684	0.655	0.665	0.625	0.628
0.578	0.604	0.643	0.580	0.615
0.473	0.544	0.618	0.527	0.597
0.367	0.477	0.583	0.465	0.569
0.263	0.406	0.538	0.399	0.529

Table 10 Distribution of the normalized stress intensity factor k/k_0 along the crack front in a cylindrical shell containing an inner or outer axial semi-elliptic surface crack (see insert in Fig. 4), $\nu = 0.3$

	Inner Crack $a=h, R_i=10h, L_0=0.2h$		Inner Crack $a=4h, R_i=10h, L_0=0.8h$		Outer Crack $a=4h, L_0=0.4h, \lambda_1=2$	
$\frac{2\phi}{\pi}$	Tension	Bending	Tension	Bending	Tension	Bending
1.0	0.812	0.799	0.161	0.078	0.773	0.747
0.894	0.807	0.797	0.160	0.082	0.764	0.743
0.789	0.792	0.792	0.157	0.094	0.736	0.731
0.684	0.766	0.782	0.153	0.109	0.693	0.710
0.578	0.730	0.765	0.147	0.124	0.637	0.683
0.473	0.685	0.739	0.138	0.139	0.572	0.652
0.367	0.628	0.700	0.126	0.149	0.500	0.612
0.263	0.559	0.642	0.114	0.154	0.426	0.562

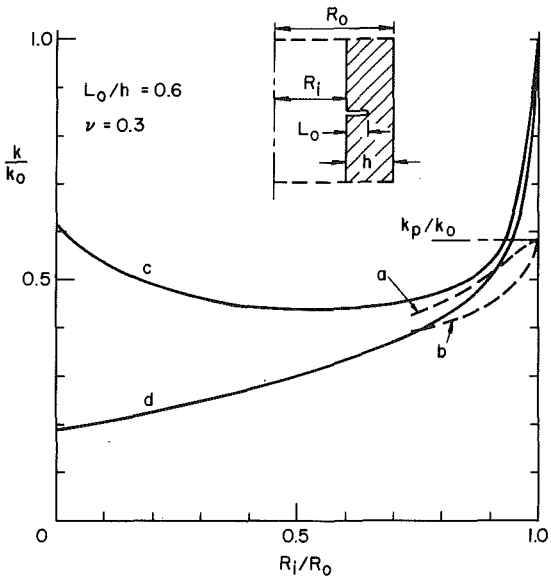


Fig. 2 Comparison of the stress intensity factors obtained from the line-spring shell model and the axisymmetric elasticity solution [21]. (a) Stress intensity factor at the deepest penetration point of an external semi-elliptic circumferential crack in the shell; (b) same as (a) for an internal surface crack; (c) elasticity solution for the external axisymmetric crack; (d) the internal axisymmetric crack. (For $L_0 = 0.6h$, $k_0 = 4.035\,\sigma_0\sqrt{L_0}$, $k_p = 0.582\,k_0$, σ_0: uniform axial stress, $a = 8h$.)

$$L = L_0\sqrt{1 - (X_2/a)^2} = L_0\sqrt{1 - y^2}. \tag{20}$$

The solution of the integral equations (17) is of the form

$$G_i(t) = \frac{\phi_i(t)}{(1 - t^2)^{1/2}}, \quad (i = 1, 2) \quad (-1 < t < 1) \tag{21}$$

where ϕ_1 and ϕ_2 are bounded functions. The functions ϕ_i may be determined from (17) to any desired degree of accuracy by using the Gauss-Chebyshev integration procedure [20]. After obtaining ϕ_1 and ϕ_2 the unknowns σ and m representing the net ligament stresses may be determined from (13) by using (14–16), (18), and (19). The stress intensity factor $K(y)$ may then be obtained from (12) and (18). For a Poisson's ratio $\nu =$ 0.3 and for various crack geometries and loading conditions, the calculated results are shown in Tables 1–10. Tables 1–8 give the normalized stress intensity factor at the deepest penetration point $y = 0$, $L = L_0$ of a semi-elliptic surface crack in a cylindrical shell under uniform membrane loading or bending. The normalizing stress intensity factor k_0 is the corresponding edge-crack value for the plane-strain problem under tension or bending and is given by

$$k_0 = \frac{K_0}{\sqrt{\pi}} = \frac{N_\infty}{\sqrt{\pi}\,h}\sqrt{h}\,g_t(\xi_0), \quad \xi_0 = \frac{L_0}{h} \tag{22}$$

for membrane loading, and

$$k_0 = \frac{K_0}{\sqrt{\pi}} = \frac{6M_\infty}{h^2\sqrt{\pi}}\sqrt{h}\,g_b(\xi_0), \quad \xi_0 = \frac{L_0}{h} \tag{23}$$

for bending.

Figures 2 and 3 show the comparison of the shell results with the stress intensity factors obtained from the corresponding axisymmetric and plane-strain problems. As

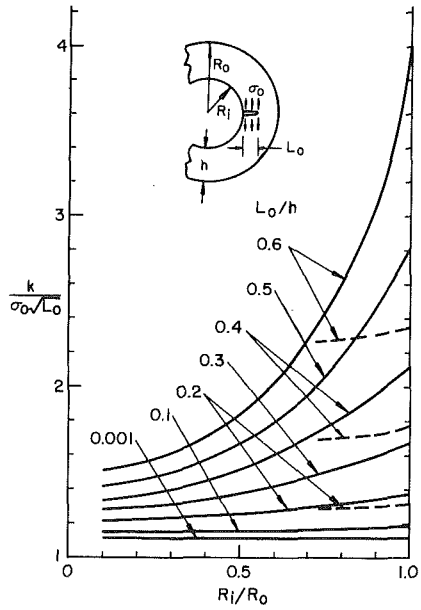


Fig. 3 Comparison of the line-spring shell, stress intensity factor at the deepest penetration point of an internal axial surface crack (dashed lines) with the corresponding plane-strain ring solution (full lines) [19], $a = 8h$

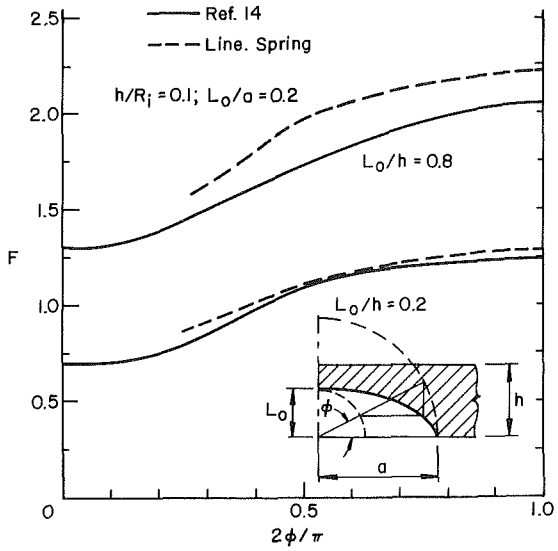


Fig. 4 Comparison of the line-spring shell results (dashed lines) with the finite element solution (full lines) [14] for a pressurized cylinder containing a semi-elliptic internal axial surface crack

Downloaded 01 May 2010 to 171.66.16.249. Redistribution subject to ASME license or copyright; see http://www.asme.org/terms/Terms_Use.cfm

$(R_i/R_0) \rightarrow 1$ the shell results approach the flat-plate solution k_p [18] having a part-through, semi-elliptic crack of the same geometry and relative dimensions. It may be noted that, as expected, the shell stress intensity factors are generally smaller than the corresponding two-dimensional values. Even though the shell results are given for $0.74 < (R_i/R_0) < 1$, because of the nature of the theory used in the shell analysis, namely the shallow shell theory, for $(R_i/R_0) < 0.9$ the results may not be very accurate. From Fig. 3 one may also observe that the difference between shell and the plane-strain results decrease with decreasing crack depth (L_0/h).[3] However, Figs. 2 and 3 also show some unexpected results. In spite of the fact that the crack length $2a$ is relatively very long ($a = 8h$), for deeper cracks and for R_i/R_0 close to unity, the difference between the part-through crack results and their limiting values (i.e., plane-strain or axisymmetrical elasticity solutions) is quite large (see Tables 1–8). For example, in the case of a flat plate ($R_i/R_0 = 1$) the stress intensity ratio k/k_0 is only 0.582 for $L_0 = 0.6h$, whereas it has a value of 0.961 for $L_0 = 0.2h$. Hence, for deep cracks, the notion that sufficiently long part-through cracks may be approximated by a plane-strain edge crack may be quite erroneous.

It should also be pointed out that even though the stress intensity ratio k/k_0 decreases with increasing crack depth L_0/h (see Tables 1–8), since the normalization factor k_0 given by (22), (23), and (18) increases with L_0/h at a much higher rate than k/k_0, the value of k itself is a monotonically increasing function of L_0/h.

Some sample results for the distribution of the stress intensity factor along the crack front are given in Tables 9 and 10. The normalization factors k_0 used in these tables and figures are also those given by (22) and (23). The variable ϕ used in the presentation of these results is the usual parametric angle of the ellipse shown in the insert of Fig. 4. For small values of ϕ the stress intensity factors given by the line-spring model are neither reliable nor meaningful and therefore are not presented.

The only shell results that exist in literature and which are obtained by using a method other than that of the line-spring model are the stress intensity factors in a pressurized cylinder containing an internal semi-elliptic axial crack [14–16]. Figure 4 shows the comparison of the stress intensity factors obtained from the line-spring model and those given in [14] which are found by using the finite element method. The parameter ϕ is again defined by the insert in Fig. 4. The stress intensity factor ratio F shown in Fig. 4 is defined by

$$F = \frac{K}{\frac{pR_i}{h}\sqrt{\pi L_0/Q}}, \qquad ,Q = [E(m)]^2, \qquad m = 1 - L_0^2/a^2, \tag{24}$$

where $K = k\sqrt{\pi}$ is the stress intensity factor along the crack front, p the internal pressure, and $E(m)$ the complete elliptic integral of the second kind. The results given in Fig. 4 include the effect of the pressure p acting on the crack surface. Considering the gross approximation involved in the formulation of the problem by using the line-spring model, and the fact that the finite element results themselves may contain a few percent error, the agreement between the two results seems to be quite good. The plane-strain results given in Fig. 3 suggest that the accuracy of the results given by the line-spring model could perhaps be further improved if the ring rather than the flat-plate solution is used to derive the functions g_t and g_b to express the stress intensity factor (see equations (12) and (18)).

[3] The plane-strain cylinder results given in Fig. 3 are obtained from [19] and the axisymmetric crack results shown in Fig. 2 are from [21].

References

1 Rice, J. R., and Levy, N., "The Part-Through Surface Crack in an Elastic Plate," ASME JOURNAL OF APPLIED MECHANICS, Vol. 39, 1972, pp. 185–194.

2 Raju, I. S., and Newman, J. C., Jr., "Stress-Intensity Factors for a Wide Range of Semi-Elliptical Surface Cracks in Finite-Thickness Plates," *Journal of Engineering Fracture Mechanics*, Vol. 11, pp. 817–829, 1979.

3 Newman, J. C., Jr., "A Review and Assessment of the Stress-Intensity Factors for Surface Cracks," NASA, Technical Memorandum 78805, Nov. 1978.

4 Atluri, S. N., Kathiresan, K., Kobayashi, A. S., and Nakagaki, M., "Inner Surface Cracks in an Internally Pressurized Cylinder Analyzed by a Three-Dimensional Displacement-Hybrid Finite Element Method," *Proc. of the 3rd Int. Conf. on Pressure Vessel Technology*, Part III, 1977, ASME, New York, pp. 527–533.

5 Smith, F. W., and Sorensen, D. R., "The Semi-Elliptical Surface Crack—A Solution by the Alternating Method," *Int. J. of Fracture*, Vol. 12, 1976, pp. 47–57.

6 Shah, R. C., and Kobayashi, A. S., "On the Surface Flaw Problem," *The Surface Crack: Physical Problems and Computational Solutions*, ed., Swedlow, J. L., 1972, pp. 79–124.

7 Parks, D. M., "The Inelastic Line-Spring: Estimates of Elastic-Plastic Fracture Mechanics Parameters for Surface-Cracked Plates and Shells," Paper 80-C2/PVP-109, ASME, 1980.

8 Rice, J. R., "The Line-Spring Model for Surface Flaws," *The Surface Crack: Physical Problems and Computational Solutions*," ed., Swedlow, J. L., ASME, New York, 1972, pp. 171–185.

9 Parks, D. M., "Inelastic Analysis of Surface Flaws Using the Line-Spring Model," *Proceedings of the 5th International Conference on Fracture*, Cannes, France, 1981.

10 Erdogan, F., and Ratwani, M., "Plasticity and Crack Opening Displacement in Shells," *Int. J. of Fracture Mechanics*, Vol. 8, pp. 413–426, 1972.

11 Reissner, E., and Wan, F. Y. M., "On the Equations of Linear Shallow Shell Theory," *Studies in Applied Mathematics*, Vol. 48, pp. 132–145, 1969.

12 Naghdi, P. M., "Note on the Equations of Elastic Shallow Shells," *Quart. Appl. Math.*, Vol. 14, 1956, pp. 331–333.

13 Kaya, A. C., and Erdogan, F., "Stress Intensity Factors and COD in an Orthotropic Strip," *Int. J. Fracture*, Vol. 16, 1980, pp. 171–190.

14 Newman, J. C., and Raju, I. S., "Stress Intensity Factors for Internal Surface Cracks in Cylindrical Pressure Vessels," NASA Technical Memorandum 80073, July 1979.

15 McGowan, J. J., and Raymund, M., "Stress Intensity Factor Solutions for Internal Longitudinal Semi-Elliptical Surface Flaws in a Cylinder under Arbitrary Loadings," *Fracture Mechanics*, ASTM, STP 677, 1979.

16 Heliot, J., and Labbens, R. C., and Pellisier-Tanon, A., "Semi-Elliptic Cracks in a Cylinder Subjected to Stress Gradients," *Fracture Mechanics*, ASTM, ST 677, 1979, pp. 341–364.

17 Delale, F., and Erdogan, F., "Transverse Shear Effect in A Circumferentially Cracked Cylindrical Shell," *Quarterly of Applied Mathematics*, Vol. 37, 1979, pp. 239–258.

18 Delale, F., and Erdogan, F., "Line-Spring Model for Surface Cracks in a Reissner Plate," to appear in the *International Journal of Engineering Science*, 1982.

19 Delale, F., and Erdogan, F., "Stress Intensity Factors in a Hollow Cylinder Containing a Radial Crack," to appear in the *International Journal of Fracture*, 1982.

20 Erdogan, F., "Mixed Boundary-Value Problems in Mechanics," *Mechanics Today*, Nemat-Nasser, S., ed., Vol. 4, Pergamon Press, 1978, Oxford, pp. 1–86.

21 Nied, H. F., "A Hollow Cylinder with an Axisymmetric Internal or Surface Crack under Nonaxisymmetric Arbitrary Loading," Ph.D. Dissertation, Lehigh University, June 1981.

Downloaded 01 May 2010 to 171.66.16.249. Redistribution subject to ASME license or copyright; see http://www.asme.org/terms/Terms_Use.cfm

J. Lyell Sanders, Jr.
Division of Applied Sciences,
Harvard University,
Cambridge, Mass. 02138
Fellow ASME

Circumferential Through-Cracks in Cylindrical Shells Under Tension

Closed-form expressions for the energy-release rate associated with circumferential through-cracks in infinitely long, thin cylindrical shells under tension loading are obtained. The analysis is valid for complete circular cylinders and is not limited to short cracks.

Introduction

The first theoretical research on the title problem was published by Folias in 1967 [1]. In a later paper, Erdogan and Ratwani [2] obtained results covering a much greater range of the parameter involved. The independent calculations of Fama and Sanders [3] served to confirm the previous work. Results in the present paper, together with concurrent work by Nicholson, Weidman, and Simmonds [4], establish the value of the energy-release rate (according to the shallow shell theory) over the whole range of the parameter, from zero to infinity.

Erdogan and Delale [5] succeeded in extending the results to include effects of transverse shear strains. Their analysis, like the others, is based on a shallow shell theory, and the problem is formulated in terms of integral equations. For any crack length, the singularities at the crack tip are significantly modified by the inclusion of transverse shear strain effects. However, there seems to be no reason to suppose that there is any significant effect on the fracture strength due to such causes except perhaps for very short cracks [6].

Barsoum, Loomis, and Stewart [7], in work done concurrently with that of [5], analyzed the problem (including transverse shear strain effects) by means of finite element methods. A significant advance over previous results was their ability to deal with long cracks. Some of their results are for cracks extending halfway around the cylinder – results that are out of reach for shallow shell theory. Their published calculations are for cylinders of finite length. The authors did not intend to include end-effects, although for some applications they could be an important consideration. Nonetheless they are there, and unfortunately preclude a valid comparison of their results with those presented here.

This paper contains an analytical solution to the cracked cylinder problem, valid everywhere except in the immediate neighborhood of the crack tips, provided the crack is sufficiently long. The solution is based on a new method of analysis for a certain class of cylindrical shell problems [8, 9]. The difficulty with the solution near the crack tips is circumvented by using path-independent integrals to calculate the energy-release rate [4, 10]. Fortunately, the range of validity of this analysis for long cracks overlaps the range of validity of the shallow shell analysis for short cracks. The connection between the two methods of analysis is herein established. Results for the energy-release rate are sufficiently simple to be given in closed form.

Fundamental Equations and Boundary Conditions

The complex displacements and stress functions in a cylindrical shell are given by [8, 9]

$$\begin{aligned} \epsilon^2 u &= \ddot{\Phi}' - \epsilon^2 \nu \varphi' & \epsilon^2 \chi_z &= -i\ddot{\Phi}' - i\epsilon^2 \nu \varphi' \\ \epsilon^2 v &= -\dot{\Phi} - \epsilon^2(2+\nu)\dot{\varphi} & \epsilon^2 \chi_\theta &= i\ddot{\Phi} + i\epsilon^2(2-\nu)\dot{\varphi} \\ w &= -\ddot{\Phi} + i(1+2i\epsilon^2)\varphi & \psi &= i\ddot{\Phi} + (1+2i\epsilon^2)\varphi \end{aligned} \tag{1}$$

where $(\,)' \triangleq \partial/\partial z(\,)$, $\dot{(\,)} \triangleq \partial/\partial\theta(\,)$. Axial distance is zR where R is the radius of the cylinder, and θ is the circumferential coordinate. The characteristic functions φ and Φ each satisfy

$$\nabla^4 \varphi + \ddot{\varphi} - i\epsilon^{-2}(1+2i\epsilon^2)\varphi'' = 0 \tag{2}$$

and are related to each other by $\Phi'' = \epsilon^2 \varphi$. The physical displacements and stress functions are the *real parts* of the expressions given by (1). Dimensional displacements and stress functions $\bar{u}$, $\bar{\chi}_z$, etc., are related to the dimensionless forms by

$$\begin{aligned} (\bar{u}, \bar{v}) &= \frac{\sigma R}{\mathrm{E}}(u, v), \quad \bar{w} = \frac{\sigma R}{\mathrm{E}\epsilon^2} w \\ (\bar{\chi}_z, \bar{\chi}_\theta) &= \sigma h R^2 \epsilon^2 (\chi_z, \chi_\theta), \quad \bar{\psi} = \sigma h R^2 \psi \end{aligned} \tag{3}$$

Here σ is the tensile stress in the cylinder at infinity, h is the shell thickness, E is Young's modulus, and ϵ is a small parameter given by

$$\epsilon^2 = (h/R)[12(1-\nu^2)]^{-1/2} \tag{4}$$

Let the opening angle of the circumferential crack be 2α. On the stress-free crack, boundary conditions on the stress functions are given by (the real parts of) (see [11]),

$$\chi_z = \chi_\theta = \psi = \psi' = 0, \quad \text{on} \quad z = 0, \quad |\theta| < \alpha \tag{5}$$

Off the crack symmetry considerations lead to

$$\chi_z = \psi' = 0, \quad u = w' = 0, \quad \text{on } z = 0, \quad \alpha < \theta < 2\pi - \alpha \tag{6}$$

Because of symmetry, the boundary value problem can be formulated for the region $z > 0$ on the cylinder.

Contributed by the Applied Mechanics Division for publication in the JOURNAL OF APPLIED MECHANICS.

Discussion on this paper should be addressed to the Editorial Department, ASME, United Engineering Center, 345 East 47th Street, New York, N.Y. 10017, and will be accepted until two months after final publication of the paper itself in the JOURNAL OF APPLIED MECHANICS. Manuscript received by ASME Applied Mechanics Division, March, 1981.

Copyright © 1982 by ASME
Downloaded 01 May 2010 to 171.66.16.249. Redistribution subject to ASME license or copyright; see http://www.asme.org/terms/Terms_Use.cfm

From (1) and (5) boundary conditions on the crack for the complete solutions φ_c and Φ_c are (in real terms)

$$\Re\{(1+i\epsilon^2\nu)\varphi_c\}=0, \quad \Re\{i\ddot{\Phi}_c+i\epsilon^2(2-\nu)\varphi_c\}=0$$
$$\Re\{\varphi_c'+i\epsilon^2(2-\nu)\varphi_c'\}=0, \quad \Re\{i\ddot{\Phi}_c'+i\epsilon^2\nu\varphi_c'\}=0 \tag{7}$$

Off the crack the boundary conditions can be written in complex form. From (1) and (6)

$$\varphi_c'=0, \quad \ddot{\Phi}_c'=0 \tag{8}$$

Some further conditions on the solution will be stated later.

Solution

The first step is to formulate a reduced boundary value problem by removing certain elementary solutions from the complete solution in such a way that the characteristic functions φ and $\ddot{\Phi}$ for the reduced problem vanish at infinity. The stresses at infinity are required to be those corresponding to simple axial tension. The solution for simple tension is given by

$$\varphi = \frac{1}{2}(1+i\epsilon^2\nu)\theta^2-\frac{1}{2}i\epsilon^2[1-i\epsilon^2(2-\nu)]z^2$$
$$\ddot{\Phi} = \frac{1}{2}i[1+i\epsilon^2(2+\nu)]\theta^2+(1+i\epsilon^2\nu)\left(\frac{1}{2}\epsilon^2z^2-i\right) \tag{9}$$

If the simple tension solution alone is removed from the complete solution, then no solution to the reduced problem is possible for which φ and $\ddot{\Phi}$ vanish at infinity. Elementary solutions corresponding to rigid body motions (for which stresses vanish) and to null solutions (for which displacements vanish) must, if they have proper symmetry, be allowed to be present at infinity. This list of solutions includes, in order: a null solution, an axial translation, a lateral translation, and a rotation given by

$$\varphi = a, \ \ddot{\Phi}=ia(1+2i\epsilon^2); \quad \varphi=i\epsilon bz, \quad \ddot{\Phi}=-\epsilon bz(1+2i\epsilon^2)$$
$$\varphi = 0, \ \ddot{\Phi}=ic\cos\theta; \quad \varphi=0, \quad \ddot{\Phi}=\epsilon dz\cos\theta \tag{10}$$

The complete solution is the linear combination

$$\varphi_c=\varphi_e+\varphi; \quad \ddot{\Phi}_c=\ddot{\Phi}_e+\ddot{\Phi} \tag{11}$$

where φ_e and $\ddot{\Phi}_e$ stand for the collection of elementary solutions (9) and (10). Boundary conditions for the reduced problem from (7), (8), and (11) are

$$\Re\{(1+i\epsilon^2\nu)\varphi\}=-a_R+\epsilon^2\nu a_I-\frac{1}{2}\theta^2 \tag{12}$$

$$\Re\{i\ddot{\Phi}+i\epsilon^2(2-\nu)\varphi\}=a_R-\epsilon^2\nu a_I+c_R\cos\theta-1+\frac{1}{2}\theta^2 \tag{13}$$

$$\Re\{\varphi'+i\epsilon^2(2-\nu)\varphi'\}=\epsilon b_I+\epsilon^3(2-\nu)b_R \tag{14}$$

$$\Re\{i\ddot{\Phi}'+i\epsilon^2\nu\varphi'\}=-\epsilon b_I-\epsilon^3(2-\nu)b_R+\epsilon d_I\cos\theta \tag{15}$$

on the crack, and

$$\varphi'=-i\epsilon b \tag{16}$$
$$\ddot{\Phi}'=\epsilon(1+2i\epsilon^2)b-\epsilon d\cos\theta \tag{17}$$

off the crack. The subscripts R and I on the constants mean real and imaginary parts. The constants are determined by conditions yet to be imposed.

For sufficiently short cracks, the whole crack lies in a region for which the characteristic functions of the reduced problem vary rapidly in both coordinates. In that case, a simplified version of (2) commonly called the shallow shell equation applies. The problem has been formulated in terms of integral equations and the solution is known [1-4]. For sufficiently long cracks, the characteristic functions of the reduced problem do not vary rapidly in the θ coordinate, i.e., $\dot{\varphi}$ and φ are the same order, except in a small region near the crack tips. Under these conditions it is possible to construct a solution that is accurate everywhere except near the crack tips [12]. The solution is a linear combination of semimembrane solutions governed by the characteristic equation

$$(\ddot{\varphi}+\varphi)^{\cdot\cdot}-i\epsilon^{-2}\varphi''=0 \tag{18}$$

and edge-effect solutions governed by

$$\varphi''-i\epsilon^{-2}\varphi=0 \tag{19}$$

In more precise terms semimembrane or edge-effect solutions have the form $\varphi(\xi,\theta,\epsilon)$ where $\xi=\epsilon z$ or $\epsilon^{-1}z$, as the case may be, and the first term in the asymptotic expansion of φ in powers of ϵ^2 satisfies (18) or (19). Well-known formal expansion procedures will, for the most part, be omitted in the present paper for the sake of brevity. A result involving semimembrane solutions, needed later, is the following

$$(\ddot{\Phi}+\Phi)^{\cdot\cdot}-i\varphi+2\epsilon^2(\ddot{\varphi}+\varphi)=0(\epsilon^4) \tag{20}$$

It seems plausible that there should be no edge-effects off the crack on $z=0$, and a precise analysis bears this out. There is, however, an edge effect on the crack. Assume a solution in the form $\varphi+\epsilon^{2-}\varphi$ where φ is semimembrane, and $\bar{\varphi}$ is edge-effect. A corresponding $\ddot{\Phi}$ is $0(\epsilon^4)$, too small to be considered. The boundary conditions (12)-(15), equation (20), and the relations $\varphi'=0(\epsilon\varphi), \bar{\varphi}'=0(\epsilon^{-1}\bar{\varphi})$ lead to

$$\Re\{\bar{\varphi}\}=\Re\{i\nu\bar{\varphi}\}$$

and

$$\Re\{\bar{\varphi}'\}=0 \quad \text{on} \quad z=0 \tag{21}$$

The solution to (19) for which $\bar{\varphi}\to 0$ as $z\to\infty$ is

$$\bar{\varphi}=\sqrt{i}G(\theta)e^{-\sqrt{i}z/\epsilon} \tag{22}$$

The conditions (21) are satisfied if G is real and

$$\Re\{\sqrt{i}G\}=\Re\{i\nu\bar{\varphi}(0.\theta)\} \tag{23}$$

The edge-effect is thus seen to be determined by boundary values of the semimembrane solution.

Equation (18), governing semimembrane solutions, calls for only two real boundary conditions on $z=0$. However, we seek a first-approximation solution only, and in view of (20), the boundary conditions (12), (14), and (16) are not independent of (13), (15), and (17), respectively. The problem has now come down to finding a (first-approximation) semimembrane solution $\ddot{\Phi}$ for which

$$\Re\{i\ddot{\Phi}\}=a_R+c_R\cos\theta-1+\frac{1}{2}\theta^2$$
$$\Re\{i\ddot{\Phi}'\}=-\epsilon b_I+\epsilon d_I\cos\theta \tag{24}$$

for $z=0$ on the crack, and

$$\ddot{\Phi}'=\epsilon b-\epsilon d\cos\theta \tag{25}$$

for $z=0$ off the crack. From the exact relation $\Phi''=\epsilon^2\varphi$ and (18) (written for Φ) follows the relation

$$\varphi=-i(\ddot{\Phi}+\Phi)^{\cdot\cdot} \tag{26}$$

to be used for obtaining φ once $\ddot{\Phi}$ is known. The mixed boundary value problem for $\ddot{\Phi}$ is still intractable.

A Fourier series solution to (18) shows that those solutions, even in θ, which vanish at $z=\infty$, necessarily satisfy the conditions

$$\int_{-\pi}^{\pi}\varphi(0,\theta)\,d\theta=0, \quad \int_{-\pi}^{\pi}\varphi(0,\theta)\cos\theta d\theta=0 \tag{27}$$

As has been shown [8] such solutions are closely approximated by solutions to a "substitute characteristics equation"

$$\varphi'=-i^{3/2}\epsilon\left(\ddot{\varphi}+\frac{1}{2}\varphi\right) \tag{28}$$

The essential simplification afforded by this approximation is

Downloaded 01 May 2010 to 171.66.16.249. Redistribution subject to ASME license or copyright; see http://www.asme.org/terms/Terms_Use.cfm

that the boundary values of φ' are expressed in terms of the boundary values of φ itself and its second derivative with respect to θ. Put

$$\ddot{\Phi}(0,\theta)=F(\theta) \tag{29}$$

then from (28)

$$\ddot{\Phi}'(0,\theta)=-i^{3/2}\epsilon\left(\ddot{F}+\frac{1}{2}F\right) \tag{30}$$

The boundary conditions (24) and (25) become

$$F_I=-a_R-c_R\cos\theta+1-\frac{1}{2}\theta^2 \tag{31}$$

$$\Re\left\{i^{1/2}\left(\ddot{F}+\frac{1}{2}F\right)\right\}=-b_I+d_I\cos\theta \tag{32}$$

on the crack, and

$$\ddot{F}+\frac{1}{2}F=i^{1/2}(b-d\cos\theta) \tag{33}$$

off the crack. Equations (31)–(33) are simply a system of ordinary differential equations for the real and imaginary parts of F.

The solution, even about $\theta=0$ and $\theta=\pi$, contains nine undetermined constants (in real terms). These are determined by the conditions (27), applied to F, and certain conditions of continuity. On physical grounds the real displacements u,v, and w must be continuous, so also must be the real X_z, X_θ, ψ, and ψ'. There are thus eleven conditions, in real terms, to be satisfied. In terms of F these require F, $\dot{F}$, $\ddot{F}$, $\Re\{i^{1/2}\dddot{F}\}$ to be continuous and (27) to be satisfied by F. The continuity conditions on X_z and ψ' are not independent conditions because the original boundary data for these functions is continuous. In effect then, there are nine independent conditions to determine the nine constants. The imaginary parts of a and c nowhere enter into the solution and can arbitrarily be set equal to zero. The constants b and d turn out to be real. The solution is

$$F=\sqrt{2}i^{1/2}\left(1-\frac{1}{2}\theta^2-a-c\cos\theta\right),\ \text{on the crack} \tag{34}$$

and

$$F=i^{1/2}\left[2(b+d\cos\theta)+\sqrt{2}P\cos\frac{\pi-\theta}{\sqrt{2}}\right],\ \text{off the crack} \tag{35}$$

where

$$\left.\begin{aligned}
\pi a&=\frac{1}{3}\alpha^3-\frac{\pi}{2}\alpha^2+\frac{\sqrt{2}}{2}\left[\sin\frac{\pi-\alpha}{\sqrt{2}}\right.\\
&\left.-\left(\frac{\pi-\alpha}{\sqrt{2}}\right)\cos\frac{\pi-\alpha}{\sqrt{2}}\right]P\\
2\pi b&=-\left(\frac{\sqrt{2}}{3}\alpha^3+\beta P\right),\Delta c=\sqrt{2}(\beta-\Delta d)\\
2\pi\Delta d&=(\sin2\alpha-2\alpha\cos2\alpha)\sin\frac{\pi-\alpha}{\sqrt{2}}\\
&+\sqrt{2}(\alpha^2+2\sin^2\alpha-3\alpha\sin\alpha\cos\alpha)\cos\frac{\pi-\alpha}{\sqrt{2}}\\
\Delta P&=2(\sin\alpha-\alpha\cos\alpha)\\
\Delta&=\sin\alpha\cos\frac{\pi-\alpha}{\sqrt{2}}+\sqrt{2}\cos\alpha\sin\frac{\pi-\alpha}{\sqrt{2}},\\
\beta&=\sin\frac{\pi-\alpha}{\sqrt{2}}+\frac{\alpha}{\sqrt{2}}\cos\frac{\pi-\alpha}{\sqrt{2}}
\end{aligned}\right\} \tag{36}$$

The solution for $\ddot{\Phi}(z,\theta)$, and by (26) for $\varphi(z,\theta)$, can be constructed by Fourier series or by means of an integral representation [9], but such results will not be needed in the subsequent analysis. The present results are what might be called an "outer solution" as part of a complete solution by the method of matched asymptotic expansions. The singularity at a crack tip according to the outer solution is not correct. It would, however, match the asymptotic form of the correct singularity according to an "inner solution" were such a solution available. The lack of an inner solution is a difficulty that can be circumvented provided one is content with less than complete information.

Energy-Release Rate

Let the energy-release rate $\bar{I}$, (with respect to α) for the crack extending at both ends, be made dimensionless according to the relation $\bar{I}=(\sigma^2R^2h/E)I$. Nicholson and Simmonds [10] have derived path-independent integrals for the calculation of I in cracked shallow shells. In particular, for the present problem

$$I=\int_{-\alpha}^{\alpha}\frac{\partial u_c}{\partial\alpha}d\theta \tag{37}$$

where $u_c\equiv u_c(0,\theta)$. The formula is easily shown to apply to the complete cylinder as well as to the shallow cylinder. For the complete cylinder the following alternative formula can be established by the same methods

$$I=\frac{\partial}{\partial\alpha}\int_{-\pi}^{\pi}u_c(z,\theta,\alpha)\ d\theta \tag{38}$$

In (38) u_c can be replaced by u_e because $\int_{-\pi}^{\pi}u d\theta=0$. Both formulas yield the same result; the second is more easily calculated to give, by means of (10) and (36)

$$I=-2\pi\epsilon^{-1}\frac{\partial b}{\partial\alpha}=\epsilon^{-1}\alpha^2g(\alpha) \tag{39}$$

where

$$g(\alpha)=2\sqrt{2}\left(1+\frac{1-\alpha\cot\alpha}{2\alpha\cot\alpha+\sqrt{2}\alpha\cot[(\pi-\alpha)/\sqrt{2}]}\right)^2 \tag{40}$$

Obviously $g(0)=2\sqrt{2}$.

In the first-approximation theory of thin shells (transverse shear strains neglected) the stretching and bending stress singularities in the neighborhood of a crack tip are the same as those in a flat plate (according to the classical theory) under loading with the same symmetry. The intensity of the singularities depends on the parameters of the shell problem. For the circumferential crack, the dimensional membrane and bending stress measures N_z and M_z on the line of the crack can be expressed in the form [3]

$$N_z\sim\sigma h\left(\frac{\alpha R}{2r}\right)^{1/2}S \tag{41}$$

$$M_z\sim\sigma Rh\epsilon^2\left(\frac{\alpha R}{2r}\right)^{1/2}(1-\nu)(3+\nu)B \tag{42}$$

where r is the distance from the crack tip. By means of path-independent integrals, Nicholson and Simmonds [10] have shown that the energy-release rate in terms of the intensity factors S and B is given by

$$I=2\pi\alpha[S^2+(1-\nu)(3+\nu)B^2] \tag{43}$$

They introduced a combined stress intensity factor C in terms of which (43) reads

$$I=2\pi\alpha C^2 \tag{44}$$

The formulas (41)–(44) have meaning for any crack length. For short cracks, shallow shell analysis leads to results in terms of a parameter $\lambda=\alpha/2\epsilon$. Numerical solution of the integral equations has been accomplished for values of λ up to 9 [4].

One might hope that the shallow shell results for large values of λ would agree in some sense with the present results

Downloaded 01 May 2010 to 171.66.16.249. Redistribution subject to ASME license or copyright; see http://www.asme.org/terms/Terms_Use.cfm

for small values of α, and this is indeed the case. According to (39) $I \sim 2\sqrt{2}\epsilon^{-1}\alpha^2$ for small α. If the two limits agree, then according to (44)

$$\lambda^{-1}C^2(\lambda) \sim 2\sqrt{2}/\pi \tag{45}$$

for large values of λ. The relation (45) is confirmed by the numerical results, but the approach to the limit is rather slow. A rational basis for (45) is discussed in the next section.

Common Limit Problem

In the limit $\epsilon \to 0$, and for any α, rapid variations in the field quantities are confined to a small region near the crack tip, except for a small edge effect which will be left out of the discussion for the sake of simplicity. A scaling of the independent variables appropriate to this state of affairs is found to be

$$\theta = \alpha\eta, \quad z = \epsilon^{-1}\alpha^2\xi \tag{46}$$

so that the characteristic equation (2) takes the form

$$\varphi_{\eta\eta\eta\eta} + 2\left(\frac{t}{\alpha}\right)^2 \nu_{\xi\xi\eta\eta} + \left(\frac{\epsilon}{\alpha}\right)^4 \varphi_{\xi\xi\xi\xi} + \alpha^2\varphi_{\eta\eta} - i\varphi_{\xi\xi} = 0 \tag{47}$$

Assume the following relation between the parameters

$$\epsilon^2 << \alpha^2 << 1 \tag{48}$$

in which case α is small and λ is large. From (47) φ is approximated by solutions to the simplified characteristics equation

$$\varphi_{\eta\eta\eta\eta} - i\varphi_{\xi\xi} = 0 \tag{49}$$

This equation contains only those terms that are common to the shallow shell equation and the semimembrane equation. With this geometry, the crack lies on $\xi = 0$, $|\eta| < 1$, and the problem can be formulated in the region $\xi > 0$, $-\infty < \eta < \infty$. The condition $\varphi \sim 1/2\theta^2$ at ∞ can be rescaled to become $\varphi \sim 1/2\eta^2$ at ∞. Boundary and other conditions are easily formulated. The usable factor of (49) in the region $\xi > 0$ is

$$\varphi_{\eta\eta} = i^{1/2}\varphi_{\xi} \tag{50}$$

Note that this agrees with the limit form of the substitute characteristic equation (28), subjected to the same scaling. The solution in its details parallels that for the semi membrane equation and need not be presented. The result for the energy-release rate is $I = 2\sqrt{2}\epsilon^{-1}\alpha^2$, as was anticipated.

Results and Discussion

The energy-release rates for long cracks and short cracks are given by (39) and (44), respectively. The latter result can be represented in closed form by means of the following formulas

$$\begin{aligned} C(\lambda) &= 1 + \frac{\pi}{16}\lambda^2 - .0293\lambda^3 \quad \lambda \le 1 \\ &= \left(\frac{2\sqrt{2}}{\pi}\lambda\right)^{.5} + \left(\frac{.179}{\lambda}\right)^{.885} \quad \lambda > 1 \end{aligned} \tag{51}$$

which fit the numerical data [13] to within 1/2 percent over the whole range of λ. Figure 1 shows results for I plotted as a function of $\alpha(0° - 40°)$ for $\epsilon = 0.1$, which corresponds to $R/h \approx 30$. As can be seen, the shallow shell and complete shell results are not greatly different. The flat plate result corresponds to $C = 1$ in (44).

The coefficients in (47) indicate that $\alpha = 0(\sqrt{\epsilon})$ divides the range of long and short cracks. The division is not a sharp one and does not impose a severe restriction on the length of short cracks for practical values of ϵ. Approximate estimates are that $\alpha < 13°$ (18°) for $R/h = 100$ (30) are short cracks. A "curve fit" formula which agrees with short crack results for small α, long crack results for large $\alpha/2\epsilon$, and is somewhat conservative in between is the following:

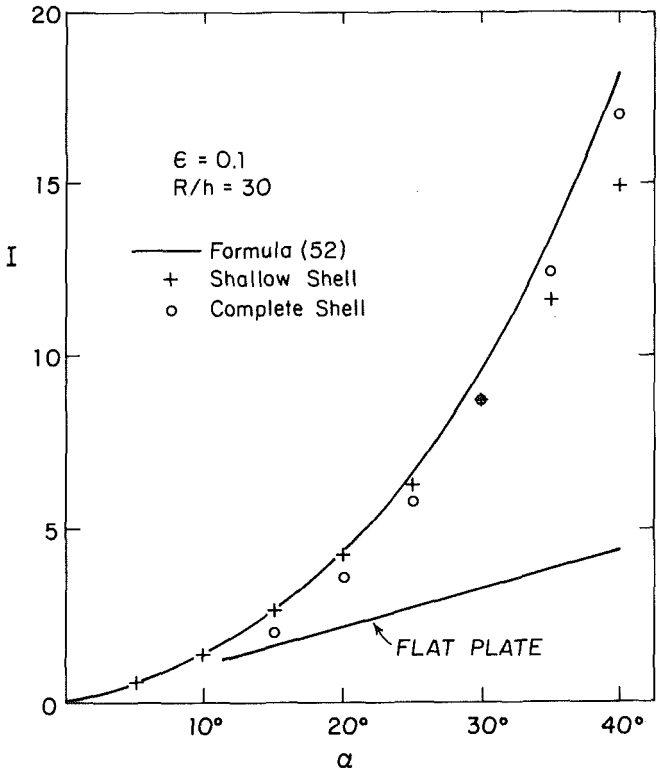


Fig. 1 Dimensionless energy-release rate versus crack angle

$$I = \epsilon^{-1}\alpha^2[g(\alpha) + \pi\lambda^{-1}C^2(\lambda) - 2\sqrt{2}] \tag{52}$$

This formula is represented graphically by the solid curve in Fig. 1. For smaller values of ϵ, (52) agrees more closely with one or the other of (39) or (44).

The present analysis does not yield the stress intensity factors S and B in (43); only the combination C is determined. However, all available evidence [2, 3, 5, 7] indicates that B is numerically small in comparison to S over the whole range of α for the geometry and loading conditions under consideration. The present analysis also omits the effects of transverse shear strains. These effects have been rather thoroughly investigated [5, 7], and found to be significant [6] only for very short cracks, $\alpha = 0(\epsilon^2)$. A fracture criterion based on a critical value of the energy-release rate seems indicated, subject to the usual restriction to small scale yeilding.

Semimembrane solutions decay very slowly in the axial direction. The validity of the present analysis is therefore limited to cylinders sufficiently long to avoid end effects. The required minimum distance between the crack and any boundary, load, or other significant disturbance is estimated to be about $2R\sqrt{R/h}$, more less independent of the crack length. Errors introduced by use of the substitute characteristic equation (28) in place of the more accurate (18) are typically the order of 1 percent, independent of ϵ. For $R/h \le 30$ such errors are no greater than those due to the use of thin shell theory.

Acknowledgment

This work was supported in part by the National Science Foundation under Grants MCS79-03227 and CME80-07477, and by the Division of Applied Sciences, Harvard University.

References

1 Folias, E. S., "A Circumferential Crack in a Pressurized Cylindrical Shell," *International Journal of Fracture Mechanics*, Vol. 3, 1967, pp. 1–11.

Downloaded 01 May 2010 to 171.66.16.249. Redistribution subject to ASME license or copyright; see http://www.asme.org/terms/Terms_Use.cfm

2 Erdogan, F., and Ratwani, M., "Fatigue and Fracture of Cylindrical Shells Containing a Circumferential Crack," *International Journal of Fracture Mechanics*, Vol. 6, 1970, pp. 379–392.

3 Duncan-Fama, M. E., and Sanders, J. L., Jr., "A Circumferential Crack in a Cylindrical Shell under Tension," *International Journal of Fracture Mechanics*, Vol. 8, 1972, pp. 15–20.

4 Nicholson, J. W., Weidman, S. T., and Simmonds, J. G., "Sanders' Energy-Release Rate Integral for a Circumferentially Cracked Cylindrical Shell," to be submitted for publication.

5 Erdogan, F., and Delale, F., "Transverse Shear Effect in a Circumferentially Cracked Cylindrical Shell," *Quarterly of Applied Mathematics*, Vol. 37, 1979, pp. 239–258.

6 Simmonds, J. G., and Duva, J., "Thickness Effects are Minor in the Energy-Release Rate Integral for Bent Plates Containing Elliptic Holes or Cracks," ASME JOURNAL OF APPLIED MECHANICS, Vol. 48, 1981, pp. 320–326.

7 Barsoum, R. S., Loomis, R. W., and Stewart, B. D., "Analysis of Through Cracks in Cylindrical Shells by the Quarter-Point Elements," *International Journal of Fracture*, Vol. 15, 1979, pp. 259–280.

8 Sanders, J. L., Jr., "Closed-Form Solution to the Semi-Infinite Cylindrical Shell Problem," *Contributions to the Theory of Aircraft Structures* (Van der Neut Volume), Delft University Press, Rotterdam, 1972, pp. 229–237.

9 Sanders, J. L., Jr., "The Cylindrical Shell Loaded by a Concentrated Normal Force," *Mechanics Today*, Vol. 5 (Reissner Volume), Pergamon Press, Oxford, 1980, pp. 427–438.

10 Nicholson, J. W., and Simmonds, J. G., "Sanders' Energy-Release Rate Integral for Arbitrarily Loaded Shallow Shells and Its Asymptotic Evaluation for a Cracked Cylinder," ASME JOURNAL OF APPLIED MECHANICS, Vol. 47, 1980, pp. 363–369.

11 Sanders, J. L., Jr., "On Stress Boundary Conditions in Shell Theory," ASME JOURNAL OF APPLIED MECHANICS, Vol. 47, 1980, pp. 202–204.

12 Reissner, E., and Simmonds, J. G., "Asymptotic Solutions of Boundary Value Problems for Elastic Semi-Infinite Circular Shells," *Journal of Mathematics and Physics*, Vol. 45, 1966, pp. 1–22.

13 Simmonds, J. G., private communication, October 1980.

Downloaded 01 May 2010 to 171.66.16.249. Redistribution subject to ASME license or copyright; see http://www.asme.org/terms/Terms_Use.cfm

K. Chandrashekhara
Professor,
Department of Civil Engineering,
Indian Institute of Science,
Bangalore 560 012, India

P. Gopalakrishnan
Assistant Professor,
Department of Civil Engineering,
College of Engineering,
Trivandrum, India

Elasticity Solution for a Multilayered Transversely Isotropic Circular Cylindrical Shell

An elasticity solution has been obtained for a long multilayered cylindrical shell of transversely isotropic layers subjected to axisymmetric radial load following Lekhnitskii's stress function method. Numerical results are presented for a two layered shell for different ratios of thickness-to-outer radius and for different ratios of the moduli of elasticity in the radial direction of the layers. The results obtained from this analysis have been compared with those obtained from the multilayered shell theory of Ambartsumian.

Introduction

The rapid development of high strength, high stiffness, and low density composite materials has resulted in the construction of laminated anisotropic plates and shells. Laminated shells exhibit properties considerably different from those of single-layer shells. In general, such shells exhibit effects due to the coupling of bending, stretching, shearing, and twisting. The analysis of various multilayered anisotropic shells, based on the assumption of nondeformable normals, have been presented in a monograph by Ambartsumian [1]. The contributions made by several investigators to the theory of anisotropic layered shells have been reviewed by Ambartsumian [2] and Habip [3]. A classified description of the studies made in anisotropic laminated plates and shells in recent years has been given by Vinson and Chou [4]. From these references, it appears that the theory of laminated anisotropic cylindrical shell has been adequately developed. The theories based on the assumption of nondeformable normals are found to be sufficiently accurate when (1) the ratio of the thickness to the lateral dimension is very small, (2) the anisotropy of each layer is not large, and (3) the material properties do not vary radically from layer to layer. In many practical applications these restrictions may not be satisfied. Therefore as a refinement, theories incorporating shear deformation and normal stress have been developed for laminated anisotropic shells. But the accuracy of these theories cannot be assessed unless they are compared with an exact solution.

The comparisons of solutions for circular cylinders by elasticity and shell theory with isotropic and transversely isotropic materials [5–8] have revealed that the shell solutions cannot be applied indiscriminately. Similar comparative study for a multilayered anisotropic cylindrical shell is of great importance to assess the accuracy of these improved shell theories.

Contributed by the Applied Mechanics Division for publication in the JOURNAL OF APPLIED MECHANICS.

Discussion on this paper should be addressed to the Editorial Department, ASME, United Engineering Center, 345 East 47th Street, New York, N. Y. 10017, and will be accepted until two months after final publication of the paper itself in the JOURNAL OF APPLIED MECHANICS. Manuscript received by ASME Applied Mechanics Division, October, 1980; final revision, July, 1981.

In this paper, an elasticity solution is presented for the foregoing problem. The solution has been obtained in terms of Lekhnitskii's [9] stress function and the final equations are arranged in matrix form using the transfer matrix approach for ease of computation. Numerical results have been obtained for a two-layered shell with different thickness-to-radius ratios and different anisotropic constants for the layers. The results obtained are compared with those of Ambartsumian [1] according to classical shell theory. A comparison of results from elasticity and shear-deformation theory [8] for a single transversely isotropic shell has indicated that incorporating the shear deformation will not in general improve the results over that of classical theory. Hence only the comparison of results from elasticity and classical shell theory has been presented here.

Problem

The problem analyzed is shown in Figs. 1(*a–c*). A long circular cylindrical shell of n layers of transversely isotropic material of constant thickness is subjected to an axisymmetric radial load. It is assumed that there is perfect adhesion between the layers so that the continuity of deformation is satisfied at the interfaces. Each layer of the shell is of transversely isotropic material and of different thickness. For the jth layer, the elastic constants of the transversely isotropic material are given as $(a_{11})_j$, $(a_{12})_j$, $(a_{13})_j$, $(a_{33})_j$, and $(a_{44})_j$. The inner and outer radii of the shell are r_0 and r_n and for the typical jth layer the inner and outer radii will be r_{j-1} and r_j.

Method of Analysis

The analysis of this problem is carried out using Lekhnitskii's [9] stress function. The final equations are arranged in matrix form using transfer matrices so that only four simultaneous equations need to be solved, regardless of the number of layers. A stress function φ_j satisfying the differential equation

$$\nabla_1^2 \nabla_2^2 \varphi_j = 0 \tag{1}$$

is chosen for the jth layer of the shell. The stresses and displacements in this layer are determined from

Copyright © 1982 by ASME
Downloaded 01 May 2010 to 171.66.16.249. Redistribution subject to ASME license or copyright; see http://www.asme.org/terms/Terms_Use.cfm

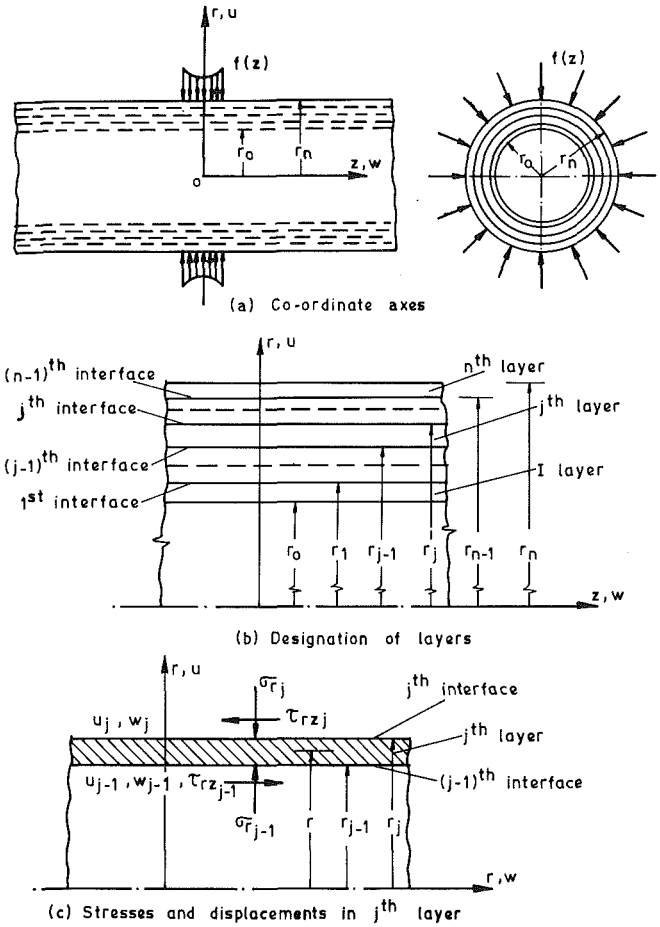


Fig. 1 Multilayered cylindrical shell subjected to axisymmetrical radial load

$$(\sigma_r)_j = -\frac{\partial}{\partial z}\left[\frac{\partial^2}{\partial r^2}+B_j\frac{1}{r}\frac{\partial}{\partial r}+A_j\frac{\partial}{\partial z^2}\right]\varphi_j$$

$$(\sigma_\theta)_j = -\frac{\partial}{\partial z}\left[B_j\frac{\partial^2}{\partial r^2}+\frac{1}{r}\frac{\partial}{\partial r}+A_j\frac{\partial^2}{\partial z^2}\right]\varphi_j$$

$$(\sigma_z)_j = -\frac{\partial}{\partial z}\left[C_j\frac{\partial^2}{\partial r^2}+C_j\frac{1}{r}\frac{\partial}{\partial r}+D_j\frac{\partial^2}{\partial z^2}\right]\varphi_j$$

$$(\tau_{rz})_j = \frac{\partial}{\partial r}\left[\frac{\partial^2}{\partial r^2}+\frac{1}{r}\frac{\partial}{\partial r}+A_j\frac{\partial^2}{\partial z^2}\right]\varphi_j$$

$$(u)_j = A_j^*\frac{\partial^2\varphi_j}{\partial r\partial z}$$

$$(w)_j = B_j^*\left[\frac{\partial^2}{\partial r^2}+\frac{1}{r}\frac{\partial}{\partial r}\right]\varphi_j+C_j^*\frac{\partial^2\varphi_j}{\partial z^2} \tag{2}$$

where

$$\nabla_i^2=\left[\frac{\partial^2}{\partial r^2}+\frac{1}{r}\frac{\partial}{\partial r}+\frac{1}{(S_i^j)^2}\frac{\partial^2}{\partial z^2}\right];\quad i=1,2 \tag{3}$$

and

$$S_{1,2}^j=\sqrt{\frac{(A_j+C_j)\pm\sqrt{(A_j+C_j)^2-4D_j}}{2D_j}}$$

where j denote values pertaining to the jth layer and A, B, C, D and A^*, B^*, C^* denote the following:

$$A=\frac{a_{13}(a_{11}-a_{12})}{(a_{11}a_{33}-a_{13}^2)};\quad B=\frac{a_{13}(a_{13}+a_{44})-a_{12}a_{33}}{(a_{11}a_{33}-a_{13}^2)};$$

$$C=\frac{a_{13}(a_{11}-a_{12})+a_{11}a_{44}}{(a_{11}a_{33}-a_{13}^2)};\quad D=\frac{a_{11}^2-a_{12}^2}{(a_{11}a_{33}-a_{13}^2)};$$

$$A^*=(a_{11}-a_{12})(B-1);\quad B^*=a_{44};\quad C^*=(Da_{33}-2Aa_{13}).$$

Boundary and Continuity Conditions

For the problem considered here the boundary conditions are

$$\text{At } r=r_0,\quad \sigma_r=0,\quad \tau_{rz}=0$$
$$\text{At } r=r_n,\quad \sigma_r=f(z),\quad \tau_{rz}=0 \tag{4}$$

The radial load $f(z)$ can be represented as a Fourier integral

$$f(z)=\int_0^\infty q(\alpha)\cos\alpha z d\alpha \tag{5}$$

where

$$q(\alpha)=\frac{2}{\pi}\int_0^\infty f(z)\cos\alpha z dz.$$

In addition to the foregoing boundary conditions, for perfect adhesion between layers, continuity conditions in terms of stresses and displacements are to be satisfied along each interface. For example, along the jth interface the continuity conditions can be written as

$$(\sigma_r)_j\Big|_{r=r_j}=(\sigma_r)_{j+1}\Big|_{r=r_j};\quad (\tau_{rz})_j\Big|_{r=r_j}=(\tau_{rz})_{j+1}\Big|_{r=r_j}$$

$$(u)_j\Big|_{r=r_j}=(u)_{j+1}\Big|_{r=r_j};\quad (w)_j\Big|_{r=r_j}=(w)_{j+1}\Big|_{r=r_j} \tag{6}$$

Nomenclature

$a_{11}, a_{12}, a_{13}, a_{33}, a_{44}$ = elastic constants for a transversely isotropic material
$E_r, E_\theta, E_z, G_{rz}$ = elastic modulii of transversely isotropic material
$f(z)$ = axisymmetric radial load acting on the outer surface of the shell
$I_0(\alpha), I_1(\alpha)$ = modified Bessel function of first kind, zero and first order, respectively
j = superscript to indicate any layer
$K_0(\alpha), K_1(\alpha)$ = modified Bessel function of second kind, zero and first order, respectively
Q = axisymmetric radial line load/unit length of circumference
$\bar{q}(\alpha)$ = $q(\alpha)\cos\alpha z$
$r_0, r_1, \ldots, r_j, \ldots, r_{n-1}$ = inside radius of layers $1,2,\ldots,j+1,\ldots,n$
r, z = cylindrical coordinate system
$(u)_j, (w)_j$ = radial and longitudinal displacements in the jth layer
α = variable of integration
$\gamma_{rz}, \gamma_{r\theta}, \gamma_{\theta z}$ = shear strains
$(\sigma_r)_j, (\sigma_\theta)_j, (\sigma_z)_j$ = normal stresses in the jth layer
$\nu_{\theta z}, \nu_{z\theta}$ = Poisson's ratios for the transversely isotropic material
$(\tau_{rz})_j$ = shear stress in the jth layer
η = E_r/E_z
μ = $(E_r)_2/(E_r)_1$

Downloaded 01 May 2010 to 171.66.16.249. Redistribution subject to ASME license or copyright; see http://www.asme.org/terms/Terms_Use.cfm

Solution

The stress function φ_j for the typical jth layer is taken as

$$\varphi_j = \int_0^\infty \frac{1}{\alpha^3} [P_j(\alpha) I_0(\alpha r/S_1^j) + Q_j(\alpha) I_0(\alpha r/S_2^j) + R_j(\alpha) K_0(\alpha r/S_1^j) + S_j(\alpha) K_0(\alpha r/S_2^j)] \sin \alpha z d\alpha \quad (7)$$

which satisfies equation (1). The stresses and displacements for the jth layer can be obtained from this stress function using equation (2). The stresses and displacements for the jth layer can be written for convenience as

$$(\sigma_r)_j = \int_0^\infty \bar{\sigma}_r(\alpha,r)_j d\alpha; \quad (\sigma_\theta)_j = \int_0^\infty \bar{\sigma}_\theta(\alpha,r)_j d\alpha$$

$$(\sigma_z)_j = \int_0^\infty \bar{\sigma}_z(\alpha,r)_j d\alpha; \quad (\tau_{rz})_j = \int_0^\infty \bar{\tau}_{rz}(\alpha,r)_j d\alpha$$

$$(u)_j = \int_0^\infty \bar{u}(\alpha,r)_j d\alpha; \quad (w)_j = \int_0^\infty \bar{w}(\alpha,r)_j d\alpha \quad (8)$$

For a jth layer the stresses and displacements (used in the continuity conditions) can be obtained in terms of the four unknown functions using equation (2). The relation can be written in compact form as

$$Z(r) = [G(\alpha,r)]\bar{p}_j(\alpha); \quad (r_{j-1} < r < r_j) \quad (9)$$

where $Z(r)$ may be called a state vector, and defined as

$$Z(r) = \begin{bmatrix} \bar{\sigma}_r(\alpha,r)_j \\ \bar{\tau}_{rz}(\alpha,r)_j \\ \bar{w}(\alpha,r)_j \\ \bar{u}(\alpha,r)_j \end{bmatrix} \text{ and } \bar{p}_j(\alpha) = \begin{bmatrix} P_j(\alpha) \\ Q_j(\alpha) \\ R_j(\alpha) \\ S_j(\alpha) \end{bmatrix} \quad (10)$$

and $[G(\alpha,r)]$ is a matrix relating the coefficients of unknown functions $P_j(\alpha), \ldots, S_j(\alpha)$ which can be obtained from equations (2) and (7).

To determine the unknown functions $P_j(\alpha)$, $Q_j(\alpha)$, $R_j(\alpha)$, and $S_j(\alpha)$ for a given value of α and z, the boundary conditions of the jth layer along the $(j-1)$th interface is to be applied, i.e., along $r = r_{j-1}$, the interface state vector $Z(r)$ will be $Z(r_{j-1})$ and the matrix $[G(\alpha,r)]$ becomes $[G(\alpha,r_{j-1})]$. Hence the coefficients of $[G(\alpha,r_{j-1})]$ are all known.

Similarly using the boundary condition along the the jth interface of the jth layer, we can write the state vectors for jth layer as

$$Z(r_j) = [F_j]Z(r_{j-1}) \quad (11)$$

where

$$[F_j] = [G(\alpha,r_j)][G(\alpha,r_{j-1})]^{-1}$$

is the transfer matrix for the jth layer. Equation (11) relates the interface vector at one end of the layer to that at the other end.

Similarly for the $(j-1)$th layer

$$Z(r_{j-1}) = [F_{j-1}]Z(r_{j-2}) \quad (12)$$

If the shell consists of n layers, then the interface vector $Z(r)$ at the outer and inner surfaces of the shell are $Z(r_n)$ and $Z(r_0)$ which represent the boundary conditions of the shell, i.e.,

$$Z(r_n) = [F_n][F_{n-1}] \ldots [F_1]Z(r_0) \quad (13)$$

From equation (13) the unknown components of the state vectors at the outer and inner boundaries of the complete shell are first determined. If the shell is subjected to a radial load on its outer surface, then for the outer surface

$$Z(r_n) = \begin{bmatrix} \bar{\sigma}_r(\alpha,r_n) \\ \bar{\tau}_{rz}(\alpha,r_n) \\ \bar{w}(\alpha,r_n) \\ \bar{u}(\alpha,r_n) \end{bmatrix} = \begin{bmatrix} \bar{q}(\alpha) \\ 0 \\ \bar{w}(\alpha,r_n) \\ \bar{u}(\alpha,r_n) \end{bmatrix} \quad (14)$$

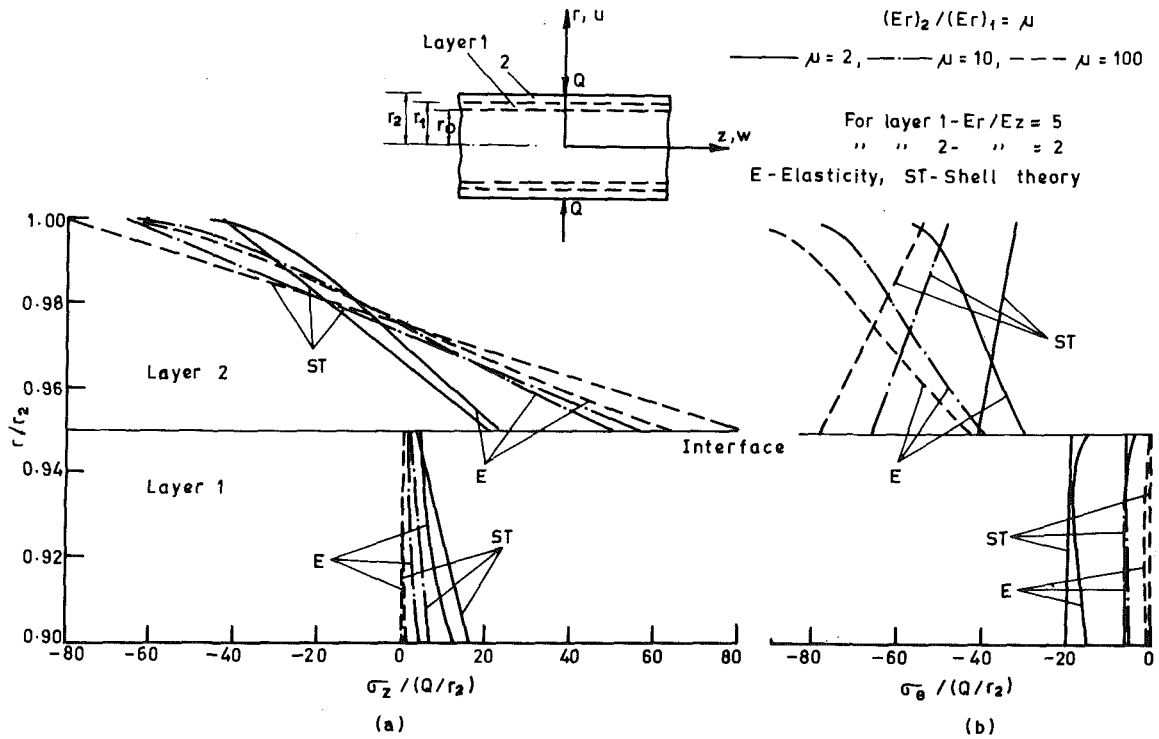


Fig. 2 Variation of longitudinal (σ_2) and circumferential (σ_θ) stresses at $z/r_2 = 0$ for $r_0/r_2 = 0.9$, $r_1/r_2 = 0.95$

Downloaded 01 May 2010 to 171.66.16.249. Redistribution subject to ASME license or copyright; see http://www.asme.org/terms/Terms_Use.cfm

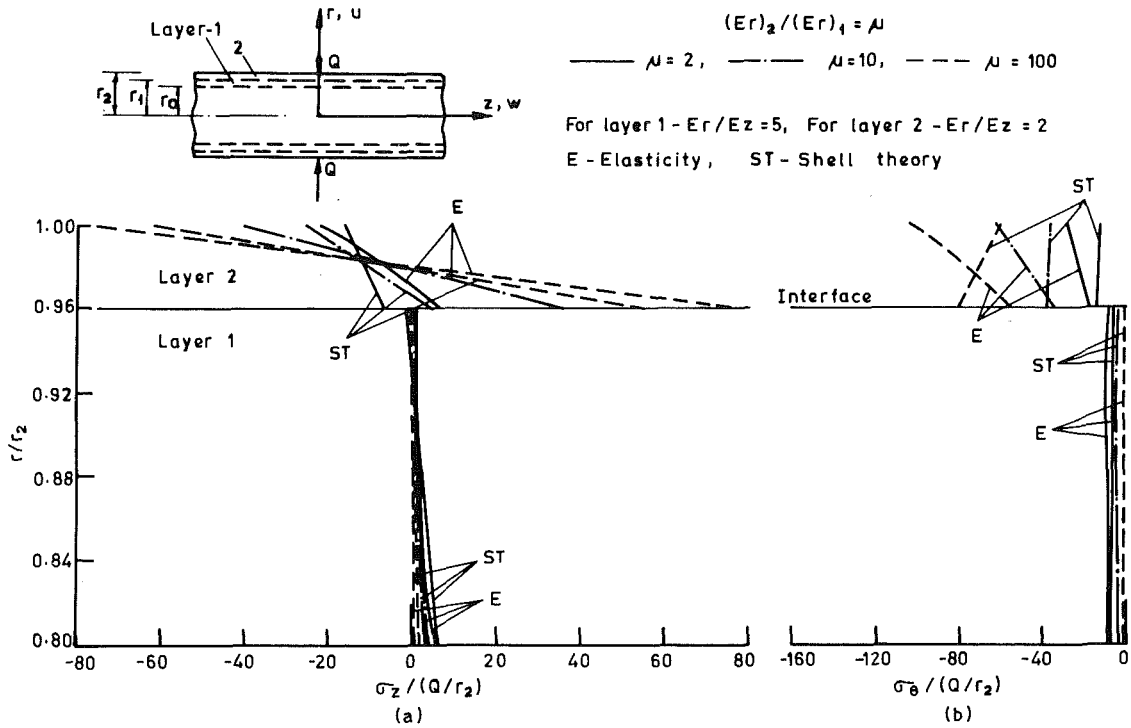


Fig. 3 Variation of longitudinal (σ_z) and circumferential (σ_θ) stresses at $z/r_2 = 0$ for $r_0/r_2 = 0.8$, $r_1/r_2 = 0.96$

and for the inner surface of the shell,

$$Z(r_0) = \begin{bmatrix} \bar{\sigma}_r(\alpha,r_0) \\ \bar{\tau}_{rz}(\alpha,r_0) \\ \bar{w}(\alpha,r_0) \\ \bar{u}(\alpha,r_0) \end{bmatrix} = \begin{bmatrix} 0 \\ 0 \\ \bar{w}(\alpha,r_0) \\ \bar{u}(\alpha,r_0) \end{bmatrix} \tag{15}$$

The unknown displacements at the boundaries can be obtained in terms of the load as well as the state vectors $Z(r_n)$ and $Z(r_0)$ from equations (13)–(15).

To determine the stresses and displacements for the jth layer, the unknown functions $P_j(\alpha), \ldots, S_j(\alpha)$ for the jth layer is determined first. These functions are obtained from equation (9) as

$$\bar{p}_j(\alpha) = [G(\alpha,r_{j-1})]^{-1} Z(r_{j-1}) \tag{16}$$

Application to Two-Layered Shell

To illustrate the applications of the general solution previously given, a long circular cylindrical shell having two layers of transversely isotropic material and subjected to an axisymmetric radial line load on the outer surface of the shell is considered. Numerical results are obtained for three different ratios of radius to thickness and for different elastic constants of the material.

First, equation (13) for a two-layered shell can be written as

$$Z(r_2) = [F_2][F_1]Z(r_0) \tag{17}$$

Since the stress components of the of the state vectors $Z(r_2)$ and $Z(r_0)$ are known, the displacement components of $Z(r_0)$ are calculated using equation (17). Once the state vector for the inner surface of the shell is known, the unknown functions $\bar{p}_j(\alpha)$ for $(j=1,2)$ the first and second layers can be determined using equation (16) and the stresses and displacements at any point can be determined. Details of the procedure for determining the stresses and displacement components is given in reference [11].

Numerical Results and Discussion

Numerical results have been obtained for a two-layered shell subjected to axisymmetric radial line load. The following elastic constants have been taken for the layers:

Layer (1): $E_r/E_z = 5$, $\nu_{r\theta} = 0.3$, $\nu_{rz} = 0.32$, $G_{rz} = E_r/11.32$
Layer (2): $E_r/E_z = 2$, $\nu_{r\theta} = 0.3$, $\nu_{rz} = 0.32$, $G_{rz} = E_r/5.28$

To illustrate the effect of different moduli in the radial direction of each layer on stresses and displacments, three different ratios, viz., $\mu = (E_r)_2/(E_r)_1 = 2$, 10, 100 have been considered. To study the effect of thickness of each layer on stresses and displacements the following cases are considered; these include a two-layered shell of equal and unequal thickness.

(*a*) $r_0/r_2 = 0.8$, $r_1/r_2 = 0.9$
(*b*) $r_0/r_2 = 0.8$, $r_1/r_2 = 0.96$
(*c*) $r_0/r_2 = 0.9$, $r_1/r_2 = 0.95$.

Numerical results have been obtained for the foregoing cases according to three-dimensional elasticity and the results have been compared with those obtained by layered shell theory as given by Ambartsumian [1]. Some typical results are presented here. It is to be noted that the stresses and displacements of the elasticity solutions involve several infinite integrals which have been evaluated numerically using Weddle's formula [10].

Figures 2–4 show the variation of longitudinal (σ_z) and circumferential (σ_θ) stresses over the thickness of a two-layered shell of equal and unequal thickness. From the figures it may be observed that when the ratio of moduli in the radial direction is very large ($\mu = 100$), the longitudinal stress variation is negligible in the inner layer indicating that the external load is completely resisted by the outer layer. It may also be seen that for $\mu = 100$, the shell theory, in general, overestimates the maximum stress in the outer layer for equal thickness of the layers, while it underestimates in the case of unequal thickness. For example, when $r_0/r_2 = 0.9$ and $r_1/r_2 = 0.95$, shell theory gives 24 percent greater value, and for $r_0/r_2 = 0.8$, $r_1/r_2 = 0.96$, it is 26 percent less. It may be

Downloaded 01 May 2010 to 171.66.16.249. Redistribution subject to ASME license or copyright; see http://www.asme.org/terms/Terms_Use.cfm

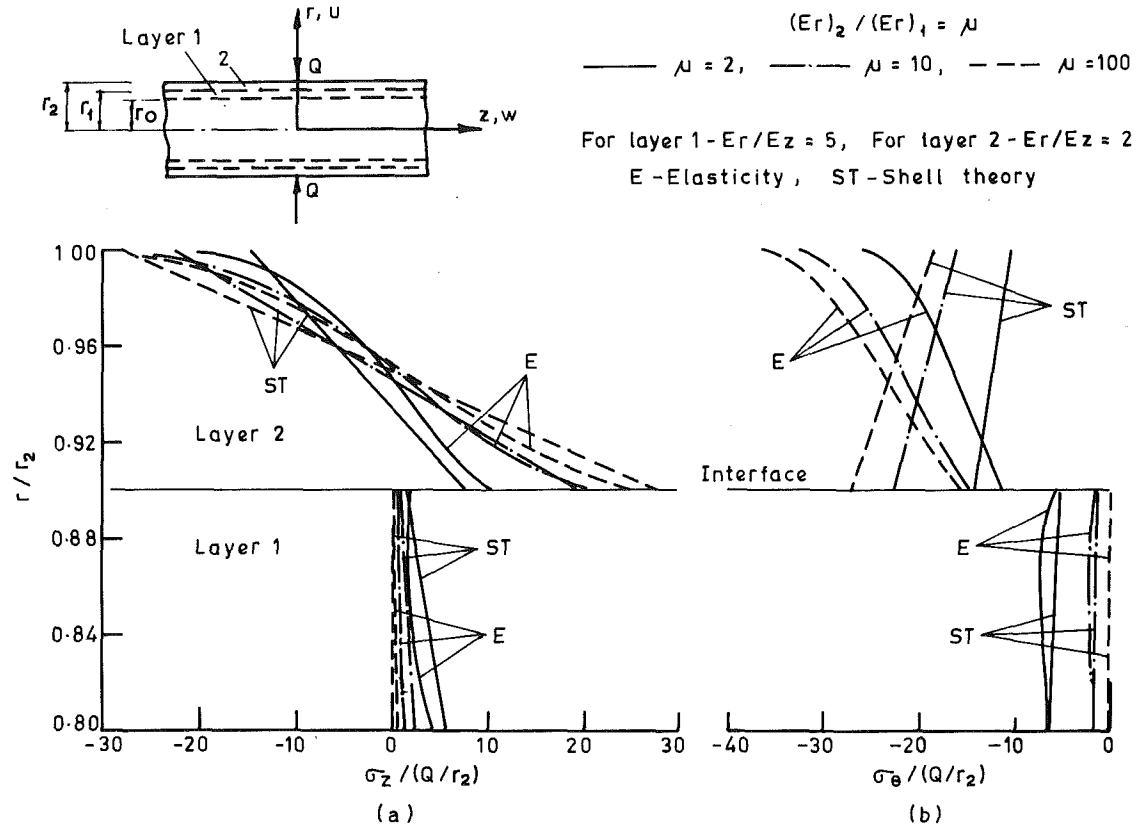


Fig. 4 Variation of longitudinal (σ_z) and circumferential (σ_θ) stresses at $z/r_2 = 0$ for $r_0/r_2 = 0.8$, $r_1/r_2 = 0.9$

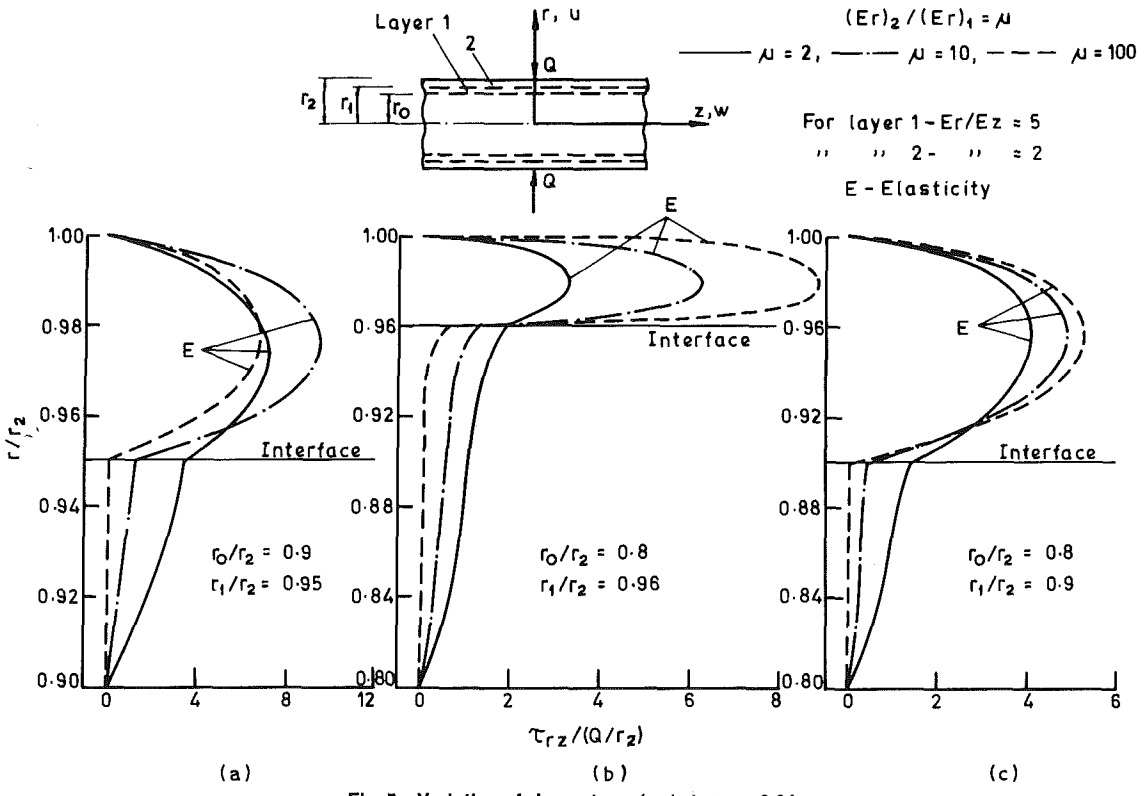


Fig. 5 Variation of shear stress (τ_{rz}) at $z/r_2 = 0.04$

observed from Figs. 2(*a*) and 4(*a*), that when the thickness of each layer is large (i.e., $r_0/r_2 = 0.8$ or less) the longitudinal stress variation, as predicted by elasticity, is nonlinear, while shell theory gives a linear variation of the stress. Figures 2(*b*) to 4(*b*), indicate that, in general, shell theory gives very poor predictions of circumferential stress for the outer layer while there is reasonable agreement between the two results for the inner layer. Figures 5(*a*)–(*c*), show the variation of shear stress

Downloaded 01 May 2010 to 171.66.16.249. Redistribution subject to ASME license or copyright; see http://www.asme.org/terms/Terms_Use.cfm

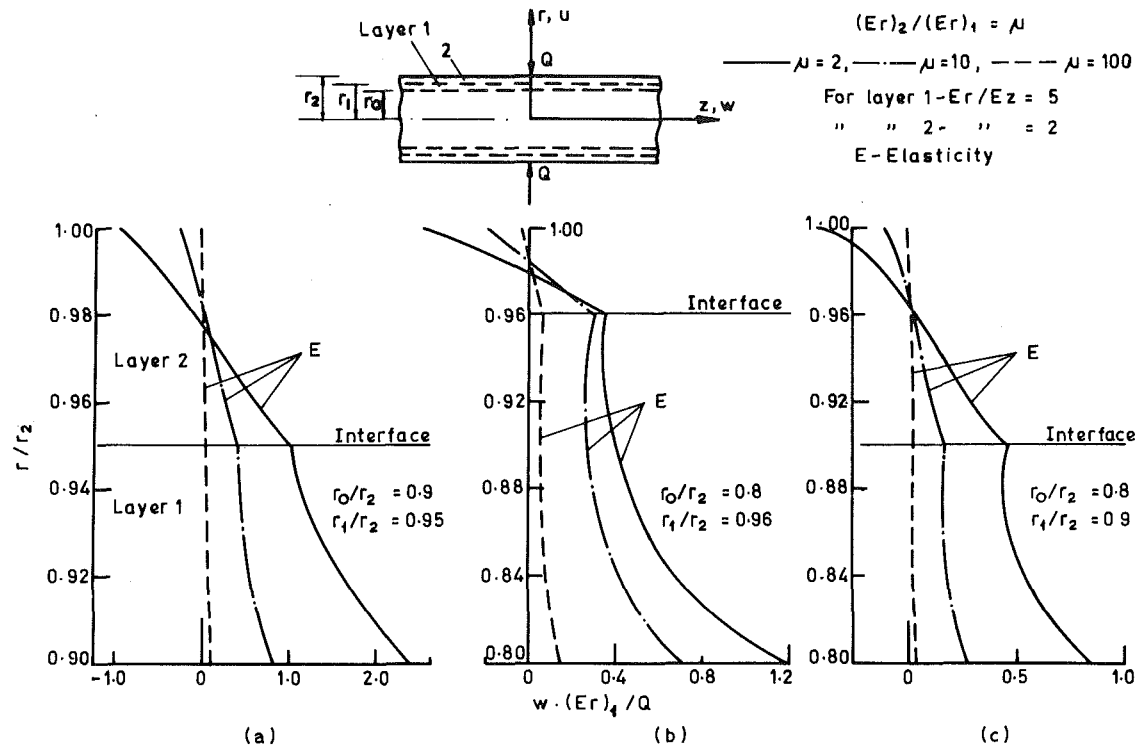


Fig. 6 Variation of longitudinal displacement (w) at $z/r_2 = 0.04$

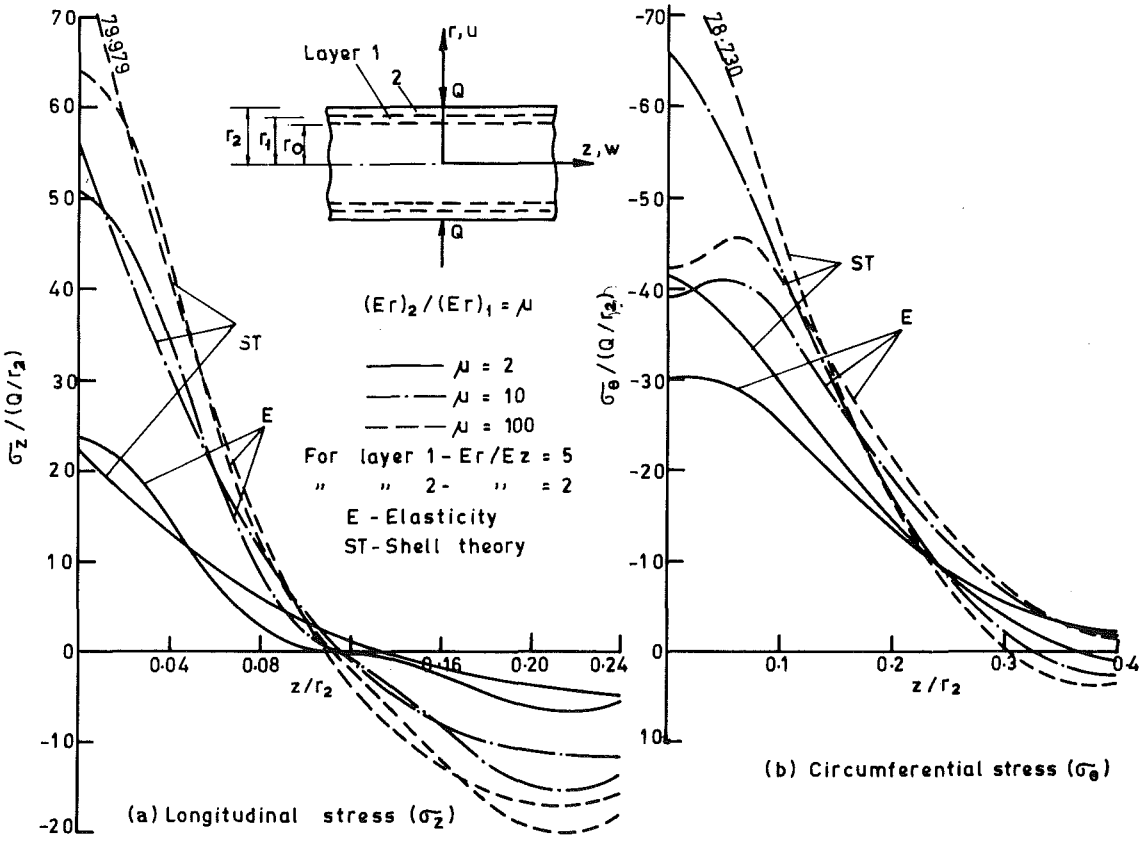


Fig. 7 Variation of stresses at the interface, ($r_0/r_2 = 0.9$, $r_1/r_2 = 0.95$)

in the outer and inner layers. It may be observed from these figures that in general, the shear stress distribution is parabolic in the outer layer and the shear stress is small in the inner layer for all the cases considered here. Figures 6(a–c), show the variation of the longitudinal displacement at $z/r_2 = 0.04$ according to the three-dimensional solution. When the thickness of the outer shell is small the variation of the longitudinal displacement is linear and it becomes nonlinear when the thickness becomes large ($r_0/r_2 \leq 0.8$). Figures 7 and 8 show the variation of interface longitudinal and cir-

Downloaded 01 May 2010 to 171.66.16.249. Redistribution subject to ASME license or copyright; see http://www.asme.org/terms/Terms_Use.cfm

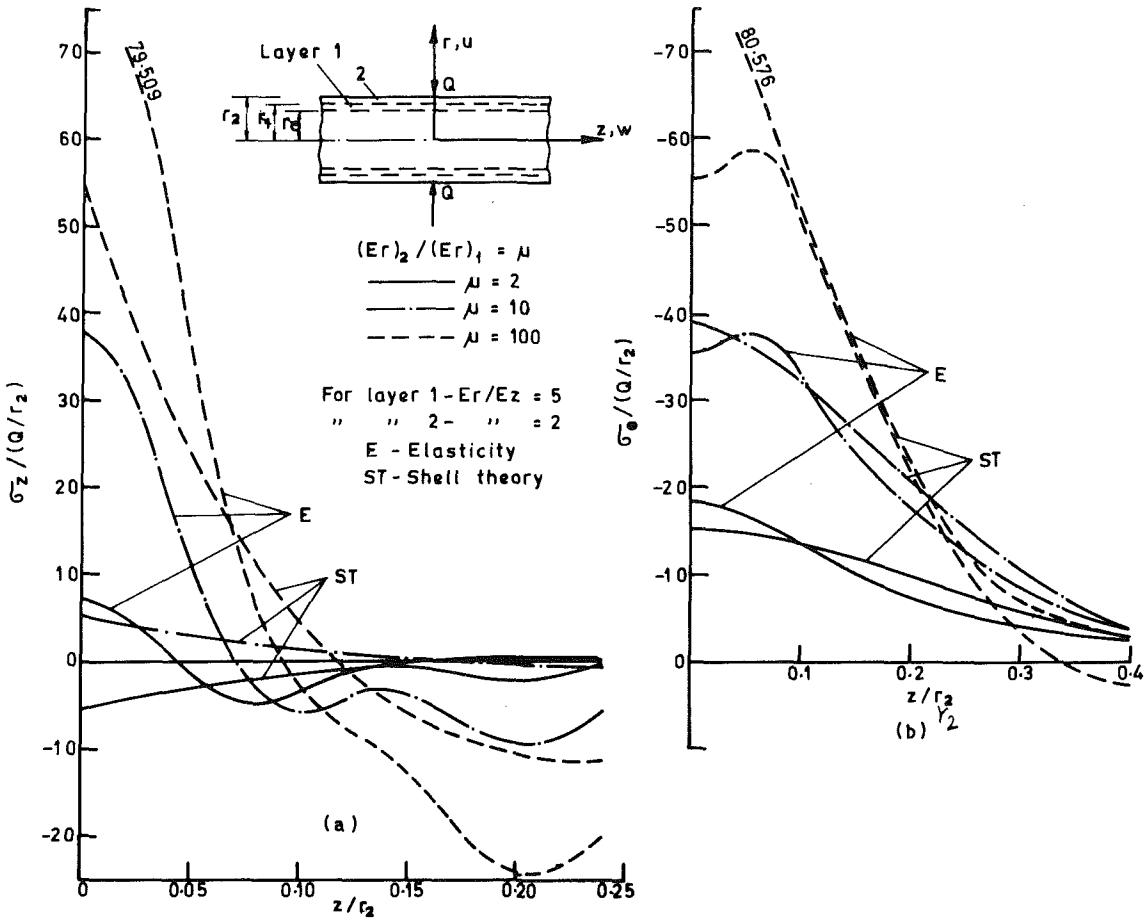


Fig. 8 Variation of stresses at the interface, ($r_0/r_2 = 0.8$, $r_1/r_2 = 0.96$)

cumferential stresses for two ratios of outer to inner thickness. It may be seen that the shell theory gives fairly accurate results for the interface longitudinal stress for $\mu = 100$ and for equal thickness (Fig. 7) while the results are poor for unequal thickness of the layers (Fig. 8). The circumferential stress of elasticity and shell theory differ greatly near the load, while at sections farther away from the load the agreement between the two results is good.

Summary and Conclusion

In this paper an elasticity solution for a multilayered transversely isotropic cylinder subjected to axisymmetric load based on a stress function approach has been presented. The numerical results obtained for a two-layered shell show that in general the magnitudes of stresses and displacements in each layer of the shell are influenced by (1) the relative elastic constants of the two layers and (2) the thickness of each layer of the shell. A comparison of the solutions of elasticity and the layered shell theory of Ambartsumian indicates that shell theory can yield reasonably good results if (*i*) the ratio of thickness to radius (r_2) of the shell is small (less than 0.1); (*ii*) the ratio of the relative elastic constant of the layers is not large (μ is small); (*iii*) the layers are of equal thickness.

References

1 Ambartsumian, S. A., "Theory of Anisotropic Shells," NASA TT F-118, 1964.

2 Ambartsumian, S. A., "Contributions to the Theory of Anisotropic Layered Shells," *Applied Mechanics Reviews*, Vol. 15, No. 4, 1962, pp. 245–249.

3 Habip, L. M., "A Review of Recent Work on Multilayered Structures," *International Journal of Mechanical Sciences*, Vol. 7, 1965, pp. 589–593.

4 Vinson, J. R., and Chou, T. W., *Composite Materials and Their Use in Structures*, Applied Science Publishers Ltd., London, 1975.

5 Klosner, J. M., and Kempner, J., "Comparison of Elasticity and Shell Theory Solutions," *AIAA Journal*, Vol. 1, No. 3, 1962, pp. 627–630.

6 Klosner, J. M., and Levine, H. S., "Further Comparison of Elasticity and Shell Theory Solutions," *AIAA Journal*, Vol. 4, No. 3, 1966, pp. 467–480.

7 Levine, H. S., and Klosner, J. M., "Transversely Isotropic Cylinders Under Band Loads," *Journal of Engineering Mechanics Division, Proceedings of the ASCE*, Vol. 93, No. EM3, June 1967, pp. 157–174.

8 Chandrashekhara, K., and Gopalakrishnan, P., "Transversely Isotropic Infinite Cylindrical Shell Subjected to Radial Axisymmetric Line Load," under publication.

9 Lekhnitskii, S. G., *Theory of Elasticity of an Anisotropic Elastic Body*, Holden-Day Inc., San Francisco, 1963.

10 Salvadori, M. G., and Baron, M. L., *Numerical Methods in Engineering*, Prentice Hall, India, 1966.

11 Gopalakrishnan, P., "Elasticity Solutions for Transversely Isotropic Single and Multilayered Cylindrical Shells Subjected to Axisymmetric Load," PhD Thesis, Indian Institute of Science, Bangalore, 1980.

Downloaded 01 May 2010 to 171.66.16.249. Redistribution subject to ASME license or copyright; see http://www.asme.org/terms/Terms_Use.cfm

G. Wempner
Georgia Institute of Technology,
Atlanta, Ga. 30332

D. Talaslidis
Ruhr Universität,
K.I.B. Lehrstuhl IV,
Postfach 10 2148,
4630 Bochum, W. Germany

C.-M. Hwang
Georgia Institute of Technology,
Atlanta, Ga. 30332

A Simple and Efficient Approximation of Shells via Finite Quadrilateral Elements

Introduction

The approximation of shells via finite elements has attracted the attention of many proponents of such methods. Peculiar difficulties can be traced to the special attributes of a shell, so thin that flexural and extensional deformations predominate while transverse stress and shear strain are incidental. In short, the hypothesis of Kirchhoff-Love is indeed an accurate basis for the overall description of the continuous body. Consequently, early attempts to develop elemental approximations were founded on the Kirchhoff-Love hypothesis and were necessarily complicated: The simplest polynomial interpolation, which preserves the requisite smoothness, assigns 16 degrees of freedom to each quadrilateral element of a plate; at least eight more are needed to accommodate the extensional deformations of a plate or shell. Moreover, the hermitian interpolation requires a polynomial of sixth degree. The literature abounds with alternative elements. Many provide good approximations to certain problems but are unreliable or inaccurate in other circumstances. Others are quite accurate but too elaborate and uneconomical for the broad spectrum of practical problems.

Our approximation by quadrilateral elements is very simple but retains the essential attributes of the shell, including effects of transverse shear. Moreover, the discrete approximation is drawn in a consistent manner from the general theory of the continuum and the mechanical behavior of the finite element, without recourse to special manipulations or computational procedures. The formulation is ultimately expressed in terms of displacements and rotations only, and exhibits the desirable attributes of such systems. Additionally, the stresses can be readily computed in accordance with consistent equations which are derived from the variational procedure. Consequently, the model is adaptable to general-purpose programs and is generally applicable to shells, thick or thin.

Basic Features

The essential step toward simpler efficient elements requires a departure from the earlier tradition of strict adherence to the Kirchhoff-Love hypothesis. Such relaxation of the kinematical basis was proposed by Wempner [1] and implemented by Kross [2] in a rudimentary form. The main feature of the element is simple trilinear approximation of the displacement. The attendant features, apparent difficulties, and alternative means of accommodation are readily displayed by the example of simple flexure: The rectangular beam of Fig. 1 lies initially along the x axis. Under the action of end couples, the homogeneous beam is deformed such that the axis forms a circular arc. The *best* bilinear approximation of the elemental displacement produces identical trapezoids. If ξ^1, ξ^2 are local coordinates emanating from the midpoint of the Nth element, ϵ_{11} and γ_{12} the extensional and shear strains according to the elementary definitions, then

$$\frac{\gamma_{12}}{\epsilon_{11}} = \frac{\xi^1}{\xi^2}$$

In a beam (plate or shell) the thickness h is small in comparison to lengths along the axis (surface). The length l of an effective element must be relatively large $l/h > 1$; it follows that the shear energy in our *best* approximation is much larger than the extensional energy

$$\frac{\iint {\gamma_{12}}^2 d\xi^1 d\xi^2}{\iint {\epsilon_{11}}^2 d\xi^1 d\xi^2} = \frac{l^2}{h^2} >> 1$$

This does not mean that our approximation fails; in the limit ($l \to 0$, $\gamma_{12} \to 0$) the approximation approaches the exact solution. It means that the unrefined approximation is impractical and some alterations are needed.

The first proposal to modify the bilinear approximation and overcome the apparent difficulty was based on the Kirchhoff-Love hypothesis. Recognizing the validity of the hypothesis in the limit, Wempner [1] proposed a discrete

Contributed by the Applied Mechanics Division for publication in the JOURNAL OF APPLIED MECHANICS.

Discussion on this paper should be addressed to the Editorial Department, ASME, United Engineering Center, 345 East 47th Street, New York, N.Y. 10017, and will be accepted until two months after final publication of the paper itself in the JOURNAL OF APPLIED MECHANICS. Manuscript received by ASME Applied Mechanics Division, May 1981; final revision, September, 1981.

Copyright © 1982 by ASME
Downloaded 01 May 2010 to 171.66.16.249. Redistribution subject to ASME license or copyright; see http://www.asme.org/terms/Terms_Use.cfm

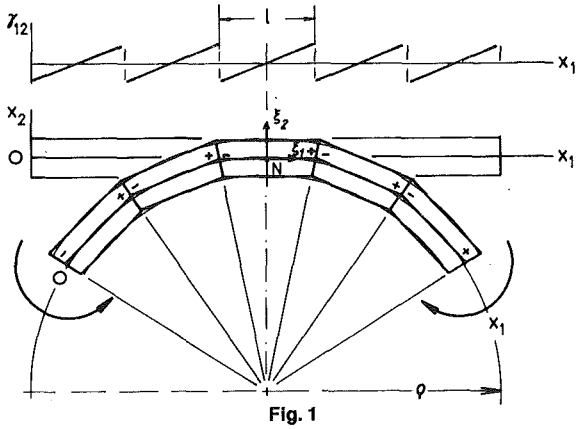


Fig. 1

counterpart, requiring the normality of an intermediate normal, insuring convergence to the Kirchhoff-Love theory and then suppressing the energy of shear at the onset. Alternative schemes are also possible to enforce a discrete Kirchhoff-Love counterpart and suppress the spurious shear energy [3, 4].

More recently the trilinear approximation has re-emerged as a means of approximating shells [5, 6]. The aforementioned shear strain and associated energy has been suppressed by computational schemes known as "reduced" or "selective integration" [7]. The basis of the scheme and the explanation are again evident in the simple example: Observe that the shear strain of Fig. 1 oscillates in the manner of sawteeth about the mean, which is zero in simple bending, but otherwise small in most practical circumstances. The "reduced integration" of the shear energy employs an intermediate value (usually the median) to approximate the integral. In the spirit of the mean-value theorem, that approximation is indeed much better than the exact integral, e.g., in pure bending of the hookean beam, the exact shear energy exceeds the flexural energy by the factor l^2/h^2, whereas the "reduced integration" provides the exact (zero) value.

Some attributes of the simplest approximation emerge: The simplest element has a trilinear approximation of displacement. Transverse shear strain can be accommodated in terms of elemental mean values. From the practical viewpoint, the discrete approximation should be formulated in terms of displacements and characterized by a symmetrical positive-definite matrix. Moreover, our goal should be achieved through consistent approximations which are systematically derived from a proven theory of the continuous shell. To achieve the objective, we turn to the general theorem of Hu-Washizu [8, 9] wherein the functional admits independent approximations of all stresses, strains, and displacements. We cast the functional in the two-dimensional space of the shell with the accepted "plane-stress" assumption ($S^{33}=0$) and a relaxed version of the Kirchhoff-Love hypothesis, which admits independent turning of the normal. In this context, we found the elemental description upon the simplest admissible approximations of the two-dimensional fields: bilinear approximations of the displacement and rotation, and piecewise constant approximations of the stresses and strains. The homogeneous stresses and strains are augmented by specific terms which are introduced to accommodate deformational modes of higher order. All are ultimately eliminated to achieve the desired formulation in terms of displacements. The essential details follow:

Kinematic Features

A typical hexilateral element is depicted in Fig. 2; it is bounded by top (S_+) and bottom (S_-) surfaces, and edges ($\theta^\alpha = a^\alpha \pm l^\alpha$). Also shown is an intermediate reference surface (S), the origin (O) of local normalized coordinates, $\xi^\alpha = (\theta^\alpha - a^\alpha)/l^\alpha$, $\xi^3 = \theta^3/h$), and nodal points (N_-, N, N_+).

Viewed as a three-dimensional finite element, the trilinear approximation of displacement $\mathbf{V}$ has the form

$$\mathbf{V} \doteq (\mathbf{W}_{NM} + \xi^3 \boldsymbol{\phi}_{NM}) \, \mathring{\jmath}_{NM}(\xi^1, \xi^2) \tag{1a}$$

$$\mathring{\jmath}_{NM} \equiv \frac{1}{4}(1+\xi_N{}^1\xi^1)(1+\xi_M{}^2\xi^2) \tag{1b}$$

where majuscule suffices signify the nodal values:

$$\mathbf{W}_{NM} \equiv \mathbf{V}(\xi_N{}^1, \xi_M{}^2, 0)$$

In accordance with the first approximation, the transverse normal stress ($S^{33}=0$) and the associated work is neglected; then the small extension of the normal is also neglected, so that

$$\boldsymbol{\phi}'_{NM} = \boldsymbol{\Phi}'_{NM} \times \mathbf{N}$$

where $\mathbf{N}$ is the unit vector along the θ^3 line; $\boldsymbol{\Phi}'_{NM}$ is the spin of that line. In the linear or incremental formulation, the relation applies as well to the small rotation as to the spin. The important feature is the reduction of freedom: Our element has 20 degrees of freedom that are, most naturally, the displacements $\mathbf{W}_{NM}$ of the nodes N on the reference surface (S) and the two components of the rotation $\boldsymbol{\phi}_{NM}$.

The effective implementation of our simple approximation follows the identification of 20 modes, which are all uncoupled in the degenerate case of the plate: six degrees of freedom correspond to rigid motions and eight modes represent the homogeneous strains (three mean extensional strains $\bar{\epsilon}_{\alpha\beta}$, three mean flexural strains $\bar{\bar{k}}_{\alpha\beta}$, and two mean shear strains $\bar{\gamma}_\alpha$). In the degenerate case, these 14 modes are expressed in the following displacements:

$$W_\alpha \doteq \bar{W}_\alpha + \bar{\omega}_{\alpha\beta}\xi^\beta + \bar{\epsilon}_{\alpha\beta}\xi^\beta \tag{2a}$$

$$W_3 \doteq \bar{W}_3 + \bar{W}_{3\alpha}\xi^\alpha \tag{2b}$$

$$\varphi^\mu e_{\alpha\mu} \doteq \bar{\gamma}_\alpha - \bar{W}_{3\alpha} - \bar{\bar{k}}_{\alpha\beta}\xi^\beta \tag{2c}$$

Here, the six constants, $\bar{W}_i$, $\bar{\omega}_{\beta\alpha} = \bar{\omega}_{\alpha\beta}$, and $\bar{W}_{3\alpha}$ represent the six degrees of small rigid motion (see reference [10], p. 62). The eight constants, $\bar{\epsilon}_{\alpha\beta}$, $\bar{\bar{k}}_{\alpha\beta}$, and $\bar{\gamma}_\alpha$, represent the homogeneous extensional, flexural and transverse shear strains.

Evidently, six additional modes are present: two extensional modes are illustrated in Fig. 3 and correspond to the bilinear terms:

$$\bar{\tilde{W}}_\alpha = \bar{\tilde{\epsilon}}_\alpha \xi^1 \xi^2 \tag{3a}$$

Similarly, two flexural modes are depicted in the edge views and correspond to the bilinear terms in rotation:

$$\varphi^\mu e_{\alpha\mu} = -\bar{\tilde{k}}_\alpha \xi^1 \xi^2 \tag{3b}$$

Two additional modes cause transverse shear strain. One is the torsional mode shown in the top view of Fig. 3 and associated with the linear rotation:

$$\phi^\alpha = -t\xi^\alpha \tag{3c}$$

The consequences are shear strains:

$$\gamma_1 = -t\xi^2, \qquad \gamma_2 = t\xi^1$$

The final mode is a warping of the middle surface, shown in the edge view of Fig. 3 and given by the displacement:

$$W_3 = \bar{\tilde{\gamma}}\xi^1\xi^2 \tag{3d}$$

At a glance, it may appear that the warping mode (3*d*) imposes unwarranted shear strains and a "locking" of higher order: The strains of warping (3*d*) follow:

$$\gamma_1 = \bar{\tilde{\gamma}}\xi^2, \qquad \gamma_2 = \bar{\tilde{\gamma}}\xi^1$$

However, our approximation of the rotation admits the simple form:

Downloaded 01 May 2010 to 171.66.16.249. Redistribution subject to ASME license or copyright; see http://www.asme.org/terms/Terms_Use.cfm

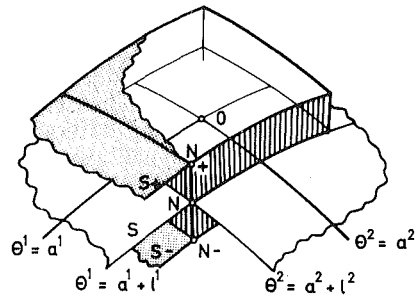


Fig. 2

$$\phi_1 = \bar{\tilde{\gamma}}\xi^1, \qquad \phi_2 = -\bar{\tilde{\gamma}}\xi^2$$

According to the usual linear equations, the combination produces the strains:

$$\gamma_1 = \gamma_2 = 0$$

$$\kappa_{12} = \frac{1}{2}[\phi_{1,1} - \phi_{2,2}] = \bar{\tilde{\gamma}}$$

The warping alone produces shear energy $0(G\bar{\tilde{\gamma}}hl^3)$ whereas the natural combination of warping and rotation produces twisting energy $0(G\bar{\tilde{\gamma}}h^3l)$ in accordance with the theory of Kirchhoff-Love. The latter statement is confirmed by the computation for the twisting of a thin plate.

In summary, the 20 modes of our element are the six rigid motions, the eight homogeneous states of strain ($\bar{\epsilon}_{\alpha\beta}$, $\bar{\kappa}_{\alpha\beta}$, $\bar{\gamma}_\alpha$) and the six additional modes ($\bar{\tilde{\epsilon}}_\alpha$, $\bar{\tilde{\kappa}}_\alpha$, t, and $\bar{\tilde{\gamma}}$). If the origin of the elemental coordinates (ξ^1,ξ^2) is at the center of a rectangular element, then the deformational modes (3*a–d*) contribute nothing to the mean values of the strains, i.e., $\bar{\epsilon}_{\alpha\beta}$, $\bar{\kappa}_{\alpha\beta}$, $\bar{\gamma}_\alpha$. It follows that our approximations of the strains (and stresses) must be augmented by six terms of higher order to provide the necessary resistance against the six modes (3*a–d*), which are otherwise uninhibited. Higher approximations of the extensional and flexural strains follow:

$$\epsilon_{11} \doteq \bar{\epsilon}_{11} + \bar{\tilde{\epsilon}}_{11}\xi^2 \tag{4a}$$

$$\epsilon_{22} \doteq \bar{\epsilon}_{22} + \bar{\epsilon}_{22}\xi^1 \tag{4b}$$

$$\epsilon_{12} \doteq \bar{\epsilon}_{12} + \underbrace{\bar{\tilde{\epsilon}}_{12}\xi^1 + \bar{\tilde{\epsilon}}_{21}\xi^2} \tag{4c}$$

$$\kappa_{11} \doteq \bar{\tilde{\kappa}}_{11} + \bar{\tilde{\kappa}}_{11}\xi^2 \tag{5a}$$

$$\kappa_{22} \doteq \bar{\tilde{\kappa}}_{22} + \bar{\tilde{\kappa}}_{22}\xi^1 \tag{5b}$$

$$\kappa_{12} \doteq \bar{\tilde{u}}_{12} + \underbrace{\bar{\tilde{\kappa}}_{12}\xi^1 + \bar{\tilde{\eta}}_{21}\xi^2} \tag{5c}$$

The additional terms of (4*a–c*) and (5*a–c*) stem from the extensional and flexural modes of Fig. 2. In our subsequent formulation, we require only four terms that are enough to inhibit these four higher modes: It is enough to retain the additional extensional terms ($\bar{\tilde{\epsilon}}_{11}$, $\bar{\tilde{\epsilon}}_{22}$) of (4*a,b*) *or* the additional terms ($\bar{\tilde{\epsilon}}_{12}$, $\bar{\tilde{\epsilon}}_{21}$) of (4*c*); likewise, it suffices to retain the flexural terms ($\bar{\tilde{\kappa}}_{11}$, $\bar{\tilde{\kappa}}_{22}$) of (5*a, b*) *or* the terms ($\bar{\tilde{\kappa}}_{12}$, $\bar{\tilde{\kappa}}_{21}$) of (5*c*). Higher approximations of the shear strains that correspond to the torsional *and* warping modes follow:

$$\gamma_1 \doteq \bar{\gamma}_1 + \bar{\tilde{\gamma}}_1\xi^2 \tag{6a}$$

$$\gamma_2 \doteq \bar{\gamma}_2 + \bar{\tilde{\kappa}}_2\xi^1 \tag{6b}$$

Variational Formulation

The basis of the elemental approximation is the variational theorem of Hu-Washizu [8,9]. The Hu-Washizu functional of all stresses, strains, and displacements in the element assumes the following form:

$$H = \int_{-1}^{+1}\int_{-1}^{+1} \{U(\epsilon_{\alpha\beta}, \kappa_{\alpha\beta}, \gamma_\alpha) - n^{\alpha\beta}[\epsilon_{\alpha\beta} - E_{\alpha\beta}(W_i)] - m^{\alpha\beta}[\kappa_{\alpha\beta} - K_{\alpha\beta}(\phi_\alpha, W_i)]$$

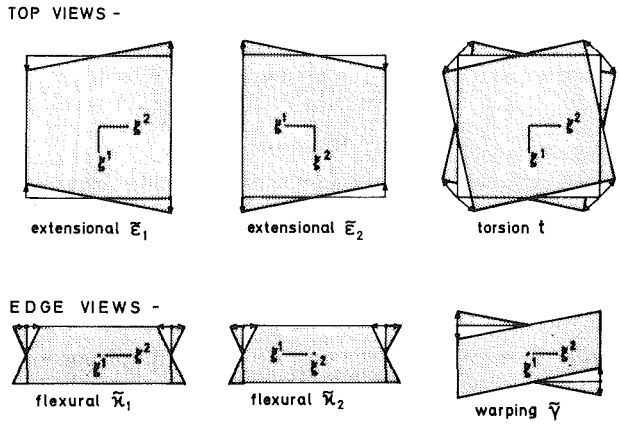


Fig. 3

$$- q^\alpha[\gamma_\alpha - G_\alpha(\phi_\alpha, W_i)] - \mathbf{F}\cdot\mathbf{W}\}A\,d\xi_1\,d\xi_2 - \int_c \{\mathbf{N}\cdot\mathbf{W} + \mathbf{M}\cdot\Phi\}\,d\xi \tag{7}$$

Here the function $A(\xi^1, \xi^2)$ is the metric of the area, U the strain-energy density; $n^{\alpha\beta}$, $m^{\alpha\beta}$, q^α are the stresses that are conjugate to the strains $\epsilon_{\alpha\beta}$, $\kappa_{\alpha\beta}$, γ_α, respectively. The applied load $\mathbf{F}$ acts on the surface; force $\mathbf{N}$ and couple $\mathbf{M}$ act on the edge C of the element. The operators $E_{\alpha\beta}$, $K_{\alpha\beta}$, and G_α express the strains $\epsilon_{\alpha\beta}$, $\kappa_{\alpha\beta}$, and γ_α in terms of the displacements W_i and rotations ϕ^α, i.e., the kinematical equations, linear or nonlinear, are the conditions that the bracketed terms vanish $[\ ] = 0$.

A crucial step in the formulation of our finite element, is the introduction of the simplest admissible approximations of each field. Accordingly, the displacement is expressed by the bilinear form (1). The approximations of the strains and stresses are also to be as simple as possible, yet consistent with established criteria: The so-called "limitation theorem" of Fraeijs de Veubeke [11] asserts that no advantages accrue from an approximation of a higher-order than one consistent with related fields. The patch test of Irons [12] requires that the element accommodate homogeneous states of strain. These criteria support our proposed approximations (4)–(6) of the strains. The eight constants represent homogeneous strains and the additional terms are only enough to accommodate the six modes of Fig. 3, which otherwise possess no energy. The approximations of the stresses follow the forms of the conjugate strains:

$$n^{11} \doteq \bar{n}^{11} + \bar{\tilde{n}}^{11}\xi^2, --, --; \tag{8a,b,c}$$

$$m^{11} \doteq \bar{m}^{11} + \bar{\tilde{m}}^{11}\xi^2, --, --; \tag{9a,b,c}$$

$$q^1 \doteq \bar{q}^1 + \bar{\tilde{q}}^1\xi^2, --; \tag{10a,b}$$

It is important to note that the supplementary terms (marked by the tilda ~) are higher order; specifically, if the gradient of the stress (or strain) is finite, then the supplementary term vanishes in the limit ($l^\alpha \to 0$).

In the rectangular element of a plate or cylindrical shell, the constants in the approximations (4–10) are orthogonal to the linear functions. In a nonrectangular element, the approximations must also account for the metric $A(\xi^1,\xi^2)$. Then the discrete counterpart of the functional (7) is a function of the form:

$$\bar{H} = \bar{U}(\bar{\epsilon}_{\alpha\beta}, \bar{\kappa}_{\alpha\beta}, \bar{\gamma}_\alpha, \bar{\tilde{\epsilon}}_{\alpha\beta}, \bar{\tilde{\kappa}}_{\alpha\beta}, \bar{\tilde{\gamma}}_\alpha) - \bar{n}^{\alpha\beta}[\bar{\epsilon}_{\alpha\beta} - \bar{E}_{\alpha\beta}(W_{NM})] - \bar{m}^{\alpha\beta}[\bar{\kappa}_{\alpha\beta} - \bar{K}_{\alpha\beta}(\phi^\alpha_{NM}, W^i_{NM})] - \frac{1}{3}\bar{\tilde{n}}^{\alpha\beta}[\bar{\tilde{\epsilon}}_{\alpha\beta} - \bar{\tilde{E}}_{\alpha\beta}(W_{NM})]$$

Downloaded 01 May 2010 to 171.66.16.249. Redistribution subject to ASME license or copyright; see http://www.asme.org/terms/Terms_Use.cfm

$$-\frac{1}{3}\bar{\bar{m}}^{\alpha\beta}[\bar{\bar{\kappa}}_{\alpha\beta}-\bar{\bar{K}}_{\alpha\beta}(\phi^{\alpha}_{NM},W^{i}_{NM})]$$
$$-\frac{1}{3}\bar{\bar{q}}^{\alpha}[\bar{\bar{\gamma}}_{\alpha}-\bar{\bar{G}}_{\alpha}(\phi^{\alpha}_{NM},W^{i}_{NM})]$$
$$-F^{NM}_{i}W^{i}_{NM}-M^{NM}_{\alpha}\phi^{\alpha}_{NM} \qquad (11)$$

Here the factor 1/3 is the result of integrating the products $(\xi^{\alpha})^2$. The function (11) is to be stationary with respect to each of the variables. The results consist of

(*a*) 20 equilibrium equations in terms of the stresses ($\bar{n}^{\alpha\beta}$, $\bar{m}^{\alpha\beta}$, $\bar{q}^{\alpha}$, $\bar{\bar{n}}^{\alpha\beta}$, $\bar{\bar{m}}^{\alpha\beta}$, $\bar{\bar{q}}^{\alpha}$), nodal forces (F^{NM}_{i}), and couples ($M_{\alpha}{}^{NM}$).

(*b*) 14 stress-strain relations. Because of the orthogonality of the functions, the equations of the isotropic hookean element are uncoupled. Specifically,

$$\bar{n}^{\alpha\beta}=C^{\alpha\beta\gamma\eta}\bar{\epsilon}_{\gamma\eta}$$
$$\bar{m}^{\alpha\beta}=\frac{h^2}{12}C^{\alpha\beta\gamma\eta}\bar{\kappa}_{\gamma\eta}$$
$$\bar{q}^{\alpha}=C^{\alpha\beta}\bar{\gamma}_{\beta} \qquad (12b)$$

The coefficients are the usual moduli of the continuous theory (see Ref. [10], p. 590).

(c) 14 strain-displacement equations that are also uncoupled. Specifically,

$$\bar{\epsilon}_{\alpha\beta}=\bar{E}_{\alpha\beta}(W_{NM})$$
$$\bar{\kappa}_{\alpha\beta}=\bar{K}_{\alpha\beta}(\phi^{\alpha}_{NM},W^{i}_{NM})$$
$$\bar{\gamma}_{\alpha}=\bar{G}_{\alpha\beta}(\phi^{\alpha}_{NM},W^{i}_{NM}). \qquad (12c)$$

The 14 equations (12*c*) can be substituted into the 14 equations (12*b*) which can be substituted into the 20 equations (12*a*) in order to obtain the elemental approximation in terms of *displacements* only.

Some features of the approximation are noteworthy:

(1) The higher-order terms (=) vanish in the limit. The remaining constitutive equations are those written explicitly under (*b*) and these approach the equations of the continuous shell. Likewise, the remaining kinematical equations are these written under (12*c*) and these difference equations approach the differential equations of the continuous shell.

(2) Five equilibrium conditions of the finite element emerge from the virtual work upon the three displacements and two rotations at each node. Like the continuum theory, rotation about the normal imposes a condition of symmetry upon the stresses ($\bar{n}^{\alpha\beta}=\bar{\bar{n}}^{\alpha\beta}$), which is inherent in our elemental approximation.

(3) The evaluation of all coefficients requires only the integration of simple functions. All can be done *exactly*, or by any accurate numerical procedure, which might be expedient to the user. Moreover, the formation of the elemental matrix requires *only direct substitutions*. Consequently, the formulation is exceedingly simple and economical.

(4) The effects of extensional and flexural behavior are represented by comparable approximations. As our examples indicate, the formulation serves as well whether extensional or flexural effects predominate.

(5) The final result of our formulation is a system of equations in terms of displacements alone. That system has the most desirable attributes of a displacement formulation: Specifically, the matrix is symmetric and positive definite.

The omission of higher-order terms reduces the internal energy, so that the element is less stiff than the element derived via minimum potential and displacements alone. Provided only that the gradients remain finite, the effects of these higher-order terms diminish as the element shrinks and, therefore, convergence is assured.

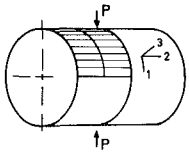
Some examples serve to demonstrate the effectiveness of this simple elemental approximation.

Example 1: Cylindrical Shell Under Radial Forces With Free Ends. The "pinched cylinder" of Fig. 4 has been used frequently for numerical testing of approximations. The radial displacement at the load is given in the table according to various authors. The deformation is predominantly flexural; indeed, the largest calculated value [13] is only 5 percent greater than that based on inextensionality [14].

For most purposes, the measure of an approximation is the number of degrees of freedom (and equations) required to obtain satisfactory results. In this respect, our simple model excels. The models of Ashwell and Sabir [15] and Dawe [19] give comparable results with fewer degrees of freedom, 20 and 30, respectively. However, the former is an element, which is especially tailored to the cylindrical shell; the latter is formed with a higher-order triangular element, which has 54 degrees of freedom based on a quintic polynomial.

It is noteworthy that our elemental matrix possesses six, and only six, *distinct* zero eigenvalues, which confirm an accurate representation of the rigid modes.

Example 2: Cylindrical Shell Under Radial Forces With Simply Supported Ends. If the ends of the "pinched



R = 4.95 in , t = 0.094 in
L = 10.35 in , P = 100 lb.
E = 10.5×10^6 lb. in.^{2}
( ): denotes degrees of freedom

Mesh in octant	Cantin [13]	Ashwell, Sabir [15]	Thomas, Gallagher [16]	Bogner, et al [17]	Cantin, Clough [18]	Dawe [19]	Present
1×1		0.104 (20)				0.106 (30)	
1×4		0.111 (50)	0.111 (67)	0.109 (120)			0.098 (32)
1×6							0.105 (48)
1×7					0.099 (96)		
1×8			0.112 (131)				0.108 (64)
1×9					0.106 (120)		
2×2	0.093 (54)	0.110 (45)				0.112 (96)	
2×4							0.099 (53)
2×6							0.106 (79)
2×9					0.107 (180)		
4×4	0.113 (150)	0.113 (125)				0.114 (374)	
6×6	0.114 (294)	0.114 (245)					

Fig. 4 Radial deflection under load in inches

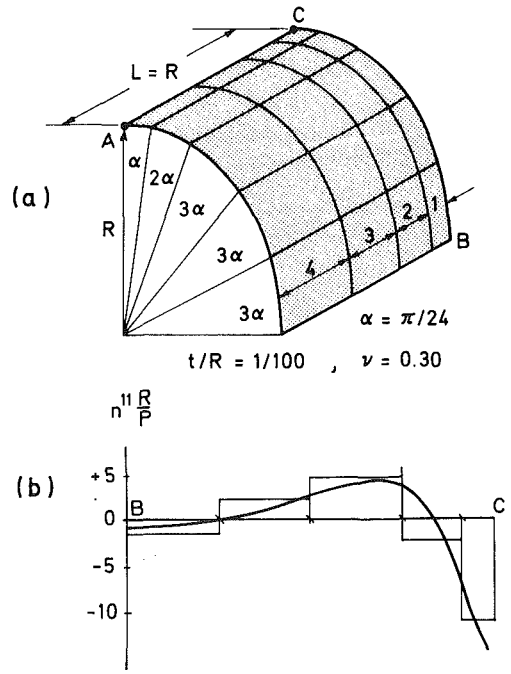


Fig. 5

Downloaded 01 May 2010 to 171.66.16.249. Redistribution subject to ASME license or copyright; see http://www.asme.org/terms/Terms_Use.cfm

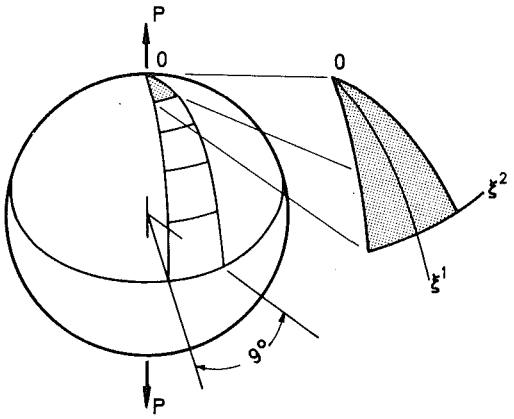


Fig. 6

cylinder" are supported by an inextensible diaphragm, then the flexure is suppressed and membrane actions prevail. Computations were made with the mesh illustrated in the octant of Figure 5(*a*), which provides 104 degrees of freedom. The radial displacement W_3 at the load (C) and axial displacement W_2 at the edge (A) are comparable to the results of Dawe [19] and Lukasiewicz [20], as follows:

	[19]	Present	[20]
EtW_3/P(at C)	164	152	155
EtW_2/P (at A)	4.11	4.06	–
Degrees of Freedom	(366)	(104)	–

The number (366) of degrees of freedom is our count according to the information given by Dawe [19]. The results given by Lukasiewicz were obtained with a few terms of a series solution; the number 155 for W_3 is estimated from his graphical presentation [20, p. 397].

The plot of Figure 5(*b*) serves to exhibit the piecewise representation of the stress n^{11}. The smooth curve is taken from the series solution, as displayed by Edwards and Webster [21].

Example 3: Spherical Shell Under Radial Forces. The spherical shell under diametrically opposed forces serves as an example in which the elements are nonrectangular. Moreover, an element at the pole degenerates to a triangle as depicted in the auxiliary view at 0 in Fig. 6. The consistent approximation of displacement and rotation in the triangular element has the form:

$$W = \bar{W} + W_1 \xi^1 + W_{12} \xi^1 \xi^2$$

Each field is determined by the three nodal values and each is compatible with the approximation of adjoining elements. The triangular element has 15 degrees of freedom, six rigid modes, eight homogeneous strains, and one warping mode which requires one additional term ($\bar{\gamma}_2 \xi^1$) in the approximation of shear:

$$\gamma_2 = \doteq \bar{\gamma}_2 + \tilde{\bar{\gamma}}_2 \xi^1$$

Here the terms of the approximations are not orthogonal in the element, since $A(\xi^1) = \sin \pi \xi^1 / 2n$, where n is the number of elements in a segment of the hemisphere, as shown. Consequently, the linear approximations introduce coupling between the mean values ($^-$) and supplementary terms ($\sim$). Otherwise, the formulation is unaffected.

Once again, the elemental matrix exhibits six *distinct* zero eigenvalues corresponding to the rigid modes.

In the numerical example, $t/R = 50$, $\nu = 0.30$. The displacement W at the pole is comparable to the result obtained by Koiter [22]:

$ETW/P = 21.2$	Koiter [22]
$\doteq 20.7$	15 Elements (87)
$\doteq 20.5$	5 Elements (27)

Here the shear modulus was amplified by a factor $0(10^3)$ to suppress the effect of transverse shear. The 15 elements were equally spaced along the meridian, whereas the five elements were unequally spaced in segments of 5 deg, 5 deg, 5 deg, 30 deg, and 45 deg to take advantage of the local deformational pattern. For purposes of testing, two-dimensional elements were employed with a breadth of 9 deg. Again, the parenthetical numbers are degrees of freedom, but these do not reflect the capabilities of the approximation, since the numbers are reduced to (44) and (14), respectively, if the symmetry is invoked at the outset and the problem is treated as one-dimensional.

Other examples of plates and arches also attest to the abilities of this elementary approximation to accommodate flexure.

Conclusion

From a practical viewpoint, the important attributes of this discrete approximation are the simplicity of the formulation and the economy of implementation. The latter is achieved without significant sacrifices in accuracy or reliability. Indeed, the comparable approximations of extensional and flexural deformations produce an element that accommodates both actions with facility. The intermediate formulations of the kinematic and constitutive equations facilitate the treatment of interactions with supporting structures and/or adjoining media.

From a theoretical viewpoint, the discrete model is derived in a consistent manner from the continuum. Each approximation is taken as simply as possible and founded entirely on mechanical and geometrical concepts. Finally, the algebraic equations of the discrete model are analogous to the corresponding equations of the continuous shell and, indeed, reproduce their counterparts in the limit.

Specific features (1)–(5), are enumerated in the "formulation."

Some distinctions between the present element and certain "mixed" elements are noteworthy: The present approximation is founded on an elaborate form (7) of *potential energy*, whereas most "mixed" elements are based on the functional of Hellinger-Reissner [23, 24], an elaboration of *complementary energy*. Our stiffness matrix has the properties of one derived from potential energy. No inversion is needed if the element is rectangular; otherwise, coupling between the constant ($-$) and higher ($=$) stresses and strains requires, at most, the inversion of 3×3 matrices. The elemental matrix of the "mixed" element requires an inversion, since the complementary formulations express displacements in terms of stresses.

The extension to finite deformations poses no inherent difficulties, but requires additional algebra and storage. The functional of Hu-Washizu [9] is generally available in terms of the Cauchy-Green components of strain and Kirchhoff-Trefftz components of stress (see reference [10] p. 443); alternatively, a precise version is also expressible in terms of engineering components of strain and Jaumann components of stress [25]. By adhering to a local convected (Lagrangian) system, the essential nonlinear terms in the discrete formulation are products of forces and relative nodal rotations, analogous to the products of forces and curvatures in the continuum theories of thin shells. Then, rigid rotations appear only where loads, surface or edge tractions, are prescribed in a fixed (Eulerian) system. Such extensions are currently under development, but beyond the scope of this initial presentation.

Acknowledgment

The authors gratefully acknowledge the support of the National Science Foundation, Grant CME-7918420 and

Downloaded 01 May 2010 to 171.66.16.249. Redistribution subject to ASME license or copyright; see http://www.asme.org/terms/Terms_Use.cfm

Grant CME-8140376, under the direction of Dr. Robert S. Ayre and Dr. John E. Goldberg, respectively.

References

1 Wempner, G. A., "New Concepts for Finite Elements of Shells," *ZAMM*, 1968, pp. T174–T176.

2 Wempner, G. A., Oden, J. T., and Kross, D., "Finite Element Analysis of Thin Shells," *Journal of Engineering Mechanics Division*, ASCE, Vol. 94, No. EM6, 1968, pp. 1273–1294.

3 Zienkiewicz, O. C., *The Finite Element Method*, McGraw-Hill, 3rd Ed., 1977, Chapter 11.7, p. 296.

4 Irons, B. M., "The Semiloof Shell Element," in *Finite Elements for Thin Shells and Curved Members* (ed., Ashwell, D. G., and Gallagher, R. H.), Wiley, 1976, Chapter 11, pp. 197–222.

5 Kanok-Nukulchai, W., "A Simple and Efficient Finite Element for General Shell Analysis," *International Journal for Numerical Methods in Engineering*, Vol. 14, 1979, pp. 179–200.

6 Kanok-Nukulchai, W., Taylor, R. L., and Hughes, T. J. R., "A Large Deformation Formulation for Shell Analysis by the Finite Element Method," *Computers and Structures*, Vol. 13, 1981, pp. 19–27.

7 Zienkiewicz, O. C., Taylor, R. L., and Too, J. M., "Reduced Integration Technique in General Analysis of Plates and Shells," *International Journal for Numerical Methods in Engineering*, Vol. 3, 1971, pp. 275–290.

8 Hu, H. C., "On Some Variational Principles in the Theory of Elasticity and Plasticity," *Scientia Sinica*, Vol. 4, 1955.

9 Washizu, K., "On the Variational Principles of Elasticity and Plasticity," Technical Report, Massachusetts Institute of Technology, 1955, report no. 25–18.

11 Fraeijs de Veubeke, B., "Displacement and Equilibrium Models in the Finite Element Method," in *Stress Analysis*, (ed., Zienkiewicz, O. C., and Holister, G. S.), Wiley, 1965, Chapter 9.

12 Irons, B. M., and Razzaque, A., "Experience with the Patch Test for Convergence of Finite Elements," in *Mathematical Foundations of the Finite Element Method with Applications to Partial Differential Equations*, (ed., Aziz, A. K.), Academic Press, 1972, pp. 557–587.

13 Cantin, G., "Rigid Body Motions in Curved Finite Elements," *AIAA Journal*, Vol. 8, 1970.

14 Timoshenko, S., and Woinowsky-Krieger, S., *Theory of Plates and Shells*, 2nd Ed., McGraw-Hill, 1959, pp. 501–506.

15 Ashwell, D. G., and Sabir, A. B., "A New Cylindrical Shell Finite Element Based on Simple Independent Strain Functions," *International Journal of Mechanical Sciences*, Vol. 14, 1972.

16 Thomas, G. R., and Gallagher, R. H., "A Triangular Element Based on Generalized Potential Energy Concepts," in *Finite Elements for Thin Shells and Curved Members* (ed., Ashwell, D. G., and Gallagher, R. H.), Wiley, New York, 1976, Chapter 9.

17 Bogner, F. K., Fox, R. L., and Schmit, L. A., "A Cylindrical Shell Discrete Element," *AIAA Journal*, Vol. 5, 1967.

18 Cantin, G., and Clough, R. W., "A Curved Cylindrical Shell Finite Element," *AIAA Journal*, Vol. 6, 1968.

19 Dawe, D. J., "High-Order Triangular Finite Element for Shell Analysis," *International Journal of Solids and Structures*, Vol. 11, 1975, pp. 1097–1110.

20 Lukasiewicz, S., *Local Loads in Plates and Shells*, Noordhoff, 1979, p. 397.

21 Edwards, G., and Webster, J. J., "Hybrid Cylindrical Shell Finite Elements," in *Finite Elements for Thin Shells and Curved Members*, (ed., Ashwell, D. G., and Gallagher, R. H.), Wiley, New York, 1976, Chapter 10.

22 Koiter, W. T., "A Spherical Shell under Point Loads at its Poles," in *Progress in Applied Mechanics*: The Prager Anniversary Volume, Macmillan, 1963.

23 Hellinger, E., "Die Algemeinen Ansätze der Mechanik der Kontinua, *Encyklopädie der Mathematischen Wissenschaften*, Vol. 4, No. 4, 1914.

24 Reissner, E., "On a Variational Theorem in Elasticity," *Journal Math. Phys.*, Vol. 25, 1950.

25 Wempner, G., "Complementary Theorems of Solid Mechanics," *Variational Methods in the Mechanics of Solids* (ed., Nemat-Nasser, S.), Pergamon Press, 1980.

Downloaded 01 May 2010 to 171.66.16.249. Redistribution subject to ASME license or copyright; see http://www.asme.org/terms/Terms_Use.cfm

Large Deflection of a Fluid-Filled Spherical Shell Under a Point Load

L. A. Taber
Biomedical Science Department,
General Motors Research Laboratories,
Warren, Mich. 48090
Assoc. Mem. ASME

Large deflection of a fluid-filled spherical shell under a concentrated load was studied analytically and experimentally. The analysis involves a strain energy approach based on thin shell theory for moderately large rotation. Load and fluid pressure from tests on rubber shells filled with water show good agreement with computed results for deflection as large as 60 percent of the radius of the shell. Deflection less than 20 percent of the radius is dominated by bending while larger deflection is governed mainly by stretching due to the displaced fluid.

Introduction

Several investigators have studied large deflection behavior of an empty spherical shell subjected to a point load [1–11]. Feng and Yang [12] dealt with the nonlinear problem of an inflated membrane compressed between two flat plates. Here we combine the two circumstances by studying the effect of an internal fluid during large deflection of a shell with significant bending rigidity. This problem is of particular interest in biomechanics since many biological structures, such as the arteries, the heart, the head, and the eyeball, can be treated as fluid-filled shells.

Most previous analytical work on empty shells is based on a shallow shell theory. Reissner [1] presented the general linear equations for small deflection of a shallow segment of a thin, spherical shell. Stress and displacement in the vicinity of a point load were computed.

Experiments with spherical shell segments [2–5] reveal that a region of reversed curvature forms under a concentrated load and spreads outward as the load increases. With this observation in mind, Ashwell [2] used Love's principle of applicable surfaces [13] to obtain a solution for large axisymmetric deformation of an empty shell with a point load. A surface is applicable if it can be derived from the original surface without stretching or folding. For a spherical shell segment, this definition corresponds to a surface of reversed curvature in which only bending strain is present. According to the principle, the deformed configuration consists of small displacement from the dimple of reversed curvature in the region near the load and from the original surface over the remainder of the shell. Ashwell [2], therefore applied the linear shallow shell relations of Reissner [1] separately to each region and obtained the overall solution by matching conditions at the edge of the dimple.

Employing the same idea along with asymptotic expansions for the nonlinear thin shell equations, Ranjan and Steele [10] studied the problem of a point load on a deep shell. Edge zone expansions in conjunction with a strain energy approach yielded a simple analytical solution that compares favorably with other numerical results. Effects of moderately large rotation and prestress were considered.

The present work extends the variational technique of Ranjan and Steele [10] to include the effect of an internal incompressible fluid. Strain is assumed to be small, i.e., material nonlinearity is not included in the analysis. In addition, shear deformation and prestress are not considered. The analytical results agree quite well with experimental data from water-filled rubber shells.

Experimental Methods

Point load tests were conducted on rubber spherical shells, i.e., commercially manufactured racquetballs. A small hole in the bottom of the "empty" shell let air flow freely into and out of the ball, which was glued into an aluminum hemispherical support (Fig. 1). For testing fluid-filled shells, tubing led from this orifice to a diaphragm pressure transducer (0–1400 kPa). The closed system was assembled under water so that all air bubbles could be removed. With the test fixture resting under a 1-mm radius aluminum indenter, a servocontrolled, hydraulic testing machine applied a ramp displacement of 30-mm amplitude at a quasi-static speed of 12 mm/s. Applied force was measured with a 22-kN diaphragm load cell while a linear voltage differential transformer measured displacement.

Four shells, each tested repeatedly with and without water, yielded virtually identical data. Therefore, results from only one shell are presented. Although hysteresis occurred, the elasticity of the shell remained intact as repeated tests with the same ball revealed negligible change in the hysteresis loop. Only data from the loading phase is considered here.

After the test, geometric and material properties of the shell were determined. A tensile test with a dumbbell-shaped specimen cut from the wall yielded the small-strain, incremental Young's modulus E as computed from the slope of the stress-strain curve near the origin. Effect of material

Contributed by the Applied Mechanics Division for publication in the JOURNAL OF APPLIED MECHANICS.

Discussion on this paper should be addressed to the Editorial Department, ASME, United Engineering Center, 345 East 47th Street, New York, N.Y. 10017, and will be accepted until two months after final publication of the paper itself in the JOURNAL OF APPLIED MECHANICS. Manuscript received by ASME Applied Mechanics Division, April 1981; final revision, September 1981.

Copyright © 1982 by ASME
Downloaded 01 May 2010 to 171.66.16.249. Redistribution subject to ASME license or copyright; see http://www.asme.org/terms/Terms_Use.cfm

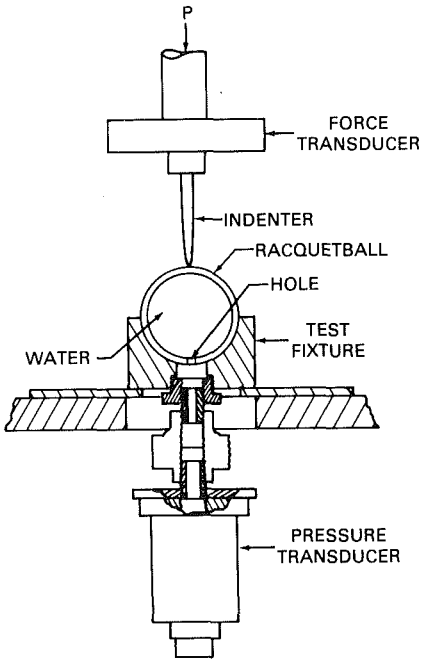


Fig. 1 Schematic of test setup

nonlinearity, i.e., variation in E with strain level, was not considered. With the radius R defined as that of the middle surface, and the thickness t measured with a micrometer, the properties of the shell are:

$$R = 26.3 \text{ mm}$$
$$t = 4.4 \text{ mm}$$
$$\mathrm{E} = 4.0 \times 10^3 \text{ kPa}$$
$$\nu = 0.5$$

where ν is Poisson's ratio for incompressible rubber.

Analytical Model

The spherical shell is assumed to be composed of a homogeneous, isotropic, elastic material with all geometric and material properties taken as constant. An incompressible fluid fills the shell which rests in a rigid hemispherical support of the same radius R. A vertical load P is applied at the apex. Since the shape of the lower half of the sphere does not change as the load is applied, the problem reduces to that of a fluid-filled hemispherical cap clamped around its edge [Fig. 2(*a*)].

The experimental shell is actually fairly thick ($R/t = 6.0$), so shear deformation may be an important factor in the experiments. However, the present analysis is based on thin shell theory which neglects shear deformation.

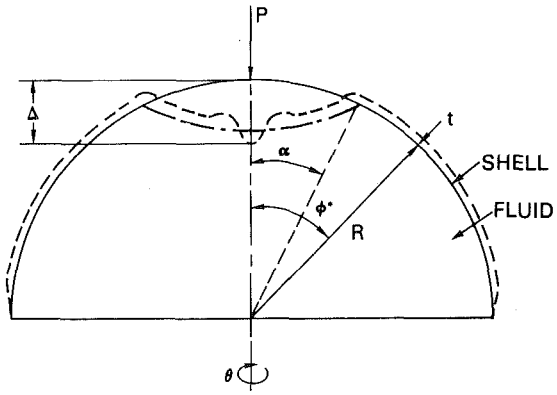


Fig. 2(*a*) Geometry for the analytical shell model

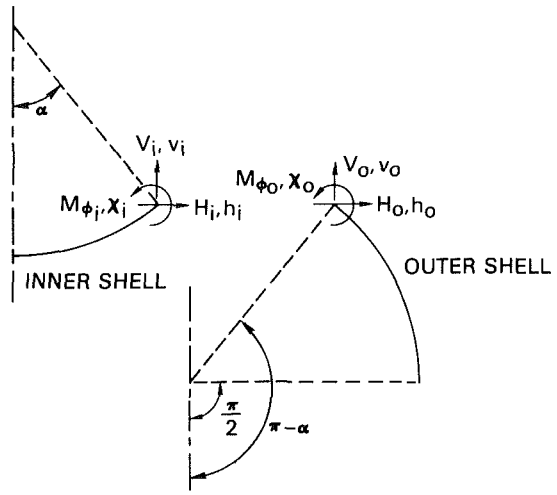


Fig. 2(*b*) Force and displacement definitions

Fig. 2

Deformation

In the experiments with fluid-filled shells, we observed that, for deflection less than about half the radius, the deformation is very similar to that of an empty shell. At larger deflection, however, there is considerable bulging caused by the displaced fluid. Taking these observations into account, we divide the deformation of the fluid-filled shell into four steps (Fig. 3).

Nomenclature

$\mathbf{A}$ = solution matrix
$\mathbf{B}_L, \mathbf{B}_{NL}$ = linear and nonlinear load vectors, respectively
c = reduced shell thickness
E = Young's modulus
h = horizontal shell displacement
H = horizontal force
M_ϕ = meridional moment
P = applied force
p = fluid pressure
R = shell radius
t = shell thickness
U_B, U_M = bending and membrane strain energy, respectively
U_L = potential energy of applied load
ΔV = change in volume
V = vertical force
v = vertical shell displacement
w = normal shell displacement
$\mathbf{y}$ = nondimensional solution vector for shell bending
$\bar{\mathbf{z}}$ = solution vector for fluid-filled shell
α = dimple edge angle
Δ_j = deflection component of load
$\epsilon_\phi, \epsilon_\theta$ = meridional and hoop strain, respectively
λ = edge-solution decay factor
ν = Poisson's ratio
Π = modified total potential energy
$\sigma_\phi, \sigma_\theta$ = meridional and hoop stress, respectively
ϕ = meridional angle
ϕ^* = general meridional angle
χ = shell rotation

Subscripts

e = edge of shell
i = inner shell
o = outer shell

Downloaded 01 May 2010 to 171.66.16.249. Redistribution subject to ASME license or copyright; see http://www.asme.org/terms/Terms_Use.cfm

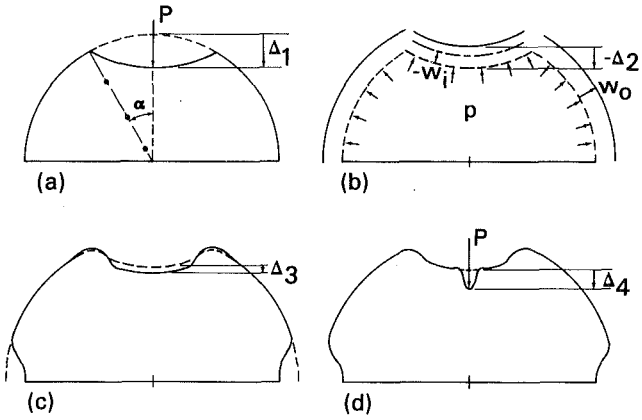


Fig. 3 Deflection components for fluid-filled shell

Consider first a spherical shell void of fluid. Under a point load, the shell deforms into a minimum energy configuration. Since stretching generally requires more energy than bending, the shell deforms with as little stretching of the middle surface as possible, i.e., the principle of applicable surfaces. Following Ranjan and Steele [10], we form a dimple of reversed curvature (the applicable surface) in the following manner. The shell is cut along the general meridional angle $\phi^* = \alpha$ [Fig. 2(*a*)]; two shells are obtained: the inner shell ($\phi^* < \alpha$) and the outer shell ($\phi^* > \alpha$) [see Fig. 2(*b*)]. Note that ϕ^* is not equal to the actual meridional angle ϕ which is defined separately for each shell. The dimple is then formed by applying equal bending moments at every point of the inner shell. According to the principle of applicable surfaces, the final configuration consists of small displacements from these two unstretched shells. And since the strain energy required to form the dimple with a free edge can be neglected in this problem [10], the shape of Fig. 3(a) serves as a reference configuration.

The incompressible fluid is now introduced. The fluid displaced under the load forces the outer shell to bulge and stretch outward. Our experiments have shown that for relatively small deflection, stretching is not significant. However, a deflection is eventually reached where the energy of stretching becomes an integral part of the deformation behavior of the system. The fluid pressured p increases, uniformly straining the inner and outer shells through radial displacements w_i and w_o, respectively [Fig. 3(*b*)].

In the following step, the shell edges bend to conform to the continuity conditions at the edge of the dimple and to the boundary conditions at the clamped lower edge [Fig. 3(*c*)]. Lastly, the displacement directly beneath the load is added [Fig. 3(*d*)] to give the final configuration. In the experiments, buckling did not occur in either the empty or the fluid-filled shell for deflection as large as the radius. Although asymmetric buckling of thinner shells is possible, here we assume that the growing dimple remains axisymmetric.

Potential Energy

Significant contributions to the potential energy of the system arise from edge bending [Fig. 3(*c*)], stretching [Fig. 3(*b*)], and the applied load. The linear displacement Δ_4 under the load [Fig. 3(*d*)] is first neglected, to be added later.

Bending. The asymptotic solution of Ranjan and Steele [10] is valid when the edges of a thin shell are "steep." In the present problem the approxpriate condition is $\lambda a >>$ where

$$\lambda = (R/c)^{1/2} \tag{1}$$

in which $c = t/[12(1-\nu^2)]^{1/2}$ is the reduced thickness and α is the dimple angle [Fig. 2(*a*)]. Although this condition does not hold near the apex, results based on edge zone expansions do not incur serious error [10].

For a thin shell, bending is significant only in narrow zones near the load and near the edges, so we assume that the solution for each edge may be considered independently. For moderately large rotation without prestress, the relations expressing the edge forces y_{1e} and y_{2e} in terms of the edge displacements y_{3e} and y_{4e} are [10]

$$y_{1e} = [(2)^{1/2} y_3 + y_4 + \lambda \cot\phi (3(2)^{1/2} y_3^2 + 2y_3 y_4)/10]_e \tag{2a}$$

$$y_{2e} = [y_3 + (2)^{1/2} y_4 + \lambda \cot\phi (y_3^2 + 2y_4^2)/10]_e \tag{2b}$$

where the nondimensional solution vector is defined as

$$\mathbf{y} = \begin{bmatrix} y_1 \\ y_2 \\ y_3 \\ y_4 \end{bmatrix} = \begin{bmatrix} M_\phi/(\mathrm{E}tc) \\ H\lambda \sin\phi_e/(\mathrm{E}t) \\ \chi/\lambda \\ h/(R \sin\phi_e) \end{bmatrix} \tag{3}$$

and the subscript "e" denotes the value at the edge of the shell. The meridional moment M_ϕ, horizontal force H, rotation χ, horizontal displacement h, and the meridional edge angle ϕ_e are defined in Fig. 2(*b*) for both the inner and the outer shell. The self-equilibrating forces are measured per unit circumferential length.

The bending strain energy due to applied edge load is

$$U_B = 2\pi R \sin\phi_e \left[\int_0^\chi M_\phi d\chi + \int_0^h H\, dh \right]_e \tag{4a}$$

which, with equation (3), may be written

$$U_B = k\lambda^3 \sin\phi_e \left[\int_0^{y_3} y_1 dy_3 + \int_0^{y_4} y_2 dy_4 \right]_e \tag{4b}$$

where $k = 2\pi \mathrm{E}tc^2$. After substitution of equations (2*a*, *b*), this expression can be integrated in closed form.

Since the force-displacement relations given by equations (2*a*, *b*) pertain to the "lower" edge of a shell segment, we define the meridional edge angle [Fig. 2(*b*)] as

$$\phi_e = \begin{cases} \alpha \text{ for edge of inner shell} \\ \pi - \alpha \text{ for top edge of outer shell} \\ \dfrac{\pi}{2} \text{ for lower edge of outer shell.} \end{cases} \tag{5}$$

After the deformation due to the fluid pressure [Fig. 3(*b*)], the displacement continuity conditions at the dimple edge are satisfied if we let

$$\left.\begin{aligned} y_{3_i} &= \bar{y}_3 - \alpha/\lambda \\ y_{4i} &= \bar{y}_4 + \Delta\bar{w}/2 \end{aligned}\right\} \text{ at } \phi_e = \alpha$$

$$\left.\begin{aligned} y_{3_o} &= \bar{y}_3 + \alpha/\lambda \\ y_{4_o} &= \bar{y}_4 - \Delta\bar{w}/2 \end{aligned}\right\} \text{ at } \phi_e = \pi - \alpha \tag{6}$$

where

$$\Delta\bar{w} = \bar{w}_o - \bar{w}_i; \quad \bar{w}_o = w_o/R; \quad \bar{w}_i = w_i/R \tag{7}$$

and the subscripts "i" and "o" denote the inner and outer shell, respectively. At the clamped edge, the boundary conditions are satisfied by

$$\left.\begin{aligned} y_{3_o} &= 0 \\ y_{4_o} &= -\bar{w}_o \end{aligned}\right\} \text{ at } \phi_e = \pi/2. \tag{8}$$

Substitution of equations (6) and (8) into the integrated form of equation (4*b*) and adding the contributions for all

Downloaded 01 May 2010 to 171.66.16.249. Redistribution subject to ASME license or copyright; see http://www.asme.org/terms/Terms_Use.cfm

three shell edges provides the total nondimensional strain energy of bending

$$\bar{U}_B = \frac{U_B}{k} = \lambda \frac{\sin\alpha}{\alpha} \{ (2)^{1/2} [\alpha^3 + \lambda^2 \alpha (\bar{y}_3^2 + \bar{y}_4^2)] + 2\lambda^2 \alpha \bar{y}_3 \bar{y}_4 - \lambda \alpha^2 \Delta \bar{w} + (2)^{1/2} \lambda^2 \alpha \Delta \bar{w}^2/4 - (\alpha \cot\alpha/10)[2(2)^{1/2} (\alpha^3 + 3\lambda^2 \alpha \bar{y}_3^2) + 4\lambda^2 \alpha \bar{y}_3 \bar{y}_4 - \lambda \Delta \bar{w} \alpha^2 - \lambda^3 \Delta \bar{w} (\bar{y}_3^2 + 2\bar{y}_4^2 + \Delta \bar{w}^2/6)] \} + \lambda^3 \sin\alpha [(2)^{1/2} \bar{w}_o^2/2 + \lambda \cot\alpha \bar{w}_o^3/15] \quad (9)$$

in which the terms in the last set of brackets represent the contribution at the clamped edge and terms multiplied by $\cot\alpha$ are nonlinear for large rotation.

Stretching. Fluid pressure induces uniform stretching of the middle surface of the outer shell and compression of the inner shell [Fig. 3(*b*)]. With the meridional and hoop strains (membrane) given by

$$\epsilon_\phi = \epsilon_\theta = \begin{cases} \bar{w}_i \text{ for } \phi^* < \alpha \\ \bar{w}_o \text{ for } \phi^* > \alpha, \end{cases} \quad (10)$$

membrane stress contributes the strain energy [14]

$$U_M = \frac{\pi E t R^2}{1-\nu^2} \int (\epsilon_\phi^2 + \epsilon_\theta^2 + 2\nu \epsilon_\phi \epsilon_\theta) \sin\phi d\phi. \quad (11a)$$

After substitution of equation (10), integration yields

$$\bar{U}_M = \frac{U_M}{k} = \frac{\lambda^4}{1-\nu} [(1-\cos\alpha)\, \bar{w}_i^2 + \cos\alpha\, \bar{w}_o^2] \quad (11b)$$

which, in the absence of material nonlinearity, involves no nonlinear terms.

Applied Load. The potential energy of the external load P is (see Fig. 3)

$$U_L = -P(\Delta_1 + \Delta_2 + \Delta_3) \quad (12)$$

with the displacement Δ_4 neglected for the moment. In terms of the nondimensional parameters

$$\bar{P} = \frac{P}{Et^2}; \quad \bar{\Delta}_j = \frac{\Delta_j}{R}, j = 1, 2, 3, 4, \quad (13)$$

equation (12) assumes the form

$$\bar{U}_L = \frac{U_L}{k} = -\frac{\lambda^2}{2\pi} \left(\frac{t}{c} \right) \bar{P} (\bar{\Delta}_1 + \bar{\Delta}_2 + \bar{\Delta}_3) \quad (14)$$

which, on substitution of the expressions derived in Appendix A for the displacement components $\bar{\Delta}_j$, becomes a function of the displacement parameters α, $\bar{w}_i$, $\bar{w}_o$, $\bar{y}_3$, and $\bar{y}_4$.

Fluid Incompressibility

The incompressible fluid constrains displacement by forcing the volume contained within the shell to remain constant during deformation. A volume change corresponds to each displacement component; the sum of the these volume changes must vanish.

The geometric problem of computing the volume changes due to the motion of the inner shell (ΔV_1, ΔV_2, ΔV_3) and the expanding outer shell (ΔV_4) is discussed in Appendix A. The volume displacement due to the deformation directly beneath the applied load [Fig. 3(*d*)] is neglected. Therefore, the total nondimensional volume change is defined as

$$\Delta \bar{V} = (\Delta V_1 + \Delta V_2 + \Delta V_3 + \Delta V_4) \left(\frac{\lambda^2}{3} \frac{t}{c} \right) \Big/ \left(\frac{2}{3} \pi R^3 \right) \quad (15)$$

which must vanish at all times as the shell deforms.

Equilibrium Solution

In nondimensional form, the modified total potential energy for the system is written

$$\bar{\Pi}(\bar{w}_i, \bar{w}_o, \bar{p}, \bar{y}_3, \bar{y}_4, \alpha; \bar{P}) = \bar{U}_B + \bar{U}_M + \bar{U}_L - \bar{p} \Delta \bar{V} \quad (16)$$

where $\bar{p}$ is a Lagrange multiplier. The physical interpretation of the multiplier is the nondimensional fluid pressure that relates to the physical pressure p by

$$\bar{p} = \frac{pR^2}{Et^2}. \quad (17)$$

After substitution of equations (9), (11*b*), (14), and (15) into equation (16), equilibrium requires

$$\frac{\partial \bar{\Pi}}{\partial \bar{w}_i} = \frac{\partial \bar{\Pi}}{\partial \bar{w}_o} = \frac{\partial \bar{\Pi}}{\partial \bar{p}} = \frac{\partial \bar{\Pi}}{\partial \bar{y}_3} = \frac{\partial \bar{\Pi}}{\partial \bar{y}_4} = \frac{\partial \bar{\Pi}}{\partial \alpha} = 0 \quad (18)$$

which, given the applied load P, provide six nonlinear algebraic equations for the six unknowns listed in equation (16). Note that the third equation provides the incompressibility condition $\Delta \bar{V} = 0$. The first five relations of equation (18), written in matrix form, are

$$\mathbf{A} \cdot \mathbf{z} = \mathbf{B}_L + \mathbf{B}_{NL} \quad (19)$$

where the solution vector is

$$\mathbf{z} = [\bar{w}_i, \bar{w}_o, \bar{p}, \bar{y}_3, \bar{y}_4]^T \quad (20)$$

and the matrix $\mathbf{A}(\alpha)$ is given in Appendix B. Terms for a solution involving linear strain measures are contained in the vector $\mathbf{B}_L$ $(\alpha; \bar{P})$, while the vector $\mathbf{B}_{NL}$ $(\bar{w}_i, \bar{w}_o, \bar{p}, \bar{y}_3, \bar{y}_4, \alpha; \bar{P})$ provides the nonlinear correction for moderately large rotation (see Appendix B).

Given α, the solution of equation (19) with $\bar{P} = \mathbf{B}_{NL} = 0$ gives a first approximation for $\mathbf{z}$. Then the last of equations (18) provides an initial estimate for $\bar{P}$. This solution is now substituted into the right-hand side of equation (19) with $\mathbf{B}_{NL}$ included, and the system is solved for the second approximation for $\mathbf{z}$, etc. For $\lambda\alpha >> 1$, this process generally converges within two or three iterations. However, when the steep shell condition does not hold, e.g., near the apex for thick shells, the system may not converge to the desired solution. Therefore, we obtained an approximate solution by assuming Δ_2, $\Delta_3 << \Delta_1$. Under this assumption, $\bar{y}_3 = \bar{y}_4 = 0$, equation (19) simplifies substantially, and the solution converges rapidly for all $\lambda\alpha$.

With the load known, the linear solution of Fig. 3(*d*) for the deflection directly beneath the load is [1]

$$\bar{\Delta}_4 = \bar{P}t/(8c) \quad (21)$$

which is based on shallow shell theory. And with $\mathbf{z}$ known, the other $\bar{\Delta}_j$ can be computed as in Appendix A, giving the total deflection of the load

$$\bar{\Delta} = \bar{\Delta}_1 + \bar{\Delta}_2 + \bar{\Delta}_3 + \bar{\Delta}_4. \quad (22)$$

Calculated results for applied load as a function of deflection are compared to experimental racquetball data in Fig. 4(*a*). The solution for an empty shell, obtained simply by setting $\bar{y}_3 = \bar{y}_4 = 0$ in the last of equations (18), is also shown with corresponding experimental measurements, and the linear solution is provided by equation (21). Curves for the computed and experimental fluid pressure are given in Fig. 4(*b*), while the effect of R/t on the results is shown in Fig. 5. Finally, bending and membrane stress distributions, computed from the one-term expansions of Ranjan [11], are illustrated in Fig. 6 for a thin shell ($R/t = 100$).

Discussion of Results

Even though the racquetball is quite thick ($R/t = 6.0$), bending theory for a thin shell describes the behavior of the empty shell under a point load accurately up to a deflection

Downloaded 01 May 2010 to 171.66.16.249. Redistribution subject to ASME license or copyright; see http://www.asme.org/terms/Terms_Use.cfm

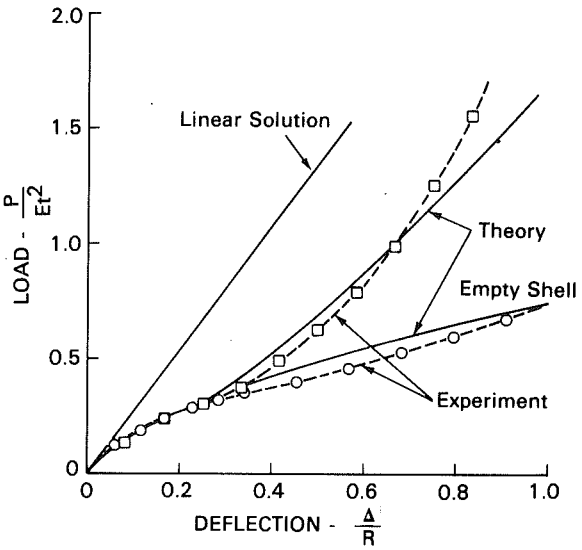


Fig. 4(*a*) Experimental and calculated load-deflection curves

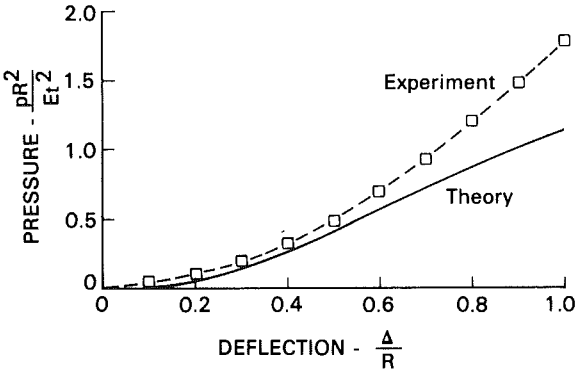


Fig. 4(*b*) Fluid pressure-deflection curves

Fig. 4 Water-filled racquetball ($R/t = 6.0$, $\nu = 0.5$)

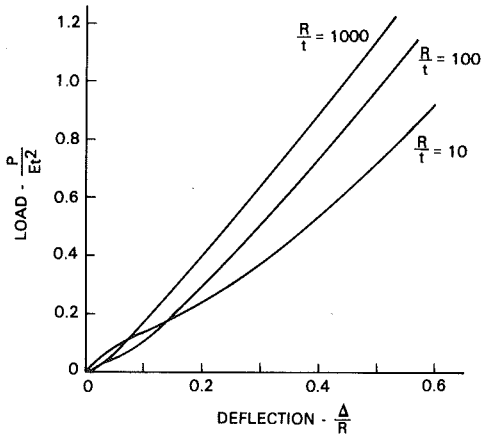


Fig. 5(*a*) Calculated load-deflection curves

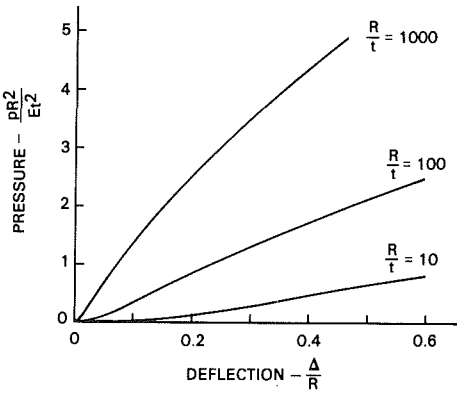


Fig. 5(*b*) Fluid pressure-deflection curves

Fig. 5 Effect of *R*/*t* on fluid-filled shells ($\nu = 0.5$)

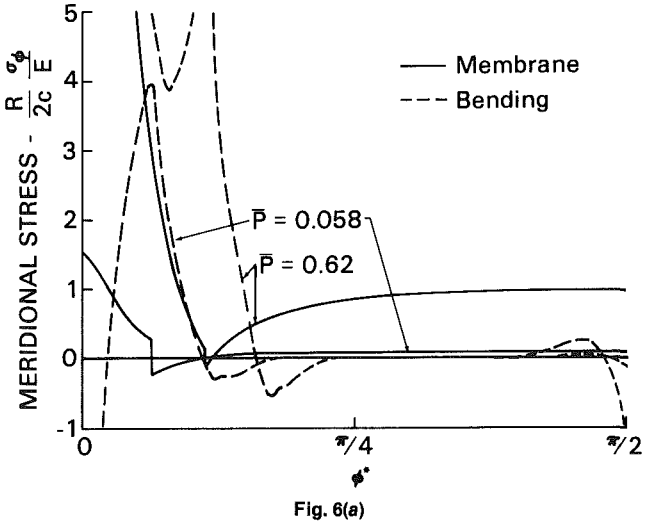


Fig. 6(*a*)

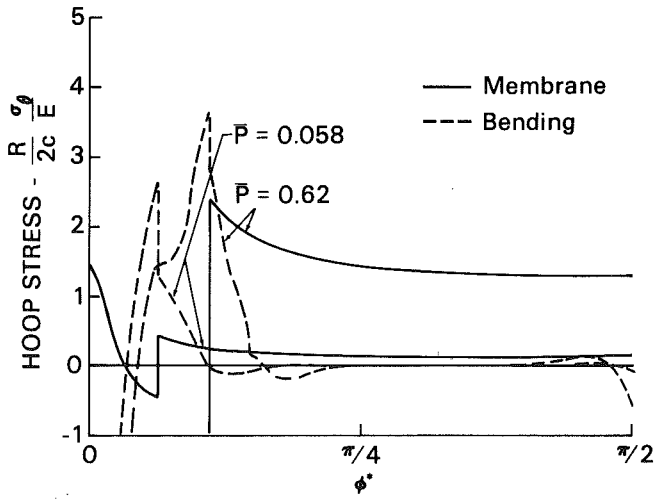


Fig. 6(*b*)

Fig. 6 Calculated membrane and bending stress distribution at outer surface of fluid-filled shell with $R/t = 100$ and $\nu = 0.5$ at two load levels

Downloaded 01 May 2010 to 171.66.16.249. Redistribution subject to ASME license or copyright; see http://www.asme.org/terms/Terms_Use.cfm

$\Delta/R = 0.25$ or 1.5 shell thicknesses [Fig. 4(*a*)]. Beyond this point, shear deformation adds to the decrease in shell stiffness with a measured load up to 15 percent lower than that calculated. When the apex deflection approaches the radius of the shell, experiments reflect the stiffening effect of the clamped lower edge. However, since we considered the solution for each edge independently, the theoretical curve does not exhibit such stiffening. In fact, the width of the edge zone is $\Delta\phi = \pi(2)^{1/2}/\lambda \cong 60$ deg for the racquetball; so, the solution at the dimple edge substantially overlaps the solution at the clamped edge. Of course, this inconsistency becomes more important as the dimple angle increases.

The load curve for the fluid-filled shell essentially follows that of the empty shell up to $\bar{\Delta} \cong 0.2$ [Fig. 4(*a*)] while the fluid pressure remains small at this deflection [Fig. 4(*b*)]. Therefore bending dominates the behavior of the system for $\bar{\Delta} \leq 0.2$. For larger deflection, enough fluid is displaced to cause significant stretching of the outer shell, and the fluid pressure and resistance to load increase substantially. The membrane stress curves of Fig. 6 illustrate the stretching. As with the empty shell, shear deformation causes the experimental load to fall slightly below the computed load.

For $\bar{\Delta} > 0.6$, the computed load and pressure begin to fall quite far below the measured values. Several factors may account for this discrepancy. First of all, as previously mentioned, displacement at the clamped edge due to bending at the dimple edge is not corrected by the solution. Secondly, the rotation of the edges is no longer "moderate" and the strain, although still small over most of the shell, becomes large near the dimple edge. Also, prestress becomes significant and the assumption $\Delta_2, \Delta_3 << \Delta_1$ does not hold for very large deflection. Finally, the deflection directly under the load becomes large and the linear solution of equation (21) is no longer valid. In view of the approximations made in the analysis, the accuracy of the computed results may be surprising.

We analyze the curves of Fig. 5 by holding the thickness of the shell constant and changing the radius. For relatively small deflection, the stiffness increases with lower values of R/t (Fig. 5(*a*)). In this region of predominant bending, the relatively thicker shell is expected to be stiffer. At larger deflection, however, geometric effects cause a higher load for the shell of larger radius. Although the strain level is actually smaller for the larger sphere, the area over which the membrane stress works increases like R^2. Likewise, while the physical fluid pressure is smaller for the larger sphere, the pressure works over an area proportional to R^2, and, as Fig. 5(*b*) shows, the effective pressure increases with R/t.

The stress distributions of Fig. 6 show high bending stress at the edge of the dimple and near the load. Both bending and membrane stress increase with the load, but the proportionate increase in membrane stress is much higher at very large deflection. The irregular behavior of the bending stress is probably due to using only the first term in the asymptotic expansion. Note that while $(\sigma_\theta)_{\text{membrane}}$ is compressive along the inner edge of the dimple, $(\sigma_\phi)_{\text{membrane}}$ is compressive at the dimple outer edge. Unlike that of the inner shell, the region of compression in the outer shell grows smaller as the load increases.

Conclusions

The major conclusions of the experimental and analytical investigation are:

1 An analysis based on axisymmetric thin shell theory predicts load and fluid pressure in good agreement with experimental data from a thick, fluid-filled spherical shell ($R/t = 6.0$) for deflection as high as 60 percent of the radius. The error due to neglecting shear deformation is less than 15 percent.

2 Deflection less than 20 percent of the radius of the shell is governed chiefly by bending while the fluid pressure increases little. Thus, small deflection behavior is similar to that of an empty shell, i.e., as the load increases, a dimple of reversed curvature spreads outward from the load and the stiffness of the shell falls.

3 For deflection greater than 20 percent of the radius, stretching due to fluid displaced by the load becomes significant. The stiffness and fluid pressure start to increase.

4 High bending stress is present at the edge of the dimple. For large deflection, however, membrane stress increases with the load more rapidly than bending stress.

Acknowledgment

The author thanks Matt M. Rodammer (General Motors Institute) and Mary E. Pope for their help in the experimental part of this work.

References

1 Reissner, E., "Stresses and Small Displacements of Shallow Spherical Shells," *Journal of Mathematics and Physics*, Vol. 25, 1946, pp. 80–85, 279–300; also, Vol. 27, 1948, p. 240.

2 Ashwell, D. G., "On the Large Deflection of a Spherical Shell with an Inward Point Load," *Proceedings of I.U.T.A.M. Symposium on the Theory of Thin Elastic Shells*, Delft, Aug. 1969, North Holland, Amsterdam, 1960, pp. 43–63.

3 Evan-Iwanowski, R. M., Cheng, H. S., and Loo, T. C., "Experimental Investigations of Deformations and Stability of Spherical Shells Subjected to Concentrated Load at the Apex," *Proceedings of the Fourth U.S. National Congress of Applied Mechanics*, 1962, pp. 563–575.

4 Penning, F. A., and Thurston, G. A., "The Stability of Shallow Spherical Shells Under Concentrated Load," *NASA CR-265*, July 1965.

5 Penning, F. A., "Experimental Buckling Modes of Clamped Shallow Shells Under Concentrated Load," ASME JOURNAL OF APPLIED MECHANICS, Vol. 33, Series E, June 1966, pp. 297–304.

6 Archer, R. R., "On the Numerical Solution of the Nonlinear Equations for Shells of Revolution," *Journal of Mathematics and Physics*, Vol. 41, 1962, pp. 165–178.

7 Mescall, J. F., "Large Deflections of Spherical Shells Under Concentrated Loads," ASME JOURNAL OF APPLIED MECHANICS, Vol. 32, Series E, Dec. 1965, pp. 936–938.

8 Bushnell, D., "Bifurcation Phenomena in Spherical Shells Under Concentrated and Ring Loads," *AIAA Journal*, Vol. 5, No. 11, Nov. 1967, pp. 2034–2040.

9 Fitch, J. R., "The Buckling and Post-Buckling Behavior of Spherical Caps Under Concentrated Load," *International Journal of Solids and Structures*, Vol. 4, 1968, pp. 421–446.

10 Ranjan, G. V., and Steele, C. R., "Large Deflection of Deep Spherical Shells Under Concentrated Load," *Proceedings, AIAA/ASME 18th Structures, Structural Dynamics, and Materials Conference*, San Diego, Mar. 21–23, 1977, pp. 269–278.

11 Ranjan, G. V., "Edge Zone Expansions for Thin Shells with Application to (1) Torispherical Pressure Vessel and (2) Large Deflection of Sphere with Point Load," PhD Dissertation, Stanford University, Nov. 1976.

12 Feng, W. W., and Yang, W.-H., "On the Contact Problem of an Inflated Spherical Nonlinear Membrane," ASME JOURNAL OF APPLIED MECHANICS, Vol. 40, Series E, 1973, pp. 209–214.

13 Love, A. E. H., *The Mathematical Theory of Elasticity*, Cambridge University Press, 4th Ed., 1927, p. 553.

14 Novozhilov, V. V., *Thin Shell Theory*, Noordhoff, Groningen, The Netherlands, 1970.

APPENDIX A

Displacement and Volume Components

The displacement components and the volume changes of Fig. 3 are determined in this Appendix. During the inversion of the inner shell to form the dimple, the load traverses a distance

$$\bar{\Delta}_1 = 2(1 - \cos\alpha). \tag{23}$$

Next, the fluid pressure causes expansion of the outer shell and contraction of the inner shell. In moving the edge of the

Downloaded 01 May 2010 to 171.66.16.249. Redistribution subject to ASME license or copyright; see http://www.asme.org/terms/Terms_Use.cfm

deformed inner shell vertically to the level of the edge of the outer shell, the load moves a distance

$$\bar{\Delta}_2 = \bar{w}_i(1-\cos\alpha) - \bar{w}_o\cos\alpha. \tag{24}$$

Finally, bending the edges produces the additional displacement [see Fig. 2(*b*)]

$$\bar{\Delta}_3 = (\bar{v}_i)_{\phi_e=\alpha} - (\bar{v}_o)_{\phi_e=\pi-\alpha} + (\bar{v}_o)_{\phi_e=}\,\pi/2 \tag{25}$$

where the vertical displacement at a steep shell edge is given by [10]

$$\bar{v}_e = \frac{v_e}{R} = -\cos\phi_e\left[y_4 + \frac{\lambda}{2(2)^{1/2}\sin 2\phi}\,(y_3^2 + y_4^2)\right]_e. \tag{26}$$

Substitution of equations (6), (8), and (26) into equation (25) yields the downward displacement component of the applied load

$$\bar{\Delta}_3 = -2\bar{y}_4\cos\alpha + \frac{\alpha}{2(2)^{1/2}\sin\alpha}\left(2\bar{y}_3 - \frac{\lambda}{\alpha}\,\bar{y}_4\Delta\bar{w}\right) - \frac{\lambda}{4(2)^{1/2}}\,\bar{w}_o^2. \tag{27}$$

With the displacement components known in terms of the problem displacement parameters, the volume changes of equation (15) can now be computed. First, the inverting dimple sweeps out a volume

$$\Delta V_1 = -\pi R^3\bar{\Delta}_1^2(6-\bar{\Delta}_1)/12. \tag{28}$$

Then, as the inner shell moves vertically downward through Δ_2, the added volume is

$$\Delta V_2 = -\Delta_2\int_0^{2\pi}\int_0^{\alpha} R^2\sin\phi\; d\phi d\theta = -2\pi R^3\bar{\Delta}_2(1-\cos\alpha). \tag{29}$$

Since bending is assumed to be localized to narrow edge zones, we neglect the fluid displaced by the deforming shell edges. Thus, the volume change produced by Δ_3 is

$$\Delta V_3 = -2\pi R^3\bar{\Delta}_3(1-\cos\alpha). \tag{30}$$

The volume displaced by the inner shell is transferred to the expanding outer shell, which, for $\bar{w}_o << 1$, adds the volume

$$\Delta V_4 = w_o\int_0^{2\pi}\int_{\pi/2}^{\pi-\alpha} R^2\sin\phi d\phi d\theta = 2\pi R^3\bar{w}_o\cos\alpha. \tag{31}$$

We neglect the volume displacement due to the deformation directly beneath the applied load.

APPENDIX B

Solution Matrices

The solution matrices of equation (19) are

$$\mathbf{A} = \begin{bmatrix} \left\{2^{-1/2} + \dfrac{2\lambda}{(1-\nu)}\dfrac{(1-\cos\alpha)}{\sin\alpha}\right\} & -2^{-1/2} & \dfrac{t}{\lambda c}\dfrac{(1-\cos\alpha)^2}{\sin\alpha} & 0 & 0 \\ -2^{-1/2} & \left\{3(2)^{-1/2} + \dfrac{2\lambda}{1-\nu}\cot\alpha\right\} & \left\{\dfrac{-t}{\lambda c}(2-\cos\alpha)\cot\alpha\right\} & 0 & 0 \\ -(1-\cos\alpha) & \cos\alpha(2-\cos\alpha) & 0 & 0 & 2\cos\alpha(1-\cos\alpha) \\ 0 & 0 & 0 & 2^{1/2} & 1 \\ 0 & 0 & \dfrac{-t}{\lambda c}(1-\cos\alpha)\cot\alpha & 1 & 2^{1/2} \end{bmatrix}, \tag{32}$$

$$\mathbf{B}_L = \begin{bmatrix} -\dfrac{\alpha}{\lambda} + \dfrac{\bar{P}}{2\pi}\dfrac{t}{\lambda c}\dfrac{(1-\cos\alpha)}{\sin\alpha} \\ \dfrac{\alpha}{\lambda} - \dfrac{\bar{P}}{2\pi}\dfrac{t}{\lambda c}\cot\alpha \\ (1-\cos\alpha)^2 \\ 0 \\ -\dfrac{\bar{P}}{2\pi}\dfrac{t}{\lambda c}\cot\alpha \end{bmatrix}, \tag{33}$$

Downloaded 01 May 2010 to 171.66.16.249. Redistribution subject to ASME license or copyright; see http://www.asme.org/terms/Terms_Use.cfm

and

$$\mathbf{B}_{NL} = \begin{bmatrix} \frac{\lambda\cot\alpha}{10}\left(\frac{\alpha^2}{\lambda^2} + \bar{y}_3^2 + 2\bar{y}_4^2 + \frac{1}{2}\Delta\bar{w}^2\right) + \frac{t}{c}\frac{\bar{y}_4}{2(2)^{1/2}\sin^2\alpha}P^* \\ \left\{\begin{array}{l} \frac{-\lambda\cot\alpha}{10}\left(\frac{\alpha^2}{\lambda^2} + \bar{y}_3^2 + 2\bar{y}_4^2 + \frac{1}{2}\Delta\bar{w}^2\right) - \frac{t}{c}\frac{\bar{y}_4}{2(2)^{1/2}\sin^2\alpha}P^* \\ \qquad - \frac{\bar{P}}{2\pi}\frac{t}{\lambda c}\cot\alpha - \frac{\lambda\cot\alpha}{5}\bar{w}_o^2 \end{array}\right\} \\ -(1-\cos\alpha)^3/3 + \frac{\alpha}{2(2)^{1/2}}\frac{(1-\cos\alpha)}{\sin\alpha}\left(2\bar{y}_3 - \frac{\lambda}{\alpha}\bar{y}_4\Delta\bar{w}\right) \\ \frac{\lambda\cot\alpha}{10}\left(6(2)^{1/2}\frac{\alpha}{\lambda}\bar{y}_3 + 2\frac{\alpha}{\lambda}\bar{y}_4 - \bar{y}_3\Delta\bar{w}\right) + \frac{t}{\lambda c}\frac{\alpha P^*}{2(2)^{1/2}\sin^2\alpha} \\ \frac{\cot\alpha}{5}(\alpha\bar{y}_3 - \lambda\Delta\bar{w}\,\bar{y}_4) - \frac{t}{c}\frac{\Delta\bar{w}}{4(2)^{1/2}\sin^2\alpha}P^* \end{bmatrix} \tag{34}$$

where

$$P^* = \frac{\bar{P}}{2\pi} - (1-\cos\alpha)\bar{p}.$$

Downloaded 01 May 2010 to 171.66.16.249. Redistribution subject to ASME license or copyright; see http://www.asme.org/terms/Terms_Use.cfm

Edge Effects in Laminated Composite Plates

S. B. Dong
Professor.
Mem. ASME

D. B. Goetschel
Formerly, Graduate Student.
Currently, Assistant Professor,
Rensselaer Polytechnic Institute,
Troy, New York

Mechanics and Structures Department,
University of California,
Los Angeles, Calif. 90024

The attenuation of self-equilibrated edge stress states into the interior of a laminated plate composed of an arbitrary number of bonded, elastic, anisotropic layers is investigated in the context of Saint-Venant's principle using the exponential decay results of Toupin, Knowles, and Horgan. To model the plate's behavior, a semianalytical method is used with finite element interpolations over the thickness and exponential decay into the plate's interior. The formulation leads to a second-order algebraic eigensystem whose eigenvalues are the characteristic inverse decay lengths, and corresponding right eigenvectors depict the displacement distributions of self-equilibrated traction states. Orthogonality relations between these right and left eigenvectors of the adjoint system are established. An eigenvector expansion for representing arbitrary self-equilibrated edge tractions is then presented. This approach is useful in revealing the interlaminar effects and their decay rates in a laminated composite plate under plane strain. Two examples are provided where the interlaminar phenomena due to eigenstates of self-equilibrated edge stress are illustrated.

Introduction

Saint-Venant's principle asserts the elastic equivalence of stress states at any point that is remote from a load region due to different but statically equivalent systems of loads. This principle on a qualitative basis has been extremely useful and extensively invoked. However, as it stands, it is not free from ambiguities and certain apparent paradoxes can be illustrated by means of well-contrived examples. Motivated by a need for clarification of this form of Saint-Venant's principle Toupin [1] in 1965 and Knowles [2] in 1966 independently presented theorems for upper bound estimates of the strain energy in a body as a function of the distance away from the region of applied tractions. The main result of their theorems is a strain energy decay inequality in the form:

$$V(x) \leq V(0) \cdot \exp(-2\gamma x) \tag{1}$$

where γ is the inverse of the characteristic decay length, $V(0)$ is the total strain energy, and $V(x)$ is the strain energy in the that part of the body beyond x. Because of the quadratic nature of strain energy in terms of the mechanical variables, an immediate consequence is the capability for pointwise estimates of displacement, strain, and stress in the forms;

$$\begin{aligned} u_i(x) &\leq K_1 \cdot \exp(-\gamma x) \\ \epsilon_{ij}(x) &\leq K_2 \cdot \exp(-\gamma x) \\ \tau_{ij}(x) &\leq K_3 \cdot \exp(-\gamma x) \end{aligned} \tag{2}$$

where K_i $(i = 1,2,3)$ are constants.

Horgan [3, 4] extended Knowles' analysis to plane problems with anisotropic domains. Choi and Horgan [5, 6] went further to analytically and numerically study two general cases of plates in plane strain, viz., a homogeneous, anisotropic composite and a sandwich construction. The formulations in references [2–6] employed the Airy stress function ϕ, which, in accordance with compatibility, leads to a generalized biharmonic governing equation. For a rectangular region, the solution form can be taken as a product function of an exponential decay away from the load region and an undetermined function in the transverse direction, i.e., if $x = 0$ is the edge with the applied tractions, then $\phi(x,y) = F(y) \cdot (-\gamma x)$. This solution form enables the eigenvalue problem to be reduced to a fourth-order ordinary differential equation in $F(y)$. The eigenvalue γ with the smallest real part characterizes the dominant exponential decay.

Herein, the same type of plane strain analysis for determining the decay rates of edge effects in a plate composed of an arbitrary number of bonded, elastic anisotropic layers is considered. We opt for a numerical approach using finite elements as a more convenient means for handling any type of laminate construction. Also, instead of the Airy function, which is used in references [2–6], we adopt the inplane displacements as the primary dependent variables. In this version of the finite element analysis, the discretization occurs over the plate's thickness with laminas, each using quadratic interpolations for the displacements. The governing equations first appear as a system of second-order ordinary differential equations. By invoking the exponential decay as given by equation (2), a second-order eigenvalue problem emerges, whose roots are the inverses of the characteristic decay lengths. The corresponding eigenvectors are displacement distributions for the self-equilibrated edge traction states. Although not demonstated herein, these eigenvectors can be shown to constitute a complete set in a mathematical sense, so that any aribtrary self-equilibrated edge disturbance can be expanded in terms of them.

High interlaminar normal and shear stresses occurring in a region near the free edge of laminated composites are sources

Contributed by the Applied Mechanics Division for publication in the JOURNAL OF APPLIED MECHANICS.

Discussion on the paper should be addressed to the Editorial Department, ASME, United Engineering Center, 345 East 47th Street, New York, N.Y. 10017, and will be accepted until two months after final publication of the paper itself in the JOURNAL OF APPLIED MECHANICS. Manuscript received by ASME Applied Mechanics Division, November, 1980; final revision, July 1981.

Copyright © 1982 by ASME
Downloaded 01 May 2010 to 171.66.16.249. Redistribution subject to ASME license or copyright; see http://www.asme.org/terms/Terms_Use.cfm

promoting structural failures [7]. Furthermore, in experimental characterization of composite material properties, issues have been raised concerning locations of strain gage placement, specimen size, and end constraint conditions in order to achieve satisfactory measurements [8–12]. To date, these problems have been primarily considered on a case-by-case basis. Methods ranging from classical plate theory to refined plate theories to approximate elasticity solutions have been employed. They include both analytical and numerical studies, including finite differences and two and three-dimensional finite element modeling. References [13–28] are indicative of this wide spectrum of activity related to the analysis of edge effects. The approach herein should provide a means for a more systematic understanding of edge effects in laminated composites. The analysis technique is useful in revealing the various interlaminar effects. Thus designs of a laminate with consideration to mitigating these effects can be evaluated analytically instead of by more costly experimental means.

Formulation of Governing Equations

Consider a semi-infinite plate composed of perfectly bonded layers with possibly distinct mechanical properties and thickness. Let (x,y,z) be rectangular Cartesian coordinates with the plate occupying the region $x \geq 0$. We will confine our attention to the case of plane strain with deformation occurring in the $x-y$ plane. Let $u = u(x,y)$ and $v = v(x,y)$ denote the components of displacement. The non-vanishing strain components $\{\epsilon\}^T = \{\epsilon_{xx}\epsilon_{yy}\gamma_{xy}\}$ are related to u and v by:

$$\epsilon_{xx} = u_{,x}; \quad \epsilon_{yy} = v_{,y}; \quad \gamma_{xy} = u_{,y} + v_{,x} \tag{3}$$

For each layer's material constitution, we will employ a relation sufficiently general to accommodate monoclinic properties and further suppose that the material's only elastic symmetry plane coincides with the $x-y$ plane. If $\{\tau\}^T = \{\tau_{xx}\tau_{yy}\tau_{xy}\}$ represent the stresses, this constitutive relation has the form:

$$\{\tau\} = [C^{(k)}]\{\epsilon\} \tag{4}$$

with

$$[C^{(k)}] = \begin{bmatrix} C_{11}^{(k)} & C_{12}^{(k)} & C_{16}^{(k)} \\ C_{12}^{(k)} & C_{22}^{(k)} & C_{26}^{(k)} \\ C_{16}^{(k)} & C_{26}^{(k)} & C_{66}^{(k)} \end{bmatrix} \tag{5}$$

where $C_j^{(k)}$ are the elastic moduli with superscript (k) denoting the kth layer.

The decay rate of end effects into the plate's interior may be posed as a boundary value problem. It calls for the fundamental equations of plane elasticity for the layers to be accompanied by traction-free exterior lateral surfaces, interface displacement and traction continuity, and prescribed traction boundary condition on the edge of the plate. Herein, the displacements are adopted as the problem's primary variables. In our finite element derivation, the governing equations will be formulated by minimization of the total potential energy Π, i.e., $\delta\Pi = 0$. For plane strain, the total potential energy has the form:

$$\Pi = \frac{1}{2}\int \left\{ \sum_k \int \{\epsilon\}^T [C^{(k)}]\{\epsilon\} dy \right\} dx - \int \left\{ \bar{\tau}_{xx} u(0,y) + \bar{\tau}_{xy} v(0,y) \right\} dy \tag{6}$$

The first integral in equation (6) represents the strain energy and the second is the potential energy of external work, where $\bar{\tau}_{xx}$ and $\bar{\tau}_{xy}$ are prescribed tractions on the edge $x = 0$.

The finite element discretization proceeds along the y-direction, with the subdivision of the plate into mathematical laminas. A mathematical lamina is distinguished from a plate layer by noting that a number of laminas may be used to model the physical behavior within a layer. In each lamina, the displacement field is taken as:

$$u(x,y) = n_1(y)\cdot u_b(x) + n_2(y)\cdot u_m(x) + n_3(y)\cdot u_f(x)$$
$$v(x,y) = n_1(y)\cdot v_b(x) + n_2(y)\cdot v_m(x) + n_3(y)\cdot v_f(x) \tag{7}$$

where generalized displacements u_b,v_b; u_m,v_m; u_f,v_f are taken at the back, mid, and front nodal surfaces of the lamina. At this point, these displacements are assumed to be undetermined functions of x. The interpolation polynomials n_i are quadratic functions given by:

$$n_1 = 1 - 3\zeta + 2\zeta^2; \quad n_2 = 4\zeta - 4\zeta^2; \quad n_3 = 2\zeta^2 - \zeta \tag{8}$$

with normalized distance ζ defined by

$$\zeta = (y - y_b)/(y_f - y_b) \tag{9}$$

where y_b, y_f are thickness coordinates of the bounding surfaces of the lamina. Inserting equation (7) into the strain-displacement relations (3) yields:

$$\{\epsilon\} = [b]\{q'\} + [a]\{q\} \tag{10}$$

where the array of the lamina's generalized displacements is ordered:

$$\{q\}^T = [u_b,v_b,u_m,v_m,u_f,v_f] \tag{11}$$

and a prime indicates differentiation with respect to x. The strain displacement transformation matrices $[a]$ and $[b]$ appear as:

$$[a] = \frac{d}{dy}\begin{bmatrix} - & - & - & - & - & - \\ - & n_1 & - & n_2 & - & n_3 \\ n_1 & - & n_2 & - & n_3 & - \end{bmatrix} \tag{12}$$

$$[b] = \begin{bmatrix} n_1 & - & n_2 & - & n_3 & - \\ - & - & - & - & - & - \\ - & n_1 & - & n_2 & - & n_3 \end{bmatrix} \tag{13}$$

Substituting the strains (10) into the strain energy portion of Π yields the lamina's strain energy:

$$V = \frac{1}{2}\int \Big[\{q'\}^T[k_1]\{q'\} + \{q'\}^T[k_2]\{q\} + \{q\}^T[k_2]^T\{q'\} + \{q\}^T[k_3]\{q\}\Big] dx \tag{14}$$

where

$$[k_1] = \int [b]^T[C^{(k)}][b]\, dy$$
$$[k_2] = \int [b]^T[C^{(k)}][a]\, dy \tag{15}$$
$$[k_3] = \int [a]^T[C^{(k)}][a]\, dy$$

Observe that $[k_1]$ and $[k_3]$ are symmetric, while $[k_2]$ is not. The elements of these matrices are listed in the Appendix.

The strain energy of the plate is found by summing the contributions from all laminas. Variation of this total strain energy gives:

$$[K_1]\{Q''\} + [K_2^*]\{Q'\} - [K_3]\{Q\} = 0 \tag{16}$$

where $\{Q\}$ is an ordered set of generalized displacements for the plate and $[K_1]$, $[K_2^*]$, $[K_3]$ are plate matrices obtained by superposing the element matrices and

Downloaded 01 May 2010 to 171.66.16.249. Redistribution subject to ASME license or copyright; see http://www.asme.org/terms/Terms_Use.cfm

$$[K_2^*] = [K_2] - [K_2]^T \tag{17}$$

Equation (16) represents a system of second-order ordinary differential equations for the nodal displacements. Note that $[K_2^*]$ is skew symmetric. We have not as yet considered the variation of the potential energy of the prescribed edge tractions. This step would lead to the boundary conditions associated with equation (16) and will not modify this governing equation.

According to the theorems of Toupin and Knowles, the x-dependence of $\{Q\}$ can be factored as follows:

$$\{Q\} = \{Q_o\} \cdot \exp(-\gamma x) \tag{18}$$

Substituting this solution form into equation (16) yields the following second-order eigenvalue problem:

$$[\gamma^2 [K_1] - \gamma[K_2^*] - [K_3]]\{Q_o\} = 0 \tag{19}$$

The solution to equation (19) is obtained by means of a Block-Stodola technique [29]. The essence of this technique is simultaneous iteration using a reduced number of coordinate vectors until convergence of a subset of eigenvalues γ to within a pre-established tolerance. The method is computationally very efficient and can treat nonsymmetric matrices and complex eigendata without difficulty.

It is remarked that there are two zero eigenvalues and their nontrivial eigenvectors contained in the eigensystem. They portray the cases of uniform extension and pure bending of the plate. Recall that a zero eigenvalue corresponds to an infinite decay length, i.e., no decay. The other eigenpairs are associated with some self-equilibrated systems of edge tractions.

Orthogonality

To develop the appropriate forms of the orthogonality relationships, it is necessary to review the solution form of equation (19). This quadratic eigenvalue problem can be reduced to a first-order problem by letting

$$\{Q_1\} = -\gamma\{Q_o\} \tag{20}$$

Then, equation (19) assumes the form

$$-\gamma[K_1]\{Q_1\} + [K_2^*]\{Q_1\} - [K_3]\{Q_o\} = 0 \tag{21}$$

Recasting equations (20) and (21) into one matrix equation gives

$$\begin{bmatrix} [0] & -[I] \\ -[K_3] & [K_2^*] \end{bmatrix} \begin{bmatrix} \{Q_o\} \\ \{Q_1\} \end{bmatrix} = \gamma \begin{bmatrix} [I] & [0] \\ [0] & [K_1] \end{bmatrix} \begin{bmatrix} \{Q_o\} \\ \{Q_1\} \end{bmatrix} \tag{22}$$

or in abbreviated notation

$$[A]\{\bar{Q}\} = \gamma[B]\{\bar{Q}\} \tag{22a}$$

The solution to equation (22a) can be stated as the transformation

$$\{\bar{Q}\} = [\bar{\phi}]\{x\} \tag{23}$$

where $[\bar{\phi}]$ contains the right eigenvectors and $\{x\}$ denotes the right normal coordinates. By virtue of equation (20), then

$$\{Q_o\} = [\phi_o]\{x\};\ \{Q_1\} = [\phi_1]\{x\} = [\phi_o][\gamma]\{x\} \tag{24}$$

where $[\gamma]$ is a diagonal matrix of the eigenvalues and $[\phi_o]$ and $[\phi_1]$ are the upper and lower partitions of $[\bar{\phi}]$, i.e.,

$$[\bar{\phi}] = \begin{bmatrix} [\phi_o] \\ \hline [\phi_1] \end{bmatrix} = \left[\begin{array}{c|c} [\phi_o] & \\ \hline -[\phi_o] & [\gamma] \end{array}\right] \tag{25}$$

Associated with equation (22) is the adjoint problem

$$\begin{bmatrix} [0] & -[K_3] \\ -[I] & -[K_2^*] \end{bmatrix} \begin{bmatrix} \{L_o\} \\ \{L_1\} \end{bmatrix} = \gamma \begin{bmatrix} [I] & [0] \\ [0] & [K_1] \end{bmatrix} \begin{bmatrix} \{L_o\} \\ \{L_1\} \end{bmatrix} \tag{26}$$

where $\{L_o\}$ and $\{L_1\}$ are the left counterparts of the generalized variables. Rewriting equation (26) in abbreviated form gives

$$[A]^T\{\bar{L}\} = \gamma \mathrm{B}]\{\bar{L}\} \tag{26a}$$

The solution to equation (26a) is written as

$$[\bar{L}] = [\bar{\psi}]\{y\} \tag{27}$$

where $[\bar{\psi}]$ and $\{y\}$ are the left eigenvectors and normal coordinates. Following the same partitioning procedure as before, equation (27) can be decomposed into

$$\{L_o\} = [\psi_o]\{y\};\ \{L_1\} = [\psi_1]\{y\} \tag{28}$$

with $[\psi_o]$ and $[\psi_1]$ as the upper and lower halves of $[\bar{\psi}]$.

The right and left eigenvectors obey the orthogonality relations

$$[\bar{\psi}]^T[B][\bar{\phi}] = [I] \tag{29}$$

$$[\bar{\psi}]^T[A][\bar{\phi}] = [\text{ diag }] \tag{30}$$

where [diag] is a diagonal matrix. In terms of $[\phi_o]$, $[\phi_1]$, $[\psi_0]$, $[\psi_1]$, they become

$$[\psi_o]^T[\phi_o] + [\psi_1]^T[K_1][\phi_1] = [I] \tag{29a}$$

$$-[\psi_1]^T[K_3][\phi_o] - [\psi_o]^T[\phi_1] + [\psi_1]^T[K_2^*][\phi_1] = [\text{ diag }] \tag{30a}$$

Going further, the orthogonality conditions can be expressed completely in terms of $[\phi_o]$ and $[\psi_o]$ by using equations (24) and (28) to give:

$$[\psi_o]^T[\phi_o] + [\gamma][\psi_o]^T[K_3]^{-1}[K_1][\phi_o][\gamma] = [I] \tag{29b}$$

$$[\gamma][\psi_o]^T[\phi_o] + [\psi_o]^T[\phi_o][\gamma] + [\gamma][\psi_o]^T[K_3]^{-1}[K_2^*][\phi_o][\gamma] = [\text{ diag }] \tag{30b}$$

Eigenvector Expansion

For edge effects, say at $x = 0$, governing equation (16) is modified by the inclusion of a consistent load vector $\{F\}$ on the right-hand side, which represents a self-equilibrated traction state:

$$[K_1]\{Q''\} + [K_2^*]\{Q'\} - [K_3]\{Q\} = \{F\}\delta(x) \tag{31}$$

This load, for example, could be the difference between an actual prescribed load and that corresponding to a variation according to classical plate theory. Recasting equation (31) into a first-order matrix differential equation gives:

$$\begin{bmatrix} [0] & -[I] \\ -[K_3] & [K_2^*] \end{bmatrix} \begin{bmatrix} \{Q\} \\ \{Q'\} \end{bmatrix} + \begin{bmatrix} [I] & [0] \\ [0] & [K_1] \end{bmatrix} \begin{bmatrix} \{Q\}' \\ \{Q'\}' \end{bmatrix} = \begin{bmatrix} \{0\} \\ \{F\}\delta(x) \end{bmatrix} \tag{32}$$

With the aid of orthogonality conditions (29) and (30) or their counterparts, equation (32) can be transformed to a system of right normal coordinates.

$$\{x'\} - [\text{ diag }]\{x\} = \{f\}\delta(x) \tag{33}$$

where

$$\{f\} = [\psi_1]^T\{F\} = [\gamma][\psi_o]^T[K_3]^{-1}\{F\} \tag{34}$$

The expansion theorem is embodied in equation (34), where it can be seen that the left eigenvectors are employed for expressing the self-equilibrated edge loads. This is an example of dual expansion techniques.

Downloaded 01 May 2010 to 171.66.16.249. Redistribution subject to ASME license or copyright; see http://www.asme.org/terms/Terms_Use.cfm

Table 1 Inverse decay lengths for homogeneous plate

	Symmetric			Antisymmetric		
Mode	Computed	Analytical	% Diff.	Computed	Analytical	% Diff.
1	0.564288	0.564288	0	0.796485	0.796485	0
2	1.134479	1.134478	<0.001	1.369817	1.369816	<0.001
3	1.751046	1.751041	<0.001	1.934698	1.934691	<0.001
4	2.100891	2.100887	<0.001	2.498649	2.498622	0.001
	±0.184676i	±0.184680i				
5				3.066716	3.066641	0.002
6	2.725580	2.725537	0.002	3.660334	3.660135	0.005
7	3.303709	3.303601	0.003	4.124063	4.123960	0.002
				±0.211119i	±0.2111132i	0.002
8	3.869578	3.869343	0.006			
9	4.433580	4.433119	0.01	4.651884	4.651237	0.01
10	5.000445	4.999603	0.02	5.238010	5.236940	0.02
11	5.583633	5.582094	0.03	5.805667	5.803916	0.03
12	6.144539	6.143946	0.01	6.370482	6.367726	0.04
	±2.062371	±0.205817i				
13				6.937329	6.933120	0.06
14	6.573874	6.570037	0.06	7.515699	7.509242	0.08
15	7.174704	7.169650	0.07	8.172515	8.171730	0.01
				±0.168462i	±0.163136i	
16	7.745562	7.738361	0.09			
17	8.312499	8.302396	0.12	8.485188	8.468500	0.20
18	8.880988	8.867031	0.16	9.117746	9.101440	0.18
19	9.458485	9.439094	0.21	9.693937	9.672621	0.22

Table 2 Inverse decay lengths for two laminated composite plates

Mode	[0/90/0/90]	[0/90/90/0]	
1	2.37127	2.67202	(S)
2	2.69332	2.67340	(A)
3	4.14039	4.43495	(S)
4	5.01693	4.66170	(S)
		±0.80848i	
5	5.05979		
	±1.02538i		
6		5.05320	(A)
7	7.18095	7.89813	(S)
8	7.80700	8.01317	(A)
9	8.86839	9.17835	(A)
		±1.52921i	
10	10.24231		
11	10.99861	10.08591	(A)
	±1.77948i		
12		10.21602	(S)
13	12.73734	13.17156	(A)
14	12.95796	13.64291	(S)
15	13.02613	13.96736	(S)
	±2.54684i	±1.38302i	
16			
17	15.07504	15.46369	(S)
18	15.54992	15.49137	(A)
19	17.97401	17.98795	(A)
	±0.94083i	±1.14093i	
20			

For [0/90/90/0] Plate: (S)—Symmetric
(A)—Antisymmetric

Homogeneous Plate

For verification of the numerical method and computer code, a homogeneous graphite/epoxy composite plate with a half-thickness of unity was considered. Properties taken for this plate are those used in reference [5], i.e.,

$$E_L = 20 \times 10^6 \text{ psi}\,; E_T = 1 + 10^6 \text{ psi}$$
$$G_{LT} = 0.6 \times 10^6 \text{ psi}\,; \nu_{LT} = \nu_{TT} = 0.25 \tag{35}$$

The elastic moduli C_{ij} corresponding to equation (35) are:

$$[C] = 10^6 \begin{bmatrix} 1.3905388 & 0.0237565 & - \\ & 0.0739303 & - \\ \text{symmetric} & & 0.0413685 \end{bmatrix} \text{ psi} \tag{36}$$

where the fiber direction coincides with the x-axis. It is mentioned that elastic compliances $[C]^{-1}$ derived from equation (36) differ slightly from those for the example in reference [5]. In order for consistency in our comparison with the analytical results, all calculations reported herein are based on equation (36). For the half-thickness model of the plate, 40 equal thickness elements (81 nodal surfaces and 162 degrees of freedom) were employed. The analysis was carried out in two phases using symmetry and antisymmetry mid-surface conditions.

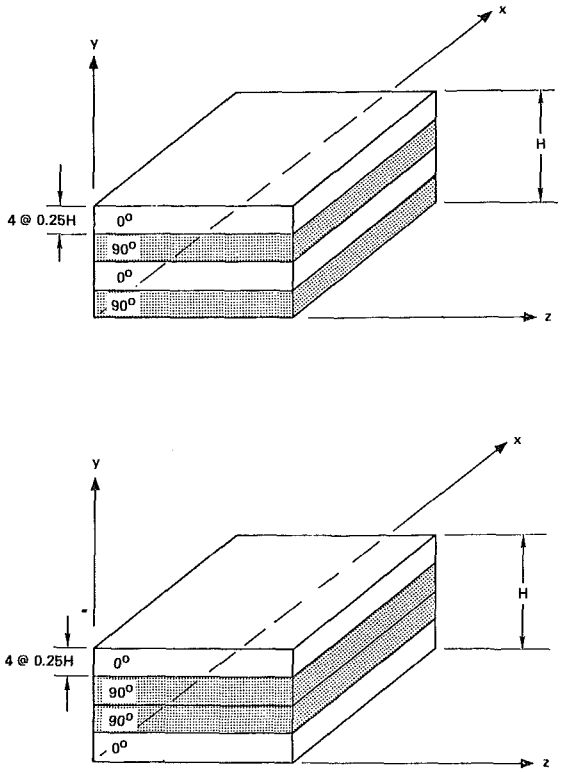


Fig. 1 Two laminated composite plates

In Table 1, the computed values of the lowest 19 (nonzero) eigenvalues for symmetric and antisymmetric deformations are listed. Also shown are the analytical values that are extracted from transcendental equation (18) of reference [5]. The accuracy of the method and the model is evidenced by the

Downloaded 01 May 2010 to 171.66.16.249. Redistribution subject to ASME license or copyright; see http://www.asme.org/terms/Terms_Use.cfm

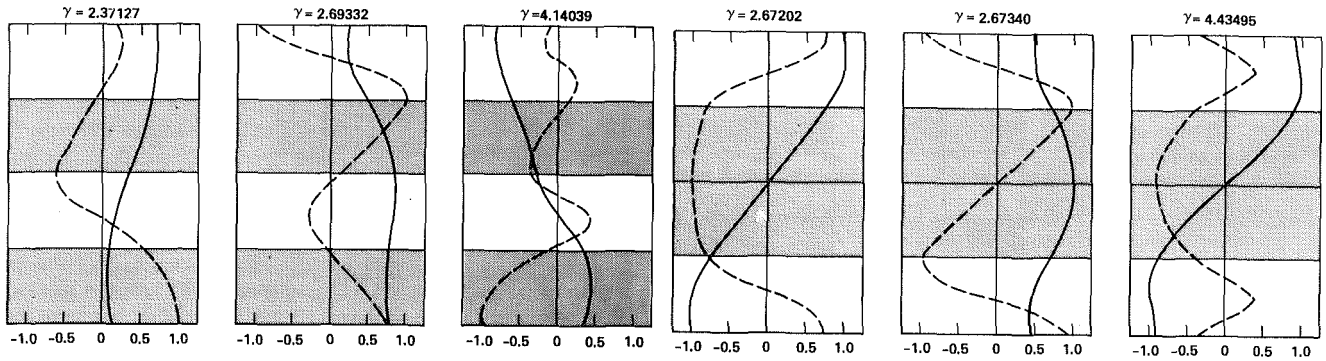


Fig. 2 Selected displacement patterns for [0/90/0/90] composite plates

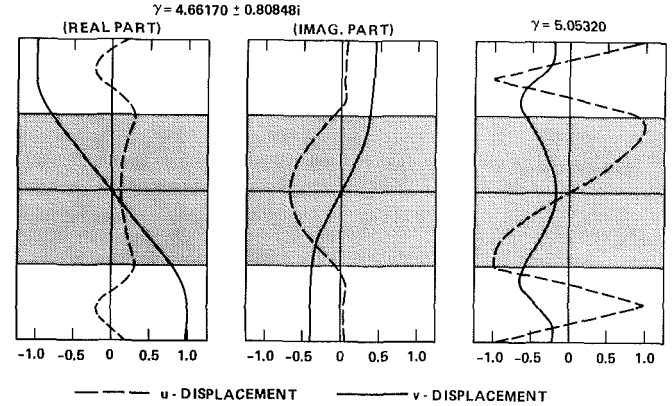


Fig. 3 Selected displacement patterns for [0/90/90/0] composite plates

remarkably small percentage differences between the computed and analytical eigenvalues. The real eigenvalues are associated with exponential decay while the complex eigenvalues pertain to damped sinusoidal decay.

Four-Ply Laminated Composite Plates

Two four-ply laminated plates, both of unit thickness, were considered. One possessed a stacking sequence of [0/90/0/90] and the other was a [0/90/90/0] lay-up as shown in Fig. 1. The elastic parameters for each ply relative to their natural elastic axis are:

$$E_L = 20.2 = 10^6 \text{ psi}; \quad E_T = 2.2 \times 10^6 \text{ psi}$$
$$G_{LT} = G_{TT} = 0.85 \times 10^6 \text{ psi}; \quad \nu_{LT} = \nu_{TT} = 0.21 \tag{37}$$

These properties are the same as those in the examples in references [23, 28]. The corresponding elastic moduli with the fiber axis parallel (0 deg) and transverse (90 deg) to the x-axis are, respectively,

$$[C]_{0\,\text{deg}} = 10^6 \begin{bmatrix} 21.28929 & 0.59201 & - \\ & 2.31864 & - \\ \text{symmetric} & & 0.85 \end{bmatrix} \text{ psi}$$

$$[C]_{90\,\text{deg}} = 10^6 \begin{bmatrix} 2.31864 & 0.50045 & - \\ & 2.31864 & - \\ & & 0.85 \end{bmatrix} \text{ psi} \tag{38}$$

For each of the two configurations, 40 equal thickness elements (81 nodal surfaces and 162 degrees of freedom) were employed in the model for the entire plate.

Table 2 lists the lowest 20 eigenvalues γ for the two stacking sequences. For the [0/90/90/0] symmetrical lay-up, the eigenvalues may be further identified according to symmetric (S) and antisymmetric (A) displacement patterns about the middle surface. Plots of displacements patterns for the first six eigensolutions for the two plates are shown in Figs. 2 and 3. Selected stress distribution plots are presented in Figs. 4 and 5. These diagrams show the unusual nature of the displacement and stress variations over the composite plate's thickness.

In the stress plots on Figs. 4 and 5, a separate scale was used for the shear and normal stresses, τ_{xy} and τ_{yy}, in order to better illustrate their variations. It is of interest to observe that the maximum shear stress in the [0/90/90/0] plate is approximately 30 percent of the maximum axial stress τ_{xx}, whereas in the [0/90/0/90] plate, it is roughly 20 percent. This clearly illustrates the salient difference between the two lay-ups as the [0/90/90/0] plate is prone to higher interlaminar shear stresses. Shearing stresses at 20 or 30 percent of the maximum normal stress in composites generally signal the occurrence of interlaminar shear failures before other modes of failure. This is due to the relatively low interlaminar shear strengths, which are typically 10 percent or less in relationship to the longitudinal strengths. Of course, the foregoing are only eigenstates of self-equilibrated edge stresses. In an actual design, a complete solution of the boundary value problem is needed to evaluate all possible failure modes.

Although not emphasized here, the analysis also yields transverse normal stresses in case the strengths in the normal direction are of concern.

Concluding Remarks

A finite element analysis of planar Saint-Venant edge effects in laminated composite plates has been presented. The method is capable of treating any laminate construction whose properties are competely anisotropic within the plane.

Downloaded 01 May 2010 to 171.66.16.249. Redistribution subject to ASME license or copyright; see http://www.asme.org/terms/Terms_Use.cfm

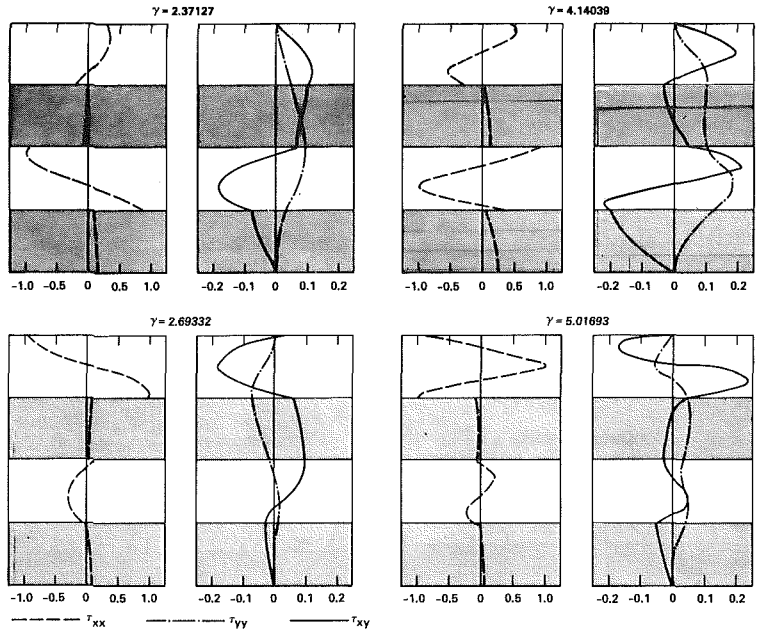


Fig. 4 Selected stress patterns for [0/90/0/90] composite plate

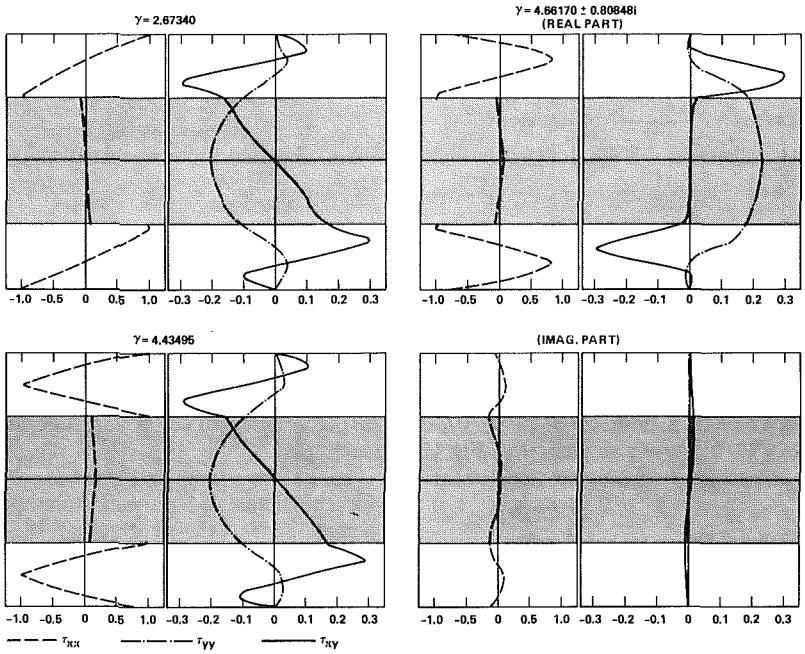


Fig. 5 Selected stress patterns for [0/90/90/0] composite plate

The analysis with displacements as the primary variables yields a second-order algebraic eigensystem, whose solution consists of a set of eigenvalues (the characteristic inverse decay lengths) and their corresponding right eigenvectors. The associated adjoint algebraic eigensystem provides the same eigenvalues, but with left eigenvectors. Orthogonality relations, as well as the method for eigenvector expansion of self-equilibrated edge tractions, are discussed. The numerical examples demonstrate the accuracy of the finite element modeling procedure and illustrate a case study of the comparison of edge phenomena and interlaminar effects in two laminated composite plates. The method is quite effective as one analysis can uncover all interlaminar effects and decay rates for a particular laminate construction under plane strain conditions.

In a discussion of edge effects in composite plates, stress singularities must be mentioned. In particular, the role of the eigenvectors of the current analysis in portrayal of such singularities must be addressed. Discontinuous edge tractions (or other discontinuous edge influences) are the primary sources for their occurrence. For the sake of discussion, consider a concentrated load on the edge or some distributed load over a very small region. These two loadings can be replaced by a statically equivalent distributed load associated with uniform straining and a system of self-equilibrated edge stresses. In the case of a point load, the eigenvector expansion of the self-equilibrated system is not convergent mathematically, i.e., an infinite number of terms are required. Therefore, it is not feasible for an eigenvector expansion of a stress singularity. An alternate approach must

Downloaded 01 May 2010 to 171.66.16.249. Redistribution subject to ASME license or copyright; see http://www.asme.org/terms/Terms_Use.cfm

be used. For example, the singularity is calculated by other means such as local asymptotic analysis. Then an eigenvector expansion may be carried out for the stress state somewhat removed from the singularity. Thus, it will be possible to capture the essence of the singularity in terms of a limited number of eigenvector. In summary, it should be remembered that the current analysis does not yield any eigenvectors embodying singular behavior.

In closure, it is mentioned that the present approach can be extended to three-dimensional edge effects in a straightforward manner. The modifications entail the revision of the displacement field to reflect all three spatial coordinates. The resultant formulations will require greater computational effort, but it will give results that will be more realistic in terms of actual applications.

References

1 Toupin, R. A., "Saint-Venant's Principle," *Archive for Rational Mechanics and Analysis,* Vol. 18, 1965, pp. 83–96.

2 Knowles, J. K., "On Saint-Venant's Principle in the Two-Dimensional Linear Theory of Elasticity," *Archive for Rational Mechanics and Analysis,* Vol. 21, 1966, pp. 1–22.

3 Horgan, C. O., "On Saint-Venant's Principle in Plane Anisotropic Elasticity," *Journal of Elasticity,* Vol. 2, 1972, pp. 169–180.

4 Horgan, C. O., "Some Remarks on Saint-Venant's Principle for Transversely Isotropic Composites," *Journal of Elasticity,* Vol. 2, 1972, pp. 335–339.

5 Choi, I., and Horgan, C. O., "Saint-Venant's Principle and End Effects in Anisotropic Elasticity," ASME JOURNAL OF APPLIED MECHANICS, Vol. 44, No. 3, 1977, pp. 424–430.

6 Choi, I., and Horgan, C. O., "Saint-Venant End Effects for Plane Deformation of Sandwich Strips," *International Journal of Solids and Structures,* Vol. 14, No. 3, 1978, pp. 187–195.

7 Pagano, N. J., and Pipes, R. B., "Some Observations on the Interlaminar Strength of Composite Laminates," *International Journal of Mechanical Sciences,* Vol. 15, 1973, pp. 679–688.

8 Pagano, N. J., and Halpin, J. C., "Influence of End Constraint in the Testing of Anisotropic Bodies," *Journal of Composite Materials,* Vol. 2, 1968, pp. 18–31.

9 Whitney, J. M., "Free Edge Effects in the Characterization of Composite Materials," *Analysis of the Test Methods for High Modulus Fibers and Composites, ASTM STP 521,* 1973.

10 Folkes, M. J., and Arridge, R. G. C., "The Measurement of Shear Modulus in Highly Anisotropic Materials: The Validity of Saint-Venant's Principle," *Journal of Physics D: Applied Physics,* Vol. 8, 1975, pp. 1053–1064.

11 Arridge, R. G. C., Barham, P. J,, Farrell, C. J., and Keller, A., "The Importance of End Effects in the Measurement of Moduli of Highly Anisotropic Materials," *Journal of Materials Science,* Vol. 11, 1976, pp. 788–790.

12 Arridge, R. G. C., and Folkes, M. J., "Effect of Sample Geometry on the Measurement of Mechanical Properties of Anisotropic Materials," *Polymer,* Vol. 17, 1976, pp. 495–500.

13 Puppo, A. H., and Evenson, H. A., "Interlaminar Shear in Laminated Composites Under Generalized Plane Stress," *Journal of Composite Materials,* Vol. 4, 1970, pp. 204–220.

14 Pipes, R. B., and Pagano, N. J., "Interlaminar Stresses in Composite Laminates Under Uniform Axial Extension," *Journal of Composite Materials,* Vol. 4, 1970, pp. 538–548.

15 Isakson, G., and Levy, A., "Finite Element Analysis of Interlaminar Shear in Fiberous Composites," *Journal of Composite Materials,* Vol. 5, 1971, pp. 273–275.

16 Levy, A., Armen, H., Jr., and Whiteside, J., "Elastic and Plastic Interlaminar Shear Deformation in Laminated Composites Under Generalized Plane Stress," *Proceedings of the 3rd Matrix Method in Stuctural Mechanics,* Wright-Patterson AFB, 1971.

17 Oplinger, D. W., "Edge Effects in Angle-Ply Composites," *AMMRC-TR-71-62,* Army Material and Mechanics Research Center, Watertown, Mass., 1971.

18 Rybicki, E. F., "Approximate Three-Dimensional Solutions for Symmetric Laminates Under Inplane Loading," *Journal of Composite Materials,* Vol. 5, 1971, pp. 354–360.

19 Pagano, N. J., "On the Calculation of Interlaminar Normal Stress in Composite Laminates," *Journal of Composite Materials,* Vol. 8, 1974, pp. 65–81.

20 Tang, S., "A Boundary Layer Theory—Part I: Laminated Composites in Plane Stress," *Journal of Composite Materials,* Vol. 9, 1975, pp. 33–41.

21 Tang, S., and Levy, A., "A Boundary Layer Theory—Part II: Extension of Laminated Finite Strip," *Journal of Composite Materials,* Vol. 9. 1975, pp. 42–52.

22 Tang, S., "Interlaminar Stresses of Uniformly Loaded Rectangular Composite Plates," *Journal of Composite Materials,* Vol. 10, 1976, pp. 69–78.

23 Hsu, P. W., and Herakovich, C. T., "A Perturbation Solution for Interlaminar Stresses in Composite Laminates," *ASTM 4th Conference on Composite Materials: Testing and Design,* Valley Forge, Pa., May 1976.

24 Hsu, P. W., and Herakovich, C. T., "Edge Effects in Angle-Ply Composite Laminates," *Journal of Composite Materials,* Vol. 11, 1977, pp. 422–427.

25 Wang, A. S. D., and Crossman, F. W., "Sone New Results on a Edge Effect in Symmetric Laminates," *Journal of Composite Materials,* Vol. 11, 1977, pp. 92–106.

26 Wang, A. S. D., and Crossman, F. W., "Edge Effects on Thermally Induced Stresses in Composite Laminates," *Journal of Composite Materials,* Vol. 11, 1977, pp. 300–312.

27 Crossman, F. W.,, and Wang, A. S. D., "Analysis of Free Edge Stress Induced Fracture of Fiber Composite Laminates," *Proceedings of the Symposium on Applications of Computer Methods in Engineering,* University of Southern California, Vol. 1, 1977, pp. 213–220.

28 Wang, J. T. S., and Dickson, J. N., "Interlaminar Stresses in Symmetric Composite Laminates," *Journal of Composite Materials,* Vol. 12, 1978, pp. 390–402.

29 Dong, S. B., "A Block-Stodola Eigensolution Technique for Large Algebraic Systems with Non-Symmetrical Matrices," *International Journal for Numerical Methods in Engineering,* Vol. 11, 1977, pp. 247–267.

APPENDIX

The elements of the matrices in equation (15) appear as follows:

$$[k_1] = \begin{bmatrix} 4a_1 & 4a_2 & 2a_1 & 2a_2 & -a_1 & -a_2 \\ & 4a_3 & 2a_2 & 2a_3 & -a_2 & -a_3 \\ & & 16a_1 & 16a_2 & 2a_1 & 2a_2 \\ & & & 16a_3 & 2a_2 & 2a_3 \\ & & & & 4a_1 & 4a_2 \\ \text{symmetric} & & & & & 4a_3 \end{bmatrix} \tag{A1}$$

$$[k_2^*] = \frac{1}{6}\begin{bmatrix} --- & 3a_4 & 8C_{16} & 4a_5 & -2C_{16} & -a_5 \\ & --- & 4a_5 & 8C_{26} & -a_5 & -2C_{26} \\ & & --- & --- & 8C_{16} & 4a_5 \\ & & & --- & 4a_5 & 8C_{26} \\ & & & & --- & -3a_4 \\ \text{antisymmetric} & & & & & --- \end{bmatrix} \tag{A2}$$

$$[k_3] = \begin{bmatrix} 7a_6 & 7a_7 & -8a_6 & -8a_7 & a_6 & a_7 \\ & 7a_8 & -8a_7 & -8a_8 & a_7 & a_8 \\ & & -16a_6 & 16a_7 & -8a_6 & -8a_7 \\ & & & 16a_8 & -8a_7 & -8a_8 \\ & & & & 7a_6 & 7a_7 \\ \text{symmetric} & & & & & 7a_8 \end{bmatrix} \tag{A3}$$

where

$$[k_2^*] = [k_2] - [k_2]^T$$

and

$$\begin{aligned} &a_1 = C_{11}h/30\,;\ a_2 = C_{16}h/30\,;\ a_3 = C_{66}h/30 \\ &a_4 = C_{66} - C_{12}\,;\ a_5 = C_{66} + C_{12}\,; \\ &a_6 = C_{66}/3h\,;\ a_7 = C_{26}/3h\,;\ a_8 = C_{22}/3h \end{aligned} \tag{A4}$$

with h as the element's thickness.

Downloaded 01 May 2010 to 171.66.16.249. Redistribution subject to ASME license or copyright; see http://www.asme.org/terms/Terms_Use.cfm

A Finite Element Formulation for Unbounded Homogeneous Continua

G. Dasgupta
Associate Professor,
Department of Civil Engineering and Engineering Mechanics,
Columbia University,
New York, N.Y. 10027
Mem. ASME

Currently available finite element formulations to model dynamic responses of unbounded continua cannot accommodate the Sommerfeld radiation condition. Discrete numerical techniques explicitly rely on analytical expressions of frequency-dependent field variables to account for the energy loss associated with outgoing waves. In the proposed method, such a dependence is eliminated. For steady dynamic responses, the analog of the quadratic eigenvalue problem (occurring in continuum mechanics) is herein constructed in the form of a quadratic matrix equation. The unknown relates to the desired stiffness matrix pertaining to the infinite or semi-infinite domain. The matrix coefficients are obtained from the conventional mass and stiffness matrices of a suitably chosen, bounded finite element. A benchmark example is included in this paper to demonstrate the very high numerical accuracy and significant computational efficiency of the proposed cloning algorithm.

Introduction

Applications of wave motions in geometrically unbounded media have generated considerable academic interests throughout the history of engineering analysis. Pioneers of continuum mechanics – Lord Kelvin, Boussinesq, Lamb (refer to Love [1]) – studied potential fields, static and dynamic responses of three-dimensional infinite elastic continua, and half spaces. For the purpose of mathematical modeling, a mechanical system is idealized to be an unbounded medium when its physical size is considerably large in comparison with the characteristic length of the problem. Some practical illustrations in various fields of engineering are: (i) soil-structure interactions of deformable embedments; (ii) responses of drilling platforms in offshore environments; (iii) electromagnetic problems for antenna and surveying for mineral deposits; (iv) propagations of dislocations in crystalline media; and (v) noise eliminations in aircraft, and so forth. This paper summarizes the essential features of the proposed novel approach of the cloning algorithm which yields a discrete model for the aforementioned cases. Details of the algebraic derivations can be found in a research report [2]. The Sommerfeld condition, which is relevant to the continuum and discrete formulations, has been elaborated in an ASME conference paper [3]. In the interest of brevity, those lengthy intermediate mathematical steps are omitted herein.

The problem of unbounded soil regions [4] occurring in structure-foundation interactions (refer to Fig. 1(*a*)) is illustrated in this paper for the purpose of deriving the numerical technique. The structure is represented as a finite

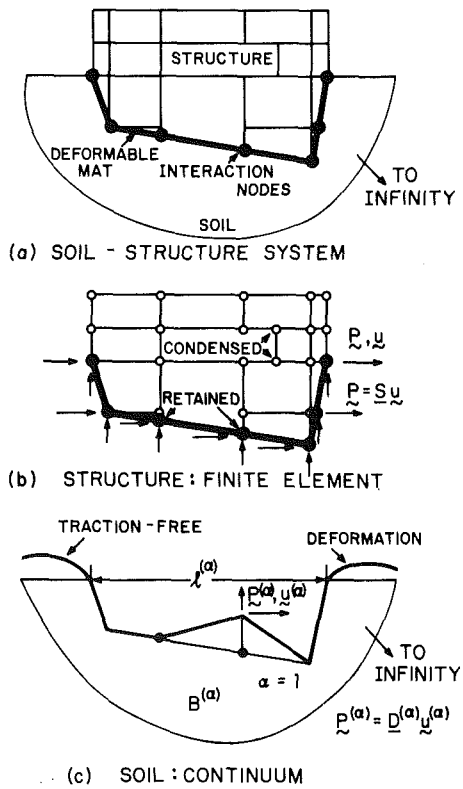


Fig. 1 Soil-structure interaction problem

Contributed by the Applied Mechanics Division for publication in the JOURNAL OF APPLIED MECHANICS.
Discussion on this paper should be addressed to the Editorial Department, ASME, United Engineering Center, 345 East 47th Street, New York, N.Y. 10017, and will be accepted until two months after final publication of the paper itself in the JOURNAL OF APPLIED MECHANICS. Manuscript received by ASME Applied Mechanics Division, May, 1981; final revision, September, 1981.

Copyright © 1982 by ASME
Downloaded 01 May 2010 to 171.66.16.249. Redistribution subject to ASME license or copyright; see http://www.asme.org/terms/Terms_Use.cfm

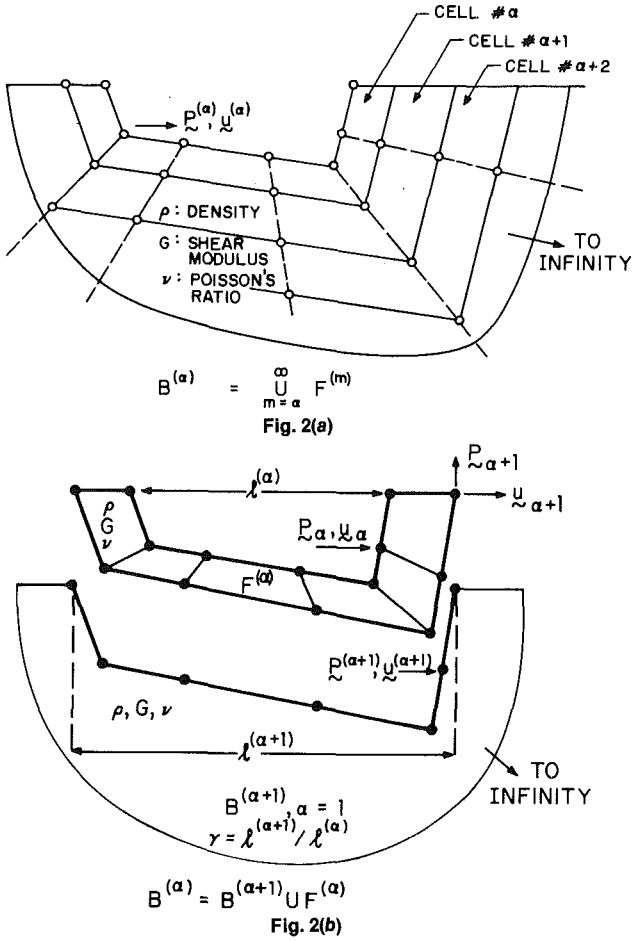


Fig. 2 Unbounded regions of similar geometry and finite element cells

element assembly. Its interaction boundary condition is furnished via the force-displacement relationship of the soil medium defined at the interface nodes. As specified in the elastic design criteria, a linear description of the soil-structure system is accepted. Since the energy loss in the soil mass (due to outgoing waves) depends on exciting frequency, the time harmonic analysis is implemented. It is then possible to carry out the substructure technique of analysis (refer to Chapter 7 of [5] for details) for the soil structure system.

The required dynamic stiffness matrix of the structure **S**, illustrated in Fig. 1(*b*), relates the steady interaction force and displacement vectors, **P** exp ($i\omega t$) and **u** exp ($i\omega t$), respectively, in the form:

$$\mathbf{P} = \mathbf{S}(\omega)\mathbf{u} \tag{1}$$

in which ω: frequency; t: time and $i:\sqrt{-1}$. It is possible to obtain very accurate values of the global mass, damping, and stiffness matrices of the structure, **M**, **C**, and **K**, respectively, according to conventional finite element formulations [5]. By prescribing zero external forces, for the system: $[\mathbf{K} + i\omega\mathbf{C} - \omega^2\mathbf{M}]$, the degrees of freedom outside the interaction region are condensed out [4]. This leads to **S** of (1). Unfortunately, there is no such conventional scheme, as described in [5], available to evaluate the dynamic stiffness matrix **D** for the unbounded soil region [refer to Fig. 1(*c*)]. It is not possible to finitely cover a semi-infinite region with bounded elements. Consequently, the concept of elements spanning to infinity [6] has been introduced. The interpolations should be complex transcendental functions to account for the radiation damping effects. In general, these distributions cannot be chosen a priori. Continuum solutions of unbounded domains should be directly used to construct **D**. For deleted half spaces, as shown in Fig. 1(*c*), these fields should simultaneously satisfy the prescribed displacements at interaction nodes and zero traction conditions all along the free surface. Such a mixed-boundary value problem pertaining to unbounded continua poses computational complexities. Singular integrals, which involve higher-order transcendental functions, need to be evaluated at a substantial computing cost. Also, the associated hybrid (discrete for structure and continuum for soil) formulations necessitate judicious interpretations of the interface equilibrium and compatibility conditions, which are satisfied only in some "average sense." Serious conceptual questions are therefore raised to justify those ad hoc discrete models of an unbounded domain.

It is, of course, desirable from the theoretical viewpoint of computational mechanics that a stand-alone finite element formulation be developed without requiring analytical expressions to supply the radiation conditions. Accordingly, the proposed cloning algorithm is designed to discretize an unbounded domain,

$$B^{(\alpha)} = \bigcup_{m=\alpha}^{\infty} F^{(m)}$$

[refer to Fig. 2(*a*)], in the Ritz sense. Only the dynamic stiffness matrix of a cell $F^{(\alpha)}$ is utilized. The necessary calculations consist of algebraic determination of eigenvalues and eigenvectors along with the solution of a system of linear equations. The size of these problems does not exceed twice the number of interaction degrees of freedom. It is thus possible to economically analyze a number of practical problems of reasonable sizes by employing standard library packages with MINI and even MICRO computers. In the interest of brevity, only the basic theoretical development of the cloning algorithm is highlighted herein. Practical illustrations relating to the response calculations of two- and three-dimensional soil-structure systems will be presented in a sequel.

Derivation

The notion of invariance, under similarity transformations associated with the finite element method of substructuring, is utilized in developing the cloning algorithm. Harmonic responses are analyzed for the unbounded media, $B^{(1)}$ and $B^{(2)}$, as depicted in Figs. 1(*c*) and 2, and the finite element region $F^{(1)}$ in Fig. 2. The constitutive properties of $B^{(2)}$ and $F^{(1)}$ in Fig. 2 are identical to those of $B^{(1)}$ in Fig. 1(*c*). Domains $B^{(1)}$ and $B^{(2)}$ are geometrically similar and the interaction degrees of freedom are located accordingly. The bounded region $F^{(\alpha)}$ is so defined that $B^{(1)} = B^{(2)} \cup F^{(1)}$. Let $\mathbf{D}^{(\alpha)}(\omega)$ denote the stiffness matrix for $B^{(\alpha)}$, $\alpha = 1,2$. Then

$$\mathbf{P}^{(\alpha)} = \mathbf{D}^{(\alpha)}\mathbf{u}^{(\alpha)}, \qquad \alpha = 1,2 \tag{2}$$

The force and displacement vectors for the unbounded regions are indicated with superscripts whereas those for the finite elements are denoted with subscripts. The dynamic stiffness matrix **S** for $F^{(1)}$ can be computed according to [7], such that

$$\begin{Bmatrix} \mathbf{P}_1 \\ \mathbf{P}_2 \end{Bmatrix} = \left[\begin{array}{c|c} \mathbf{S}_{11} & \mathbf{S}_{12} \\ \hline \mathbf{S}_{21} & \mathbf{S}_{22} \end{array}\right] \begin{Bmatrix} \mathbf{u}_1 \\ \mathbf{u}_2 \end{Bmatrix} \tag{3}$$

or

$$\begin{aligned} \mathbf{P}_1 &= \mathbf{S}_{11}\mathbf{u}_1 + \mathbf{S}_{12}\mathbf{u}_2 \\ \mathbf{P}_2 &= \mathbf{S}_{21}\mathbf{u}_1 + \mathbf{S}_{22}\mathbf{u}_2 \end{aligned} \tag{4}$$

in which the force and displacement vectors and the submatrices refer to the boundary degrees of freedom indicated by the subscripts. Consider the equilibrium of $B^{(1)}$ containing $B^{(2)}$ and $F^{(1)}$ in Fig. 2, that is, impose the compatibility: $\mathbf{u}^{(\alpha)} =$

Downloaded 01 May 2010 to 171.66.16.249. Redistribution subject to ASME license or copyright; see http://www.asme.org/terms/Terms_Use.cfm

$\mathbf{u}_\alpha$ and equilibrium: $\mathbf{P}^{(1)} = \mathbf{P}_1$ and $\mathbf{P}^{(2)} + \mathbf{P}_2 = \mathbf{0}$. One now obtains from (2) and (4):

$$\mathbf{D}^{(1)}\mathbf{u}_1 = \mathbf{S}_{11}\mathbf{u}_1 + \mathbf{S}_{12}\mathbf{u}_2$$

$$-\mathbf{D}^{(2)}\mathbf{u}_2 = \mathbf{S}_{21}\mathbf{u}_1 + \mathbf{S}_{22}\mathbf{u}_2 \tag{5}$$

Eliminating $\mathbf{u}_1$ and $\mathbf{u}_2$, the substructure equation (refer to Chapter 7.22 of [5]) is obtained in the form:

$$\mathbf{D}^{(1)} = \mathbf{S}_{11} - \mathbf{S}_{12}[\mathbf{D}^{(2)} + \mathbf{S}_{22}]^{-1}\mathbf{S}_{21} \tag{6}$$

The only difference between $\mathbf{D}^{(1)}$ and $\mathbf{D}^{(2)}$ is that those are associated with different characteristic lengths $l^{(1)}$, $l^{(2)}$, respectively. Hence the set of matrices $\{\mathbf{D}^{(\alpha)}\}$ possesses a nondimensional invariant $\mathbf{X}$, which is governed by the common shape of $\{B^{(\alpha)}\}$. This fact, which furnishes another relationship between $\mathbf{D}^{(1)}$ and $\mathbf{D}^{(2)}$, is utilized to reduce (6) into an equation with a single unknown matrix.

A nondimensional frequency $a_0{}^{(\alpha)}$ is defined to be:

$$a_0{}^{(\alpha)} \equiv \omega l^{(\alpha)}/C_v \tag{7}$$

in which C_v is a representative wave speed and is often taken to be a shear wave velocity. The corresponding nondimensional forms $\mathbf{v}$ and $\mathbf{V}$ for the displacement and force vectors, respectively, are given by:

$$\mathbf{v}^{(\alpha)} = \mathbf{u}^{(\alpha)}/l^{(\alpha)}; \qquad \mathbf{V}^{(\alpha)} = \mathbf{P}^{(\alpha)}/l^{(\alpha)}b_0; \qquad b_0{}^{(\alpha)} = \mu[l^{(\alpha)}]^{K-2} \tag{8}$$

in which μ is a shear modulus and K is the spatial dimension (2 or 3) of $\{B^{(\alpha)}\}$. The nondimensional form for $\mathbf{D}^{(\alpha)}(\omega)$ from (2) and (8) is then

$$\mathbf{X}(a_0{}^{(\alpha)}) = \mathbf{D}^{(\alpha)}/b_0{}^{(\alpha)} \quad \text{such that} \quad \mathbf{V}^{(\alpha)} = \mathbf{X}\mathbf{v}^{(\alpha)} \tag{9}$$

The nondimensional forms for the submatrices of $\mathbf{S}$ in (3) according to the aforementioned scaling factors (8) are:

$$\mathbf{Z}_{11} = \mathbf{S}_{11}{}^{(1)}/b_0{}^{(1)}; \qquad \mathbf{Z}_{12} = \gamma\mathbf{S}_{12}{}^{(1)}/b_0{}^{(1)};$$
$$\mathbf{Z}_{21} = \gamma^{(1-k)}\mathbf{S}_{21}{}^{(1)}/b_0{}^{(1)}$$
$$\mathbf{Z}_{22} = \gamma^{(2-k)}\mathbf{S}_{22}{}^{(1)}/b_0{}^{(1)}; \qquad \gamma = l^{(2)}/l^{(1)} \tag{10}$$

The nondimensional form for the substructure equation (6), according to (9) and (10), is

$$\mathbf{X}(a_0{}^{(1)}) = \mathbf{Z}_{11} - \mathbf{Z}_{12}[\mathbf{X}(a_0{}^{(2)}) + \mathbf{Z}_{22}]^{-1}\mathbf{Z}_{21} \tag{11}$$

This equation could be interpreted to be a functional relationship for two distinct frequency parameters, $a_0{}^{(1)}$ and $a_0{}^{(2)}(= a_0{}^{(1)}/\gamma)$ involving the dynamic stiffness map $\mathbf{X}$ defined for $\{B^{(\alpha)}\}$. Then (11) could be reduced to an algebraic equation of reasonably simpler form if it is possible to approximate $\mathbf{X}(a_0{}^{(2)})$ by $\mathbf{X}(a_0{}^{(1)})$.

It is well known that all frequency response quantities pertaining to unbounded media are devoid of sharp peaks (due to the absence of any real natural frequency). In practical numerical computations [4] it is a routine procedure to approximate $\mathbf{X}(a_0{}^{(2)})$ by $\mathbf{X}(a_0{}^{(1)})$ for up to 10 percent difference in the two corresponding nondimensional frequencies. Hence, restricting the mesh parameter for the finite element $F^{(\alpha)}$ in Fig. 2 (e.g., γ to be less than 1.1), the error $\|\mathbf{X}(a_0{}^{(1)}) - \mathbf{X}(a_0{}^{(2)})\|$ should be well within the overall tolerance of the finite element formulation. In the lower frequency regime, the stiffness parameters increase rather gently with frequencies. On the other hand, for comparatively high frequencies, the characteristic mesh size in the interaction region [refer to Fig. 1(*a*)], is always designed to be smaller than the wave length of the associated harmonic excitation. Thus the aforementioned restriction on the value of γ (to be close to unity) does, by no means, impose any further stringent requirement. In the derivation that follows, $a_0{}^{(1)}$ and $a_0{}^{(2)}$ will be replaced by their average value. For mere convenience γ raised to fractional

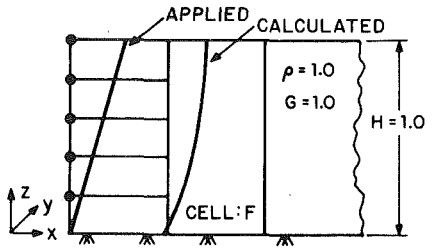


Fig. 3 Antiplane Motion of a layer

powers will not be distinguished from unity. *This is the only approximation invoked in this derivation.* Thus (11) becomes

$$\mathbf{X} = \mathbf{Z}_{11} - \mathbf{Z}_{12}[\mathbf{X} + \mathbf{Z}_{22}]^{-1}\mathbf{Z}_{21} \tag{12}$$

It is now a straightforward algebraic task to rearrange (refer to [2] for details of substitutions) the terms containing the unknown $\mathbf{X}$ in order to reduce the approximated substructure equation (12) into the following familiar quadratic form:

$$\mathbf{Y}\mathbf{Y} - \mathbf{Q}\mathbf{Y} + \mathbf{R} = \mathbf{0} \tag{13}$$

in which

$$\mathbf{Y} = [\mathbf{X} + \mathbf{Z}_{22}]\mathbf{Z}_{21}{}^{-1}; \qquad \mathbf{Q} = \mathbf{G}\mathbf{Z}_{21}{}^{-1}$$
$$\mathbf{G} = [\mathbf{Z}_{11} + \mathbf{Z}_{22}]; \qquad \mathbf{R} = \mathbf{Z}_{12}\mathbf{Z}_{21}{}^{-1} \tag{14}$$

Existence of inverses for the off-diagonal submatrices of $\mathbf{S}$ and $\mathbf{Z}$, in (3) and (10), respectively, is unconditionally guaranteed according to [8]. It has been demonstrated that the discrete dynamic analog of Almansi's theorems [9], which deals with a nonclassical boundary value problem (Cauchy type in the spatial coordinates), demands that

$$\det[\mathbf{S}_{12}] \neq 0, \text{ consequently, } \det[\mathbf{Z}_{12}] \neq 0 \text{ and } \det[\mathbf{Z}_{21}] \neq 0 \tag{15}$$

The proposed cloning algorithm has led to the formulation of the quadratic matrix equation (13). The unknown $\mathbf{Y}$ contains the nondimensional dynamic stiffness matrix $\mathbf{X}$ for unbounded regions $\{B^{(\alpha)}\}$ whereas the coefficient matrices $\mathbf{Q}$ and $\mathbf{R}$ are completely defined from the finite element mass and stiffness matrices of the bounded region $F^{(\alpha)}$ in Fig. 2.

Unique Solution: Sommerfeld Condition

The unknown matrix $\mathbf{Y}$ is determined by solving the quadratic matrix equation (13) according to the eigenvalue decomposition technique. Let λ_i and $\mathbf{y}_i$ be an eigenvalue and eigenvector pair, respectively, for $\mathbf{Y}$, i.e.,

$$\mathbf{Y}\mathbf{y}_i = \lambda_i\mathbf{y}_i; \qquad i = 1 \text{ to } n\text{: size of } \mathbf{Y},\ \mathbf{Q},\ \mathbf{R} \tag{16}$$

Then postmultiplication of (13) with $\mathbf{y}_i$ yields a quadratic eigenvalue problem:

$$\lambda_i{}^2\mathbf{y}_i - \lambda_i\mathbf{Q}\mathbf{y}_i + \mathbf{R}\mathbf{y}_i = \mathbf{0} \tag{17}$$

The preceding equation is rewritten, utilizing (14), in the following alternative form:

$$[\lambda_i{}^2\mathbf{Z}_{21} - \lambda_i\mathbf{G} + \mathbf{Z}_{12}]\mathbf{W}_i = \mathbf{0}; \quad \text{in which} \quad \mathbf{W}_i = \mathbf{Z}_{21}{}^{-1}\mathbf{y}_i \tag{18}$$

All the matrix coefficients in the foregoing problem are nonsingular [refer to (14) and (15)]. Hence for $\mathbf{Y}$ of size $n \times n$ there exist, as has been demonstrated in [10], $2n$ nonzero λ_i and $\mathbf{W}_i$; consequently there are $2n$ number of nonzero $\mathbf{y}_i$. The particular structure of (18) suggests the following important pairing relation between the elements of the set $\{\lambda_i\}$. Equation (18) is rewritten to be:

$$[\beta_i{}^2\mathbf{Z}_{12} - \beta_i\mathbf{G} + \mathbf{Z}_{21}]\mathbf{W}_i = \mathbf{0}; \quad \text{in which} \quad \beta_i = 1/\lambda_i \tag{19}$$

This eigenproblem is adjoint to (18) since $\mathbf{G}$ is symmetric from (14), (10), and (3). Hence, the sets $\{\lambda_i\}$ and $\{\beta_i\}$ are identical. Thus for each λ_i there exists a β_i, which is also another eigenvalue of $\mathbf{Y}$ such that $\beta_i = 1/\lambda_i$ or $\beta_i\lambda_1 = 1$. For

Downloaded 01 May 2010 to 171.66.16.249. Redistribution subject to ASME license or copyright; see http://www.asme.org/terms/Terms_Use.cfm

convenience, the complete set of eigenvalues of (17) can then be partitioned into two sets Λ_1 and Λ_2 so that

$$\Lambda_1 = \{\lambda_i \text{ such that } |\lambda_i| > 1\}$$
$$\Lambda_2 = \{\lambda_i \text{ such that } |\lambda_i| \leq 1\} \tag{20}$$

The physical implications of β_i and $\mathbf{W}_i$ in (19) can now be deduced. If $\mathbf{u}_1$ and $\mathbf{u}_2$ in (4) are so selected that $\mathbf{u}_2 = -\theta\mathbf{u}_1$ then from (5), (9), and (14) one obtains:

$$[\theta^2\mathbf{Z}_{12} - \theta\mathbf{G} + \mathbf{Z}_{21}]\mathbf{u}_1 = \mathbf{0}$$

The aforementioned equation is identical to (19) when β_i and $\mathbf{W}_i$ are replaced by θ and $\mathbf{u}_1$, respectively. In the light of the decay conditions for field variables in $\{B^{(\alpha)}\}$, a certain restriction on $\theta(= \beta_i = 1/\lambda_i)$ is necessary. The nondimensional form (18) suggests that for any pair of unbounded regions $B^{(\alpha)}$ and $B^{(\alpha+1)}$ with same $\gamma = l^{(\alpha+1)}/l^{(\alpha)}$ as in (10), an eigenvalue β_i can be taken to be a scaling factor θ so that vectors $\mathbf{u}_\alpha$ and $\mathbf{u}_{\alpha+1}$ are parallel in $\mathcal{R}^n$.

Sommerfeld condition [11] dictates that a pertinent dynamic solution for an unbounded medium is characterized by outgoing waves. These are associated with the outward decay of displacement fields. Thus the factor θ should be a contraction,[1] i.e., $|\theta| < 1$, which implies β_i in (19), consequently λ_i in (18), should be contained in Λ_2 and Λ_1 of (20), respectively. Hence, there is a unique set of n eigenvalues $\{\lambda_i\}$ satisfying the Sommerfeld condition out of $2n$ eigenvalues, which satisfy the quadratic eigenproblem (17). This leads to a unique value of the matrix $\mathbf{Y}$ (according to the theorem of polar decomposition) in the form:

$$\mathbf{Y} = \{\mathbf{y}_i\} < \lambda_i > \{\mathbf{y}_i\}^{-1}$$

In the equation, $<\lambda_i>$ is the diagonal matrix of eigenvalues of (17), each $|\lambda_i| > 1$, and $\{\mathbf{y}_i\}$ is the matrix consisting of corresponding eigenvectors stored as columns. The complete set of eigenvectors and eigenvalues of (17) can be evaluated by solving the following conventional problem:

$$\begin{bmatrix} \mathbf{0} & \mathbf{I} \\ -\mathbf{R} & \mathbf{0} \end{bmatrix} \begin{Bmatrix} y_i \\ \lambda_i \mathbf{y}_i \end{Bmatrix} = \lambda_i \begin{bmatrix} \mathbf{I} & \mathbf{0} \\ -\mathbf{Q} & \mathbf{I} \end{bmatrix} \begin{Bmatrix} \mathbf{y}_i \\ \lambda_i \mathbf{y}_i \end{Bmatrix}$$

in which $\mathbf{0}$ and $\mathbf{I}$ are the null and identity matrices of size $n \times n$.

It is desirable to establish that the dynamic stiffness matrix $\mathbf{D}^{(\alpha)}$ in (9) for $\mathbf{B}^{(\alpha)}$ calculated from $\mathbf{Y}$ in (18) is indeed symmetric. From (14) it is then sufficient to deduce that

$$\mathbf{X} + \mathbf{Z}_{22} = \mathbf{Y}\mathbf{Z}_{21} = \mathbf{Z}_{21}\{\mathbf{W}_i\} < \lambda_i > \{\mathbf{W}_i\}^{-1}$$

is symmetric [refer to (18)]. Consider the quadratic eigenvalue problem (18) for two distinct eigenpairs with indices i and j leading to:

$$\mathbf{W}_j{}^T[\lambda_i\mathbf{Z}_{21} - \mathbf{G} + \frac{1}{\lambda_i}\mathbf{Z}_{12}]\mathbf{W}_i = \mathbf{0}$$

$$\mathbf{W}_i{}^T[\lambda_j\mathbf{Z}_{21} - \mathbf{G} + \frac{1}{\lambda_j}\mathbf{Z}_{12}]\mathbf{W}_j = \mathbf{0}$$

or

$$\mathbf{W}_j{}^T[\frac{1}{\lambda_j}\mathbf{Z}_{21} - \mathbf{G} + \lambda_j\mathbf{Z}_{12}]\mathbf{W}_i = \mathbf{0}$$

Since G is symmetric from (14), then

$$(\lambda_i\lambda_j - 1)\mathbf{W}_j{}^T\mathbf{Z}_{21}\mathbf{W}_i\lambda_i = (\lambda_i\lambda_j - 1)\lambda_j\mathbf{W}_j{}^T\mathbf{Z}_{12}\mathbf{W}_i$$

$\lambda_i, \lambda_j \epsilon \Lambda_1$ in (20) hence $|\lambda_i\lambda_j| > 1$. The matrix form of the foregoing identity (considering the complete set of eigenvalues and eigenvectors) is then

[1] $\theta = 1$ is only possible for two-dimensional static cases.

Table 1 Comparison of displacements (at $x = 1/32$, $z = 1.0$ of Fig. 3)

Frequency	Analytical	Proposed cloning
0.0	0.906239 $-i0.0$	0.905952 $-i0.0$
1.0	0.915355 $-i0.0$	0.914910 $-i0.0$
1.5	0.934183 $-i0.0$	0.933754 $-i0.0$
1.6	0.945983 $-i0.00770791$	0.945545 $-i0.00774400$
2.0	0.945942 $-i0.0313506$	0.945508 $-i0.0313768$

$$\{\mathbf{W}_i\}^T\mathbf{Z}_{21}\{\mathbf{W}_i\} < \lambda_i > = < \lambda_i > \{\mathbf{W}_i\}^T\mathbf{Z}_{12}\{\mathbf{W}_i\}$$

or

$$\mathbf{Z}_{21}\{\mathbf{W}_i\} < \lambda_i > \{\mathbf{W}_i\}^{-1} = [\{W_i\}^T]^{-1}\{\lambda_i\}\{\mathbf{W}_i\}^T\mathbf{Z}_{12}$$

The matrix $\mathbf{X} + \mathbf{Z}_{22}$, which is indeed the left-hand side of the preceding equation [refer to (19)], is symmetric since the right-hand side is the transpose of the left-hand one.

This concludes the formal development of the proposed cloning algorithm.

Numerical Results

The numerical accuracy of the proposed cloning algorithm is ascertained in this section. An elastic, homogeneous, uniform layer (depicted in Fig. 3), is analyzed as the benchmark problem. Analytical solutions are available for the case of the layer undergoing antiplane (S_H) harmonic oscillations. A survey paper [12] recommends this to be a suitable example for verifying calculations of the dynamic stiffness matrices for unbounded media.

The height of the layer, the density, and the shear modulus are taken to be unity. Cell F (see Fig. 3) of the layer is discretized with 32 square elements. The degrees of freedom are the nodal displacements along the y-direction. The quadratic matrix equation (13) has 32×32 coefficient matrices, which are well within the storage capacity of a small DEC20 computer employed herein. This discretization guarantees four elements per rise of wave up to an excitation frequency of 2.0. The stiffness matrix for the elements is taken from [13]. The diagonal mass matrix is used in the calculation for convenience.

The continuum solution for the layer problem is available in [13]. A linear displacement profile with unit amplitude at the free surface is introduced at the boundary wall. Displacements at a distance $x = 1/32$ are calculated according to the analytical method. An excellent comparison of the cloning results can be readily observed from Table 1. The latter needed 20.9 of CPU time in a DEC20 whereas almost 20 CPUs were necessary for the same computations in a much faster machine, viz. the CDC 6400, according to the existing absorbing boundary formulation [13]. Thus the efficiency and the accuracy of the proposed cloning algorithm is hereby established.

Conclusion

A novel formulation is presented to model dynamic responses of an infinite or semi-infinite domain. Frequency-dependent complex stiffness matrices are numerically evaluated for such an unbounded medium. Algebraic operations, viz. an eigensolution and a matrix inversion, on the database furnished by a finite element cell lead to the desired results. Those cells, which are of similar geometry, indeed provide an infinite covering for the aforementioned continuum. The proposed method is, therefore, christened the Cloning Algorithm.

Downloaded 01 May 2010 to 171.66.16.249. Redistribution subject to ASME license or copyright; see http://www.asme.org/terms/Terms_Use.cfm

The finite element methodology is hereby so enhanced that it satisfies the qualitative prescription of the Sommerfeld radiation condition. Hence the expensive calculations of infinite integrals involving higher-order transcendental functions, which originate in analytical solutions, are no longer necessary. It is demonstrated that the proposed cloning algorithm yields very accurate numerical results (including a precise estimation of cutoff frequencies). The method is anticipated to economize computations of field variables that satisfy the Helmholtz equation in unbounded domains.

Acknowledgment

The present investigation was carried out as a faculty research project; funding for computations was granted by the Department of Civil Engineering and Engineering Mechanics, Columbia University.

References

1 Love, A. E. H., *A Treatise on the Mathematical Theory of Elasticity*, Dover, New York, 1944.

2 Dasgupta, G., "Cloning Algorithm," *Columbia University Report*, Civil Engineering, Columbia University, New York, 1981.

3 Dasgupta, G., "Sommerfeld's Radiation Conditions and Cloning Algorithm," *New Concepts in Finite Element Methods*, Proceedings of ASME Summer Conference, Boulder, Colo., 1981.

4 Chopra, A. K., Chakrabarti, P., and Gupta, S., "Earthquake Response of Concrete Gravity Dams Including Hydrodynamic and Foundation Interaction Effects," Report No. EERC-80-01, Earthquake Engineering Research Center, University of California, Berkeley, Calif., 1980.

5 Zienkiewicz, O. C., *The Finite Element Method*, 3rd ed. McGraw-Hill, New York, 1977.

6 Bettess, P., and Zienkiewicz, O. C., "Diffraction and Refraction of Surface Waves Using Finite and Infinite Elements," *International Journal for Numerical Methods in Engineering*, Vol. 11, 1977, pp. 1271–1290.

7 Taylor, R. L., "Computer Procedure for Finite Element Analysis," Chapter 24, *The Finite Element Method*, Zienkiewicz, O. C., Ed., 3rd ed., McGraw Hill, New York, 1977, pp. 667–756.

8 Dasgupta, G., "Wellposedness of Substructure Deletion Formulation," *Proceedings, 16th Midwestern Mechanics Conference*, University of Kansas, Manhattan, Kan., 1979, pp. 207–211.

9 Almansi, E., "Un Teorema Sulle Deformazioni Elastiche dei Solidi Isotropi, *Atti della reale accademia dei nazionale Lincei*, Vol. 16, 1907, pp. 865–868.

10 Davis, G. J., "Numerical Solution of a Quadratic Matrix Equation," PhD. Dissertation, University of New Mexico, Albuquerque, N.M., 1979.

11 Sommerfeld, A., *Partial Differential Equations in Physics* Chapter 28, Academic Press, New York, 1949.

12 Kausel, E., and Tassoulas, J. L., "Transmitting Boundaries: A Closed Form Comparison," *Bulletin of the Seismological Society of America*, Vol. 71, No. 1, February, 1981, pp. 143–150.

13 Lysmer, J., and Waas, G., "Shear Waves in Plane Infinite Structures," *Journal of the Engineeriong Mechanics Division*, American Society of Civil Engineers, Vol. 98, No. EM 1, 1972, pp. 859–877.

Downloaded 01 May 2010 to 171.66.16.249. Redistribution subject to ASME license or copyright; see http://www.asme.org/terms/Terms_Use.cfm

S. K. Datta
Professor,
Department of Mechanical Engineering,
University of Colorado,
Boulder, Colo.
Mem. ASME

A. H. Shah
Associate Professor,
Department of Civil Engineering,
University of Manitoba,
Winnipeg, Canada

N. El-Akily
Assistant Professor,
Department of Mechanical Engineering,
University of Colorado,
Boulder, Colo.

Dynamic Behavior of a Buried Pipe in a Seismic Environment

Axisymmetric dynamic response of a buried pipe due to an incident compressional wave is the subject of this investigation. The pipe has been modeled as a thin cylindrical shell of linear homogeneous isotropic elastic material embedded in a linear isotropic homogeneous elastic medium of infinite extent. The response characteristics of the pipe due to changes in the material properties of the surrounding medium have been carefully studied. It is found that even at long wavelengths and low frequencies, the dynamic response is significantly altered by the changes in the Poisson's ratio and the rigidity modulus of the surrounding medium. Further, it is found that there are real resonant frequencies of the pipe that are also significantly dependent on these quantities, as well as on the wavelength.

Introduction

Dynamic response of buried pipelines to seismic excitation has been a subject of considerable interest in recent years. The interest in the subject originates from the desire to design lifelines like gas and water/sewer pipelines against severe damage from earthquakes. The damage to buried pipelines is caused by landslides, liquefaction of soil, faulting, and is also due to shaking by traveling seismic waves.

Several investigators have recently studied the dynamic response of underground pipelines to seismic excitation. References to these works can be found in the review articles [1–4]. Most of these works have treated the pipeline as a continuous or segmented beam and have not taken into account the dynamic interaction between the pipe and its surrounding medium.

The departure from the beam model is in the works of Ariman, et al. [2, 5], and in those of Novak and his coworkers [6–8], where the authors have considered the shell model of the pipe. However, the interaction of the pipe and the soil has not been considered in the sense that equations governing the three-dimensional wave motion of the surrounding ground have not been solved simultaneously with the equations of motion of the pipeline.

In recent studies [9,10], it has been shown that the dynamic interaction between the pipe and its environment significantly influences the displacements of the pipe wall and the stresses arising in it. It has also been found that the depth of the embedment of the pipe also affects the pipe response. Because the problem of three-dimensional motion of an embedded pipe in a semi-infinite elastic medium is very complex, attention was focused on the two-dimensional (plane strain) problem in [9, 10].

The object of the present investigation is to quantitatively assess the effects of the dynamic interaction between the pipe and the surrounding ground when the pipe is disturbed by waves moving along its length. For simplicity of analysis only, the axisymmetric motion of a pipe in an infinite elastic medium caused by longitudinal wave moving along the pipe has been considered here. Admittedly, this is a rather simplified version of the very complex problem of pipeline motion due to seismic excitation. However, the object here is to ascertain what effects the wavelength and frequency of excitation and the material properties of the pipe and its surroundings have on the dynamic behavior of an embedded pipeline. An understanding of the influence of these parameters on the dynamic behavior of embedded pipelines would be helpful in their seismic resistant design.

It may be mentioned that the related problems of the free and forced vibrations of a pipe in an acoustic medium have received considerable attention in the past [11,12]. The vibration of a pipe in an elastic medium is complicated by the coupling of the longitudinal and shear waves generated in the surrounding medium. As in the case of a freely vibrating pipe in an acoustic medium, it is found that there may exist resonant frequencies for a pipe freely vibrating in an elastic medium. However, in the latter case, the existence of the resonant frequencies depends on the rigidity ratio of the pipe and its surrounding elastic medium and these frequencies are well beyond the predominant frequencies of seismic excitation.

For the sake of compactness, the governing equations of motion of a cylindrical shell in an elastic medium will not be developed here. The derivation of the equations governing the motion of cylindrical shells have been discussed in [13], where shear deformation and rotary inertia effects were included. The equations used here are those discussed in [13] with the

Contributed by the Applied Mechanics Division for publication in the JOURNAL OF APPLIED MECHANICS.
Discussion on this paper should be addressed to the Editorial Department, ASME, United Engineering Center, 345 East 47th Street, New York, N. Y. 10017, and will be accepted until two months after final publication of the paper itself in the JOURNAL OF APPLIED MECHANICS. Manuscripts received by ASME Applied Mechanics Division September, 1980; final revision, April 1981.

Copyright © 1982 by ASME
Downloaded 01 May 2010 to 171.66.16.249. Redistribution subject to ASME license or copyright; see http://www.asme.org/terms/Terms_Use.cfm

inclusion of the traction forces acting on the shell due to the surrounding elastic medium.

Equations and Solution

It can be shown that the equations governing the axisymmetric motion of a shell element are given by

$$\left[-\frac{1}{R^2}(E_p+D/R^2)+k_x^2Gh\frac{\partial^2}{\partial x^2}-\rho_s h\frac{\partial^2}{\partial t^2}\right]w + k_x^2Gh\frac{\partial\Psi_x}{\partial x}-\frac{E_p\nu}{R}\frac{\partial u}{\partial x}+p_1^*=0 \quad (1)$$

$$-k_x^2Gh\frac{\partial w}{\partial x}+\left[D\frac{\partial^2}{\partial x^2}-k_x^2Gh-\rho_x I\frac{\partial^2}{\partial t^2}\right]\Psi_x + \left[\frac{D}{R}\frac{\partial^2}{\partial x^2}-\frac{\rho_s I}{R}\frac{\partial^2}{\partial t^2}\right]u+p_2^*=0 \quad (2)$$

$$\frac{E_p\nu}{R}\frac{\partial w}{\partial x}+\left[\frac{D}{R}\frac{\partial^2}{\partial x^2}-\frac{\rho_s I}{R}\frac{\partial^2}{\partial t^2}\right]\Psi_x+\left[E_p\frac{\partial^2}{\partial x^2} -\rho_s h\frac{\partial^2}{\partial t^2}\right]u+p_3^*=0 \quad (3)$$

In equations (1-3), the x-axis is measured along the axis of the shell; u, and w are the axial and radial displacements of a point on the shell-middle surface (see Fig. 1) and Ψ_x is the rotation of the normal to this surface in the meridional plane. The other shell parameters are defined as follows.

$R \equiv$ mean radius
$h \equiv$ thickness
$E_p = \dfrac{EH}{1-\nu^2}$, $E \equiv$ Young's modulus, $\nu \equiv$ Poisson's ratio
$D = \dfrac{E_p h^2}{12}$
$G \equiv$ shear modulus
$\rho_s \equiv$ density
$I = \dfrac{h^3}{12}$
$k_x \equiv$ shear correction factor, taken as $\dfrac{\pi}{\sqrt{12}}$

These equations include the shear deformation and rotary inertia terms and have been developed following the analysis of [13].

The vector $\mathbf{p}^*$ represents the force and moment exerted per unit area by the surrounding medium on the shell and has the components

$$p_1^*=\left(1+\frac{h}{2R}\right)\tau_{rr}^*,\quad p_2^*=\frac{h}{2}p_3^*,\quad p_3^*=\left(1+\frac{h}{2R}\right)\tau_{rx}^* \quad (4)$$

The normal and shear stress components τ_{rr}^* and τ_{rx}^* arise from the motion of the surrounding medium and are evaluated at $r=R+h/2$.

The displacement $\mathbf{u}(r, \theta, x, t)$ of a point of the outer medium satisfies the equations of motion

$$\tau^2\nabla\nabla\cdot\mathbf{u}-\nabla\wedge\nabla\wedge\mathbf{u}=\frac{1}{c_2^2}\frac{\partial^2\mathbf{u}}{\partial t^2} \quad (5)$$

where

$$\tau=\sqrt{\frac{2(1-\sigma)}{1-2\sigma}},\quad c_2=\sqrt{\frac{\mu}{\rho}}$$

σ is the Poisson's ratio and c_2 is the shear wave speed.

Since the object of the present investigation is to analyze the motion of the shell excited by a longitudinal wave moving along the axis of the pipe, the displacement $\mathbf{u}$ will have two

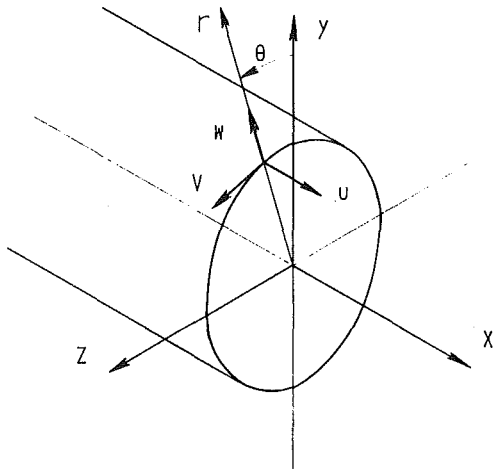


Fig. 1 Geometry of the problem

parts. The part due to the incident disturbance will be denoted by $\mathbf{u}^{(i)}$, whose components may be represented for axisymmetric motion as

$$u_r^{(i)}=-u_o R\sqrt{\xi^2-k_1^2}I_1\left(\sqrt{\xi^2-k_1^2}r\right)\cos\xi(x-ct)$$
$$u_x^{(i)}=u_o\xi R I_o\left(\sqrt{\xi^2-k_1^2}r\right)\sin\xi(x-ct) \quad (6)$$

where I_n $(n=0, 1)$ is the modified Bessel function of the first kind. Note that k_1 is the wave number given by $k_1=\omega/c_1$, c_1 being the longitudinal wave speed in the medium and ω the circular frequency. Clearly $\mathbf{u}^{(i)}$ given by (6) satisfies (5) and is a traveling wave of wavelength $\lambda=2\pi/\xi$, moving with speed $c(=\omega/\xi)$ along the axis of the pipe. If the excitation is due to a *plane* longitudinal wave moving at an angle α with the axis of the pipe, then (6) will represent the axisymmetric component of that wave. Physically, the apparent wave speed c of such a wave along the axis of the pipe will be $c_1/\cos\alpha$. In the particular case of a plane longitudinal wave moving along the axis of the pipe, (6) will reduce to

$$u_r^{(i)}=0,\ u_x^{(i)}=u_o\xi R\sin\xi(x-c_1t) \quad (7)$$

The other part of $\mathbf{u}$, denoted by $\mathbf{u}^{(s)}$, may then be written as

$$u_r^{(s)}=-\left[A\frac{\gamma}{R}K_1\left(\gamma\frac{r}{R}\right)+B\xi K_1\left(\delta\frac{r}{R}\right)\right]\cos\xi(x-ct)$$
$$u_x^{(s)}=\left[A\xi K_o\left(\gamma\frac{r}{R}\right)+B\frac{\delta}{R}K_o\left(\delta\frac{r}{R}\right)\right]\sin\xi(x-ct) \quad (8)$$

Here K_n $(n=0,1)$ is the modified Bessel function of the second kind and

$$\gamma=\sqrt{l^2-\epsilon^2},\ \delta=\sqrt{l^2-\tau^2\epsilon^2},\ \epsilon=\omega R/c_1,\ l=\xi R \quad (9)$$

The constants A and B are chosen so that the displacement is continuous at the shell outer surface, that is,

$$u_r^{(s)}=w-u_r^{(i)},\ u_x^{(s)}=u+\frac{h}{2}\Psi_x-u_x^{(i)} \quad (10)$$

Once $u_r^{(s)}$, $u_x^{(s)}$ are known, they can be used to calculate the stresses $\tau_{rr}^{(s)*}$, $\tau_{rx}^{(x)*}$ arising from them at $r=R+h/2$. Assuming that

$$w=\bar{w}\cos\xi(x-ct),\quad \Psi_x=\bar{\Psi}_x\sin\xi(x-ct),\quad u=\bar{u}\sin\xi(x-ct) \quad (11)$$

it can be shown, after some lengthy algebra,

$$p_1^*=\frac{\mu}{R}\left[T_{11}w_o+\frac{h}{2}T_{12}\bar{\Psi}_x+T_{13}u_o\right]\cos\xi(x-ct) + \left(1+\frac{m}{2}\right)\tau_{rr}^{(i)*}$$

Downloaded 01 May 2010 to 171.66.16.249. Redistribution subject to ASME license or copyright; see http://www.asme.org/terms/Terms_Use.cfm

$$p_3^* = \frac{\mu}{R}\left[T_{13}w_o + \frac{h}{2}T_{23}\bar{\Psi}_x + T_{33}u_o\right]\sin\xi(x-ct) + \left(1+\frac{m}{2}\right)\tau_{rx}^{(i)*} \tag{12}$$

$$p_2^* = \frac{h}{2}p_3^*$$

where the elements T_{ij} of the matrix T are given by

$$T_{11} = -(1+m/2)\left[\delta\frac{\tau^2\epsilon^2 K_o(\mathfrak{B})K_o(\mathfrak{A})}{\mathfrak{D}} + \frac{2}{1+m/2}\right]$$

$$T_{12} = T_{21} = T_{13} = T_{31} = -l(1+m/2)\times \left[2 - \frac{\tau^2\epsilon^2 K_1(\mathfrak{B})K_o(\mathfrak{A})}{\mathfrak{D}}\right] \tag{13}$$

$$T_{22} = T_{33} = T_{23} = T_{32} = -\frac{(1+m/2)\tau^2\epsilon^2\gamma K_1(\mathfrak{A})K_1(\mathfrak{B})}{\mathfrak{D}}$$

$$\mathfrak{D} = l^2 K_o(\mathfrak{A})K_1(\mathfrak{B}) - \gamma\delta K_1(\mathfrak{A})K_o(\mathfrak{B})$$

and

$$m = h/R, \quad w_o = \bar{w} + u_o\gamma I_1(\mathfrak{A}), \quad u_o = \bar{u} - u_o l I_o(\mathfrak{A})$$

$$\mathfrak{A} = (1+m/2)\gamma, \quad \mathfrak{B} = (1+m/2)\delta$$

μ is the modulus of rigidity of the surrounding medium.

Finally, equations for the determination of $\bar{w}$, $\bar{\Psi}_x$, and $\bar{u}$ are obtained by substituting (11) and (12) in (1)-(3). In matrix notation, these can be written as

$$[A - MT - \Omega^2 B]U = -MTU^{(i)} + MT^{(i)} \tag{14}$$

Here A and B are symmetric 3 × 3 matrices having the elements

$$\begin{aligned} A_{11} &= 2Nm(1+m^2/12) + k_x^2 m l^2, \quad B_{11} = 1 \\ A_{12} &= -2k_x^2 l, \quad B_{12} = 0 \\ A_{13} &= 2N\nu lm, \quad B_{13} = 0 \\ A_{22} &= \frac{4}{m}\left(\frac{N}{6}m^2 l^2 + k_x^2\right), \quad B_{22} = \frac{1}{3} \\ A_{23} &= \frac{1}{3}Nm^2 l^2, \quad B_{22} = \frac{m}{6} \\ A_{33} &= 2Nml^2, \quad B_{33} = 1 \end{aligned} \tag{15}$$

also,

$$M = \mu/G, \quad N = \frac{1}{1-\nu}, \quad U_1^{(i)} = -\gamma I_1(\mathfrak{A})$$

$$U_2^{(i)} = 0, \quad U_3^{(i)} = l I_o(\mathfrak{A})$$

$$T_1^{(i)} = (\tau^2\epsilon^2 - 2l^2)I_o(\mathfrak{A}) + \frac{2\gamma}{1+m/2}I_1(\mathfrak{A})$$

$$T_2^{(i)} = T_3^{(i)} = 2\gamma l I_1(\mathfrak{A})$$

$$U_1 = \bar{w}/u_o, \quad U_2 = \frac{h}{2}\bar{\Psi}_x/u_o, \quad U_3 = \bar{u}/u_o$$

$$\Omega^2 = \frac{\rho_s hR}{G}\omega^2 = \tau^2\epsilon^2 Mm\left(\frac{\rho_s}{\rho}\right)$$

It should be pointed out here that equation (14) represents the equation for the determination of the displacement of, and the rotation normal to, the middle surface when the pipe is excited by an axially propagating longitudinal wave. The excitation is represented by the right-hand side of equation (14). Note that the matrix T depends solely on the geometry of the pipe, the material properties of the surrounding medium, and, of course, on the wavelenth and wave-speed of the excitation. So for a different excitation, only $U^{(i)}$ and $T^{(i)}$ will be changed. Further, the equation determining the frequency of free vibration of the pipe in an elastic medium is given by

$$\det[A - MT - \Omega^2] = 0 \tag{16}$$

In general, these frequencies are complex and depend on M as well as on other material and geometrical parameters of the shell and its surrounding medium. The real frequencies can exist only if

$$\epsilon < l/\tau \tag{17}$$

These are discussed in the following section. Note that (17) implies that $c < c_2$. Thus resonances cannot occur if the pipe is excited by a plane longitudinal wave.

A parametric study has been performed in this paper analyzing the dependence of the amplitudes (radial and axial) of oscillation of the pipe on the material parameters M (ratio of the rigidities of the ground and the pipe) and σ (Poisson's ratio of the ground), and the excitation parameters ω and ξ. The results are discussed in the next section.

Numerical Results and Discussions

In order to see whether there are real resonating frequencies of the pipeline within the range of predominant frequencies of seismic excitation, equation (16) was solved for real frequencies for different values of M and the Poisson's ratio, σ, of the outer medium. These are shown in Tables 1 and 2. The following parameters were chosen for the shell representing a steel shell in soil.

$$h/R = .05, \quad \nu = 0.3, \quad \rho_s/\rho = 2.9266$$

It was found that there were no real frequencies for small M and for M between 0.1 and 1 there is only one real frequency, which lies between the frequencies of the first and second flexural modes of free vibration of the pipe in vacuum. It is further noted that if $l \leq \pi/3$, then there are no real frequencies for any value of M. This is to be contrasted with the case of a shell vibrating in an acoustic medium in which case it was found [12] that there was always one real frequency for all l. Also, the real frequency exists for smaller values of l as M increases. For example, when $M = 0.1$, the real frequency occurs first for $l = 5\pi/3$ whereas when $M = 0.3$, it occurs first for $l = 5\pi/6$ and when $M = 1$, it is for $l = 2\pi/3$. It is observed that the frequency of free vibration decreases with the increase in the rigidity ratio of the soil and the pipe. Increasing the Poisson's ratio also decreases the frequency.

It may be noted that for a steel pipe embedded in a rocky material, the rigidity ratio would be about 0.3085 and in a soft clay this ratio is about 0.01. The density ratio is nearly the same in both cases. The Poisson's ratio of rock may be taken as 0.25 and 0.45 for soft clay. It is seen from Tables 1 and 2 that for the particular problem considered, the pipe will not resonate in soft soil and it may resonate in hard or rocky soil if the wavelength is of the order of the diameter of the shell. The resonating frequency is quite high. For example, when $\lambda/2R = 1.2$ then $\omega = 1kHz$ for $R = 1.2m$. This is well beyond the frequency content of seismic excitation.

Equation (14) and its simplified version obtained by neglecting the shear deformation and rotory inertia were then solved for the two particular cases previously mentioned. The difference between the results obtained by solving the simplified equation and the more exact equation (14) was not found to be large except at very short wavelengths. The results presented in Figs. 2-13 are from the simpler (Flügge's) equation. Figures 2 and 3 show the ratios of the dynamic amplitudes of the radial and axial displacement components and their static values for a steel shell in hard ground. Figure 4 shows the amplitude ratio of the dynamic axial stress and its static value. These figures show that for long wavelengths, the

Downloaded 01 May 2010 to 171.66.16.249. Redistribution subject to ASME license or copyright; see http://www.asme.org/terms/Terms_Use.cfm

Table 1 Real vibrational frequencies ($\epsilon = \omega R/C_1$) of the shell in an elastic medium ($m = 0.05$, $\nu = 0.3$, $\sigma = 0.25$, $\rho^* = 2.9266$)

	$M = \mu/G$			
l	0.10	0.30	1.0	10
0	None	None	None	None
0.523599				
1.047198				
1.570796	None	None	None	0.90349
2.094395	None	None	1.186374	1.156917
2.617994	None	1.503563	1.441541	1.386536
3.141593	None	1.778986	1.686290	1.598974
3.665191	None	2.045781	1.923659	1.795699
4.188700	None	2.306060	2.155022	1.976985
4.712389	None	2.560788	2.381172	2.142921
5.235988	2.995772	2.810588	2.602665	2.293865
5.759587	3.266147	3.055966	2.819936	2.430641
6.283185	3.530997	3.297378	3.033356	2.554559
				3.571390

Table 2 Real vibrational frequencies ($\epsilon = \omega R/C_1$) of the shell in an elastic medium ($m = 0.05$, $\nu = 0.3$, $\sigma = 0.45$, $\rho^* = 2.9266$)

	$M = \mu/G$			
l	0.10	0.30	1.0	10
0	None	None	None	None
0.523599				
1.047197				
3.141592	None	0.9339887	0.8997447	0.8699774
6.283185	1.845795	1.741516	1.646022	1.865283

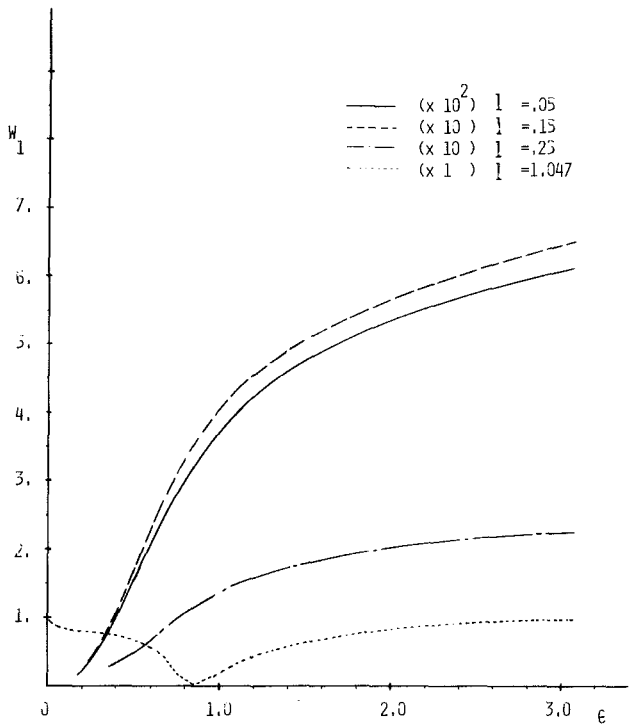


Fig. 2 Variation of the dynamic amplification of the radial displacement with ϵ and l in a hard ground

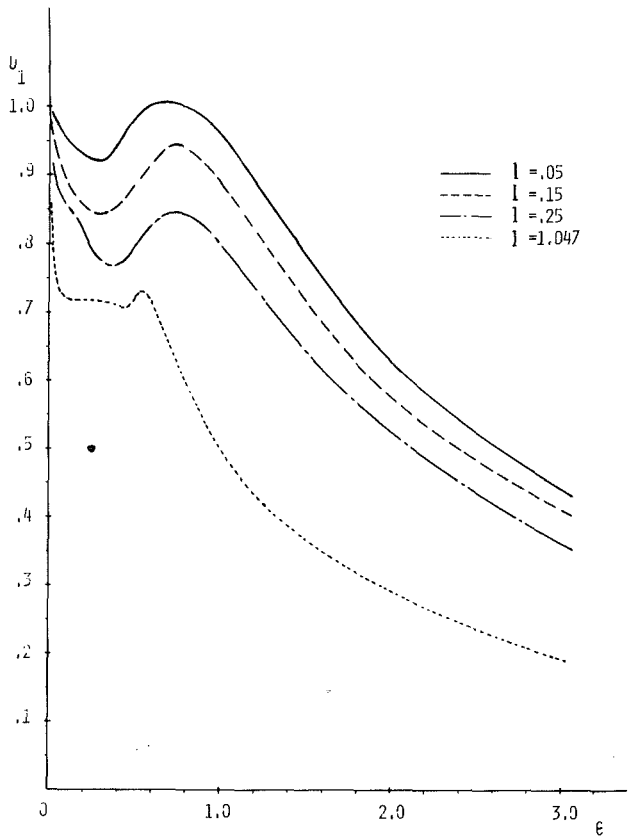


Fig. 3 Variation of the dynamic amplification of the axial displacement with ϵ and l in a hard ground

Downloaded 01 May 2010 to 171.66.16.249. Redistribution subject to ASME license or copyright; see http://www.asme.org/terms/Terms_Use.cfm

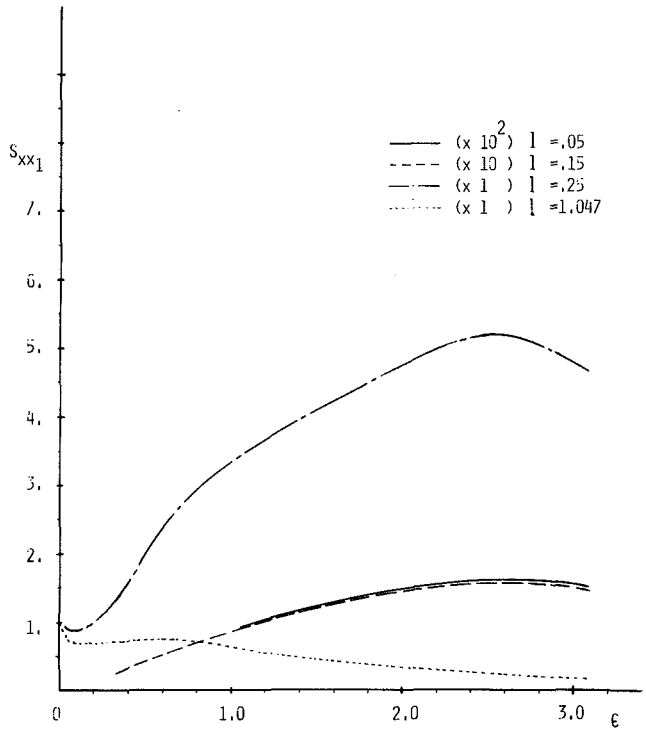


Fig. 4 Variation of the dynamic amplification of the axial stress in a hard ground

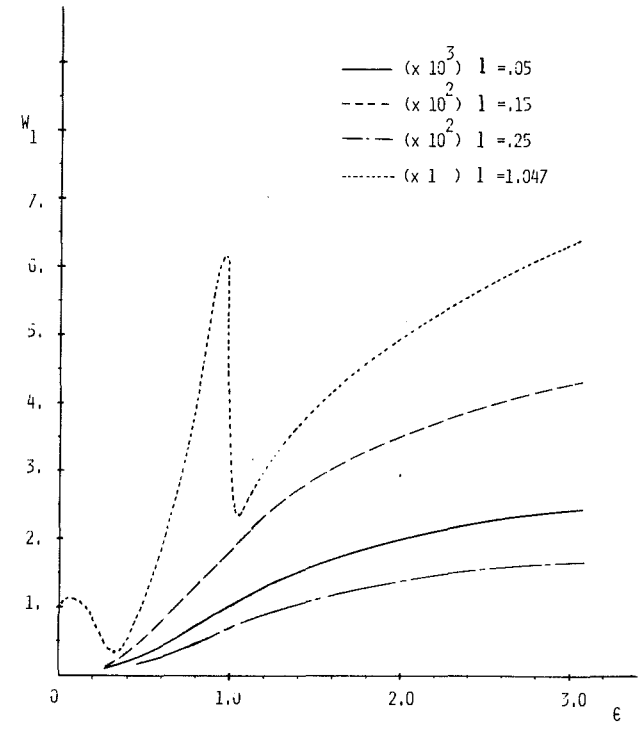


Fig. 6 Dynamic amplification of the radial displacement in a soft ground

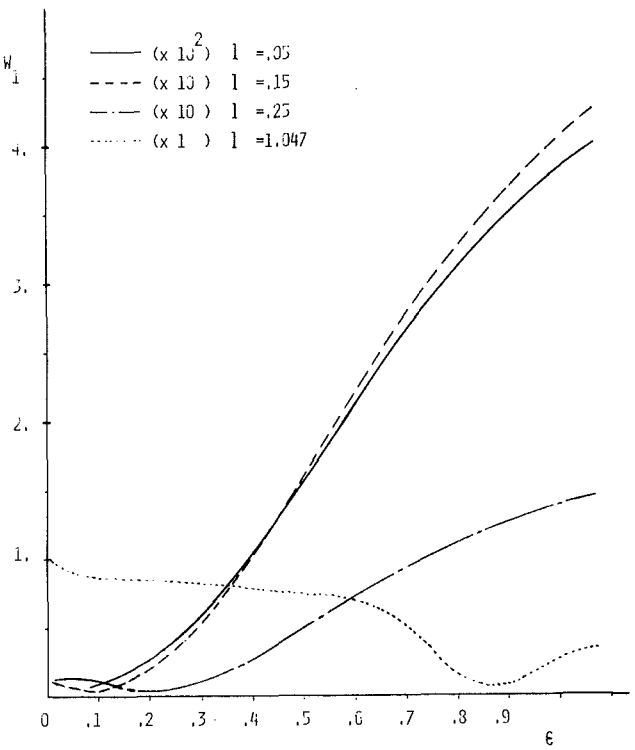


Fig. 5 Dynamic amplification of the radial displacement at low frequencies and long wavelengths

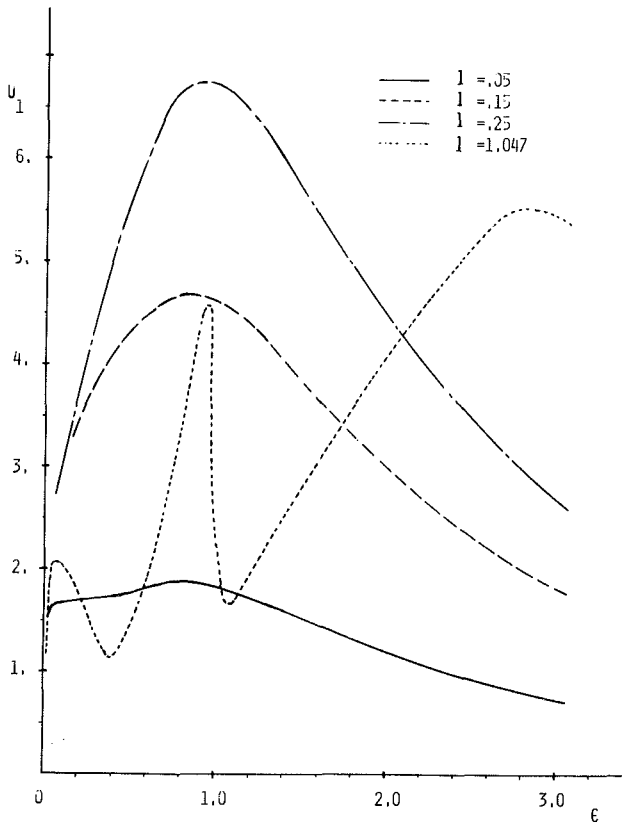


Fig. 7 Dynamic amplification of the axial displacement in a soft ground

Downloaded 01 May 2010 to 171.66.16.249. Redistribution subject to ASME license or copyright; see http://www.asme.org/terms/Terms_Use.cfm

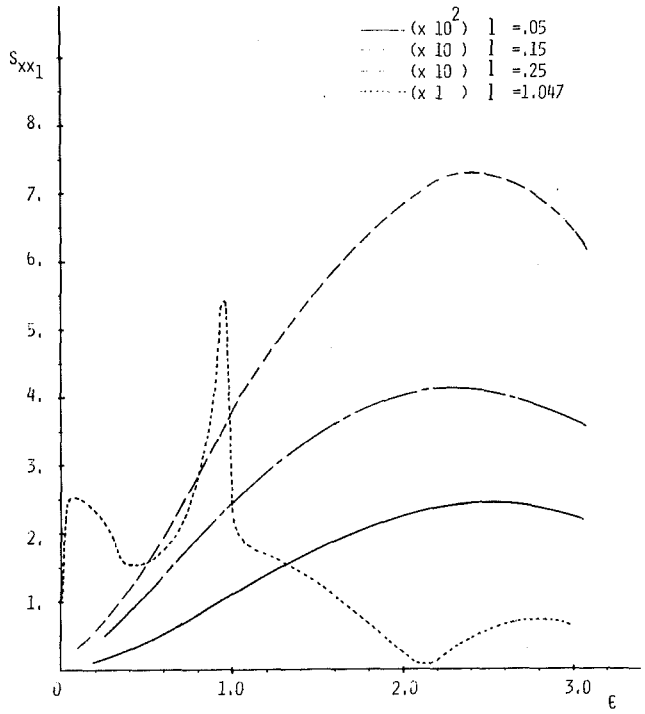


Fig. 8 Dynamic amplification of the axial stress in a soft ground

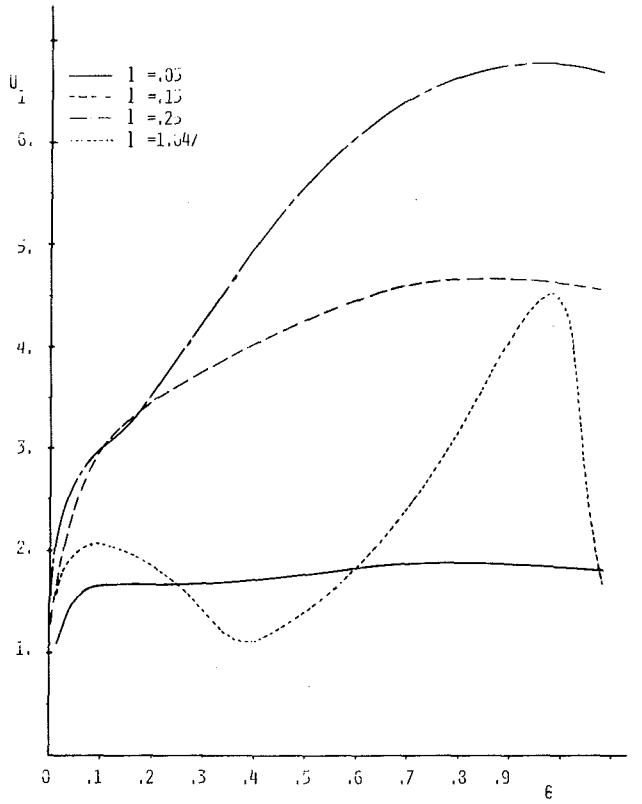


Fig. 10 Dynamic amplification of the axial displacement at low frequencies in a soft ground

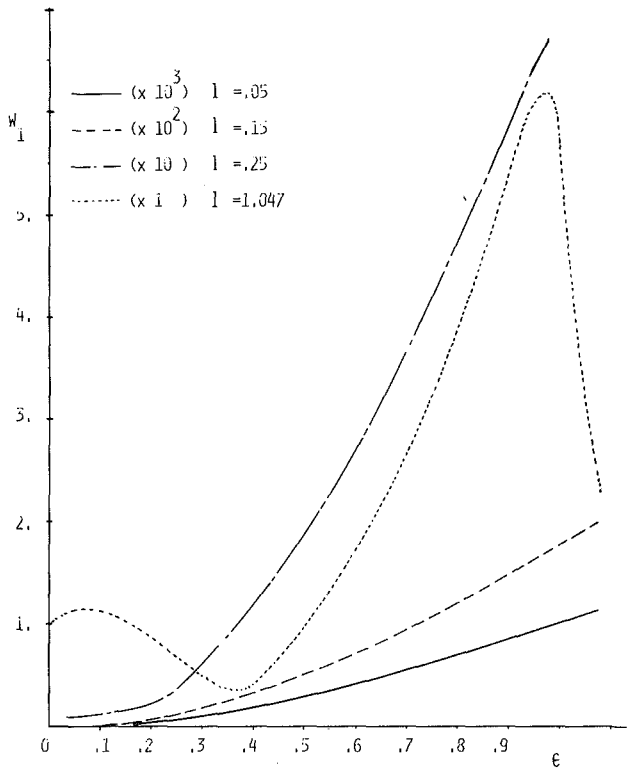


Fig. 9 Dynamic amplification of the radial displacement at low frequencies in a soft ground

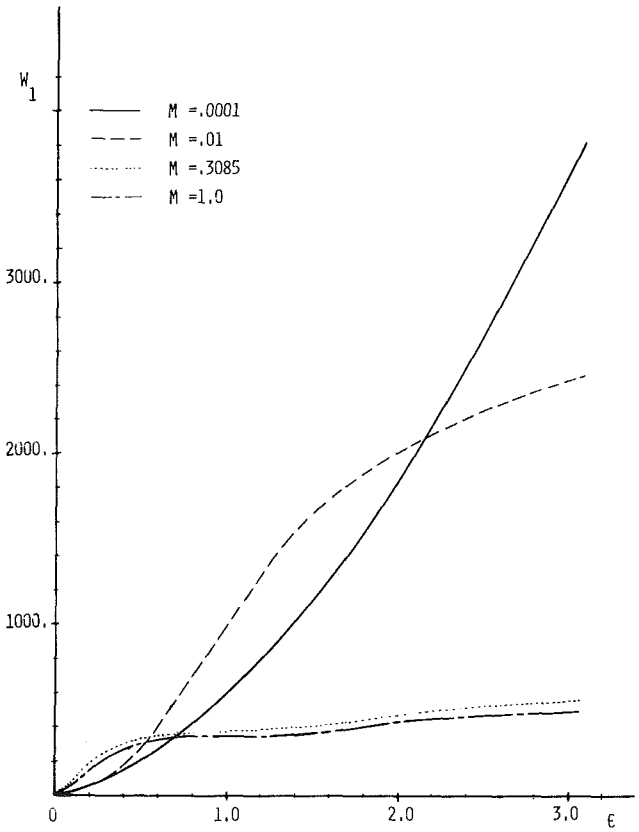


Fig. 11 Dynamic amplification of the radial displacement for various *M* at *l* = 0.05 in a soft ground

Downloaded 01 May 2010 to 171.66.16.249. Redistribution subject to ASME license or copyright; see http://www.asme.org/terms/Terms_Use.cfm

dynamic amplification of the radial displacement and axial stress increase rapidly with increasing frequency. As the wavelength increases, the amplification decreases. It is noted that the rate of increase of amplification with frequency is most rapid for $\epsilon < 0.5$, a range of interest in seismic excitation of pipelines. This is further illustrated in Fig. 5. The behavior of the same pipeline in a soft soil is illustrated in Figs. 6–10. As in the case of hard soil, it is seen that the amplification is most severe for long wavelengths. In this case, however, there are some distinct differences in the behavior of the pipeline. There is large amplification of the axial displacement of the pipeline in soft soil. This is to be contrasted with the deamplification observed in hard ground. It is seen that the amplification first increases with decreasing wavelength, but then decreases. For short wavelengths, the amplification in all the quantities shown has oscillatory behavior at low frequencies ($\epsilon < 1$). Of special significance is the fact that in soft soil, the dynamic amplification is much larger than in a hard ground. Finally, in Figs. 11–13, the dynamic amplification of the displacement components for various rigidity ratios in soft and hard soils are shown when $2R/\lambda = 0.05/\pi$. These figures show that for the same wavelength, amplification in the radial displacement increases with increasing M up to $M = 0.31$ for low frequencies. At high frequencies, however, the amplification tends to level off for large M. It is seen from Fig. 12 that the amplification in the axial displacement in soft soil is very large when M is very small. But as M increases, the amplication is nearly the same for all M.

Thus the following conclusions may be drawn from these observations.

(1) For long wavelengths when the rigidity ratio of the ground and the pipe is kept at the same small value, larger axial stresses in the pipe are caused in a softer ground. For large rigidity ratios, on the other hand, just the reverse occurs, except when frequency is low.

(2) Pipe resonance occurs only when the rigidity ratio is large and the wavelength is small. No resonance occurs in a soft soil.

(3) For long wavelengths, it appears that dynamic amplification of the displacement of the pipe wall is much larger in a softer ground.

(4) It is interesting to note that whereas dynamic amplication of the axial displacement increases with frequency in a soft ground, it decreases in a hard ground. Also of interest to note is that in a hard ground, amplification decreases with decreasing wavelength. But in a soft soil, it increases initially with decreasing wavelength.

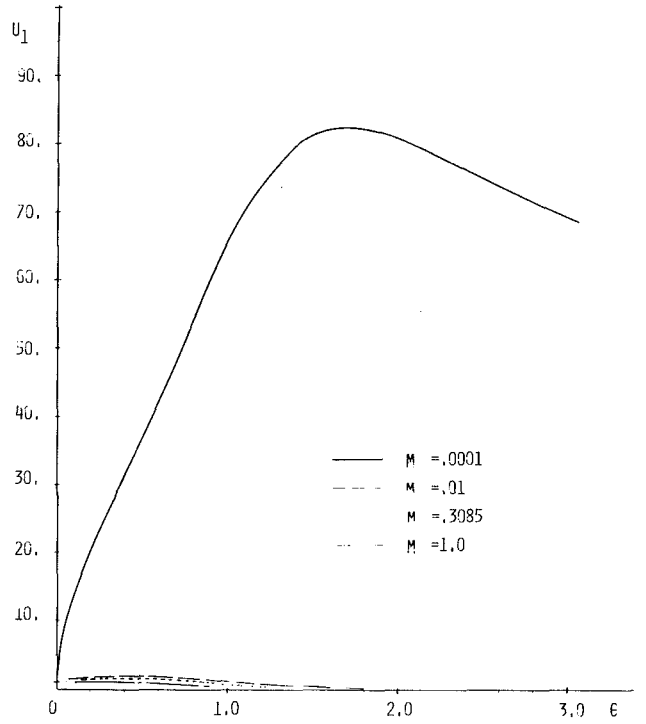


Fig. 12 Dynamic amplification of the axial displacement for various M at $l = 0.05$ in a soft ground

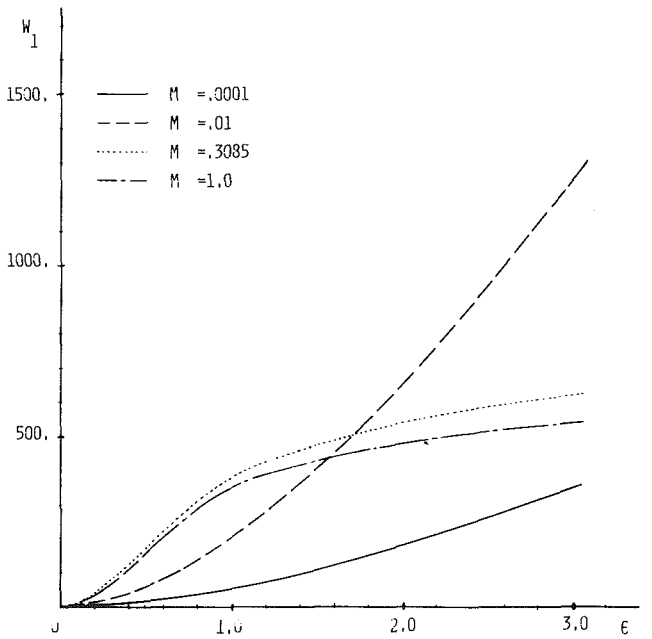


Fig. 13 Dynamic amplification of the radial displacement in a hard soil at $l = 0.05$

Acknowledgment

The work was supported in part by the Problem Focused Research Division of the National Science Foundation (Grant No. PFR-7822848) under the Earthquake Hazards Mitigation Program. The program manager was Dr. W. W. Hakala. Part of the work was done while the first author (S. K Datta) was at the Department of Applied Mathematics, Calcutta University. He is grateful to Professor P. K. Ghosh for his support and help. Thanks are also due to Natural Science and Engineering Science Council of Canada for providing partial support to AHS.

References

1 Wang, L. R. L., and O'Rourke, M., "State of the Art of Buried Lifeline Earthquake Engineering," *Proceedings of the Current State of Lifeline Earthquake Engineering, ASCE,* Los Angeles, Calif., Aug. 30–31, 1977, pp. 252–266.

2 Ariman, T., and Muleski, G. E., "Recent Developments in Seismic Analysis of Buried Pipelines," *Proceedings of the 2nd U.S. National Conference on Earthquake Engineering*, Earthquake Engineering Research Institute, Berkeley, Calif., Aug. 22–24, 1979, pp. 643–652.

3 Nelson, I., and Weidlinger, P., "Dynamic Seismic Analysis of Long Segmented Lifelines," ASME *Journal of Pressure Vessel Technology*, Vol. 101, 1979, pp. 10–20.

4 Kubo, K., Katayama, T., and Ohashi, M., "Lifeline Earthquake Engineering in Japan," *Journal of the Technical Councils of ASCE*, TC1, Apr. 1979, pp. 221–238.

5 Muleski, G. E., Ariman, T., and Aumen, C. E., "A Shell Model of a Buried Pipe in a Seismic Environment," ASME *Journal of Pressure Vessel Technology*, Vol. 101, 1979, pp. 44–50.

6 Novak, M., and Hindy, A., "Dynamic Response of Buried Pipelines," *Proceedings of the 6th European Conference on Earthquake Engineering*, Dubrovnik, Yugoslavia, Sept. 1978, Vol. 2, pp. 533–540.

7 Hindy, A., and Novak, M., "Earthquake Response of Underground Pipelines," *International Journal of Earthquake Engineering and Structural Dynamics*, Vol. 7, 1979, pp. 451–476.

Downloaded 01 May 2010 to 171.66.16.249. Redistribution subject to ASME license or copyright; see http://www.asme.org/terms/Terms_Use.cfm

8 Novak, M., and Hindy, A., "Seismic Analysis of Underground Tubular Structures," *Proceedings of the 7th World Conference on Earthquake Engineering*, Sept. 8–13, Vol. 8, 1980, pp. 287–294.

9 El-Akily, N., and Datta, S. K., "Response of a Circular Cylindrical Shell to Disturbances in a Half-Space," to appear in the *International Journal of Earthquake Engineering and Structural Dynamics*, 1981.

10 N. El-Akily, and Datta, S. K., "Response of a Buried Pipe to Seismic Waves," *Proceedings of the 7th World Conference on Earthquake Engineering*, Sept. 8–13, Vol. 8, 1980, pp. 217–224.

11 Bleich, H. H., and Baron, M. L., "Free and Forced Vibrations of an Infinitely Long Cylindrical Shell in an Infinite Acoustic Medium," ASME JOURNAL OF APPLIED MECHANICS, Vol. 21, 1954, pp. 167–177.

12 Junger, M. C., "Dynamic Behavior of Reinforced Cylindrical Shells in a Vacuum and in a Fluid," ASME JOURNAL OF APPLIED MECHANICS, Vol. 21, 1954, pp. 35–41.

13 Mirsky, I., and Herrmann, G. H., "Nonaxially Symmetric Motion of Cylindrical Shells," *Journal of the Acoustical Society of America*, Vol. 29, 1957, pp. 1116–1123.

Downloaded 01 May 2010 to 171.66.16.249. Redistribution subject to ASME license or copyright; see http://www.asme.org/terms/Terms_Use.cfm

Transverse Impact on Fluid-Filled Cylindrical Tubes

F. Katsamanis
Lecturer,
Naval College,
Athens, Greece

W. Goldsmith
Professor,
Department of Mechanical Engineering,
University of California,
Berkeley, Calif. 94720
Fellow ASME

An analytical and experimental study was conducted regarding the effects produced by transverse impact of spherical steel projectiles on circular elastic tubes either empty or else containing stationary or flowing fluids. Similar tests were also executed on acrylic (PMMA) tubes that exhibit viscoelastic behavior. Transients were generated by pneumatically propelled 12.7 mm (1/2 in.) and 4.8 mm (3/16 in.) diameter projectiles striking the midpoint of two types of 3 m long 2024-T3 aluminum tubes with an outer diameter of 25.4 mm and wall thicknesses of 2.41 and 1.25 mm, respectively, and PMMA tubes with outer diameters of 34.93 and 31.75 mm and wall thicknesses of 3.17 and 1.58 mm, respectively. The targets were ballistically suspended by means of strings, and filled either with distilled water or a high-density capacitor fluid, Fluorinert. Most of the tests were performed with stationary liquids when the tube ends were stoppered; in some of the experiments, laminar flow in the hollow cylinders was produced by means of a blood pump. The initial and final projectile velocities were measured by means of a set of two multiple coils wound around an acrylic tube through which the striker passed; the impact force was determined from a sandwiched quartz crystal arrangement placed ahead of the contact point on the targets. Axial and hoop strain histories were ascertained by means of foil strain gages mounted at two stations on the outer hollow cylinder surface. Antisymmetric strain records were compared with the predictions of a modified Timoshenko-beam model; good agreement was noted between these results, particularly for the case of thick-walled tubes.

Introduction

Substantial interest has prompted a study of the propagation of waves in liquid-filled tubes in connection with flow in blood vessels, ducts, and pipelines, including the phenomenon of the water hammer. The vast majority of the efforts have been concerned only with the delineation of wave speeds or else the behavior under steady-state or harmonic excitation conditions, and, furthermore, have primarily dealt with axisymmetric rather than antisymmetric propagation conditions. Recent contributions in this area have been published by Skalak [1] and Walker and Phillips [2, 3].

There have been no investigations of the transient response of fluid-filled containers under transverse impact as was executed recently for the corresponding case of longitudinal axisymmetric impact on elastic and viscoelastic tubes containing either inviscid or viscous liquids [4]. That analysis was carried out using one-dimensional bar-like or membrane-shell representations of the container, incorporating its viscous features when appropriate.

The present work is intended as an initial counterpart for transverse loading on empty and fluid-filled tubes, represented by an elastic model, filled with two different fluids, treated analytically as inviscid and compressible, using a modified Timoshenko-beam theory for a representation of the system. Two sizes of aluminum and two types of PMMA tubes with lengths much greater than the tube radius were subjected to central transverse impact by pneumatically propelled steel spheres whose initial and rebound velocities, as well as the resultant force history generated, were monitored. Measured axial strain histories were compared to corresponding analytical results obtained in integral form and evaluated by means of a digital computer.

Analysis

An optimum theoretical development for the present problem should provide maximum insight into the effect of the various system parameters on the response to permit a good quantitative prediction of the major features of the propagation phenomena; this normally requires a solution in quadratures rather than a completely numerical one. These considerations strongly pointed to the choice of a modified Timoshenko beam [5, 6] as a suitable model, constituting a substantial improvement over a Euler beam (although incapable of predicting fluid parameters), yet not requiring the excessive computational labor demanded by a membrane-shell or Pochhammer-Chree representation.

The presence of a fluid inside a container can be incorporated by its inclusion in the transverse inertia term of the Timoshenko-beam equation involving an equivalent density, $\rho_e \equiv (\rho_t A_t + \rho_F A_F)/A_t$, where subscripts t and F denote tube and fluid, respectively. The deflection w at any position x and time t is produced by a bending moment M created by an applied force per unit length $f^*(x,t)$.

Contributed by the Applied Mechanics Division for publication in the JOURNAL OF APPLIED MECHANICS.

Discussion on this paper should be addressed to the Editorial Department, ASME, United Engineering Center, 345 East 47th Street, New York, N.Y. 10017, and will be accepted until two months after final publication of the paper itself in the JOURNAL OF APPLIED MECHANICS. Manuscript received by ASME Applied Mechanics Division, March 1981; final revision, July, 1981.

Copyright © 1982 by ASME
Downloaded 01 May 2010 to 171.66.16.249. Redistribution subject to ASME license or copyright; see http://www.asme.org/terms/Terms_Use.cfm

The phase velocity $c = (p/f)$ is determined from the equation

$$\left(\frac{c}{c_0}\right)^4 - \left[1 + \frac{1}{C}\left(\beta + \frac{1}{4\pi^2\left(\frac{k}{\Lambda}\right)^2}\right)\right]\left(\frac{c}{c_0}\right)^2 + \frac{\beta}{C} = 0$$

$$\text{with} \quad C \equiv \frac{2(1+\nu)}{\eta} \text{ and } \beta \equiv \frac{\rho_t}{\rho_e} \tag{1}$$

The ratio of average shear to that at the neutral axis used here [7] is

$$\eta = \frac{6(1+\nu)^2(1+n^2)^2}{(7+34n^2+7n^4)+\nu(12+48n^2+12n^4)+\nu^2(4+16n^2+4n^4)} \tag{2}$$

with values given in Table 3, where $n = R_i/R_0$ is the ratio of inner to outer tube radius. For large wave numbers, the positive roots of equation (1) yield two nondispersive limiting speeds, $c_I = (G\eta/\rho_e)^{1/2}$ and $c_{II} = (E/\rho_t)^{1/2}$. The first mode speed c_I depends significantly on the presence of the fluid; it is smaller for the fluid-filled than for an empty tube with differences of the order of 65 percent for the present configurations. However, the limiting value of the second mode, c_{II}, is independent of liquid properties. In contrast, the tube phase velocity for the Euler beam, $c = c_0 fk$, is dispersive for all wave numbers.

For the long wavelength limit $f \to 0$, equation (1) yields two roots for the frequency p_t, identical to the case of an empty tube, namely, $p_t{}^I = 0$ and $p_t{}^{II} = (GA_t\eta/\rho_t I)^{1/2}$. The second represents a cutoff frequency where beam motion corresponds to pure shear.

The corresponding group velocity ratio is given by

$$\frac{c_g}{c_0} = \frac{c}{c_0}\left[1 + \left(4\pi^2\left[\frac{k}{\Lambda}\right]^2 C\left\{1 + \frac{1}{C}\left[\beta + \left(\frac{\Lambda}{2\pi k}\right)^2\right] - 2\left(\frac{c}{c_0}\right)^2\right\}\right)^{-1}\right] \tag{3}$$

Thus, the ratio of either phase or group velocity for the solid-fluid system to that for the empty tube depends on wave length Λ, while that based on a Euler-Bernoulli beam is $(\rho_t/\rho^*)^{1/2}$. However, in the short wave length limit, the same ratio is also obtained for the group velocities of the filled versus empty tube, i.e.,

$$c_g{}^f/c_g{}^e = c^f/c^e = (\rho_t/\rho^*)^{1/2} = \beta^{1/2} \tag{4}$$

The dimensionless form of the modified Timoshenko-beam equation is given by

$$k^{*2}\frac{\partial^4 W}{\partial X^4} - k^{*2}(1+C^*)\frac{\partial^2 W}{\partial X^2 \partial \tau^2} + \frac{\partial^2 W}{\partial \tau^2} + k^{*2}C^*\frac{\partial^4 W}{\partial \tau^4} = F^*(X,\tau) \tag{5}$$

where $X = x/R_m$, $W = w/R_m$, $\tau = (c_0/R_m)t$, $k^* = (k/R_m)(\beta)^{1/2}$, $C^* = (C/\beta)$, the nondimensional force per unit length is $F^*(X,\tau) = f^*(x,t)\,R_m/(\rho_t A_t c_0{}^2)$, and R_m is the mean radius of the tube. This corresponds to the Timoshenko relation for a homogeneous beam with the same Young's modulus E and density ρ_t, but with a radius of gyration and Poisson's ratio ν_e given by

$$k_e = k(\beta)^{1/2} \text{ and } \nu_e = \{(\nu+1)/\beta\} - 1 \tag{6}$$

respectively. This may yield values of an equivalent Poisson's ratio greater than the theoretical maximum of 0.5 and would thus have no meaning for a homogeneous beam; for example, in the present case of an aluminum tube filled with water, this ratio is $\nu_e = 1.27$. This consideration does not arise in the analysis of an equivalent Euler-Bernoulli beam for a fluid-filled container. However, the formal solutions available for the usual Timoshenko-beam relations will still provide the appropriate result for the combined system.

Consequently, the present problem will be treated as an infinitely long modified Timoshenko beam subjected to an impulsively applied, concentrated transverse force at the coordinate origin with the loading function $f^*(x,t)$ expressed in terms of a double Dirac delta function by

$$f^*(x,t) = \delta(x)\,\delta(t) \tag{7}$$

The solution to equation (5) subject to an impulse of unit nondimensional magnitude of the type given by equation (7) is presented in reference [6]. It is utilized here by initially changing the dummy variable ξ appearing there to ξ_1/b and ξ_1/a, for the first and second integrals, respectively, so as to normalize the interval of integration, where $a = 2[k(C-1)]^{-1}$ and $b = [k\sqrt{C}]^{-1}$, and adapting it to the solid-fluid system

Nomenclature

a = $2k/(C\text{-}1)$
A = cross-sectional area
b = $(kC^{1/2})^{-1}$
B = arbitrary positive number less than unity
c = phase velocity
c_0 = rod wave velocity = $(E/\rho_t)^{1/2}$
c_g = group velocity
C = $2(1+\nu)/\eta$
C^* = C/β
E = Young's modulus
f = wave number
f^* = transverse load per unit length
F^* = nondimensional transverse force per unit length = $f^*(x,t)R_m/(\rho_t A_t c_0{}^2)$
G = shear modulus
I = moment of inertia of tube
k = radius of gyration = I/A_t
k^* = nondimensional radius of gyration = $(k/R_m)(\beta)^{1/2}$
L = tube length
m = nondimensional bending moment = $M/ER_m{}^3$
M = bending moment
n = ratio of inner to outer tube radius = R_i/R_0
p = frequency
R = tube radius
t = time
u_1 = funciton of ξ_1
w = transverse displacement
W = nondimensional transverse displacement = w/R_m
x = horizontal coordinate
X = nondimensional horizontal coordinate = x/R_m
β = density ratio = ρ_t/ρ_e
γ = dummy variable
δ = delta function
η = average shear to shear at neutral axis
Λ = wave length
ν = Poisson's ratio
ξ_1 = variable
ρ = density
ρ_e = equivalent density = $(\rho_t A_t + \rho_F A_F)/A_t$
τ = nondimensional time = $c_0 t/R_m$

Subscripts

e = equivalent
F = fluid
i = inner
m = mean
0 = outer
t = tube

Superscripts

e = empty
f = filled

Downloaded 01 May 2010 to 171.66.16.249. Redistribution subject to ASME license or copyright; see http://www.asme.org/terms/Terms_Use.cfm

upon replacement of constants k and C by k^* and C^*. In terms of the nondimensional bending moment $m(\tau,X) = M/ER_m{}^3$, the solutions for a unit nondimensional impulse after some manipulations are given by

$$\text{I)} \quad m(\tau,X)=0;\ \tau<X \tag{8}$$

$$\text{II)} \quad m(\tau,X)=I_1-(I_2+I_3+I_4+I_5);\ X<\tau<(C^*)^{1/2}X \tag{9}$$

$$\text{III)} \quad m(\tau,X)=I_1;\ (C^*)^{1/2}X<\tau \tag{10}$$

where

$$I_1=\int_0^1 F_1(u_1,\tau,X)du_1, I_2=\int_0^{0.8} G_2(u_1,\tau,X)du_1,$$

$$I_3=\int_0^{0.8} G_3(u_1,\tau,X)du_1, I_4=\int_0^{0.6} G_4(u_1,\tau,X)du_1, \tag{11}$$

$$I_5=\int_0^{0.6} G_5(u_1,\tau,X)du_1$$

$$F_1(u_1,\tau,X)=$$

$$\frac{[N(a^{*2}+b^{*2}u_1{}^4)^{1/2}-b^*u_1{}^2]^{1/2}}{\pi M_1 N(a^{*2}+b^{*2}+b^{*2}u_1{}^4)^{1/2}}b^{*1/2}\cos(b^*u_1{}^2\tau)\cosh(SX) \tag{12}$$

$$G_2(u_1,\tau,X)=$$

$$\frac{(R_1+a^*u_1{}^2)^{1/2}\cos(M_1X\phi_1)\cosh(a^*u_1{}^2\tau-M_1X\zeta_1)}{\pi M_1 N[2a^*(1-u_1{}^4)]^{1/2}} \tag{13}$$

$$G_3(u_1,\tau,X)=$$

$$\frac{(R_1-a^*u_1{}^2)^{1/2}\sin(M_1X\phi_1)\sinh(a^*u_1{}^2\tau-M_1X\zeta_1)}{\pi M_1 N[2a^*(1-u_1{}^4)]^{1/2}} \tag{14}$$

$$G_4(u_1,\tau,X)=$$

$$\frac{[R_2+a^*(1-u_1{}^2)]^{1/2}\cos(M_1X\phi_2)\cosh[a^*(1-u_1{}^2)\tau-M_1X\zeta_2]}{\pi M_1 N[2a^*(1-u_1{}^2)(2-u_1{}^2)]^{1/2}} \tag{15}$$

$$G_5(u_1,\tau,X)=$$

$$\frac{[R_2-a^*(1-u_1{}^2)]^{1/2}\sin(M_1X\phi_2)\sinh[a^*(1-u_1{}^2)\tau-M_1X\zeta_2]}{\pi M_1 N[2a^*(1-u_1{}^2)(2-u_1{}^2)]^{1/2}} \tag{16}$$

and

$$S=M_1b^{*1/2}u_1[N(a^{*2}+b^{*2}u_1{}^4)^{1/2}-b^*u_1{}^2]^{1/2},$$

$$R_1=a^*[u_1{}^4+N^2(1-u_1{}^4)]^{1/2}$$

$$\zeta_1=u_1\left[\frac{a^*(R_1+a^*u_1{}^2)}{2}\right]^{1/2}, \phi_1=u_1\left[\frac{a^*(R_1-a^*u_1{}^2)}{2}\right]^{1/2}$$

$$R_2=a^*[(1-u_1{}^2)^2+N^2u_1{}^2(2-u_1{}^2)]^{1/2},$$

$$\zeta_2=\left[\frac{a^*(1-u_1{}^2)[R_2+a^*(1-u_1{}^2)]}{2}\right]^{1/2}$$

$$\phi_2=\left[\frac{a^*(1-u_1{}^2)[R_2-a^*(1-u_1{}^2)]}{2}\right]^{1/2},$$

$$M_1=\left(\frac{C^*+1}{2}\right)^{1/2}, N=\frac{C^*-1}{C^*+1}$$

$$a^*=\frac{2}{k^*(C^*-1)}, b^*=\frac{1}{k^*(C^*)^{1/2}} \tag{17}$$

The original integral functions exhibited removable singularities of the order 1/2 that corresponding to F_1 occurred at $\xi_1=0$ and was removed by substitution of $u_1{}^2=\xi_1$. The original integrand functions for G_2, G_3, G_4, and G_5 had singularities at both limits of integration which were removed by substitution of $u_1{}^2=\xi_1$ in the range $0\le\xi_1\le B$ and $u_1{}^2=1-\xi_1$ in the range $B\le\xi_1\le 1$, where B is an arbitrary number in the range $0<B<1$. For convenience, B was chosen as 0.64 so that the upper limits of the integrals for the transformed variables are 0.8 and 0.6 for the functions G_2, G_3, and G_4, G_5, respectively.

The integrand functions, equations (12–16), are highly oscillatory requiring substantial precision in their numerical evaluation. Conversion of the results from the solution for an impulse to that corresponding to a finite-duration force history is effected by the convolution integral yielding the nondimensional moment m_f due to nondimensional input force $F^*(\tau,0)$ as

$$m_f(\tau,X)=\int_0^\tau F^*(\gamma)m(\tau-\gamma,X)\,d\gamma \tag{18}$$

Force F^* is determined experimentally for the system, and $m(\tau,X)$ is calculated from equations (8–10). The numerical evaluations and the plotting of the results were performed with the aid of a PDP-11 Computer. A comparison can then be provided between the experimentally determined, longitudinal strain at the outer tube radius R_0 yielding the corresponding experimental nondimensional bending moment m_e and the value predicted by equation (18). However, a similar comparison of circumferential strain (and fluid pressure) requires employment of at least a coupled membrane-shell theory for the tube and an inviscid potential representation for the fluid.

Experimental Arrangement and Procedure

The dimensions and properties of the specimens used are listed in Table 1. They were tested when empty or filled, either with distilled water or an electrical condenser liquid, Fluorinert[1]; these have a mass density ρ_F of 1.0 and 1.94 g/cm^3, respectively. The well-established elastic constants for aluminum were accepted here; however, those of PMMA were determined from impacts on a Hopkinson bar of the identical material. Signals from strain gages placed in pairs both longitudinally and circumferentially at two sections of a rod were used to measure both the rod wave velocity $c_0=(E/\rho_l)^{1/2}$ and a dynamic Poisson's ratio. This permitted calculation of the constants for the presumed elastic behavior of the bar.

Transverse impact was executed at several tube positions by the propulsion of 4.8 mm (3/16 in.) or 12.7 mm (1/2 in.) diameter steel spheres fired from a pneumatic gun with two interchangeable barrels. The initial striker velocity was determined using the device described in reference (8). A blood type pump forcing liquid from an open surface reservoir to prevent entrapment of air bubbles through 15.875 (5/8 in.) o.d., 9.525 mm (3/8 in.) i.d. Tygon tubing attached to caps at the tube ends provided laminar-flow circulation. The maximum pump capacity is 454 L/hr (120 gal/hr) at a liquid pressure of 172 kPa (25 psi). Flow was measured by a calibrated meter.

Each tube was furnished with two instrumentation stations consisting of two sets of 3.17 mm (1/2 in.) foil gages cemented longitudinally at opposite ends of a diameter and a similar single transverse gage 90 deg from the longitudinal pair along corresponding tube generators. All gages were connected in potentiometric circuits. The impact force history was measured by a 6.35 mm (0.25 in.) diameter X-cut quartz

[1] FC-48, Electronic Liquid, 3M Corp.

Downloaded 01 May 2010 to 171.66.16.249. Redistribution subject to ASME license or copyright; see http://www.asme.org/terms/Terms_Use.cfm

Downloaded 01 May 2010 to 171.66.16.249. Redistribution subject to ASME license or copyright; see http://www.asme.org/terms/Terms_Use.cfm

Table 1 Tube dimensions and properties

Specimen	Length, L, m	Outer radius, R_0 mm	Mean radius, R_m mm	Wall thickness, h, mm	h/R_m	Mass density ρ_t, g/cm^3	Young's modulus, E, GPa	Poisson's ratio, ν
Thick aluminum 2024-T3	3.046	12.70	11.51	2.413	0.210	2.70	73.0	0.33
Thin aluminum 2024-T3	3.050	12.70	12.08	1.245	0.103			
Thick PMMA	1.833	17.46	15.88	3.175	0.200	1.18	5.25	0.36
Thin PMMA	1.850	15.88	15.08	1.588	0.105			

Table 2 Transducer stations relative to impact position

Tube specimen	Distance between the stations 1–2	Distance of impact points from station 1 (cm)			
		Symmetric with respect to stations 1 and 2	Stations 1 and 2 on the same tube side from impact point		
		(I)	(II)	(III)	(IV)
Thick aluminum	$32R_m$ (36.83 cm)	$-16R_m$ (-18.42 cm)	$8R_m$ (9.21 cm)	$16R_m$ (18.42 cm)	$32R_m$ (36.83 cm)
Thin aluminum	$32R_m$ (38.66 cm)	$-16R_m$ (-19.33 cm)	$8R_m$ (9.66 cm)	$16R_m$ (19.33 cm)	$32R_m$ (38.66 cm)
Thick PMMA	$16R_m$ (25.41 cm)	$-8R_m$ (-12.70 cm)	$8R_m$ (12.70 cm)	$16R_m$ (25.41 cm)	–
Thin PMMA	$16R_m$ (24.13 cm)	$-8R_m$ (-12.06 cm)	$8R_m$(-12.06 cm)	$16R_m$ (24.13 cm)	–

R_m = mean tube radius

Table 3 Shear-coefficient and other relevant parameters for the solid-fluid systems

Tube	Shear coefficient η	Parameter $C = \frac{2(\nu_1+1)}{\eta}$	Empty			Water			Fluorinert		
			$\beta = \frac{\rho_t}{\rho_e}$	C^*	k^*	$\beta = \frac{\rho_t}{\rho_e}$	C^*	k^*	$\beta = \frac{\rho_t}{\rho_e}$	C^*	k^*
Thick aluminum	0.581	4.579	1.0	4.58	0.71	0.586	7.81	0.54	0.421	10.88	0.46
Thin aluminum	0.573	4.643	1.0	4.64	0.71	0.382	12.15	0.44	0.242	19.18	0.35
Thick PMMA	0.587	4.634	1.0	4.63	0.71	0.367	17.63	0.43	0.230	20.15	0.34
Thin PMMA	0.579	4.697	1.0	4.70	0.71	0.216	21.75	0.33	0.124	37.89	0.24

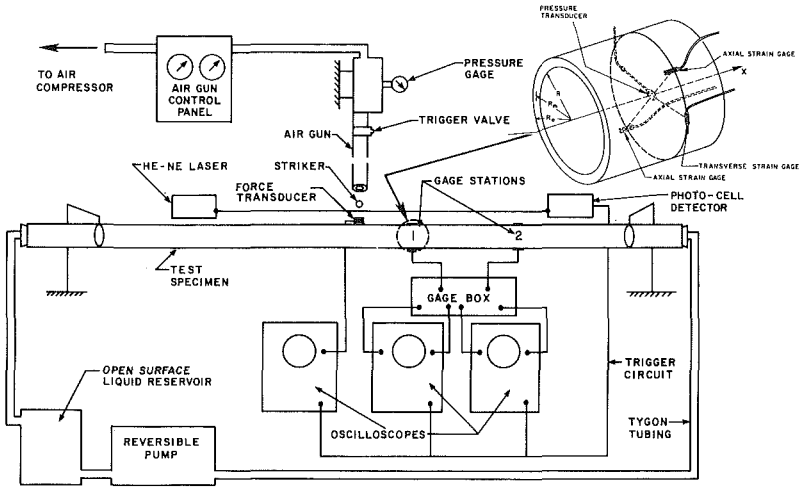


Fig. 1 Experimental arrangement and gage station

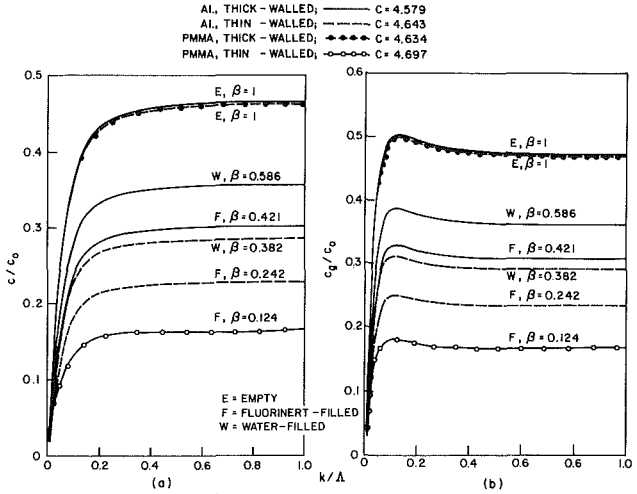


Fig. 2 Dispersion curves for flexural waves in a modified Timoshenko beam model (*a*) first mode phase velocities (*b*) first mode group velocities

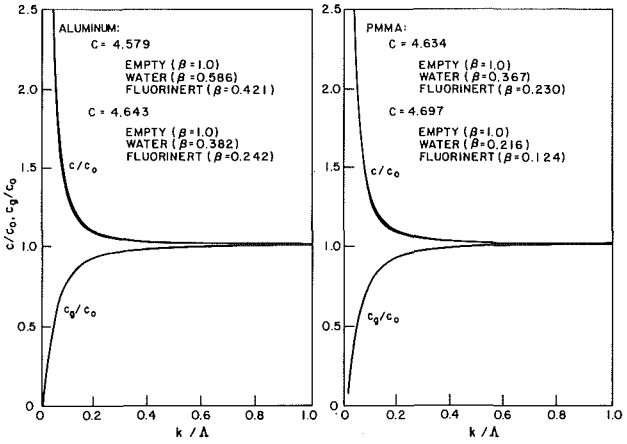


Fig. 3 Dispersion curves for the second-mode phase and group velocities of flexural waves in a modified Timoshenko beam for both thicknesses of aluminum and PMMA tubes

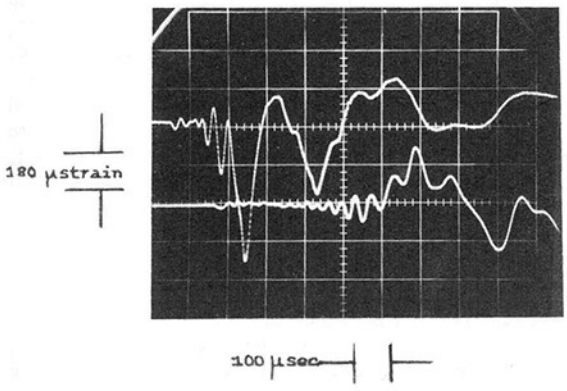


Fig. 4(*a*) Empty

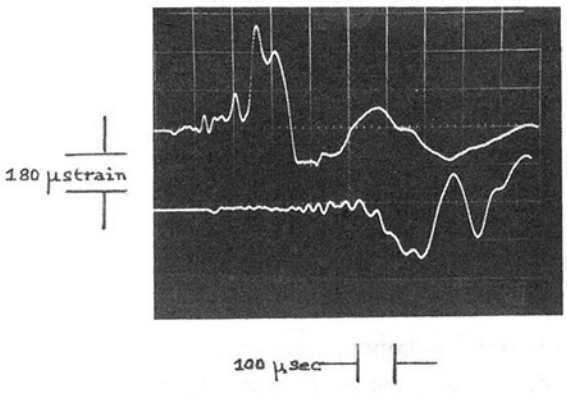


Fig. 4(*b*) Filled with water

Fig. 4 Antisymmetric strain records for the thick-walled PMMA tube struck by a 12.7 mm diameter steel sphere at impact position II at a velocity of 4 m/s

Downloaded 01 May 2010 to 171.66.16.249. Redistribution subject to ASME license or copyright; see http://www.asme.org/terms/Terms_Use.cfm

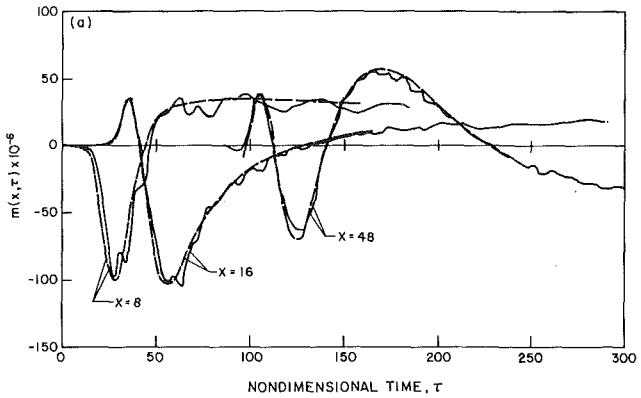


Fig. 5(a) Comparison of the experimental and theoretical nondimensional bending moment history for the empty thick-walled aluminum tube struck by the 12.7 mm diameter sphere

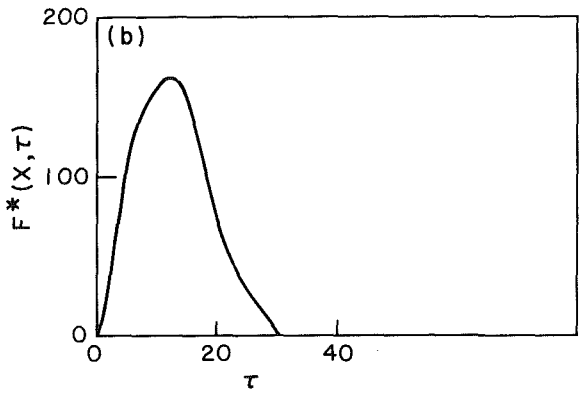


Fig. 5(b) Corresponding input force history

Fig. 5

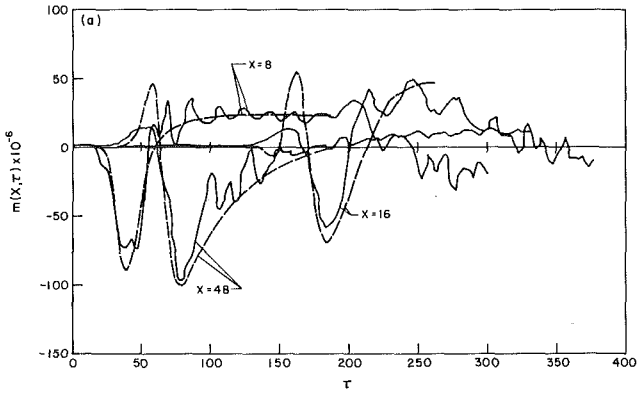


Fig. 6(a) Comparison of the experimental and theoretical nondimensional bending moment history for the Fluorinert-filled thick-walled aluminum tube struck by the 12.7 mm diameter sphere

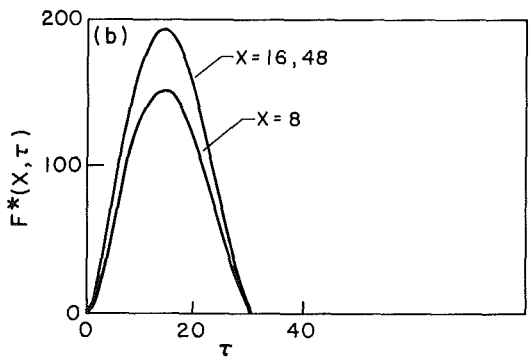


Fig. 6(b) Corresponding input force histories

Fig. 6

crystal with silvered end surfaces sandwiched between two thin aluminum disks of identical diameter. Sufficient parallel capacitance was added here so that the overall capacitance of the circuit was 2200 pF.

All signals were displayed and photographed on Tektronix 565 dual-beam oscilloscopes with amplifiers flat from d-c to about 1 MHz. A schematic of the experimental arrangement including a sketch of a typical instrumentation station is presented in Fig. 1. Table 2 summarizes the location of the two transducer stations relative to each of the four impact points employed. For each such position, repeated runs for both strikers were executed to obtain the desired records, with reproducibility monitored by measurement of impact force history. Successive tests under identical initial conditions indicated excellent repeatability of the signals.

The tubes were suspended horizontally by means of two strings. Transient phenomena were generally produced by transverse impact at an initial speed of 4 m/s and 15 m/s of the 12.7 mm diameter and 4.8 mm diameter steel spheres, respectively; for some tests at higher velocities, the force transducer was not employed to avoid its destruction. The oscilloscopes were triggered by the signal generated from the interruption by the striker of a laser beam.

Results and Discussion

Table 3 presents the values of the shear coefficient η, the density ratio β, and the coefficients C, C^*, and k^* for the present experimental configurations. Figure 2 presents representative phase and group velocities for the first-mode propagation of flexural waves in the solid-fluid Timoshenko model calculated from equations (1) and (3). The shape of the curves for the phase and group velocities, respectively, are virtually identical due to the small changes in the value of C for the four tubes. The influence of this parameter cannnot be detected for the second mode, shown in Fig. 3 for all solid-fluid combinations, nor does the density ratio β appear to govern this speed.

A typical set of antisymmetric strain records for the thick PMMA tube, either empty or water-filled, subjected to transverse impact by the 12.7 mm diameter sphere at station II is presented in Fig. 4, with an overall experimental error estimated to be about 3–4 percent. These histories are comprised of a combination of a local elastic contact phenomenon and the structural response of the tube to transverse loading. Employment of the thinner tube or smaller strikers emphasized higher-order and coupling effects, whereas use of a metal tube diminished the influence of these phenomena.

The most effective comparison between the predictions of the present analysis and experimental data was considered to be the computed and derived nondimensional moment, the latter evaluated from the measured antisymmetric strain histories, with the force data serving as the boundary condition. Figures 5–10 show this comparison for the four tubes employed either in the empty or fluid-filled condition using the 12.7 mm diameter striker. Figure 5 depicts the excellent predictive capability of the theory for the empty thick-walled aluminum tube, except for the presence of some low-amplitude, high-frequency oscillations in the data that are due to higher-order effects not encompassed by the present theory. This feature is emphasized in the presence of fluid as shown in Fig. 6; furthermore, the predicted peak moment is slightly smaller than that observed, attributed to energy conversion in the fluid, not incorporated analytically, to some form other than transverse inertia effects. Identical, although

Downloaded 01 May 2010 to 171.66.16.249. Redistribution subject to ASME license or copyright; see http://www.asme.org/terms/Terms_Use.cfm

more pronounced effects due to coupling are noted in the results for the thin-walled aluminum tube, as exemplified by Fig. 7, corresponding to the Fluorinert-filled condition.

Satisfactory correlation is also noted in the case of the thick-walled PMMA tube (Figs. 8 and 9) although the increment in the peak value of the prediction compared to the data is larger than that for the aluminum tube. This is attributed to the influence of viscoelastic behavior of the tube material that particularly affects the higher-frequency components concentrated around the peak of the transient. The correspondence deteriorates further for the thin-walled PMMA tube tests exemplified by Fig. 10 where shell response, viscoelastic behavior, and stronger solid-fluid coupling are more pronounced. An additional reason for the discrepancies in the peak magnitude in the calculations is the presence of multiple peaks in the force input that requires far greater numerical accuracy than for the case of a smooth loading history.

However, overall, excellent agreement exists between prediction and test results demonstrating that the modified Timoshenko-beam model satisfactorily describes the basic antisymmetrical propagation mode of the coupled system provided that the impact duration is sufficiently long and the shear coefficient η is properly selected. Numerical experimentation with this last parameter indicates an increase in the difference of arrival time of two successive major pulse components and a decrease in their relative amplitudes together with a somewhat later arrival of the first wave as this parameter is increased, although the differences diminish with increasing time after initial wave arrival at a given station.

Reduction of the impact duration by use of a smaller striker yielded a set of very complex strain records whose prediction appeared to require utilization of a more comprehensive model than employed. Consequently, no data of this nature will be presented or analyzed here. One of the principal mechanisms for this behavior is due to the breathing mode of the container. As expected, the presence of a streaming rather than a stationary fluid did not appear to have any effect on signals propagated in the tube due to a difference of three decades in their velocities. This would not be the case if the fluid and wave velocities were of the same order.

Placement of the impact position halfway between measuring stations resulted in axial strain records that were not mirror images, indicating the absence of pure bending in the system. As noted in reference [6], the loading generates a superposed symmetric and antisymmetric response propagating outward from the impact point; while those investigators chose their conditions so that the response at their transducers indicated essentially antisymmetric conditions, this situation arises in the present tests only for large values of X. Use of the Timoshenko theory for detailing the response of solid bars loaded flexurally yielded excellent correspondence with experimental results for all but the shortest pulses for impact loads with durations above about 2 μs [6], [9], and [10]. In comparison with the current results, it must be concluded that employment of the modified Timoshenko model for a solid-fluid system degrades more rapidly than for the homogeneous case even when a thick-walled tube is utilized, but that the antisymmetric strain component is best represented by that analysis compared to other field variables.

A description of the fluid response and effects on the system due to its presence will be provided in a companion paper.

Conclusions

An analytical and experimental study of the behavior of either empty or fluid-filled tubes of aluminum or PMMA loaded by the transverse impact of steel spheres indicated that

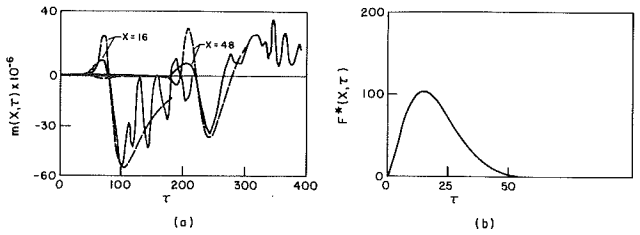


Fig. 7 Comparison of the experimental and theoretical nondimensional bending moment history (*a*) for the Fluorinert-filled thin-walled aluminum tube struck by the 12.7 mm diameter sphere (*b*) input force histories

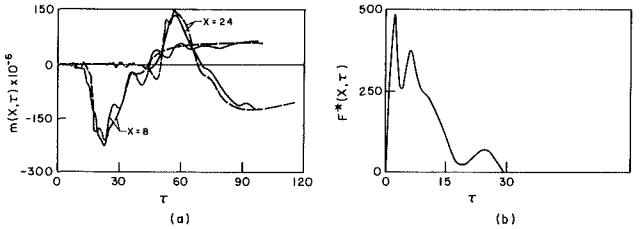


Fig. 8 Comparison of the experimental and theoretical nondimensional bending moment history (*a*) for the empty thick-walled PMMA tube struck by the 12.7 mm diameter sphere (*b*) input force history

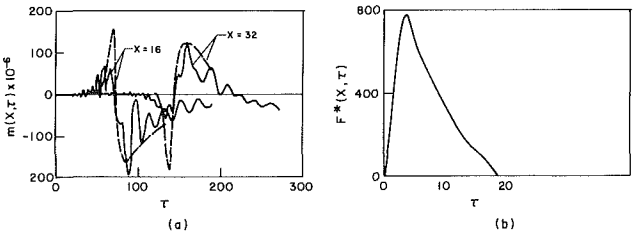


Fig. 9 Comparison of the experimental and theoretical nondimensional bending moment history (*a*) for the Fluorinert-filled thick walled PMMA tube struck by the 12.7 mm diameter sphere (*b*) input force history

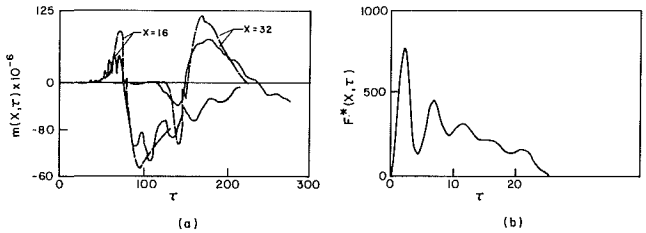


Fig. 10 Comparison of the experimental and theoretical nondimensional bending moment history (*a*) for the water-filled thin-walled PMMA tube struck by the 12.7 mm diameter sphere (*b*) input force history

1 The numerical predictions of a modified Timoshenko-beam analysis are in good correspondence with antisymmetrical strain records for impacts of moderate duration, of the order of 20 μs or more.

2 Strain records generated by shorter loading histories exhibited complicated features requiring a higher-order type of analysis for correlation. Such a theory would also be required to predict resultant fluid pressure histories.

3 The viscoelastic character of the PMMA tubes was manifested by a greater reduction in the ratio of observed to predicted peak amplitude compared to the case of aluminum vessels.

4 The observed propagation velocity of the first signal in the tube wall is not affected by the presence of a fluid, while the propagation velocity of the dominant flexural transient decreases as the density of the fluid increases, in accord with the requirements of the present analysis.

Downloaded 01 May 2010 to 171.66.16.249. Redistribution subject to ASME license or copyright; see http://www.asme.org/terms/Terms_Use.cfm

5 Prediction of higher-order effects manifested in the strain records, the most prominent being associated with the breathing mode of the tube, requires a more comprehensive analytical representation than employed.

Acknowledgment

The authors would like to express their appreciation to Drs. M. Kabo and A. Kumano for substantial experimental assistance and to Professor H. Matsumoto for valuable suggestions in the theoretical aspect of the investigation. The work was sponsored by the National Institutes of Health under Grant number 5 R01 AM 18284.

References

1 Skalak, R., "An Extension of the Theory of Water Hammer," Technical Report No. 15, Dept. of Civil Eng. and Eng. Mechanics, Columbia University, New York, AFSWP No. 922, Mar. 1955.

2 Phillips, J. W., and Walker, J. S., "A Study of Classical Water Hammer Theory," T. and A.M. Dept. Report No. 411, Dept. of Theoretical and Applied Mechanics, University of Illinois, Urbana, 1976.

3 Walker, J. S., and Phillips, J. W., "Pulse Propagation in Fluid-Filled Tubes," ASME JOURNAL OF APPLIED MECHANICS, Vol. 44, 1977, pp. 31–35.

4 Barez, F., Goldsmith, W., and Sackman, J. L., "Longitudinal Waves in Liquid-Filled Tubes," I. Theory, II. Experiments. *Int. J. Mechanical Sciences*, Vol. 21, 1976, pp. 213–221, 223–236.

5 Timoshenko, S. P., "On the Transverse Vibrations of Bars of Uniform Cross-Section," *Philosophical Magazine*, Vol. 43, series 6, 1922, pp. 125–131.

6 Goland, M., Wickersham, P. D., and Dengler, M. A., "Propagation of Elastic Impact in Beams in Bending," ASME JOURNAL OF APPLIED MECHANICS, Vol. 77, 1955, pp. 1–7.

7 Stephen, N. G., "Timoshenko's Shear Coefficient from a Beam Subjected to Gravity Loading," ASME JOURNAL OF APPLIED MECHANICS, Vol. 47, 1980, pp. 121–127.

8 Calder, C. A., "A Simple Inexpensive Projectile Velocity Gauge," *J. Scientific Instruments*, series 2, Vol. 1, 1968, pp. 882–883.

9 Ripperger, E. A., and Abramson, H. N., "A Study of the Propagation of Flexural Waves in Elastic Beams," ASME JOURNAL OF APPLIED MECHANICS, Vol. 24, 1957, pp. 431–434.

10 Plass, H. J., and Steyer, C. C., "Studies in Longitudinal and Bending Waves in Long Elastic Rods," University of Texas, Austin, Defense Research Lab. Rept. DRL-376, CM-860, 1956.

Downloaded 01 May 2010 to 171.66.16.249. Redistribution subject to ASME license or copyright; see http://www.asme.org/terms/Terms_Use.cfm

Stress Wave Propagation in a Bar of Arbitrary Cross Section

K. Nagaya
Professor,
Department of Mechanical Engineering,
Faculty of Engineering,
Gunma University,
Kiryu, Gunma, Japan

In this paper a method for solving wave propagation problems of an infinite bar of arbitrary cross section has been presented. The frequency equation for finding phase velocites for longitudinal, torsional, and flexural waves have been obtained by making use of the Fourier expansion collocation method which has been developed by the author on the vibration and dynamic response problems of membranes and plates. As a numerical example, the phase velocities versus wave numbers are calculated for elliptical and truncated elliptical cross-section bars.

Introduction

Many investigations have been made for wave propagation in an infinite bar of typical cases such as the circular [1], rectangular [1–11], and elliptical cross sections [12–14]. It is difficult to satisfy both the wave equation and the boundary conditions for complicated cross-section bars. Hence the problem of general cross-section bars has not been discussed thoroughly. For such problems, Rosenfeld and Miklowitz [15] have treated the transient wave propagation in rods of arbitrary cross section. In that paper the boundary conditions of stresses are satisfied using the double integration over the area of the rod. They have performed numerical calculations for a typical case of a circular rod only. Baltrukonis, et al. [16], also discussed complex problems of star-shaped bars by use of the conformal mapping method. Another interesting method is the Rayleigh-Ritz procedure given by Aalami [17]. However he has discussed a typical case of rectangular cross-section bars only in the numerical example. In these methods the analysis must be made for each shape of the cross section. Therefore it seems to be important to give a more straightforward method from which the result with reasonable accuracy being obtained directly. From this standpoint, this paper gives a frequency equation which is applicable to a bar of general cross section. In the analysis the exact solutions have been derived from the wave equations based on the three-dimensional theory of elasticity. The boundary conditions along the free surface of arbitrary cross section have been satisfied directly by means of the Fourier expansion collocation method which has been developed in the author's previous reports concerning vibration and dynamic response problems of membranes [18] and plates [19, 20] of arbitrary shape. As a demonstration of this method, numerical calculations have been carried out for elliptical and truncated elliptical cross-section bars. A comparison between the present and previously published results for circular and elliptical cross-section bars has also been made.

Contributed by the Applied Mechanics Division for publication in the JOURNAL OF APPLIED MECHANICS.
Discussion on this paper should be addressed to the Editorial Department, ASME, United Engineering Center, 345 East 47th Street, New York, N. Y. 10017, and will be accepted until two months after final publication of the paper itself in the JOURNAL OF APPLIED MECHANICS. Manuscript received by ASME Applied Mechanics Division, February, 1981; final revision, June, 1981.

Derivation of the Frequency Equation

If the cylindrical coordinates are taken as r,θ, and z from an arbitrary point in the cross section, and the corresponding displacements are u_r, u_θ, and u_z, the wave equations based on the three-dimensional theory of elasticity may be written

$$\left.\begin{aligned}
\rho\frac{\partial^2 u_r}{\partial t^2} &= (\lambda+2\mu)\frac{\partial\Delta}{\partial r} - \frac{2\mu}{r}\frac{\partial\omega_z}{\partial\theta} + 2\mu\frac{\partial\omega_\theta}{\partial z} \\
\rho\frac{\partial^2 u_\theta}{\partial t^2} &= (\lambda+2\mu)\frac{1}{r}\frac{\partial\Delta}{\partial\theta} - 2\mu\frac{\partial\omega_r}{\partial z} + 2\mu\frac{\partial\omega_z}{\partial r} \\
\rho\frac{\partial^2 u_z}{\partial t^2} &= (\lambda+2\mu)\frac{\partial\Delta}{\partial z} - \frac{2\mu}{r}\frac{\partial}{\partial r}(r\omega_\theta) + \frac{2\mu}{r}\frac{\partial\omega_r}{\partial\theta}
\end{aligned}\right\} \quad (1)$$

where ρ is the mass density, t is the time, λ and μ are Lame's constants, Δ is the dilatatin in cylindrical coordinates, ω_r, ω_θ, ω_z are the components of the rotation about three orthogonal directions [21]. For harmonic wave propagation, we may write

$$\left.\begin{aligned}
\Delta &= \sum_{n=0}^{\infty}\epsilon_n(\Delta_n\cos n\theta + \bar{\Delta}_n\sin n\theta)\exp[j(\eta z+pt)] \\
u_r &= \sum_{n=0}^{\infty}\epsilon_n(U_n\cos n\theta + \bar{U}_n\sin n\theta)\exp[j(\eta z+pt)] \\
u_\theta &= \sum_{z=0}^{\infty}\epsilon_n(V_n\sin n\theta - \bar{V}_n\cos n\theta)\exp[j(\eta z+pt)] \\
u_z &= \sum_{n=0}^{\infty}\epsilon_n(W_n\cos n\theta + \bar{W}_n\sin n\theta)\exp[j(\eta z+pt)]
\end{aligned}\right\} \quad (2)$$

where $\epsilon_n = 1/2$ for $n=0$, $\epsilon_n = 1$ for $n \geqq 1$, $j=\sqrt{-1}$, η is the wave number and p is the circular frequency of the harmonic wave. Substituting equations (2) into equations (1) and (3) and taking the solution for solid uniform bars, we obtain

$$\left.\begin{aligned}
\Delta_n &= -[p^2\rho/(\lambda+2\mu)]A_nJ_n - (\bar{\alpha}r) \\
U_n &= A_n\partial J_n(\bar{\alpha}r)/\partial r + B_n\eta\partial J_n(\bar{\beta}r)/\partial r \\
&\quad + C_n(n/r)J_n(\bar{\beta}r)
\end{aligned}\right.$$

Copyright © 1982 by ASME
Downloaded 01 May 2010 to 171.66.16.249. Redistribution subject to ASME license or copyright; see http://www.asme.org/terms/Terms_Use.cfm

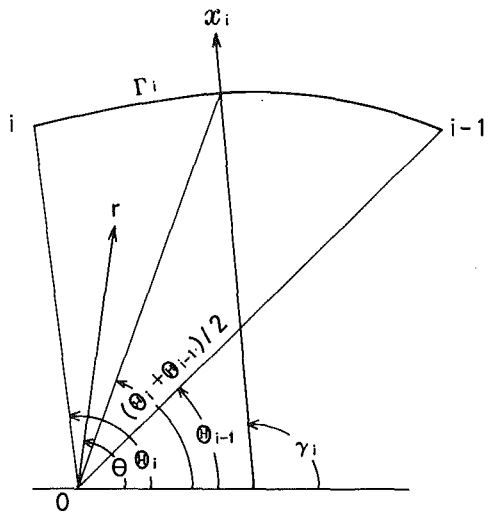


Fig. 1 Geometry of a segment of curved boundaries of the cross section

$$
\left.
\begin{aligned}
V_n &= -[A_n (n/r) J_n(\bar{\alpha} r) + B_n \eta (n/r) J_n(\bar{\beta} r) \\
&\quad + C_n \partial J_n(\bar{\beta} r)/\partial r] \\
W_n &= j[A_n \eta J_n(\bar{\alpha} r) - B_n \bar{\beta}^2 J_n(\bar{\beta} r)] \\
\bar{\alpha}^2 &= p^2\rho/(\lambda+2\mu) - \eta^2,\ \bar{\beta}^2 = p^2\rho/\mu - \eta^2
\end{aligned}
\right\} \quad (3)
$$

where A_n, B_n, and C_n are the constants of integration, and $J_n(\bar{\beta}r)$ and $J_n(\bar{\alpha}r)$ are the Bessel functions of the first kind of order n. The equations for $\bar{\Delta}_n$, $\bar{U}_n$, $\bar{V}_n$, and $\bar{W}_n$ have the same forms as Δ_n, U_n, V_n, and W_n but in which A_n, B_n, and C_n are replaced by $\bar{A}_n$, $\bar{B}_n$, and $\bar{C}_n$, respectively.

The boundary conditions for an infinite bar of stress-free surface are

$$(\sigma_{qq})_i = (\sigma_{qs})_i = (\sigma_{zq})_i = 0 \quad (4)$$

where q is the coordinate normal to the boundary and s is the coordinate in the tangential direction, σ_{qq} is the normal stress, σ_{qs} and σ_{zq} are the shearing stresses and $(\ )_i$ is the value at ith boundary. It is difficult to find the transformed expressions of the stresses in cases of the arbitrary cross-section bars because the coordinates q and s vary with the angle θ. To obtain the general transformed expressions which are applicable to the problem of general cross-section bars, the curved boundary is divided into small segments as shown in Fig. 1, and the variations of the direction of the stresses along the segments are neglected. The direction of the coordinate normal to the segment is therefore assumed to be constant. By making use of this assumption, since the angle γ_i between the normal to the segment and the reference axis has a constant value, we can assume the curvilinear coordinate s as the orthogonal coordinate y_i, and the coordinate q as the orthogonal coordinate x_i approximately. Therefore we have the following relations:

$$
\begin{aligned}
u_x &= u_r \cos(\theta-\gamma_i) - u_\theta \sin(\theta-\gamma_i), \\
u_y &= u_\theta \cos(\theta-\gamma_i) + u_r \sin(\theta-\gamma_i)
\end{aligned} \quad (5)
$$

where u_x and u_y are the displacements in the x_i and y_i-directions, respectively. The relations between the coordinates r, θ and x_i and y_i are given in references [19, 20]. Substituting these equations into the relations between the stresses and the displacements yield

$$
\left.
\begin{aligned}
\sigma_{xx} &= \lambda\Delta + 2\mu(\partial u_x/\partial x_i) \\
&= \lambda\Delta + 2\mu\{(\partial u_r/\partial r)\cos^2(\theta-\gamma_i) \\
&\quad + (1/r)(u_r + \partial u_\theta/\partial\theta)\sin^2(\theta-\gamma_i) \\
&\quad + 0.5[u_\theta/r - (1/r)\partial u_r/\partial\theta - \partial u_\theta/\partial r] \\
&\quad \times \sin 2(\theta-\gamma_i)\} \\
\sigma_{xy} &= \mu(\partial u_y/\partial x_i + \partial u_x/\partial y_i) \\
&= \mu\{[\partial u_r/\partial r - (1/r)\partial u_\theta/\partial\theta - u_r/r]\sin 2(\theta-\gamma_i) \\
&\quad + [(1/r)\partial u_r/\partial\theta + \partial u_\theta/\partial r - u_\theta/r] \\
&\quad \times [\cos^2(\theta-\gamma_i) - \sin^2(\theta-\gamma_i)]\} \\
\sigma_{zx} &= \mu(\partial u_x/\partial z + \partial u_z/\partial x_i) \\
&= \mu\{(\partial u_r/\partial z + \partial u_z/\partial r)\cos(\theta-\gamma_i) \\
&\quad - [\partial u_\theta/\partial z + (1/r)\partial u_z/\partial\theta]\sin(\theta-\gamma_i)\}
\end{aligned}
\right\} \quad (6)
$$

Substituting equations (2) into (6), the transformed expressions of the normal and the shearing stresses with respect to the ith boundary of the surface can be obtained. The transformed equations for the straight line boundary are also the same as equations (6), but the angle γ_i has a constant value in one straight line boundary. For the present problem, the sign in the square roots of the variables $\bar{\alpha}$ and $\bar{\beta}$ changes according to the value of the phase velocity. Therefore the solution is separated into three cases, that is, (a) the phase velocity is less than the shear wave velocity, (b) the shear wave velocity is less than the phase velocity and the dilatational wave velocity is greater than the phase velocity, and (c) the phase velocity is greater than the dilatational wave velocity. The transformed expressions of equations (4) are written as follows by using the phase velocity $c=p/\eta$ and the velocity $c_0=\sqrt{E/\rho}$ of infinitely long waves in a bar:

$$
\left.
\begin{aligned}
&[(s_{xx})_i + (\bar{S}_{xx})_i]\exp[j(\eta z + pt)] = 0 \\
&[(S_{xy})_i - (\bar{S}_{xy})_i]\exp[j(\eta z + pt)] = 0 \\
&[(S_{zx})_i + (\bar{S}_{zx})_i]\exp[j(\eta z + pt)] = 0
\end{aligned}
\right\} \quad (7)
$$

where E is Young's modulus and where

$$
\left.
\begin{aligned}
S_{xx} &= 0.5\, e_0{}^1(r,\theta)A_0 + 0.5\, e_0{}^2(r,\theta)B_0{}^* \\
&\quad + \sum_{n=1}^{\infty}[e_n{}^1(r,\theta)A_n + e_n{}^2(r,\theta)B_n{}^* \\
&\quad + e_n{}^3(r,\theta)C_n] \\
S_{xy} &= 0.5\, f_0{}^1(r,\theta)A_0 + 0.5\, f_0{}^2(r,\theta)\, B_0{}^* \\
&\quad + \sum_{n=1}^{\infty}[f_n{}^1(r,\theta)\, A_n + f_n{}^2(r,\theta)\, B_n{}^* \\
&\quad + f_n{}^3(r,\theta)\, C_n] \\
S_{zx} &= 0.5\, g_0{}^1(r,\theta)\, A_0 + 0.5\, g_0{}^2(r,\theta)\, B_0{}^* \\
&\quad + \sum_{n=1}^{\infty}[g_n{}^1(r,\theta)\, A_n + g_n{}^2(r,\theta)B_n{}^* \\
&\quad + g_n{}^3(r,\theta)\, C_n] \\
\bar{S}_{xx} &= 0.5\, \bar{e}_0{}^3(r,\theta)\, \bar{C}_0 + \sum_{n=1}^{\infty}[\bar{e}_n{}^1(r,\theta)\bar{A}_n \\
&\quad + \bar{e}_n{}^2(r,\theta)\bar{B}_n{}^* + \bar{e}_n{}^3(r,\theta)\bar{C}_n]
\end{aligned}
\right\} \quad (8)
$$

Downloaded 01 May 2010 to 171.66.16.249. Redistribution subject to ASME license or copyright; see http://www.asme.org/terms/Terms_Use.cfm

$$\bar{S}_{xy} = 0.5\bar{f}_0{}^3(r,\theta)\bar{C}_0 + \sum_{n=1}^{\infty}[\bar{f}_n{}^1(r,\theta)\bar{A}_n + \bar{f}_n{}^2(r,\theta)\bar{B}_n{}^* + \bar{f}_n{}^3(r,\theta)\bar{C}_n]$$

$$\bar{S}_{zx} = 0.5\bar{g}_0{}^3(r,\theta)\bar{C}_0 + \sum_{n=1}^{\infty}[\bar{g}_n{}^1 r,\theta)\bar{A}_n + \bar{g}_n{}^2(r,\theta)\bar{B}_n{}^* + \bar{g}_n{}^3(r,\theta)\bar{C}_n]$$

$B_n{}^* = B_n/b$, where b is the reference length which is included to obtain dimensionless expressions. The equations for $e_n{}^1 \sim \bar{g}_n{}^3$ are given in the Appendix.

The boundary conditions along the whole range of the boundary cannot be satisfied directly. To satisfy the boundary conditions, the Fourier expansion is performed to the equations of the boundary conditions along the boundary line of the cross section. For the present case, one straight line is considered to be one segment, while one curved line must be divided into many segments according to the convergence of the solution [18–20]. The Fourier coefficients are therefore obtained by the addition of these for the separately considered boundaries. When the cross section is symmetric about an axis, the analysis can be separated into symmetric and antisymmetric cases. Hence, when the coordinate θ is chosen from an axis of symmetry, the boundary conditions are expanded into the following Fourier series:

$$\left.\begin{aligned}
&\sum_{m=0}^{\infty}\epsilon_m[E^1_{m0}A_0 + E^2_{m0}B_0^* + \sum_{n=1}^{\infty}(E^1_{mn}A_n + E^2_{mn}B_n^* + E^3_{mn}C_n)]\cos m\theta = 0\\
&\sum_{m=1}^{\infty}[F^1_{m0}A_0 + F^2_{m0}B_0^* + \sum_{n=1}^{\infty}(F^1_{mn}A_n + F^2_{mn}B_n^* + F^3_{mn}C_n)]\sin m\theta = 0\\
&\sum_{m=0}^{\infty}\epsilon_m[G^1_{m0}A_0 + G^2_{m0}B_0^* + \sum_{n=1}^{\infty}(G^1_{mn}A_n + G^2_{mn}B_n^* + G^3_{mn}C_n)]\cos m\theta = 0
\end{aligned}\right\} \quad (9a)$$

for the symmetric mode, and

$$\left.\begin{aligned}
&\sum_{m=1}^{\infty}[\bar{E}^3_{m0}\bar{C}_0 + \sum_{n=1}^{\infty}(\bar{E}^1_{mn}\bar{A}_n + \bar{E}^2_{mn}\bar{B}_n{}^* + \bar{E}^3_{mn}\bar{C}_n)]\sin m\theta = 0\\
&\sum_{m=0}^{\infty}\epsilon_m[\bar{F}^3_{m0}\bar{C}_0 + \sum_{n=1}^{\infty}(\bar{F}^1_{mn}\bar{A}_n + \bar{F}^2_{mn}\bar{B}_n{}^* + \bar{F}^3_{mn}\bar{C}_n)]\cos m\theta = 0\\
&\sum_{m=1}^{\infty}[\bar{G}^3_{m0}\bar{C}_0 + \sum_{n=1}^{\infty}(\bar{G}^1_{mn}\bar{A}_n + \bar{G}^2_{mn}\bar{B}_n{}^* + \bar{G}^3_{mn}\bar{C}_n)]\sin m\theta = 0
\end{aligned}\right\} \quad (9b)$$

for the antisymmetric mode, where

$$\left.\begin{aligned}
E^I_{mn} &= (2\epsilon_n/\pi)\sum_{i=1}^{I}\int_{\Theta_{i-1}}^{\Theta_i} e^I_n(R_i,\theta)\cos m\theta\, d\theta,\\
F^I_{mn} &= (2\epsilon_n/\pi)\sum_{i=1}^{I}\int_{\Theta_{i-1}}^{\Theta_i} f^I_n(R_i,\theta)\sin m\theta\, d\theta\\
G^I_{mn} &= (2\epsilon_n/\pi)\sum_{i=1}^{I}\int_{\Theta_{i-1}}^{\Theta_i} g^I_n(R_i,\theta)\cos m\theta\, d\theta
\end{aligned}\right\} \quad (10a)$$

$$\left.\begin{aligned}
\bar{E}^I_{mn} &= (2\epsilon_n/\pi)\sum_{i=1}^{I}\int_{\Theta_{i-1}}^{\Theta_i} \bar{e}^I_n(R_i,\theta)\sin m\theta\, d\theta,\\
\bar{F}^I_{mn} &= (2\epsilon_n/\pi)\sum_{i=1}^{I}\int_{\Theta_{i-1}}^{\Theta_i} \bar{f}^I_n(R_i,\theta)\cos m\theta\, d\theta\\
\bar{G}^I_{mn} &= (2\epsilon_n/\pi)\sum_{i=1}^{I}\int_{\Theta_{i-1}}^{\Theta_i} \bar{g}^I_n(R_i,\theta)\sin m\theta\, d\theta
\end{aligned}\right\} \quad (10b)$$

and where $\epsilon_m = 1/2$ for $m=0$, $\epsilon_m = 1$ for $m \geqq 1$. I is the number of the segments including the straight line boundaries in the range $\theta=0$ to $\theta=\pi$ and R_i is the coordinate r at ith segment which is expressed as a function of θ. The frequency equation for determining the phase velocities may be obtained by putting the determinant of coefficients of equations (9) to zero.

The equation for a bar of which cross section having no symmetric axes is obtained in the same way. In such a case the Fourier expansion must be performed in the range $\theta=0$ to $\theta=2\pi$ with both sine and cosine terms included.

Numerical Examples

Numerical results for an elliptical cross-section bar have been obtained by Fraser [12] and Sato [13]. To investigate the accuracy of this method, numerical calculations are carried out first for this problem. As an application, numerical calculations are demonstrated to a truncated elliptical cross-section bar which has not been treated in the previous papers.

Elliptical Cross Section. If we consider a uniform bar with elliptical cross section of major axis $2a$ and minor axis $2b$, we have the following relations taking the length b as a reference length:

$$R_i/b = (a/b)/[\cos^2\theta + (a/b)^2\sin^2\theta]^{1/2} \quad (11a)$$

$$\left.\begin{aligned}
&\gamma_i = \pi/2 - \arctan[(b/a)^2/\tan\Theta_i^*]\\
&\quad \text{for} \quad \Theta_i^* < \pi/2, \quad \gamma_i = \pi/2 \quad \text{for} \quad \Theta_i^* = \pi/2,\\
&\gamma_i = \pi/2 + \arctan[(b/a)^2/|\tan\Theta_i^*|]\\
&\quad \text{for} \quad \Theta_i^* > \pi/2
\end{aligned}\right\} \quad (11b)$$

where the angle θ is chosen from the major axis and where $\Theta_i^* = (\Theta_i + \Theta_{i-1})/2$. Substituting equations (11) into equations (9) and (10), the integrands in equations (10) become expressed as functions of the independent variable θ only. The integration in equations (10) can be performed numerically, and hence the dimensionless phase velocity c/c_0

Downloaded 01 May 2010 to 171.66.16.249. Redistribution subject to ASME license or copyright; see http://www.asme.org/terms/Terms_Use.cfm

Table 1 Comparison between the present and Sato's exact values [13] for the first branch of phase velocities c/c_0 of a bar of elliptical cross section with Poisson's ratio $\nu = 0.3$

		(a)		(b)	
a/b	b/Λ	Author	Sato	Author	Sato
1	0.05	0.9978	0.9977	0.1507	0.1503
	0.1	0.9905	0.9905	0.2698	0.2699
	0.2	0.9541	0.9541	0.4133	0.4133
	0.3	0.8697	0.8696	0.4840	0.4840
	0.4	0.7636	0.7636	0.5218	0.5218
	0.5	0.6882	0.6881	0.5436	0.5436
	0.8	0.6011	0.6011	0.5703	0.5720
	1.0	0.5853	0.5852	0.5752	0.5752
2	0.05	0.9940	0.9940	0.1503	0.1502
	0.1	0.9680	0.9680	0.2691	0.2691
	0.2	0.7513	0.7513	0.4098	0.4098
	0.3	0.6451	0.6450	0.4778	0.4778
	0.4	0.6131	0.6131	0.5140	0.5140
	0.5	0.6012	0.6012	0.5350	0.5351
	0.8	0.5878	0.5872	0.5674	0.5626
	1.0	0.5789	0.5802	0.5502	0.5691
3	0.05	0.9862	0.9862	0.1501	0.1500
	0.1	0.8766	0.8766	0.2677	0.2677
	0.2	0.6473	0.6471	0.4037	0.4037
	0.3	0.6083	0.6081	0.4681	0.4681
	0.4	0.5999	0.5992	0.5028	0.5027
	0.5	0.5998	0.5962		0.5237
	0.8	0.5876	0.5882	0.5576	0.5544

(a) First branch of longitudinal mode

(b) First branch of flexural mode about the major axis

Table 2 Comparison between the present and Fraser's values [12] for the second branch of phase velocities c/c_0 of a bar of elliptical cross section with $a/b = 1.6667$ (the ellipticity is 0.8) and $\nu = 0.3$

	(a)		(b)	
b/Λ	Author	Fraser	Author	Fraser
0.12732	1.308	1.307	1.240	
0.15916	1.104	1.103	1.050	1.049
0.19099	1.013	1.013	0.9318	0.9311
0.25465	0.9137	0.9138	0.7977	0.7971
0.31831	0.8174	0.8174	0.7277	0.7273
0.38197	0.7412	0.7411	0.6869	0.6866
0.47747	0.6701	0.6700	0.6516	0.6514
0.54113	0.6420	0.6419	0.6373	0.6371
0.57296	0.6317	0.6316	0.6317	0.6316

(a) Second branch of longitudinal modes

(b) Second branch of flexural modes about the major axis

is evaluated from equations (9). For the present problem, there are four kinds of basic independent modes of wave propagation, that is, longitudinal, torsional, and two flexural modes.

(*a*) *Longitudinal Mode.* Since the vibration displacements are symmetrical about both the major and the minor axes in cases of the longitudinal mode, both terms of n and m are chosen as 0,2,4,6, . . . in equations (9*a*). In this case, since the boundary consists of a curve, the boundary line

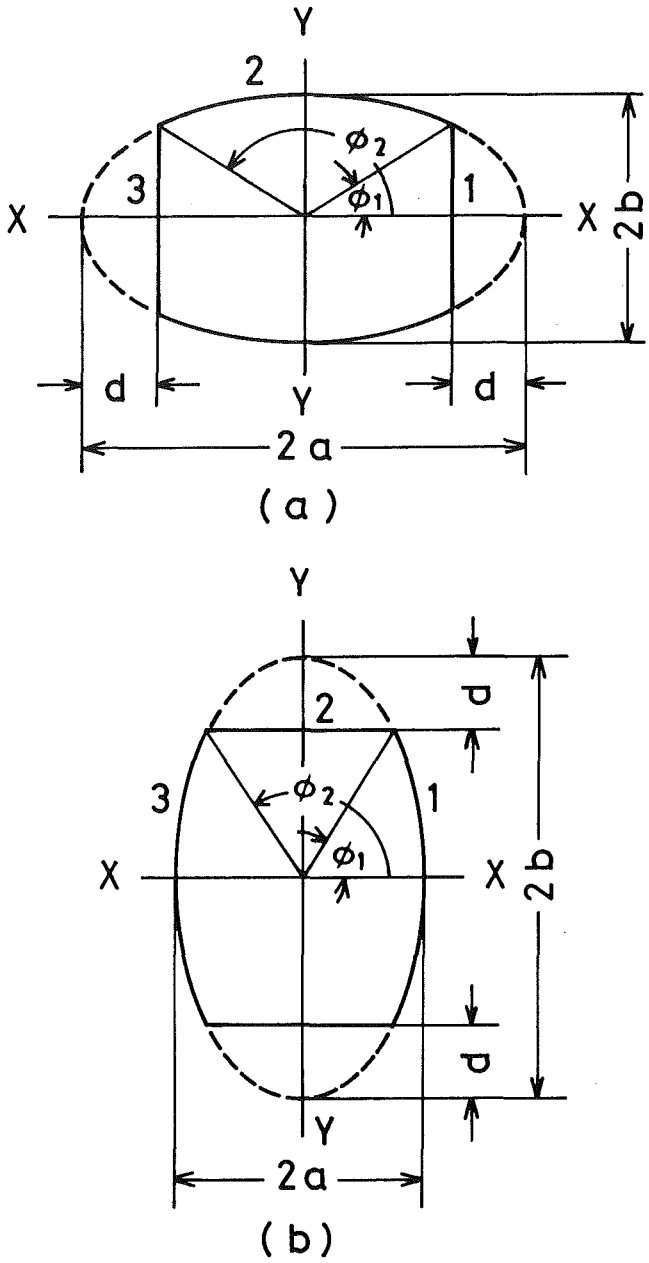


Fig. 2 Geometry of the truncated elliptical cross section

must be divided into small segments according to the convergence of the solution. In the numerical calculation an elliptical curve in the range $\theta = 0$ to $\theta = \pi$ has been divided into 15 segments and the integration for a segment is performed numerically by use of the five point Gaussian formula. The convergence of the Fourier series is good and up to five terms (n,m = 0,2,4,6,8) have been included. Table 1(*a*) depicts the comparison between the present and Sato's exact values [13] of the first branch of dimensionless phase velocities c/c_0 ($c_0 = \sqrt{E/\rho}$) of the longitudinal mode for various values of $(b/\Lambda) = (\eta b/2\pi)$, where Λ is the wavelength. Table 2(*a*) shows the present and Fraser's results for the second branch of the phase velocities c/c_0. It can be noted that the present results almost coincide with the previously published ones.

(*b*) *Torsional Mode.* Since the vibration displacements are antisymmetrical about both the axes in cases of the torsional mode, the frequency equation may be obtained from equations (9*b*) by choosing $n,m = 0,2,4, \ldots$.

(*c*) *Flexural Mode.* If we consider the flexural mode about the major axis, the vibration displacements are sym-

Downloaded 01 May 2010 to 171.66.16.249. Redistribution subject to ASME license or copyright; see http://www.asme.org/terms/Terms_Use.cfm

Table 3 Dimensionless phase velocities c/c_0 of the first branch of longitudinal modes for a bar of truncated elliptical cross section with $\nu = 0.3$

a/b	b/Λ	d/a = 0	0.1	0.2	0.3	0.4	0.5
1	0.05	0.9977	0.9978	0.9980	0.9980	0.9981	0.9983
	0.1	0.9905	0.9909	0.9913	0.9917	0.9921	0.9925
	0.2	0.9541	0.9559	0.9565	0.9562	0.9552	0.9533
	0.4	0.7636	0.7742	0.7999	0.8461	0.9077	0.9736
	0.5	0.6882	0.6966	0.7156	0.7518	0.8091	0.8911
	0.6	0.6432	0.6498	0.6636	0.6895	0.7344	0.8051
	0.7	0.6169	0.6112	0.6324	0.6505	0.6825	0.7388
	0.8	0.6011	0.6069	0.6137	0.6261	0.6489	0.6917
	0.9	0.5914	0.5931	0.6024	0.6105	0.6267	0.6587
	1.0	0.5853	0.5871	0.5956	0.6004	0.6116	0.6355
2	0.05	0.9940	0.9946	0.9953	0.9959	0.9966	0.9972
	0.1	0.9680	0.9725	0.9772	0.9816	0.9851	0.9879
	0.2	0.7513	0.7705	0.8027	0.8513	0.9063	0.9377
	0.3	0.6450	0.6511	0.6621	0.6851	0.7234	0.7766
	0.4	0.6131	0.6142	0.6160	0.6245	0.6414	0.6636
	0.5	0.6012	0.6007	0.5989	0.6017	0.6092	0.6402
	0.7	0.5914	0.5912	0.6009	0.5994	0.5891	0.5889
	0.8	0.5872	0.5878	0.5905	0.5895	0.5857	0.5844

metrical about the minor axis and antisymmetrical about the major axis. Hence the frequency equation may be obtained from equations (9*b*) by choosing $n,m = 1,3,5,7, \ldots$. Table 1(*b*) and Table 2(*b*) depict the comparison between the present and the other author's results [12, 13] for flexural modes about the major axis. The present results are in very good agreement with the previously published ones. However it is important to point out that in the present method the convergence of the Fourier series becomes poor as the cross section becomes slender.

Truncated Elliptical Cross Section. Figure 2 shows the geometry of the truncated elliptical cross section. In this case there are also four independent modes of wave propagation.

(*a*) *Longitudinal Mode.* For longitudinal modes the vibration displacements are symmetrical about the both axes $X-X$ and $Y-Y$ in Fig. 2(*a*). Therefore the terms n and m are chosen as 0,2,4,6, . . . in equations (9*a*). The geometrical values R_i and γ_i are calculated as

$$R_i/b = (a-d)/b \cos\theta, \quad \gamma_i = 0 \quad \text{for} \quad \theta \leqq \phi_1 \tag{12a}$$

for the boundary 1, and

$$R_i/b = -(a-d)/b \cos\theta, \quad \gamma_i = \pi \quad \text{for} \quad \theta \geqq \phi_2 \tag{12b}$$

for the boundary 3, where

$$\phi_1 = \arctan\{[b/(a-d)][1-(a-d)^2/a^2]^{1/2}\},$$
$$\phi_2 = \pi - \phi_1 \tag{12c}$$

The expressions of R_i and γ_i for the boundary 2 ($\phi_1 < \theta < \phi_2$) are the same as equations (11). The numerical results for this mode are tabulated in Tables 3[1] and 4. Figure 3 depicts the phase velocities c/c_0 versus the dimensionless aspect ratio d/a up to fourth branches.

(*b*) *Torsional Mode.* The vibration displacements are antisymmetrical about both axes (see Fig. 2(*a*)). Hence $n,m = 0,2,4,6, \ldots$ must be substituted in equations (9*b*).

(*c*) *Flexural Mode.* There are two independent flexural modes, that is, the mode with respect to the major axis and that to the minor axis. For the mode about the major axis, the geometrical relations in equations (11) and (12) may also be

[1] Values for $d/a = 0$ in Tables 3, 5, and 7 denote Sato's exact results [13].

Table 4 Dimensionless phase velocities c/c_0 of the second branch of longitudinal modes for a bar of truncated elliptical cross section with $\nu = 0.3$

a/b	b/Λ	d/a = 0	0.1	0.2	0.3	0.4	0.5
1	0.15	1.526	1.572	1.630	1.664	1.672	1.673
	0.2		1.193	1.234	1.260	1.271	1.277
	0.25	0.9187	0.9205	0.9163	0.9066	0.8963	0.8891
	0.3	0.8406	0.8465	0.8403	0.8256	0.8115	0.8030
	0.4	0.7145	0.7166	0.7128	0.7015	0.6896	0.6827
	0.5	0.6578	0.6568	0.6516	0.6423	0.6376	0.6325
2	0.1	1.418	1.482	1.592	1.749	1.951	2.175
	0.15	1.071	1.086	1.123	1.193	1.301	1.439
	0.2	0.9880	0.9877	0.9887	0.9941	1.016	1.085
	0.25	0.9180	0.9160	0.9121	0.9063	0.8986	0.9161
	0.3	0.8382	0.8368	0.8333	0.8276	0.8207	0.8257
	0.4	0.7178	0.7172	0.7150	0.7112	0.7083	0.7191
	0.5	0.6541	0.6536	0.6518	0.6491	0.6481	0.6571

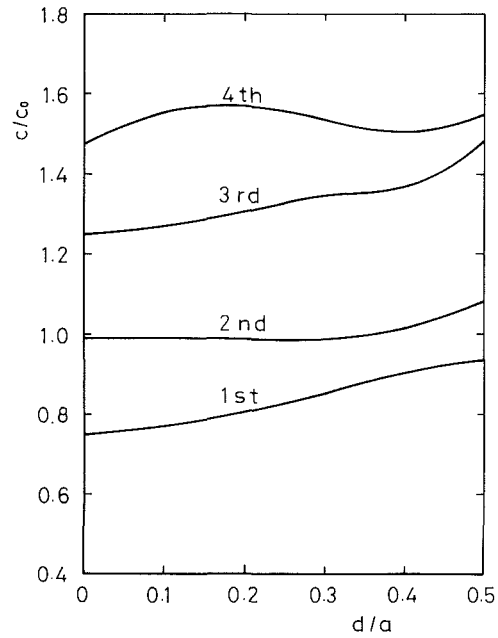


Fig. 3 Dimensionless phase velocities c/c_0 versus aspect ratios d/a of various longitudinal modes for a bar of truncated elliptical cross section with $a/b = 2$, $b/\Lambda = 0.2$, and $\nu = 0.3$

utilized, and $n,m = 1,3,5,7, \ldots$ are substituted in equations (9*b*). The phase velocities c/c_0 versus b/Λ for the flexural mode about the axis $X-X$ (see Fig. 2(*a*)) are depicted in Tables 5[1] and 6.

For the mode about the minor axis, we have the following relations (see Fig. 2(*b*)):

$$R_i/b = (1-d/b)/\sin\theta, \quad \gamma_i = \pi/2 \quad \text{for} \quad \phi_1 < \theta < \phi_2 \tag{13a}$$

for the boundary 2, where

$$\phi_1 = \arctan\{(b/a - d/a)/[1-(1-d/b)^2]^{1/2}\},$$
$$\phi_2 = \pi - \phi_1 \tag{13b}$$

The expressions for the boundaries 1 and 3 are also the same as equations (11), but the angle θ is chosen for the axis $X-X$ in Fig. 2(*b*). Table 7 depicts the numerical results of this mode.[1]

Conclusion

This paper is concerned with a method for solving wave propagation problems of an infinite uniform bar with arbitrary cross section. The frequency equation which presents

Downloaded 01 May 2010 to 171.66.16.249. Redistribution subject to ASME license or copyright; see http://www.asme.org/terms/Terms_Use.cfm

Table 5 Dimensionless phase velocities c/c_0 of the first branch of flexural modes about the major axis for a bar of truncated elliptical cross section with $\nu = 0.3$ (see Fig. 2(*a*))

a/b	b/A	d/a 0	0.1	0.2	0.3	0.4	0.5
	0.05	0.1503	0.1535	0.1556	0.1594	0.1612	0.1620
	0.1	0.2699	0.2730	0.2773	0.2814	0.2844	0.2857
	0.2	0.4133	0.4160	0.4190	0.4219	0.4236	0.4232
	0.3	0.4840	0.4859	0.4872	0.4885	0.4887	0.4866
	0.4	0.5218	0.5231	0.5233	0.5234	0.5229	0.5195
1	0.5	0.5436	0.5446	0.5441	0.5436	0.5427	0.5385
	0.6	0.5568	0.5576	0.5569	0.5561	0.5552	0.5506
	0.7	0.5651	0.5658	0.5651	0.5642	0.5634	0.5590
	0.8	0.5720	0.5710	0.5705	0.5696	0.5690	0.5653
	0.9	0.5734	0.5742	0.5740	0.5733	0.5729	0.5701
	1.0	0.5752	0.5761	0.5762	0.5757	0.5755	0.5738
	0.05	0.1502	0.1534	0.1589	0.1623	0.1637	0.1658
	0.1	0.2691	0.2744	0.2829	0.2874	0.2886	0.2911
	0.2	0.4098	0.4169	0.4265	0.4303	0.4296	0.4311
	0.3	0.4778	0.4853	0.4939	0.4965	0.4949	0.4958
	0.4	0.5140	0.5213	0.5281	0.5299	0.5283	0.5293
2	0.5	0.5351	0.5417	0.5467	0.5479	0.5469	0.5482
	0.6	0.5482	0.5537	0.5572	0.5581	0.5577	0.5595
	0.7	0.5568	0.5609	0.5632	0.5640	0.5642	0.5663
	0.8	0.5626	0.5651	0.5667	0.5674	0.5681	0.5703
	0.9	0.5665	0.5658	0.5678	0.5694	0.5704	0.5727
	1.0	0.5691	0.5594	0.5657	0.5698	0.5717	0.5739

the phase velocities of harmonic wave propagating a bar of arbitrary cross section has been given. Numerical calculations have been carried out for two cases of an elliptical cross-section bar and a truncated elliptical cross-section bar. A comparison between the present results and previously published ones shows very good agreement for an elliptical bar.

Numerical results can be obtained directly for the same frequency equation by substituting the geometrical values of the boundary of the cross section analytically or numerically. The solution yields satisfactory convergence, and the results with reasonable accuracy may be obtained easily using a minicomputer. Therefore this method has many advantages as compared with other general approximate methods.

Acknowledgments

The author wishes to thank heartily Mr. S. Ikai, Gunma University, for his various contributions throughout the progress of the present investigation. The author is also indebted to the reviewers for their useful comments.

References

1 Meeker, T. R., and Meitzler, A. H., "Physical Acoustics," Pt. A, 1964, pp. 111-167, Academic Press.

2 Morse, R. W., "Dispersion of Compressional Waves in Isotropic Rods of Rectangular Cross Section," *Journal of the Acoustical Society of America,* Vol. 20, 1948, pp. 833-838.

3 Nigro, N. J., "Steady-State Propagation in Infinite Bars of Noncircular Cross Section," *Journal of the Acoustical Society of America,* Vol. 40, 1966, pp. 1501-1508.

4 Kynch, G. J., and Green, W. A., "Vibration of Beams, I. Longitudinal Modes," *Quarterly Journal of Mechanics and Applied Mathematics,* Vol. X, 1957, pp. 63-73.

5 Fraser, W. B., "Stress Wave Propagation in Rectangular Bars," *International Journal of Solids and Structures,* Vol. 5, 1967, pp. 379-397.

6 Barr, A. D. S., "Torsional Waves in Uniform Rods of Noncircular Cross Section," *Journal of Mechanical Engineering Science,* Vol. 4, 1962, pp. 127-135.

7 Aalami, B., and Atozori, B., "Flexural Vibrations and Timoshenko's Beam Theory," *AIAA Journal,* Vol. 12, 1974, pp. 679-685.

8 Medick, M. A., "One-Dimensional Theories of Wave Propagation and Vibrations in Elastic Bars of Rectangular Cross Section," ASME JOURNAL OF APPLIED MECHANICS, Vol. 33, 1966, pp. 489-495.

Table 6 Dimensionless phase velocities c/c_0 of the second branch of flexural modes about the major axis for a bar of truncated elliptical cross section with $\nu = 0.3$ (see Fig. 2(*a*))

a/b	b/A	d/a 0	0.1	0.2	0.3	0.4	0.5
	0.1	2.091	2.071	2.038	2.003	1.971	1.945
	0.15	1.563	1.559	1.548	1.532	1.515	1.501
	0.2	1.302	1.311	1.315	1.312	1.304	1.297
1	0.25	1.136	1.154	1.173	1.182	1.181	1.179
	0.3	1.019	1.040	1.069	1.090	1.099	1.100
	0.4	0.8685	0.8839	0.9127	0.9491	0.9793	0.9860
	0.5	0.7828	0.7906	0.8072	0.8338	0.8765	0.8926
	0.6	0.7307	0.7321	0.7405	0.7568	0.7856	0.8149
	0.1	1.217	1.302	1.443	1.615	1.834	1.918
	0.15	0.9129	0.9698	1.058	1.161	1.311	1.452
	0.2	0.7804	0.8239	0.8860	0.9552	1.064	1.213
2	0.25	0.7116	0.7474	0.7946	0.8438	0.9261	1.067
	0.3	0.6719	0.7026	0.7402	0.7771	0.8421	0.9782
	0.4	0.6312	0.6549	0.6810	0.7051	0.7508	0.9005
	0.5	0.6126	0.6309	0.6500	0.6697	0.7060	0.7704
	0.6	0.6030		0.6309	0.6501	0.6785	0.7106

Table 7 Dimensionless phase velocities c/c_0 of the first branch of flexural modes about the minor axis for a bar of truncated circular cross section with $\nu = 0.3$ and $a/b = 1$ (see Fig. 2(*b*)).

b/A	d/a 0	0.1	0.2	0.3	0.4	0.5
0.05	0.1503	0.1441	0.1336	0.1171	0.1033	
0.1	0.2699	0.2602	0.2435	0.2221	0.1969	0.1695
0.2	0.4133	0.4039	0.3868	0.3633	0.3334	0.2973
0.3	0.4840	0.4767	0.4630	0.4432	0.4165	0.3826
0.4	0.5218	0.5164	0.5058	0.4899	0.4678	0.4384
0.5	0.5436	0.5396	0.5315	0.5189	0.5007	0.4758
0.6	0.5568	0.5539	0.5477	0.5377	0.5227	0.5015
0.7	0.5651	0.5631	0.5583	0.5504	0.5379	0.5199
0.8	0.5720	0.5689	0.5654	0.5592	0.5489	0.5332
0.9	0.5734	0.5727	0.5702	0.5653	0.5568	0.5432
1.0	0.5752	0.5751	0.5735	0.5698	0.5628	0.5508

9 Medick, M. A., "On Dispersion of Longitudinal Waves in Rectangular Bars," ASME JOURNAL OF APPLIED MECHANICS, Vol. 34, 1967, pp. 714-717.

10 Mindrin, R. D., and Fox, F. A., "Vibrations and Waves in Elastic Bars of Rectangular Cross Section," ASME JOURNAL OF APPLIED MECHANICS, Vol. 27, 1960, pp. 152-158.

11 Tanaka, K., and Iwahashi, Y., "Dispersion Relation of Elastic Waves in Bars of Rectangular Cross Section," *Trans. Japan Society of Mechanical Engineers* (in Japanese), Vol. 42, 1976, pp. 3771-3779.

12 Fraser, W. B., "Dispersion of Elastic Waves in Elliptical Bars," *Journal of Sound and Vibration,* Vol. 10, 1969, pp. 247-260.

13 Sato, K., "Elastic Wave Propagation in an Infinite Bars of Elliptical Cross Section," *Bulletin of the JSME,* Vol. 21, 1978, pp. 203-209.

14 Wong, W. K., Miklowitz, J., and Scott, R. A., "Propagation of Harmonic Flexural Waves in an Infinite Elastic Rod of Elliptical Cross Section," *Journal of the Acoustical Society of America,* Vol. 40, 1966, pp. 393-398.

15 Rosenfeld, R. L., and Miklowitz, J., "Elastic Wave Propagation in Rods of Arbitrary Cross Section," ASME JOURNAL OF APPLIED MECHANICS, Vol. 32, 1965, pp. 290-294.

16 Baltrukonis, J. H., Chi, M., and Laura, P. A. A., "Axial-Shear Vibrations of Star Shaped Bars-Kohn-Kato Bounds," *Developments in Mechanics, Proceedings of the Eight Midwestern Conference,* Case Institute of Technology, 1963, pp. 449-467.

17 Aalami, B., "Waves in Prismatic Guides of Arbitrary Cross Section," ASME JOURNAL OF APPLIED MECHANICS, Vol. 40, 1973, pp. 1067-1072.

18 Nagaya, K., "Dynamic Response of a Membrane With Both Curved and Straight Line Boundaries," ASME JOURNAL OF APPLIED MECHANICS, Vol. 46, 1979, pp. 667-671.

19 Nagaya, K., "Method for Solving Vibration Problems of a Plate With Arbitrary Shape," *Journal of the Acoustical Society of America,* Vol. 67, 1980, pp. 2029-2033.

Downloaded 01 May 2010 to 171.66.16.249. Redistribution subject to ASME license or copyright; see http://www.asme.org/terms/Terms_Use.cfm

20 Nagaya, K., "Dynamic Response of a Plate With Arbitrary Shape," ASME JOURNAL OF APPLIED MECHANICS, Vol. 47, 1980, pp. 620-626.
21 Love, A. E. H., *A Treatise on the Mathematical Theory of Elasticity*, 4th ed., Dover Publications, 1944, pp. 287-292.

APPENDIX

The equations for $e_n{}^1(r,\theta) \sim g_n{}^3(r,\theta)$ in equations (8) are obtained in the following three cases:

(a) For $(c/c_0) < [1/2(1+\nu)]^{1/2}$

$$e_n{}^1(r,\theta) = \{[2\nu(1+\nu)/(1-\nu)](4\pi^2/\alpha^2 b^2) \times (b^2/\Lambda^2)(c/c_0)^2 \cos n\theta - (2/\alpha^2 r^2) \times [(n^2+n+\alpha^2 r^2)\cos^2(\theta-\gamma_i)\cos n\theta - (n^2+n)\sin^2(\theta-\gamma_i)\cos n\theta - (n^2+n) \times \sin 2(\theta-\gamma_i)\sin n\theta]\}I_n(\alpha r) - (2/\alpha r)[-\cos^2(\theta-\gamma_i)\cos n\theta + \sin^2(\theta-\gamma_i) \times \cos n\theta + n\sin 2(\theta-\gamma_i)\sin n\theta]I_{n-1}(\alpha r)$$

$$e_n{}^2(r,\theta) = \eta b\{-(2\delta^2/\beta^2 r^2)[(n^2+n+\beta^2 r^2) \times \cos^2(\theta-\gamma_i)\cos n\theta - (n^2+n)\sin^2(\theta-\gamma_i) \times \cos n\theta - (n^2+n)\sin 2(\theta-\gamma_i)\sin n\theta]I_n(\beta r) - (2\delta^2/\beta r)[-\cos^2(\theta-\gamma_i) \times \cos n\theta + \sin^2(\theta-\gamma_i)\cos n\theta + n\sin 2(\theta-\gamma_i)\sin n\theta]I_{n-1}(\beta r)\}$$

$$e_n{}^3(r,\theta) = -(2\delta^2/\beta^2 r^2)\{n(n+1)[\sin^2(\theta-\gamma_i) - \cos^2(\theta-\gamma_i)]\cos n\theta + (n^2+n+0.5\beta^2 r^2)\sin 2(\theta-\gamma_i)\sin n\theta\}I_n(\beta r) - (2\delta^2/\beta r)\{n[\cos^2(\theta-\gamma_i) - \sin^2(\theta-\gamma_i)]\cos n\theta - \sin 2(\theta-\gamma_i)\sin n\theta\}I_{n-1}(\beta r)$$

$$f_n{}^1(r,\theta) = -(2/\alpha^2 r^2)\{(n^2+n+0.5\alpha^2 r^2) \times \sin 2(\theta-\gamma_i)\cos n\theta + (n^2+n)[\cos^2(\theta-\gamma_i) - \sin^2(\theta-\gamma_i)]\sin n\theta\}I_n(\alpha r) + (2/\alpha r)\{\sin 2(\theta-\gamma_i)\cos n\theta + n[\cos^2(\theta-\gamma_i) - \sin^2(\theta-\gamma_i)]\sin n\theta\}I_{n-1}(\alpha r)$$

$$f_n{}^2(r,\theta) = \eta_b\{-(2\delta^2/\beta^2 r^2)\{(n^2+n+0.5\beta^2 r^2) \times \sin 2(\theta-\gamma_i)\cos n\theta + (n^2+n)[\cos^2(\theta-\gamma_i) - \sin^2(\theta-\gamma_i)]\sin n\theta\}I_n(\beta r) + (2\delta^2/\beta r)\{\sin 2(\theta-\gamma_i)\cos n\theta + n[\cos^2(\theta-\gamma_i) - \sin^2(\theta-\gamma_i)]\sin n\theta\}I_{n-1}(\beta r)\}$$

$$f_n{}^3(r,\theta) = -(2\delta^2/\beta^2 r^2)\{-(n^2+n+0.5\beta^2 r^2) \times [\cos^2(\theta-\gamma_i) - \sin^2(\theta-\gamma_i)]\sin n\theta - (n^2+n)\sin 2(\theta-\gamma_i)\cos n\theta\}I_n(\beta r) - (2\delta^2/\beta r)\{[\cos^2(\theta-\gamma_i) - \sin^2(\theta-\gamma_i)]\sin n\theta + n\sin 2(\theta-\gamma_i)\cos n\theta\}I_{n-1}(\beta r) \quad (14)$$

$$g_n{}^1(r,\theta) = (2n/\alpha r)[-\cos(\theta-\gamma_i)\cos n\theta + \sin(\theta-\gamma_i)\sin n\theta]I_n(\alpha r) + 2I_{n-1}(\alpha r)\cos(\theta-\gamma_i)\cos n\theta$$

$$g_n{}^2(r,\theta) = \eta b\{(n\delta/\beta r)(1+\zeta^2)[-\cos(\theta-\gamma_i)\cos n\theta + \sin(\theta-\gamma_i)\sin n\theta]I_n(\beta r) + \delta(1+\zeta^2)I_{n-1}(\beta r)\cos(\theta-\gamma_i)\cos n\theta\}$$

$$g_n{}^3(r,\theta) = (n\delta/\beta r)[\cos(\theta-\gamma_i)\cos n\theta - \sin(\theta-\gamma_i) + \sin n\theta]I_n(\beta r) + \delta I_{n-1}(\beta r)\sin(\theta-\gamma_i)\sin n\theta$$

$$\alpha = (2\pi/\Lambda)[1-(1+\nu)(1-2\nu)(c/c_0)^2/(1-\nu)]^{1/2}$$

$$\beta = (2\pi/\Lambda)[1-2(1+\nu)(c/c_0)^2]^{1/2}$$

$$\delta = \{[1-2(1+\nu)(c/c_0)^2]/[1-(1+\nu)(1-2\nu) \times (c/c_0)^2/(1-\nu)]\}^{1/2}$$

$$\zeta = [1-2(1+\nu)(c/c_0)^2]^{1/2}$$

(b) For $[1/2(1+\nu)]^{1/2} < (c/c_0) < [(1-\nu)/(1+\nu)(1-2\nu)]^{1/2}$

$$e_n{}^2(r,\theta) = \eta b\{-(2\delta^2/\beta^2 r^2)[(n^2+n-\beta^2 r^2) \times \cos^2(\theta-\gamma_i)\cos n\theta - (n^2+n)\sin^2(\theta-\gamma_i) \times \cos n\theta - (n^2+n)\sin 2(\theta-\gamma_i)\sin n\theta]J_n(\beta r) - (2\delta^2/\beta r)[-\cos^2(\theta-\gamma_i)\cos n\theta + \sin^2(\theta-\gamma_i)\cos n\theta + n\sin 2(\theta-\gamma_i) + \sin n\theta]J_{n-1}(\beta r)\}$$

$$e_n{}^3(r,\theta) = -(2\delta^2/\beta^2 r^2)\{n(n+1)[\sin^2(\theta-\gamma_i) - \cos^2(\theta-\gamma_i)]\cos n\theta + (n^2+n-0.5\beta^2 r^2) \times \sin 2(\theta-\gamma_i)\sin n\theta\}J_n(\beta r) - (2\delta^2/\beta r)\{n[\cos^2(\theta-\gamma_i) - \sin^2(\theta-\gamma_i)]\cos n\theta - \sin 2(\theta-\gamma_i)\sin n\theta\}J_{n-1}(\beta r)$$

$$f_n{}^2(r,\theta) = \eta b\{-(2\delta^2/\beta^2 r^2)\{(n^2+n-0.5\beta^2 r^2) \times \sin 2(\theta-\gamma_i)\cos n\theta + (n^2+n)[\cos^2(\theta-\gamma_i) - \sin^2(\theta-\gamma_i)]\sin n\theta\}J_n(\beta r) + (2\delta^2/\beta r)\{\sin 2(\theta-\gamma_i)\cos n\theta + n[\cos^2(\theta-\gamma_i) - \sin^2(\theta-\gamma_i)]\sin n\theta\}J_{n-1}(\beta r)\}$$

$$f_n{}^3(r,\theta) = -(2\delta^2/\beta^2 r^2)\{-(n^2+n-0.5\beta^2 r^2)$$

Downloaded 01 May 2010 to 171.66.16.249. Redistribution subject to ASME license or copyright; see http://www.asme.org/terms/Terms_Use.cfm

$$+[\cos^2(\theta-\gamma_i)-\sin^2(\theta-\gamma_i)]\sin n\theta$$
$$-(n^2+n)\sin 2(\theta-\gamma_i)\cos n\theta\}J_n(\beta r)$$
$$-(2\delta^2/\beta r)\{[\cos^2(\theta-\gamma_i)-\sin^2(\theta-\gamma_i)]\sin n\theta$$
$$+n\sin 2(\theta-\gamma_i)\cos n\theta\}J_{n-1}(\beta r)$$

$$g_n{}^2(r,\theta)=\eta b\{(n\delta/\beta r)(1-\zeta^2)[-\cos(\theta-\gamma_i)\cos n\theta$$
$$+\sin(\theta-\gamma_i)\sin n\theta]J_n(\beta r)$$
$$+\delta(1-\zeta^2)J_{n-1}(\beta r)\cos(\theta-\gamma_i)\cos n\theta\}$$

$$g_n{}^3(r,\theta)=(n\delta/\beta r)[\cos(\theta-\gamma_i)\cos n\theta$$
$$-\sin(\theta-\gamma_i)\sin n\theta]J_n(\beta r) \qquad (15)$$
$$+\delta J_{n-1}(\beta r)\sin(\theta-\gamma_i)\sin n\theta$$

$$\alpha=(2\pi/\Lambda)[1-(c/c_0)^2(1+\nu)(1-2\nu)/(1-\nu)]^{1/2}$$

$$\beta=(2\pi/\Lambda)[2(c/c_0)^2(1+\nu)-1]^{1/2}$$

$$\delta=\{[2(c/c_0)^2(1+\nu)-1]/[1-(c/c_0)^2(1+\nu)$$
$$\times(1-2\nu)/(1-\nu)]\}^{1/2}$$

$$\zeta=[2(c/c_0)^2(1+\nu)-1]^{1/2}$$

where $I_n(\alpha r)$ and $I_n(\beta r)$ are the modified Bessel functions of the first kind of order n, E is Young's modulus, ν is Poisson's ratio, b is the reference length which is used to obtain the nondimensional expressions, and Λ is the wavelength. In this case the expressions for $e_n^1(r,\theta)$, $f_n^1(r,\theta)$, and $g_n^1(r,\theta)$ are the same as equations (14).

(c) For $[(1-\nu)/(1+\nu)(1-2\nu)]^{1/2} < (c/c_0)$

$$e_n{}^1(r,\theta)=\{-[2\nu(1+\nu)/(1-\nu)](4\pi^2/\alpha^2b^2)(b/\Lambda)^2$$
$$\times(c/c_0)^2\cos n\theta+(2/\alpha^2r^2)[(n^2+n-\alpha^2r^2)$$
$$\times\cos^2(\theta-\gamma_i)\cos n\theta-(n^2+n)\sin^2(\theta-\gamma_i)\cos n\theta$$
$$-(n^2+n)\sin 2(\theta-\gamma_i)\sin n\theta]\}J_n(\alpha r)$$
$$+(2/\alpha r)[-\cos^2(\theta-\gamma_i)\cos n\theta+\sin^2(\theta-\gamma_i)$$
$$+\cos n\theta+n\sin 2(\theta-\gamma_i)\sin n\theta]J_{n-1}(\alpha r)$$

$$e_n{}^2(r,\theta)=\eta b\{(2\delta^2/\beta^2r^2)[(n^2+n-\beta^2r^2)$$
$$\times\cos^2(\theta-\gamma_i)\cos n\theta-(n^2+n)\sin^2(\theta-\gamma_i)\cos n\theta$$
$$-(n^2+n)\sin 2(\theta-\gamma_i)\sin n\theta]J_n(\beta r)$$
$$+(2\delta^2/\beta r)[-\cos^2(\theta-\gamma_i)\cos n\theta$$
$$+\sin^2(\theta-\gamma_i)\cos n\theta+n\sin 2(\theta-\gamma_i)$$
$$\times\sin n\theta]J_{n-1}(\beta r)\}$$

$$e_n{}^3(r,\theta)=(2\delta^2/\beta^2r^2)\{n(n+1)[\sin^2(\theta-\gamma_i)$$
$$-\cos^2(\theta-\gamma_i)]\cos n\theta+(n^2+n-0.5\beta^2r^2)$$
$$\times\sin 2(\theta-\gamma_i)\sin n\theta\}J_n(\beta r)$$
$$+(2\delta^2/\beta r)\{n[\cos^2(\theta-\gamma_i)-\sin^2(\theta-\gamma_i)]$$
$$\times\cos n\theta-\sin 2(\theta-\gamma_i)\sin n\theta\}J_{n-1}(\beta r)$$

$$f_n{}^1(r,\theta)=(2/\alpha^2r^2)\{(n^2+n-0.5\alpha^2r^2)$$
$$\times\sin 2(\theta-\gamma_i)\cos n\theta+(n^2+n)[\cos^2(\theta-\gamma_i)$$
$$-\sin^2(\theta-\gamma_i)]\sin n\theta\}J_n(\alpha r)$$
$$-(2/\alpha r)\{\sin 2(\theta-\gamma_i)\cos n\theta$$
$$+n[\cos^2(\theta-\gamma_i)-\sin^2(\theta-\gamma_i)]\sin n\theta\}J_{n-1}(\alpha r)$$

$$f_n{}^2(r,\theta)=\eta b\Big\{(2\delta^2/\beta^2r^2)\{(n^2+n-0.5\beta^2r^2)$$
$$\times\sin 2(\theta-\gamma_i)\cos n\theta+(n^2+n)[\cos^2(\theta-\gamma_i)$$
$$-\sin^2(\theta-\gamma_i)]\sin n\theta\}J_n(\beta r)$$
$$-(2\delta^2/\beta r)\{\sin 2(\theta-\gamma_i)\cos n\theta+n[\cos^2(\theta-\gamma_i)$$
$$-\sin^2(\theta-\gamma_i)]\sin n\theta\}J_{n-1}(\beta r)\Big\}$$

$$f_n{}^3(r,\theta)=(2\delta^2/\beta^2r^2)\{-(n^2+n-0.5\beta^2r^2)$$
$$\times[\cos^2(\theta-\gamma_i)-\sin^2(\theta-\gamma_i)]\sin n\theta$$
$$-(n^2+n)\sin 2(\theta-\gamma_i)\cos n\theta\}J_n(\beta r)$$
$$+(2\delta^2/\beta r)\{[\cos^2(\theta-\gamma_i)-\sin^2(\theta-\gamma_i)] \qquad (16)$$
$$\times\sin n\theta+n\sin 2(\theta-\gamma_i)\cos n\theta\}J_{n-1}(\beta r)$$

$$g_n{}^1(r,\theta)=(2n/\alpha r)[-\cos(\theta-\gamma_i)\cos n\theta$$
$$+\sin(\theta-\gamma_i)\sin n\theta]J_n(\alpha r)$$
$$+2J_{n-1}(\alpha r)\cos(\theta-\gamma_i)\cos n\theta$$

$$g_n{}^2(r,\theta)=\eta b\{(n\delta/\beta r)(1-\zeta^2)[-\cos(\theta-\gamma_i)\cos n\theta$$
$$+\sin(\theta-\gamma_i)\sin n\theta]J_n(\beta r)$$
$$+\delta(1-\zeta^2)J_{n-1}(\beta r)\cos(\theta-\gamma_i)\cos n\theta\}$$

$$g_n{}^3(r,\theta)=(n\delta/\beta r)[\cos(\theta-\gamma_i)\cos n\theta$$
$$-\sin(\theta-\gamma_i)\sin n\theta]J_n(\beta r)$$
$$+\delta J_{n-1}(\beta r)\sin(\theta-\gamma_i)\sin n\theta$$

$$\alpha=(2\pi/\Lambda)[(c/c_0)^2(1+\nu)(1-2\nu)/(1-\nu)-1]^{1/2}$$

$$\beta=(2\pi/\Lambda)[2(c/c_0)^2(1+\nu)-1]^{1/2}$$

$$\delta=\{[2(1+\nu)(c/c_0)^2-1]/[(1+\nu)(1-2\nu)$$
$$\times(c/c_0)^2/(1-\nu)-1]\}^{1/2}$$

$$\zeta=[2(1+\nu)(c/c_0)^2-1]^{1/2}$$

The expressions for $\bar{e}_n^1(r,\theta)\sim\bar{g}_n^3(r,\theta)$ have the same forms as $e_n^1(r,\theta)\sim g_n^3(r,\theta)$ in equations (14)–(16), but in which cos $n\theta$ is replaced by sin $n\theta$ and sin $n\theta$ is replaced by $-\cos n\theta$.

Downloaded 01 May 2010 to 171.66.16.249. Redistribution subject to ASME license or copyright; see http://www.asme.org/terms/Terms_Use.cfm

K. J. Bathe
Associate Professor.
Mem. ASME

C. A. Almeida
Graduate Student.

Department of Mechanical Engineering,
Massachusetts Institute
of Technology,
Cambridge, Mass. 02139

A Simple and Effective Pipe Elbow Element—Interaction Effects

Our elbow element presented in an earlier communication is enhanced to account for interaction effects between elbows and rigid flanges, elbows of different curvatures, and elbows joining straight pipe sections. The interaction effects are modeled by including the appropriate additional strain terms in the stiffness matrix formulation and by using a penalty procedure to enforce the continuity of the derivatives in the pipe skin radial displacements. The enhancement in the formulation has been implemented and the results of various sample analyses are presented.

1 Introduction

In a previous communication, we presented a basic elbow pipe element [1], which we formulated using the displacement-based finite element method. The essential ingredients of the formulation are the specific displacement assumptions used and the stress and strain components included in the evaluation of the strain energy of the element.

The displacements used to formulate the element are, first, axial, torsional, and bending displacements with the assumption that the cross section of the elbow remains plane. Considering the element in Fig. 1, we have the cubic displacement interpolation

$$u_i(r,s,t) = \sum_{k=1}^{4} h_k u_i^k + t\sum_{k=1}^{4} \bar{a}_k h_k V_{ti}^k + s\sum_{k=1}^{4} \bar{a}_k h_k V_{si}^k;\ i = 1,2,3 \tag{1}$$

with

$$\mathbf{V}_t^k = \theta^k \times {}^0\mathbf{V}_t^k$$
$$\mathbf{V}_s^k = \theta^k \times {}^0\mathbf{V}_s^k \tag{2}$$

where

- r,s,t = isoparametric coordinates [2]
- u_i = Cartesian displacement of material point (r,s,t)
- $h_k(r)$ = isoparametric interpolation functions [1,2]
- u_i^k = Cartesian displacements of nodal point k
- θ^k = rotations at nodal point k
- $\bar{a}_k$ = outer radius of element at nodal point k
- ${}^0V_{ti}^k$ = component i of unit vector ${}^0\mathbf{V}_t^k$, in direction t at nodal point k
- ${}^0V_{si}^k$ = component i of unit vector ${}^0\mathbf{V}_s^k$, in direction s at nodal point k

The displacement interpolations in equation (1) correspond to the displacements of a beam with a circular cross section which does not distort either in or out of its plane.

The second displacement assumption is that the elbow can ovalize with the displacement patterns, see Fig. 2,

$$w_\xi(r,\phi) = \sum_{k=1}^{4}\Bigg(\underbrace{\sum_{m=1}^{N_c} h_k c_m^k \sin 2m\phi}_{\text{in-plane bending}} + \underbrace{\sum_{m=1}^{N_d} h_k d_m^k \cos 2m\phi}_{\text{out-of-plane bending}}\Bigg) \tag{3}$$

where the assumption is that (see reference [1])

$$w_\zeta = -\frac{dw_\xi}{d\phi} \tag{4}$$

and the c_m^k and d_m^k, $k = 1, 2, 3, 4$, are the unknown generalized ovalization displacements. Depending on the pipe geometry and the type of loading, it can be sufficient to include only the first, or first two, terms of one (or both) double summation(s). In the implementation of the element, we have allowed N_c to be 0 (no ovalization), 1, 2, or 3, and similarly for N_d [1]. The total displacements of the element are the sum of the displacements presented in equations (1) and (3). Hence, for example, with N_c and N_d equal to 3, a typical nodal point k carries the unknown displacements

$$\mathbf{u}^{kT} = [u_1^k\ u_2^k\ u_3^k\ \theta_1^k\ \theta_2^k\ \theta_3^k \mid c_1^k\ c_2^k\ c_3^k \mid d_1^k\ d_2^k\ d_3^k] \tag{5}$$

The element stiffness matrix of the elbow was obtained by including in the strain energy the usual longitudinal and shear strains corresponding to a curved circular cross section beam whose cross section does not distort and the strains due to ovalization. Using the coordinate axes defined in Figs. 1 and 2, the ovalization strains included were

$$(\epsilon_{\eta\eta})_{ov} = \frac{w_R}{R - a\cos\phi} \tag{6}$$

and

$$(\epsilon_{\xi\xi})_{ov} = -\frac{1}{a^2}\left[w_\zeta + \frac{d^2 w_\zeta}{d\phi^2}\right]\zeta \tag{7}$$

Contributed by the Applied Mechanics Division for publication in the JOURNAL OF APPLIED MECHANICS.
Discussion on this paper should be addressed to the Editorial Department, ASME, United Engineering Center, 345 East 47th Street, New York, N.Y. 10017, and will be accepted until two months after final publication of the paper itself in the JOURNAL OF APPLIED MECHANICS. Manuscript received by ASME Applied Mechanics Division, March, 1981; final revision, July, 1981.

Copyright © 1982 by ASME
Downloaded 01 May 2010 to 171.66.16.249. Redistribution subject to ASME license or copyright; see http://www.asme.org/terms/Terms_Use.cfm

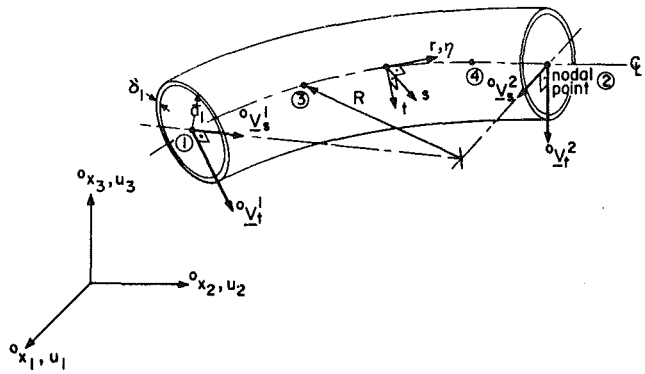


Fig. 1 Geometry of pipe elbow element

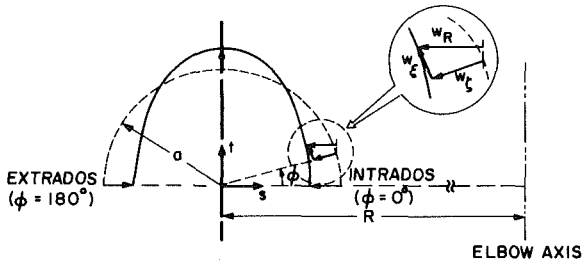


Fig. 2 Displacement of deformed cross section. (First von Kármán mode; w_ζ is shown negative.) Pipe mean radius is a.

The basic assumption in using the foregoing strain components only is that, in essence, each differential length of the elbow can ovalize independently, although by virtue of using equation (3), the ovalization displacements are continuous within an element and across element boundaries. Therefore, the interaction effects in the ovalization between elbows of different curvatures, an elbow and a straight pipe section, and an elbow and a rigid flange cannot be properly modeled. As we pointed out in [1], to render the element applicable to such situations, it is necessary to extend the basic formulation.

The objective in this paper is to amend our element formulation given in [1] in a very simple way to also account for interaction effects. This is achieved by including in the formulation additional important strain terms formulation that are identified using thin shell theory, and using a penalty procedure to enforce the required continuity conditions.

In the next section of this paper, we discuss the additional strain terms that are included in the formulation so that the element is applicable to the modeling of interaction effects. The presentation shows that it is then also necessary to enforce continuity in the derivatives of the ovalization displacements w_ζ with respect to the longitudinal membrane coordinate η. This continuity is imposed using a penalty procedure as discussed in Section 3. The amendments in the formulation of the element have been implemented in the computer program ADINAP, and in Section 4 we give the results obtained in the analyses of some problems.

2 Strain Terms Used in our Elbow Formulation

Considering the skin of the elbow to be a doubly curved thin shell [3], we can identify the following important strain terms, which have not been included in our original formulation and which are due to a variation of ovalization along the longitudinal axis of the elbow,

$$(\epsilon^I_{\eta\eta})_{ov} = -\left[\left(\frac{1}{R-a\cos\phi}\right)^2 \frac{d^2 w_\zeta}{d\theta^2}\right]\zeta \tag{8}$$

and

$$(\gamma^I_{\eta\xi})_{ov} = \left(\frac{1}{R-a\cos\phi}\right)\frac{dw_\xi}{d\theta} \tag{9}$$

In equations (8) and (9), the superscript "I" refers to the fact that these strain terms need be included in the formulation if interaction effects are important.

The strain term in equation (8) is due to longitudinal bending of the pipe skin and can directly be evaluated using the interpolation of w_ζ given in equations (3) and (4). However, since this term contains the second derivative of the pipe skin radial displacement, it is necessary to enforce in the finite element formulation continuity in the first derivative [2]. This is achieved using a penalty procedure as described in Section 3.

The shear strain term in equation (9) is a function of $dw_\xi/d\theta$ and therefore only requires continuity in w_ξ, which is already assured in the formulation.

Using the strain expressions in equations (8) and (9) and the displacement interpolation in equations (3) and (4), we can now directly amend the strain-displacement matrix given in reference [1]. Namely, to include the foregoing strain terms in our elbow formulation, we simply need to add to the matrices $\mathbf{B}^k_{ov1}$ and $\mathbf{B}^k_{ov3}$ defined in reference [1], and the following contributions, respectively,

$$\mathbf{B}^{Ik}_{ov1} = \frac{d}{dr}\begin{bmatrix} \frac{dh_k}{dr} & (a^I_1 & a^I_2 & a^I_3) \\ h_k & (b^I_1 & b^I_2 & b^I_3) \\ & 0 & 0 & 0 \end{bmatrix} \tag{10}$$

where,

$$a^I_l = \left[\frac{2}{(R_n - a\cos\phi)\theta_n}\right]^2 (m)\cos(m\phi)\zeta \tag{11}$$

$$b^I_l = \left[\frac{2}{(R_n - a\cos\phi)\theta_n}\right]\sin(m\phi) \tag{12}$$

$m = 2l$; $R_n\theta_n$ = length of elbow at center line

$$\mathbf{B}^{Ik}_{ov3} = \frac{d}{dr}\begin{bmatrix} \frac{dh_k}{dr} & (\tilde{a}^I_1 & \tilde{a}^I_2 & \tilde{a}^I_3) \\ h_k & (\tilde{b}^I_1 & \tilde{b}^I_2 & \tilde{b}^I_3) \\ & 0 & 0 & 0 \end{bmatrix} \tag{13}$$

where,

$$\tilde{a}^I_l = -\left[\frac{2}{(R_n - a\cos\phi)\theta_n}\right]^2 (m)\sin(m\phi)\zeta \tag{14}$$

$$\tilde{b}^I_l = \left[\frac{2}{(R_n - a\cos\phi)\theta_n}\right]\cos(m\phi) \tag{15}$$

The foregoing expressions are for a curved pipe. If a straight pipe is considered, the term $[2/(R_n - a\cos\phi)\theta_n]$ needs to be replaced by $[2/l]$ where l is the total length of the element.

3 Imposition of Continuity on Derivative of Pipe Skin Radial Displacement

The objective is to enforce continuity on the first derivative of the ovalization displacement w_ζ between elements without introducing additional degrees of freedom. In the classical analysis of beam structures, this continuity is achieved by introducing beam rotational degrees of freedom. However, we can enforce the continuity in our formulation without the use of rotational degrees of freedom using a penalty

Downloaded 01 May 2010 to 171.66.16.249. Redistribution subject to ASME license or copyright; see http://www.asme.org/terms/Terms_Use.cfm

procedure. The basic technique in this method is to add the constraint to be achieved in the solution, say,

$$\text{CONSTRAINT} = 0 \tag{16}$$

to the variational indicator of the problem in the following form,

$$\Pi = U - W + \frac{\alpha}{2}\int_0^{2\pi} (\text{CONSTRAINT})^2\, d\phi \tag{17}$$

where U and W are the total strain energy and total potential of the external loads, respectively, and α is the penalty parameter. The solution obtained using equation (17) with $\delta\Pi = 0$ will satisfy the condition in equation (16) to the required accuracy provided α is selected to be sufficiently large [2, 4–6].

Considering our elbow element, we want to be able to impose the constraints corresponding to two different conditions: first, the fixity condition when an element is clamped to a rigid flange and, second, the continuity condition when elements are joined.

3.1 Fixity Condition. When an element is fixed or clamped to a rigid flange, as shown schematically in Fig. 3(*a*), the boundary conditions are that at $x = 0$ there is no ovalization and $dw_\zeta/dx = 0$. Hence, we have, corresponding to equation (3)

$$c_m^i = d_m^i = 0 \quad (\text{all } m) \tag{18}$$

and

$$\left[\frac{2}{(R_n - a\cos\phi)\theta_n}\right]\frac{dw_\zeta}{dr}\bigg|_{r=-1} = 0 \tag{19}$$

where

$$\frac{dw_\zeta}{dr}\bigg|_{r=-1} = -\sum_{k=1}^{4}\left(\sum_{m=1}^{N_c} 2m\, c_m^k \frac{dh_k}{dr}\bigg|_{r=-1}\cos 2m\phi - \sum_{m=1}^{N_d} 2m\, d_m^k \frac{dh_k}{dr}\bigg|_{r=-1}\sin 2m\phi\right) \tag{20}$$

The constraint in equation (18) simply means that the ovalization degrees of freedom at node i must be set equal to zero, whereas the constraint in equation (19) is imposed with a penalty parameter. Using, in accordance with equation (16),

$$\text{CONSTRAINT} = \left[\frac{2}{(R_n - a\cos\phi)\theta_n}\frac{dw_\zeta}{dr}\bigg|_{r=-1} - 0\right] \tag{21}$$

then substituting into equation (17) and invoking the stationarity condition on Π results into the following penalty matrix

$$\mathbf{K}_p^F = \alpha\int_0^{2\pi} \mathbf{G}_F{}^T\left[\frac{2}{(R_n - a\cos\phi)\theta_n}\right]^2 \mathbf{G}_F\, d\phi \tag{22}$$

where

$$\mathbf{G}_F = [\ldots \bar{a}_1^k\ \bar{a}_2^k\ \bar{a}_3^k\ \bar{b}_1^k\ \bar{b}_2^k\ \bar{b}_3^k \ldots] \tag{23}$$

$$\bar{a}_m^k = -2m\frac{dh_k}{dr}\bigg|_{r=-1}\cos 2m\phi \tag{24}$$

$$\bar{b}_m^k = 2m\frac{dh_k}{dr}\bigg|_{r=-1}\sin 2m\phi \tag{25}$$

and $\mathbf{K}_p^F$ is defined corresponding to the degrees of freedom

$$\mathbf{u}^{F^T} = [\ldots \underbrace{c_1^k\ c_2^k\ c_3^k\ d_1^k\ d_2^k\ d_3^k}_{\text{node } k}\ \ldots] \tag{26}$$

The matrix $\mathbf{K}_p^F$ with a relatively large value of α is added using the usual direct stiffness matrix procedure [2] to enforce the constraint in equation (21). The study in Section 4 illustrates how an appropriate magnitude for α is chosen.

3.2 Continuity Condition. At the intersection of two elbow elements, as shown in Fig. 3(*b*), the ovalization is automatically continuous because the same ovalization degrees of freedom pertain to both elements. In addition, we have the continuity condition

$$\text{CONSTRAINT} = \left[\frac{2}{(R_n - a\cos\phi)\theta_n}\right]\frac{dw_\zeta}{dr}\bigg|_{r=+1} - \left[\frac{2}{(R_{n+1} - a\cos\phi)\theta_{n+1}}\right]\frac{dw_\zeta}{dr}\bigg|_{r=-1} \tag{27}$$

We impose this condition using the penalty method already employed in Section 3.1. Substituting into equation (17) from equation (27), we now obtain the penalty matrix

$$\mathbf{K}_p^C = \alpha\int_0^{2\pi} \mathbf{G}_C{}^T\,\mathbf{G}_C\, d\phi \tag{28}$$

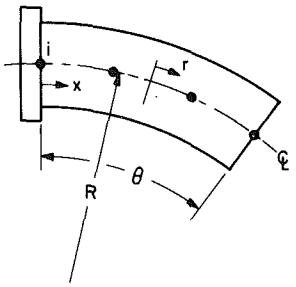
where

$$\mathbf{G}_C = [\ldots \bar{a}_1^{k(n)}\ \bar{a}_2^{k(n)}\ \bar{a}_3^{k(n)}\ \bar{b}_1^{k(n)}\ \bar{b}_2^{k(n)}\ \bar{b}_3^{k(n)}\ \ldots \bar{a}_1\ \bar{a}_2\ \bar{a}_3\ \bar{b}_1\ \bar{b}_2\ \bar{b}_3 \ldots$$
$$\ldots \bar{a}_1^{k(n+1)}\ \bar{a}_2^{k(n+1)}\ \bar{a}_3^{k(n+1)}\ \bar{b}_1^{k(n+1)}\ \bar{b}_2^{k(n+1)}\ \bar{b}_3^{k(n+1)}\ \ldots] \tag{29}$$

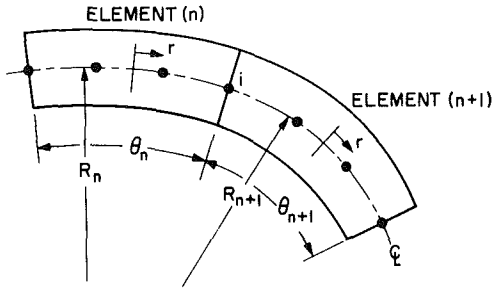
$$\left.\begin{aligned}\bar{a}_m^{k(n)} &= -\left[\frac{2}{(R_n - a\cos\phi)\theta_n}\right]2m\frac{dh_k{}^{(n)}}{dr}\bigg|_{r=+1}\cos 2m\phi \quad (30)\\ \bar{b}_m^{k(n)} &= \left[\frac{2}{(R_n - a\cos\phi)\theta_n}\right]2m\frac{dh_k{}^{(n)}}{dr}\bigg|_{r=+1}\sin 2m\phi \quad (31)\end{aligned}\right\} k \neq 2$$

$$\left.\begin{aligned}\bar{a}_m^{k(n+1)} &= \left[\frac{2}{(R_{n+1} - a\cos\phi)\theta_{n+1}}\right]2m\frac{dh_k{}^{(n+1)}}{dr}\bigg|_{r=-1}\cos 2m\phi \quad (32)\\ \bar{b}_m^{k(n+1)} &= -\left[\frac{2}{(R_{n+1} - a\cos\phi)\theta_{n+1}}\right]2m\frac{dh_k{}^{(n+1)}}{dr}\bigg|_{r=-1}\sin 2m\phi \quad (33)\end{aligned}\right\} k \neq 1$$

Downloaded 01 May 2010 to 171.66.16.249. Redistribution subject to ASME license or copyright; see http://www.asme.org/terms/Terms_Use.cfm



(a) ELBOW WITH A RIGID FLANGE AT NODE i



(b) ELBOWS OF DIFFERENT RADII JOINED AT NODE i

Fig. 3 Interactions considered in analyses

and for the common node (i) of the two elements,

$$\bar{a}_m = \left\{ -\left[\frac{2}{(R_n - a\cos\phi)\theta_n}\right]\frac{dh_2^{(n)}}{dr}\bigg|_{r=+1} + \left[\frac{2}{(R_{n+1} - a\cos\phi)\theta_{n+1}}\right]\frac{dh_1^{(n+1)}}{dr}\bigg|_{r=-1}\right\} 2m\cos 2m\phi \tag{34}$$

$$\bar{b}_m = \left\{ \left[\frac{2}{(R_n - a\cos\phi)\theta_n}\right]\frac{dh_2^{(n)}}{dr}\bigg|_{r=+1} - \left[\frac{2}{(R_{n+1} - a\cos\phi)\theta_{n+1}}\right]\frac{dh_1^{(n+1)}}{dr}\bigg|_{r=-1}\right\} 2m\sin 2m\phi \tag{35}$$

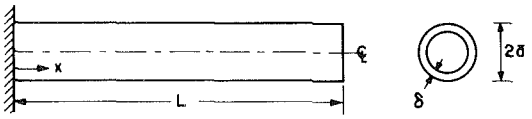
This penalty matrix corresponds to the degrees of freedom

$$\mathbf{u}^{cT} = [\ldots \underbrace{c_1^{k(n)}\ c_2^{k(n)}\ c_3^{k(n)}\ d_1^{k(n)}\ d_2^{k(n)}\ d_3^{k(n)}}_{\text{node } k \text{ of element } (n),\ k\neq 2} \ldots \underbrace{c_1\ c_2\ c_3\ d_1\ d_2\ d_3}_{\text{node } i} \ldots$$

$$\ldots \underbrace{c_1^{k(n+1)}\ c_2^{k(n+1)}\ c_3^{k(n+1)}\ d_1^{k(n+1)}\ d_2^{k(n+1)}\ d_3^{k(n+1)}}_{\text{node } k \text{ of element } (n+1),\ k\neq 1} \ldots] \tag{36}$$

4 Sample Analyses

We have implemented the foregoing enhancements to our elbow formulation in the computer program ADINAP [7]. The following analysis results are presented to indicate the applicability and effectiveness of these enhancements.



OVALIZATION BOUNDARY CONDITIONS

AT $x = 0$: $w_\zeta = 0.$, $\frac{dw_\zeta}{dx} = 0.$

AT $x = L$: $C_1 = 0.5$ in. (CORRESPONDING TO UNIT OVALIZATION IN FIRST VON KÁRMÁN MODE)

ANALYSIS PARAMETERS

$L = 4.8$ in. $\quad E = 2.8 \times 10^7$ psi

$\bar{\delta} = 8.0$ in.

$\delta = 0.37$ in.

Fig. 4 Straight cantilever pipe test problem, E = Young's modulus

4.1 Analysis of a Straight Pipe. The straight cantilever pipe shown in Fig. 4 was analyzed for a prescribed ovalization at its right end. The purpose of this analysis was to investigate the effects of the element size and penalty parameter size on the response predicted, and thus arrive at some guidelines for the use of the element in modeling more complex piping systems.

Figure 5 shows the response predicted in the analysis when using four equal size elements. It is seen that, although dw_ζ/dx is continuous, the second derivative of w_ζ with respect to x is strongly discontinuous at the junction of the first and second elements. Hence, the bending strain (in equation (8)) displays a large jump at this point and a finer finite element mesh is required at the fixed end if the stress distribution is to be predicted accurately.

The appropriate element size for stress continuity between elements is evaluated by recognizing that in the stiffness matrix the bending strain contribution due to equation (8) should be at least as large as the shearing strain contribution in equation (9). This condition gives that for an element in which the terms in equations (8) and (9) are important, we want $\delta/l > 1/4$ where l is the element length. Figure 6 shows the response predicted using a fine finite element idealization for which this criterion is satisfied. It is seen that in the predicted response, the second derivative of w_ζ is now continuous. It is also impoprtant to note that the ovalization displacement w_ζ has changed very little from the response given in Fig. 5.

To investigate the effect of the size of the penalty parameter α, the 16-element model of the cantilevered pipe was analyzed using the values of α listed in Fig. 7. As expected, when α is very small, the fixity condition at $x = 0$ is not properly imposed and when α is very large, the complete element stiffness matrix is singular. However, for a large range of α (see Cases 2 and 3) an identical response is predicted. In practice, it is effective to choose α equal to the largest value in the stiffness matrix corresponding to the ovalization degrees of freedom and this is done automatically in the program.

4.2 Analysis of a Flanged Pipe Bend. The flanged pipe bend shown in Fig. 8 was analyzed using the finite element model given. Figures 9–13 show the computed response for

Downloaded 01 May 2010 to 171.66.16.249. Redistribution subject to ASME license or copyright; see http://www.asme.org/terms/Terms_Use.cfm

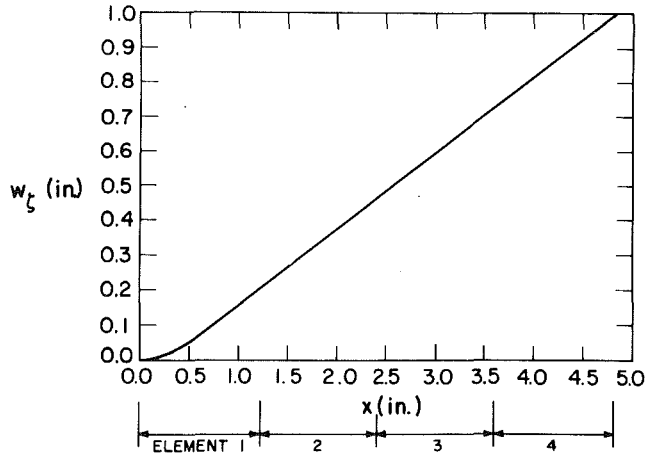


Fig. 5 Predicted response of cantilevered pipe using four equal elements

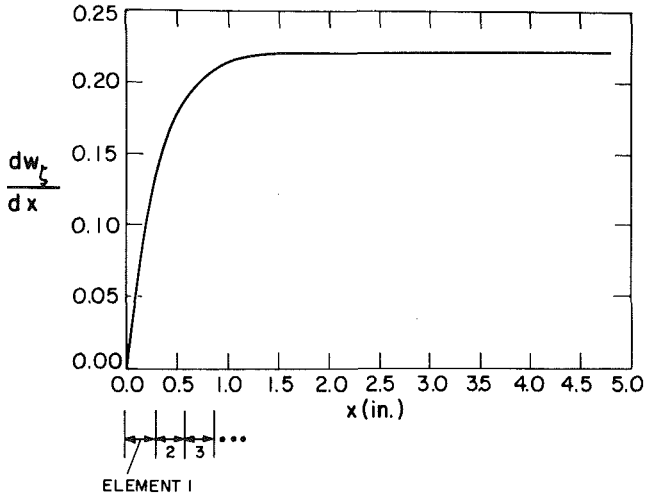


Fig. 6 (cont.)

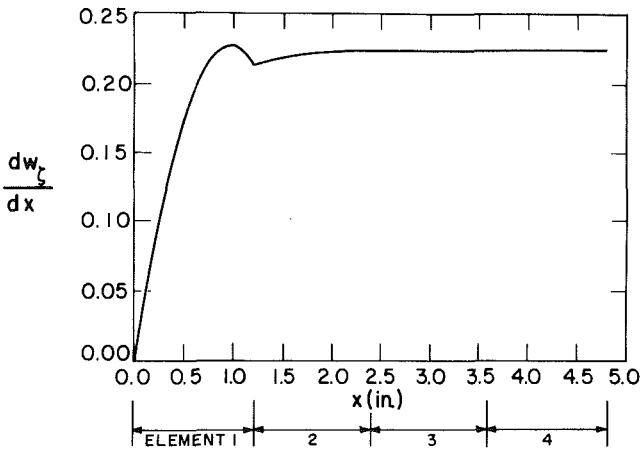


Fig. 5 (cont.)

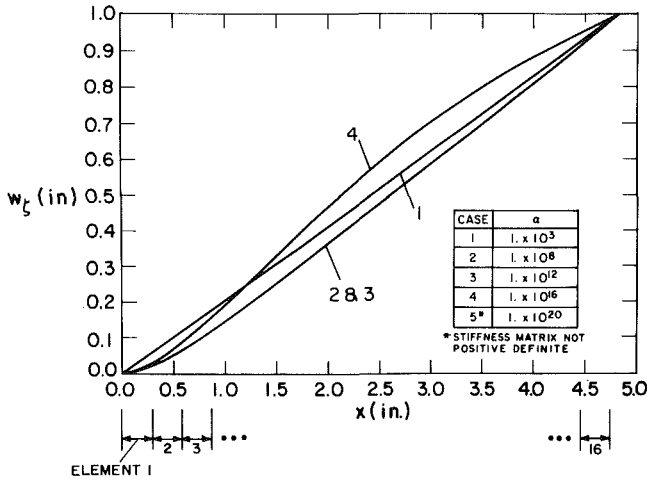


Fig. 7 Effect of size of penalty parameter on predicted response of cantilevered pipe

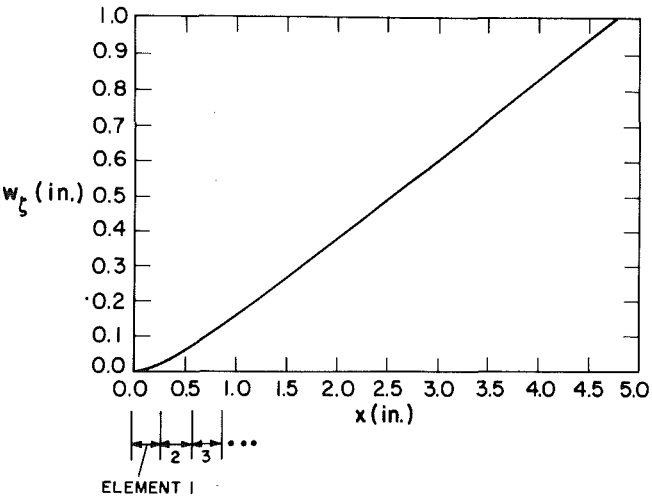


Fig. 6 Predicted response of cantilevered pipe using fine finite element idealization (same response obtained using 16 elements of length 0.3 in. or 6 elements of 0.3 in. and 1 element of 3.0 in.)

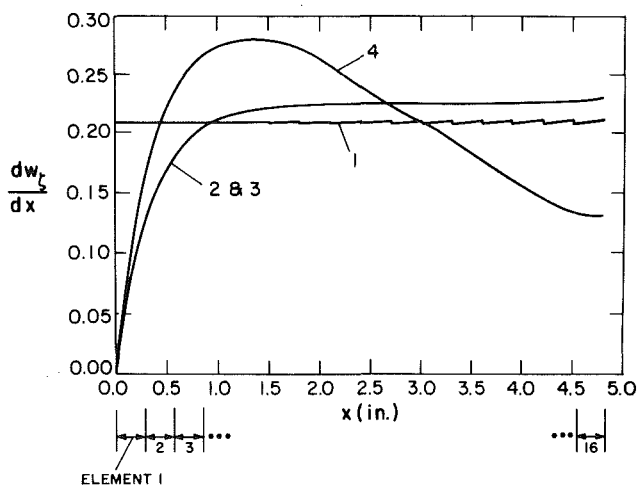


Fig. 7 (cont.)

Downloaded 01 May 2010 to 171.66.16.249. Redistribution subject to ASME license or copyright; see http://www.asme.org/terms/Terms_Use.cfm

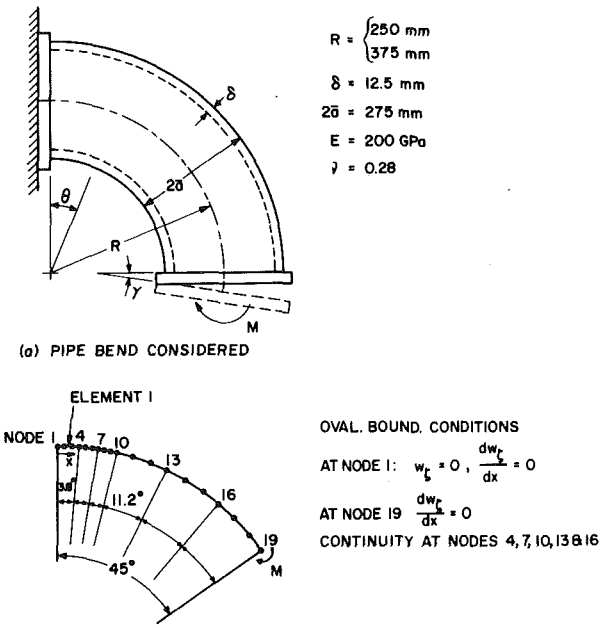


Fig. 8 Whatham pipe bend, E = Young's modulus, ν = Poisson's ratio

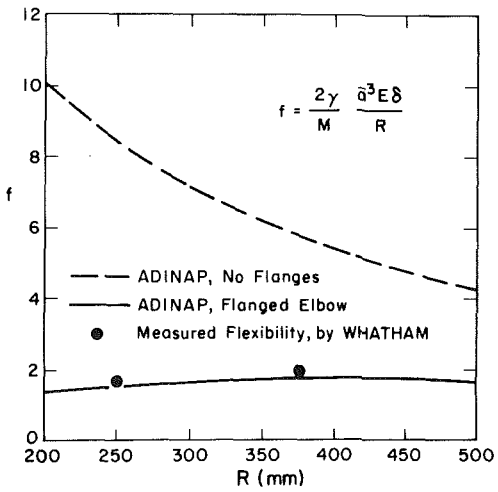


Fig. 9 Predicted flexibility factors for Whatham pipe bend

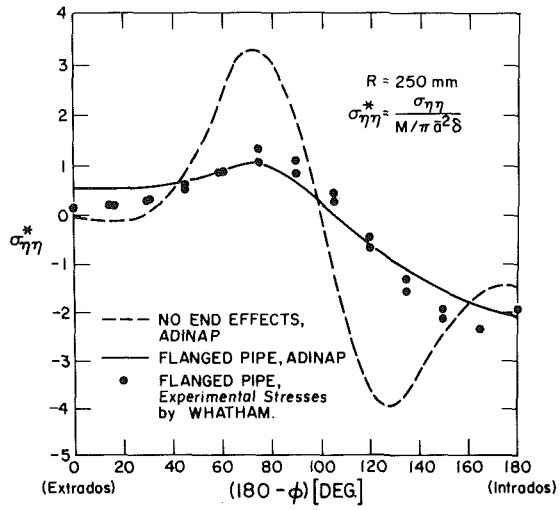


Fig. 10 Predicted longitudinal stresses at θ = 45 deg and at outside surface in analysis of Whatham pipe bend, R = 250 mm

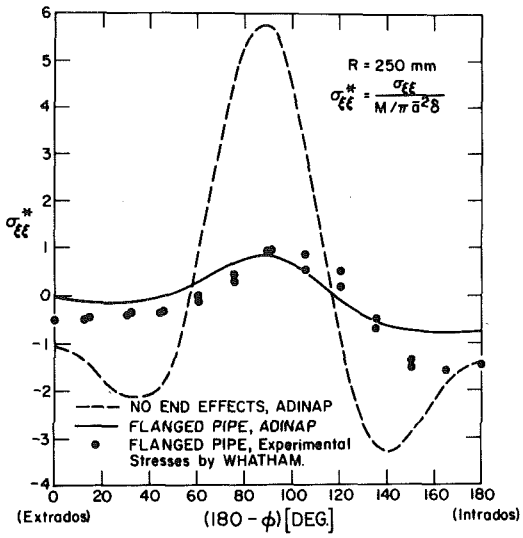


Fig. 11 Predicted circumferential stresses at θ = 45 deg and at outside surface in analysis of Whatham pipe bend, R = 250 mm

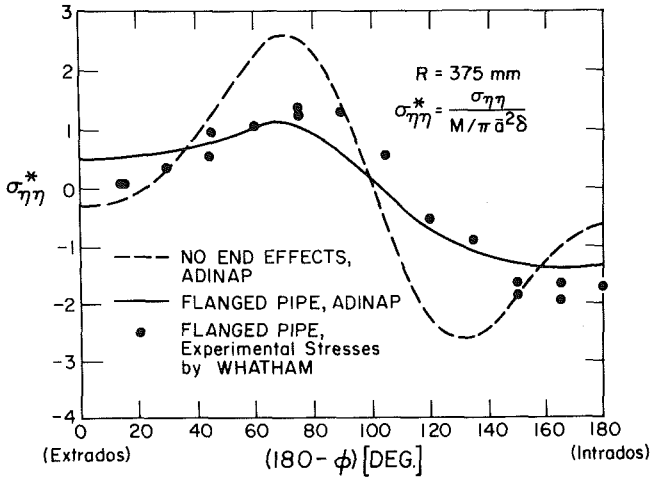


Fig. 12 Predicted longitudinal stresses at θ = 45 deg and at outside surface in analysis of Whatham pipe bend, R = 375 mm

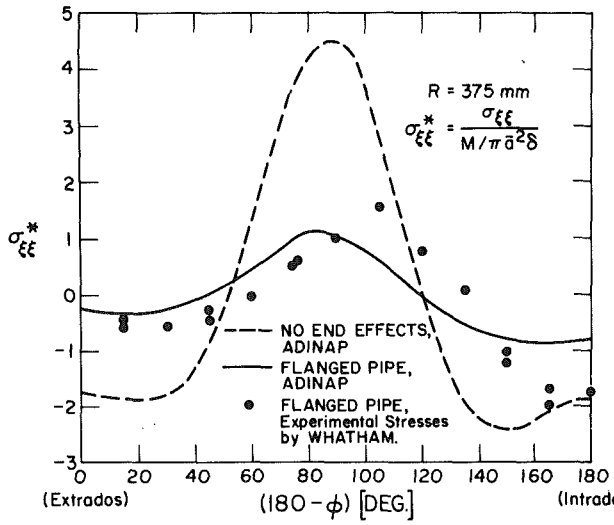


Fig. 13 Predicted circumferential stresses at θ = 45 deg and outside surface in analysis of Whatham pipe bend, R = 375 mm

Downloaded 01 May 2010 to 171.66.16.249. Redistribution subject to ASME license or copyright; see http://www.asme.org/terms/Terms_Use.cfm

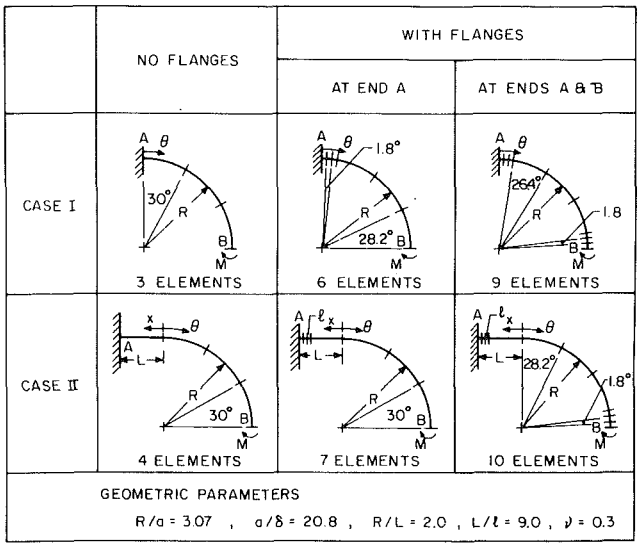


Fig. 14 Pipe bends and finite element models used

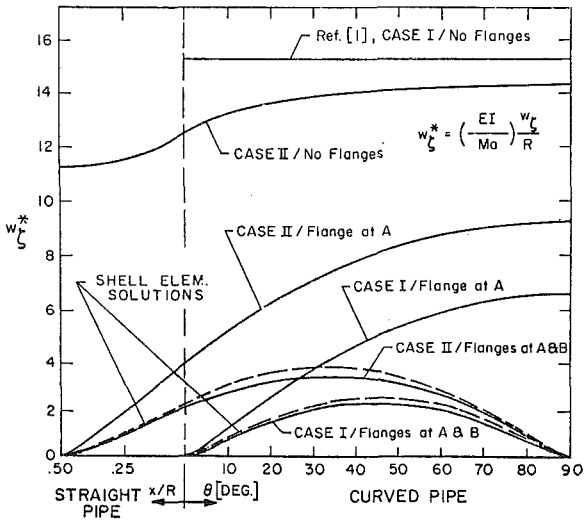


Fig. 15 Predicted ovalization response of bends defined in Fig. 14. Ovalization measured at $\phi = 90$ deg.

two different bend radii and give also experimental results [8]. It is seen that the correspondence between the computed and experimental flexibility factors and longitudinal stresses is good, but there is less good corrrespondence between the measured and computed circumferential stresses.

4.3 Analysis of a Second Pipe Bend. The pipe bend shown in Fig. 14 was analyzed in reference [1] and in previous studies [9, 10]. In these analyses, interaction effects were not considered. Figure 15 shows the response predicted when now including interaction effects using the idealizations described in Fig. 14. For comparison, also the response predicted using a finite element shell idealization of the piping system with flanges at A and B is shown. The shell element used in these analyses is the triangular flat 18 degrees of the freedom element described in [11]. The following shell element mesh was used: 12 layers of elements around half the circumference (one layer being two triangles), 9 layers for the 90 deg bend, and 3 layers for the straight. Thus, a total of 216 and 288 shell elements were used to model Case I/flanges at A and B and Case II/flanges at A and B, respectively. Figure 15 shows that the ovalizations predicted using our elbow element are close to the ovalizations calculated with the shell element idealizations. Considering the response of the piping structures, we note that the ovalizations of the piping systems are reduced very significantly when the interaction effects are included.

Conclusions

Our elbow element presented in reference [1] has been enhanced to also account for interaction effects with rigid flanges and straight piping sections. The interaction effects are included in a novel, but very simple and efficient manner using a penalty function formulation. The results of some sample solutions have been presented which indicate the applicability of the element. However, the total element formulation is based on a number of assumptions and further detailed studies of the element performance are required in order to identify the limit of range of problems for which the element can be employed.

Acknowledgment

We gratefully acknowledge the support of CNEN and PUC/RJ, Brazil, for C. A. Almeida's studies.

References

1 Bathe, K. J., and Almeida, C. A., "A Simple and Effective Pipe Elbow Element — Linear Analysis," ASME JOURNAL OF APPLIED MECHANICS, Vol. 47, No. 1, 1980, pp. 93–100.

2 Bathe, K. J., *Finite Element Procedures in Engineering Analysis,* Prentice-Hall, 1981.

3 Novozhilov, V. V., *Thin Shell Theory,* translated by P. G. Lowe, P. Noordhoff Ltd., Groningen, Netherlands, 1964.

4 Zienkiewicz, O. C., *The Finite Element Method,* McGraw-Hill, New York, 1977.

5 Felippa, C. A., "Interactive Procedures for Improving Penalty Function Solutions of Algebraic Systems," *International Journal of Numerical Methods in Engineering,* Vol. 12, 1978, pp. 821–836.

6 Oden, J. T., "Exterior Penalty Methods for Contact Problems in Elasticity," *Nonlinear Finite Element Analysis in Structural Mechanics* W. Wunderlich, et al., eds., S pringer-Verlag, Berlin, 1981.

7 ADINAP, Arthur D. Little Report, 1979.

8 Whatham, J. F., "In-Plane Bending of Flanged Elbows," *Proceedings, Metal Structures Conference,* the Institution of Engineers, Australia, Perth, Nov. 30–Dec. 1, 1978.

9 Clark, R. A., and Reissner, E., "Bending of Curved Tubes," *Advances in Applied Mechanics,* Vol. 2, 1951, pp. 93–122.

10 Sobel, L. H., "In-Plane Bending of Elbows," *Journal Computers and Structures,* Vol. 7, 1977, pp. 701–715.

11 Bathe, K. J., and Ho, L. W., "A Simple and Effective Element for Analysis of General Shell Structures," *Journal of Computers and Structures,* Vol. 13, 1981, pp. 673–681.

Downloaded 01 May 2010 to 171.66.16.249. Redistribution subject to ASME license or copyright; see http://www.asme.org/terms/Terms_Use.cfm

H. Stolarski
Research Associate.

T. Belytschko
Professor of Civil and Nuclear Engineering.
Mem. ASME

Department of Civil Engineering,
The Technological Institute,
Northwestern University,
Evanston, Il. 60201

Membrane Locking and Reduced Integration for Curved Elements

The behavior of a curved beam element is studied by comparison to an analytic solution. In the curved beam element, curvature effects are incorporated through a "shallow-shell" type theory. It is shown that when low-order, inplane displacement fields are used for the element, the curvature terms increase the bending stiffness due to contributions from the membrane strains; this is called "membrane locking." Reduced integration yields a bending stiffness, which is in better agreement with the analytic value, and yet it retains the bending-membrane coupling, which is characteristic of curved elements. The results of the analysis are verified by several numerical examples.

1 Introduction

Curved elements may provide significant advantages over flat elements for the analysis of shells. While bending-membrane coupling is represented only for an assemblage of flat elements, this coupling appears in individual curved elements. Furthermore, curved elements eliminate "discontinuity moments" that plague flat elements [1].

There are basically three approaches that may be used for formulation of curved elements: degenerate continuum elements [2–4]; intrinsic curved elements, where the governing equations are developed in a curvilinear system [1,5]; and elements based on theories for shallow structures [6–8]. A disadvantage of all of these curved elements is the tendency to be too stiff unless the inplane displacement field is of sufficiently high order. When low-order, inplane displacements are used, an artificial constraint appears that causes a bending-dominated response to be replaced by a membrane-dominated response; here, this effect is called "membrane locking." Although a low-order, inplane displacement field is not advantageous in many applications, it is quite desirable for transient analysis by explicit-time integration, since it significantly increases the stable time step.

In this paper, the elimination of membrane locking by reduced integration is investigated. The analysis is limited to shallow-structure formulations, although the results of this analysis also pertain to the other types of elements. As found in other contexts [9,10] where artificial constraints appear, it is shown that selective-reduced integration eliminates the undesirable constraint and the resulting locking mechanism. While the beneficial effects of reduced integration on membrane locking have previously been mentioned in the literature [11,12], the phenomenon has not been clearly identified nor analyzed. In this paper it is shown, by means of a simple analysis, that membrane locking results from the effects of the curvature on the bending stiffness, whenever membrane displacements are represented by polynomials of lower order. Furthermore, it is shown that elements based on the theory of shallow structures accurately reproduce membrane-bending coupling on an element level. The analysis presented here is restricted to arches, which can serve as a model for many types of shell behavior, except those associated with the effects of double curvature.

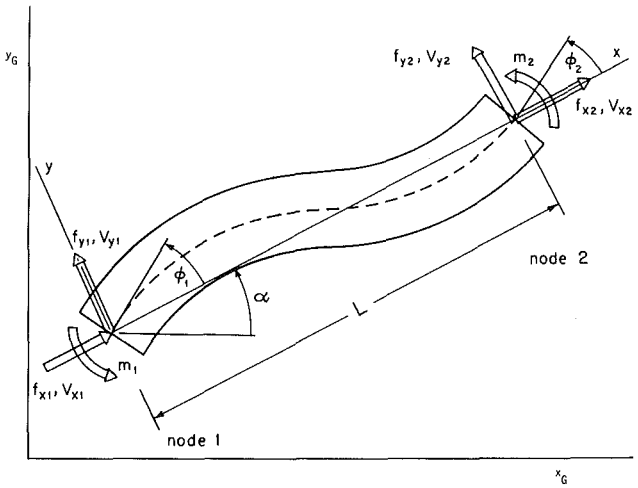


Fig. 1 Nomenclature for curved beam element

In the next section, the basic equations for the finite element representations of arches are presented; a corotational formulation in which only the deformation modes appear [13–17] is chosen for simplicity. The sources of excessive constraint are then explained. This is followed by a discussion of the role of underintegration in eliminating the constraints. Examples and conclusions are given in the last two sections, respectively.

2 Basic Relationships

Consider a curved beam element with a local corotational coordinate system x, y, shown in Fig. 1. If, at any instant, the shape of the beam, described by the function w, is such that

Contributed by the Applied Mechanics Division for publication in the JOURNAL OF APPLIED MECHANICS.

Discussion on this paper should be addressed to the Editorial Department, ASME, United Engineering Center, 345 East 47th Street, New York, N.Y. 10017, and will be accepted until two months after final publication of the paper itself in the JOURNAL OF APPLIED MECHANICS. Manuscript received by ASME Applied Mechanics Division, April, 1981; final revision, August, 1981.

Copyright © 1982 by ASME
Downloaded 01 May 2010 to 171.66.16.249. Redistribution subject to ASME license or copyright; see http://www.asme.org/terms/Terms_Use.cfm

$$\frac{w}{L}=0(e) \qquad w_{,x}=0(e) \qquad w_{,xx}=0(e^2) \tag{1}$$

where e is a small number and L is the length of the element, the corotational component of the velocity strain tensor containing terms of order e^2 can be shown to be

$$D_x = \dot{\epsilon}_x + y\dot{\kappa}_x \tag{2a}$$

$$\dot{\epsilon}_x = V_{x,x} + w_{,x}V_{y,x} \tag{2b}$$

$$\dot{\kappa}_x = -V_{y,xx} \tag{2c}$$

In the foregoing, the rigid body motion has been excluded so V_x, V_y are the deformational velocities relative to the rotating x, y frame. The comma denotes differentiation with respect to the following variables. The only term in equation (2) that differs from the standard linear strain-displacement relation is the second term in (2b), which corresponds to the nonlinear term given by Marguerre [18] for shallow shells.

The deformation velocity fields are approximated in each element by the shape functions as follows:

$$V_x = V_{x2}\xi \tag{3a}$$

$$V_y = \dot{\phi}_1 L(\xi^3 - 2\xi^2 + \xi) + \dot{\phi}_2 L(\xi^3 - \xi^2) \tag{3b}$$

$$\xi = \frac{x}{L} \tag{3c}$$

where $\dot{\phi}_I$ are the nodal rotations relative to the corotational system, which are given in terms of total rotations $\dot{\theta}_I$ and total velocities V^t_{y2}, V^t_{y1} by

$$\dot{\phi}_I = \dot{\theta}_I - \frac{1}{L}(V^t_{y2} - V^t_{y1}) \tag{4}$$

The same shape functions are used to describe the current shape of the element

$$w = \phi_1 L(\xi^3 - 2\xi^2 + \xi) + \phi_2 L(\xi^3 - \xi^2) \tag{5}$$

The initial configuration determines the initial values of ϕ_I; subsequently ϕ_I and hence w, is updated through the integration of $\dot{\phi}_I$.

The matrix form of the kinematical relationships presented in equations (2)–(5) follows

$$D_x = \mathbf{B}\mathbf{v} \tag{6}$$

where

$$\mathbf{B} = \mathbf{B}^L + \mathbf{B}^H \tag{7a}$$

$$\mathbf{B}^L = \frac{1}{L}\begin{bmatrix} 1 \\ -y(6\xi-4) \\ -y(6\xi-2) \end{bmatrix}^{\mathrm{T}} \tag{7b}$$

$$\mathbf{B}^H = \begin{bmatrix} 0 \\ w_{,x}(3\xi^2-4\xi+1) \\ w_{,x}(3\xi^2-2\xi) \end{bmatrix}^{\mathrm{T}} \tag{7c}$$

$$\mathbf{v} = \begin{Bmatrix} V_{x2} \\ \phi_1 \\ \phi_2 \end{Bmatrix} \tag{7d}$$

The nodal forces corresponding to the deformation nodal velocities, equation (7d) are then given by

$$\begin{Bmatrix} f_{x2} \\ m_1 \\ m_2 \end{Bmatrix} = \int_0^L \int_{h/2}^{h/2} \mathbf{B}^T T_x \, dy \, dx \tag{8}$$

where h is the depth of the element, T_x is the normal component of the Cauchy stress, and m_I are the nodal moments. The remaining nodal forces are given by equilibrium

$$f_{x1} = -f_{x2} \tag{9a}$$

$$f_{y1} = -f_{y2} = \frac{m_1 + m_2}{L} \tag{9b}$$

The stiffness matrix for a homogeneous, elastic beam can then be written as

$$\mathbf{K} = \mathbf{K}^L + \mathbf{K}^H \tag{10a}$$

$$\mathbf{K}^L = \frac{Eh}{L}\begin{bmatrix} 1 & 0 & 0 \\ 0 & 4r^2 & 2r^2 \\ 0 & 2r^2 & 4r^2 \end{bmatrix} \tag{10b}$$

$$\mathbf{K}^H = \frac{Eh}{L}\int_0^1 \begin{bmatrix} 0 & w_{,\xi}N_{1,\xi} & w_{,\xi}N_{2,\xi} \\ & (w_{,\xi}N_{1,\xi})^2 & w_{,\xi}^2 N_{1,\xi}N_{2,\xi} \\ \text{symmetric} & & (w_{,\xi}N_{2,\xi})^2 \end{bmatrix} d\xi \tag{10c}$$

and

$$r^2 = \frac{h^2}{12}, \qquad N_1 = \xi^3 - 2\xi^2 + \xi, \qquad N_2 = \xi^3 - \xi^2$$

The first part, $\mathbf{K}^L$, corresponds to the stiffness for a straight beam element. Note that the straight element has no coupling between axial and bending response, i.e., on an element basis, membrane-moment coupling will be absent. The second term, $\mathbf{K}^H$, provides two effects: the addition of K^H_{12} and K^H_{13}, which represent membrane-moment coupling on an element level, and K^H_{ij} (i = 2,3; j = 2,3), which modifies the bending behavior of the element.

From the assumed approximations and from equation (2b) it can now be seen that $\dot{\epsilon}_x$ is a polynomial of fourth order, since $V_{x,x}$ is constant but $w_{,x}$ and $V_{y,x}$ are both quadratic. If a structure is subjected to only pure bending, the stretching $\dot{\epsilon}_x$ therefore cannot vanish. This indicates that in all the cases where the predominant type of deformation is bending, the stretching resulting from a disagreement between the structural theory and the shape functions may distort results significantly. Moreover, since for flexible structures, stretching absorbs relatively more energy, displacements resulting from the foregoing approximation can be expected to be too small. We will call this phenomenon "membrane locking."

As indicated in the Introduction, it has been noted in the literature [11] that higher-order approximations for V_x eliminate the difficulty. However, for explicit time integration, this approach reduces the stable time step dramatically; from that standpoint it is often inappropriate. Another remedy consists of underintegrating the terms of the stiffness matrix $\mathbf{K}^H$ (or the internal nodal forces) which are associated with the nonlinear term of equation (2b), and thus with polynomials of higher order. This, in a sense, is the opposite approach to a higher-order approximation for V_x, which also permits the bending mode of deformation in a structure to be restored.

3 Influence of the Reduced Integration

To study the influence of the underintegration on the matrix $\mathbf{K}^H$ we have considered a problem of a beam with the shape prescribed by equation (5) and boundary conditions $V^t_{x1} = V^t_{y1} = V^t_{y2} = \dot{\theta}_1 = 0$ (in the corotational framework only the

Downloaded 01 May 2010 to 171.66.16.249. Redistribution subject to ASME license or copyright; see http://www.asme.org/terms/Terms_Use.cfm

Table 1 Analytic and numerically integrated values of K_{12}^H and K_{22}^H

Numbers of Gauss points	K_{12}^H	K_{22}^H
Analytic	$\frac{2}{15}\phi_1 - \frac{1}{30}\phi_2$	$\left(\frac{1}{42} - \frac{2}{45}\frac{h^2}{L^2}\right)\phi_1^2 - \left(\frac{1}{60} - \frac{1}{50}\frac{h^2}{L^2}\right)\phi_1\phi_2 + \left(\frac{17}{2100} - \frac{2}{45}\right)\phi_2^2$
1	$-\frac{1}{16}\phi_1 + \frac{1}{16}\phi_2$	$\frac{1}{512}\phi_1^2 - \frac{1}{256}\phi_1\phi_2 + \frac{1}{512}\phi_2^2$
2	$0.084\phi_1 - 0.084\phi_2$	$0.0070\phi_1^2 - 0.0140\phi_1\phi_2 + 0.0070\phi_2^2$
3	$\frac{2}{15}\phi_1 - \frac{1}{30}\phi_2$	$0.0375\phi_1^2 - 0.0027\phi_1\phi_2 + 0.0185\phi_2^2$
4	$\frac{2}{15}\phi_1 - \frac{1}{30}\phi_2$	$0.0870\phi_1^2 - 0.0175\phi_1\phi_2 + 0.0030\phi_2^2$

Table 2 Values of K_{12}^H and K_{22}^H for $\phi_1 = \phi_2$ and $\phi_1 = -\phi_2$

Number of Gauss points	K_{12}^H/ϕ_1^2		K_{22}^H/ϕ_1^2	
	$\phi_1 = -\phi_2$	$\phi_1 = \phi_2$	$\phi_1 = -\phi_2$	$\phi_1 = \phi_2$
Analytic	0.167	0.100	0.0486	0.0152
1	0.125	0	0.0080	0
2	0.168	0	0.028	0
3	0.167	0.100	0.083	0.029
4	0.167	0.100	0.108	0.073

condition $\dot{\phi}_1 = 0$ is needed). The stiffness matrix $\mathbf{K}^H$ can then be reduced to the form:

$$\mathbf{K}^H = Eh \begin{bmatrix} 0 & K_{12}^H \\ K_{12}^H & LK_{22}^H \end{bmatrix} \begin{matrix} \dot{f}_{2x} \\ \dot{m}_2 \end{matrix} \qquad (11)$$

$$V_{2x} \qquad \dot{\phi}_2$$

Entries of the foregoing matrix evaluated numerically are compared to the analytical solution in Table 1.

Values of these terms when $\phi_1 = -\phi_2$ and $\phi_1 = \phi_2$ are given in Table 2. Since for most meshes of interest $(h/L)^2 << 1$, the terms containing this factor in the analytical solution have been neglected.

It is worth noting that, in view of equations (10) and (11), $K_{12} = K_{12}^H$, whereas for $\phi_1 = -\phi_2$ or $\phi_1 = \phi_2$

$$K_{22} = \frac{Eh^3}{L}\left[\frac{1}{3} + \left(\frac{L}{h}\right)^2 K_{22}^H(\phi_1)\right] \qquad (12)$$

The last result indicates that for thick (small L/h) or very shallow (small ϕ_1) elements, the change in K_{22} due to initial curvature is small. The effect of the initial curvature of the element is then predominantly due to the coupling term K_{12}. However, for the values L/h of order 10, and ϕ_1 of order 0.1, which can often be met in practice, $L\phi_1/h$ is of order 1, and the results given in Table 2 show a significant difference between stiffnesses of the straight and curved elements. For quadrature with four Gauss points, when $\phi_1 = -\phi_2$, the difference can be as large as 30 percent – this has remarkable influence on the results and has not been reported in the literature.

To draw some conclusions as to the number of Gauss points to be used, the numerical results presented in Table 2 should be compared to the analytical solution. The following features can then be noted:

1 K_{12}^H (membrane-moment coupling), which is a fourth-order term in x, is integrated almost exactly with two Gauss points, and when $\phi_1 = -\phi_2$ there is almost no error; if $\phi_1 = \phi_2$, with two point integration, the membrane-moment coupling vanishes. The exact integration of these terms does not stiffen the element beyond the analytic solution.

2 K_{22}^H, which reflects the effect of curvature on the bending stiffness, is too large when more than two Gauss points are used.

In summary, the excessive stiffness does not appear in the moment-membrane coupling, but in the effects of the curvature on the bending terms. Even in the latter, the stiffening due to full integration is not particularly severe, but the effect on a solution can be dramatic, as shown in the next section.

2 Examples

In all problems reported here, symmetry was used and the number of elements given is for half of the structure. The geometric and material properties are given in Table 3.

The first example is an elastic circular ring shown in Fig. 2. Both geometrically linear and nonlinear solutions have been obtained. The results for the linear solutions are presented along with the numerical results in Table 4. The membrane locking effect due to overintegration is quite clear and only with reduced integration is the curved element accurate. However, in a structure that is relatively thick and does not have strong membrane-bending coupling, such as this one, the curved element provides no advantage compared to straight elements. This is also apparent in the geometrically nonlinear results for the same structure, shown in Fig. 2

For more shallow arches, the curved elements provide an advantage over straight elements. This is mostly due to membrane-bending coupling. Results are presented for two shallow arches, for which the parameters are given in Table 3, the results in Figs. 3 and 4. In both cases, the curved elements agree more closely with the expected solution. It can also be seen from these results that the need for reduced integration depends on the ratio of the bending to the axial stiffness. For the shallow beam ($\Lambda = 11.63$), reduced integration improves the results markedly, whereas for the deep beam ($\Lambda = 3$), the effects of reduced integration are negligible. Apparently in the latter, the additional bending stiffness K_{22}^H, due to membrane

Downloaded 01 May 2010 to 171.66.16.249. Redistribution subject to ASME license or copyright; see http://www.asme.org/terms/Terms_Use.cfm

Table 3 Parameters for sample problems

A Elastic Ring (Fig. 2)

Depth of section h: 0.125 in.
Width of section: 1.2 in.
Young's modulus E: 1.05×10^7 psi
Radius of ring 2.97 in.

B Shallow Arch 1, $\Lambda = \dfrac{2H}{h} = 3$ (Fig. 3)

Depth of section h: 2 in.
Width of section: 1 in.
Span of arch: 48.51 in.
Rise of arch H: 3 in.
Radius of arch: 100 in.
Young's modulus E: 10^7 psi

C Shallow Arch 2, $\Lambda = \dfrac{2H}{h} = 11.63$ (Fig. 4)

Depth of section h: 0.1875 in.
Width of section: 1 in.
Span of arch: 34 in.
Rise of arch: 1.09 in.
Radius of arch: 133.114 in.
Young's modulus E: 10^7 psi

D Elastic-Plastic Ring (Fig. 5)

Initial yield stress: 4.28×10^4 psi
Ultimate yield stress: 5.0×10^5 psi
Plastic modulus: 7.87×10^4 psi
Density: 2.61×10^{-4} lb-in./s^4
Geometric parameters identical to problem *A*

Table 4 Linear solution for circular ring (see Fig. 2)

	Number of integration points	Force/deflection at load (lbs/in.)
Analytic solution		471.09
8 curved elements	2	450.13
8 curved elements	3	702.56
8 curved elements	4	698.28
8 straight elements	2	482.13

locking, is small compared to the linear bending stiffness, K_{22}^L, so the number of integration points used is immaterial.

We finally present a dynamic, elastic-plastic problem to examine the effects of reduced integration and curved elements in this setting. The problem parameters are given in Table 3. The problem was solved by central difference integration in time. The loading consisted of an initial velocity applied over a 60 deg arc as shown in Fig. 5. The elastic-plastic material law included piecewise-linear, isotropic hardening and perfectly plastic behavior after the ultimate stress. This problem was one of the motivations for this study, because in elastic-plastic problems, extra integration points are often desirable to capture the spread of the plastic domain. As can be seen from Fig. 5, use of more than two integration points causes complete failure, whereas with two points the convergence is excellent. However, as for the linear static response of the same structure (example *A*), straight elements perform as well as the curved elements.

5 Discussion and Conclusions

Several points come to mind in considering these results. First, why have the locking effects of "shallow-structure" formulations for curved elements not plagued previous investigations [6] and [8]? In studying [6], we find that in the interest of computational efficiency, linear approximations were used for the terms corresponding to $\mathbf{K}^H$ in [6]. Thus a form of reduced integration was used for efficiency and also

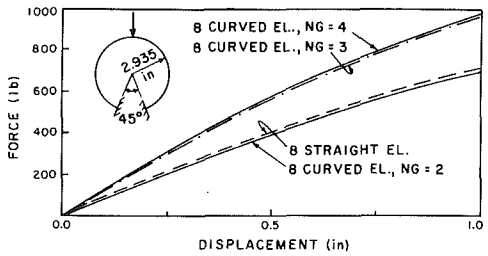


Fig. 2 Displacement under the load for nonlinear response of the circular, elastic ring (NG is the number of Gauss integration points; the numbers of elements used for half the structure are cited)

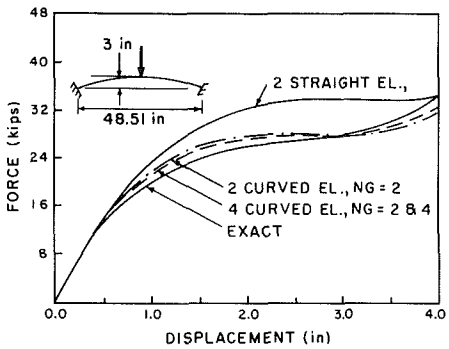


Fig. 3 Centerpoint displacement for shallow arch with $\Lambda = 3$; exact solution from Masur and Schreyer [19]

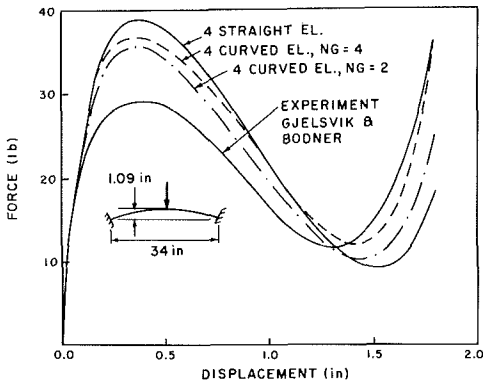


Fig. 4 Centerpoint displacement for shallow arch with $\Lambda = 11.63$

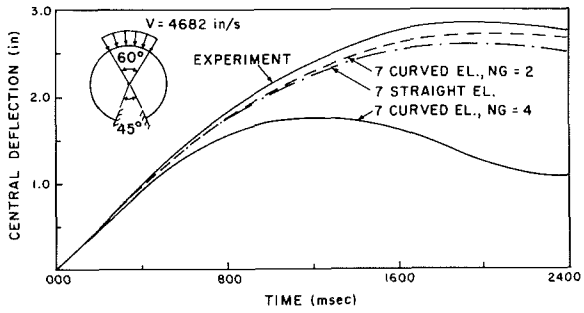


Fig. 5 Time history of centerpoint displacement for elastic-plastic impulsively loaded ring; experimental result from Balmer and Witmer [21]

overcame the locking problem. Similarly, in [8], a trapezoidal rule was used in the coupling terms.

A second point of interest is the relationship of this study to the underintegration of membrane energies reported for curved degenerate elements in [9] and [12]. Although the similarity of the phenomena in degenerate elements and shallow shell elements is not immediately apparent, the mechanical behavior of the two elements is basically identical,

Downloaded 01 May 2010 to 171.66.16.249. Redistribution subject to ASME license or copyright; see http://www.asme.org/terms/Terms_Use.cfm

and the analysis presented here should throw some light on the benefits of reduced integration in degenerate elements. Obviously, in an isoparametric degenerate element, the terms corresponding to $w_{,x}\ V_{y,x}$ in equation (2*b*) are of higher order than $V_{x,x}$, so reduced integration must be used to prevent excess bending stiffness in thin elements. For thicker elements, the contribution of the curvature to the bending stiffness is small, as for the example in Fig. 3, so reduced integration is not necessary to prevent membrane locking.

An obvious remedy for membrane locking in shallow structure elements would be to use higher-order fields for the membrane displacements. This alternative is, however, quite unpalatable in explicit time integration programs; when going from a linear to a quadratic membrane field, the stable time step is reduced by $\sqrt{6}/6$ when membrane frequencies are maximum [22], so the advantage in accuracy of higher-order membrane fields must indeed be substantial to justify their use.

Membrane locking may be avoided by approximating the stress resultants by lower-order polynomials in mixed elements, as in the work of Noor and coworkers [23, 24]. The analogy between this approach and reduced integration is identified in [10]. However, the use of mixed methods complicates the formulation substantially. It is also interesting to note that reference [24] contains many results for the displacement method in which the agreement with the correct solution is very poor because of the use of full integration.

The results of this study indicate that the use of higher-order fields for shallow shell elements is not necessary if reduced integration is used. Furthermore, the effect of underintegration has been shown to manifest itself primarily in the affects of the curvature on the bending stiffness, so care is needed primarily for thin structures. The advantage of shallow structural elements over flat elements is not yet clear.

Acknowledgment

The support of the Electric Power Research Institute is gratefully acknowledged.

References

1 Ashwell, D. G., and Gallagher, R. H., eds., *Finite Elements for Thin Shells and Curved Members*, Wiley, London, 1976.

2 Ahmad, S., "Pseudo-isoparametric Finite Elements for Shell and Plate Analysis," Proc. Conf. on Recent Advances in Stress Analysis, *JBCSA Royal Aeuronautical Society*, 1968, pp. 6-21.

3 Ahmad, S., Irons, B. M., and Zienkiewicz, O. C., "Analysis of Thick and Thin Shell Structures by Curved Finite Elements," *Int. J. for Numerical Methods in Eng.*, Vol. 2, 1970, pp. 419-451.

4 Hughes, T. J. R ., and Liu, W. K., "Nonlinear Finite Element Analysis of Shells; Part I. Three-Dimensional Shells," *Computer Methods in Applied Mechanics and Engineering*, Vol. 26, No. 3, 1981, pp. 331-362.

5 Dupuis, G., and Goël, J. J., "A Curved Finite Element for Thin Elastic Shells," Report No. N00014-0007/4, Dec. 1969, Division of Engineering, Brown University, Providence, R.I.

6 Bergan, P. G., and Clough, R. W., "Large Deflection Analysis of Plates and Shallow Shells Using the Finite Element Method," *Int. J. for Numerical Methods in Eng.*, Vol. 5, 1973, pp. 543-556.

7 Vos, R. G., "Generalization of Plate Finite Elements to Shells," *Proc. ASCE, Journal of Engineering Mechanics Division*, Vol. 98, EM2, 1972, pp. 385-400.

8 Belytschko, T., and Glaum, L. W., "Applications of Higher Order Corotational Stretch Theories to Nonlinear Finite Element Analysis," *Computers and Structures*, Vol. 10, 1979, pp. 175-182.

9 Zienkiewicz, O. C., Taylor, R. L., and Too, J. M., "Reduced Integration Techniques in General Analysis of Plates and Shells," *Int. J. for Numerical Methods in Eng.*, Vol. 3, pp. 1971, 275-290.

10 Malkus, D. S., and Hughes, T. J. R., "Mixed Finite Element Methods—Reduced and Selective Integration Techniques: A Unification of Concepts," *Computer Methods in Applied Mechanics and Engineering*, Vol. 15, No. 1, 1978, pp. 63-81.

11 Fried, I., "Finite Element Analysis of Thin Elastic Shells With Residual Energy Balancing and the Role of Rigid Body Modes, ASME JOURNAL OF APPLIED MECHANICS, Vol. 42, 1975, pp. 99-104.

12 Parish, H., "A Critical Survey of the Nine-Node Degenerated Shell Element With Special Emphasis on Thin Shell Application and Reduced Integration," *Computer Methods in Applied Mechanics and Engineering*, Vol. 20, 1979, pp. 323-350.

13 Argyris, J. H., Kelsey, S., and Kamel, H., "Matrix Methods of Structural Analysis: A Precis of Recent Developments" in *Matrix Methods of Structural Analysis*, edited by deVeubeke, E. F., Agardograph, 72, Pergamon Press, New York, 1964.

14 Wempner, G. A., "Finite Elements, Finite Rotation and Small Strains of Flexible Shells," *Int. Journal of Solids and Structures*, Vol. 5, 1969, pp. 117-153.

15 Murray, D. W., and Wilson, E. L., "Finite Element Large Deflection Analysis of Plates," *Proc. ASCE, Journal of Engineering Mechanics Division*, Vol. 95, 1969, pp. 143-165.

16 Belytschko, T., and Hsieh, B. J., "Nonlinear Transient Finite Element Analysis With Convected Coordinates," *Int. Journal for Numerical Methods in Engineering*, Vol. 3, 1973, pp. 255-272.

17 Belytschko, T., and Marchertas, A. H., "Nonlinear Finite Element Methods of Plate and Its Application to Dynamic Response of Reactor Fuel Subassemblies," ASME *Journal of Pressure Vessel Technology*, 1974, pp. 251-257.

18 Marguerre, K., "Zur Theorie Der Gekrummten Platte Grosser Formanderung," *Proc. 5th Int. Congress Appl. Mech.*, 1938, pp. 93-101.

19 Masur, E. F., and Schreyer, H., "A Second Approximation to the Problem of Elastic Instability," *Proc. Symp. Theory Shells* (Donnell Anniversary Volume) University of Houston, 1967, pp. 229-250.

20 Gjelsvik, A., and Bodner, S., "The Energy Criterion and Snapthrough of Arches," *Proc. ASCE, Journal of the Engineering Mechanics Division*, Vol. EM 5, 1971, pp. 1397-1412.

21 Balmer, H. A., and Witmer, E. A., "Theoretical-Experimental Correlation of Large Dynamic and Permanent Deformation of Impulsively Loaded Simple Structures," Report FDL-TDR-64-108, Air Force Flight Dyn. Lab., Wright-Patterson AFB, Ohio, 1964.

22 Belytschko, T., "Explicit time integration of structure-mechanical systems," *Advanced Structural Dynamics*, ed. by J. Donea, Applied Science Publishers, pp. 97-122, 1980.

23 Noor, A. K., and Andersen, C. M., "Mixed Isoparametric Finite Element Models of Laminated Composite Shells," *Computer Methods in Applied Mechanics and Engineering*, Vol. 11, 1977, pp. 255-280.

24 Noor, A. K., and Peters, J. M., "Mixed Models and Reduced/Selective Integration Displacement Models for Nonlinear Analysis of Curved Beams," *Int. Journal for Numerical Methods in Engineering*, Vol. 17, No. 4, 1981, pp. 615-632.

Downloaded 01 May 2010 to 171.66.16.249. Redistribution subject to ASME license or copyright; see http://www.asme.org/terms/Terms_Use.cfm

G. Baker
Research Student.

M. N. Pavlović
Lecturer.

Department of Civil Engineering,
Imperial College of Science
& Technology,
University of London,
London SW7 2AZ, U.K.

Elastic Stability of Simply Supported Rectangular Plates Under Locally Distributed Edge Forces

Introduction

The elastic stability of a simply supported rectangular plate under the action of two equal and opposite concentrated forces has been investigated by several authors [1-5]. Similarly, the problem where the load is distributed uniformly over a finite portion l of the plate width b (Fig. 1) has also been studied [2, 4, 5]. However, the ensuing results are only approximate since all previous workers in this field have used a simplified stress distribution in the buckling analysis. In the present work the latter source of inaccuracy is removed by the use of Mathieu's exact solution for the plane elasticity problem with rectangular boundaries that are subjected to arbitrary surface forces [6]. Thus, our computed buckling coefficients can be considered to be "exact," and hence, may be used with confidence in design computations; furthermore, they might also prove useful as a data basis for comparison of finite elements or other numerical techniques.

Problem Formulation

In some of the previous attempts to solve the problem under consideration, the actual eigenvalue problem is tackled by means of the approximate energy method [1, 2, 4] while in others a more general approach is adopted by the use of the differential equation of neutral equilibrium [3, 5]. Since the actual boundary conditions of simple support permit the ready identification of a "suitable" deflected shape, either method can be used to generate "exact" solutions. For example, Yamaki [5] computed stresses by means of both the foregoing techniques and found that three or four terms of the series approximating the transverse deflexion w of the plate were sufficient to establish an accuracy of four significant figures.

In the present work we adopt the energy method, and choose the following expression for the out-of-plane deflexion w of the plate at buckling:

$$w=\sin\frac{s\pi}{a}\left(x+\frac{a}{2}\right)\sum_{r}^{\infty}W_r\cdot\cos\left(\frac{r\pi y}{b}\right) \tag{1}$$

where s is a positive integer representing the number of half waves in the x-direction (Fig. 1), i.e.,

$$s=1, 2, 3, 4, 5, \ldots \tag{2}$$

and

$$r=1, 3, 5, 7, 9, \ldots \tag{3}$$

while W_r are the undefined amplitude coefficients. The assumed deflected shape satisfies, term by term, the boundary conditions of a plate simply supported on all four edges, thus ensuring convergence to the correct answer.

The hinged conditions of support permit a simplification in the general expression for the strain energy in bending U [7]. The simplified form is then

$$U=+\frac{D}{2}\int_{-a/2}^{+a/2}\int_{-b/2}^{+b/2}\left[\frac{\partial^2 w}{\partial x^2}+\frac{\partial^2 w}{\partial y^2}\right]^2 dx\,dy \tag{4}$$

where D is the flexural rigidity of the plate given by

$$D=\frac{\mathrm{E}t^3}{12(1-\nu^2)} \tag{5}$$

and the symbols E, ν, and t have the usual meaning, namely Young's modulus, Poisson's ratio, and plate thickness, respectively.

By introducing the deflected shape (1) into expression (4) we obtain

$$U=D\left(\frac{\pi}{b}\right)^2\frac{\pi^2 s^2}{8\phi}\sum_{r}^{\infty}W_r{}^2\left(\frac{s}{\phi}+\frac{r^2\phi}{s}\right)^2 \tag{6}$$

where the aspect ratio ϕ is defined as

$$\phi=a/b \tag{7}$$

with the plate dimensions a and b shown in Fig. 1.

To obtain the stress distribution throughout the plate, it is necessary to express the external loading $f(y)$ applied at the edges $x=\pm a/2$ as a half-range Fourier expansion. Choosing an even series with period b we obtain

$$f(y)=A_0+\sum_{n}^{\infty}A_n\cos ny \tag{8}$$

Contributed by the Applied Mechanics Division for publication in the JOURNAL OF APPLIED MECHANICS.

Discussion on this paper should be addressed to the Editorial Department ASME, United Engineering Center, 345 East 47th Street, New York, N.Y. 10017, and will be accepted until two months after final publication of the paper itself in the JOURNAL OF APPLIED MECHANICS. Manuscript received by ASME Applied Mechanics Division, October, 1980; final revisions, October, 1981.

Copyright © 1982 by ASME
Downloaded 01 May 2010 to 171.66.16.249. Redistribution subject to ASME license or copyright; see http://www.asme.org/terms/Terms_Use.cfm

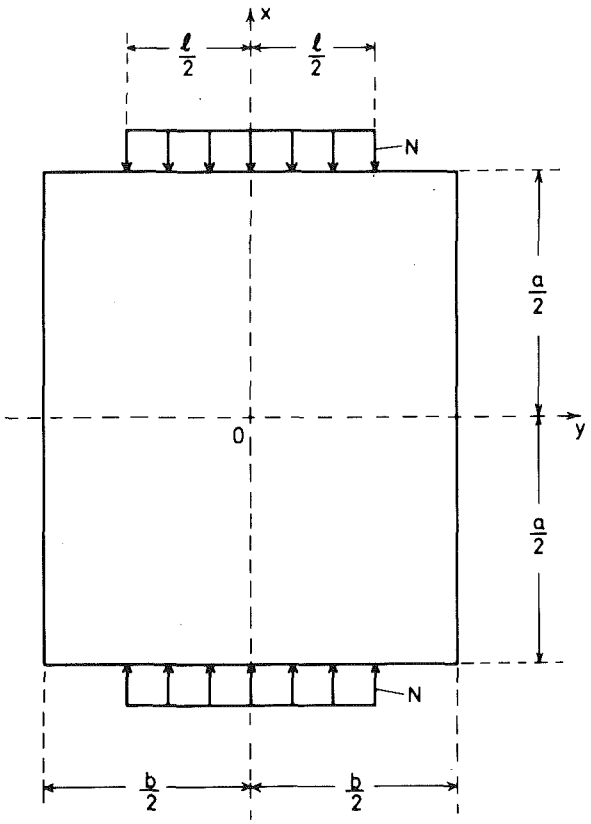


Fig. 1 Thin plate acted on by two equal and opposite, uniformly distributed loads

where

$$A_0 = N\gamma; \qquad A_n = \frac{2N}{\pi q} \sin \pi q \gamma \tag{9}$$

and

$$\gamma = \frac{l}{b} \tag{10}$$

where l is the portion of the plate width on which the load N (force per unit length) acts (Fig. 1); n is defined below. The exact stress distribution is then [6]:

$$N_x = A_0 + \sum_n C_n^{(1)} \cdot \cosh(nx) \cdot \cos(ny)$$

$$+ \sum_n^{\infty} C_n^{(2)} \cdot nx \cdot \sinh(nx) \cdot \cos(ny)$$

$$+ \sum_m^{\infty} C_m^{(3)} \cdot \cosh(my) \cdot \cos(mx)$$

$$+ \sum_m^{\infty} C_m^{(4)} \cdot my \cdot \sinh(my) \cdot \cos(mx) \tag{11}$$

$$N_y = \sum_m^{\infty} C_m^{(5)} \cdot \cosh(my) \cdot \cos(\mathrm{mx})$$

$$+ \sum_m^{\infty} C_m^{(6)} \cdot my \cdot \sinh(my) \cdot \cos(mx)$$

$$+ \sum_n^{\infty} C_n^{(7)} \cdot \cosh(nx) \cdot \cos(ny)$$

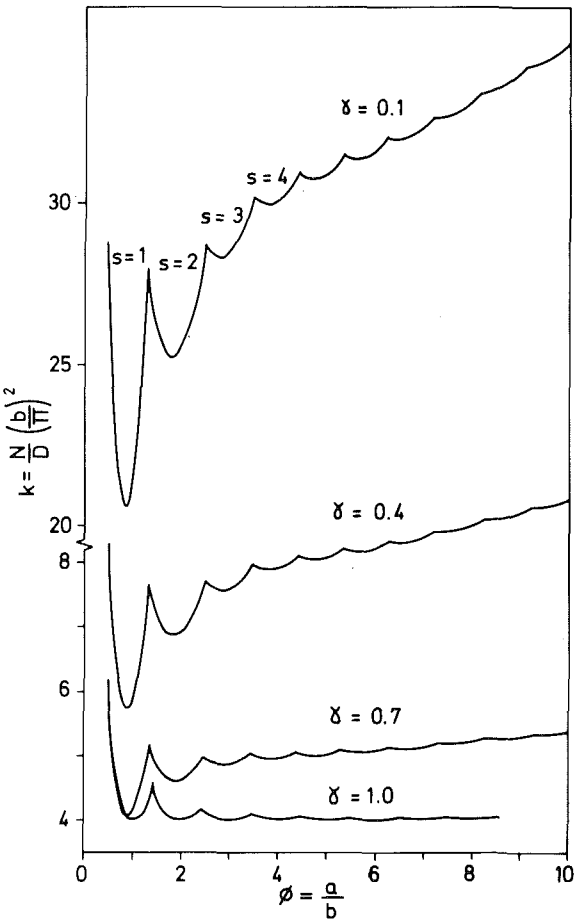


Fig. 2 k versus ϕ plots for γ = 1.0, 0.7, 0.4, 0.1

$$+ \sum_n^{\infty} C_n^{(8)} \cdot nx \cdot \sinh(nx) \cdot \cos(ny) \tag{12}$$

$$N_{xy} = \sum_n^{\infty} C_n^{(9)} \cdot \sinh(nx) \cdot \sin(ny)$$

$$+ \sum_n^{\infty} C_n^{(10)} \cdot nx \cdot \cosh(nx) \cdot \sin(ny)$$

$$+ \sum_m^{\infty} C_m^{(11)} \cdot \sinh(my) \cdot \sin(mx)$$

$$+ \sum_m^{\infty} C_m^{(12)} \cdot my \cdot \cosh(my) \cdot \sin(mx) \tag{13}$$

where (N_x, N_y, N_{xy}) are the stress resultants (i.e., stress × plate thickness) and the integers m and n are given by

$$m = \frac{2\pi p}{a}, \quad p = 1, 2, 3, 4, 5, \ldots \tag{14}$$

$$n = \frac{2\pi q}{b}, \quad q = 1, 2, 3, 4, 5, \ldots \tag{15}$$

The 12 constants $C_n^{()}$ *and* $C_m^{()}$ are themselves infinite series which are a function of the coefficients A_n [6].

The potential energy of the system, V, is given by

$$V = -\frac{1}{2} \int_{-a/2}^{+a/2} \int_{-b/2}^{+b/2} \left[N_x \cdot \left(\frac{\partial w}{\partial x}\right)^2 + N_y \cdot \left(\frac{\partial w}{\partial y}\right)^2 + 2N_{xy} \cdot \left(\frac{\partial w}{\partial x} \cdot \frac{\partial w}{\partial y}\right) \right] dx\, dy \tag{16}$$

Downloaded 01 May 2010 to 171.66.16.249. Redistribution subject to ASME license or copyright; see http://www.asme.org/terms/Terms_Use.cfm

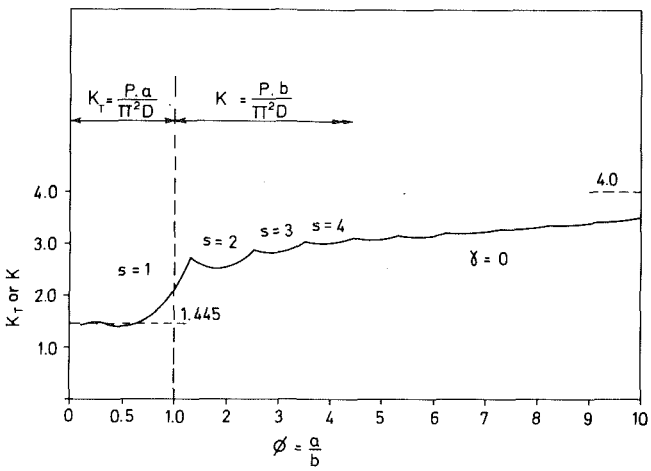


Fig. 3 K_T (or K) versus ϕ plot for $\gamma = 0$

In computing V it is convenient to break it up into 13 components, corresponding to the 13 terms appearing in expressions (11)–(13). The resulting integrals are relatively straightforward but rather lengthy and, for our present purposes, their actual forms need not be given here; it suffices to mention that they consist of single, double, or triple infinite series, a typical term of which is given by the undefined coefficents W muliplied by a factor which we denote by I.

We can now write the total energy of the system (Π) as

$$\Pi = U + V \tag{17}$$

The condition that Π be minimum is then

$$\frac{\partial \Pi}{\partial W_r} = 0 \tag{18}$$

which leads to the following expression for the state of incipient instability:

$$\frac{\pi^2 s^2}{8\phi}\left(\frac{s}{\phi} + \frac{r^2\phi}{s}\right)^2 \cdot W_r + \frac{k}{N}\Big[I_{x0} \cdot W_r + \sum_{i}^{\infty} W_i \Big[\sum_{q^*}^{\infty} (I_{x1} + I_{x2}) + (I_{x3} + I_{x4}) + (I_{y1} + I_{y2}) + \sum_{\bar{q}}^{\infty} (I_{y3} + I_{y4}) + \sum_{\mathbf{q}}^{\infty} (I_{xy1} + I_{xy2}) + (I_{xy3} + I_{xy4})\Big]\Big] = 0 \tag{19}$$

The integer i takes on all positive odd values while the integers q^*, $\bar{q}$, and $\mathbf{q}$ can only adopt a more restricted range of values. The x and/or y subscript(s) denote(s) the stress resultant with which the factor I is associated; the second subscript in the I's identifies the corresponding term in the expression for that stress resultant (for example, I_{x0} and I_{y3} refer to the first term in (11) and the third term in (12), respectively). Finally, k is the buckling coefficient, defined in the usual way [7]:

$$k = \frac{N \cdot b^2}{\pi^2 D} \tag{20}$$

Expression (19) represents an infinite set of simultaneous homogeneous linear equations, the nontrivial solution of which is given by the condition that the determinant of their coefficients be zero. The lowest eigenvalue gives the solution for k.

Problem 1: Plate Buckling Under Locally Distributed Edge Forces

The buckling coefficients for the problem depicted in Fig. 1 have been solved to an accuracy of four significant figures. The results for $\gamma = 0.1$, 0.4, 0.7, and 1.0 appear as plots of k versus ϕ in Fig. 2. For long plates, k tends to $4/\gamma$, a result consistent with St. Venant's hypothesis, since then most of the plate can be considered to be under uniaxial compression N_x/γ. Table 1 lists some actual numerical values of k for various ϕ and γ, which may be used as a basis of comparison for the accuracy of numerical techniques applied to similar problems.

Table 1 Numerical values of k for finite γ

γ \ ϕ	0.7	1.0	1.3
1.0	4.530	4.000	4.281
0.7	4.388	4.181	5.003
0.4	6.087	5.935	7.460
0.1	21.681	21.458	27.503

Table 2 Numerical values of K_T ($\phi \leq 1$) and K($\phi \geq 1$) for $\gamma = 0$

ϕ	0.7	1.0	1.3
K_T (or K)	1.501	2.127	2.737

Problem 2: Plate Buckling Under Concentrated Edge Forces

We let l, $\gamma \to 0$ so that, in the limit, the problem of Fig. 1 is reduced to that of a plate acted on by two concentrated end forces P. The terms in the Fourier series now become

$$A_0 = P/b; \quad A_n = 2P/b \tag{21}$$

It is convenient to define the buckling coefficient for this problem as

$$K_T = \frac{P \cdot a}{\pi^2 D} \text{ for } \phi \leq 1 \tag{22}$$

$$K = \frac{P \cdot b}{\pi^2 \cdot D} \text{ for } \phi \geq 1 \tag{23}$$

The former tends to 1.455 as $\phi \to 0$ while the later approaches 4.000 as $\phi \to \infty$. The results appear in Fig. 3 and some numerical values are also listed in Table 2.

Acknowledgments

The present results form part of an extensive program of investigation into the stability of plates under arbitrary edge forces and subject to various conditions of support. The authors are grateful to Prof. Ian Munro, Imperial College, University of London, for his advice concerning the choice of results appearing in this paper. Thanks are also due to Prof. Gerald A. Wempner, Georgia Institute of Technology, whose suggestions helped shape the present technical abstract.

References

1 Timoshenko, S. P., "Stabilität einer rechteckigen Platte, die durch einzelne Kräfte gedrückt wird," *Zeitschrift für Mathematik und Physik,* Vol. 58, 1910, pp. 357–360.

2 Hopkins, H. G., "Elastic Stability of Infinite Strips," *Proceedings of the 7th International Congress of Applied Mechanics,* London, Vol. 1, 1948, p. 413.

3 Leggett, D. M. A., "The Effect of Two Isolated Forces on the Elastic Stability of a Flat Rectangular Plate," *Proceedings of the Cambridge Philosophical Society,* Vol. 33, 1937, pp. 325–339.

4 Yamaki, N., "Buckling of a Rectangular Plate under Locally Distributed Forces Applied on the Two Opposite Edges," Institute of High Speed Mechanics Reports, Tōhoku University, Vol. 3, No. 26, 1953, pp. 71–87.

5 Yamaki, N., "Buckling of a Rectangular Plate under Locally Distributed Forces Applied on the Two Opposite Edges," Institute of High Speed Mechanics Reports, Tōhoku University, Vol. 3, No. 27, 1953, pp. 89–98.

6 Mathieu, E., Théorie de l'Elasticité des Corps Solides, Part 2, Chapter 10, Gauthier-Villars, Paris, 1890, pp. 140–179.

7 Timoshenko, S. P., and Gere, J. M., *Theory of Elastic Stability,* McGraw-Hill, New York, 1961.

Downloaded 01 May 2010 to 171.66.16.249. Redistribution subject to ASME license or copyright; see http://www.asme.org/terms/Terms_Use.cfm

K. Miya
Associate Professor.

T. Takagi
Graduate Student.

M. Uesaka
Graduate Student.

K. Someya
Assistant Professor.

Nuclear Engineering Research Laboratory, Faculty of Engineering, University of Tokyo, Tokyo, Japan

Finite Element Analysis of Magnetoelastic Buckling of Eight-Coil Superconducting Full Torus

A method of numerical analysis of the magnetoelastic buckling of toroidal field coils is shown on the basis of finite element method. Lagrange's equation is used to deduce an eigenvalue equation determining the buckling current of the toroidal coils. The Lagrangian consists of elastic strain energy and magnetic energy. Since the coil is unidirectional, fiber-reinforced composite material, the theory of orthotropy is applied to determine elastic constants at 4.2 K.

A buckling experiment on the eight superconducting-coil full torus was conducted to verify the numerical method developed here. A comparison of the numerical results with the experimental result is fairly good.

Introduction

Remarkable progress in plasma confinement technology has been achieved in recent years. Reflecting this accomplishment, larger machines such as TFTR [1] and JET [2] are now being constructed to prove scientific feasibility for plasma confinement. Hence, actual engineering problems associated with fabrication and operation of large-scale experimental devices have already been recognized to be very important and must be urgently studied. Coil engineering is one of the very important fusion engineering problems, especially when superconducting coils are employed.

In a Tokamak type reactor, which is the most advanced at the present time, a set of discrete superconducting coils will be used to generate a toroidal magnetic field high enough for the plasma confinement. As is well known, several patterns of magnetic loads such as centering force, circumferential tension, and overturning torque would act on each of the superconducting toroidal field coils. However, the mutual attractions, which also act on each of the coils, are caused by the rest of the coils and are balanced to result in zero force because of a symmetric array of the coils. Conversely, this symmetric array would cause a magnetoelastic instability of a set of the toroidal field coils if the coil current is sufficiently high to overcome the bending stiffness of the coil. Experimental evidence of this magnetoelastic instability of the toroidal coils was first demonstrated by Moon [3]. Moon also developed a modal analysis of the magnetoelastic buckling of the toroidal coils. Since his simple theory is based on the modal analysis, it cannot predict the buckling current without knowing the natural frequency of the coil. Therefore development of some numerical methods has been required for a solution of the magnetoelastic buckling of full-scale, superconducting, toroidal field coils. Applications of the finite element method to the problem have already been demonstrated, with one based on the equivalent plate magnet concept [4] and with another based on the principle of stationary potential energy [5] by Miya and Takagi. The concept of the equivalent plate magnet, which is an extension of the magnetic torque exerting on a ferromagnetic beam plate placed in a magnetic field [6], limits a general application of the theory because the total magnetic torque acting on the coil is assumed to distribute uniformly through an elastic region of the toroidal coil. One of the ways to avoid this limitation is to apply the vector potential method to a direct calculation of a perturbed magnetic energy as shown in reference [5].

In this paper, an eigenvalue equation, from which the buckling current can be obtained, is deduced with the help of Lagrange's equation. Strain energy stored in the toroidal coil and magnetic energy generated by the coil current are needed to construct the Lagrangian. The eigenvalue equation is deduced by substituting the Lagrangian in Lagrange's equation. This method of deduction is simpler than a consideration of balance of force.

On the other hand, orthotropic characteristics of the toroidal coils used in this study must be taken into consideration in the finite element analysis of the experimental results. In reference [5] two simplified models giving upper and lower bounds of elastic constants were applied. In this paper, a new experiment was conducted with the use of an

Contributed by the Applied Mechanics Division for publication in the JOURNAL OF APPLIED MECHANICS.

Discussion on this paper should be addressed to the Editorial Department, ASME, United Engineering Center, 345 East 47th Street, New York, N.Y. 10017, and will be accepted until two months after final publication of the paper itself in the JOURNAL OF APPLIED MECHANICS. Manuscript received by ASME Applied Mechanics Division, March 1981; final revision, September 1981.

Copyright © 1982 by ASME
Downloaded 01 May 2010 to 171.66.16.249. Redistribution subject to ASME license or copyright; see http://www.asme.org/terms/Terms_Use.cfm

eight-coil full torus and a more accurate model of the composite coil, which was proposed by Uemura and Yamada, was applied to give better agreement between theory and experiment.

Theory of Magnetoelastic Buckling of Toroidal Coils

Basic Equations. Any of the toroidal coils experience attractive forces from the rest of the coils since the coil currents flow in the same direction. These attractive forces are balanced when the coils are symmetrically arrayed in a torus. However, the balance of the forces could be broken when a perturbed displacement of some coil occurs. An unbalance of the forces could be caused by an increase in the coil current to a critical one as observed in a buckling of a column loaded with axial compressive force. The coil current is considered to correspond to the axial force in the Euler buckling of the column.

In this paper, our concern is placed on showing a numerical method to calculate the critical current corresponding to the buckling of the toroidal coils. For this purpose, a perturbed magnetic energy stored in the coil system must be taken into consideration together with an elastic strain energy.

Letting U_m and U_e denote magnetic and strain energies, respectively, both are expressed as follows,

$$U_m = \frac{1}{2}\sum_i \int\int \mathbf{A}\cdot\mathbf{J} h dx dy \tag{1}$$

$$U_e = \frac{1}{2}\sum_i \int\int \{\epsilon\}^T \{\sigma\} dx dy \tag{2}$$

where

$\mathbf{A}$ = vector potential
$\mathbf{J}$ = current density
$\{\epsilon\}, \{\sigma\}$ = generalized strain and stress, respectively
h = thickness of the coil

Summations of both energies are carried out over all the coils. In general the Lagrangian "L" is defined by

$$L = T - U_e + U_m \tag{3}$$

where T is kinetic energy. The kinetic energy is not needed in the magnetoelastic buckling problem. An equilibrium equation deduced from the Lagrangian is given by

$$\frac{d}{dt}\left(\frac{\partial L}{\partial \dot{w}}\right) - \frac{\partial L}{\partial w} = F \tag{4}$$

where F and w are external force and deflection normal to a coil plane, respectively. Since $\partial L/\partial \dot{w} = 0$ and $F = 0$, Lagrange's equation is given by

$$\frac{\partial}{\partial w}(U_m - U_e) = 0 \tag{5}$$

This simple equation determines the buckling current of the toroidal coils as proved in the following section.

Perturbation of Magnetic Energy. A perturbation of the magnetic energy is caused by a lateral movement of the coil and is given as a difference of the magnetic energies before and after the deflection. Now let us consider an expression for the perturbation of the magnetic energy in a single coil. The magnetic energy given by equation (1) is summed twice for each coil. Thus a change of the magnetic energy for the coil is given by

$$\Delta U_m = \int\int \mathbf{A}'\cdot\mathbf{J}' h dx dy - \int\int \mathbf{A}_0\cdot\mathbf{J}_0 h dx dy \tag{6}$$

where $\mathbf{A}'$ and $\mathbf{A}_0$, for example, are the vector potentials at the coil after and before the deflection, respectively. The vector potential as well as the current density vector will change in value and direction with deflection of the coil. In other words, the translational movement in the toroidal direction causes the change of only the vector potential ($\mathbf{A}' \neq \mathbf{A}_0$, but $\mathbf{J}' = \mathbf{J}_0$) and the two rotations defined by $\partial w/\partial y$ and $-\partial w/\partial x$ causes the change of only the current density ($\mathbf{J}' \neq \mathbf{J}_0$, but $\mathbf{A}' = \mathbf{A}_0$).

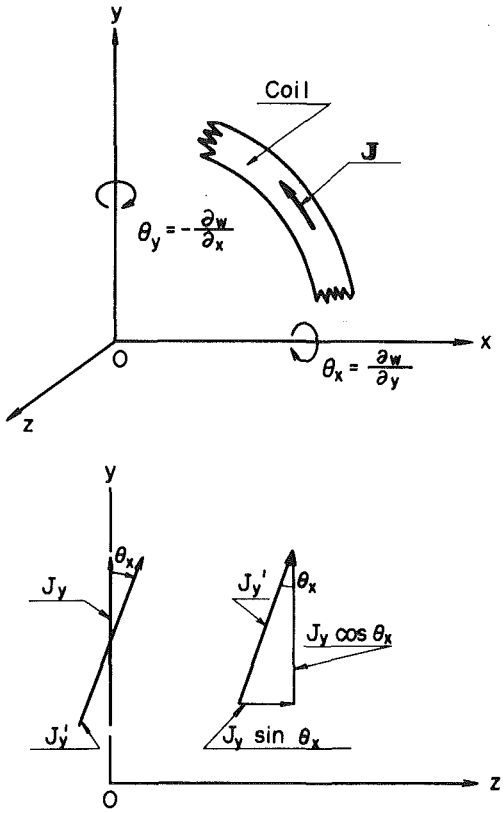


Fig. 1 Change of current density vector due to rotation of coil

Figure 1 shows the change of the current density due to the rotation around the x-axis. Referring to the figure, the new current density vector $\mathbf{J}'$ after the rotation is given by

$$\mathbf{J}' = \mathbf{J}_0 - \left\{\frac{1}{2}J_{x0}\left(\frac{\partial w}{\partial x}\right)^2, \quad \frac{1}{2}J_{y0}\left(\frac{\partial w}{\partial y}\right)^2, \quad J_{y0}\frac{\partial w}{\partial y} + J_{x0}\frac{\partial w}{\partial x}\right\}^T \tag{7}$$

where J_{x0} and J_{y0} are x and y components of the original current density $\mathbf{J}_0$ and thus

$$\mathbf{J}_0 = \{J_{x0}, \quad J_{y0}, \quad 0\}^T \tag{8}$$

The superscript "T" means a transpose of the vector. On the other hand, the vector potential at any point of the coil after the deflection is given by the following Taylor's expansion,

$$\mathbf{A}' = \mathbf{A}_0 + \mathbf{A}_1 w + \mathbf{A}_2 w^2 + \mathbf{A}_3 w^3 + \ldots \tag{9}$$

where the original vector potential $\mathbf{A}_0$ is expressed by

$$\mathbf{A}_0 = \{A_{x0}, A_{y0}, 0\}^T \tag{10}$$

The second term in the right-hand side of equation (9) will not contribute to the magnetic energy when the toroidal coils are arrayed symmetrically in a full torus as shown in Photo 1. If the array of the coils is not symmetric, the problem reduces to one where the deformation needs to be solved. It is also confirmed, upon calculating the coefficients in equation (9), that the odd terms in the deflection "w" will not contribute to the magnetic energy if the array is symmetric. Thus $\mathbf{A}'$ can be approximated by,

$$\mathbf{A}' = \mathbf{A}_0 + \mathbf{A}_2 w^2 \tag{11}$$

Substituting equation (7) and (11) in equation (6), we obtain

Downloaded 01 May 2010 to 171.66.16.249. Redistribution subject to ASME license or copyright; see http://www.asme.org/terms/Terms_Use.cfm

$$\Delta U_m = -\frac{1}{2}\iint\left[J_{x0}A_{x0}\left(\frac{\partial w}{\partial x}\right)^2 + J_{y0}A_{y0}\left(\frac{\partial w}{\partial y}\right)^2\right]hdxdy + \iint[J_{x0}A_{x2} + J_{y0}A_{y2}]w^2 hdxdy \tag{12}$$

where

$$\mathbf{A}_2 = \{A_{x2}, A_{y2}, 0\}^T \tag{13}$$

Here we should notice that as predicted by Faraday's law of induction, the coil currents always change when they change mutual distances between themselves. However, the current change was compensated to keep the coil currents constant by a power supply in a common experiment as carried out in this study. This work done by the electric source is always negative and twice that given by the second term in the right-hand side of equation (12). Thus equation (12) must be modified as follows,

$$\Delta U_m = -\frac{1}{2}\iint\left[J_{x0}A_{x0}\left(\frac{\partial w}{\partial x}\right)^2 + J_{y0}A_{y0}\left(\frac{\partial w}{\partial y}\right)^2\right]hdxdy - \iint[J_{x0}A_{x2} + J_{y0}A_{y2}]w^2 hdxdy \tag{14}$$

Calculation of the coefficients A_{x2}, A_{y2} is shown in reference [5]. The first and second terms in equation (14) represent the energy changes due to the rotations ($\theta_x = \partial w/\partial y$, $\theta_y = -\partial w/\partial x$) and the deflection "$w$," respectively.

Strain Energy in Orthotropic Coil. The toroidal coil is assumed to be a plate, which allows us to treat the buckling of the coil as a plate bending. As generally defined in a treatment of the plate bending, generalized strains and stresses are expressed with curvatures and moments like

$$\{\epsilon\} = \left\{-\frac{\partial^2 w}{\partial x^2}, -\frac{\partial^2 w}{\partial y^2}, -2\frac{\partial^2 w}{\partial x \partial y}\right\}^T \tag{15}$$

$$\{\sigma\} = \{M_x, M_y, M_{xy}\}^T \tag{16}$$

Hooke's law is given by

$$\{\sigma\} = [D]\{\epsilon\} \tag{17}$$

where $[D]$ is the elasticity matrix, a function of Young's modulus, Poisson's ratio, and thickness of the coil. Since the coil used in this study consisted of NbTi wire and epoxy resin, it should be treated as an orthotropic elastic plate.

Actually the coil in the experiment can be considered as a unidirectional, fiber-reinforced composite material. A schematic cross section of the coil is shown in Fig. 2(*a*). In a previous paper [5], elastic constants of the coil were assumed to be between those of Type I and Type II models, which are also shown in Figs. 2(*b*) and 2(*c*). A reason why a prediction of the elastic constants is needed in the buckling analysis of the experimental results is that Young's modulus, E_T, and Poisson's ratio, ν_T, normal to a winding direction of the fiber, were almost impossible to determine from the bending test at 4.2 K because of the narrow width of the coil, whereas E_L and ν_L in a winding direction could be determined from the specimen cut from a straight portion of the coil.

A set of formulas [7] for the Type I model is,

$$E_L{}^{(\mathrm{I})} = E_f V_f + E_m(1 - V_f) \tag{18}$$

$$E_T{}^{(\mathrm{I})} = E_f E_m / [E_m V_f + E_f(1 - V_f)] \tag{19}$$

$$G_{LT}{}^{(\mathrm{I})} = G_f G_m / [G_m V_f + G_f(1 - V_f)] \tag{20}$$

$$\nu_L{}^{(\mathrm{I})} = \nu_f V_f + \nu_m(1 - V_f) \tag{21}$$

and a set of the formulas [7] for the Type II model is,

$$E_L{}^{(\mathrm{II})} = E_T{}^{(\mathrm{II})} = E_f V_f + E_m(1 - V_f) \tag{22}$$

$$G_{LT}{}^{(\mathrm{II})} = G_f V_f + G_m(1 - V_f) \tag{23}$$

$$\nu_L{}^{(\mathrm{II})} = [\nu_f E_f V_f + \nu_m E_m(1 - V_f)]/E_L{}^{(\mathrm{II})} \tag{24}$$

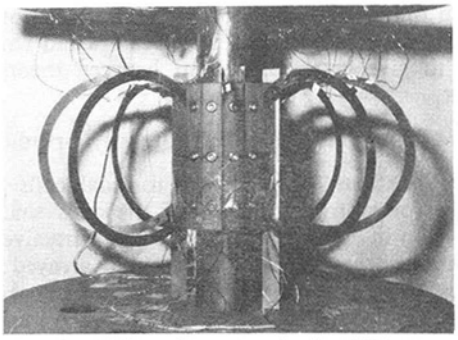


Photo 1 Eight-coil superconducting full torus

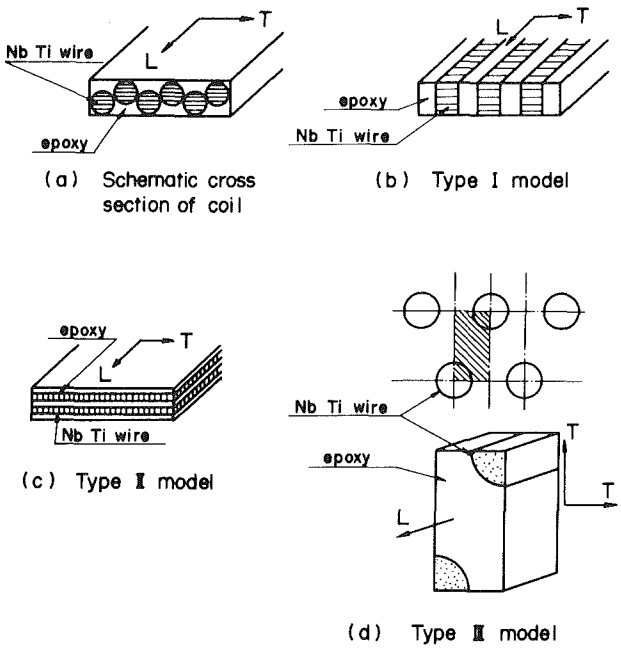


Fig. 2 Schematic configuration of orthotropic coil and its models

where subscripts "f" and "m" refer to the fiber (NbTi wire) and the matrix (epoxy resin), respectively. V_f and G_{LT} are a volume fraction of the fiber and shear modulus of the coil, respectively. A Poisson's ratio, ν_T, which does not appear in the foregoing equations, is given by the reciprocal theorem as

$$\nu_T = (E_T/E_L)\nu_L \tag{25}$$

On the other hand, a set of the formulas for a hexagonal array of reinforced fibers is,

$$E_L{}^{(\mathrm{III})} = E_f V_f + E_m(1 - V_f) \tag{26}$$

$$1/E_T{}^{(\mathrm{III})} = 1.36(K_f - K_m)/[(K_f - K_m)^2 - (\nu_f K_f - \nu_m K_m)^2] + (1 - 1.05\sqrt{V_f})/E_m \tag{27}$$

$$1/G_{LT}{}^{(\mathrm{III})} = 1.36/(G_f - G_m) + (1 - 1.05\sqrt{V_f})/G_m \tag{28}$$

$$\nu_L = 1.05\sqrt{V_f}(\nu_f - \nu_m)K_f/(K_f - K_m) + \nu_m \tag{29}$$

where

$$K_f = E_f/(1 - \nu_f{}^2), \qquad K_m = E_m/(1 - \nu_m{}^2)$$

$$G_f = E_f/2(1 + \nu_f), \qquad G_m = E_m/2(1 + \nu_m)$$

A model for the hexagonal array of reinforced fibers is shown schematically in Fig. 2(*d*), and the foregoing formulas for the model were given by Uemura and Yamada [8]. When we apply any set of the formulas shown in the preceding equations, elastic matrix $[D]$ of the orthotropic coil in equation (17) can be determined as

Downloaded 01 May 2010 to 171.66.16.249. Redistribution subject to ASME license or copyright; see http://www.asme.org/terms/Terms_Use.cfm

$$[D] = \begin{bmatrix} D_x & D_1 & 0 \\ D_1 & D_y & 0 \\ 0 & 0 & D_{xy} \end{bmatrix} \tag{30}$$

where

$$D_1 = \nu_T E_L h^3/12(1-\nu_L\nu_T)$$
$$D_x = E_T h^3/12(1-\nu_L\nu_T)$$
$$D_y = E_L h^3/12(1-\nu_L\nu_T)$$
$$D_{xy} = G_{LT} h^3/12$$

In the local coordinate system fixed to a triangular element, which is selected in the finite element computer code, the y-axis is taken to be in the winding direction of the wire. The strain energy stored in a single coil is expressed as

$$U_e = \frac{1}{2}\int\int \{\epsilon\}^T [D]\{\epsilon\} dxdy \tag{31}$$

Finite Element Formulation of Buckling Equation. Since triangular plate elements are used in this analysis, a shape function proposed by Tocher [9] is employed, which is given by

$$w = \alpha_1 + \alpha_2 x + \alpha_3 y + \alpha_4 x^2 + \alpha_5 xy + \alpha_6 y^2 + \alpha_7 x^3 + \alpha_8(x^2 y + xy^2) + \alpha_9 y^3 \tag{32}$$

This is simply rewritten with a matrix expression like

$$w = [R]\{\alpha_i\} \tag{33}$$

A nodal vector $\{q\}$ for an element of which nodal points are numbered as i, j, k is defined by

$$\{q\}^T = \left\{w_i, \left(\frac{\partial w}{\partial y}\right)_i, -\left(\frac{\partial w}{\partial x}\right)_i, w_j, \left(\frac{\partial w}{\partial y}\right)_j, -\left(\frac{\partial w}{\partial x}\right)_j, w_k, \left(\frac{\partial w}{\partial y}\right)_k, -\left(\frac{\partial w}{\partial x}\right)_k\right\} \tag{34}$$

Introducing equation (32) and coordinates at nodal points in equation (34), we obtain,

$$\{q\} = [H]\{\alpha_i\} \tag{35}$$

From equations (34) and (35), we obtain,

$$w = [R][H]^{-1}\{q\} \tag{36}$$

Substitution of equation (36) in equation (15) gives,

$$\{\epsilon\} = [Q][H]^{-1}\{q\} \tag{37}$$

where

$$[Q] = -\left\{\frac{\partial^2}{\partial x^2}, \frac{\partial^2}{\partial y^2}, 2\frac{\partial^2}{\partial x \partial y}\right\}^T [R] \tag{38}$$

From equations (17) and (37), we obtain,

$$\{\sigma\} = [D][Q][H]^{-1}\{q\} \tag{39}$$

Finally we obtain an expression for the strain energy from substitution of equation (37) in equation (31).

$$U_e = \frac{1}{2}\{q\}^T\left\{\int\int([H]^{-1})[Q]^T[D][Q][H]^{-1} dxdy\right\}\{q\} \tag{40}$$

The shape function of a triangular element is given from equation (36) as follows

$$[N] = [R][H]^{-1} \tag{41}$$

And thus

$$\theta_x = \frac{\partial w}{\partial y} = \frac{\partial [N]}{\partial y}\{q\}, \qquad \theta_y = -\frac{\partial w}{\partial x} = -\frac{\partial [N]}{\partial x}\{q\} \tag{42}$$

Substituting equation (42) in equation (14) we obtain a final expression for the perturbed magnetic energy:

$$\Delta U_m = -\frac{1}{2}\{q\}^T\left[\int\int\left(J_{x0}A_{x0}\frac{\partial [N]^T}{\partial x}\frac{\partial [N]}{\partial x} + J_{y0}A_{y0}\frac{\partial [N]^T}{\partial y}\frac{\partial [N]}{\partial y}\right)hdxdy + 2\int\int(J_{x0}A_{x2} + J_{x0}A_{y2})([H]^{-1})^T[R]^T[R][H]^{-1}hdxdy\right]\{q\} \tag{43}$$

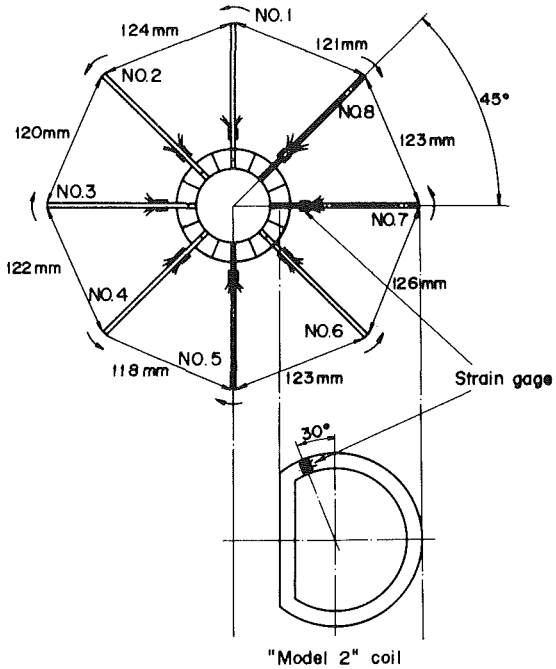


Fig. 3 Top view of the eight-coil superconducting full torus, showing the toroidal buckling mode and the positions of strain gage

Hence, equations (40) and (43) can be written in a matrix form as

$$U_e = \frac{1}{2}\{q\}^T[K_e]\{q\} \tag{44}$$

$$\Delta U_m = \frac{1}{2}\{q\}^T[K_m]\{q\} \tag{45}$$

where $[K_e]$ is a well-known stiffness matrix and $[K_m]$ may be conveniently called a magnetic stiffness matrix. The magnetic stiffness matrix physically corresponds to a magnetic spring constant, and when it is negative, the magnetic force acts on the elastic body carrying a current as a destabilizing force. The critical current for the magnetoelastic buckling can be obtained from solutions of equation (5). Substitution of equations (44) and (45) in equation (5) gives,

$$|[K_e] - [K_m]|\{q\} = 0 \tag{46}$$

For this equation to give nontrivial solution, the following equation must have eigenvalues.

$$|[K_e] - [K_m]| = 0 \tag{47}$$

The buckling current can be given by the first of the eigenvalues obtained from equation (47).

Experiment and Result

Experimental Procedure. The magnetoelastic buckling experiments of the three-coil partial torus with and without a lateral support have been conducted and analyzed with application of the Type I and II models shown in Fig. 2(*b*) and 2(*c*) [5]. In this study, the buckling experiment of an eight-coil full torus without a support was conducted, and the finite element analysis of all the experimental results, including the data from the three-coil partial torus, were analyzed with an application of the accurate Type III model proposed by Uemura and Yamada, which is shown in Fig. 2(*d*). As shown in Photo 1 and Fig. 3, the full torus consists of eight D-shaped

Downloaded 01 May 2010 to 171.66.16.249. Redistribution subject to ASME license or copyright; see http://www.asme.org/terms/Terms_Use.cfm

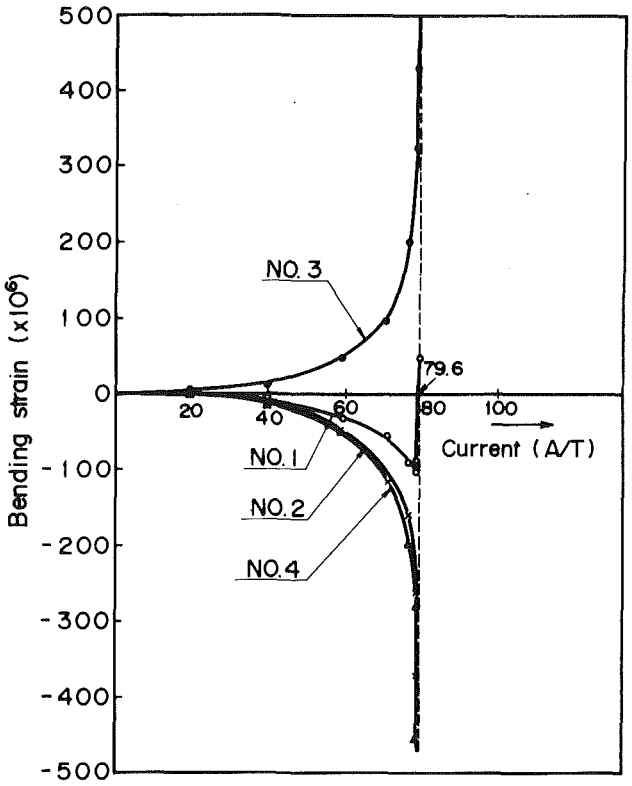


Fig. 4 Current strain curves of the coils (Nos. 1-4) obtained from the buckling experiment on the eight-coil superconducting full torus

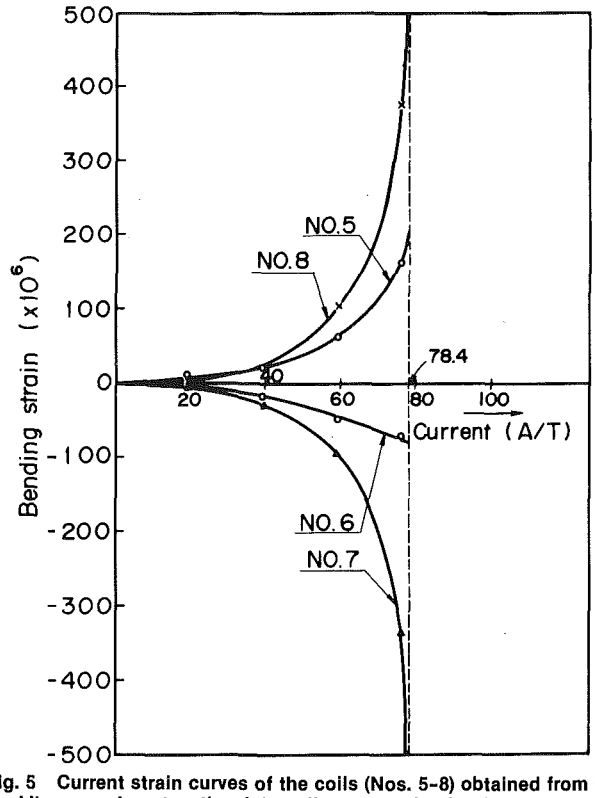


Fig. 5 Current strain curves of the coils (Nos. 5-8) obtained from the buckling experiment on the eight-coil superconducting full torus

coils which are circular over a 270 deg arc of radius 60 mm, and straight along a 90 deg section. Each coil was made from 19-turn NbTi wires potted in epoxy. The NbTi wire was 0.45 mm diameter (copper/superconductor ratio = 1.35). Two pairs of strain gages were attached to every coil to measure the bending strain and to detect the buckling current as shown in Figs. 4 and 5. A vibration method, which is another way of determining the buckling current, was not applied in this study. Although a magnetoresistance of a strain gage would make a significant effect for a very high magnetic field [10], the effect is very small in the present experiment because the magnetic field is small (B_{max} at an inner part of the coil is less than 0.12 Tesla). If any, the effect does not inhibit from determining a buckling current. Figure 3 shows a top view of the full torus and location of the strain gages attached to it. Initial distances between two neighboring coils are also noted in the figure to show a misalignment of the coil array. The whole apparatus was set in a cryostat of 400 mm diameter and liquid helium was poured in the cryostat to conduct the experiment at 4.2 K. Current-bending strain curves shown in Figs. 4 and 5 were recorded on a X-Y chart recorder. The power supply designed for a superconductor has a capacity of up to a direct current of 200 A.

Experimental Results. Direction of deflection of each coil is marked with an arrow in Fig. 3. There are eight kinds of toroidal modes that occur for this set of the toroidal coils. The first mode that occurs is a pairing mode defined so that two neighboring coils move closer to each other. However, the toroidal set had a slightly significant misalignment as shown in Fig. 3. The maximum difference was 6.7 percent ((126-118) × 100/118). This misalignment was supposed to make a complete pairing mode not occur as a whole. Nevertheless, three pairs that move closer to each other are found in the figure (No. 2, No. 3, No. 4, No. 5, No. 7, and No. 8 coils). A buckling current of this partial pairing mode can be approximated with that of a complete pairing mode as discussed

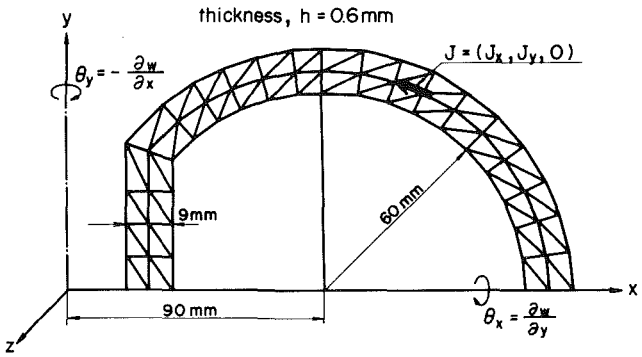


Fig. 6 Mesh division of half coil with triangular element

later. Bending strain versus toroidal-coil current curves are shown in Figs. 4 and 5. In the figures, strains of No. 1, No. 5, and No. 6 are much smaller compared with those of the rest for the coil current near the buckling current. This indicates that No. 1, No. 5, and No. 6 coils still did not buckle when the rest of the coils did drastically. The buckling currents of No. 7 and No. 8 coils are almost the same (78.4 A/turn) and slightly smaller than that of No. 2, No. 3, and No. 4 coils (79.6 A/turn), but this is not a significant difference. The Southwell plot of the curves could give us almost the same buckling currents, which are not shown here.

Numerical Analysis of Experimental Results

Figure 6 shows a mesh division of the coil. The total numbers of elements and nodal points are 80 and 63, respectively. The thickness of the coil is 0.6 mm. The upper half of the coil was analyzed, considering symmetry. A straight portion was clamped to give a fixed boundary condition. In the local coordinates set to an element, the y-axis is chosen in the flow direction of the coil current. Figure 7 shows numerical results for buckling currents of various toroidal

Downloaded 01 May 2010 to 171.66.16.249. Redistribution subject to ASME license or copyright; see http://www.asme.org/terms/Terms_Use.cfm

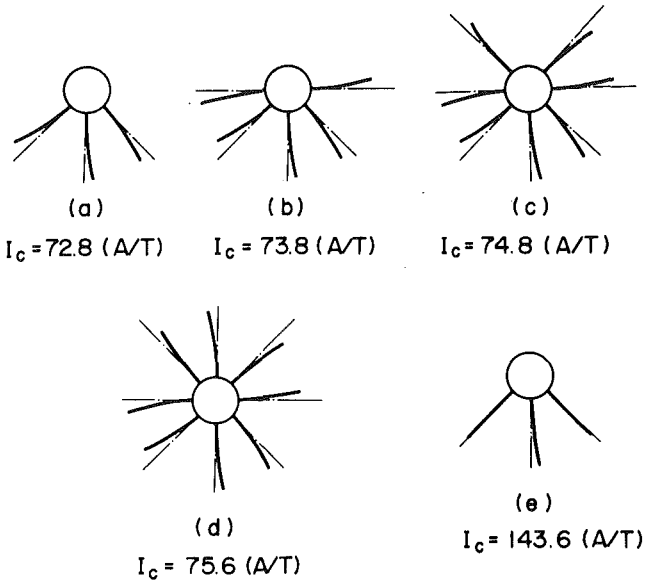


Fig. 7 Buckling currents for various toroidal modes

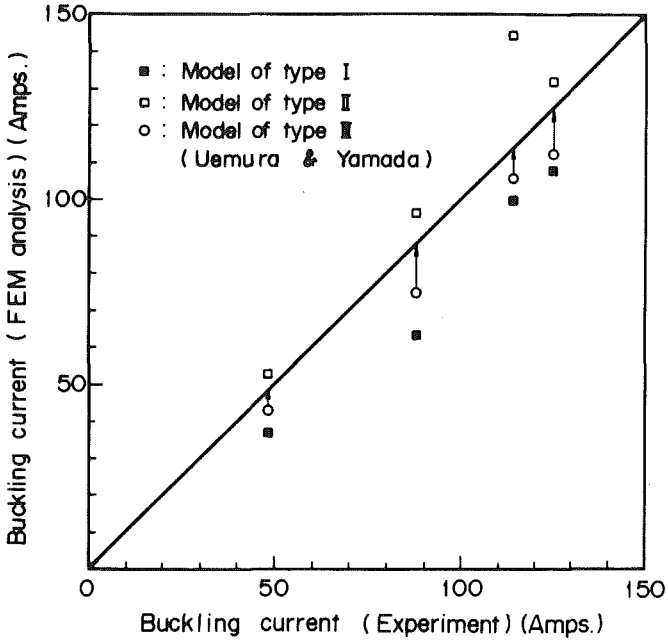


Fig. 8 Comparison of numerical results with experimental ones for buckling current

Table 1 Comparison of buckling currents between FEM analysis and experiment

		Experiment	FEM analysis		
			Type I	Type II	Type III
Three-coil torus	Model I	114.0	100	145	106.0
	Model II	47.8	37	53	43.2
	Model II (support)	125.0	108	132	112.0
Full torus	Model II	78.4			
		79.6	63.2	96.7	75.6

Note: Diameters of NbTi wire used in Model I and Model II are 0.68 and 0.45 mm, respectively.

modes when the number of coils increases, and the corresponding buckling modes are also shown. An increase of the number of coils would lead to a slight increase of the buckling current. Roughly speaking, however, a significant difference does not occur. The buckling current determined from the present experiment may be expected close to that of the pairing mode of Fig. 7(*d*) because a dominant effect will be given to one coil by a pairing coil. In the case of the three-coil partial tori [Fig. 7(*a*) and Fig. 7(*e*)], a boundary condition of two side coils yield a very significant effect on the buckling current. In case of Fig. 7(*e*), the buckling current is 143.6 (A/turn), which is twice that of Fig. 7(*a*).

To obtain accurate numerical results, the mechanical behavior of the orthotropic coil must be evaluated as exactly as possible. Fortunately the coils used in the series of our magnetoelastic buckling experiments are unidirectional fiber-reinforced composite material. Although several formulas for the elastic constants have been proposed, those proposed by Uemura and Yamada seem better. A comparison of numerical results with all the experimental results obtained thus far is shown in Table 1. All the experimental and numerical results listed in Table 1 are shown in Fig. 8, where the experimental results are plotted on the abscissa and numerical results on the ordinate. If the plotted data were on the 45 deg, declined line, the agreement between theory and experiment would be complete. Blank circles calculated with application of Uemura and Yamada's formula are nearer to the line.

As Moon discussed in his paper [11], an extensional force could make the coil stiff for the out-of-plane displacement. The tension stiffening effect, however, was not evaluated in this paper. Moon's paper [11] showed that the buckling current is increased by about 7 percent for a toroidal coil current of 100 A/turn. Applying a correction given by equation (9) in reference [11] to the present numerical results, the theoretical results in Table 1 tend to approach more closely to the experimental results.

Conclusions

The following conclusions are drawn from the theoretical and experimental study on the magnetoelastic buckling of the toroidal field coils.

1 The work done by the electric field due to a rotation of the coil current, must be included as a contribution to the potential energy.

2 The method of numerical analysis of the magnetoelastic buckling has been completely established based on the finite element method.

3 The theory of orthotropic material was applied to the evaluation of the elastic behavior of the coil with success.

Acknowledgment

This work has been done with the financial support of the Controlled Thermonuclear Reactor Committee (Chairman, Prof. R. Kiyose), Faculty of Engineering, the University of

Downloaded 01 May 2010 to 171.66.16.249. Redistribution subject to ASME license or copyright; see http://www.asme.org/terms/Terms_Use.cfm

Tokyo. The authors would like to express their sincere gratitude to Mr. H. Yanagi for his help in the experiment. The authors also appreciate discussions and comments on this work with Prof. F. C. Moon, Cornell University.

References

1 Smith, G. E., and Punchard, W. F. B., "TFTR Toroidal Field Coil," *Proceedings of the 7th Symposium on Engineering Problems of Fusion Research*, 1977, pp. 15–19.

2 Huguet, M., Booth, J. A., and Pohlchen, R., "The Design and Manufacture of the Joint European Torus (JET) Toroidal Field Coils," *Proceedings of the 7th Symposium on Engineering Problems of Fusion Research*, 1977, pp. 28–32.

3 Moon, F. C., "Buckling of a Superconducting Coil Nested in a Three-Coil Toroidal Segment," *Journal of Applied Physics*, Vol. 47, No. 3, Mar. 1976.

4 Miya, K., and Takagi, T., "Finite Element Analysis of Electromagnetoelastic Buckling of Superconducting Magnet in a Magnetic Fusion Reactor," ASME *Journal of Pressure Vessel Technology*, 1978, pp. 1–24.

5 Miya, K., Takagi, T., and Uesaka, M., "Finite Element Analysis of Magnetoelastic Buckling and Experiments on a Three-Coil Superconducting Partial Torus," ASME *Journal of Mechanical Design*, Vol. 41, 1980, pp. 91–107.

6 Miya, K., Takagi, T., and Ando, Y., "Finite-Element Analysis of Magnetoelastic Buckling of Ferromagnetic Beam Plate," ASME JOURNAL OF APPLIED MECHANICS, Vol. 47, No. 2, 1980, pp. 377–382.

7 Uemura, M. et al., "Elastic Constants of Filament Wound Composite Materials," Report of Institute of Space & Aeronautical Science, Univ. of Tokyo, Vol. 4, No. 3(B), 1968, pp. 448–463.

8 Uemura, M., and Yamada, N., "Elastic Constants of Carbon Fiber Reinforced Plastic Materials," *J. Society of Material Science of Japan (Zairyo)*, Vol. 24, No. 257, 1965, pp. 156–163.

9 Tocher, J. L., "Analysis of Plate Bending Using Triangular Elements," Ph.D. dissertation, Civil Engineering Department, University of California, Berkeley, Calif. 1962.

10 Walstrom, P. L., "The Effect of High Magnetic Fields on Metal Foil Strain Gages at 4.2 K," *Cryogenics*, May 1975, pp. 270–272.

11 Moon, F. C., "Experiments on Magnetoelastic Buckling in a Superconducting Torus," ASME JOURNAL OF APPLIED MECHANICS, Vol. 46, 1979, pp. 145–150.

Downloaded 01 May 2010 to 171.66.16.249. Redistribution subject to ASME license or copyright; see http://www.asme.org/terms/Terms_Use.cfm

Dynamic Instability in Ice-Lifting From a Flat Road Surface Through Penetration With a Sharp Blade[1]

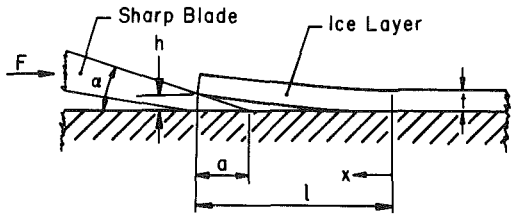
N. C. Huang
Department of Aerospace and Mechanical Engineering, University of Notre Dame, Notre Dame, Ind. 46556
Mem. ASME

This paper is concerned with the problem of dynamic instability during ice-lifting from a flat surface through penetration of the interface by means of a sharp blade. The blade is subjected to a horizontal impulsive load and a constant horizontal thrust, both applied suddenly and simultaneously. The principle of the balance of energy is used to analyze the deformation of the ice associated with the crack propagation along the interface. In our formulation, the effect of wave propagation in the ice is neglected. However, the inertia force due to the acceleration of the blade is included. The motion of the blade is investigated by the numerical solution of a complex, nonlinear, initial value problem. It is found that under a given horizontal thrust, if the initial velocity of the blade is sufficiently small, the motion of the blade may stop. However, if the initial velocity of the blade is sufficiently large, the motion of the blade is always forward and the crack can propagate indefinitely along the interface.

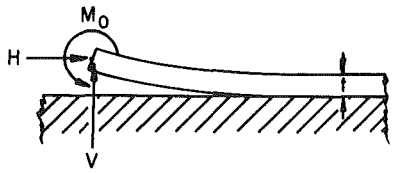
Introduction

At present, the most common and reliable method for ice removal from the road surface is the application of a mechanical tool with a sharp edge such as blades, chisels, and shovels. With the use of the mechanical method, impact force is usually applied to the tool in addition to a constant thrust. The ice layer can be lifted from the road surface as the crack propagates along the ice-road interface. A quasi-static problem of ice-lifting from the surface under the action of a horizontal thrust applied to a sharp blade has been studied by Huang [1]. The author assumes that an initial crack exists at the end of the interface. His study finds that when the thrust reaches a certain magnitude, the crack can propagate indefinitely along the interface. In the same study, the effect of the inertia force is also investigated for the case of impulsive loading, but the stress wave in the ice is neglected. It is noted that if the applied force is purely impulsive, then the velocity of the blade decreases continuously and there is no dynamic instability involved in ice-lifting.

In this paper, we shall generalize the dynamic problem of reference [1] to the case of combined loading of a constant thrust and an impulsive force both applied suddenly and simultaneously. The impulsive load can cause an initial velocity of the blade. Under a given thrust, if the initial velocity of the blade is sufficiently small, the forward motion of the blade may stop at a certain point. In this case, we have either a situation of limited crack propagation or no crack propagation. When the initial velocity of the blade is beyond a certain limit, the motion of the blade is always forward and the crack can propagate indefinitely along the interface. Thus when we increase the initial velocity of the blade gradually, the pattern of the motion of the blade can change drastically at a certain velocity. We refer to this phenomenon as dynamic instability. Our interest is to find the critical condition of the applied thrust and the initial velocity of the blade for dynamic instability.



(a) Geometry of the problem



(b) Forces and moment acting on the ice layer

Fig. 1 Lifting of an ice layer by a sharp blade

[1]This work has been supported by the Department of Transportation, URBAN MASS TRANSPORTATION ADMINISTRATION, under contract IN-06-0009, titled Cold Weather Transit Technology Program.

Contributed by the Applied Mechanics Division for publication in the JOURNAL OF APPLIED MECHANICS.

Discussion on this paper should be addressed to the Editorial Department, ASME, United Engineering Center, 345 East 47th Street, New York, N.Y. 10017, and will be accepted until two months after final publication of the paper itself in the JOURNAL OF APPLIED MECHANICS. Manuscript received by ASME Applied Mechanics Division, April, 1981; final revision, September 1981.

Copyright © 1982 by ASME
Downloaded 01 May 2010 to 171.66.16.249. Redistribution subject to ASME license or copyright; see http://www.asme.org/terms/Terms_Use.cfm

Outline of the Quasi-Static Problem

Let us consider a layer of ice of width b and thickness t. The ice is lifted by a sharp blade with blade angle α, as shown in Fig. 1(a). When the blade is penetrated by a distance a, the length of the lifted ice is l. The blade is subjected to a horizontal thrust F. The forces and moment acting at the end of the lifted ice are shown in Fig. 1(b). In the case of small deflection, the effect of the horizontal force H can be neglected. We shall treat the ice layer as an elastic Timoshenko beam of cantilever type, and analyze the problem based on the principle of the balance of energy, i.e., the total work done by the vertical force V, the end moment M_0, and the weight of the lifted ice layer is equal to the sum of the strain energy stored in the ice and the surface energy for separating the ice from the flat surface. In our investigation, we shall first consider a quasi-static problem where the effect of all inertia forces is neglected. An eigenvalue problem can be formulated for the initiation of crack propagation. The solution has been found in reference [1]. It can be summarized as follows:

Let EI be the bending stiffness of the ice; G the shear modulus of the ice; ρ the density of the ice; and ψ the angle of friction between the blade and the flat surface. By Timoshenko beam theory, we obtain the horizontal displacement of the blade as

$$a=\frac{1}{3EI}Fl^3\frac{\cos\alpha\cot\alpha\cos\psi}{\sin(\alpha+\psi)}-\frac{1}{4EI}Fl^2t\frac{\cos\alpha\cos\psi}{\sin(\alpha+\psi)}-\frac{1}{8EI}\rho btl^4\cot\alpha+\frac{3Fl}{2btG}\frac{\cos\alpha\cot\alpha\cos\psi}{\sin(\alpha+\psi)}-\frac{3\rho l^3}{4G}\cot\alpha. \quad (1)$$

Let δF, δl, and δa be the increments of F, l, and a, respectively. The balance of energy requires that

$$\left[-\frac{1}{3EI}Fl^3\frac{\cos^2\alpha\cos^2\psi}{\sin^2(\alpha+\psi)}+\frac{1}{4EI}Ftl^2\frac{\sin\alpha\cos\alpha\cos^2\psi}{\sin^2(a+\psi)}-\frac{3}{2btG}Fl\frac{\cos^2\alpha\cos^2\psi}{\sin^2(\alpha+\psi)}\right]\delta F+\left[\frac{1}{8EI}\rho^2b^2t^2l^4-\frac{1}{4EI}F^2l^2\frac{\cos^2\alpha\cos^2\psi}{\sin^2(\alpha+\psi)}+\frac{1}{4EI}F^2tl\frac{\sin\alpha\cos\alpha\cos^2\psi}{\sin^2(\alpha+\psi)}+\frac{3}{4G}\rho^2btl^2-\frac{3}{4btG}F^2\frac{\cos^2\alpha\cos^2\psi}{\sin^2(\alpha+\psi)}-Tb\right]\delta l+F\frac{\cos\psi\sin\alpha}{\sin(\alpha+\psi)}\delta a=0. \quad (2)$$

Let ν be Poisson's ratio of the ice; T the surface energy per unit area between the ice and the flat surface; l_0 the initial crack length at the interface measured from the end of the ice layer, and

$$\mu=(1+\nu)\cot^2\alpha,\qquad f=\frac{F\cos\alpha\cot\alpha\cos\psi}{\rho bt^2\sin^2(\alpha+\psi)},$$

$$\lambda=\frac{ET\cot^4\alpha}{6\rho^2t^3},\qquad \gamma=\frac{l\cot\alpha}{t},$$

$$\gamma_0=\frac{l_0\cot\alpha}{t},\qquad \beta=\frac{Ea\cot^3\alpha}{12\rho t^2}. \quad (3)$$

Equation (1) can be expressed in terms of the dimensionless quantities as

$$\beta=\frac{\gamma}{24}[\gamma(8f\gamma-6f-3\gamma^2)+3\mu(2f-\gamma)]. \quad (4)$$

The incremental form of equation (4) is

$$\delta\beta=\frac{1}{12}[\gamma(4\gamma^2-3\gamma+3\mu)\delta f+3(4f\gamma^2-2f\gamma-2\gamma^3+4f-\mu\gamma)\delta\gamma]. \quad (5)$$

Equation (2) can also be expressed in terms of the dimensionless quantities as

$$\delta\beta=\frac{1}{24f}[2f\gamma(4\gamma^2-3\gamma+3\mu)\delta f-3(\gamma^4-4f^2\gamma^2+2f^2\gamma+\mu\gamma^2-\mu f^2-4\lambda)\delta\gamma]. \quad (6)$$

Equations (5) and (6) can be combined as

$$[f^2(4\gamma^2-2\gamma+\mu)-2f\gamma(\mu+2\gamma^2)+\gamma^4+\mu\gamma^2-4\lambda]\delta\gamma=0. \quad (7)$$

We have either

$$\delta\gamma=0 \quad (8)$$

or

$$f^2(4\gamma^2-2\gamma+\mu)-2f\gamma(\mu+2\gamma^2)+\gamma^4+\mu\gamma^2-4\lambda=0 \quad (9)$$

which leads to

$$f=\frac{\gamma(\mu+2\gamma^2)+[\gamma^2(\mu+2\gamma^2)^2-(4\gamma^2-2\gamma+\mu)(\gamma^4+\mu\gamma^2-4\lambda)]^{1/2}}{4\gamma^2-2\gamma+\mu} \quad (10)$$

Equation (8) corresponds to the case of no crack propagation. In this case, β is related to f by equation (4) with $\gamma=\gamma_0$. After crack propagation, f is related to γ by equation (10), hence the $f-\beta$ relation can be determined by equations (4) and (10) with γ as a parameter.

For $\mu=48.25$, $\gamma_0=11.34$, and $\mu=4.529\times10^9$, thus $f-\beta$ relation is shown in Fig. 2. It is found that for $\beta<3.423\times10^6$, there is no crack propagation and the $f-\beta$ relation is nearly linear. When f is increased to a value of 5.799×10^3, $\beta=3.423\times10^6$ and bifurcation occurs. Under this value of f,

Nomenclature

a = penetration of the blade
b = width of ice
E = modulus of elasticity of the ice
F = effective horizontal thrust for ice-lifting
F_a = applied horizontal thrust
f = equation (1)
f_a = equation (4)
f_c = critical value of f for crack propagation
G = shear modulus of the ice
I = moment of inertia of the cross section
l = length of the crack
l_0 = initial length of the crack
m = mass of the blade
T = surface energy between the ice and the flat surface
t = thickness of the ice
t_0 = time
V_b = velocity of the blade
V_0 = initial velocity of the blade
v_b = equation (4)
v_0 = equation (4)
v_{oc} = critical value of v_0 for dynamic instability
α = blade angle
β = equation (1)
γ = equation (1)
γ_0 = equation (1)
λ = equation (1)
μ = equation (1)
ν = Poisson's ratio of the ice
ρ = density of the ice
σ_b = maximum tensile stress in the ice
τ = equation (4)
τ_b = equation (12)
ψ = angle of friction between the blade and the flat surface

Downloaded 01 May 2010 to 171.66.16.249. Redistribution subject to ASME license or copyright; see http://www.asme.org/terms/Terms_Use.cfm

the crack begins to propagate. With the initiation of crack propagation, f decreases with increasing β. Hence, the point of bifurcation is also a maximum point where an instability of the snapping type can be expected under the bifurcation load.

Analysis of the Dynamic Problem

In our dynamic problem we shall include the effect of the inertia force of the blade but neglect the phenomenon of stress wave propagation in the ice. Thus the ice layer acts as a nonlinear spring with the force-displacement relation shown in Fig. 2. The blade is subjected to a horizontal thrust, which is a step function of time of the magnitude F_a. The blade is also subjected to an initial velocity V_0. The velocity of the blade at any time t_0 is denoted by V_b. Let us introduce the following dimensionless quantities:

$$\tau = \left[\frac{Eb\cot^2\alpha\sin(\alpha+\psi)}{12m\cos\alpha\cos\psi}\right]^{\frac{1}{2}} t_0,$$

$$v_b = \left[\frac{Em\cot^4\alpha\cos\alpha\cos\psi}{12\rho^2 t^4 b\sin(\alpha+\psi)}\right]^{\frac{1}{2}} V_b,$$

$$v_0 = \left[\frac{Em\cot^4\cos\alpha\cos\psi}{12\rho^2 t^4 b\sin(\alpha+\psi)}\right]^{\frac{1}{2}} V_0,$$

$$f_a = \frac{F_a\cos\alpha\cot\alpha\cos\psi}{\rho bt^2\sin(\alpha+\psi)}, \tag{11}$$

where m is the mass of the blade. We have

$$v_b = \frac{d\beta}{d\tau}, \tag{12}$$

and the effective force for ice lifting is the sum of the applied force f_a and the D'Alemberet's inertia force $-d^2\beta/d\tau^2$, i.e.,

$$f = f_a - \frac{d^2\beta}{d}$$

Equations (4) and (10) still hold in the dynamic problem. At $\tau = 0$, we have the following initial conditions:

$$\beta(0) = f(0) = 0, \qquad \gamma(0) = \gamma_0 \qquad \text{and} \qquad v_b(0) = v_0. \tag{14}$$

When τ is sufficiently small, there is no crack propagation and β is related to f by equation (4) with $\gamma = \gamma_0$. When τ is sufficiently large, the crack may propagate depending on the value of v_0.

Our initial value problem will be solved numerically. The numerical scheme adopted here is similar to what has been used in reference [1]. With a two-term Taylor's expansion, we can relate the increments in β and τ, $\delta\beta$ and $\delta\tau$, by

$$\delta\beta = \frac{d\beta}{d\tau}\delta\tau + \frac{1}{2}\frac{d^2\beta}{d\tau^2}\delta\tau^2$$

$$= v_b\delta\tau + \frac{1}{2}(f_a - f)\delta\tau^2. \tag{15}$$

Therefore,

$$\delta\tau = \frac{1}{f - f_a}\left\{v_b \pm [v_b^2 - 2(f - f_a)\delta\beta]^{\frac{1}{2}}\right\}, \tag{16}$$

where we take the plus sign for $v_b < 0$ and the minus sign for $v_b > 0$. From equations (12) and (13) we have,

$$\frac{dv_b}{d\tau} = f_a - f, \tag{17}$$

which leads to

$$\delta v_b = (f_a - f)\,\delta\tau. \tag{18}$$

For given values of μ, λ, γ_0, f_a, and v_0, we first calculate the bifurcation load f_c according to equation (10) with $\gamma = \gamma_0$. The value of f increases gradually from zero until it reaches f_c. For each value of f, we compute β from equation (4) with $\gamma = \gamma_0$. The increments $\delta\tau$ and δv_b can be determined from equations (16) and (18). The new values of τ and v_b are now $\tau + \delta\tau$ and $v_b + \delta v_b$, respectively. When f reaches the value f_c, the crack begins to propagate and the value of f decreases with increasing crack length γ. In this case, we assign values for γ, and find f, β, $\delta\tau$, and δv_b successively from equations (10), (4), (16), and (18), respectively.

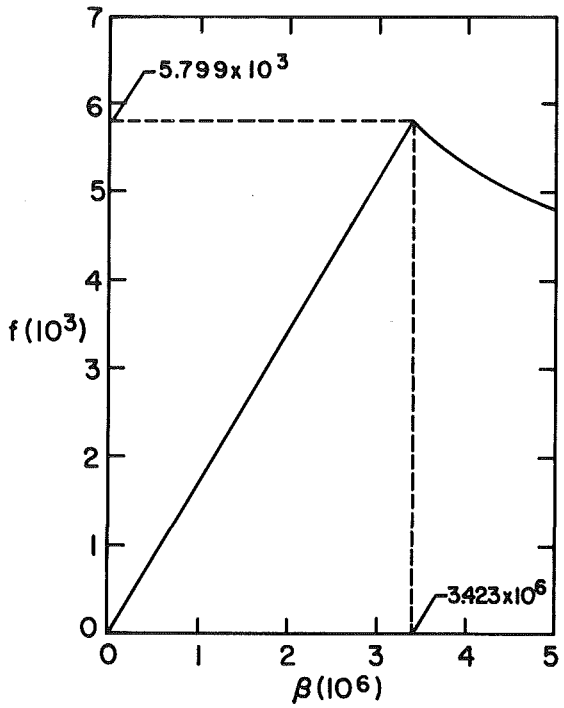


Fig. 2 f versus β curve for $\mu = 48.25$, $\gamma_0 = 11.34$, and $\lambda = 4.529 \times 10^9$

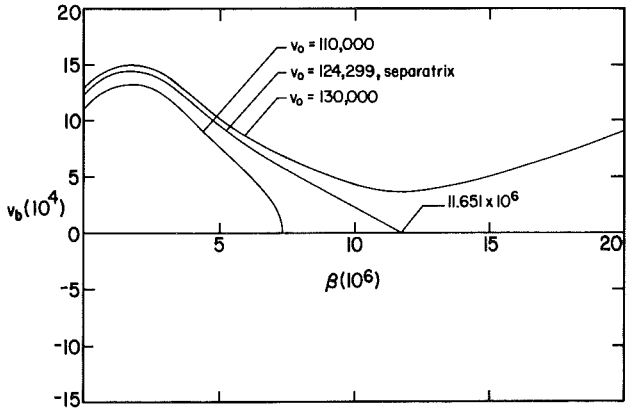


Fig. 3 Phase plane diagram for $\mu = 48.25$, $\gamma_0 = 11.34$, and $\lambda = 4.529 \times 10^9$; $f_a = 3000$ and different values of v_0

In Fig. 3, we have plotted the phase plane diagram, v_b versus β curves, for $\mu = 48.25$, $\gamma_0 = 11.34$, $\lambda = 4.529 \times 10^9$, $f_a = 3000$, and different values of v_0. It is found that when the value of v_0 is small, the trajectory in the phase plane diagram is bounded within a certain region. In this case, the value of v_b can reduce to zero at a certain time. When $\psi > \alpha$, due to the friction, the backward motion of the blade may not occur. When the value of v_0 is sufficiently large, the trajectory in the phase plane diagram becomes unbounded. In this case, motion of the blade is forward and the crack will propagate indefinitely along the interface. The behavior of the transition from a bounded trajectory to an unbounded trajectory in the phase plane diagram is referred to as dynamic instability. The

Downloaded 01 May 2010 to 171.66.16.249. Redistribution subject to ASME license or copyright; see http://www.asme.org/terms/Terms_Use.cfm

critical value of the initial velocity for the dynamic instability is denoted by v_{0c}. When $v_0 = v_{0c} = 124{,}299$, the trajectory is referred to as a separatrix, which corresponds to the critical condition for dynamic instability. At the equilibrium point on the separatrix, $\beta = 11.65 \times 10^6$, $v_b = 0$, and the acceleration $d^2\beta/d\tau^2$ is also zero. Hence, the motion will stop at the equilibrium point. Note that it will take an infinite time to reach the equilibrium point on the separatrix. In Fig. 4, we have plotted f_a versus v_{0c} for $\mu = 48.25$, $\gamma_0 = 11.34$, and $\lambda = 4.529 \times 10^9$. For any combination of f_a and v_0 corresponding to a point below the curve, the motion of the blade is stable. In this case, there is either no crack propagation or a limited crack propagation. On the other hand, if the combination of f_a and v_0 locates a point above the curve in Fig. 4, the motion of the blade is dynamically unstable and the crack propagation is indefinite. Note that when f approaches 0, v_{oc} approaches infinity. This indicates that the crack length is always finite under a purely inpulsive load. This result can be seen from the condition of the conservation of energy. Without the step function load f_a, the total energy input is merely the initial kinetic energy of the blade and hence, the crack length must be bounded.

It is interesting to note that when $v_0 = 0$, the critical value of f_a is 3823, which is smaller than the quasi-static bifurcation load 5799. This substantial decrease in the critical load is due to the fact that the inertia force, due to the deceleration of the blade, can increase the value of the effective thrust and hence, reduces the critical value of the applied thrust. The behavior that the dynamic buckling load for snap-through is smaller than the corresponding static buckling load has also been observed by Nachbar and Huang in a problem of the dynamic snap-through of a shallow simple truss [2].

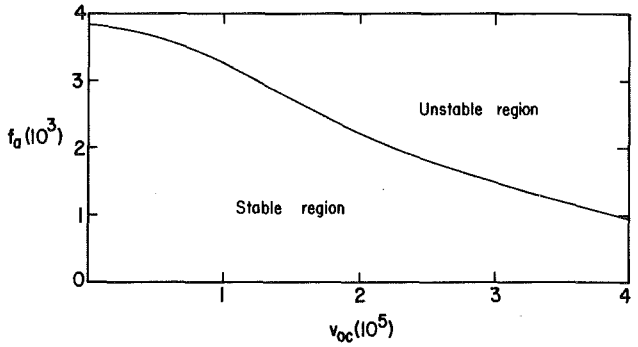


Fig. 4 Critical condition for dynamic instability for $\mu = 48.25$, $\gamma = 11.34$, and $\lambda = 4.529 \times 10^9$

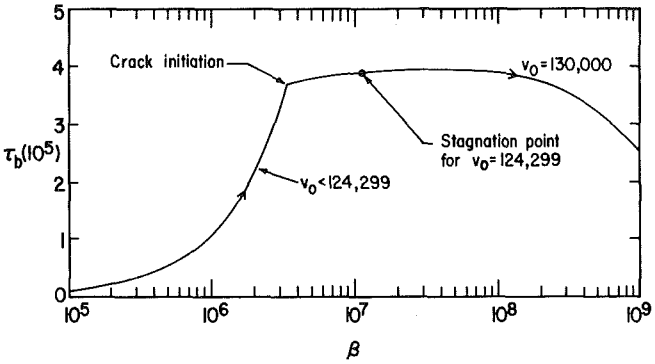


Fig. 5 τ_b versus β curves for $\mu = 48.25$, $\gamma_0 = 11.34$, and $\lambda = 4.529 \times 10^9$; $f_a = 3000$ and different values of v_0

Fracture of Ice

When the length of the interface crack reaches a certain limit, the bending stress in the ice would exceed the maximum tensile strength of the ice and the lifted ice will break at the tip of the interface crack. Let the maximum tensile stress in the ice due to the combined action of bending and direct compression be σ_b and

$$\tau_b = \frac{\sigma_b}{\rho t} \cot^2\alpha. \tag{19}$$

It is found in reference [1] that

$$\tau_b = 2f(3\gamma - 2) - 3\gamma^2. \tag{20}$$

When τ_b exceeds the critical value, fracture of the ice will be introduced. In Fig. 5, we have plotted the maximum tensile stress τ_b versus the penetration β, for $\mu = 48.25$, $\gamma_0 = 11.34$, $\lambda = 4.529 \times 10^9$, $f_a = 3000$, and different values of v_0 corresponding to the cases of dynamic stability, dynamic instability, and their transition. It is found that, prior to crack propagation, the maximum stress in the ice increases rapidly with the penetration of the blade. However, with the crack propagation, the maximum stress increases slowly with the penetration until it reaches a maximum value and then decreases. As we have pointed out previously, if we neglect the effect of the stress wave propagation in the ice, the ice acts simply as a nonlinear spring with the force-penetration relation as shown in Fig. 2. Hence, during the forward motion of the blade, the maximum stress in the ice is actually governed by the quasi-static relation equations (4), (10), and (20), which are independent of the values of f_a and v_0.

Conclusions

It is found that the critical initial velocity for dynamic instability decreases with increasing horizontal thrust. As the result of the inertia force of the blade, even if the initial velocity approaches zero, the critical horizontal thrust for dynamic stability is smaller than its corresponding value for static instability. It is also found that, prior to crack propagation, the maximum stress in the ice increases rapidly with the penetration of the blade. However, after crack propagation, the maximum stress in the ice increases slowly with the penetration until it reaches a maximum value and then decreases. In order to have a large size of the ice chip, it is necessary for us to choose a sufficiently large value of v_0 for dynamic instability. During crack propagation, the maximum stress in the ice depends on the geometrical and physical parameters of the ice and the blade. Although the motion of the blade is controlled by the magnitudes of the applied impulsive and constant forces, the maximum stress in the ice is independent of the applied forces.

Acknowledgment

The author wishes to express his appreciation and thanks to the Department of Transportation for the support of the research; to Mr. K. H. Liu for his assistance in the preparation of illustrations.

References

1 Huang, N. C., "Mechanics of Ice-Lifting from a Flat Surface Through Penetration with a Sharp Blade," Technical Report, Project UMTA, College of Engineering, University of Notre Dame, Notre Dame, Indiana, December, 1980, to appear in ASME JOURNAL OF APPLIED MECHANICS.

2 Nachbar, W., and Huang, N. C., "Dynamic Snap-Through of a Simple Viscoelastic Truss," *Quarterly of Applied Mathematics*, Vol. 25, 1967, pp. 65–82.

Downloaded 01 May 2010 to 171.66.16.249. Redistribution subject to ASME license or copyright; see http://www.asme.org/terms/Terms_Use.cfm

Some Principles of Elastic Shaft Stability Including Variational Principles

R. C. Shieh
MRJ, Inc.,
10400 Eaton Place,
Suite 300,
Fairfax, Va. 22030

Flutter instability problems of (i) a rotating circular elastic shaft subjected to both follower end torque(s) and dead force, and (ii) a rotating elliptical elastic shaft subjected to axial compressive dead force are studied, and some instability and variational principles are established in an "equivalent energy" term.

1 Introduction

Following the pioneering work of Nikolai [1] and Ziegler [2], the local stability problems of a flexible elastic shaft subjected to follower-type nonconservative forces (such as axial or tangential torques) has been studied by many authors (see references in [3–5]). In particular, Ziegler [2] and Troesch [6], through use of the vibration method, showed that undamped cantilever and clamped-hinged circular shafts are unstable under the action of infinitesimally small axial torque while the simply supported circular shaft is stable if the axial torque is smaller than a certain critical value. The latter agrees with the result of Greenhill [7] established by the equilibrium (static) method. It is probable but has not been rigorously proved thus far that the cantilever or clamped-hinged shafts are unstable for all values of the axial torque (see [4]).

According to Ziegler's classification [3], a conservatively loaded, undamped elastic shaft subjected to a constant axial angular rotation falls into the category of gyroscopic conservative systems. Earlier studies [3, 17] revealed that gyroscopic forces may stabilize an otherwise unstable conservative system and thus, may cause the system to exhibit multiple regions of stability. Furthermore, in the presence of gyroscopic forces, the positive-definiteness of the potential energy of the system is no longer a necessary condition for stability [3]. A necessary and sufficient general stability criterion for both discrete and continuous gyroscopic conservative systems in an "equivalent energy" term was later formulated [9] by the author, who also established two variational principles and extended the Rayleigh-Ritz type stability analysis to such systems [8]. These studies [8, 9] also (*a*) revealed that gyroscopic forces, after having stabilized an otherwise divergent unstable conservative system, may also cause such a stabilized system to lose stability by flutter, and (*b*) established a necessary and sufficient condition against flutter instability. Following these studies, the flutter instability behavior was further examined in [18, 19] (also see [20]).

Contributed by the Applied Mechanics Division for publication in the JOURNAL OF APPLIED MECHANICS.

Discussion on this paper should be addressed to the Editorial Department, ASME, United Engineering Center, 345 East 47th Street, New York, N. Y. 10017, and will be accepted until two months after final publication of the paper itself in the JOURNAL OF APPLIED MECHANICS. Manuscript received by ASME Applied Mechanics Division, August, 1980; final revision, June, 1981.

Naturally, these stability and variational principles are also applicable to conservatively loaded, undamped shafts subjected to a constant axial angular rotation. It is well known that an unloaded, rotating circular elastic shaft is always stable except at the discrete critical speeds (at which the system is divergent critical) [17] while an unloaded, elliptical shaft may lose stability by divergence in certain rotating speed ranges and still retain the property of multiple regions of stability. If a rotating shaft is also subjected to a compressive dead force, the shaft may also lose stability by flutter [8]. This phenomenon was further examined in [19], including the case of shafts with unequal principal stiffnesses.

In the present study, local stability of a rotating circular or elliptical shaft subjected to a dead, end compressive force and/or end follower torque(s) is studied through the use of an "equivalent energy" approach [8–11].

2 Instability of a Rotating Circular Shaft Subjected to End, Axial Torsion and Dead Force

(A) Governing Equations of Motion. Let t be the time and z the axial coordinate of a circular shaft of length l and mass per unit length m, carrying a concentrated mass M at $z = \mu l (0 < \mu \leq 1)$ and subjected to an end dead compressive force P and axial follower torque T (see Fig. 1). Let $u_1(z, t)$ and $u_2(z, t)$ denote, respectively, the two components of small lateral displacement of the shaft. The equations of motion, in terms of the complex displacement $w(z, t) = \mu_1 + i\mu_2$ ($i = \sqrt{-1}$) are obtained from equation (2.73) of [5] by adding the concentrated inertia force term $M\delta(z-\mu l)\ddot{w}$ (e.g., see [16]) as

$$EIw^{IV} - iT''' + Pw'' + [m + M\delta(z-\mu l)]\ddot{w} = 0$$

in which $\delta(x)$ is the Dirac delta function of x

$$\text{(i.e., } \delta(x) = 0 \text{ if } c \neq 0; \int_{-\infty}^{\infty} \delta(x)\,dx = 1), \tag{1}$$

and in which the dots and primes indicate differentiations of a function with respect to time t and axial coordinate z, respectively. We now let the shaft, together with the rectangular coordinate frame $oxyz$ rotate uniformly with a constant angular velocity Ω about the undeformed shaft axis oz. The complex force induced by the rotating motion is

Copyright © 1982 by ASME
Downloaded 01 May 2010 to 171.66.16.249. Redistribution subject to ASME license or copyright; see http://www.asme.org/terms/Terms_Use.cfm

$$f=[m+M\delta(z-\mu l)]\,(2i\Omega\dot{w}-\Omega^2 w) \tag{2}$$

and thus, the complex equation of motion of the rotating system becomes

$$EIw^{IV}-i\,Tw'''+Pw''$$
$$+[m+M\delta(z-\mu l)](\ddot{w}+2i\Omega\dot{w}-\Omega^2 w)=0 \tag{3}$$

in which rotatory inertia and gyroscopic moment effects have been neglected.

The boundary conditions of the shafts shown in Fig. 1 may be written as

$$\left.\begin{aligned} &w(EIw'''-iTw''+Pw')=0\\ &w'(EIw''-(1-\alpha)iTw')=0\end{aligned}\right\}\ \text{at } z=0,l \tag{4}$$

where $\alpha = 0$ and $\alpha = 1$ (Fig. 1) correspond to the axial and tangential torque [3–5] loading cases, respectively, and where the two factors in each condition of equation (4) do not vanish simultaneously.

Substitution of

$$w(z,t)=\phi(z)e^{i\omega t} \tag{5}$$

into equations (3) and (4) leads to the complex eigenvalue problem in ω and ϕ:

$$EI\phi^{IV}-iT\phi'''+P\phi''-[m+M\delta(z-\mu l)](\omega+\Omega)^2\phi=0 \tag{6a}$$

$$\left.\begin{aligned} &\phi[EI\phi'''-iT\phi''+P\phi']=0\\ &\phi'(EI\phi''-(1-\alpha)iT\phi')=0\end{aligned}\right\}\ \text{at } z=0,l \tag{6b}$$

Equations (6*a*, *b*) admit the eigensolutions

$$\omega=\omega_n,\quad \phi=\phi_n\ (n=1,2,\ldots) \tag{7}$$

where ϕ_n is the eigenfunction associated with the nth eigenvalue ω_n. The undisturbed rotating state ($u_1 = u_2 = \phi = 0$) is then said to be quasi-stable [12][1] if all ω_n are real and nonvanishing and not repeated; divergent (*d*-) or flutter (*f*-) critical if in the foregoing ω_n conditions at least a pair of ω_n becomes repeated with $\omega_n = 0$ or repeated with $\omega_n \neq 0$; *d*- or *f*- unstable if at least a pair of ω_n becomes purely imaginary or complex provided that in the flutter case no divergent instability occurs simultaneously.

[1] Called "stable" in the common engineering practice, and "critical" in the Liapunov sense of stability [13].

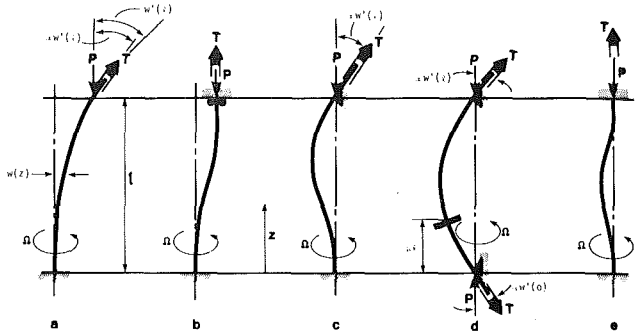


Fig. 1 Shaft end and loading conditions

We now multiply equation (6*a*) by $\bar{\phi}$, the complex conjugate of ϕ, integrate the result over $z=0$ to $z=l$ and use the boundary conditions (6*b*) to obtain

$$-K\omega^2-2\Omega K\omega+Q-iF=0\quad (Q\equiv V-\Omega^2 K) \tag{8}$$

where

$$K = M\phi(\mu l)\,\bar{\phi}(\mu l)+\int_0^l m\phi\bar{\phi}\,dz,$$

$$V = \int_0^l [EI\bar{\phi}''\phi''-P\bar{\phi}'\phi'+\frac{1}{2}iT(\phi''\bar{\phi}'-\phi'\bar{\phi}'')]dz,$$

$$F = \frac{T}{2}[\phi'(l)\,\bar{\phi}'(l)-\phi'(0)\bar{\phi}'(0)](1-2\alpha). \tag{9}$$

are real quantities. The quantities $-K\omega^2$, $-2\Omega K\omega$, Q, and F in equation (8) for real ω are, respectively, *associated* with the kinetic energy, gyroscopic potential, potential energy, and

Nomenclature

A = real functional defined in equation (27)
C = positive-definite function defined in equation (34)
E = Young's modulus
F = equivalent work energy contributed by the nonconservative part of circulatory forces
f = expression in equation (2)
G = scalar functional given in equation (26)
I = second moment of inertia of a circular shaft
I_1, I_2 = two moments of inertia of an elliptical shaft
i = $\sqrt{-1}$
K = scalar functional given in equations (9) or (26)
κ_1, κ_2 = positive real constants (see equation (22))
l = shaft length
M = concentrated mass
m = shaft mass per unit length
P = dead compressive end force
p = PC/U_1
Q = scalar functional given in equation (8)
Q_n = scalar functionals defined in equations (26) ($n=1,2$)
q = $K\Omega^2/U_1$
T = follower torque
t = time
U_n = scalar functionals defined in equation (34) ($n=1,2$)
u_1, u_2 = two components of small lateral displacement vector of the shaft
V = equivalent incremental potential energy of the system contributed by all forces except for the centrifugal forces (see equation (9))
w = $u_1 + iu_2$ = complex shaft lateral displacement
X, Y, Z = real stability functionals defined in equation (28)
z = shaft axial coordinate
α = parameter defining type of follower torque (see Fig. 1)
γ = $U_2/U_1 = I_2/I_1$
δ = variational symbol
$\delta(X)$ = Dirac delta function of X
μ = $z_{(\text{mass } M)}/l$ = nondimensional axial coordinate of the concentrated mass M
Φ_j = eigenfunction defined by equation (17), i.e., $u_j=\Phi_j e^{i\omega t}$ ($j=1,2$)
ϕ = eigenfunction in expression $w = \phi e^{i\omega t}$; $\phi=\Phi_1+i\Phi_2$
$\bar{\phi}$ = complex conjugate of ϕ
ψ = eigenfunction related to Φ_1 and Φ_2 by equation (22)
$\bar{\psi}$ = complex conjugate of ψ
Ω = shaft rotating speed
ω = eigenfrequency

Downloaded 01 May 2010 to 171.66.16.249. Redistribution subject to ASME license or copyright; see http://www.asme.org/terms/Terms_Use.cfm

nonconservative contribution of work energy of the system with respect to the rotating frame. These quantities, which have the dimension of an energy but are fictitious quantities, are, therefore, appropriate to be called "equivalent energy" quantities [8–11] as opposed to the actual ones. They were also called "generalized energy" quantities elsewhere [21].

(B) Stability-Instability Theorems. According to equation (8) and the stability definition given in Section 2(*A*), we obtain the quasi-stability condition as follows:

Theorem 1. *The undisturbed state is (quasi-) stable against divergent (d-) instability if and only if*

$$V>0 \qquad \text{for } \Omega = 0 \tag{10a}$$

$$Q \equiv V-\Omega^2 K \neq 0 \quad \text{for } \Omega \neq 0 \tag{10b}$$[2]

and (quasi-) stable against flutter (f-) instability if and only if

$$F = 0 \quad \text{for } \Omega = 0, \tag{11a}$$

$$F = 0 \; V>0 \quad \text{for } \Omega \neq 0 \tag{11b}$$

for all eigenfunctions $\phi = \phi_n$ $(n = 1, 2, \ldots)$, and stable against all types of instability if and only if all previous conditions are satisfied.

From the expression of F in equations (9) and the necessary condition for stability of the undisturbed state against *f*-instability, i.e., $F = 0$ in equations (11), it is obvious that: *For $T \neq 0$, $\Omega^2 > 0$, $\alpha \neq 1/2$, and $P^2 > 0$, the undisturbed state can be stable only if*

$$\phi'(l) = \pm \phi'(0) \quad (\phi = \phi_n; n = 1, 2, \ldots) \tag{12}$$

Discussion. From equations (10)–(12) the following conclusions can be drawn:

(*a*) *Conservative Torque Cases.* For the case of $\alpha = 1/2$ (for which the torque is of a semi-tangential type [3-5]) or the cases of the shafts in Fig. 1(*b*) and 1(*e*), $F \equiv 0$, and therefore, the systems are conservative if $\Omega = 0$ and gyroscopic conservative if $\Omega \neq 0$. In both conservative and generalized conservative cases, the stability condition is

$$V>0 \quad \text{and} \quad Q \equiv V-\Omega^2 K \neq 0 \; (\text{for } \Omega \neq 0)$$
$$\text{for all } \phi = \phi_n \; (n = 1, 2, \ldots) \tag{13}$$

Furthermore, it is readily shown that the variational principles

$$\delta Q = 0, \quad \delta V = 0 \tag{14}$$

hold for all kinematically admissible function[3] ϕ at a divergent critical state ($Q=0$) and flutter critical state ($V=0$), respectively; in equation (14) the symbol δ denotes conventional variational symbol.

(*b*) *The Cases of the Cantilever Shaft (Fig. 1(a)) and Clamped-Hinged Shaft (Fig. 1(c)).* These shafts are always unstable if $\alpha \neq 1/2$, $T \neq 0$, $\Omega^2 \geq 0$, and $P^2 \geq 0$; furthermore, instability is always of flutter type because $\phi_n'(l) \neq \pm \phi_n'(0)$ $(F \neq 0)$ for all principal modes of vibration. A special case of this instability result, namely, the shafts in Figs. 1(*a*, *c*), are always unstable under the action of any small axial torque (T small; $\alpha = \Omega = P = 0$), was established by Troesch [6][4] through the direct expansion of the characteristic equation in terms of the small torque parameter $\beta = T/EI$.

(*c*) *The Case of the Simply Supported Shaft (Fig. 1(d)) without a Disk ($M \equiv 0$) or Carrying a Disk at Its Midspan ($\mu = 1/2$, $M \neq 0$).* In this case, the shaft vibration problem is symmetric with respect to the midspan section, $z = l/2$. In view that the principal modes of vibration for such a symmetric system are either symmetric or anatisymmetric, i.e., $\phi_n(0) = \pm \phi_n(l)$ $(n = 1, 2, \ldots)$ one has $F=0$ (which means that the nonconservative part of work energy is zero). Consequently, the critical stability load, T_{cr}, needs not to be zero in this case; i.e., the undisturbed state is stable as long as the stability condition, equation (13), is satisfied. Furthermore, it can be shown that the variational principles given by equation (14) also hold for the present case provided that the admissible function ϕ (z) now should also satisfy the additional kinematical condition

$$\phi'(0) = \phi'(l) \text{ or } \phi'(0) = -\phi'(l). \tag{15}$$

Therefore, with this modification, one can extend and use the Rayleigh-Ritz type variational method to the critical load analysis of this (or this class of) gyroscopic "quasi-conservative" shaft stability problems(s) [8] in which the nonconservative part of work energy vanishes under all principal modes of vibration (rather than, as in the conservative loading case, vanishes under any kinematically admissible motions). In this respect it is perhaps appropriate to call such a system in the absence of gyroscopic forces ($\Omega = 0$) as a "quasi-conservative" system. Also, for such a system it is apparent from equation (15), which implies $F = 0$ in equation (11), that the undisturbed state cannot lose stability by flutter if $\Omega = 0$. Therefore, the equilibrium (static) method alone is sufficient for the critical force analysis of the present special case (simply supported shaft with $\Omega = 0$, $P > 0$, $T \neq 0$, and $M = 0$ or $M \neq 0$ and $\mu = 1/2$) of the stability problem despite that it was regarded as an inadmissible method in [3] for the analysis of nonconservative stability problems of circulatory type.[5] Indeed, Greenhill [7] has obtained the critical value $T = 2.0\,\pi/l$ for the simply supported shaft case (with $M = P = \Omega = 0$) through the use of the static method and Ziegler [2] and Troesch [6] have obtained the same through the use of the kinetic (vibration) method.

(*d*) *Case of the Simply Supported Shaft With an Unsymmetrically Located Disk ($M \neq 0$, $0 < \mu < 1$ and $\mu \neq 1/2$).* In this case, $F \neq 0$ for all eigenfunctions $\phi = \phi_n$; therefore, the shaft is always unstable if $T \neq 0$.

3 Instability of a Rotating Elliptical Shaft Subjected to Dead Axial Force

The equations of small lateral motion of a rotating elliptical elastic shaft (see Fig. 2) subjected to a dead compressive force P may be written as

$$EI_j u_j^{IV} + P u_j'' + [m + M\,\delta(z-\mu l)]\,(\ddot{u}_j - 2\,\Omega e_{j\kappa}\dot{u}_\kappa - \Omega^2 u_j) = 0$$
$$(j,\kappa = 1,2; \text{ no sum on } j, \text{ but sum on repeated } \kappa). \tag{16}$$

where $e_{11} = e_{22} = 0$, $e_{12} = -e_{21} = 1$ and EI_j $(j = 1, 2)$ are the bending stiffnesses about the y and x-axes, respectively. The other notations are defined as in Section 2. With

$$u_j(z,t) = \Phi_j(z)\, e^{i\omega t} \quad (j = 1, 2, \quad i = \sqrt{-1}) \tag{17}$$

Equations (16) becomes

$$EI_j\,\Phi_j^{IV} + P\Phi_j'' - [m + M\,\delta(z-\mu l)](\omega^2 \Phi_j + 2i\Omega\, e_{j\kappa}\Phi_\kappa + \Omega^2\,\Phi_j) = 0 \quad (j = 1, 2) \tag{18}$$

[2] If $Q=0$ for $\Omega \neq 0$, the equilibrium state is divergent critical; no divergent instability is possible if $\Omega \neq 0$.

[3] A function is said to be admissible if it satisfies the geometric boundary conditions and required smoothness conditions.

[4] A similar study was given by Ziegler in an earlier paper [2].

[5] A force is called circulatory if it is displacement-dependent and nonconservative, and a system is called circulatory if it is an elastic system subjected to circulatory forces.

Downloaded 01 May 2010 to 171.66.16.249. Redistribution subject to ASME license or copyright; see http://www.asme.org/terms/Terms_Use.cfm

Multiplication of the second of equations (18) by $i = \sqrt{-1}$ and addition to the first equation, then multiplication of the resulting equation with $\bar{\phi} = \bar{\Phi}_1 - i\bar{\Phi}_2$ (the complex conjugate of $\phi = \Phi_1 + i\Phi_2$), integration of the result over $z = 0$ to l and finally use of the boundary conditions

$$(EI_1\Phi_1''' + iEI_2\Phi_2''' + P\phi')\bar{\phi} = (EI_1\Phi_1'' + iEI_2\Phi_2'')\bar{\phi}' = 0 \quad \text{at} \quad z = 0, l \tag{19}$$

leads to the scalar equation

$$-K^*\omega^2 - 2\Omega K^*\omega + (V^* - \Omega^2 K^*) + iF^* = 0 \tag{20}$$

Here, K^*, V^*, F^* are real functionals of Φ_1 and Φ_2 defined by

$$K^* = M\phi(\mu l)\bar{\phi}(\mu l) + \int_0^l m\phi\bar{\phi}dz$$

$$V^* = \int_0^l \left\{\frac{1}{2}[E(I_1 + I_2)\bar{\phi}''\phi'' - E(I_2 - I_1)(\Phi_1''\bar{\Phi}_1'' - \Phi_2''\bar{\Phi}_2'')] - P\phi'\bar{\phi}'\right\}dz$$

$$F^* = \frac{1}{2}\int_0^l E(I_2 - I_1)(\bar{\Phi}_1''\Phi_2'' + \Phi_1''\bar{\Phi}_2'')dz \tag{21}$$

In order that the undisturbed equilibrium state be stable (i.e., all ω real, nonvanishing and not repeated), it is necessary that $F^* = 0$ for *all* eigenfunctions ϕ (cf. equation (20)). This condition is equivalent to

$$\Phi_1(z) = \kappa_1\psi(z), \ \Phi_2(z) = i\kappa_2\psi(z) \ (\kappa_1^2 + \kappa_2^2 \neq 0) \tag{22}$$

for some complex function $\psi(z)$ and real constants κ_j ($j = 1, 2$) with $0 < \kappa_j^2 < \infty$ and $\kappa_1^2 + \kappa_2^2 \neq 0$. Substitution of equations (22) into equations (18) and (19) leads to

$$\kappa_1[EI_1\psi^{IV} + P\psi'' - (\omega^2 + \Omega^2)(m + M\delta(z - \mu l))\psi] + 2(m + M\delta(z - \mu l))\Omega\omega\kappa_2\psi = 0 \tag{23a}$$

$$\kappa_2[EI_2\psi^{IV} + P\psi'' - (\omega^2 + \Omega^2)(m + M\delta(z - \mu l))\psi] + 2(m + M\delta(z - \mu l))\Omega\omega\kappa_1\psi = 0 \tag{23b}$$

$$\kappa_n'[EI_n\psi^{III} + P\psi']\bar{\psi} = 0 (z = 0, 1) \tag{24a}$$

$$\kappa_n^2 EI_n\psi''\bar{\psi}' = 0 \quad (z = 0, l) \quad (n = 1, 2) \tag{24b}$$

Equations (23) and (24) define a new eigenvalue problem, which is assumed to yield the eigenvalues $\omega = \omega_j$ and eigenfunctions $\psi = \psi_j$ ($j = 1, 2, \ldots$). Multiplying equations (23*a*, *b*) by $\bar{\psi}$, the complex conjugate of ψ, integrating the results over $z = 0$ to l and making use of boundary conditions (24*a*, *b*), there are obtained:

$$\left.\begin{aligned} \kappa_1(Q_1 - \omega^2 K) + \kappa_2 G\omega &= 0 \quad (25a) \\ \kappa_1 G\omega + \kappa_2(Q_2 - \omega^2 K) &= 0 \quad (25b) \end{aligned}\right\} (\omega^2 \geq 0)$$

where $K\omega^2$, $G\omega$, and Q_n are real scalar functions (equivalent energy quantities) given by

$$\begin{aligned} K &= \frac{1}{2}M\psi(\mu l)\psi(\mu l) + \frac{1}{2}\int_0^l m\bar{\psi}\psi dz \\ G &= -2\Omega K \\ Q_n &= -\Omega^2 K + \frac{1}{2}\int_0^l (EI_n\psi''\bar{\psi}'' - P\bar{\psi}'\psi')dz \quad (n = 1, 2) \end{aligned} \tag{26}$$

Elimination of κ_1 and κ_2 between equations (25*a*) and (25*b*) gives

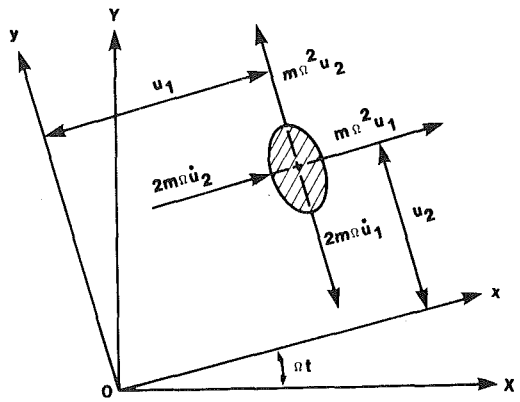


Fig. 2 Lateral forces acting on a rotating elliptical elastic shaft

$$A \equiv \omega^4 K - \omega^2(KQ_1 + KQ_2 + G^2) + Q_1Q_2 = 0 \quad (\omega^2 > 0) \tag{27}$$

Thus, from equation (27) and the definitions of quasi-stability and critical conditions, we obtain the following theorem:

Theorem 2. The undisturbed state is (*i*) stable if and only if

$$X \equiv Q_1Q_2 > 0, \quad Y \equiv K(Q_1 + Q_2) + G^2 > 0,$$

$$Z \equiv K^2(Q_2 - Q_1)^2 + 2K(Q_1 + Q_2)G^2 + G^4 > 0 \tag{28}$$

for all eigenfunctions $\psi = \psi_j$ ($j = 1, 2, \ldots$), (*ii*) divergent critical if and only if

$$Q_1 = 0 \quad \text{or} \quad Q_2 = 0 \quad (Y > 0), \tag{29}$$

and flutter critical if and only if

$$Z = 0 \ (Y > 0) \tag{30}$$

for at least one pair of eigenfunctions while the remaining eigenfunctions satisfy conditions (28), and (*iii*) in a boundary state between flutter and divergent instabilities if and only if

$$Z = 0 \quad \text{and} \quad Y < 0 \tag{31}$$

for a pair of eigenfunctions.

Similary, from the definition of instability and equation (25) we obtain

Corrollary 1: The undisturbed state is divergent-unstable if and only if

$$X = Q_1Q_2 < 0 \tag{32a}$$

or

$$Y < 0, \quad Z > 0 \tag{32b}$$

and flutter-unstable if and only if

$$Z < 0 \quad (X > 0) \tag{33}$$

for at least one eigenfunction.

If we substitute the second and the third of equation (26) into equation (28) and let

$$U_n = \frac{1}{2}\int_0^l EI_n\psi''\bar{\psi}''dz, \quad C = \frac{1}{2}\int_0^l \bar{\psi}'\psi'dz \quad (n = 1, 2) \tag{34}$$

we get more explicit stability conditons

$$\begin{aligned} P &< (U_1 - \Omega^2 K)/C \quad (\text{i.e., } Q_1 > 0, Q_2 > 0), \\ P &> (U_2 - \Omega^2 K)/C \quad (\text{i.e., } Q_1 < 0, Q_2 < 0), \\ P &< \frac{1}{2}(U_1 + U_2)/C + K\Omega^2/C \quad (\text{i.e., } Y > 0), \\ P &< \frac{1}{2}(U_1 + U_2)/C + \frac{1}{16}(U_2 - U_1)^2/\Omega^2 KC \quad (\text{i.e., } Z > 0) \end{aligned} \tag{35}$$

These stability-instability conditions are shown in Fig. 3 in the nondimensional p–q plane, where

Downloaded 01 May 2010 to 171.66.16.249. Redistribution subject to ASME license or copyright; see http://www.asme.org/terms/Terms_Use.cfm

$$p=PC/U_1 \quad q=K\Omega^2/U_1, \quad \gamma=U_2/U_1=I_2/I_1 \qquad (36)$$

This figure coincides with that (e.g., Fig. 5.7 of [20]) of a rotating two-degrees-of-freedom shaft system (e.g., massless shaft, $m=0$, $M\neq 0$, in equation 18) if p and q are interpreted as nondimensional compressive force and square of rotating shaft speed, respectively.

Variational Principle: If we repeat the same procedure followed in obtaining equations (25), but now multiplying equations (23) by $\delta\bar{\psi}$ instead of $\bar{\psi}$, and add the resulting equations to their respective complex conjugate equations, we obtain

$$\kappa_1(\delta Q_1-\omega^2\delta K)+\kappa_2\omega\,\delta G = 0 \qquad (37a)$$

$$\kappa_1\omega\delta G+\kappa_2(\delta Q_2-\omega^2\delta K) = 0 \qquad (37b)$$

in which δ is the variational symbol. Elimination of κ_1 and κ_2 between equations (37*a*) and (25*b*), and between equations (37*b*) and (25*a*), and addition of the resulting equations, lead to the variational equation

$$\delta A=0 \quad \text{(no variation on } \omega) \qquad (38)$$

where A is defined as in equation (27). Furthermore, if we note that the critical flutter frequency (corresponding to the coalescence of two ω's in equation (27)) is

$$\omega_{cr}=\pm\left[\frac{K(Q_1+Q_2)+G^2}{2K^2}\right]^{1/2}=\pm\left[\frac{Q_1Q_2}{K^2}\right]^{1/4} \qquad (39)$$

it is easily seen that the relations

$$\delta A(\psi,\bar{\psi},\omega)=0 \quad \text{(variation on } \omega) \qquad (40)$$

and

$$\delta Z=0 \qquad (41)$$

also hold at a flutter critical state. Therefore, we may state the following theorem and corollary:

Theorem 3. Of all admissible functions ψ, the eigenfunction associated with the eigenvalue ω is characterized by

$$(i) \quad \delta A = 0 \quad \text{for} \quad \omega^2>0. \quad \text{(no variation on } \omega) \qquad (42)$$

$$(ii) \quad \delta Q_1 = 0 \quad \text{or} \quad \delta Q_2=0 \quad \text{for} \quad \omega=0 \quad \text{(divergent critical)} \qquad (41b)$$

$$(iii) \quad \delta Z = 0\ (Y>0) \quad \text{for} \quad \omega=\left[\frac{K(Q_1+Q_2)+G^2}{2K^2}\right]^{1/2} \quad \text{(flutter critical)} \qquad (42)$$

Corollary 2: For all admissible functions ψ and arbitrary ω ($\omega^2>0$), the flutter critical state is characterized by

$$\delta A(\phi_1,\bar{\phi}_1,\omega)=0 \quad \text{(variation on } \omega) \qquad (43)$$

Discussion. Based on the stability-instability conditions (28)–(35) (or Fig. 3) the following conclusions are readily drawn: (*i*) The first condition in equation (35) (that is, $Q_2>Q_1>0$) alone is a sufficient condition for stability, and is equivalent to the classical stability criterion [14]. (*ii*) Flutter instability can occur only in the regions (in loading space) where $Q_1Q_2>0$ and $Z<0$ (which implies $Q_1+Q_2<0$), that is, in the regions where the components Q_1 and Q_2 of the equivalent potential energy are both negative (cf. (33)). (*iii*) an unloaded rotating elliptical shaft can lose stability by divergence (buckling) only (cf. (35) for $P=0$). The divergent loads can be obtained from the instability-critical conditions

$$U_1/K\leq\Omega^2\leq U_2/K \qquad (44)$$

through the use of the Rayleigh-Ritz method; for a massless shaft, equation (44) may be written as

$$EI_1\kappa^*/M\leq\Omega^2\leq EI_2\kappa^*/M$$

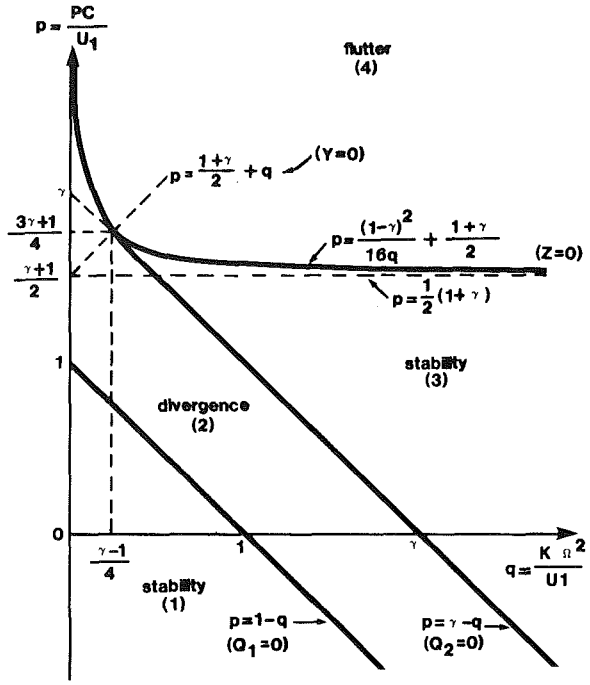


Fig. 3 Stability-instability regions for a rotating elliptical elastic shaft in compression ($\gamma = I_2/I_1 = 2$)

$$\left(\kappa^*=\int_0^1\phi_1''\bar{\phi}_1''\,dz/\phi_1(\mu l)\,\bar{\phi}_1(\mu l)>0\right) \qquad (45)$$

which forms an alternate (but more convenient) version of Grammel's formula [15]. (*iv*) A rotating elliptical shaft, as in the case of a circular shaft, exhibits multiple regions of stability [3, 9] in which $Q_1Q_2>0$ and $Z>0$ (cf. (35) or Fig. 3). (*v*) A sufficient condition against flutter instability is (cf. (33) and (35))

$$P\leq\frac{1}{2}(U_1+U_2)/C \qquad (46)$$

and thus a sufficient condition against both flutter and divergent instabilities is

$$P<(U_1-\Omega^2U_2)/C \quad P>(U_2-\Omega^2K)/C$$

$$P\leq\frac{1}{2}(U_1+U_2)/C=\frac{1}{2}(1+I_2/I_1)U_1/C \qquad (47)$$

which correspond to Regions 1 and 3 in Fig. 3, provided that the upper boundary of Region 3 now is the horizontal asymptotic line of the original flutter boundary curve. These conditions are in a convenient quotient form for approximate critical load analysis in a manner of Rayleigh-Ritz.

Finally, it should be mentioned that all principles and results obtained in this section are equally applicable to the case in which the shaft has unequal principal stiffness.

4 Concluding Remarks

Stability of undamped elastic shafts, carrying a concentrated mass and subjected to a constant axial rotation, a dead compressive force and/or follower type end torque has been studied. The cases studied are (*i*) the circular shaft case in the presence of all these forces, and (*ii*) the elliptical shaft (or shaft with unequal principal stiffness) case in which the follower torque is not present. Stability/instability criteria have been formulated, and variational principles obtained for the elliptical shaft case and the special subcases of the circular shaft case in which the systems are gyroscopic conservative

Downloaded 01 May 2010 to 171.66.16.249. Redistribution subject to ASME license or copyright; see http://www.asme.org/terms/Terms_Use.cfm

(i.e., the torque is semitangental, $\alpha = 1/2$ in Fig. 1, or the shafts shown in Figs. 1(*b* and *e*)) or gyroscopic "quasi-conservative," i.e., the simply supported shaft (Fig. 1(*d*)) in which the disk (if any) is attached at the shaft midspan section; for these cases, the nonrotating shaft cannot lose stability by flutter and thus the static equilibrium method may be used in the divergent critical load analysis. For the other circular shafts shown in Fig. 1, including the simply supported shaft case in which the disk is not attached to the midspan section, it was shown that the shaft cannot be stable in the presence of the nonconservative follower torque ($\alpha \neq 1/2$ in Fig. 1). The critical conditions and variational principles obtained are suitable for the critical load analysis via the Rayleigh-Ritz type variational approach.

Acknowledgment

This work was completed partially at NASA Langley Research Center while the author was a Postdoctoral Resident Research Associate of the National Research Council, National Academy of Sciences.

References

1 Nikolai, E. L., "On the Stability of the Rectilinear Form of a Bar in Compression and Torsion," *Izv. Leningr. politekjn.*, in-ta 31, 1928.

2 Ziegler, H., "Stabilitats probleme bei geraden Staben und Wellen," *Zeitschrift für Angewandte Mathematik und Physik,* Vol. 2, 1951, pp. 265–289.

3 Ziegler, H., "On the Concept of Elastic Stability," *Adv. in Applied Mechanics,* Vol. 4, Academic Press, N. Y., 1956, pp. 351–403.

4 Ziegler, H., *Principles of Structural Stability,* Braisdell Publishing Co., Boston, 1967.

5 Bolotin, V., *Nonconservative Problems of the Theory of Elastic Stability,* The Macmillan Company, N. Y., 1963, Chapters 2 and 3.

6 Troesch, A., "Stabilitats probleme bei tordierten Staben und Wellen," *Ingenieur-Archive,* Vol. 20, 1952, pp. 258–277.

7 Greenhill, A. G., "On the Strength of Shafting When Exposed Both to Torsion and End Thrust," *Proceedings of the Institution of Mechanical Engineers,* London 21883, pp. 182–209.

8 Shieh, R., "Energy and Variational Principles for Generalized (Gyroscopic) Conservative Problems," *International Journal of Nonlinear Mechanics,* Vol. 5, 1971, pp. 495–509.

9 Shieh, R., and Masur, E., "Some General Principles of Dynamic Instability of Solid Bodies," *Zeitschrift für Augewandte Mathematic und Physik,* Vol. 19, 1968, pp. 927–941.

10 Shieh, R. C., "Asymptotic Stability Analysis of Viscoelastic Systems," *Journal of the Engineering Mechanics Division ASCE,* EM2, 1971, pp. 193–203.

11 Shieh, R., "Variational Method in the Stability Analysis of Nonconservative Problems," *Zutschrift fur Augewandte Mathematic und Physik,* Vol. 21, 1970, pp. 88–100.

12 Bolotin, V., and Zhinzher, N. I., "Effects of Damping on Stability of Elastic Systems Subjected to Nonconservative Forces," *International Journal of Solids and Structures,* Vol. 5, 1969, pp. 965–989.

13 Minorski, N., *Nonlinear Oscillations,* D. Van Nostrand Co., Princeton, N. J., 1962, pp. 144–145.

14 Pearson, C., "General Theory of Elastic Stability," *Quarterly of Applied Mathematics,* Vol. 14, 1956, pp. 134–144.

15 Biezeno, C. B., and Grammel, R., *Technische Dynamik,* Vol. II, Springer, Berlin, 1953, p. 164.

16 Yu, Y. Y., "Thermally Induced Vibration and Flutter of a Flexible Boom," AIAA 7th Aerospace Sciences, New York City, January 20–22, 1969, AIAA Paper No. 69–21.

17 Thomson, W., and Tait, G., *A Treatise on Natural Philosophy,* Vol. 1, *Part I, Cambridge University Press, Cambridge, England, 1879.*

18 Huseyin, K., and Plaut, R., "Transverse Vibrations and Stability of Systems With Gyroscopic Forces," *Journal of Structural Mechanics,* Vol. 3 (2), 1974, pp. 163–177.

19 Huseyin, K., and Plaut, R., "Divergence and Flutter Boundaries of Systems Under Combined Conservative and Gyroscopic Forces," IUTAM Symposium on Dynamics of Rotors, Lyngby/Denmark, August 12–16, 1974, pp. 182–204.

20 Huseyin, K., *Vibrations and Stability of Multiple-Parameter Systems,* Sijthoff & Noordhoff, 1978.

21 Leipholz, H., *Direct Variational Methods and Eigenvalue Problems in Engineering,* Noordhoff International Publishing, Leyden, 1977.

Downloaded 01 May 2010 to 171.66.16.249. Redistribution subject to ASME license or copyright; see http://www.asme.org/terms/Terms_Use.cfm

A. D. Wright
Research Engineer,
Rockwell International,
Wind Systems Group,
Rocky Flats,
Golden, Colo. 80401

C. E. Smith
Professor.
Mem. ASME

R. W. Thresher
Professor.
Mem. ASME

J. L. C. Wang
Graduate Assistant.

Department of Mechanical Engineering,
Oregon State University,
Corvallis, Ore. 97331

Vibration Modes of Centrifugally Stiffened Beams

The method of Frobenius is used to solve for the exact frequencies and mode shapes for rotating beams in which both the flexural rigidity and the mass distribution vary linearly. Results are tabulated for a variety of situations including uniform and tapered beams, with root offset and tip mass, and for both hinged root and fixed root boundary conditions. The results obtained for the case of the uniform cantilever beam are compared with other solutions, and the results of a conventional finite-element code.

Introduction

The design of helicopter rotors, long, flexible, rotating space booms, wind turbines, and probably other devices have motivated a number of studies of the modes of flexural vibration of rotating beams. The analysis leads to a variable-coefficient differential equation for the mode shapes, for which only approximations to its solutions have been used in previous analyses. Convergent power series for the deflection of the beam are developed here, giving precise values of both natural frequencies and corresponding mode shapes.

The results presented should be useful for direct analysis in situations in which the parameters correspond closely to those used here. In addition, the results can provide criteria with which approximate methods can be evaluated. For example, a finite-element method would probably be most practicable for analyzing beams with relatively complicated distributions of density or flexural rigidity, and development of such methods can be considerably facilitated if precise values for a number of special cases are available for verification.

Basic Equations

The system to be analyzed is illustrated in Fig. 1. The rotor spins about a fixed axis at a constant angular speed Ω, and the beam is free to vibrate in the axial (y) direction. Circumferential displacement components w are assumed to be negligible, and the radial components u are assumed to be related to the axial components v in such a way that the length of the central axis of the beam does not change upon deformation. For small $\partial v/\partial x$, this relationship is

$$u(x,t) = -\frac{1}{2}\int_0^x \left(\frac{\partial v}{\partial \xi}\right)^2 d\xi \tag{1}$$

With these assumptions, the kinetic energy can be expressed as

$$T = \tfrac{1}{2}\int_0^L \rho A\left[\left(\int_0^x v_\xi v_{\xi t}\, d\xi\right)^2 + v_t^2 + \Omega^2\left(a + x - \tfrac{1}{2}\int_0^x v_\xi^2\, d\xi\right)^2\right] dx$$

$$- \tfrac{1}{2}M\left[\left(\int_0^L v_x v_{xt}\, dx\right)^2 + v_t^2(L,t) + \Omega^2\left(a + L - \tfrac{1}{2}\int_0^L v_x^2\, dx\right)^2\right]$$

where the subscripts imply differentiation. Neglecting terms of the order of $(\int v_x^2 dx)^2$ reduces this to

$$T = \tfrac{1}{2}\int_0^L \rho A\left[v_t^2 - (a+x)\Omega^2\int_0^x v_\xi^2\, d\xi\right] dx + \frac{M}{2}\left[v_t^2(L,t) - (a+L)\Omega^2\int_0^L v_x^2\, dx\right] + \text{constant}$$

Contributed by the Applied Mechanics Division for publication in the JOURNAL OF APPLIED MECHANICS.

Discussion on this paper should be addressed to the Editorial Department, ASME, United Engineering Center, 345 East 47th Street, New York, N. Y. 10017, and will be accepted until two months after final publication of the paper itself in the JOURNAL OF APPLIED MECHANICS. Manuscript received by ASME Applied Mechanics Division, February, 1980; final revision, July, 1981.

Copyright © 1982 by ASME
Downloaded 01 May 2010 to 171.66.16.249. Redistribution subject to ASME license or copyright; see http://www.asme.org/terms/Terms_Use.cfm

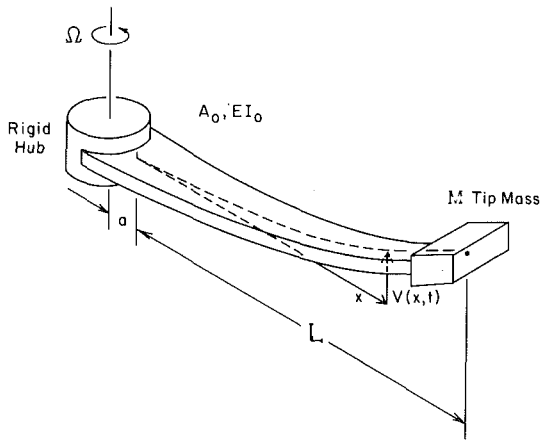


Fig. 1 Deformed beam

A more useful form results after integrating by parts the term containing the factor Ω^2. This form is

$$T=\frac{1}{2}\int_0^L \left[\rho A v_t{}^2-\Omega^2 G(x) v_x{}^2\right]dx+\frac{M}{2}v_t{}^2(L,t) \qquad (2)$$

in which

$$G(x)=\int_x^L \rho A(\xi)(a+\xi)d\xi+M(a+L) \qquad (3)$$

is the first moment, about the spin axis, of the mass that is located beyond the section at x.

The potential energy is given by

$$V=\tfrac{1}{2}\int_0^L EI\, v_{xx}{}^2 dx \qquad (4)$$

Application of Hamilton's principle with the foregoing energy expressions and the customary integration by parts show that the displacement $v(x,t)$ must satisfy the Euler-Lagrange equation

$$(EIv_{xx})_{xx}-\Omega^2(Gv_x)_x+\rho A\, v_{tt}=0$$

in the interval $0 < x < L$, and the boundary conditions

$$EIv_{xx}=0$$

$$(EIv_{xx})_x-M(a+L)\Omega^2 v_x-Mv_{tt}=0$$

at the tip, where $x = L$.

Two types of connection with the hub—clamped and hinged—are examined here. Both satisfy the boundary condition

$$v(0,t)=0$$

while the cantilevered and pinned attachments are distinguished from one another by the respective boundary conditions

$$v_x(0,t)=0$$

$$v_{xx}(0,t)=0$$

In order to reduce the number of parameters in the equations, the following dimensionless quantities are introduced:

$$\alpha=\frac{a}{L}\quad \mu=\frac{M}{\rho A_0 L}\quad \eta^2=\frac{\rho A_0 L^4\Omega^2}{EI_0}$$

$$\xi=\frac{x}{L}\quad \tau=\sqrt{\frac{EI_0}{\rho A_0 L^4}}t$$

$$f(\xi)=\frac{EI(L\xi)}{EI_0}\quad g(\xi)=\int_\xi^1 h(x)(\alpha+x)dx+\mu(1+\alpha)$$

$$h(\xi)=\frac{\rho A(L\xi)}{\rho A_0}$$

In terms of these, the equations of motion become

$$(fv'')''-\eta^2(gv')'+h\ddot{v}=0\quad 0<\xi<1 \qquad (5)$$

$$v(0,\tau)=0 \qquad (6)$$

$$v'(0,\tau)=0\quad \text{or}\quad v''(0,\tau)=0 \qquad (7a,b)$$

$$v''(1,\tau)=0 \qquad (8)$$

$$(fv'')'(1,\tau)-\mu(1+\alpha)\eta^2 v'(1,\tau)-\mu\ddot{v}(1,\tau)=0 \qquad (9)$$

in which the primes denote differentiation with respect to ξ and the dots denote differentiation with respect to τ.

These equations can be expected to admit solutions that represent normal mode motions

$$v(\xi,\tau)=\phi(\xi)\cos(\omega\tau+\theta)$$

Substitution leads to the following ordinary differential equation and boundary conditions that govern ϕ:

$$(f\phi'')''-\eta^2(g\phi')'-\omega^2 h\phi=0 \qquad (10)$$

Nomenclature

a = radius of rigid hub
C_r = constants in general solution for mode shape (equation (21))
$EI(x)$ = flexural rigidity of beam at section x
EI_0 = flexural rigidity of attachment point
$f(\xi)$ = $EI(L\xi)/EI_0$
$G(x)$ = first moment of mass beyond section x (equation (3))
$g(\xi)$ = dimensionless form of $G(x)$
$h(\xi)$ = $\rho A(L\xi)/\rho A_0$
L = length
$\mathcal{L}$ = Lagrangian
M = mass of particle attached to tip
P_n = natural (angular) frequency
R = Rayleigh quotient (equation (16))
s = subscript, equal to 1 for hinge attachment, equal to 2 for cantilever attachment
T = kinetic energy
t = time
$u_r(\xi), v_r(\xi)$ = solutions that form mode shapes
u = radial displacement component
v = axial displacement component
w = tangential displacement component
x = radial coordinate
α = hub radius to beam length ratio, a/L
β = rate of decrease of flexural rigidity (equation (17))
γ = rate of decrease of mass per unit length (equation (18))
δ = $\alpha + \frac{1}{2}(1-\alpha\gamma) - 1/3\gamma + \mu(1+\alpha)$
η = $\sqrt{\rho A_0 L^4\Omega^2/EI_0}$
μ = $m/\rho A_0 L$
ξ = x/L
$\rho A(x)$ = mass per unit length of beam at section x
ρA_0 = mass per unit length of beam at attachment point
τ = $\sqrt{\frac{EI_0}{\rho A_0 L^4}}t$
$\phi(\xi)$ = mode shape
Ω = rotation rate
ω_n = $p_n\sqrt{\frac{EI_0}{\rho A_0 L^4}}$

Downloaded 01 May 2010 to 171.66.16.249. Redistribution subject to ASME license or copyright; see http://www.asme.org/terms/Terms_Use.cfm

$$\phi(0)=0 \tag{11}$$

$$\phi'(0)=0 \quad \text{or} \quad \phi''(0)=0 \tag{12a,b}$$

$$\phi''(1)=0 \tag{13}$$

$$(f\phi'')'(1)-\mu(1+\alpha)\eta^2\phi'(1)+\omega^2\mu\phi(1)=0 \tag{14}$$

The values of ω for which nontrivial solutions to equations (10)–(14) exist give the natural frequencies of the system as

$$p_n=\sqrt{\frac{EI_0}{\rho A_0 L^4}}\omega_n \tag{15}$$

and the corresponding solutions $\phi_n(\xi)$ are the associated mode shapes.

The Rayleigh quotient (which forms the basis for some approximate methods) can be readily obtained from the energy expressions and is

$$R(\phi)=\frac{\int_0^L EI\phi_{xx}{}^2dx+\Omega^2\int_0^L G\phi_x{}^2dx}{\int_0^L \rho A\phi^2dx+M\phi^2(1)}$$

$$=\frac{EI_0}{\rho A_0 L^4}\frac{\int_0^1 f\phi''{}^2d\xi+\eta^2\int_0^1 g\phi'{}^2d\xi}{\int_0^1 h\phi^2d\xi+\mu\phi^2(1)} \tag{16}$$

When ϕ is one of the solutions to equations (10)–(14), $\sqrt{R}$ has the value of the corresponding natural frequency; also, R is stationary with respect to variations in ϕ at each of these points.

Exact Solution

When f and h are analytic, power series representing solutions to equation (10) can be constructed by the method of Frobenius [1]. This is done here for beams in which both flexural rigidity and density vary linearly

$$f(\xi)=1-\beta\xi \tag{17}$$

$$h(\xi)=1-\gamma\xi \tag{18}$$

Of course these contain the uniform beam as the special case $\beta=\gamma=0$. Several wind turbine blades have been designed such that stiffness and density vary approximately in this way; thus the results will be directly applicable for estimating vibration modes in a number of designs.

Four solutions that are linearly independent have the form

$$u_r(\xi)=\sum_{k=r}^{\infty}a_{rk}\xi^k \quad r=0,1,2,3 \tag{19}$$

Substitution of (19) into (10) and equating coefficients of like powers of ξ lead to the recursion relationships

$$a_{rk}=\frac{\beta(k-2)}{k}a_{r(k-1)}+\frac{\eta^2\delta}{k(k-1)}a_{r(k-2)}$$

$$-\frac{\alpha\eta^2(k-3)}{k(k-1)(k-2)}a_{r(k-3)}$$

$$-\frac{\frac{1}{2}\eta^2(1-\alpha\gamma)(k-3)(k-4)-\omega^2}{k(k-1)(k-2)(k-3)}a_{r(k-4)}$$

$$+\gamma\frac{\frac{1}{3}\eta^2(k-3)(k-5)-\omega^2}{k(k-1)(k-2)(k-3)}a_{r(k-5)} \tag{20}$$

in which

$$\delta=\alpha+\tfrac{1}{2}(1-\alpha\gamma)-\tfrac{1}{3}\gamma+\mu(1+\alpha)$$

and it is to be understood that the coefficient a_{rk} is zero whenever the second subscript k is less than r. The lead coefficient a_{rr} in each series is arbitrary. With each of these set equal to 1, the first three terms in each series are given by

$$u_0=1-\frac{\beta}{2}\xi+\frac{\eta^2\delta}{2}\xi^2+\ldots$$

$$u_1=\xi+\frac{\eta^2\delta}{6}\xi^3+\frac{\eta^2(2\beta\delta-\alpha)}{24}\xi^4+\ldots$$

$$u_2=\xi^2+\frac{\beta}{3}\xi^3+\frac{2\beta^2+\eta^2\delta}{12}\xi^4+\ldots$$

$$u_3=\xi^3+\frac{\beta}{2}\xi^4+\frac{6\beta^2+\eta^2\delta}{20}\xi^5+\ldots$$

The general solution to equation (10) can be expressed as

$$\phi(\xi)=\sum_{r=0}^{3}C_r u_r(\xi) \tag{21}$$

The boundary conditions (11) and (12) give, for the clamped attachment,

$$\phi(0)=C_0=0$$

$$\phi'(0)=-\frac{\beta}{2}C_0+C_1=0$$

and, for the hinged attachment,

$$\phi(0)=C_0=0$$

$$\phi''(0)=\eta^2\delta C_0+2C_2=0$$

Therefore, for these two attachments,

$$\phi(\xi)=C_s u_s(\xi)+C_3 u_3(\xi)$$

where $s=1$ for the hinge attachment and $s=2$ for the cantilever attachment. The boundary conditions (13) and (14) can now be written as

$$\begin{bmatrix} b_{1s} & b_{13} \\ b_{2s} & b_{23} \end{bmatrix}\begin{Bmatrix} C_s \\ C_3 \end{Bmatrix}=\begin{Bmatrix} 0 \\ 0 \end{Bmatrix} \tag{22}$$

in which, for $k=s,3$,

$$b_{1k}=u_k''(1)$$

$$b_{2k}=(1-\beta)u_k'''(1)-\beta u_k''(1)-\mu(1+\alpha)\eta^2u_k'(1)+\mu\omega^2u_k(1) \tag{23}$$

For a nontrivial $\{C\}$, the determinant of the square matrix in equation (22) must be equal to zero. The values of ω which make this determinant vanish give the natural frequencies of the system through equation (15). To determine these values, the elements $b_{ij}(\omega)$ are computed according to equations (23), using a sufficient number of terms in the series defined by (19) and (20) and with trial values of ω. A root search is then employed to find the desired values of ω.

The mode shape can then be determined by solving either of the equations in (22) for the ratio C_s/C_3; using the first equation gives

$$\frac{C_s}{C_3}=-\frac{b_{13}}{b_{1s}}=-\frac{u_3''(1)}{u_s''(1)}$$

The mode shape is then given by

$$\phi(\xi)=C_3\left[-\frac{u_3''(1)}{u_s''(1)}u_s(\xi)+u_3(\xi)\right] \tag{24}$$

Some results of this analysis are presented and discussed in a later section.

The expressions used in the foregoing converge reasonably rapidly for all values of the parameters covered in this study, except cases in which β is near unity. In such cases slower convergence is to be expected, since the singular point $\xi=1/\beta$

Downloaded 01 May 2010 to 171.66.16.249. Redistribution subject to ASME license or copyright; see http://www.asme.org/terms/Terms_Use.cfm

Table 1 Comparison of exact frequency ratios with approximate estimates for the cantilever beam with zero root offset and zero tip mass; $\alpha=0, \beta=0, \gamma=0, \mu=0$

	Frequency Ratio	Rotation Speed Ratio			
		$\eta=0$	$\eta=3$	$\eta=6$	$\eta=12$
ω_1	Exact	3.5160	4.7973	7.3604	13.1702
	Peters' Formula (2)	3.5160	4.7964	7.3561	13.1634
	SAP-V (3)	3.500	4.908	7.629	13.65
	Hoa's Method	3.5160	4.7973	7.3604	13.1706
	Hodges' Method	3.5160	4.7973	7.3604	13.1702
ω_2	Exact	22.0345	23.3203	26.8091	37.6031
	Peters' Formula	22.0345	23.3188	26.7933	37.5155
	SAP-V	21.69	23.18	27.17	39.27
	Hoa's Method	22.0352	23.3210	26.8098	37.6050
	Hodges' Method	22.0345	23.3203	26.8091	37.6031
ω_3	Exact	61.6972	62.9850	66.6840	79.6145
	Peters' Formula	61.6973	62.9720	66.5421	78.7188
	SAP-V	60.12	61.55	65.65	79.88
ω_4	Exact	120.902	122.236	126.140	140.534
	Peters' Formula	120.901	122.194	125.759	138.322
	SAP-V	116.6	118.0	122.2	137.6

of equation (10) is then near the point $\xi = 1$ used in the boundary conditions (23). To better handle computations in these cases, series expansions about the regular singular point $\xi = 1/\beta$ were constructed. Four linearly independent solutions resulting from this are

$$v_0(\xi) = \log\left(\frac{1}{\beta}-\xi\right)\sum_{k=0}^{\infty}\bar{a}_{0k}\left(\frac{1}{\beta}-\xi\right)^k + \sum_{k=0}^{\infty}\bar{a}'_{0k}\left(\frac{1}{\beta}-\xi\right)^k$$

$$v_1(\xi) = \log\left(\frac{1}{\beta}-\xi\right)v_2(\xi) + \sum_{k=0}^{\infty}\bar{a}'_{1k}\left(\frac{1}{\beta}-\xi\right)^{k+1}$$

$$v_2(\xi) = \sum_{k=0}^{\infty}\bar{a}_{1k}\left(\frac{1}{\beta}-\xi\right)^{k+1}$$

$$v_3(\xi) = \sum_{k=0}^{\infty}\bar{a}_{2k}\left(\frac{1}{\beta}-\xi\right)^{k+2}$$

in which the coefficients $\bar{a}_{rk}$ satisfy the recurrence relationships

$$\bar{a}_{rk} = -\frac{a}{(k+r)(k+r-1)}\bar{a}_{r(k-1)} - \frac{(k+r-2)b}{(k+r)(k+r-1)^2}\bar{a}_{r(k-2)} - \frac{(k+r-3)(k+r-2)c+e}{(k+r)(k+r-1)^2(k+r-2)}\bar{a}_{r(k-3)} - \frac{(k+r-4)(k+r-2)d+f}{(k+r)(k+r-1)^2(k+r-2)}\bar{a}_{r(k-4)}$$

the coefficients $\bar{a}'_{rk}$ are given by

$$\bar{a}'_{rk} = \left(\frac{\partial\bar{a}_{\sigma k}}{\partial\sigma}\right)_{\sigma=r}$$

and the abbreviations

$$a = -\frac{\eta^2}{\beta}\left[\left(1-\frac{1}{\beta}\right)\alpha + \frac{1}{2}\left(1-\frac{1}{\beta^2}\right)(1-\alpha\gamma) - \frac{1}{3}\left(1-\frac{1}{\beta^3}\right)\gamma\right]$$

$$b = -\frac{\eta^2}{\beta}\left[\alpha + \frac{1}{\beta}(1-\alpha\gamma) - \frac{\gamma}{\beta^2}\right]$$

$$c = -\frac{\eta^2}{\beta}\left[\frac{\gamma}{\beta} - \frac{1}{2}(1-\alpha\gamma)\right]$$

$$d = \frac{\eta^2\gamma}{3\beta}$$

$$e = -\frac{\omega^2}{\beta}\left(1-\frac{\gamma}{\beta}\right)$$

$$f = -\frac{\omega^2\gamma}{\beta}$$

have been introduced. The general solution can then be represented as

$$\phi = \sum_{r=0}^{3} C_r v_r \tag{25}$$

and the boundary conditions (11)–(14) written as

$$\begin{bmatrix} b_{00} & b_{01} & b_{02} & b_{03} \\ b_{10} & b_{11} & b_{12} & b_{13} \\ b_{20} & b_{21} & b_{22} & b_{23} \\ b_{30} & b_{31} & b_{32} & b_{33} \end{bmatrix}\begin{Bmatrix} C_0 \\ C_1 \\ C_2 \\ C_3 \end{Bmatrix} = \begin{Bmatrix} 0 \\ 0 \\ 0 \\ 0 \end{Bmatrix} \tag{26}$$

in which

$$b_{oj} = v_j(0)$$

$$b_{1j} = \begin{cases} v_j'(0) & \text{for the cantilever attachment} \\ v_j''(0) & \text{for the hinge attachment} \end{cases}$$

$$b_{2j} = v_j''(1)$$

$$b_{3j} = (1-\beta)v_j'''(1) + \beta v_j''(1) - \mu(1+\alpha)\eta^2 v_j'(1) - \mu\omega^2 v_j(1)$$

As with equation (22), a root search is used to find values of ω that make the determinant of the square matrix in equation (26) vanish. The corresponding mode shape is found by setting $C_0 = 1$, computing C_1, C_2, and C_3 from

$$\begin{Bmatrix} C_1 \\ C_2 \\ C_3 \end{Bmatrix} = -\begin{bmatrix} b_{11} & b_{12} & b_{13} \\ b_{21} & b_{22} & b_{23} \\ b_{31} & b_{32} & b_{33} \end{bmatrix}^{-1}\begin{Bmatrix} b_{10} \\ b_{20} \\ b_{30} \end{Bmatrix}$$

and substituting these values into equation (25).

Results and Conclusions

The natural frequencies for the system are determined by numerically computing the values of ω which make the determinant of the square matrix in either equations (22) and (26) vanish. Before presenting a tabulation of results, it will be useful to compare some of the results of the exact solution with other approximate solutions available in the literature. Table 1 provides such a comparison for the simple case of a uniform cantilever beam with no root off set or tip mass. The table provides a comparison of the results using the finite-element program, SAP-V (3). Peter's formula is reputed to provide a simple expression having errors of only few percent over a wide frequency range for the uncoupled frequencies of rotating uniform cantilever beams. As can be seen from Table 1, Peter's formula is extremely accurate even at relatively large rotation rates and does not appear to suffer a significant decrease in accuracy for the higher modes. The constants used were computed to the appropriate number of significant figures.

The SAP-V results were obtained using 10 beam elements and the geometric stiffness matrix option to account for

Downloaded 01 May 2010 to 171.66.16.249. Redistribution subject to ASME license or copyright; see http://www.asme.org/terms/Terms_Use.cfm

Table 2 Frequency ratios of a uniform hinged beam with zero root offset and zero tip mass; $\alpha = 0, \beta = 0, \gamma = 0, \mu = 0$

η	ω_1	ω_2	ω_3	ω_4	ω_5
0.0	0.0000	15.4182	49.9649	104.248	178.270
1.0	1.0000	15.6242	50.1437	104.420	178.440
2.0	2.0000	16.2261	50.6760	104.936	178.949
3.0	3.0000	17.1807	51.5498	105.789	179.794
4.0	4.0000	18.4313	52.7463	106.971	180.970
5.0	5.0000	19.9197	54.2419	108.469	182.469
6.0	6.0000	21.5944	56.0099	110.270	184.283
7.0	7.0000	23.4133	58.0223	112.356	186.401
8.0	8.0000	25.3436	60.2513	114.709	188.812
9.0	9.0000	27.3601	62.6705	117.313	191.504
10.0	10.0000	29.4439	65.2554	120.146	194.462
11.0	11.0000	31.5809	67.9842	123.192	197.673
12.0	12.0000	33.7603	70.8373	126.431	201.122

Table 3 Frequency ratios of a uniform cantilever beam with zero root offset and zero tip mass; $\alpha = 0, \beta = 0, \gamma = 0, \mu = 0$

η	ω_1	ω_2	ω_3	ω_4	ω_5
0.0	3.5160	22.0345	61.6972	120.902	199.860
1.0	3.6817	22.1810	61.8418	121.051	200.012
2.0	4.1373	22.6149	62.2732	121.497	200.467
3.0	4.7973	23.3203	62.9850	122.236	201.223
4.0	5.5850	24.2734	63.9668	123.261	202.277
5.0	6.4495	25.4461	65.2050	124.566	203.622
6.0	7.3604	26.8091	66.6840	126.140	205.253
7.0	8.2996	28.3341	68.3860	127.972	207.161
8.0	9.2568	29.9954	70.2930	130.049	209.338
9.0	10.2257	31.7705	72.3867	132.358	211.775
10.0	11.2023	33.6404	74.6493	134.884	214.461
11.0	12.1843	35.5890	77.0638	137.614	217.385
12.0	13.1702	37.6031	79.6145	140.534	220.536

Table 4 Frequency ratios of a tapered hinged beam with zero root offset and zero tip mass; $\alpha = 0, \beta = 0.95, \gamma = 0.8, \mu = 0$

η	ω_1	ω_2	ω_3	ω_4	ω_5
0.0	0.0000	16.7328	48.4691	97.1704	163.002
1.0	1.0000	16.8711	48.5872	97.2823	163.111
2.0	2.0000	17.2794	48.9395	97.6172	163.438
3.0	3.0000	17.9388	49.5210	98.1727	163.983
4.0	4.0000	18.8233	50.3234	98.9450	164.741
5.0	5.0000	19.9022	51.3360	99.9287	165.711
6.0	6.0000	21.1456	52.5463	101.117	166.889
7.0	7.0000	22.5260	53.9405	102.504	168.269
8.0	8.0000	24.0195	55.5042	104.079	169.847
9.0	9.0000	25.6060	57.2230	105.835	171.618
10.0	10.0000	27.2692	59.0828	107.762	173.573
11.0	11.0000	28.9956	61.0700	109.850	175.708
12.0	12.0000	30.7745	63.1722	112.090	178.105

Table 5 Frequency ratios of a tapered cantilever beam with zero root offset and zero tip mass; $\alpha = 0, \beta = 0.95, \gamma = 0.8, \mu = 0$

η	ω_1	ω_2	ω_3	ω_4	ω_5
0.0	5.2738	24.0041	59.9701	112.909	183.024
1.0	5.3903	24.1069	60.0696	113.009	183.124
2.0	5.7249	24.4130	60.3669	113.307	183.424
3.0	6.2402	24.9149	60.8590	113.803	183.923
4.0	6.8928	25.6013	61.5412	114.492	184.619
5.0	7.6443	26.4581	62.4069	115.372	185.509
6.0	8.4653	27.4693	63.4483	116.439	186.591
7.0	9.3347	28.6185	64.6566	117.685	187.862
8.0	10.2379	29.8894	66.0222	119.107	189.316
9.0	11.1650	31.2669	67.5351	120.696	190.950
10.0	12.1092	32.7369	69.1851	122.446	192.759
11.0	13.0657	34.2871	70.9622	124.350	194.737
12.0	14.0313	35.9064	72.8565	126.401	196.880

rotational stiffness effects. SAP-V assumes lumped mass for computing the beam element inertia matrix, rather than using a consistent mass matrix, so even for the nonrotating beam the results are not exact as can be seen from Table 1. However, SAP-V is versatile in that it can be used for beams with rather complicated mass and stiffness distribution; perhaps most important, SAP-V is widely available at a rather nominal cost. Although the SAP-V results are not as accurate as Peter's formula they do provide reasonable estimates for many applications.

A comparison has also been made to a computational approach due to Hodges [4] using what is called the Ritz finite-element method. This method has the versatility of

Table 6 Effect of root offset on the first two frequency ratios of a uniform hinges beam with zero tip mass; $\beta = 0, \gamma = 0, \mu = 0$

	α=0.0		α=0.1		α=1.0	
η	ω_1	ω_2	ω_1	ω_2	ω_1	ω_2
0.0	0.0000	15.4182	0.0000	15.4182	0.0000	15.4182
1.0	1.0000	15.6242	1.0724	15.6537	1.5806	15.9161
2.0	2.0000	16.2261	2.1447	16.3389	3.1586	17.3179
3.0	3.0000	17.1807	3.2170	17.4186	4.7333	19.4142
4.0	4.0000	18.4313	4.2892	18.8218	6.3056	21.9897
5.0	5.0000	19.9197	5.3613	20.4785	7.8765	24.8804
6.0	6.0000	21.5944	6.4334	22.3291	9.4467	27.9770
7.0	7.0000	23.4133	7.5054	24.3263	11.0166	31.2103
8.0	8.0000	25.3436	8.5775	26.4345	12.5865	34.5373
9.0	9.0000	27.3601	9.6495	28.6272	14.1563	37.9304
10.0	10.0000	29.4439	10.7215	30.8851	15.7263	41.3720
11.0	11.0000	31.5809	11.7935	33.1939	17.2963	44.8504
12.0	12.0000	33.7603	12.8656	35.5428	18.8665	48.3572

Table 7 Effect of root offset on the first two frequency ratios of a uniform cantilever beam with zero tip mass; $\gamma = 0, \beta = 0, \mu = 0$

	α=0.0		α=0.1		α=1.0	
η	ω_1	ω_2	ω_1	ω_2	ω_1	ω_2
0.0	3.5160	22.0345	3.5160	22.0345	3.5160	22.0345
1.0	3.6817	22.1810	3.7029	22.2005	3.8888	22.3750
2.0	4.1373	22.6149	4.2123	22.6912	4.8337	23.3660
3.0	4.7973	23.3203	4.9412	23.4863	6.0818	24.9277
4.0	5.5850	24.2734	5.8026	24.5559	7.4751	26.9573
5.0	6.4495	25.4461	6.7414	25.8655	8.9404	29.3528
6.0	7.3604	26.8091	7.7260	27.3797	10.4439	32.0272
7.0	8.2996	28.3341	8.7384	29.0653	11.9691	34.9116
8.0	9.2568	29.9954	9.7682	30.8930	13.5074	37.9538
9.0	10.2257	31.7705	10.8092	32.8377	15.0541	41.1154
10.0	11.2023	33.6404	11.8578	34.8784	16.6064	44.3682
11.0	12.1843	35.5890	12.9116	36.9981	18.1625	47.6916
12.0	13.1702	37.6031	13.9692	39.1829	19.7215	51.0701

Table 8 Frequency ratios for uniform, hinged beam, zero root offset ($\alpha = \beta = \gamma = 0$)

$\omega_1 = \eta$ for all μ

	ω_2			
η	μ=0	μ=0.5	μ=1.0	μ=2.0
0	15.4182	11.3340	10.7144	10.3274
1	15.6242		11.3592	
2	16.2261		13.1029	
3	17.1807		15.5786	
4	18.4313		18.4941	
5	19.9197		21.6727	
6	21.5944		25.0141	
7	23.4133		28.4612	
8	25.3436		31.9798	
9	27.3601		35.5486	
10	29.4439		39.1541	
11	31.5809		42.7867	
12	33.7603	37.3369	46.4402	61.7736

finite elements and can be made to converge to the exact solution by either increasing the number of elements, as is the case with the conventional finite-element method, or by increasing the number of admissible functions in each element. The comparison was made for the uniform cantilever beam at rotation speeds of $\eta = 0, 3, 6, 12$ and showed that for the first two modes the results were identical with this paper's computations to six significant figures. Hodges' program appears to be very useful and varsatile for this type of computation. Recently Hodges and Rutkowski [5] published results for the Hoa [8] with a correction, and presented results compared to Hodges [4]. The corrected results for [8] also appear in Table 1.

A variety of results are tabulated for general use in Tables 2–9. These cover a range of situations including uniform and tapered beams, with root offset and tip mass, for both the hinged and fixed root boundary conditions. The results are presented in tabular, rather than graphical form so that the full six-figure accuracy can be retained. It is hoped that these tabulated results of high accuracy can serve as test cases for the development of other more specialized computation methods and not just as a source of basic design data for situations which happen to fall within the tabulation parameters. There are, for example, many practical problems

Downloaded 01 May 2010 to 171.66.16.249. Redistribution subject to ASME license or copyright; see http://www.asme.org/terms/Terms_Use.cfm

Table 9 Frequency ratios for uniform, clamped beam, zero root offset ($\alpha = \beta = \gamma = 0$)

	ω_1				ω_2			
n	μ=0	μ=0.5	μ=1.0	μ=2.0	μ=0	μ=0.5	μ=1.0	μ=2.0
0	3.5160	2.0163	1.5573	1.1582	22.0345	16.9014	16.2500	15.8609
1	3.6817		1.9017		22.1810		16.7570	
2	4.1373		2.6696		22.6149		18.1910	
3	4.7973		3.5823		23.3203		20.3504	
4	5.5850		4.5429		24.2734		23.0229	
5	6.4495		5.5218		25.4461		26.0415	
6	7.3604		6.5090		26.8091		29.2917	
7	8.2996		7.5005		28.3341		32.6984	
8	9.2568		8.4945		29.9954		36.2134	
9	10.2257		9.4899		31.7705		39.8048	
10	11.2023		10.4864		33.6404		43.4517	
11	12.1843		11.4836		35.5890		47.1399	
12	13.1702	12.6352	12.4814	12.3517	37.6031	43.0415	50.8594	63.8567

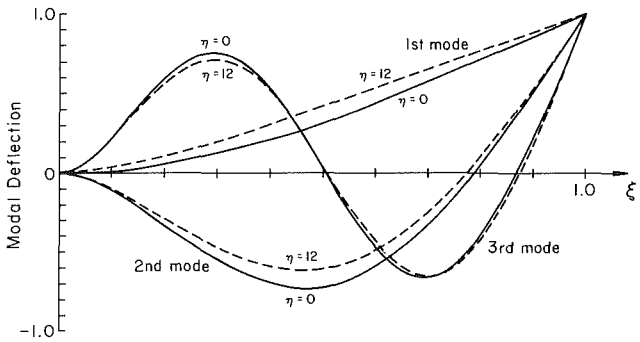


Fig. 2 Mode shapes, cantilevered beam

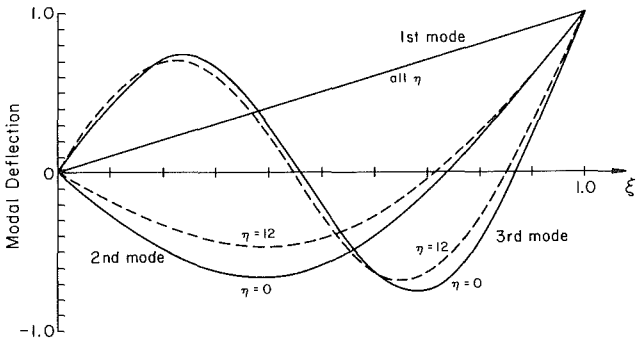


Fig. 3 Mode shapes, hinged beam

of great design interest involving the coulped vibration of propellers, helicopter, and wind turbine blades, such as described in references [5–9], where limited test cases could be used to check computer codes. As a final result, Figs. 2 and 3 present the mode shapes for the uniform cantilever and uniform hinged beam and illustrate the decreasing influence of centrifugal stiffening with increasing mode numbers.

Acknowledgments

The authors wish to acknowledge that this work was sponsored in part by the Department of Energy, under Contract EY-76-S-06-2227, and Oregon State University, Mechanical Engineering Department, with computational support provided by the Computer Center at Oregon State University. The authors are indebted to Dr. T. C. Kennedy of Oregon State University for making the SAP-V computer runs for this work. In addition, we would like to thank the reviewers for their very helpful comments, suggestions, and personal computations. The responsibility for the results and the opinions expressed are those of the authors and not the United States Government or Oregon State University.

References

1 Ince, E. L., *Ordinary Differential Equations,* Longmans, Green and Co., Ltd., New York, 1927.

2 Peters, D. A., "An Approximate Solution for the Free Vibration of Rotating Uniform Cantilever Beams," NASA N78-33289, formerly NASA TM X-62,299, Sept. 1973, Revised 8-28-78.

3 SAP-V, "A Structural Analysis Program for Static and Dynamic Response of Linear Systems," University of Southern California, Department of Civil Engineering, Report No. EERC 73-11.

4 Hodges, D. H., "Vibration and Response of Nonuniform Rotating Beams With Discontinuities," *Journal of the American Helicopter Society,* Vol. 24, No. 5, pp. 43–50.

5 Hodges, D. H., and Rutkowski, M. J., "Comments on Vibration of a Rotating Beam With Tip Mass," Vol. 72, No. 4, pp. 547–549.

6 Murthy, V. R., "Dynamic Characteristics of Rotor Blades," *Journal of Sound and Vibration,* Vol. 49, No. 3, pp. 483–500.

7 White, W. F., and Malatino, R. W., "A Numerical Method for Determining the Natural Vibration Characteristics of Rotating Nonuniform Cantilever Blades," NASA TM X-72, 751, Oct. 1975.

8 Hoa, S. V., "Vibration of a Rotating Beam With Tip Mass," *Journal of Sound and Vibration,* Vol. 67, No. 3, pp. 369–381.

9 Kumar, R., "Flexural Vibrations of a Beam Under a Centrifugal Tension Field," *Proceedings, 4th Canadian Congress of Applied Mechanics,* p. 447.

10 Yntema, R. T., "Simplified Procedures and Charts for the Rapid Estimation of Bending Frequencies of Rotating Beams," NACA TN 3459.

Downloaded 01 May 2010 to 171.66.16.249. Redistribution subject to ASME license or copyright; see http://www.asme.org/terms/Terms_Use.cfm

Stability Analysis of an Extrapolated Force Correction Method for Nonlinear Structural Dynamics

D. M. Trujillo
TRUCOMP,
Fountain Valley, Calif. 92708
Mem. ASME

In this paper, conditions for the unconditional stability of an extrapolated force correction method have been identified. The analysis assumed a nonlinear elastodynamic system for which energy is conserved. Some numerical examples are included to demonstrate the performance of the method.

Introduction

The force correction method is the Newmark ($\beta = 1/4$) method adapted to nonlinear problems [1, 2]. The principal feature is that all of the nonlinear terms are incorporated into a force correction term on the right-hand side of the integration formulas. This has the computational advantage of requiring only a single matrix factorization for the solution of nonlinear structural dynamic problems. The method, however, can exhibit numerical instabilities. This paper derives some conditions that assure the unconditional stability of the force correction method. Some numerical examples are included to demonstrate the effectiveness of the conditions.

It would be desirable to identify the conditions under which an integration technique would be unconditionally stable for all classes of nonlinear problems. However, this is a difficult task since nonlinear problems can include such complexities as plasticity, large deflections, friction, and almost any other imaginable physical concept. Thus, one must define and, in a sense, limit the nonlinearity in order to make any meaningful analysis. One simple concept is to consider nonlinear elastodynamics in which the energy is identically conserved in the absence of external forces. T. J. R. Hughes, et. al. [3], proposes an integration technique that preserves this conservation property and thus assures that unconditional stability is attained. Their method incorporates an iterative procedure at each time step which can involve a matrix factorization. The force correction method [1, 2] is an integration technique that, in effect, transfers the nonlinear terms to the right-hand side of the integration formula. The principal advantage is that only a single matrix factorization is required for the entire process. Also, only the internal nodal forces are required, which avoids the evaluation of the tangent stiffness matrix [6]. There are other analyses of implicit methods that assure stability [4, 5]. However, these require continual evaluations of the stiffness matrix, which in turn requires a matrix factorization.

This paper attempts to identify the conditions under which the force correction method will be unconditionally stable. It should be emphasized that this does not necessarily imply accuracy. There is no better substitute for assuring the accuracy of solutions other than using smaller integration step sizes, especially for nonlinear problems.

Preliminaries

Following Hughes, et al. [3], consider the semidiscrete equations

$$\mathbf{M}\ddot{\mathbf{x}} + \mathbf{N}(\mathbf{x}) = \mathbf{F}(t) \tag{1}$$

$\mathbf{M}$ = mass matrix (symmetric and positive-definite)
$\mathbf{N}(\mathbf{x})$ = vector of internal forces
$\mathbf{F}$ = externally applied forces
$\mathbf{x}$ = generalized displacement vector

The internal forces are assumed to be the gradient of a strain energy function, $U(\mathbf{x})$.

$$\mathbf{N}(\mathbf{x}) = \begin{bmatrix} \dfrac{\partial U}{\partial x_1} \\ \dfrac{\partial U}{\partial x_2} \\ \vdots \\ \dfrac{\partial U}{\partial x_j} \\ \vdots \end{bmatrix} \tag{2}$$

$U(\mathbf{x})$ is assumed to be nonnegative and also if $U(\mathbf{x})$ is bounded then so is $\mathbf{x}$. With the initial conditions

$$\mathbf{x}(0) = \mathbf{x}_o \qquad \dot{\mathbf{x}}(0) = \mathbf{v}_o \tag{3}$$

Contributed by the Applied Mechanics Division for publication in the JOURNAL OF APPLIED MECHANICS.

Discussion on this paper should be addressed to the Editorial Department, ASME, United Engineering Center, 345 East 47th Street, New York, N.Y. 10017, and will be accepted until two months after final publication of the paper itself in the JOURNAL OF APPLIED MECHANICS. Manuscript received by ASME Applied Mechanics Division, November, 1980; final revision, May, 1980.

Copyright © 1982 by ASME
Downloaded 01 May 2010 to 171.66.16.249. Redistribution subject to ASME license or copyright; see http://www.asme.org/terms/Terms_Use.cfm

The foregoing set of equations are stable in the sense that total energy is conserved. The energy E is defined as

$$\mathrm{E}(\mathbf{x},\dot{\mathbf{x}}) = \tfrac{1}{2}(\dot{\mathbf{x}},\mathbf{M}\dot{\mathbf{x}}) + \mathbf{U}(\mathbf{x}) \tag{4}$$

and also

$$\frac{d}{dt}U(\mathbf{x}) = (\mathbf{N}(\mathbf{x}),\dot{\mathbf{x}})$$

where the inner product of the two vectors $\mathbf{x}$ and $\mathbf{y}$ is denoted by $(\mathbf{x},\mathbf{y})$. With an inner product of equation (1) with $\dot{\mathbf{x}}$ and a simple integration, one can arrive at the following conservation of energy

$$\tfrac{1}{2}(\mathbf{M}\dot{\mathbf{x}},\dot{\mathbf{x}}) + \mathbf{U}(\mathbf{x}) = \tfrac{1}{2}(\mathbf{M}\mathbf{v}_0,\mathbf{v}_0) + U(\mathbf{x}_0) \tag{5}$$

for the system without externally applied forces.

An Extrapolated Force Correction Method

One method of applying Newmark's method to nonlinear systems is to consider $N(x)$ to be of the form

$$\mathbf{N}(\mathbf{x}) = \mathbf{K}\mathbf{x} - \mathbf{q}(\mathbf{x}) \tag{6}$$

This should generally be thought of as a definition of $\mathbf{q}(\mathbf{x})$. That is, one can select *any* positive-definite, symmetric matrix $\mathbf{K}$ and knowing $\mathbf{N}(\mathbf{x})$, $\mathbf{q}(\mathbf{x})$ must then satisfy equation (6). The arbitrary choice of $\mathbf{K}$ is important because it need not necessarily be chosen as the initial stiffness matrix, although in the majority of cases, it is the best choice. It will be shown in this paper that for some systems, choosing $\mathbf{K}$ to be the intitial stiffness matrix will lead to unstable solutions.

An extrapolated force correction method [1, 2] expressed in terms of the three displacements $\mathbf{x}_{n+1}$, $\mathbf{x}_n$, and $\mathbf{x}_{n-1}$ is

$$(\mathbf{M} + \frac{h^2}{4}\mathbf{K})\mathbf{x}_{n+1} = (2\mathbf{M} - \frac{h^2}{2}\mathbf{K})x_n - (\mathbf{M} + \frac{h^2}{4}\mathbf{K})\mathbf{x}_{n-1} + \frac{h^2}{2}[\mathbf{q}(\mathbf{x}_n) + \mathbf{q}(\mathbf{x}_{n-1})] \tag{7}$$

Damping and the externally applied forces have been excluded for this analysis. There are other choices for the term $\tfrac{1}{2}[\mathbf{q}(\mathbf{x}_n) + \mathbf{q}(\mathbf{x}_{n-1})]$ such as $\mathbf{q}(\mathbf{x}_n)$ or $\tfrac{1}{4}[3\mathbf{q}(\mathbf{x}_n) + \mathbf{q}(\mathbf{x}_{n-1})]$. These are obtained from the original forcing term $\tfrac{1}{4}\mathbf{q}(\mathbf{x}_{n+1}) + 2\mathbf{q}(\mathbf{x}_n) + \mathbf{q}(\mathbf{x}_{n-1})]$ by approximating $\mathbf{q}(\mathbf{x}_{n+1})$ with combinations of $\mathbf{q}(\mathbf{x}_n)$ and $\mathbf{q}(\mathbf{x}_{n-1})$. In this study, the choice was to replace $\mathbf{q}(\mathbf{x}_{n+1})$ with $\mathbf{q}(\mathbf{x}_{n-1})$. The main feature of equation (7) is that all of the nonlinearities have been accumulated into the terms $\mathbf{q}(\mathbf{x}_n)$ and $\mathbf{q}(\mathbf{x}_{n-1})$. This means that the matrix expression $(\mathbf{M} + h^2/4\mathbf{K})$ on the left-hand side need only be factored once. This affords a tremendous savings in computational effort and also eases the programming effort required to solve nonlinear problems, that is, only the nodal forces are needed and not a tangential stiffness matrix. For analysis purposes, a more convenient form of the force correction method are the following one-step implicit formulas involving the velocities and the displacements.

$$\mathbf{M}\mathbf{x}_{n+1} - \frac{h}{2}\mathbf{M}\mathbf{v}_{n+1} = \mathbf{M}\mathbf{x}_n + \frac{h}{2}\mathbf{M}\mathbf{v}_n \tag{8}$$

$$\mathbf{M}\mathbf{v}_{n+1} + \frac{h}{2}\mathbf{K}\mathbf{x}_{n+1} = \mathbf{M}\mathbf{v}_n - \frac{h}{2}\mathbf{K}\mathbf{x}_n + h\mathbf{q}_n \tag{9}$$

Equation (7) can be obtained from these equations by first eliminating $\mathbf{v}_n$. This gives

$$h\mathbf{M}\mathbf{v}_{n+1} = (\mathbf{M} - \frac{h^2}{4}\mathbf{K})\mathbf{x}_{n+1} - (\mathbf{M} + \frac{h^2}{4}\mathbf{K})\mathbf{x}_n + \frac{h^2}{2}\mathbf{q}_n$$

By shifting the recursive index $n+1$ to n, an equation for $\mathbf{v}_n$ is obtained.

$$h\mathbf{M}\mathbf{v}_n = (\mathbf{M} - \frac{h^2}{4}\mathbf{K})\mathbf{x}_n - (\mathbf{M} + \frac{h^2}{4}\mathbf{K})\mathbf{x}_{n-1} + \frac{h^2}{2}\mathbf{q}_{n-1}$$

Substituting these into equation (9) and regrouping produces equation (7).

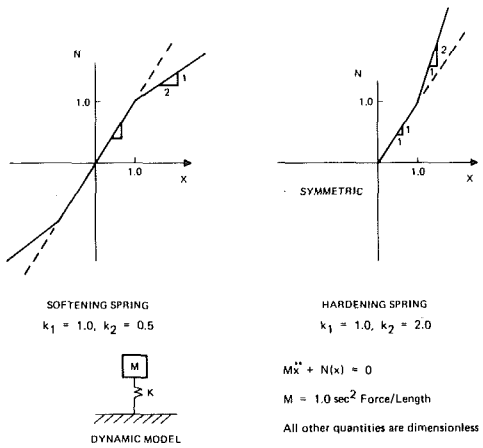


Fig. 1 Nonlinear springs and models

Equations (8) and (9) can be rewritten in terms of $\mathbf{N}_n$ and reorganized to give

$$\mathbf{M}(\mathbf{x}_{n+1} - \mathbf{x}_n) = \frac{h}{2}\mathbf{M}(\mathbf{v}_{n+1} + \mathbf{v}_n) \tag{10}$$

$$\mathbf{M}(\mathbf{v}_{n+1} - \mathbf{v}_n) = -\frac{h}{2}\mathbf{K}(\mathbf{x}_{n+1} + \mathbf{x}_n) + h(\mathbf{K}\mathbf{x}_n - \mathbf{N}_n) \tag{11}$$

Taking inner products of equation (10) with $(\mathbf{v}_{n+1} - \mathbf{v}_n)$ and equation (11) with $(\mathbf{x}_{n+1} - \mathbf{x}_n)$ and subtracting gives

$$\tfrac{1}{2}(\mathbf{M}(\mathbf{v}_{n+1} + \mathbf{v}_n),\mathbf{v}_{n+1} - \mathbf{v}_n) + \tfrac{1}{2}(\mathbf{K}(\mathbf{x}_{n+1} - \mathbf{x}_n), \mathbf{x}_{n+1} - \mathbf{x}_n) + (\mathbf{N}_n,\mathbf{x}_{n+1} - \mathbf{x}_n) = 0 \tag{12}$$

For the potential function U, we will assume that the following holds

$$U(\mathbf{x}_{n+1}) = U(\mathbf{x}_n) + (\mathbf{N}_n,\mathbf{x}_{n+1} - \mathbf{x}_n) + \tfrac{1}{2}(\mathbf{K}^*(\mathbf{x}_{n+1} - \mathbf{x}_n),\mathbf{x}_{n+} - x_n) \tag{13}$$

where $\mathbf{K}^*$ is related to the tangent stiffness matrix. Strictly speaking, Taylor's theorem only postulates that a $\mathbf{K}^*$ can be found using component values of $\mathbf{x}$ between $\mathbf{x}_n$ and $\mathbf{x}_{n+1}$. Thus, $\mathbf{K}^*$ is not strictly the tangent stiffness at $\mathbf{x}_n$, but for all practical purposes it can be thought of as such. Using equation (13) to replace $(\mathbf{N}_n,\mathbf{x}_{n+1} - \mathbf{x}_n)$ in equation (12) gives

$$\tfrac{1}{2}(\mathbf{M}\mathbf{v}_{n+1},\mathbf{v}_{n+1}) + U(\mathbf{x}_{n+1}) = \tfrac{1}{2}(\mathbf{M}\mathbf{v}_n,\mathbf{v}_n) + U(\mathbf{x}_n) - \tfrac{1}{2}((\mathbf{K} - \mathbf{K}^*)(\mathbf{x}_{n+1} - \mathbf{x}_n),\mathbf{x}_{n+1} - \mathbf{x}_n)) \tag{14}$$

Or in terms of energies

$$E_{n+1} = E_n - \tfrac{1}{2}((\mathbf{K} - \mathbf{K}^*)(\mathbf{x}_{n+1} - \mathbf{x}_n),\mathbf{x}_{n+1} - \mathbf{x}_n) \tag{15}$$

This is the relationship that we desired. If the method is to be stable, then the energy must decrease or remain constant, $E_{n+1} \leq E_n$, which implies that the remaining term must be negative. This can be assured if the matrix difference $\mathbf{K} - \mathbf{K}^*$ remains positive-definite throughout the solution. Since the time step does not enter into equation (15), this also assures unconditional stability. For linear problems, $\mathbf{K}^*$ is constant and choosing $\mathbf{K}$ equal to $\mathbf{K}^*$ results in the well-known fact that energy is preserved for linear problems.

The major conclusion to be made is that in order for the force correction method to remain stable, the stiffness matrix $\mathbf{K}$ should be chosen "stiffer" than any anticipated stiffness $\mathbf{K}^*$ expected during the analysis. When this is true, then the relationship in equation (15) will assure the stability.

Equation (15) points out another feature of the force correction method which pertains to the accuracy of the solution. Clearly, if the total energy is to be conserved, then smaller differences between $\mathbf{K}$ and $\mathbf{K}^*$ would be desirable. This could lead to schemes that would update $\mathbf{K}$ periodically during the process in order to minimize the loss of energy. However, this introduces more computations and defeats the

Downloaded 01 May 2010 to 171.66.16.249. Redistribution subject to ASME license or copyright; see http://www.asme.org/terms/Terms_Use.cfm

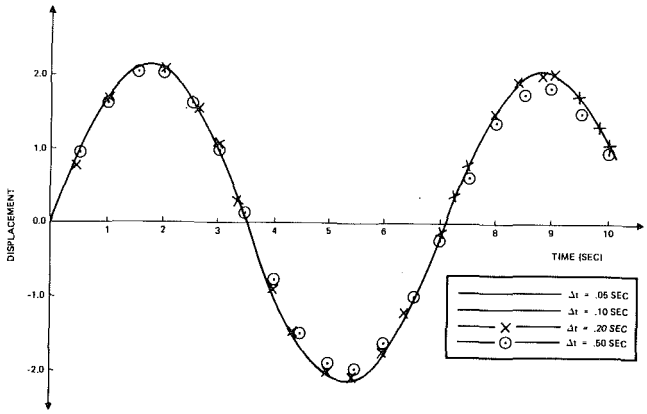


Fig. 2 Plot of displacement versus time for comparison test: $k = 1.0$, $k_1 = 1.0$, $k_2 = 0.50$, various Δt

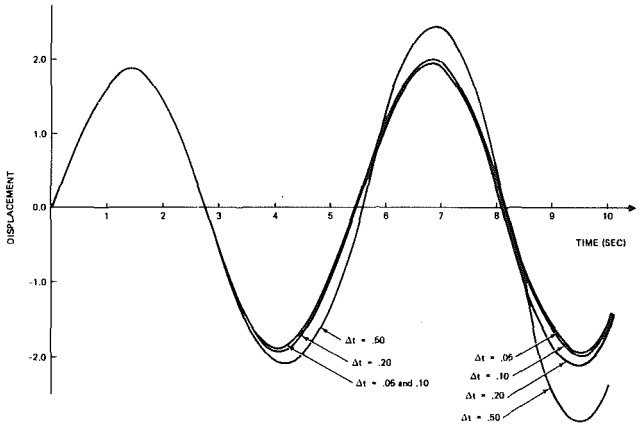


Fig. 3 Plot of displacement versus time, hardening spring, $k = 1.0$ and various Δt

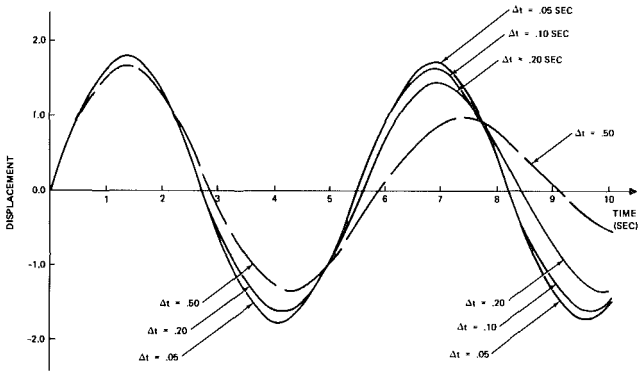


Fig. 4 Plot of displacement versus time, hardening spring, $k = 20$ and various Δt

principal advantage of the force correction method. It seems more logical to restrict the method to mildly nonlinear problems for which it is best suited.

Numerical Examples

In order to explore the effectiveness of the ideas presented in the previous section, some simple, one-dimensional nonlinear problems were integrated. These include a nonlinear softening spring and a similar hardening one. Figure 1 shows all of the pertinent data.

From the relationship in equation (15), the softening spring should be stable if the initial stiffness is used. The results confirm this and are shown in Fig. 2. The time step was varied from 0.05 to 0.50 s. The results for 0.05 and 0.10 are virtually identical. The larger time steps showed a definite decrease in the amplitudes.

On the other hand, the hardening spring should be unstable if the initial stiffness is used. Figure 3 shows this to be the case. However, if an initial stiffness of $k = 2.0$ is used, then the integration should be stable and Fig. 4 shows this to be the case.

Conclusions

The conditions that produce an unconditionally stable force correction method have been identified. The simple one-dimensional examples show that the conditions are valid for those cases. In the multidimensional case, the computation of the stiffness matrix that will bound the nonlinearities is a matter of future investigation. Clearly, a very stiff matrix will produce stability, but may require very small integration step sizes to produce accurate results. The choice will probably be problem-dependent. For mildly nonlinear problems, the choice should be obvious and easily implemented.

References

1 Stricklin, J. A., et al., "Nonlinear Dynamic Analysis of Shells of Revolution by Matrix Displacement Method," Report 69-77, Aerospace Engineering Department, Texas A & M University, College Station, Texas, Feb. 1970.

2 Klein, S., "The Nonlinear Dynamic Analysis of Shells of Revolution with Asymmetric Properties by the Finite Element Method," ASME *Journal of Pressure Vessel Technology*, Aug. 1975, pp. 163-171.

3 Hughes, T. J. R., Caughey, T. K., and Liu, W. K., "Finite Element Methods for Nonlinear Elastodynamics which Conserve Energy," ASME JOURNAL OF APPLIED MECHANICS, Vol. 45, 1978, pp. 366-370.

4 Belytschko, T., and Schoeberle, D. F., "On the Unconditional Stability of an Implicit Algorithm for Nonlinear Structural Dynamics," ASME JOURNAL OF APPLIED MECHANICS, Dec. 1975, pp. 865-869.

5 Park, K. C., "An Improved Stiffly Stable Method for Direct Integration of Nonlinear Structural Dynamic Equations," ASME JOURNAL OF APPLIED MECHANICS, June 1975, pp. 464-470.

6 Belytschko, T., and Hsieh, B. J., "Nonlinear Transient Finite Element Analysis with Convected Co-Ordinates," *Int. J. Num. Meth. Engr.*, Vol. 7, 1973, pp. 255-271.

Downloaded 01 May 2010 to 171.66.16.249. Redistribution subject to ASME license or copyright; see http://www.asme.org/terms/Terms_Use.cfm

Free Vibration Analysis of Stiffened Plates by Including the Effect of Inplane Inertia[1]

G. Aksu
Mechanical Engineering Department,
Middle East Technical University,
Gaziantep Campus,
Gazinatep-Turkey

A method based on the variational principles in conjunction with the finite difference technique is applied to determine the dynamic characteristic of eccentrically stiffened plates. The inplane deformations in both directions of the plate have been considered and the inplane inertia has been included into the analysis. The strain and kinetic energy for the plate and the stiffener are expressed in terms of discrete displacement components using the finite difference method. The energy functional is minimized with respect to discretized displacement components and the natural frequencies and corresponding mode shapes are obtained from the solution of a linear eigenvalue problem. The effect of inplane deformations of the plate and the stiffener and also the effect of inplane inertia on free vibration characteristics of uniaxial and cross-stiffened plates have been examined.

Introduction

Most of the present publications of stiffened plates are dedicated to approximation and a commonly used one is to approximate the plate by an orthotropic one, that is to define the flexural rigidities in two dimensions. The idea is such an approximation is that stiffeners are integrated with the plate. Wah [1] used an orthotropic plate to increase the accuracy of simulating the vibration modes of a stiffened plate. Initially he has used the combination of classical theories for an isotropic plate and beam to find the theoretical frequencies. Then the results are compared to those of orthotropic plate theory.

A more rigorous analysis for stiffened panels simply supported along the edges normal to the direction of stiffening has been reported by Long [2] and Smith [3]. They have used a composite beam-plate method (CBP) for this analysis. Later, Long [4] further simplified the analysis by neglecting inplane displacement in the direction normal to the direction of stiffening. Kirk [5] determined the natural frequencies of the first symmetric and the first antisymmetric modes of a simply supported rectangular stiffened plate by using the Ritz method. Shimizu [6] presented a matrix method analysis of the free vibration of plates, stiffened in one direction and simply supported along all the edges.

Besides the approximation methods mentioned above, the finite element method can be used by defining the plate elements and brick elements for the beam. However, the finite element method is more powerful for concentrical stiffeners. Alternatively Aksu and Ali [7] have used finite difference formulation with unequal intervals for the vibration analysis of a orthotropic plate. Later Aksu and Ali [8] , [9] have developed a variational technique in conjunction with finite difference formulation in order to obtain the free vibration frequencies and mode shapes of a stiffened plate. In this analysis, inplane displacements and inertia in the direction of stiffener have been considered. Comparison with CBP has been given. Recently, Aksu [10] applied the developed technique to cross-stiffened plates. However, in this analysis the inplane displacements have been neglected.

So far, the effect of inplane inertia in the direction normal to the stiffener has been neglected and also the studies are limited to the plates stiffened in one direction only when both inplane deformations and inertia are included in the analysis. The numerical technique developed by Aksu and Ali [9] has been extended to include the effect of inplane inertia in both directions and the results obtained for stiffened plates in one direction have been compared with those given by the stiffness method as proposed by Long [4] and Aksu and Ali [9]. Present study has been applied to cross-stiffened plates and the effects of inplane displacements and inertia has been examined by comparing the results with those obtained by Aksu [10].

Formulation of the Problem

A stiffened plate considered here is shown in Fig. 1. It is assumed that stiffeners are an integral part of the stiffened plate, i.e., no slippage occurs between the plate and stiffeners. The strain energy due to bending and inplane stresses and kinetic energy of an isotropic plate as given by Szilard [11] based on the nondimensional parameters $\zeta = x/a$, $\eta = y/a$, $w' = w/a$, $v' = v/a$, $u' = u/a$, and $\gamma = b/a$ can be expressed as

[1] A condensed version of this paper was first presented at TBTAK VI, Science Congress, Izmir, Turkey, October, 1978.

Contributed by the Applied Mechanics Division for publication in the JOURNAL OF APPLIED MECHANICS.

Discussion on this paper should be addressed to the Editorial Department, ASME, United Engineering Center, 345 East 47th Street, New York, N. Y. 10017, and will be accepted two months after final publication of the paper itself in the JOURNAL OF APPLIED MECHANICS. Manuscript received by ASME Applied Mechanics Division, January 1981; final revison, June, 1981.

Copyright © 1982 by ASME
Downloaded 01 May 2010 to 171.66.16.249. Redistribution subject to ASME license or copyright; see http://www.asme.org/terms/Terms_Use.cfm

$$U_p = \frac{1}{2}\int_0^\gamma\int_0^1 \Big\{D\Big[\Big(\frac{\partial^2 w'}{\partial\zeta}\Big)2 + 2\nu\Big(\frac{\partial^2 w'}{\partial\zeta}\Big)\Big(\frac{\partial^2 w'}{\partial\eta^2}\Big) + \Big(\frac{\partial^2 w'}{\partial\eta^2}\Big)^2 + 2(1-\nu)\Big(\frac{\partial^2 w'}{\partial\zeta\partial\eta}\Big)^2\Big] + \frac{hEa^2}{(1-\nu^2)}\Big[\Big(\frac{\partial u'}{\partial\zeta}\Big)^2 + 2\nu\Big(\frac{\partial u'}{\partial\zeta}\Big)\Big(\frac{\partial v'}{\partial\eta}\Big) + \Big(\frac{\partial v'}{\partial\eta}\Big)^2\Big] + \frac{hEa^2}{2(1+\nu)}\Big[\Big(\frac{\partial u'}{\partial\eta}\Big)^2 + 2\Big(\frac{\partial u'}{\partial\eta}\Big)\Big(\frac{\partial v'}{\partial\zeta}\Big) + \Big(\frac{\partial v'}{\partial\zeta}\Big)^2\Big]\Big\}d\zeta d\eta \quad (1)$$

$$T_p = \frac{1}{2}a^4\rho h\int_0^\gamma\int_0^1\Big[\Big(\frac{\partial u'}{\partial t}\Big)^2 + \Big(\frac{\partial v'}{\partial t}\Big)^2 + \Big(\frac{\partial w'}{\partial t}\Big)^2\Big]d\zeta d\eta \quad (2)$$

The stiffener is subjected to normal and shear loading as shown. The strain energy of the stiffener due to bending and axial stretching are both considered. In addition, the stiffener undergoes nonlinear twisting about on axis $x = a/2$ lying in the middle surface of the plate. The torsion of stiffener leads to warping of the cross sections along the stiffener length. Thus in addition to strain energy due to torsion, there is an additional strain energy due to warping. The total strain and kinetic energies given by Aksu and Ali [9] based on nondimensional parameters can be written as,

$$\bar{U}_s = \int_0^\gamma \frac{EI_s}{a}\Big[\Big(\frac{\partial w'}{\partial\zeta}\Big)^2 - eEA\Big(\frac{\partial v'}{\partial\zeta}\Big)\Big(\frac{\partial^2 w'}{\partial\eta^2}\Big) + \frac{E\Gamma}{a^3}\Big(\frac{\partial^3 w'}{\partial\zeta\partial\eta}\Big)\Big]d\eta + \frac{1}{2}\int_0^\gamma\Big[EAa\Big(\frac{\partial v'}{\partial\eta}\Big)^2 + \frac{GJ}{a}\Big(\frac{\partial^2 w'}{\partial\zeta\partial\eta}\Big)^2\Big]d\eta \quad (3)$$

$$\bar{T}_s = \frac{1}{2}\int_0^\gamma\Big\{a^3\rho A\Big[\Big(\frac{\partial v'}{\partial t}\Big)^2 + \Big(\frac{\partial w'}{\partial t}\Big)^2\Big] + I_p a\Big(\frac{\partial^2 w'}{\partial\zeta\partial t}\Big)^2\Big\}d\eta \quad (4)$$

where $I_s = I + e^2A$ is the second moment of inertia about an axis in the midplane of the plate. In determining the total strain energy of the stiffened plate, use is made of the fact that the corresponding element displacement components of a common node must be equal.

In the case of a rectangular-section stiffener of width d and depth f, it is assumed that for the stiffener to be effective, its depth must be equal to or greater than its width. The Saint-Venant torsion constant J is taken from Dowty [12] and is as follows,

$$\frac{GJ}{a} = \frac{G\Psi(a\phi)^3}{16}\Big\{5.333 - \Big(3.36\frac{Q\phi}{\Psi}\Big)\Big[1 - 0.0833\frac{Q\phi^4}{\Psi}\Big]\Big\} \quad (5)$$

where $Q = a/h$. The warping constant Γ is given by

$$\frac{E\Gamma}{a} = \frac{Ea\phi\Psi^3}{36Q^3}\Big[\Big(1+\frac{0.5}{\Psi}\Big)^3 - \Big(\frac{0.5}{\Psi}\Big)^3\Big] \quad (6)$$

The polar mass moment of inertia I_p can be expressed as

$$I_p = \rho A k_r^2$$

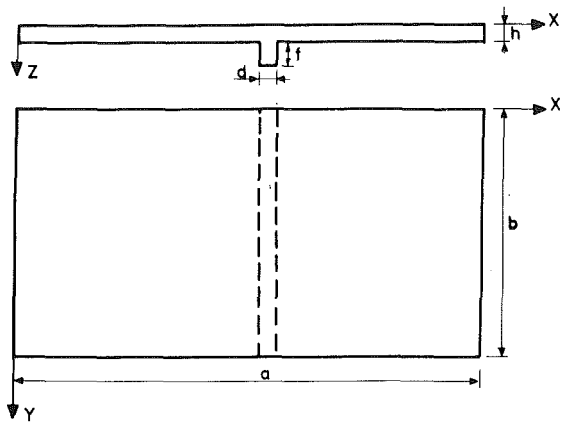
$$aI_p = \frac{\rho a^4 h\phi\Psi}{4Q^2}\Big[\frac{1}{3}(Q^2\phi^2 + 4\Psi^2) + 2\Psi + 1\Big] \quad (7)$$

The integrals in the strain energy expressions are replaced by finite approximate sums based on the mesh covering the plate. Subsequently, with the use of standard finite difference formulas, the total strain energy of the plate and beam can be expressed as quadratic form F in discrete displacement variables

Nomenclature

a,b = length and width of a plate, respectively
$[A],[B]$ = coefficient matrices, respectively
A = cross-sectional area of stiffener
D = flexural rigidity for an isotropic plate
E = elastic moduli for the plate and stiffener
e = stiffener eccentricity
d,f = width and depth of a stiffener with a rectangular cross section
F = quadratic function in discrete displacement variables
G = modulus of elasticity in shear for plate and stiffener
h = thickness of plate
H = linear function of the squares of discrete velocities
I_p = polar mass moment of inertia
I_s = second moment of inertia of stiffener about the middle surface of the plate
J = torsion constant
k_r = radius of gyration
$\bar{M}_x$ = bending moment for stiffener
m,n = mode numbers
N = numbers of equations
$\bar{N}y$ = normal forces for a stiffener in direction of y axis
MM,NN = numbers of rows and columns in the node set, respectively
Q = nondimensional parameter (a/h)
q_j,r_j = unequal mesh interval parameters in x direction
$\bar{s},\bar{q}$ = loads applied on the beam by the plate in y and z directions, respectively
T = kinetic energy
U = potential energy
p_i,s_i = unequal mesh interval parameter in y direction
U,V,W = displacement components
$\bar{V},\bar{W}$ = displacement components for stiffener
$\bar{v}_a$ = axial displacement for a stiffener
$\bar{v}_b$ = inplane displacement due to bending
u',v',w' = nondimensional displacement components
U,V,W = displacement components independent of time
x,y,z = rectangular coordinates
α = ratio of finite difference increments in orthogonal directions
γ = aspect ratio (b/a)
ϕ = nondimensional parameter (d/a)
L = Lagrangian
ζ,η = x/a, y/a nondimensional coordinates
$\Delta\zeta,\Delta\eta$ = finite difference increments
λ = eigenvalue
θ = angular displacements
ν = Poisson's ratio
ρ = mass density
ω = radian frequency of vibration
Ψ = nondimensional parameter (f/h)
Γ = warping constant

Downloaded 01 May 2010 to 171.66.16.249. Redistribution subject to ASME license or copyright; see http://www.asme.org/terms/Terms_Use.cfm



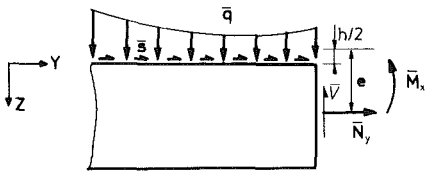


Fig. 1 A stiffened plate and the forces on the stiffener

$$F(w'_{ij}) = U_p + \bar{U}_s \tag{8}$$

Similar approximations reduce the kinetic energy to a linear function H of the squares of discrete velocities,

$$H\left[\left(\frac{\partial w'}{\partial t}\right)^2_{i,j}\right] = T_p + \bar{T}_s \tag{9}$$

Applying Euler's necessary condition to minimize the total energy of the system gives the relations

$$\frac{d}{dt}\left(\frac{\partial L}{\partial \dot{w}'}\right) - \left(\frac{\partial L}{\partial w'}\right) = 0 \tag{10}$$

where Lagrangian is

$$L = U_p + \bar{U}_s - T_p - \bar{T}_s \tag{11}$$

The solution of hormonic motion may be assumed in the form of the product

$$\begin{aligned} w'(\zeta,\eta,t) &= (A \text{ Cos } \omega t + B \text{ Sin } \omega t)\ W(\zeta,\eta) \\ v'(\zeta,\eta,t) &= (\text{A Cos } \omega t + B \text{ Sin } \omega t)\ V,(\zeta,\eta) \\ u'(\zeta,\eta,t) &= (A \text{ Cos } \omega t + B \text{ Sin } \omega t)\ U(\zeta,\eta) \end{aligned} \tag{12}$$

Equation (10) can be expressed as a matrix eigenvalue problem as follows.

$$\begin{aligned} A\{X\} &= \lambda[B]\{X\} \\ \lambda &= a^4 \rho h \omega^2 \end{aligned} \tag{13}$$

A computer program was developed for this analysis. The program carried out the substitution of finite difference equations and performed the partial differentiation required by equation (10).

Finite Difference Formulation

The finite difference formulation of the integral expressions for the strain energy due to bending of the plate and for the total strain energy of the beam was obtained by a first and second-order Lagrangian polynomials as discussed by Aksu and Ali [8, 9].

The concept of interlacing grids and nodal subdomains are applied for the strain energy expression due to inplane displacements and a modified finite difference method is used

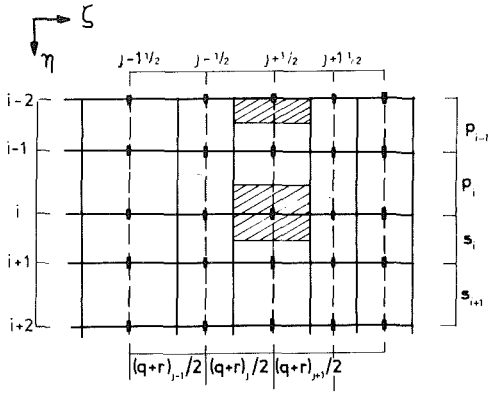


Fig. 2 Nodes and nodal subdomains for inplane displacements

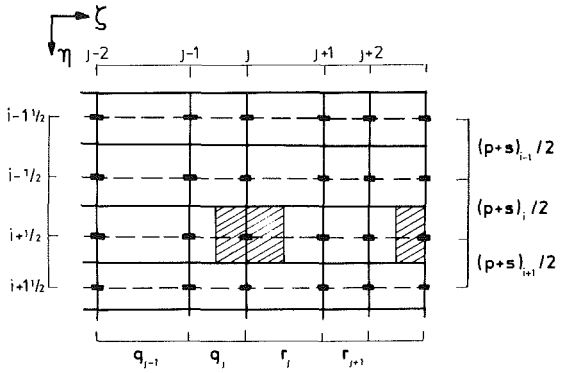


Fig. 3 Nodes and nodal subdomains for inplane displacements

in the formulation. For the application of the method, the inplane strain energy expression of the plate is divided into substrain energies as follows

$$U_m = \int_0^{\gamma}\int_0^{1}\left[U_1 + U_2 + U_3 + U_4\right] d\zeta d\eta \tag{14}$$

where

$$U_1 = \frac{Eha^2}{2(1-\nu^2)}\left(\frac{\partial u'}{\partial \zeta}\right)^2 + \frac{ha^2}{4(1+\nu)}\left(\frac{\partial v}{\partial \zeta}\right)^2$$

$$U_2 = \frac{Eha^2}{4(1+\nu)}\left(\frac{\partial u'}{\partial \eta}\right)^2 + \frac{Eha^2}{2(1-\nu^2)}\left(\frac{\partial v'}{\partial \eta}\right)^2$$

$$U_3 = \frac{ha^2}{(1-\nu^2)}\left(\frac{\partial u'}{\partial \zeta}\right)\left(\frac{\partial v'}{\partial \eta}\right)$$

$$U_4 = \frac{Eha^2}{2(1+\nu)}\left(\frac{\partial u'}{\partial \eta}\right)\frac{\partial v'}{\partial \zeta}$$

The nodal subdomains used for substrain energies U_1 and U_2 are shown in Figs. 2 and 3, respectively. For substrain energies U_3 and U_4, a combination of nodal subdomains for the substrain energies U_1 and U_2 are used. The strain energy associated with inplane stresses are computed as the sum of strain energies summed over the set of nonoverlapping subdomains. Employing two sets of interlacing grids provides a finite difference formulation with a reduced mesh size and results in reduced discretization error.

The intervals $\Delta\zeta$ and $\Delta\eta$ as shown in Fig. 4, are defined when the plate is divided into (MM-1) and (NN-1) subdivisions in each coordinate direction, respectively:

$$\Delta\zeta = \frac{1}{MM\text{-}1}, \Delta\eta = \frac{\gamma}{NN\text{-}1}, \propto = \frac{\gamma(MM\text{-}1)}{NN\text{-}1} \tag{15}$$

then the use of unequal intervals, where more accurate results

Downloaded 01 May 2010 to 171.66.16.249. Redistribution subject to ASME license or copyright; see http://www.asme.org/terms/Terms_Use.cfm

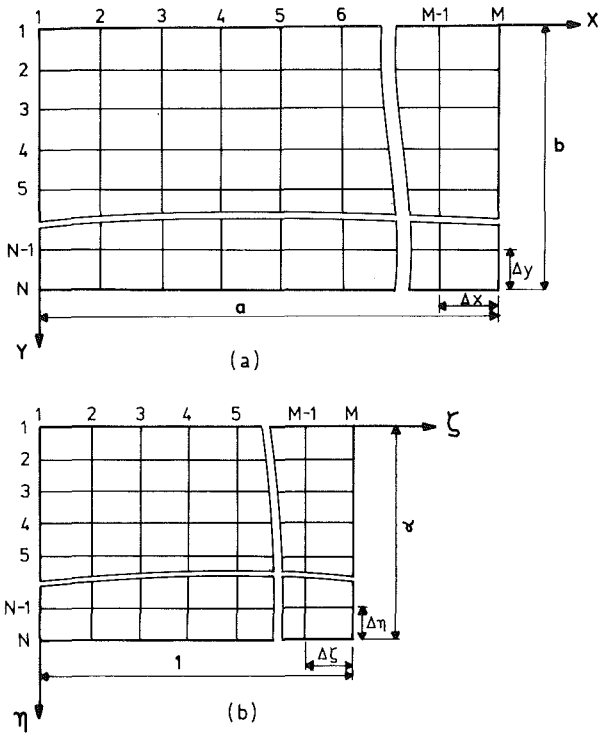


Fig. 4 Mesh used for the plate

are obtained by Aksu and Ali [7], introduces the following conditions to be satisfied,

$$N\text{-}1 = \frac{1}{2}\left[\sum_{i=1}^{NN}(p_i + s_i) - (p_1 + s_{NN})\right] \tag{16}$$

$$M\text{-}1 = \frac{1}{2}\left[\sum_{J=1}^{MM}(q_j - r_j) - (q_1 + r_{MM})\right] \tag{17}$$

Transforming the inplane displacement $u'(\zeta,\eta,t)$ and $v'(\zeta,\eta,t)$ to $U(\zeta,\eta)$ and $V(\zeta,\eta)$, respectively, the finite difference equations are obtained by using Lagrangian interpolation polynomial as developed by Aksu and Ali [9].

Results and Discussions

The numerical method developed in this study is applied to several rectangular plate systems simply supported on all edges, which have integral stiffeners in one or two directions.

In the first example, the stiffened plate system studied by Long [4] and Aksu [9] is examined. This system consists of a plate simply supported on all the edges and with dimensions 16 in. × 24 × 0.25 in. (406 mm × 610 mm × 6.35 mm) and an eccentric stiffener 0.875 in. × 0.5 in. (22.22 mm × 12.70 mm) placed across the shorter span. The solution is obtained by considering the lateral displacement w' restrained along all simply supported edges and inplane displacements v' and u' are restrained along the edges parallel to η and ζ axis, respectively.

In Table 1, the results obtained by Long [4] for the stiffened plate are given. In this analysis inplane displacement in the stiffening direction is included, but inplane inertia is excluded. Considering the results obtained by Aksu [9], it is observed that the inplane inertia in one direction only has a considerable effect on the first and third symmetric modes. The discrepancy when comparing to the stiffness method for the first mode is 6.6 percent. Due to inherent error in the finite difference technique, the expected increase in the natural frequency calculation by introducing inplane inertia into the analysis is more than 6.6 percent and its effect is increased as expected for higher modes. For the second mode, since the stiffener does not experience bending, the effect of inplane inertia is diminished.

When inplane displacement v' is included into the analysis, the discrepancy compared to the method given by Long [4] is increased to 13.8 percent for the first mode and 5.6 percent for the third mode while only 1.5 percent discrepancy is observed for the second mode which is not symmetric.

Since we have observed quite a considerable increase in the natural frequencies, especially for the first mode, which is of greatest interest in practical applications, the inplane displacement u' should be included into the analysis.

The characteristics of inplane displacements for the first and third mode are shown in Figs. 5-8. The inplane displacement u' is zero along the beam. It is zero at inflection points of the wave form of lateral displacement w' along the $-\zeta$ direction. The mode shape of v' along the ζ direction is similar to the mode shape of u' along the η direction. However inplane displacement v' along the beam direction are of a higher order of magnitude when compared to the transverse displacement u'.

When u' displacement is included into the analysis, generally, v' displacement are reduced. Its effects is high where u' displacements are maximum. The reduction in v' displacement corresponds to a relative increase in lateral displacement w'. In addition to increase in stiffness of the structure by including inplane displacements with resulting inplane inertia, the overall stiffness of the structure is further

Table 1 Frequencies (Hz) for a plate 410| × |600| × |6.33 mm with a centrally spaced stiffener 22.22| × |12.70 mm and all the sides are simply supported (E = 2.11 × 10^6 kg/cm ^{2}, ν = 0.3 ρ = 7.83 × 10^{-3} kg/cm^3)

Displacement Components Considered		Stiffness Method [4] (w + v)	Finite Differences [9] (w + v)			Present Analysis (w + v + u)	
Mesh	NN		6	8	9	6	9
	MM		9	11	13	9	13
Number of Equations			70	126	176	112	284
Mode	m=1, n=1	224.0	233.60	238.82	240.24	243.96	254.94
	m=2, n=1	273.6	261.83	267.02	269.71	264.22	269.46
	m=3, n=1	484.9	468.69	483.23	490.13	478.35	511.64

Downloaded 01 May 2010 to 171.66.16.249. Redistribution subject to ASME license or copyright; see http://www.asme.org/terms/Terms_Use.cfm

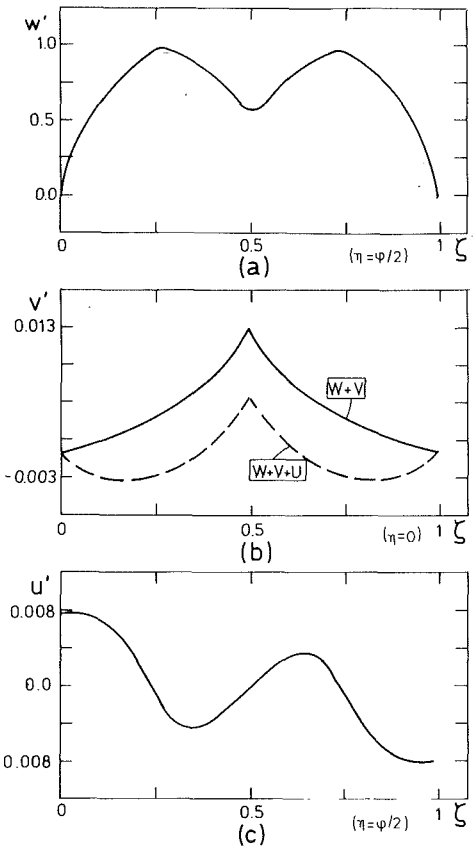


Fig. 5 Mode shape functions of the first mode for example 1

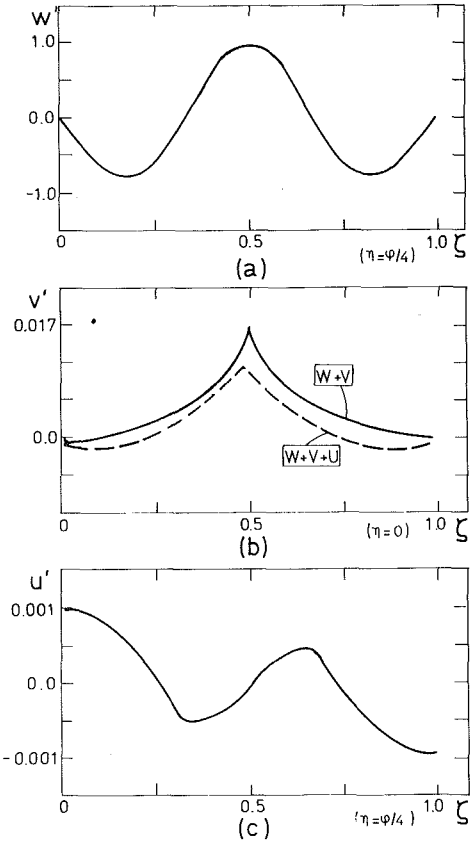


Fig. 7 Mode shape functions of the third mode for example 1

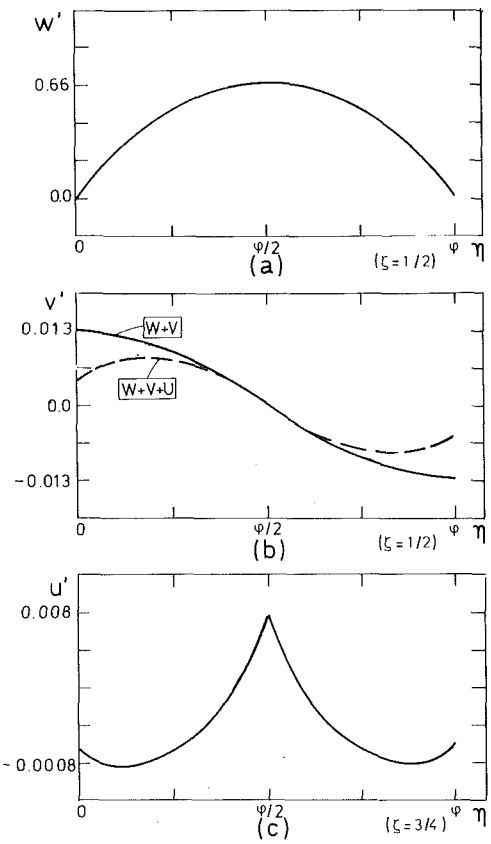


Fig. 6 Mode shape functions of the first mode for example 1

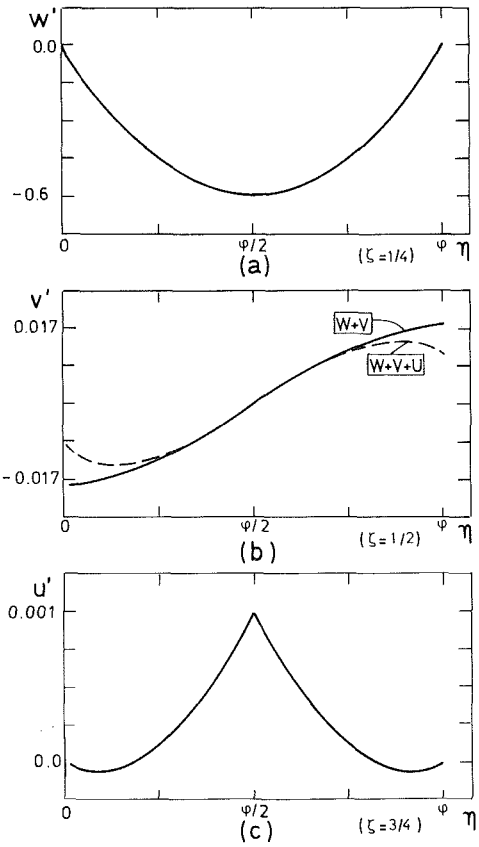


Fig. 8 Mode shape functions of the third mode for example 1

Downloaded 01 May 2010 to 171.66.16.249. Redistribution subject to ASME license or copyright; see http://www.asme.org/terms/Terms_Use.cfm

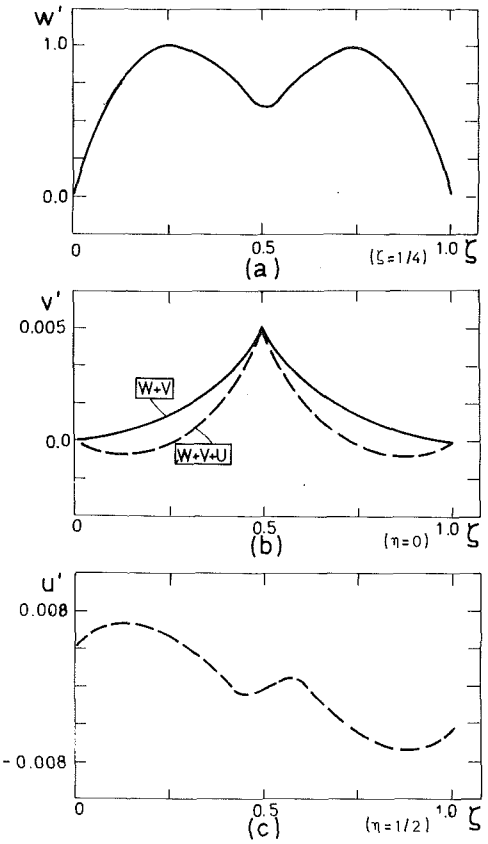


Fig. 9 Mode shape functions for the fundamental mode of cross-stiffened plate (example 2)

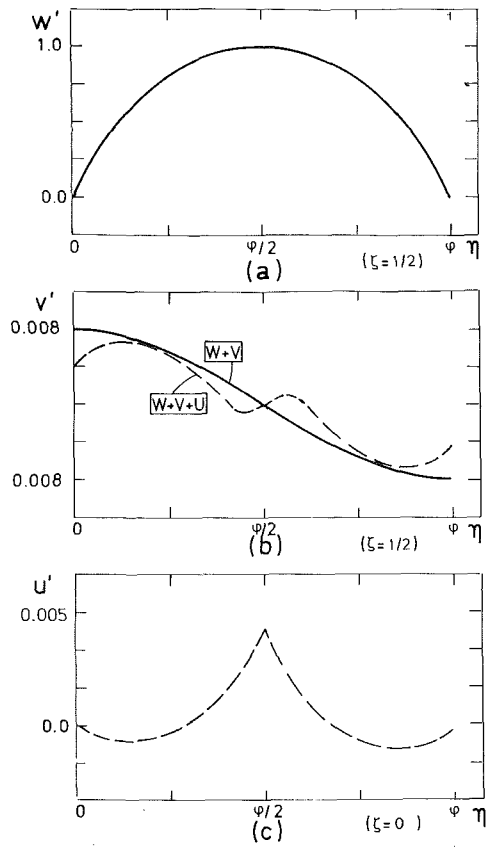


Fig. 10 Mode shape functions for the fundamental mode of cross-stiffened plate (example 2)

Table 2 Frequencies (Hz) for a cross-stiffened plate, $a = 635$ mm, $Q = 250$, $\phi = 0.01$, and $\psi = 10$ with all edges ss ($\nu = 0.3$, $E = 2.11 \times 10^6$ kg/cm^2, $\rho = 7.83$ kg/cm^3.)

Mode	Exact Solution [11] Unstiffened Plate h=2.54 mm	h=3.43 mm	Finite Differences w(10) (9 x 9)	w+v (9 x 9)	w+v+u (9 x 9)
m=1, n=1	30.79	41.57	127.73	126.05	129.08
m=2, n=2	76.97	103.91	150.33	143.48	158.10
m=2, n=2	123.16	166.27	149.21	175.81	182.75

increased due to bending stiffness of the stiffener. It implies that the natural frequencies of symmetric modes tends to an increase particularly toward the higher modes.

In the second example, the cross-stiffened plate system is examined. This system consists of a 25 in. (635 mm) square plate 0.1 in. (2.54 mm) thick, simply supported on all the edges and has two integral stiffeners 0.975 in. × 0.5 in. (22.22 mm × 12.7 mm) placed on the axes of symmetry. The natural frequencies for the first three modes are given in Table 2. In column 1, the natural frequencies of an unstiffened plate is obtained by an exact solution. Then, the natural frequencies of the unstiffened plate, which is equal in mass to the cross-stiffened plate, are determined and the results are indicated in column 2 of the table.

In column 3, the results obtained for the cross-stiffened plate by Aksu [10] are given. The inplane displacements u' and v' are neglected in this analysis and the stiffener bending is assumed to be about an axis in the middle surface of the plate, which implies an upper bound to the stiffener flexural rigidity. These results show that the effect of stiffening decreases for higher modes. Since the effect of bending is replaced by torsion and warping of the stiffener gradually in second and third modes.

In column 4 of the table, the results are obtained when inplane displacements and inertia in both directions are included into the analysis. The discrepancy in natural frequencies comparing to the results given by Aksu [10] increases gradually to the higher modes since the inplane displacements relatively increases due to mode shapes of vibration in higher modes. Due to the effect of inertia force resulted by inplane motion, the natural frequency of vibration in the third mode increases about 29 percent which is absolutely considerable. The mode shape functions for the fundamental mode are given in Figs. 9 and 10.

Conclusions

The numerical method based on variational principles in conjunction with the finite difference technique that is developed here is used for comparisons on the effects of stiffening, inplane displacements and inplane inertia on the natural frequencies of an eccentricically stiffened rectangular plate. When inplane displacement normal to the direction of stiffening is included in the analysis, the inplane displacement in the direction of stiffening is reduced, which corresponds to a relative increase in lateral displacement of stiffener. Overall stiffness of structure is increased due to the effect of considering the inplane stiffness of the plate in the direction normal to the stiffener and bending stiffness of stiffener, which is resulted by relative increase in the lateral displacement. The discrepancy in natural frequencies of vibration for symmetric modes increases gradually in higher modes.

Downloaded 01 May 2010 to 171.66.16.249. Redistribution subject to ASME license or copyright; see http://www.asme.org/terms/Terms_Use.cfm

Acknowledgments

I acknowledge the valuable help of my research student Yaman Akar for his support in running the computer programs and in preparation of drawings for the realization of this study.

References

1 Wah, T., "Vibration of Stiffened Plates," *Aeronautical Quarterly*, Vol. XV, 1964, p. 285.

2 Long, B. R., "Vibration of Eccentrically Stiffened Plates," *Shock Vib. Bull.*, Vol. 38, 1960.

3 Smith, C. S., "Bending, Buckling and Vibration of Orthotropic Plate-Beam Structures," *J. Ship Research*, Vol. 12, No. 4, 1968.

4 Long, B. R., "A Stifness-Type Analysis of the Vibration of a Class of Stiffened Plates," *J. Sound and Vibration*, Vol. 16, No. 3, 1971, pp. 323–335.

5 Kirk, C. L., "Natural Frequencies of Stiffened Rectangular Plates," *J. Sound and Vibration*, Vol. 13, No. 4, 1970, pp. 375–388.

6 Shimizu, S., "Free Vibration of Stiffened Plates," *Adv. in Compt. Math. in Str. Mech. and Design*, 2nd U.S. and Japan Seminar, 1972.

7 Aksu, G., and Ali, R., "Prediction of Dynamic Characteristics of Orthotropic Plates by a Finite Difference Unequal Interval Formulation," *J. Sound and Vibration*, Vol. 35, No. 1, 1974, pp. 119–128.

8 Aksu, G., and Ali, R., "Determination of Dynamic Characteristics of Rectangular Plates with Cutouts Using a Finite Difference Formulation," *J. Sound and Vibration*, Vol. 44, 1976, pp. 147–158.

9 Aksu, G., and Ali, R., "Free Vibration Analysis of Stiffened Plates Using Finite Difference Method," *J. Sound and Vibration*, Vol. 48, 1976, pp. 15–25.

10 Aksu, G., "Free Vibration Analysis of Cross Stiffened Rectangular Plates," *METU J. Pure and Applied Sciences*, Vol. 9, No. 2, 1976, pp. 209–226.

11 Szilard, R., *Theory of Plates*, Prentice Hall, New York, 1975.

12 Dowty G. H., *Structural Principles and Data*, Handbook of Aeronautics, No. 1, Royal Aeronautical Society, 1952.

Downloaded 01 May 2010 to 171.66.16.249. Redistribution subject to ASME license or copyright; see http://www.asme.org/terms/Terms_Use.cfm

A Linear Algebra Approach to the Analysis of Rigid Body Displacement From Initial and Final Position Data

A. J. Laub
Department of Electrical Engineering – Systems.

G. R. Shiflett
Department of Mechanical Engineering. Assoc. Mem. ASME

University of Southern California, Los Angeles, Calif. 90007

The location and orientation of a rigid body in space can be defined in terms of three noncollinear points in the body. As the rigid body is moved through space, the motion may be described by a series of rotations and translations. The sequence of displacements may be conveniently represented in matrix form by a series of displacement matrices that describe the motion of the body between successive positions. If the rotations and translations (and hence the displacement matrix) are known then succeeding positions of a rigid body may be easily calculated in terms of the initial position. Conversely, if successive positions of three points in the rigid body are known, it is possible to calculate the parameters of the corresponding rotation and translation. In this paper, a new solution is presented which provides explicit formulas for the rotation and translation of a rigid body in terms of the initial and final positions of three points fixed in the rigid body. The rotation matrix is determined directly whereupon appropriate rotation angles and other information can subsequently be calculated if desired.

1 Introduction

The kinematics of rigid body motion is an intriguing problem that has attracted the attention of many authors. Beatty [1] has provided a short bibliographic sketch of many of the papers on rigid body rotation which have appeared in recent years. The origin of classical kinematic theory may be traced to Euler and Chasles; in a standard treatise on classical dynamics, Whittaker [2] discusses their work and provides geometric proofs of several important theorems. The central problem in the study of finite displacements of a rigid body is to describe successive positions of a rigid body by a linear transformation which is, for the most general case, a combination of translation(s) and rotation(s). Typically, the problem is one in which the angle(s) of rotation, the translation between successive positions of the rigid body, and the initial position of the rigid body as defined by three points within the body are given and the elements of the transformation must first be evaluated before the final position of the body may be calculated.

Although it has received somewhat less attention, a problem of equal interest is that of calculating the transformation relating successive positions of the rigid body (and hence the rotational and translational parameters of the displacement) from a knowledge of the actual positions of the rigid body. Methods for calculating the appropriate transformation have been provided by Paul [3], Bottema and Roth [4], Suh and Radcliffe [5], and Beggs [6]. With the use of precise position data for the successive positions of the three points each technique will yield equivalent results. However, if a rigid body is moved through space and the successive positions of the three points are actually measured, some degree of measurement error is incorporated into the position data and the foregoing techniques may no longer yield equivalent results. In fact, each of the foregoing techniques can lead to several possible transformations. The method of Bottema and Roth alone may provide three separate possible transformations depending on the order in which the points are considered. In the presence of imprecise data, which transformation best describes the motion becomes a serious question. Typically, only rotations are considered and a least squares procedure is used (see, for instance, Ström and Svensson [13]).

The present paper grew out of an attempt to determine the transformation that best describes the displacement of a rigid body for the more general case of rotation and translation from imprecise data for the initial and final positions of three points fixed in the body. A new linear algebra approach is employed for the solution. Such an approach offers two distinct advantages. First, a direct analysis of the imprecise data case is greatly facilitated through the ability to bring to bear some matrix perturbation theory on the problem. Second, the solution involves only simple arithmetic operations (add, subtract, multiply, divide – no trigonometric functions, for example) and hence is easily implemented on a

Contributed by the Applied Mechanics Division for publication in the JOURNAL OF APPLIED MECHANICS.

Discussion on this paper should be addressed to the Editorial Department, ASME, United Engineering Center, 345 East 47th Street, New York, N.Y. 10017, and will be accepted until two months after publication of the paper itself in the JOURNAL OF APPLIED MECHANICS. Manuscript received by ASME Applied Mechanics Division, June, 1980; final revision, March, 1981.

Copyright © 1982 by ASME
Downloaded 01 May 2010 to 171.66.16.249. Redistribution subject to ASME license or copyright; see http://www.asme.org/terms/Terms_Use.cfm

microprocessor. The perturbation analysis and details of the microprocessor implementation are beyond the scope of this paper and will be reported separately. Here, the linear algebraic solution and its interpretation will be presented.

Briefly, the paper is organized as follows: Section 2 defines some of the notation used and reviews two results from matrix theory; Section 3 reviews rigid body displacement and defines the problem to be solved in the paper; Section 4 derives the formulas that solve the problem, and finally, a numerical example and some details of implementation are provided in Section 5.

2 Some Notation and Matrix Theory Results

Uppercase Latin letters will be used to denote matrices while lowercase Latin letters will denote (column) vectors. The inverse, transpose, inverse transpose, and determinant of a matrix A will be denoted, respectively, by A^{-1}, A^T, A^{-T}, and $\det A$. The vector norm will be the usual Euclidean norm:

$$\|x\| := \left(\sum_{i=1}^{n} x_i^2\right)^{1/2}$$

Throughout this paper $:=$ means "is defined as."

Definition 1. An $n \times n$ matrix R is an *orthogonal matrix* if $RR^T = R^T R = I$ and R is a *rotation* or *proper orthogonal* matrix if R is orthogonal and $\det R = +1$. The Euclidean norm $\|\circ\|$ is unitarily invariant, i.e., $\|Rx\| = \|x\|$ if R is orthogonal.

Lemma 1. For compatibly dimensioned matrices and assuming the indicated inverses exist we have the following determinant identities:

1. $\det \begin{bmatrix} A & B \\ C & D \end{bmatrix} = \det A \cdot \det (D - CA^{-1}B)$; or

2. $\det \begin{bmatrix} A & B \\ C & D \end{bmatrix} = \det D \cdot \det (A - BD^{-1}C)$

Proof: 1 follows immediately upon noting that

$$\begin{bmatrix} A & B \\ C & D \end{bmatrix} = \begin{bmatrix} I & 0 \\ CA^{-1} & I \end{bmatrix} \begin{bmatrix} A & B \\ 0 & D - CA^{-1}B \end{bmatrix}$$

The proof of 2 follows similarly.

Lemma 2. (Sherman-Morrison-Woodbury [7, 8]): For compatibly dimensioned matrices:

$$(A + BDC)^{-1} = A^{-1} - A^{-1}B(D^{-1} + CA^{-1}B)^{-1}CA^{-1}$$

assuming the indicated inverses exist.

3 Rigid Body Displacement

It is well known that, relative to a fixed inertial reference frame, the configurations of a vector fixed in a rotating rigid body are related by

$$v_k = R_{jk} v_j \tag{1}$$

where v_k, v_j denote the kth and jth configurations of the vector v that is fixed in the body; and R_{jk} is the orthogonal (rotation) transformation from j to k. Since v_i may be related to the ith positions p_i and r_i in the inertial frame of two points, p and r, fixed in the body by $v_i = p_i - r_i$ (1), can be rewritten as

$$p_k - r_k = R_{jk}(p_j - r_j) \tag{2}$$

Rearranging (2) yields

$$p_k = R_{jk} p_j + s_{jk} \tag{3}$$

where $s_{jk} := r_k - R_{jk} r_j$.

Since the spatial location and orientation of a rigid body may be described in terms of three noncollinear points fixed in the body and since (3) holds for any point in the body, successive positions of the rigid body can be related by writing (3) for three noncollinear points in the body and combining the results to form

$$P_k = R_{jk} P_j + s_{jk} h^T \tag{4}$$

where: P_j, P_k are 3×3 matrices, the columns of which are the jth and kth spatial coordinates, respectively, of three points fixed in the body; $h^T := (1\ 1\ 1)$; and s_{jk} is the same as before.

The rotation matrix, R_{jk}, used in (1)–(4) represents the rotation(s) of the body (or points within the body) about an arbitrary set of axes. The rotations are often defined as rotations about a fixed, right-handed set of Cartesian axes, relative rotations about axes fixed in the body (Euler angles), or as a single rotation about a specific axis in space. The last approach is particularly appealing for it views the displacement of a rigid body as a screw displacement in terms of a single rotation and a single translation. Beatty [1, 9, 10], Thurnauer [11], Schwartz [12], and others (see bibliography in [1]) have given formulas by which the elements of the rotation matrix, R_{jk}, may be evaluated given the rotation angle(s) and axes of rotation thus permitting calculation of the kth position and orientation of the rigid body.

A related problem (in effect, the "inverse" problem), however, is determination of the rotation matrix, R_{jk} when the successive positions of three noncollinear points in the body are already known. Beggs [6] and Suh and Radcliffe [5] derive methods by which the rotation matrix is calculated after which the displacement parameters are found. Bottema and Roth [4] use the opposite approach and first find the displacement in terms of screw parameters before calculating the rotation matrix. Both approaches, however, share the common trait of designating one of the three points as a reference point within the body, that is, as the origin of a set of vectors fixed in the body. Once the rotation is calculated, the translation of the body is calculated from the successive positions of the specially designated point.

In the case for which the successive positions of three noncollinear points in the body are known unambiguously, the choice of one of the three points as the reference is immaterial – any of the various methods will yield equivalent results. However, if the successive positions of the three noncollinear points are actually measured (possibly inaccurately), the resolution of the measurement system affects the outcome of each method. Not only will the results of the various methods be different but, depending on which point is chosen as the reference, each individual method may itself lead to several different results. Clearly a method is required that will yield unambiguously a good estimate of the displacement parameters given data that are known to contain some degree of ambiguity – a method that does not also depend on the choice of one of the three noncollinear points as a reference.

The method presented in this paper is the result of preliminary research in applying perturbation analysis to the problem posed with imprecise data. The method begins with the general form of rigid body displacement as given by (4). Clearly, there is no loss of generality in assuming that P_j is nonsingular (a physical interpretation of the nonsingularity of either P_j or P_k would be that no two of the three points fixed in the body are collinear with the origin of the fixed inertial coordinate system) and it will then be more convenient in the sequel to postmultiply by P_j^{-1} and work with the equation

$$R_{jk} = Q_{jk} - s_{jk} v_j^T \tag{5}$$

where

Downloaded 01 May 2010 to 171.66.16.249. Redistribution subject to ASME license or copyright; see http://www.asme.org/terms/Terms_Use.cfm

$$Q_{jk} := P_k P_j^{-1}\ ;\ \text{and}$$
$$v_j := P_j^{-T} h$$

For simplicity in the sequel we shall henceforth write $j = 1$, $k = 2$, and drop the unnecessary subscripts so that (4) will be written in the form

$$P_2 = RP_1 + sh^T \tag{4a}$$

while (5) will be written in the form

$$R = Q - sv^T \tag{5a}$$

Note that $Q = P_2 P_1^{-1}$ and $v = P_1^{-T} h$ are the given data while s and thus R are to be determined.

One final point that must be mentioned here is that even if P_1 in (4*a*) is nonsingular, P_2 may still be singular. For example (see [6]) if

$$P_1 = \begin{bmatrix} 1 & 4 & 7 \\ 1 & 7 & 10 \\ 7 & 1 & 10 \end{bmatrix}, R = \frac{1}{3}\begin{bmatrix} 2 & -1 & 2 \\ 2 & 2 & -1 \\ -1 & 2 & 2 \end{bmatrix},$$
$$s = \begin{bmatrix} 2 \\ 2 \\ 2 \end{bmatrix} \text{ then } P_2 = \begin{bmatrix} 7 & 3 & 10 \\ 1 & 9 & 10 \\ 7 & 6 & 13 \end{bmatrix}$$

which obviously is singular. But we claim that it is no loss of generality to also assume that P_2 (and hence Q) is nonsingular. For if P_1 and P_2 are given data arising from rigid body motion with singular P_2, we can always find a vector $\hat{s}$ such that $P_2' := P_2 + \hat{s}h^T$ is nonsingular.[1] It then suffices to consider the modified problem

$$P_2' = RP_1 + s'h^T \tag{4b}$$

where $s' := s + \hat{s}$. Since it will be convenient in the sequel to assume that Q is nonsingular, we shall henceforth assume that P_2 is also nonsingular. However, it will be evident from the final form of the actual solution that nonsingularity of Q or P_2 is not necessary.

4 Problem Solution

With Q and v given, it suffices to determine s in (5*a*) so that $Q - sv^T$ is a rotation. First note that by Lemma 1

$$\det \begin{bmatrix} Q & s \\ v^T & 1 \end{bmatrix} = (1 - v^T Q^{-1} s) \cdot \det Q$$

while by Lemma 2

$$\det \begin{bmatrix} Q & s \\ v^T & 1 \end{bmatrix} = 1 \cdot \det (Q - sv^T)$$

$$(1 - v^T Q^{-1} s) \det Q = 1 \tag{6}$$

Furthermore, by Lemma 2 we have

$$(Q - sv^T)^{-1} = Q^{-1} + \frac{Q^{-1} s v^T Q^{-1}}{1 - v^T Q^{-1} s}$$
$$= Q^{-1} + (\det Q) Q^{-1} s v^T Q^{-1}$$

by (6). Since the inverse of an orthogonal matrix is equal to its transpose we can write

$$Q^T - vs^T = Q^{-1} + (\det Q) Q^{-1} s v^T Q^{-1}$$

or, upon premultiplication by Q,

$$-Qvs^T - (\det Q) s v^T Q^{-1} + QQ^T - I = 0 \tag{7}$$

Also, we must have

$$I = (Q - sv^T)(Q - sv^T)^T$$

which becomes, on multiplying out and rearranging,

$$(v^T v) ss^T - Qvs^T - sv^T Q^T + QQ^T - I = 0 \tag{8}$$

Subtracting (7) from (8) we have

$$s\left[(v^T v) s^T + v^T \left((\det Q) Q^{-1} - Q^T\right)\right] = 0 \tag{9}$$

Now if Q is already a rotation s must be 0. If $s \neq 0$ we conclude from (9) that

$$s = \frac{1}{v^T v}\left[Q - (\det Q) Q^{-T}\right] v \tag{10}$$

Note also that $s = 0$ in (10) if Q is a rotation for then $Q = (\det Q) Q^{-T}$. Finally, R becomes

$$R = Q - sv^T$$
$$= Q - \frac{1}{v^T v}\left[Q - (\det Q) Q^{-T}\right] v v^T \tag{11}$$

Equations (10) and (11) constitute the desired analytic solution to our problem.

The solution can also be written in terms of the data P_1 and P_2 as follows:

$$s = \frac{1}{h^T P_1^{-1} P_1^{-T} h}\left[P_2 P_1^{-1} P_1^{-T} - \left(\frac{\det P_2}{\det P_1}\right) P_2^{-T}\right] h \tag{12}$$

and

$$R = P_2 P_1^{-1} - sh^T P_1^{-1}$$
$$= P_2 P_1^{-1}\left(I - \frac{P_1^{-T} h h^T P_1^{-1}}{h^T P_1^{-1} P_1^{-T} h}\right) +$$
$$\frac{(\det P_2)}{(\det P_1) h^T P_1^{-1} P_1^{-T} h} P_2^{-T} h h^T P_1^{-1} \tag{13}$$

Note that (10) and (11) are indicative of a more efficient arrangement of the calculations than the more formidable forms in (12) and (13). Note also that the matrix $Q - (\det Q) Q^{-T}$ in (10) can be written in the form

$$\begin{bmatrix} q_{11} + q_{23} q_{32} - q_{22} q_{33} & q_{12} + q_{21} q_{33} - q_{23} q_{31} & q_{13} + q_{22} q_{13} - q_{21} q_{32} \\ q_{21} + q_{12} q_{33} - q_{13} q_{32} & q_{22} + q_{13} q_{31} - q_{11} q_{33} & q_{23} + q_{11} q_{32} - q_{12} q_{31} \\ q_{31} + q_{13} q_{22} - q_{12} q_{23} & q_{32} + q_{11} q_{23} - q_{13} q_{21} & q_{33} + q_{12} q_{21} - q_{11} q_{22} \end{bmatrix} \tag{14}$$

Since $Q - sv^T$ is a rotation with determinant $+1$ we clearly must have

(where q_{ij} are the elements of Q) showing directly that, as mentioned above, it is not necessary that Q be nonsingular.

To summarize then, we have the following:

Theorem 1. Given 3×3 matrices P_1 and P_2 such that

$$\|P_1 x\| = \|P_2 x\| \text{ for all } x \text{ such that } h^T x = 0 \tag{15}$$

(i.e., rigid body motion) where $h^T = (1, 1, 1)$ then there exists

[1] To see why this must be so, suppose such an $\hat{s}$ did not exist. Then there would have to exist a vector $x \neq 0$ such that $(P_2 + \hat{s}h^T) x = 0$ for any $\hat{s}$. In particular, we could take $\hat{s} = -s$ whereupon from (4*b*) we would have $RP_1 x = 0$ which would contradict the nonsingularity of RP_1.

Downloaded 01 May 2010 to 171.66.16.249. Redistribution subject to ASME license or copyright; see http://www.asme.org/terms/Terms_Use.cfm

a (unique) s given by (12) and rotation R given by (13) such that

$$P_2 = RP_1 + sh^T \tag{4a}$$

Conversely (4*a*) is possible only if (15) holds (this is obvious since from (4*a*) we have $P_2x = R\,P_1x$ if $h^Tx = 0$ and $\|\circ\|$ is unitarily invariant).

Theorem 2. Given a 3 × 3 matrix Q and $v \neq 0$ such that

$$\|Q\,x\| = \|x\| \text{ for all } x \text{ such that } v^Tx = 0 \tag{16}$$

then there exists a (unique) s given by (10) and rotation R given by (11) such that

$$R = Q - s\,v^T \tag{5a}$$

Conversely (5*a*) is possible only if (16) holds (this is obvious since from (5*a*) we have $Rx = Qx$ if $v^Tx = 0$ and $\|\bullet\|$ is unitarily invariant).

Note that the solution for the rotation matrix, R, and the vector, s, depends neither on a particular form for R nor on a particular initial location for the reference point and may thus be used for Euler or Cartesian displacements as well as screw displacements.

5 An Example

A simple numerical example is included which may prove useful in comparing with previous results (e.g. [6]). Consider the data at the end of Section 3 but choose $\hat{s} = \begin{pmatrix} 1 \\ 0 \\ 0 \end{pmatrix}$ so that

$$\begin{pmatrix} 7 & 3 & 10 \\ 1 & 9 & 10 \\ 7 & 6 & 13 \end{pmatrix} + \hat{s}h^T \text{ is nonsingular. Thus we shall consider}$$

$$P_1 = \begin{pmatrix} 1 & 4 & 7 \\ 1 & 7 & 10 \\ 7 & 1 & 10 \end{pmatrix}$$

$$P_2 = \begin{pmatrix} 8 & 4 & 11 \\ 1 & 9 & 10 \\ 7 & 6 & 13 \end{pmatrix}$$

Then

$$Q = \frac{1}{12}\begin{pmatrix} -64 & 41 & 17 \\ -40 & 38 & 2 \\ -52 & 38 & 14 \end{pmatrix} \text{ and } v = \begin{pmatrix} -2 \\ \frac{5}{4} \\ \frac{1}{4} \end{pmatrix}$$

Hence

$$s = \frac{1}{v^Tv}[Q - (\det Q)\,Q^{-T}]v = \begin{pmatrix} 3 \\ 2 \\ 2 \end{pmatrix} \text{ and } R = Q - sv^T \begin{pmatrix} \frac{2}{3} & -\frac{1}{3} & \frac{2}{3} \\ \frac{2}{3} & \frac{2}{3} & -\frac{1}{3} \\ -\frac{1}{3} & \frac{2}{3} & \frac{2}{3} \end{pmatrix}$$

Note that the true s is $\begin{pmatrix} 2 \\ 2 \\ 2 \end{pmatrix}$ when $\hat{s}$ is subtracted.

The formulas (10), (11), and (14) are easily implemented using standard linear equation software. Only an LU factorization of a 3 × 3 matrix (P_1)—a fairly routine matter—and some matrix/vector multiplications are required. A microprocessor-based implementation is currently under investigation by the authors.

References

1 Beatty, M. F., "Vector Analysis of Finite Rigid Rotations," ASME Journal of Applied Mechanics, Vol. 44, 1977, pp. 501-502.

2 Whittaker, E. T., *Analytical Dynamics*, Cambridge University Press, Cambridge, 1927, Chapter 1.

3 Paul, B., "On the Composition of Finite Rotations," *American Mathematical Monthly*, Vol. 70, 1963, pp. 859-862.

4 Bottema, O., and Roth, B., *Theoretical Kinematics*, North-Holland, Amsterdam, 1979, Chapter 3.

5 Suh, C., and Radcliffe, C., *Kinematics and Mechanisms Design*, Wiley, New York, 1978, Chapter 3.

6 Beggs, J. S., *Advanced Mechanism*, Macmillan, New York, 1966, Chapter 2.

7 Sherman, J., and Morrison, W. J., "Adjustment of an Inverse Matrix Corresponding to Changes in the Elements of a Given Column or a Given Row of the Original Matrix," *Ann. Math. Statist.*, Vol. 20, 1949, p. 621.

8 Woodbury, M., "Inverting Modified Matrices," Memorandum Report 42, Statistical Research Group, Princeton, 1950.

9 Beatty, M. F., "Kinematics of Finite, Rigid Body Displacements," *American Journal of Physics*, Vol. 34, 1966, pp. 949-954.

10 Beatty, M. F., "Kinematics of Finite Rigid Body Rotations—Revisited," *American Journal of Physics*, Vol. 45, 1977, p. 1006.

11 Thurnauer, P. J., "Kinematics of Finite, Rigid Body Displacements," *American Journal of Physics*, Vol. 35, 1967, pp. 1145-1154.

12 Schwartz, H. M., "Derivation of the Matrix of Rotation About a Given Direction as a Simple Exercise in Matrix Algebra," *American Journal of Physics*, Vol. 31, 1963, pp. 730-731.

13 Ström, T., and Svensson, P., "On the Determination of an Orthogonal Transformation," *J. Comp. Appl. Math.*, Vol. 2, 1976, pp. 7-11.

Downloaded 01 May 2010 to 171.66.16.249. Redistribution subject to ASME license or copyright; see http://www.asme.org/terms/Terms_Use.cfm

A Generalized Hill's Method for the Stability Analysis of Parametrically Excited Dynamic Systems

S. T. Noah
Assistant Professor.
Mem. ASME

G. R. Hopkins
Professor and Head.
Mem. ASME

Department of Mechanical Engineering,
Texas A&M University,
College Station, Texas 77843

A method is described for investigating the stability of the null solution for a general system of linear second-order differential equations with periodic coefficients. The method is based on a generalization of Hill's analysis and leads to a generalized Hill's infinite determinant. Following a proof of its absolute convergence, a closed-form expression for the characteristic infinite determinant is obtained. Methods for the stability analysis utilizing different forms of the characteristic determinant are discussed. For cases where the instabilities are of the simple parametric type, a truncated form of the determinant may be used directly to locate the boundaries of the resonance regions in terms of appropriate system parameters. The present generalized Hill's method is applied to a multidegree-of-freedom discretized system describing pipes conveying pulsating fluid. It is demonstrated that the method is a flexible and efficient computational tool for the stability analysis of general periodic systems.

Introduction

In the analysis of various dynamical systems, respresentation of the motion involved frequently leads to a system of second-order linear differential equations with periodic coefficients. Examples include structural members under periodic loads [1], rotors subjected to pulsating torque [2], pipes with pulsating fluid [3, 4], aeroelastic stability of helicopter blades [5], and liquid parametric sloshing in flexible containers [6]. Other applications include missiles subjected to pulsating thrusts [7], attitude stability of spinning satellites [8], and applications in linear control theory [9]. A comprehensive list of reported applications may be found in [10, 11].

Various methods have been devised for investigating the nature of the general solution to a set of linear homogeneous equations with periodic coefficients [12, 13]. In most of these investigations, a small parameter is utilized in conjunction with assumed small periodic coefficients. In addition, restrictions are usually imposed on the form of the coefficient matrices of the differential equations describing the system. Investigations utilizing a small parameter may best be represented by the work of Starzhinski [14], Hsu [15], Nishikawa and Willems [16], Fu and Nemat-Nasser [17], and Lee [18].

In many applications, however, the assumption of small variations in the amplitude of the periodic coefficients cannot be justified. For these cases, only a limited number of methods is available for the analysis of the associated differential equations. The available methods, which vary in their general applicability and numerical efficiency, are essentially based on Floquet's work [19]. Hill [20] utilized the form of solution provided by Floquet to show that the stability of a second-order differential equation with periodic coefficients could be determined from a single transcendental equation involving the characteristic exponents of the assumed solution. Later, Liapunov [21] introduced the so-called "Liapunov transformation" of reducible systems which is of utmost importance in the study of the nature of solutions to systems of linear differential equations with harmonic coefficients.

The existing methods for investigating the stability of a general *system* of second-order differential equations with periodic coefficients of *finite* amplitude may be grouped into two categories:

1 Those utilizing the so-called "Numerical Floquet-Liapunov Approach" [22], in which one examines the eigenvalues (characteristic multipliers) of the state transition (monodromy) matrix of the system. The transition matrix is determined through numerical integration of the reduced system of first-order equations over one period of the coefficients. This method was utilized in several studies; see, for example, [23–26]. However, as pointed out in [24], the method is computationally time-consuming, and in some cases requires very accurate numerical integration of the system of equations.

Contributed by the Applied Mechanics Division for publication in the JOURNAL OF APPLIED MECHANICS.

Discussion on this paper should be addressed to the Editorial Department, ASME, United Engineering Center, 345 East 47th Street, New York, N. Y. 10017, and will be accepted until two months after final publication of the paper itself in the JOURNAL OF APPLIED MECHANICS. Manuscript received by ASME Applied Mechanics Division, April, 1981; final revision, July, 1981.

Copyright © 1982 by ASME
Downloaded 01 May 2010 to 171.66.16.249. Redistribution subject to ASME license or copyright; see http://www.asme.org/terms/Terms_Use.cfm

An alternative method to evaluate the transition matrix is that recently developed by Hsu [27, 28]. In that method, common period of the coefficients is divided into a number of equal parts and the equations over each interval are then considered as a set of differential equations with constant coefficients. Friedmann and Silverthorn [5] applied the foregoing method to helicopter rotor blade instability problems and reported the method to be highly efficient.

2 Those based on variations on Hill's infinite determinant method to accommodate a system of differential equations. A method due to Bolotin [1] is concerned with seeking periodic solutions for the system of equations, leading to infinite determinant expressions by which the boundaries of instability regions are determined. However, as discussed in [29], the method is based on insufficient conditions for determining the instability boundaries. The method for instance is not capable of locating the regions of parametric instabilities of the combination (second) type [30]. Lindh and Likins [31] pointed out that on the boundaries of the combination resonance regions, almost-periodic rather than periodic solutions exist. They proposed an extension of Bolotin's method to enable the determination of all the instability regions for a system described by canonical equations coupled by a skew-symmetric velocity-coefficient matrix.

More recently, Szemplinska-Stupnicka [32] made an attempt to generalize Bolotin's method to allow the determination of the combination resonance regions. He considered the motion of a mechanical system described by a system of second-order differential equations of symmetric coefficient matrices, with the generalized coordinates coefficient matrix harmonic in time. A determinant expression was derived through which the boundary of the principal combination resonance region can be determined in the first approximation.

Other methods, using infinite determinant-type approach, were developed for determining the stability of the solution for a given set of system parameters. Valeev [33–35] utilized Laplace transforms to transform a periodic system of differential equations into an infinite system of algebraic equations. He showed the convergence of the associated infinite determinant and derived the characteristic equation in the form of an infinite series of continued fractions. However, the form of the characteristic equation introduces the difficulty of implementing the method numerically.

Investigating the stability of flexible missiles under pulsating thrusts, Beal [7] used Hill's type of approach and obtained the characteristic equation in the form of a polynomial in the characteristic exponents. The absence of damping terms made it possible to demonstrate the convergence of the associated characteristic infinite determinant. Crimi [36] treated a coupled periodic system of equations of general damping and stiffness matrices by closely following Hill's approach to arrive at a closed-form expression for the characteristic equation. He resorted to a lengthy procedure of differentiating the system of differential equations twice in order to arrive at an infinite characteristic determinant in a convenient form for the theory of convergence of infinite determinants to be directly applicable. The solution sought is that which is common to the two systems of equations resulting from differentiation and to the original system.

In the present study, we consider the stability of the null solution for a general coupled system of linear ordinary differential equations with periodic coefficients. Utilizing Hill's type of approach, convergence of the associated characteristic infinite determinant is proved and a closed-form expression for the characteristic equation is obtained. Methods for the stability analysis utilizing different forms of the characteristic determinant are discussed.

The System

Consider the motion of an N-degrees-of-freedom system described by a linear set of differential equations with periodic coefficients that may be expressed as finite sums of trigonometric functions. The equations are written in the form

$$\frac{d^2}{dt^2}\{X(t)\}+\sum_{q=-h}^{h} e^{iqt}[F]^{(q)}\frac{d}{dt}\{X(t)\}$$

$$+\sum_{q=-h}^{h} e^{iqt}[G]^{(q)}\{X(t)\}=0;\quad i^2=-1 \tag{1}$$

where $\{X(t)\}=\{x_1(t), x_2(t), \ldots, x_N(t)\}^T$ is a column matrix of the generalized coordinates, t is the time, $[F]^{(q)}=[f_{rs}]^{(q)}$ and $[G]^{(q)}=[g_{rs}]^{(q)}$, $r,s=1, \ldots, N$, are constant $N\times N$ coefficient matrices with the index $q=-h, -h+1, \ldots, +h$. The coefficient matrices, $[F]^{(q)}$ and $[G]^{(q)}$ are general matrices whose elements are finite. The matrix equation (1), therefore, represents a general coupled system of equations with periodic coefficients.

In order to investigate the stability of possible solutions of system (1), a new method based on a generalization of Hill's infinite determinant method is developed in the subsequent sections.

The Generalized Hill's Method

According to Floquet [19], a particular solution of (1) may be written in the form

$$\{X(t)\}=e^{\lambda t}\{Y(t)\} \tag{2}$$

where λ is a characteristic constant and $\{Y(t)\}$ is a column matrix of the periodic functions $y_r(t)$. Expanding $\{Y(t)\}$ in a complex Fourier series form, the solution (2) can be expressed as

$$\{X(t)\}=\sum_{n=-\infty}^{\infty} e^{(\lambda+in)t}\{C\}^{(n)} \tag{3}$$

where $\{C\}^{(n)}$ are constant column matrices of N rows.

Substituting (3) into (1), with a shaft in indices, and equating the terms of like powers of e^{int} to zero, the following infinite set of algebraic equations is obtained:

$$(\lambda+in)^2\{C\}^{(n)}+\sum_{q=-h}^{h}[(\lambda+i(n-q))[F]^{(q)}$$

$$+[G]^{(q)}]\{C\}^{(n-q)}=0;\quad n=\ldots,-2,-1,0,1,2,\ldots \tag{4}$$

Each of the equations in (4) may be multiplied by a constant matrix $[-n^2[I]+\text{dia}\,[G]^{(0)}-(\text{dia}\,[F/2]^{(0)})^2]^{-1}$, where $[I]$ is the unit matrix, without altering the solution if the cases where any of the terms $g^0_{rr}-(f^0_{rr}/2)^2$ being equal to n^2 are excluded. The resulting system of equations is represented by the matrix equation

$$[B]\{C\}=0 \tag{5}$$

in which $\{C\}$ is an infinite column matrix composed of the submatrices $\{C\}^{(p)}$, $p=n-q$, and $[B]$ is an infinite square matrix of submatrices $[B]^{(np)}$. The superscripts n and p denote, respectively, the row and column indices of the matrix $[B]$. The diagonal and off-diagonal elements of these submatrices are given by, respectively,

$$b^{nn}_{rr}=\frac{(\lambda+in)^2+(\lambda+in)f^0_{rr}+g^0_{rr}}{-n^2+g^0_{rr}-(f^0_{rr}/2)^2} \tag{6}$$

and

$$b^{np}_{rs}=\frac{(\lambda+ip)f^{n-p}_{rs}+g^{n-p}_{rs}}{-n^2+g^0_{rr}-(f^0_{rr}/2)^2} \tag{7}$$

Downloaded 01 May 2010 to 171.66.16.249. Redistribution subject to ASME license or copyright; see http://www.asme.org/terms/Terms_Use.cfm

where r denotes the row index and s the column index of the elements within a particular submatrix $[B]^{(np)}$. In expressions (6) and (7), $f_{rs}^{n-p} = g_{rs}^{n-p} \equiv 0$ for $|n-p| > h$, in which $n, p = \ldots, -1, 0, 1, \ldots$, while $r, s = 1, 2, \ldots, N$. The infinite matrix $[B]$ is, therefore, a banded matrix with bandwidth $2\eta + 1$, where $\eta = N(h+1) - 1$.

A necessary condition for the existence of a nontrivial solution of (5) is for the determinant of $[B]$, denoted henceforth by $\Delta(\lambda)$, to vanish, or

$$\Delta(\lambda) = \det[B] = 0 \tag{8}$$

Following Hill's procedure [37], $\Delta(\lambda)$ can be shown to be absolutely convergent and therefore may be expressed in closed form in the characteristic exponents λ. According to Hill, an infinite determinant converges provided the product of the diagonal elements converges absolutely and the sum of the off-diagonal elements is also absolutely convergent. In mathematical terms, for the determinant of $[b_{jk}]_{-\infty}^{\infty}$ to be convergent, the following two conditions must be satisfied:

$$\prod_{j=-\infty}^{\infty} |b_{jj}| = D_1 \quad \text{and} \quad \prod_{j,k=-\infty}^{\infty} |b_{jk}| = D_2;\ j \neq k$$

where D_1 and D_2 are finite numbers and $|\ |$ indicates an absolute value. For the determinant $\Delta(\lambda)$, whose elements are given by (6) and (7), satisfaction of the aforementioned convergence conditions is not evident.

To show that $\Delta(\lambda)$ is indeed convergent, it is convenient to first establish the convergence of a new determinant $\Delta_1(\lambda)$, which is formed by factoring out of each row of $\Delta(\lambda)$ the element on the principal diagonal. The elements of $\Delta_1(\lambda)$ are hence given by

$$d_{rr}^{nn} = 1 \tag{9}$$

and

$$d_{rs}^{np} = \frac{(\lambda + ip) f_{rs}^{n-p} + g_{rs}^{n-p}}{(\lambda+in)^2 + (\lambda+in) f_{rr}^{0} + g_{rr}^{0}} \tag{10}$$

The determinant $\Delta(\lambda)$ may then be expressed as

$$\Delta(\lambda) = \Delta_1(\lambda) \prod_{r=1}^{N} \lim_{k\to\infty} \prod_{n=-k}^{k} \frac{(\lambda+in)^2 + (\lambda+in) f_{rr}^{0} + g_{rr}^{0}}{-n^2 + g_{rr}^{0} - (f_{rr}^{0}/2)^2} \tag{11}$$

To show the convergence of $\Delta_1(\lambda)$, it is necessary to prove a theorem on the convergence of a class of infinite determinants.

Proof of Convergence

Consider an infinite banded-diagonal determinant of η super and subdiagonals and with ones along the principal diagonal. The determinant expansion for a $2\rho + 1$ by $2\rho + 1$ determinant D_ρ of elements a_{j_l, j_m} centered at the origin of the foregoing infinite determinant is

$$D_\rho = \sum_{\mu} (\epsilon_{j_1 j_2 \cdots j_{2\rho+1}}) a_{-\rho, j_1} \cdots a_{j_l, j_m} \cdots a_{\rho, j_{2\rho+1}} \tag{12}$$

where $j_l, j_m = -\rho, \ldots, 0, \ldots, +\rho$ and $l, m = 1, 2, \ldots, 2\rho+1$, with $\mu = (2\rho+1)!$ permutations of $j_1, j_2, \ldots, j_{2\rho+1}$. The symbol $\epsilon_{j_1 j_2 \cdots j_{2\rho+1}}$ denotes a permutation symbol where

$$\epsilon_{j_1 j_2 \ldots j_{2\rho+1}} = \begin{cases} +1 & \text{for indices, } j_l, \text{ of even permutations,} \\ -1 & \text{for indices of odd permutations,} \\ 0 & \text{if any of the indices are repeated.} \end{cases}$$

By forming the product

$$P_\rho = \prod_{k=-\rho}^{\rho} \left({}_{\alpha_l} \sum {}_{\beta_l} \left| a_{\alpha_1, \beta_1} \ldots a_{\alpha_{2\rho+1}, \beta_{2\rho+1}} \right| \right) \tag{13}$$

in which $\alpha_l = \{k-\rho, \ldots, k, \ldots, k+\rho\}$, $\beta_l = \{k-\rho, \ldots k, \ldots, k+\rho\}$, and α_l, Σ_{β_l} denotes the sum of all distinct permutations of α_l and β_l, the absolute values of the terms in the D_ρ expansion are contained in the expansion P_ρ when $\rho < \eta$. In fact it is possible to form a new product P'_ρ by setting certain terms of P_ρ to zero and changing the sign of others so that $P'_\rho \equiv D_\rho$.

When D_ρ is considered where $\rho > \eta$, it is sufficient that each product in the ${}_{\alpha_l}, \Sigma_{\beta_l}$ series of expansion (13) contains only $2\eta + 1$ elements, since $a_{\alpha_l, \beta_m} \equiv 0$ for $|\alpha_l - \beta_m| > \eta$. That is,

$$P_\rho = \prod_{k=-\rho}^{\rho} \left({}_{\alpha_l} \sum {}_{\beta_l} \left| a_{\alpha_1, \beta_1} \ldots a_{\alpha_{2\eta+1}, \beta_{2\eta+1}} \right| \right) \tag{14}$$

where $\alpha_l = \{k-\eta, \ldots, k, \ldots, k+\eta\}$, $\beta_l = \{k-\eta, \ldots, k, \ldots, k+\eta\}$. The absolute value of each of the terms of expansion (12) is contained in the expansion P_ρ, (14). As before, P_ρ can be altered to form P'_ρ such that $P'_\rho \equiv D_\rho$.

It follows that for each term in the expansion D_ρ, there is a corresponding term in the expansion P_ρ of equal or greater modulus. Hence

$$|D_{\gamma+\rho} - D_\rho| \leqq P_{\gamma+\rho} - P_\rho \tag{15}$$

Therefore, if P_ρ tends to a limit as $\rho \to \infty$ then D_ρ must also approach a limit as $\rho \to \infty$.

Since the class of determinants being considered have only ones along the principal diagonal, the product P_ρ, for $\rho > \eta$, may be written as

$$P_\rho = \prod_{k=-\rho}^{\rho} \left(1 + {}_{\alpha_l} \sum\nolimits^{1}_{\beta_l} \left| a_{\alpha_1, \beta_1} \ldots a_{\alpha_{2\eta+1}, \beta_{2\eta+1}} \right| \right) \tag{16}$$

where ${}_{\alpha_l} \Sigma^1_{\beta_l}$ denotes the sum of all distinct permutations of α_l and β_l, as defined in (14), except those where the α_l sequence is identically equal to the β_l sequence; in which case the term $|a_{\alpha_1, \beta_1} \ldots a_{\alpha_{2\eta+1}, \beta_{2\eta+1}}|$ is equal to unity since it is the product of the ones along the principal diagonal.

A necessary and sufficient condition for

$$P = \lim_{\rho\to\infty} \prod_{k=-\rho}^{\rho} \left(1 + {}_{\alpha_l} \sum\nolimits^{1}_{\beta_l} \left| a_{\alpha_1, \beta_1} \ldots a_{\alpha_{2\eta+1}, \beta_{2\eta+1}} \right| \right) \tag{17}$$

to be absolutely convergent is for the series

$$SP = \sum_{k=-\infty}^{\infty} {}_{\alpha_l} \sum\nolimits^{1}_{\beta_l} \left| a_{\alpha_1, \beta_1} \ldots a_{\alpha_{2\eta+1}, \beta_{2\eta+1}} \right| \tag{18}$$

to be convergent [37]. The following theorem may now be stated.

Theorem. An infinite banded-diagonal determinant with η super and subdiagonals and ones along the principal diagonal is absolutely convergent if the series, SP given by (18), where $a_{\alpha_l, \beta_l} \equiv 0$ for $|\alpha_l - \beta_l| > \eta$, is convergent.

It is noted that the determinant $\Delta_1(\lambda)$, as defined by equations (9) and (10), is of the class of determinants considered by the previous theorem. Its convergence therefore depends on the convergence of the series SP made up from its elements in the form (18), with $\eta = N(h+1) - 1$. To check the convergence of the formed series, it is observed that the expansion $\Sigma^1_{\alpha_l,\ \beta_l} |a_{\alpha_1, \beta_1} \ldots a_{\alpha_{2\eta+1},\ \beta_{2\eta+1}}|$ of that series is equivalent to the expansion

$$+ {}_{\alpha_l} \sum\nolimits^{*}_{\beta_l} \left| a_{\alpha_1, \beta_1} \ldots a_{\alpha_{2\eta+1}, \beta_{2\eta+1}} \right|$$

Downloaded 01 May 2010 to 171.66.16.249. Redistribution subject to ASME license or copyright; see http://www.asme.org/terms/Terms_Use.cfm

where $\Sigma^*_{\alpha_l,\beta_l}$ denotes the sum of all permutations of α_l and β_l in the subscripts, except those where $\alpha_l = \beta_l$.

From expression (10) for the off-diagonal elements of $\Delta_1(\lambda)$, it can be seen that

$$\sum\nolimits^*_{\alpha_l,\beta_l} \left| a_{\alpha_1,\beta_1}\, a_{\alpha_2,\beta_2} \right| = \left| 0\left(\frac{1}{k^2}\right) \right|, \tag{19}$$

since the only way for terms like $(a_{\alpha_1,\beta_1}\, a_{\alpha_2,\beta_2})$ to exist is if $\alpha_1 = \beta_2$ and $\beta_1 = \alpha_2$. Similarly

$$_{\alpha_l}\sum\nolimits^*_{\beta_l} \left| a_{\alpha_1,\beta_1} a_{\alpha_2,\beta_2} a_{\alpha_3,\beta_3} \right| = \left| 0\left(\frac{1}{k^3}\right) \right|,$$

$$_{\alpha_l}\sum\nolimits^*_{\beta_l} \left| a_{\alpha_1,\beta_1} \cdots\cdots a_{\alpha_{2\eta+1},\beta_{2\eta+1}} \right| = \left| 0\left(\frac{1}{k^{2\eta+1}}\right) \right|,$$

hence

$$_{\alpha_l}\sum\nolimits^1_{\beta_l} \left| a_{\alpha_1,\beta_1} \cdots\cdots a_{\alpha_{2\eta+1},\beta_{2\eta+1}} \right| = \left| 0\left(\frac{1}{k^2}\right) \right|, \tag{20}$$

since terms like

$$_{\alpha_l}\sum\nolimits^*_{\beta_l} \left| a_{\alpha_1,\beta_1} \right| \text{ do not exist.}$$

The condition for the convergence of $\Delta_1(\lambda)$ is that for

$$\lim_{\rho\to\infty} \sum_{k=-\rho}^{\rho} \left| 0\left(\frac{1}{k^2}\right) \right|$$

to exist. Since this limit does in fact exist, $\Delta_1(\lambda)$ is an absolutely convergent determinant.

Since $\Delta_1(\lambda)$ is convergent, the determinant $\Delta(\lambda)$ is also convergent if it is recognized that the infinite product in (11) is of finite magnitude. This can be readily shown by utilizing the product expansion for the sine function [38] as follows:

$$\prod_{n=-\infty}^{\infty} \frac{(\lambda+in)^2 + (\lambda+in) f^0_{rr} + g^0_{rr}}{-n^2 + g^0_{rr} - (f^0_{rr}/2)^2}$$

$$= \prod_{n=-\infty}^{\infty} \frac{g^0_{rr} - (f^0_{rr}/2)^2 - [i(\lambda + f^0_{rr}/2) - n]^2}{-n^2 + g^0_{rr} - (f^0_{rr}/2)^2}$$

$$= \frac{-\sin\pi\{i(\lambda+f^0_{rr}/2) - [g^0_{rr} - (f^0_{rr}/2)^2]^{1/2}\} \sin\pi\{i(\lambda+f^0_{rr}/2) + [g^0_{rr} - (f^0_{rr}/2)^2]^{1/2}\}}{\sin^2(\pi[g^0_{rr} - (f^0_{rr}/2)^2]^{1/2})} \tag{21}$$

Thus equation (11) can be written as

$$\Delta(\lambda) = (-1)^N \Delta_1(\lambda) \prod_{r=1}^{N} \frac{\sin\pi\{i(\lambda+f^0_{rr}/2) - [g^0_{rr} - (f^0_{rr}/2)^2]^{1/2}\}}{\sin^2(\pi[g^0_{rr} - (f^0_{rr}/2)^2]^{1/2})} \cdot \sin\pi\{i(\lambda+f^0_{rr}/2) + [g^0_{rr} - (f^0_{rr}/2)^2]^{1/2}\} \tag{22}$$

The convergence of $\Delta(\lambda)$ follows from the fact that $\Delta(\lambda)$ is equal to the product of $\Delta_1(\lambda)$, which is convergent, and a finite number of sine terms.

The Characteristic Equation

$\Delta(\lambda)$ is analytic everywhere in λ as may be seen from its elements (6) and (7). $\Delta_1(\lambda)$ has simple poles at

$$\lambda^r_{1,2} = -f^0_{rr}/2 \pm i[g^0_{rr} - (f^0_{rr}/2)^2]^{1/2}, \tag{23}$$

Thus the constants κ^r_1 and κ^r_2 may be chosen so that the function

$$\bar{\Delta}(\lambda) = \Delta_1(\lambda) - \sum_{r=1}^{N} [\kappa^r_1 \cot i\pi(\lambda-\lambda^r_1) - \kappa^r_2 \cot i\pi(\lambda-\lambda^r_2)] \tag{24}$$

will have no simple poles at the points λ^r_1 or λ^r_2.

On writing $\Delta_1(\lambda)$ in full, it is evident that $\Delta_1(\lambda) = \Delta_1(\lambda+i)$; hence, $\Delta_1(\lambda)$ is a periodic function of λ with period i. Since $\Delta_1(\lambda)$ and the terms in brackets in equation (24) are periodic functions of the same period i, it follows that $\bar{\Delta}(\lambda)$ is also periodic of period i. Since $\bar{\Delta}(\lambda)$ has no simple poles at λ^r_1 or λ^r_2, it has no simple poles at the points $(\lambda^r_1 \pm in)$ or $(\lambda^r_2 \pm in)$.

The determinant expansion for $\Delta_1(\lambda)$ illustrates that each term in the expansion is at least $0(1/\lambda)$ except the product of the diagonal terms which is equal to unity. Therefore, the $\lim_{\mathrm{Re}(\lambda)\to\pm\infty} \Delta_1(\lambda)$ exists and $\Delta_1(\lambda)$ is bounded. Thus $\bar{\Delta}(\lambda)$ is also a bounded function. Since $\bar{\Delta}(\lambda)$ is an analytic and bounded function for the cases considered, it satisfies the postulates of Liouville's theorem [37] and is, therefore, a constant. This constant can be evaluated by considering

$$\lim_{\mathrm{Re}(\lambda)\to\pm\infty} \bar{\Delta}(\lambda) = \lim_{\mathrm{Re}(\lambda)\to\pm\infty} \left\{ \Delta_1(\lambda) - \sum_{r=1}^{N} [\kappa^r_1 \cot i\pi(\lambda-\lambda^r_1) - \kappa^r_2 \cot i\pi(\lambda-\lambda^r_2)] \right\}$$

$$= 1 \pm \sum_{r=1}^{N} (\kappa^r_1 - \kappa^r_2) = \text{constant}$$

Hence, as in [36]

$$\sum_{r=1}^{N} (\kappa^r_1 - \kappa^r_2) = 0 \tag{25}$$

Therefore, $\bar{\Delta}(\lambda) = 1$ and so

$$\Delta_1(\lambda) = 1 + \sum_{r=1}^{N} [\kappa^r_1 \cot i\pi(\lambda-\lambda^r_1) - \kappa^r_2 \cot i\pi(\lambda-\lambda^r_2)] \tag{26}$$

It is of interest to note that if the λ^r_1's and λ^r_2's are complex numbers, the constants κ^r_2 will be the conjugates of the constants κ^r_1. However, the constants κ^r_1 and κ^r_2 should be generally assumed distinct to account for all possible values of the $\lambda^r_{1,2}$'s.

Substitution of (26) into (22), utilizing (23), yields

$$\Delta(\lambda) = (-1)^N \sum_{r=1}^{N} \frac{\sin i\pi(\lambda-\lambda^r_1) \sin i\pi(\lambda-\lambda^r_2)}{\sin^2(\pi[g^0_{rr} - (f^0_{rr}/2)^2]^{1/2})} \cdot \left\{ 1 + \sum_{r=1}^{N} [\kappa^r_1 \cot i\pi(\lambda-\lambda^r_1) - \kappa^r_2 \cot i\pi(\lambda-\lambda^r_2)] \right\} \tag{27}$$

Expression (27) is the closed-form representation sought for the generalized Hill's determinant $\Delta(\lambda)$ whose roots (characteristic exponents λ) determine the nature of solutions for the system of equations (1).

An alternative form of (27) can be obtained as a $2N$-degree polynomial in the characteristic multipliers, z, which are related to the exponents λ by [22]

$$z = e^{2\pi\lambda} \tag{28}$$

Substitution from (28) into (27) yields, after some manipulation, the characteristic equation in the form

$$f(z) = \prod_{s=1}^{N} (c^s_1 z - 1)(c^s_2 z - 1) - i \sum_{r=1}^{N} \left\{ \left[\prod_{\substack{s=1 \\ s\neq r}}^{N} (c^s_1 z - 1)(c^s_2 z - 1) \right] \cdot [\kappa^r_1 (c^r_1 z + 1)(c^r_2 z - 1) - \kappa^r_2 (c^r_2 z + 1)(c^r_1 z - 1)] \right\} = 0 \tag{29}$$

Downloaded 01 May 2010 to 171.66.16.249. Redistribution subject to ASME license or copyright; see http://www.asme.org/terms/Terms_Use.cfm

where $c^r_{1,2} = e^{-2\pi\lambda^r_{1,2}}$.

It remains now to determine the constants $\kappa^r_{1,2}$. To that end, equation (26) is written as

$$\left(\prod_{r=1}^{N} \frac{1}{\lambda^2 + \lambda f^0_{rr} + g^0_{rr}}\right)\Delta_1^*(\lambda) =$$

$$= 1 + \sum_{r=1}^{N} \frac{\kappa^r_1 \sin i\,\pi(\lambda-\lambda^r_2)\cos i\,\pi(\lambda-\lambda^r_1) - \kappa^r_2 \cos i\,\pi(\lambda-\lambda^r_2)\sin i\,\pi(\lambda-\lambda^r_1)}{\sin i\,\pi(\lambda-\lambda^r_1)\sin i\,\pi(\lambda-\lambda^r_2)} \tag{30}$$

where $\Delta_1^*(\lambda)$ is formed by multiplying the N rows of the central submatrices (where $n=0$) of $\Delta_1(\lambda)$ by the corresponding $\lambda^2 + \lambda f^0_{rr} + g^0_{rr}$; $r = 1, 2, \ldots, N$. Consequently, the elements of $\Delta_1^*(\lambda)$ will be the same as those of $\Delta_1(\lambda)$ except for those where $n=0$, and $\Delta_1^*(\lambda)$ will have no poles at the λ^r_1's and λ^r_2's. The constants κ^s_1 and κ^s_2 may be determined by successively multiplying (30) by $\{\sin i\,\pi(\lambda-\lambda^s_1) \cdot \sin i\,\pi(\lambda-\lambda^s_2)\}$ and letting $\lambda\to\lambda^s_1$ or $\lambda\to\lambda^s_2$ for $s = 1, 2, \ldots, N$, yielding

$$\kappa^s_{1,2} = \frac{\pi\Delta_1^*(\lambda^s_{1,2})}{2[g^0_{ss} - (f^0_{ss}/2)^2]^{1/2}} \prod_{\substack{r=1 \\ r\neq s}}^{N} \frac{1}{(\lambda^s_{1,2})^2 + \lambda^s_{1,2} f^0_{rr} + g^0_{rr}}, \tag{31}$$

where $\Delta_1^*(\lambda^s_1)$ and $\Delta_1^*(\lambda^s_2)$, hence κ^s_1 and κ^s_2, are conjugates for complex $\lambda^s_{1,2}$.

Stability Analysis

Depending on the objectives of the analysis, different techniques may be effectively utilized to determine the stability of the null solution for a system given by (1). For a given set of system parameters, the specific values, or mere existence, of exponents λ with positive real parts may be determined through numerical implementation of the argument principle [39], in conjunction with the analytic function $\Delta(\lambda)$ as given by (27). More effectively, the argument principle can be used with $f(z)$ as given by (29) to check whether all of the roots, z, exist within the circle $|z| = 1$. Alternatively, the Schur-Cohn criterion [40] may be utilized for that same purpose. In cases where knowledge of the specific values of the z-roots is required, an efficient numerical method, such as that of Newton-Raphson's, can be used in conjunction with (29).

The present generalized Hill's method can be also be used to locate, in a more direct fashion, the boundaries of the parametric resonance regions of the simple (first) type. This is done by assigning the values of either zero or $\pm 0.5i$ to λ and seek values for the sytem parameters for which the convergent determinant $\Delta_1^*(\lambda)$ (or $\Delta(\lambda)$) vanishes. The values of the parameters so determined locate the boundaries of the resonance regions on which the solutions of (1) are periodic of period 2π or 4π, corresponding to $\lambda = 0$ or $\pm 0.5i$, respectively [31]. This procedure is similar to that proposed by Bolotin [1].

Applications

To illustrate the generalized Hill's method developed in this paper, the method is applied to a multidegree of freedom system representing a Galerkin approximation to the continuous system of a pipe conveying pulsating fluid.

The small motion of an N-degrees-of-freedom discretized pipe-fluid system can be expressed in the nondimensional matrix form [26]

$$\frac{d^2}{d\tau^2}\{X(\tau)\} + \left[\gamma\lceil\omega_r^2\rfloor + 2u_0\,\mu^{1/2}(1+\epsilon\cos\Omega\tau)\,[D]\right]\frac{d}{d\tau}\{X(\tau)\}$$

$$+ [\lceil\omega_r^2\rfloor + u_0^2(1+\epsilon\cos\Omega\tau)^2[H]$$

$$+ \epsilon\Omega u_0\mu^{1/2}\,[[A]-[H]]\sin\Omega\tau]\{X(\tau)\} = 0 \tag{32}$$

where τ is the dimensionless time, γ is the dimensionless damping coefficient of the pipe's material, ω_r, $r=1, \ldots, N$, are the dimensionless natural frequencies in absence of fluid flow, u_0 is the nondimensional flow velocity, μ is the fluid mass to fluid plus pipe mass ratio, ϵ is a positive parameter of magnitude less than one, and Ω is the dimensionless frequency of fluid flow pulsations. Also, in equation (32), $[A]$, $[D]$, and $[H]$ are $N\times N$ matrices whose elements are definite integrals involving the eigenvectors of the abbreviated problem ($u_0 \equiv 0$).

Expressing τ as t/Ω in equation (32) and comparing it with equation (1) yields the coefficient matrices as

$$[F]^{(0)} = \frac{2\mu^{1/2}u_0}{\Omega}\,[D] + \frac{\gamma}{\Omega}\lceil\omega_r^2\rfloor$$

$$[F]^{(2)} = [F]^{(-2)} = 0, \quad [F]^{(1)} = [F]^{(-1)} = \frac{\epsilon\mu^{1/2}u_0}{\Omega}\,[D] \tag{33}$$

and

$$[G]^{(0)} = \frac{1}{\Omega^2}\lceil\omega_r^2\rfloor + \frac{u_0^2}{\Omega^2}\left(1+\frac{\epsilon^2}{2}\right)[H],$$

$$[G]^{(-2)} = [G]^{(2)} = \frac{\epsilon^2 u_0^2}{4\Omega^2}\,[H],$$

$$[G]^{(1),(-1)} = \frac{\epsilon u_0^2}{\Omega^2}\,[H] \mp i\frac{\epsilon u_0\mu^{1/2}}{2\Omega}\,[[A]-[H]] \tag{34}$$

Two types of end supports are considered for the pipe, clamped-clamped and clamped-free. The dynamic behavior of the equivalent pipe-fluid systems with steady flow is distinctly different with the two types of supports [3]. The numerical results for the selected systems are obtained taking $N = 4$.

Clamped-Clamped Pipe. The system considered is that of Fig. 6 in reference [25], where $u_0 = 4$, $\mu = 0.2$, and $\gamma = 0.001$. With steady flow, the equivalent system would become first unstable by divergence for $u_0 > 2\pi$, [3]. The frequency and perturbation parameter of the fluid flow are selected as $\Omega/\omega_{0_1} = 6$ and $\epsilon = 0.3$, respectively, where ω_{0_1} is the fundamental frequency of the lateral oscillations of the pipe in absence of fluid flow. The present generalized Hill's method was applied for the stability analysis as follows.

The values for the poles $\lambda^r_{1,2}$, $r=1, \ldots, 4$, together with the elements of the 4×4 matrices $[F]^{(q)}$ and $[G]^{(q)}$, as given by (33) and (34), were used to calculate the values of the determinants $\Delta_1^*(\lambda^r_{1,2})$. These values are in turn used to determine the constants $\kappa^r_{1,2}$ as

$$\kappa^1_{1,2} = 0.00034 \mp 0.01560\,i, \qquad \kappa^2_{1,2} = 0.04388 \mp 0.00176\,i,$$

$$\kappa^3_{1,2} = -0.00523 \pm 0.01610\,i, \quad \kappa^4_{1,2} = 0.05095 \pm 0.00126\,i.$$

The central 33×33 elements of $\Delta_1^*(\lambda^r_{1,2})$ were found to be more than sufficient in determining the values of the determinants. Equation (29) was then utilized to obtain the characteristic polynomial as

$$f(z) = z^8 + 0.189\,z^7 - 0.384\,z^6 + 0.770\,z^5 + 0.943\,z^4$$
$$- 0.083\,z^3 + 0.135\,z^2 + 0.239\,z + 0.064 = 0 \tag{35}$$

A Newton-Raphson method was used to calculate the roots

Downloaded 01 May 2010 to 171.66.16.249. Redistribution subject to ASME license or copyright; see http://www.asme.org/terms/Terms_Use.cfm

of the aforementioned equation. Among the calculated roots, two were found whose modulii are greater than unity, namely,

$$z_{1,2} = 0.7044 \pm 0.7316\, i, \tag{36}$$

indicating loss of stability by combination resonance, since the two roots are conjugates. Using (28) and recalling that $t = \Omega\tau$, the imaginary parts of the corresponding $\Omega\lambda_{1,2}$ are given by $\pm$ 17.19. Since the values are determined up to an integral multiple of Ω ($=$ 134.2), it can be shown that they are approximately those of the first and third "modes" of the pipe (ω_1 and ω_3) with steady flow of $u_0 = 4$, where $\omega_1 = 16.9$ and $\omega_3 = 114.5$. This is in agreement with reference [25] in which the instability was identified as a combination resonance of the sum type, with the value of Ω being close to that of ($\omega_1 + \omega_3$). The values of the roots as given in (36) also coincided with those obtained using the numerical Floquet-Liapunov method.

The instability of the foregoing system can also be determined without knowledge of the specific values of the characteristic multipliers, z. In that respect, the argument principle proves to be a highly efficient computational tool. The argument principle was applied to the just mentioned system in conjunction with (35). The total change in $\arg f(z)$ corresponding to tracing the circle $|z| = 1$ in the z-plane was observed to be exactly that of 12 π. This indicates the presence of six roots of modulii less than unity. The remaining two roots are thus located outside the unit circle, indicating the given system to be unstable.

Cantilevered Pipe. The parameters selected in this case are those of $\gamma = 0$, $\mu = 0.15$, $u_0 = 5.2$, $\epsilon = 0.25$, and $\Omega = 38.7$. In contrast to the foregoing system, these values would lend the equivalent cantilevered system with steady flow unstable. The instability first occurs at $u_0 = 5$ and is of the oscillatory type.

The generalized Hill's method was applied to the cantilevered pipe with pulsatile flow to reveal that the system is unstable by combination resonance of the difference type involving the second and third "modes." Again, the central 33×33 elements of $\Delta_1^*(\lambda_{1,2}')$ were found to be more than adequate for the analysis and the calculated roots coincided with those obtained using the Floquet-Liapunov method.

Concluding Remarks

The generalized Hill's method presented in this study is an effective analytical tool for the stability analysis of the null solution for a *general* system of linear differential equations with periodic coefficients. The method can be readily programmed for digital computation and requires significantly less computer core space than those of other comparable techniques.

The main appeal of the method, however, lies with its flexibility in meeting different objectives for performing the stability analysis. The method is capable of yielding the values of the characteristic exponents associated with a given system, from which a complete characterization of the nature of the null solution may be determined. This may best be achieved by first calculating the roots of the characteristic polynomial, using a Newton-Raphson algorithm, and if desired, deduce the system's characteristic exponents. The overall numerical efficiency here is comparable to that of the numerical Floquet-Liapunov technique.

The generalized Hill's method is particularly effective, on the other hand, if the objective of the analysis is to merely determine whether a given system is stable. In this case, the argument principle can be effectively utilized, in conjunction with the characteristic polynomial, to detect whether any roots of moduli greater than unity exist. The present method can also be utilized to locate, in a more direct fashion, the boundaries of the instability regions of the simple parametric resonance type.

References

1 Bolotin, V. V., *The Dynamic Stability of Elastic Systems,* Holden-Day, San Francisco, 1964.

2 Eshleman, R. L., and Eubanks, R. A., "On the Critical Speeds of a Continuous Rotor," ASME *Journal of Engineering for Industry,* Vol. 91, Nov. 1969, pp. 1180–1188.

3 Paidoussis, M. P., and Issid, N. T., "Dynamic Stability of Pipes Conveying Fluid," *Journal of Sound and Vibration,* Vol. 33, No. 3, 1974, pp. 267–294.

4 Paidoussis, M. P., Issid, N. T., and Tsui, M., "Parametric Resonance Oscillations of Flexible Slender Cylinders in Harmonically Perturbed Axial Flow, Part 1: Theory," ASME JOURNAL OF APPLIED MECHANICS, Vol. 47, 1980, pp. 709–714.

5 Friedmann, P., and Silverthorn, L. J., "Aeroelastic Stability of Periodic Systems With Application to Rotor Blade Flutter," *American Institute of Aeronautics and Astronautics Journal,* Vol. 12, No. 11, Nov. 1974, pp. 1559–1565.

6 Khandelwal, R. S., and Nigam, N. C., "Parametric Instabilities of a Liquid Free Surface in a Flexible Container Under Vertical Periodic Motion," *Journal of Sound and Vibration,* Vol. 74, No. 2, 1981, pp. 243–249.

7 Beal, T. R., "Dynamic Stability of a Flexible Missile Under Constant and Pulsating Thrusts," *American Institute of Aeronautics and Astronautics Journal,* Vol. 3, No. 3, Mar. 1965, pp. 486–494.

8 Wallace, F., and Meirovitch, L., "Attitude Instability Regions of a Spinning Symmetric Satellite in an Elliptical Orbit," *American Institute of Aeronautics and Astronautics Journal,* Vol. 5, No. 9, Sept. 1967, pp. 1642–1650.

9 James, D. J. G., "Stability of a Model Reference Control System," *American Institute of Aeronautics and Astronautics Journal,* Vol. 9, No. 5, May 1971, pp. 950–952.

10 Ibrahim, R. A., "Parametric Vibration-Part III: Current Problems (1)," *Shock and Vibration Digest,* U.S. Naval Research Lab., Vol. 10, No. 3, 1978, pp. 41–57.

11 Ibrahim, R. A., "Parametric Vibration-Part IV: Current Problems (2)," *Shock and Vibration Digest,* U.S. Naval Research Lab., Vol. 10, No. 4, 1978, pp. 19–47.

12 Cesari, L., *Asymptotic Behavior and Stability Problems in Ordinary Differential Equations,* Springer Verlag, New York, 1971.

13 Evan-Iwanowski, R. M., *Resonance Oscillations in Mechanical Systems,* Elsevier Scientific Publ., New York, 1976.

14 Starzhinski, V. M., "On the Stability of a Trivial Solution of a Linear System With Periodic Coefficients," *Journal of Applied Mathematics and Mechanics* (translation of *Prikladnaya Matematika i Mekhanika*), Vol. 22, No. 5, 1958, pp. 907–921.

15 Hsu, C. S., "On the Parametric Excitation of a Dynamic System Having Multiple Degrees of Freedom," ASME JOURNAL OF APPLIED MECHANICS, Vol. 30, 1963, pp. 367–372.

16 Nishikawa, Y., and Willems, P., "A Method for Stability Investigation of a Periodic Dynamic System With Many Degrees of Freedom," *Journal of The Franklin Institute,* Vol. 287, No. 2, Feb. 1969, pp. 143–157.

17 Fu, F. C. L., and Nemat-Nasser, S., "Stability of Solution of Systems of Linear Differential Equations With Harmonic Coefficients," *American Institute of Aeronautics and Astronautics Journal,* Vol. 10, No. 1, Jan. 1972, pp. 30–36.

18 Lee, T., "A Study of Coupled Mathieu Equations by Use of Infinite Determinants," ASME JOURNAL OF APPLIED MECHANICS, Vol. 43, June 1976.

19 Floquet, G., "Sur les Équation Différentielles Linéaires à Coefficients Periodiques," *Annales de École Normale,* 2-e Série, Paris, Vol. 12, 1883, pp. 47–89.

20 Magnus, W., and Winkler, S., *Hill's Equation,* Interscience Publishers, New York, 1966.

21 Liapunov, M. A., *General Problem of the Stability of Motion,* Annals of Mathematics Studies, Princeton University Press, Princeton, 1947.

22 Meirovitch, L., *Methods of Analytical Dynamics,* McGraw-Hill, New York, 1970.

23 Kane, T. R., and Sobala, D., "A New Method for Attitude Stabilization," *American Institute of Aeronautics and Astronautics Journal,* Vol. 1, No. 6, June 1963, pp. 1365–1367.

24 Bohn, M. P., and Herrmann, G., "The Dynamic Behavior of Articulated Pipes Conveying Fluid With Periodic Flow Rate," ASME JOURNAL OF APPLIED MECHANICS, Vol. 41, 1974, pp. 55–62.

25 Paidoussis, M. P., and Sundararajan, C., "Parametric and Combination Resonances of a Pipe Conveying Pulsating Fluid," ASME JOURNAL OF APPLIED MECHANICS, Vol. 42, 1975. pp. 780–784.

26 Noah, S. T., and Hopkins, G. R., "Dynamic Stability of Elastically Supported Pipes Conveying Pulsating Fluid," *Journal of Sound and Vibration,* Vol. 71, No. 1, July 1980, pp. 103–116.

27 Hsu, C. S., and Cheng, W. H., "Applications of the Theory of Impulsive Parametric Excitation and New Treatments of General Parametric Excitation Problems," ASME JOURNAL OF APPLIED MECHANICS, Vol. 40, 1973, pp. 78–86.

Downloaded 01 May 2010 to 171.66.16.249. Redistribution subject to ASME license or copyright; see http://www.asme.org/terms/Terms_Use.cfm

28 Hsu, C. S., "On Approximating a General Linear Periodic System," *Journal of Mathematical Analysis and Applications,* Vol. 45, 1974, pp. 234–251.

29 Fu, F. C. L., and Nemat-Nasser, S., "Stability of Dynamic Systems Subjected to Nonconservative and Harmonic Forces," *American Institute of Aeronautics and Astronautics Journal,* Vol. 8, No. 6, June 1970, pp. 1174–1176.

30 Mettler, E., "Combination Resonance in Mechanical Systems Under Harmonic Excitations," *Proceedings of the Fourth International Conference on Nonlinear Oscillations,* Academia Publ. House of the Czechoslovak of Science, Prague, 1968, pp. 51–70.

31 Lindh, K. G., and Likins, P. W., "Infinite Determinant Methods for Stability Analysis of Periodic-Coefficient Differential Equations," *American Institute of Aeronautics and Astronautics Journal,* Vol. 8, No. 4, Apr. 1970, pp. 680–686.

32 Szemplinska-Stupnicka, W., "The Generalized Harmonic Balance Method For Determining the Combination Resonance in the Parametic Dynamic Systems," *Journal of Sound and Vibration,* Vol. 58, No. 3, 1978, pp. 347–361.

33 Valeev, K. C., "On the Solution and Characteristic Exponents of Solutions of Some Systems of Linear Differential Equations With Periodic Coefficients," *Journal of Applied Mathematics and Mechanics* (translation of *Prikladnaya Matematika i Mekhanika*), Vol. 24, No. 4, 1960, pp. 877–902.

34 Valeev, K. G., "On Hill's Method in the Theory of Linear Differential Equations With Periodic Coefficients," *Journal of Applied Mathematics and Mechanics* (translation of *Prikladnaya Metamatika i Mekhanika*), Vol. 24, No. 6, 1960, pp. 1493–1505.

35 Valeev, K. G., "On Hill's Method in the Theory of Linear Differential Equations With Periodic Coefficients," *Journal of Applied Mathematics and Mechanics,* (translation of *Prikladnaya Matematika i Mekhanika*), Vol. 25, No. 2, 1961, pp. 460–466.

36 Crimi, P., "Stability of Dynamic Systems with Periodically Varying Parameters," *American Institute of Aeronautics and Astronautics Journal,* Vol. 8, No. 10, Oct. 1970, pp. 1760–1764.

37 Whittaker, E. T., and Watson, G. N., *A Course of Modern Analysis,* 4th ed., Cambridge University Press, Cambridge, 1962.

38 Irving, J., and Millineux, N., *Mathematics in Physics and Engineering,* Academic Press, New York, 1959, p. 789.

39 Kaplan, W., *Introduction to Analytical Functions,* Addison-Wesley, Massachusetts, 1966, p. 110.

40 Marden, M., *Geometry of Polynomials,* Mathematical Surveys No. 3, American Mathematical Society, Rhode Island, 1966, p. 198.

Downloaded 01 May 2010 to 171.66.16.249. Redistribution subject to ASME license or copyright; see http://www.asme.org/terms/Terms_Use.cfm

Journal of Applied Mechanics

Brief Notes

A Brief Note is a short paper that presents a specific solution of technical interest in mechanics but which does not necessarily contain new general methods or results. A Brief Note should not exceed 1500 words *or equivalent* (a typical one-column figure or table is equivalent to 250 words; a one line equation to 30 words). Brief Notes will be subject to the usual review procedures prior to publication. After approval such Notes will be published as soon as possible. The Notes should be submitted to the Technical Editor of the JOURNAL OF APPLIED MECHANICS. Discussions on the Brief Notes should be addressed to the Editorial Department, ASME, United Engineering Center, 345 East 47th Street, New York, N. Y. 10017, or to the Technical Editor of the JOURNAL OF APPLIED MECHANICS. Discussions on Brief Notes appearing in this issue will be accepted until two months after publication. Readers who need more time to prepare a Discussion should request an extension of the deadline from the Editorial Department.

Stress Singularities at the Edge of a Cylindrical Slider

R. Solecki[1] and R. J. Conant[2]

Introduction

When analyzing the state of stress and deformation in a cantilevered, elastic, circular cylinder pressed against a moving, rough, rigid surface [1] the authors were faced with necessity of determining the stress singularities at the edge of the sliding end of the cylinder. This problem may have wider applications, in particular because it is applicable to any elastic right cylinder with an arbitrary smooth contour.

The two-dimensional counterpart of the present problem, that is, the effect of Coulomb friction on the stress distribution at the corner of an elastic wedge pressed against a surface has been addressed previously.

Gdoutos and Theocaris [2], using Williams' technique [3], determined the stress singularity at the apex of an elastic wedge sliding with friction over an elastic half plane. A special case of the foregoing constituted part of the studies of Dasgupta and Prasad [4] and Prasad, Chiu, and Dasgupta [5], who determined the characteristic equation for the strength of the singularity at the corners of an elastic rectangular sliding with friction along a rigid base. Comninou [6] also studied the problem investigated in [2]. She employed the Mellin transformation, following Sternberg and Koiter [7] and others. This approach allowed for a more detailed study of the singularity and enabled her to draw rather general conclusions, in particular with respect to the logarithmic singularity.

Characteristic Equation

Consider a cylinder with planform shown in Fig. 1. Only the behavior of stresses in the vicinity of the edge is presently of interest. Therefore, asymptotically, there is no difference between this problem and the problem of an elastic isotropic quarter-space sliding in a direction inclined at an angle α to the edge (Fig. 2).

For a homogeneous problem none of the displacements depend on z. Therefore, Navier's equations of equilibrium reduce to

$$\mu \nabla^2 \mathbf{u} + (\lambda + \mu) \nabla (\nabla \cdot \mathbf{u}) = \mathbf{0} \tag{1}$$

$$\nabla^2 w = 0 \tag{2}$$

where $\mathbf{u} = (u, v)$ and $u = u(x, y)$, $v = v(x,y)$, $w = w(x,y)$, and λ and μ are the Lame constants. The homogeneous boundary conditions applicable here are

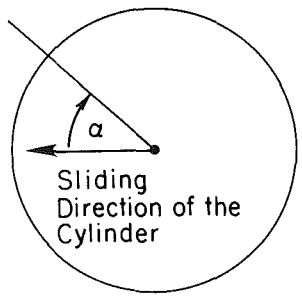


Fig. 1

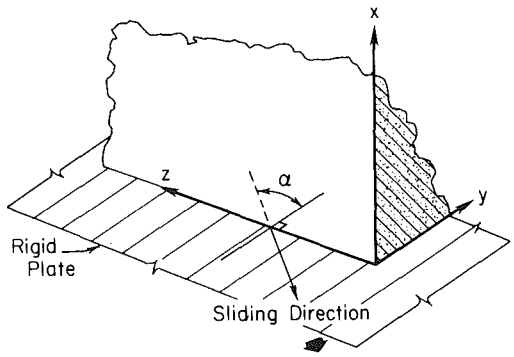


Fig. 2

[1] Professor, Mechanical Engineering Department, University of Connecticut, Storrs, Conn. 06268. Mem. ASME.

[2] Instructor, Mechanical Engineering Department, University of Connecticut. Presently, Assistant Professor, Mechanical Engineering Department, Montana State University, Bozeman, Mont. 59715. Mem. ASME

Manuscript received by ASME Applied Mechanics Division, June, 1981.

Copyright © 1982 by ASME
Downloaded 01 May 2010 to 171.66.16.249. Redistribution subject to ASME license or copyright; see http://www.asme.org/terms/Terms_Use.cfm

$$u=0, \qquad \text{at} \quad x=0, y>0 \quad (3)$$

$$\mu\frac{\partial v}{\partial x}=k\left[(\lambda+2\mu)\frac{\partial u}{\partial x}+\lambda\frac{\partial v}{\partial y}\right]\cos\alpha \quad \text{at} \quad x=0, y>0 \quad (4)$$

$$\mu\frac{\partial w}{\partial x}=k\left[(\lambda+2\mu)\frac{\partial u}{\partial x}+\lambda\frac{\partial u}{\partial y}\right]\sin\alpha \quad \text{at} \quad x=0, y>0 \quad (5)$$

$$\frac{\partial u}{\partial y}+\frac{\partial v}{\partial x}$$
$$=0, \lambda\left(\frac{\partial u}{\partial x}+\frac{\partial u}{\partial u}\right)+2\mu\frac{\partial v}{\partial y}=0, \qquad \text{at} \quad y=0, x>0 \quad (6)$$

where k is the coefficient of Coulomb friction.

It is seen that u and v can be found independent of w which can be determined subsequently using equation (2) and the boundary conditions (5) and (6) (one-sided coupling). Hence, the present problem differs from those considered in [2, 6] only in that $k\cos\alpha$ replaces k.[3]

The characteristic equation is obtained following the technique described by Bogy [8]. First, polar coordinates are introduced. Next, the stresses (and displacements) are expressed in terms of Airy's stress function ϕ, and finally the Mellin transformation is applied to find the transform of ϕ and of the boundary conditions (3), (4), $(6)_1$, and $(6)_2$. A detailed description of the procedure can be found in [8]. Similarly, the Mellin transform is applied to the differential equation (2) and the remaining boundary conditions. The solution of transformed equation (2) takes the form

$$\hat{\bar{w}}(s,\theta)=e(s)\cos(s+1)\theta+f(s)\sin(s+1)\theta \quad (7)$$

where s is the parameter of Mellin transformation, $e(s)$ and $f(s)$ are arbitrary functions of s, and $\hat{\bar{w}}(s,\theta)=\int_0^\infty r^{s-1}(rw)\,dr$.

Application of the transformed boundary conditions to the transforms of the unknown functions results in the following characteristic equation, where $p-1$ is the strength of the singularity and $0<p=-s-1<1$ (see [8]):

$$\mathfrak{D}(p)\equiv p^3(p+1)\sin\frac{p\pi}{2}\{-2(1-\nu)\sin p\pi$$
$$-k(1-2\nu)\cos\alpha\cos p\pi$$
$$+k\cos\alpha[2p^2+4(1-\nu)p+1-2\nu]\}=0 \quad (8)$$

The symbol $\mathfrak{D}$ replaces Comninou's determinant $\mathfrak{D}(b, a, \alpha, \beta, \rho)$ where α, β are Dundurs' parameters [9] and ρ is the friction coefficient.

Strengths of the Power Singularities. The absolute values of the strengths of stress singularities $\gamma=|p-1|$ for various k and for limiting values of $\nu(\nu=0$, and $\nu=0.5)$ are given in Fig. 3 for $0\le\alpha\le\pi/2$.

One can easily prove that for $\pi/2<\alpha<\pi$ (trailing edge) the characteristic equation (8) has no real roots for all admissible values of ν and p.

Logarithmic and Oscillatory Singularities. The logarithmic singularity is present if $\partial\mathfrak{D}/\partial p=0$ at $p=1$ (see [10, 6]). In the present case this condition leads to the following equation:

$$\pi(1-\nu)+2(9-8\nu)k\cos\alpha=0 \quad (9).$$

For assumed values of ν and k one can obtain from equation (9) the value of α at which the logarithmic singularity occurs. It is seen that α must be greater than $\pi/2$. Also, the following condition must be satisfied: $-\pi/18<k\cos\alpha<-\pi/20$. Hence k must be at least greater than $\pi/20\simeq 0.15708$ for the logarithmic singularity to be present. For each such value of k, the logarithmic singularity appears at only one value of α. As $k\to\infty$ the logarithmic singularity appears when α tends to $\pi/2$.

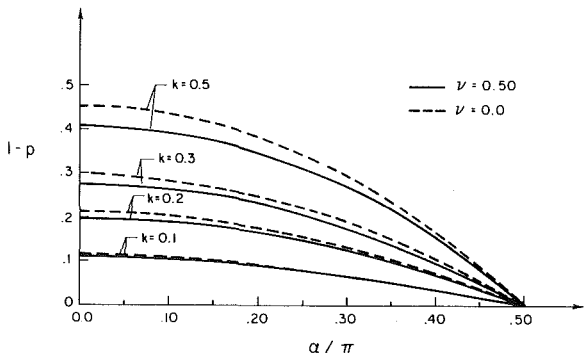


Fig. 3

Oscillatory singularities occur if the real part of $p=\xi+i\eta$ is in the strip $0<\xi<1$.

By splitting equation (8) into its real and imaginary parts, it can be shown that no oscillatory singularities exist.

Conclusions

It was found that power singularity appears only at the leading edge of the cylindrical slider. Two isolated logarithmic singularities may appear at the trailing edge if the coefficient of friction k is sufficiently large. There are no oscillatory singularities.

References

1 Conant, R. J., and Solecki, R., "The End Problem of a Finite Elastic Cylinder Pressed Against a Rough, Rigid, Sliding Surface," submitted for publication.

2 Gdoutos, E. E., and Theocaris, P. S., "Stress Concentrations at the Apex of a Plane Indenter Acting on an Elastic Half Plane," ASME JOURNAL OF APPLIED MECHANICS, Vol. 42, 1975, pp. 688-692.

3 Williams, M. L., "Stress Singularities Resulting From Various Boundary Conditions in Angular Corners of Plates in Extension," ASME JOURNAL OF APPLIED MECHANICS, Vol. 19, 1952, pp. 526-528.

4 Dasgupta, S., and Prasad, S. N., "On the Phenomenon of Separation During Compression and Frictional Sliding of an Elastic Rectangle," ASME JOURNAL OF APPLIED MECHANICS, Vol. 43, 1976, pp. 268-274.

5 Prasad, S. N., Chiu, P. K., and Dasgupta, S., "Compression and Sliding of an Elastic Rectangle Fixed Rigidly at the Base," *International Journal of Engineering Science*, Vol. 14, 1976, pp. 617-629.

6 Comninou, M., "Stress Singularity at a Sharp Edge in Contact Problems With Friction," *Journal of Applied Mathematics and Physics (ZAMP)*, Vol. 27, 1976, pp. 493-494.

7 Sternberg, E., and Koiter, W. R., "The Wedge Under a Concentrated Couple: A Paradox in Two-Dimensional Theory of Elasticity," ASME JOURNAL OF APPLIED MECHANICS, Vol. 25, 1958, pp. 575-581.

8 Bogy, D. B., "Edge-Bonded Dissimilar Orthogonal Elastic Wedges Under Normal and Shear Loading," ASME JOURNAL OF APPLIED MECHANICS, Vol. 35, 1968, pp. 460-466.

9 Dundurs, J., Discussion of [8], ASME JOURNAL OF APPLIED MECHANICS, Vol. 36, 1969, pp. 650-652.

10 Bogy, D. B., "Two Edge-Bonded Elastic Wedges of Different Materials and Wedge Angles Under Surface Tractions," ASME JOURNAL OF APPLIED MECHANICS, Vol. 38, 1971, pp. 377-386.

[3] This confirms the opinion expressed by Prof. Maria Comninou of the University of Michigan at Ann Arbor in a private conversation with the authors. The authors are indebted to Professor Comniou for her valuable comments.

Rotation of a Free Elastic Rod

C. -Y. Wang [1]

Introduction and Formulation

Centrifugal forces due to rotation of space structures are

[1] Professor, Department of Mathematics, Michigan State University, East Lansing, Mich. 48824.

Manuscript received by ASME Applied Mechanics Division, March 1981; final revision, August 1981.

Downloaded 01 May 2010 to 171.66.16.249. Redistribution subject to ASME license or copyright; see http://www.asme.org/terms/Terms_Use.cfm

$$u=0, \qquad \text{at} \quad x=0, y>0 \quad (3)$$

$$\mu\frac{\partial v}{\partial x}=k\left[(\lambda+2\mu)\frac{\partial u}{\partial x}+\lambda\frac{\partial v}{\partial y}\right]\cos\alpha \quad \text{at} \quad x=0, y>0 \quad (4)$$

$$\mu\frac{\partial w}{\partial x}=k\left[(\lambda+2\mu)\frac{\partial u}{\partial x}+\lambda\frac{\partial u}{\partial y}\right]\sin\alpha \quad \text{at} \quad x=0, y>0 \quad (5)$$

$$\frac{\partial u}{\partial y}+\frac{\partial v}{\partial x}$$

$$=0, \lambda\left(\frac{\partial u}{\partial x}+\frac{\partial u}{\partial u}\right)+2\mu\frac{\partial v}{\partial y}=0, \qquad \text{at} \quad y=0, x>0 \quad (6)$$

where k is the coefficient of Coulomb friction.

It is seen that u and v can be found independent of w which can be determined subsequently using equation (2) and the boundary conditions (5) and (6) (one-sided coupling). Hence, the present problem differs from those considered in [2, 6] only in that $k\cos\alpha$ replaces k.[3]

The characteristic equation is obtained following the technique described by Bogy [8]. First, polar coordinates are introduced. Next, the stresses (and displacements) are expressed in terms of Airy's stress function ϕ, and finally the Mellin transformation is applied to find the transform of ϕ and of the boundary conditions (3), (4), $(6)_1$, and $(6)_2$. A detailed description of the procedure can be found in [8]. Similarly, the Mellin transform is applied to the differential equation (2) and the remaining boundary conditions. The solution of transformed equation (2) takes the form

$$\hat{\bar{w}}(s,\theta)=e(s)\cos(s+1)\theta+f(s)\sin(s+1)\theta \quad (7)$$

where s is the parameter of Mellin transformation, $e(s)$ and $f(s)$ are arbitrary functions of s, and $\hat{\bar{w}}(s,\theta)=\int_0^\infty r^{s-1}(rw)\,dr$.

Application of the transformed boundary conditions to the transforms of the unknown functions results in the following characteristic equation, where $p-1$ is the strength of the singularity and $0<p=-s-1<1$ (see [8]):

$$\mathfrak{D}(p)\equiv p^3(p+1)\sin\frac{p\pi}{2}\{-2(1-\nu)\sin p\pi$$
$$-k(1-2\nu)\cos\alpha\cos p\pi$$
$$+k\cos\alpha[2p^2+4(1-\nu)p+1-2\nu]\}=0 \quad (8)$$

The symbol $\mathfrak{D}$ replaces Comninou's determinant $\mathfrak{D}(b, a, \alpha, \beta, \rho)$ where α, β are Dundurs' parameters [9] and ρ is the friction coefficient.

Strengths of the Power Singularities. The absolute values of the strengths of stress singularities $\gamma=|p-1|$ for various k and for limiting values of $\nu(\nu=0$, and $\nu=0.5)$ are given in Fig. 3 for $0\le\alpha\le\pi/2$.

One can easily prove that for $\pi/2<\alpha<\pi$ (trailing edge) the characteristic equation (8) has no real roots for all admissible values of ν and p.

Logarithmic and Oscillatory Singularities. The logarithmic singularity is present if $\partial\mathfrak{D}/\partial p=0$ at $p=1$ (see [10, 6]). In the present case this condition leads to the following equation:

$$\pi(1-\nu)+2(9-8\nu)k\cos\alpha=0 \quad (9).$$

For assumed values of ν and k one can obtain from equation (9) the value of α at which the logarithmic singularity occurs. It is seen that α must be greater than $\pi/2$. Also, the following condition must be satisfied: $-\pi/18<k\cos\alpha<-\pi/20$. Hence k must be at least greater than $\pi/20\simeq 0.15708$ for the logarithmic singularity to be present. For each such value of k, the logarithmic singularity appears at only one value of α. As $k\to\infty$ the logarithmic singularity appears when α tends to $\pi/2$.

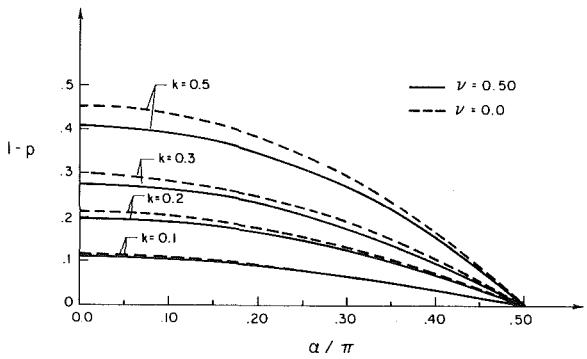


Fig. 3

Oscillatory singularities occur if the real part of $p=\xi+i\eta$ is in the strip $0<\xi<1$.

By splitting equation (8) into its real and imaginary parts, it can be shown that no oscillatory singularities exist.

Conclusions

It was found that power singularity appears only at the leading edge of the cylindrical slider. Two isolated logarithmic singularities may appear at the trailing edge if the coefficient of friction k is sufficiently large. There are no oscillatory singularities.

References

1 Conant, R. J., and Solecki, R., "The End Problem of a Finite Elastic Cylinder Pressed Against a Rough, Rigid, Sliding Surface," submitted for publication.

2 Gdoutos, E. E., and Theocaris, P. S., "Stress Concentrations at the Apex of a Plane Indenter Acting on an Elastic Half Plane," ASME JOURNAL OF APPLIED MECHANICS, Vol. 42, 1975, pp. 688-692.

3 Williams, M. L., "Stress Singularities Resulting From Various Boundary Conditions in Angular Corners of Plates in Extension," ASME JOURNAL OF APPLIED MECHANICS, Vol. 19, 1952, pp. 526-528.

4 Dasgupta, S., and Prasad, S. N., "On the Phenomenon of Separation During Compression and Frictional Sliding of an Elastic Rectangle," ASME JOURNAL OF APPLIED MECHANICS, Vol. 43, 1976, pp. 268-274.

5 Prasad, S. N., Chiu, P. K., and Dasgupta, S., "Compression and Sliding of an Elastic Rectangle Fixed Rigidly at the Base," *International Journal of Engineering Science*, Vol. 14, 1976, pp. 617-629.

6 Comninou, M., "Stress Singularity at a Sharp Edge in Contact Problems With Friction," *Journal of Applied Mathematics and Physics (ZAMP)*, Vol. 27, 1976, pp. 493-494.

7 Sternberg, E., and Koiter, W. R., "The Wedge Under a Concentrated Couple: A Paradox in Two-Dimensional Theory of Elasticity," ASME JOURNAL OF APPLIED MECHANICS, Vol. 25, 1958, pp. 575-581.

8 Bogy, D. B., "Edge-Bonded Dissimilar Orthogonal Elastic Wedges Under Normal and Shear Loading," ASME JOURNAL OF APPLIED MECHANICS, Vol. 35, 1968, pp. 460-466.

9 Dundurs, J., Discussion of [8], ASME JOURNAL OF APPLIED MECHANICS, Vol. 36, 1969, pp. 650-652.

10 Bogy, D. B., "Two Edge-Bonded Elastic Wedges of Different Materials and Wedge Angles Under Surface Tractions," ASME JOURNAL OF APPLIED MECHANICS, Vol. 38, 1971, pp. 377-386.

[3] This confirms the opinion expressed by Prof. Maria Comninou of the University of Michigan at Ann Arbor in a private conversation with the authors. The authors are indebted to Professor Comniou for her valuable comments.

Rotation of a Free Elastic Rod

C. -Y. Wang [1]

Introduction and Formulation

Centrifugal forces due to rotation of space structures are

[1] Professor, Department of Mathematics, Michigan State University, East Lansing, Mich. 48824.

Manuscript received by ASME Applied Mechanics Division, March 1981; final revision, August 1981.

Copyright © 1982 by ASME
Downloaded 01 May 2010 to 171.66.16.249. Redistribution subject to ASME license or copyright; see http://www.asme.org/terms/Terms_Use.cfm

sometimes desirable and other times unavoidable. This paper studies the equilbrium configurations of a free, thin, originally straight, elastic rod rotating in space. If the angular velocity Ω is low, the rod remains straight with two possible equilibrium orientations: rotation longitudinally along its axis and rotation perpendicular to its axis about the midpoint. When Ω is large enough the rod may assume curved equilibrium configurations as well. We shall only be concerned with configurations that are symmetric or antisymmetric as in Fig. 1. There may be other forms.

Let us assume the rod is slender enough so that it can be considered as an elastica, and let us put the origin of a cartesian coordinate system (x', y') at the centroid of the rotating rod. The axis of rotation is the x' axis. A local balance of moment gives

$$\frac{d^2\theta}{ds^2} = J^4 u\cos\theta, \quad \frac{d^2 u}{ds^2} = \sin\theta \tag{1}$$

where

$$u \equiv \int_1^s \text{yds}, \quad J^4 \equiv \frac{\rho\Omega^2 l^4}{EI}. \tag{2}$$

Here ρ is the mass per unit length, l is the half length of the rod, θ is the local angle of inclination, s is the arc length from the origin, and EI is the flexural rigidity. All lengths have been normalized by l. The important nondimensional parameter J represents the relative importance of density, angular velocity, and length to flexural rigidity. The boundary conditions are

$$\theta(0) = 0, \quad u(0) = 0, \quad u(1) = 0,$$
$$\frac{d\theta}{ds}(1) = 0, \quad \text{symmetric case.} \tag{3}$$

$$\frac{d\theta}{ds}(0) = 0, \quad \frac{du}{ds}(0) = 0 \quad u(1) = 0,$$
$$\frac{d\theta}{ds}(1) = 0, \quad \text{antisymmetric case.} \tag{4}$$

Equations (1-4) are nonlinear and closed-form solutions do not exist.

Bifurcations of the straight, axially rotating rod

The stability of axially rotating rods was briefly surveyed in Love [1]. This paper concerns the free-free rod which has not been investigated before. Assuming both θ and u are small, equations (1) linearizes to

$$\frac{d^4\theta}{ds^4} = J^4\theta. \tag{5}$$

The general solution is

$$\theta = C_1\sinh Js + C_2\cosh Js + C_3\sin Js + C_4\cos Js. \tag{6}$$

For the symmetric case, we apply the boundary conditions of equation (3). In order for nontrivial solutions to exist, the determinant of the coefficient matrix of C_1, C_2, C_3, C_4 must be zero. After some work, we obtain the condition

$$\cosh J\sin J + \cos J\sinh J = 0. \tag{7}$$

The roots are at $J = 0$, 2.365020, 5.497804, . . . The other roots are well approximated by $(n - 1/4)\pi$, $n = 3,4,5 \ldots$. Similarly the condition for the antisymmetric case is

$$\cosh J\sin J - \cos J\sinh J = 0. \tag{8}$$

The roots are at $J = 0$, 3.926602, 7.068583, . . . with the other roots near $J = (n + 1/4)\pi, n = 3,4,5 \ldots$.

Note that $J = 0$ corresponds to the nonrotating case. The (straight) rod can be in equilibrium at any angle θ constant.

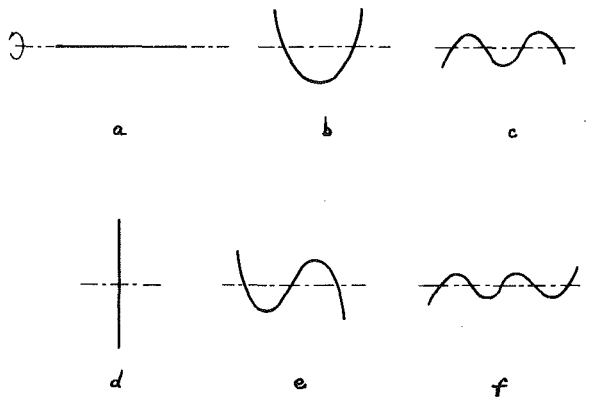


Fig. 1 Symmetric equilbrium configurations (a-c); antisymmetric equilbrium configurations (d-f); _._._ is the axis of rotation

Curved equilibrium configurations bifurcate at the values of $J = 2.365$, 3.927, 5.498, 7.069 etc., corresponding to Fig. 1(*b*), (*e*), (*c*), and (*f*), respectively.

Numerical Integration

When θ ceases to be small, the solution must be obtained numerically. In what follows we shall transform the equations into a much simpler one-parameter shooting problem. Set

$$t \equiv Js, \quad v \equiv J^2 u. \tag{9}$$

The governing equations become

$$\frac{d^2\theta}{dt^2} = v\cos\theta, \quad \frac{d^2 v}{dt^2} = \sin\theta. \tag{10}$$

For the symmetric case, we start with the initial conditions $\theta(0) = 0$, $v(0) = 0$, any fixed $d\theta/dt(0)$, and guess $dv/dt(0)$. Equation (10) is then integrated by the fourth-order Runge-Kutta algorithm until $v = 0$ again. A solution is found if $d\theta/dt$ is zero there. If not, $dv/dt(0)$ is adjusted and equations (10) is integrated again. Let $t = t^*$ be the place where both v and $d\theta/dt$ become zero. Then

$$J = t^* \tag{11}$$

$$M = \frac{m'(0)}{EI/l} = \frac{d\theta}{ds}(0) = t^*\frac{d\theta}{dt}(0) \tag{12}$$

$$y(0) = \frac{du}{ds}(0) = \frac{1}{t^*}\frac{dv}{dt}(0) \tag{13}$$

$$y(1) = \frac{du}{ds}(1) = \frac{1}{t^*}\frac{dv}{dt}(t^*) \tag{14}$$

where M is the maximum moment experienced. This gives the bifurcation solutions corresponding to Fig. 1(*b*). If we integrate until $v = 0$ the third time, initial values for Fig. 1(*c*) will be obtained . For the actual equilibrium configuration, equations (1), (3), (12), and (13) are integrated with $x(0) = 0$ and

$$\frac{dx}{ds} = \cos\theta, \quad \frac{dy}{ds} = \sin\theta \tag{15}$$

Similarly, for the antisymmetric case, Fig. 1(*e*), we take $d\theta/dt(0) = 0$, $du/dt(0) = 0$, any fixed $\theta(0)$, and guess $v(0)$. Equation (10) is integrated as an initial value problem until $v = 0$ the second time. A solution is found at $t = t^*$ if $d\theta/dt$ is also zero. Then

$$J = t^* \tag{16}$$

$$F = u(0) = (t^*)^{-2}v(0) \tag{17}$$

$$y(1) = \frac{1}{t^*}\frac{dv}{dt}(t^*) \tag{18}$$

Downloaded 01 May 2010 to 171.66.16.249. Redistribution subject to ASME license or copyright; see http://www.asme.org/terms/Terms_Use.cfm

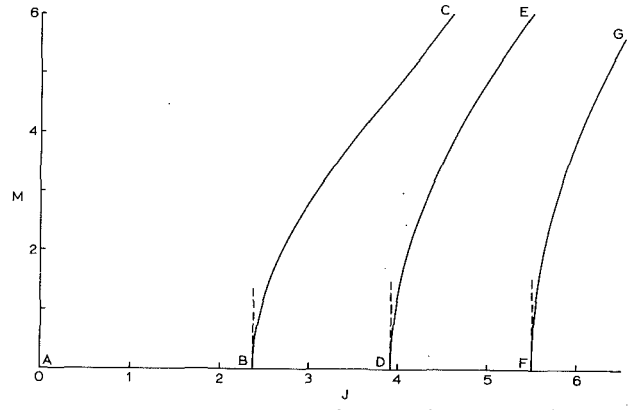


Fig. 2 The maximum moment M as a function of J showing bifurcation branches. Dashed lines represent stability theory.

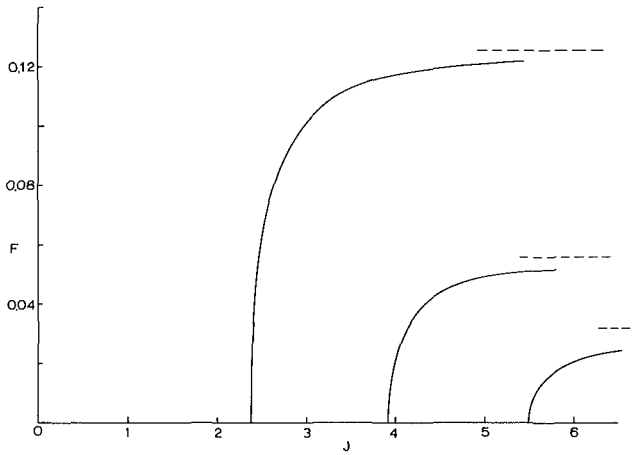


Fig. 3 The maximum force F. Dashed lines are asymptotes.

where F is the maximum force normalized by $\rho\Omega^2 l^2$. For the case depicted by Fig. 1(f), we integrate till $v=0$ the third time.

Results and Discussion

Figure 2 shows the results for the normalized maximum moment M as a function of the rotation parameter J. When $J=0$ (point A), the rod is straight and can be in equilibrium at any orientation. The vertical straight rod (Fig. 1(d)) is stable for all J but the moment is zero. The horizontal straight rod (Fig. 1(a)), is the only other solution for $0<J<2.365020$ (segment AB). The horizontal straight rod becomes unstable and may assume the bifurcation solution of Fig. 1(b) when $J>2.365020$ (segment BC). When $J>3.926602$ the configuration of Fig. (e) may occur (segment DE), and when $J>5.497804$ Fig. 1(c) is also possible (segment FG). The maximum moment for the symetric case occurs at $s=0$ while the maximum moment for the antisymmetric case occurs near $s=1/3, 1/5, 1/7, \ldots$.

Figure 3 shows the normalized maximum force F as a function of J. F equals 1/2 for the vertical rotating rod (not shown in the figure). The bifurcation solutions approach 1/8, 1/18, 1/32, respectively. The maximum force for the antisymmetric case occurs at $s=0$ (17) while the maximum force for the symmetric case occurs near $s=1/2, 1/4, \ldots$.

Figure 4 shows representative configuration for the branch BC. As rotation or J is increased the configuration becomes more like a rotating hairpin. Figure 5 shows the next higher branch DE, which is antisymmetric. Due to force considerations, the originally straight, free, rotating elastic rod could only be in equilibrium in a plane containing the rotation axis.

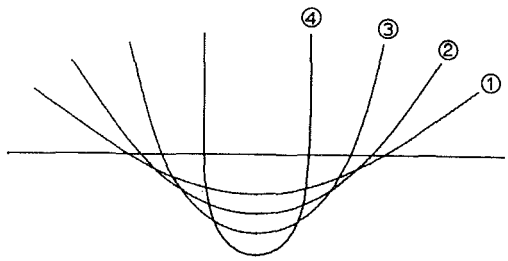


Fig. 4 Configurations for the branch BC. ①: $J=2.4875$; ②: $J=2.6844$; ③: $J=3.1439$; ④: $J=4.9107$.

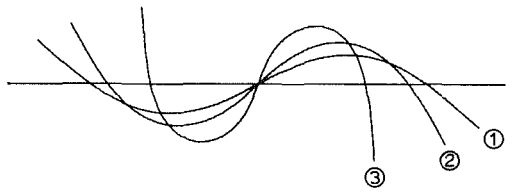


Fig. 5 Configurations for the branch DE. ①: $J=4.1422$; ②: $J=4.4529$; ③: $J=5.6047$.

The related problem of an axially rotating rod with one end free and one end clamped has been considered by several authors. Odeh and Tadjbakhsh [2] proved existence using several methods. Bazley and Zwahlen [3] determined the number of possible equilibrium solutions. Antman and Nachman [4] answered several qualitative questions. Although similar analyses could be done in our case, we favor the actual determination of the entire bifurcation picture and the equilibrium configurations of the free-free rotating rod as presented in this paper.

References

1 Love, A. E. H., *A Treatise on the Mathematical Theory of Elasticity*, Dover, New York, 1944, pp. 442-443.

2 Odeh, F., and Tadjbakhsh, I., "A Nonlinear Eigenvalue Problem for Rotating Rods," *Arch. Rat. Mech. Anal.*, Vol. 20, 1965, pp. 81-94.

3 Bazley, N., and Zwahlen, B., "Remarks on the Bifurcation of Solutions of a Nonlinear Eigenvalue Problem," *Arch. Rat. Mech. Anal.*, Vol. 28, 1968, pp. 51-58.

4 Antman, S. S., and Nachman, A., "Large Buckled States of Rotating Rods," *Nonlinear Analysis*, Vol. 4, 1980, pp. 303-327.

Vibrations of Simply Supported Shallow Shells on Elliptical Bases

J. R. Coleby[1] and J. Mazumdar[1]

Introduction

In the past, several authors, in particular Reissner [1] and Hoppman [2], have studied the axisymmetric vibrations of shallow spherical shells and obtained results for the mode shapes and frequencies of vibration. Recently, Jones and Mazumdar [3] applied the method of constant-deflection contours to the problem of transverse vibrations of shallow shells of arbitrary geometric plan form and, as an illustration, reported the fundamental frequencies for clamped shallow shells on elliptical bases for a variety of physical parameters.

The purpose of the present note is to provide solutions for the mode shapes and frequencies for simply supported shallow elliptical domes which, to the authors' knowledge, have not yet been discussed in the literature.

[1]Department of Applied Mathematics, The University of Adelaide, Adelaide, South Australia.

Manuscript received by ASME Applied Mechanics Division, October, 1980; final revision, March, 1981.

Downloaded 01 May 2010 to 171.66.16.249. Redistribution subject to ASME license or copyright; see http://www.asme.org/terms/Terms_Use.cfm

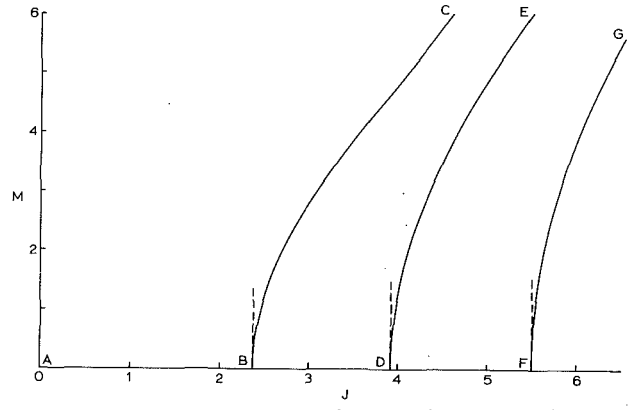


Fig. 2 The maximum moment M as a function of J showing bifurcation branches. Dashed lines represent stability theory.

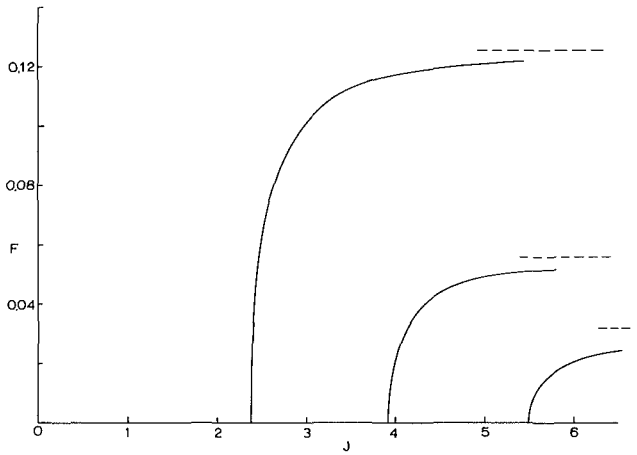


Fig. 3 The maximum force F. Dashed lines are asymptotes.

where F is the maximum force normalized by $\rho\Omega^2 l^2$. For the case depicted by Fig. 1(f), we integrate till $v=0$ the third time.

Results and Discussion

Figure 2 shows the results for the normalized maximum moment M as a function of the rotation parameter J. When $J=0$ (point A), the rod is straight and can be in equilibrium at any orientation. The vertical straight rod (Fig. 1(d)) is stable for all J but the moment is zero. The horizontal straight rod (Fig. 1(a)), is the only other solution for $0<J<2.365020$ (segment AB). The horizontal straight rod becomes unstable and may assume the bifurcation solution of Fig. 1(b) when $J>2.365020$ (segment BC). When $J>3.926602$ the configuration of Fig. (e) may occur (segment DE), and when $J>5.497804$ Fig. 1(c) is also possible (segment FG). The maximum moment for the symetric case occurs at $s=0$ while the maximum moment for the antisymmetric case occurs near $s=1/3, 1/5, 1/7, \ldots$.

Figure 3 shows the normalized maximum force F as a function of J. F equals 1/2 for the vertical rotating rod (not shown in the figure). The bifurcation solutions approach 1/8, 1/18, 1/32, respectively. The maximum force for the antisymmetric case occurs at $s=0$ (17) while the maximum force for the symmetric case occurs near $s=1/2, 1/4, \ldots$.

Figure 4 shows representative configuration for the branch BC. As rotation or J is increased the configuration becomes more like a rotating hairpin. Figure 5 shows the next higher branch DE, which is antisymmetric. Due to force considerations, the originally straight, free, rotating elastic rod could only be in equilibrium in a plane containing the rotation axis.

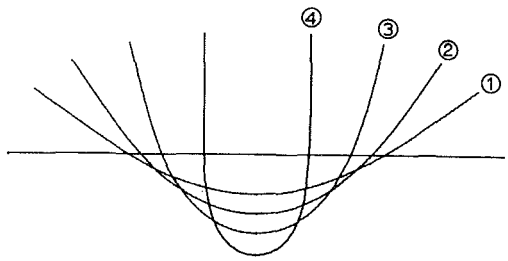


Fig. 4 Configurations for the branch BC. ①: $J=2.4875$; ②: $J=2.6844$; ③: $J=3.1439$; ④: $J=4.9107$.

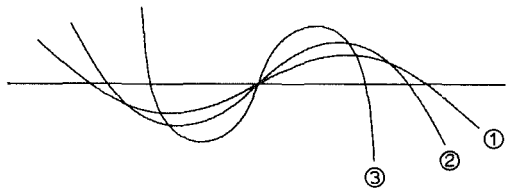


Fig. 5 Configurations for the branch DE. ①: $J=4.1422$; ②: $J=4.4529$; ③: $J=5.6047$.

The related problem of an axially rotating rod with one end free and one end clamped has been considered by several authors. Odeh and Tadjbakhsh [2] proved existence using several methods. Bazley and Zwahlen [3] determined the number of possible equilibrium solutions. Antman and Nachman [4] answered several qualitative questions. Although similar analyses could be done in our case, we favor the actual determination of the entire bifurcation picture and the equilibrium configurations of the free-free rotating rod as presented in this paper.

References

1 Love, A. E. H., *A Treatise on the Mathematical Theory of Elasticity*, Dover, New York, 1944, pp. 442-443.

2 Odeh, F., and Tadjbakhsh, I., "A Nonlinear Eigenvalue Problem for Rotating Rods," *Arch. Rat. Mech. Anal.*, Vol. 20, 1965, pp. 81-94.

3 Bazley, N., and Zwahlen, B., "Remarks on the Bifurcation of Solutions of a Nonlinear Eigenvalue Problem," *Arch. Rat. Mech. Anal.*, Vol. 28, 1968, pp. 51-58.

4 Antman, S. S., and Nachman, A., "Large Buckled States of Rotating Rods," *Nonlinear Analysis*, Vol. 4, 1980, pp. 303-327.

Vibrations of Simply Supported Shallow Shells on Elliptical Bases

J. R. Coleby[1] and J. Mazumdar[1]

Introduction

In the past, several authors, in particular Reissner [1] and Hoppman [2], have studied the axisymmetric vibrations of shallow spherical shells and obtained results for the mode shapes and frequencies of vibration. Recently, Jones and Mazumdar [3] applied the method of constant-deflection contours to the problem of transverse vibrations of shallow shells of arbitrary geometric plan form and, as an illustration, reported the fundamental frequencies for clamped shallow shells on elliptical bases for a variety of physical parameters.

The purpose of the present note is to provide solutions for the mode shapes and frequencies for simply supported shallow elliptical domes which, to the authors' knowledge, have not yet been discussed in the literature.

[1]Department of Applied Mathematics, The University of Adelaide, Adelaide, South Australia.

Manuscript received by ASME Applied Mechanics Division, October, 1980; final revision, March, 1981.

Copyright © 1982 by ASME
Downloaded 01 May 2010 to 171.66.16.249. Redistribution subject to ASME license or copyright; see http://www.asme.org/terms/Terms_Use.cfm

Table 1 Representative solutions of the frequency equation (10)

μ	M^4	λ_1	λ_2	λ_3	λ_4	λ_5
0	0.0	2.1080	5.4188	8.5920	11.741	14.8962
	10.0	2.2775	5.4207	8.5922	11.7472	14.8962
	100.0	3.0827	5.4386	8.5940	11.7475	14.8963
	500.0	4.2964	5.5594	8.6024	11.7492	14.8968
1/3	0.0	2.2324	5.4551	8.6135	11.7624	14.9081
	10.0	2.3767	5.4570	8.6137	11.7624	14.9081
	100.0	3.1176	5.4754	8.6155	11.7628	14.9082
	500.0	4.2988	5.5966	8.6241	11.7645	14.9087

General Solutions

As shown in reference [3], the general solutions for the normal functions W and ϕ, representing the mode shape and the stress function, respectively, are given by

$$W = A_0 J_0(\lambda f) + A_1 Y_0(\lambda f) + A_2 I_0(\lambda f) + A_3 K_0(\lambda f) + A_4, \quad (1)$$

and

$$\phi = -\frac{4EH\gamma}{\lambda^2}[A_0 J_0(\lambda f) + A_1 Y_0(\lambda f) - A_2 I_0(\lambda f) - A_3 K_0(\lambda f)] + \frac{D\eta^4 f^2}{\gamma} A_4 + A_5 \log f, \quad (2)$$

where $A_0, \ldots A_5$ are integration constants to be determined, E is Young's modulus, $D = Eh^3/12(1-\mu^2)$ is the flexural rigidity, μ is Poisson's ratio, h is the shell thickness, J_0, Y_0, I_0, and K_0 are zeroth-order Bessel and modified Bessel functions of the first and second kinds, respectively, and where

$$\gamma = \left(\frac{1}{b^2 R_x} + \frac{1}{a^2 R_y}\right) a^4 b^4/(3a^4 + 2a^2 b^2 + 3b^4),$$

$$\eta^4 = \frac{\rho h \omega^2 a^4 b^4}{2D(3a^4 + 2a^2 b^2 + 3b^4)}, \quad (3)$$

and

$$\lambda^4 = 16(\eta^4 - Eh\gamma^2/D).$$

Here, a and b are, respectively, the semimajor and semiminor axes, R_x and R_y are the radii of curvature, ρ is the mass density, and ω is the circular frequency.

To obtain the foregoing solutions, it has been assumed that the iso-amplitude contour lines, $u(x,y)$ = constant, form similar and similarly situated ellipses given by

$$u(x,y) = 1 - x^2/a^2 - y^2/b^2 = \text{constant}, \quad (4)$$

and a new variable f, defined by $f^2 = 1 - u$, has been introduced.

Simply Supported Boundary Conditions

For the case of shallow shells with simply supported edges, the conditions to be imposed on W and ϕ for $f = 1$ are as follows:

$$\text{(I)} \quad W = 0,$$

$$\text{(II)} \quad \frac{d^2 W}{df^2} + \frac{\mu}{f}\frac{dW}{df} = 0,$$

and

$$\text{(III)} \quad \frac{d^2\phi}{df^2} - \frac{\mu}{f}\frac{d\phi}{df} = 0. \quad (5)$$

The second condition in equation (5) arises from the requirement for zero normal moment [4], while the third is derived from Reissner's vanishing circumferential strain condition [3].

These conditions, together with the regularity conditions for W and ϕ at the center ($f = 0$), determine the values of the constants $A_0, \ldots A_5$ to within a constant multiplier. Consequently, we obtain

$$A_1 = A_3 = A_5 = 0, \quad (6)$$

$$A_0 J_0(\lambda) + A_2 I_0(\lambda) + A_4 = 0, \quad (7)$$

$$A_0 J_0(\lambda) - A_2 I_0(\lambda) + \frac{1-\mu}{\lambda}[A_0 J_0'(\lambda) + A_2 I_0'(\lambda)] = 0 \quad (8)$$

$$A_0 J_0(\lambda) + A_2 I_0(\lambda) + \frac{1+\mu}{\lambda}[A_0 J_0'(\lambda) - A_2 I_0'(\lambda)] + \frac{(1-\mu)D\eta^4}{2Eh\gamma^2} A_4 = 0. \quad (9)$$

On invoking the condition of vanishing of the determinant of the system (7)–(9), and after some algebraic manipulation with the Bessel functions and their derivatives, the following frequency equation is obtained:

$$J_0(\lambda) I_1(\lambda) + J_1(\lambda) I_0(\lambda) - \frac{2\lambda(\lambda^4 - M^4) J_0(\lambda) I_0(\lambda) - 4(1-\mu) M^4 J_1(\lambda) I_1(\lambda)/\lambda}{(1-\mu)(\lambda^4 - M^4) - 2M^4} = 0, \quad (10)$$

where the parameter M^4, a measure of the shell curvature, is given by

$$M^4 = \frac{16(1+\mu)Eh\gamma^2}{(1-\mu)D} = 48(1+\mu)^2\left(\frac{2\gamma}{h}\right)^2. \quad (11)$$

There exists an infinite number of roots, λ_i, of equation (10) for each value of M^4 and each value of Poisson's ratio. Some representative values of the first five roots are shown in Table 1. Also, corresponding to each λ_i there exists a mode shape W_i given by

$$W_i = [I_0(\lambda_i) - \frac{1-\mu}{\lambda_i} I_1(\lambda_i)] J_0(\lambda_i f) + [J_0(\lambda_i) - \frac{1-\mu}{\lambda_i} J_1(\lambda_i)] I_0(\lambda_i f) + \frac{4M^4 J_0(\lambda_i) I_0(\lambda_i)}{(1-\mu)(\lambda_i^4 - M^4) - 2M^4} - \frac{4M^4(1-\mu)^2 J_1(\lambda_i) I_1(\lambda_i)}{\lambda_i^2[(1-\mu)(\lambda_i^4 - M^4) - 2M^4]}. \quad (12)$$

It is interesting to note that if one sets $M = 0$, the case of zero curvature, in equations (10) and (12) one gets the simply supported elliptical plate equations as given in reference [4].

Following reference [1], an expression for the circular frequency, ω, may now be derived from the relations (3) and (11):

$$\omega = \left[\frac{Eh^2(3a^4 + 2a^2 b^2 + 3b^4)}{8\rho a^4 b^4}\right]^{1/2} \times \left[\frac{\lambda^4}{12(1-\mu^2)} + \frac{M^4}{12(1+\mu)^2}\right]^{1/2}, \quad (13)$$

where λ can be calculated for particular values of the

Downloaded 01 May 2010 to 171.66.16.249. Redistribution subject to ASME license or copyright; see http://www.asme.org/terms/Terms_Use.cfm

Table 2 Frequencies of vibration for spherical shells (HZ)[a]

	$H/a = 0.0$[b]		0.0833		0.167		0.267	
Mode	Present	reference [2]	Present	reference [2]	Present	reference [2]	Present	reference [2]
1	2162	2100	8904	9000	15633	16000	21535	21000
2	12907	12760	14465	15000	19819	20000	29541	29000
3	32180	31850	32727	32000	34355	34000	37823	38000

[a] $E = 20.685 \times 10^{10}\ N/m^2$, $\rho = 7705\ \text{kg/m}^3$, $h/a = 1/24$, $a = 0.1524\text{m}$, $\mu = 1/3$.
[b] H is the shell rise height.

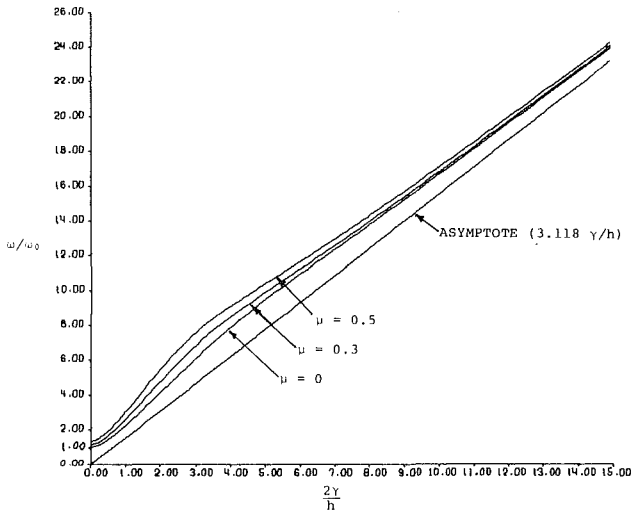


Fig. 1 The lowest frequency ω/ω_0, for elliptic dome with simply supported edge, in units of the corresponding frequency for a flat plate with zero Poisson's ratio

parameters M^4 and μ as it is related to them by equation (10). This leads to the following nondimensional form:

$$\frac{\omega}{\omega_0} = [1-\mu_0^2]^{1/2}\left[\frac{1}{1-\mu^2}\left(\frac{\lambda}{\lambda_0}\right)^4 + \frac{48}{\lambda_0^4}\left(\frac{2\gamma}{h}\right)^2\right]^{1/2}, \quad (14)$$

where ω_0 and λ_0 denote the values of ω and λ corresponding to a flat plate ($M = 0$) and a particular value of Poisson's ratio i.e., ($\mu = \mu_0$). In this paper, for consistency, $\mu_0 = 0$ is used throughout [1, 3].

Results

Since to the authors' knowledge there are no exact theoretical or experimental results for simply supported elliptical domes with which comparisons can be made, we may consider, as a basis for comparison and also as confirmation of the proposed method, the limiting case when $a \to b$ and $R_x \to R_y$ for which solutions exist in references [2, 5].

First, on using the present definition of ω_0 and recalculating the exact value of the ratio ω/ω_0 for a simply supported spherical shell as given in reference [5], one obtains the value 10.2, which compares favorably with the value of 9.92 produced by the present method.

Second, some results obtained by using equations (13) are displayed in Table 2 together with the corresponding results from reference [2]. It is clear that there is remarkable agreement between the two sets of results.

Finally, the ratio ω/ω_0 for various values of Poisson's ratio and $2\gamma/h$ is shown in Fig. 1. It is interesting to note the features of the figure that are different from those for the clamped shell case [3]: the considerably greater slope of the asymptote and the stronger dependence of ω/ω_0 on Poisson's ratio.

Conclusion

We have thus obtained a simple closed-form frequency expression for a simply supported shallow shell on an elliptical base. Results obtained for the limiting case of a spherical shell exhibit excellent agreement with results previously obtained in the literature.

Acknowledgment

The authors gratefully acknowledge one of the referees for his particularly helpful comments on the earlier version of this note.

The first author is also most thankful for the financial support provided by an Australian Government Public Service Board Postgraduate Award, which has enabled him to complete this work.

References

1 Reissner, E., "On Axisymmetrical Vibrations of Shallow Spherical Shells," *Quarterly of Applied Mechanics*, Vol. 13, No. 3, 1955, pp. 279-290.

2 Hoppmann, W. H., II, "Frequencies of Vibration of Shallow Spherical Shells," ASME JOURNAL OF APPLIED MECHANICS, Vol. 28, 1961, pp. 305-307.

3 Jones, R., and Mazumdar, J., "Transverse Vibrations of Shallow Shells by the Method of Constant Deflection Contours," *Journal of the Acoustical Society of America*, Vol. 56, No. 5, 1974, pp. 1487-1492.

4 Mazumdar, J., "Transverse Vibration of Elastic Plates by the Method of Constant Deflection Lines," *Journal of Sound and Vibration*, Vol. 18, No. 2, 1971, pp. 147-155.

5 Kalnins, A., and Naghdi, P. M., "Axisymmetric Vibrations of Shallow Elastic Spherical Shells," *Journal of the Acoustical Society of America*, Vol. 32, No. 3, 1960, pp. 342-347.

The Local Stress State at a Sharp Corner of an Expanding Inclusion

Celina Gómez[1] and John Dundurs[2]

The object of this Note is to explore the local nature of stresses at a sharp corner of an inclusion that undergoes a uniform expansion. This problem arises in several applications, but in its simplest terms it may be thought of as the situation realized when a composite body is made at a certain temperature, and stresses are induced by unequal thermal expansion as the temperature later changes.

For the study of the local stress state in the vicinity of the corner, by what in elasticity is now called the Williams technique [1], the inclusion is taken as the unbounded domain $0 < r < \infty$, $0 < \theta < \pi/2$, and the matrix as $0 < r < \infty$, $-3\pi/2 < \theta < 0$ (see Fig. 1). The elastic constants of the inclusion are μ_1, κ_1, with μ denoting the shear modulus, $\kappa = 3 - 4\nu$ for plane strain, and ν being Poisson's ratio. Suppose that the inclusion is disconnected from the matrix so that it can expand freely. Then it undergoes a stress-free deformation with the displacement components $v_x = \omega(1 + \nu_1)x$ and $v_y = \omega(1 + \nu_1)y$, where ω is the free expansion strain of the inclusion, and the factor $1 + \nu_1$ enters because of the plane

[1] Graduate Student, Department of Civil Engineering, Northwestern University, Evanston, Ill.. 60201.

[2] Professor, Department of Civil Engineering, Northwestern University, Evanston, Ill. 60201.

Manuscript received by ASME Applied Mechanics Division, May 1981; final revision, September 1981.

Downloaded 01 May 2010 to 171.66.16.249. Redistribution subject to ASME license or copyright; see http://www.asme.org/terms/Terms_Use.cfm

Table 2 Frequencies of vibration for spherical shells (HZ)[a]

	$H/a = 0.0$[b]		0.0833		0.167		0.267	
Mode	Present	reference [2]	Present	reference [2]	Present	reference [2]	Present	reference [2]
1	2162	2100	8904	9000	15633	16000	21535	21000
2	12907	12760	14465	15000	19819	20000	29541	29000
3	32180	31850	32727	32000	34355	34000	37823	38000

[a] $E = 20.685 \times 10^{10}\ N/m^2$, $\rho = 7705\ \text{kg/m}^3$, $h/a = 1/24$, $a = 0.1524\text{m}$, $\mu = 1/3$.
[b] H is the shell rise height.

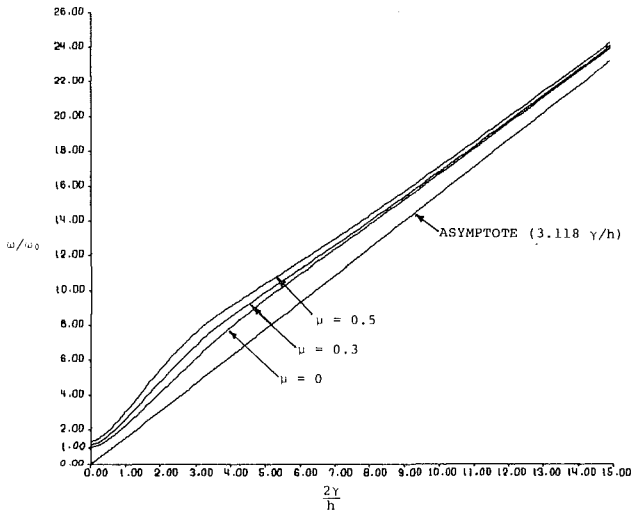


Fig. 1 The lowest frequency ω/ω_0, for elliptic dome with simply supported edge, in units of the corresponding frequency for a flat plate with zero Poisson's ratio

parameters M^4 and μ as it is related to them by equation (10). This leads to the following nondimensional form:

$$\frac{\omega}{\omega_0} = [1-\mu_0^2]^{1/2}\left[\frac{1}{1-\mu^2}\left(\frac{\lambda}{\lambda_0}\right)^4 + \frac{48}{\lambda_0^4}\left(\frac{2\gamma}{h}\right)^2\right]^{1/2}, \quad (14)$$

where ω_0 and λ_0 denote the values of ω and λ corresponding to a flat plate ($M = 0$) and a particular value of Poisson's ratio i.e., ($\mu = \mu_0$). In this paper, for consistency, $\mu_0 = 0$ is used throughout [1, 3].

Results

Since to the authors' knowledge there are no exact theoretical or experimental results for simply supported elliptical domes with which comparisons can be made, we may consider, as a basis for comparison and also as confirmation of the proposed method, the limiting case when $a \to b$ and $R_x \to R_y$ for which solutions exist in references [2, 5].

First, on using the present definition of ω_0 and recalculating the exact value of the ratio ω/ω_0 for a simply supported spherical shell as given in reference [5], one obtains the value 10.2, which compares favorably with the value of 9.92 produced by the present method.

Second, some results obtained by using equations (13) are displayed in Table 2 together with the corresponding results from reference [2]. It is clear that there is remarkable agreement between the two sets of results.

Finally, the ratio ω/ω_0 for various values of Poisson's ratio and $2\gamma/h$ is shown in Fig. 1. It is interesting to note the features of the figure that are different from those for the clamped shell case [3]: the considerably greater slope of the asymptote and the stronger dependence of ω/ω_0 on Poisson's ratio.

Conclusion

We have thus obtained a simple closed-form frequency expression for a simply supported shallow shell on an elliptical base. Results obtained for the limiting case of a spherical shell exhibit excellent agreement with results previously obtained in the literature.

Acknowledgment

The authors gratefully acknowledge one of the referees for his particularly helpful comments on the earlier version of this note.

The first author is also most thankful for the financial support provided by an Australian Government Public Service Board Postgraduate Award, which has enabled him to complete this work.

References

1 Reissner, E., "On Axisymmetrical Vibrations of Shallow Spherical Shells," *Quarterly of Applied Mechanics*, Vol. 13, No. 3, 1955, pp. 279-290.

2 Hoppmann, W. H., II, "Frequencies of Vibration of Shallow Spherical Shells," ASME JOURNAL OF APPLIED MECHANICS, Vol. 28, 1961, pp. 305-307.

3 Jones, R., and Mazumdar, J., "Transverse Vibrations of Shallow Shells by the Method of Constant Deflection Contours," *Journal of the Acoustical Society of America*, Vol. 56, No. 5, 1974, pp. 1487-1492.

4 Mazumdar, J., "Transverse Vibration of Elastic Plates by the Method of Constant Deflection Lines," *Journal of Sound and Vibration*, Vol. 18, No. 2, 1971, pp. 147-155.

5 Kalnins, A., and Naghdi, P. M., "Axisymmetric Vibrations of Shallow Elastic Spherical Shells," *Journal of the Acoustical Society of America*, Vol. 32, No. 3, 1960, pp. 342-347.

The Local Stress State at a Sharp Corner of an Expanding Inclusion

Celina Gómez[1] and John Dundurs[2]

The object of this Note is to explore the local nature of stresses at a sharp corner of an inclusion that undergoes a uniform expansion. This problem arises in several applications, but in its simplest terms it may be thought of as the situation realized when a composite body is made at a certain temperature, and stresses are induced by unequal thermal expansion as the temperature later changes.

For the study of the local stress state in the vicinity of the corner, by what in elasticity is now called the Williams technique [1], the inclusion is taken as the unbounded domain $0 < r < \infty$, $0 < \theta < \pi/2$, and the matrix as $0 < r < \infty$, $-3\pi/2 < \theta < 0$ (see Fig. 1). The elastic constants of the inclusion are μ_1, κ_1, with μ denoting the shear modulus, $\kappa = 3 - 4\nu$ for plane strain, and ν being Poisson's ratio. Suppose that the inclusion is disconnected from the matrix so that it can expand freely. Then it undergoes a stress-free deformation with the displacement components $v_x = \omega(1 + \nu_1)x$ and $v_y = \omega(1 + \nu_1)y$, where ω is the free expansion strain of the inclusion, and the factor $1 + \nu_1$ enters because of the plane

[1] Graduate Student, Department of Civil Engineering, Northwestern University, Evanston, Ill.. 60201.

[2] Professor, Department of Civil Engineering, Northwestern University, Evanston, Ill. 60201.

Manuscript received by ASME Applied Mechanics Division, May 1981; final revision, September 1981.

Copyright © 1982 by ASME
Downloaded 01 May 2010 to 171.66.16.249. Redistribution subject to ASME license or copyright; see http://www.asme.org/terms/Terms_Use.cfm

strain constraint. When the inclusion is connected to the matrix, the expansion induces stresses with the components σ_{xx}, σ_{xy} and σ_{yy}, which are related by Hooke's law to the derivatives of the displacement components u_x and u_y. Using these symbols, the boundary conditions of the problem are

$$u_x^{(1)} + \omega(1+\nu_1)x = u_x^{(2)}, \qquad u_y^{(1)} = u_y^{(2)} \tag{1}$$

$$\sigma_{xy}^{(1)} = \sigma_{xy}^{(2)}, \qquad \sigma_{yy}^{(1)} = \sigma_{yy}^{(2)} \tag{2}$$

on $x > 0, y = 0$,

and

$$u_x^{(1)} = u_x^{(2)}, \qquad u_y^{(1)} + \omega(1+\nu_1)y = u_y^{(2)} \tag{3}$$

$$\sigma_{xx}^{(1)} = \sigma_{xx}^{(2)}, \qquad \sigma_{xy}^{(1)} = \sigma_{xy}^{(2)} \tag{4}$$

on $x = 0, y = > 0$, where the superscripts 1 and 2 refer to the inclusion and matrix, respectively.

The boundary conditions are nonhomogeneous which suggests that terms with logarithms be included in the asymptotic analysis [2]. The analysis is thus based on eight sets of elastic fields instead of four, as customarily encountered in the Williams technique. The eight sets are (cf. the Appendices in [3, 4] with $\lambda = 0$)

$$\{A\}: \ 2\mu u_x = (\kappa-1)x, \quad 2\mu u_y = (\kappa-1)y,$$

$$\sigma_{xx} = \sigma_{yy} = 2, \quad \sigma_{xy} = 0 \tag{5}$$

$$\{B\}: \ 2\mu u_x = -(\kappa+1)y, \quad 2\mu u_y = (\kappa+1)x,$$

$$\sigma_{xx} = \sigma_{xy} = \sigma_{yy} = 0 \tag{6}$$

$$\{C\}: \ 2\mu u_x = -x, \quad 2\mu u_y = y,$$

$$\sigma_{xx} = -1, \quad \sigma_{xy} = 0, \quad \sigma_{yy} = 1 \tag{7}$$

$$\{D\}: \ 2\mu u_x = y, \quad 2\mu u_y = x, \quad \sigma_{xx} = \sigma_{yy} = 0, \quad \sigma_{xy} = 1 \tag{8}$$

$$\{E\}: \ 2\mu u_x = x[(\kappa-1)\log r - 1] - (\kappa+1)y\theta,$$

$$2\mu u_y = y[(\kappa-1)\log r - 1] + (\kappa+1)x\theta$$

$$\sigma_{xx} = 2(\log r + 1) - \frac{x^2-y^2}{r^2}, \quad \sigma_{xy} = -\frac{2xy}{r^2},$$

$$\sigma_{yy} = 2(\log r + 1) + \frac{x^2-y^2}{r^2} \tag{9}$$

$$\{F\}: \ 2\mu u_x = -(\kappa+1)y\log r - (\kappa-1)x\theta,$$

$$2\mu u_y = (\kappa+1)x\log r - (\kappa-1)y\theta$$

$$\sigma_{xx} = -2\theta - \frac{2xy}{r^2}, \quad \sigma_{xy} = \frac{x^2-y^2}{r^2}, \quad \sigma_{yy} = -2\theta + \frac{2xy}{r^2} \tag{10}$$

$$\{G\}: \ 2\mu u_x = -x\log r + y\theta, \quad 2\mu u_y = y\log r + x\theta$$

$$\sigma_{xx} = -\log r - 1, \quad \sigma_{xy} = \theta, \quad \sigma_{yy} = \log r + 1 \tag{11}$$

$$\{H\}: \ 2\mu u_x = y\log r + x\theta, \quad 2\mu u_y = x\log r - y\theta$$

$$\sigma_{xx} = \theta, \quad \sigma_{xy} = \log r + 1, \quad \sigma_{yy} = -\theta \tag{12}$$

The total fields are formed as liner combinations of the eight sets with the unknown coefficients $A_1, B_1, \ldots, H_1$ and $A_2, B_2, \ldots, H_2$ where the subscripts 1 and 2 refer, respectively, to the inclusion and the matrix. The boundary conditions (1-4), which must be identically satisfied, yield 16

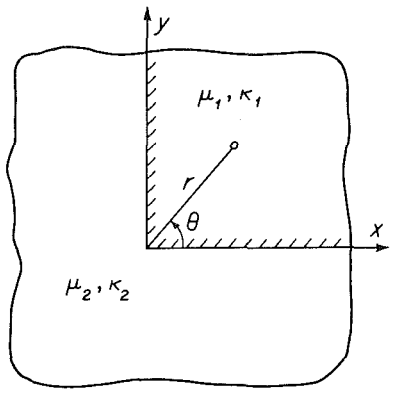


Fig. 1

equations for the unknown coefficients. However, the simultaneous equations contain various degeneracies depending on the combination of materials, and several cases must be treated separately. Using the notation

$$\Gamma = \mu_2/\mu_1, \quad L = 2\omega\mu(1+\nu_1)/(\kappa_2+1),$$

$$M = 2\omega\mu_2(1+\nu_1)/(\Gamma-1) \tag{13}$$

we only give the *nonvanishing coefficients* in the sequel (B_1 and B_2 are of no interest because they give rigid body displacements).

Case 1: $\Gamma - 1 = 0$

$$A_2 = L + A_1(\kappa_1+1)/(\kappa_2+1),$$

$$C_2 = -2L + 2A_1(\kappa_2-\kappa_1)/(\kappa_2+1) + C_1 \tag{14}$$

$$D_2 = D_1, \quad H_1 = H_2 = (2/\pi)[L - A_1(\kappa_2-\kappa_1)/(\kappa_2+1)] \tag{15}$$

where A_1, C_1, and D_1 remain free.

Case 2: $\Gamma - 1 \neq 0, \Gamma(\kappa_1 + 1) - (\kappa_2 + 1) = 0$

$$A_2 = 2M - 3A_1, \quad C_1 = (-M + 2A_1)[2\Gamma(\kappa_1+1)/(\Gamma-1) - 1] \tag{16}$$

$$C_2 = (-M + 2A_1)[2\Gamma(\kappa_1+1)/(\Gamma-1) + 3],$$

$$F_1 = F_2 = (2/\pi)(-M + 2A_1) \tag{17}$$

where A_1 remains arbitrary.

Case 3: $\Gamma - 1 \neq 0, \Gamma(\kappa_1 + 1) - (\kappa_2 + 1) \neq 0,$ $\Gamma(\kappa_1 - 1) - (\kappa_2 - 1) = 0$

$$A_2 = A_1, \quad D_1 = D_2 = (\pi/2)M[2(\Gamma\kappa_1+1)/(\Gamma-1) - 1],$$

$$E_1 = E_2 = M \tag{18}$$

where A_1 remains free.

Case 4: $\Gamma - 1 \neq 0, \Gamma(\kappa_1 + 1) - (\kappa_2 + 1) \neq 0,$ $\Gamma(\kappa_1 - 1) - (\kappa_2 - 1) \neq 0$

$$A_1 = A_2 = -2\omega\mu_2(1+\nu_1)/[\Gamma(\kappa_1-1) - (\kappa_2-1)] \tag{19}$$

A logarithmic singularity appears in the stresses whenever at least one of the coefficients E, F, G, and H does not vanish (Cases 1, 2, and 3). It is noteworthy that in Case 1 for $\kappa_1 = \kappa_2$ (identical materials) and Case 3, the asymptotic analysis not only establishes the nature of the singularity, as is usually the case, but also determines its *magnitude*. This is not so for Case 1 if $\kappa_1 \neq \kappa_2$ and Case 2, in which an isotropic and

Downloaded 01 May 2010 to 171.66.16.249. Redistribution subject to ASME license or copyright; see http://www.asme.org/terms/Terms_Use.cfm

homogeneous state of stress can interact with or even cancel the logarithmic singularity through the coefficient A_1. An unexpected result is also that the logarithmic singularity occurs in the problem with the nonhomogeneous boundary conditions (1) and (3) only for special combinations of materials, as the stresses remain finite in Case 4, which corresponds to a general combination of materials with the three restrictions listed. Note that for Case 4 both the inclusion and the matrix are in the same isotropic state of stress, and that the uniform strain in the matrix caused by stress is equal to the strain in the inclusion caused by stress plus the free expansion strain.

The stress singularity for this geometry under the homogeneous boundary conditions corresponding to $\omega = 0$ in (1-4) has been studied before by Bogy and Wang [5]. It was found that, depending on the combination of materials, the homogeneous system leads to either power or oscillatory singularities (a logarithmic singularity was also found from the homogeneous system for $\Gamma = 1$). In the solution of specific boundary value problems, the power singularity will dominate the problem mathematically near $r = 0$, but the fields given here have a longer range and they may be useful in energy considerations and constructing approximation.

Acknowledgment

The results reported here were obtained in the course of research supported by the Onada Cement Co., Ltd.

References

1 Williams, M. L., "Stress Singularities For Various Boundary Conditions in Angular Corners of Plates in Extension," ASME JOURNAL OF APPLIED MECHANICS, Vol. 19, 1952, pp. 526-528.

2 Dempsey, J. P., and Sinclair, G. B., "On the Stress Singularities in the Plane Elasticity of the Composite Wedge," *Journal of Elasticity,* Vol. 9, 1979, pp. 373-391.

3 Comninou, M., "The Interface Crack," ASME JOURNAL OF APPLIED MECHANICS, Vol. 44, 1977, pp. 631-636.

4 Comninou, M., and Dundurs, J., "On the Barber Boundary Conditions for Thermoelastic Contact," ASME JOURNAL OF APPLIED MECHANICS, Vol. 46, 1979, pp. 849-853.

5 Bogy, D. B., and Wang, K. C., "Stress Singularities at Interface Corners in Bonded Dissimilar Isotropic Elastic Materials," *International Journal of Solids and Structures,* Vol. 7, 1971, pp. 993-1005.

Stick/Slip Conditions for a Thin, Incomplete, Elastic Ring Impinging on a Frictional Barrier

R. C. Benson[1]

Introduction

In a recent paper [1] the author examined the large deformation of a thin, incomplete, elastic ring in a channel with friction. Here the related problem of a ring impinging on a frictional barrier is studied. Through a perturbation analysis it is possible to obtain closed-form stick/slip conditions for the initial contact. Designers of machines such as plain paper copiers, self-threading tapes, and sewing machines should find the results useful and easy to apply.

Stick/Slip Geometry

In Fig. 1, a ring, of radius R and flexural rigidity D, is passed through a partial clamp (which restrains only transverse motion) until the leading edge just meets a frictional barrier. This is shown by the dashed circular arc. Subsequently an additional length ΔL is forced through the clamp, and in the absence of slip the ring deforms to the solid curve in the figure. A small reaction ΔF inclined at an angle Ψ is required to hold the edge of the ring in place. Whether the ring sticks or slips depends on an elementary constraint between Ψ, the surface pitch Ψ^*, and the friction angle $\tan^{-1}(\mu)$:

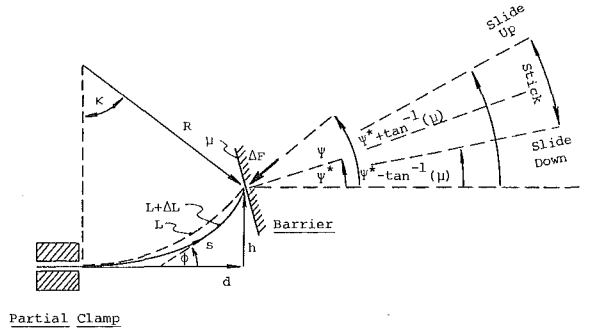


Fig. 1 Geometry

$$\Psi > \Psi^* + \tan^{-1}(\mu) => \text{slide up},$$

$$\Psi^* - \tan^{-1}(\mu) < \Psi < \Psi^* + \tan^{-1}(\mu) => \text{stick},$$

$$\Psi < \Psi^* - \tan^{-1}(\mu) => \text{slide down}. \quad (1)$$

Since Ψ^* and μ are known, the problem reduces to a calculation of Ψ.

The Reaction Angle

Assuming plane-strain, inextensible bending, the ring may be treated as a wide Euler-Bernoulli "beam" of constant curvature [2]. The problem is formulated using the nonlinear theory of the elastica [2, 3] and then linearized [4] for small initial deformation.

Neglecting gravity and transient effects the differential equation and boundary conditions for the deformed beam are:

$$D\frac{d^2\phi}{ds^2} = \Delta F \sin(\Psi - \phi), \quad (2)$$

$$\phi(0) = 0, \quad \frac{d\phi}{ds}(L+\Delta L) = \frac{1}{R}, \quad (3)$$

where s is the distance along the beam measured from the partial clamp, and $\phi(s)$ is the slope with respect to the horizontal. Before and after deformation the coordinates of the beam tip remain unchanged:

$$d = R\sin(L/R) = \int_0^{L+\Delta L} \cos\phi\, ds, \quad (4)$$

$$h = R - R\cos(L/R) = \int_0^{L+\Delta L} \sin\phi\, ds. \quad (5)$$

The problem is next nondimensionalized by dividing lengths by L and the force by D/L^2:

$$\xi = s/L, \quad \kappa = L/R,$$

$$\overline{\Delta L} = \Delta L/L, \quad \overline{\Delta F} = \Delta F/(D/L^2). \quad (6)$$

The nondimensional curvature κ may be negative if the beam in Fig. 1 curves downward. Additionally $\overline{\Delta\phi}$ will denote the change in slope from the undeformed value of $s/R = \kappa\xi$:

$$\phi = \kappa\xi + \overline{\Delta\phi}. \quad (7)$$

Thus equations (2)-(5) become:

[1] Assistant Professor, Department of Mechanical and Aerospace Sciences, University of Rochester, Rochester, N.Y. 14627. Assoc. Mem. ASME

Manuscript received by ASME Applied Mechanics Division, May 1981; final revision, July 1981.

Downloaded 01 May 2010 to 171.66.16.249. Redistribution subject to ASME license or copyright; see http://www.asme.org/terms/Terms_Use.cfm

homogeneous state of stress can interact with or even cancel the logarithmic singularity through the coefficient A_1. An unexpected result is also that the logarithmic singularity occurs in the problem with the nonhomogeneous boundary conditions (1) and (3) only for special combinations of materials, as the stresses remain finite in Case 4, which corresponds to a general combination of materials with the three restrictions listed. Note that for Case 4 both the inclusion and the matrix are in the same isotropic state of stress, and that the uniform strain in the matrix caused by stress is equal to the strain in the inclusion caused by stress plus the free expansion strain.

The stress singularity for this geometry under the homogeneous boundary conditions corresponding to $\omega = 0$ in (1-4) has been studied before by Bogy and Wang [5]. It was found that, depending on the combination of materials, the homogeneous system leads to either power or oscillatory singularities (a logarithmic singularity was also found from the homogeneous system for $\Gamma = 1$). In the solution of specific boundary value problems, the power singularity will dominate the problem mathematically near $r = 0$, but the fields given here have a longer range and they may be useful in energy considerations and constructing approximation.

Acknowledgment

The results reported here were obtained in the course of research supported by the Onada Cement Co., Ltd.

References

1 Williams, M. L., "Stress Singularities For Various Boundary Conditions in Angular Corners of Plates in Extension," ASME JOURNAL OF APPLIED MECHANICS, Vol. 19, 1952, pp. 526-528.

2 Dempsey, J. P., and Sinclair, G. B., "On the Stress Singularities in the Plane Elasticity of the Composite Wedge," *Journal of Elasticity,* Vol. 9, 1979, pp. 373-391.

3 Comninou, M., "The Interface Crack," ASME JOURNAL OF APPLIED MECHANICS, Vol. 44, 1977, pp. 631-636.

4 Comninou, M., and Dundurs, J., "On the Barber Boundary Conditions for Thermoelastic Contact," ASME JOURNAL OF APPLIED MECHANICS, Vol. 46, 1979, pp. 849-853.

5 Bogy, D. B., and Wang, K. C., "Stress Singularities at Interface Corners in Bonded Dissimilar Isotropic Elastic Materials," *International Journal of Solids and Structures,* Vol. 7, 1971, pp. 993-1005.

Stick/Slip Conditions for a Thin, Incomplete, Elastic Ring Impinging on a Frictional Barrier

R. C. Benson[1]

Introduction

In a recent paper [1] the author examined the large deformation of a thin, incomplete, elastic ring in a channel with friction. Here the related problem of a ring impinging on a frictional barrier is studied. Through a perturbation analysis it is possible to obtain closed-form stick/slip conditions for the initial contact. Designers of machines such as plain paper copiers, self-threading tapes, and sewing machines should find the results useful and easy to apply.

Stick/Slip Geometry

In Fig. 1, a ring, of radius R and flexural rigidity D, is passed through a partial clamp (which restrains only transverse motion) until the leading edge just meets a frictional barrier. This is shown by the dashed circular arc. Subsequently an additional length ΔL is forced through the clamp, and in the absence of slip the ring deforms to the solid curve in the figure. A small reaction ΔF inclined at an angle Ψ is required to hold the edge of the ring in place. Whether the ring sticks or slips depends on an elementary constraint between Ψ, the surface pitch Ψ^*, and the friction angle $\tan^{-1}(\mu)$:

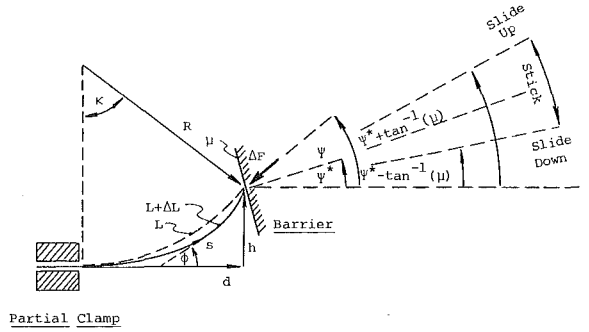


Fig. 1 Geometry

$$\Psi > \Psi^* + \tan^{-1}(\mu) => \text{slide up},$$

$$\Psi^* - \tan^{-1}(\mu) < \Psi < \Psi^* + \tan^{-1}(\mu) => \text{stick},$$

$$\Psi < \Psi^* - \tan^{-1}(\mu) => \text{slide down}. \quad (1)$$

Since Ψ^* and μ are known, the problem reduces to a calculation of Ψ.

The Reaction Angle

Assuming plane-strain, inextensible bending, the ring may be treated as a wide Euler-Bernoulli "beam" of constant curvature [2]. The problem is formulated using the nonlinear theory of the elastica [2, 3] and then linearized [4] for small initial deformation.

Neglecting gravity and transient effects the differential equation and boundary conditions for the deformed beam are:

$$D\frac{d^2\phi}{ds^2} = \Delta F \sin(\Psi - \phi), \quad (2)$$

$$\phi(0) = 0, \quad \frac{d\phi}{ds}(L+\Delta L) = \frac{1}{R}, \quad (3)$$

where s is the distance along the beam measured from the partial clamp, and $\phi(s)$ is the slope with respect to the horizontal. Before and after deformation the coordinates of the beam tip remain unchanged:

$$d = R\sin(L/R) = \int_0^{L+\Delta L} \cos\phi\, ds, \quad (4)$$

$$h = R - R\cos(L/R) = \int_0^{L+\Delta L} \sin\phi\, ds. \quad (5)$$

The problem is next nondimensionalized by dividing lengths by L and the force by D/L^2:

$$\xi = s/L, \quad \kappa = L/R,$$

$$\overline{\Delta L} = \Delta L/L, \quad \overline{\Delta F} = \Delta F/(D/L^2). \quad (6)$$

The nondimensional curvature κ may be negative if the beam in Fig. 1 curves downward. Additionally $\overline{\Delta\phi}$ will denote the change in slope from the undeformed value of $s/R = \kappa\xi$:

$$\phi = \kappa\xi + \overline{\Delta\phi}. \quad (7)$$

Thus equations (2)-(5) become:

[1] Assistant Professor, Department of Mechanical and Aerospace Sciences, University of Rochester, Rochester, N.Y. 14627. Assoc. Mem. ASME

Manuscript received by ASME Applied Mechanics Division, May 1981; final revision, July 1981.

Copyright © 1982 by ASME
Downloaded 01 May 2010 to 171.66.16.249. Redistribution subject to ASME license or copyright; see http://www.asme.org/terms/Terms_Use.cfm

$$\frac{d^2(\overline{\Delta\phi})}{d\xi^2} = \overline{\Delta F}\sin(\Psi - \kappa\xi - \overline{\Delta\phi}), \tag{8}$$

$$\overline{\Delta\phi}(0) = 0, \quad \frac{d(\overline{\Delta\phi})}{d\xi}(1 + \overline{\Delta L}) = 0; \tag{9}$$

$$\frac{\sin\kappa}{\kappa} \int_0^{1+\overline{\Delta L}} \cos(\kappa\xi + \overline{\Delta\phi})d\xi, \tag{10}$$

$$\frac{1-\cos\kappa}{\kappa} = \int_0^{1+\overline{\Delta L}} \sin(\kappa\xi + \overline{\Delta\phi})d\xi. \tag{11}$$

For the perturbed geometry, each of the quantities $\overline{\Delta L}$, $\overline{\Delta F}$, and $\overline{\Delta\phi}$ will be small and equations (8), (10), and (11) may be linearized to become:

$$\frac{d^2(\overline{\Delta\phi})}{d\xi^2} = \overline{\Delta F}\sin(\Psi - \kappa\xi), \tag{12}$$

$$\frac{\sin\kappa}{\kappa} = \int_0^{1+\overline{\Delta L}} \cos(\kappa\xi)d\xi - \int_0^1 \overline{\Delta\phi}\sin(\kappa\xi)\,d\xi, \tag{13}$$

$$\frac{1-\cos\kappa}{\kappa} = \int_0^{1+\overline{\Delta L}} \sin(\kappa\xi)\,d\xi + \int_0^1 \overline{\Delta\phi}\cos(\kappa\xi)\,d\xi. \tag{14}$$

Integrating the first term on the right-hand side of equations (13) and (14), and retaining only first-order terms in ΔL gives the respective results:

$$\overline{\Delta L}\cos\kappa = \int_0^1 \overline{\Delta\phi}\sin(\kappa\xi)\,d\xi,$$

$$-\overline{\Delta L}\sin\kappa = \int_0^1 \overline{\Delta\phi}\cos(\kappa\xi)\,d\xi. \tag{15}$$

$\overline{\Delta L}$ is eliminated from constraint (15) by multiplying through the first equation by $\sin(\kappa)$, the second equation by $\cos(\kappa)$, and adding:

$$0 = \int_0^1 \overline{\Delta\phi}\cos(\kappa - \kappa\xi)\,d\xi. \tag{16}$$

Next, equation (12) is integrated, making use of boundary conditions (9) to get:

$$\overline{\Delta\phi} = \frac{\overline{\Delta F}}{\kappa^2}[\sin\Psi - \sin(\Psi - \kappa\xi) - \kappa\xi\cos(\Psi - \kappa)]. \tag{17}$$

Substituting (17) into (16), and dividing through by the nonzero amount $\Delta F/\kappa^2$ gives:

$$0 = \int_0^1 \cos(\kappa - \kappa\xi)[\sin\Psi - \sin(\Psi - \kappa\xi) - \kappa\xi\cos(\Psi - \kappa)]d\xi. \tag{18}$$

After integration and some trigonometry this produces:

$$0 = \sin\Psi\ [2\sin\kappa\cos\kappa - \kappa\cos\kappa - \sin\kappa] + \cos\Psi\ [2\cos^2\kappa + \kappa\sin\kappa - 2\cos\kappa], \tag{19}$$

which may be solved for the reaction angle:

$$\Psi = \tan^{-1}\left[\frac{\kappa\sin\kappa - 2\cos\kappa(1-\cos\kappa)}{\cos\kappa + \sin\kappa(1-2\cos\kappa)}\right]. \tag{20}$$

Here it has been shown that the reaction angle of a beam that sticks at first contact is completely determined by the nondimensional curvature κ. This should then be substituted into (1) to see if the beam does indeed stick, or else slip under a small, but unbalanced, load. A simplification of equation (20), which is so concise and accurate that it deserves mentioning, is the Taylor series expansion through order κ^2:

$$\Psi \approx \frac{5}{8}\kappa \tag{21}$$

For most of the industrial applications mentioned earlier, κ will be sufficiently small to merit the use of equation (21) in place of equation (20). Both functions are graphed in Fig. 2.

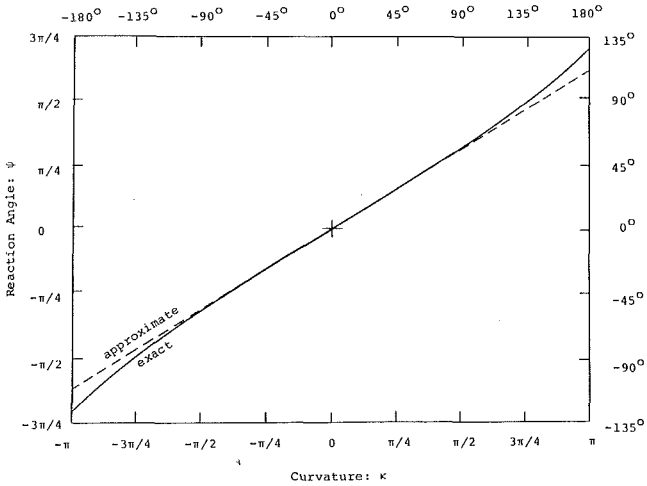


Fig. 2 Reaction angle

References

1 Benson, R. C., "The Deformation of a Thin, Incomplete, Elastic Ring in a Frictional Channel," accepted for publication in ASME JOURNAL OF APPLIED MECHANICS, Vol. 48, Dec. 1981, pp. 895-899.

2 Frisch-Fay, R., *Flexible Bars*, Butterworth, Washington, 1962.

3 Conway, H. D., "The Nonlinear Bending of Thin Circular Rods," ASME JOURNAL OF APPLIED MECHANICS, Vol. 23, Mar. 1956, pp. 7-10.

4 Timoshenko, S. P., and Gere, J. M., *Theory of Elastic Stability*, McGraw-Hill, N.Y., 1961.

On the Derivation of Two-Dimensional Strain Displacement Relations for Small Finite Deformations of Shear-Deformable Plates[1]

E. Reissner[2]

Introduction

In what follows, we give a brief rational derivation of a nonlinear system of strain displacement relations for shear-deformable plates, which has previously been put forward on the basis of considerations involving a measure of speculativity [1].

In obtaining the results of this Brief Note, we depart from the formulation of shell theory in terms of equilibrium and compatibility equations in [3]. Insofar as the special case of plates is concerned, we now complement this theory by a *derivation* of strain displacement relations for *small* finite displacements. The nature of our derivation is such that the possibility of extending it to shells will be evident. We expect that this extension may, in certain respects, have advantages over Simmonds' and Danielson's results in terms of a Rodrigues rotation vector [2].

Translational and Rotational Displacement Representations for Two-Dimensional Plates

We consider a plate with undeformed (middle) surface

[1] Supported by the Office of Naval Research.

[2] Department of Applied Mechanics and Engineering Sciences, University of California, San Diego, La Jolla, Calif. 92093. Fellow ASME.

Manuscript received by ASME Applied Mechanics Division, December 1980; final revision, September 1981.

Downloaded 01 May 2010 to 171.66.16.249. Redistribution subject to ASME license or copyright; see http://www.asme.org/terms/Terms_Use.cfm

$$\frac{d^2(\overline{\Delta\phi})}{d\xi^2} = \overline{\Delta F}\sin(\Psi - \kappa\xi - \overline{\Delta\phi}), \tag{8}$$

$$\overline{\Delta\phi}(0) = 0, \quad \frac{d(\overline{\Delta\phi})}{d\xi}(1 + \overline{\Delta L}) = 0; \tag{9}$$

$$\frac{\sin\kappa}{\kappa} \int_0^{1+\overline{\Delta L}} \cos(\kappa\xi + \overline{\Delta\phi})d\xi, \tag{10}$$

$$\frac{1-\cos\kappa}{\kappa} = \int_0^{1+\overline{\Delta L}} \sin(\kappa\xi + \overline{\Delta\phi})d\xi. \tag{11}$$

For the perturbed geometry, each of the quantities $\overline{\Delta L}$, $\overline{\Delta F}$, and $\overline{\Delta\phi}$ will be small and equations (8), (10), and (11) may be linearized to become:

$$\frac{d^2(\overline{\Delta\phi})}{d\xi^2} = \overline{\Delta F}\sin(\Psi - \kappa\xi), \tag{12}$$

$$\frac{\sin\kappa}{\kappa} = \int_0^{1+\overline{\Delta L}} \cos(\kappa\xi)d\xi - \int_0^1 \overline{\Delta\phi}\sin(\kappa\xi)\,d\xi, \tag{13}$$

$$\frac{1-\cos\kappa}{\kappa} = \int_0^{1+\overline{\Delta L}} \sin(\kappa\xi)\,d\xi + \int_0^1 \overline{\Delta\phi}\cos(\kappa\xi)\,d\xi. \tag{14}$$

Integrating the first term on the right-hand side of equations (13) and (14), and retaining only first-order terms in ΔL gives the respective results:

$$\overline{\Delta L}\cos\kappa = \int_0^1 \overline{\Delta\phi}\sin(\kappa\xi)\,d\xi,$$

$$-\overline{\Delta L}\sin\kappa = \int_0^1 \overline{\Delta\phi}\cos(\kappa\xi)\,d\xi. \tag{15}$$

$\overline{\Delta L}$ is eliminated from constraint (15) by multiplying through the first equation by $\sin(\kappa)$, the second equation by $\cos(\kappa)$, and adding:

$$0 = \int_0^1 \overline{\Delta\phi}\cos(\kappa - \kappa\xi)\,d\xi. \tag{16}$$

Next, equation (12) is integrated, making use of boundary conditions (9) to get:

$$\overline{\Delta\phi} = \frac{\overline{\Delta F}}{\kappa^2}[\sin\Psi - \sin(\Psi - \kappa\xi) - \kappa\xi\cos(\Psi - \kappa)]. \tag{17}$$

Substituting (17) into (16), and dividing through by the nonzero amount $\Delta F/\kappa^2$ gives:

$$0 = \int_0^1 \cos(\kappa - \kappa\xi)[\sin\Psi - \sin(\Psi - \kappa\xi) - \kappa\xi\cos(\Psi - \kappa)]d\xi. \tag{18}$$

After integration and some trigonometry this produces:

$$0 = \sin\Psi\ [2\sin\kappa\cos\kappa - \kappa\cos\kappa - \sin\kappa] + \cos\Psi\ [2\cos^2\kappa + \kappa\sin\kappa - 2\cos\kappa], \tag{19}$$

which may be solved for the reaction angle:

$$\Psi = \tan^{-1}\left[\frac{\kappa\sin\kappa - 2\cos\kappa(1-\cos\kappa)}{\cos\kappa + \sin\kappa(1-2\cos\kappa)}\right]. \tag{20}$$

Here it has been shown that the reaction angle of a beam that sticks at first contact is completely determined by the nondimensional curvature κ. This should then be substituted into (1) to see if the beam does indeed stick, or else slip under a small, but unbalanced, load. A simplification of equation (20), which is so concise and accurate that it deserves mentioning, is the Taylor series expansion through order κ^2:

$$\Psi \approx \frac{5}{8}\kappa \tag{21}$$

For most of the industrial applications mentioned earlier, κ will be sufficiently small to merit the use of equation (21) in place of equation (20). Both functions are graphed in Fig. 2.

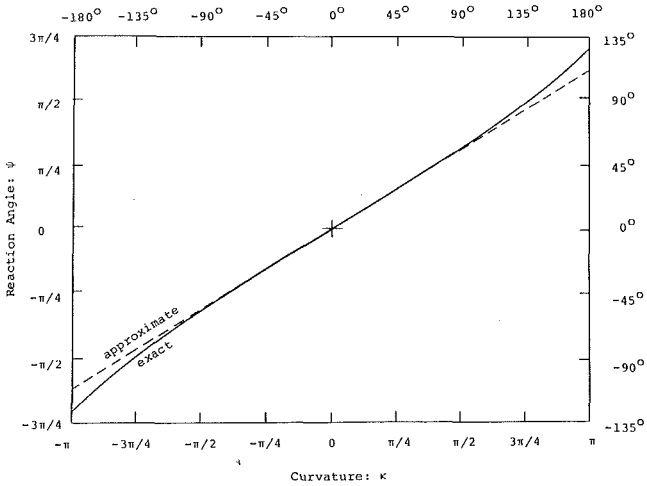


Fig. 2 Reaction angle

References

1 Benson, R. C., "The Deformation of a Thin, Incomplete, Elastic Ring in a Frictional Channel," accepted for publication in ASME JOURNAL OF APPLIED MECHANICS, Vol. 48, Dec. 1981, pp. 895-899.

2 Frisch-Fay, R., *Flexible Bars*, Butterworth, Washington, 1962.

3 Conway, H. D., "The Nonlinear Bending of Thin Circular Rods," ASME JOURNAL OF APPLIED MECHANICS, Vol. 23, Mar. 1956, pp. 7-10.

4 Timoshenko, S. P., and Gere, J. M., *Theory of Elastic Stability*, McGraw-Hill, N.Y., 1961.

On the Derivation of Two-Dimensional Strain Displacement Relations for Small Finite Deformations of Shear-Deformable Plates[1]

E. Reissner[2]

Introduction

In what follows, we give a brief rational derivation of a nonlinear system of strain displacement relations for shear-deformable plates, which has previously been put forward on the basis of considerations involving a measure of speculativity [1].

In obtaining the results of this Brief Note, we depart from the formulation of shell theory in terms of equilibrium and compatibility equations in [3]. Insofar as the special case of plates is concerned, we now complement this theory by a *derivation* of strain displacement relations for *small* finite displacements. The nature of our derivation is such that the possibility of extending it to shells will be evident. We expect that this extension may, in certain respects, have advantages over Simmonds' and Danielson's results in terms of a Rodrigues rotation vector [2].

Translational and Rotational Displacement Representations for Two-Dimensional Plates

We consider a plate with undeformed (middle) surface

[1] Supported by the Office of Naval Research.

[2] Department of Applied Mechanics and Engineering Sciences, University of California, San Diego, La Jolla, Calif. 92093. Fellow ASME.

Manuscript received by ASME Applied Mechanics Division, December 1980; final revision, September 1981.

Copyright © 1982 by ASME
Downloaded 01 May 2010 to 171.66.16.249. Redistribution subject to ASME license or copyright; see http://www.asme.org/terms/Terms_Use.cfm

equation $\mathbf{r} = x_1\mathbf{i}_1 + x_2\mathbf{i}_2$ and with deformed middle surface equation $\boldsymbol{\rho} = \mathbf{r} + \mathbf{u}$.

In addition to the foregoing state of translational displacement, we introduce a state of rotational displacement by the stipulation that an element of the plate, which before deformation is defined by the unit vectors $\mathbf{t}_1 = \mathbf{i}_1$, $\mathbf{t}_2 = \mathbf{i}_2$, $\mathbf{n} = \mathbf{i}_3$, will, after deformation, be defined by a different set of mutually perpendicular unit vectors $\mathbf{T}_1$, $\mathbf{T}_2$, $\mathbf{N}$, with the "difference" between the set ($\mathbf{t}_i$, $\mathbf{n}$) and the set ($\mathbf{T}_i$, $\mathbf{N}$) being a measure of the state of rotational displacement. It is the choice of appropriate expressions for the vectors $\mathbf{T}_1$, $\mathbf{T}_2$, and $\mathbf{N}$ that is the essential element of the results which are to be deduced in what follows.

Evidently, the formulas for $\mathbf{T}_1$, $\mathbf{T}_2$, and $\mathbf{N}$ must involve *three* scalar measures of rotation. Our formulation is based on the thought that the pair $\mathbf{T}_1$, $\mathbf{T}_2$, for physical reasons, ought to be treated in a symmetrical manner, with this symmetry not including $\mathbf{N}$. With this in mind, we first introduce two "interim" mutually perpendicular tangent unit vectors $\hat{\mathbf{T}}_1$, $\hat{\mathbf{T}}_2$ in the form

$$A_1\hat{\mathbf{T}}_1 = \mathbf{i}_1 - \phi_1\mathbf{i}_3 - \beta\mathbf{i}_2, \qquad A_1^2 = 1 + \phi_1^2 + \beta^2, \tag{1a}$$

$$A_2\hat{\mathbf{T}}_2 = \mathbf{i}_2 - \phi_2\mathbf{i}_3 - \beta\mathbf{i}_1, \qquad A_2^2 = 1 + \phi_2^2 + \beta^2. \tag{1b}$$

Evidently, for $\hat{\mathbf{T}}_1$ and $\hat{\mathbf{T}}_2$ to be mutually perpendicular the coefficient β in (1) must depend on the two rotational displacement components ϕ_1, ϕ_2 in the form

$$\beta = \frac{1}{2}\phi_1\phi_2. \tag{2}$$

Having $\hat{\mathbf{T}}_1$ and $\hat{\mathbf{T}}_2$, we introduce the vector $\mathbf{N}$ by the cross-product formula $\mathbf{N} = \hat{\mathbf{T}} \times \hat{\mathbf{T}}_2$, with this giving as expression for $\mathbf{N}$ in terms of ϕ_1 and ϕ_2,

$$A_1A_2\mathbf{N} = (1 - \beta^2)\mathbf{i}_3 + (\phi_1 + \beta\phi_2)\mathbf{i}_1 + (\phi_2 + \beta\phi_1)\mathbf{i}_2. \tag{3}$$

Having $\mathbf{N}$, we finally obtain $\mathbf{T}_1$ and $\mathbf{T}_2$ as functions of $\hat{\mathbf{T}}_1$ and $\hat{\mathbf{T}}_2$ in terms of a *third* rotational displacement component ω by writing

$$B\mathbf{T}_1 = \hat{\mathbf{T}}_1 + \omega\hat{\mathbf{T}}_2, \qquad B\mathbf{T}_2 = \hat{\mathbf{T}}_2 - \omega\hat{\mathbf{T}}_1, \qquad B^2 = 1 + \omega^2. \tag{4a,b}$$

We will, for the time being, leave $\mathbf{T}_1$, $\mathbf{T}_2$ in the foregoing undeveloped form.

With (3) and (4) as representations of $\mathbf{N}$, $\mathbf{T}_1$, and $\mathbf{T}_2$, in terms of three rotational displacement components, we now turn to the question of how to define scalar components of the translational displacement vector $\mathbf{u}$. In the present context there are at least two distinct ways in which to represent $\mathbf{u}$. One of these is in terms of components in the direction of $\mathbf{t}_1$, $\mathbf{t}_2$, $\mathbf{n}$. The other is in terms of components in the direction of $\mathbf{T}_1$, $\mathbf{T}_2$, $\mathbf{N}$. We shall consider both of these possibilities and write,

$$\mathbf{u} = u_1\mathbf{t}_1 + u_2\mathbf{t}_2 + w\mathbf{n} = U_1\mathbf{T}_1 + U_2\mathbf{T}_2 + W\mathbf{N}. \tag{5a,b}$$

Formulas for Small Finite Rotational Displacements. While it is possible to carry through a complete formulation of two-dimensional plate theory on the basis of the expression for $\mathbf{T}_1$, $\mathbf{T}_2$, and $\mathbf{N}$ in equations (4) and (3) as they stand, we here limit attention to the case of *small* finite rotations. By small finite rotations we mean, for present purposes, a theory that is of the *second degree* in terms of the components ϕ_i, and of the *first degree* in terms of the component ω.

Considering the defining equation (2) for β, we have from equation (3) as expression for $\mathbf{N}$ in this small finite rotation theory,

$$\mathbf{N} = \left(1 - \frac{1}{2}\phi_1^2 - \frac{1}{2}\phi_2^2\right)\mathbf{i}_3 + \phi_1\mathbf{i}_1 + \phi_2\mathbf{i}_2, \tag{6}$$

and from equations (4) and (1) as expressions for $\mathbf{T}_1$ and $\mathbf{T}_2$

$$\mathbf{T}_1 = \left(1 - \frac{1}{2}\phi_1^2\right)\mathbf{i}_1 - \phi_1\mathbf{i}_3 + \left(\omega - \frac{1}{2}\phi_1\phi_2\right)\mathbf{i}_2, \tag{7a}$$

$$\mathbf{T}_2 = \left(1 - \frac{1}{2}\phi_2^2\right)\mathbf{i}_2 - \phi_2\mathbf{i}_3 - \left(\omega + \frac{1}{2}\phi_1\phi_2\right)\mathbf{i}_1. \tag{7b}$$

Derivation of Strain Displacement Relations

Defining relations for forces strain components ϵ_{ij}, γ_i, and moment strain components κ_{ij}, λ_i, consistent with the defining relations $\mathbf{N}_i = N_{ij}\mathbf{T}_j + Q_i\mathbf{N}$ and $\mathbf{M}_i = M_{ij}\mathbf{N} \times \mathbf{T}_j + P_i\mathbf{N}$ for stress resultant and couple vectors via an appropriate use of the principle of virtual work [3], come out to be of the form

$$\boldsymbol{\rho}_{,1} = \mathbf{i}_1 + \mathbf{u}_{,1} = (1 + \epsilon_{11})\mathbf{T}_1 + \epsilon_{12}\mathbf{T}_2 + \gamma_1\mathbf{N}, \tag{8a}$$

$$\boldsymbol{\rho}_{,2} = \mathbf{i}_2 + \mathbf{u}_{,2} = \epsilon_{21}\mathbf{T}_1 + (1 + \epsilon_{22})\mathbf{T}_2 + \gamma_2\mathbf{N}, \tag{8b}$$

and

$$\mathbf{T}_{1,1} = \lambda_1\mathbf{T}_2 - \kappa_{11}\mathbf{N}, \qquad \mathbf{T}_{2,1} = -\lambda_1\mathbf{T}_1 - \kappa_{12}\mathbf{N}, \qquad \mathbf{N}_{,1} = \kappa_{11}\mathbf{T}_1 + \kappa_{12}\mathbf{T}_2, \tag{9a}$$

$$\mathbf{T}_{1,2} = \lambda_2\mathbf{T}_2 - \kappa_{21}\mathbf{N}, \qquad \mathbf{T}_{2,2} = -\lambda_2\mathbf{T}_1 - \kappa_{22}\mathbf{N}, \qquad \mathbf{N}_{,2} = \kappa_{21}\mathbf{T}_1 + \kappa_{22}\mathbf{T}_2, \tag{9b}$$

with the moment strain components λ_i being without physical significance, except for plates that are able to sustain stress couples P_i turning about the normals to the deflected plate surface.

With the defining relations (9) and (8) we now obtain, up to second degree terms in ϕ_i and first degree terms in ω,

$$\kappa_{11} = \mathbf{T}_1 \cdot \mathbf{N}_{,1} = \phi_{1,1}, \qquad \kappa_{12} = \mathbf{T}_2 \cdot \mathbf{N}_{,1} = \phi_{2,1}, \tag{10a}$$

$$\kappa_{21} = \mathbf{T}_1 \cdot \mathbf{N}_{,2} = \phi_{1,2}, \qquad \kappa_{22} = \mathbf{T}_2 \cdot \mathbf{N}_{,2} = \phi_{2,2}, \tag{10b}$$

with these expressions being the same as in linear theory, in agreement with the results in [1].

In the same way we obtain, with the help of equations (9) and (7),

$$\lambda_1 = \mathbf{T}_2 \cdot \mathbf{T}_{1,1} = \omega_{,1} + \frac{1}{2}\phi_2\phi_{1,1} - \frac{1}{2}\phi_1\phi_{2,1}, \tag{10c}$$

with this result being in agreement with the applicable portion of equation (27) in [1].

As regards the problem of deriving force strain components we have, on the basis of equations (8),

$$(1 + \epsilon_{11}) = (\mathbf{i}_1 + \mathbf{u}_{,1}) \cdot \mathbf{T}_1, \qquad \epsilon_{12} = (\mathbf{i}_1 + \mathbf{u}_{,1}) \cdot \mathbf{T}_2, \qquad \gamma_1 = (\mathbf{i}_1 + \mathbf{u}_{,1}) \cdot \mathbf{N}, \tag{11}$$

with corresponding relations for ϵ_{21}, ϵ_{22} and γ_2.

In evaluating (11) the results depend on whether we use (5*a*) or (5*b*) as representation for $\mathbf{u}$. We will establish contact with the contents of [1] by evaluating the consequences of the representation (5*b*). With the retention of second degree terms in W and first-degree terms in U_i, corresponding to the earlier retention of second degree terms in ϕ_i and first degree terms in ω, we then have $\gamma_1 = W_{,1} + \phi_1$ and

$$\epsilon_{11} = U_{1,1} + \phi_{1,1}W - \frac{1}{2}\phi_1^2, \quad \epsilon_{12} = U_{2,1} - \omega + \phi_{2,1}W - \frac{1}{2}\phi_1\phi_2, \tag{12}$$

with these formulas being in agreement with the correspondiong formulas in equations (29), (30), and (8*a*) in [1].

Force Strains in Terms of Cartesian Displacement Components. We complement the foregoing by related results which were not considered in [1], by introducing the representation (5*a*) in (1). In this way we obtain $\gamma_1 = w_{,1} + \phi_1$ and

$$\epsilon_{11} = u_{1,1} - w_{,1}\phi_1 - \frac{1}{2}\phi_1^2, \quad \epsilon_{12} = u_{2,1} - \omega - w_{,1}\phi_2 - \frac{1}{2}\phi_1\phi_2. \tag{13}$$

Downloaded 01 May 2010 to 171.66.16.249. Redistribution subject to ASME license or copyright; see http://www.asme.org/terms/Terms_Use.cfm

In comparing equations (12) and (13) we note the appearance, in both cases, of the terms $1/2\ \phi_1^2$ and $1/2\ \phi_1\phi_2$. The difference in assumption concerning the geometrical nature of the translational displacement components manifests itself in the appearance of the "mixed" terms $\phi_{1,1} W$, $w_{,1}\phi_1$, etc.

For the purpose of satisfying boundary conditions, it will sometimes be of advantage to have displacements in terms of strains, rather than vice versa. It is readily seen that equation (8), in conjunction with (5*a*), (6), and (7), gives the relations

$$u_{1,1} = \epsilon_{11} + \gamma_1\phi_1 - \frac{1}{2}\phi_1^2, \quad u_{2,1} = \epsilon_{12} + \omega + \gamma_1\phi_2 - \frac{1}{2}\phi_1\phi_2, \tag{14}$$

with corresponding expressions for $u_{1,2}$, $u_{2,2}$.

Equations of Equilibrium

The subject of equilibrium equations, which are consistent with the strain displacements (10) and (12) via application of the principle of virtual work, has been dealt with in [1] and [3] and does not need to be reconsidered here. A complete statement of these equations, for the purpose of a specific application, may be found in [4].

References

1 Reissner, E., "On the Equations of Non-Linear Shallow Shell Theory," *Studies Appl. Math.*, Vol. 48, 1969, pp. 171-175.

2 Simmonds, J. G., and Danielson, D. A., "Non-Linear Shell Theory With Finite Rotation and Stress Function Vectors," ASME JOURNAL OF APPLIED MECHANICS, Vol. 39, 1972, pp. 1085-1090.

3 Reissner, E., "Linear and Non-Linear Shell Theory," *Symposium on Thin Shell Structures*, Fung, Y. C., and Sechler, E., eds., 1974, pp. 29-44.

4 Reissner, E., "On a One-Dimensional Theory of Finite Torsion and Flexure of Anisotropic Plates," ASME JOURNAL OF APPLIED MECHANICS, Vol. 48, 1981, pp. 601-605.

Unsteady Incompressible Boundary-Layer Flow Over a Rotating Sphere

M. Kumari[1] and G. Nath[2]

Introduction

The design of rotodynamic machines, projectiles, and missiles requires accurate prediction of flow and heat transfer characteristics of the unsteady flow over rotating bodies. As far as these authors are aware, this problem has not been studied so far. However, the analogous steady case has been studied by several investigators [1-5]. Recently, Kumari [6] restudied the foregoing problem using an implicit finite-difference scheme.

The aim of this Brief Note is to study the unsteady flow and heat transfer over a rotating sphere in a forced flow when the free-stream velocity, wall temperature, and rotation of the body vary arbitrarily with time. The partial differential equations governing the unsteady, nonsimilar flow involving three independent variables have been solved numerically using an implicit finite-difference scheme [7]. The results have been compared with the available results.

Governing Equations

We consider the unsteady laminar, incompressible boundary-layer flow with mass transfer over a rotating sphere placed in a uniform stream with its axis of rotation parallel to the free-stream velocity. The free-stream velocity, wall temperature, and rotation of the body are assumed to vary arbitrarily with time. Also, the fluid at the edge of the boundary layer is maintained at a constant temperature T_∞. Under the foregoing assumptions, the boundary-layer equations in dimensionless form governing the flow can be expressed in the form [5-6]

$$F'' + \varphi fF' + \beta\varphi(1 - F^2) + \varphi^{-1}\varphi_1^2\alpha s^2 - P[F_t^* - \varphi^{-1}\varphi_t^*(1 - F)] = 2\xi\varphi(FF_\xi - f_\xi F') \tag{1a}$$

$$s'' + \varphi fs' - \varphi\alpha_1 Fs - P[s_t^* + \varphi_1^{-1}(\varphi_1)_t^* s] = 2\xi\varphi(F_{s\xi} - f_{\xi s}') \tag{1b}$$

$$\mathrm{Pr}^{-1}g'' + \varphi fg' + \mathrm{Br}(u_s/u_\infty)^2\varphi^2[F'^2 + (r\omega/u_s)^2(\varphi^{-1}\varphi_1)^2 s'^2] - Pg_t^* = 2\xi\varphi(F_{g\varphi} - f_{\xi g}') \tag{1c}$$

The boundary conditions are

$$F(\xi,0,t^*) = s(\xi,0,t^*) = 0, \qquad g(\xi,0,t^*) = \varphi_2(t^*) \tag{2a}$$

$$F(\xi,\infty,t^*) = s(\xi,\infty,t^*) = g(\xi,\infty,t^*) = 1 \tag{2b}$$

where

$$\xi = (1 - \cos\bar{x})^2(2 + \cos\bar{x})/2,\ \alpha = \lambda\beta,\ \bar{x} = x/R,\ u_s/u_\infty = 1.5\sin\bar{x}$$
$$\beta = (2/3)[\cos\bar{x}(2 + \cos\bar{x})/(1 + \cos\bar{x})^2],\ \alpha_1 = 2\beta,\ u_e/u_\infty = (u_s/u_\infty)\varphi(t^*)$$
$$\lambda = (4/9)(\omega R/u_\infty)^2,\ P = (2/3)(2 + \cos\bar{x})(1 + \cos\bar{x})^{-2} \tag{3}$$
$$f = \int_0^\eta F d\eta + f_w,\ f_w = A\varphi^{-1}[2/(2 + \cos\bar{x})]^{1/2},\ A = -(w_w/u_\infty)(\mathrm{Re}_L)^{1/2}$$

The initial conditions are obtained by putting

$$\varphi(t^*) = \varphi_1(t^*) = 1,\ \varphi_2(t^*) = \varphi_t^* = (\varphi_1)_t^* = F_t^* = s_t^* = g_t^* = 0 \tag{4}$$

in (1*a-c*). The skin-friction coefficients in the x and y directions (C_f, $\bar{C}_f$) and the heat-transfer coefficient in the terms of Nusselt number Nu are given by

$$C_f(\mathrm{Re}_L)^{1/2} = (9/2)\sin\bar{x}(1 + \cos\bar{x})(2 + \cos\bar{x})^{-1/2}\varphi(t^*)F_w'$$
$$\bar{C}_f(\mathrm{Re}_L)^{1/2} = (9/2)\lambda^{1/2}\sin\bar{x}(1 + \cos\bar{x})(2 + \cos\bar{x})^{-1/2}\varphi_1(t^*)s_w' \tag{5}$$
$$\mathrm{Nu}(\mathrm{Re}_L)^{-1/2} = (3/2)(1 + \cos\bar{x})(2 + \cos\bar{x})^{-1/2}g_w'$$

Here $F(f')$ and s are the dimensionless velocity components in the x and y directions, respectively; g is the dimensionless temperature; λ, Br, Pr, and Re_L are, respectively, the rotation parameter, Brinkman number, Prandtl number, and Reynolds number; F_w' and s_w' are the skin-friction parameters in the x and y directions, respectively; g_w' is the heat-transfer parameter; A is a constant, $A > 0$ for suction, and $A < 0$ for injection; φ and φ_1 are arbitrary functions of t^* representing, respectively, the nature of unsteadiness in the free-stream velocity and rotation of the body and have continuous first derivative for $t^* \geq 0$; φ_2 is an arbitrary function of t^* representing the variation of the wall temperature with time. The prime denotes derivatives with respect to η and the subscripts t^* and ξ denote derivatives with respect to t^* and ξ, respectively. Other symbols are defined in [5-6].

Results and Discussion

The set of equations (1) under boundary conditions (2) and initial conditions, obtained by using the relations (4) in (1a-*c*), has been solved numerically using an implicit finite-difference scheme [7]. The unsteady free-stream velocity distributions, rotation of the body, and the wall temperature considered here are, respectively, given by

[1] Research Scholar, Department of Applied Mathematics, Indian Institute of Science, Bangalore-560012, India.

[2] Professor, Department of Applied Mathematics, Indian Institute of Science, Bangalore-560012, India.

Manuscript received by ASME Applied Mechanics Division, April, 1981; Final revision, August, 1981.

Downloaded 01 May 2010 to 171.66.16.249. Redistribution subject to ASME license or copyright; see http://www.asme.org/terms/Terms_Use.cfm

In comparing equations (12) and (13) we note the appearance, in both cases, of the terms $1/2\ \phi_1^2$ and $1/2\ \phi_1\phi_2$. The difference in assumption concerning the geometrical nature of the translational displacement components manifests itself in the appearance of the "mixed" terms $\phi_{1,1} W$, $w_{,1}\phi_1$, etc.

For the purpose of satisfying boundary conditions, it will sometimes be of advantage to have displacements in terms of strains, rather than vice versa. It is readily seen that equation (8), in conjunction with (5*a*), (6), and (7), gives the relations

$$u_{1,1} = \epsilon_{11} + \gamma_1\phi_1 - \frac{1}{2}\phi_1^2, \quad u_{2,1} = \epsilon_{12} + \omega + \gamma_1\phi_2 - \frac{1}{2}\phi_1\phi_2, \tag{14}$$

with corresponding expressions for $u_{1,2}$, $u_{2,2}$.

Equations of Equilibrium

The subject of equilibrium equations, which are consistent with the strain displacements (10) and (12) via application of the principle of virtual work, has been dealt with in [1] and [3] and does not need to be reconsidered here. A complete statement of these equations, for the purpose of a specific application, may be found in [4].

References

1 Reissner, E., "On the Equations of Non-Linear Shallow Shell Theory," *Studies Appl. Math.*, Vol. 48, 1969, pp. 171-175.

2 Simmonds, J. G., and Danielson, D. A., "Non-Linear Shell Theory With Finite Rotation and Stress Function Vectors," ASME JOURNAL OF APPLIED MECHANICS, Vol. 39, 1972, pp. 1085-1090.

3 Reissner, E., "Linear and Non-Linear Shell Theory," *Symposium on Thin Shell Structures*, Fung, Y. C., and Sechler, E., eds., 1974, pp. 29-44.

4 Reissner, E., "On a One-Dimensional Theory of Finite Torsion and Flexure of Anisotropic Plates," ASME JOURNAL OF APPLIED MECHANICS, Vol. 48, 1981, pp. 601-605.

Unsteady Incompressible Boundary-Layer Flow Over a Rotating Sphere

M. Kumari[1] and G. Nath[2]

Introduction

The design of rotodynamic machines, projectiles, and missiles requires accurate prediction of flow and heat transfer characteristics of the unsteady flow over rotating bodies. As far as these authors are aware, this problem has not been studied so far. However, the analogous steady case has been studied by several investigators [1-5]. Recently, Kumari [6] restudied the foregoing problem using an implicit finite-difference scheme.

The aim of this Brief Note is to study the unsteady flow and heat transfer over a rotating sphere in a forced flow when the free-stream velocity, wall temperature, and rotation of the body vary arbitrarily with time. The partial differential equations governing the unsteady, nonsimilar flow involving three independent variables have been solved numerically using an implicit finite-difference scheme [7]. The results have been compared with the available results.

Governing Equations

We consider the unsteady laminar, incompressible boundary-layer flow with mass transfer over a rotating sphere placed in a uniform stream with its axis of rotation parallel to the free-stream velocity. The free-stream velocity, wall temperature, and rotation of the body are assumed to vary arbitrarily with time. Also, the fluid at the edge of the boundary layer is maintained at a constant temperature T_∞. Under the foregoing assumptions, the boundary-layer equations in dimensionless form governing the flow can be expressed in the form [5-6]

$$F'' + \varphi f F' + \beta\varphi(1 - F^2) + \varphi^{-1}\varphi_1^2\alpha s^2 - P[F_t^* - \varphi^{-1}\varphi_t^*(1 - F)] = 2\xi\varphi(FF_\xi - f_\xi F') \tag{1a}$$

$$s'' + \varphi f s' - \varphi\alpha_1 F s - P[s_t^* + \varphi_1^{-1}(\varphi_1)_t^* s] = 2\xi\varphi(F_{s\xi} - f_{\xi s}') \tag{1b}$$

$$\mathrm{Pr}^{-1} g'' + \varphi f g' + \mathrm{Br}(u_s/u_\infty)^2\varphi^2[F'^2 + (r\omega/u_s)^2(\varphi^{-1}\varphi_1)^2 s'^2] - P g_t^* = 2\xi\varphi(F_{g\varphi} - f_{\xi g}') \tag{1c}$$

The boundary conditions are

$$F(\xi,0,t^*) = s(\xi,0,t^*) = 0, \qquad g(\xi,0,t^*) = \varphi_2(t^*) \tag{2a}$$

$$F(\xi,\infty,t^*) = s(\xi,\infty,t^*) = g(\xi,\infty,t^*) = 1 \tag{2b}$$

where

$$\xi = (1 - \cos\bar{x})^2(2 + \cos\bar{x})/2,\ \alpha = \lambda\beta,\ \bar{x} = x/R,\ u_s/u_\infty = 1.5\sin\bar{x}$$

$$\beta = (2/3)[\cos\bar{x}(2 + \cos\bar{x})/(1 + \cos\bar{x})^2],\ \alpha_1 = 2\beta,\ u_e/u_\infty = (u_s/u_\infty)\varphi(t^*)$$

$$\lambda = (4/9)(\omega R/u_\infty)^2,\ P = (2/3)(2 + \cos\bar{x})(1 + \cos\bar{x})^{-2} \tag{3}$$

$$f = \int_0^\eta F d\eta + f_w,\ f_w = A\varphi^{-1}[2/(2 + \cos\bar{x})]^{1/2},\quad A = -(w_w/u_\infty)(\mathrm{Re}_L)^{1/2}$$

The initial conditions are obtained by putting

$$\varphi(t^*) = \varphi_1(t^*) = 1,\ \varphi_2(t^*) = \varphi_t^* = (\varphi_1)_t^* = F_t^* = s_t^* = g_t^* = 0 \tag{4}$$

in (1*a-c*). The skin-friction coefficients in the x and y directions (C_f, $\bar{C}_f$) and the heat-transfer coefficient in the terms of Nusselt number Nu are given by

$$\begin{aligned} C_f(\mathrm{Re}_L)^{1/2} &= (9/2)\sin\bar{x}(1 + \cos\bar{x})(2 + \cos\bar{x})^{-1/2}\varphi(t^*)F_w' \\ \bar{C}_f(\mathrm{Re}_L)^{1/2} &= (9/2)\lambda^{1/2}\sin\bar{x}(1 + \cos\bar{x})(2 + \cos\bar{x})^{-1/2}\varphi_1(t^*)s_w' \\ \mathrm{Nu}(\mathrm{Re}_L)^{-1/2} &= (3/2)(1 + \cos\bar{x})(2 + \cos\bar{x})^{-1/2} g_w' \end{aligned} \tag{5}$$

Here $F(f')$ and s are the dimensionless velocity components in the x and y directions, respectively; g is the dimensionless temperature; λ, Br, Pr, and Re_L are, respectively, the rotation parameter, Brinkman number, Prandtl number, and Reynolds number; F_w' and s_w' are the skin-friction parameters in the x and y directions, respectively; g_w' is the heat-transfer parameter; A is a constant, $A > 0$ for suction, and $A < 0$ for injection; φ and φ_1 are arbitrary functions of t^* representing, respectively, the nature of unsteadiness in the free-stream velocity and rotation of the body and have continuous first derivative for $t^* \geq 0$; φ_2 is an arbitrary function of t^* representing the variation of the wall temperature with time. The prime denotes derivatives with respect to η and the subscripts t^* and ξ denote derivatives with respect to t^* and ξ, respectively. Other symbols are defined in [5-6].

Results and Discussion

The set of equations (1) under boundary conditions (2) and initial conditions, obtained by using the relations (4) in (1a-*c*), has been solved numerically using an implicit finite-difference scheme [7]. The unsteady free-stream velocity distributions, rotation of the body, and the wall temperature considered here are, respectively, given by

[1] Research Scholar, Department of Applied Mathematics, Indian Institute of Science, Bangalore-560012, India.

[2] Professor, Department of Applied Mathematics, Indian Institute of Science, Bangalore-560012, India.

Manuscript received by ASME Applied Mechanics Division, April, 1981; Final revision, August, 1981.

Copyright © 1982 by ASME

Downloaded 01 May 2010 to 171.66.16.249. Redistribution subject to ASME license or copyright; see http://www.asme.org/terms/Terms_Use.cfm

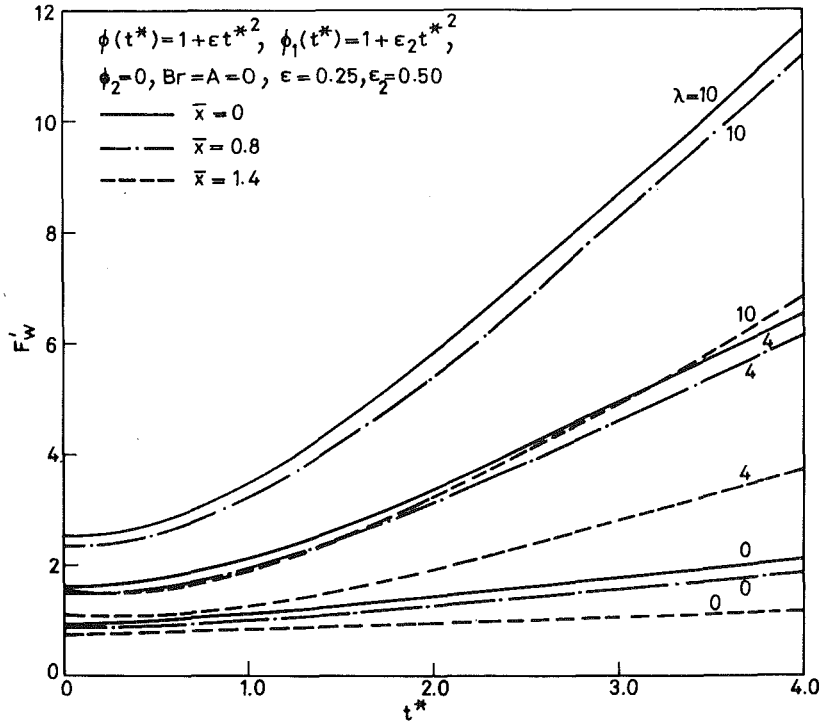


Fig. 1 Effect of rotation of the body on skin friction in the x direction for $t^* \geq 0$

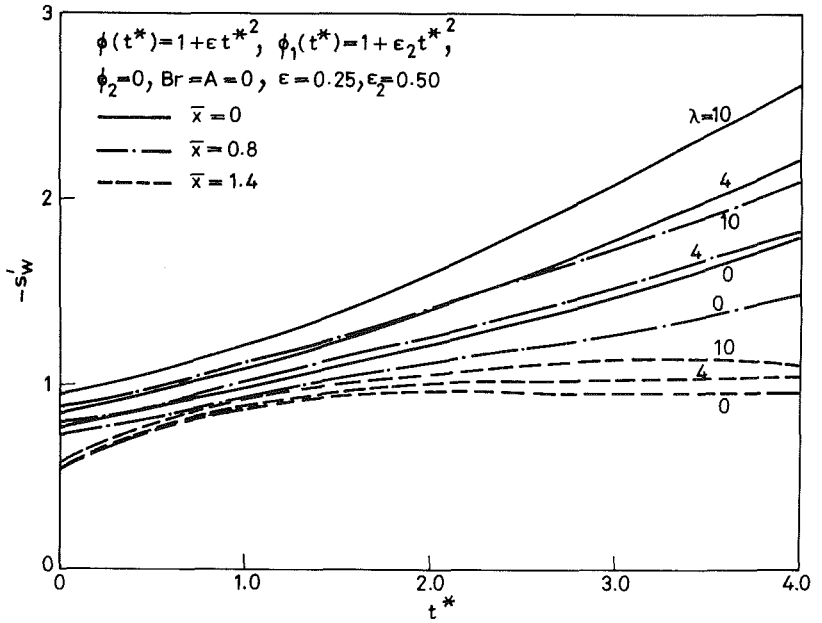


Fig. 2 Effect of rotation of the body on skin friction in the y direction for $t^* \geq 0$

$$\varphi(t^*) = 1+\epsilon t^{*2}, \qquad \varphi(t^*)=1+\epsilon_1 \sin^2(\omega^* t^*)$$
$$\varphi_1(t^*) = 1+\epsilon_2 t^{*2}, \qquad \varphi_2(t^*)=\epsilon_3 t^* \tag{6}$$

where ϵ, ϵ_1, ϵ_2, and ϵ_3 are small positive constants, and ω^* is the frequency parameter. To assess the accuracy of the present method, we have compared our skin-friction and heat-transfer results (F'_w, g'_w) at $t^* = 0$ (steady-state case) with those of finite-difference scheme [6] and found them in excellent agreement.

The skin-friction and heat-transfer results F'_w, $-s'_w$, and g'_w, showing the effects of time and rotation of the body on them at various streamwise locations $\bar{x}$ for the constantly accelerating free-stream velocity distribution $\varphi(t^*) = 1 + \epsilon t^{*2}$, are shown in Figs. 1-3. The skin-friction and heat-transfer parameters F'_w, $-s'_w$, and g'_w ($\varphi_2(t^*) = 0$) increase as t^* increases (in some cases after a certain time t^*). The rate of increase is more pronounced when the body rotates ($\lambda > 0$) than when it is at rest ($\lambda = 0$). Also, F'_w, $-s'_w$, and g'_w increase as λ increases, but they decrease as $\bar{x}$ increases. Figure 3 also shows the effect of the variation of wall temperature with time on heat transfer (skin friction is unaffected). When the wall temperature increases with time ($\varphi_2(t^*)=\epsilon_3 t^*$, $\epsilon_3 > 0$), g'_w continuously decreases, whereas for the constant wall temperature case ($\varphi_2(t^*) \downarrow 0$), it generally increase with time. The effect of the wall temperature decreasing with time results in increase in g'_w with time (not shown in the figure).

Downloaded 01 May 2010 to 171.66.16.249. Redistribution subject to ASME license or copyright; see http://www.asme.org/terms/Terms_Use.cfm

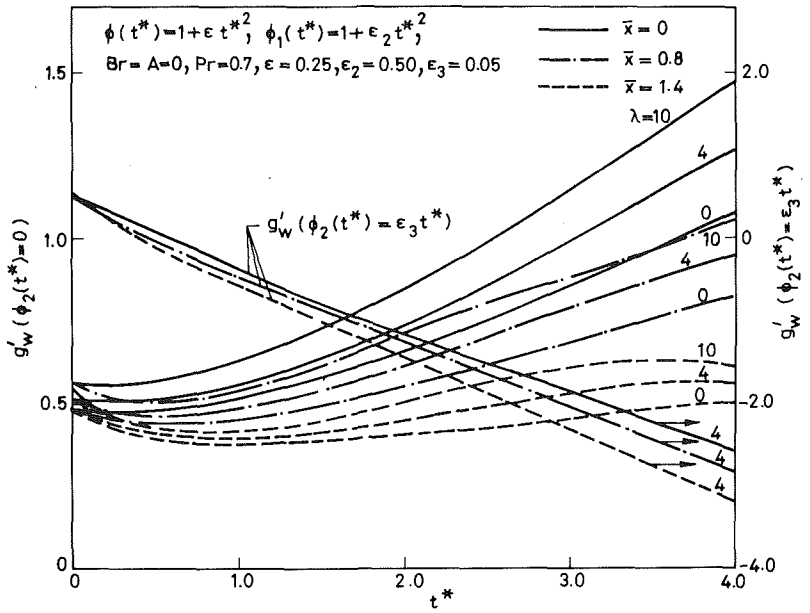


Fig. 3 Effect of rotation of the body on heat transfer for $t^* \geq 0$

The effect of mass transfer on F'_w, $-s'_w$, and g'_w, and the effect of the Prandtl number Pr and the Brinkman number Br (dissipation parameter) on g'_w have also been studied, but not shown in the figures for the sake of brevity.[3] As expected, suction ($A > 0$) increases F'_w, $-s'_w$, and g'_w, whereas injection ($A < 0$) does the reverse. Furthermore, suction delays the separation, whereas injection causes the separation to occur earlier. It is found that g'_w is strongly affected by both Pr and Br. For small values of Pr, the thermal boundary layer is much thicker than the velocity boundary layer. The effect of the rotation of the body λ and time t^* on the separation of the fluid from the boundary has been investigated, and it is found that both λ and t^* cause the point of separation (i.e., the point of zero skin friction ($F'_w = 0$)) to move forward toward the equator ($\bar{x} = \pi/2$). However, they are not shown here to conserve space.[3]

The effects of oscillatory free-stream velocity $\varphi(t^*) = 1 + \epsilon_1 \sin^2(\omega^* t^*)$ on the skin friction and heat transfer (F'_w, $-s'_w$, g'_w) have been considered, but to limit the number of figures, they are not presented here.[3] It is observed that for the stationary body ($\lambda = 0$) F'_w responds more to the fluctuations of the free-stream velocity as compared to $-s'_w$ and g'_w. For the rotating body ($\lambda > 0$), F'_w, $-s'_w$, and g'_w respond more to the unsteadiness in the rotation of the body than to the free-stream velocity distribution.

Conclusions

The unsteady free-stream velocity distribution and rotation of the body strongly affect the skin friction and heat transfer. Rotation of the body, unsteadiness, and injection cause the separation to occur earlier. Prandtl number, dissipation parameter, and the variation of the wall temperature with time strongly affect the heat transfer and the effect is more pronounced for large times. Suction increases the skin friction and heat transfer, whereas injection does the reverse.

References

1 Hoskin, N. E., "The Laminar Boundary Layer on a Rotating Sphere," In Gortler, H., and Tollmien, W., eds., 50 Jahre Grenzschichtforchung, *Fredr. Vieweg u. Sohn Braunschweig*, 1955, pp. 127-131.

2 Siekmann, I., "The Calculation of the Thermal Laminar Boundary Layer on Rotating Sphere," *S. Angew. Math. Phys.*, Vol. 13, No. 5, 1962, pp. 468-482.

3 Chao, B. T., and Grief, R., "Laminar Forced Convection over Rotating Bodies," ASME *Journal of Heat Transfer*, Vol. 96, No. 4, Nov. 1974, pp. 463-466.

4 Chao, B. T., "An Analysis of Forced Convection over Nonisothermal Surfaces via Universal Functions," *Recent Advances in Engineering Science, Proceedings of the 4th Annual Meeting of the Society of Engineering Science*, Lehigh University, 1977, pp. 471-483.

5 Lee, M. H., Jeng, D. R., and DeWitt, K. T., "Laminar Boundary Layer Transfer over Rotating Bodies in Forced Flow," ASME *Journal of Heat Transfer*, Vol. 100, No. 3, Aug. 1978, pp. 496-502.

6 Kumari, M., "Investigation of Laminar Boundary-Layer Flows Using Finite-Difference Method," Ph.D. Thesis, Indian Institute of Science, Bangalore, Chapter II, 1980.

7 Marvin, J. G., and Sheaffer, Y. S., "A Method for Solving Nonsimilar Laminar Boundary Layer Equations Including Foreign Gas Injection," NASA TN5516, 1969.

[3] They may be obtained from the authors.

Photoelastic Analysis of the Stress Field Around Cuspidal Points of Rigid Inclusions

E. E. Gdoutos[1]

The stress field around a cuspidal point of a rigid inclusion embedded in an elastic plate can be expressed in terms of two stress-intensity factors k_1 and k_2 in an analogous manner as in the case of a crack under mixed-mode loading conditions [1]. As in crack problems the stresses present an inverse square root singularity. It is the objective of the present work to present computer generated isochromatic patterns around cuspidal points of rigid inclusions and to show that the method of photoelasticity can be used for the determination of k_1 and k_2.

Introducing the expressions of the stress components into the photoelastic stress-optical law we obtain after lengthy calculations the following expression for the radius r of the isochromatic fringe of order N:

[1] Professor of Applied Mechanics, Democritus University of Thrace, Xanthi, Greece; present address, Institute of Fracture and Solid Mechanics, Packard Laboratory, Building 19, Lehigh University, Bethlehem, Pa. 18015. Mem. ASME.

Manuscript received by ASME Applied Mechanics Division, March, 1981; final revision, June, 1981.

Downloaded 01 May 2010 to 171.66.16.249. Redistribution subject to ASME license or copyright; see http://www.asme.org/terms/Terms_Use.cfm

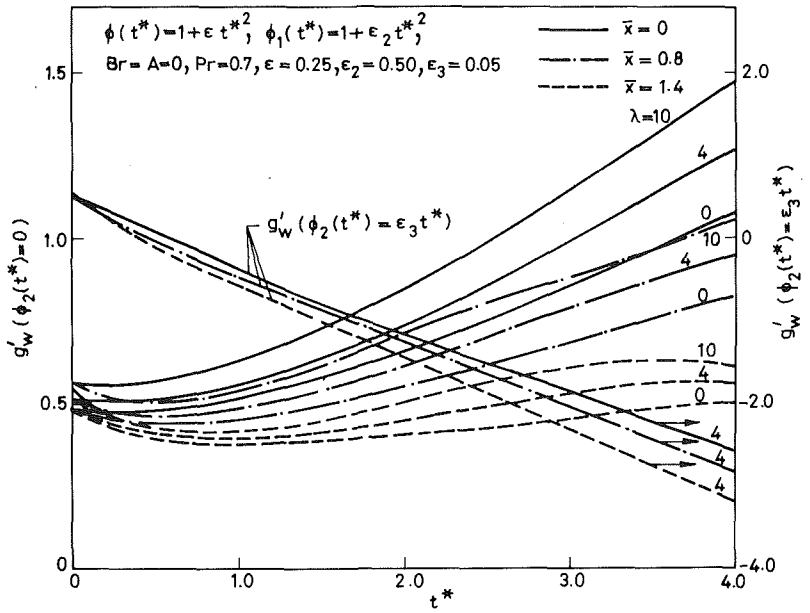


Fig. 3 Effect of rotation of the body on heat transfer for $t^* \geq 0$

The effect of mass transfer on F'_w, $-s'_w$, and g'_w, and the effect of the Prandtl number Pr and the Brinkman number Br (dissipation parameter) on g'_w have also been studied, but not shown in the figures for the sake of brevity.[3] As expected, suction ($A > 0$) increases F'_w, $-s'_w$, and g'_w, whereas injection ($A < 0$) does the reverse. Furthermore, suction delays the separation, whereas injection causes the separation to occur earlier. It is found that g'_w is strongly affected by both Pr and Br. For small values of Pr, the thermal boundary layer is much thicker than the velocity boundary layer. The effect of the rotation of the body λ and time t^* on the separation of the fluid from the boundary has been investigated, and it is found that both λ and t^* cause the point of separation (i.e., the point of zero skin friction ($F'_w = 0$)) to move forward toward the equator ($\bar{x}=\pi/2$). However, they are not shown here to conserve space.[3]

The effects of oscillatory free-stream velocity $\varphi(t^*) = 1 + \epsilon_1 \sin^2(\omega^* t^*)$ on the skin friction and heat transfer (F'_w, $-s'_w$, g'_w) have been considered, but to limit the number of figures, they are not presented here.[3] It is observed that for the stationary body ($\lambda = 0$) F'_w responds more to the fluctuations of the free-stream velocity as compared to $-s'_w$ and g'_w. For the rotating body ($\lambda > 0$), F'_w, $-s'_w$, and g'_w respond more to the unsteadiness in the rotation of the body than to the free-stream velocity distribution.

Conclusions

The unsteady free-stream velocity distribution and rotation of the body strongly affect the skin friction and heat transfer. Rotation of the body, unsteadiness, and injection cause the separation to occur earlier. Prandtl number, dissipation parameter, and the variation of the wall temperature with time strongly affect the heat transfer and the effect is more pronounced for large times. Suction increases the skin friction and heat transfer, whereas injection does the reverse.

References

1 Hoskin, N. E., "The Laminar Boundary Layer on a Rotating Sphere," In Gortler, H., and Tollmien, W., eds., 50 Jahre Grenzschichtforchung, *Fredr. Vieweg u. Sohn Braunschweig*, 1955, pp. 127–131.

2 Siekmann, I., "The Calculation of the Thermal Laminar Boundary Layer on Rotating Sphere," *S. Angew. Math. Phys.*, Vol. 13, No. 5, 1962, pp. 468–482.

3 Chao, B. T., and Grief, R., "Laminar Forced Convection over Rotating Bodies," ASME *Journal of Heat Transfer*, Vol. 96, No. 4, Nov. 1974, pp. 463–466.

4 Chao, B. T., "An Analysis of Forced Convection over Nonisothermal Surfaces via Universal Functions," *Recent Advances in Engineering Science, Proceedings of the 4th Annual Meeting of the Society of Engineering Science*, Lehigh University, 1977, pp. 471–483.

5 Lee, M. H., Jeng, D. R., and DeWitt, K. T., "Laminar Boundary Layer Transfer over Rotating Bodies in Forced Flow," ASME *Journal of Heat Transfer*, Vol. 100, No. 3, Aug. 1978, pp. 496–502.

6 Kumari, M., "Investigation of Laminar Boundary-Layer Flows Using Finite-Difference Method," Ph.D. Thesis, Indian Institute of Science, Bangalore, Chapter II, 1980.

7 Marvin, J. G., and Sheaffer, Y. S., "A Method for Solving Nonsimilar Laminar Boundary Layer Equations Including Foreign Gas Injection," NASA TN5516, 1969.

[3] They may be obtained from the authors.

Photoelastic Analysis of the Stress Field Around Cuspidal Points of Rigid Inclusions

E. E. Gdoutos[1]

The stress field around a cuspidal point of a rigid inclusion embedded in an elastic plate can be expressed in terms of two stress-intensity factors k_1 and k_2 in an analogous manner as in the case of a crack under mixed-mode loading conditions [1]. As in crack problems the stresses present an inverse square root singularity. It is the objective of the present work to present computer generated isochromatic patterns around cuspidal points of rigid inclusions and to show that the method of photoelasticity can be used for the determination of k_1 and k_2.

Introducing the expressions of the stress components into the photoelastic stress-optical law we obtain after lengthy calculations the following expression for the radius r of the isochromatic fringe of order N:

[1] Professor of Applied Mechanics, Democritus University of Thrace, Xanthi, Greece; present address, Institute of Fracture and Solid Mechanics, Packard Laboratory, Building 19, Lehigh University, Bethlehem, Pa. 18015. Mem. ASME.

Manuscript received by ASME Applied Mechanics Division, March, 1981; final revision, June, 1981.

Copyright © 1982 by ASME
Downloaded 01 May 2010 to 171.66.16.249. Redistribution subject to ASME license or copyright; see http://www.asme.org/terms/Terms_Use.cfm

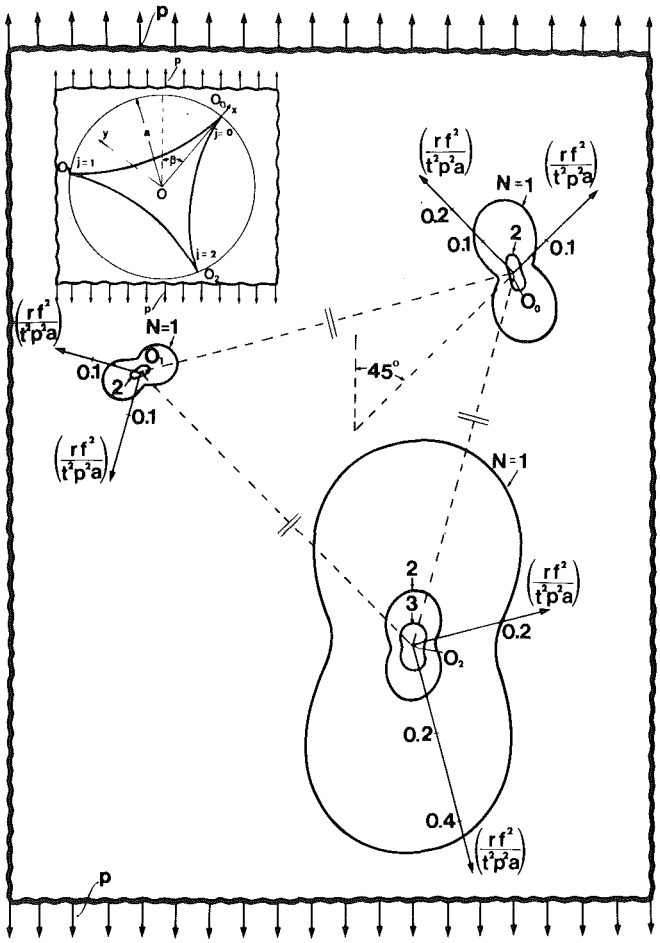


Fig. 1 Isochromatic patterns developed at the cuspidal points $j = 0$ (0_0) and $j = 3$ (0_3) of an astroidal inclusion for $\beta = 30°$ and $\kappa = 1.8$

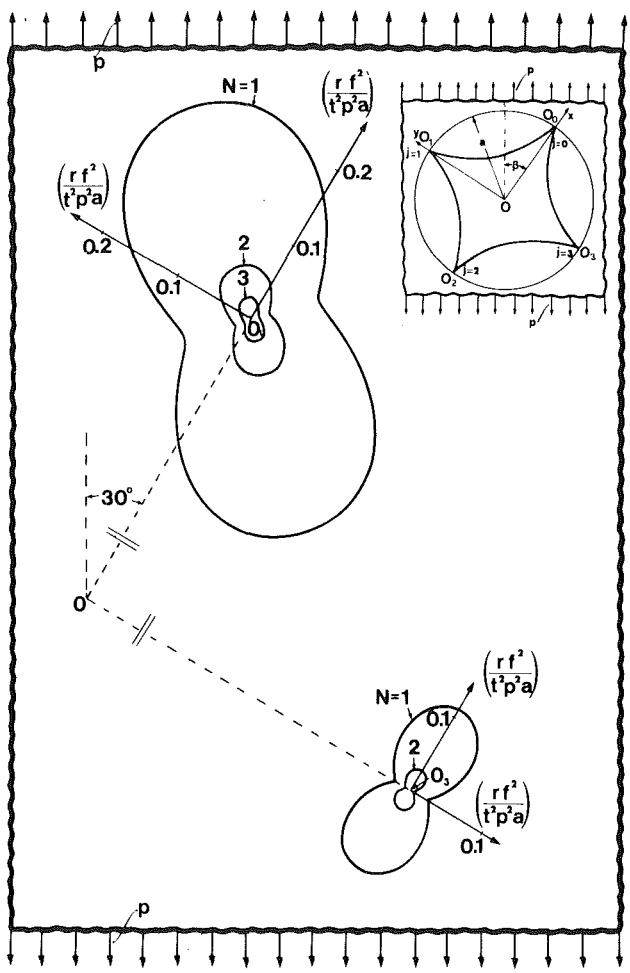


Fig. 2 Isochromatic patterns developed at the cuspidal points $j = 0$ (0_0), $j = 1$ (0_1) and $j = 2$ (0_2) of a hypocycloidal inclusion for $\beta = 45°$ and $\kappa = 1.8$

$$r = \frac{1}{2}\left(\frac{t}{Nf}\right)^2 (a_{11}k_1^2 + 2a_{12}k_1k_2 + a_{22}k_2^2) \tag{1}$$

with

$$\begin{aligned} a_{11} &= (1+\kappa)^2 - (1+2\kappa)\sin^2\theta \\ a_{12} &= -\kappa \sin 2\theta \\ a_{22} &= (1-\kappa)^2 + (2\kappa-1)\sin^2\theta \end{aligned} \tag{2}$$

In these relations f is the stress-optical constant of the material of the matrix, t the thickness of the plate, and κ is equal to 3-4ν or (3-ν)/(1 + ν) for plane-strain or generalized plane-stress conditions, respectively, with ν the Poisson's ratio. The polar angle θ is measured in a counterclockwise sense from the tangent of the inclusion at the cuspidal point.

It is worthwhile to observe that relations (1) and (2) for $\kappa = -1$ give the well-known formula of the radius of the isochromatic fringes for the case of a crack in a mixed mode stress field (reference [2], relation 9)). However, the value $\kappa = -1$ does not have any physical significance.

In order to obtain an idea of the form of isochromatic patterns we will consider the cases of the astroidal and hypocycloidal inclusions embedded in a plate which is subjected to uniaxial tension.

For the astroidal inclusion (Fig. 1) the stress-intensity factors k_1 and k_2 are given by [1]

$$\begin{aligned} k_1^{(j)} &= \frac{\sqrt{3a}}{4\kappa} p\left[\frac{k-1}{2} + \frac{3k}{3k+1}\cos(\pi j - 2\beta)\right] \\ k_2^{(j)} &= \frac{\sqrt{3a}}{4} p \frac{3}{3\kappa-1}\sin(\pi j - 2\beta) \end{aligned} \tag{3}$$

with $j = 0, 1, 2, 3$ for the four cuspidal points of the inclusion.

Introducing these expressions of stress-intensity factors into relations (1) and (2) we obtain the values of the non-dimensional quantity (rN^2f^2/t^2p^2a) for each of the four cuspidal points of the inclusion as a function of the angle β of inclination of the inclusion and the material constant κ of the matrix.

Figure 1 presents the isochromatic patterns developed at the cuspidal points $j = 0$ (0_0) and $j = 3$ (0_3) of the astroidal inclusion for $\beta = 30°$. The material constant κ took the value 1.8. We observe that the isochromatic fringes form closed loops which do not pass from the cuspidal points as it happens in the case of cracks.

For the hypocycloidal inclusion (Fig. 2) the stress-intensity factors k_1 and k_2 are given by [1]

$$\begin{aligned} k_1^{(j)} &= \frac{\sqrt{2a}}{3\kappa} p\left[\frac{\kappa-1}{2} + \cos\left(\frac{4\pi j}{3} - 2\beta\right)\right] \\ k_2^{(j)} &= \frac{\sqrt{2a}}{3\kappa} p \sin\left(\frac{4\pi j}{3} - 2\beta\right) \quad j = 0, 1, 2 \end{aligned} \tag{4}$$

Working as in the previous case of the astroidal inclusion the isochromatic patterns around all three cuspidal points were determined. Fig. 2 presents these patterns for $\beta = 45°$.

The isochromatic patterns developed around the cuspidal points of rigid inclusions can be used for the determination of k_1 and k_2 stress-intensity factors. As in crack problems, one easily measurable quantity in the isochromatic pattern is the

Downloaded 01 May 2010 to 171.66.16.249. Redistribution subject to ASME license or copyright; see http://www.asme.org/terms/Terms_Use.cfm

angle θ_m that the tangent of the inclusion at the cuspidal point subtends with the line connecting this point with the farthest point on a given isochromatic loop. The condition of determining the position on an isochromatic loop which has the largest distance from the cuspidal point is expressed by the following relation:

$$\frac{\partial \tau_{\max}}{\partial \theta} = 0 \tag{5}$$

which by taking into account relations (1) and (2) leads to the following equation:

$$\frac{2\kappa - 1}{2\kappa + 1}\left(\frac{k_2}{k_1}\right)^2 - \frac{4\kappa}{2\kappa + 1}\left(\frac{k_2}{k_1}\right)\cot 2\theta_m - 1 = 0 \tag{6}$$

Equation (6) for $k = -1$ gives the well-known equation for the case of a crack in a mixed-mode stress field (equation (15) of reference [2]). This equation enables the direct determination of the ratio (k_2/k_1) by measuring the angle θ_m on the isochromatic loops. If now the thus determined ratio (k_2/k_1) is introduced into equations (1) and (2) the value of k_1 can be determined from one measurement on the isochromatic pattern.

Determination of k_1 and k_2 can also be made by applying relations (1) and (2) to two points of the isochromatic pattern with known values of the fringe order N. The values of k_1 and k_2 are calculated from the solution of the derived system of two equations with unknowns k_1 and k_2. It is evident that the measurements on the isochromatic pattern must be made in the close vicinity of the cuspidal point since, as we recede from it, relations (1) and (2) do not hold any more. For such cases, higher-order terms should be incorporated into the expressions of the stress components.

References

1 Panasyuk, V. V., Berezhnitskii, L. T., and Trush, I. I., "Stress Distribution About Defects Such as Rigid Sharp-Angled Inclusions," *Problemy Prochnosti,* Vol. 7, 1972, pp. 3–9.

2 Gdoutos, E. E., and Theocaris, P. S., "A Photoelastic Determination of Mixed-Mode Stress-Intensity Factors," *Experimental Mechanics,* Vol. 18, 1978, pp. 87–96.

Boundary Condition Effect on Forced Torsional Vibrations of a Cylindrical Rod Connected to an Elastic Half Space

H. Wada[1]

Introduction

When torsional vibrations of a cylindrical rod, one end of which is connected to an elastic half space, are considered, the boundary conditions at the interface between the rod and the half space are the continuity of circumferential displacement and that of shear stress. However, when the elementary theory of torsional vibrations is applied, it is impossible to satisfy the boundary conditions at the interface exactly, because the displacement and stress on the cross section of the rod are assumed to undergo a pure rotation about the rod axis. Therefore, the approximate boundary conditions must be devised. This Note discusses the effect of these approximate boundary conditions on the response curves of the system.

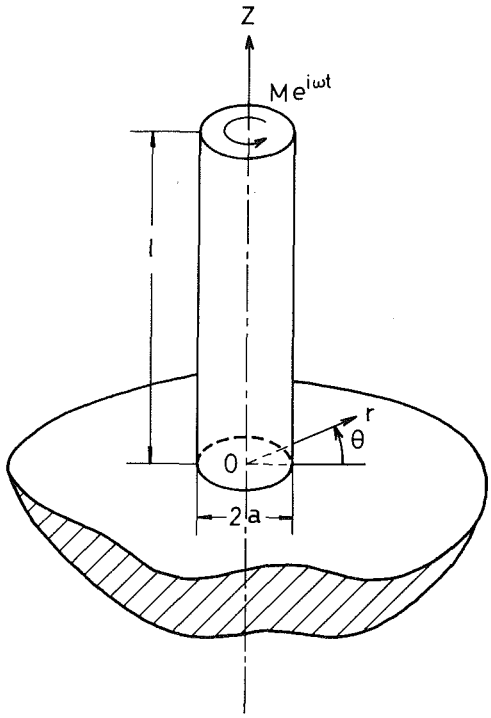


Fig. 1 Cylindrical rod connected to elastic half space

Analysis

As shown in Fig. 1, consider an elastic cylindrical rod of length l and radius a, one end of which is attached to an elastic half space and the other end subjected to a harmonic disturbing moment $Me^{i\omega t}$. The rotation of the rod is taken to be θ_R. Then, the corresponding equation for the torsional vibrations of the rod is

$$\frac{\partial^2 \theta_R}{\partial t^2} = C_R^2 \frac{\partial^2 \theta_R}{\partial z^2}, \tag{1}$$

with

$$C_R = \sqrt{G_R/\rho_R}, \tag{2}$$

where ρ_R is the density of the rod, G_R is the shear modulus, and t is the time. The equation of motion for the half space is

$$\frac{\partial^2 v}{\partial z^2} + \frac{\partial}{\partial r}\left\{\frac{1}{r}\frac{\partial}{\partial r}(rv)\right\} = \frac{1}{C^2}\frac{\partial^2 v}{\partial t^2}, \tag{3}$$

with

$$C = \sqrt{G/\rho}, \tag{4}$$

where v is the circumferential displacement component, ρ is the density, and G is the shear modulus.

At the interface between the rod and the half space, the displacement and stress must be continuous. Therefore, the boundary conditions become

$$v(r,0,t) = r\theta_R, \quad 0 \leqq r \leqq a, \tag{5}$$

$$\tau_{Z\theta}(r,0,t) = G_R r \partial\theta_R/\partial z, \quad 0 \leqq r \leqq a, \tag{6a}$$

$$= 0, \quad a < r. \tag{6b}$$

However, as just mentioned, it is impossible to satisfy boundary conditions (5) and (6) simultaneously. Consequently, two specific boundary conditions are considered: i.e., linear shear stress distribution at the interface (A) and linear circumferential displacement distribution at the interface (B).

[1] Instructor, Department of Mechanical Engineering, Tohoku University, Sendai 980, Japan.

Manuscript received by ASME Applied Mechanics Division, December, 1980.

Downloaded 01 May 2010 to 171.66.16.249. Redistribution subject to ASME license or copyright; see http://www.asme.org/terms/Terms_Use.cfm

angle θ_m that the tangent of the inclusion at the cuspidal point subtends with the line connecting this point with the farthest point on a given isochromatic loop. The condition of determining the position on an isochromatic loop which has the largest distance from the cuspidal point is expressed by the following relation:

$$\frac{\partial \tau_{\max}}{\partial \theta} = 0 \tag{5}$$

which by taking into account relations (1) and (2) leads to the following equation:

$$\frac{2\kappa - 1}{2\kappa + 1}\left(\frac{k_2}{k_1}\right)^2 - \frac{4\kappa}{2\kappa + 1}\left(\frac{k_2}{k_1}\right)\cot 2\theta_m - 1 = 0 \tag{6}$$

Equation (6) for $k = -1$ gives the well-known equation for the case of a crack in a mixed-mode stress field (equation (15) of reference [2]). This equation enables the direct determination of the ratio (k_2/k_1) by measuring the angle θ_m on the isochromatic loops. If now the thus determined ratio (k_2/k_1) is introduced into equations (1) and (2) the value of k_1 can be determined from one measurement on the isochromatic pattern.

Determination of k_1 and k_2 can also be made by applying relations (1) and (2) to two points of the isochromatic pattern with known values of the fringe order N. The values of k_1 and k_2 are calculated from the solution of the derived system of two equations with unknowns k_1 and k_2. It is evident that the measurements on the isochromatic pattern must be made in the close vicinity of the cuspidal point since, as we recede from it, relations (1) and (2) do not hold any more. For such cases, higher-order terms should be incorporated into the expressions of the stress components.

References

1 Panasyuk, V. V., Berezhnitskii, L. T., and Trush, I. I., "Stress Distribution About Defects Such as Rigid Sharp-Angled Inclusions," *Problemy Prochnosti,* Vol. 7, 1972, pp. 3–9.

2 Gdoutos, E. E., and Theocaris, P. S., "A Photoelastic Determination of Mixed-Mode Stress-Intensity Factors," *Experimental Mechanics,* Vol. 18, 1978, pp. 87–96.

Boundary Condition Effect on Forced Torsional Vibrations of a Cylindrical Rod Connected to an Elastic Half Space

H. Wada[1]

Introduction

When torsional vibrations of a cylindrical rod, one end of which is connected to an elastic half space, are considered, the boundary conditions at the interface between the rod and the half space are the continuity of circumferential displacement and that of shear stress. However, when the elementary theory of torsional vibrations is applied, it is impossible to satisfy the boundary conditions at the interface exactly, because the displacement and stress on the cross section of the rod are assumed to undergo a pure rotation about the rod axis. Therefore, the approximate boundary conditions must be devised. This Note discusses the effect of these approximate boundary conditions on the response curves of the system.

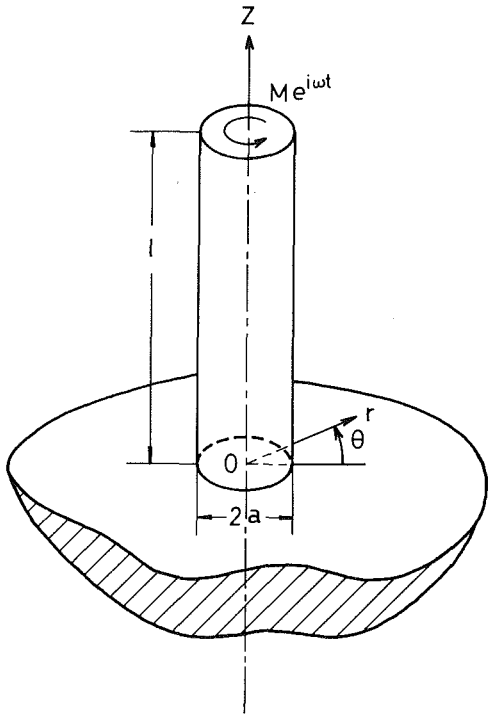


Fig. 1 Cylindrical rod connected to elastic half space

Analysis

As shown in Fig. 1, consider an elastic cylindrical rod of length l and radius a, one end of which is attached to an elastic half space and the other end subjected to a harmonic disturbing moment $Me^{i\omega t}$. The rotation of the rod is taken to be θ_R. Then, the corresponding equation for the torsional vibrations of the rod is

$$\frac{\partial^2 \theta_R}{\partial t^2} = C_R^2 \frac{\partial^2 \theta_R}{\partial z^2}, \tag{1}$$

with

$$C_R = \sqrt{G_R/\rho_R}, \tag{2}$$

where ρ_R is the density of the rod, G_R is the shear modulus, and t is the time. The equation of motion for the half space is

$$\frac{\partial^2 v}{\partial z^2} + \frac{\partial}{\partial r}\left\{\frac{1}{r}\frac{\partial}{\partial r}(rv)\right\} = \frac{1}{C^2}\frac{\partial^2 v}{\partial t^2}, \tag{3}$$

with

$$C = \sqrt{G/\rho}, \tag{4}$$

where v is the circumferential displacement component, ρ is the density, and G is the shear modulus.

At the interface between the rod and the half space, the displacement and stress must be continuous. Therefore, the boundary conditions become

$$v(r,0,t) = r\theta_R, \quad 0 \leqq r \leqq a, \tag{5}$$

$$\tau_{Z\theta}(r,0,t) = G_R r \partial\theta_R/\partial z, \quad 0 \leqq r \leqq a, \tag{6a}$$

$$= 0, \quad a < r. \tag{6b}$$

However, as just mentioned, it is impossible to satisfy boundary conditions (5) and (6) simultaneously. Consequently, two specific boundary conditions are considered: i.e., linear shear stress distribution at the interface (A) and linear circumferential displacement distribution at the interface (B).

[1] Instructor, Department of Mechanical Engineering, Tohoku University, Sendai 980, Japan.

Manuscript received by ASME Applied Mechanics Division, December, 1980.

Copyright © 1982 by ASME
Downloaded 01 May 2010 to 171.66.16.249. Redistribution subject to ASME license or copyright; see http://www.asme.org/terms/Terms_Use.cfm

(*A*) Linear Shear Stress Distribution at the Interface. In this case, boundary condition (6) is applicable. Instead of the rotation of the half space at the interface θ_h $(= v(r, 0, t)/r)$, the approximate mean rotation $\theta_{h,\text{mean}}$ is developed in the following form:

$$\theta_{h,\text{mean}} = \frac{1}{\pi a^2}\int_0^{2\pi}\int_0^a \theta_h r dr d\theta = \frac{2}{a^2}\int_0^a v(r,0,t)\,dr. \tag{7}$$

This mean rotation is considered to be equal to that of the rod. Taking account of these equations and introducing the following dimensionless quantities:

$$\Omega = \omega l/C_R, \quad K = C_R/C, \quad \kappa = a/l, \tag{8}$$

the rotation of the rod at $z = l$ is ultimately obtained as

$$\Theta = \theta_{R,z=l}\Big/\frac{Ml}{G_R I_R} = \frac{2(G_R/G)\Omega F_1 \cos\Omega + \sin\Omega}{\Omega\{-2(G_R/G)\Omega F_1 \sin\Omega + \cos\Omega\}} e^{i\omega t}, \tag{9}$$

with

$$I_R = \pi a^4/2, \tag{10}$$

$$F_1 = \int_0^\infty \frac{1}{\sqrt{\zeta^2 - K^2\Omega^2}} J_2(\zeta\kappa)\{1 - J_0(\zeta\kappa)\}\frac{d\zeta}{\zeta}, \tag{11}$$

where $J_n(\ )$ is the Bessel function of order n. This equation coincides with [1, 2].

(*B*) Linear Circumferential Displacement Distribution at the Interface. Next, boundary conditions (5) and (6*b*) are applied. Utilizing essentially the same method as [3], the rotation of the half space at the interface is obtained as

$$\theta_H = \frac{9}{8}\frac{G_R}{G}\frac{I_R}{\pi a^3}\frac{\partial\theta_R}{\partial z}_{z=0} \int_0^\infty \frac{1}{\alpha}\frac{\{\sin(\xi a) - \xi a\cos(\xi a)\}^2}{(\xi a)^3} d\xi e^{i\omega t}, \tag{12}$$

where

$$\alpha = \sqrt{\xi^2 - \omega^2/C^2}. \tag{13}$$

Substituting equation (12) into boundary condition (5), the rotation of the rod at $z = l$ is evaluated as

$$\Theta = \theta_{R,z=l}\Big/\frac{Ml}{G_R I_R} = \frac{\frac{9}{16}\frac{G_R}{G}\kappa\Omega F_2 \cos\Omega + \sin\Omega}{\Omega\left(-\frac{9}{16}\frac{G_R}{G}\kappa\Omega F_2 \sin\Omega + \cos\Omega\right)} e^{i\omega t}, \tag{14}$$

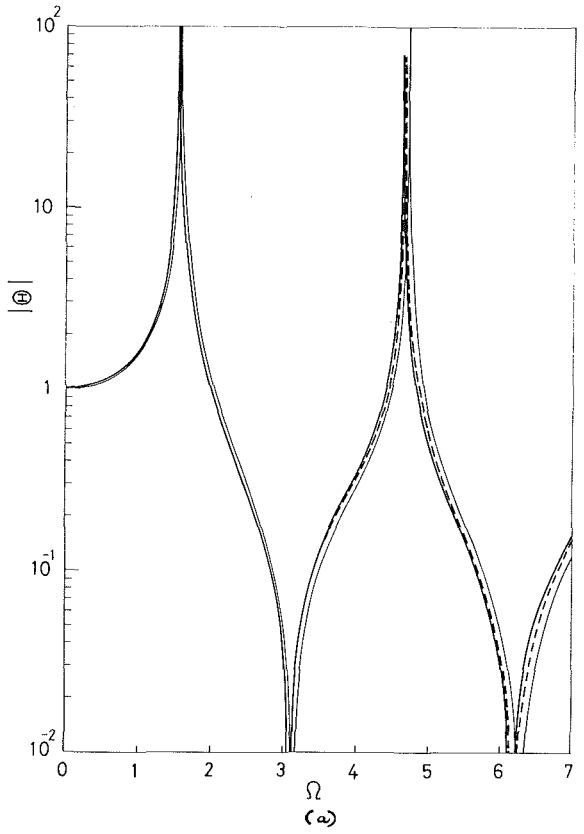
where

$$F_2 = \int_0^\infty \frac{1}{\sqrt{\zeta^2 - K^2\Omega^2}} \frac{\{\sin(\zeta\kappa) - \zeta\kappa\cos(\zeta\kappa)\}^2}{(\zeta\kappa)^3} d\zeta. \tag{15}$$

Numerical Results and Conclusions

Given the values of shear modulus ratio G_R/G, velocity ratio K and slenderness ratio κ, the relationships between rotational amplitude of the rod at $z = l$, $|\Theta|$, and the forcing frequency Ω are obtained. In Fig. 2, the solid line curves are derived from linear shear stress distribution (*A*), the broken line curves from linear circumferential displacement distribution (*B*) and the fine solid line curves from the limiting case of a rigid half space.

Comparing the curves of Case (*A*) with those of Case (*B*), it can be seen that the curves almost coincide with each other when $G_R/G = 1$ and $K = 1$ as shown in Fig. 2(*a*), and that the differences are still small even when G_R/G and K are large as depicted in Fig. 2(*b*). Therefore, it may be said that the shape of shear stress distribution at the interface has almost no effect on the response curves of the system. Since Case (*A*) will give the lower limit of the shear stress distribution at the interface and Case (*B*) the upper limit, it might be more accurate to assume that the actual state of the response curves is given by the mean of the respective values of Cases (*A*) and (*B*).



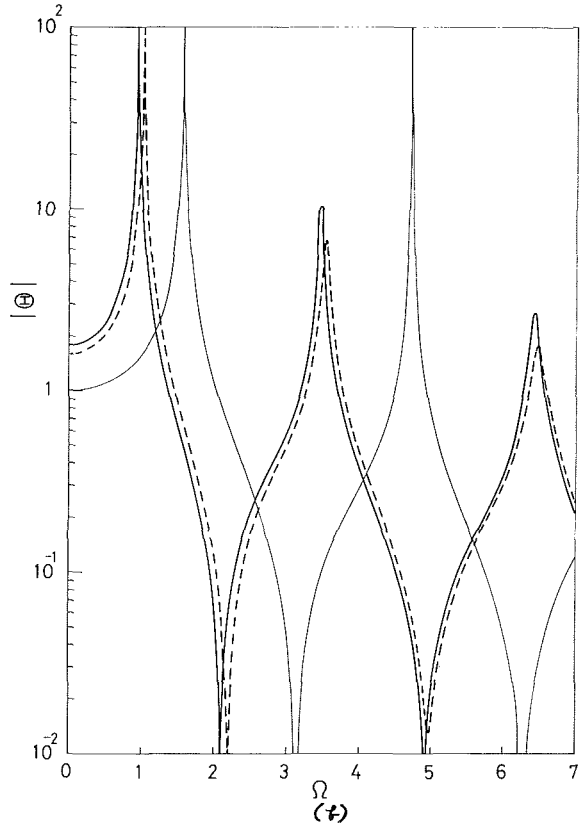


Fig. 2 Response curves of the rotation at the free end of the rod. (*a*) $G_R/G = 1, K = 1, \kappa = 0.05$; (*b*) $G_R/G = 20, K = 3, \kappa = 0.1$. ——, linear shear stress distribution; -----, linear circumferential displacement distribution; ——, $G = \infty$.

Downloaded 01 May 2010 to 171.66.16.249. Redistribution subject to ASME license or copyright; see http://www.asme.org/terms/Terms_Use.cfm

Acknowledgment

The author is deeply indebted to Professor Hideo Saito of Tohoku University for his consistent guidance.

References

1 Paul, H. S., and Sridharan, K., "Forced Torsional Vibration of an Elastic Circular Rod on an Elastic Half Space and on an Elastic Stratum," *Journal of the Acoustical Society of America*, Vol. 65, 1979, pp. 391–398.

2 Wada, H., "Forced Torsional Vibrations of a Cylindrical Rod Connected to an Elastic Half Space," *Journal of Sound and Vibration*, Vol. 66, No. 2, 1979, pp. 265–275.

3 Saito, H., and Wada, H., "Forced Vibrations of a Mass Connected to an Elastic Half Space by an Elastic Rod or a Spring," *Journal of Sound and Vibration*, Vol. 50, No. 4., 1977, pp. 519–532.

Dynamic Response of Rigid-Plastic Circular Plates in a Damping Medium

A. Kumar[1] and M. Hegde[2]

Introduction

In this Note, the motion of a thin circular plate (radius R) of rigid-plastic material in a damping medium is studied. The plate is subjected to a uniformly distributed load which is applied suddenly at time $t = 0$, kept constant at an intensity p during $0 < t < \tau$, and suddenly removed at $t = \tau$. The plate material obeys the Tresea yield criterion and the associated flow rule. The damping resistance is taken to be $f = \alpha V$ where V is the transverse velocity of the plate and α is a constant. Hopkins and Prager [1] studied the problem when damping was absent and found that the nature of the motion depends on whether the load is medium ($p_0 < p \leq 2p_0$) or high ($p > 2p_0$), where p_0 is the static limit load intensity.

In the present case, the equation of dynamic equilibrium is

$$\frac{\partial}{\partial r}(rM) - N = -\int_0^r (p - \mu\ddot{w} - \alpha\dot{w})\, r\, dr \qquad (1)$$

where M and N are the radial and the circumferential moments, respectively, μ is the mass per unit area of the middle surface whose deflection is w, and dots indicate differentiation with respect to time. Following a procedure similar to that in [1], the results are summarized as follows.

Medium Load

Phase I. $(0 < t < \tau)$. The moment distribution is

$$\frac{M}{M_0} = 1 - \frac{pr^2}{p_0 R^2} + \frac{r^2}{R^2}\left(2 - \frac{r}{R}\right)\left(\frac{p}{p_0} - 1\right) \qquad (2)$$

The central deflection is given by

$$w(0,t) = \frac{2(p-p_0)}{\alpha}\left[t + \frac{\mu}{\alpha}\left\{\exp\left(-\frac{\alpha t}{\mu}\right) - 1\right\}\right] \qquad (3)$$

Phase II. $(\tau < t < T)$. The plate comes to rest at time T given by

$$T = \frac{\mu}{\alpha}\log\left[\frac{p}{p_0}\left\{\exp\left(\frac{\alpha\tau}{\mu}\right) - 1\right\} + 1\right] \qquad (4)$$

Then, the final deflection is of the form

$$w(r,T) = \frac{2p}{\alpha}\left(\tau - \frac{p_0}{p}T\right)\left(1 - \frac{r}{R}\right) \qquad (5)$$

The variation of the moment M is given as

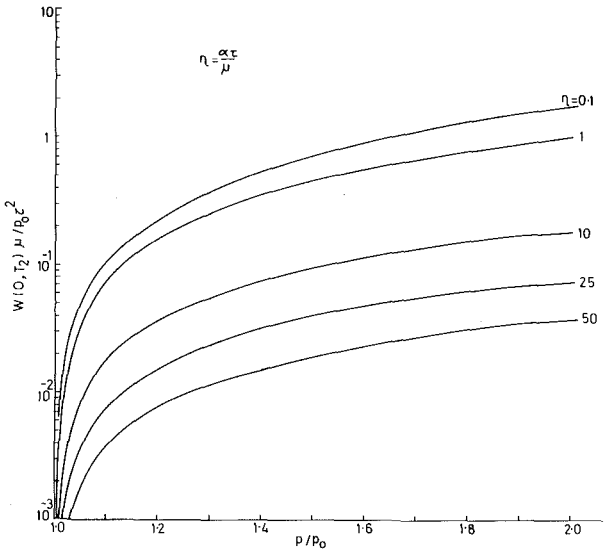


Fig. 1 Effect of damping on central plate deflection for the case of medium load

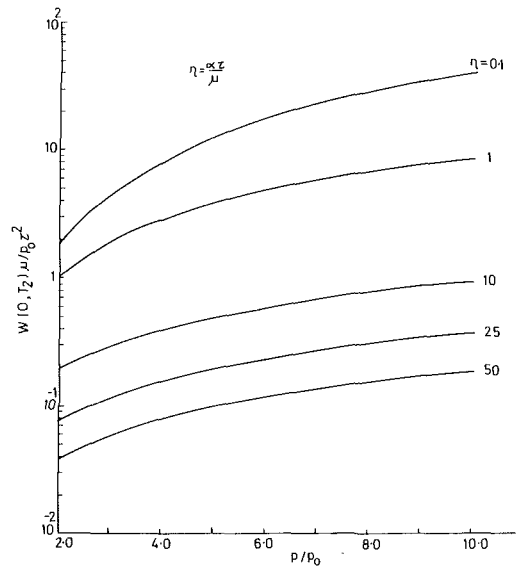


Fig. 2 Effect of damping on central plate deflection for the case of high load

$$\frac{M}{M_0} = 1 - \frac{r^2}{R^2}\left(2 - \frac{r}{R}\right) \qquad (6)$$

High Load

Phase I. $(0 < t < \tau)$. The deformation field throughout the plate is

$$w(r,t) = \begin{cases} \dfrac{p}{\alpha}\left[t + \dfrac{\mu}{\alpha}\exp\left(-\dfrac{\alpha t}{\mu}\right) - \dfrac{\mu}{\alpha}\right]; & 0 \leq r \leq \rho_0 \\ \dfrac{p}{\alpha}\left[t + \dfrac{\mu}{\alpha}\exp\left(-\dfrac{\alpha t}{\mu}\right) - \dfrac{\mu}{\alpha}\right]\left(\dfrac{R-r}{R-\rho_0}\right); & \rho_0 \leq r \leq R \end{cases} \qquad (7)$$

where ρ_0, the radius of the stationary hinge circle, is given by

$$(\rho_0/R)^3 - (\rho_0/R)^2 - (\rho_0/R) = (2p_0/p - 1) \qquad (8)$$

The expression for the moment is

[1] Assistant Professor, Department of Civil Engineering, I.I.T. Kanpur, Kanpur-208016, India.

[2] Research Student, Department of Civil Engineering, I.I.T. Kanpur, Kanpur-208016, India.

Manuscript received by ASME Applied Mechanics Division, April, 1981; final revision, July, 1981.

Downloaded 01 May 2010 to 171.66.16.249. Redistribution subject to ASME license or copyright; see http://www.asme.org/terms/Terms_Use.cfm

Acknowledgment

The author is deeply indebted to Professor Hideo Saito of Tohoku University for his consistent guidance.

References

1 Paul, H. S., and Sridharan, K., "Forced Torsional Vibration of an Elastic Circular Rod on an Elastic Half Space and on an Elastic Stratum," *Journal of the Acoustical Society of America*, Vol. 65, 1979, pp. 391–398.

2 Wada, H., "Forced Torsional Vibrations of a Cylindrical Rod Connected to an Elastic Half Space," *Journal of Sound and Vibration*, Vol. 66, No. 2, 1979, pp. 265–275.

3 Saito, H., and Wada, H., "Forced Vibrations of a Mass Connected to an Elastic Half Space by an Elastic Rod or a Spring," *Journal of Sound and Vibration*, Vol. 50, No. 4., 1977, pp. 519–532.

Dynamic Response of Rigid-Plastic Circular Plates in a Damping Medium

A. Kumar[1] and M. Hegde[2]

Introduction

In this Note, the motion of a thin circular plate (radius R) of rigid-plastic material in a damping medium is studied. The plate is subjected to a uniformly distributed load which is applied suddenly at time $t = 0$, kept constant at an intensity p during $0 < t < \tau$, and suddenly removed at $t = \tau$. The plate material obeys the Tresea yield criterion and the associated flow rule. The damping resistance is taken to be $f = \alpha V$ where V is the transverse velocity of the plate and α is a constant. Hopkins and Prager [1] studied the problem when damping was absent and found that the nature of the motion depends on whether the load is medium ($p_0 < p \leq 2p_0$) or high ($p > 2p_0$), where p_0 is the static limit load intensity.

In the present case, the equation of dynamic equilibrium is

$$\frac{\partial}{\partial r}(rM) - N = -\int_0^r (p - \mu\ddot{w} - \alpha\dot{w})\, r\, dr \qquad (1)$$

where M and N are the radial and the circumferential moments, respectively, μ is the mass per unit area of the middle surface whose deflection is w, and dots indicate differentiation with respect to time. Following a procedure similar to that in [1], the results are summarized as follows.

Medium Load

Phase I. $(0 < t < \tau)$. The moment distribution is

$$\frac{M}{M_0} = 1 - \frac{pr^2}{p_0 R^2} + \frac{r^2}{R^2}\left(2 - \frac{r}{R}\right)\left(\frac{p}{p_0} - 1\right) \qquad (2)$$

The central deflection is given by

$$w(0,t) = \frac{2(p-p_0)}{\alpha}\left[t + \frac{\mu}{\alpha}\left\{\exp\left(-\frac{\alpha t}{\mu}\right) - 1\right\}\right] \qquad (3)$$

Phase II. $(\tau < t < T)$. The plate comes to rest at time T given by

$$T = \frac{\mu}{\alpha}\log\left[\frac{p}{p_0}\left\{\exp\left(\frac{\alpha\tau}{\mu}\right) - 1\right\} + 1\right] \qquad (4)$$

Then, the final deflection is of the form

$$w(r,T) = \frac{2p}{\alpha}\left(\tau - \frac{p_0}{p}T\right)\left(1 - \frac{r}{R}\right) \qquad (5)$$

The variation of the moment M is given as

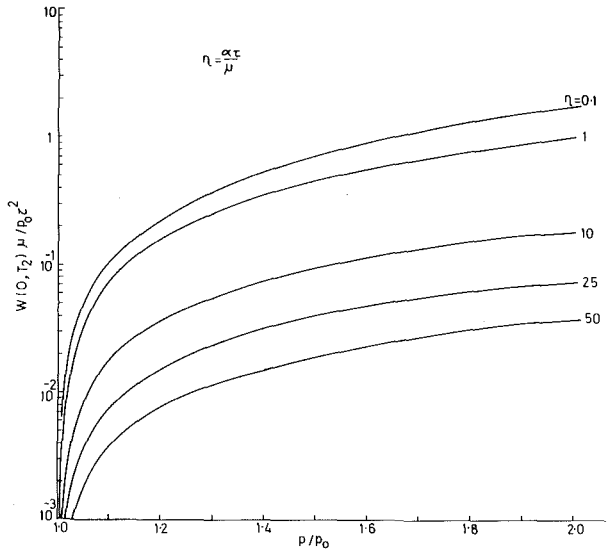


Fig. 1 Effect of damping on central plate deflection for the case of medium load

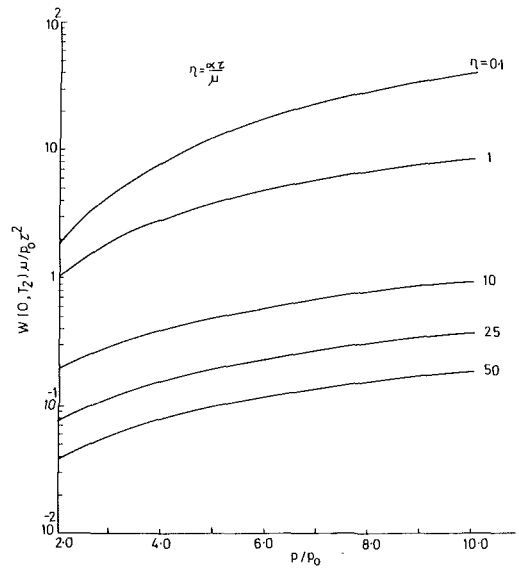


Fig. 2 Effect of damping on central plate deflection for the case of high load

$$\frac{M}{M_0} = 1 - \frac{r^2}{R^2}\left(2 - \frac{r}{R}\right) \qquad (6)$$

High Load

Phase I. $(0 < t < \tau)$. The deformation field throughout the plate is

$$w(r,t) = \begin{cases} \dfrac{p}{\alpha}\left[t + \dfrac{\mu}{\alpha}\exp\left(-\dfrac{\alpha t}{\mu}\right) - \dfrac{\mu}{\alpha}\right]; & 0 \leq r \leq \rho_0 \\ \dfrac{p}{\alpha}\left[t + \dfrac{\mu}{\alpha}\exp\left(-\dfrac{\alpha t}{\mu}\right) - \dfrac{\mu}{\alpha}\right]\left(\dfrac{R-r}{R-\rho_0}\right); & \rho_0 \leq r \leq R \end{cases} \qquad (7)$$

where ρ_0, the radius of the stationary hinge circle, is given by

$$(\rho_0/R)^3 - (\rho_0/R)^2 - (\rho_0/R) = (2p_0/p - 1) \qquad (8)$$

The expression for the moment is

[1] Assistant Professor, Department of Civil Engineering, I.I.T. Kanpur, Kanpur-208016, India.

[2] Research Student, Department of Civil Engineering, I.I.T. Kanpur, Kanpur-208016, India.

Manuscript received by ASME Applied Mechanics Division, April, 1981; final revision, July, 1981.

Copyright © 1982 by ASME

Downloaded 01 May 2010 to 171.66.16.249. Redistribution subject to ASME license or copyright; see http://www.asme.org/terms/Terms_Use.cfm

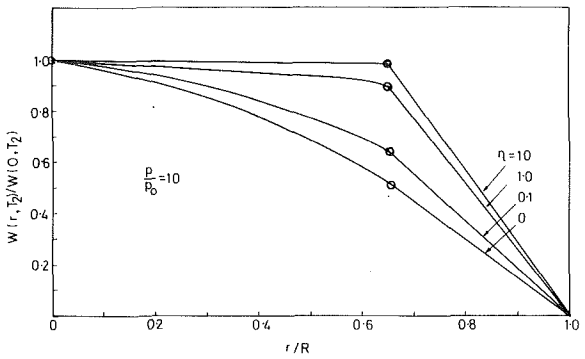


Fig. 3 Variation of final deflection across plate, expressed in terms of central deflection, with damping coefficient η for $p/p_0 = 10$

$$\frac{M}{M_0} = 1 - \frac{R(r-\rho_0)^3\,(r+\rho_0)}{r(R-\rho_0)^3\,(R+\rho_0)} \tag{9}$$

Phase II. $(\tau < t < T_1)$. The hinge circle ρ shrinks to zero at $t = T_1$, given by

$$T_1 = \frac{\mu}{\alpha}\log\left[1+\frac{p}{2p_0}\left\{\exp\left(\frac{\alpha\tau}{\mu}\right)-1\right\}\right] \tag{10}$$

Then, the central deflection is

$$w(0,T_1) = \frac{p\tau}{\alpha} - \frac{p\mu}{\alpha^2}\left\{\exp\left(\frac{\alpha\tau}{\mu}\right)-1\right\}\exp\left(1-\frac{\alpha T_1}{\mu}\right) \tag{11}$$

Phase III. $(T_1 < t < T_2)$. The plate comes to rest at $t = T_2$

$$T_2 = \frac{\mu}{\alpha}\log\left[1+\frac{p}{p_0}\left\{\exp\left(\frac{\alpha\tau}{\mu}\right)-1\right\}\right] \tag{12}$$

The final deflection in the central circular region, $0 \le r \le \rho_0$, is

$$w(r,T_2) = \left[\frac{2p_0}{\alpha}(T_1-T_2) - \frac{2p_0\mu}{\alpha^2}\right]\left(1-\frac{r}{R}\right) + \frac{p\tau}{\alpha} + \frac{p\mu}{\alpha^2} \cdot \frac{2p_0}{[2p_0 + p\{\exp(\alpha\tau/\mu)-1\}]} \cdot \left[\frac{2p_0}{p}\left(1-\frac{r}{R}\right) + \left\{\exp\left(\frac{\alpha\tau}{\mu}\right)-1\right\}\left(1-\frac{2r}{R}\right) - \frac{p\{\exp(\alpha\tau/\mu)-1\}^2}{2p_0 + p\{\exp(\alpha\tau/\mu)-1\}}\frac{1}{2}\left(\frac{r^2}{R^2}+\frac{r^3}{R^3}\right)\right] \tag{13}$$

Outside this region, the shape of the plate is conical.

Discussion

It is found that the variation of M during the motion is independent of damping. However, the plate deformation is affected by the damping force. In Figs. 1 and 2, the non-dimensional central plate deflection is plotted, on a logarithmic scale, against different values of *medium* and *high* loads for some specific values of the damping parameter $\eta(=\alpha\tau/\mu)$. When the damping coefficient α tends to zero, it is verified that the present solutions reduce to those obtained by Hopkins and Prager [1]. In Fig. 3, the variation of $w(r,T_2)/w(0,T_2)$ with r/R is shown for some representative value of η when $p/p_0 = 10$. It may be mentioned that the circle on each curve indicates the position of the hinge circle in Phase I.

Reference

1 Hopkins, H. G., and Prager, W., "On the Dynamics of Plastic Circular Plates," *Zeitschrift für Angewandte Mathematik und Physik,* Vol. 5, No. 4, 1954, pp. 317–330.

Index Evaluation for Nonlinear Systems of Order Higher Than Two

R. S. Guttalu[1] and C. S. Hsu[2]

For second-order nonlinear systems Poincaré's theory of index [1] is a remarkable one because it deals with truly global properties of the system. In [2] the theory of index is generalized for systems of order higher than two by using the concept of the degree of a map. In [2, 3] the theory is also applied to point mapping dynamical systems. Besides its intrinsic theoretical value, this theory of index can also be used to advantage to help search periodic solutions of strongly nonlinear systems, often a very difficult task, and to verify the existence and the number of these solutions within a given region of the state space.

The application of the generalized index theory to a very simple third-order system has been presented in [2]. However, because of space limitation, other examples of application and the numerical schemes and the practicality by which the specific index formula derived in [2] can be evaluated could not be included there; this we shall do in this Brief Note. It is believed that this is the first time a completely numerical index evaluation for systems of order higher than two has been carried out.

Index Formula

Consider an n-dimensional Euclidean space $\mathbf{X}$. Let $\mathbf{F}$ be a continuous real-valued vector field defined on $\mathbf{X}$ with only isolated singular points. Let $\mathbf{S}$ be a compact and oriented hypersurface of dimension $(n-1)$ in $\mathbf{X}$ not passing through any singular points of $\mathbf{F}$. Then, according to the theory of index, associated with $\mathbf{S}$ and $\mathbf{F}$ is an index $I(\mathbf{S},\mathbf{F})$ which is entirely determined by the number and character of the singular points of $\mathbf{F}$ residing in the interior of $\mathbf{S}$. In [2] the index formula is discussed in detail. If the hypersurface $\mathbf{S}$ is a sphere of radius R centered at the origin of $\mathbf{X}$, then the index formula is given by

$$I(\mathbf{S}(R),\mathbf{F}) = \frac{\Gamma\left(\frac{n}{2}+1\right)}{n\pi^{n/2}}\int_{\mathbf{S}} \det\left\{\mathbf{C}\frac{\partial \mathbf{y}}{\partial \mathbf{F}}\frac{\partial \mathbf{F}}{\partial \mathbf{x}}\frac{\partial \mathbf{x}}{\partial \mathbf{u}}\right\} du^1\,du^2\ldots du^{n-1} \tag{1}$$

where u^i, $i=1,2,\ldots,n-1$ are the generalized spherical coordinates on $\mathbf{S}$, and $\mathbf{C}$, $\partial\mathbf{y}/\partial\mathbf{F}$, $\partial\mathbf{x}/\partial\mathbf{u}$ are given by (38), (34), and (35) of [2]. Essentially, to evaluate the index $I(\mathbf{S}(R),\mathbf{F})$ we need to carry out an integration over $\mathbf{S}$.

If the size of $\mathbf{S}$ is increased, then everytime it moves across a singular point of $\mathbf{F}$ the index is expected to change by one unit. Thus, by finding the variation of the index as a funcion of R, one can determine the radial distribution of the singular points of $\mathbf{F}$ in the space $\mathbf{X}$.

Numerical Integration

To evaluate the multiple integral we use Simpson's 1/3-rule which requires two intervals for each application of the rule and hence a composite rule requires an even number of intervals in each dimension. By a "basic cell" we mean a parallelpiped in the integration space of dimension $(n\text{-}1)$ consisting of two intervals in each direction. We also employ here a semiadaptive integration procedure to achieve the desired integration accuracy. A basic cell of selected size is

[1]Research, Associate, Department of Mechanical Engineering, University of California, Berkeley, Calif. 94720.

[2]Professor of Applied Mechanics, Department of Mechanical Engineering, University of California, Berkeley, Calif. 94720. Fellow ASME.

Manuscript received by ASME Applied Mechanical Division, June, 1981.

Downloaded 01 May 2010 to 171.66.16.249. Redistribution subject to ASME license or copyright; see http://www.asme.org/terms/Terms_Use.cfm

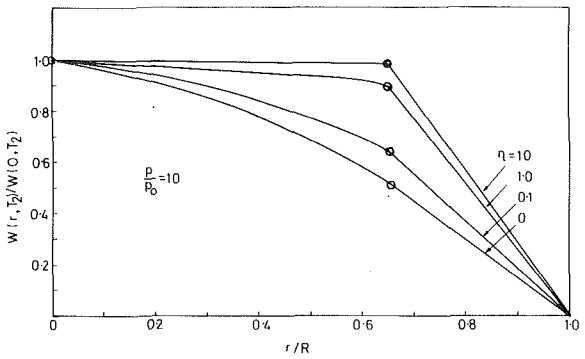


Fig. 3 Variation of final deflection across plate, expressed in terms of central deflection, with damping coefficient η for $p/p_0 = 10$

$$\frac{M}{M_0} = 1 - \frac{R(r-\rho_0)^3\,(r+\rho_0)}{r(R-\rho_0)^3\,(R+\rho_0)} \tag{9}$$

Phase II. $(\tau < t < T_1)$. The hinge circle ρ shrinks to zero at $t = T_1$, given by

$$T_1 = \frac{\mu}{\alpha}\log\left[1+\frac{p}{2p_0}\left\{\exp\left(\frac{\alpha\tau}{\mu}\right)-1\right\}\right] \tag{10}$$

Then, the central deflection is

$$w(0,T_1) = \frac{p\tau}{\alpha} - \frac{p\mu}{\alpha^2}\left\{\exp\left(\frac{\alpha\tau}{\mu}\right)-1\right\}\exp\left(1-\frac{\alpha T_1}{\mu}\right) \tag{11}$$

Phase III. $(T_1 < t < T_2)$. The plate comes to rest at $t = T_2$

$$T_2 = \frac{\mu}{\alpha}\log\left[1+\frac{p}{p_0}\left\{\exp\left(\frac{\alpha\tau}{\mu}\right)-1\right\}\right] \tag{12}$$

The final deflection in the central circular region, $0 \le r \le \rho_0$, is

$$w(r,T_2) = \left[\frac{2p_0}{\alpha}(T_1-T_2) - \frac{2p_0\mu}{\alpha^2}\right]\left(1-\frac{r}{R}\right) + \frac{p\tau}{\alpha} + \frac{p\mu}{\alpha^2} \cdot \frac{2p_0}{[2p_0 + p\{\exp(\alpha\tau/\mu)-1\}]} \cdot \left[\frac{2p_0}{p}\left(1-\frac{r}{R}\right) + \left\{\exp\left(\frac{\alpha\tau}{\mu}\right)-1\right\}\left(1-\frac{2r}{R}\right) - \frac{p\{\exp(\alpha\tau/\mu)-1\}^2}{2p_0 + p\{\exp(\alpha\tau/\mu)-1\}}\frac{1}{2}\left(\frac{r^2}{R^2}+\frac{r^3}{R^3}\right)\right] \tag{13}$$

Outside this region, the shape of the plate is conical.

Discussion

It is found that the variation of M during the motion is independent of damping. However, the plate deformation is affected by the damping force. In Figs. 1 and 2, the non-dimensional central plate deflection is plotted, on a logarithmic scale, against different values of *medium* and *high* loads for some specific values of the damping parameter $\eta(=\alpha\tau/\mu)$. When the damping coefficient α tends to zero, it is verified that the present solutions reduce to those obtained by Hopkins and Prager [1]. In Fig. 3, the variation of $w(r,T_2)/w(0,T_2)$ with r/R is shown for some representative value of η when $p/p_0 = 10$. It may be mentioned that the circle on each curve indicates the position of the hinge circle in Phase I.

Reference

1 Hopkins, H. G., and Prager, W., "On the Dynamics of Plastic Circular Plates," *Zeitschrift für Angewandte Mathematik und Physik*, Vol. 5, No. 4, 1954, pp. 317–330.

Index Evaluation for Nonlinear Systems of Order Higher Than Two

R. S. Guttalu[1] and C. S. Hsu[2]

For second-order nonlinear systems Poincaré's theory of index [1] is a remarkable one because it deals with truly global properties of the system. In [2] the theory of index is generalized for systems of order higher than two by using the concept of the degree of a map. In [2, 3] the theory is also applied to point mapping dynamical systems. Besides its intrinsic theoretical value, this theory of index can also be used to advantage to help search periodic solutions of strongly nonlinear systems, often a very difficult task, and to verify the existence and the number of these solutions within a given region of the state space.

The application of the generalized index theory to a very simple third-order system has been presented in [2]. However, because of space limitation, other examples of application and the numerical schemes and the practicality by which the specific index formula derived in [2] can be evaluated could not be included there; this we shall do in this Brief Note. It is believed that this is the first time a completely numerical index evaluation for systems of order higher than two has been carried out.

Index Formula

Consider an n-dimensional Euclidean space $\mathbf{X}$. Let $\mathbf{F}$ be a continuous real-valued vector field defined on $\mathbf{X}$ with only isolated singular points. Let $\mathbf{S}$ be a compact and oriented hypersurface of dimension $(n-1)$ in $\mathbf{X}$ not passing through any singular points of $\mathbf{F}$. Then, according to the theory of index, associated with $\mathbf{S}$ and $\mathbf{F}$ is an index $I(\mathbf{S},\mathbf{F})$ which is entirely determined by the number and character of the singular points of $\mathbf{F}$ residing in the interior of $\mathbf{S}$. In [2] the index formula is discussed in detail. If the hypersurface $\mathbf{S}$ is a sphere of radius R centered at the origin of $\mathbf{X}$, then the index formula is given by

$$I(\mathbf{S}(R),\mathbf{F}) = \frac{\Gamma\left(\frac{n}{2}+1\right)}{n\pi^{n/2}}\int_{\mathbf{S}} \det\left\{\mathbf{C}\frac{\partial \mathbf{y}}{\partial \mathbf{F}}\frac{\partial \mathbf{F}}{\partial \mathbf{x}}\frac{\partial \mathbf{x}}{\partial \mathbf{u}}\right\} du^1 du^2 \ldots du^{n-1} \tag{1}$$

where u^i, $i = 1,2,\ldots,n-1$ are the generalized spherical coordinates on $\mathbf{S}$, and $\mathbf{C}$, $\partial\mathbf{y}/\partial\mathbf{F}$, $\partial\mathbf{x}/\partial\mathbf{u}$ are given by (38), (34), and (35) of [2]. Essentially, to evaluate the index $I(\mathbf{S}(R),\mathbf{F})$ we need to carry out an integration over $\mathbf{S}$.

If the size of $\mathbf{S}$ is increased, then everytime it moves across a singular point of $\mathbf{F}$ the index is expected to change by one unit. Thus, by finding the variation of the index as a funcion of R, one can determine the radial distribution of the singular points of $\mathbf{F}$ in the space $\mathbf{X}$.

Numerical Integration

To evaluate the multiple integral we use Simpson's 1/3-rule which requires two intervals for each application of the rule and hence a composite rule requires an even number of intervals in each dimension. By a "basic cell" we mean a parallelpiped in the integration space of dimension $(n\text{-}1)$ consisting of two intervals in each direction. We also employ here a semiadaptive integration procedure to achieve the desired integration accuracy. A basic cell of selected size is

[1] Research, Associate, Department of Mechanical Engineering, University of California, Berkeley, Calif. 94720.

[2] Professor of Applied Mechanics, Department of Mechanical Engineering, University of California, Berkeley, Calif. 94720. Fellow ASME.

Manuscript received by ASME Applied Mechanical Division, June, 1981.

Copyright © 1982 by ASME
Downloaded 01 May 2010 to 171.66.16.249. Redistribution subject to ASME license or copyright; see http://www.asme.org/terms/Terms_Use.cfm

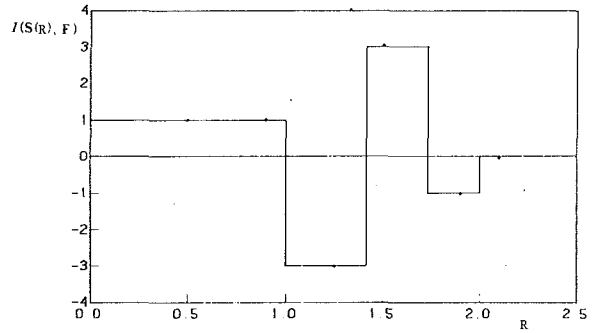


Fig. 1 Variation of the index $I(\mathbf{S}(R),F)$ of S with respect to vector field F of Example 1 as a function of R

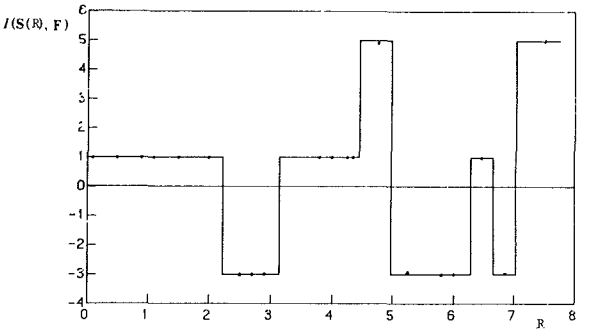


Fig. 2 Variation of the index $I(\mathbf{S}(R),F)$ of S with respect to the vector field $F = G - I$ of Example 2 for $\alpha = 5$, $\mu_1 = 0.1\pi$, $\mu_2 = 0.2\pi$

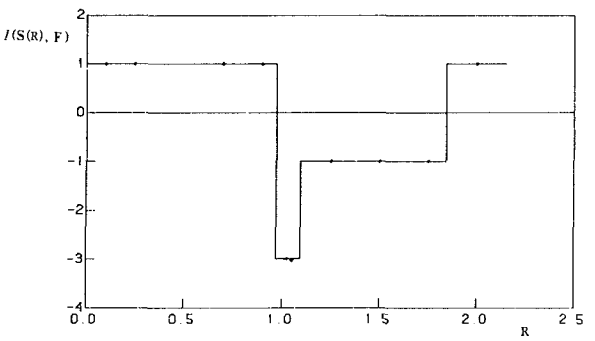


Fig. 3 Variation of the index $I(\mathbf{S}(R),F)$ of S with respect to the vector field $F = G^2 - I$ of Example 3 for $\alpha = 5$, $\mu_1 = 0.1\pi$, $\mu_2 = 0.2\pi$

integrated by applying Simpson's rule, and then the intervals in the cell are halved in size and the composite Simpson's rule is applied to the cell. If the difference of the two integrations is smaller than the required accuracy, the integration over this cell is terminated and we proceed to integrate over the next cell. Otherwise, we again halve the intervals and re-evaluate the integral over the cell. This process is repeated until the desired accuracy is achieved or the number of times of halving the intervals exceeds a preset value. For a detailed discussion of this numerical integration procedure the reader is referred to [4]. Since S is here a hypersurface of a sphere of dimension $(n-1)$, the ranges of integration for the variables are from 0 to π for $u^1, u^2, \ldots, u^{n-2}$ and from 0 to 2π for u^{n-1}.

Example 1

We first consider the following fourth-order system for which the complete distribution of its singular points is easily determined.

$$\dot{x}_k = F_k(\mathbf{x}) = x_k^2 - x_k, \quad k = 1, 2, 3, 4. \tag{2}$$

There are 16 singular points for this system. So far as the radial distribution is concerned, there is one with index $+1$ located at $R = 0$, four with index -1 located at $R = 1$, six with index $+1$ at $R = 2^{1/2}$, four with index -1 at $R = 3^{1/2}$, and one with index $+1$ at $R = 2$. Thus the variation of the index $I(\mathbf{S}(R),F)$ with R follows the solid line in Fig. 1. The numerical evaluation of the index formula (1) for this system is shown by the dots in Fig. 1. The results confirm completely the prediction of the index theory.

Example 2

Next we consider a two-degrees-of-freedom system studied in [5]. The system consists of two identical rigid bars free to rotate about a common axis. The two bars are coupled and anchored through linear rotational dampers and they are subjected to simultaneous periodic impact loads. The behavior of the system is shown [5] to be governed by the following point mapping $\mathbf{G}$:

$$\begin{aligned}
x_1(n+1) &= G_1(\mathbf{x}(n)) = x_1(n) + C_1[x_3(n) \\
&\quad - \alpha \sin x_1(n) \cos x_2(n)] \\
x_2(n+1) &= G_2(\mathbf{x}(n)) = x_2(n) + C_2[x_4(n) \\
&\quad - \alpha \cos x_1(n) \sin x_2(n)] \\
x_3(n+1) &= G_3(\mathbf{x}(n)) = D_1[x_3(n) \\
&\quad - \alpha \sin x_1(n) \cos x_2(n)] \\
x_4(n+1) &= G_4(\mathbf{x}(n)) = D_2[x_4(n) \\
&\quad - \alpha \cos x_1(n) \sin x_2(n)]
\end{aligned} \tag{3}$$

where

$$C_1 = \frac{1 - e^{-2\mu_1}}{2\mu_1}, \qquad C_2 = \frac{1 - e^{-2\mu_2}}{2\mu_2}$$
$$D_1 = e^{-2\mu_1}, \qquad D_2 = e^{-2\mu_2}. \tag{4}$$

In (3) and (4) x_1 and x_3 are the in-phase mode angular displacement and velocity, x_2 and x_4 are the out-of-phase mode displacement and velocity, μ_1 and μ_2 are, respectively, the in-phase mode and the out-of-phase mode damping coefficients, and α is the excitation strength.

First, we study the radial distribution of the periodic solutions of period 1 of the point mapping $\mathbf{G}$. This corresponds to studying the singular points of a vector field $\mathbf{F} = \mathbf{G} - \mathbf{I}$. The results of numerical evaluation of the index formula (1) for this vector field with $\alpha = 5$, $\mu_1 = 0.1\pi$ and $\mu_2 = 0.2\pi$ are shown by the dots in Fig. 2. These dots are seen to lie on the solid line which represents the true index value based upon a complete study of the precise locations of the periodic solutions of period 1 for this system, thus confirming the prediction of the index theory.

Example 3

Here we consider the same two-degrees-of-freedom system as in Example 2, except that now we study the radial distribution of the periodic solutions of period 2 of the point mapping $\mathbf{G}$. This corresponds to studying the singular points of a vector field $\mathbf{F} = \mathbf{G}^2 - \mathbf{I}$. The results of numerical evaluation of the index formula (1) for this vector field with $\alpha = 5$, $\mu_1 = 0.1\pi$ and $\mu_2 = 0.2\pi$ are again shown as dots in Fig. 3. They are seen to lie on the solid line which represents the true index value based upon an exhaustive and very involved study of the locations of the periodic solutions of period 2 of the system. For a more detailed discussion of the numerical evaluation of Examples 2 and 3 the reader is referred to [4].

Concluding Remarks

The purpose of this Note is to show how the index formula

Downloaded 01 May 2010 to 171.66.16.249. Redistribution subject to ASME license or copyright; see http://www.asme.org/terms/Terms_Use.cfm

can be evaluated and how the evaluation can contribute to the knowledge of the distribution of the singular points of the dynamical system in the state space. The index theory is a truly global theory and it deserves much more attention than it has received in the past. Hopefully the results reported here might encourage further exploitation and development of this interesting approach to the study of global properties of highly nonlinear systems.

Acknowledgment

This material is based upon work supported by the National Science Foundation under Grant No. CME-8019274.

References

1 Minorsky, N., *Nonlinear scillations,* D. Van Nostrand Co., Princeton, N.J., 1962.

2 Hsu, C. S., "Theory of Index for Dynamical Systems of Order Higher Than Two," ASME JOURNAL OF APPLIED MECHANICS, Vol. 47, 1980, pp. 421-427.

3 Hsu, C. S., "A Theory of Index for Point Mapping Dynamical Systems," ASME JOURNAL OF APPLIED MECHANICS, Vol. 47, 1980, pp. 185-190.

4 Guttalu, R. S., *"On Point Mapping Methods for Studying Nonlinear Dynamical Systems,"* PhD Dissertation, Department of Mechanical Engineering, University of California, Berkeley, Calif. June 1981.

5 Hsu, C. S., "Nonlinear Behavior of Multibody Systems Under Impulsive Parametric Excitation," IUTAM Symposium on Dynamics of Multibody Systems, Munich, 1977; *Dynamics of Multibody Systems,* ed., Mangus, K., Springer-Verlag, 1978, pp. 63-74.

Large Deflections of Circular Plates of Variable Thickness

B. Banerjee[1]

The large deflection of a clamped circular plate of variable thickness under uniform load has been investigated using von Karman's equations. Numerical results obtained for the deflections and stresses at the center of the plate have been given in tabular forms.

Introduction

The study of the behavior of thin elastic plates has interested scientists for many years. With the increased use of strong and light-weight structures, many problems of nonlinear deformations have become of interest in recent years. It is well known that if the deflections of a thin elastic plate become comparable with its thickness, the standard procedure for determining the deformation of the plate consists in the application of two partial differential equations of the fourth order involving the deflection and the membrane stress funtion as two dependent variables.

These equations, initially derived by von Karman [1], are nonlinear in character, their solution is intricate, and is known only in more simple cases. Various approximate methods for the solution of these equations have been followed by various workers [2-11] for thin plates with different edge conditions. These papers are confined to plates of uniform thickness only.

Plates of nonuniform thickness are sometimes encountered in the design of machine parts, such as diaphragms of steam turbines and pistons of reciprocating engines. Investigations of plates of nonuniform thickness based on linear theory have been done by many workers and the bibliography of these workers is given in [2].

[1]Head of the Dept. of Mathematics, Jalpaiguri Government Engineering College, Jalpaiguri, West Bengal, India

Manuscript received by ASME Applied Mechanics Division, December 1980; final revision, August 1981.

In this paper, the large deflection of a clamped circular plate of variable thickness has been investigated following von Karman's equations expressed in terms of displacement components. The thickness of the plate has been assumed to vary exponentially and this type of thickness variation has been discussed fully in [2] for the corresponding small deflection problem. The final cubic equation determining the central deflection has been obtained by Galerkin's procedure. Deflections and membrane stresses have been calculated at the center of the plate and the numerical results thus obtained have been given in tabular forms.

Analysis

Let us consider a circular plate of radius a with the center of the plate taken as the origin. Considering equation of equilibrium for an element of the plate, one gets [2]

$$N_r - N_t + r\frac{dN_r}{dr} = 0 \tag{1}$$

where

$$N_r = \frac{Eh}{1-\nu^2}\left[\frac{du}{dr} + \frac{1}{2}\left(\frac{dw}{dr}\right)^2 + \frac{\nu u}{r}\right]$$

$$N_t = \frac{Eh}{1-\nu^2}\left[\frac{u}{r} + \frac{\nu du}{dr} + \frac{\nu}{2}\left(\frac{dw}{dr}\right)^2\right] \tag{1a}$$

Also, from the contributions of shearing stresses, one gets

$$\phi_r = -N_r\frac{dw}{dr} - \frac{1}{r}\int_o^r qrdr = -D\left[\frac{d^3w}{dr^3} + \frac{1}{r}\frac{d^2w}{dr^2} - \frac{1}{r^2}\frac{dw}{dr}\right] \tag{2}$$

where q is the intensity of uniform loading, $D = Eh^3/12(1-\nu^2)$ and W is the deflection of the middle plane of the plate. Considering (1) and (2) and remembering that the plate thickness h is a variable quantity, one can write the following set of differential equations

$$h\frac{d^2u}{dr^2} + \frac{1}{r}\frac{du}{dr}\left(h + r\frac{dh}{dr}\right) + \frac{u}{r}\left(\frac{\nu dh}{dr} - \frac{h}{r}\right)$$

$$= -\frac{h}{2r}(1-\nu)\left(\frac{dw}{dr}\right)^2 - h\frac{d^2w}{dr^2}\cdot\frac{dw}{dr}$$

$$-\frac{1}{2}\frac{dh}{dr}\left(\frac{dw}{dr}\right)^2 \tag{3}$$

$$\frac{d^3w}{dr^3} + \frac{1}{r}\frac{d^2w}{dr^2} - \frac{1}{r^2}\frac{dw}{dr} + 3\frac{dh}{dr}\frac{1}{rh}\left(r\frac{d^2w}{dr^2} + \frac{\nu dw}{dr}\right)$$

$$-\frac{12}{h^2}\left\{\frac{dw}{dr}\frac{du}{dr} + \frac{1}{2}\left(\frac{dw}{dr}\right)^3 + \frac{\nu u}{r}\frac{dw}{dr}\right\} = \frac{6(1-\nu^2)}{Eh^3}qr \tag{4}$$

if q = const

$$e - \frac{\beta r^2}{6a^2}$$

Let

$$h = h_o\rho \tag{5}$$

This variation of thickness has been discussed fully in [2] for the corresponding small deflection problem.

Substituting (5) into (4) and (3) one gets

$$\frac{d^2u}{dr^2} + \left(\frac{1}{r} - \frac{\beta r}{3a^2}\right)\frac{du}{dr} - u\left(\frac{\nu\beta}{3a^2} + \frac{1}{r^2}\right) = \frac{\nu-1}{2r}\left(\frac{dw}{dr}\right)^2$$

Downloaded 01 May 2010 to 171.66.16.249. Redistribution subject to ASME license or copyright; see http://www.asme.org/terms/Terms_Use.cfm

can be evaluated and how the evaluation can contribute to the knowledge of the distribution of the singular points of the dynamical system in the state space. The index theory is a truly global theory and it deserves much more attention than it has received in the past. Hopefully the results reported here might encourage further exploitation and development of this interesting approach to the study of global properties of highly nonlinear systems.

Acknowledgment

This material is based upon work supported by the National Science Foundation under Grant No. CME-8019274.

References

1 Minorsky, N., *Nonlinear scillations,* D. Van Nostrand Co., Princeton, N.J., 1962.

2 Hsu, C. S., "Theory of Index for Dynamical Systems of Order Higher Than Two," ASME JOURNAL OF APPLIED MECHANICS, Vol. 47, 1980, pp. 421-427.

3 Hsu, C. S., "A Theory of Index for Point Mapping Dynamical Systems," ASME JOURNAL OF APPLIED MECHANICS, Vol. 47, 1980, pp. 185-190.

4 Guttalu, R. S., *"On Point Mapping Methods for Studying Nonlinear Dynamical Systems,"* PhD Dissertation, Department of Mechanical Engineering, University of California, Berkeley, Calif. June 1981.

5 Hsu, C. S., "Nonlinear Behavior of Multibody Systems Under Impulsive Parametric Excitation," IUTAM Symposium on Dynamics of Multibody Systems, Munich, 1977; *Dynamics of Multibody Systems,* ed., Mangus, K., Springer-Verlag, 1978, pp. 63-74.

Large Deflections of Circular Plates of Variable Thickness

B. Banerjee[1]

The large deflection of a clamped circular plate of variable thickness under uniform load has been investigated using von Karman's equations. Numerical results obtained for the deflections and stresses at the center of the plate have been given in tabular forms.

Introduction

The study of the behavior of thin elastic plates has interested scientists for many years. With the increased use of strong and light-weight structures, many problems of nonlinear deformations have become of interest in recent years. It is well known that if the deflections of a thin elastic plate become comparable with its thickness, the standard procedure for determining the deformation of the plate consists in the application of two partial differential equations of the fourth order involving the deflection and the membrane stress funtion as two dependent variables.

These equations, initially derived by von Karman [1], are nonlinear in character, their solution is intricate, and is known only in more simple cases. Various approximate methods for the solution of these equations have been followed by various workers [2-11] for thin plates with different edge conditions. These papers are confined to plates of uniform thickness only.

Plates of nonuniform thickness are sometimes encountered in the design of machine parts, such as diaphragms of steam turbines and pistons of reciprocating engines. Investigations of plates of nonuniform thickness based on linear theory have been done by many workers and the bibliography of these workers is given in [2].

[1]Head of the Dept. of Mathematics, Jalpaiguri Government Engineering College, Jalpaiguri, West Bengal, India

Manuscript received by ASME Applied Mechanics Division, December 1980; final revision, August 1981.

In this paper, the large deflection of a clamped circular plate of variable thickness has been investigated following von Karman's equations expressed in terms of displacement components. The thickness of the plate has been assumed to vary exponentially and this type of thickness variation has been discussed fully in [2] for the corresponding small deflection problem. The final cubic equation determining the central deflection has been obtained by Galerkin's procedure. Deflections and membrane stresses have been calculated at the center of the plate and the numerical results thus obtained have been given in tabular forms.

Analysis

Let us consider a circular plate of radius a with the center of the plate taken as the origin. Considering equation of equilibrium for an element of the plate, one gets [2]

$$N_r - N_t + r\frac{dN_r}{dr} = 0 \tag{1}$$

where

$$N_r = \frac{Eh}{1-\nu^2}\left[\frac{du}{dr} + \frac{1}{2}\left(\frac{dw}{dr}\right)^2 + \frac{\nu u}{r}\right]$$

$$N_t = \frac{Eh}{1-\nu^2}\left[\frac{u}{r} + \frac{\nu du}{dr} + \frac{\nu}{2}\left(\frac{dw}{dr}\right)^2\right] \tag{1a}$$

Also, from the contributions of shearing stresses, one gets

$$\phi_r = -N_r\frac{dw}{dr} - \frac{1}{r}\int_o^r qrdr = -D\left[\frac{d^3w}{dr^3} + \frac{1}{r}\frac{d^2w}{dr^2} - \frac{1}{r^2}\frac{dw}{dr}\right] \tag{2}$$

where q is the intensity of uniform loading, $D = Eh^3/12(1-\nu^2)$ and W is the deflection of the middle plane of the plate. Considering (1) and (2) and remembering that the plate thickness h is a variable quantity, one can write the following set of differential equations

$$h\frac{d^2u}{dr^2} + \frac{1}{r}\frac{du}{dr}\left(h + r\frac{dh}{dr}\right) + \frac{u}{r}\left(\frac{\nu dh}{dr} - \frac{h}{r}\right)$$

$$= -\frac{h}{2r}(1-\nu)\left(\frac{dw}{dr}\right)^2 - h\frac{d^2w}{dr^2}\cdot\frac{dw}{dr}$$

$$-\frac{1}{2}\frac{dh}{dr}\left(\frac{dw}{dr}\right)^2 \tag{3}$$

$$\frac{d^3w}{dr^3} + \frac{1}{r}\frac{d^2w}{dr^2} - \frac{1}{r^2}\frac{dw}{dr} + 3\frac{dh}{dr}\frac{1}{rh}\left(r\frac{d^2w}{dr^2} + \frac{\nu dw}{dr}\right)$$

$$-\frac{12}{h^2}\left\{\frac{dw}{dr}\frac{du}{dr} + \frac{1}{2}\left(\frac{dw}{dr}\right)^3 + \frac{\nu u}{r}\frac{dw}{dr}\right\} = \frac{6(1-\nu^2)}{Eh^3}qr \tag{4}$$

if q = const

$$e - \frac{\beta r^2}{6a^2}$$

Let

$$h = h_o\rho \tag{5}$$

This variation of thickness has been discussed fully in [2] for the corresponding small deflection problem.

Substituting (5) into (4) and (3) one gets

$$\frac{d^2u}{dr^2} + \left(\frac{1}{r} - \frac{\beta r}{3a^2}\right)\frac{du}{dr} - u\left(\frac{\nu\beta}{3a^2} + \frac{1}{r^2}\right) = \frac{\nu-1}{2r}\left(\frac{dw}{dr}\right)^2$$

Copyright © 1982 by ASME
Downloaded 01 May 2010 to 171.66.16.249. Redistribution subject to ASME license or copyright; see http://www.asme.org/terms/Terms_Use.cfm

Table 1 $\nu = 0.3$

Boundary condition	A_1	B_1	β	A_1	B_1
	Immovable	Edge		Movable	Edge
Plate clamped	0.471	0.171	0	0.146	0.171
	0.597	0.217	1	0.203	0.217
	0.728	0.275	2	0.256	0.275
	0.824	0.349	3	0.306	0.349

$$-\frac{d^2w}{dr^2}\frac{dw}{dr}+\frac{\beta r}{6a^2}\left(\frac{dw}{dr}\right)^2 \tag{6}$$

$$\frac{d^3w}{dr^3}+\frac{1}{r}\frac{d^2w}{dr^2}-\frac{1}{r^2}\frac{dw}{dr}-\frac{\beta}{a^2}\left\{r\frac{d^2w}{dr^2}+\nu\frac{dw}{dr}\right\}-\frac{12}{h_o{}^2}e^{\frac{\beta r^2}{3a^2}}$$

$$\times\left\{\frac{dw}{dr}\cdot\frac{du}{dr}+\frac{1}{2}\left(\frac{dw}{dr}\right)^3+\frac{\nu u}{r}\frac{dw}{dr}\right\}=\frac{6(1-\nu^2)}{Eh_o{}^3}qre^{\frac{\beta r^2}{2a^2}} \tag{7}$$

Let

$$w=W_0\left(1-\frac{r^2}{a^2}\right)^2 \tag{8}$$

which satisfies clamped edge conditions. Putting (8) into (6), one gets the following differential equation for u.

$$\frac{d^2u}{dr^2}+\left(\frac{1}{r}-\frac{\beta r}{3a^2}\right)\frac{du}{dr}-\left(\frac{\nu\beta}{3a^2}+\frac{1}{r^2}\right)u = Ar+Br^3+Cr^5+Dr^7 \tag{9}$$

where

$$A = \frac{8W_o{}^2}{a^4}(\nu-3),\ B=-\frac{16\,W_o{}^2}{a^6}\left(\nu-5-\frac{\beta}{6}\right)$$

$$C = \frac{8W_o{}^2}{a^8}\left(\nu-7-\frac{2}{3}\beta\right),\ D=\frac{8}{3}W_o{}^2\beta\frac{1}{a^{10}}$$

The solution of (9) can be stated as

$$u=a_1\left[r+\sum_{n=1}^{\infty}\left(\frac{\beta}{3a^2}\right)^n\frac{(1+\nu)(3+\nu).\ldots.(2n-1+\nu)}{2.4.4.6.6.\ldots.2n.2n.(2n+2)}r^{2n+1}\right]$$
$$+\lambda_1 r^7+\lambda_2 r^5+\lambda_3 r^3+\lambda_4 r$$
$$=a_1\left[r+\sum_{n=1}^{\infty}F_n(\beta)r^{2n+1}\right]+\lambda_1 r^7+\lambda_2 r^5+\lambda_3 r^3+\lambda_4 r \tag{10}$$

where

$$F_n(\beta)=\left(\frac{\beta}{3a^2}\right)^n\frac{(1+\nu)(3+\nu).\ldots.(2n-1+\nu)}{2.4.4.6.6.\ldots.2n.2n.(2n+2)}$$

a_1 is a constant of integration to be determined from the boundary conditions, movable or immovable edge, and

$$\lambda_1 = \frac{3a^2D}{\beta(7+\nu)},\quad \lambda_2=-\left[\frac{C\beta(7+\nu)+144a^2D}{\beta^2(5+\nu)(7+\nu)}\right]3a^2$$

$$\lambda_3 = \frac{[B\beta^2(5+\nu)(7+\nu)+72a^2\,C\beta(7+\nu)+144a^2D]}{\beta^3(5+\nu)(7+\nu)(3+\nu)}3a^2$$

$$\lambda_4 = -\frac{(A-8\lambda_3)\cdot 3a^2}{\beta(1+\nu)}$$

The series $F_n(\beta)$ is rapidly convergent and is excellent for numerical computation.

For immovable edges $u = o$ at $r = a$. Thus

$$a_1=\frac{-(\lambda_1a^6+\lambda_2a^4+\lambda_3a^2+\lambda_4)}{1+F_n(\beta)a^{2n}}$$

For movable edges $N_r = o$ at $r = a$. This gives

$$a_1=\frac{-[\lambda_1a^6(\nu+7)+\lambda_2a^4(\nu+5)+\lambda_3(\nu+3)^{xa^2}+\lambda_4(\nu+1)]}{(1+\nu)+F_n(\beta)a^{2n}x(\nu+2n+1)}$$

Thus u is determined completely.

Let us now turn to equation (7). Substituting (8) and (10) into (7) and applying Galerkin's method, we get the following cubic equation determining W_o

$$\frac{Wo}{ho}\left(\frac{256}{105}=\frac{64\beta\nu}{315}\right)+\frac{12W_o}{h_o{}^3}\sum_{s=0}^{\infty}\left(\frac{\beta}{2a^2}\right)^s\frac{a^{2s}}{/s}$$
$$\left[4\lambda_4(1+\nu)a^2\left\{\frac{3}{5+2s}-\frac{3}{2s+7}+\frac{1}{2s+9}-\frac{1}{2s+3}\right\}\right.$$
$$+\ 4\lambda_3(3+\nu)a^4\left\{\frac{3}{7+2s}-\frac{3}{2s+9}+\frac{1}{11+2s}-\frac{1}{2s+5}\right\}$$
$$+\ 4\lambda_2(5+\nu)a^6\left\{\frac{3}{9+2s}-\frac{3}{2s+11}+\frac{1}{13+2s}-\frac{1}{2s+7}\right\}$$
$$+\ 4\lambda_1(7+\nu)a^8\left\{\frac{3}{11+2s}-\frac{3}{2s+13}+\frac{1}{13+2s}-\frac{1}{2s+9}\right\}$$
$$+\ 4a_1(1+\nu)a^2\left\{\frac{3}{2s+5}-\frac{3}{2s+7}+\frac{1}{2s+9}-\frac{1}{2s+3}\right\}$$
$$+\sum_{n=1}^{\infty}4a_1(2n+1+\nu)F_n(\beta)a^{2n+2}$$
$$\left\{\frac{3}{2s+2n+5}-\frac{3}{2s+2n+7}+\frac{1}{2s+2n+9}-\frac{1}{2s+2n+3}\right\}$$
$$\left.+32\left\{\frac{5}{2s+7}-\frac{1}{2s+5}-\frac{10}{2s+9}+\frac{10}{2s+11}-\frac{5}{2s+13}+\frac{1}{2s+15}\right\}\right]$$
$$=\frac{6(1-\nu^2)qa^4}{Eh_o{}^4}\sum_{s=o}^{\infty}\frac{\left(\frac{\beta}{2a^2}\right)^s a^{2s}}{/s}\left[\frac{1}{2s+3}-\frac{2}{2s+5}+\frac{1}{2s+7}\right] \tag{11}$$

Equation (11) is of the following form

$$\frac{W_o}{h_o}+A_1\frac{W_o{}^3}{h_o^3}=B_1\frac{q\,a^4}{E\,h_o{}^4} \tag{12}$$

Numerical Results

Numerical results have been calculated for deflections and membrane stresses at $r = o$ for different values of β and given in the following tables.

From Table 1, it is clear that as $\beta \to o$, the results of the present study agree exactly with those in [2] for the corresponding large deflection circular plate problem of uniform thickness. If the nonlinear term $(W_o/h_o)^3$ is discarded, the results of the present study agree very well with those in [2] for the corresponding linear circular plate problem of variable thickness.

From relation 1(*a*), membrane stress at the center of the

Downloaded 01 May 2010 to 171.66.16.249. Redistribution subject to ASME license or copyright; see http://www.asme.org/terms/Terms_Use.cfm

Table 2

Clamped immovable α	β	Clamped movable α
0.976	0	0.500
0.901	1	0.452
0.812	2	0.431
0.705	3	0.382

plate is calculated and is given by $6\sigma a^2/Eh_o^2 = \alpha(w_o/h_o)^2$. Different values of α for various σ are tabulated in Table 2.

From Table 2, it is also clear that $\beta \to o$, the membrane stresses at the center of the plate both for movable and immovable edges agree exactly with those in [2] for corresponding large deflection circular plate problem of uniform thickness.

References

1 von Karman, Th., "Encyklopädie der Mathematischen Wissenschaften," Vol. IV, 1910, p. 349.

2 Timoshenko, S., and Woinowsky-Krieger, S., *Theory of Plates and Shells*, 2nd Edition, McGraw-Hill, New York, pp. 402, 407, 422.

3 Nowinski, J., "Non-Linear Transverse Vibrations of Circular Elastic Plates Built-In at the Boundary," *Proceedings of the 4th U.S. National Congress of Applied Mechanics*, 1962, pp. 325-334.

4 Yamaki, N., "Influence of Large Amplitudes on Flexural Vibrations of Elastic Plates," *Zeitschrift für Angewandte Mathematik and Mechanik*, Berlin, East Germany, Vol. 41, No. 12, 1961, pp. 501-510.

5 Way, S., *Trans.* ASME, Vol. 56, 1934, pp. 627.

6 Schmidt, R., "Large Deflections of a Clamped Circular Plate," *J. Eng. Mech. Div., ASCE*, 1968, p. 1605.

7 Perry, C. L., "The Bending of Thin Elliptical Plates," *Proceedings of Symposia in Applied Mathematics*, Vol. III, *Elasticity*, McGraw-Hill, New York, 1950, pp. 131-139.

8 Weil, N. A., and Newmark, N. M., "Large Deflections of Elliptical Plates," ASME JOURNAL OF APPLIED MECHANICS, Vol. 78, 1956, pp. 21-26.

9 Nash, W. A., and Cooley, I. D., "Large Deflections of a Clamped Elliptical Plate Subjected to Uniform Pressure," ASME JOURNAL OF APPLIED MECHANICS, 1959, pp. 291-293.

10 Bolton, R., "Stresses in Circular Plates on Elastic Foundations," *J. Eng. Mech. Div., ASCE* Vol. 98, No. EM3, 1972, pp. 629-659.

11 Datta, S., "Large Deflections of Elliptic Plates Exhibiting Rectilinear Orthotropy," ASME JOURNAL OF APPLIED MECHANICS, Vol. 43, 1976, pp. 690-692.

On Nontrivial Solutions for a Compressed Linear Viscoelastic Rod

Morton E. Gurtin,[1] Victor J. Mizel,[1] and David W. Reynolds[2]

Introduction

In this Note we consider the linearized equation for the buckling of a viscoelastic rod from an undeformed virgin state. We show that this equation has only the trivial solution for axial end thrusts which—after application—are held constant. Though this result is apparently known, there appears to be no proof available in the literature.

We show further that if the load is allowed to vary with time, then, in contrast to elastica theory, there is an uncountably infinite number of nontrivial solutions.

1 Basic Equations

Consider a thin inextensible rod, pinned[3] at the ends, and acted on by an axial end thrust $P(t)$ in such a way that its center line bends in a plane. For each material point x and time t, let $\varphi(x,t)$ denote the angle between the horizontal axis and the tangent to the rod at x (Fig. 1), and let $m(x,t)$ designate the bending moment at x. Here, for convenience, we label material points by their positions $x \in [0,L]$ in the undeformed, straight configuration the rod is assumed to be in prior to time zero.

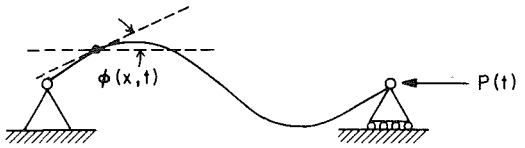


Fig. 1 The deformed rod

We work within the *quasi-static* theory; thus balance of moments has the form[4]

$$m' + P\sin\varphi = 0, \tag{1}$$

where $m' = \partial m/\partial x$. We assume that the rod is linearly viscoelastic in the sense of the constitutive equation[5]

$$m(x,t) = \beta\varphi'(x,t) + \int_0^t \alpha(t-s)\varphi'(x,s)\,ds \tag{2}$$

giving the bending moment as a function of the past history of the curvature φ'. Here $\beta > 0$ is the instantaneous flexural rigidity, while α, assumed continuous and <0, measures internal dissipation; the unique solution $G(s)$, $s \geq 0$, of the initial-value problem

$$\dot{G}(s) = \alpha(s), \quad G(0) = \beta$$

is the (moment-curvature) relaxation function.

Equations (1) and (2) yield the integro-differential equation

$$\beta\varphi''(x,t) + \int_0^t \alpha(t-s)\varphi''(x,s)\,ds + P(t)\sin\varphi(x,t) = 0,$$

or equivalently, using the standard notation for convolutions,

$$\beta\varphi'' + \alpha * \varphi'' + P\sin\varphi = 0.$$

Since the ends of the rod are pinned, the relevant boundary conditions are

$$m(0,t) = m(L,t) = 0$$

for all t, or, by (2) and the standard uniqueness theorem for linear Volterra integral equations,

$$\varphi'(0,t) = \varphi'(L,t) = 0$$

for all t. Further, as the end of the rod corresponding to the material point $x = L$ can move only horizontally, we have the additional constraint

$$\int_0^L \sin\varphi(x,t)\,dx = 0.$$

In this Note we confine our attention to the linear theory and hence replace $\sin\varphi$ by φ in the foregoing equations. The resulting boundary-value problem then takes the form[6]

$$\begin{aligned} \beta\varphi'' + \alpha*\varphi'' + P\varphi &= 0, \\ \varphi'(0,t) = \varphi'(L,t) &= 0, \\ \int_0^L \varphi(x,t)\,dx &= 0. \end{aligned} \tag{3}$$

2 Impossibility of Nontrivial Solutions When $P(t)$ = Constant

In this section we show that the problem (3) has only the zero solution when

[1] Professors of Mathematics, Department of Mathematics, Carnegie-Mellon University, Pittsburgh, Pa. 15213.

[2] Research Assistant, Department of Mathematics, Carnegie-Mellon University, Pittsburgh, Pa. 15213.

[3] In the interest of brevity, we consider only pinned ends. Our results go through, without change, for any of the standard boundary conditions. (In this connection, cf. [1].)

Manuscript received by ASME Applied Mechanics Division, April, 1981; final revision, July, 1981.

[4] Cf., e.g., [2, Section 262].

[5] Here we use the fact that $\varphi(x,t) = 0$ for $t < 0$.

[6] Cf. [3, 4] for a discussion of equations similar to $(3)_1$, but with P = constant. To our knowledge no previous paper has allowed $P(t)$ to depend on t.

Downloaded 01 May 2010 to 171.66.16.249. Redistribution subject to ASME license or copyright; see http://www.asme.org/terms/Terms_Use.cfm

Table 2

Clamped immovable α	β	Clamped movable α
0.976	0	0.500
0.901	1	0.452
0.812	2	0.431
0.705	3	0.382

plate is calculated and is given by $6\sigma a^2/Eh_o^2 = \alpha(w_o/h_o)^2$. Different values of α for various σ are tabulated in Table 2.

From Table 2, it is also clear that $\beta \to o$, the membrane stresses at the center of the plate both for movable and immovable edges agree exactly with those in [2] for corresponding large deflection circular plate problem of uniform thickness.

References

1 von Karman, Th., "Encyklopädie der Mathematischen Wissenschaften," Vol. IV, 1910, p. 349.

2 Timoshenko, S., and Woinowsky-Krieger, S., *Theory of Plates and Shells*, 2nd Edition, McGraw-Hill, New York, pp. 402, 407, 422.

3 Nowinski, J., "Non-Linear Transverse Vibrations of Circular Elastic Plates Built-In at the Boundary," *Proceedings of the 4th U.S. National Congress of Applied Mechanics*, 1962, pp. 325-334.

4 Yamaki, N., "Influence of Large Amplitudes on Flexural Vibrations of Elastic Plates," *Zeitschrift für Angewandte Mathematik and Mechanik*, Berlin, East Germany, Vol. 41, No. 12, 1961, pp. 501-510.

5 Way, S., *Trans.* ASME, Vol. 56, 1934, pp. 627.

6 Schmidt, R., "Large Deflections of a Clamped Circular Plate," *J. Eng. Mech. Div., ASCE*, 1968, p. 1605.

7 Perry, C. L., "The Bending of Thin Elliptical Plates," *Proceedings of Symposia in Applied Mathematics*, Vol. III, *Elasticity*, McGraw-Hill, New York, 1950, pp. 131-139.

8 Weil, N. A., and Newmark, N. M., "Large Deflections of Elliptical Plates," ASME JOURNAL OF APPLIED MECHANICS, Vol. 78, 1956, pp. 21-26.

9 Nash, W. A., and Cooley, I. D., "Large Deflections of a Clamped Elliptical Plate Subjected to Uniform Pressure," ASME JOURNAL OF APPLIED MECHANICS, 1959, pp. 291-293.

10 Bolton, R., "Stresses in Circular Plates on Elastic Foundations," *J. Eng. Mech. Div., ASCE* Vol. 98, No. EM3, 1972, pp. 629-659.

11 Datta, S., "Large Deflections of Elliptic Plates Exhibiting Rectilinear Orthotropy," ASME JOURNAL OF APPLIED MECHANICS, Vol. 43, 1976, pp. 690-692.

On Nontrivial Solutions for a Compressed Linear Viscoelastic Rod

Morton E. Gurtin,[1] Victor J. Mizel,[1] and David W. Reynolds[2]

Introduction

In this Note we consider the linearized equation for the buckling of a viscoelastic rod from an undeformed virgin state. We show that this equation has only the trivial solution for axial end thrusts which—after application—are held constant. Though this result is apparently known, there appears to be no proof available in the literature.

We show further that if the load is allowed to vary with time, then, in contrast to elastica theory, there is an uncountably infinite number of nontrivial solutions.

1 Basic Equations

Consider a thin inextensible rod, pinned[3] at the ends, and acted on by an axial end thrust $P(t)$ in such a way that its center line bends in a plane. For each material point x and time t, let $\varphi(x,t)$ denote the angle between the horizontal axis and the tangent to the rod at x (Fig. 1), and let $m(x,t)$ designate the bending moment at x. Here, for convenience, we label material points by their positions $x \in [0,L]$ in the undeformed, straight configuration the rod is assumed to be in prior to time zero.

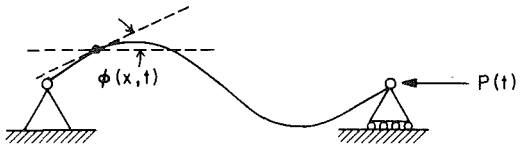


Fig. 1 The deformed rod

We work within the *quasi-static* theory; thus balance of moments has the form[4]

$$m' + P\sin\varphi = 0, \tag{1}$$

where $m' = \partial m/\partial x$. We assume that the rod is linearly viscoelastic in the sense of the constitutive equation[5]

$$m(x,t) = \beta\varphi'(x,t) + \int_0^t \alpha(t-s)\varphi'(x,s)\,ds \tag{2}$$

giving the bending moment as a function of the past history of the curvature φ'. Here $\beta > 0$ is the instantaneous flexural rigidity, while α, assumed continuous and <0, measures internal dissipation; the unique solution $G(s)$, $s \geq 0$, of the initial-value problem

$$\dot{G}(s) = \alpha(s), \quad G(0) = \beta$$

is the (moment-curvature) relaxation function.

Equations (1) and (2) yield the integro-differential equation

$$\beta\varphi''(x,t) + \int_0^t \alpha(t-s)\varphi''(x,s)\,ds + P(t)\sin\varphi(x,t) = 0,$$

or equivalently, using the standard notation for convolutions,

$$\beta\varphi'' + \alpha * \varphi'' + P\sin\varphi = 0.$$

Since the ends of the rod are pinned, the relevant boundary conditions are

$$m(0,t) = m(L,t) = 0$$

for all t, or, by (2) and the standard uniqueness theorem for linear Volterra integral equations,

$$\varphi'(0,t) = \varphi'(L,t) = 0$$

for all t. Further, as the end of the rod corresponding to the material point $x = L$ can move only horizontally, we have the additional constraint

$$\int_0^L \sin\varphi(x,t)\,dx = 0.$$

In this Note we confine our attention to the linear theory and hence replace $\sin\varphi$ by φ in the foregoing equations. The resulting boundary-value problem then takes the form[6]

$$\begin{aligned} \beta\varphi'' + \alpha*\varphi'' + P\varphi &= 0, \\ \varphi'(0,t) = \varphi'(L,t) &= 0, \\ \int_0^L \varphi(x,t)\,dx &= 0. \end{aligned} \tag{3}$$

2 Impossibility of Nontrivial Solutions When $P(t)$ = Constant

In this section we show that the problem (3) has only the zero solution when

[1] Professors of Mathematics, Department of Mathematics, Carnegie-Mellon University, Pittsburgh, Pa. 15213.

[2] Research Assistant, Department of Mathematics, Carnegie-Mellon University, Pittsburgh, Pa. 15213.

[3] In the interest of brevity, we consider only pinned ends. Our results go through, without change, for any of the standard boundary conditions. (In this connection, cf. [1].)

Manuscript received by ASME Applied Mechanics Division, April, 1981; final revision, July, 1981.

[4] Cf., e.g., [2, Section 262].

[5] Here we use the fact that $\varphi(x,t) = 0$ for $t < 0$.

[6] Cf. [3, 4] for a discussion of equations similar to $(3)_1$, but with P = constant. To our knowledge no previous paper has allowed $P(t)$ to depend on t.

Copyright © 1982 by ASME
Downloaded 01 May 2010 to 171.66.16.249. Redistribution subject to ASME license or copyright; see http://www.asme.org/terms/Terms_Use.cfm

$$P(t) = P = \text{constant for } t \geq 0.$$

With this in mind, let $0 < P_1 < P_2 < \ldots < P_n < \ldots$ and $\psi_1(x)$, $\psi_2(x)$, ..., $\psi_n(x)$, ... denote the eigenvalues and eigenvectors of the corresponding *elastic problem:*

$$\begin{aligned} &\beta\psi_n'' + P_n\psi_n = 0, \\ &\psi_n'(0) = \psi_n'(L) = 0, \\ &\int_0^L \psi_n(x)\,dx = 0; \end{aligned} \tag{4}$$

i.e.,

$$\psi_n(x) = \cos\frac{n\pi x}{L}, \quad P_n = \beta\frac{n^2\pi^2}{L^2}, \quad n = 1,2,\ldots \tag{5}$$

Suppose that $\varphi(x,t)$ is a sufficiently smooth solution of (3) and define

$$\varphi_n(t) = \int_0^L \varphi(x,t)\,\psi_n(x)\,dx. \tag{6}$$

Then, since φ and ψ_n have vanishing spatial derivatives at the ends of the rod, two integrations by parts in conjunction with $(4)_1$ yield

$$\int_0^L \varphi''\psi_n dx = \int_0^L \varphi\psi_n'' dx = -\frac{P_n}{\beta}\varphi_n.$$

Thus multiplying $(3)_1$ by ψ_n and integrating with respect to x over the interval $(0,L)$ results in the integral equation

$$(P - P_n)\varphi_n - \frac{P_n}{\beta}\alpha * \varphi_n = 0 \tag{7}$$

for $n = 1,2,\ldots$.

If $P \neq P_n$, (7) is a Volterra equation of the second kind, which has the unique solution

$$\varphi_n(t) = 0 \tag{8}$$

for all t. On the other hand, if $P = P_n$,

$$\alpha * \varphi_n = 0,$$

and hence, by Titchmarsh's theorem,[7] (8) holds in this case as well. By (6) and (8), φ is orthogonal to each function ψ_n of the form $(5)_1$. This is clearly possible only if $\varphi(x,t)$ is independent of x, and the desired conclusion, $\varphi \equiv 0$, follows from $(3)_3$.

The foregoing result, of course, does not imply that an actual rod will not buckle under the constant thrust $P \equiv P_1$. As is well known, buckling cannot be satisfactorily explained within a linear thoery, and by replacing sin φ by φ in (1) we neglected a geometrical nonlinearity. But even our linear theory indicates that a rod will not remain straight under the load $P \equiv P_1$, for the straight solution $\varphi \equiv 0$ is highly unstable. Indeed, one can approximate[8] $P \equiv P_1$ by $P(t) = P_1$ for $t = 0$ and $t \geq \epsilon$, $P(t) < P_1$ for $0 < t < \epsilon$ in such a way that there is a nontrivial solution $\varphi(x,t)$ which becomes infinite as $t \to \epsilon^-$. This makes precise the assertion that for $P \equiv P_1$ the rod buckles instantly with infinite amplitude.

3 Existence of Nontrivial Solutions With $P(t) \neq$ Constant

There are nontrivial solutions for certain nonconstant loads. To see this consider solutions of the form

$$\varphi(x,t) = \gamma(t)\,\psi_n(x)$$

for $t \geq 0$. By $(4)_{2,3}$ this function satisfies the boundary conditions $(3)_2$ and the constraint condition $(3)_3$. Moreover, by $(4)_1$, φ will satisfy the differential equation $(3)_1$ provided γ and P satisfy the integral equation

$$[P(t) - P_n]\gamma(t) - \frac{P_n}{\beta}\int_0^t \alpha(t-s)\gamma(s)\,ds = 0. \tag{9}$$

This equation can have *many* solutions. A simple example is

$$\gamma(t) = \text{constant}, \quad P(t) = P_n\mathcal{G}(t),$$

with

$$\mathcal{G}(t) = \frac{G(t)}{G(0)}.$$

For this solution the angle $\varphi(x,t)$ *jumps* to its elastic shape at $t = 0$ and remains there for $t > 0$. The requisite axial thrust is initially the elastic buckling load P_n, but for $t > 0$, $P(t)$ *decreases* in proportion to the relaxation function $G(t)$.

Solutions continuous in time at $t = 0$ are also possible. For example,

$$\gamma(t) = At \ (A = \text{constant}), \quad P(t) = P_n\frac{1}{t}\int_0^t \mathcal{G}(s)\,ds,$$

forms a solution. (Note that, again, $P(0^+) = P_n$.)

More generally, (9) can be rewritten as

$$\frac{P(t)}{P_n} = \frac{\gamma(t) + \gamma * \dot{\mathcal{G}}(t)}{\gamma(t)}; \tag{10}$$

thus *any* function $\gamma > 0$ on $[0,\infty)$ yields a nontrivial solution with P given by (10). It is not difficult to show that $P(0^+)$ exists when $\gamma(0^+) = 0$, provided $\dot{\gamma}(0^+) > 0$. Thus any smooth function γ on $[0,\infty)$ with $\gamma > 0$ on $(0,\infty)$, $\gamma(0) = 0$, and $\dot{\gamma}(0^+) > 0$ also generates a solution.[9]

Thus, interestingly, in contrast to elastica theory there is an uncountable infinite number of solutions (even modulo multiplicative constants).

The results in this section do not apply to a Kelvin material, nor, for that matter, to any material with instantaneous creep compliance $J(0) = 0$. For such materials the resulting boundary-value problem has only the zero solution for *any* axial thrust $P(t)$. An argument analogous to that used in Section 2 easily shows this. In the particular case of a Kelvin material, this zero solution loses stability to initial disturbances at $P \equiv P_1$. (This fact was pointed out to us by the referee.)

Acknowledgment

This work was supported by the Army Research Office (MEG, DWR) and the National Science Foundation (VJM).

References

1 Reynolds, D. W., "On the Buckling of Viscoelastic Rods," in preparation.

2 Love, A. E. H., *A Treatise on the Mathematical Theory of Elasticity*, Dover, New York, 1944, 4th edition.

3 Distéfano, J. N., Sulla stabilita in regime viscoelastico a comportamento lineare I. Atti Acad. Naz. Lincei Rend. Cl. Sci. Fis. Mat. Natur, Vol. (8) 27, 1960, pp. 356-361.

4 Distéfano, J. N., "Creep Buckling of Slender Columns," *Journal of Structural Division, Proceedings of ASCE*, Vol. 91, 1965, pp. 127-150.

5 Titchmarsh, E. C., *Introduction to the Theory of Fourier Integrals*, Oxford, Oxford, 1948, 2nd edition.

[7] Cf., e.g., [5, Theorem 152].

[8] Cf. [1].

[9] Conditions on $P(t)$ which insure the existence of nontrivial $\gamma(t)$ are given in [1]. This paper also investigates the asymptotic behavior of these solutions.

Downloaded 01 May 2010 to 171.66.16.249. Redistribution subject to ASME license or copyright; see http://www.asme.org/terms/Terms_Use.cfm

On the Stability of Linear Systems: A Turbulent Flow Classification Scheme for Dilute Polymer Solutions

N. Phan-Thien[1] and J. D. Atkinson[1]

Introduction

The stability of the equilibrium solution of a finite system of linear equations of the form

$$\dot{\mathbf{x}} = (\mathbf{A} + \mathbf{F}(t))\mathbf{x},$$
$$\mathbf{x}(0) = \mathbf{c}, \tag{1}$$

has been investigated by several authors [1-4]. Here $\mathbf{A}$ is a stability matrix and $\mathbf{F}(t)$ is a stationary, ergodic process, and $\mathbf{c}$ is a constant vector. In [1-3] the Gronwall-Bellman's inequality and Lyapunov techniques were applied whereby the ergodic properties of $\mathbf{F}(t)$ were invoked to yield sufficient conditions for almost-sure stability of the sample solution.

In particular, assuming that $F_{ij}(t)$ satisfy the following:

$$\left.\begin{array}{ll} (i) & F_{ij}(t) \text{ are continuous on } (0,\infty) \text{ with probability one} \\ (ii) & F_{ij}(t) \text{ are strictly stationary} \\ (iii) & F_{ij}(t) \text{ are ergodic processes in time} \end{array}\right\} \tag{2}$$

then Theorem $A1$ of Caughey and Gray [1] asserts that the system (1) is almost-surely stable if $\mathbf{A}$ is a stability matrix and that

$$E\{\|\mathbf{P}^{-1/2}\mathbf{F}^T(t)\mathbf{P}^{1/2} + \mathbf{P}^{1/2} + \mathbf{P}^{1/2}\mathbf{F}(t)\mathbf{P}^{-1/2}\|\} \tag{3}$$

exists and is less than $1/\lambda_M$.

Here $E\{\cdot\}$ is the mathematical expectation, $\mathbf{P}$ is a symmetric, positive-definite matrix such that [5]

$$\mathbf{PA} + \mathbf{A}^T\mathbf{P} = -\mathbf{I}, \tag{4}$$

and λ_M is the maximum (positive) eigenvalue of $\mathbf{P}$, viz., there is an orthogonal transformation θ such that

$$\theta^T\theta = \mathbf{I}, \quad \theta^T\mathbf{P}\theta = \text{diag}\{\lambda_i\}. \tag{5}$$

In this Note we derive a slightly more restrictive stability criterion than that given by (3) which is based on Caughey and Gray's [2] method. The result is then applied to a turbulent flow of dilute polymer solutions to obtain a weak flow criterion in which there is not much distortion to the microstructure. If one hypothesises that the famous drag reduction is somehow connected with the microstructure distortion, then this weak flow criterion may be thought of as providing an indirect evidence of the "time hypothesis" for the onset of drag reduction.

Statement and Proof of Main Results

Definition. The trivial solution, $\mathbf{x} = 0$, of (1) is said to be almost-surely stable in the sense of Lyapunov [1-3] if for all $\mathbf{c}$,

$$\lim_{t\to\infty} \|\mathbf{x}(t;\mathbf{c})\| = 0,$$

where $\|\cdot\|$ is the norm of a vector.

Theorem. Equation (1) is almost-surely stable in the sense of Lyapunov if

1 The matrix $\mathbf{A}$ is a stability matrix.
2 $\mathbf{F}(t)$ satisfy conditions (2).
3 $E\{\sigma_M\}$ exists and is less than $1/\lambda_M$.

Here σ_M is the largest eigenvalue of the matrix

$$\mathbf{Q} = \mathbf{P}^{-1/2}\mathbf{F}^T(t)\mathbf{P}^{1/2} + \mathbf{P}^{1/2}\mathbf{F}(t)\mathbf{P}^{-1/2} \tag{6}$$

The proof of this theorem follows essentially that of Caughey and Gray [2] the main feature of which is reported here.

Since $\mathbf{A}$ is a stability matrix, we can define $\mathbf{P}$, and consequently any powers of $\mathbf{P}$ according to (4) and (5). By letting

$$v = \mathbf{x}^T\mathbf{P}\mathbf{x} \tag{7}$$

It follows that

$$\dot{v} = -x^2 + \mathbf{x}^T(\mathbf{F}^T\mathbf{P} + \mathbf{PF})\mathbf{x}. \tag{8}$$

From (5) and (7) $-x^2 \le -v/\lambda_M$, and (8) yields

$$\dot{v} \le -v/\lambda_M + \mathbf{y}^T\mathbf{Q}\mathbf{y}, \tag{9}$$

where $\mathbf{Q}$ is given by (6) and $\mathbf{y} = \mathbf{P}^{1/2}\mathbf{x}$.

Since $\mathbf{Q}$ is symmetric, it has n real eigenvalues σ_i and n eigenvectors $\mathbf{p}_i$ which form an orthonormal system (n is the dimension of the system).

Thus a representation of $\mathbf{Q}$ is

$$\mathbf{Q} = \sum_i \sigma_i \mathbf{p}_i\mathbf{p}_i \tag{10}$$

from which the second term on the right-hand side of (9) can be estimated as

$$\mathbf{y}^T\mathbf{Q}\mathbf{y} = \sum_i \sigma_i(\mathbf{y}\cdot\mathbf{p}_i)^2 \le \sigma_M \sum_i (\mathbf{y}\cdot\mathbf{p}_i)^2,$$

and, since $\{\mathbf{p}_i\}$ form an orthonormal basis,

$$\mathbf{y}^T\mathbf{Q}\mathbf{y} \le \sigma_M y^2 = \sigma_M v, \tag{11}$$

where $\sigma_M = \max_i \{\sigma_i\}$.

Returning to (9),

$$\dot{v} \le (-1/\lambda_M + \sigma_M)v \tag{12}$$

which implies

$$v(t) \le v_0 \exp\left\{\left(-1/\lambda_M + \frac{1}{t}\int_0^t \sigma_M(\eta)\,d\eta\right)t\right\} \tag{13}$$

The conditions (2) and (3) of the theorem guarantees that

$$\lim_{t\to\infty} \frac{1}{t}\int_0^t \sigma_M(\eta)\,d\eta = E\{\sigma_M\}$$

with probability one.

Thus, if

$$E\{\sigma_M\} \le 1/\lambda_M \tag{14}$$

then $\lim_{t\to\infty} v(t) = 0$ and consequently $\lim_{t\to\infty} \|\mathbf{x}\| = 0$, and the system (1) is almost-surely stable in the sense of Lyapunov.

Next, for any eigenvector $\mathbf{p}_i$,

$$\|\mathbf{Q}\mathbf{p}_i\| = |\sigma_i| \le \|\mathbf{Q}\|. \tag{15}$$

Thus the present criterion (14) is always more restrictive than of (3). Note that if $E\{\sigma_m\} \ge 1/\lambda_m$, where $\lambda_m = \min_i \{\lambda_i\}$ and $\sigma_m = \min_i \{\sigma_i\}$ then (1) is a runaway process; that is, it is almost-surely unstable.

Application to Turbulent Flow of Dilute Polymer Solution

The solution to boundary-value problems in non-Newtonian fluid mechanics proceeds in a peculiar way. First, the major aspects of the flow kinematics are guessed, often with reference to the same flow problem for a Newtonian fluid. A flow classification scheme is then employed to give an indication of the how a given fluid would behave in the given flow field. With this knowledge, a constitutive equation for the fluid is chosen and the full analysis on the flow is carried out either analytically (which is rare) or numerically.

[1] Department of Mechanical Engineering, University of Sydney, Sydney, N.S.W. 2006, Australia

Manuscript received by ASME Applied Mechanics Division, April, 1981.

Copyright © 1982 by ASME
Downloaded 01 May 2010 to 171.66.16.249. Redistribution subject to ASME license or copyright; see http://www.asme.org/terms/Terms_Use.cfm

Clearly, a sound flow classification scheme is desirable. This idea is not a recent one; indeed Truesdell and Noll [6] and Huilgol [7] have employed a kinematic flow classification scheme that achieves the separation of viscometric flows from all other homogeneous steady flows. However, this scheme does not distinguish betwen a steady elongational (~strong) and the eccentric disk viscometer (~weak) flow. The desire to separate these flows stems from microstructural studies where it can be shown that the microstructural distortion can be very severe in an elongational flow whereas the microstructure is more or less at equilibrium in the eccentric disk viscometer flow.

This separation was achieved in Tanner's [8] and Hinch's [9] classification scheme. They considered the microstructure to be represented by $\mathbf{r}(t)$, where

$$\dot{\mathbf{r}} + \frac{1}{2\lambda}\mathbf{r} = \mathbf{L}\mathbf{r}. \tag{16}$$

Here $\mathbf{r}$ can be regarded as the end-to-end vector of an elastic polymer molecule advected with the local bulk flow so that the velocity gradient $\mathbf{L}$ should be evaluated as a function of time in a Lagrangian frame.

Thus, if $\mathbf{L}$ is constant in time (the only case considered by Tanner [8] and Hinch [9]), then the flow is "weak" if $\mathbf{L} - \mathbf{I}/2\lambda$ is a stability matrix, i.e., if the largest eigenvalue of $\mathbf{L}$ is smaller than or equal to $1/2\lambda$. Otherwise the flow is "strong," i.e., the microstructural distortion is expected to be large.

As far as we are aware, there is no sound flow classification scheme when the flow is intrinsically unsteady in the Lagrangian sense. This is an important problem in the drag reduction phenomenon where only a few parts per million by weight of some suitable polymer solution can drastically reduce the pressure drop in a turbulent flow through a circular pipe as compared to the Newtonian value. Assuming that the drag reducing effectiveness of the polymer is connected with the microstructural distortion (there is a large amount of indirect evidence for this [9]), a good flow classification scheme would allow us to say something about the onset of drag reduction.

In this instance, the microstructure can be aptly represented by (16) where $\mathbf{L}(t)$ is now a stochastic process. The matrix $\mathbf{A}$ discussed in the first part of this Note is identified as $-\mathbf{I}/2\lambda$ and λ_M as λ. Thus, if $\mathbf{L}(t)$ satisfies conditions (2), then (16) is stable, viz., the flow is *weak*, if the expectation of the largest eigenvalue of $\mathbf{D} = \frac{1}{2}(\mathbf{L}+\mathbf{L}^T)$, d_M, exists and is less than $1/2\lambda$.

Since $\mathbf{D}$ is symmetric, it has three real eigenvalues; moreover tr $\mathbf{D}=0$ if we assume that the fluid is incompressible. Thus there is at least one (at most two) negative eigenvalue. Then d_M is positive, and the criterion for weak flow is

$$E\{d_M\} < 1/2\lambda. \tag{17}$$

A more refined criterion can be derived by splitting $\mathbf{L}$ into a constant mean, $<\mathbf{L}>$, and a fluctuating component $\mathbf{l}(t)$. As we are primarily interested in phenomena near the wall, we adopt a mean shear flow where the Jordan canonical form of $<\mathbf{L}>$ is [10]

$$<\mathbf{L}> = \begin{pmatrix} 0 & \gamma & 0 \\ 0 & 0 & 0 \\ 0 & 0 & 0 \end{pmatrix}.$$

Note that γ is the mean shear rate and that all eigenvalues of $<\mathbf{L}>$ are zero; consequently $\mathbf{A} = <\mathbf{L}> - \mathbf{I}/2\lambda$ is always stable (the mean flow is always weak).

It can be shown that

$$\mathbf{P} = \lambda \begin{pmatrix} 1 & \lambda\gamma & 0 \\ \lambda\gamma & 1+2\lambda^2\gamma^2 & 0 \\ 0 & 0 & 1 \end{pmatrix}, \tag{19}$$

and the extreme eigenvalues of $\mathbf{P}$ are

$$\lambda_M = \lambda(1+\lambda^2\gamma^2)^{1/2}[(1+\lambda^2\gamma^2)^{1/2} + \lambda|\gamma|], \tag{20}$$

$$\lambda_m = \lambda(1+\lambda^2\gamma^2)^{1/2}[(1+\lambda^2\gamma^2)^{1/2} - \lambda|\gamma|] \geq 0. \tag{21}$$

Thus a more refined criterion than (17) is

$$E\{\sigma_M\} < 1/\{\lambda(1+\lambda^2\gamma^2)^{1/2}[(1+\lambda^2\gamma^2)^{1/2} + \lambda|\gamma|]\}, \tag{22}$$

where σ_M is the maximum eigenvalue of the matrix $\mathbf{P}^{-1/2}\mathbf{l}^T(t)\mathbf{P}^{1/2} + \mathbf{P}^{1/2}\mathbf{l}(t)\mathbf{P}^{-1/2}$. Note that the minimum eigenvalue of this matrix is negative (its trace is zero) whereas λ_m is positive; hence there is nothing one can say about instability criterion.

If (17) or (22) is violated, then some distortion to the microstructure may be expected. Since $E\{\sigma_M\}$ can be regarded as an inverse of the "residence" time, the criterion (17) or (22) points to a "time hypothesis" for the onset of drag reduction. Experimentally the time scale deduced from the turbulent wall strain rate is of the order of the relaxation time λ of the fluid; but there is a wide scatter in the data. A refined time hypothesis based on (17) or (22) could reduce the scatter.

References

1 Kozin, F., "On Almost-Sure Stability of Linear Systems With Random Coefficients," *MIT Journal of Mathematics and Physics,* Vol. 42, 1963, pp. 59–67.

2 Caughey, T. K., and Gray, A. H., Jr., "On the Almost-Sure Stability of Linear Dynamic Systems With Stochastic Coefficients," ASME JOURNAL OF APPLIED MECHANICS, Vol. 32, 1965, pp. 365–372.

3 Mehr, C. B., and Wang, P. K. C., "Discussion on a paper by Caughey and Gray," ASME JOURNAL OF APPLIED MECHANICS, Vol. 33, 1966, pp. 234–236.

4 Kozin, F., and Wu, C-M., "On the Stability of Linear Stochastic Differential Equations," ASME JOURNAL OF APPLIED MECHANICS, Vol. 40, 1973, pp. 87–92.

5 Bellman, R., *Introduction to Matrix Analysis,* McGraw-Hill, New York, 1960, pp. 242–243.

6 Truesdell, C., and Noll, W., "The Nonlinear Field Theories of Mechanics," *Handbuch der Physik,* III/3, Springer-Berlin, 1965.

7 Huilgol, R. R., *Continuum Mechanics of Viscoelastic Liquids,* Hindustan Publishing Corp., Delhi, 1975.

8 Tanner, R. I., "A Test Particle Approach to Flow Classification for Viscoelastic Fluids," *AIChJ,* Vol. 22, 1976, pp. 910–918.

9 Hinch, E. J., "Mechanical Models of Dilute Polymer Solutions in Strong Flows," *Physics of Fluids,* Vol. 20, 1977, pp. S22–S30.

10 Martin, A. D., and Mizel, V. J., *Introduction to Linear Algebra,* McGraw-Hill, New York, 1966.

Numerical Generation of Curvilinear Coordinate Systems

B. S. Berger[1] and D. M. Curtis[2]

Introduction

The efficient construction of coordinate systems for domains of various shapes is of importance in computational

[1] Professor, Department of Mechanical Engineering, University of Maryland, College Park, Md. 20742. Assoc. Mem. ASME.

[2] Senior Mechanical Engineer, NKF Engineering Associates, Inc., 8150 Leesburg Pike, Suite 700, Vienna, Va. 22180. Assoc. Mem. ASME.

[3] Manuscript received by ASME Applied Mechanics Division, April, 1981; final revision, August, 1981.

Downloaded 01 May 2010 to 171.66.16.249. Redistribution subject to ASME license or copyright; see http://www.asme.org/terms/Terms_Use.cfm

Clearly, a sound flow classification scheme is desirable. This idea is not a recent one; indeed Truesdell and Noll [6] and Huilgol [7] have employed a kinematic flow classification scheme that achieves the separation of viscometric flows from all other homogeneous steady flows. However, this scheme does not distinguish betwen a steady elongational (~strong) and the eccentric disk viscometer (~weak) flow. The desire to separate these flows stems from microstructural studies where it can be shown that the microstructural distortion can be very severe in an elongational flow whereas the microstructure is more or less at equilibrium in the eccentric disk viscometer flow.

This separation was achieved in Tanner's [8] and Hinch's [9] classification scheme. They considered the microstructure to be represented by $\mathbf{r}(t)$, where

$$\dot{\mathbf{r}} + \frac{1}{2\lambda}\mathbf{r} = \mathbf{L}\mathbf{r}. \tag{16}$$

Here $\mathbf{r}$ can be regarded as the end-to-end vector of an elastic polymer molecule advected with the local bulk flow so that the velocity gradient $\mathbf{L}$ should be evaluated as a function of time in a Lagrangian frame.

Thus, if $\mathbf{L}$ is constant in time (the only case considered by Tanner [8] and Hinch [9]), then the flow is "weak" if $\mathbf{L} - \mathbf{I}/2\lambda$ is a stability matrix, i.e., if the largest eigenvalue of $\mathbf{L}$ is smaller than or equal to $1/2\lambda$. Otherwise the flow is "strong," i.e., the microstructural distortion is expected to be large.

As far as we are aware, there is no sound flow classification scheme when the flow is intrinsically unsteady in the Lagrangian sense. This is an important problem in the drag reduction phenomenon where only a few parts per million by weight of some suitable polymer solution can drastically reduce the pressure drop in a turbulent flow through a circular pipe as compared to the Newtonian value. Assuming that the drag reducing effectiveness of the polymer is connected with the microstructural distortion (there is a large amount of indirect evidence for this [9]), a good flow classification scheme would allow us to say something about the onset of drag reduction.

In this instance, the microstructure can be aptly represented by (16) where $\mathbf{L}(t)$ is now a stochastic process. The matrix $\mathbf{A}$ discussed in the first part of this Note is identified as $-\mathbf{I}/2\lambda$ and λ_M as λ. Thus, if $\mathbf{L}(t)$ satisfies conditions (2), then (16) is stable, viz., the flow is *weak*, if the expectation of the largest eigenvalue of $\mathbf{D} = \frac{1}{2}(\mathbf{L}+\mathbf{L}^T)$, d_M, exists and is less than $1/2\lambda$.

Since $\mathbf{D}$ is symmetric, it has three real eigenvalues; moreover tr $\mathbf{D}=0$ if we assume that the fluid is incompressible. Thus there is at least one (at most two) negative eigenvalue. Then d_M is positive, and the criterion for weak flow is

$$E\{d_M\} < 1/2\lambda. \tag{17}$$

A more refined criterion can be derived by splitting $\mathbf{L}$ into a constant mean, $<\mathbf{L}>$, and a fluctuating component $\mathbf{l}(t)$. As we are primarily interested in phenomena near the wall, we adopt a mean shear flow where the Jordan canonical form of $<\mathbf{L}>$ is [10]

$$<\mathbf{L}> = \begin{pmatrix} 0 & \gamma & 0 \\ 0 & 0 & 0 \\ 0 & 0 & 0 \end{pmatrix}.$$

Note that γ is the mean shear rate and that all eigenvalues of $<\mathbf{L}>$ are zero; consequently $\mathbf{A} = <\mathbf{L}> - \mathbf{I}/2\lambda$ is always stable (the mean flow is always weak).

It can be shown that

$$\mathbf{P} = \lambda \begin{pmatrix} 1 & \lambda\gamma & 0 \\ \lambda\gamma & 1+2\lambda^2\gamma^2 & 0 \\ 0 & 0 & 1 \end{pmatrix}, \tag{19}$$

and the extreme eigenvalues of $\mathbf{P}$ are

$$\lambda_M = \lambda(1+\lambda^2\gamma^2)^{1/2}[(1+\lambda^2\gamma^2)^{1/2} + \lambda|\gamma|], \tag{20}$$

$$\lambda_m = \lambda(1+\lambda^2\gamma^2)^{1/2}[(1+\lambda^2\gamma^2)^{1/2} - \lambda|\gamma|] \geq 0. \tag{21}$$

Thus a more refined criterion than (17) is

$$E\{\sigma_M\} < 1/\{\lambda(1+\lambda^2\gamma^2)^{1/2}[(1+\lambda^2\gamma^2)^{1/2} + \lambda|\gamma|]\}, \tag{22}$$

where σ_M is the maximum eigenvalue of the matrix $\mathbf{P}^{-1/2}\mathbf{l}^T(t)\mathbf{P}^{1/2} + \mathbf{P}^{1/2}\mathbf{l}(t)\mathbf{P}^{-1/2}$. Note that the minimum eigenvalue of this matrix is negative (its trace is zero) whereas λ_m is positive; hence there is nothing one can say about instability criterion.

If (17) or (22) is violated, then some distortion to the microstructure may be expected. Since $E\{\sigma_M\}$ can be regarded as an inverse of the "residence" time, the criterion (17) or (22) points to a "time hypothesis" for the onset of drag reduction. Experimentally the time scale deduced from the turbulent wall strain rate is of the order of the relaxation time λ of the fluid; but there is a wide scatter in the data. A refined time hypothesis based on (17) or (22) could reduce the scatter.

References

1 Kozin, F., "On Almost-Sure Stability of Linear Systems With Random Coefficients," *MIT Journal of Mathematics and Physics,* Vol. 42, 1963, pp. 59–67.

2 Caughey, T. K., and Gray, A. H., Jr., "On the Almost-Sure Stability of Linear Dynamic Systems With Stochastic Coefficients," ASME JOURNAL OF APPLIED MECHANICS, Vol. 32, 1965, pp. 365–372.

3 Mehr, C. B., and Wang, P. K. C., "Discussion on a paper by Caughey and Gray," ASME JOURNAL OF APPLIED MECHANICS, Vol. 33, 1966, pp. 234–236.

4 Kozin, F., and Wu, C-M., "On the Stability of Linear Stochastic Differential Equations," ASME JOURNAL OF APPLIED MECHANICS, Vol. 40, 1973, pp. 87–92.

5 Bellman, R., *Introduction to Matrix Analysis,* McGraw-Hill, New York, 1960, pp. 242–243.

6 Truesdell, C., and Noll, W., "The Nonlinear Field Theories of Mechanics," *Handbuch der Physik,* III/3, Springer-Berlin, 1965.

7 Huilgol, R. R., *Continuum Mechanics of Viscoelastic Liquids,* Hindustan Publishing Corp., Delhi, 1975.

8 Tanner, R. I., "A Test Particle Approach to Flow Classification for Viscoelastic Fluids," *AIChJ,* Vol. 22, 1976, pp. 910–918.

9 Hinch, E. J., "Mechanical Models of Dilute Polymer Solutions in Strong Flows," *Physics of Fluids,* Vol. 20, 1977, pp. S22–S30.

10 Martin, A. D., and Mizel, V. J., *Introduction to Linear Algebra,* McGraw-Hill, New York, 1966.

Numerical Generation of Curvilinear Coordinate Systems

B. S. Berger[1] and D. M. Curtis[2]

Introduction

The efficient construction of coordinate systems for domains of various shapes is of importance in computational

[1] Professor, Department of Mechanical Engineering, University of Maryland, College Park, Md. 20742. Assoc. Mem. ASME.

[2] Senior Mechanical Engineer, NKF Engineering Associates, Inc., 8150 Leesburg Pike, Suite 700, Vienna, Va. 22180. Assoc. Mem. ASME.

[3] Manuscript received by ASME Applied Mechanics Division, April, 1981; final revision, August, 1981.

Copyright © 1982 by ASME
Downloaded 01 May 2010 to 171.66.16.249. Redistribution subject to ASME license or copyright; see http://www.asme.org/terms/Terms_Use.cfm

solid and fluid mechanics [2–7]. Coordinate generation procedures have been based on conformal mapping and the solution of related integral equations [1, 2, 7], solutions of elliptic partial differential equations [3, 4], and direct geometric constructions [5, 6, 8]. For a more comprehensive bibliography see [8].

The conformal mapping techniques are inherently limited to two dimensions and in the control of grid spacing and shape. Furthermore, it was found that the conformal algorithms are unsatisfactory for highly elongated shapes [8] (see Fig. 1).

Techniques based on the solution of elliptic partial differential equations have to some extent overcome these limitations. Aside from the difficulties in using a forcing function to control grid size and shape, however, these methods require elaborate programs together with considerable computer storage and execution time [3, 4].

In assuring a one-to-one coordinate transformation, the two previous methods have recourse to solutions of an integral equation or a set of partial differential equations. Geometric methods, however, can satisfy the same requirements [5, 6]. In the case of boundary deformation coordinates, one or both sets of coordinate lines are generated by deforming one set of the boundary curves of a domain into another set in such a way that the coordinate transformation is one-to-one and the required continuity is maintained. Since, at most, an initial value problem for an ordinary differential equation must be solved, it follows that execution and storage requirements are generally less than those required by the methods of [3, 4].

Boundary-Deformation Coordinates

Let $X_2 = f(X_1)$ define the upper boundary, 1, of the simply connected cross section shown in Fig. 1. Assume that $f(X_1)$ is single-valued and nonnegative. Let x_1 and x_2 be curvilinear coordinates defined over the rectangle $0 \le x_1 \le 1$, $0 \le x_2 \le 1$. Define the x_2 coordinate line implicitly by

$$X_2 = h_1(x_1)[1 - h_3(x_1)h_4(x_2)]f(X_1) \tag{1}$$

where $h_1(0) = 0, h_1(1) = 1, h_1(x_1)$ is monotonic, $h_3(1) = 0$, $h_3(x_1)$ is monotonic and decreasing, and $h_4(x_2)$ is a nonnegative function such that $h_3(x_1)h_4(x_2) < 1$ for all x_1 and x_2. For $x_1 = 0$ in equation (1), $X_2 = 0$, which corresponds to the horizontal axis in Fig. 1. For $x_1 = 1$, in equation (1), $X_2 = f(X_1)$, which is the upper boundary, 1, in Fig. 1. The functions $h_1(x_1)$, $h_3(x_1)$ and $h_4(x_2)$ allow the variation of coordinate line geometry as a function of x_1 and x_2. Forms of (1) applicable to unsymmetric domains are given in [8]. The x_1 lines may be defined to form either an orthogonal or a nonorthogonal coordinate system [8]. For the orthogonal case, the x_1 lines are taken to be the orthogonal trajectories of the x_2 lines. The slope of the x_1 lines is therefore given by [9], $dX_2/dX_1 = (\partial\phi/\partial X_2)/(\partial\phi/\partial X_1)$ where $\phi = X_2 - h_1(x_1)[1 - h_3(x_1)h_4(x_2)]f(X_1)$. Equation (2)

$$\frac{dX_2}{dX_1} = -\left[X_2 \frac{f'(X_1)}{f(X_1)} - h_1(x_1)h_3(x_1)h_4'(x_2)\frac{f(X_1)}{h_2'(x_2)}\right]^{-1} \tag{2}$$

together with (1) then defines the x_1 coordinate lines. The x_2 coordinate may be defined geometrically in terms of the X_1 coordinate, $X_1(0)$, of the intersection of the x_1 coordinate line with the X_1 axis, (Fig. 1). Then $X_1(0) = h_2(x_2)$ where $h_2(x_2)$ is a monotonic function such that $h_2(0) = 0$ and $h_2(1) = l_1$, assuming that the right and left extremities of the domain are $X_1 = 0$ and $X_1 = l_1$. The spacing of the x_1 coordinate lines assuming a uniform Δx_2 is controlled by $h_2(x_2)$. Since the x_2 coordinate lines are nonintersecting their orthogonal trajectories, the x_1 lines, do not intersect within the figure. Let X_1 denote the X_1 coordinate of the intersection of either the right or left boundary of the domain with the X_1 axis (Fig. 1). Then an x_1 coordinate line will correspond to a right or left boundary if either $f(X_1) = 0$ or if $f'(X_1) = 0$ and the boundary is a vertical straight line.

The coordinate system defined by (1) and (2) is one of a large set of possible, distinct, boundary deformation coordinate systems. Consider the following for elongated domains for which a coordinate system approaching Cartesian is appropriate near the origin and one approaching polar is appropriate neat the extremity (Fig. 2). An effective mapping into the rectangle is given by defining the x_2 coordinate lines parametrically as $X_1 = f_2(x_1, X_1, \alpha), X_2 = f_3(x_1, X_1, \alpha)$ where

$$f_2(x_1, X_1, \alpha) = h_6(\alpha) + h_1(x_1)D(X_1, \alpha)\cos h_5(\alpha) \tag{3}$$

$$f_3(x_1, X_1, \alpha) = h_1(x_1)\sin h_5(\alpha)\, D(X_1, \alpha) \tag{4}$$

$D(X_1, (\alpha) = [f_1^2(X_1) + (X_1 - \alpha)^2]^{1/2}, X_2 = f_1(X_1)$ defines the boundary curve 1, $\theta = h_5(\alpha), h_5(0) = \pi/2, h_5(1) = 0, h_5(\alpha)$ is monotonic for $0 \le \alpha \le 1, h_1(0) = 0, h_1(1) = 1, h_1(x_1)$ is monotonic for $0 \le x_1 \le 1, h_6(0) = 0, h_6(1) \le L, x = h_6(\alpha)$, and $h_6(\alpha)$ is monotonic. The x_2 coordinate is related to the X_1 coordinate of a point on $f_1(X_1)$. It may be shown that the x_2 coordinate lines do not intersect within the figure. The slope of the x_1 orthogonal coordinate lines is given by

$$\frac{dX_2}{dX_1} = -\left[\frac{\partial f_3}{\partial X_1} + \frac{\partial f_3}{\partial \alpha}\left(1 - \frac{\partial f_2}{\partial X_1}\right)\Big/\frac{\partial f_2}{\partial \alpha}\right]^{-1} \tag{5}$$

For domains bounded by curves that do not satisfy end orthogonality, nonorthogonal coordinate lines may be advantageous. Let $X_2 = f_1(X_1), X_2 = f_3(X_1), X_1 = f_2(X_2), X_1 = f_4(X_2)$ with $f_1(X_1) < 0, f_3(X_1) > 0, f_2(X_2) > 0$, and $f_4(X_2) < 0$. Assume that the line segments so defined outline a simply connected quadrilateral (Fig. 3). Define the curvilinear coordinates $-1 \le x_1 \le +1$ and $-1 \le x_2 \le +1$ such that

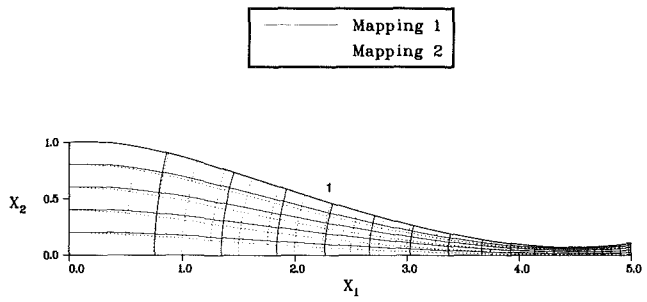


Fig. 1

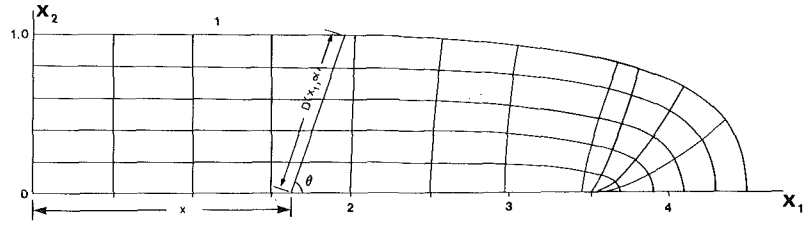


Fig. 2

Downloaded 01 May 2010 to 171.66.16.249. Redistribution subject to ASME license or copyright; see http://www.asme.org/terms/Terms_Use.cfm

$$X_2 = ax_1 + Q(x_1)[f_3(X_1) - a], 0 \le x_1 \le 1 \quad (6)$$

$$X_2 = ax_1 + Q(x_1)[f_1(X_1) + a], -1 \le x_1 \le 0 \quad (7)$$

$$X_1 = ax_2 + Q(x_2)[f_2(X_2) - a], 0 \le x_2 \le 1 \quad (8)$$

$$X_1 = ax_2 + Q(x_2)[f_4(X_2) + a], -1 \le x_2 \le 0 \quad (9)$$

with $a > 0$, $Q(x) = |x|^n(1+\epsilon)/(|x|^{n-1} + \epsilon), 0 < \epsilon < 1$, and $n \ge 2$. Letting $x_1 = 1$, 0 and -1 in (6) and (7) gives $X_2 = f_3(X_1)$, $X_2 = 0$, and $X_2 = f_1(X_1)$, while (8) and (9) give $X_1 = f_2(X_2)$, $X_1 = 0$, and $X_1 = f_4(X_2)$ for $x_2 = 1$, 0, and -1. The coordinate lines are nearly orthogonal Cartesian in the neighborhood of $X_1 = 0$, $X_2 = 0$. By choosing n to be sufficiently large, the continuity of derivatives of any order across the axes may be assured.

Numerical Studies

In (1) let $h_1(x_1) = x_1$, $h_4(x_2) = 0$, $f(X_1) = 1.001915 + 0.078934\,X_1 - 0.291029\,X_1^2 + 0.096388\,X_1^3 - 0.014604\,X_1^4 + 0.000982\,X_1^5$ and $h_2(x_2) = 17.14\,x_2 - 53.81\,x_2^2 + 165.185\,x_2^3 - 293.364\,x_2^4 + 249.725\,x_2^5 - 80.179\,x_2^6$. Substituting into (2) and solving the first-order nonlinear differential equations using a Runge-Kutta subroutine resulted in Mapping 1, Fig. 1. The x_1 coordinate lines were evaluated for $x_2 = 0.05$–1.0 with $\Delta x_2 = 0.05$. $h_2(x_2)$ was constructed to fit a curve representing the desired distribution of x_1 coordinate lines along the X_1 axis. The x_2 coordinate lines correspond to $x_1 = 0.0$–1.0 with $\Delta x_1 = 0.20$.

To demonstrate the control of grid shape, let $h_1(x_1) = x_1$, $h_3(x_1) = 1 - x_1$, $h_4(x_2) = x_2/1.1$, and $h_2(x_2) = 5x_2$ in (1). Solving (2) and evaluating (1) yields Mapping 2 (Fig. 1). The x_2 coordinate lines correspond to $x_1 = 0.0$–1.0, $\Delta x_1 = 0.2$, while the x_1 lines correspond to $x_2 = 0.1$–1.0, $\Delta x_2 = 0.05$.

The boundary of the elongated shape in Fig. 2 is defined by $f_1(X_1) = [2 - \exp(X_1/5)^4]^{1/2}$. The functions appearing in (3) and (4) are $h_1(x_1) = x_1$, $h_5(\alpha) = (\pi/2)\ [2 - \exp(c\alpha)^4]^{1/2}$, $c = 0.912444304$, and $h_6(\alpha) = 3.5\alpha$. Solving (5) results in the coordinate lines shown in Fig. 2. The x_2 lines correspond to $x_1 = 0.0$–1.0, $\Delta x_1 = 0.2$, and the x_1 lines to $x_2 = 0.143$, 0.286, . . .

The irregularly shaped quadrilateral shown in Fig. 3 is defined by (6–9), $f_1(X_1) = 0.03\ X_1/(0.01 + X_1^2) - 1 - 0.03X_1/1.01$, $f_2(X_2) = 1 + 0.5\cos(\pi X_2/2) + 0.1\cos(5\pi X_2/2)$, $f_3(X_1) = 1 - 0.5\sin(\pi X_1)$, and $f_4(X_2) = 0.5\ [\cos(\pi X_2/2)]^{100} - 0.1\cos(\pi X_2/2) - 1$. For the plot shown $n = 4$, $a = 1$, $\epsilon = 0.1$, $\Delta x_1 = 0.1$, and $\Delta x_2 = 0.1$. The coordinate lines are nearly rectangular Cartesian in the neighborhood of the origin.

The boundary deformation coordinate techniques developed here produce sets of equally spaced nodal points in the x_i coordinates for the finite difference solution of partial differential equations as well as generate meshes in the X_i coordinates for finite element discretizations. A more comprehensive discussion is given in [8].

Acknowledgment

All computations were performed at the Computer Science Center, University of Maryland, College Park, Maryland.

References

1 Hayes, J. K., Kahaner, D. K., and Kellner, R. G., "A Numerical Comparison of Integral Equations of the First and Second Kind for Conformal Mapping," *Math. Comp.*, Vol. 29, 1975, pp. 512–521.

2 Barfield, W. D., "An Optimal Mesh Generator for Lagrangian Hydrodynamic Calculations in Two Space Dimensions," *J. Comp. Phys.*, Vol. 6, 1970, pp. 417–429.

3 Thompson, J. F., Thames, F. C., and Mastin, C. W., "TOMCAT—A Code for Numerical Generation of Body-Fitted Curvilinear Coordinate Systems on Fields Containing Any Number of Arbitrary Two-Dimensional Bodies," *J. Comp. Phys.*, Vol. 24, 1977, pp. 274–302.

4 Mobley, C. D., and Stewart, R. J., "On the Numerical Generation of Boundary-Fitted Orthogonal Curvilinear Coordinate Systems," *J. Comp. Phys.*, Vol. 34, 1980, pp. 124–135.

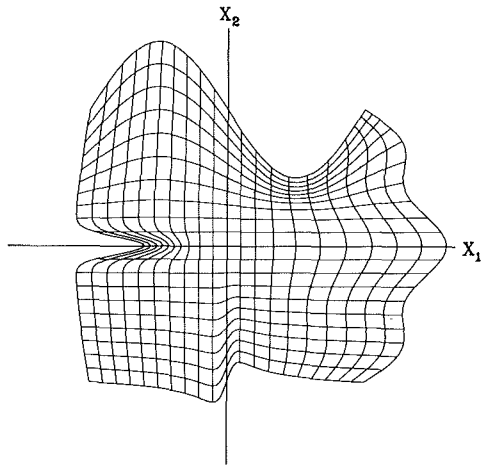


Fig. 3

5 Zienkiewicz, O. C., and Phillips, D. V., "An Automatic Mesh Generation Scheme for Plane and Curved Surfaces by Isoparametric Coordinates," *Int. J. Num. Methods Eng.*, Vol. 3, 1971, pp. 519–528.

6 Eiseman, P. R., "A Coordinate System for a Viscous Transonic Cascade Analysis," *J. Comp. Phys.*, Vol. 26, 1978, pp. 307–338.

7 Berger, B. S., and Alabi, B., "Solution of Navier's Equation in Cylindrical Curvilinear Coordinates," ASME JOURNAL OF APPLIED MECHANICS, Vol. 45, 1978, pp. 812–816.

8 Curtis, D. M., "Finite Difference Boundary Deformation Techniques in the Analysis of Elastic Bodies of Revolution," Ph.D. thesis, Department of Mechanical Engineering, University of Maryland, 1980.

9 Ince, E. L., *Ordinary Differential Equations*, Dover Publications, Inc., first American edition.

Laminar Flow Along a Porous Vertical Wall

P. D. Verma,[1] K. C. Sarangi[1] and P. D. Ariel[2]

The behavior of boundary layer thickness, film thickness is investigated for steady laminar flow along a porous vertical wall. Using a sixth-degree velocity profile the resulting equation from the Von Karman integral equation has been integrated numerically. The boundary layer thickness, film thickness are shown graphically for different values of suction parameter $\lambda_1 = v_0 h_0/\nu$ *and a dimensionless parameter*

$$\phi = \left(\frac{3\nu u_0}{g h_0^2}\right)^{1/2}.$$

Nomenclature

u = velocity component in x-direction
u_0 = entrance flow velocity
u_s = free stream velocity
v = velocity component in y-direction
x = coordinate axis along direction of motion
y = coordinate axis normal to the wall

[1] Department of Mathematics, University of Rajasthan, Jaipur, India
[2] Department of Mathematics, M.R. Engineering College, Jaipur, India

Manuscript received by ASME Applied Mechanics Division, March, 1981; final revision, July, 1981.

Downloaded 01 May 2010 to 171.66.16.249. Redistribution subject to ASME license or copyright; see http://www.asme.org/terms/Terms_Use.cfm

$$X_2 = ax_1 + Q(x_1)[f_3(X_1) - a], 0 \le x_1 \le 1 \quad (6)$$

$$X_2 = ax_1 + Q(x_1)[f_1(X_1) + a], -1 \le x_1 \le 0 \quad (7)$$

$$X_1 = ax_2 + Q(x_2)[f_2(X_2) - a], 0 \le x_2 \le 1 \quad (8)$$

$$X_1 = ax_2 + Q(x_2)[f_4(X_2) + a], -1 \le x_2 \le 0 \quad (9)$$

with $a > 0$, $Q(x) = |x|^n(1+\epsilon)/(|x|^{n-1}+\epsilon), 0 < \epsilon < 1$, and $n \ge 2$. Letting $x_1 = 1$, 0 and -1 in (6) and (7) gives $X_2 = f_3(X_1)$, $X_2 = 0$, and $X_2 = f_1(X_1)$, while (8) and (9) give $X_1 = f_2(X_2)$, $X_1 = 0$, and $X_1 = f_4(X_2)$ for $x_2 = 1$, 0, and -1. The coordinate lines are nearly orthogonal Cartesian in the neighborhood of $X_1 = 0$, $X_2 = 0$. By choosing n to be sufficiently large, the continuity of derivatives of any order across the axes may be assured.

Numerical Studies

In (1) let $h_1(x_1) = x_1$, $h_4(x_2) = 0$, $f(X_1) = 1.001915 + 0.078934\,X_1 - 0.291029\,X_1^2 + 0.096388\,X_1^3 - 0.014604\,X_1^4 + 0.000982\,X_1^5$ and $h_2(x_2) = 17.14\,x_2 - 53.81\,x_2^2 + 165.185\,x_2^3 - 293.364\,x_2^4 + 249.725\,x_2^5 - 80.179\,x_2^6$. Substituting into (2) and solving the first-order nonlinear differential equations using a Runge-Kutta subroutine resulted in Mapping 1, Fig. 1. The x_1 coordinate lines were evaluated for $x_2 = 0.05$–1.0 with $\Delta x_2 = 0.05$. $h_2(x_2)$ was constructed to fit a curve representing the desired distribution of x_1 coordinate lines along the X_1 axis. The x_2 coordinate lines correspond to $x_1 = 0.0$–1.0 with $\Delta x_1 = 0.20$.

To demonstrate the control of grid shape, let $h_1(x_1) = x_1$, $h_3(x_1) = 1 - x_1$, $h_4(x_2) = x_2/1.1$, and $h_2(x_2) = 5x_2$ in (1). Solving (2) and evaluating (1) yields Mapping 2 (Fig. 1). The x_2 coordinate lines correspond to $x_1 = 0.0$–1.0, $\Delta x_1 = 0.2$, while the x_1 lines correspond to $x_2 = 0.1$–1.0, $\Delta x_2 = 0.05$.

The boundary of the elongated shape in Fig. 2 is defined by $f_1(X_1) = [2 - \exp(X_1/5)^4]^{1/2}$. The functions appearing in (3) and (4) are $h_1(x_1) = x_1$, $h_5(\alpha) = (\pi/2)\ [2 - \exp(c\alpha)^4]^{1/2}$, $c = 0.912444304$, and $h_6(\alpha) = 3.5\alpha$. Solving (5) results in the coordinate lines shown in Fig. 2. The x_2 lines correspond to $x_1 = 0.0$–1.0, $\Delta x_1 = 0.2$, and the x_1 lines to $x_2 = 0.143$, 0.286, . . .

The irregularly shaped quadrilateral shown in Fig. 3 is defined by (6–9), $f_1(X_1) = 0.03\ X_1/(0.01 + X_1^2) - 1 - 0.03X_1/1.01$, $f_2(X_2) = 1 + 0.5\cos(\pi X_2/2) + 0.1\cos(5\pi X_2/2)$, $f_3(X_1) = 1 - 0.5\sin(\pi X_1)$, and $f_4(X_2) = 0.5\ [\cos(\pi X_2/2)]^{100} - 0.1\cos(\pi X_2/2) - 1$. For the plot shown $n = 4$, $a = 1$, $\epsilon = 0.1$, $\Delta x_1 = 0.1$, and $\Delta x_2 = 0.1$. The coordinate lines are nearly rectangular Cartesian in the neighborhood of the origin.

The boundary deformation coordinate techniques developed here produce sets of equally spaced nodal points in the x_i coordinates for the finite difference solution of partial differential equations as well as generate meshes in the X_i coordinates for finite element discretizations. A more comprehensive discussion is given in [8].

Acknowledgment

All computations were performed at the Computer Science Center, University of Maryland, College Park, Maryland.

References

1 Hayes, J. K., Kahaner, D. K., and Kellner, R. G., "A Numerical Comparison of Integral Equations of the First and Second Kind for Conformal Mapping," *Math. Comp.*, Vol. 29, 1975, pp. 512–521.

2 Barfield, W. D., "An Optimal Mesh Generator for Lagrangian Hydrodynamic Calculations in Two Space Dimensions," *J. Comp. Phys.*, Vol. 6, 1970, pp. 417–429.

3 Thompson, J. F., Thames, F. C., and Mastin, C. W., "TOMCAT—A Code for Numerical Generation of Body-Fitted Curvilinear Coordinate Systems on Fields Containing Any Number of Arbitrary Two-Dimensional Bodies," *J. Comp. Phys.*, Vol. 24, 1977, pp. 274–302.

4 Mobley, C. D., and Stewart, R. J., "On the Numerical Generation of Boundary-Fitted Orthogonal Curvilinear Coordinate Systems," *J. Comp. Phys.*, Vol. 34, 1980, pp. 124–135.

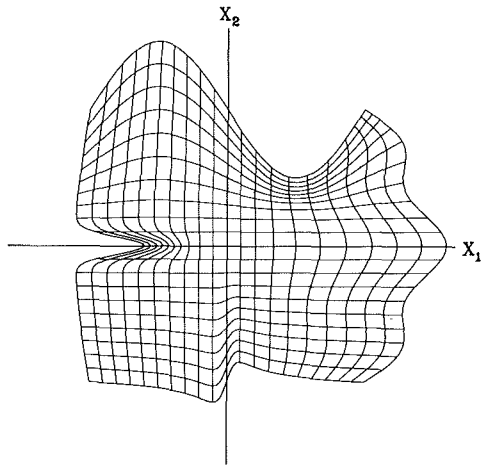


Fig. 3

5 Zienkiewicz, O. C., and Phillips, D. V., "An Automatic Mesh Generation Scheme for Plane and Curved Surfaces by Isoparametric Coordinates," *Int. J. Num. Methods Eng.*, Vol. 3, 1971, pp. 519–528.

6 Eiseman, P. R., "A Coordinate System for a Viscous Transonic Cascade Analysis," *J. Comp. Phys.*, Vol. 26, 1978, pp. 307–338.

7 Berger, B. S., and Alabi, B., "Solution of Navier's Equation in Cylindrical Curvilinear Coordinates," ASME JOURNAL OF APPLIED MECHANICS, Vol. 45, 1978, pp. 812–816.

8 Curtis, D. M., "Finite Difference Boundary Deformation Techniques in the Analysis of Elastic Bodies of Revolution," Ph.D. thesis, Department of Mechanical Engineering, University of Maryland, 1980.

9 Ince, E. L., *Ordinary Differential Equations*, Dover Publications, Inc., first American edition.

Laminar Flow Along a Porous Vertical Wall

P. D. Verma,[1] K. C. Sarangi[1] and P. D. Ariel[2]

The behavior of boundary layer thickness, film thickness is investigated for steady laminar flow along a porous vertical wall. Using a sixth-degree velocity profile the resulting equation from the Von Karman integral equation has been integrated numerically. The boundary layer thickness, film thickness are shown graphically for different values of suction parameter $\lambda_1 = v_0 h_0/\nu$ *and a dimensionless parameter*

$$\phi = \left(\frac{3\nu u_0}{g h_0^2}\right)^{1/2}.$$

Nomenclature

u = velocity component in x-direction
u_0 = entrance flow velocity
u_s = free stream velocity
v = velocity component in y-direction
x = coordinate axis along direction of motion
y = coordinate axis normal to the wall

[1] Department of Mathematics, University of Rajasthan, Jaipur, India
[2] Department of Mathematics, M.R. Engineering College, Jaipur, India

Manuscript received by ASME Applied Mechanics Division, March, 1981; final revision, July, 1981.

Copyright © 1982 by ASME
Downloaded 01 May 2010 to 171.66.16.249. Redistribution subject to ASME license or copyright; see http://www.asme.org/terms/Terms_Use.cfm

$\bar{x}$ = dimensionless distance = x/h_0
δ = boundary layer thickness
$\bar{\delta}$ = dimensionless boundary layer thickness = δ/h_0
η = dimensionless distance = y/δ
h_0 = initial film thickness
h = film thickness
g = gravitational acceleration
ν = kinematic viscosity
ϕ = defined by equation (23)
Λ = shape factor = $g\delta^2/\nu u_s$
ξ = defined by equation (24)
λ_1 = suction parameter = $v_0 h_0/\nu$
λ = $\lambda_1 \bar{\delta}$
v_0 = uniform suction/injection velocity ($v_0 > 0$ for injection, $v_0 < 0$ for suction)

Introduction

The flow problems along a vertical wall occur frequently in trickling filters, evaporation, and gas absorption experiments.

Hassan [1] and Haugen [2] have discussed the laminar flow along a vertical wall under the influence of gravity. Haugen [2] assumed a second-degree velocity profile and integrated the equation of continuity and motion to obtain boundary layer thickness, film thickness, and fully developed flow condition. Lal [3] discussed the problem taking a fourth-degree velocity profile. Introducing a shape factor in the expression of velocity profile, Jain [4] discussed the problem of Lal [3], and Goyal and Jain [5] solved the problem for a porous vertical wall and found expressions for boundary layer thickness, film thickness using the Karman-Pohlhausen integral technique. But in the analysis presented in [4] and [5] the authors have assumed the shape factor $\Lambda = g\delta^2/\nu u_s$, and the suction parameter $\lambda = v_0\delta/\nu$ as constants. However, they are functions of x, the distance along the wall and therefore cannot be assumed to be constants. Moreover, in their analysis, as they have used Pohlhausen's fourth-degree velocity profile and the boundary conditions

at $y = 0$, $u = 0$

$$\frac{\partial^2 u}{\partial y^2} = -g + v_0\left(\frac{\partial u}{\partial y}\right)$$

at $y = \delta$, $u = u_s$

$$\frac{\partial u}{\partial y} = \frac{\partial^2 u}{\partial y^2} = 0$$

the velocity becomes infinite at a particular value of suction and the separation occurs at $\Lambda = -12$, which is independent of suction.

Torda [6] attributed these shortcomings to the use of three or more boundary conditions at the edge, and one at the wall. Jain [7] consequently improved the solution of Torda [6] by taking a sixth-degree velocity profile. His solution was free of the aforementioned drawbacks.

In the present paper, following Jain [7], we have also assumed a sixth-degree velocity profile and used two boundary conditions besides the no-slip condition at the wall and four at the edge of the boundary layer. We have taken the shape factor $\Lambda(x) = g\delta^2/\nu u_s$ and $\lambda(x) = \lambda_1 \bar{\delta}$ where the suction parameter $\lambda_1 = v_0 h_0/\nu$ (constant).

The resulting velocity profile is substituted in the Von Karman integral equation for the incompressible viscous fluid and a first-order differential equation, governing the behavior of the boundary layer thickness $\delta(x)$, is obtained which is integrated numerically using the fourth-order Runge-Kutta method on IBM 1130.

Formulation of the Problem

The boundary layer equations governing the flow are

$$\frac{\partial u}{\partial x} + \frac{\partial v}{\partial y} = 0 \tag{1}$$

$$u\frac{\partial u}{\partial x} + v\frac{\partial u}{\partial y} = g + \nu\frac{\partial^2 u}{\partial y^2} \tag{2}$$

with the boundary conditions

$$y = 0, \quad u = 0, \quad v = v_0$$

and

$$y = \delta, \quad u = u_s, \quad \frac{\partial u}{\partial y} = 0 \tag{3}$$

Integrating (1) between the limits $y = 0$ and $y = h$ and (2) between the limits $y = 0$ and $y = \delta$ we get (compare reference [2])

$$\int_0^\delta u dy + u_s(h - \delta) - v_0 x = \text{const} = u_0 h_0 \tag{4}$$

and

$$u_s\frac{d}{dx}\int_0^\delta u dy - \frac{d}{dx}\int_0^\delta u^2 dy - v_0 u_s + g\delta = \nu\left(\frac{\partial u}{\partial y}\right)_{y=0} \tag{5}$$

Let us assume a sixth-degree velocity profile

$$\frac{u}{u_s} = \sum_{i=0}^{6} a_i \eta^i, 0 \le \eta \le 1 \tag{6}$$

with the following boundary conditions and compatibility conditions to determine a_i's.

(I) at $y = 0$, $u = 0$, $v = v_0$

$$v_0\left(\frac{\partial u}{\partial y}\right)_{y=0} = g + \nu\left(\frac{\partial^2 u}{\partial y^2}\right)_{y=0}$$

$$v_0\left(\frac{\partial^2 u}{\partial y^2}\right)_{y=0} = \nu\left(\frac{\partial^3 u}{\partial y^3}\right)_{y=0} \tag{7}$$

(II) at $y = \delta$, $u = u_s$

$$\left(\frac{\partial u}{\partial y}\right)_{y=\delta} = 0, \quad \left(\frac{\partial^2 u}{\partial y^2}\right)_{y=\delta} = 0, \quad \left(\frac{\partial^3 u}{\partial y^3}\right)_{y=\delta} = 0 \tag{8}$$

Under these conditions the coefficients are given by

$$a_0 = 0 \tag{9}$$

$$a_1 = \frac{120 + 12\Lambda + \Lambda\lambda}{D} \tag{10}$$

$$a_2 = \frac{30(2\lambda - \Lambda)}{D} \tag{11}$$

$$a_3 = \frac{10\lambda(2\lambda - \Lambda)}{D} \tag{12}$$

$$a_4 = \frac{5}{D}(12\Lambda + 4\Lambda\lambda - 9\lambda^2 - 36\lambda - 60) \tag{13}$$

$$a_5 = \frac{3}{D}(120 + 64\lambda + 12\lambda^2 - 20\Lambda - 5\Lambda\lambda) \tag{14}$$

$$a_6 = \frac{1}{D}(18\Lambda + 4\Lambda\lambda - 10\lambda^2 - 60\lambda - 120) \tag{15}$$

where

$$D = 60 + 12\lambda + \lambda^2 \tag{16}$$

$$\Lambda = \frac{g\delta^2}{\nu u_s} \tag{17}$$

$$\lambda = \frac{v_0\delta}{\nu} \tag{18}$$

Downloaded 01 May 2010 to 171.66.16.249. Redistribution subject to ASME license or copyright; see http://www.asme.org/terms/Terms_Use.cfm

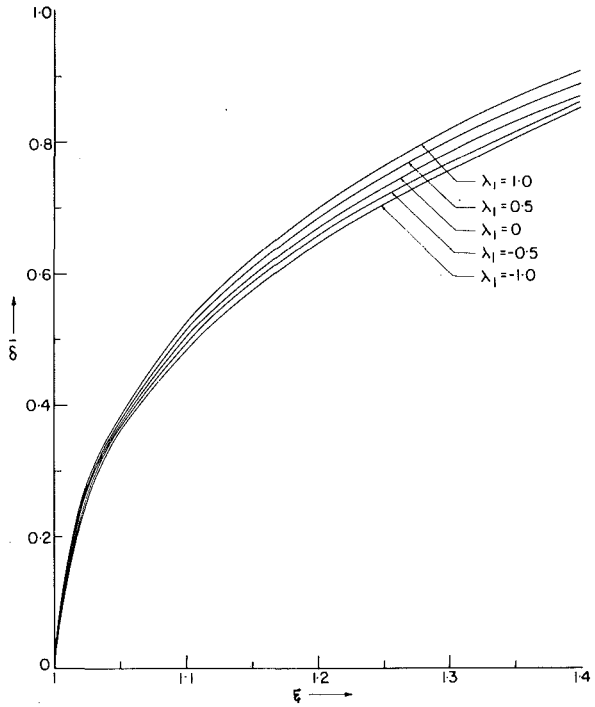


Fig. 1 Variation of dimensionless boundary layer thickness $\bar{\delta}$ with dimensionless distance ξ for $\phi = 0.5$

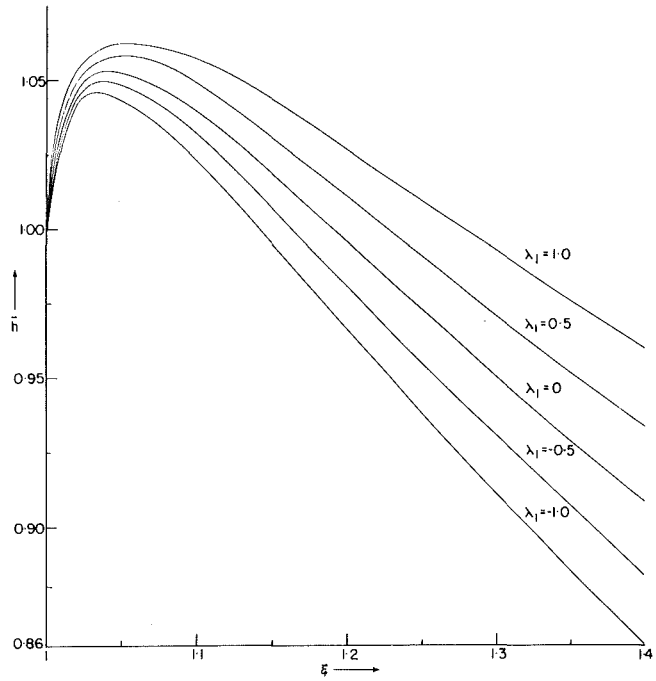


Fig. 3 Variation of dimensionless film thickness $\bar{h}$ with dimensionless distance ξ for $\phi = 0.5$

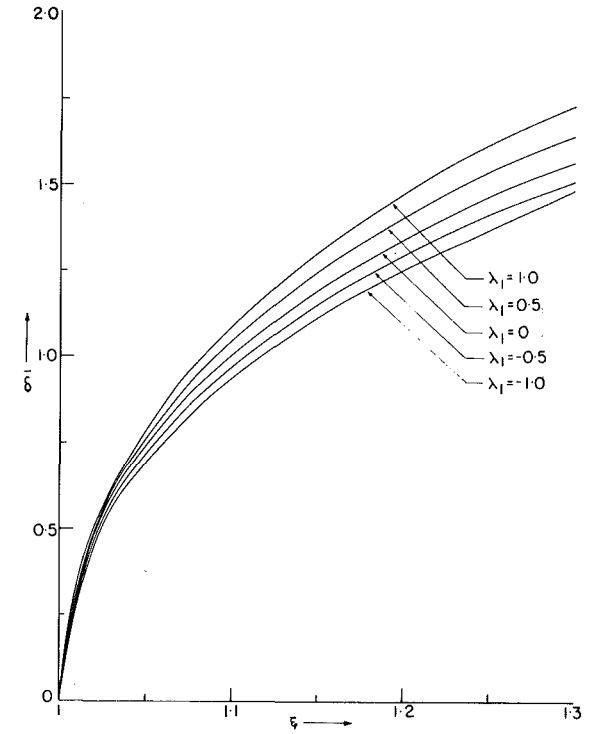


Fig. 2 Variation of dimensionless boundary layer thickness $\bar{\delta}$ with dimensionless distance ξ for $\phi = 1.0$

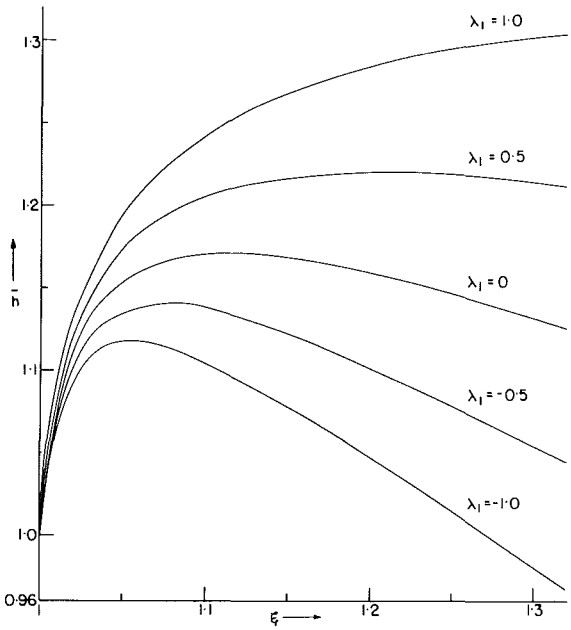


Fig. 4 Variation of dimensionless film thickness $\bar{h}$ with dimensionless distance ξ for $\phi = 1.0$

It is noted that for no real value of suction velocity the coefficients become infinite since the denominator of the coefficients has imaginary roots.

Now from equation (5) using the velocity profile given by (6) we get

$$\lambda + a_1 + \frac{u_s \delta}{\nu}(A - B)\frac{d\delta}{dx} + \Lambda(2A - B - 1) + \frac{u_s \delta^2}{\nu}\sum_{j=1}^{6} M_j \frac{da_j}{dx} = 0 \tag{19}$$

where

$$A = \sum_{i=1}^{6}\sum_{j=1}^{6} \frac{a_i a_j}{i+j+1} \tag{20}$$

$$B = \sum_{i=1}^{6} \frac{a_i}{i+1} \tag{21}$$

$$M_j = 2\sum_{i=1}^{6} \frac{a_i}{i+j+1} - \frac{1}{j+1} \quad (j = 1,6) \tag{22}$$

Let us introduce

Downloaded 01 May 2010 to 171.66.16.249. Redistribution subject to ASME license or copyright; see http://www.asme.org/terms/Terms_Use.cfm

$$\bar{x}=\frac{x}{h_0},\quad \bar{\delta}=\frac{\delta}{h_0},$$

$$\phi^2=\frac{3\nu u_0}{gh_0^2} \tag{23}$$

$$\xi^2=\left(\frac{us}{u_0}\right)^2=1+\frac{2gh_0\bar{x}}{u_0^2} \tag{24}$$

and we have $\Lambda = 3\bar{\delta}^2/\phi^2\xi$, $\lambda = \lambda_1\,\bar{\delta}$ with $\lambda_1 + v_0h_0/\nu$

Using the aforementioned nondimensional quantities and substituting for a_i's, equation (19) becomes

$$\frac{3}{\phi^2}\left[(A-B)+\sum_{i=1}^{6}M_i\left(\frac{6\bar{\delta}^2}{\phi^2\xi}\lambda_1 c_1\bar{\delta}\right)\right]\frac{d\bar{\delta}^2}{d\xi}$$
$$=-2\left[\frac{3\bar{\delta}^2}{\phi^2\xi}(2A-B-1)+(\lambda_1\bar{\delta}+a_1)-\frac{9\bar{\delta}^4}{\phi^2\xi 2}\sum_{i=1}^{6}b_iM_i\right] \tag{25}$$

where

$$b_1=\frac{1}{D}(12+\lambda) \tag{26}$$

$$b_2=-\frac{30}{D} \tag{27}$$

$$b_3=-\frac{10\lambda}{D} \tag{28}$$

$$b_4=\frac{20}{D}(3+\lambda) \tag{29}$$

$$b_5=-\frac{15}{D}(4+\lambda) \tag{30}$$

$$b_6=\frac{2}{D}(2\lambda+9) \tag{31}$$

$$c_1=-\frac{1}{D^2}[\Lambda(\lambda^2+24\lambda+84)+(240\lambda+1440)] \tag{32}$$

$$c_2=\frac{1}{D^2}[60\Lambda(\lambda+6)-60(\lambda^2-60)] \tag{33}$$

$$c_3=\frac{1}{D^2}[10\Lambda(\lambda^2-60)+240\lambda(\lambda+10)] \tag{34}$$

$$c_4=-\frac{1}{D^2}[20\Lambda(\lambda^2+6\lambda-24)+120(3\lambda^2+40\lambda+60)] \tag{35}$$

$$c_5=\frac{1}{D^2}[15\Lambda(\lambda^2+8\lambda-12)+240(\lambda^2+15\lambda+30)] \tag{36}$$

$$c_6=-\frac{1}{D^2}[4\Lambda(\lambda^2+9\lambda-6)+60(\lambda^2+16\lambda+36)] \tag{37}$$

Equation (25) is to be solved under the initial condition $\bar{\delta}(1) = 0$.

Now from equation (4) we have for the dimensionless film thickness

$$\bar{h}=\frac{h}{h_0}=\frac{u_0}{u_s}+\frac{v_0}{u_s}\frac{x}{h_0}+\frac{\delta}{h_0}-\frac{1}{h_0}\int_0^{\delta}\frac{u}{u_s}dy$$

or

$$\bar{h}=\frac{1}{\xi}+\lambda_1\frac{\phi^2}{6}\left(\xi-\frac{1}{\xi}\right)+\bar{\delta}\left[1-\sum_{i=1}^{6}\frac{a_i}{i+1}\right] \tag{38}$$

Solution for the fully developed flow is given by putting $\bar{\delta} = \bar{h}$ in (38)
i.e.,

$$\bar{\delta}\sum_{i=1}^{6}\frac{a_i}{i+1}=\frac{1}{\xi}+\frac{\lambda_1}{6}\phi^2\left(\xi-\frac{1}{\xi}\right) \tag{39}$$

Discussion

Equation (25) is integrated numerically by the fourth-order Ringe-Kutta method with the condition $\xi = 1$, $\bar{\delta} = 0$ for $\lambda_1 = -1, -0.5, 0, 0.5, 1$ and $\phi = 0.5, 1$.

In Figs. (1) and (2) the variation of dimensionless boundary layer thickness $\bar{\delta}$ with dimensionless distance ξ have been shown. It is observed that withdrawal of fluid through the wall controls the boundary layer.

The variation of dimensionless film thickness with the dimensionless distance ξ have been shown in Figs. (3) and (4). It is noted that in both the cases, film thickness $\bar{h}$ first increases to its maximum value and then decreases with the distance along the wall.

Acknowledgment

One of the authors (K. C. S.) is thankful to the University Grants Commission for the award of a teacher fellowship under the U.G.C. faculty improvement program.

References

1 Hassan, N. A., "Laminar Flow Along a Vertical Wall," ASME JOURNAL OF APPLIED MECHANICS, Vol. 34, Sept. 1967, pp. 535-537.

2 Haugen, R., "Laminar Flow Along a Vertical Wall," ASME JOURNAL OF APPLIED MECHANICS, Vol. 35, Dec. 1968, pp. 631-633.

3 Lal, K., "Laminar Flow Along a Vertical Wall," *Journal of Institute of Engineers*, India, I.M.E., Vol. 56, July 1975, pp. 24-27.

4 Jain, N. C., "A Numerical Study of the Laminar Flow Along a Vertical Wall," *Acta Technica CSAV*, No. 5, 1978, pp. 549-556.

5 Goyal, M. C., and Jain, N. C., "An Integral Approach for the Flow Along a Porous Vertical Wall," *Bulletin of the Technical University of Istanbul*, Vol 31, No. 1, 1978, pp. 40-55.

6 Torda, T. P., "Boundary Layer Control by Continous Surface Suction or Injuction," *J. Math. Phys.*, Vol. 31, 1952, pp. 206-213.

7 Jain, A. C., "On Boundary Layer Control by Continuous Suction," *Proceedings of the National Institute of Science*, Vol. 26, A, No. 3, 1960. pp. 298-304.

Plastic Wave Propagation in a Circular Cylindrical Rod[1]

J. W. Swegle[2] and T. C. T. Ting[3]

1 Introduction

The classical theory of plastic wave propagation in a thin rod was developed independently by von Karman [1], Taylor [2], and Rakhmatulin [3] during World War II, although Donnell [4] was in fact the first one to investigate the problem. Rate-independent one-dimensional theory predicts that the precursor wave front propagates at the plastic wave speed if the rod is prestressed into a plastic state. Experiments by Sternglass and Stewart [5] and Bell [6] show otherwise. They found the precursor wave front propagated at the elastic

[1] This work was partially supported by the U.S. Department of Energy (DOE), under Contract DE-AC04-76-DP00789, and partially by the U.S. Army Research Office, Durham, under Grant DAAG 29-G-0121 to the University of Illinois at Chicago Circle.

[2] Sandia National Laboratories, A U.S. Department of Energy Facility, Albuquerque, New Mex. 87185.

[3] Department of Materials Engineering, University of Illinois at Chicago Circle, Chicago, Ill. 60680 Mem. ASME

Manuscript received by ASME Applied Mechanics Division, January 1981.

Downloaded 01 May 2010 to 171.66.16.249. Redistribution subject to ASME license or copyright; see http://www.asme.org/terms/Terms_Use.cfm

$$\bar{x}=\frac{x}{h_0},\quad \bar{\delta}=\frac{\delta}{h_0},$$

$$\phi^2=\frac{3\nu u_0}{gh_0^2} \tag{23}$$

$$\xi^2=\left(\frac{us}{u_0}\right)^2=1+\frac{2gh_0\bar{x}}{u_0^2} \tag{24}$$

and we have $\Lambda = 3\bar{\delta}^2/\phi^2\xi$, $\lambda = \lambda_1\,\bar{\delta}$ with $\lambda_1 + v_0h_0/\nu$

Using the aforementioned nondimensional quantities and substituting for a_i's, equation (19) becomes

$$\frac{3}{\phi^2}\left[(A-B)+\sum_{i=1}^{6}M_i\left(\frac{6\bar{\delta}^2}{\phi^2\xi}\lambda_1 c_1\bar{\delta}\right)\right]\frac{d\bar{\delta}^2}{d\xi}$$
$$=-2\left[\frac{3\bar{\delta}^2}{\phi^2\xi}(2A-B-1)+(\lambda_1\bar{\delta}+a_1)-\frac{9\bar{\delta}^4}{\phi^2\xi 2}\sum_{i=1}^{6}b_iM_i\right] \tag{25}$$

where

$$b_1=\frac{1}{D}(12+\lambda) \tag{26}$$

$$b_2=-\frac{30}{D} \tag{27}$$

$$b_3=-\frac{10\lambda}{D} \tag{28}$$

$$b_4=\frac{20}{D}(3+\lambda) \tag{29}$$

$$b_5=-\frac{15}{D}(4+\lambda) \tag{30}$$

$$b_6=\frac{2}{D}(2\lambda+9) \tag{31}$$

$$c_1=-\frac{1}{D^2}[\Lambda(\lambda^2+24\lambda+84)+(240\lambda+1440)] \tag{32}$$

$$c_2=\frac{1}{D^2}[60\Lambda(\lambda+6)-60(\lambda^2-60)] \tag{33}$$

$$c_3=\frac{1}{D^2}[10\Lambda(\lambda^2-60)+240\lambda(\lambda+10)] \tag{34}$$

$$c_4=-\frac{1}{D^2}[20\Lambda(\lambda^2+6\lambda-24)+120(3\lambda^2+40\lambda+60)] \tag{35}$$

$$c_5=\frac{1}{D^2}[15\Lambda(\lambda^2+8\lambda-12)+240(\lambda^2+15\lambda+30)] \tag{36}$$

$$c_6=-\frac{1}{D^2}[4\Lambda(\lambda^2+9\lambda-6)+60(\lambda^2+16\lambda+36)] \tag{37}$$

Equation (25) is to be solved under the initial condition $\bar{\delta}(1) = 0$.

Now from equation (4) we have for the dimensionless film thickness

$$\bar{h}=\frac{h}{h_0}=\frac{u_0}{u_s}+\frac{v_0}{u_s}\frac{x}{h_0}+\frac{\delta}{h_0}-\frac{1}{h_0}\int_0^{\delta}\frac{u}{u_s}dy$$

or

$$\bar{h}=\frac{1}{\xi}+\lambda_1\frac{\phi^2}{6}\left(\xi-\frac{1}{\xi}\right)+\bar{\delta}\left[1-\sum_{i=1}^{6}\frac{a_i}{i+1}\right] \tag{38}$$

Solution for the fully developed flow is given by putting $\bar{\delta} = \bar{h}$ in (38)
i.e.,

$$\bar{\delta}\sum_{i=1}^{6}\frac{a_i}{i+1}=\frac{1}{\xi}+\frac{\lambda_1}{6}\phi^2\left(\xi-\frac{1}{\xi}\right) \tag{39}$$

Discussion

Equation (25) is integrated numerically by the fourth-order Ringe-Kutta method with the condition $\xi = 1$, $\bar{\delta} = 0$ for $\lambda_1 = -1, -0.5, 0, 0.5, 1$ and $\phi = 0.5, 1$.

In Figs. (1) and (2) the variation of dimensionless boundary layer thickness $\bar{\delta}$ with dimensionless distance ξ have been shown. It is observed that withdrawal of fluid through the wall controls the boundary layer.

The variation of dimensionless film thickness with the dimensionless distance ξ have been shown in Figs. (3) and (4). It is noted that in both the cases, film thickness $\bar{h}$ first increases to its maximum value and then decreases with the distance along the wall.

Acknowledgment

One of the authors (K. C. S.) is thankful to the University Grants Commission for the award of a teacher fellowship under the U.G.C. faculty improvement program.

References

1 Hassan, N. A., "Laminar Flow Along a Vertical Wall," ASME JOURNAL OF APPLIED MECHANICS, Vol. 34, Sept. 1967, pp. 535-537.

2 Haugen, R., "Laminar Flow Along a Vertical Wall," ASME JOURNAL OF APPLIED MECHANICS, Vol. 35, Dec. 1968, pp. 631-633.

3 Lal, K., "Laminar Flow Along a Vertical Wall," *Journal of Institute of Engineers*, India, I.M.E., Vol. 56, July 1975, pp. 24-27.

4 Jain, N. C., "A Numerical Study of the Laminar Flow Along a Vertical Wall," *Acta Technica CSAV*, No. 5, 1978, pp. 549-556.

5 Goyal, M. C., and Jain, N. C., "An Integral Approach for the Flow Along a Porous Vertical Wall," *Bulletin of the Technical University of Istanbul*, Vol 31, No. 1, 1978, pp. 40-55.

6 Torda, T. P., "Boundary Layer Control by Continous Surface Suction or Injuction," *J. Math. Phys.*, Vol. 31, 1952, pp. 206-213.

7 Jain, A. C., "On Boundary Layer Control by Continuous Suction," *Proceedings of the National Institute of Science*, Vol. 26, A, No. 3, 1960. pp. 298-304.

Plastic Wave Propagation in a Circular Cylindrical Rod[1]

J. W. Swegle[2] and T. C. T. Ting[3]

1 Introduction

The classical theory of plastic wave propagation in a thin rod was developed independently by von Karman [1], Taylor [2], and Rakhmatulin [3] during World War II, although Donnell [4] was in fact the first one to investigate the problem. Rate-independent one-dimensional theory predicts that the precursor wave front propagates at the plastic wave speed if the rod is prestressed into a plastic state. Experiments by Sternglass and Stewart [5] and Bell [6] show otherwise. They found the precursor wave front propagated at the elastic

[1] This work was partially supported by the U.S. Department of Energy (DOE), under Contract DE-AC04-76-DP00789, and partially by the U.S. Army Research Office, Durham, under Grant DAAG 29-G-0121 to the University of Illinois at Chicago Circle.

[2] Sandia National Laboratories, A U.S. Department of Energy Facility, Albuquerque, New Mex. 87185.

[3] Department of Materials Engineering, University of Illinois at Chicago Circle, Chicago, Ill. 60680 Mem. ASME

Manuscript received by ASME Applied Mechanics Division, January 1981.

Copyright © 1982 by ASME
Downloaded 01 May 2010 to 171.66.16.249. Redistribution subject to ASME license or copyright; see http://www.asme.org/terms/Terms_Use.cfm

bar velocity c_0 regardless of whether the rod was prestressed into a plastic state or not. The contradiction between the experiments and the classical rate-independent theory has been attributed to the fact that the real material is rate-dependent, in which case theory predicts that the precursor wave front propagates at the elastic bar velocity c_0 regardless of the magnitude of the prestress on the rod [7].

One-dimensional theory provides only an approximate solution, since the actual stress in the rod is a three-dimensional combined stress state for which analytical solutions are not available. However, various problems of combined stress have been studied, and it was found that under certain loading conditions the precursor wave front can propagate at an elastic wave speed in a body which is prestressed into a plastic state [8–10]. A recent study of plastic wave speeds in three-dimensional isotropically work-hardening plastic media [11] shows that the fast plastic wave speed can be identical to the elastic dilation wave speed, depending on the prestressed state and the direction of propagation. Therefore, the fact that the precursor wave front propagates at the elastic wave speed in a plastically prestressed rod may not be due entirely to the strain-rate effect of the material. The combined stress state in the rod and the three-dimensional nature of the rod may also contribute to this phenomenon. The purpose of this study is to use a finite-difference scheme to investigate whether or not the precursor wave front in a plastically prestressed rod propagates at the elastic bar velocity c_0 if the rod is treated as a three-dimensional circular cylinder.

2 Constitutive Equations

We will assume that the material is isotropically work hardening and obeys a von Mises yield condition. Therefore, the relations between the stress σ_{ij} and the strain ϵ_{ij} are

$$\dot{\epsilon}_{ij} = \dot{\epsilon}^e_{ij} + \dot{\epsilon}^p_{ij} \tag{1}$$

$$\dot{\epsilon}^e_{ij} = \frac{1+\nu}{E}\delta_{ij} - \frac{\nu}{E}\delta_{ij}\dot{\sigma}_{ll} \tag{2}$$

$$\dot{\epsilon}^p_{ij} = G(k)s_{ij}s_{mn}\dot{\sigma}_{mn} \tag{3}$$

$$s_{ij} = \sigma_{ij} - \frac{1}{3}\delta_{ij}\sigma_{ll} \tag{4}$$

$$J = \frac{1}{2}s_{ij}s_{ij} = k^2 \tag{5}$$

where E is Young's modulus, ν is the Poisson's ratio, and G is a function of k to be specified later.

Let W^p be the plastic work so that

$$\dot{W}^p = \sigma_{ij}\dot{\epsilon}^p_{ij} \tag{6}$$

Substituting equation (3) into (6) and making use of equations (4) and (5), we obtain

$$G(k) = \frac{1}{4k^3}\frac{dW^p}{dk} \tag{7}$$

On the other hand, if we specialize equations (1)–(5) to the case of simple tension in which $\sigma_{11} = \sigma$ is the only non-vanishing stress component, we obtain, letting $\epsilon_{11} = \epsilon$,

$$\frac{1}{g(\sigma)} = \frac{d\epsilon}{d\sigma} = \frac{1}{E} + \frac{4}{9}G\left(\frac{1}{\sqrt{3}}\sigma\right)\sigma^2 \tag{8}$$

where $g(\sigma)$ is the slope of the stress-strain curve in simple tension. Since equation (5) reduces to $\sigma^2/3 = k^2$ for the case of simple tension, we have

$$G(k) = \frac{3}{4k^2}\left\{\frac{1}{g(\sqrt{3}k)} - \frac{1}{E}\right\} \tag{9}$$

Elimination of $G(k)$ between equations (7) and (9) yields the relation

$$W^p = \int_{y_0/\sqrt{3}}^{Y/\sqrt{3}} 3k\left\{\frac{1}{g(\sqrt{3}k)} - \frac{1}{E}\right\}dk \tag{10}$$

where Y_0 and Y are the initial and the current yield strength in simple tension, respectively. Therefore, the current yield strength Y is a function of the plastic work. Equations (1)–(5) apply whenever the material is in a plastic state. If

$$J_2 < Y^2/3 \tag{11}$$

the material is in an elastic state and

$$\dot{\epsilon}^p_{ij} = 0, \quad \dot{\epsilon}_{ij} = \dot{\epsilon}^e_{ij} \tag{12}$$

It remains to specify the function $g(\sigma)$ which is the slope of the stress-strain curve in simple tension. In this study, we will assume the following special form for $g(\sigma)$

$$g(\sigma) = \frac{d\sigma}{d\epsilon} = E\left(\frac{Y_0}{\sigma}\right)^2 \tag{13}$$

Substitution of equation (13) into (10) yields the relation

$$Y = Y_0\left(1 + \sqrt{\frac{4EW^p}{Y_0^2}}\right)^{1/2} \tag{14}$$

which gives the current yield strength Y in terms of the plastic work.

3 Initial and Boundary Values

We will use a cylindrical coordinate system (r,θ,z) to describe wave propagation in a circular cylindrical rod whose center line is on the z-axis. The wave motion considered here is axially symmetric so that all physical quantitites are independent of θ. Let u_r and u_z be the particle displacement in the r and z-direction, respectively.

We assume that at $t = 0$ the rod is prestressed longitudinally at value σ^- but otherwise is at rest. Hence

$$\begin{aligned} &u_r(r,z,0) = u_z(r,z,0) = 0 \\ &\sigma_{rz}(r,z,0) = \sigma_{rr}(r,z,0) = \sigma_{\theta\theta}(r,z,0) = 0 \\ &\sigma_{zz}(r,z,0) = \text{constant} = \sigma^- \end{aligned} \tag{15}$$

As to the boundary condition, let a be the radius of the circular cross section of the cylinder. The boundary conditions for $t > 0$ are

$r = a$

$$\sigma_{rz}(a,z,t) = \sigma_{rr}(a,z,t) = 0 \tag{16}$$

$z = 0$

$$\begin{aligned} &\sigma_{rz}(r,0,t) = 0 \\ &\sigma_{zz}(r,0,t) = \text{constant} = \sigma^+ . \end{aligned} \tag{17}$$

We will consider the following two cases for σ^+ and σ^-.

$$\text{Case I} \qquad \sigma^- = 0, \qquad \sigma^+ = 2Y_0 \tag{18}$$

$$\text{Case II} \qquad \sigma^- = 1.8\ Y_0, \qquad \sigma^+ = 2Y_0 \tag{19}$$

4 Numerical Solution

A numerical solution to the problem discussed in Sections 2 and 3 was obtained using the two-dimensional Lagrangian finite-difference wavecode TOODY [12]. The code solves the finite-difference analogs to the differential equations of motion in cylindrical coordinates using a two-dimensional extension of the artificial viscosity method of von Neumann and Richtmyer [13]. The code has previously been validated for numerical solution of problems involving wave propagation in cylindrical rods [14].

Calculations were done for a rod 1 cm in radius and 30 cm in length. All quantities were initialized to the proper initial conditions for the case being run, and at time $t = 0$ a pressure was applied uniformly over one end of the rod. The calculations were run until just before the first signal reached

Downloaded 01 May 2010 to 171.66.16.249. Redistribution subject to ASME license or copyright; see http://www.asme.org/terms/Terms_Use.cfm

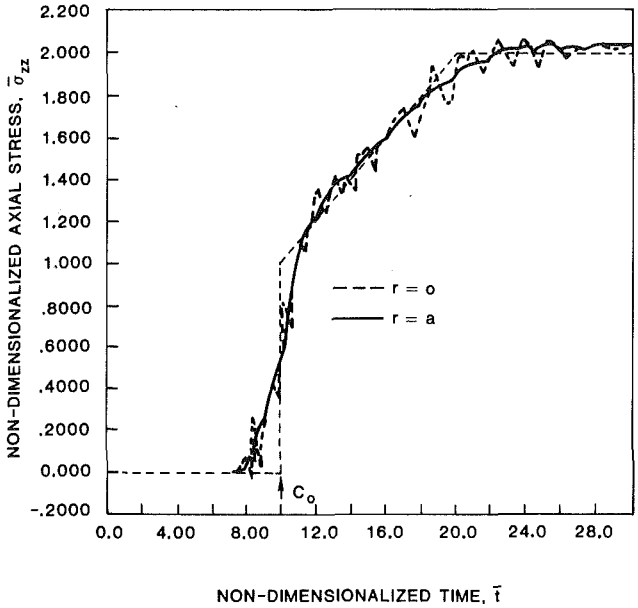


Fig. 1 Axial stress history at $z = 10a$, $r = 0$, and $r = a$; initially unstressed rod; predicted arrival time of bar wave, velocity c_0, is indicated

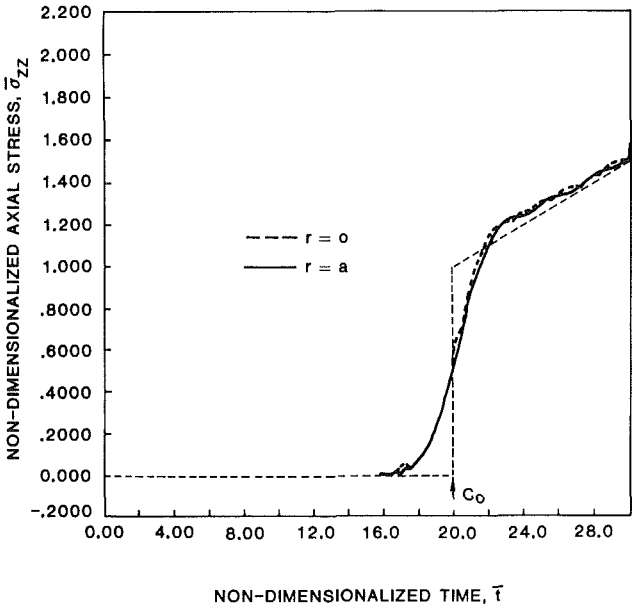


Fig. 2 Axial stress history at $z = 20a$, $r = 0$ and $r = a$; initially unstressed rod; predicted arrival time of bar wave, velocity c_0, is indicated

the opposite end of the rod so that the finite length of the rod had no influence on the solution. Histories of axial stress were kept at $r = 0$ and $r = a$ at positions 10 and 20 cm from the applied pressure end of rod, corresponding to 10 and 20 rod radii.

In order to implement the finite-difference technique, the rod is discretized into an array of square zones. Calculations were done for high resolution zoning with 20 zones through the rod radius and low resolution zoning with four zones through the rod radius; resulting in a total of 480 and 12,000 zones, respectively, for the low and high resolutions. The physical quantities were nondimensionalized in the following manner:

$$\bar{t} = \frac{c_0 t}{a}, \quad c_0^2 = \frac{E}{\rho}, \quad \bar{\sigma}_{ij} = \frac{\sigma_{ij}}{Y_0}. \tag{20}$$

Thus the results depend only on the values of ν, σ^- / Y_0, and σ^+ / Y_0. All calculations used a value of 1/3 for ν, and the two

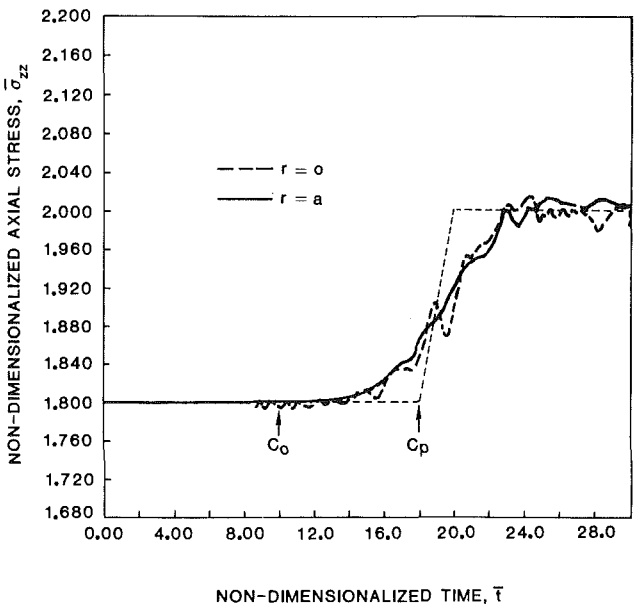


Fig. 3 Axial stress history at $z = 10a$, $r = 0$ and $r = a$; prestressed rod; predicted arrival times of bar wave, velocity c_0, and uniaxial strain plastic wave, velocity c_p, are indicated

cases for the values of σ^- / Y_0 and $\sigma^+ Y_0$ are summarized in equation (18) and (19). With this nondimensionalization, the arrival time at a point a distance $z = na$ from the applied pressure end of the rod is $\bar{t} = n$ for a wave traveling with velocity c_0, and according to uniaxial stress theory and the stress-strain curve given by equation (13), the arrival time of the plastic wave increment which brings the axial stress to the value σ is $\bar{t} = n\sigma / Y_0$.

5 Discussion of the Results

Several calculations were run with varying zone sizes, artificial viscosity, and time step. The results showed that these variables had only a minor effect on the form of the solution and the overall features of the solution were the same for all values tested. The following results are for a given set of values, but may be taken to be representative of all the calculations.

Numerical solutions are compared to one-dimensional theory (straight dotted line) in Figs. 1 and 2 for Case I and in Fig. 3 for Case II. In Case II, the one-dimensional theory predicts that the precursor wave front propagates at the plastic wave speed c_p. The results indicate essential agreement between the one-dimensional theory and the three-dimensional solutions. The major difference is that the waves show more spread in the calculations than is predicted by one-dimensional theory. However, the half-amplitude point arrives at the time predicted by the one-dimensional theory. The wave shape appears to be unchanged with propagation distance, although more runs to much greater propagation distances would be required to verify this. Thus it appears that the waves travel with the velocity predicted by the one-dimensional theory, although they have larger rise-times. It should be noted that this wave spreading is characteristic of artificial viscosity, finite-difference methods. Thus the method will alter a discontinuous jump into a smooth wave with a finite rise-time. However, this type of smearing is dependent upon the amount of artificial viscosity used and the resolution of the zoning. In the calculations described here, the amount of spread was independent of the amount of artificial viscosity and the resolution of the calculations. This indicates that it is a real feature of the problem and is geometric dispersion rather than numerical dispersion.

Downloaded 01 May 2010 to 171.66.16.249. Redistribution subject to ASME license or copyright; see http://www.asme.org/terms/Terms_Use.cfm

Infinitesimal amplitude noise which runs ahead of the main wave can be seen in the calculations. The velocity and amount of this noise were found to be highly dependent on the numerics of the calculation. Physically, one might expect infinitesimal amplitude sound signals to propagate into the rod with a velocity greater than that predicted by the one-dimensional theory, with the relative importance of these signals decreasing with propagation distance. It is well known that infinitesimal amplitude noise can be propagated in a numerical calculation of this type with a velocity which is not related to physical wave speeds. In either case, the noise is negligible with respect to the main wave. Thus the calculations show that any experimental deviation from the one-dimensional theory cannot be accounted for purely on the basis of three-dimensional effects.

References

1 von Karman, T., Bohnenblust, H. F., and Hyers, D. H., "The Propagation of Plastic Waves in Tension Specimens of Finite Length," NDRC Report A-103 (OSRD No. 946), 1943.

2 Taylor, G. I., "The Plastic Wave in a Wire Extended by an Impact Load," *Scientific Papers*, Vol. 1, 1958, p. 467.

3 Rakhmatulin, Kh. A., "On the Propagation of Waves of Unloading," *Prikladnaya Matematika i Mekhanika*, Vol. 9, 1945, pp. 91–100.

4 Donnell, L. H., "Longitudinal Wave Transmission and Impact," ASME JOURNAL OF APPLIED MECHANICS, Vol. 52, 1930, p. 153.

5 Sternglass, E. J., and Stuart, D. A., "An Experimental Study of Propagation of Transient Longitudinal Deformations in Elasto-Plastic Media," ASME JOURNAL OF APPLIED MECHANICS, Vol. 20, 1953, pp. 427–434.

6 Bell, J. F., "Propagation of Plastic Waves in Prestressed Bars," Department of Mechanical Engineering, The Johns Hopkins University Technical Report No. 5, Navy Contract N6-ONR-243.

7 Malvern, L. E., "The Propagation of Longitudinal Waves of Plastic Deformation in a Bar of Material Exhibiting a Strain-Rate Effect," ASME JOURNAL OF APPLIED MECHANICS, Vol. 18, 1951, p. 203.

8 Clifton, R. J., "An Analysis of Combined Longitudinal and Torsional Plastic Waves in a Thin-Walled Tube," *Proceedings of the Fifth U.S. National Congress of Applied Mechanics*, ASME, 1966, pp. 456–480.

9 Ting, T. C. T., "The Initiation of Combined Stress Waves in a Thin-Walled Tube Due to Impact Loadings," *International Journal of Solids and Structures*, Vol. 8, 1972, pp. 269–293.

10 Ting, T. C. T., "On Wave Propagation Problems in Which $c_f = c_s = c_2$ Occurs," *Quarterly of Applied Mathematics*, Vol. 31, No. 3, 1973, pp. 275–286.

11 Ting, T. C. T., "Plastic Wave Speeds in Isotropically Work-Hardening Materials," ASME JOURNAL OF APPLIED MECHANICS, Vol. 44, 1977, pp. 68–72.

12 Swegle, J. W., "Toody IV—A Computer Program for Two-Dimensional Wave Propagation," Sandia Laboratories, SAND78-0552, Sept. 1978.

13 von Neumann, J., and Richtmyer, R. D., "A Method for the Numerical Calculation of Hydrodynamic Shocks," *Journal of Applied Physics*, Vol. 21, 1950, p. 232.

14 Bertholf, L. D., "Feasibility of Two-Dimensional Numerical Analysis of the Split Hopkinson Pressure Bar System," ASME JOURNAL OF APPLIED MECHANICS, Vol. 41, 1974, p. 137.

Downloaded 01 May 2010 to 171.66.16.249. Redistribution subject to ASME license or copyright; see http://www.asme.org/terms/Terms_Use.cfm

Journal of Applied Mechanics

Discussion

Creeping Viscous Flow Around a Heat-Generating Solid Sphere[1]

P. R. Dawson.[2] The author has provided a useful analytical solution for the problem of thermally induced motion of a heat-producing sphere. The magnitude of the velocities was compared to numerical results for a similar problem. However, the comparison was not totally valid. In the report by Dawson and Tillerson [2] cited by the author, the steady-state velocities were obtained as upper bounds of canister motion by computing the velocities that would result if the heat sources did not decay and the temperatures reached steady state. The velocities predicted in these cases are much higher than those predicted for decaying sources. These computations were intended to show that even under such unrealistic conditions significant canister motion would not occur.

The report also included the predicted motion of a heat source with a 30 year half-life for a period of 150 years. A direct comparison to Krenk's work is not possible since our numerical analysis included the effects of a temperature-dependent viscosity. The report does mention that for a constant viscosity and decaying heat source, the velocity predicted after 10 years is 1.5 pm/s. This value is quite close to the value apparent from Fig. 4 of the author's article (1.6 to 1.7 pm/s).

Thus, when the proper comparison of the two analyses is made, the results appear to be consistent. The minor differences can be a result of the variations in solid sphere geometry and material properties between the two analyses.

Author's Closure

I appreciate the comments of Dr. Dawson concerning the consistency of the two methods of calculation. Unfortunately reference [2] does not include a full transient analysis under the simplifying assumptions used in [1]. An essential difference between the two methods is the lack of finite boundaries in [1], and as a consequence no steady-state solution exists in this model. The steady-state velocity from [2] was therefore included to indicate an upper limit. As expected, the time delay of the buoyancy in the transient problem leads to a maximum upward velocity considerably below this value.

A central point in comparing the two methods is the difference in boundary conditions. The influence of this difference is expected to increase with time, and although the 10-year velocities mentioned by Dr. Dawson look encouraging, it appears that a definite conclusion would require additional computations.

[1] Krenk, S., and published in the June 1981, issue of the ASME JOURNAL OF APPLIED MECHANICS, Vol. 48, pp. 239-242.

[2] Dawson, P. R., and Tillerson, J. R., "Nuclear Waste Canister Thermally Induced Motion," Report SAND-78-0566, Sandia National Laboratories, June 1978.

Nonlinear Harmonic Oscillations of Gyroscopic Structural Systems and the Case of a Rotating Ring[1]

C. W. Bert[2]. This problem was first attacked by Padovan [1] in 1976. He used the Lindstedt-Poincaré procedure, but achieved results somewhat different from those of Professor Maewal. Padovan found that all branches, backward and forward, exhibit a softening behavior, whereas Maewal found the backward waves to have a hardening behavior and the forward waves to transition from a hardening behavior to a softening behavior as the rotational speed is increased.

References

1 Padovan, J., "Coriolis Effects on Nonlinear Oscillations of Rotating Cylinders and Rings," *Advances in Engineering Science* (13th Annual Meeting, Society of Engineering Science, Hampton, Va., Nov. 1976), NASA CP-2001, Vol. 2, pp. 409-416.

Author's Closure

I am thankful to Professor Bert for his interest in my paper.

It is perhaps evident from the introductory section of the paper that the primary motivation of the developments therein is the phenomenon of disappearance of circumferentially standing waves as normal modes of free vibrations of rotating shells of revolution. A primary result of my analysis is a description of this phenomenon in terms of secondary bifurcation, with the conclusions being valid for arbitrary shells of revolution in view of the rather general formulation. Inasmuch as this issue is not even explicitly addressed in the paper [1] cited by Professor Bert, I find it difficult to agree with his characterization of the relationship between the two investigations.

As has been demonstrated in a related context in references [6] and [7] of my paper, satisfactory solution of a nonlinear harmonic oscillations problem, correct to the lowest order, can be obtained only if an expression for strain energy, which is accurate up to and including the quartic terms, is utilized. The strain energy functional used in Padovan's work [1] differs from the one I have used even in the quadratic term. Because of this difference, and due to the different assumption made by Padovan on the membrane stiffness of the ring, it is not expected that the solution obtained by him should necessarily be the same as what I obtained, mainly to illustrate my more general results.

[1] By A. Maewal, and published in the September, 1981, issue of the ASME JOURNAL OF APPLIED MECHANICS, Vol. 48, pp. 627-633.

[2] Perkinson Professor of Engineering, School of Aerospace, Mechanical and Nuclear Engineering, The University of Oklahoma, Norman, Oklahoma, 73019. Mem. ASME.

Copyright © 1982 by ASME
Downloaded 01 May 2010 to 171.66.16.249. Redistribution subject to ASME license or copyright; see http://www.asme.org/terms/Terms_Use.cfm

Some Considerations on Thermal Shock Problems in a Plate[1]

P. Puri.[2] The authors have discussed an important problem in thermoelasticity and have brought out some very interesting features of the problem.

However the authors' conclusion that Singh's solution is valid only for a short time is not entirely correct. The displacement solution in [1] (authors' reference [4]) is valid only for the time that it takes the wave front to reach the other end of the plate, but the expression for stress is valid for all times. Further Puri [2] (authors' reference [5]) corrected the oversight in [1] and obtained a bounded solution for the displacement, which is valid for all times.

References

1 Singh, A., and Puri, P., "Dynamic Thermal Stresses in an Infinite State," *Arch. Mech. Stosw.*, Vol. 15, 1963, pp. 77-88.

2 Puri, P., "One-Dimensional Dynamic Problems of Thermoelasticity." *Arch. Mech. Stosw.*, Vol. 16, 1964, pp. 93-102.

Author's Closure

We understand Professor Puri's comment. In our first impression we imagined that actual time $t = 100$ is pretty small in dimensionless time; then we considered his result. We agree with his opinion; however, there are still the following important features in our paper:

i In industry, it is more important to find solution of σ_{yy} instead of σ_{xx}.

ii For realistic materials, dynamic effects have disappeared, but the coupling effects have clear effects. For example, some axisymmetric thermal stress problems have about 30-40 percent deviations in stress distributions [1] when the coupling is taken into account.

References

1 Takeuti, Y., and Tanigawa, Y., "On a New Method for Axisymmetric Thermoelastic Problems," *Journal of Thermal Stresses*, Vol. 4, No. 3, 1981.

[1] By Y. Takeuti and T. Furukawa, and published in the March, 1981, issue of the ASME JOURNAL OF APPLIED MECHANICS, Vol. 48, pp. 113-118.

[2] Department of Mathematics, University of New Orleans, New Orleans, La. 70112.

Stress Concentrations in Cylindrically Orthotropic Composite Plates With a Circular Hole[1]

C.H. Parr[2]. Professor Hoff has given some interesting insights into a basic problem area for composite materials. However, I would give a different interpretation to the root $p_3 = 2$ in equation (56).

The case resulting from taking $n = 0$ in the stress function ϕ, equation (7), is axisymmetric stress but not axisymmetric displacement. The term $p_3 = 2$ corresponds to a tangential displacement of the form

$$v = \text{constant} \times r\,\theta.$$

The boundary conditions (54) need only be supplemented by another boundary condition,

$$v \equiv 0,$$

for the dilemma to be resolved. The root $p_3 = 2$ results in a displacement distribution that is multivalued and not unique. However, it is not a spurious solution as indicated by Professor Hoff.

Author's Closure

Mr. Parr's discussion deals largely with a matter of semantics but it leads to an explanation of the conclusion of the paper that a state of constant stress $\sigma_r = \sigma_\vartheta = C =$ constant, $\tau_{r\vartheta} = 0$ cannot exist in a cylindrically orthotropic circular plate (without a hole) subjected to a constant radial traction C at its outer edge $r = R$ except when $S_{rr} = S_{\vartheta\vartheta}$. The relations

$$\phi = (C/2)r^2 \quad u = C(S_{rr} + S_{r\vartheta})r \quad v = C(S_{\vartheta\vartheta} - S_{rr})r\vartheta$$

represent a solution if a sector has been cut out of the plate between $\vartheta = 2\pi - \alpha$ and $\theta = 2\pi$ (provided that a circumferential traction C is applied to the two edges so created); but this solution is not admissible when the circular plate is complete (uncut) because then two different values are obtained for v at $\vartheta = 0$ and $\theta = 2\pi$. The only exception is the case when $S_{rr} = S_{\vartheta\vartheta}$ because then v vanishes identically.

Incidentally, an error in the original text should be corrected. On page 568, under the section "Discussion of Results," on the third line of the second paragraph, the word "uniaxial" should be replaced with the word "radial."

[1] By N.J. Hoff, and published in the September, 1981, issue of the ASME JOURNAL OF APPLIED MECHANICS, Vol. 48, pp. 563-569.

[2] Manager, Composites and Plastics Research and Development, Lord Kinematics, Lord Corporation, 1635 West 12th Street, P.O. Box 2051, Erie, Pa. 16512.

Copyright © 1982 by ASME
Downloaded 01 May 2010 to 171.66.16.249. Redistribution subject to ASME license or copyright; see http://www.asme.org/terms/Terms_Use.cfm

Journal of Applied Mechanics

Book Reviews

Limit Analysis of Structures at Thermal Cycling. By D. A. Gokhfeld and O. F. Cherniavsky. Sijthoff and Noordhoff, The Netherlands, 1980, Pages xxviii–537. Price $110.00.

REVIEWED BY PHILIP G. HODGE, JR.[1]

The contents of this book can be roughly separated into three parts: basic theory and simple examples, applications to nontrivial problems, and advanced theoretical concepts. The first part is separated into five chapters beginning with a presentation of fundamental ideas in terms of simple two-and three-bar trusses followed by general mathematical statements and proofs of the theorems of limit analysis and shakedown. Chapter 3 discusses the value and some of the severe limitations of generalized variables in shakedown analysis. Chapters 4 and 5 give simple illustrative examples of the statical and kinematical theorems, respectively, including many computational details.

The second part contains one chapter each devoted to turbines, plates, and shells. A great deal of detail is given and comparisons are made with some experimental results. Both circular and rectangular solid plates are covered in Chapter 7, and a section on perforated plates is included. Chapter 8 includes cylindrical, conical, and spherical shells together with sections on a liquid fuel rocket engine and a nuclear fuel element.

The final part begins with a chapter exploring the case of thermal cycling under negligible mechanical loads. Several examples of rachetting and incremental thermal buckling are considered. Chapter 10 is on shakedown in contact problems and the final chapter discusses possible simplifications in proceeding directly to a steady stress cycle in investigating shakedown.

The book is clearly designed for an engineering audience. Basic ideas are presented first in terms of simple examples. Two- or three-dimensional symbolic diagrams are used to present fundamental ideas in a geometric terminology. Mathematics is kept as simple as possible. Index notation is used, but explained, and the reader need only be familiar with such classical concepts as summations, inequalities, and linear differential equations.

In the second part the emphasis is on solution of real problems. This is particularly true of the turbine disks in Chapter 6 and some of the shell-type structures in Chapter 8.

The presentation of the material is excellent. Figures are extremely clear and easy to read. The text is obviously written by someone to whom English is not a native language, but this results only in a slight awkwardness of sentence construction and inappropriate use (or nonuse) of the definite article. The meaning is always perfectly clear, both in total and sentence-by-sentence. Over 300 references are given to both the Russian and Western literature. The index appears to be adequate.

In summary, this book appears to do a thorough job of covering the current state of knowledge about mechanical shakedown theory and application, and to extend the ideas, often for the first time, to thermal loading as well.

Fracture and Fatigue. Edited by J. C. Radon. Pergamon Press, New York. 1981. Pages ix–488. Price $60.00.

REVIEWED BY: J. W. HUTCHINSON[2]

This volume of almost 500 pages is a collection of papers on fracture mechanics which make up the Proceedings of the Third Colloquium on Fracture, held at Imperial College, London, in September, 1980. The meeting was organized by the European Group on Fracture. The book is subdivided into three main headings: elastoplastic fracture mechanics, micromechanisms of fracture, and thin-sheet fracture mechanics. For the most part, the papers represent the state of the art in fracture analysis and testing as practiced in Europe, including the United Kingdom.

Stable crack growth receives more attention than any other single topic. It is treated in several review papers, a number of experimental papers on tearing resistance, and in several analytical papers. This subject has seen rapid and parallel developments in both the United Kingdom and in the United States, and this volume reveals that there appears to be less divergence in these two approaches than was evident in some of the earlier developments in fracture mechanics. The section on thin sheets also contains papers on tearing resistance, which is particularly welcomed since fracture under plane stress conditions tends to get short shrift in this country.

The volume includes a survey paper on recent work on micromechanisms of fracture. It also includes several papers on mixed mode fracture and on fatigue. Most of the papers are oriented toward the fracture of metals, but one paper does deal with stable crack growth in ceramics. Taken together, this collection of papers indicates a vital European fracture community with much in common with its counterpart in the United States.

Computational Methods in Structural Dynamics. By L. Meirovitch. Sijthoff & Noordhoff, The Netherlands. 1980. Pages xiv–439. Price $35.00.

REVIEWED BY P. P. FRIEDMANN[3]

During the last two decades the field of structural dynamics has been very active, mainly due to the combined influence of

[1] University of Minnesota, Department of Aerospace Engineering and Mechanics, 107 Akerman Hall, Minneapolis, Minnesota 55455.

[2] Professor, Division of Applied Sciences, Harvard University, Cambridge, Mass. 02138.

[3] Professor, Mechanics and Structures Department, University of California, Los Angeles, Calif. 90024.

Copyright © 1982 by ASME
Downloaded 01 May 2010 to 171.66.16.249. Redistribution subject to ASME license or copyright; see http://www.asme.org/terms/Terms_Use.cfm

finite element modeling of structural dynamic systems coupled with the tremendous advances in computer technology. Much of this activity has been centered on the development and refinement of computational methods capable of dealing with structural systems having a large number of degrees of freedom. Professor Meirovitch's excellent book on this subject represents a timely and valuable treatment of this important field, which is a natural sequel to his previous book (*Analytical Methods in Vibrations*, Macmillan, 1967). The book is self-contained and presents a large amount of material on the subject in a complete and very readable manner.

The book has a very logical structure. The first chapter presents a collection of concepts from linear algebra which is essential to the understanding of the subject matter treated subsequently in the book. Chapter 2 deals with the free vibration of discrete systems, presenting the necessary background and tools for formulating free vibration problems for undamped, damped, and gyroscopic systems. The material in this chapter is, by necessity, condensed and the uninitiated reader will find it useful to consult Professor Meirovitch's previous book for the additional clarification of some fundamental concepts. Chapter 3 presents a general overview of the eigenvalue problem for a variety of structural dynamic systems without delving into numerical details. Thus, it essentially contains additional material from linear algebra required for the complete and proper understanding of eigenanalysis.

Chapter 4 is devoted to the qualitative behavior of the eigensolution based on Rayleigh's principle. Various additional important topics such as the minimax theorem, the inclusion principle, Gerschgorin's theorem, and first-order perturbations of the eigenvalue problem are discussed in a lucid manner.

Chapter 5 contains a (72 pages long) detailed discussion of the computational methods used in eigensolution. Starting from the power and Jacobi's methods, more advanced methods such as Givens, Housholder, Sturm, and *QR* methods are discussed in detail.

Chapter 6 is devoted to the response calculation of linear discrete systems both damped and undamped. Direct numerical integration methods in the conventional sense, are not considered in this chapter.

Chapter 7 and 8 are closely related. Chapter 7 presents a few exact solutions to simple, continuous, free vibration problems while Chapter 8 considers approximations to the same problem by global discretization methods such as the Rayleigh-Ritz and weighted residual methods. Chapter 9 continues the treatment of spatial discretization, except that it is now accomplished on a local level, by using finite elements. This relatively detailed chapter (50 pages) presents the finite element method in a relatively complete manner.

The introduction of the finite element method yields structural dynamic systems having a large number of degrees of freedom; the treatment of such systems is the objective of the last two chapters of the book. Chapter 10 considers reduction of system size by static condensation, mass condensation, or the calculation of the lowest modes only by direct simultaneous iteration or subspace iteration. Chapter 11 concludes this topic by presenting a number of substructuring methods such as component mode synthesis, branch-mode analysis, component-mode substitution, and substructure synthesis.

The book also contains a considerable number of small examples illustrating the basic aspects of the various methods presented. These examples however are restricted to systems having four degrees of freedom or less. It would have been nice to see in a computational book, such as this one, some more complicated examples including computational treatments utilizing actual computer programs that contain algorithmic implementations. The book is remarkably complete, considering the wide scope of the subject matter; however, direct numerical integration of the equations of motion also should have been included, since it deserves at least one whole chapter in a book having a computational flavor.

The book can serve as an excellent textbook for a graduate level course on this topic. It is also highly recommended to engineer analysts and researchers working in the field of structural dynamics.

Topics in Finite Elasticity. By M. E. Gurtin. Society for Industrial and Applied Mathematics, Philadelphia, Pa., 1980, Price $9.50.

REVIEWED BY JAMES K. KNOWLES[4]

This little-book—it is only 58 pages long—is the published version of a series of lectures given by the author at the University of Tennesee and sponsored by the National Science Foundation under the auspices of the Conference Board of the Mathematical Sciences. There are 15 short, tightly written chapters, of which the first 10, together with Chapter 13, might be regarded as setting out the basic ingredients of the theory of finite *equilibrium* deformations of elastic solids. The remaining four chapters deal with loosely related special topics which represent some of the currently active areas in finite elastostatics: the variational formulation of the basic boundary value problem (Chapter 11), stability and uniqueness (Chapter 12), the multiplicity of possible deformations of an incompressible cube under uniform all-around tensile loading (Chapter 14), and finite antiplane shear (Chapter 15).

The presentation of the fundamental theory of finite elasticity as given here is clear, direct and well organized, but necessarily so concise that the potential reader who is curious about—but unfamiliar with—continuum mechanics might find the going a bit hard. (Chapter 13 is only one page long!) Some results are proved, but of course others are not; references to appropriate sources are given. The dynamical theory is not treated, nor is the connection between finite elasticity and the classical linear theory of infinitesimal deformations of an elastic solid.

Chapter 11 on the variational formulation of the "mixed" boundary value problem of the theory deals with weak solutions and establishes the principle of stationary potential energy for them. In this connection, there is some discussion of the role played by such possible restrictions on the strain energy function as quasi-convexity or the Legendre-Hadamard condition.

The discussion of stability and uniqueness in Chapter 12 is devoted primarily to recent joint work of Gurtin and S. J. Spector. It focuses on the relation between certain static (or quasi-static) notions of stability on the one hand and local uniqueness of weak solutions on the other.

The lack of uniqueness that may arise when finite deformations are taken into account is illustrated in Chapter 14 by an explicit analysis of the homogeneous deformations possible in an incompressible cube of Neo-Hookean material subject to uniformly distributed equal tensile normal forces on all of its deformed faces.

Finally, the subject of finite antiplane shear of a cylindrical incompressible solid appears in Chapter 15, supplying as it usually does the simplest setting in which to explore some aspect of the general theory. In this case, the question studied

[4] Division of Engineering and Applied Science 104-44, California Institute of Technology, Pasadena, Calif. 91125

Copyright © 1982 by ASME
Downloaded 01 May 2010 to 171.66.16.249. Redistribution subject to ASME license or copyright; see http://www.asme.org/terms/Terms_Use.cfm

concerns the consequences for the equilibrium problem of nonconvexity of the potential energy functional. The chapter is based on recent joint work of R. Temam and the author.

A list of some 49 references is included. This little monograph conveys nicely some of the features of finite elasticity which make it an active flourishing field today. I found it enjoyable reading.

The Dynamics of Arches. By Josef Henrych. Elsevier, Amsterdam and New York. 1981. Pages 00–463. Price $85.00.

REVIEWED BY G. J. SIMITSES[5]

This book primarily deals with the subject of linear small oscillations (free and forced) of mainly planar arches and frames. The geometry of the configurations is very general and the analysis includes the effects of nonuniformity in the cross section, rotatory inertia, tangential inertia, transverse shear, and extensionality (compressibility) of the neutral axis. Solution procedures are presented with great detail and sophistication for specialized geometries, such as the circular arch and straight bars. In all of these solutions, the various effects previously mentioned for both free and forced vibrations can be fully assessed from the derived formulas. In the case of forced vibrations, both the method of resolution according to normal modes of vibration and the method of decomposition into forced motion and free vibration are presented. The question of accuracy of the two methods is continuously addressed, and a comparison between the two methods is given. Moreover, these two methods are applied in the analysis of frames with straight and curved bars, which are excited either by (dynamic) forces or kinematically. In addition, the vibration analysis of some space frames is presented. The space frame may also be excited kinematically. Finally, some numerical (computer-obtained) results are presented for a few special configurations (simple geometries). These results were contributed by Dr. J. Pavlik and Mr. F. Cermak.

This book is recommended to the practicing engineer who is concerned with vibration analysis of arches, beams, and frames. The derived formulas and equations can be programmed, and extensive parametric studies can be performed to assess the effect of various parameters on the vibration response characteristics of the analyzed systems. It is also recommended as a reference text to the student of structural dynamics. Unfortunately because of the course structure in American technical universities and because of the highly specialized topics covered in the book, it cannot possibly be adopted as a text for a course in structural dynamics (small oscillations, theory of vibrations, etc.) regardless of the field of study (aerospace, civil, mechanical, or mechanics).

[5]Professor of Engineering Science and Mechanics, George Institute of Technology, Atlanta Georgia, 30332.

Downloaded 01 May 2010 to 171.66.16.249. Redistribution subject to ASME license or copyright; see http://www.asme.org/terms/Terms_Use.cfm

concerns the consequences for the equilibrium problem of nonconvexity of the potential energy functional. The chapter is based on recent joint work of R. Temam and the author.

A list of some 49 references is included. This little monograph conveys nicely some of the features of finite elasticity which make it an active flourishing field today. I found it enjoyable reading.

The Dynamics of Arches. By Josef Henrych. Elsevier, Amsterdam and New York. 1981. Pages 00–463. Price $85.00.

REVIEWED BY G. J. SIMITSES[5]

This book primarily deals with the subject of linear small oscillations (free and forced) of mainly planar arches and frames. The geometry of the configurations is very general and the analysis includes the effects of nonuniformity in the cross section, rotatory inertia, tangential inertia, transverse shear, and extensionality (compressibility) of the neutral axis. Solution procedures are presented with great detail and sophistication for specialized geometries, such as the circular arch and straight bars. In all of these solutions, the various effects previously mentioned for both free and forced vibrations can be fully assessed from the derived formulas. In the case of forced vibrations, both the method of resolution according to normal modes of vibration and the method of decomposition into forced motion and free vibration are presented. The question of accuracy of the two methods is continuously addressed, and a comparison between the two methods is given. Moreover, these two methods are applied in the analysis of frames with straight and curved bars, which are excited either by (dynamic) forces or kinematically. In addition, the vibration analysis of some space frames is presented. The space frame may also be excited kinematically. Finally, some numerical (computer-obtained) results are presented for a few special configurations (simple geometries). These results were contributed by Dr. J. Pavlik and Mr. F. Cermak.

This book is recommended to the practicing engineer who is concerned with vibration analysis of arches, beams, and frames. The derived formulas and equations can be programmed, and extensive parametric studies can be performed to assess the effect of various parameters on the vibration response characteristics of the analyzed systems. It is also recommended as a reference text to the student of structural dynamics. Unfortunately because of the course structure in American technical universities and because of the highly specialized topics covered in the book, it cannot possibly be adopted as a text for a course in structural dynamics (small oscillations, theory of vibrations, etc.) regardless of the field of study (aerospace, civil, mechanical, or mechanics).

[5]Professor of Engineering Science and Mechanics, George Institute of Technology, Atlanta Georgia, 30332.

Copyright © 1982 by ASME
Downloaded 01 May 2010 to 171.66.16.249. Redistribution subject to ASME license or copyright; see http://www.asme.org/terms/Terms_Use.cfm